Preprints

THIRD CONFERENCE ON SATELLITE METEOROLOGY AND OCEANOGRAPHY

February 1–5, 1988

Anaheim, Calif.

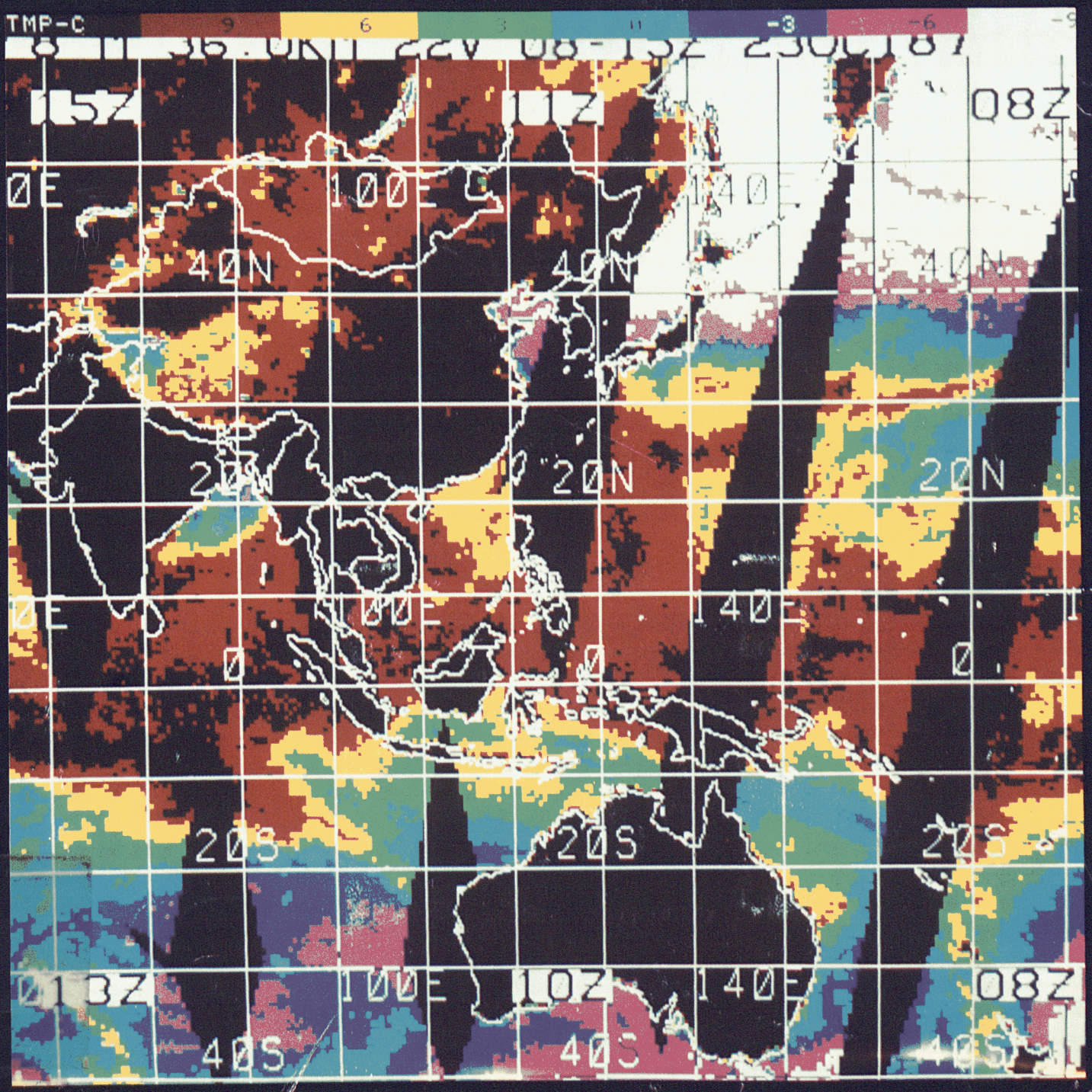

AMERICAN METEOROLOGICAL SOCIETY

AMERICAN METEOROLOGICAL SOCIETY

45 BEACON STREET, BOSTON, MASSACHUSETTS 02108

PERIODICALS—1988°

	Nonmember Prices
JOURNAL OF THE ATMOSPHERIC SCIENCES (ISSN 0022-4928) Volume 45, 1988. Semi-monthly Original research papers related to the atmospheres of the earth and other planets with emphasis on the quantitative and deductive aspects of the physics and dynamics of atmospheric processes and phenomena.	$200.00* $30.00†
JOURNAL OF APPLIED METEOROLOGY (ISSN 0894-8763) Volume 27, 1988. Monthly Original papers and critical surveys concerned with the applications of the atmospheric sciences to operational and practical goals. Its editorial scope encompasses the full range of applications of meteorology to safety, health, industry, the economy, and general well-being of the human community.	$120.00* $20.00†
JOURNAL OF PHYSICAL OCEANOGRAPHY (ISSN 0022-3670) Volume 18, 1988. Monthly Original research and survey papers devoted to the communication of knowledge concerning the physics and chemistry of the oceans and of the processes coupling the sea to the atmosphere. Papers will deal with the theoretical and observational aspects of topics such as: ocean circulation, surface waves, internal waves, inertial oscillations, oceanic turbulence, interpretive regional studies, and oceanic tides and other long-wave phenomena.	$120.00* $20.00†
MONTHLY WEATHER REVIEW (ISSN 0027-0644) Volume 116, 1988. Monthly Original research and survey papers concerned with weather analysis and forecasting (non-operational); observed and modeled circulations including techniques development and verification studies, and seasonal-annual weather summaries.	$120.00* $20.00†
JOURNAL OF ATMOSPHERIC AND OCEANIC TECHNOLOGY (ISSN 0739-0572) Volume 5, 1988. Bimonthly Original research and survey papers related to instrument-system descriptions, exploratory measurement techniques, calibration methods, and performance analyses for the mainstream of atmospheric and oceanic technology, including the development of data-acquisition hardware, real-time and post-analysis software, and signal-processing techniques.	$100.00* $15.00†
WEATHER AND FORECASTING (ISSN 0882-8156) Volume 3, 1988. Quarterly Original research and survey papers immediately related to the operational forecasting or weather events significant to operational forecast problems including such topics as operational-forecasting techniques, applications of new analysis methods, forecasting-verification studies, and case studies with direct application to forecasting.	$80.00* $15.00†
JOURNAL OF CLIMATE (ISSN 0894-8755) Volume 1, 1988. Monthly Articles concerned with climate data and analysis, long-term atmospheric variability (seasonal, interannual), climate change and prediction on seasonal and longer time scales, and the impacts of climate change on society.	$120.00* $20.00†
BULLETIN OF THE AMERICAN METEOROLOGICAL SOCIETY (ISSN 0003-0007) Volume 69, 1988. Monthly The official organ of the Society, devoted to editorials, topical reports to members, articles, professional and membership news, conference announcements, programs, and summaries, book reviews, and Society activities.	$60.00* $20.00†
METEOROLOGICAL & GEOASTROPHYSICAL ABSTRACTS (ISSN 0026-1130) Volume 39, 1988. Monthly Abstracts of current world literature in meteorology, climatology, aeronomy, planetary atmospheres, solar-terrestrial relations, hydrology, oceanography, glaciology, cosmic rays, and radioastronomy. The abstracts of books, articles, and reprints are arranged by subject categories with extensive cross-referencing. Monthly author, subject, and geographical indexes. Information on the computerized MGA data base, 1970–1985, may be obtained by writing to the Society.	$450.00* $20.00†
METEOROLOGICAL & GEOASTROPHYSICAL ABSTRACTS (ANNUAL INDEXES) Vol. 37, Jan.–Dec. 1986. Annually Cumulative Author, Subject, and Geographic Indexes.	$150.00 $3.00†

°The availability and prices of back issues of AMS periodicals will be furnished on request.

*Subscriptions are accepted on calendar year basis only. †Surface postage and handling for foreign subscriptions.

TL
798
.M4
C61
1988

THIRD CONFERENCE ON SATELLITE METEOROLOGY AND OCEANOGRAPHY

February 1-5, 1988

LIBRARY
DEC 0 7 1988
N.O.A.A.
U.S. Dept. of Commerce

Anaheim, Calif.

SPONSORED BY

American Meteorological Society

COVER PHOTO: Successive images from DMSP SSM/I, the first operational microwave imager, from 23 October 1987 over the western Pacific and Indian Oceans. Brightness temperatures are shown from the 22 GHz channel. This frequency is on the wings of a water vapor absorption band and is used to estimate total atmospheric water vapor. The data is presented such that brightness count varies inversely with brightness temperature. Therefore, over the ocean low brightness counts represent warm brightness temperatures and high water vapor content. Note the high water vapor content from about 30°N to 20°S. Image analysis courtesy of Mr. James Clark and Dr. Andreas K. Goroch, Naval Environmental Prediction Facility, Monterey, CA.

Copyright© 1987, American Meteorological Society. This copyright notice applies to only the overall collection of papers; authors retain their individual rights and should be contacted directly for permission to use their material separately. Contact AMS for permission pertaining to the overall collection.

The manuscripts reproduced in this collection of extended abstracts are unrefereed papers presented at the Third Conference on Satellite Meteorology and Oceanography; their appearance in this collection does not constitute formal publication.

AMERICAN METEOROLOGICAL SOCIETY
45 Beacon St., Boston, Mass. 02108 U.S.A.

National Oceanic and Atmospheric Administration
TIROS Satellites and Satellite Meteorology

ERRATA NOTICE

One or more conditions of the original document may affect the quality of the image, such as:

Discolored pages
Faded or light ink
Binding intrudes into the text

This has been a co-operative project between the NOAA Central Library and the Climate Database Modernization Program, National Climate Data Center (NCDC). To view the original document contact the NOAA Central Library in Silver Spring, MD at (301) 713-2607 x124 or Library.Reference@noaa.gov.

HOV Services
Imaging Contractor
12200 Kiln Court
Beltsville, MD 20704-1387
January 26, 2009

Blank page retained for pagination

FOREWORD

It is just twenty months since the 2nd Conference in Williamsburg and we are ready once again to present current research activities in the science of remote sensing of the atmosphere and oceans. A total of 96 papers in regular sessions and 18 papers in joint sessions will be presented during the week. This intense activity suggests a growing and vital community. Also, the opportunity for joint sessions here and at previous conferences suggests the vital role satellite observations play in current research in many subfields.

In 1986 the name of the AMS committee and the conference were changed to include Oceanography. It is especially appropriate that we have scheduled a joint session with the Ocean-Atmosphere Interaction Conference here in Anaheim. A joint session with the Interactive Information Processing conference is also planned. Other highlights of the week include:

1) A session on New and Future Systems to include discussion of remote sensing platforms planned for the 1990s.

2) For the first time a session on Ocean Remote Sensing.

3) An update on ISCCP (International Satellite Cloud Climatology Project) progress including some results from the recent regional experiment.

4) A wide array of additional topics from atmospheric sounding techniques to weather and forecasting applications to radiation budget studies.

A careful examination of the program reveals that the remote sensing community is in transition in two respects. First, we await the next generation of operational satellites and an array of international efforts especially in exploitation of microwave frequencies (passive and active). Many new techniques using these sensors are being anticipated. Some of them will render current satellite techniques obsolete. Second, we continue to increase our contributions to the resolution of some fundamental questions about the atmosphere and oceans (ERB, cloud climatology, severe storm dynamics, air-sea interaction, SST, ocean circulation systems). This is in contrast to traditional, technique oriented studies where new methods of observation are developed. Evidence of this is also apparent in other conferences where satellite studies of fundamental issues are appearing with greater frequency. These transitions ensure a growing and vigorous community and, in the short term, an exciting week of presentations and discussions.

Philip A. Durkee
Program Chairman

PROGRAM COMMITTEE

Philip A. Durkee
Dennis Chesters
Floyd Hauth
Kenneth R. Hardy
Stanley Q. Kidder
Dale Lowry
David S. McDougal
Erik Mollo-Christensen
Anthony Mostek
Gregory S. Wilson
Thomas Vonder Haar

Blank page retained for pagination

TABLE OF CONTENTS

Page

FOREWORD iii

AUTHOR INDEX xiii

SESSION 1: TEMPERATURE RETRIEVALS

Chairperson: Dennis Chesters, NASA/Goddard Space Flight Center (GSFC), Greenbelt, Md.

1.1 EVALUATION OF SATELLITE SAMPLING OF THE MIDDLE ATMOSPHERE USING THE GFDL SKYHI GENERAL CIRCULATION MODEL. Denise Stephenson Graves, AT&T Bell Labs., Whippany, N.J 1

1.2 A CLIMATOLOGY OF ATMOSPHERIC STABILITY FOR THE TROPICS DERIVED FROM TOVS. Siri Jodha Singh Khalsa and Ellen J. Steiner, Univ. of Colorado, Boulder, Colo. 7

1.3 RETRIEVAL OF AIR SURFACE TEMPERATURES OVER OCEANS FROM SATELLITE RADIANCE MEASUREMENTS USING STRATIFICATION TECHNIQUES. Larry M. McMillin, NOAA/Satellite Research Lab., Washington, D.C. 10

1.4 A METHOD OF NOISE REDUCTION FOR THE IMPROVEMENT OF CLEAR COLUMN IN PARTLY CLOUDY AREAS. Anand Swaroop, A. J. Nappi and Hal J. Bloom, ST Systems Corp., Lanham, Md.; and Larry M. McMillin, NOAA/NESDIS, Washington, D.C. 13

1.5 OPERATIONAL IMPLEMENTATION OF THE MINIMUM VARIANCE SIMULTANEOUS RETRIEVAL METHOD. Henry E. Fleming, NOAA/National Environmental Satellite Data Information Service (NESDIS)/Satellite Research Lab., Washington, D.C.; Mitchell D. Goldberg, ST Systems Corp., Lanham, Md.; and David S. Crosby, American Univ., Washington, D.C. 16

1.6 A METHOD FOR OBTAINING AN IMPROVED INITIAL APPROXIMATION FOR THE TEMPERATURE/MOISTURE RETRIEVAL PROBLEM. Mitchell D. Goldberg and Jaime M. Daniels, ST Systems Corp., Lanham, Md.; and Henry E. Fleming, NOAA/NESDIS, Washington, D.C. 20

1.7 COMPARISONS BETWEEN PHYSICALLY RETRIEVED TEMPERATURE AND MOISTURE FIELDS FROM NOAA-7, NOAA-9 and CONVENTIONAL ANALYSES OF RADIOSONDE DATA. N. Husson, Y. Tahani, N. A. Scott, A. Chedin, LMD/CNRS Ecole Polytechnique, Palaiseau, France 24

1.8 TOVS OPERATIONAL SOUNDINGS WITHOUT TROPOSPHERIC MICROWAVE DATA. Anthony Reale, D. Gray and M. Chalfant, NOAA/NESDIS, Washington, D.C.; and A. Nappi, ST Systems Corp., Lanham, Md. 30

1.9 IMPROVED VAS REGRESSION SOUNDINGS OF MESOSCALE TEMPERATURE FEATURES OBSERVED DURING THE ATMOSPHERIC VARIABILITY EXPERIMENT ON 6 MARCH 1982. Dennis Chesters, D. A. Keyser, D. E. Larko and L. Uccellini, NASA/GSFC, Greenbelt, Md. 35

1.10 RELATIONS BETWEEN VAS PHYSICAL RETRIEVALS AND THEIR FIRST GUESS INPUT. John L. Beven II and Henry E. Fuelberg, Florida State Univ., Tallahassee, Fla. 41

1.11 A SPECTRAL APPROACH TO THE UNIFICATION OF SATELLITE AND CONVENTIONAL TEMPERATURE DATA. Kyung-Sup Shin and James R. Scoggins, Texas A&M Univ., College Station, Tex. 47

1.12 SPATIAL AND TEMPORAL VARIABILITY OF VAS RADIANCE MEASUREMENTS BY STRUCTURE AND CORRELATION ANALYSIS. Donald W. Hillger, A. S. Jones, J. F. W. Purdom and T. H. Vonder Haar, Colorado State Univ., Ft. Collins, Colo. 51

*Abstract available; see p. 428.
**Manuscript not available; if received in time, it will appear at back of book.

Page

1.13 OPERATIONAL VAS SOUNDINGS AT PROFS. John S. Snook, NOAA/ERL/ESG/PROFS, Boulder, Colo. 55

SESSION 2: WATER VAPOR RETRIEVALS

Chairperson: Anthony Mostek, National Meteorological Center, Washington, D.C.

2.1 ON THE INTERPRETATION OF INTEGRATED WATER VAPOR PATTERNS IN MIDLATITUDE CYCLONES DERIVED FROM THE NIMBUS 7 SCANNING MULTICHANNEL MICROWAVE RADIOMETER. Lynn A. McMurdie and Kristina B. Katsaros, Univ. of Washington, Seattle, Wash. 60

2.2 PRECIPITABLE WATER DERIVED FROM NIMBUS-7 SMMR MEASUREMENTS AND ITS COMPARISON TO FGGE III-B DATA DURING JANUARY 10-FEBRUARY 13, 1979. Huo-Jin (Alex) Huang, Univ. of North Carolina, Asheville, N.C.; Dayton G. Vincent, Purdue Univ., W. Lafayette, Ind.; and Franklin R. Robertson, NASA/MSFC, Huntsville, Ala. 64

2.3 AN EXAMPLE OF ESTIMATES OF PRECIPITABLE WATER DERIVED FROM NIMBUS-7 SMMR SATELLITE MEASUREMENTS AND FGGE UPPER AIR DATA. Douglas K. Miller and Dayton G. Vincent, Purdue Univ., W. Lafayette, Ind. 70

2.4 TOTAL PRECIPITABLE WATER MEASUREMENTS FROM THE SSM/I. John C. Alishouse, NOAA/NESDIS/Satellite Research Lab., Washington, D.C.; and Jennifer Vongsathorn, S. M. Systems and Research Corp., Lanham, Md. 74

2.5 MOISTURE PROFILE ESTIMATES IN CLOUDY LAYERS UTILIZING GEOSTATIONARY SATELLITE DATA. Jacques Halle, Canadian Meteorological Centre, Dorval, Que., Canada 76

2.6 PROFS QUANTITATIVE PRECIPITABLE WATER PRODUCT. Daniel Birkenheuer, NOAA/ERL/ESG/PROFS, Boulder, Colo. 80

2.7 AN EXTENSION OF THE SPLIT WINDOW TECHNIQUE FOR THE RETRIEVAL OF PRECIPITABLE WATER: EXPERIMENTAL VERIFICATION. Thomas J. Kleespies, Air Force Geophysics Lab. (AFGL), Hanscom AFB, Bedford, Mass.; and Larry M. McMillin, NOAA/NESDIS, Washington, D.C. 84

2.8 DETERMINATION OF LOW-LEVEL PRECIPITABLE WATER VARIABILITY FROM SPLIT WINDOW CHANNEL RADIANCE DATA. Gary J. Jedlovec, NASA/Marshall Space Flight Center (MSFC), Huntsville, Ala. 89

SESSION 3: MULTIPLE PARAMETER STUDIES

Chairperson: Dale A. Lowry, National Weather Service, Silver Spring, Md.

3.1 REMOTE SENSING OF SURFACE AIR TEMPERATURE AND HUMIDITY OVER OCEANIC AREAS WITH APPLICATION TO CLIMATOLOGY AND WEATHER PREDICTION. Louis Garand, Atmospheric Environment Service, Dorval, Que., Canada 95

3.2 DETERMINATION OF SURFACE AND ATMOSPHERIC PARAMETERS USING THE ADVANCED MICROWAVE SOUNDING UNIT. Norman C. Grody, NOAA/NESDIS, Washington, D.C. 100

3.3 ENHANCED IMAGE PRODUCTS BY LIMB-CORRECTION AND SMOOTHING OF VAS RADIANCE MEASUREMENTS. Andrew S. Jones, D. W. Hillger, J. F. W. Purdom and T. H. Vonder Haar, Colorado State Univ., Ft. Collins, Colo. 105

3.4 ESTIMATION OF METEOROLOGICAL PARAMETERS OVER MESOSCALE REGIONS FROM SATELLITE AND IN SITU DATA. Jan L. Behunek and Chi-Fan Shih, METSAT, Inc.; and Thomas H. Vonder Haar, Colorado State Univ., Ft. Collins, Colo. 109

3.5 TEMPORAL AND SPATIAL VARIABILITY AND CONTAMINATION OF 6.7 AND 7.3 MICROMETER WATER VAPOR RADIANCES. K. G. Blackwell, J. P. McGuirk and A. H. Thompson, Texas A&M Univ., College Station, Tex. 115

*Abstract available; see p. 428.
**Manuscript not available; if received in time, it will appear at back of book.

Page

3.6 IDENTIFICATION AND RECOVERY OF DISCONTINUOUS SYNOPTIC FEATURES IN SATELLITE-RETRIEVED BRIGHTNESS TEMPERATURES USING A RADIATIVE TRANSFER MODEL. G. A. White, J. P. McGuirk and A. H. Thompson, Texas A&M Univ., College Station, Tex. 121

SESSION 4: RADIATION BUDGET STUDIES

Chairperson: T. H. Vonder Haar, Colorado State Univ., Ft. Collins, Colo.

4.1 SPATIAL SCALE OF RADIATION TO SPACE -- A SPECTRAL AND STRUCTURE FUNCTION ANALYSIS OF SATELLITE IMAGERY. G. G. Campbell and T. H. Vonder Haar, Colorado State Univ., Ft. Collins, Colo. 128

4.2 DECONVOLUTION RESULTS FOR WIDE-FIELD-OF-VIEW RADIOMETER MEASUREMENTS OF REFLECTED SOLAR RADIATION. G. Louis Smith, Langley Research Center; and David Rutan, PRC Kentron, Inc., Hampton, Va. 132

4.3 INTERCOMPARISON OF OUTGOING LONGWAVE RADIATION OBTAINED FROM ERBE AND NOAA OPERATIONAL SATELLITE: A PRELIMINARY RESULT. Shi-Keng Yang and B. Liebmann, Univ. of Maryland, College Park, Md.; and A. Gruber and A. Miller, NOAA, Washington, D.C. 138

4.4 ERB STATISTICS FROM NFOV DAILY DATA: COMPARISON BETWEEN NOAA AND NIMBUS-7 POLAR ORBITING SATELLITES. Laura D. Smith and Thomas H. Vonder Haar, Colorado State Univ., Ft. Collins, Colo. 142

4.5 NIMBUS-7 EARTH RADIATION BUDGET MEASUREMENTS AND THEIR RELATIONSHIP TO THE ENERGETICS OF THE GENERAL CIRCULATION. David L. Randel and Thomas H. Vonder Haar, Colorado State Univ., Ft. Collins, Colo. 148

SESSION 5: FORECASTING AND WEATHER ANALYSIS

Chairperson: Floyd Hauth, First Weather Wing, Hickam AFB, Hawaii

5.1 THE COMBINING OF METEOROLOGICAL RADAR AND SATELLITE DATA FOR THE SHORT-TERM PREDICTION OF RAINFALL AND SEVERE WEATHER. G. L. Austin, A. Bellon and A. Kilambi, McGill Radar Weather Observatory, Quebec, Canada *

5.2 SATELLITE INTERPRETATION TECHNIQUES INVOLVING THUNDERSTORMS. Ernest H. Goetsch, National Weather Service (NWS) Forecast Office, Louisville, Ky. 152

5.3 STORM DIAGNOSTIC/PREDICTIVE IMAGES DERIVED FROM A COMBINATION OF LIGHTNING AND SATELLITE IMAGERY. Steven J. Goodman, Dennis E. Buechler and Paul E. Meyer, NASA/MSFC, Huntsville, Ala. 158

5.4 USING SATELLITE DATA TO AID IN DIAGNOSING AND FORECASTING CONVECTIVE DEVELOPMENT AND INTENSITY ALONG ARC CLOUD LINES. James F. W. Purdom and Peter C. Sinclair, Colorado State Univ., Ft. Collins, Colo. 166

5.5 ASSIMILATION OF SATELLITE SURFACE WIND SPEED DATA USING THE GLA ANALYSIS/FORECAST SYSTEM. S. C. Bloom and R. Atlas, NASA/GSFC, Greenbelt, Md. 172

5.6 INTEGRATION OF SATELLITE SCATTEROMETER AND RADIOMETER MEASUREMENTS. Marie C. Colton and Allan B. Caughey, NEPRF, Monterey, Calif. 178

5.7 ERROR ANALYSIS OF AUTOMATED WINDS DERIVED FROM GOES MULTISPECTRAL IMAGERY. Steven D. Swadley, NEPRF, Monterey, Calif., 181

5.8 PAPER WITHDRAWN

5.9 AUTOMATIC ANALYSIS OF STEREOSCOPIC IMAGE PAIRS FROM GOES SATELLITES. A. F. Hasler and J. Strong, NASA/GSFC, Greenbelt; and R. Morris and H. Pierce, General Sciences Corp., Laurel, Md. 187

*Abstract available; see p. 428.
**Manuscript not available; if received in time, it will appear at back of book.

Page

5.10 FORECASTING CYCLOGENESIS USING GOES WATER VAPOR SATELLITE IMAGERY AND NUMERICAL MODELS. LeRoy E. Spayd, Jr., NWS/National Meteorological Center (NMC), Camp Springs, Md. 192

5.11 TROPOPAUSE ADJUSTMENT TO TROPICAL CYCLONES AS INFERRED FROM SATELLITE OZONE OBSERVATIONS. Edward B. Rodgers, NASA/GSFC, Greenbelt,; J. Stout and J. Steranka, General Sciences Corp., Laurel, Md; and S. Chang, Naval Research Lab., Washington, D.C. 197

5.12 RELATIONS BETWEEN WATER VAPOR IMAGERY, VERTICAL MOTION AND TROPOPAUSE FOLDS. Steven R. Moore and Henry E. Fuelberg, Florida State Univ., Tallahassee, Fla. 203

5.13 THE USE OF POLAR ORBITER DATA IN TROPICAL WEATHER SYSTEM ANALYSIS. Debra A. Lubich, Colorado State Univ.; and Raymond M. Zehr, NOAA/NESDIS, Ft. Collins, Colo. 209

5.14 USING THE VAS DATA UTILIZATION CENTER (VDUC) FOR THE ANALYSIS AND FORECASTING OF HEAVY RAINFALL PRODUCING MESOSCALE CONVECTIVE SYSTEMS (MCSS). Roderick A. Scofield, NOAA/NESDIS, Washington, D.C. 215

5.15 VAS MODEL IMPACT STUDIES AT NMC. Anthony Mostek, A. Siebers, R. Petersen and D. Keyser, NWS/NMC, Camp Springs, Md.; C. Hayden and W. P. Menzel, NOAA/NESDIS, Washington, D.C. 222

5.16 VERTICAL MOTION AS INFERRED BY THE VAS 6.7 MICROMETER WATER VAPOR CHANNEL. John Stout and J. Steranka, General Sciences Corp., Laurel, Md.; and E. Rodgers and R. A. Petersen, NASA/GSFC, Greenbelt, Md. 231

5.17 TROPICAL SYNOPTIC SIGNATURES IN COMPOSITED 6.7 MICROMETER WATER VAPOR IMAGERY. A. H. Thompson, J. P. McGuirk and D. J. Ulsh, Texas A&M Univ., College Station, Tex. 235

5.18 SATELLITE DIAGNOSIS OF TROPICAL CYCLONES. Raymond M. Zehr, Colorado State Univ., Ft. Collins, Colo. 241

5.19 SATELLITE-DETERMINED SYNOPTIC AND MESOSCALE VARIATIONS OF LOW CLOUDS AND RADIO PROPAGATION CONDITIONS OVER THE OCEAN. J. S. Rosenthal, S. W. Lyons, A. D. Fox and R. A. Helvey, Pacific Missile Test Center, Point Mugu, Calif. *

SESSION J3: OCEAN APPLICATIONS (JOINT WITH 4 INTERACTIVE INFORMATION PROCESSING CONFERENCE)

Cochairpersons: Carlyle H. Wash, Naval Postgraduate School, Monterey, Calif., and Glenn A. Flittner, NOAA/National Ocean Service, Washington, D.C.

J3.1 VISSR SENSOR INTRODUCED MODIFICATIONS IN THE PRESENCE OF LARGE TEMPERATURE GRADIENTS. E. V. Cherna, G. L. Austin, A. Bellon and A. Kilambi, McGill Radar Weather Observatory, St. Anne de Bellevue, Que., Canada J9

J3.2 OPERATIONAL CALIBRATION OF THE METEOSAT IR CHANNEL USING SEA SURFACE TEMPERATURE OBSERVATIONS. Volker Gaertner, European Space Operations Center (ESOC), Darmstadt, Fed. Rep. of Germany J14

J3.3 AUTOMATIC NAVIGATION FOR METEOROLOGICAL SATELLITES. Robert Pyzalski, David Santek and J. T. Young, Univ. of Wisconsin, Madison, Wis. J17

J3.4 A REAL-TIME INTERACTIVE SYSTEM TO PROCESS TIROS ASVHRR, TOVS, AND ARGOS DATA FOR USE IN METEOROLOGY, OCEANOGRAPHY, AND OTHER APPLICATIONS. Charles H. Vermillion and F. Stetina, NASA/GSFC, Greenbelt, Md.; J. Hill, Louisiana State Univ., Baton Rouge, La.; G. Shaffer, Science Systems and Applications, Inc., Beltsville, Md. J40

J3.5 A SYSTEM FOR MANAGEMENT, DISPLAY AND ANALYSIS OF OCEANOGRAPHIC TIME SERIES AND HYDROGRAPHIC DATA. Nancy N. Soreide and S. P. Hayes, NOAA/Pacific Marine Environmental Lab. (PMEL), Seattle, Wash. J20

*Abstract available; see p. 428.
**Manuscript not available; if received in time, it will appear at back of book.

Page

J3.6 A PC-BASED INTERACTIVE GRAPHICS SYSTEM TO PERFORM SATELLITE DERIVED OCEANOGRAPHIC THERMAL ANALYSIS. Marcia L. Weaks, Kim Buttleman and W. B. Campbell, NOAA/NESDIS, Camp Springs, Md. J1

J3.7 PROTOTYPE SATELLITE DATA PROCESSING AND ANALYSIS SOFTWARE SYSTEM FOR EARTH'S ATMOSPHERE AND SURFACE RESEARCH. Brian Dealy, C. Gauthier, R. Frouin, J. Bates, D. Lingner and J. Y. Simonot, Scripps Inst. of Oceanography, La Jolla, Calif. J23

J3.8 A SOFTWARE SYSTEM FOR PROCESSING TOVS ON A PERSONAL COMPUTER. W. L. Smith, R. G. Redecker, H. M. Woolf, H. B. Howell, W. P. Menzel and Qu Wanni, Univ. of Wisconsin, Madison, Wis. J40

J3.9 AN OVERVIEW OF INTERAGENCY TRAINER COORDINATED WORKING GROUP ACTIVITIES. Michael F. Squires, Dept. of the Air Force (DNTN), Scott AFB, Ill. J40

J3.10 SATELLITE TRAINING DEVELOPMENT ACTIVITIES: A STATUS REPORT. H. Michael Mogil, NOAA/NESDIS, Washington, D.C. J29

J3.11 INTEGRATED SATELLITE APT AND WEATHER RADIO BROADCAST PROCESSOR. Kenneth W. Ruggles, Systems West Inc., Carmel, Calif. J35

J3.12 A SYSTEM FOR GOES RECEPTION AND PROCESSING IN PERU. P. D. Erickson, L. Laba and L. W. Diehl, MacDonald Dettwiler and Associates, Ltd., Richmond, B.C., Canada *

SESSION 6: NEW AND FUTURE SYSTEMS

Chairperson: Gregory S. Wilson, NASA/MSFC, Huntsville, Ala.

6.1 SUGGESTED GOES I-M SATELLITE OPERATIONAL SCENARIOS. William E. Shenk, NASA/GSFC, Greenbelt, Md.; W. P. Menzel, Advanced Satellite Products Project, Madison, Wis.; F. Mosher, NOAA/NSSFC, Kansas City, Mo.; and R. T. Merrill, Univ. of Wisconsin, Madison, Wis. 247

6.2 THE DETECTION AND LOCATION OF LIGHTNING FROM GEOSTATIONARY ORBIT. H. J. Christian, NASA/MSFC, Huntsville, Ala. 253

6.3 CONCEPT FOR GEOSTATIONARY EXPERIMENTAL TEMPERATURE AND MOISTURE SOUNDER. J. B. Kumer et al., Lockheed Palo Alto Research Lab., Palo Alto, Calif. 257

6.4 HIGH RESOLUTION INTERFEROMETER SOUNDER -- THE RETRIEVAL OF ATMOSPHERIC TEMPERATURE AND WATER VAPOR PROFILES. W. L. Smith, H. M. Woolf, H. B. Howell, H. E. Revercomb and H.-L. Huang, Univ. of Wisconsin, Madison, Wis. 266

6.5 NASA'S EARTH SCIENCE GEOSTATIONARY PLATFORM. Gregory S. Wilson, NASA/MSFC, Huntsville, Ala.; Robert J. Curran and Dixon M. Butler, NASA Headquarters, Washington, D.C. 272

6.6 THE EARTH AS A SYSTEM: STUDYING THE HYDROLOGIC CYCLE WITH THE POLAR-ORBITING, EARTH OBSERVING SYSTEM. James C. Dodge, NASA Headquarters, Washington, D.C. *

6.7 DOPPLER LIDAR WIND MEASUREMENTS ON THE EOS: LAWS. Daniel E. Fitzjarrald, NASA/MSFC, Huntsville, Ala. 278

6.8 THE GLOBAL BACKSCATTER EXPERIMENT (GLOBE) MEASUREMENT AND MODELING PROGRAM. David A. Bowdle, NASA/MSFC, Huntsville, Ala. *

6.9 AEROSOL BACKSCATTER VARIABILITY AT 10.6 MICRONS OVER COLORADO HIGH PLAINS DURING JAWS EXPERIMENT. Jeff Rothermel and D. Bowdle, Univ. Space Research Association, Huntsville, Ala; and J. M. Vaughan, Royal Signals and Radar Establishment, Great Malvern, United Kingdom 280

6.10 DIRECT MEASUREMENT OF BOUNDARY LAYER WINDS OVER THE OCEANS USING A SPACE-BASED DOPPLER LIDAR WIND SOUNDER. G. D. Emmitt, Simpson Weather Associates, Inc., Charlottesville, Va. 284

*Abstract available; see p. 428.
**Manuscript not available; if received in time, it will appear at back of book.

Page

6.11 THE TROPICAL RAINFALL MEASURING MISSION (TRMM). John S. Theon, NASA Headquarters, Washington, D.C. 287

6.12 DMSP SSM/I STATUS OF CALIBRATION AND EVALUATION. James P. Hollinger and Gene A. Poe, Naval Research Lab., Washington, D.C. **

SESSION 7: RAINFALL OBSERVATIONS

Chairperson: Stanley Q. Kidder, Colorado State Univ., Ft. Collins, Colo.

7.1 SATELLITE MICROWAVE RAINFALL SIMULATIONS WITH A THREE-DIMENSIONAL DYNAMICAL CLOUD MODEL. Robert F. Adler, W.-K. Tao, N. Prasad, J. Simpson and Hwa-Young Yeh, NASA/GSFC, Greenbelt, Md. 290

7.2 THE 1982-83 ENSO GLOBAL CONVECTIVE PRECIPITATION ANOMALY DERIVED FROM NIMBUS-7 SMMR 37 GHZ SCATTERING MEASUREMENTS. Roy W. Spencer and H. Michael Goodman, NASA/MSFC, Huntsville, Ala. 296

7.3 THUNDERSTORM ICE INDUCED BRIGHTNESS TEMPERATURE DEPRESSIONS AT 18, 37 and 92 GHZ DURING COHMEX AND THEIR IMPLICATIONS FOR SATELLITE PRECIPITATION RETRIEVALS. Robbie E. Hood and Roy W. Spencer, NASA/MSFC, Huntsville, Ala. 303

7.4 COMPARISON OF WEATHER RADAR AND SATELLITE-BASED PASSIVE MICROWAVE OBSERVATIONS OF RAINFALL OVER LAND AND OCEANS. Ralph R. Ferraro and Joseph V. Fiore, Jr., Research and Data Systems Corp., Lanham, Md.; and John C. Alishouse, NOAA/NESDIS, Washington, D.C. 309

7.5 A PILOT STUDY TO DETERMINE RELATIONSHIPS BETWEEN NORTH PACIFIC PRECIPITATION FROM NIMBUS-7 SCANNING MULTICHANNEL MICROWAVE RADIOMETER DATA AND ASSOCIATED ATMOSPHERIC CONDITIONS. Mark R. Anderson and John O. Roads, Scripps Inst. of Oceanography, La Jolla, Calif. 315

7.6 PRECIPITATION ESTIMATION USING VISIBLE AND INFRARED SATELLITE AND SURFACE DATA. C. E. Motell and C. H. Wash, Naval Postgraduate School, Monterey, Calif. 319

7.7 THE ADDITION OF VISIBLE CHANNEL DATA TO SATELLITE INFRARED RAIN ESTIMATION SCHEMES. Andrew J. Negri and Robert F. Adler, NASA/GSFC, Greenbelt, Md. 325

7.8 GLOBAL PRECIPITATION DERIVED FROM HIRS2/MSU SOUNDINGS. Man-Li Wu and Joel Susskind, NASA/GSFC, Greenbelt, Md. 331

7.9 VERTICAL PROFILES OF HEATING DERIVED FROM IR-BASED PRECIPITATION ESTIMATES DURING FGGE SOP-1. Franklin R. Robertson, NASA/MSFC, Huntsville, Ala.; and Dayton G. Vincent, Purdue Univ., W. Lafayette, Ind. 334

7.10 THE EVALUATION OF SIMPLE APPROACHES FOR THE DELINEATION OF RAIN AREA FROM SATELLITE IMAGERY. Anastasios A. Tsonis, Univ. of Wisconsin, Milwaukee, Wis. 340

7.11 VARIATION OF SATELLITE RAIN RELATIONSHIPS IN SPACE AND TIME. Patrick King and Tsoi-ching Yip, Atmospheric Environment Service (AES), Downsview, Ont., Canada 346

7.12 MID-LATITUDE EVALUATION OF SOME SATELLITE RAINFALL ESTIMATION TECHNIQUES. W. D. Hogg, A. J. Hanssen, A. Niitsoo and V. L. Polavarapu, AES, Downsview, Ont., Canada 352

7.13 COMPARISON OF SATELLITE IR RAIN ESTIMATES WITH RADAR RAIN OBSERVATIONS IN HURRICANES. K. Robert Morris, General Sciences Corp., Laurel; and Andrew J. Negri and Robert F. Adler, NASA/GSFC, Greenbelt, Md. 358

7.14 RAIN ESTIMATION FROM SATELLITES: AREAL RAINFALL-RAIN AREA RELATION. Long S. Chiu, Applied Research Corporation, Landover, Md. 363

*Abstract available; see p. 428.
**Manuscript not available; if received in time, it will appear at back of book.

Page

SESSION 8: DETECTION OF CLOUDS AND CLOUD PARAMETERS

Chairperson: *David S. McDougal, NASA/LRC*, Hampton, Va.

8.1 FIRE: A MULTIDISCIPLINE PROGRAM TO IMPROVE CLOUD OBSERVATION FROM SATELLITES. *David S. McDougal, NASA/Langley Research Center*, Hampton, Va. (Invited Paper) **

8.2 INTENSIVE FIELD OBSERVATIONS OF CIRRUS CLOUDS. David O'C. Starr, SUNY, Albany, N.Y. **

8.3 INTENSIVE OBSERVATIONS OF MARINE STRATOCUMULUS CLOUDS DURING FIRE. Bruce Albrecht, Pennsylvania State Univ., University Park, Penn. (Invited Paper) 369

8.4 CLOUD COVER STATISTICS FROM GOES/VAS. *Donald Wylie, Peter Grimm*, Univ. of Wisconsin; and W. P. Menzel, NOAA/NESDIS Advanced Satellite Products Project, Madison, Wis. 373

8.5 ANNUAL AND INTERANNUAL VARIATIONS IN THE VERTICAL DISTRIBUTION OF COLD CLOUDINESS OVER THE EASTERN PACIFIC AND THE AMERICAS. Phillip A. Arkin, NOAA/NWS/NMC/Climate Analysis Center, Washington, D.C. 377

8.6 SNOW AND LOW-CLOUD DISCRIMINATION FROM MULTISPECTRAL SATELLITE MEASUREMENTS. Robert C. Allen, P. A. Durkee and C. H. Wash, Naval Postgraduate School, Monterey, Calif. 383

8.7 AN IMPROVED METHOD FOR THE RETRIEVAL OF CLOUD HEIGHT AND AMOUNT FROM SATELLITE RADIANCE MEASUREMENTS. Andrew J. Nappi, Anand Swaroop and Larry M. McMillin, ST Systems Corp., Lanham, Md. 388

8.8 RESOLUTION DEPENDENCE IN SATELLITE IMAGERY: MULTIFRACTAL ANALYSIS. P. Gabriel, S. Lovejoy and D. Schertzer, McGill Univ., Montreal, Canada 392

8.9 MODELING THE SCALE DEPENDENCE OF VISIBLE SATELLITE IMAGES BY RADIATIVE TRANSFER IN FRACTAL CLOUDS. S. Lovejoy, P. Gabriel, D. Schertzer and G. L. Austin, McGill Univ., Montreal, Canada 395

8.10 EFFECTS OF DATA RESOLUTION ON MARINE STRATIFORM CLOUD DETECTION USING AVHRR AND VISSR SATELLITE DATA. Chi-Fan Shih, Melanie Wetzel and Thomas H. Vonder Haar, Colorado State Univ., Ft. Collins, Colo. 401

8.11 ANALYSIS OF CLOUD DYNAMICS WITH MULTISPECTRAL TECHNIQUES. Andreas K. Goroch and James R. Clark, NEPRF, Monterey, Calif. 404

8.12 DUAL-IMAGE PROCESSING TO ENHANCE LOW CLOUDS AND DELINEATE PRECIPITATION. A. D. Fox, S. W. Lyons and G. W. Rainey, Pacific Missile Test Center, Point Mugu, Calif. *

SESSION 9: OCEAN REMOTE SENSING

Chairperson: Erik Mollo-Christensen, NASA/GSFC, Greenbelt, Md.

9.1 WIDE SWATH RADAR ALTIMETRY: TOPOGRAPHIC MAPPING SYSTEMS OF THE FUTURE. Chester Parsons, NASA/GSFC, Greenbelt, Md. (Invited Paper) *

9.2 TIROS-N MULTICHANNEL SEA SURFACE TEMPERATURE ANALYSES FIELDS FOR THE FGGE PERIOD. Ziauddin Ahmad, Jordan L. Sutton and Alan Strong, ST Systems Corp., Lanham, Md. *

9.3 EVALUATION OF 3.7 MICROMETERS SPLIT WINDOWS FOR ESTIMATING SURFACE TEMPERATURE. David S. Crosby, Larry M. McMillin and John C. Alishouse, NOAA/NESDIS, Washington, D.C. 406

9.4 EOF ANALYSIS OF AVHRR AND CZCS IMAGERY. Gary S. E. Lagerloef, Science Applications International Corp., Bellevue, Wash. 410

*Abstract available; see p. 428.
**Manuscript not available; if received in time, it will appear at back of book.

Page

9.5 NIMBUS-7 SMMR DERIVED SEA-ICE CONCENTRATIONS OVER ANTARCTICA. Ralph R. Ferraro and E. R. Major, Research and Data Systems Corp., Lanham, Md.; and J. D'Aguanno and J. D. Tarpley, NOAA/NESDIS, Washington, D.C. 416

9.6 MODELLING OF SURFACE WAVES AND SEA STATE-DEPENDENT WIND STRESS FOR THE NORTHEAST PACIFIC OCEAN USING SEASAT SCATTEROMETER DATA. Hans C. Graber, K. A. Kelly and R. C. Beardsley, Woods Hole Oceanographic Inst., Woods Hole, Mass.; and S. Hasselman, Max-Planck Inst. für Meteorologie, Hamburg, Fed. Rep. of Germany 421

9.7 WIND AND WIND STRESS CURL FIELDS FOR THE NORTHEAST PACIFIC OCEAN USING SATELLITE SCATTEROMETER DATA. Kathryn A. Kelly, Hans C. Graber and Robert C. Beardsley, Woods Hole Oceanographic Inst. Woods Hole, Mass. 425

SESSION J9: JOINT WITH 7 OCEAN-ATMOSPHERE CONFERENCE

Chairperson: Andreas K. Goroch, NEPRF, Monterey, Calif.

J9.1 X-BAND SCATTEROMETER MEASUREMENTS AT LOW WINDS IN A WAVETANK. Mary Ruth Keller and William J. Plant, Naval Research Lab., Washington, D.C. J41

J9.2 USING SATELLITE SCATTEROMETER DETERMINED WINDFIELDS TO OBTAIN SYNOPTIC-SCALE SURFACE PRESSURE FIELDS. R. A. Brown, Univ. of Washington, Seattle, Wash. J44

J9.3 DETERMINING EQUIVALENT DEPTHS OF THE ATMOSPHERIC BOUNDARY LAYER OVER THE OCEANS. Tsann-wang Yu, NOAA/NSW/NMC, Washington, D.C. J46

J9.4 MARINE BOUNDARY LAYER DEPTH AND HUMIDITY ESTIMATION FROM SATELLITE MEASURED OPTICAL DEPTH AND TOTAL WATER CONTENT. P. A. Durkee, R. Kren and S. Smolinski, Naval Postgraduate School, Monterey, Calif. J52

J9.5 MESOSCALE SATELLITE DERIVED TEMPERATURE AND HUMIDITY PROFILES FOR THE FASINEX CAMPAIGN: COMPARISONS WITH CONVENTIONAL PRODUCTS. Claire Levy, F. M. Breon, A. Chedin and N. A. Scott, Ecole Polytechnique, Paliseau, France J56

J9.6 HURRICANE-OCEAN INTERACTION NEAR THE SUBTROPICAL FRONT. Peter G. Black, NOAA/Atlantic Oceanographic and Marine Labs (AOML), Miami, Fla. J60

J9.7 INFLUENCE OF SEA SURFACE TEMPERATURE ON INTRA- AND INTER-ANNUAL VARIATIONS OF ITCZ. Jaime M. Daniels, ST Systems Corp., Lanham; and Anandu V. Vernekar, Univ. of Maryland, College Park, Md. J61

Please note: In an attempt to save space in the Table of Contents multiple authors have been grouped according to affiliation. For the correct order, please refer to the paper.

*Abstract available; see p. 428.
**Manuscript not available; if received in time, it will appear at back of book.

AUTHOR INDEX

		Paper	Page
A	Adler, Robert F.	7.1	290
		7.7	325
		7.13	358
	Ahmad, Ziauddin	9.2	*
	Albrecht, Bruce	8.3	369
	Alishouse, John C.	2.4	74
		7.4	309
		9.3	406
	Allen, Robert C.	8.6	383
	Anderson, Mark R.	7.5	315
	Arkin, Phillip A.	8.5	377
	Atlas, R.	5.5	172
	Austin, G. L.	5.1	*
		J3.1	J9
		8.9	395
B	Bates, J.	J3.7	J23
	Beardsley, Robert C.	9.6	421
		9.7	425
	Behunek, Jan L.	3.4	109
	Bellon, A.	5.1	*
		J3.1	J9
	Beven, John L., II,	1.10	41
	Birkenheuer, Daniel	2.6	80
	Black, Peter G.	J9.6	J60
	Blackwell, K. G.	3.5	115
	Bloom, Hal J.	1.4	13
	Bloom, S.	5.5	172
	Bowdle, David A.	6.8	*
		6.9	280
	Breon, F. M.	J9.5	J56
	Brown, R. A.	J9.2	J44
	Buechler, Dennis E.	5.3	158
	Butler, Dixon M.	6.5	272
	Buttleman, Kim	J3.6	J1
C	Campbell, G. G.	4.1	128
	Campbell, W. B.	J3.6	J1
	Chalfant, M.	1.8	30
	Chang, Simon	5.11	197
	Chedin, A.	1.7	24
		J9.5	J56
	Cherna, E. V.	J3.1	J9
	Chesters, Dennis	1.9	35
		6.3	257
	Chiu, Long S.	7.14	363
	Christian, H. J.	6.2	253
	Clark, James R.	8.11	404
	Colton, Marie C.	5.6	178
	Caughey, Allan B.	5.6	178
	Crosby, David S.	1.5	16
		9.3	406
	Curran, Robert J.	6.5	272
D	D'Aguanno, Jane	9.5	416
	Daniels, Jaime M.	1.6	20
		J9.7	J61
	Dealy, Brian	J3.7	J23
	Diehl, L. W.	J3.12	*
	Dodge, James C.	6.6	*
	Durkee, P. A.	8.6	383
		J9.4	J52
E	Emmitt, G. D.	6.10	284
	Erickson, P. D.	J3.12	*
F	Ferraro, Ralph R.	7.4	309
		9.5	416
	Fiore, Joseph V., Jr.	7.4	309
F	Fitzjarrald, Daniel E.	6.7	278
	Fleming, Henry E.	1.5	16
		1.6	20
	Fox, A. D.	5.19	*
		8.12	*
	Frouin, R.	J3.7	J23
	Fuelberg, Henry E.	1.10	41
		5.12	203
G	Gabriel, P.	8.8	392
		8.9	395
	Gaertner, Volker	J3.2	J14
	Garand, Louis	3.1	95
	Gauthier, C.	J3.7	J23
	Goetsch, Ernest H.	5.2	152
	Goldberg, Mitchell D.	1.5	16
		1.6	20
	Goodman, H. Michael	7.2	296
	Goodman, Steven J.	5.3	158
	Goroch, Andreas K.	8.11	404
	Graber, Hans C.	9.6	421
		9.7	425
	Graves, Denise S.	1.1	1
	Gray, D.	1.8	30
	Grimm, Peter	8.4	373
	Grody, Norman C.	3.2	100
	Gruber, Arnold	4.3	138
H	Halle, Jacques	2.5	76
	Hanssen, A. J.	7.12	352
	Hasler, A. F.	5.9	187
	Hasselman, Susanne	9.6	421
	Hayden, Christopher	5.15	222
	Hayes, S. P.	J3.5	J20
	Helvey, R. A.	5.19	*
	Hill, J.	J3.4	J40
	Hillger, Donald W.	1.12	51
		3.3	105
	Hogg, W. D.	7.12	352
	Hollinger, James P.	6.12	**
	Hood, Robbie E.	7.3	303
	Howell, H. B.	J3.8	J40
		6.4	266
	Huang, H.-L.	6.4	266
	Huang, Huo-Jin (Alex)	2.2	64
	Husson, N.	1.7	24
J	James, T. C.	6.3	257
	Jedlovec, Gary J.	2.8	89
	Jones, Andrew S.	1.12	51
		3.3	105
K	Katsaros, Kristina B.	2.1	60
	Keller, Mary Ruth	J9.1	J41
	Kelly, Kathryn A.	9.6	421
		9.7	425
	Keyser, Dennis A.	1.9	35
		5.15	222
	Khalsa, Siri Jodha Singh	1.2	7
	Kilambi, A.	5.1	*
		J3.1	J9
	King, Patrick	7.11	346
	Kleespies, Thomas J.	2.7	84
	Koenig, E. W.	6.3	257
	Kren, R.	J9.4	J52
	Kumer, J. B.	6.3	257
L	Laba, L.	J3.12	*
	Lagerloef, Gary S. E.	9.4	410

*Abstract available; see p. 428.
**Manuscript not available; if received in time, it will appear in back of book.

AUTHOR INDEX

		Paper	Page
L	Larko, D. E.	1.9	35
	Levy, Claire	J9.5	J56
	Liebmann, Brant	4.3	138
	Lingner, D.	J3.7	J23
	Lovejoy, S.	8.8	392
		8.9	395
	Lubich, Debra A.	5.13	209
	Lyons, S. W.	5.19	*
		8.12	*
M	Major, Eugene R.	9.5	416
	McDougal, David S.	8.1	**
	McGuirk, J. P.	3.5	115
		3.6	121
		5.17	235
	McMillin, Larry M.	1.3	10
		1.4	13
		2.7	84
		8.7	388
		9.3	406
	McMurdie, Lynn A.	2.1	60
	Menzel, W. P.	J3.8	J40
		5.15	222
		6.1	247
		8.4	373
	Merrill, R. T.	6.1	247
	Meyer, Paul E.	5.3	158
	Miller, Alvin	4.3	138
	Miller, Douglas K.	2.3	70
	Mogil, H. Michael	J3.10	J29
	Moore, Steven R.	5.12	203
	Morris, K. Robert	5.9	187
		7.13	358
	Mosher, F.	6.1	247
	Mostek, Anthony	5.15	222
	Motell, C. E.	7.6	319
	Murray, D. O.	6.3	257
N	Naes, L. G.	6.3	257
	Nappi, Andrew J.	1.4	13
		1.8	30
		8.7	388
	Nast, T. C.	6.3	257
	Negri, Andrew J.	7.7	325
		7.13	358
	Niitsoo, A.	7.12	352
O	Ostling, A. R.	6.3	257
P	Parsons, Chester	9.1	*
	Perscheid, G. A.	6.3	257
	Petersen, R. A.	5.15	222
		5.16	231
	Pierce, H.	5.9	187
	Plant, William J.	J9.1	J41
	Poe, Gene A.	6.12	**
	Polavarapu, V. L.	7.12	352
	Potter, J. F.	6.3	257
	Prasad, N.	7.1	290
	Purdom, J. F. W.	1.12	51
		3.3	105
		5.4	166
	Pyzalski, Robert	J3.3	J17
R	Rainey, G. W.	8.12	*
	Randel, David L.	4.5	148
	Reale, Anthony	1.8	30
	Redecker, R. G.	J3.8	J40
	Revercomb, H. E.	6.4	266
R	Roads, John O.	7.5	315
	Robertson, Franklin R.	2.2	64
		7.9	334
	Roche, A. E.	6.3	257
	Rodgers, Edward B.	5.11	197
		5.16	231
	Rosenberg, W. J.	6.3	257
	Rosenthal, J. S.	5.19	*
	Rothermel, Jeff	6.9	280
	Ruggles, Kenneth W.	J3.11	J35
	Rutan, David	4.2	132
S	Santek, David	J3.3	J17
	Schertzer, D.	8.8	392
		8.9	395
	Scofield, Roderick A.	5.14	215
	Scoggins, James R.	1.11	47
	Scott, N. A.	1.7	24
		J9.5	J56
	Shaffer, G.	J3.4	J40
	Shenk, William E.	6.1	247
		6.3	257
	Shih, Chi-Fan	3.4	109
		8.10	401
	Shin, Kyung-Sup	1.11	47
	Siebers, Anthony	5.15	222
	Simonot, J. Y.	J3.7	J23
	Simpson, J.	7.1	290
	Sinclair, Peter C.	5.4	166
	Smith, G. Louis	4.2	132
	Smith, Laura D.	4.4	142
	Smith, W. L.	J3.8	J40
		6.4	266
	Smolinski, S.	J9.4	J52
	Snook, John S.	1.13	55
	Soreide, Nancy N.	J3.5	J20
	Spayd, LeRoy E., Jr.	5.10	192
	Spencer, Roy W.	7.2	296
		7.3	303
	Springer, L. A.	6.3	257
	Squires, Michael F.	J3.9	J40
	Starr, David O'C.	8.2	**
	Steakley, B. C.	6.3	257
	Steiner, Ellen J.	1.2	7
	Steranka, J.	5.11	197
		5.16	231
	Sterrit, L. W.	6.3	257
	Stetina, F.	J3.4	J40
	Stout, John	5.11	197
		5.16	231
	Strong, Alan	9.2	*
	Strong, J.	5.9	187
	Susskind, J.	6.3	257
		7.8	331
	Sutton, Jordan L.	9.2	*
	Swadley, Steven D.	5.7	181
	Swaroop, Anand	1.4	13
		8.7	388
T	Tahani, Y.	1.7	24
	Tao, Wei-Kuo	7.1	290
	Tarpley, J. D.	9.5	416
	Theon, John S.	6.11	287
	Thompson, A. H.	3.5	115
		3.6	121
		5.17	235
	Tsonis, Anastasios A.	7.10	340
U	Uccellini, Louis	1.9	35

*Abstract available; see p. 428.
**Manuscript not available; if received in time, it will appear in back of book.

AUTHOR INDEX

		Paper	Page
U	Ulsh, D. J.	5.17	235
V	Vaughan, J. M.	6.9	280
	Vermillion, Charles H.	J3.4	J40
	Vernekar, Anandu V.	J9.7	J61
	Vincent, Dayton G.	2.2	64
		2.3	70
		7.9	334
	Vonder Haar, Thomas H.	1.12	51
		3.3	105
		3.4	109
		4.1	128
		4.4	142
		4.5	148
		8.10	401
	Vongsathorn, Jennifer	2.4	74
W	Wanni, Qu	J3.8	J40
W	Wash, C. H.	7.6	319
		8.6	383
	Weaks, Marcia L.	J3.6	J1
	Wetzel, Melanie	8.10	401
	White, G. A.	3.6	121
	Wilson, Gregory S.	6.5	272
	Woolf, H. M.	J3.8	J40
		6.4	266
	Wu, Man-Li	7.8	331
	Wylie, Donald	8.4	373
Y	Yang, Shi-Keng	4.3	138
	Yeh, H.-Y.	7.1	290
	Yip, Tsoi-ching	7.11	346
	Young, J. T.	J3.3	J17
	Yu, Tsann-wang	J9.3	J46
Z	Zehr, Raymond M.	5.13	209
		5.18	241

*Abstract available; see p. 428.
**Manuscript not available; if received in time, it will appear in back of book.

1.1

EVALUATION OF SATELLITE SAMPLING OF THE MIDDLE ATMOSPHERE USING THE GFDL SKYHI GENERAL CIRCULATION MODEL

Denise Stephenson Graves
AT&T Bell Laboratories
Whippany, NJ 07981

1.0 INTRODUCTION

Atmospheric data gathered via the satellite platform currently provides more than 4 times the global meteorological information available from the traditional radiosonde-rawinsonde-rocketsonde-oceanic sensor network. The majority of the traditional ground-based measurement stations are located in the Northern Hemisphere while the maritime sensor network provides most of its meteorological coverage over the principal maritime regions. The satellite however, gives complete global coverage, providing a massive data base containing the majority of meteorological data gathered over global maritime regions as well as over land areas in the Southern Hemisphere.

Atmospheric data obtained from the aforementioned traditional means have historically been accepted by the scientific community as "truth". Temperature and wind fields calculated from satellite-based measurements have been routinely compared to this "truth" to determine the validity of the satellite's indirect method of measurement. Because the satellite platform routinely provides a more complete and consistent data set over maritime regions relative to other atmospheric sensors, the routine use of weather ships and weather reconnaissance has been abandoned. This decrease in the traditional sources of data, particularly over oceanic areas, has resulted in less observational data available to aid in the validation of data from the satellite platform. Consequently, the importance of satellite data in describing the atmosphere over these regions has increased.

The overall objective of this study is to examine the validity of various "meteorologically-significant" dynamical diagnostics calculated from data measured from the satellite platform with principal focus within the northern hemisphere, wintertime middle atmosphere. Two items are of particular concern in this study. These are (1) the accuracy of the structure of global atmospheric temperature fields calculated from satellite measurements and (2) the sensitivity of various meteorological fields defined from satellite temperatures to errors in these temperature fields. The satellite platform provides the most complete and consistent global coverage of the earth's atmosphere. Because the data obtained from this platform are frequently used to examine mathematical theories thought to describe fluid motions of the earth's atmosphere, a thorough understanding of the attributes and limitations of the satellite's meteorological data base is desirable.

The approach taken here to study this problem is to simulate a nadir-viewing, near polar-orbiting satellite that samples the earth's middle atmosphere. Numerically simulated satellite measurements of the atmosphere's longwave and microwave radiation are used in a mathematical inversion scheme to convert the satellite's measured radiation to temperatures. Using the vertical temperature profiles defined from the simulated satellite radiation data, meteorological fields of geopotential height (Z), zonal (U) and meridional (V) winds, heat and momentum fluxes, the Ertel's isentropic potential vorticity and the divergence of the Eliassen-Palm flux are calculated. Direct comparisons are then made between the satellite's view of these meteorological variables and the "true" variables.

2.0 DATA AND ANALYSIS PROCEDURE

The current study assumes that the verification data set (the "true" meteorological variables that describe the earth's atmospheric state) is defined by calculations from the National Oceanic and Atmospheric Administration (NOAA) Geophysical Fluid Dynamics Laboratory's (GFDL) SKYHI general circulation model (GCM). Several versions of the SKYHI GCM exist which differ primarily in the degree of resolution of the model's horizontal grid. The version of the SKYHI GCM used in this study has horizontal resolution of 3° of latitude by 3.6° of longitude (N30 version) with 40 vertical levels extending from the earth's surface to approximately 80km. (See Fels et al. (1980) for further details of the version of SKYHI used in this study.) Data from SKYHI are used in this study in lieu of actual measurements of the earth's atmosphere because the GCM provides a complete, consistent set of global, synoptic data with known spatial, vertical and temporal resolution. This type of resolution can be obtained from traditional observations only after extensive interpolative/extrapolative analysis and concatenation of measurements from a myriad of observing instruments (each instrument having a different accuracy) have been performed. The advantage of using the SKYHI GCM data is that concerns such as (a) the impact of undersampling in describing the atmospheric state, (b) the impact of instrumental error upon measured meteorological fields, (c) the effect of measurements obtained at different times (asynoptic) in describing the global atmosphere at a specific instance in time (synoptic) and (d) the influence of human intervention in subjectively analyzing the measured fields becomes moot.

The time of year selected for this case study, January, contains both quiescent and highly transient meteorological episodes. This was done because the true test of the reliability of the satellite as an investigative tool lies in its ability to characterize accurately, highly variable phenomenon, e.g., the evolution of major and minor stratospheric sudden warming events. These extreme situations are both provided to some degree in the January SKYHI GCM data used here.

The analysis techniques used in this study for calculating vertical temperature profiles from satellite radiances are designed to parallel the operational procedures of NOAA/National Environmental Satellite Data Information Service (NOAA/NESDIS) in Suitland, Maryland. (See Weinreb and Hill (1980) and Weinreb et al. (1981) for details of the computer analysis techniques.) From an asynoptic sample of temperatures for the month of January, transmittances and radiances are defined which correspond to the instruments comprising the Television Infrared Operating Sounder (TIROS-N) Operational Vertical Sounder (TOVS). The TOVS satellite system is comprised of three instruments that measure the atmosphere's emitted radiation. These instruments are the High Resolution Infrared Sounder (HIRS-2), the Stratospheric Sounding Unit (SSU), and the Microwave Sounding Unit (MSU). NOAA/NESDIS uses the mathematical technique of statistical linear regression analysis to define vertical temperature profiles from satellite radiances measured by each of these instruments.

(See Smith and Woolf (1976) for details of the technique of statistical linear regression analysis employed by NOAA/NESDIS.) This technique requires the use of predefined vertical profiles of temperature and water vapor mixing ratio to infer the vertical atmospheric temperature structure from the satellite's radiation measurements. The predefined fields of temperature and water vapor mixing ratio used by NOAA/NESDIS are comprised of climatological and near real time data obtained from the traditional radiosonde and rocketsonde networks. This observational data network has been simulated in the current study and the resultant meteorological data are used in the inference of vertical temperature structure from the satellite's radiation field.

Several issues are examined in this study before comparisons are performed between the meteorological variables calculated from the nadir-viewing satellite's temperature fields and the "true" variables of the SKYHI atmosphere. These include:

i. similarities and differences between the SKYHI GCM and the earth's atmosphere

ii. the limitations of using the quasi-geostrophic approximations to define the atmosphere's true zonal mean zonal wind, meridional fluxes of heat and momentum and the Eliassen-Palm (E-P) flux divergence, *divF*

iii. the limitations of a discrete, synoptic sample of the atmospheric temperature field in defining the true character of the temperature field

iv. the attributes and limitations of objective analysis techniques employed to convert asynoptic satellite data to a synoptic form, and

v. the impact of the density of the global radiosonde/rocketsonde data measurement network in defining vertical temperature profiles from satellite radiance measurements

The importance of portions of items (ii) and (v) are addressed in this paper. Further details of the work presented in this paper and the meteorological issues listed but not discussed can be found in Graves(1986).

3.0 DISCUSSION

Comparisons were made between data from the SKYHI GCM and observational data analyses to assess the realism of SKYHI relative to the earth's atmosphere. These comparisons were performed to determine the appropriateness of using the SKYHI GCM data as a surrogate for the earth's atmosphere for purpose of conducting a study that models the retrieval of atmospheric field data (i.e. temperature, wind and other derived dynamical quantities) from satellite measurements of the earth's radiation field. Using three climatological data sets, Geller, Wu and Gelman (1983), Hamilton (1982), and Labitzke and Collaborators (1972) as indicators of the earth's true atmospheric character, the time averaged, horizontally varying and zonally averaged fields of temperature, wind, meridional eddy fluxes of momentum and temperature and the Eliassen-Palm flux divergence were examined relative to those diagnostics from SKYHI. Also, the realism between vertical profiles of temperature and zonal and meridional winds from SKYHI at selected rocketsonde station locations was examined relative to these data defined in the Range Reference Atmosphere atlases (e.g.,1983). The SKYHI results are representative of a single year of GCM data while the climatologies are defined from several years of observations.

Concluded from this comparative analysis was that SKYHI is a reasonable substitute for the earth's atmosphere for purposes of this simulated satellite study. Two comparisons that were made have a direct influence on the simulated satellite results presented here. These are

i. comparisons between the use of the geostrophic and gradient wind equations in approximating the zonal winds of SKYHI and

ii. comparison between SKYHI's actual Eliassen-Palm flux divergence and this divergence calculated from the SKYHI data using the quasi-geostrophic potential vorticity equation.

The first comparison resulted in the use of the gradient wind equation to define the simulated satellite meteorological parameters. Concluded from the second comparison was that the eddy-induced E-P flux divergence eddies calculated from the meridional flux of quasi-geostrophic potential vorticity underestimates the true magnitude of SKYHI's *divF* by 10% within the upper stratosphere and by larger percentages in the lower mesosphere. The errors inherent in the satellite inferred *divF* can only exceed these estimates. The impact of this final comparison upon actual meteorological analyses cannot be addressed in reality but only through a simulated study of this nature.

An understanding of the mathematical method used to infer vertical temperature structure from satellite measurements of radiation emitted from the atmosphere is paramount to understanding the results of this study. The process of inferring vertical temperature structure from measurements of the radiation emitted from the atmosphere requires the numerical inversion of the equation of radiative transfer. The radiance, $\hat{I}(\theta)$, can be defined in terms of the spectral response function, $\hat{\Phi}(\nu)$, given as a function of the inverse monochromatic frequency, ν, and the monochromatic radiance, $I(\nu,\theta)$, upwelling from the atmosphere as a function of ν and zenith angle θ as

$$\hat{I}(\theta) = \int_{\nu_1}^{\nu_2} \hat{\Phi}(\nu) I(\nu,\theta) d\nu \qquad (1)$$

Instruments for measuring the earth's emitted radiation, that is, radiometers, must be quantitatively definable so that calculations can be made of the radiation emitted within a finite spectral (i.e., frequency) interval. The term "channel" is used to describe this finite frequency range within which radiation is being measured. Spectral response functions, $\Phi(\nu)$, defined as a function of wavenumber, describe the nonuniform way in which the various channels of the radiometer react to radiation incident upon them. The monochromatic radiance is represented by the equation

$$I(\nu,\theta) = \epsilon(\nu,\theta) B(\nu,T_s)\tau(\nu,\theta,p_s) - \int_0^{p_s} B(\nu,T(p)) \frac{\partial\tau(\nu,\theta,p)}{\partial p} dp \qquad (2)$$

$I(\nu,\theta)$ is defined for a non-scattering, plane-parallel atmosphere in local thermodynamic equilibrium. Also, other variables in equation (2) are:

$B(\nu,\tau)$: Planck function

$\tau(\nu,\theta,p)$: fractional transmittance from level p to the altitude of the radiometer (∞)

$\epsilon(\nu,\theta)$: surface emissivity.

s (subscript): surface

The problem of inverting the integral equation of radiative transfer given by (1) is an ill-conditioned one. This equation is ill-conditioned because there are only a *finite* number of measurements available to infer the atmosphere's temperature profile which is a *continuous* function of pressure.

There are many methods available to solve equation (1) for the earth's unknown temperature profile. The solutions obtained, however, are not unique. The technique of statistical linear

regression used by NOAA/NESDIS calculates an atmospheric temperature as the deviation of an unknown temperature T from "some" climatological mean temperature. This deviation can be expressed as a linear combination of the deviation of the *measured* equivalent brightness temperature (determined from the satellite's channel radiance measurements) from "some" climatological mean equivalent brightness temperature.

SKYHI GCM data were used to reconstruct the indirect retrieval of vertical temperature profiles from satellite radiances above 100mb. The process begins by defining asynoptic temperature (later referred to in section 4 as SKYHI SAT), relative humidity and surface pressure profiles from SKYHI corresponding to the subsatellite ground track of a nadir-viewing, near polar orbiting satellite. Computer programs used in performing the SKYHI temperature to simulated satellite temperature calculations were provided by M. Chalfant of NOAA/NESDIS in Suitland, MD.

Transmittances and radiances representative of the instruments comprising the TOVS system of NOAA's TIROS-N satellite system were calculated from the SKYHI data. Satellite simulated temperatures were then calculated using the technique of statistical regression analysis from the SKYHI radiances and two climatological temperature data bases. These data bases are

i. a SKYHI climatological data base that has spatial locations contiguous with radiosonde stations; lags the satellite simulated temperatures in time by two weeks and

ii. the PDS1200 data currently employed by NOAA/NESDIS for temperature inversions *above* 10mb.

The PDS1200 is a permanent data set (PDS) comprised of 1200 *instantaneous* vertical profiles of atmospheric temperature and relative humidity measured from rocketsondes during the time period 1963 through 1972. These profiles are representative of high latitude, middle latitude and tropical environments but are predominantly northern hemisphere (NH) data.

A fundamental question regarding the use of the technique of statistical linear regression analysis is how sensitive are the inferred satellite temperatures to the information contained in the climatological data bases. This question is addressed in the next section by using three different data sets to initialize the regression technique. These data sets are generically referred to as initialization data sets. The initialization data set used by NOAA/NESDIS in the inference of atmospheric temperatures is *always* comprised of PDS1200 data *above* the 10mb pressure level and near real time radiosonde data *below* the 10mb level. The coupling of these *independent* data sets at 10mb defines a discontinuity in the information used to infer temperatures from satellite measurements using the technique of statistical linear regression analysis. The implications of using each of these data sets in calculating vertical temperatures via the technique of statistical linear regression analysis are discussed in the next section.

Three initialization data sets are used in this study to analyze their influence on temperatures inferred from satellite measurements. The data comprising each of the initialization data sets used in this study and the acronyms representing each are

i. PDS: PDS1200 data

ii. NHCONT: SKYHI GCM data spatially located at existing NH radiosonde sites; data are sampled randomly in time within the two weeks preceding the simulated satellite temperature retrievals

iii. NHDISCONT: NHCONT data from 100mb to 10mb; PDS1200 data above 10mb. (This data set mimics the operational procedure currently employed by NOAA/NESDIS.)

The satellite temperatures were interpolated onto a regular grid prior to defining the geopotential height and wind fields for each day in January. The daily SKYHI 100mb synoptic geopotential height was used as the reference surface when the geopotential height field was calculated using the hypsometric equation. Fourier transforms of the T, U, V and Z fields were used to interpolate these data onto an even global spatial grid that has the same spatial resolution as the SKYHI GCM. These fields were then used to calculate the quasi-geostrophic Eliassen-Palm flux divergence from the quasi-geostrophic potential vorticity. Comparisons were then made between the simulated satellite fields of these meteorological quantities and the original SKYHI fields.

4.0 RESULTS

Simulated satellite temperature fields and Eliassen-Palm flux divergence maps are compared with these meteorological fields calculated from SKYHI GCM data. Temperature comparisons show that the accuracy of satellite-inferred temperatures determined from the use of the technique of statistical linear regression analysis is highly dependent upon the initialization data set used. Finally, the comparison of satellite estimates of the Eliassen-Palm flux divergence with the true SKYHI GCM fields shows differences in both the magnitude and sign of *divF* within the middle atmosphere.

4.1 Temperatures

The experiment comparison to follow uses the initialization data sets described in the previous section, namely, PDS, NHCONT and NHDISCONT to calculate satellite temperatures using the method of statistical linear regression analysis. Shown in Figure 1 are three contour plots depicting zonal mean temperature differences for January 1 defined as a function of latitude and pressure. The first depicts the difference between the SKYHI GCM asynoptic temperatures (SKYHI SAT) and PDS while Figure 1b defines the difference between SKYHI SAT and NHCONT. In the winter hemisphere (NH), the magnitude of temperature errors using either initialization data set is comparable, generally less than 5°K throughout the middle atmosphere. Exceptions, however, dominate the lower mesosphere where errors exceed 12°K for both initialization data sets. The large temperature errors in the summer hemisphere middle atmosphere using either PDS or NHCONT are an artifact of inferring summer temperature structure from a NH initialization data set.

Errors from use of PDS in equatorial regions above 5mb are on the order of 10°K while the errors from use of NHCONT in this region are double this value above 1mb. This is a region of high gravity wave activity within the SKYHI GCM (Miyahara, Hayashi and Mahlman, 1985). The sampled data comprising NHCONT can only approximate the true wave activity in the tropics to a limited degree. The sparseness of radiosonde station locations in the tropics reflected in both of the initialization data sets used here and the accuracy of the temperature variability defined from these station data contribute to the large errors.

Shown in Figure 1c are contours of the temperature difference between SKYHI SAT and NHDISCONT. A comparison between Figures 1b and 1c indicates significant increases in temperature differences. Differences from 5°K to 20°K are noted at the level of discontinuity, 10mb, and in the lower mesosphere when the continuous data, Figure 1a, are compared with the discontinuous data Figure 1c. It should be noted that temperature differences are significantly less as a result of improved temperature inferences within the stratosphere, when the vertically continuous PDS data are used in lieu of the discontinuous data (NHDISCONT). Therefore, this comparison indicates that a more realistic approximation of vertical temperature structure in

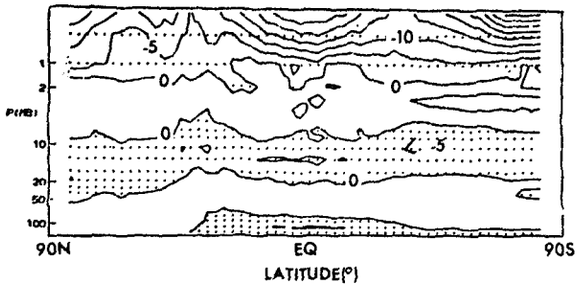

(a) SKYHI SAT minus PDS.

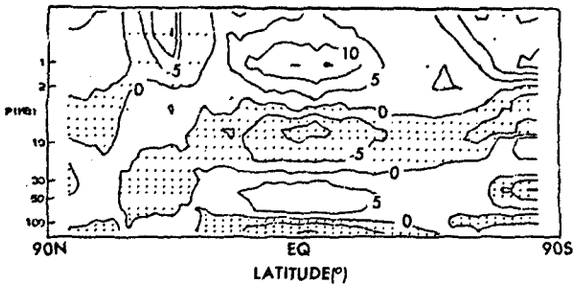

(b) SKYHI SAT minus NHCONT.

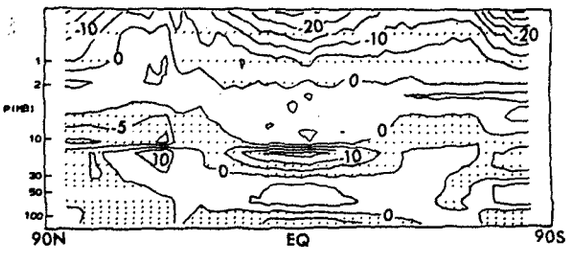

(c) SKYHI SAT minus NHDISCONT.

Figure 1. Zonal Mean Temperature Differences for January 1. (Units: °K)

the vicinity of the 10mb level would result from use of the continuous PDS1200 data.

For both data comparisons, SKYHI SAT vs. NHCONT and SKYHI SAT vs. NHDISCONT, there is a systematic pattern of regions of positive and negative temperature differences throughout the equatorial middle atmosphere. This may be indicative of a misrepresentation of the vertical phase of the true SKYHI temperature waves by the satellite temperature.

Shown in Figure 2 is a latitude/pressure map depicting the difference between the SKYHI SAT temperatures and the temperatures in the PDS1200 initialization data set. This figure differs from Figure 1a in that the temperature differences in Figure 1a are defined between SKYHI SAT and the satellite's temperatures *inferred from the use of the PDS1200* as the initialization data set. In contrast, Figure 2 describes the temperature differences between SKYHI SAT and the *latitude band averaged* temperatures in the PDS1200 initialization data set. Comparisons between Figures 1a and 2 indicate similar patterns of temperature differences within the tropical middle atmosphere. Particularly evident from a comparison of Figures 1a and 2 is the fact that the technique employed by NOAA/NESDIS does a remarkably good job of approximating the SKYHI SAT temperatures within the extratropical

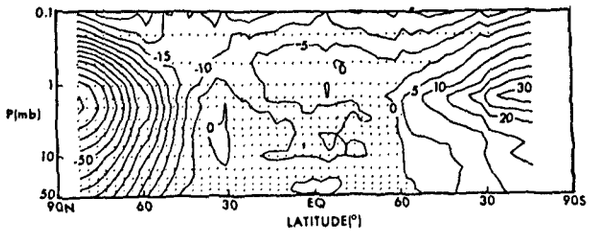

Figure 2. SKYHI SAT minus the temperatures comprising the PDS1200 (Latitude band spatial averages are used to define the contoured temperature differences.) (Units: °K)

atmosphere. This excellent aggreement is achieved in spite of the existence of extremely large temperature differences between the SKYHI SAT zonally averaged temperatures and the latitudinal band averaged temperatures comprising the PDS1200 data set (Figure 2).

4.2 Eliassen-Palm Flux Divergences

The Eliassen-Palm flux divergence is a meteorological diagnostic that defines the influence of eddy motions in forcing the zonally-averaged zonal flow. Because of the importance of *divF* as an indicator of atmospheric behavior, it is important to determine its fidelity as derived from satellite radiance measurements relative to that defined given the true temperature and wind fields. *DivF* is numerically defined for this study as the zonally averaged meridional eddy flux of quasi-geostrophic potential vorticity.

Shown in Figure 3 are three latitude/pressure maps of *divF* averaged for seven days during the time period 01-14 January. The first defines *divF* as calculated geostrophically from the SKYHI GCM data. The second and third maps display contours of *divF* as derived from the two sets of satellite temperature data, NHCONT and NHDISCONT, respectively.

Poleward of 60°N latitude, the region of convergent *divF* in SKYHI (Figure 3a) is also defined by both the NHCONT and NHDISCONT data. The magnitude of maximum convergence differs for the three cases, SKYHI indicates $22.8 * 10^{-5} m/sec^2$ while NHCONT defines a value of $25.1 * 10^{-5} m/sec^2$ and NHDISCONT $-28.3 * 10^{-5} m/sec^2$ for 60°N latitude at the 1mb pressure level. The degree of agreement/disagreement indicated by these values highlight the fact that many of the essential features of *divF* are not accurately represented from the satellite data. For example, both estimates of *divF* from the satellite data define a small region of divergence poleward of 60°N latitude in the middle to upper stratosphere, not indicated by the SKYHI data. Also, equatorward of 50°N latitude there is very poor agreement between SKYHI's *divF* and that calculated from the satellite temperatures.

There are many reasons for the failure of the simulated satellite data to accurately define the magnitude and sign of *divF*, particularly poleward of 60°N in the upper stratosphere. Before beginning an elaboration of these reasons, it must be emphasized that the calculation of the meteorological diagnostic, *divF*, requires several differentiations of the geopotential height field, which is, in turn, determined from temperatures inferred from satellite radiance measurements. *To retain accuracy, a differentiated field must be virtually free of "noise" or errorless on the scale on which the differentiation occurs.* If this is not the case, then erroneous differentiations will result in incorrect diagnostics.

There is a high percentage of spatial temperature variance in SKYHI equatorward of 50° latitude in the upper stratosphere that cannot be explained from sampled satellite temperatures. At best, the temperature information defined for spatial scales larger

than wavenumber 6 will be aliased by the measurements and temperature inferences into smaller wavenumbers. This information is vitally important when defining a highly differentiated field. In contrast, the NH stratospheric midlatitude dynamics are dominated by large amplitude, long waves that are more accurately characterized from the nadir viewed satellite data. This explains the more accurate representation of *divF* by the satellite data in this region. Without an accurate description of spatial variations, it is improbable that accurate values of *divF* can result.

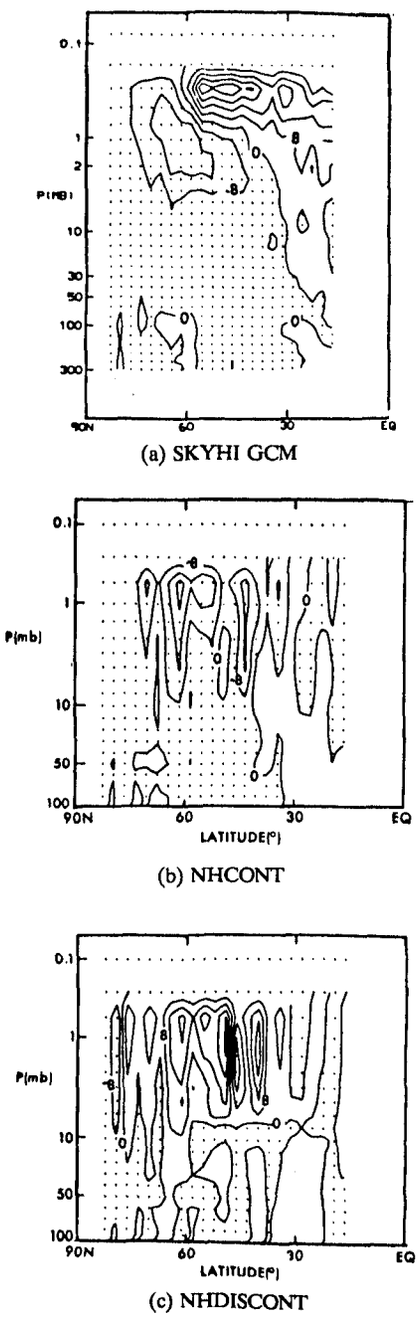

Figure 3. Time averaged, Latitude/Pressure Maps of the Eliassen-Palm Flux Divergence. Data averaged for 7 days during the time period 01-14 January. (Units: $10^{-5} m/sec^2$)

5.0 SUMMARY AND CONCLUDING REMARKS

A simulated case study has been performed to examine and define the limitations of various "meteorologically-significant" dynamical diagnostics calculated from data measured from the satellite platform relative to the true diagnostics in the atmosphere. In research of this study objective, two items of particular concern were highlighted in this paper. They are

i. the accuracy of the structure of global atmospheric temperature fields calculated from satellite radiance measurements and

ii. the sensitivity of the Eliassen-Palm flux divergence defined from satellite temperatures to errors in these temperature fields.

The role played by climatological data in the inference of temperature from satellite measured radiances using the method of statistical linear regression analysis is illustrated. Temperature differences between asynoptic SKYHI temperatures and simulated satellite temperatures of less than 3°K can be found in the midlatitude lower stratosphere but can exceed 10°K equatorward of 50°N in the upper stratosphere/lower mesosphere. The divergence of the Eliassen-Palm flux as defined from the satellite radiances significantly differs in both magnitude and sign from that of SKYHI throughout the middle atmosphere.

Results of this study have indicated that measurements of atmospheric radiation obtained from the satellite platform can be successfully used to provide a broad gamut of meteorological information. Measurements from the satellite platform, at present, provide indirect measures of the atmosphere's vertical structure. The results of this study have identified limitations concerning the practical use of the technique of statistical linear regression currently used by NOAA/NESDIS to define temperature from satellite channel radiances. In particular, the fact that if different initialization data sets are used to calculate temperature from identical satellite radiances using the NOAA/NESDIS technique, then the results can differ *dramatically*.

The eradication of the majority of these limitations appear plausible based upon the research conducted within this study. Others, however, require additional study and possibly a change in the analysis approach currently employed by NOAA/NESDIS to calculate temperature from satellite radiances. The most obvious change in the current system signals the need for more rocketsonde data in the upper atmosphere high latitude regions, within the tropics and within the Southern Hemisphere. The addition of a nominal number of additional sites, judicially positioned could mean the difference between accurate retrievals and retrievals that are *severely biased*. Further examination and implementation of the suggestions made throughout this text and in Graves (1986) will result in more reliable and *robust* satellite derived meteorological quantities.

6.0 REFERENCES

Dickinson, R.E., 1969: Theory of planetary wave-zonal flow interaction. J. Atmos. Sci., *26*, 73-81.

Fels, S.B., 1985: Radiative-dynamical interactions in the middle atmosphere. Adv. in Geophys., *28A*, 277-300. J. Atmos. Sci., 38, 2187-2197

Graves.D.S., 1986: Evaluation of satellite sampling of the middle atmosphere using the GFDL SKYHI general circulation model. Ph.D thesis, Princeton University, Princeton, NJ.

Geller,M.A., M.-F. Wu and M.E.Gelman, 1983: Troposphere-stratosphere (surface-55km) monthly winter general circulation statistics for the northern hemisphere - four year averages. J. Atmos. Sci., 40(5), 1334-1352.

Hamilton,K., 1982: Stratospheric circulation statistics. NCAR Tech. Note-191+STR, 174pp.

Labitzke,K. and Collaborators, 1972: Climatology of the stratosphere in the northern hemisphere part I: heights, temperatures and geostrophic resultant wind speeds at 100, 50, 30 and 10mb. Verlag von Dietrich Reimer in Berlin.

Miyahara,S., Y.Hayashi and J.D.Mahlman, 1986: Interactions between gravity waves and planetary scale flow simulated by the "SKYHI" general circulation model. Submitted for publication to J. Atmos. Sci.

Range Reference Atmosphere 0-70km Altitude, 1983. Cape Canaveral, FLA. Meteorology Group, Range Commanders Council, Doc. 361-83, 203pp.

Smith,W.L. and H.M.Woolf,1976: The use of eigenvectors of statistical covariance matrices for interpreting satellite sounding radiometer observations. J. Atmos. Sci., 33(7), 1127-1140.

Weinreb,M.P. and M.L.Hill, 1980: Calculations of atmospheric radiances and brightness temperatures in infrared window channels of satellite radiometers. NOAA Tech. Rep. NESS 80, 40pp.

_____, H.E.Fleming, L.M.McMillin and A.C.Neuendorffer, 1981: Transmittances for the TIROS operational vertical sounder. NOAA TR NESS 85, 60pp.

1.2

A CLIMATOLOGY OF ATMOSPHERIC STABILITY FOR THE TROPICS DERIVED FROM TOVS

Siri Jodha Singh Khalsa
Ellen J. Steiner

Cooperative Institute for Research in Environmental Sciences
University of Colorado
Boulder, Colorado 80309-0449

1. INTRODUCTION

The climatological distribution of deep convection over the tropical oceans has been observed to be approximately coincident with areas of highest sea surface temperature (SST) and with surface wind convergence. The influence of high SST on deep convection is assumed to take place through increased moisture availability and decreased atmospheric stability. Lack of adequate upper-air data over the tropical oceans has made it difficult to verify the role of atmospheric stability in determining the location and intensity of deep convection.

The TIROS Operational Vertical Sounder (TOVS) has provided daily, near-global coverage of atmospheric temperature and moisture since 1979. Although the vertical resolution of TOVS is relatively coarse, we have found that in the tropics the information returned is adequate to estimate the static stability under most conditions (Khalsa and Steiner, 1987a).

Mean monthly values of a stability index (SI) based on TOVS data have been computed for the period 1982 - 1986. A subset of this data is examined and compared with highly reflective cloud (HRC, which is a measure of organized deep convection), and SST for the global tropics. The period 1982-1985 was used to compute means for SI and HRC in order to match the interval for which SST data was available.

2. DATA SETS

2.1 TOVS

The operational TOVS product, as archived by NESDIS, is used for this study. Fifteen values of layer-averaged virtual temperature and 3 values of precipitable water are contained in the data set. Data from individual soundings, up to 16,000 per day, have been extrapolated onto daily 5 x 5° grids for the ±30° tropical strip (for details see Khalsa and Steiner, 1987b).

The suitability of TOVS for determining atmospheric stability in the tropics is discussed in Khalsa and Steiner (1987a). There, through comparisons with *in situ* soundings made in the eastern Pacific, it was shown that it was possible to derive an index that in most cases represented the stability of the atmosphere to deep convection.

This stability index is defined as the difference between the saturated equivalent potential temperature in the 700 - 500 mb layer and the equivalent potential temperature in the 1000 - 850 mb layer:

$$SI = \Theta_{es}(700\text{-}500) - \Theta_{e}(1000\text{-}850) \qquad (1)$$

Since equivalent potential temperature is conserved under moist adiabatic ascent, this difference provides a measure of the buoyant restoring force acting on a low-level parcel when it is lifted to midtroposphere. A negative value means an unstable stratification, i.e. the parcel will continue to rise.

2.2 Sea Surface Temperature

The source of SST for this study is the blended analysis from the Climate Analysis Center. This data set is based on both ship reports and AVHRR determinations of surface temperature.

2.3 Deep Convection

The HRC data set is used as a proxy for deep convection in the tropics. Daily mosaics of POES imagery are subjectively analyzed for evidence of deep convection (Garcia, 1985). Here, HRC will be expressed as number of days per month at a given location. The gridded data exists for the ±25° tropical strip.

3. RESULTS

3.1 January

In Fig. 1 the mean of the stability index for January is contoured for values smaller than 8K. In Fig. 2 the January mean of SST is contoured for values exceeding 27.5° C. In both Figs. 1 and 2 regions of HRC are shown by various densities of shading described in the figure captions. As expected for the northern hemisphere winter, extrema in all three variables occur mostly south of the equator.

Over the oceans HRC occurs almost entirely within the SI = 8 contour (Fig. 1). The region of greatest instability (SI < 0) encompasses most of the over-ocean locations with HRC > 4 days.

SI is usually positive (stable) over continents because TOVS returns relatively low near-surface values of equivalent potential temperature. SI is never found to be smaller than 8 over the African Continent but over the near-equatorial regions of South American low values of SI do occur. We are currently working on refinements in the stability criterion for continental regions.

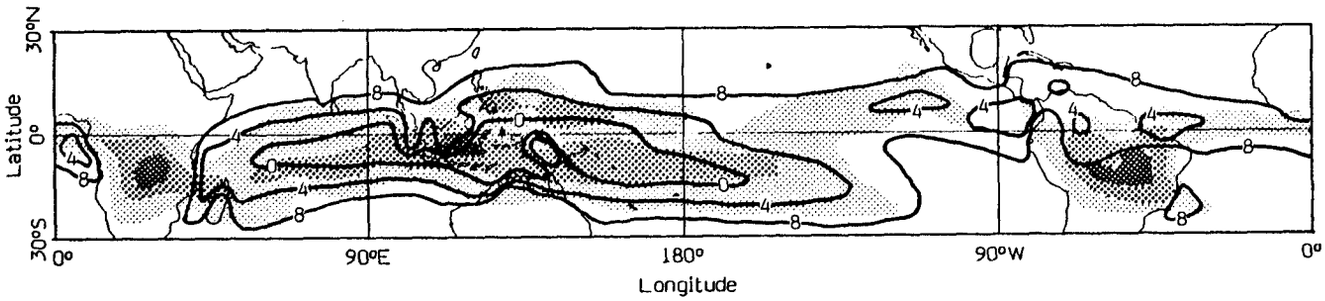

Figure 1. Mean stability index for January 1982-1985, contoured for values less than 8K. Shading indicates presence of highly reflective cloud (HRC): lightest shade, 1-3 days; medium shade [illegible] darkest shade, > 8 days.

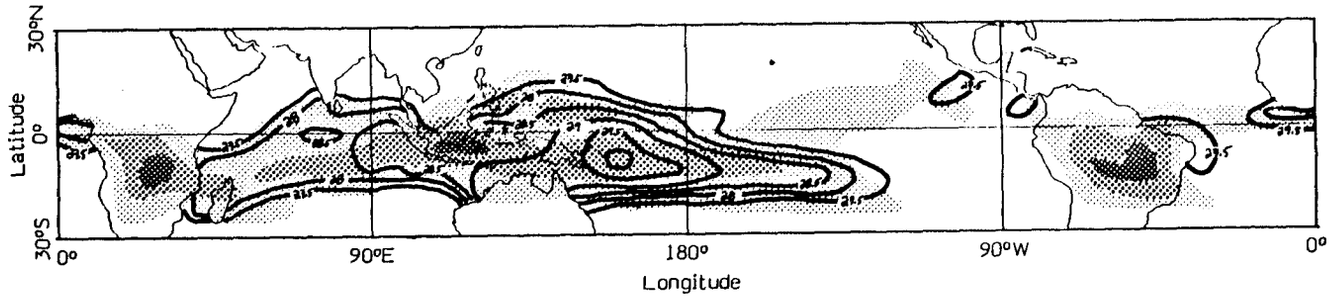

Figure 2. Mean sea surface temperature for January 1982-1985 contoured for values exceeding 27.5°C. Shading indicates presence of HRC as described in Fig. 1.

The 27.5° C isotherm of SST is seen to encompass most of the convection in the central and western Pacific and Indian oceans but misses much of the convection in the near-equatorial convergence zones in the eastern Pacific and Atlantic oceans

3.2 July

Mean conditions for July 1982-1985 show that SI minima, SST and HRC maxima are all concentrated north of the equator with much of the northern subtropics now having low SI (Figs. 3 and 4). There is a large region in the western Pacific and Eastern Indian oceans having SI < -4. Over-ocean HRC now mostly occurs within the SI < 4 contour and HRC > 4 d occur mostly within the SI < 0 contour, as for the January mean case. Regions of HRC > 8 days off the coasts of southern Mexico and Central America occur within the SI < -4 contour. A contour of SI < -4 also extends up towards the Bay of Bengal where HRC > 8 days reflects Indian monsoon convection.

Over-ocean HRC falls almost entirely within the SST > 27.5° C isotherm. The correspondence between higher SST's and regions of HRC > 4 in the eastern Pacific is relatively

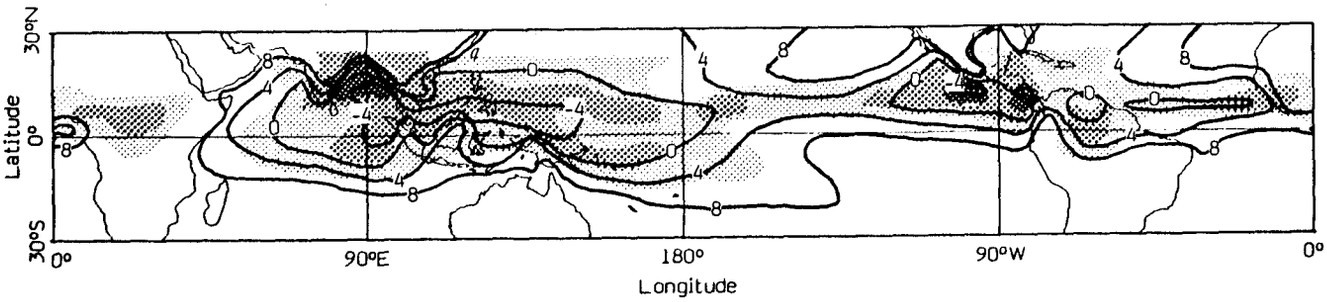

Figure 3. Mean stability index and HRC for July 1982-1985, as described in Fig. 1.

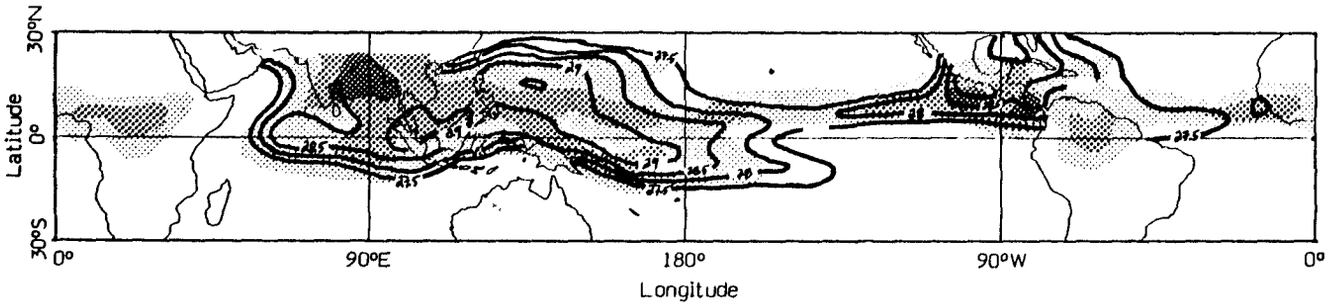

Figure 4. Mean sea surface temperature and HRC for July 1982-1985, as described in Fig. 2

close but elsewhere it is not as good. In particular, the region of warmest water, 29° C, in the western Pacific and Indian oceans encloses only a fraction of the HRC > 4 area whereas SI < 0 encompasses essentially all of it.

3.3 January 1983

In Figs. 5 and 6 conditions for January 1983, near the peak of the strong El Nino event, are shown. Convection is concentrated near and east of the Dateline. The SI < 8 contour encompasses almost all over-ocean HRC. There are only a few small areas of SI < 0, all occurring where HRC > 8 days.

Regions of SST greater than 29° C exist between 90° E and the Dateline and between 125 and 150° W. These warmest waters encompass only a fraction of the area with HRC > 8 days.

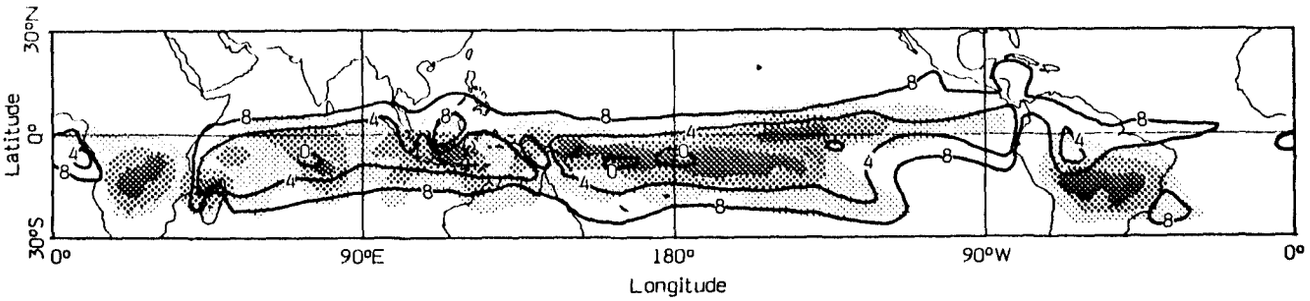

Figure 5. Stability index and HRC for January 1983, as described in Fig. 1.

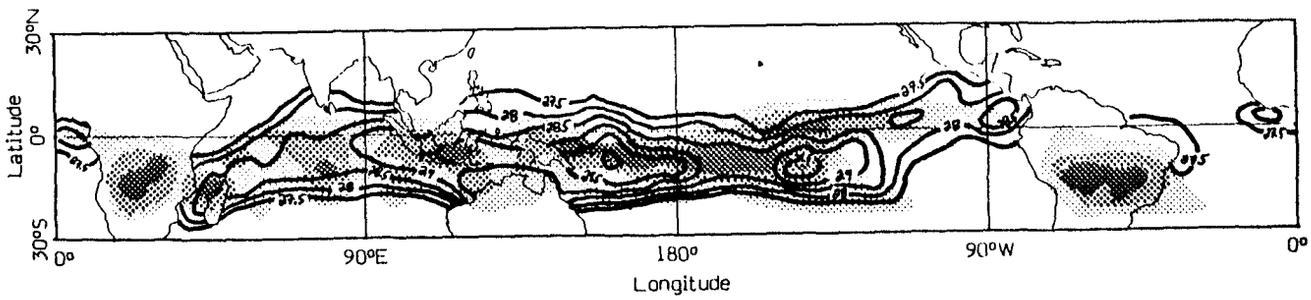

Figure 6. Sea surface temperature and HRC for January 1983, as described in Fig. 2.

4. SUMMARY

In this first examination of atmospheric stability for the entire global tropics, it appears that areas of deep convection occur primarily in those areas with the lowest stability. Although a threshold value of 27.5° C for sea surface temperature appeared to provide an envelope for tropical convection, it was found that often the areas of highest SST did not correspond well with the most intense convection. A similar result was obtained by Steiner and Khalsa (1987). In contrast, the stability index gave both a threshold for HRC and a favored location for highest HRC values corresponding to the lowest stability.

The gross correspondence between SI and SST is relatively high, i.e. low atmospheric stability generally occurs over high sea surface temperatures. This indicates the important role played by surface conditions in determining stability on monthly time scales. On shorter time scales, midtropospheric conditions can have more of an influence. A study of the 30-60 day oscillation in the global tropics has shown that midtropospheric warming can increase stability when low-level conditions remain constant. (Khalsa, Weickmann and Steiner, 1987).

5. REFERENCES

Garcia, O., 1985: *Atlas of highly reflective clouds for the global tropics: 1971-1983*, NOAA/ERL, Boulder, CO, 365pp.

Khalsa, S. J. S., and E. Steiner, 1987a: Vertical structure in the near-equatorial atmosphere from the TIROS Operational Vertical Sounders (TOVS). Extended Abstracts, *17th Conf. on Hurricanes and Tropical Meteorology*, Miami, FL, April 7-10, 1987. Amer. Meteor. Soc., Boston, MA, 137-141.

Khalsa, S. J. S., and E. Steiner, 1987b: A TOVS data set for the study of low-latitude ocean-atmosphere interaction. submitted to *J. Climate Appl. Meteorol.*

Khalsa, S. J. S., K. M. Weickmann, and E. Steiner, 1987: Thermodynamical aspects of the 30-60 day oscillation in the global tropics. Proc. *Twelfth Annual Climate Diagnostics Workshop*, Salt Lake City, UT, Oct. 12-16, 1987. NOAA/NMC/Climate Analysis Center, Washington D. C., (in press).

Steiner, E. J., and S. J. S. Khalsa, 1987: Sea surface temperature, low-level moisture, and convection in the tropical Pacific, 1982-1985. *J. Geophys. Res., 92*, (in press).

RETRIEVAL OF AIR SURFACE TEMPERATURES OVER OCEANS FROM SATELLITE RADIANCE MEASUREMENTS USING STRATIFICATION TECHNIQUES

Larry M. McMillin

National Oceanic and Atmospheric Administration
National Environmental Satellite, Data, and Information Service
Satellite Research Laboratory
Washington, D.C. 20233

1. INTRODUCTION

Most retrieval algorithms used to convert satellite based measurements of atmospheric radiance to temperature are based on linear models. Linear models work well in the middle of the atmosphere where the lapse rate is fairly constant over large height intervals. However, linear approaches have difficulty producing accurate results near the surface and the tropopause where the temperature profile may have a local maximum or minimum. In the past several years, several authors have investigated various classification (stratification) approaches to producing temperature soundings. Uddstrom and Wark (1985), Wark (1986), and Thompson (1985) investigated various approaches with simulated data, and McMillin (1985 & 1986) has evaluated classification approaches based on actual measurements. In a related paper, Thompson et al. (1987) discuss the distinction between a problem that is ill-posed in a mathematical sense and one that is ill-posed in a practical sense. They demonstrated that although many mathematical functions can be added to a profile to produce different atmospheric profiles with the same radiances, in practice, profiles producing the same radiance are unique, because many of the mathematical perturbations produce layers that are extremely superadiabatic or otherwise physically impossible. Results based on both simulated and actual measurements demonstrate that the classification technique produces substantial increases in retrieval accuracy over the current operational retrieval method used by the National Environmental Satellite, Data, and Information Service (NESDIS).

Atmospheric measurements on the current NESDIS polar satellites are made with the TIROS Operational Vertical Temperature Sounder (TOVS), which consists of three separate instruments. The High resolution Infrared Radiation Sounder is a twenty channel instrument to sound the lower atmosphere. Channels 1-7 use the 15 μm region of the spectrum to sense atmospheric temperature, channel 8 uses the 10-12 μm window region region to sense the surface temperature, and channels 10-12 are used to sense water vapor. These 12 channels are all in the infrared region of the spectrum. Channels 13-19 form a second set of sounding channels in the near infrared region that is particularly useful for measuring temperatures near the ground. Channels 13-17 respond to the atmospheric temperature while channels 18 and 19 respond to the surface temperature. In this study, only channels 13-15 were used since channels 18 and 19 essentially duplicate the information given by channel 8. Channel 17 is affected by stimulated emission and it is difficult to relate the value of this channel to an atmospheric temperature in day light.

The Microwave Sounding Unit (MSU) is a 4 channel sounder. While the infrared measurements are affected by clouds, measurements in the infrared region penetrate many clouds, giving the microwave channels an advantage in cloudy areas. Channels 22-24 sense atmospheric temperature in the microwave region, and channel 21 senses the surface radiance. One of the disadvantages of the microwave measurements is that the surface emissivity is more variable than it is in the infrared.

The Stratospheric Sounding Unit (SSU) is an instrument designed to measure the upper atmosphere. The measurements of this instrument are not relevant to the topic covered in this paper.

One of the problems associated with the use of atmospheric radiances is the lack of vertical resolution. The radiance for a particular channel represents a weighted average temperature over some region of the atmosphere. The width of the region is determined by the physics of atmosphere and the technology used to limit the bandpass of the channel. With the filter instruments used on the TIROS Operational Vertical Sounder (TOVS), it is difficult to obtain sufficient resolution to resolve features such as surface inversions. As an example, a sample of 1921 profiles had 367 profiles for which the lapse rate between 1000 and 950 hPa had an inversion. In the same sample, channel 10 had a lower brightness temperature than channel 8, the surface channel, 62 times, channel 13 was lower only 10 times, and channel 7 was lower only 1 time. The one channel that frequently responds to the inversion is channel 10.

It is difficult to use channel 10 to infer temperature in a conventional retrieval method because the concentration of the water vapor has to be known. Water vapor concentrations can be

highly variable. However, a classification approach does not depend on knowledge of the concentration. Because there is such a large correlation between atmospheric moisture and temperature, a classification approach can use the temperature information in the moisture channel in a non-linear way to obtain temperature information about the surface layers.

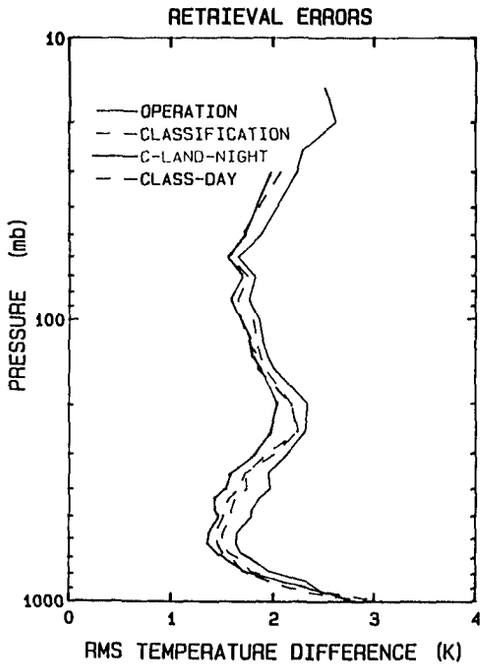

Fig. 1. Retrieval accuracies for the operational approach, a single classification, and a classification separated into land night (inversion) and all other cases (lapse).

2. APPROACH

Work on classification approaches in NESDIS started with the work of Uddstrom and Wark (1985) which was done in the early 80's. In this paper, the authors discussed the results of using typical shape functions to classify the atmosphere. The results were based on simulated data. Later, Wark (1986) discussed the results of using an eigenvector approach for the classification on simulated data. McMillin (1985) discussed the results of using the typical shape function approach on real measurements. As a result of these studies, it was decided to use the eigenvector approach suggested by Wark (1986). Although the distinction may be somewhat obscure in many cases, the typical shape function approach is a clustering method. With the switch to eigenvectors, the approach switched from one of putting data into clusters to one of stratifying the data into groups that are evenly spaced over the range. In the stratification, an attempt is made to make the groups far enough apart to be distinct, yet close enough together that the distance from any sounding to its appropriate mean will always be small. In a strict clustering approach, it is possible for a sounding to be far from any group, and the sounding will be made with a poor first guess. Although cases far from a cluster are rare, the rare cases are weather and the common cases are climatology. The results of applying the eigenvector stratification method to real data are given by McMillin (1986).

After 1986, the method was refined by separating the retrievals into two groups, one containing the ocean cases and the day cases over land; and one containing the night cases over land. The separation was made on the assumption that soundings in the first group would have lapse conditions near the ground and that soundings in the second group would have inversions. Figure 1 compares the accuracies of the operational NESDIS soundings, stratification without the separation into expected lapse groups, and stratification with the separation. There is a definite advantage to doing the separation. Even though the increase in accuracy resulting from the separation is substantial (0.3 to 0.4 K throughout most of the atmosphere), it is more appealing to detect the lapse conditions from a more direct indicator such as the radiance data.

Uddstrom and Wark (1985) showed the value of subtracting a mean profile temperature before attempting a classification (stratification). In the case of the eigenvector approach, the eigenvectors are then free to capture the shape of the profile without being affected by temperature shifts. For the surface, channels 4-8, 10-15, and 22 were selected to be used for the stratification, and channels 5-8, 10-15, and 22 were averaged and subtracted.

The eigenvectors of the covariance matrix of channels 4-8, 10-15, and 22 were calculated. Coefficients of the eigenvectors associated with the four largest eigenvalues were calculated for the dependent data set, and the maximum and minimum of each was found and used to determine the range. Each eigenvector range was then divided into a number of groups, and the boundaries of these groups were calculated and saved. For each group, the mean value of the brightness temperatures and the temperatures were then calculated. When a retrieval is done, the brightness temperatures of the selected channels are averaged for that profile and then the average is subtracted from the vector of observed radiances to calculate a selection vector. The eigenvector coefficients of the selection vector are then calculated and compared with the group boundaries to determine the class. Then the mean brightness temperature and temperature for that class are used as the first step in the retrieval process.

3. TEST PROCEDURE

The method was evaluated on a sample of satellite measurements that were collocated with radiosondes. In the collocation, the satellite soundings were required to be within ± 6 hours of the radiosonde and within a distance that varies with latitude zone because the of the varying number of radiosondes present. The distances ranged up to 3° of latitude in data sparse areas near the South Pole, but 1° is typical. In addition, where possible, two radiosondes twelve hours apart were averaged to the time of the satellite observation.

Measurements from all latitude zones were included in the data set. Coefficients and initial results were generated from data collected in the May of 1987. Tests are being run on data collected in August and September.

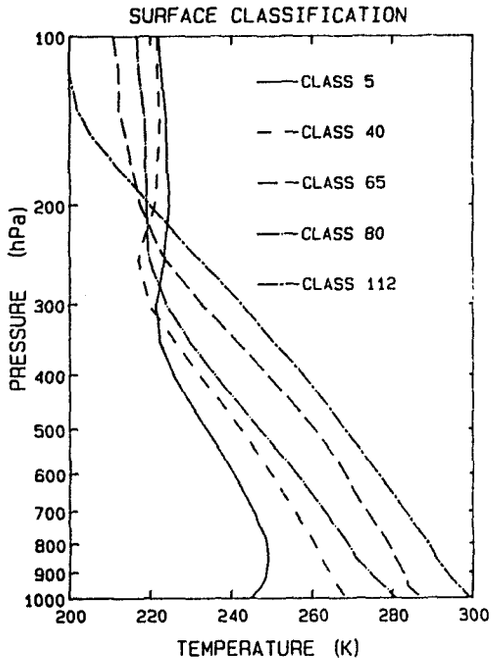

Fig. 2. Mean profiles of selected classes.

4. RESULTS

The evaluation of the method progressed in two stages. In the first stage, the mean radiosonde profiles for the classes were examined. As the class number increased, the profiles progressed from a lapse condition to an inversion condition. Figure 2 shows the mean profiles for selected classes. As expected, the classes tend to follow the gross structure changes associated with the change from tropical to polar cases. This is shown by the progression of the profiles from cold to warm near the surface with increasing class number. Note, however, that class 80 occurs before class 65. This is due to the difference in lapse rate at the surface.

In the second stage, temperature retrievals were obtained for the classes. A covariance matrix was constructed by using the eigenvector coefficients to identify the class for a given profile and subtracting the class mean from the profile. The resulting deviations were treated as a single sample to calculate a single covariance matrix covering all classes. Regression coefficients were then generated to relate retrieved temperatures to the observed radiances using the procedure described in McMillin (1986). Figure 3. shows the results of the stratification retrieval. In contrast to the method used in Fig. 1, this stratification was optimized for the surface and shows a substantial increase in accuracy over the operation from 600 hPa to the surface. As expected, the accuracy of the stratified result was not as good in the upper atmosphere. However, a retrieval based on the surface stratification for layers near the surface and the atmospheric stratification for other layers would provide the best of both results. Ideally, the mixing of the two stratifications would be a smooth function of height.

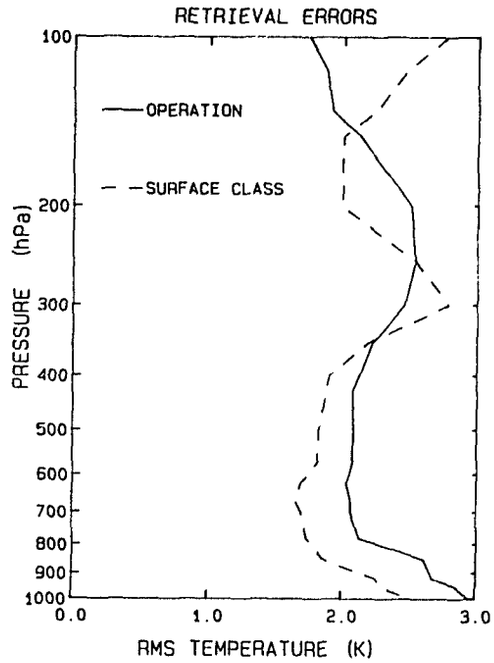

Fig. 3. Retrieval accuracies for the operational approach and stratification optimized for the surface.

5. REFERENCES

McMillin, L.M., 1985: The use of typical shape functions of radiance vectors in satellite retrievals. Advances in Remote Sensing Retrieval Methods (eds. A.Deepak, H.Fleming&M.Chahine), A. Deepak Publishing, Hampton, Va.

McMillin, L.M., 1986: The use of classification procedures to improve the accuracy of satellite soundings of temperature and moisture. Second Conference on Satellite Meteorology/Remote Sensing and Applications, Williamsburg, Va., 1-4.

Thompson, O.E., M.D. Goldberg, and D.A. Dazlich, 1985: pattern recognition in the satellite temperature problem. J. Climate & Appl. Meteor., 24, 30-48.

Thompson, O.E., D.D. Dazlich, and Yu-Tai Hou, 1986; The Ill-posed Nature of the Satellite Temperature Retrieval Problem and the Limits of Retrievability, J. Atmos. Oceanic Technol., 3, 643-649.

Uddstrom, M.J., and D.Q. Wark, 1985: A classification scheme for satellite temperature retrievals. J. Climate & Appl. Meteor., 24,16-29.

Wark, D.Q., 1986: Temperature profiles derived from a restricted range of solutions using satellite measurements. Advances in Remote Sensing Retrieval Methods (eds. A.Deepak, H.Fleming & M.Chahine), A. Deepak Publishing, Hampton, Va.

A METHOD OF NOISE REDUCTION FOR THE IMPROVEMENT OF CLEAR COLUMN RADIANCE ESTIMATION IN PARTLY CLOUDY AREAS

Anand Swaroop, Andrew J. Nappi and Hal J. Bloom

ST Systems Corporation (STX)
4400 Forbes Blvd., Lanham, MD 20706

Larry M. McMillin

NOAA/NESDIS
Washington, D.C. 20233

1. INTRODUCTION

Atmospheric temperature profiles are retrieved operationally from TIROS-N Operational Vertical Sounder (TOVS) radiances in all atmospheres - clear, partly cloudy and overcast, at NOAA/NESDIS (Smith, et al. 1979). The TOVS consists of three instruments; a High-resolution Infrared Radiation Sounder Version 2 (HIRS/2), a Microwave Sounding Unit (MSU), and a Stratospheric Sounding Unit (SSU). The HIRS instrument has 20 channels and measures the upwelling thermal energy in the infrared region of the spectrum. The infrared radiances from HIRS are contaminated by the presence of clouds and pose a serious problem in retrieving temperature profiles in partially cloudy and overcast regions. In regions of partial cloudiness, the infrared radiances are corrected for the cloud contamination through use of the adjacent pair technique (Smith, 1968, McMillin, 1978). This approach is also known as the N* technique. Multiple level cloudiness, along with noise in the sample of radiance data, introduce sources of error into the cloud-clearing procedure. Since cloud cleared radiances are treated as clear radiances by the statistical regression based retrieval algorithm, the residual errors in cloud cleared radiances result in less accurate retrievals in partly cloudy areas than in clear areas. There have been considerable efforts directed towards refining the cloud-clearing procedure. Operationally, screening for multiple level clouds is done in an attempt to produce a consistent sample of data from which to compute N* and to subsequently correct the partially cloudy radiances. This screening procedure doesn't remove all cases of multiple level cloudiness, however. Additionally, enough noise remains in the samples to adversely affect retrieval accuracy. This paper describes a method being developed for reducing residual noise in radiances and for providing the improved cloud cleared radiances.

2. REVIEW OF CURRENT CLOUD-CLEARING PROCEDURE

The current operational cloud clearing approach utilizes adjacent radiance measurements in a retrieval area comprised of 9 Fields of View (FOVs). The concept of N*, which is essentially a ratio of cloud amounts, N_1 and N_2, at two adjacent FOVs, is introduced and is defined as:

$$N^* = \frac{N_1}{N_2} = \frac{I(\nu,1) - I(\nu,c)}{I(\nu,2) - I(\nu,c)} \quad \text{where} \qquad (1)$$

$I(\nu,c)$ is the clear radiance at wavenumber ν,
$I(\nu,1)$ and $I(\nu,2)$ are radiance measurements for two adjacent FOVs within the area of observation

The assumption is made that N* is independent of wavenumber so that once N* is obtained for one channel, it can be applied to radiances of all the other infrared channels via equation 1, to estimate clear column radiances as follows:

$$I(\nu,c) = [N^* I(\nu,2) - I(\nu,1)]/(N^*-1) \qquad (2)$$

Before N* can be used to correct for all other channel radiances, the non-trivial problem of initially computing N* for one channel must be solved. The method used in TOVS is based on the adjacent pair technique in which two FOVs in a sounding area are used and N* values are derived from interchannel regression relationships as detailed by McMillin and Dean (1982). Two separate calculations of N* are performed and are compared for consistency. First, an N* value using only HIRS data is computed. A regression scheme is used to predict the 4.3 micron channel radiance from the measured radiances in the 15 micron band channels. Neither observation is cloud-free but the radiances in these two regions respond differently to clouds. The HIRS channels 6, 7, 8 and 10 are used to predict HIRS channel 13. An iterative method described by McMillin and Dean (1982) is used in deriving the N* value. A second N* value based upon Microwave Sounding Unit (MSU) data for the same sounding area is computed. A cloudy microwave pseudo-radiance for MSU channel 2 (53.74 GHz), scaled to HIRS channel 6 wavenumber, is calculated via regression utilizing the cloud contaminated HIRS channels 5, 6, 7 and 8 radiances. An equivalent clear radiance value for HIRS channel 6 is obtained by converting observed radiances for MSU channel 2 since microwave radiances are essentially unaffected by clouds. These two estimates of N* are compared and averaged together where consistent. Once N* is calculated, it is a fairly straight-forward technique to produce the clear column radiances for the remaining HIRS channels.

The cloud-clearing algorithm assumes that clear and cloudy radiances are uniform over the area covered by the FOVs used to calculate an N* value and are linearly related to cloud amounts. A change from the original TOVS Operational Processing System to Enhanced TOVS System in 1986 (Swaroop, et al., 1985, Reale, et al. 1986) caused this assumption to be less valid. The original system produced an average N* value from screened pairs of adjacent FOVs in a large area (63 FOVs). This allowed for greater consistency in the N* process. The Enhanced System, however, produces N* values for much smaller FOV areas, thereby losing much of the consistency of the earlier system. Cloud height and amount may vary dramatically in these areas, causing partly cloudy radiances to change greatly within one retrieval region. This adds noise to the procedure. The upgraded N* algorithm attempts to compensate for these effects.

3. THE UPGRADED N* ALGORITHM

The upgrades to the N* algorithm include improved radiance screening procedures to remove multiple level cloud effects and the use of averaging techniques to reduce noise. The adjacent pair technique is replaced by the use of two radiance measurements representative of the sounding area. Despite these changes, techniques used in the actual cloud-clearing process are retained by the new algorithm. The HIRS and MSU based N* values are calculated via the same relationships outlined in Section 2, and the clear radiances are produced using the N* values in the same general manner as in the operational algorithm.

The screening technique for removal of multiple level clouds is accomplished in the following manner: Two channels whose weighting functions peak close to the surface are selected. The radiances for one channel for all 63 FOVs representing a large sounding area are ordered from lowest to highest as illustrated in Figure 1. Radiances for the second channel are examined and if for any FOV, the second channel radiances are not in the same order as the first channel, then that FOV is discarded. The selection is done so that the FOVs corresponding to the highest clouds remain. This examination process is repeated for all the FOVs and FOVs are discarded until a monotonic sample is attained. Figure 2 represents the screened subset of points which were presented in Figure 1. Addition of this strict screening procedure further removes the FOVs with multiple level clouds whose radiances are not linearly related with other FOVs.

The use of an averaging technique to remove noise from the sample represents a return to the concept of using differences of averaged radiances in a sounding area to compute N*. This replaces the current operational approach which utilizes the average of differences of adjacent FOVs. The method of using averaged radiances is correct for single level clouds (Smith, 1967) but will be in error for multiple level clouds. For this reason, it is important to include the previously described screening of multiple level clouds along with the averaging technique to produce an accurate estimate of N* and clear radiances. The averaging approach has been shown to produce very accurate results in the upper troposphere (Susskind et al. 1984). The adjacent pair technique, in the absence of multiple level clouds, produces accurate results in the lower troposphere. The new algorithm attempts to combine the best portions of both approaches.

The averaging technique utilizes the monotonic sample FOVs to generate a least squares line fit for the two selected channel radiances. The outliers are then rejected to reduce the noise and establish high correlation between two selected channels. The remaining monotonic sample FOVs are also used to derive least squares lines for all the infrared channels relative to HIRS channel 7. The slope and the intercept of the line are used along with the highest and lowest radiances from HIRS channel 7 to derive the highest and lowest radiances in the area for all the other HIRS channels. These highest and lowest radiances replace the adjacent spots in the operational technique to compute the N*. Since the line fitting technique requires the screened sample of the 63 FOV sounding area, but the retrievals are produced on the 9 FOV sub-area, the highest and lowest radiances for the 9 FOV region must be obtained. In practice, a predicted highest radiance for the 63 FOV area is obtained via a regression scheme using radiances from HIRS channels 1, 2 and 3 and MSU channels 2, 3 and 4, which are all relatively cloud-free. The difference between the predicted highest radiance and the actual high radiance is assumed to be constant over the 63 FOV area and is used as an offset in estimating highest radiance for the 9 FOV areas. Once the high and low spots are obtained, the method of computing the clear column radiance is essentially the same as the current operational method.

4. RESULTS

Testing of this algorithm on a few test cases has shown improvements over the operational method. Generally, the new method produces fewer partly cloudy soundings than the operational method does. The rejected data are classified as cloudy. The actual decrease in partly cloudy soundings is sensitive to the tightness of the screening procedure and noise reduction. For example, the correlation coefficient limit of the least squares line was tightened from 0.90 to 0.99 in one set of experiments. The resulting decrease in N* soundings was on the order of 5-8%. Testing is continuing to select the optimal level of screening. Some case study results comparing the operational and new algorithm are presented below. Since clear retrievals are the highest quality TOVS soundings and the purpose of a cloud clearing technique is to approximate clear radiances, clear and partly cloudy retrievals in the same general area should be similar. One means of evaluating the results, therefore, is by analyzing the differences between the clear and partly cloudy soundings from

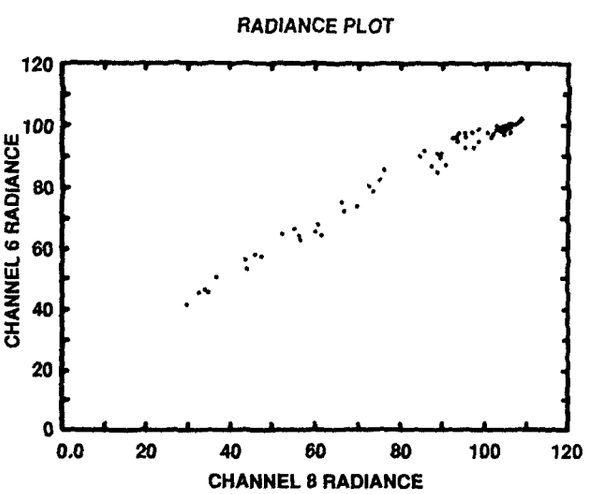

Fig. 1. The HIRS channel 6 radiance against HIRS channel 8 radiance plot for all 63 FOVs.

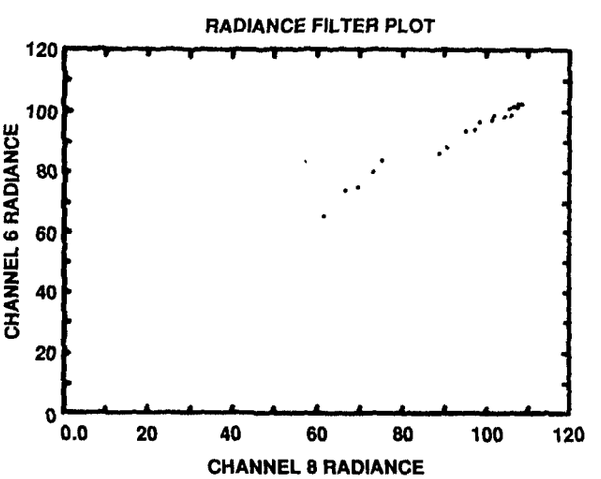

Fig. 2. The HIRS channel 6 radiance against HIRS channel 8 radiance plot for the remaining monotonic FOVs.

both the operational and the new techniques. Figure 3 shows plotted 850 mb retrieval temperature values. The partly cloudy retrievals from the operational and the new algorithm are shown respectively within square brackets and parentheses. Remaining values show clear soundings. Inspection of the data reveals that generally the new algorithm appears to be producing a less noisy, more accurate sample of partly cloudy retrievals which are in better agreement with the clear retrievals. Significant improvements of 5 degrees or more are noted at locations A and B with improvements of 0.4 to 1.0 degrees at locations C, D, E and F. No appreciable improvements, or very slight degradations are found only at locations G, H and I. The improvements made are significant and further tuning of the algorithm should lead to additional improvement.

5. SUMMARY

A new method for noise reduction and elimination of multiple level cloud effects on partly cloudy radiances has been developed. Retrievals made with this algorithm in partly cloudy regions are shown to be more consistent and in better agreement with the clear retrievals than operational partly cloudy retrievals are. Some partly cloudy radiances produced by the current system prove to be too noisy to be accepted by the new algorithm and are screened out and called cloudy

6. ACKNOWLEDGEMENTS

The authors which to acknowledge Mr. Charles Novak and Mr. Michael Chalfant of NOAA/NESDIS for their support for this effort. The authors also wish to thank Ms. Christine Mitchell for typing the manuscript and Ms. Lisa Markel and Ms. Jennifer Forman for drafting the figures.

7. REFERENCES

McMillin, L.M., 1978: An improved technique for obtaining clear column radiances from cloud-contaminated radiances. Monthly Weather Review, 106, 1590-1597.

McMillin, L.M., and C. Dean, 1982: Evaluation of a new operational technique for producing clear radiances. Journal of Applied Meteorology, 21, 1005-1014.

McMillin, L.M. and Nappi, A., 1986: Some modifications to the NESDIS operational clear column radiance procedure, The Third International TOVS Study Conference, Madison, WI, pp. 160-172.

Reale, A.L., D.G. Gray, M.W. Chalfant, A. Swaroop and A. Nappi, 1986: Higher resolutional operational satellite retrievals. Second Conference on Satellite Meteorology/Remote Sensing and Applications, Williamsburg, VA, May 13-16, 1986.

Smith, W.L., 1968: An improved method for calculating tropospheric temperature and moisture from satellite radiometer measurements. Monthly Weather Review, 96, 387-396.

Smith, W., H. Woolf, C. Hayden, D. Wark, and L. McMillin, 1979: The TIROS-N operational vertical sounder. Bulletin of the American Meteorological Society, 60, 1177-1187.

Susskind, J., J. Rosenfield, D. Reuter, and M.T. Chahine, 1984: Remote sensing of weather and climate parameters from HIRS/MSU on TIROS-N, J. of Geophys. Res., 89, 4677-4679.

Swaroop, A., A. Nappi, Z. Ahmad, M. Chalfant and L.M. McMillin, 1985: Enhanced soundings over oceans from NOAA-9 polar orbiting satellite. MTS/IEEE Conference and Exposition, "Oceans 85", San Diego, CA, Nov. 12-14, 1985, pp. 333-338.

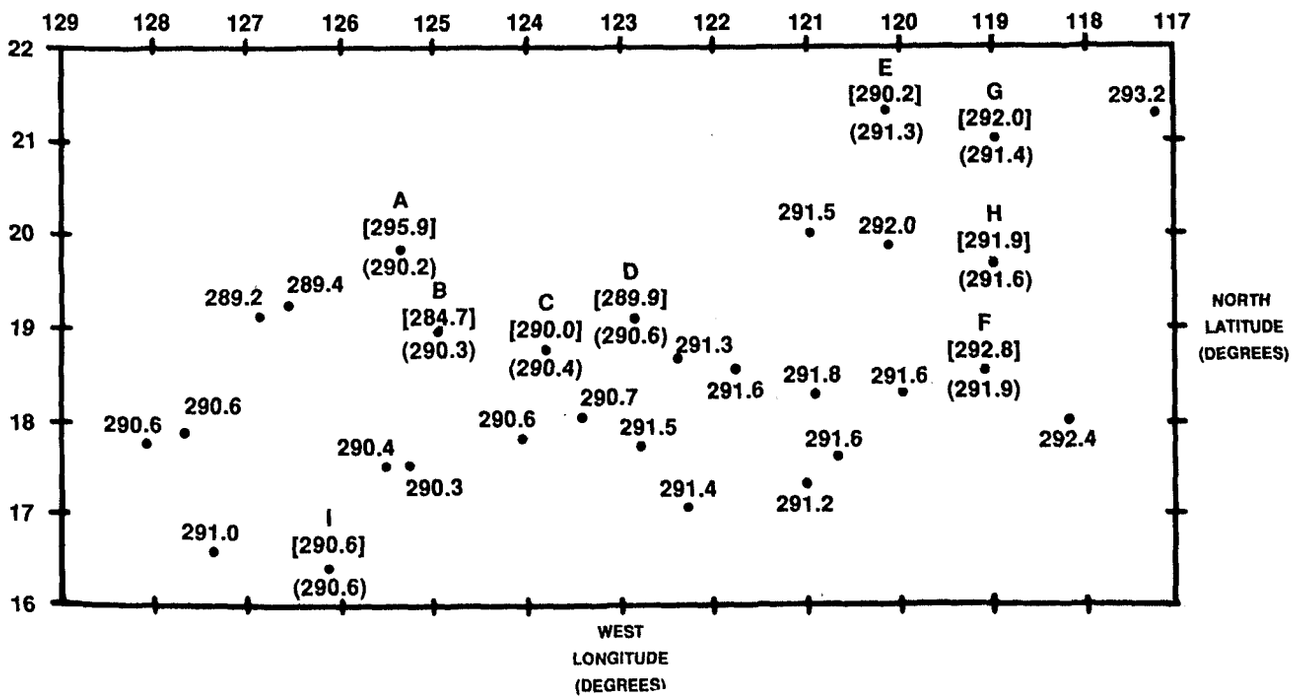

Fig. 3. The retrieved 850 mb. temperatures for clear and partly cloudy conditions. The partly cloudy temperatures from the operational and new algorithm are shown within square brackets and parenthesis respectively.

OPERATIONAL IMPLEMENTATION OF THE MINIMUM VARIANCE SIMULTANEOUS RETRIEVAL METHOD

Henry E. Fleming
National Oceanic and Atmospheric Administration
National Environmental Satellite, Data, and Information Service
Satellite Research Laboratory
Washington, D.C. 20233

Mitchell D. Goldberg
ST Systems Corporation
Lanham, Maryland 20706

David S. Crosby*
The American University
Washington, D.C. 20016
(*Also affiliated with NOAA/NESDIS, Washington, D.C. 20233)

1. INTRODUCTION

At the Second Conference on Satellite Meteorology and Oceanography, we presented a paper by Fleming, et al. (1986b) that described an algorithm for the simultaneous retrieval of temperature and moisture from satellite radiance measurements. Here we are concerned with the practical implementation of that algorithm in an operational setting in which large volumes of satellite data must be processed almost in real time. Major changes to the original algorithm are required in order to satisfy these operational constraints.

The changes include linearization of the operator to eliminate the iterations required by the original nonlinear operator, operator scaling to compensate for the linearization, an improved initial approximation to the solution, and the transference of certain computations done online to an offline procedure. Details of these changes are presented in the next six sections. In Section 8, results are presented which compare retrieval accuracies of the new linearized minimum variance simultaneous (MVS) retrieval system with those of the original nonlinear MVS retrieval system. A summary and conclusions are given in the ninth, and final, section.

2. THE TUNING SETS

The minimum variance simultaneous (MVS) retrieval system is a so-called "physical" retrieval method in that it is derived from the physical model of the radiative transfer equation. This is in contrast to statistical retrieval methods, such as regression, which rely on compilations of matched data. The matched data are radiosonde temperature and moisture profiles matched in place and time with the radiances measured by satellite. While such data sets are not needed in theory by physical retrieval methods, this is not true in practice. Because certain physical parameters, such as spectral line parameters, that enter into the physical model are not known with complete accuracy, small matched data sets are needed to correct (i.e., tune) for these uncertainties. Hence, these data sets are known as "tuning sets". A tuning set is much smaller than the matched data sets required by statistical retrieval methods. It is compiled from high quality radiosonde data and cloud-free radiance data which are selected to be representative of, and well distributed within, a specific latitudinal and longitudinal sector, a land or sea category, and a season (actually a period of several weeks). On the other hand, if air mass classification is used, these categories are replaced by air mass classes. Just how these sets are used for tuning is explained in detail in Fleming, et al. (1986a). Here we have additional uses for them, which are explained subsequently.

3. LINEARIZATION OF THE OPERATOR

The solution vector of the minimum variance simultaneous (MVS) retrieval method is of the form

$$V = [T_1, \ldots, T_t, T_s, Q_1, \ldots, Q_q]^T \qquad (1)$$

where the vector elements T and Q represent temperature and water vapor mixing ratio, respectively, the superscript T indicates vector transpose, and the subscripts t and q represent, respectfully, the number of temperature and mixing ratio elements in V, but the subscript s represents the surface. The number of elements in V is

$$m = t + q + 1 \; . \qquad (2)$$

The nonlinear operator C for the MVS retrieval method is of the form

$$C = SA^T(ASA^T + N)^{-1} \qquad (3)$$

where "-1" denotes the matrix inverse, S is the covariance matrix of the vector V whose dimensions are mxm, A is the matrix of weighting functions with dimensions nxm (n is the number of channels), and N is the system noise covariance matrix whose dimensions are nxn. Covariance

matrix S is a block matrix with three principal submatrices having dimensions txt, 1x1, and qxq, respectively. The matrix A also is in block form, but is a row of three submatrices of dimension nxt, nx1, and nxq, respectively. For a complete description of S, including the off-diagonal submatrices, and A see Fleming, et al. (1986b).

In its complete and correct form, the matrix operator C is nonlinear because the matrix A, and hence C, depends on the solution vector V. The usual method for treating such a problem is to evaluate A for some initial solution vector V_0, insert A in (3), use (3) to solve for V_1, and repeat the process by iteratively evaluating A (and hence C) for V_k and solving for V_k+1. However, this procedure is computationally too time consuming for our operational setting. To get around this difficulty, we linearize the operator C as follows.

Using the temperature/moisture profile vectors from the tuning set for a given latitudinal and longitudinal sector, land/sea category, and season described in Section 2, we evaluate a separate, nonlinear matrix A for each individual profile vector in the set. This produces a set of individual matrices A_i which yield the single average matrix A, i.e.,

$$\bar{A} = (1/I)\sum_{i=1}^{I} A_i \tag{4}$$

Then by applying the matrix $\bar{A}$ to (3), one obtains the linearized operator $\bar{C}$, given explicitly by

$$\bar{C} = S\bar{A}^T(\bar{A}S\bar{A}^T + N)^{-1} \tag{5}$$

This operator is used operationally to retrieve the solution vector V, i.e.,

$$V = \bar{V} + \bar{C}(T^* - \bar{T}^*) \tag{6}$$

where T^* is the satellite-measured brightness temperature and $\bar{V}$ and $\bar{T}^*$ are the initial temperature/moisture and brightness temperature vectors, respectively, which are vector averages from the tuning set as per Fleming, et al. (1986a).

4. OPERATOR SCALING AND VECTOR DISPLACEMENT

Equations (5) and (6) are not quite correct as given because of scaling and displacement factors which arise from the fact that the exact matrix A, denoted A[V] to indicate dependence upon V, has been replaced by an approximate (average) one. In other words, the nonlinear matrix form of the radiative transfer equation is

$$A[V]\ V = T^* \tag{7}$$

but the linearized form is

$$\bar{A}V = \hat{T}^* \tag{8}$$

where $\hat{T}^*$ differs from the brightness temperature T^* because of averaging. A successful approach to compensating for the discrepancy between the two brightness temperatures is by the following operator scaling and vector displacement procedure.

It turns out that T^* and $\hat{T}^*$ are, to a first approximation, linearly related, i.e.,

$$T^* = a\ \hat{T}^* + b \tag{9}$$

where the slopes a and the intercepts b are determined by a least squares fit. The variables T^* and $\hat{T}^*$ are obtained by using the appropriate tuning set in eqs. (7) and (8). Of course, coefficients a and b are functions of channel as well as of the tuning set. Consequently, if (5) and (6) are rederived using (9), they become, respectively,

$$\bar{C} = S\bar{A}^TD(D\bar{A}S\bar{A}^TD + N)^{-1} \tag{10}$$

and

$$V = \bar{V} + \bar{C}(T^* - \bar{T}^* - B) \tag{11}$$

where D is a diagonal matrix of the form $D = \mathrm{diag}(a_1, \ldots, a_n)$ and B is a vector of the form $B = [b_1, \ldots, b_n]^T$. Retrievals are calculated using (10) and (11), not (5) and (6).

5. IMPROVED INITIAL APPROXIMATIONS

So far we have concentrated on improving the efficiency of the operational MVS retrieval method, but we also have improved the retrieval accuracy. This was accomplished by improving the initial approximations used in (11) by implementing the so-called "library search technique", which is described next.

Reduced to its essentials, the library search technique is one in which the given brightness temperature vector T^* used to do a specific retrieval is compared with every brightness temperature vector in each of the tuning sets. The twenty such vectors that are closest to the given T^* are saved and averaged. (A weighted vector norm is used as the measure of closeness.) The resulting average brightness temperature vector is used for $\bar{T}^*$ in (11). Then the twenty radiosonde profile vectors V corresponding to the twenty averaged brightness temperature vectors also are averaged. This second average vector is used for $\bar{V}$ in (11).

In practice the number twenty is found to be a good compromise between having enough vectors to average out noise and anomalous structures, and not having too many so that the accuracy and fine structure of a good first approximation are washed out. A comprehensive discussion of the library search procedure and results are presented in a companion paper of this Preprint Volume by Goldberg, et al. (1988). Both the improved initial approximations of the library search technique and the linearization of the operator described in Sections 3 and 4 are used in the MVS retrieval method to meet operational time schedule and accuracy requirements.

6. OFFLINE PROCEDURES

The operator linearization technique described above permits us to transfer much of the computational burden from online to an offline procedure, thereby allowing us to better meet operational processing time requirements. Central to the offline procedures are the matched tuning data sets, which are called "bins" in the offline mode. At all times there are available 27 such bins organized as follows. There are nine latitudinal belts (90-60N, 60-45N, 45-30N,

30-15N, 15N-15S, 15-30S, 30-45S, 45-60S, 60-90S) times the three categories of LAND/DAY, LAND/NIGHT, and SEA/DAY&NIGHT for a total of 27 bins. None of the data are are older than three weeks.

The bulk of the offline work is in compiling the bin data. The remaining steps of the offline procedures are as follows:

1. Generate the individual weighting function matrices A based on the data in each bin.
2. Average the $\underline{A}$ matrices in each bin to obtain an average $\bar{A}$ for each bin.
3. Determine the elements of the matrix D and vector B by least squares from the bin data.
4. Select the proper covariance matrix S for each bin. They have been precalculated from climatological data and stored.
5. Assemble the matrix components $S\bar{A}^TD$ and $D\bar{A}S\bar{A}^TD$.

Note that the complete matrix operator $\bar{C}$ cannot be assembled offline because if a channel fails on the instrument, we have to be able to strip out, online, the appropriate column from $S\bar{A}^TD$ and the appropriate row and column from $D\bar{A}S\bar{A}^TD$. Also, the matrix N must be computed online.

7. ONLINE PROCEDURES

Since most of the computational work is done offline, the online computations can be done efficiently. Futhermore, this paper deals only with the retrieval algorithm; therefore, it is assumed that the brightness temperatures have been corrected for clouds, surface elevation, precipitation, cloud liquid water, limb effects, etc. in an earlier part of the online processing system. Consequently, the online procedures for retrieval processing reduce to the following steps:

1. Decide the channel combination to be used based on channel failures (if any) and whether the field of view is clear or overcast.
2. Choose the appropriate bin out of the 27 available based on location, time of day, and land/sea criteria described in Section 6.
3. Call in the a priori bin data from storage as determined by Step 2.
4. Set up the noise covariance matrix N based on the instrumental noise, cloud amount in the original field of view, and any other factor that contributes to the overall system noise.
5. If fewer than the full complement of channels is to be used, delete the appropriate rows and/or columns from the individual components of the retrieval operator.
6. Assemble the retrieval operator, which includes calculating the inverse matrix.
7. Do a library search, as described in Section 5, to obtain the initial approximations for the retrieval.
8. Execute the retrieval using eqs. (10) and (11) given in Section 4.

These steps constitute the essential steps of the retrieval process. There are other procedures such as quality assurance, that are required in any retrieval process. However, since these are standard procedures, they are not discussed.

8. RESULTS

Two tests were conducted to determine the validity of linearizing the retrieval operator in the manner described in Sections 3 and 4. In the first test the full nonlinear operator (3) was used to do the retrievals and in the second test the linearized operator (10) was used. Since we did not want to test two new concepts at the same time, the library search procedure was not used in either of the tests. Instead, the average vectors of V and T* from the appropriate bins (tuning sets) were used for the initial approximations.

The data used in the tests were a sample of 334 cases of brightness temperature vectors from the TOVS sounder on the NOAA 9 satellite in the summer of 1986. Included in the data were 132 midlatitudinal sea cases, 89 tropical sea cases, and 113 midlatitudinal land cases. The sample set included both day and night cases, but were limited to clear sky cases to avoid having the results of the tests being influenced by the cloud-clearing algorithm. Tables 1 and 2 show the results of the two tests for temperature and water vapor mixing ratio, respectively.

TABLE 1. Rms temperature retieval errors using the nonlinear and linearized operators as a function of pressure.

Pressure (mb)	Linearized operator (C)	Nonlinear operator (C)
115	2.09	2.08
135	2.21	2.19
150	2.22	2.22
200	2.27	2.16
250	2.05	2.05
300	1.74	1.75
350	1.60	1.54
400	1.50	1.43
430	1.40	1.35
475	1.35	1.33
500	1.37	1.35
570	1.36	1.35
620	1.43	1.43
670	1.45	1.45
700	1.61	1.57
780	1.96	1.86
850	2.43	2.36
920	2.14	2.17
950	2.25	2.27
1000	2.25	2.15

TABLE 2. Rms water vapor mixing ratio retrieval error using the nonlinear linear and linearized operators as a function of pressure.

Pressure (mb)	Linearized operator (C)	Nonlinear operator (C)
300	.10	.09
350	.21	.20
400	.35	.32
430	.43	.42
475	.61	.55
500	.70	.62
570	.98	.89
620	1.18	1.07
670	1.38	1.29
700	1.57	1.45
780	2.08	1.91
850	2.35	2.18
920	2.28	2.07
950	2.14	2.07
1000	2.09	2.08

It is evident from Tables 1 and 2 that both the temperature and the water vapor mixing ratio retrievals from the true nonlinear operator are (with a few minor exceptions) more accurate than those from the approximate linearized operator. These results are what one would expect; however, the surprise is how little the linearized operator results differ from the nonlinear operator results.

Results from testing the library search technique are not given here because they are presented in a companion paper of this Preprint Volume by Goldberg, et al. (1988). The results of that paper show that there is an improvement

in retrieval accuracy when using the library search initial vectors in the MVS linearized method as opposed to using the average bin vectors.

9. SUMMARY AND CONCLUSIONS

We have shown how the nonlinear retrieval operator can be linearized to improve the efficiency of the operational retrieval processing system. The improvement in efficiency is of the order of ten times in CPU time over the nonlinear approach. We also have shown how one calculates and applies operator scaling factors and brightness temperature displacement vectors to compensate for errors introduced by the linearization process. In addition to achieving significant improvement in efficiency, we have effected improvement in retrieval accuracy through the library search technique.

The operator linearization procedure achieves much of its computational advantage by transferring certain online computations to offline processing. A listing of the new offline and online steps are summarized in Sections 6 and 7, respectively.

Finally, tuning sets of matched radiosonde/radiance data were described and were shown to be central to the whole linearization and retrieval process. Their importance is emphasized by the many ways in which they are used, namely:

1. To tune the retrieval algorithm for uncertainties in the physical model.
2. To linearize the operator by averaging individual operators based on the tuning set.
3. To derive coefficients by least squares for operator scaling and vector displacement.
4. To provide data sets on which the library search conducted.

We conclude that the minor degradation in accuracy resulting from the linearization of the nonlinear MVS operator can easily be tolerated in view of the large gain in computational efficiency. But, in the final analysis this loss of accuracy is even less than that shown by the results of Tables 1 and 2 because they do not include the gain in accuracy achieved by using the library search technique. Thus, the incorporation of the techniques of operator linearization and library search into the operational processing system yields a retrieval system that is both computationally efficient and accurate.

10. REFERENCES

Fleming, H.E., D.S. Crosby and A.C. Neuendorffer, 1986a: Correction of satellite temperature retrieval errors due to errors in atmospheric transmittances. J. Climate Appl. Meteor., 25, 869-882.

Fleming, H.E., M.D. Goldberg and D.S. Crosby, 1986b: Minimum variance simultaneous retrieval of temperature and water vapor from satellite radiance measurements. Proceedings of 2nd Conf. Satellite Meteor./Remote Sensing and Appl., Williamsburg, Va., Amer. Meteor. Soc., 20-23.

Goldberg, M.D., J.M. Daniels and H.E. Fleming, 1988: A method for obtaining an improved initial approximation for the temperature/moisture retrieval problem. In this Preprint Volume.

1.6

A METHOD FOR OBTAINING AN IMPROVED INITIAL APPROXIMATION FOR THE TEMPERATURE/MOISTURE RETRIEVAL PROBLEM

Mitchell D. Goldberg and Jaime M. Daniels

ST Systems Corporation (STX)
4400 Forbes Blvd., Lanham, MD 20706

Henry E. Fleming

Satellite Research Laboratory
NOAA/NESDIS
Washington, D.C. 20233

1. INTRODUCTION

The primary purpose of satellite derived temperature and moisture retrievals is to provide information over regions where conventional radiosonde data are either sparse or non-existent. Retrieval accuracy comparable to radiosonde measurements continues to be the long term objective, but the low vertical resolution of present-day radiometers precludes this. One way of reducing retrieval error and improving retrieval structure is to improve the initial approximation used in the retrieval.

Retrieval structure is predominantly carried over from the structure of the initial approximation. The initial approximation, also referred to as the first guess, has traditionally been derived from a mean condition of an ensemble of apriori data representing some given range of latitude and season. The problem with this approach is that ensemble means are typically smooth, resulting in smooth retrievals. The solution to this problem is to use a first guess representative of the ambient condition, in terms of structure.

The focus of this paper is to present a pattern recognition library search technique for improving the initial approximation. This technique was derived from the concept that if a set of indistinguishable radiance vectors existed and was matched to "ground truth" radiosonde profiles of temperature and moisture, the ground truth, due to non-uniqueness and the limited vertical resolution of the radiometer, would not be indistinguishable but very similar in both magnitude and structure. We assume that severe occurrences of non-uniqueness (i.e., two quite different atmospheric profiles, resulting in the same set of radiance vectors) are statistically uncommon. Other library search approaches have been reported by Chedin and Scott (1985), Goldberg, et al. (1985) and Thompson, et al. (1985).

The objective of the library search technique is to find a small sub-set of radiance vectors from a historical library of matched data that are similar to the ambient radiance. These matched data are satellite radiances matched in time and space with radiosonde temperature and moisture profiles. The small sub-set of radiance vectors, along with their matched temperature and moisture profiles, are used to generate the first guess vectors for the retrieval algorithm.

The library search technique is presently used in the Minimum Variance Simultaneous (MVS) algorithm (Fleming, et al. 1988). Results based on the library search are compared to the more common approach of using mean conditions representing a latitudinal and seasonal regime of which the ambient condition is a member.

2. APPROACH

The library search method uses nearest neighbor discriminate analysis to compute a "closeness measure" between the ambient condition and each radiance member in the library. The closeness measure, ρ, between the ambient radiance vector, r, and the κth library radiance member $\tilde{r}$ is defined as

$$\rho_\kappa = (r_i - \tilde{r}_{i\kappa})\, S^{-1}\, (r_i - \tilde{r}_{i\kappa})^T \qquad (1)$$

$$i = 1 \ldots I \text{ channels}$$

where the superscript "T" denotes matrix transposition, "-1" denotes matrix inversion, and S is the covariance matrix of the radiance measurements within the library.

Instead of using the temperature, moisture and radiance vectors associated with the minimum ρ value, the first guess is obtained by averaging the vectors associated with the n smallest ρ values. After some experimentation, the best value of n was found to be 20. The closest neighbor by itself is not used for three reasons. First, due to non-uniqueness of solutions to the radiative transfer equation, the nearest neighbor in radiance space, can theoretically be a distant neighbor in temperature space. Second, satellite radiometers do not have the vertical resolution of the radiosonde, and therefore, radiances are insensitive to small scale structure in temperature/moisture profiles, hence the closest neighbor might not correspond to the most representative ambient structure. Finally, there are always some discrepancies between matching real satellite observations with radiosonde data, since the radiometer has a relatively large horizontal resolution and the satellite overpass time rarely coincides with the time of the radiosonde observation.

3. APPLICATION

The library search technique supplies first guess information to the Minimum Variance Simultaneous (MVS) retrieval algorithm, which has been used in processing NOAA-10 retrievals since March 1987 in parallel with the current operational regression algorithm at NOAA/NESDIS. The same channels are used for both library search and the retrieval. The library is updated on a daily basis with radiances matched to radiosonde data, based on a fixed set of 200 geographically distributed radiosonde stations. In this operational environment,

approximately 50000 retrievals are processed daily from radiance data collected over 14 orbits. The library search technique can be used for each sounding, however, to avoid the needless generation of redundant first guess information, we test the applicability of the library search first guess, used in the previous sounding, to the current data.

To test for first guess redundancy, a "redundancy" closeness measure, based on equation 1, is computed between the ambient radiance vector and the most recent library search first guess radiance vector. A threshold limit, defined as the mean of the twenty smallest ρ values associated with the most recent library search, is compared to the redundancy closeness measure. A new first guess is generated only if the threshold is exceeded, otherwise, the first guess applied in the previous sounding is used. On the average, only 30% of all soundings required the generation of new first guess information.

4. DATA

Results in this paper are derived from channel radiance data collected from the High-resolution Infrared Radiation Sounder (HIRS/2), Microwave Sounding Unit (MSU), and the Stratospheric Sounding Unit (SSU) on board the NOAA-10 polar orbiting satellite for the period of October 6-16, 1987. A complete description of these instruments can be found in Smith et al. (1978). To evaluate the retrievals, radiosonde temperature and moisture profiles are matched to retrievals, under the condition that the matched pairs are within 3 hours and within a 3° spatial window. Only clear and cloud-corrected (N*) radiances (McMillin and Dean, 1982) are used in the evaluation. The matched data are sorted into the following latitude zones to facilitate the evaluation:

a)	Zone 1 (60-90°N)	1309 cases
b)	Zone 2 (30-60°N)	1784 cases
c)	Zone 3 (30°S-30°N)	588 cases

The channel combination used for clear and partly-cloudy retrievals are HIRS 2-7 and 13-16, MSU 2-4, and SSU 1-3.

5. RESULTS

Before the development and implementation of the library search technique, the ensemble means from 27 bins of matched radiosonde/radiance data sets (see Table 1), were used for the initial approximation in the MVS retrieval algorithm. To demonstrate the library search approach, results based on library search are compared to results based on ensemble means. However, we will first demonstrate the high degree of ambient representation generated by the library search procedure. Figures 1(a-b) and 2(a-b) are displays of thermal gradients, generated using a VICOM computer-based interactive graphics system (Brown, et al. 1988). Figures 1a and 2a show the approximation of the ambient thermal field generated by the library search technique at 250 mb and 750 mb, whereas Figures 1b and 2b show the corresponding retrieved thermal field. Overall, the first guess field appears to be a very good first approximation of the ambient field, but notice that the retrieval sharpens the features detected by library search.

Table 1. The 27 MVS Retrieval Bins

Latitude	Sea*	Land/Day	Land/Night
60 < LAT ≤ 90N	1	10	19
45 < LAT ≤ 60N	2	11	20
30 < LAT ≤ 45N	3	12	21
15 < LAT ≤ 30N	4	13	22
15S < LAT ≤ 15N	5	14	23
15 < LAT ≤ 30S	6	15	24
30 < LAT ≤ 45S	7	16	25
45 < LAT ≤ 60S	8	17	26
60 < LAT ≤ 90S	9	18	27

* No Day/Night Breakdown over Ocean

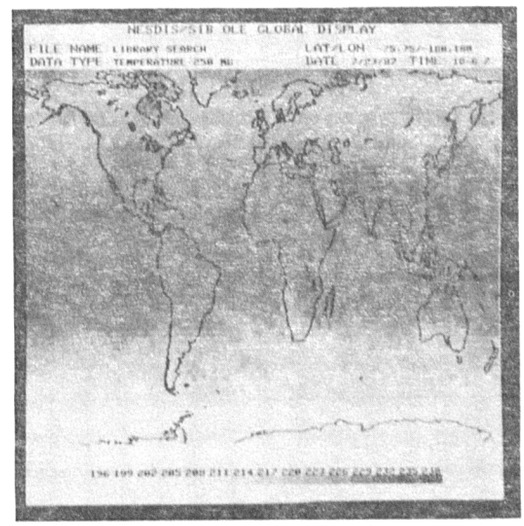

Figure 1a. Library search first guess field at 250 mb.

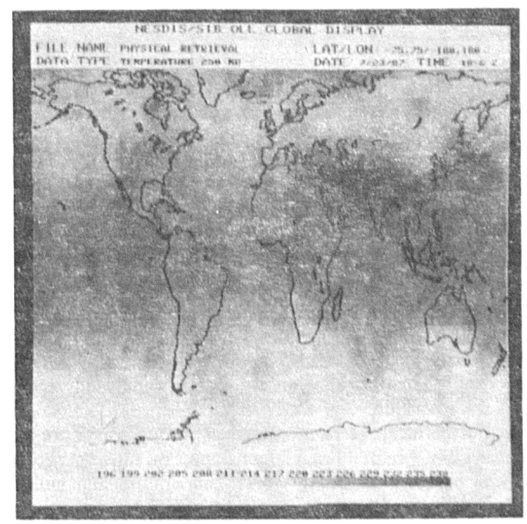

Figure 1b. MVS retrieval field at 250 mb, using the library search first guess field.

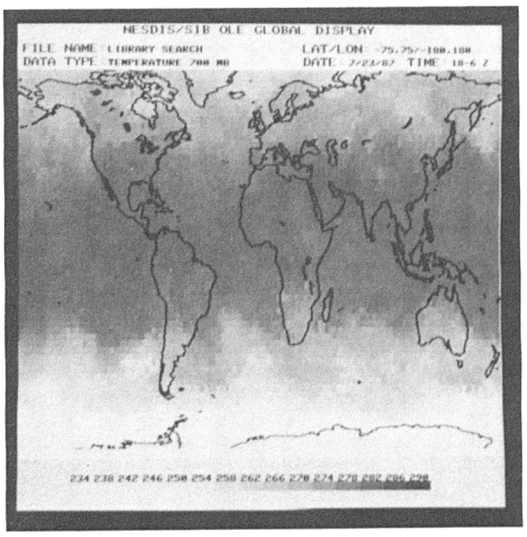

Figure 2a. Library search first guess field at 700 mb.

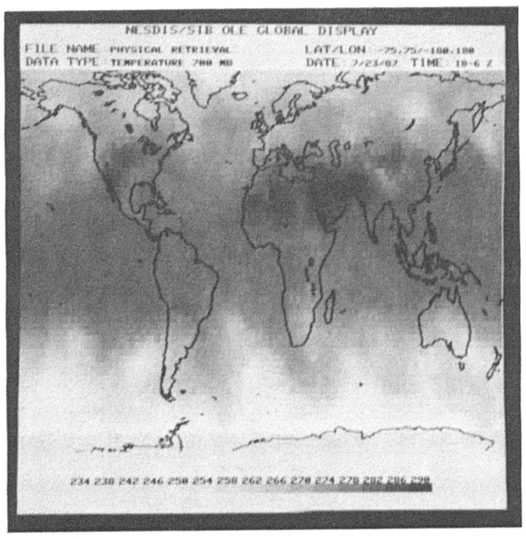

Figure 2b. MVS retrieval field at 700 mb, using the library search first guess field.

Retrieval RMS errors (retrieval vs. radiosonde) and first guess errors (retrieval vs.first guess) are shown in Figures 3(a-b), 4(a-b) and 5(a-b) for Zones 1, 2 and 3, respectively. All three figures clearly illustrate that library search significantly reduces both the temperature and water vapor mixing ratio first guess errors. Furthermore, retrievals based on library search are more accurate. Library search has a larger impact on retrieval accuracy in regions of the atmosphere where temperature and moisture have the highest variability, more specifically, this includes regions near the surface and above 500 mb.

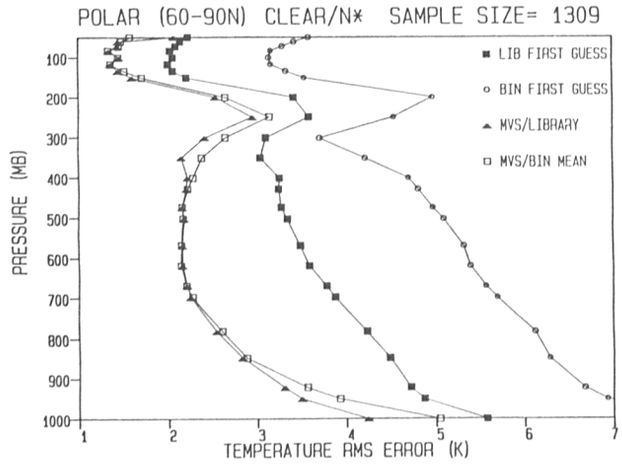

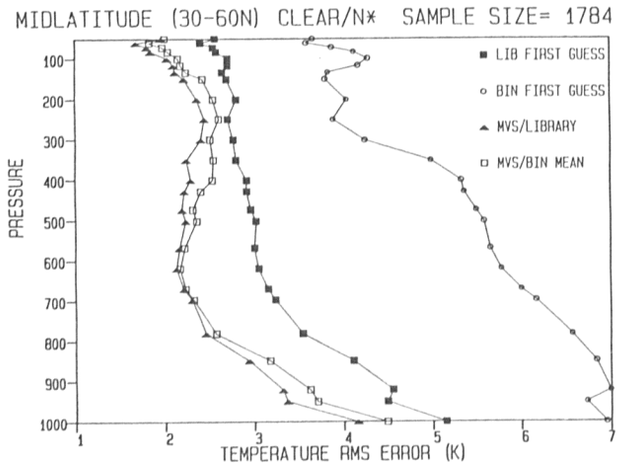

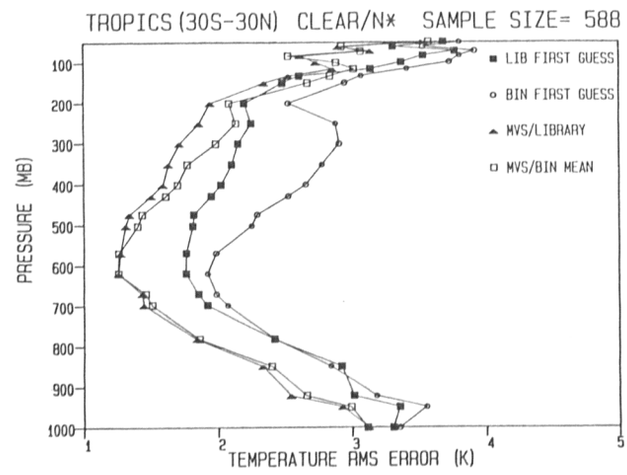

Figures 3a-5a. Temperature MVS retrieval and first guess error profiles using library search and bin means for polar, mid-latitudes and tropics, respectively.

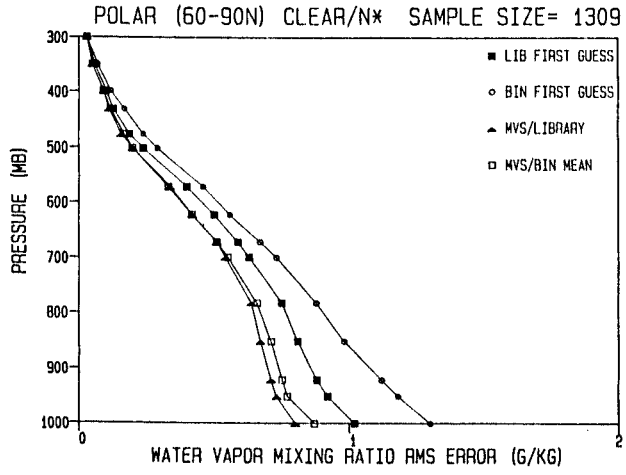

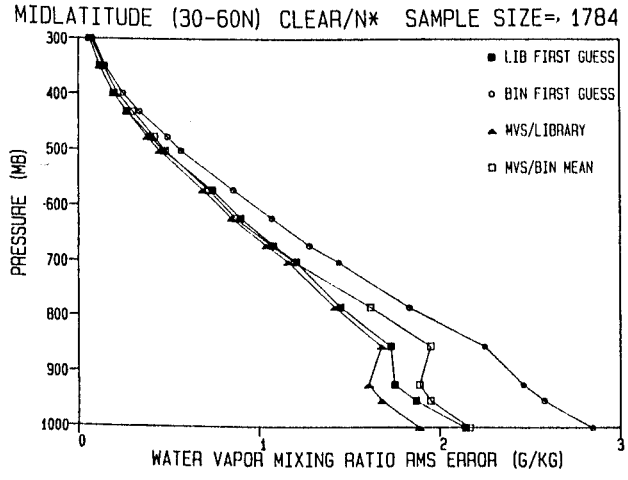

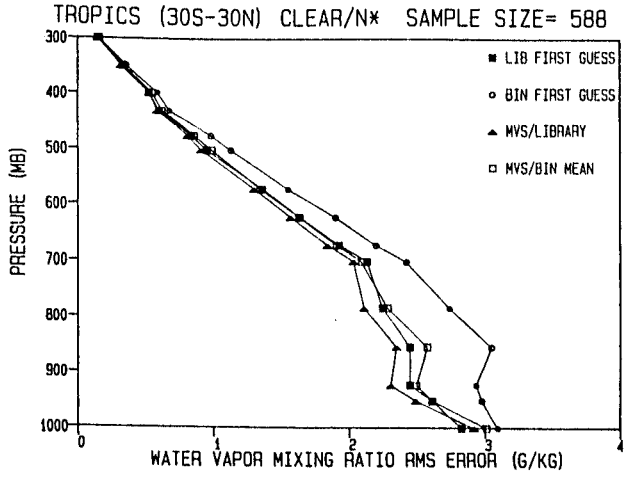

Figures 3b-5b. Water vapor mixing ratio MVS retrieval and first guess error profiles using library search and bin means for polar, mid-latitudes and tropics, respectively.

Notice that in Zones 2 and 3, library search water vapor first guess errors are smaller near the surface than the errors associated with retrievals based on ensemble means. This is probably a consequence of the high variability of moisture in the horizontal and the relatively poor horizontal resolution of the radiometer. Remember, first guess temperature and water vapor profiles are derived from point measurements (radiosonde), whereas a retrieval represents an average condition defined by the horizontal and vertical resolution of the radiometer.

Observing the significant reduction of first guess errors, one might have expected library search to have a much larger impact on retrieval accuracy. However, retrieval accuracy is also defined by the retrieval operator. Apparently, the retrieval operator, which incorporates radiative transfer physics and apriori covariance relationships of temperature and water vapor, plays an important role. The role of the first guess is to provide information on the vertical structure of atmosphere, that cannot be resolved by present-day radiometers.

6. CONCLUSIONS

It was demonstrated that library search can generate a good approximation of the ambient thermal and moisture field. Furthermore, the use of library search in conjunction with a physical retrieval algorithm resulted in more accurate retrievals, especially in regions of high variability. An important feature of this technique is that apriori data sets are not partitioned into different regimes of latitude and season, as required by the traditional ensemble approach.

7. ACKNOWLEDGEMENTS

The authors wish to acknowledge Charles Novak and Michael Chalfant of NESDIS for providing the resources to conduct the study and to Charles Brown of ST Systems Corp. The authors are also indebted to Lisa Markel for drafting, and Chris Mitchell for typing the manuscript.

8. REFERENCES

Brown, C.E., K. Fakhrai, M. Liu, A. Swaroop, and A.L. Reale, 1988: An image processing display system for evaluation of operational meteorological products. Preprint Volume: Fourth Conference on Interactive Information and Processing Systems for Meteorology, Oceanography, and Hydrology, Feb. 1-5, 1988, Anaheim, Calif. Published by Amer. Meteor. Soc., Boston, MA

Chedin, A., and N.A. Scott, 1985: The 3I (Improved Initialization Inversion) method applied to the satellites of the TIROS-N series. In Deepak, A., H.E. Fleming, and M.T. Chahine (Eds.), Advances in Remote Sensing Retrieval Methods, A. Deepak Publishing, Hampton, Virginia

Fleming, H.E., M.D. Goldberg, and D.S. Crosby, 1988: Operational implementation of the minimum variance simultaneous retrieval method. Preprint Volume: Third Conference on Satellite Meteorology and Oceanography, Jan. 31-Feb. 5, 1988, Anaheim, Calif. Published by Amer. Meteor. Soc., Boston, MA

Goldberg, M.D., N.C. Grody, and O.E. Thompson, 1985: Analog temperature retrievals using a library search procedure. In Deepak, A., H.E. Fleming, and M.T. Chahine (Eds.), Advances in Remote Sensing Retrieval Methods, A. Deepak Publishing, Hampton, Virginia, 461-470.

McMillin, L.M., C. Dean, 1982: Evaluation of a new operational technique for producing clear radiances. J. Appl. Meteor., 21, 1005-1014.

Smith, W.L., H.M. Woolf, C.M. Hayden, D.Q. Wark, and L.M. McMillin, 1979: The TIROS-N operational vertical sounder. Bull. Amer. Meteor. Soc., 60, 1177-1187.

Thompson, O.E., M. Goldberg and D. Dazlich, 1985: Pattern recognition in the satellite temperature retrieval problem. J. Clim. Appl. Meteor., 24, 30-48.

COMPARISONS BETWEEN PHYSICALLY RETRIEVED TEMPERATURE AND MOISTURE FIELDS FROM NOAA-7 AND NOAA-9 AND CONVENTIONAL ANALYSES OR RADIOSONDE DATA

N. Husson, Y. Tahani, N.A. Scott, and A. Chedin

Laboratoire de Météorologie Dynamique du CNRS
Ecole Polytechnique, 91128 Palaiseau Cedex, France

1. INTRODUCTION

The quality of the instruments aboard the present generation of operational meteorological satellites (the Tiros-N series) and the increasing capability of the so-called physical inversion methods to accurately retrieve atmospheric parameters from the multi-spectral radiative measurements, explain the increasing compatibility of these remote observations with the requirements of most of the present or planned meteorological or climatological programmes, as far as the atmospheric structure (temperature, moisture, cloudiness, etc...) is concerned. This essentially results from the actual taking account of the physical and statistical (a priori information) aspects of the phenomena - very often through a coupling of the various instruments (e.g. infrared and microwave sounders).

The "3I" (Improved Initialisation Inversion) algorithm (Chedin et al., 1985a, 1985b, 1986) has been designed with the purpose of retrieving geophysical parameters from space radiometric measurements and oriented towards the processing of the Tiros-N series observations made by the TOVS (Tiros-N Operational Vertical Sounder) instruments : HIRS-2, a 20-channel infrared radiometer, and MSU, a 4-channel microwave radiometer.

This procedure is a physico-statistical type method which relies on a "pattern recognition" type approach. The inversion of the radiative transfer equation is splitted into two steps, both of which take satellite measurements as their source data. The first step "inverts" these measurements according to the principle of "best initial profile" from among a vast selection of atmospheric situations archived in advance and classified in groups according to air mass type. This "library" of atmospheres, "TIGR" (TOVS Initial Guess Retrieval data set) (see above references), consists at present of about 1200 situations carefully sampled by statistical analysis methods. The selected set of observed brightness temperatures is "compared" to each of the computed sets of brightness temperatures and the "closest" is retained.

From the initial profile obtained in this manner, the second step performs the radiative transfer equation inversion. The basis for the retrieval of the exact solution is a maximum probability estimation procedure aimed at minimizing the differences between the brightness temperatures associated with the initial guess and the observed ones. Use is made of the Jacobian associated with the retrieved initial guess, in the "TIGR" data set.

The use of the so-called "Ψ-method" (see above references) relying on a coupling of the infrared and microwave channels, to obtain "equivalent clear radiances" in cloudy areas, preserves as far as possible the nominal vertical resolution of the instruments.

Resulting from a compromise between the spatial resolutions of the two sounders HIRS-2 (infrared) and MSU (microwaves) and from an over-sampling along the subsatellite track, the 3I algorithm produces one retrieval every 100 x 30 km^2.

Algorithm "3I" is producing thermal structure and other products such as : geopotential thicknesses, thermal winds, cloud parameters such as altitude, cloud amounts, relative humidities and water vapor amounts.

Retrievals of water vapor quantities (relative humidities, total amount of precipitable water vapor) are made for 3 layers delimited by the levels 1000, 800, 500 and 300 mb. Following the temperature profile retrieval, the brightness temperatures associated with the initial guess are corrected for the deviations between the initial temperature profile and the final solution giving rise to the initial guess for water vapor and surface temperature retrievals. The method used is based upon a simultaneous physical inversion of the water vapor amounts and of the surface temperature.

Four HIRS-2 channels are presently used : 8, 10, 11, 12 for the day-time observations and 18, 10, 11, 12 for the night-time observations. A ridge type estimation procedure is used :

$$\Delta\beta = (X'X + \gamma I)^{-1} X' \Delta Y$$

where X (X' transpose of X) is the matrix of the partial derivatives of the brightness temperatures with respect to relative humidities and surface temperature. ΔY is the difference between observed (cleared) brightness temperatures and the initial values of the parameters considered, γ is a smoothing parameter (Lagrangian parameter).

The "3I" method has been applied to NOAA-7 and NOAA-9 satellite observations over Europe, to assess its capability to produce accurate temperature soundings or geopotential thicknesses, as well as water vapor related quantities. Systematic comparisons with either operational analyses or colocated radiosoundings data have been performed.

2. PRESENTATIONS OF THE SITUATIONS ADOPTED

2.1 The NOAA-7 "situations"

Six "situations" were selected, corresponding either to a single satellite pass (giving a more restricted geographic zone of coverage), or to two successive satellite passes. They are generally related to complex atmospheric situations, often characterized by a very rapid evolution and have resulted in substantial errors in forecasting either by the European Center in Reading (ECMWF) or by the French Met. Office or both. The dates range from September to December 1983 (see Chedin et al., 1987).

In such cases, the differences between retrievals and operational analyses must be interpreted having in mind the forecast errors, the main purpose being to properly assess the real benefit brought by such remote observations.

A total of nine scenes have been studied. The 2 situations reported here are for September 27, 1983, orbit nb. 11664 at 14:35Z and for December 28, 1983, orbit nb. 12963 at 14:17Z (see also Chedin et al., 1987).

They have been selected as the ones corresponding to the slightest errors in the forecasts, the first one being however more complex than the second.

2.2 The NOAA-9 situations

Observations from NOAA-9 were chosen, for two satellite passes over the "HAPEX-MOBILHY" ("Hydrology - Atmospheric Pilot Experiment" - "Modélisation du Bilan Hydrique") experiment site (André et al., 1987) corresponding to June 9, 1987, orbit nb. 7676 at 2:02 pm, and to June 19, 1987, orbit nb. 7817 (C. Ottlé, Private Communication).

3. RESULTS OF COMPARISONS BETWEEN CONVENTIONAL ANALYSIS AND 3I ALGORITHM RESULTS FOR THE NOAA-7 AND NOAA-9 CASES

The quality of retrieved products (thermal structure as well as water vapor related quantities) has been estimated, for the NOAA-7

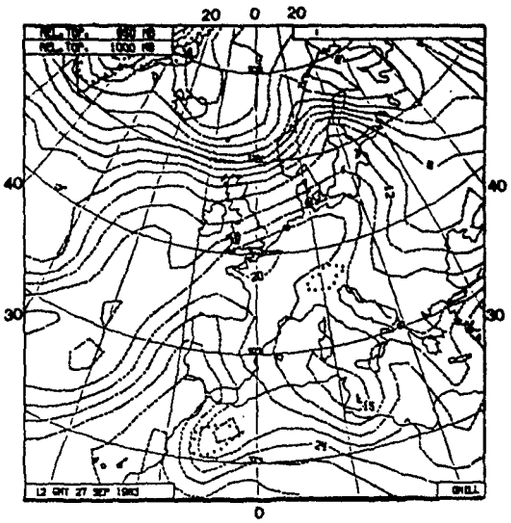

fig 1 : ECMWF operational analysis : thicknesses 1000-850 mb, in °C (virtual temperatures)

NOAA7 orb. 11664, September 27,1983, 14.35z

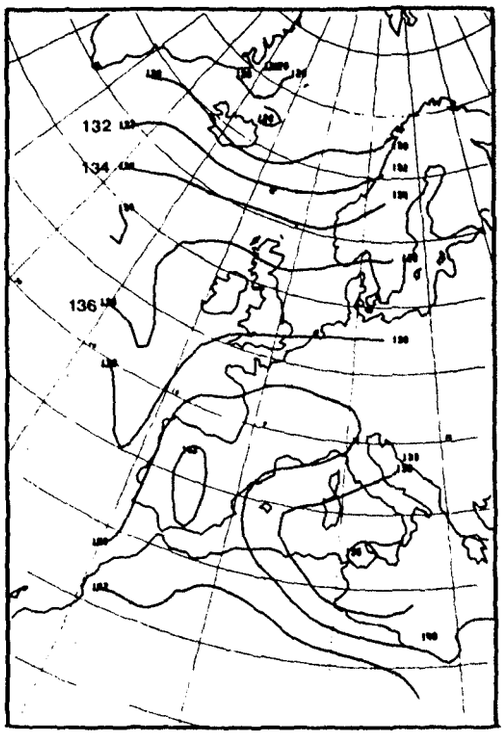

fig 2 : 1000-850 mb geopotential thicknesses retrieved from the 3I algorithm

and NOAA-9 situations mentioned above, through comparisons with ECMWF (European Center for Medium Range Weather Forecast) conventional analyses. Visual comparisons have also been made on the basis of geopotential thickness fields.

3.1 Temperature structure

1) Orbit number 11664

On a qualitative point of view, operational analyses of 1000-850 mb and 1000-500 mb geopotential thicknesses of the ECMWF (expressed in virtual temperatures), are presented in Figures 1 and 3 respectively. Figures 2 and 4 display the corresponding "3I" thickness charts. 3I fields appear quite similar to those resulting from operational analyses both as regard value and aspect. For a more detailed and precise analysis of the differences between the two fields, see Chedin et al., 1987.

A quantitative assessment of the accuracy of the retrieved products has been approached by a statistical analysis of the deviations between the 3I retrievals and the ECMWF thickness fields. The results of this statistical evaluation are reported on Figure 5 which displays statistics on the differences between 3I retrieved geopotential thicknesses and corresponding analysis from ECMWF, for 7 layers : 1000-850, 850-700, 700-500, 500-300, 300-100, 100-70 and 70-50 mb. Mean and standard deviations are in percentage of geopotential thickness of corresponding layer for the US standard atmosphere. Comparisons with analyses comprise about 1660 "3I" samples over a total of 1752 for this orbit.

2) Orbit 12963

Quantitative results of the statistical evaluation of the differences between 3I retrieved geopotential thicknesses and ECMWF are shown on Figure 6. Over a total of 1475 samples for this orbit, about 1410 are involved in this evaluation.

3) NOAA-9 selected passes

Figure 7 displays the same kind of results as Figures 5 and 6 for the NOAA-9 pass, orbit 7817.

A few remarks come out of these results. The two NOAA-7 passes show a standard deviation of about 0.6% throughout the atmospheric column except for the lowest layer where it reaches 0.9 to 1%. Biases are more important for orbit 11664 (the most complex). They are less than the standard deviations (one exception). The NOAA-9 pass nb. 7676, corresponding to a more "classical" meteorological situation, displays results (not shown) similar to NOAA-7 pass number11963 when the second one (7817) shows a standard deviation still better of 0.3% to 0.5% with a peak at about 0.8% for the lowest layer.

These results are considered as satisfactory.

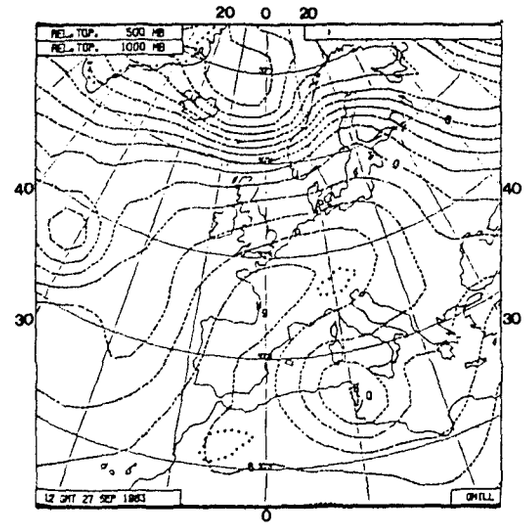

fig 3 : ECMWF operational analysis : thicknesses 1000-500 mb, in ^{o}C (virtual temperatures)

NOAA7 orb. 11664, September 27,1983, 14.35z

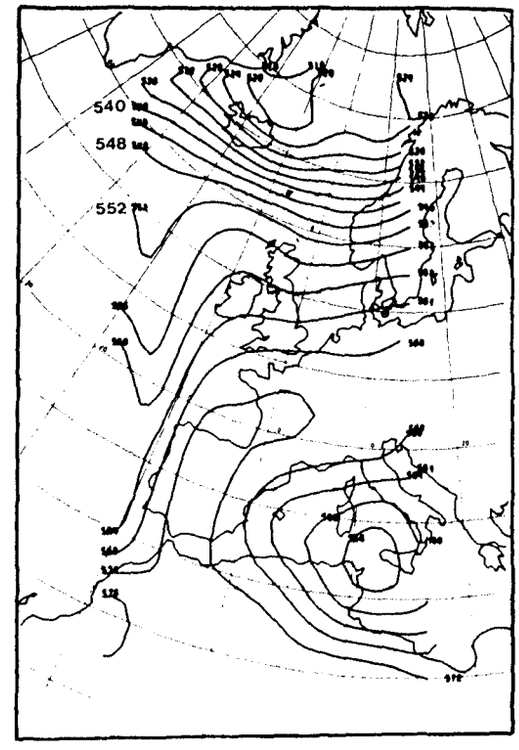

fig 4 : 1000-500 mb geopotential thicknesses retrieved from the 3I algorithm

3.2 Water vapor structure

Results of the statistics on the differences of total water vapor content between "3I" retrievals and ECMWF corresponding analyses are given in Table 1 for the two NOAA-7 orbits and in Table 2 for the two NOAA-9 orbits.

orbit NOAA7	11664	12963
mean content	1.92	1.51
biais	-0.53	-0.27
std. dev.	0.72	0.36
sample	902	975

table 1 : Differences between 3I retrieved and ECMWF analysed total water vapor contents (g.cm-2) for the two NOAA7 passes.

The number of samples retained is not as important as for the thickness fields because of the cloudy rejection flag : 60% is the adopted limit nebulosity value for proceeding to water vapor retrievals.

orbit NOAA9	7676	7817
mean content	1.99	2.00
biais	-0.09	-0.07
std. dev.	0.48	0.60
sample	592	546

table 2 : Differences between 3I retrieved and ECMWF analysed total water vapor contents (g.cm-2) for the two NOAA9 passes.

From these results, it appears that rms values ranging from 25% to 30% of the total water vapor content are obtained except for orbit NOAA-7 number 11664 for which it reaches the surprisingly bad value of 46%. Going deeper into the analysis of this result has led us to point out an area for which discrepancies between 3I retrieved and ECMWF analysed total water vapor contents are very large. This is shown on Figs. 8 and 9 : over Spain, values of the order of 4 $g.cm^{-2}$ are given by ECMWF when 3I retrieves values of the order of 1.5 $g.cm^{-2}$. As a preliminary attempt to elucidate this question, comparisons have been made between radiosonde data, 3I retrievals and ECMWF values. They are shown in Table 3 which concludes in favor of 3I.

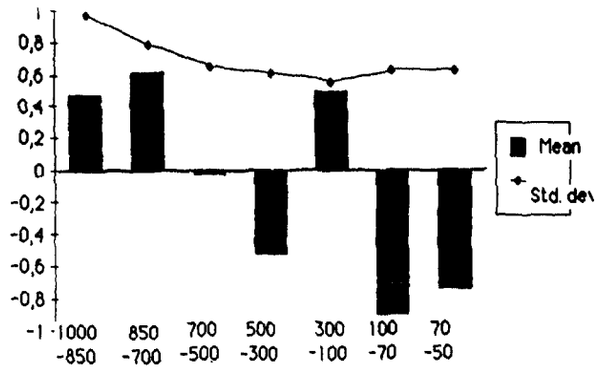

fig 5 : NOAA7, orbit 11664, statistics on the differences between 3I retrieved geopotential thicknesses and corresponding analysis from ECMWF

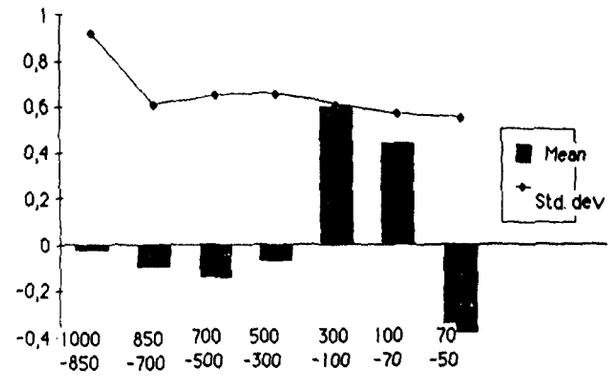

fig 6: NOAA7, orbit 12963, statistics on the differences between 3I retrieved geopotential thicknesses and corresponding analysis from ECMWF

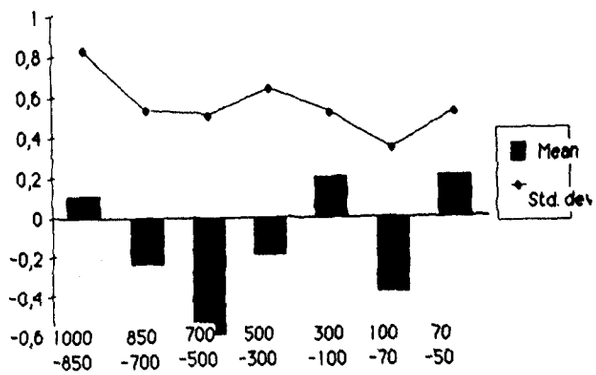

fig 7: NOAA9, orbit 7817, statistics on the differences between 3I retrieved geopotential thicknesses and corresponding analysis from ECMWF

Station	R/S data	3I	ECMWF
Madrid	1.34	1.40	4.58
Gibraltar	2.60	2.55	3.44
La Coruna	2.33	1.86	3.12

table 3 : comparison between radiosonde data, 3I retrieval and ECMWF analysis values of total water vapor (in g/cm2)

4. CONCLUSION

This study of a few selected cases confirms previous results obtained through the 3I retrieval algorithm. Departures between 3I-retrieved and ECMWF-analysed geopotential thicknesses generally display standard deviations ranging from 0.3% ("classical" meteorological situation) to 0.6% (complex situation) with a peak for the lowest layer (0.8% to 1%). For the total water vapor content, rms values are of the order of 25% to 30% of the mean content. In one case, a much larger value (46%) has been explained in large part, in favor of 3I. Further comparisons are in progress in cooperation with Dr. G. J. Prangsma from KNMI (Netherlands).

Acknowledgements :

We are happy to thank C. Ottlé (CRPE) who provided us with the NOAA-9 satellite data from the HAPEX-MOBILHY campaign. F.M. Bréon, J.F. Flobert (involved in the NOAA-7 analysis) and C. Levy from ARA/LMD group helped us at various stages of this work. Help and support from G. Rochard (CMS-Lannion) and his colleagues are gratefully acknowledged. Processing of the data has been done on the computers of CIRCE (Centre Inter Régional de Calcul Electronique).

REFERENCES

Chedin, A., and N.A. Scott, 1985a: Initialization of the radiative transfer equation inversion problem from a pattern recognition type approach. Application to the satellites of the Tiros-N series. *Advances in Remote Sensing Retrieval Methods.* Academic Press, A. Deepak Ed., 495-515.

Chedin, A., N.A. Scott, C. Wahiche, and P. Moulinier, 1985b: The Improved Initialization Inversion method : a high resolution physical method for temperature retrievals from the Tiros-N series. *J. Clim. Appl. Meteor.*, 24, 128-143.

Chedin, A., N.A. Scott, C. Wahiche, P. Moulinier, N. Husson, and P. Sitbon, 1986: The 3I procedure applied to the retrieval of meteorological and climate parameters from NOAA-7. *Ocean-Air Interactions*, 1, 29-42.

Chedin, A., N.A. Scott, J.F. Flobert, N. Husson, C. Levy, G. Rochard, Q. Quéré, B. Bellec, and J. Siméon, 1987 : Analyse des champs d'épaisseurs obtenus par la méthode "3I" d'inversion des observations satellitaires de la série Tiros-N. *La Météorologie*, 16, 24-34.

André, J.C., J.P. Goutorbe, A. Perrier, et al., 1987: Hapex-Mobilhy : First results from the Special Observing Period. *Bull. Amer. Meteor. Soc.*, To be published.

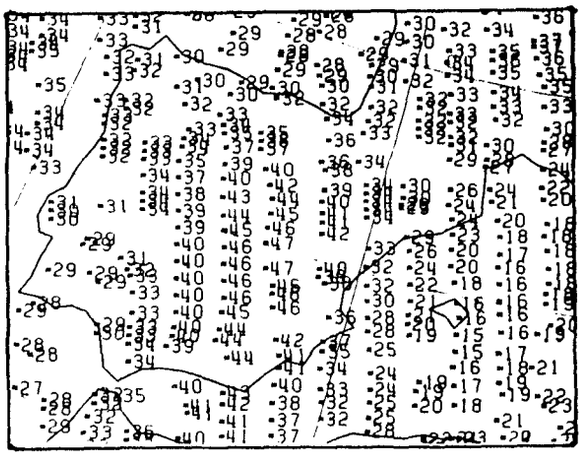

fig 8 : NOAA7, orbit 11664, ECMWF analysed total water vapor content (in mm)

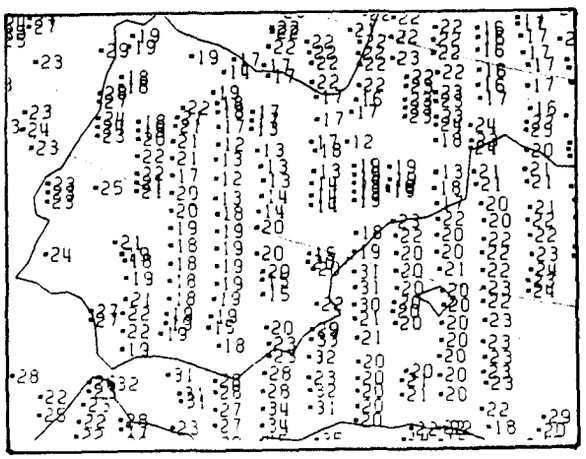

fig 9 : NOAA7, orbit 11664, 3I retrieved total water vapor content (in mm)

Blank page retained for pagination

TOVS OPERATIONAL SOUNDINGS WITHOUT TROPOSPHERIC MICROWAVE DATA

Anthony L. Reale
Donald G. Gray
Michael W. Chalfant

National Oceanic and Atmospheric Administration
National Environmental Satellite, Data
and Information Service
Washington, D.C. 20233

Andrew Nappi

ST Systems Corporation
4400 Forbes Boulevard
Lanham, MD 20706

1. INTRODUCTION

NOAA/NESDIS produces operational temperature and water vapor soundings from the TIROS Operational Vertical Sounder (TOVS) on board the NOAA TIROS-N series polar orbiting satellites. NESDIS operates two sun synchronous, polar orbiting satellites, an odd-numbered satellite for mid-day and mid-night measurements and an even-numbered satellite for morning and evening measurements. The TOVS consists of three instruments; the second version of the High-resolution Infrared Sounder (HIRS/2), the Microwave Sounding Unit (MSU) and the Stratospheric Sounding Unit (SSU). The HIRS/2 supplemented by the MSU are primarily used to generate tropospheric sounding products.

Due to the failure of MSU channels 2 (53.73 GHZ) and 3 (54.96 GHZ) on board NOAA-9, sounding products from NOAA-9 were discontinued on March 17, 1987. Global sounding products became solely dependent on NOAA-10 with a 50% reduction in coverage. This included the loss of timely sounding data from the northeast Pacific region for direct input into the National Meteorological Center's (NMC) Nested Grid Model (NGM) for numerical weather prediction. At that time, a system to generate tropospheric sounding products without the MSU channels 2 and 3 did not exist. These are the primary tropospheric sounding channels of the MSU and are required to validate the HIRS/2 data and to produce soundings in cloudy atmospheres.

NESDIS has since developed a system to generate TOVS sounding products without MSU channels 2 and 3. This system became operational for NOAA-9 on September 1, 1987. NOAA-9 soundings were evaluated by NMC during September and found to be usable. NMC was scheduled to begin using NOAA-9 products in the NGM and other forecast models by November 1987, as well as distribution to the European Center for Medium-range Weather Forecasting. Worldwide distribution of NOAA-9 products over the Global Telecommunication System was also scheduled to resume during November.

The following paper describes modifications to the TOVS processing system to generate soundings without Tropospheric MSU data that were implemented for NOAA-9. An evaluation technique and results comparing the observed accuracy of NOAA-9 and NOAA-10 soundings are presented. Results showing the impact on sounding accuracy of the removal of specified TOVS channels are also presented. Results are for soundings generated using a statistical regression algorithm.

2. SYSTEM DESCRIPTION

The sounding system for NOAA-9 does not require MSU channels 2 and 3. The HIRS/2 channel 16 (4.4 μm) is also not available. MSU channels 1 (50.31 GHZ) and 4 (57.95 GHZ) are available and used in the processing. Figure 1 shows the atmospheric sensitivity of the various TOVS channels. A gap in the sensitivity is present in the vicinity of the tropopause (200mb). The loss of MSU channel 3 and HIRS channel 16 for NOAA-9 amplifies this problem.

Sounding products for NOAA-9 are generated similar to those for NOAA-10. Prior to the cloud clearing step the only difference is that the MSU channels 2 and 3 are not available as predictors for limb and water vapor correction. The main difference in processing occurs in the cloud clearing procedure. Tests to identify cloud contaminated HIRS/2 data using MSU channels 2 and 3 are not done. It was also found that the calculation of clear column brightness temperatures (McMillin, 1987) for HIRS/2 data without MSU channels 2 and 3 is unstable, therefore, it is not done. Only HIRS/2 data in cloud-free areas are processed into tropospheric products.

Prior to the retrieval step, objective analysis of the clear HIRS/2 data is done and a quality indicator is set. Normally, these procedures use MSU channels 2 and 3 together with HIRS/2 data to identify outliers. For NOAA-9, separate channels of the HIRS/2 are used to check other HIRS/2 channels. This procedure cannot be used over high terrain (>1.2 km) and for these cases the quality indicator is set to questionable.

NOAA-9 products consist of tropospheric (1000 mb. to 115 mb.) and stratospheric (100 mb. to .1 mb.) soundings for cloud free regions and only stratospheric soundings in cloudy regions. Accurate tropospheric soundings cannot be retrieved in cloudy atmospheres without MSU channels 2 and 3. No products are distributed over high terrain.

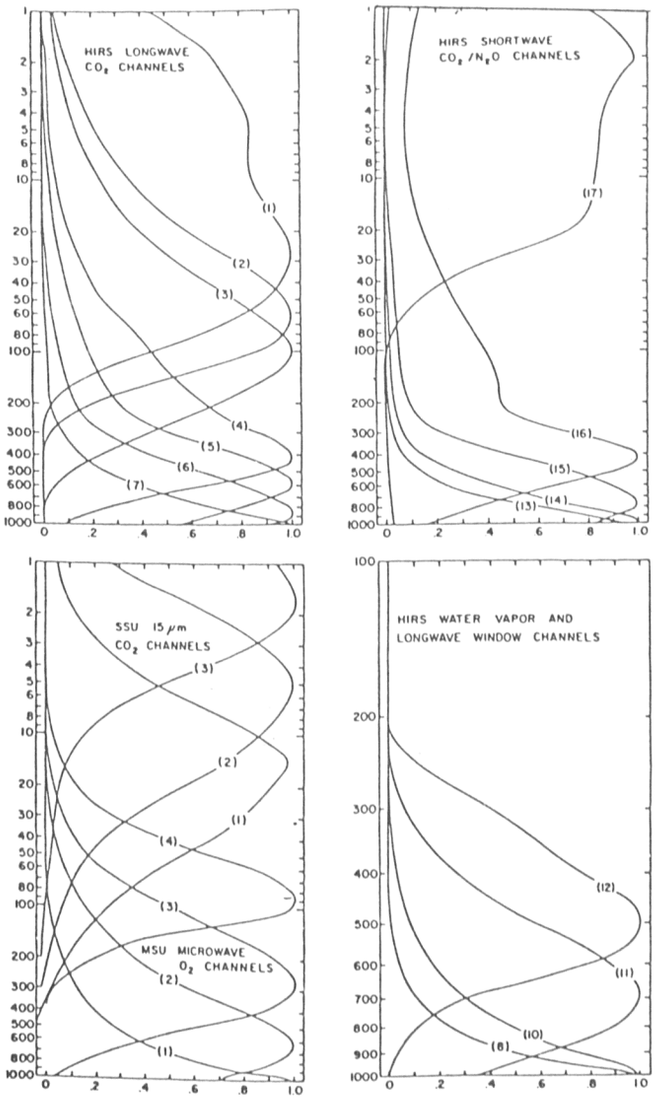

Fig. 1: Normalized Atmospheric Weighting Functions for TOVS Channels.

Clear tropospheric soundings are computed using the HIRS/2 sounding channels and MSU channel 4. Stratospheric soundings are produced similar to the normal TOVS operation except that the MSU channel 3 is not used. The MSU channel 4 is also used for coefficient interpolation between TOVS latitude zones (same as normal TOVS system).

Clear soundings comprise about 30% of the total number of soundings produced for NOAA-9. Figure 2 shows an example of the tropospheric sounding coverage for NOAA-9 over a 24-hour period. The dark areas represent cloud free regions for which NOAA-9 tropospheric products were generated and the white areas cloudy regions. The corresponding NOAA-10 picture would have shown complete global coverage.

3. RESULTS

3.1 Evaluation Technique

Several methods are available to compute error statistics for sounding systems. The re-retrieval method, was chosen for this paper. This method uses archived data-sets of TOVS sounding and upper-air radiosonde (raob) matchups. A dependent sample (21 days) of matchups is used to generate "new" retrieval coefficients (using statistical regression) and an independent sample (7 days) is used for evaluation. The evaluation is done by re-retrieving the soundings in the independent sample with the "new" coefficients and computing error statistics relative to the raobs.

Raob and sounding matchups are collected daily and stored on a 28-day rotating file during routine TOVS processing with a separate file for each satellite. The distance window for matchups ranges from 25 km. to 300 km. depending upon the latitude zone (and raob density). Linear time interpolation of the raob data to the sounding time is done if the time difference for the matchup exceeds 3 hours. The matchup files are archived by NESDIS every 15 days for research and development purposes and system backup.

The re-retrieval method is applied in two ways to evaluate the impact of removing specified TOVS channels from the processing.

Procedure "A" evaluates observed NOAA-9 and NOAA-10 error statistics using the separate matchup files archived for each satellite. The dependent and independent samples from each satellite are selected for the same time period. This procedure directly measures the impact removing MSU channels 2 and 3 and HIRS/2 channel 16 using coincident data from NOAA-9 and NOAA-10. However, this procedure also reflects differences due to the different samples for each satellite which can distort the results.

Procedure "B" evaluates the impact of removing each of the following channels from the TOVS processing system:

- o HIRS/2 channel 16,
- o HIRS/2 channel 16 and MSU channels 2 & 3, and
- o All MSU channels.

This is done using the NOAA-10 matchup data only. The dependent and independent matchup samples are identical for each of the above scenarios with separate "new" coefficients for each. This avoids the problem of comparing results for different samples. However, evaluation results do not necessarily reflect the actual performance of a particular satellite (i.e., NOAA-9).

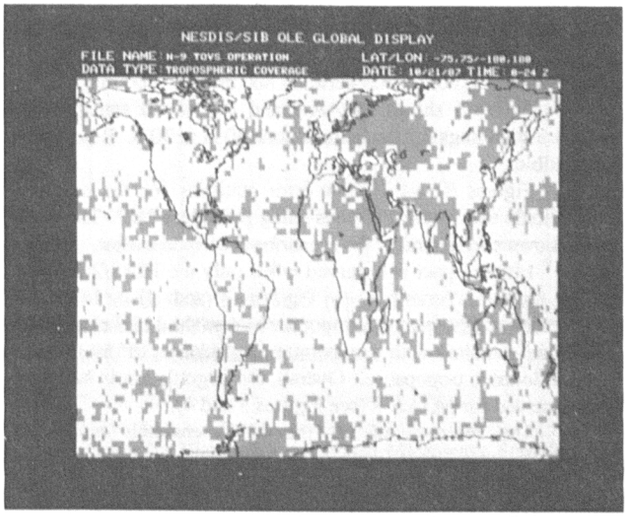

Fig. 2: NOAA-9 Tropospheric Coverage for a 24-hour Period, White Areas Indicate No Coverage Due to Clouds.

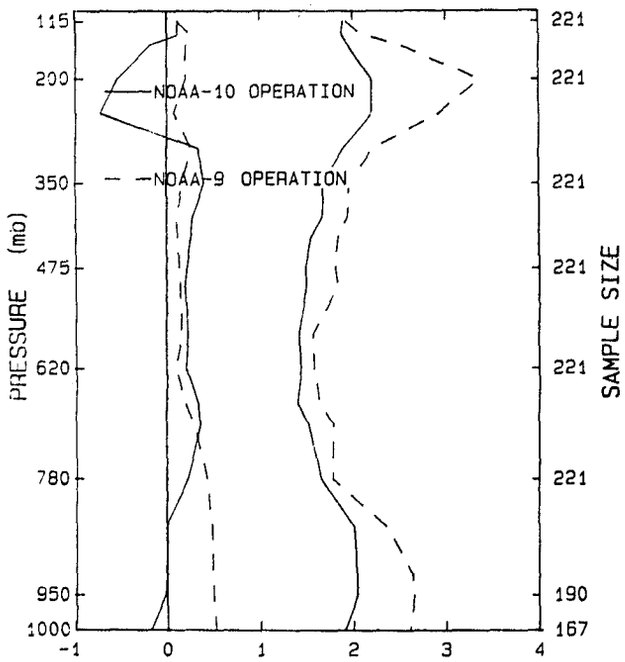

Fig. 3: Mean (left) and RMS (right) Error (°K) Statistics for Temperature Soundings in the Latitude Zone 60 N to 30 N Using Procedure "A", 9/28/87 - 10/4/87.

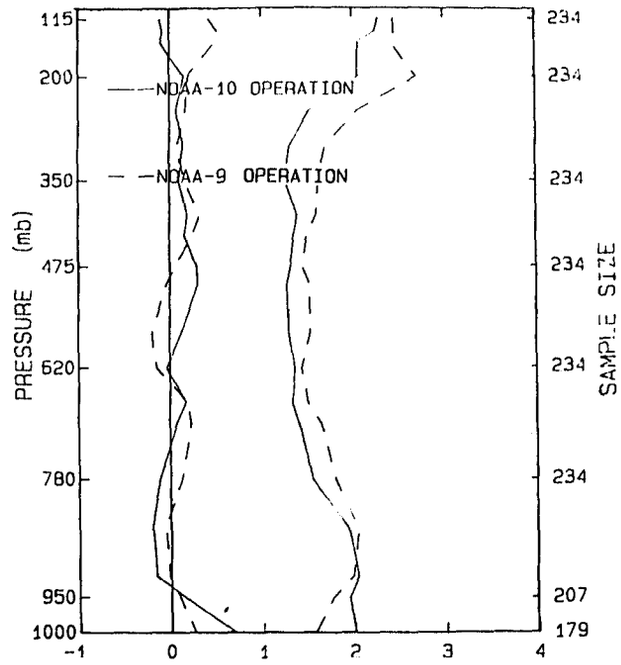

Fig. 4: Mean (left) and RMS (right) Error (°K) Statistics for Temperature Soundings in the Latitude Zone 30 N to 30 S Using Procedure "A", 9/28/87 - 10/4/87.

3.2 Evaluation Results

Results comparing the mean and rms error statistics for the various sounding system scenarios are summarized below. Only tropospheric data are shown, results in the stratosphere being least affected by the channels removed. Results are for clear TOVS soundings. The evaluation period chosen was September 28 through October 4, 1987.

Figures 3 and 4 show error statistics for temperature soundings for the latitude zones 60 N to 30 N and 30 N to 30 S using procedure "A." NOAA-9 soundings (dashed line) appear worse than those for NOAA-10 (solid line) particularly near the tropopause (200 mb.) in both zones. A maximum degradation of 1.1° rms occurs at the mid-latitude tropopause (although the NOAA-9 mean error is smaller for this case). NOAA-9 is about .3° rms worse in both zones between 800 mb. and 300 mb.

Figure 5 shows NOAA-9 and NOAA-10 statistics for moisture soundings for the latitude zone 30 N to 30 S. Results are compatible.

Figures 6 and 7 show error statistics for the northern mid-latitude and tropical regions using procedure "B." The three plots shown correspond to the scenarios described earlier.

Little impact is observed when only the HIRS/2 channel 16 is removed (compare to Figures 3 and 4). Increased degradation occurs near the tropopause when the MSU channels 2 and 3 are removed with a maximum degradation of .5° rms for the mid-latitude tropopause. Overall, the degradation is less than that observed for NOAA-9 (see Figures 3 and 4).

The removal of all the MSU channels results in significant degradation in the north mid-latitude region but no degradation in the tropics. This may be due to the wider range of atmospheric conditions encountered in the mid-latitudes as well as the location of the tropopause relative to the TOVS atmospheric sensitivity gaps (see Figure 1). It may also reflect the impact of replacing MSU channel 4 with a stratospheric

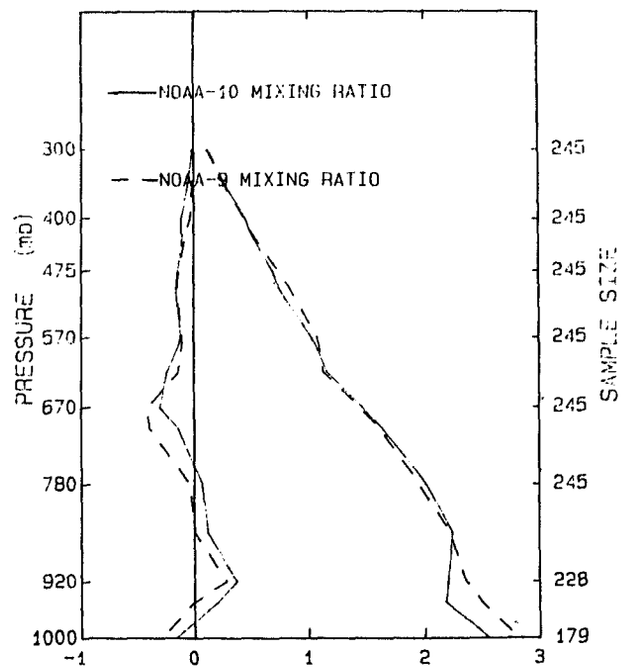

Fig. 5: Mean (left) and RMS (right) Error (G/KG) Statistics for Moisture Soundings in the Latitude Zone 30 N to 30 S Using Procedure "A", 9/28/87 -10/4/87.

HIRS/2 channel, whose noise level is higher, for coefficient interpolation.

Figures 8 and 9 summarize error statistics for the latitude zone 30 S to 60 S using procedures "A" and "B", respectively. Overall, these results support those reported for the northern mid-latitude region.

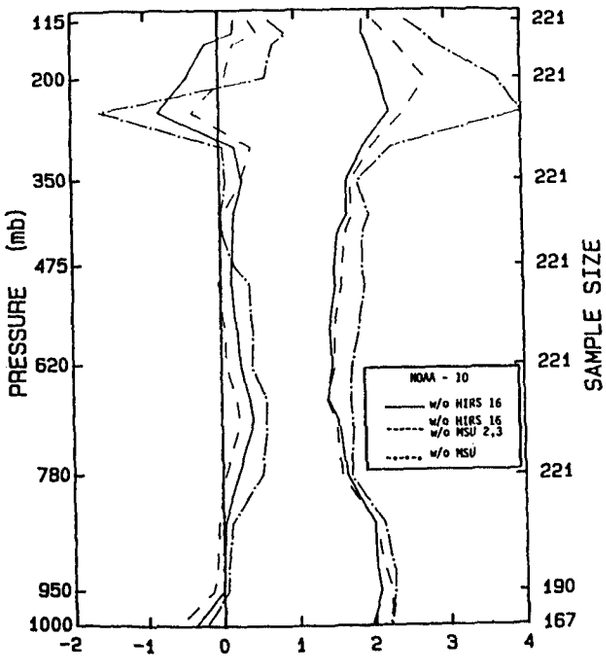

Fig. 6: Mean (left) and RMS (right) Error (°K) Statistics for Temperature Soundings in the Latitude Zone 60 N to 30 N Using Procedure "B", 9/28/87 - 10/4/87.

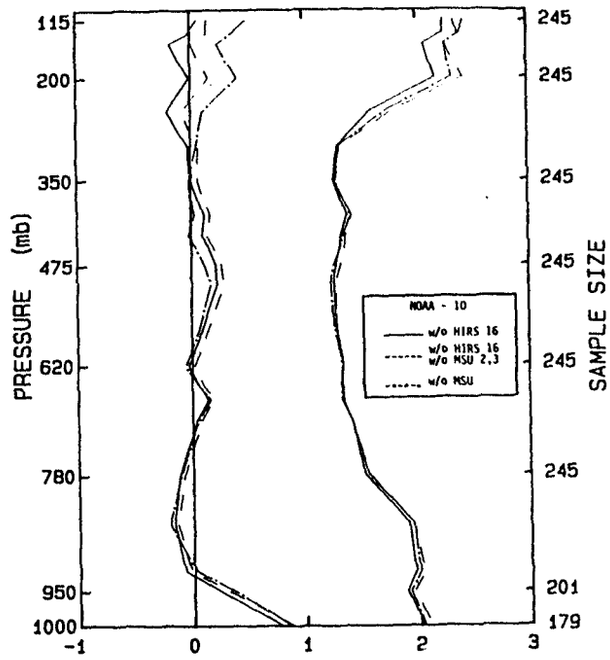

Fig. 7: Mean (left) and RMS (right) Error (°K) Statistics for Temperature Soundings in the Latitude Zone 30 N to 30 S Using Procedure "B", 9/28/87 - 10/4/87.

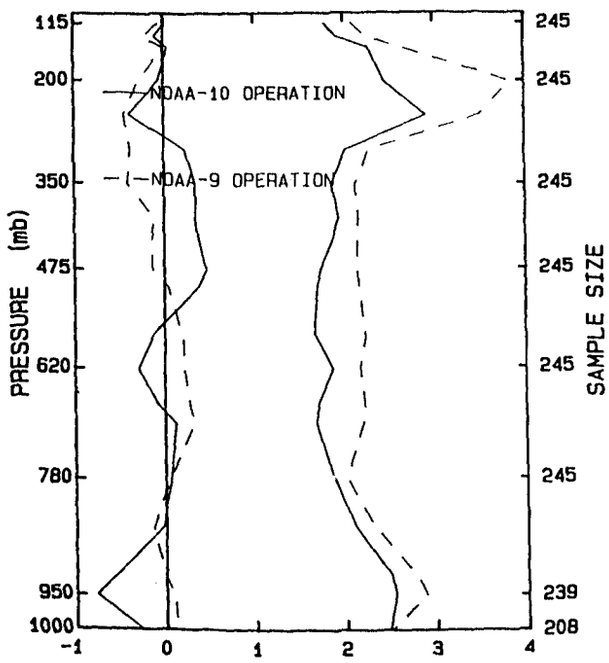

Fig. 8: Mean (left) and RMS (right) Error (°K) Statistics for Temperature Soundings in the Latitude Zone 30 S to 60 S Using Procedure "A", 9/28/87 - 10/4/87.

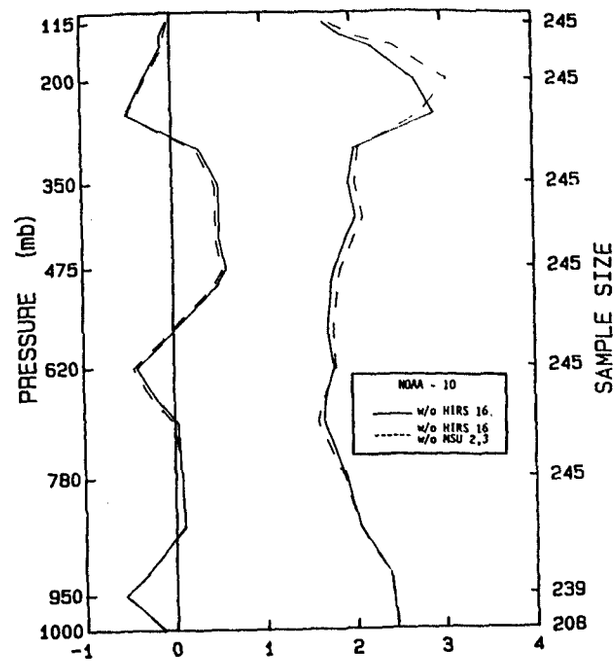

Fig. 9: Mean (left) and RMS (right) Error (°K) Statistics for Temperature Soundings in the Latitude Zone 30 S to 60 S Using Procedure "B", 9/28/87 - 10/4/87.

4. OTHER APPLICATIONS

The generation of TOVS sounding products without tropospheric MSU data has recently become an issue at NESDIS. During 1987, it was decided that an infrared-only sounding capability would be developed for the NOAA-K, L, M polar orbiter series. In this new series the SSU and MSU sounders are replaced by the 20-channel Advanced Microwave Sounding Unit and the HIRS/2 by the HIRS/3. Instrument design for the HIRS/3 includes a stand-alone operational capability. This combined with the loss of timely sounding products in the northeast Pacific for NMC forecast models prompted the development of the "HIRS/2-only" sounding system for NOAA'9. Previously, such an operation was not sanctioned by NESDIS.

In the 1990 timeframe, NESDIS plans to launch the first in a series of improved geostationary satellites (GOES I-M). Onboard will be an improved 18 channel infrared sounder, nearly identical to the HIRS/3 instrument. Since the GOES I-M series will not have a microwave sensing capability, the atmospheric soundings will be retrieved using infrared-only algorithms. NESDIS plans to investigate the applicability of the infrared only techniques developed for the polar orbiting NOAA-K, L, M series to the geostationary sounding system. This could move NESDIS closer to the goal of employing similar scientific methods for the retrieval of atmospheric soundings from all operational satellites (polar, geostationary, military, etc.)

5. SUMMARY

Modification of the TOVS processing system to generate tropospheric sounding products without using the tropospheric MSU sounding channels is described. This was necessitated by the failure of MSU channels 2 and 3 onboard NOAA-9.

Results are presented which show that there is a degradation in sounding quality particularly near the tropopause when the MSU tropospheric channels are removed. Furthermore, without MSU support, accurate TOVS tropospheric soundings can only be produced in clear atmospheres. This reduces global tropospheric coverage to about 30% of normal.

Despite these deficiencies, the soundings from NOAA-9 provide timely and valuable information for global and regional numerical weather prediction models. This system became operational at NESDIS on September 1, 1987. NMC is scheduled to begin using NOAA-9 products in their models in early November, 1987. The success of the processing system for NOAA-9 is an important step for future developments in the NOAA-K, L, M and GOES sounding systems.

6. REFERENCES

McMillin, L.M. and C. Dean: An Evaluation of A New Operational Technique for Producing Clear Radiances, Journal of Applied Meteorology, Vol. 12, NO. 7, July 1982.

McMillin, L.M, et al., U.S. Department of Commerce: The Complementary Roles of Microwave and Infrared Instruments in Atmospheric Sounding. NOAA Technical Report, NESDIS 29, Feb. 1987.

Reale, A., D. Gray, M. Chalfant, A. Swaroop and A. Nappi: Higher Resolution Operational Satellite Retrievals, 2nd Conference on Satellite Meteorology/Remote Sensing and Applications, AMS, May 13-16, 1986. Williamsburg, Va.

Smith, W., H. Woolf, C. Hayden, D. Wark and L. McMillin: TIROS-N Operational Vertical Sounder. Bull. Amer. Meteor. Soc., 60, 10, 1177-1187, Oct. 1979.

Smith, W.L.: The Retrieval of Atmospheric Profiles from VAS Geostationary Radiance Observations. J. Atmos. Sci., 40,2025-2035, 1983.

Werbowetzki, A., U.S. Dept. of Commerce, 1981: Atmospheric Sounding Users's Guide. NOAA Tech. Re. NESS 83, April 1981.

7. ACKNOWLEDGMENTS

The authors thank Pauline Mazzella, Betty Wilson and John Shadid of the Satellite Applications Laboratory of NESDIS, and Charles Brown of ST Systems Corporation for their support in preparing this document. We also acknowledge Charles Novak, Chief of the Sounding Implementation Branch, for his contributions.

1.9

IMPROVED VAS REGRESSION SOUNDINGS OF MESOSCALE TEMPERATURE FEATURES OBSERVED DURING THE ATMOSPHERIC VARIABILITY EXPERIMENT ON 6 MARCH 1982

DENNIS CHESTERS, DENNIS A. KEYSER[1,2], DAVID E. LARKO[3] AND LOUIS W. UCCELLINI

Laboratory for Atmospheres
NASA/Goddard Space Flight Center
Greenbelt, MD 20711

1. INTRODUCTION

The VISSR Atmospheric Sounder (VAS) on the Geosynchronous Operational Environmental Satellites (GOES) has twelve infrared channels designed to provide frequent, high-resolution temperature and moisture soundings over the United States. In 1982, an Atmospheric Variability Experiment (AVE) was performed to verify VAS's mesoscale sounding capabilities (Dodge *et al.*, 1985). Radiosondes were launched at 3 hour intervals from an AVE mesoscale network consisting of 13 special mobile sites in north-central Texas while VAS simultaneously gathered radiometric data. To monitor the surrounding region, the National Weather Service (NWS) stations in the central United States also launched balloons at 3 hour intervals, forming a supplementary AVE regional network. Figure 1 illustrates the entire AVE network late in the afternoon of 6 March 1982, after a winter storm had passed over Texas. The strong temperature gradients in the cloud-free post-frontal environment over north-central Texas provide optimal conditions for verifying VAS temperature soundings using the AVE mesoscale observations.

Jedlovec (1985) and Fuelberg and Meyer (1986) have compared VAS soundings to the AVE radiosonde observations for 6 March 1982. They found that the previous VAS retrievals for this case do a poor job of detecting temperature profile deviations from the average lapse rate, including features such as the tropopause, a mid-level cold pool and a low-level inversion over north-central Texas (Fig. 2). Although VAS vertical resolution is limited by the nature of passive radiation transfer, a cold pool should significantly decrease the brightness of several infrared channels. Poor mid-tropospheric resolution in the geosynchronous satellite soundings under ideal conditions is a cause for concern because thermal features indicate important mesoscale dynamic processes, such as jets and vertical motions, which are difficult to detect in clear air using passive remote sensing techniques.

The purpose of this paper is to determine whether the cold pool can be retrieved from the 6 March 1982 VAS radiances, using an enhanced version of a ridge-regression algorithm originally applied to VAS data by Lee *et al.* (1983). Two simple enhancements are introduced in this paper: (1) the regression matrix is calculated using the AVE asynoptic radiosondes launched from NWS sites in the region (see Fig. 3); and (2) the statistical conditioning factor is changed from a conservative 10/1 signal/noise ratio to an optimistic 100/1 ratio for those VAS channels which are most sensitive to tropospheric temperature (see Fig. 5). The intent is to sensitize the VAS regression retrieval algorithm without introducing horizontal structure into the first-guess field (as does Smith *et al.*'s (1983) physical algorithm) and without drawing upon the special mesoscale AVE "ground truth" radiosondes used for independent verification over north-central Texas.

The AVE "ground truth" soundings are compared to the original "VAS1" and the enhanced "VAS2" satellite soundings for resolution and accuracy. Successful resolution of the cold bubble would indicate that the poor VAS1 results were due to limitations in the sounding algorithm, not to the VAS radiometer.

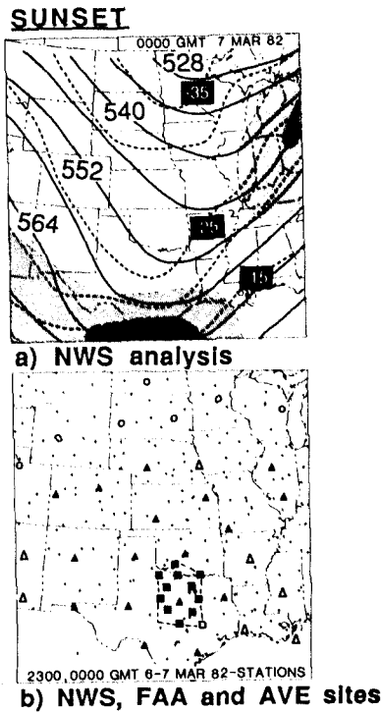

FIG. 1. The central United States at 2300-0000 GMT on 6-7 March 1982: (a) a synoptic upper-air analysis of 500 mb geopotential height (solid, dam), 500 mb temperature (dashed, °C), and 300 mb wind speeds (lightly stippled for 45 to 55 m sec^{-1} and darkly stippled above 55 m sec^{-1}); and (b) a map showing the location of FAA surface reports (+), radiosonde profiles from the synoptic NWS operational network (O), from the asynoptic AVE regional network (Δ), and from the special AVE mesoscale (Π) network. Cloud-free radiosonde sites are marked with filled symbols, and cloudy sites are marked with unfilled symbols. A trough with a jet to the south is passing through the AVE mesoscale network in north-central Texas.

[1] General Sciences Corporation, Landover, MD 20785.
[2] Present affiliation: NOAA/NMC, Camp Springs, MD 20748.
[3] Research and Data Systems, Lanham, MD 20706.

2. OBSERVATIONS

This case is characterized by a late winter storm which passed over the south-central United States, producing snow in Colorado, Oklahoma and northern Texas and cold rain from central Texas to the Gulf Coast. Behind the storm system, cold dry air pushed rapidly southeastward into the region, so that a cloud-free post-frontal environment prevailed over north-central Texas after 1700 GMT. Figure 4 presents a time-series of the operational surface analyses and corresponding GOES visible imagery for the afternoon of 6 March. The GOES images in Fig. 4-b depict the rapid clearing across Oklahoma and north-central Texas behind the storm system, with melting snow cover across southern Colorado and the Texas-Oklahoma panhandle. The surface temperature fields in Fig. 4-a indicate that a strong temperature gradient is present beneath the cloud cover behind the front along the Gulf Coast, that cooler temperatures are maintained by snow cover in Colorado and the Texas-Oklahoma panhandle, maintaining a low-level inversion, while mid-afternoon solar heating warms the dry air in the boundary layer over west-central Texas.

The upper air environment illustrated in Fig. 1-a contains strong low- and mid-level temperature gradients associated with a subtropical jet streak at the base of a mid- and upper-level trough which extends from the upper-Mississippi valley southeastward into Texas. The clear zone depicted in Fig. 4-b over north-central Texas and Oklahoma extends across the AVE regional and mesoscale network providing ideal conditions for calculating VAS temperature soundings which can be compared to the special AVE radiosondes operating that day. More complete analyses for this case are described by Jedlovec (1985) and Fuelberg and Meyer (1986).

Figure 3 summarizes the datasets gathered during the VAS/AVE operations on 6 March. Five periods of contemporaneous data were obtained within ±1 hour at 3 hour intervals. The local time periods are dawn, morning, noon, mid-afternoon and sunset. Only the last three periods (collectively called "afternoon") are analyzed in this study because clouds covered most of the Texas-Oklahoma region prior to 1700 GMT. The database includes four conventional radiosonde and surface datasets and two geosynchronous satellite datasets, and is more completely described by Chesters *et al.* (1987).

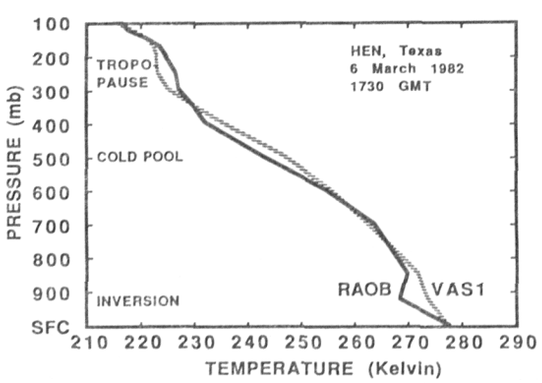

FIG. 2. The AVE radiosonde temperature (solid, °C) profile from Henrietta, Texas (HEN) at 1700 GMT located on the northern edge of the special mesoscale network and compared to the corresponding VAS1 satellite retrieval at 1730 GMT (dashed). Significant temperature deviations from the average lapse rate occur in an inversion just above the surface, through a cold pool near 500 mb, and at the tropopause. The previous VAS1 retrievals scarcely resolved these features.

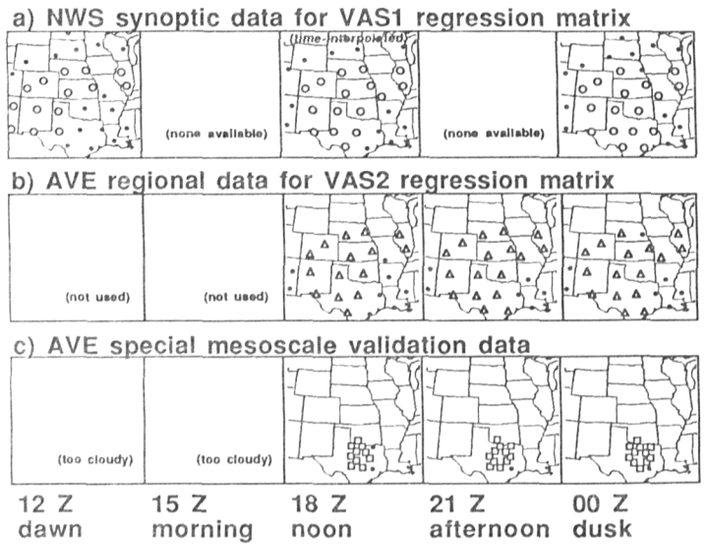

FIG. 3. Statistical design for VAS1 and VAS2 regression soundings on 6 March 1982: (a) the locations of NWS radiosonde profiles used to calculate the VAS1 regression matrix, including some time-interpolated "synthetic" profiles at 18 Z; (b) the locations of AVE regional radiosonde profiles launched from NWS sites at 3 hour intervals and used to calculate the VAS2 regression matrix; and (c) the locations of the AVE special mesoscale radiosonde sites used for independent verification of the VAS1 and VAS2 satellite soundings. Cloud-free radiosonde sites are marked with large unfilled symbols, and cloudy sites are marked with dots. Because the number of radiosonde sites and spatial coverage for the VAS1 and VAS2 regression training are similar, the improvement in VAS2 retrieval accuracy is provided by the timeliness of the asynoptic profile network.

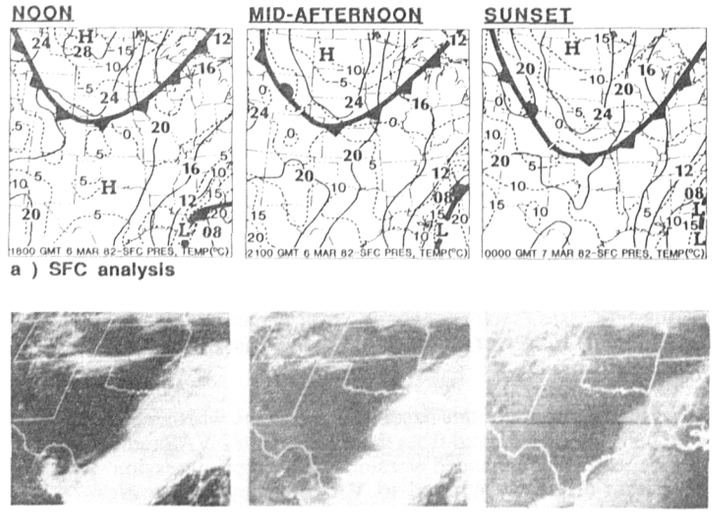

FIG. 4. Operational data during the last three AVE observing periods over the central United States on the afternoon of 6 March 1982, following a late winter storm over the Texas-Oklahoma region: (a) analyses of surface pressure (solid, mb), temperature (dashed, °C) and surface fronts; and (b) GOES visible images. The bright areas in the visible images of the Texas-Oklahoma panhandle are melting snow cover, not clouds. At sunset, the faintly lit clouds are difficult to distinguish in southeastern Texas.

3. THE VAS REGRESSION ALGORITHM

VAS soundings are calculated by a "ridge regression" algorithm that utilizes a combination of VAS radiances and ancillary FAA surface data to predict atmospheric temperature, moisture and stability values over the United States (Lee *et al.*, 1983). Statistical conditioning, in the form of an *a priori* signal/noise ratio (S/N), is used to suppress noisy channels and stabilize a regression matrix calculated from a modest number of observations (Marquardt and Snee, 1975). The "signal" is the atmospheric variance (±°C, air temperature) and the "noise" is observational error (±K, brightness temperature). For the original VAS1 soundings, S/N=10/1 was used for all predictors, based upon relatively conservative signal and noise estimates, ±5°C and ±0.5 K, respectively. For the VAS2 soundings, S/N=100/1 is used for the VAS and surface predictors of atmospheric temperature, based upon more optimistic signal and noise estimates for the lower troposphere, ±10°C and ±0.1 K, respectively. For all retrievals, S/N=1/10 is used for suppressing the effects of reflected sunlight in channel 12, and S/N=10/1 is applied to the upper air water vapor channels 9 and 10.

Figure 5 presents the weighting functions for the VAS channels. Because the mid-level cold pool on 6 March 1982 is approximately 4°C colder through a layer that is approximately one-quarter the thickness of a VAS weighting function, the cold pool should decrease the brightness temperature by approximately 1 K for those VAS channels which are sensitive to mid-level temperature. This "signal" must compete with radiometric noise (at least ±0.25 K) and with the effects of other temperature variations above and below the cold pool. Attempts were made to detect the cold pool using direct multispectral imaging techniques with linear combinations of VAS channels 3, 4, 5 and 6, but the cold pool's net effect is too faint to detect so easily.

The original VAS1 regression matrix was calculated from a total of 50 cloud-free synoptic scale observations for three observing periods illustrated in Fig. 3-a, including 15 time-interpolated profiles at local noon (18 Z). The VAS2 regression matrix was calculated from a total of 49 cloud-free regional scale observations from the three afternoon observing periods illustrated in Fig. 3-b. The VAS1 and VAS2 satellite profiles are each statistically verified against the same independent set of 32 mesoscale radiosonde observations obtained during the last three observing periods by the AVE special network over north-central Texas as illustrated in Fig. 3-c.

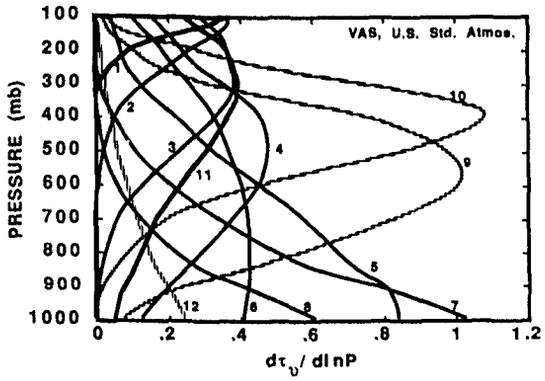

FIG. 5. VAS weighting functions using the US Standard Atmosphere profile. Dashed lines indicate those channels which do not receive more optimistic signal/noise conditioning in the VAS2 soundings. A cold pool from 400 to 600 mb should affect several VAS temperature sounding channels.

4. TEMPERATURE SOUNDINGS

Fig. 6 presents a comparison between a time-series of 500 mb temperature analyses for the AVE, VAS1 and VAS2 soundings during the three afternoon periods on 6 March. The AVE "ground truth" analyses (Fig. 6-a) clearly captures the cold pool moving southeastward across north-central Texas and the frontal gradient moving across the Gulf Coast. The original VAS1 temperature soundings (Fig. 6-b) capture some of the pool and temperature gradient at noon, but fail to properly resolve the horizontal structure during the late-afternoon soundings. The new VAS2 temperature soundings (Fig. 6-c) are much more temporally consistent than the VAS1 analyses, capturing the cold pool as a distinct structure at all three times. The VAS2 soundings still underestimate the intensity of the cold pool, but are consistent in centering this feature over the AVE data-sparse region of eastern Oklahoma. Across the southern portion of the mesoscale, the VAS2 temperature gradient network is stronger than the corresponding VAS1 gradient and is also more properly aligned with the northwest-southeast direction indicated in the AVE analyses.

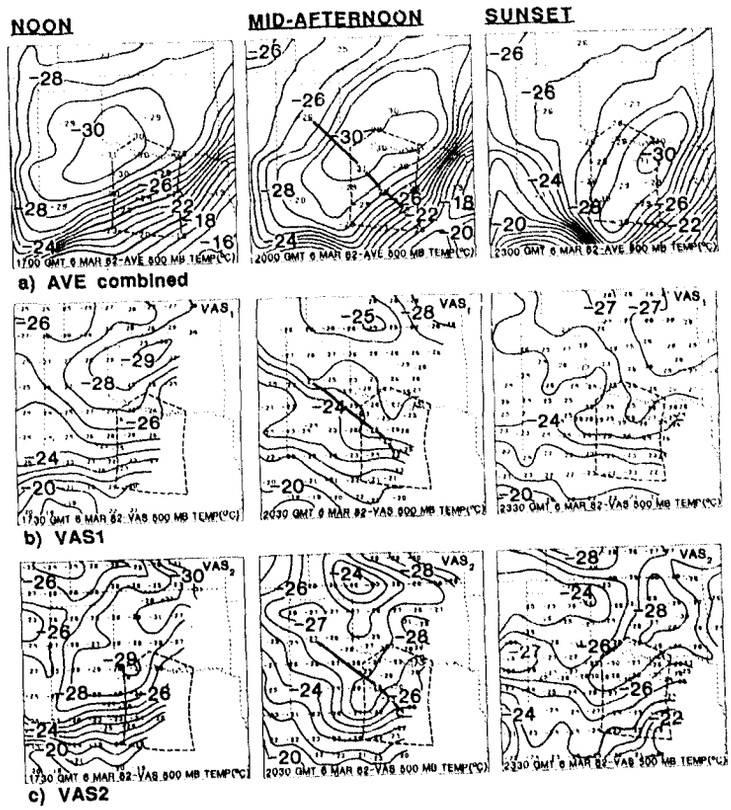

FIG. 6. A time-series of temperature (°C) analyses at 500 mb over north-central Texas and Oklahoma during the three cloud-free observing periods on 6 March 1982 for: (a) AVE regional and mesoscale radiosondes combined; (b) original VAS1 soundings; and (c) enhanced VAS2 soundings. Vertical cross sections of potential temperature are presented in Fig. 8 along the paths indicated by the thick solid lines drawn diagonally across the mid-afternoon fields. The enhanced VAS2 soundings resolve more thermal features, especially the cold pool over north-central Texas during the late afternoon.

The root mean square (RMS) differences between the VAS1 and VAS2 profiles and the independent AVE mesoscale verification radiosondes are presented in Fig. 7. The error maxima for the VAS1 soundings correspond to the problem levels indicated in Fig. 4: the tropopause, the cold pool and the boundary layer. The VAS2-AVE errors in the temperature soundings are approximately ±1.0°C smaller in these three layers, demonstrating the effectiveness of the VAS2 algorithm enhancement. The greatest residual errors still occur at 500 mb, and are reflected in the differences between the VAS and AVE analyses in Fig. 6. Nevertheless, approximately one-half of the "signal" from the cold pool is recovered using only the enhanced VAS2 regression algorithm and no horizontal structure in the first guess.

Because satellite soundings can mis-assign a 500 mb temperature variation to adjacent levels, the vertical blurring in VAS soundings should result in thickness observations that are still approximately correct for layer averages. To test this hypothesis, vertical cross sections of potential temperature θ(p) were calculated and are presented in Fig. 8 for the AVE, VAS1 and VAS2 soundings during the mid-afternoon episode, when the cold pool was entering the mesoscale network from the northwest. The cross sections extend from the Texas panhandle into the special mesoscale network along the diagonal lines drawn on the corresponding mid-afternoon panels in Fig. 6. Each cross section is based upon an objective analysis of potential temperature drawn from four individual soundings indicated with vertical lines in Fig 8. The VAS cross sections in Figs. 8-b and 8-c do not extend quite as far to the southeast as the AVE cross section due to lingering cloud cover above the southeastern edge of the special radiosonde network at this time. The AVE θ(p) cross section in Fig. 8-a clearly delineates the tropopause, cold pool, and low-level inversion,. The VAS1 θ(p) cross section scarcely resolves any of these structures. By contrast, the VAS2 θ(p) cross section determines these structures clearly, and the 500 mb cold pool is especially well defined. Therefore, the new VAS2 algorithm is successful in delineating the bulk thermodynamic effect of the cold pool over a deep layer.

Geosynchronous satellite soundings provide very detailed horizontal resolution over large regions. The AVE mesoscale network depicted in Fig. 3-c provides 100 km resolution, but only in a limited area over north-central Texas, while the VAS soundings provide 60 km resolution over the entire cloud-free region. Fig. 9 indicates the effects of different resolution and coverage on 500 mb temperature analyses at local sunset (2300 to 0000 GMT). The NWS synoptic observations in Fig. 9-a contain a single report of -29°C at Stephenville, Texas (SEP) in the center of the AVE special network, but the 500 mb cold pool is resolved only by the mutually supporting radiosonde data from the AVE mesoscale network. However, even the AVE combined analysis in Fig. 9-b provides little resolution across the northern Texas panhandle and Oklahoma, where the VAS2 soundings in Fig. 9-c apparently resolve several additional features: 1) another cold pool over the Texas-New Mexico border, 2) a warm pool over the Texas-Oklahoma panhandle, and 3) an extension to the original cold pool over central Oklahoma. Although these thermal features are too far north and west to be verified by using the AVE mesoscale radiosondes, the additional structures appear to be just as creditable as the thermal gradient and cold pool verified by the VAS2 soundings over the AVE mesoscale network in north-central Texas. The VAS2 results indicate that ground-based asynoptic regional temperature profiles and high resolution satellite radiances can be successfully combined to provide mesoscale resolution of upper-air thermal features which are scarcely resolved by a ground-based regional network alone.

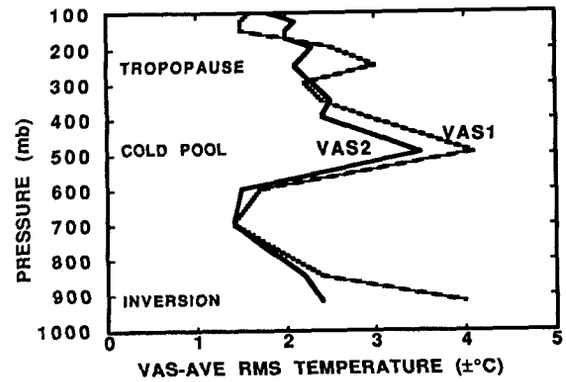

FIG. 7. RMS errors in the retrieved temperature (°C) profiles, comparing the original VAS1 and enhanced VAS2 retrievals to co-located profiles from the independent AVE mesoscale network during the last three observing periods on 6 March 1982. The enhanced VAS2 soundings are significantly improved by using asynoptic profile observations to calculate the retrieval matrix.

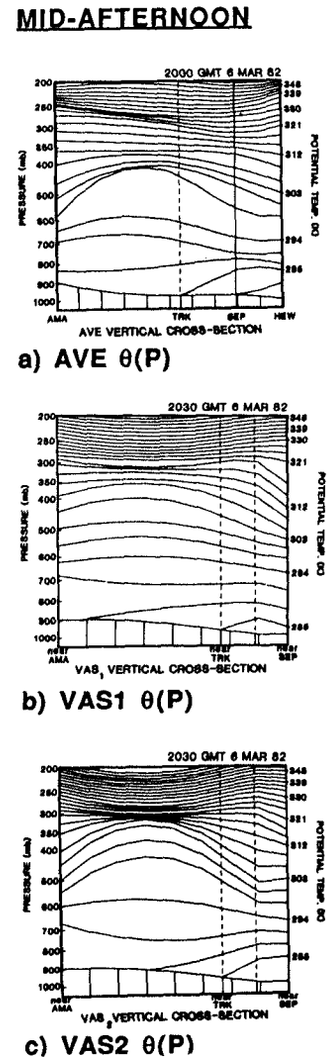

FIG. 8. Vertical cross-sections of potential temperature (θ(p), Kelvin) across north-central Texas at mid-afternoon on 6 March 1982 based upon temperature profiles from: (a) the AVE regional and mesoscale networks, (b) the original VAS1 soundings and (c) the enhanced VAS2 soundings. The cross sectional path is indicated on the corresponding mid-afternoon analyses in Fig. 6. The original VAS1 soundings suffer poor vertical resolution while the enhanced VAS2 soundings capture a cold pool.

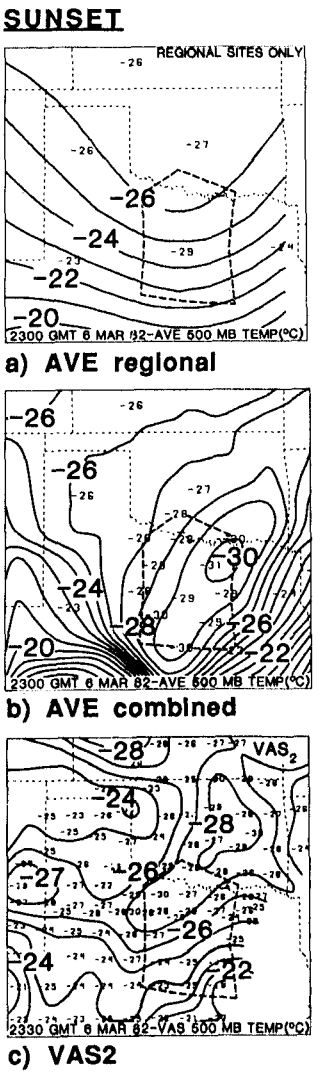

FIG. 9. Temperature (°C) analyses at 500 mb during the sunset period on March 6, indicating the effect of inreased horizontal resolution over the Texas-Oklahoma region for: (a) the regional network of radiosondes launched at NWS sites; (b) a combination of AVE regional and mesoscale radiosondes; and (c) the VAS2 satellite soundings. The mesoscale radiosonde and satellite soundings both capture thermal structures which are completely unresolved by the regional radiosonde network. Although VAS2 gradients are less distinct for the cold pool verified by the mesoscale radiosonde network over north-central Texas, the satellite analysis suggests that this cold pool actually extends into central Oklahoma and is accompanied by a warm pool over the Oklahoma panhandle and by other smaller pools.

5. SUMMARY AND CONCLUSIONS

In order to verify geosynchronous satellite soundings from the VISSR Atmospheric Sounder (VAS), an Atmospheric Variability Experiment (AVE) launched radiosondes at 3 hour intervals from a special mesoscale network over the north-central Texas during 6 March 1982. Previous VAS soundings for this case scarcely detected significant temperature structures, including a mid-tropospheric cold pool and a low-level inversion. In order to determine whether these mesoscale thermal features could be retrieved from VAS radiances without introducing any horizontal structure into the first-guess, the 6 March 1982 case was re-processed using an enhanced version of a regression retrieval algorithm. The principal enhancement is the use of asynoptic radiosondes observed at the same time as the midday satellite data in order to construct a more appropriate regression matrix. In the dataset used to calculate the regression matrix, neither the number of radiosondes nor their spatial distribution was enhanced, only the time of observation.

The enhanced algorithm better detects the significant temperature variations from a mean lapse rate and delineates three dimensional mesoscale temperature fields with improved accuracy. Therefore, the enhanced VAS2 soundings better resolve the faint atmospheric temperature structures which were poorly retrieved by the original VAS1 soundings. However, the improvement in the VAS retrievals in this case required the use of some asynoptic temperature profiles collected at NWS radiosonde sites during midday satellite observations.

This type of profile data is not normally available. Other case studies using VAS midday soundings have had mixed success in providing an impact upon analyses of storm environments (Kitzmiller, 1986; Shoeni and Mosher, 1986; Mostek *et al.*, 1986; Petersen and Keyser, 1987) and upon numerical forecast models (Mostek and Olsen, 1986; Aune *et al.*, 1987). Perhaps these other cases also failed to utilize all of the information available in the VAS radiances because of the lack of ground-based asynoptic profiles. Indeed, Mostek *et al.*, (1986) note that the lack of midday radiosondes over the United States is a major inhibiting factor in deriving accurate VAS retrievals.

Because most of the improvement to the accuracy of VAS midday soundings in the March 6 case stems from the use of asynoptic radiosonde observations at NWS sites, the results from this paper imply that a regional temperature profiling network might be required to bridge the gap between the operational synoptic network and mesoscale satellite soundings. A combined satellite- and ground-based sounding system has the potential for exploiting the strengths of each observing system to provide accurate, high resolution datasets for analysis and prediction. The ground-based system could be selected radiosonde releases, upward-looking microwave Profilers, or a combination of the two. In such a scheme, the ground-based profiles provide accurate temperature and moisture information at a few points in a region, while the satellite sounder provides radiance information with good horizontal resolution and coverage to fill in the mesoscale structure during each asynoptic observing period. Westwater *et al.*, (1984) have already demonstrated that the vertical resolution of remotely-sensed temperature and moisture profiles can be improved by calculating them from a combination of ground-based upward-looking microwave Profiler data and downward-looking satellite-based infrared and microwave data from a polar orbiter.

An asynoptic regional network of radiosondes and/or ground-based microwave Profilers, combined with the GOES Sounder, might provide the accuracy and resolution required for useful mesoscale sounding and analysis of convective environments. Of course, the eventual development of such a system will require mesoscale "ground truth" cases for algorithm development and verification, a situation currently being considered as part of NOAA's STORM project.

Other VAS retrieval algorithms could benefit from ground-based asynoptic profile data. For example, the physical algorithm developed by Smith *et al.* (1983) requires a good first-guess temperature and moisture field from a numerical forecast model, but the retrievals are quite sensitive to model forecast errors. An asynoptic ground-based profiling network could provide the first-guess field instead.

For this 6 March 1982 case study, the satellite-based mesoscale temperature retrievals are more accurate using the enhanced VAS regression retrieval algorithm than the corresponding retrievals (see Jedlovec (1985) and Fuelberg and Meyer (1986)) from a physical retrieval algorithm developed by Smith *et al.* (1983). Furthermore, Chesters *et al.* (1986) have shown that the regression approach is fast enough to meet realtime imaging and analysis requirements for processing VAS soundings at mesoscale resolution, and it also is simple enough to implement using a modest computer system. It is therefore possible that a regression-based retrieval system could provide the speed, coverage and accuracy required for operational mesoscale soundings by marrying a few ground-based profiles from the region of interest with large volumes of simultaneously observed geosynchronous satellite radiances.

Acknowledgments The AVE/VAS experiment and subsequent assessments have been supported by Dr. James Dodge of NASA's Severe Storm Research Program. A complete set of GOES observations for 6 March 1982 were assembled by combining VAS data capture tapes at Goddard Space Flight Center (GSFC) in Greenbelt, Maryland with tapes provided by the Space Sciences and Engineering Center (SSEC) in Madison, Wisconsin. Data processing was performed on the Atmospheric and Oceanographic Image Processing System (AOIPS) at GSFC, with assistance from Mr. Anthony Mostek, Mr. Wayne Robinson and Dr. Tay-How Lee.

6. REFERENCES

Aune, R.M., L.W. Uccellini, R.A. Petersen and J.T. Tuccillo, 1987: A VAS numerical model impact study using the Gal-Chen variational approach. *Mon. Wea. Rev.*, **115**, accepted for the April issue.

Chesters, D., A. Mostek and D.A. Keyser, 1986: VAS sounding images of atmospheric stability parameters. *Weather and Forecasting*, **1**, 5-22.

Chesters, D., D.A. Keyser, D.E. Larko and L.W. Uccellini, 1987: Improved VAS regression soundings of mesoscale temperature features observed during the Atmospheric Variability Experiment on 6 March 1982. NASA TM-100679, 44 pages.

Dodge, J., J.R. Greaves and H.E. Montgomery, 1985: AVE/VAS ground truth experiment. *VAS demonstration: (VISSR Atmospheric Sounder) description and final report.* H.E. Montgomery and L.W. Uccellini, Eds. NASA RP-1151 [NTIS 86N13867], 50-54.

Fuelberg, H.E. and P.J. Meyer, 1986: An analysis of mesoscale VAS retrievals using statistical structure functions. *J. Climate Appl. Meteor.*, **25**, 60-76.

Jedlovec, G.J., 1985: An evaluation and comparison of vertical profile data from the VISSR Atmospheric Sounder (VAS). *J. of Atmos. and Oceanic Technology*, **2**, 559-581.

Lee, T.H., D. Chesters and A. Mostek, 1983: The impact of conventional surface data upon VAS regression retrievals in the lower troposphere. *J. Climate Appl. Meteor.*, **22**, 1853-1874.

Marquardt, D.W., and R.D. Snee, 1975: Ridge regression in practice. *Amer. Stat.*, **29**, 3-20.

Mostek, A. and D.A. Olsen, 1986: Eastern Pacific model impact study (EPAC) at the National Meteorological Center. *Preprint, 2nd Conf. on Satellite/Remote Sensing and Applications*, Williamsburg, Amer. Meteor. Soc., 164-167.

Mostek, A., L.W. Uccellini, R.A. Petersen and D. Chesters, 1986: Assessment of VAS soundings in the analysis of a preconvective environment. *Mon. Wea. Rev.*, **114**, 62-87.

Petersen, R.A. and D.A. Keyser, 1987: An evaluation of various forms of VAS retrievals in the analysis of a preconvective environment. Accepted by *Meteor. and Atmos. Physics.*

Shoeni, T.R. and F.R. Mosher, 1986: Real-time use of VAS data at the National Severe Storms Forecast Center. *Preprint, 11th Conf. on Weather Forecasting and Analysis*, Kansas City, Amer. Meteor. Soc., 411-415.

Smith, W.L., 1983: The retrieval of atmospheric profiles from VAS geostationary radiance observations. *J. Atmos. Sci.*, **40**, 2025-2035.

Westwater, E.R., W.B. Swezy, L.M. McMillin and C. Dean, 1984: Determination of atmospheric temperature profiles from a statistical combination of ground-based profiler and operational NOAA 6/7 satellite retrievals. *J. Climate Appl. Meteor.*, **23**, 689-703.

RELATIONS BETWEEN VAS PHYSICAL RETRIEVALS AND THEIR FIRST GUESS INPUT

John L. Beven
Henry E. Fuelberg

Department of Meteorology
Florida State University
Tallahassee, FL 32306

1. INTRODUCTION

The VISSR Atmospheric Sounder (VAS) on GOES satellites measures radiation in the visible band plus 12 channels of the Infrared spectrum. VAS-derived products are utilized at the National Severe Storms Forecast Center and the National Hurricane Center. Two algorithms have been used operationally to retrieve vertical profiles of temperature and dewpoint from VAS radiances. Both are physical procedures in which the radiative transfer equation is inverted (Smith, 1983; Smith and Woolf, 1984). Since the solution is not unique, a "first guess" sounding must be provided as input. An iterative technique is employed to compute the profiles of temperature and humidity, and after obtaining initial values, an analytical least squares procedure enhances their vertical structure.

The AVE/VAS Ground Truth Field Experiment was held in 1982 to assess VAS's capabilities. A number of investigators have utilized the 6-7 March dataset, including Jedlovec (1985) and Fuelberg and Meyer (1986). This study will investigate results from the Smith (1983) algorithm on that day to determine the relative influences of the first guess and radiance data on VAS retrievals.

2. METHODOLOGY

a. Theory

The use of structure and correlation functions on a time series of data at a single site was described by Gandin (1963). The modification used in this study that permits the analysis of a field of data at individual times was developed by Hillger and Vonder Haar (1979) and Maddox and Vonder Haar (1979). At the single time, the anisotropic structure value of a quantity f at observation sites $\vec{r}_1$ and $\vec{r}_2$ is given by

$$STR(\vec{r}_1, \vec{r}_2) = \frac{1}{K}\Sigma[f'(\vec{r}_1) - f'(\vec{r}_2)]^2, \qquad (1)$$

where $f'(\vec{r}) = f(\vec{r}) - \bar{f}$, $\bar{f}$ is the spatial mean, and K is the number of station pairs within intervals of station separation, e.g., 125 km and 15°since anisotropic separation depends on both distance and direction. If the data are assumed to be homogeneous and isotropic, the separation becomes a function of distance (ρ) only:

$$\rho = |\vec{r}_2 - \vec{r}_1|, \qquad (2)$$

and (1) reduces to:

$$STR(\rho) = \frac{1}{K}\Sigma[f(\vec{r}_1) - f(\vec{r}_2)]^2. \qquad (3)$$

The covariance function (COV) can be defined:

$$COV(\vec{r}_1, \vec{r}_2) = \frac{1}{K}\Sigma[f'(\vec{r}_1)f'(\vec{r}_2)]. \qquad (4)$$

The correlation function (CORR) arises by normalizing the covariance function by the variance (VAR) which we obtained as:

$$VAR(\vec{r}_1, \vec{r}_2) = \frac{1}{2K}\Sigma[(f'(\vec{r}_1))^2 + (f'(\vec{r}_2))^2]. \qquad (5)$$

Thus, CORR becomes:

$$\frac{COV}{VAR}. \qquad (6)$$

Note that the variance differs for each separation interval. If homogeneous and isotropic conditions are assumed, the correlation depends only on scalar separation ρ. The main advantage of the correlation function is its lack of units, thereby allowing differing data types to be directly compared.

b. Data

Four types of data were used in the study. The first was VAS sounding retrievals of temperature and dewpoint over the southcentral United States at 7 times on 6-7 March 1982. These profiles were created at the National Environmental Satellite, Data and Information Service (NESDIS) at the University of Wisconsin, and were at spacings of 75–100 km over cloud free areas. The second data type was "first guess" (FG) profiles used to create the retrievals. They were based on time interpolation of 12 h output from the Limited Fine Mesh (LFM) model. The FG profile sites were identical to those of the VAS retrievals. The third data type was 12 channels of VAS brightness temperatures. Although all 12 channels are be-

ing examined, this report is limited to the 14 μm mid-level temperature channel (Channel 4), the 11.2 μm surface window channel (Channel 8), and the 6.7 μm middle tropospheric water vapor channel (Channel 10). Finally, rawinsonde (RAOB) profiles from the AVE/VAS Experiment served as ground truth. More information on the various data can be found in Jedlovec (1985) and Fuelberg and Meyer (1986).

c. Data Processing

The data underwent a variety of processing before use. A four step procedure was employed for the brightness temperatures. First, garbled or missing scan lines were removed. Second, the originally oversampled scan lines were averaged into larger fields of view (i.e., 4 FOVS of 4 × 14 km were averaged into 1 FOV of 16 × 14 km). Third, all detectable cloud contaminated points were removed based on: (1) The split window technique of Smith (1983), (2) Examination of visible satellite imagery, and (3) Examination of surface weather charts. Finally, a correction for varying satellite zenith angle was applied. Hillger and Vonder Haar (1979) noted that radiances could be linearly corrected in terms of $sec^{\frac{1}{2}}\theta$, where θ is the satellite zenith angle. In this study, however, results from a radiative transfer routine at NASA's Marshall Space Flight Center were used to develop a channel dependent polynomial relation between the brightness temperatures and $sec^{\frac{1}{2}}\theta$. Corrections were applied to all channels except Channel 8.

Processing of the VAS retrievals and FG data involved the removal of soundings not located in the clear sky region of the radiance data. This was necessary because our cloud detection criteria were more stringent than those used during the original preparation of retrievals. The only processing of the RAOB data was a time adjustment for non-simultaneous release described in Jedlovec (1985).

d. Procedures

Two approaches were employed to investigate the retrieval algorithm. The first was a simple level-by-level comparison between the RAOB data and nearby VAS/FG profiles. Specifically, each RAOB site was paired with the nearest VAS retrieval within 100 km, with consideration of sonde drift being included. This procedure permitted the statistical evaluation of the retrievals against their FG input and the "ground-truth" sonde data.

The second and primary approach was an analysis by structure and correlation functions. Previous investigators who have employed similar techniques on satellite retrievals include Hillger and Vonder Haar (1979), Fuelberg and Meyer (1986), and Hillger *et al.* (1986). Our first step was to calculate structure functions on the brightness temperatures, VAS, and FG data at the 7 single times and for the composite period. Both isotropic and anisotropic assumptions were investigated. Once completed, structure-derived random error estimates (σ) were obtained from the isotropic functions using:

$$\sigma = \sqrt{\frac{STR(0)}{2}}, \tag{7}$$

where STR(0) is the structure value at zero separation. STR(0) was determined by fitting an n-degree polynomial to the structure data with the restrictions that: (1) STR(0) $\geq$ 0.0, (2) The curve must be concave up, and (3) The slope of the polynomial curve must be approximately zero near zero separation. Various degrees of polynomials were investigated, with the final selection being determined by the best fit with the original structure values.

Correlation functions then were calculated for single times and the composite period, again for both isotropic and anisotropic cases. Using the structure-derived error σ, the corrected correlation function CORR was obtained from

$$CORR(\vec{r}_1, \vec{r}_2) = CORR^*(\vec{r}_1, \vec{r}_2)[1 + (\sigma^2/VAR(0))], \tag{8}$$

where $CORR^*$ is the original uncorrected function.

To better compare the brightness temperatures with the retrievals and FG data, we prepared an equivalent sounding value for each VAS and FG profile that would approximate what the satellite would "see" in each particular channel. Specifically, RAOBs from various sites within the data domain of 6-7 March were input to a radiative transfer model to determine weighting functions for each channel. Results from the various locations then were averaged and normalized to get a single weighting function for each channel. Then, for the temperature and window channels, these functions were multiplied by the temperature profile to get a "weighted sounding" value. For the mid-tropospheric water vapor channel, however, precipitable water was calculated over the 300–500 mb layer, with this value being used in subsequent calculations of structure and correlation.

For the isotropic calculations, a separation interval of 28 km was used for the brightness temperatures, while 125 km was used for the VAS/FG data. Anisotropic calculations used a radial separation of 125 km and an angular separation of 15° for all data types.

3. RESULTS

a. Pairings

Results from pairing the radiosonde sites with nearby VAS retrievals are given in Fig. 1. One should recall that sonde data were available from the special network at 3 h intervals during the experiment period. Thus, values at most levels of the figure are based on at least 90 pairings and are for the composite of the 7 observation times. The lack of sonde-derived humidity above 400 mb prevented calculations in the upper troposphere, and there was an insufficient number of pairings at the individual times to warrant separate calculations, due mostly to extensive cloud cover early in the period.

Concerning mean arithmetic differences between VAS- and sonde-derived temperatures (Fig. 1). the VAS-RAOB profile shows smaller differences than the FG-RAOB profile below 700 mb. This means that the VAS

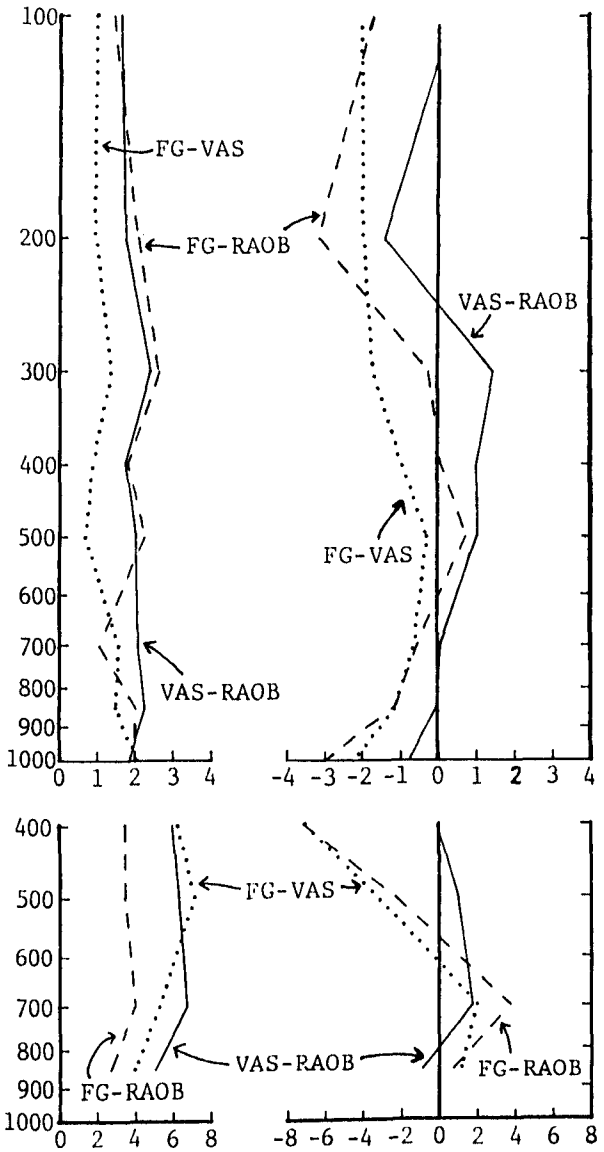

Fig. 1. Means (right) and standard deviations (left) of differences between paired sets of first guess and radiosonde data (FG-RAOB), VAS retrievals and radiosonde data (VAS-RAOB), and first guess and VAS retrievals (FG-VAS). Temperature values (°C) are at the top while dew point results (°C) are at the bottom.

retrievals are closer to the ground truth than are the guess profiles from the LFM. Conversely, however, the FG data are closer to observed values between 700–300 mb. Finally, above 300 mb, the VAS-RAOB profile once again exhibits the smaller mean difference. Absolute values of the mean differences are less than approximately 3°C, with the greatest (negative) differences being located near the surface and 200 mb where both the retrievals and guess profiles are colder than the verifying sonde data. The FG-VAS profile shows that VAS-derived temperatures are warmer than the guess values from which they were obtained, and that mean differences between the input and output data are less than 2°C.

Standard deviations of the FG-RAOB and VAS-RAOB pairings (Fig. 1) are very similar at most levels, approximately 2°C, except near 700 mb where the guess deviations are smaller (1.1°C). Above 500 mb, the retrievals agree better with the sonde data than do the guess values, but the improvement is less than 1°C. Nearer the surface, the guess profiles are slightly superior. Finally, the FG-VAS profile reiterates the small difference between the guess and retrieval data. Although the small contrasts between the guess and observed sonde data indicate that the LFM prognosis was quite good, it is somewhat surprising that the algorithm was only able to improve it by such a small amount.

Pairing results for the dew point data (Fig. 1) are very interesting. It is encouraging that mean differences for the VAS-derived values are smaller than those of the FG data at most levels; however, standard deviations of differences are very large. The smaller standard deviations of the FG-RAOB pairings is partly attributable to the smoothness of the LFM dew point patterns, although even those deviations are approximately 3.5°C.

b. Isotropic Functions

Results of the pairing procedure suggested that we statistically compare horizontal patterns of the VAS soundings against those of the retrieval algorithm's inputs of radiance and first guess profiles. Structure and correlation function analyses for that purpose were performed at the 7 individual times, but due to space limitations, only correlation functions for a single time are presented here. Figure 2 contains correlation functions for Channels 4 and 8 at 0830 GMT 7 March and Channel 10 at 0230 GMT. In each case, the profile for brightness temperatures is accompanied by those for the first guess and VAS sounding equivalents, based on the weighting procedures described earlier. Functions of brightness temperatures are based on a maximum of approximately 550,000 pairs in the most populated separation bins (28 km intervals), while the FG and VAS data have maxima of 600–1000. A minimum number of pairings, 4000 for the brightness temperatures and 25 for the soundings, was specified to insure the validity of results. Concerning the interpretation of correlation functions, their rate of decrease versus distance is directly proportional to the horizontal gradient of the feature being considered, and is inversely proportional to its scale. Thus, a function that decreases to 0 at 400 km describes stronger gradients than one reading 0 at 800 km. Finally, one should recall that the effects of random data error have been removed from the correlation functions via the procedure described earlier using structure functions.

Correlation functions involving window Channel 8 (11 μm) reveal several important points (Fig. 2). First, each data type exhibits the same basic shape and becomes 0 at approximately 800 km. Second, the retrieval curve lies between those of the first guess and brightness temperatures, thereby indicating that the algorithm has compromised between the stronger gradients of the brightness temperatures and the slightly weaker gradients of the LFM guess data. The brightness temperatures have strongest gradients at small separations whereas retrieval gradients

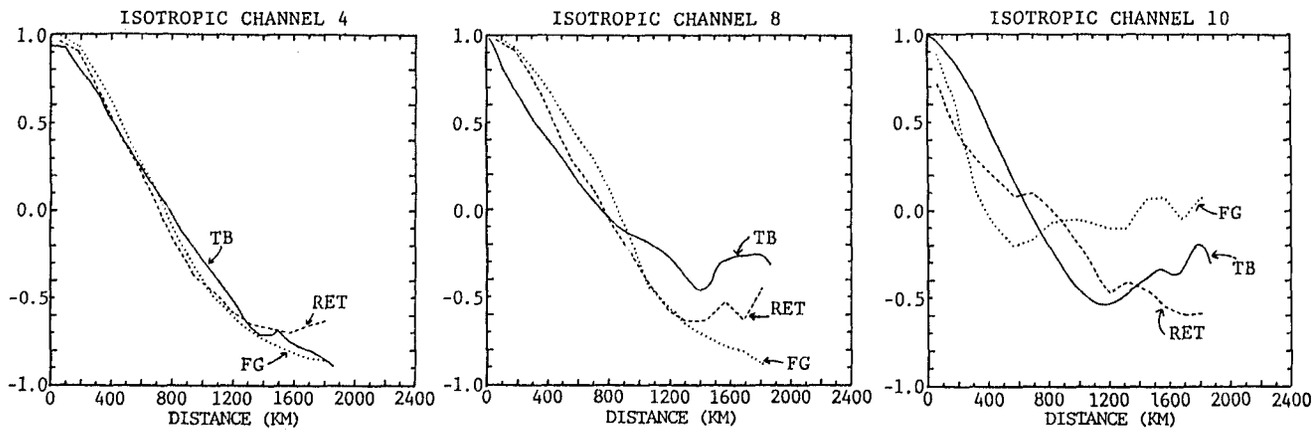

Fig. 2. Isotropic correlation functions pertaining to VAS Channels 4 and 8 at 0830 GMT 7 March 1982 and Channel 10 at 0230 GMT. Functions are for brightness temperature (TB), first guess data (FG), and VAS retrievals (RET). Separations are in km.

are strongest at greater distances. A time sequence of the functions (not shown) indicates a slow weakening of gradients during the experimental period that probably is related to evolving synoptic conditions and the diurnal heating cycle.

Some of the above mentioned characteristics also are evident in midtropospheric temperature Channel 4 (14 μm), but there are important differences as well (Fig. 2). Specifically, although the three curves have similar shapes, the one for FG portrays stronger gradients than does the function for brightness temperatures. Furthermore, instead of the blending process noted with Channel 8, VAS retrieval gradients appear more similar to those of the guess pattern than the brightness temperatures.

Correlation functions relating to mid tropospheric water vapor content (Fig. 2 Channel 10), reach 0 at smaller distances than their counterparts for the temperature channels. Thus, horizontal gradients of vapor are greater than those of temperature. Correlation function evaluations of radiosonde data have shown that the variance of humidity is greater than that of any other basic parameter (Barnes and Lilly, 1975; Fuelberg and Meyer, 1984). Thus, the relative steepness of the Channel 10 FG equivalent and brightness curves is not surprising. On the other hand, the very rapid drop of the retrieval curve appears to be due, in large part at least, to data uncertainty. This conclusion is based on a contour analysis of the dew point fields at these levels. Specifically, although there are many small scale features with strong gradients, few have good spatial or temporal continuity.

c. Anisotropic Functions

Anisotropic correlation functions for Channels 4, 8 and 10 along with their associated sounding equivalent parameters are given in Fig. 3 for 0830 GMT 7 March. Maximum pairings in the 125 km $\times$ 15°sectors were approximately 260,000 (90) for the brightness temperatures (sounding parameters), while the cutoff imposed for plotting purposes was 4000 (25). To interpret the diagrams, a close spacing of the isopleths along a given direction corresponds to strong horizontal gradients.

In the case of the window channel (8), the noncircular orientation of the contours (Fig. 3) indicates that the three data types are highly anisotropic. In fact, strongest gradients of brightness temperatures are oriented along a northwest-southeast direction, whereas they have a northeast-southwest arrangement in the first guess field. The axis of strongest retrieval gradients is intermediate to those of the input data. Along these axes of maximum gradient, isopleth spacing is slightly smaller for the retrievals than for either the guess or radiance data, thereby indicating strongest gradients. This was not apparent in the isotropic version (Fig. 2) in which all site configurations were grouped together.

Each of the parameters related to midtropospheric temperature (Channel 4, Fig. 3) also is highly anisotropic, but there is less difference between the orientations of strongest gradient. The axis for the guess data is aligned northeast-southwest, but maximum gradients for the retrievals appear more along a north-south direction, in closer agreement with the brightness temperatures. As noted in the isotropic representation (Fig. 2), gradient magnitudes of the VAS retrievals are similar in most directions to those of the first guess fields, but weaker than observed for the brightness temperatures.

Anisotropic functions for Channel 10 (Fig. 3) reveal several points that were not evident in the isotropic versions (Fig. 2). The brightness temperatures exhibit maximum gradient along a north-south direction. The first guess field, on the other hand, is more nearly isotropic, at least at separations smaller than 400 km. At longer separations, however, strongest gradients are oriented east-west, or perpendicular to those of the brightness temperatures. VAS-derived humidity data in the upper tropospheric are portrayed by a very chaotic correlation pattern. Even though the radiance and first guess patterns both had relatively simple features, it appears that the retrieval algorithm was unable to transform them into a meaningful field of precipitable water. As noted earlier, this lack of coherence is readily apparent in a simple hand analysis of the data.

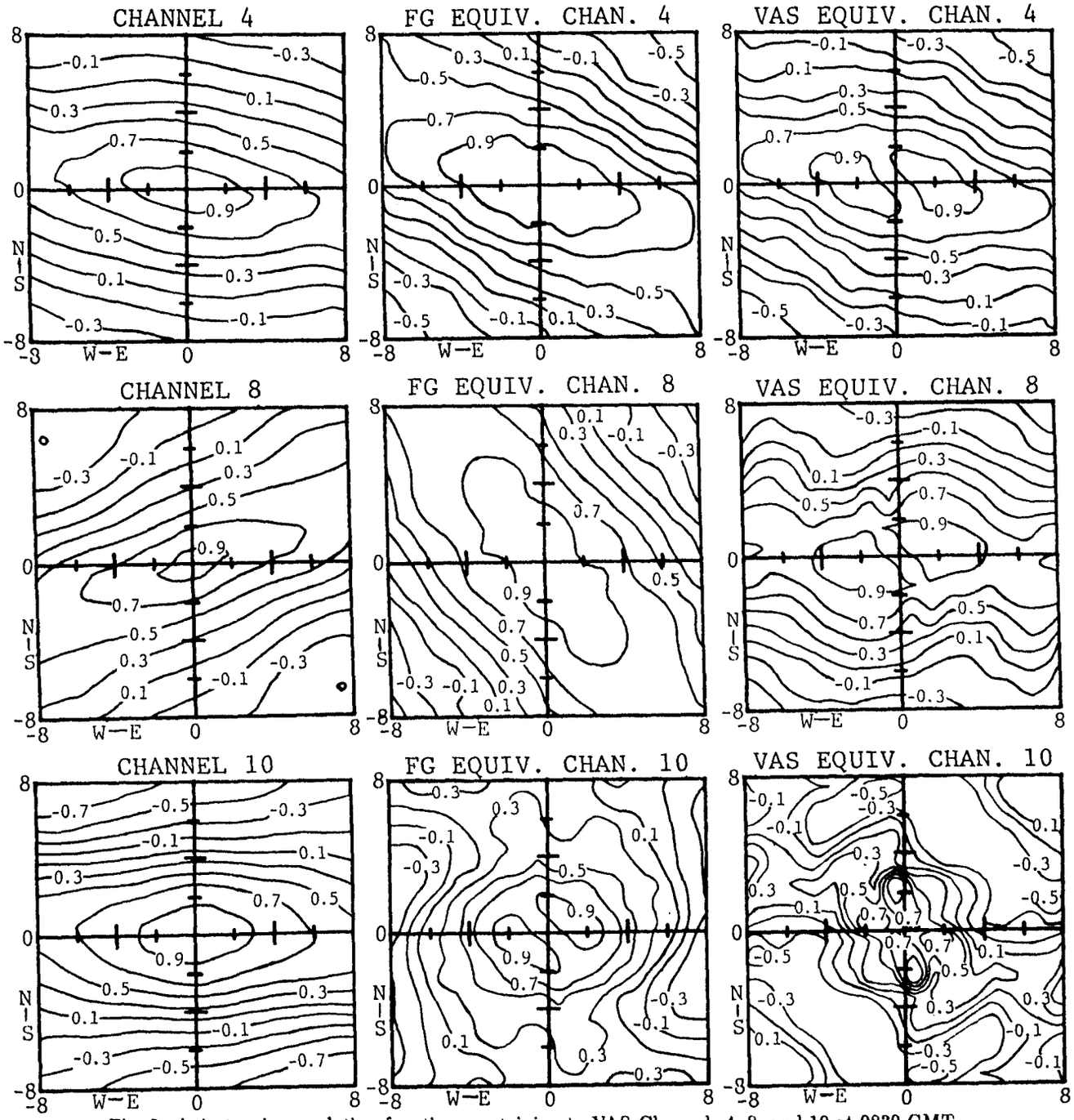

Fig. 3. Anisotropic correlation functions pertaining to VAS Channels 4, 8, and 10 at 0830 GMT 7 March 1982. Functions are for brightness temperature, the first guess equivalent, and the VAS equivalent. North-south and east-west directions are indicated, and separations are in 10^2 km.

4. CONCLUSIONS

Smith's (1983) physical retrieval algorithm is designed to produce mesoscale soundings by blending first guess LFM-derived profiles with VAS-detected radiance data through an inversion of the radiative transfer equation. By pairing the guess and retrieval values with observed radiosonde data, we found that the retrievals sometimes were better related to the "ground truth" data than the guess profiles at some levels. At other levels, however, the first guess profiles were slightly superior to the retrievals. In general, the various statistics suggest that the retrievals often were not greatly different from the first guess. This may be partly attributable to the goodness of the LFM-derived guess field on this particular day, i.e., major improvement is not possible to an already good solution.

Correlation functions related to the window (Channel 8) and mid-tropospheric (Channel 4) temperature channels indicated that magnitudes and orientations of horizontal retrieval gradients were intermediate to those of the guess data and brightness temperatures. With the middle level humidity Channel 10, however, the retrievals bore little resemblance to either form of input and did not exhibit horizontal patterns with suitable time and space continuity. It should be noted, however, that Jedlovec (1985) and Fuelberg and Meyer (1986) found low level satellite-derived humidity distributions on 6-7 March to be much more meaningful. Space limitations did not permit our discussion of those channels in this report.

To our knowledge, studies similar to this have not been reported in the literature. Thus, it is important to emphasize that current results are based on only one case, and may not be representative of a majority of situations. In any event, they suggest that more study is needed before we will understand the degree to which VAS retrievals are an improvement over model-derived soundings.

ACKNOWLEDGEMENTS

Several individuals have been very helpful during this investigation. Dr. Gary Jedlovec of NASA/Marshall Space Flight Center (MSFC) supplied data for the study, assisted us in using his radiative transfer routines, and was a valuable source of information. Drs. Don Hillger of Colorado State University and Christopher Hayden of NOAA/NESDIS also provided valuable insight into the data and procedures. The text was expertly prepared by Mrs. Cynthia Wheatley-Lovoy. Finally, the authors gratefully acknowledge the support of NASA through Grant NAG8-033, under the auspices of the Remote Sensing Branch of MSFC.

REFERENCES

Barnes, S. L., and D. K. Lilly, 1975: Covariance analysis of severe storm environments. *Preprints, Ninth Conf. Severe Local Storms*, Norman, Amer. Meteor. Soc., 301-306.

Fuelberg, H. E., and P. J. Meyer, 1984: An analysis of the AVE-SESAME I period using statistical structure and correlation functions. *Mon. Wea. Rev.*, **112**, 1562-1576.

———, and ———, 1986: An analysis of mesoscale VAS retrievals using statistical structure functions. *J. Climate Appl. Meteor.*, **25**, 59–76.

Gandin, L. S., 1963: Objective analysis of meteorological fields. Translated from Russian, Israel Program for Scientific Translations, Jerusalem, 242 pp. [NTIS TT-65-50007].

Hillger, D. W., and T. H. Vonder Haar, 1979: An analysis of satellite infrared soundings at the mesoscale using statistical structure and correlation functions. *J. Atmos. Sci.*, **36**, 287-305.

———, J. F. W. Purdom, and T. H. Vonder Haar, 1986: The use of structure function analysis to estimate noise levels and the potential resolution of satellite measurements. *Preprints, Second Conf. Satellite Meteor./Remote Sensing and Applications*, Williamsburg, Amer. Meteor. Soc., 102-107.

Jedlovec, G. J., 1985: An evaluation and comparison of vertical profile data from the VISSR atmospheric sounder (VAS). *J. Atmos. Oceanic Tech.*, **2**, 559-581.

Maddox, R. A., and T. H. Vonder Haar, 1979: Covariance analyses of satellite-derived mesoscale wind fields. *J. Appl. Meteor.*, **18**, 1327-1334.

Smith, W. L., 1983: The retrieval of atmospheric profiles from VAS geostationary radiance observations. *J. Atmos. Sci.*, **40**, 2025-2035.

———, and H. Woolf, 1984: Improved vertical soundings from an amalgamation of polar and geostationary radiance observations. *Preprints, Conf. on Satellite Meteor./Remote Sensing and Applications*, Clearwater Beach, Amer. Meteor. Soc., 45-48.

1.11

A SPECTRAL APPROACH TO THE UNIFICATION OF SATELLITE AND CONVENTIONAL TEMPERATURE DATA

Kyung-Sup Shin and James R. Scoggins

Department of Meteorology
Texas A&M University
College Station, Texas 77843

1. Introduction

In this study, a new method to combine temperature soundings derived from VAS[1] radiance observations with conventional data is proposed. Unlike similar previous attempts (Mostek *et al.*, 1986; O'Lenic, 1986), only a portion of the signal contained in the VAS temperature soundings was combined with conventional data. This approach is based on the fact that the independent information in satellite radiance observations is small relative to the scale of natural variations in the temperature structure of the atmosphere. Resulting poor vertical resolution in VAS temperature retrievals (Smith, 1983) make it difficult to determine the accuracy of satellite soundings when they are compared to rawinsonde soundings which provide point measurements. Differences between the soundings strongly depend on the degree of existence of small scale features in a particular weather pattern (Koehler *et al.*, 1983; Jedlovec, 1984). It is required that comparisons of the two types of data be *on the basis of the same vertical scale rather than on direct level-by-level comparisons.* Then, a reasonable comparison between the two types of soundings may be achieved. The portion of signal in the satellite soundings can be identified by considering variations larger than the scales that satellite data can represent. Since the retrieval constraints and observations cannot be decoupled in the operational retrieval of VAS temperature profiles, this study also approaches the vertical resolution question from an empirical standpoint.

2. Spectral Characteristics of VAS Temperature Profiles

a. Data and Analysis

The data from the AVE[2] /VAS Ground Truth Field Experiment (Hill and Turner, 1983) were used in this study. The rawinsonde soundings consist of those made at the regular National Weather Service (NWS) stations over the central United States, and those taken at the special meso-network (approximately 120 km spacing) set up in central Texas. The VAS temperature profiles retrieved by the physical-mathematical retrieval (Smith, 1983) were used. The satellite soundings have 75-100 km spacing which is comparable with that in the special meso-network.

In order to compare the two types of profiles based on the same vertical scale, the mean vertical temperature profile represented by the U.S. Standard Atmosphere was subtracted from both profiles, then the perturbation profiles were represented by Fourier cosine series. The harmonic coefficients, a_n, of both soundings were compared for collocated pairs and at grid points. In this way, more reasonable comparisons between the profiles which have different vertical resolutions may be achieved. The mean perturbation, $a_0/2$, is referred to as the amplitude of the zeroth harmonic.

b. Comparison of Coefficients

A total of 47 pairs of collocated soundings (separation $\leq$ 50 km) was selected at 0000 and 0300 GMT 7 March 1982. The coefficients of each harmonic in VAS temperature profiles were tested by a simple regression model such that

$$a^s_{n_i} = \alpha_n + \beta_n a^r_{n_i} + \epsilon_{n_i}$$

where $a^s_{n_i}$ and $a^r_{n_i}$ represent the coefficients of the n-th harmonic in satellite and rawinsonde profiles, respectively. The α_n and β_n represent the intercept and slope of the n-th harmonic, respectively, and ϵ_{n_i} is the unexplained error in the model. By using the least squares estimation of α_n and β_n, and the coefficient of determination (R^2) for each harmonic number, the relationship between $a^r_{n_i}$ and $a^s_{n_i}$ was established. The results for harmonics up to the tenth are summarized in Table 1.

Table 1 shows that coefficients of the zeroth and first harmonics in VAS temperature profiles agree well with those in rawinsonde profiles. As the harmonic number increases, the slopes and R^2 values become smaller, which indicates the poor agreements between the harmonics. The statistics beyond the fifth (small vertical scale) indicate poor agreement between the VAS and rawinsonde soundings.

To see the spatial variations of each harmonic, the coefficients were interpolated to a grid with equal spacing of grid points. Two grid systems were established for synoptic scale and mesoscale representations of each harmonic coefficient in the temperature profiles. The synoptic scale grid system had 10 x 11 grid points with a spacing of 158 km over the central United States, and the mesoscale grid system had 9 x 10 grid points with a spacing of 50 km in central Texas where the special meso-network was operated. The interpolation method

[1] Visible and Infrared Spin-Scan Radiometer Atmospheric Sounder

[2] Atmospheric Variability Experiment

Table 1 Comparisons of harmonic coefficients for collocated profiles. Statistics are mean coefficient, and regressional fit of intercept, slope, and coefficient of determination for each harmonic. Total of 47 pairs at 0000 GMT and 0300 GMT 7 March were selected.

Harmonic number	Mean coefficient		Intercept		Slope		Coefficient of determination
n	$\overline{a^r_{n_i}}$	$\overline{a^s_{n_i}}$	α_n	C.L.*	β_n	C.L.*	R^2
0**	-3.85	-3.71	-0.26	±0.37	0.90	±0.08	0.92
1	-4.30	-5.11	-1.40	±0.33	0.86	±0.07	0.94
2	0.96	0.45	-0.23	±0.29	0.71	±0.13	0.74
3	-1.71	-1.44	-0.30	±0.48	0.67	±0.20	0.51
4	0.03	-0.66	-0.68	±0.17	0.43	±0.11	0.59
5	0.21	0.43	0.30	±0.22	0.62	±0.19	0.50
6	-1.13	-1.46	-1.34	±0.29	0.11	±0.24	0.02
7	1.02	0.61	0.16	±0.26	0.44	±0.21	0.29
8	-1.56	-1.30	-1.05	±0.16	0.16	±0.09	0.21
9	0.90	0.23	-0.10	±0.18	0.36	±0.17	0.28
10	-1.12	-0.95	-0.81	±0.15	0.12	±0.12	0.09

* 95% confidence limits ** 1/2 a_0

proposed by Barnes (1964) was used to grid the coefficients.

For comparison purposes, three statistical parameters were used: mean difference ($\bar{S} - \bar{R}$); standard deviation ratio (σ_S/σ_R), and; correlation coefficient. S and R refer to satellite and rawinsonde, respectively. The results at 0300 GMT 7 March 1982 are summarized in Table 2. The results indicate that the zeroth and first harmonics in the VAS temperature profiles represent synoptic scale variations almost the same as those in the rawinsonde temperature profiles. It is suggested that VAS soundings can measure synoptic scale variability of the second to the fifth harmonics in temperature profiles to some degree, but the variations are generally weakly detected (small standard deviation ratio). Beyond the fifth, the agreement between the coefficients is very poor, which is consistent with the results for the collocated soundings.

It should be emphasized that the rawinsonde soundings also contain measurement errors although they were considered as ground truth here. Therefore, the differences between coefficients are not due totally to errors in VAS soundings. However, if errors in rawinsonde temperature are random, the errors may be attributed to higher harmonics, while the lower harmonics will represent real variations. The poor agreement between coefficients higher than the fifth may have been due, in part, to the different vertical resolution of the two soundings and to some measurement errors in rawinsonde soundings.

Results of mesoscale representation of the VAS temperature soundings were different from those of synoptic-scale representation. The correlation between the zeroth harmonics was relatively poor (0.73), indicating some discrepancies in VAS temperature profiles compared to rawinsonde temperature profiles in representing mesoscale mean atmospheric temperature variations. On the other hand, high correlations were found for the first harmonic, but the horizontal variation was smoothed. Other har-

Table 2 Comparisons of horizontal variations of harmonic coefficients at grid points. Statistics are mean difference (SAT - RAW), standard deviation ratio, and correlation coefficient of each harmonic. Synoptic scale and mesoscale representations at 0300 GMT 7 March 1982.

harmonic number n	mean difference (°C)	standard deviation ratio (σ^s/σ^r)	correlation coefficient
			Synoptic scale
0	-0.05	0.99	0.97
1	-0.71	0.87	0.95
2	-0.11	0.84	0.62
3	0.26	0.72	0.93
4	-0.88	0.68	0.74
5	0.31	0.89	0.85
6	-0.35	0.57	0.19
7	-0.40	0.89	0.68
8	-0.09	0.25	0.46
9	-0.53	0.70	0.45
10	0.23	0.32	0.36
			Mesoscale
0	0.71	1.09	0.73
1	-0.22	0.75	0.92
2	-1.08	0.68	0.72
3	-0.62	1.47	0.66
4	-1.01	0.43	0.89
5	-0.10	1.04	-0.42
6	-0.29	0.50	0.33
7	-0.73	0.65	0.04
8	0.85	0.14	-0.39
9	-0.87	0.35	0.43
10	0.48	0.19	-0.29

monics show even greater disagreements between the soundings. Although the VAS soundings represent some of the mesoscale temperature variations at lower harmonics, especially the first harmonic, they generally missed important mesoscale features indicated in rawinsonde soundings in the special meso-network (not shown). Fuelberg and Meyer (1986) suggested that VAS retrievals could be valuable for meso-α scale analysis but uncertain for meso-β scale analysis. This is consistent with our results.

The low correlations beyond the fifth harmonic are probably related to limitations of the satellite sounding system. In order to represent the first five cosine harmonics, at least six data points in the profile are required. Because VAS has six infrared channels to determine vertical temperature profiles, there are six degrees of freedom in principle. Although the retrieval method is not directly mathematical, one would expect that relatively reasonable representations up to the fifth harmonic are possible. However, the observations in each channel are not completely independent. There are large overlaps between weighting functions. Therefore, the actual number of degrees of freedom is smaller than six. If additional uncertainties in the transmittance functions and observational errors are considered, accuracy must be restricted even more. This suggests why only the zeroth and first harmonics are correctly represented and why the second to the fifth harmonics contain uncertainties in describing synoptic scale temperature variations.

3. Unified Data and Quality Verification

a. Unified Data

As demonstrated in the previous section, VAS soundings detect synoptic scale temperature variations well at vertical scales of the zeroth and first harmonics. To be conservative, only these portions in the VAS temperature soundings are treated as signal although the second to fifth harmonic also contain some of temperature variations (especially the third harmonic). Only the signal in the VAS temperature soundings is combined with the conventional data for the purpose of developing the unified data set.

The unified data set was obtained by combining rawinsonde and VAS soundings as follows. Let the vertical temperature profile from conventional data at each grid point be represented by

$$T^r(p^*) = \bar{T}(p^*) + \frac{1}{2}a_0^r + a_1^r \cos p^* + RES^r(p^*)$$

and that of the VAS temperature profile by

$$T^s(p^*) = \bar{T}(p^*) + \frac{1}{2}a_0^s + a_1^s \cos p^* + RES^s(p^*)$$

where the superscripts r and s denote the conventional and VAS data, respectively, subscripts 0 and 1 indicate the harmonic numbers, RES represents the residual (sum of all other harmonics), and p^* indicates the pressure level transformed to 0 to π (1000 and 100 mb). Then the unified profile will be represented by

$$T^u(p^*) = \bar{T}(p^*) + \frac{1}{2}a_0^s + a_1^s \cos p^* + RES^r(p^*)$$

Therefore, the difference between the conventional data and unified data is the replacement of the zeroth and first harmonics from VAS. If the conventional data is a good representation of atmospheric temperature structure in the zeroth and first harmonics, the conventional and unified data will be close. However, if some conventional data are not a sufficiently good representation of the thermal structure, the initial state can be improved by the unified data to the extent of the difference accounted for by the zeroth and first harmonics. Such situations are expected in regions where rawinsonde observations are restricted or not available.

b. Quality of Unified Data

The quality of the unified data may be examined by its capability for describing weather systems with respect to other data sets. Since vertical motion is closely related to cloud patterns indicated by satellite images, the vertical motion patterns calculated by use of a diagnostic model for all data sets were compared with satellite images to determine the quality of the unified data. A diagnostic linear balance model with convective parameterization (Kuo 1965, 1974) was constructed for this purpose and used for computing the vertical motion patterns over oceanic regions. NMC initialized data and VAS data from GOES-EAST were available over the eastern United States and the western Atlantic ocean on selected days during August 1983. Three consecutive days, 22-24 August 1983 were selected for the case study, based on the availability of both NMC and VAS data and the existence of well identified weather systems over the ocean. The unified (UNI) data were recomposed at each grid point by replacing the zeroth and first harmonics in the NMC temperature profile with those of VAS.

Results from one of the three case studies are shown here. Fig. 1 shows vertical motion fields at the 500 mb level derived from the NMC, VAS, and UNI data at 1200 GMT 24 August 1983. The GOES-EAST visible and infrared images are displayed in Fig. 2 for comparison. The visible imagery for 1500 GMT was used because most of the western part of the United States is still in shadow at 1200 GMT. If we assume no abrupt change in cloud patterns in three hours, this imagery may be useful for deducing the visible imagery at 1200 GMT.

The NMC data describe the convective activity well. The isolated tropical storm near Florida was pronounced and convection related to the front over Cape Hatteras and the banded nature of convection east of there were indicated. Due to the large data gaps caused by clouds, results from VAS data were not as good as the NMC data in describing convective systems at this time. The tropical storm is almost lost and frontal convection is poorly described. However, the strong downward motion northeast of Haiti is better depicted than that from the NMC data. This is in a region essentially free of clouds.

The omega fields from UNI data show good agreement with satellite images. They depict well both the tropical storm and convection over Cape Hatteras. The

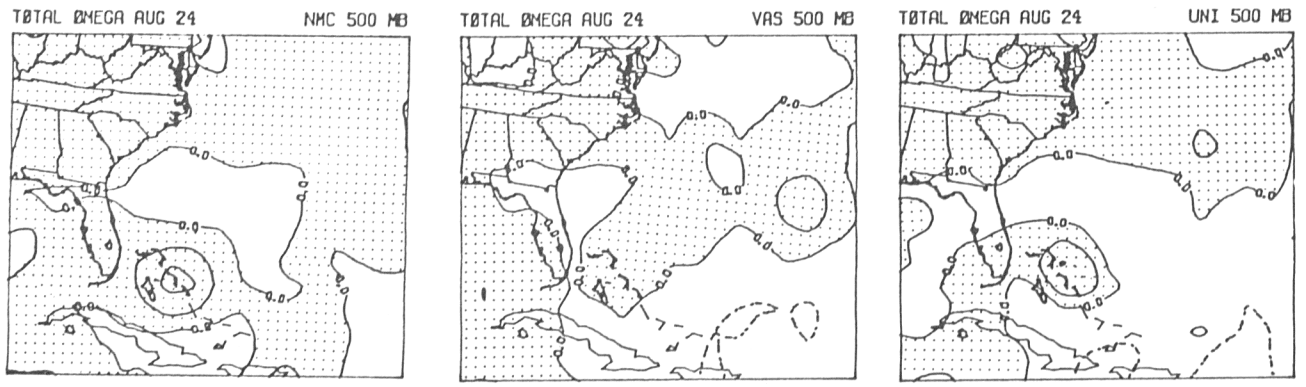

Fig. 1 The omega fields calculated from NMC, VAS, and UNI data for 500 mb level at 1200 GMT 24 August 1983. Contour interval is 1.0 μbs^{-1} and positive values are represented by dashed lines. Regions of upward motion are shaded.

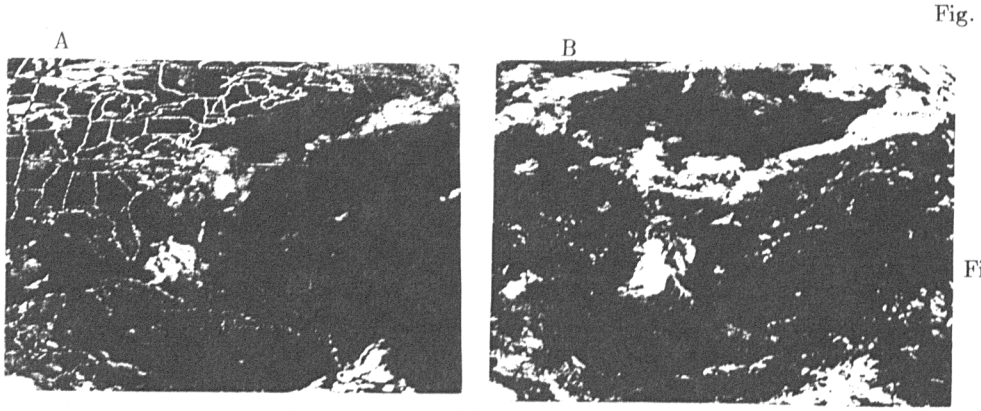

Fig. 2 The GOES-EAST infrared and visible images. Infrared imagery (A) is at 1200 GMT and visible imagery (B) is at 1500 GMT 24 August 1983.

omega fields from NMC and UNI data were similar. However, the downward motion area east of Barry, which is well depicted in VAS data, was also indicated in the UNI data. Therefore, the isolated features of the tropical storm were described better in UNI data than in NMC data.

Commenting on the other two cases which are not shown, the UNI data also showed better agreement with satellite images on 22 August, while the UNI data were as good as the NMC data on 23 August. We could not address the significance of these improvements; however, they demonstrate potential of the UNI data proposed in this study.

4. Conclusions

The information content in the VAS temperature soundings may be limited to the zeroth and first harmonics in describing synoptic scale temperature variations. In the three case studies considered over the western Atlantic, the vertical motion fields derived from the unified data showed some improvements over oceans around the developing tropical depression in two cases. Results of another one case showed that analyses from the unified data were as good as those from NMC data. Generally, the zeroth and first harmonics in the NMC temperature data were comparable to those in the VAS data. Therefore, overall improvements in the unified data seem to be small. Improvement in the second (and higher) harmonic in the VAS temperature retrievals is required to improve the potential of the unified data over ocean areas where the conventional data are restricted. Further development of methods for combining profiles using objective analysis schemes may enchance the potential of unified data.

REFERENCES

Barnes, S. L., 1964: A technique for maximizing detail in numerical weather map analysis. *J. Appl. Meteor.*, 3, 396-409.

Hill, C. K., and R. E. Turner, 1983: NASA's AVE/VAS program. *Bull. Amer. Meteor. Soc.*, 64, 796-797.

Jedlovec, G. J., 1984: A statistical evaluation and comparison of VISSR Atmospheric Sounder (VAS) data and corresponding rawinsonde measurements. NASA TM 82575, 11 pp.

Koehler, T. L., J. C. Derber, B. D. Schmidt and L. H. Horn, 1983: An evaluation of soundings, analysis and model forecasts derived from TIROS-N and NOAA-6 satellite data. *Mon. Wea. Rev.*, 111, 562-571.

Kuo, H. L., 1965: On formation and intensification of tropical cyclones through latent heat release by cumulus convection. *J. Atmos. Sci.*, 22, 40-63.

——, 1974: Further studies of the parameterization of the influence of cumulus convection on large-scale flow. *J. Atmos. Sci.*, 31, 1232-1240.

Mostek, A., L. W. Uccellini, R. A. Petersen and D. Chesters, 1986: Assessment of VAS soundings in the analysis of a preconvective environment. *Mon. Wea. Rev.*, 114, 62-87.

O'Lenic, E. A., 1986: The effect if VISSR Atmospheric Sounder data on some LFM analysis and forecasts. *Mon. Wea. Rev.*, 114, 1832-1846.

Smith, W. L., 1983: The retrieval of atmospheric profiles from VAS geostationary radiance observation. *J. Atmos. Sci.*, 40, 2025-2035.

1.12

SPATIAL AND TEMPORAL VARIABILITY OF VAS RADIANCE MEASUREMENTS BY STRUCTURE AND CORRELATION ANALYSIS

Donald W. Hillger[1,2]
Andrew S. Jones[2,3]
James F. W. Purdom[1,2]
Thomas H. Vonder Haar[2,3]

[1]Regional and Mesoscale Meteorology Branch,
Satellite Applications Laboratory, NOAA/NESDIS

[2]Cooperative Institute for Research in the Atmosphere (CIRA)

[3]U.S. Army Center for Geosciences

Colorado State University
Fort Collins, CO 80523-0033

1.0 INTRODUCTION

A very important aspect of satellite remote-sensing measurements is their ability to detect changes in atmospheric temperatures and water vapor in both space and time. Temperature and water vapor variations are important atmospheric features for weather analysis and forecasting, and correct sampling resolution is necessary to measure this atmospheric variability (Hillger and Vonder Haar, 1987).

In order to measure atmospheric variability statistical structure function analysis is applied to VISSR Atmospheric Sounder (VAS) measurements. Unlike previous work which dealt only with spatial (horizontal) structure, the analysis has been extended to include time. The resulting structure plots are shown in 2 dimensions (2 spatial dimensions or 1 spatial dimension and time) but they give an indication of 3-dimensional measurement variability. The analyses which include time as a coordinate also give an indication of the mean speed and direction of motion of the analyzed data.

VAS variability along the analysis coordinates (space and/or time) can be used to determine correct sampling resolutions (in space and time). Results for 3-hourly VAS data indicate that sampling at high frequency (approximately 1 hour) is needed in order to correctly monitor temporal variability in VAS measurements equivalent to that being measured at high spatial resolution.

2.0 STRUCTURE ANALYSIS OF SATELLITE DATA

A statistical tool which can be used to quantify atmospheric variability is the structure function (Gandin, 1963). The structure is the mean-squared difference between measurements as a function of either space or time, and therefore is a measure of the mean gradient in space or the mean change in time. The structure is computed by identifying all possible combinations of pairs of measurements and grouping the pairs according to separation in either space or time or both. The result will be a structure function which summarizes atmospheric variability in a statistical-mean sense (Hillger and Vonder Haar, 1979).

The satellite data analyzed were infrared measurements from the GOES VISSR Atmospheric Sounder (VAS) on GOES-5. As is typical of most satellite data, the measurements are obtained in lines composed of individual elements. Measurements were at a resolution, or spacing, of about 14 km in the line (east-west) orientation and about 23 km in the element (north-south) orientation. Time resolution was 3 hours. Fields of 30 x 30 measurements were analyzed at 4 times over a period of 9 hours. Water vapor measurements for VAS channel 10 at 6.8 µm and channel 9 at 7.3 µm were analyzed, as well as temperature measurements from VAS channel 6 at 4.5 µm. The VAS measurements were given in terms of effective blackbody temperatures. For water vapor channels lower values signal more atmospheric absorption and therefore more water vapor in the atmosphere. For the temperature channels, higher values signal warmer temperatures in the layer of the atmosphere being measured.

A function inversely related to the structure is the correlation function. The correlation is a normalized function and decreases from near 1.0 at zero separation in space or time. The advantage of the correlation analysis over the structure analysis is the ability to compare VAS channels which have different absolute values. The correlations are normalized compared to unnormalized structure values.

Figure 1 shows the spatial correlation of effective blackbody temperatures for VAS water vapor channel 10 at 6.8 µm. The correlation was computed in two spatial orientations, aligned with the lines and elements of the satellite data. Note that the spatial correlation differs with the orientation of the data indicating that the correlation is anisotropic.

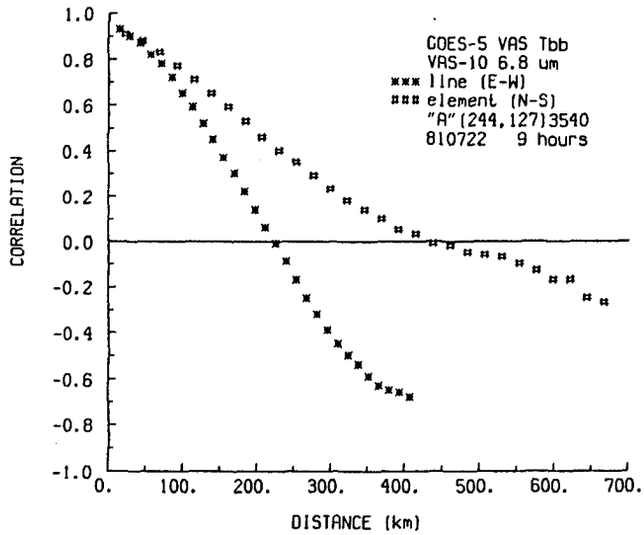

Figure 1. Spatial correlation of measurements from VAS water vapor channel 10 at 6.8 µm. Different correlations in the two orientations indicate that the correlation is anisotropic.

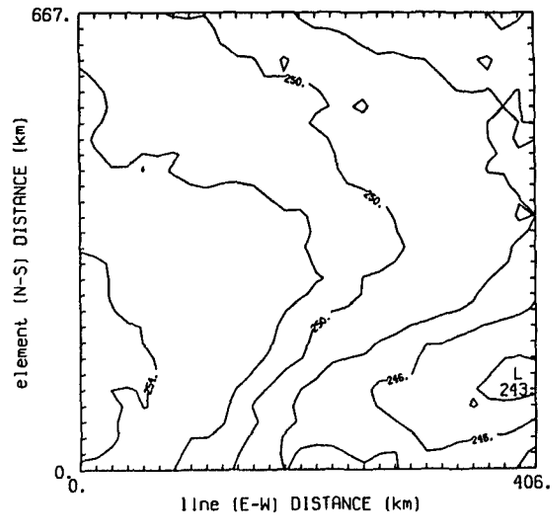

Figure 3. Contours of 30 x 30 effective blackbody temperatures for VAS channel 10 at 6.8 µm at 1800 UTC on 22 July 1987. These are the measurements on which the correlations in Figures 1 and 2 were computed.

A better way to analyze the dependence upon orientation is to compute the correlation in 2 spatial dimensions. Figure 2 is the 2-dimensional spatial correlation for the same data from VAS water vapor channel 10. The structure was computed anisotropically (as a function of spatial distance and orientation). The correlation origin is at the center of the horizontal axis with the distance between tic marks equal to the spatial resolution of the measurements. Since the correlation is axially symmetric, it is only necessary to show the top half of the figure; the bottom half contains redundant information. The maximum correlation, or minimum gradient, is oriented in the north-south direction which is parallel to the dominant contours of the VAS measurements in Figure 3. Similarly, the minimum correlation, or maximum gradient, is in the east-west orientation, which is perpendicular as the major contour lines in Figure 3. The 2-dimensional spatial correlation therefore contains not only gradient information but also contains information on the orientation of the maximum and minimum gradient.

Figure 4 is a 2-dimensional correlation plot of the same area but for measurements from VAS water vapor channel 9. In this case the orientation of the maximum correlation (minimum water vapor gradient) is again nearly north-south, but there is a greater anisotropy in the measurements for VAS channel 9. These two channels measure water vapor at different levels in the atmosphere; thus the different dependence of the spatial correlation on orientation.

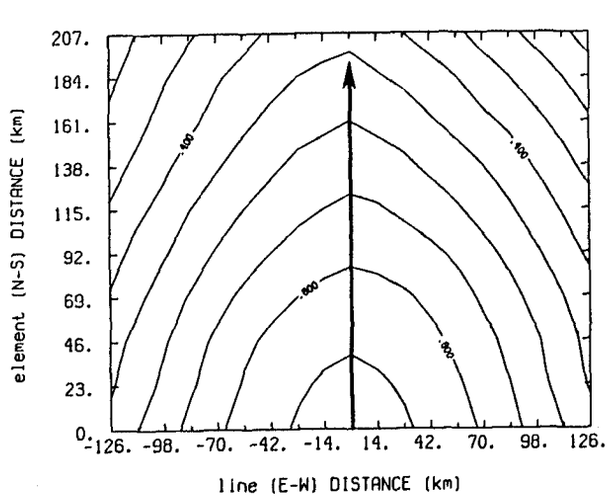

Figure 2. Two-dimensional spatial correlation analysis of VAS water vapor channel 10 at 6.8 µm. The maximum correlation (minimum gradient) is oriented along a north-south line as indicated by the arrow.

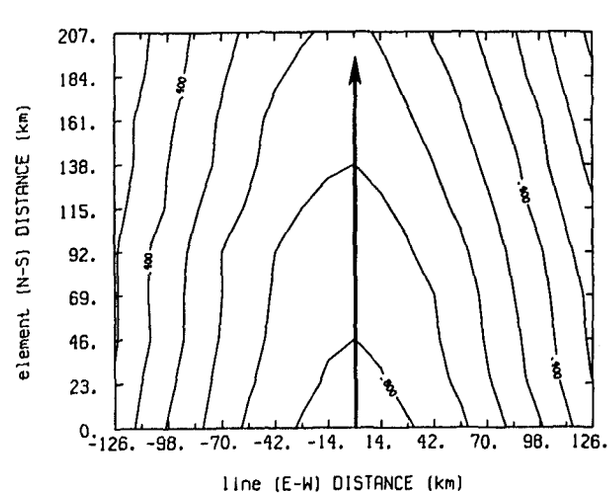

Figure 4. Two-dimensional correlation analysis of VAS water vapor channel 9 at 7.3 um. This figure shows a more anisotropic correlation compared to VAS channel 10 in Figure 2, but the maximum correlation as indicated by the arrow is in the same orientation.

Compared to the water vapor channels, which show only minimal difference in the orientation and magnitude of their maximum correlation, the 2-dimensional correlation analysis of VAS temperature channel 6 in Figure 5 is quite different. The orientation of the maximum correlation is in a northeast-southwest direction, at a large angle compared to the maximum correlation of water vapor in either Figures 2 and 4. This indicates that the temperature and water vapor gradients are not parallel. These VAS channels measure in the troposphere, but not at the same levels, so the difference may be partially due to the vertical separation. However, temperature and water vapor gradients at different angles imply water vapor advection as well as possible differences in instability.

2.1 Temporal Correlations

Given a formulation for computing spatial correlation, it is straightforward to adopt it for computing temporal correlations as well. The temporal and spatial correlations can be plotted together, as for VAS channel 10 in Figures 6a and 6b. Each figure depicts the time variability along with one of the two perpendicular spatial orientations. Figure 6a shows a lower spatial correlation than Figure 6b at the same distance, which agrees with the maximum gradient from Figure 2 being in an east-west orientation.

An interesting feature of the time and space correlation plots is the ability to detect mean motion of the field. This would be indicated by a spatial shift of the maximum correlation with time, which signals a horizontal movement of the measured features. In Figures 6a and 6b the mean movements are to the west and north, respectively. In 6 hours the maximum correlation moved only slightly to the west and about 70 km to the north. Correlations of course drop with time as the water vapor features not only move in space but change in shape and magnitude. This tracking process is similar to the lag-correlation used by automatic cloud-motion (wind) algorithms.

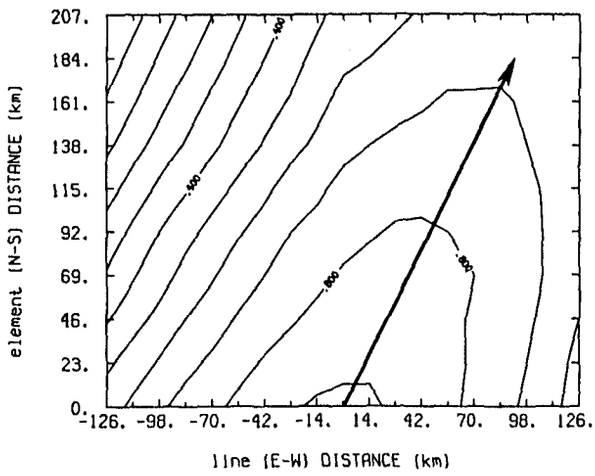

Figure 5. Two-dimensional correlation analysis of VAS temperature channel 6 at 4.5 um. The arrow indicates a northeast-southwest orientation of the maximum correlation. This is at a large angle compared to the maximum water vapor correlation in Figures 2 or 4.

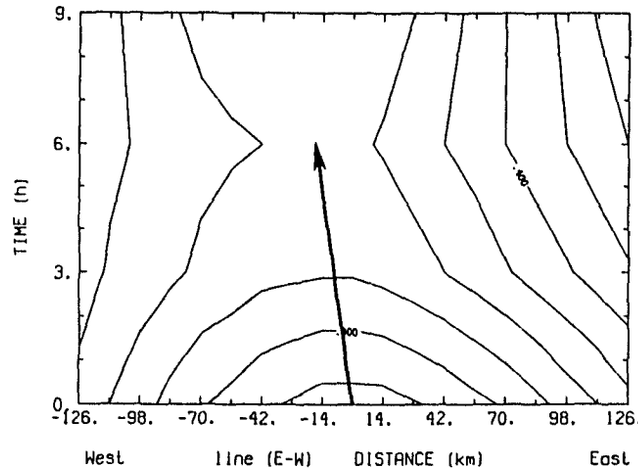

Figure 6a. Time and east-west spatial correlation for VAS water vapor channel 10 at 6.8 µm. The arrow along the maximum correlation indicates a mean shift of the field slightly to the west in time.

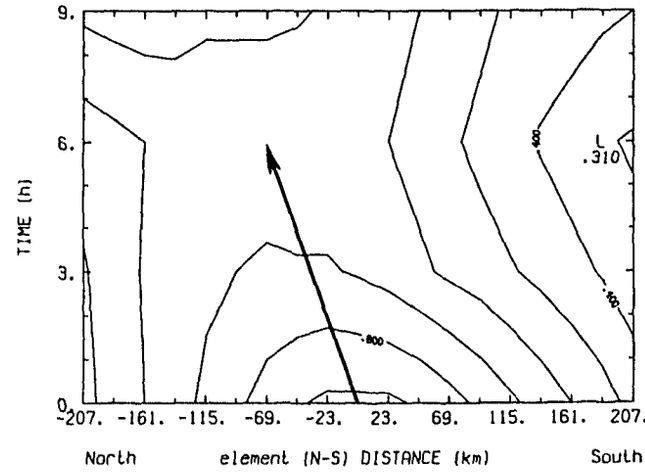

Figure 6b. Same as Figure 6a except for time and north-south spatial correlation. The arrow along the maximum correlation indicates a mean shift in the field of about 70 km to the north in 6 hours.

The equivalence between space and time can be seen by comparing the spatial and temporal axes at equal correlations. For this purpose the isotropic (non-directional) correlation was computed and plotted against the temporal correlation as in Figure 7 for VAS channel 10. According to this figure the correlation falls off more rapidly in 3 hours (one time sample) than it does at a distance of about 100 km. The correlation in both cases is about 0.7. By examining Figures 6a and 6b the number of spatial samples represented by a correlation of 0.7 is about 6 and 5, respectively. This indicates that these water vapor features are less persistent between time samples than they are coherent in space, at least for short time scales. For longer times the correlation does not continue to drop off as rapidly. However, this is not true for VAS channel 6 in Figure 8. In this case the correlation falls off to less than 0.1 in 9 hours.

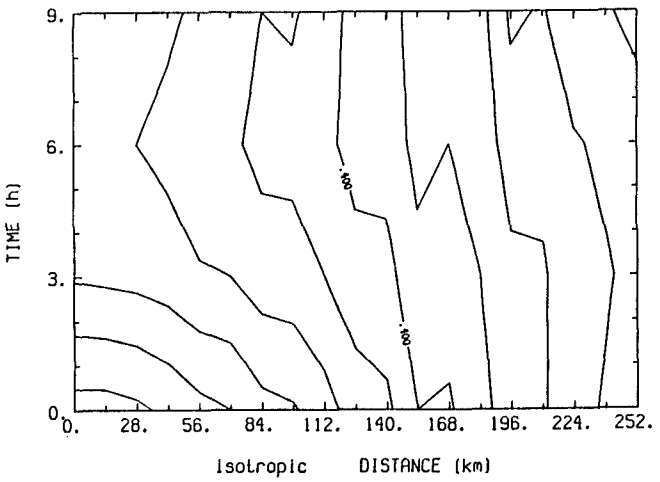

Figure 7. Time and isotropic correlation for VAS water vapor channel at 7.3 µm. The correlation drops off more rapidly in 3 hours than it does at 100 km.

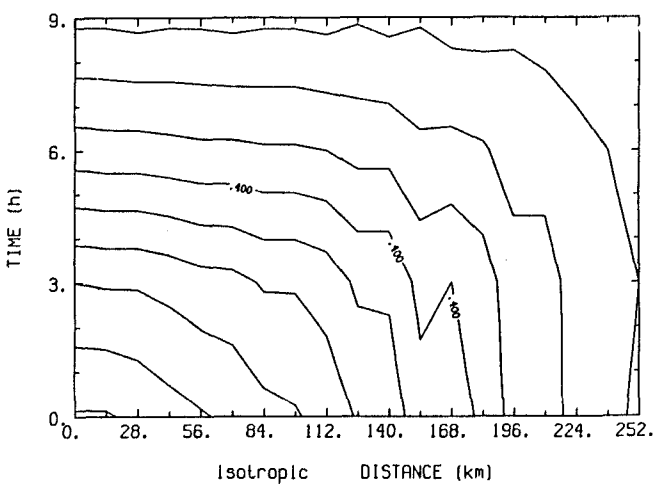

Figure 8. Time and isotropic correlation for VAS temperature channel 6 at 4.5 µm. The correlation drops off more rapidly at longer times than it does for VAS channel 10 in Figure 7.

The same correlation occurs at a distance of about 250 km. Because this channel is influenced by variability in surface characteristics, the more rapid decrease in correlation with time is not unexpected, due to diurnal variations.

The same amount of atmospheric variability can therefore be quantified in both space and time. This has important implications for spatial and temporal sampling concerning the question of whether or not spatial resolution and sampling time are sufficient to measure atmospheric variability. A high correlation between adjacent measurements in space or time might be an indication of excessive sampling. On the other hand, a correlation which drops off rapidly would signal variations in space or time which are not sufficiently sampled by the measurement resolution or spacing. In the case of VAS channel 10 in Figure 7 even though the correlation appears to drop off more slowly in time, the correlation drops off more rapidly between time samples of 3 hours than it does over several adjacent samples. The correlation at 1 hour is closer to the correlation at minimum spatial resolution. This implies that temporal resolution less than 3 hours is necessary to measure atmospheric variability equivalent to that being sampled in space.

3.0 CONCLUSIONS

Structure or correlation analysis provides a convenient method to look at atmospheric variability both spatially and temporally. Two-dimensional correlation plots indicate the magnitude and orientation of gradient information. When time is included, the maximum correlation can indicate the mean movement of the data. Equivalent sampling distances and times can also be quantified for the satellite measurements which were analyzed. In this study it was found that VAS temporal resolution of 1 hour minimum is needed to detect variability equivalent to that being measured at minimum spatial resolution.

ACKNOWLEDGEMENTS

This research was jointly funded by NOAA Grant NA85RAH05045, NASA Contract NAS8-36472, and ARO Grant DAAL03-86-G-0190. We wish to thank Mrs. Debbie Eckdahl for expertly typing the manuscript.

REFERENCES:

Gandin, L.S., 1963: Objective Analysis of Meteorological Fields. Translated from Russian, Israel Program for Scientific Translations, Jerusalem, 242 pp. (NTIS Ref:TT-65-50007).

Hillger, D.W., and T.H. Vonder Haar, 1979: An analysis of satellite infrared soundings at the mesoscale using statistical structure and correlation functions. J. Atmos. Sci., 36, 287-305.

Hillger, D.W., and T.H. Vonder Haar, 1987: Estimating noise levels of remotely-sensed measurements from satellites using spatial structure analysis. Accepted by J. Atmos. Ocean. Tech., 30 pp.

1.13

OPERATIONAL VAS SOUNDINGS AT PROFS

John S. Snook*

Program for Regional Observing and Forecasting Services
National Oceanic and Atmospheric Administration
Boulder, Colorado 80303

1. INTRODUCTION

A primary focus of the Program for Regional Observing and Forecasting Services (PROFS) is to develop products from alternative data sources and to implement and evaluate their analysis and forecast utility, specifically for the improvement of short-range local area forecasts (Reynolds, 1983). High-quality, timely soundings derived from radiance data collected by the Visible and Infrared Spin-Scan Radiometer (VISSR) Atmospheric Sounder (VAS) instrument on board the Geostationary Operational Environmental Satellite (GOES) can provide upper air temperature and moisture data at much greater spatial and temporal resolutions than the conventional Radiosonde Observation (RAOB) network. Prior to 1986, PROFS received VAS soundings via a telephone link with the University of Wisconsin-Madison. To improve reliability and to increase flexibility, PROFS initiated development of a system to produce in-house VAS soundings. During May 1987, PROFS implemented a totally automated system to generate real-time VAS soundings which could be accessed through the PROFS meteorological workstation (Reynolds, 1983; MacDonald, 1985). VAS soundings were monitored on a daily basis in conjunction with the PROFS 1987 real-time summer forecast experiment. All soundings were archived for post-experiment analysis. This paper investigates VAS sounding quality, problems, and possible improvements to the system at PROFS. The forecast utility of VAS soundings during the summer experiment is discussed. Discussions of the future of VAS sounding data at PROFS and better methods which take full advantage of the positive features of VAS sounding data follow.

2. OPERATIONAL VAS SOUNDING GENERATION

The VAS sounding generation system at PROFS uses a direct, physical approach developed at the University of Wisconsin-Madison (Smith, 1983). The approach uses radiance measurements from various infrared wavelengths collected on board the GOES 7 platform. Temperature and mixing ratio are computed for 40 levels ranging from the surface to 0.1 mb. Geopotential height is computed hypsometrically. Soundings are generated every 90 minutes for a 110 km grid covering the continental United States. Real-time soundings are produced at rates of better than 100 per minute; thus, national coverage is achieved approximately ten minutes following raw data ingest. Since the number of vertical levels generated exceeds the number of VAS wavelengths available, a first guess profile of temperature and moisture is required. The upper air first guess for the national grid is generated from RAOB, profiler, and aircraft data at 0000 and 1200 UTC by the PROFS Mesoscale Analysis and Prediction System (MAPS) group (Benjamin, 1985). Climatology is used for levels above 150 mb. The surface first guess is produced hourly from Surface Aviation Observations (SAO).

VAS radiance data may be contaminated by clouds since infrared radiation from the ground is absorbed by clouds and re-emitted at colder temperatures than it is when it passes through the clear atmosphere. These cold cloud-contaminated VAS brightness temperatures can severely affect the quality of VAS soundings. Thus, a scheme to eliminate the adverse effects of clouds is necessary. It must also be automated and efficient to satisfy PROFS real-time requirements. The technique currently in use subtracts the 11.2 μm window band brightness temperature from the collocated surface temperature (Snook, 1987). If the difference is greater than 10 K, the pixel is flagged as cloudy.

Soundings are generated for 11 by 11 infrared pixel (80 km by 80 km) fields of view to reduce the effects of signal noise in the radiance measurements. The sounding generation system uses transmittance functions to relate measured radiance values to brightness temperature for each infrared wavelength. Since GOES 7 transmittance functions were not immediately available, GOES 6 functions were used during the summer experiment. This undoubtedly introduced some systematic bias to VAS sounding quality. Following the experiment, new GOES 7 functions were installed.

3. VAS SOUNDING QUALITY

VAS sounding quality is evaluated through a direct comparison with the nearest RAOB sounding in space and time. Discrepancies can occur with this type of comparison since the RAOB is a point observation while the VAS sounding is a volume observation. Even for the best cases, the VAS cannot be expected to have

---

* Contract with T. S. Infosystems, Inc., Lanham, MD 20706.

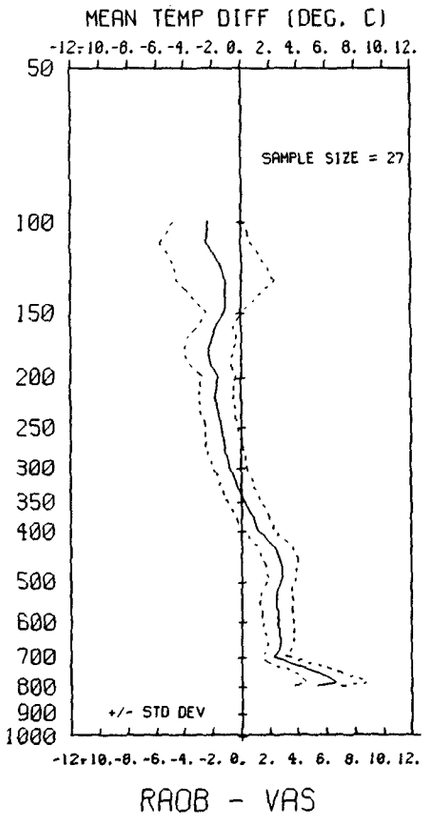

Fig. 1. Mean vertical temperature (°C) comparison for 1200 UTC Denver RAOB and 1245 UTC VAS sounding using 27 clear to partly cloudy cases from June, July, and August 1987. The VAS sounding is located approximately 30 km south of the Denver RAOB. The solid line depicts the mean temperature difference of VAS subtracted from RAOB. The surrounding dashed lines indicate the positive and negative standard deviations.

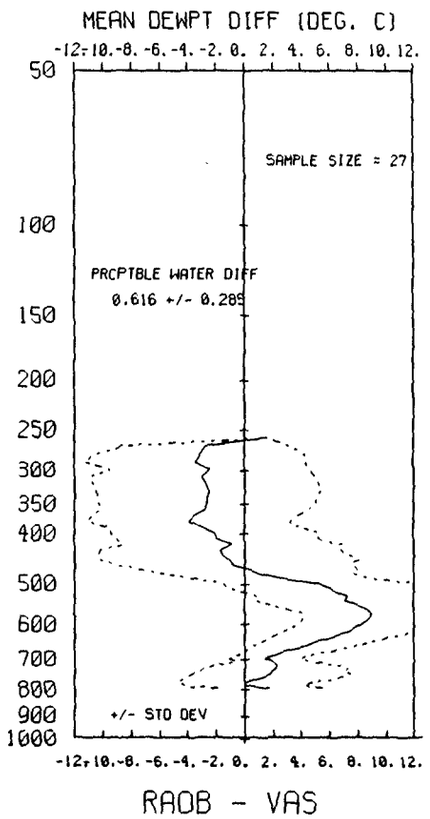

Fig. 2. Mean vertical dew point (°C) comparison for the cases in Figure 1. The solid line depicts the mean dew point difference of VAS subtracted from RAOB. The surrounding dashed lines indicate the positive and negative standard deviations. The mean total column precipitable water difference is also shown.

as much vertical resolution as the RAOB, especially for the moisture profile. Regardless, this comparison remains the best available for this study and has been used by others (Jedlovec, 1985; Bruce et al., 1977).

Figure 1 shows the 1200 UTC Denver RAOB and 1245 UTC VAS mean temperature sounding comparison for 27 days in the months of June, July, and August 1987. The VAS sounding is located approximately 30 km south of the RAOB, and only cases with more than 33% clear pixels within the VAS sounding field of view are used. The solid line depicts the mean temperature difference of VAS subtracted from RAOB. Thus, positive temperature differences indicate the VAS to be colder than the RAOB while negative temperature differences show the VAS to be warmer than the RAOB. The surrounding dashed lines indicate the positive and negative standard deviations. Note the consistent cold bias below 350 mb and the consistent warm bias above. Preliminary results from later VAS sounding comparisons attribute much of the bias above 700 mb to the use of the GOES 6 transmittance functions. Since the VAS sounding grid point is over higher terrain than the Denver RAOB, the cold temperature bias between 700 and 800 mb is mostly due to the unfair comparison of the VAS surface temperature with the warmer RAOB boundary layer inversion temperature. More important is the magnitude of the standard deviation. Values are less than 2 °C for all levels below 150 mb, which is consistent with other reports (Jedlovec, 1985), indicating that reasonable temperature soundings can be achieved with the removal of the consistent biases.

Figure 2 shows the corresponding RAOB and VAS mean dewpoint sounding comparison. A dry (cold) dewpoint bias is evident below 475 mb, with a moist (warm) bias above. As expected, the magnitudes of the standard deviation are larger than those of the mean temperature difference. Values range from less than 3 °C at 700 mb to approximately 7 °C at 500 mb and above. Again, preliminary results from later VAS sounding comparisons attribute much of the dry and moist bias to the use of the GOES 6 transmittance functions. Differences in the lowest layer are due to the variation in surface elevation between the VAS sounding grid point and the Denver RAOB location. Standard deviation values are expected to increase with height since small errors in mixing ratio will create much larger errors in dewpoint at high

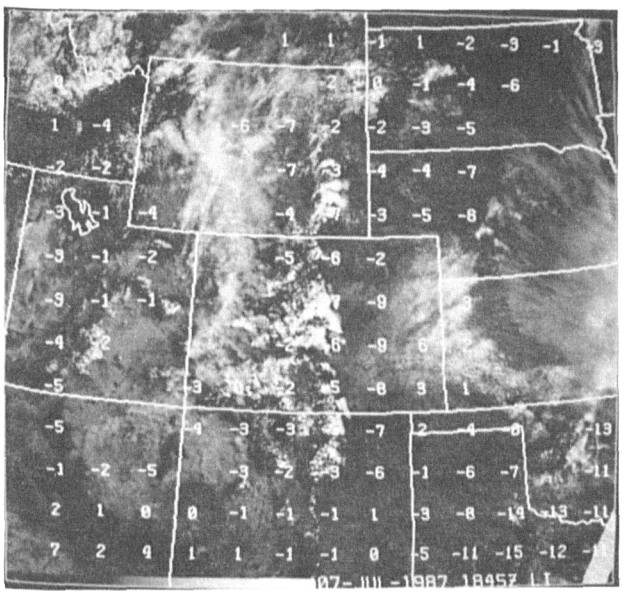

Fig. 3. VAS surface based lifted indices (°C) for 1845 UTC 7 July 1987 superimposed on a satellite image for same time. Lower lifted indices indicate areas of greater convective potential.

levels than at low levels. Low-level water vapor is generally more important for diagnosing convective potential, thus VAS soundings should be able to produce reasonable moisture profiles for this purpose. The mean total column precipitable water difference of .62 cm (Figure 2) is due to the lower tropospheric cold dewpoint bias noted above. The standard deviation of .29 cm indicates that the VAS precipitable water is a parameter useful for evaluating the convective environment, especially when compared to neighboring values. Similar results were found for other areas of the United States as well.

4. SHORT-RANGE FORECAST UTILITY OF VAS SOUNDINGS

As with previous forecast experiments (Birkenheuer and Snook, 1985), forecaster acceptance of VAS sounding data during the 1987 summer experiment was limited. Although locally generated VAS soundings improved data reliability and timeliness, many of the same quality problems still existed. When sounding data do not exactly agree with RAOB data, the VAS data are dismissed as erroneous. However, proper application will produce positive results. Since the VAS soundings are volume observations, bulk stability parameters (e.g., lifted index, precipitable water, positive buoyant energy, and negative buoyant energy) have proved useful for evaluating the pre-convective environment (Birkenheuer and Snook, 1985; Snook and Birkenheuer, 1986). Figure 3 shows VAS lifted indices for 1845 UTC 7 July 1987 superimposed on a visible satellite image. The lifted indices indicate the area of greatest convective potential to be from central Wyoming to just east of the Colorado front range into

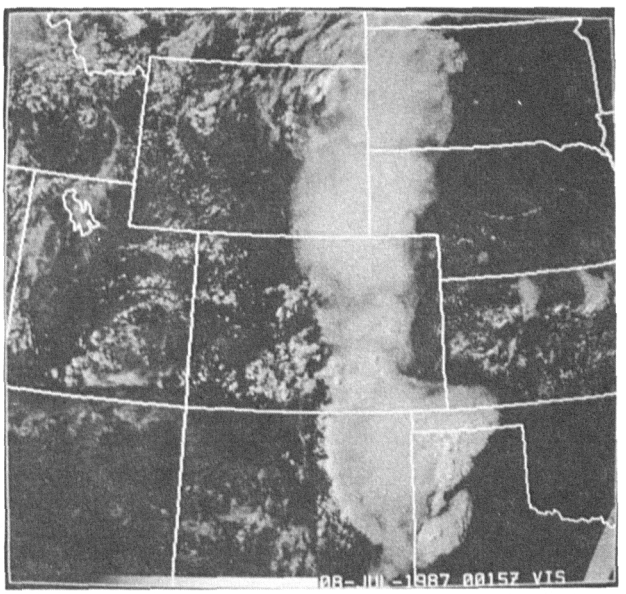

Fig. 4. Visible satellite image for 0015 UTC 8 July 1987.

northern New Mexico and the Texas panhandle. The visible image from 0015 UTC 8 July 1987 (Figure 4) shows that the strongest activity occured in these regions.

To enhance forecaster confidence, the sounding quality needs to be improved such that it corroborates other data sources. In addition, alternative products which exploit the advantages of the data need to be developed.

5. FUTURE WORK AND METHODS TO BETTER UTILIZE VAS SOUNDING DATA

There is much potential for the improvement of VAS sounding quality at PROFS. The mean temperature difference profiles indicate that soundings with less than a two-degree mean error compared to the RAOB can be produced. The use of GOES 7 transmittance functions will eliminate some of the biases already noted, although it is likely some biases will remain. If this is the case, a statistical approach is necessary to adjust the channel radiances.

Better use of the sounding data is necessary. Since consistent biases do exist, it has been suggested that sounding gradient (spatial and temporal) information be utilized (Jedlovec, 1985). The variational analysis technique to combine RAOB data and VAS sounding gradient data (McGinley, 1987; Birkenheuer, 1987) is currently being evaluated at PROFS. Imaging numerical VAS sounding products is another method which exploits the gradient information (Smith et al., 1985). Figure 5 illustrates an imaged Barnes analysis of the lifted indices field shown in Figure 3. When sounding data images are animated, changes in space and time are easily identified. Several methods to integrate sounding data and sounding gradient data into the MAPS mesoscale model are being evaluated (Benjamin et al., 1988). Since the VAS sounding is a volume observation, in

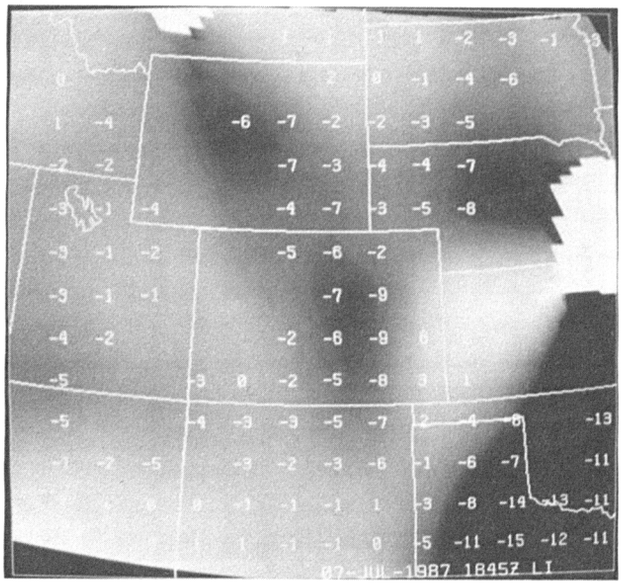

Fig. 5. Imaged Barnes analysis of VAS surface based lifted indices from Figure 3. Darkest areas indicate areas of greatest convective potential.

contrast to the RAOB point observation, a high quality VAS sounding may provide a more accurate representation of the atmosphere for computer model input.

The potential to produce higher spatial resolution soundings exists. Hillger et al. (1986) suggest that a three by three infrared pixel (16 km by 16 km) sounding field of view is sufficiently large to maintain the accuracy necessary for the VAS sounding generation process. Quality VAS soundings at this resolution could provide analysis and forecast utility on the meso-alpha scale and may supply valuable input to local area computer models.

6. SUMMARY

PROFS generates real-time VAS soundings every 90 minutes for a mesoscale grid covering the continental United States. An evaluation of VAS sounding quality during the PROFS 1987 summer forecast experiment revealed consistent biases in the temperature and moisture profiles. However, results indicate that the VAS soundings can provide valuable short-range analysis and forecast information if the consistent biases can be removed.

The VAS soundings generated at PROFS during the 1987 summer forecast exercise showed short-range forecast utility similar to previous experiments. The bulk stability parameters were most useful for defining areas of potential convective development. The potential to produce higher quality soundings with better spatial resolution in combination with more imaginative methods to use the data should allow VAS sounding data to become a valuable short-range forecast tool in the operational environment.

7. ACKNOWLEDGMENTS

Christopher Hayden has provided technical assistance towards the improvement of VAS sounding quality at PROFS. The author thanks Steve Zimmerman for software support and James Ramsay for technical assistance in preparing the manuscript.

8. REFERENCES

Benjamin, S. G., D. Birkenheuer, R. McPherson, T. Smith, J. S. Snook, 1988: Experiments in the assimilation of radiance observations from VAS. *Preprints, Eighth Conference on Numerical Weather Prediction*, Baltimore, February 22 - 26, 1988, AMS, Boston, in press.

Benjamin, S. G., R. S. Lieberman, T. W. Schlatter, R. G. Rasmussen, 1985: Preliminary tests of a regional objective analysis and short-range numerical forecasting system. *Preprints, Seventh Conference on Numerical Weather Prediction*, Montreal, June 17-20, 1985, AMS, Boston, 440-443.

Birkenheuer, D., 1987: Horizontal shape matching applied to VAS data. *Proc., Symp. Mesoscale Analysis and Forecasting*, Vancouver, Canada, August 17-19, 1987, ESA SP-282, 91-95.

Birkenheuer, D., and J. S. Snook, 1985: A review of the VAS assessment during the 1985 PROFS summer exercise. *NOAA Tech. Memo. ERL ESG-19*, Environmental Research Laboratories, Boulder, Colo., 18 p.

Bruce, R. E., L. D. Duncan, J. H. Pierluissi, 1977: Experimental study of the relationship between radiosonde temperatures and satellite-derived temperatures. *Mon. Wea. Rev.*, **105**, 493-496.

Hillger, D. W., J. F. W. Purdom, T. H. Vonder Haar, 1986: The use of structure function analysis to estimate noise levels and the potential resolution of satellite measurements. *Preprints, Second Conference on Satellite Meteorology/Remote Sensing and Applications*, Williamsburg, Va., May 13-16, 1986, AMS, Boston, 102-107.

Jedlovec, G. J., 1985: An evaluation and comparison of vertical profile data from the VISSR Atmospheric Sounder (VAS). *NASA Tech. Paper 2425*, Marshall Space Flight Center, Alabama, 38 p.

MacDonald, A. E., 1985: Design considerations of operational meteorological systems: a perspective based upon the PROFS experience. *Preprints, International Conference on Interactive Information and Processing Systems for Meteorology, Oceanography, and Hydrology*, Los Angeles, Calif., January 7-11, 1985, AMS, Boston, 16-23.

McGinley, J. A., 1987: The use of satellite IR data in the enhancement of surface thermal fields. *Proc., Symp. Mesoscale Analysis and Forecasting*, Vancouver, Canada, August 17-19, 1987, ESA SP-282, 123-128.

Reynolds, D. W., 1983: Prototype workstation for mesoscale forecasting. *Bull. Amer. Meteor. Soc.*, **64**, 264-273.

Smith, W. L., 1983: The retrieval of atmospheric profiles from VAS geostationary radiance observations. *J. Atmos. Sciences*, **40**, 2025-2035.

Smith, W. L., G. S. Wade, H. M. Woolf, 1985: Combined atmospheric sounding/cloud imagery-a new forecast tool. *Bull. Amer. Meteor. Soc.*, **66**, 138-141.

Snook, J. S., 1987: Operational cloud-clearing techniques of VAS radiance data. *Proc., Symp. Mesoscale Analysis and Forecasting*, Vancouver, Canada, August 17-19, 1987, ESA SP-282, 103-106.

Snook, J. S. and D. Birkenheuer, 1986: Utilization of VAS data in PROFS 1985 forecasting exercise. *Preprints, Eleventh Conference Weather Forecasting and Analysis*, Kansas City, Mo., June 17-20, 1986, AMS, Boston, 155-159.

ON THE INTERPRETATION OF INTEGRATED WATER VAPOR PATTERNS IN MIDLATITUDE CYCLONES DERIVED FROM THE NIMBUS 7 SCANNING MULTICHANNEL MICROWAVE RADIOMETER

Lynn A. McMurdie
Kristina B. Katsaros

University of Washington
Seattle, Washington

1. INTRODUCTION

The initiation and development of midlatitude cyclones often occurs over oceans. However, the sparsity of data in these regions severly inhibits the study and forecasting of these storms. In the last 20 years, satellite-borne instruments have begun to fill the information gap. Infrared and visible satellite images have been very useful in identifying cloud systems associated with midlatitude cyclones, and they have improved our ability to locate surface fronts and upper level features (Anderson et. al, 1969). Currently, passive microwave instruments on polar orbiting satellites are able to measure a wide range of atmospheric and surface quantities. Specifically, the Scanning Multichannel Microwave Radiometer (SMMR) that is on the Nimbus 7 satellite measures sea surface temperature, surface windspeed, integrated water vapor, sea ice and rainrate over oceanic regions, (Gloersen et. al, 1984). Integrated water vapor values derived from SMMR are accurate for a wide range of conditions (Katsaros et. al, 1981), and have a rms error of 2.1 kg m^{-2} (Chang et. al, 1984). The horizontal distribution of vapor is well suited for locating surface fronts and waves along fronts (McMurdie and Katsaros, 1985, Katsaros and Lewis, 1986). In addition, the patterns are well correlated with surface convergence derived from the Seasat-A Scatterometer (McMurdie, et. al, 1987).

In the work described here, we further explore ways to interpret the SMMR vapor patterns and how they relate to the dynamical structure of individual midlatitude storms. We use gridded meteorological data from the First GARP Global Experiment (FGGE) special observing period to calculate diagnostic quantities. We compare SMMR patterns for a storm at a weak stage determined from the diagnostic quantites to SMMR patterns for the storm at a stronger stage and document the differences. From this information, a more complete interpretation of the SMMR patterns is possible.

2. DATA ANALYSIS

Brightness temperatures measured by SMMR at 18 and 21 GHz channels (vertical and horizontal polarizations) were input to a water vapor algorithm outlined in Chang et. al (1984) and corrections were applied to account for drift in the 21 GHz channel over time. The horizontal resolution of the data is 50 x 50 km^2, and the swath width is 800 km. The integrated water vapor values for individual passes were mapped, and the National Meteorological Center (NMC) surface frontal analysis at the closest synoptic time was overlayed.

Many unique data sources in addition to the standard surface and upper level observations were used as input to a four-dimensional data-assimilation system at the European Centre for Medium Range Weather Forecasts (ECMWF) to produce the FGGE level III-b gridded data set. Details about the model and assimilation procedure are given in Bengtsson et. al (1982). The ECMWF FGGE III-b data set consists of basic analysis parameters and derived parameters at 15 vertical levels (1000 to 10 mb) that have a spacial resolution of 1.875 degrees latitude and longitude and temporal resolution of a six hours. The basic analysis parameters are uninitialized and they include geopotential height, sea level pressure, and horizontal wind components. The derived components are computed from the initialized fields and include temperature, relative humidity and vertical velocity. The vertical velocity was derived by ECMWF using the kinematic (mass continuity) method from the initialized divergences.

In this work, the diagnostic fields used are the vertical velocity fields at the 700 mb and 500 mb levels obtained directly from the FGGE data set, and divergence of the "Q-vector" at the 700 mb and 500 mb levels obtained from the FGGE geopotential fields. The Q-vector is defined as

$$\mathbf{Q} = \left[\frac{\partial \mathbf{V}_g}{\partial x} \cdot \nabla\left(\frac{\partial \Phi}{\partial P}\right), \frac{\partial \mathbf{V}_g}{\partial Y} \cdot \nabla\left(\frac{\partial \Phi}{\partial P}\right) \right] \qquad (1)$$

where $\mathbf{V}_g$ is the horizontal geostrophic wind at a particular pressure level and $\frac{\partial \Phi}{\partial P}$ is the thickness of the atmosphere between two pressure levels. The derivation of the Q-vector equation and it's interpretation is given in Hoskins et. al (1978) and Hoskins and Pedder (1980). The Q-vector can provide an approximate picture of the ageostrophic horizontal wind in the lower branch of the circulation that develops in order to maintain thermal wind balance in an evolving synoptic disturbance. The divergence of Q vectors is exactly equivalent to the forcing for quasi-geostrophic vertical motion. The full vertical velocity equation

$$\nabla^2\omega + \frac{f^2}{\sigma}\frac{\partial^2\omega}{\partial P^2} = -2\nabla\cdot\mathbf{Q} - \frac{R}{C_p P}\nabla^2 H \qquad (2)$$

has two main forcing mechanisms: quasi-geostrophic terms that are summarized by the divergence of Q, $\nabla\cdot\mathbf{Q}$, and diabatic heating, $\nabla^2 H$, most often due to the release of latent heat by

condensation. A comparison of the vertical velocity fields and the divergence of Q-vector fields can give indications of the relative importance of these two mechanisms in the resulting vertical motion fields.

We concentrate on diagnostic fields that indicate vertical motion because variations in integrated water vapor in a midlatitude storm as it develops could be due to variations of vertical motion. In this work, we explore one North Pacific storm as it develops and examine the relationship between the diagnostic fields and the SMMR vapor patterns.

3. RESULTS

The storm we chose to examine, 8-14 January 1979, arrived in the western Pacific as an occluded mature system and had an upper level flow that was nearly zonal with a weak short wave trough. At 12 GMT 10 January, the time of the first SMMR overpass, the upper level flow was west-northwesterly and the surface occluded and cold fronts were not associated with a surface low pressure center. The GOES-W satellite picture at this time had only a thin cloud band associated with the surface fronts. By 18 GMT 12 January, the time of the second SMMR overpass, the upper level flow deepened into a major trough, a new surface low formed, and the clouds associated with the surface fronts were much more extensive.

The SMMR pass, orbit number 1081 at 1150 GMT 10 January along with the NMC frontal analysis is given in fig. 1. The region of maximum water vapor lies just ahead of the cold front, and has a magnitude of 19 kg m^{-2}. Our previous work (unpublished) indicates that this is less than the average for this region and season (24 kg m^{-2}). There is a weak gradient behind the cold front to a minimum of 8 kg m^{-2}.

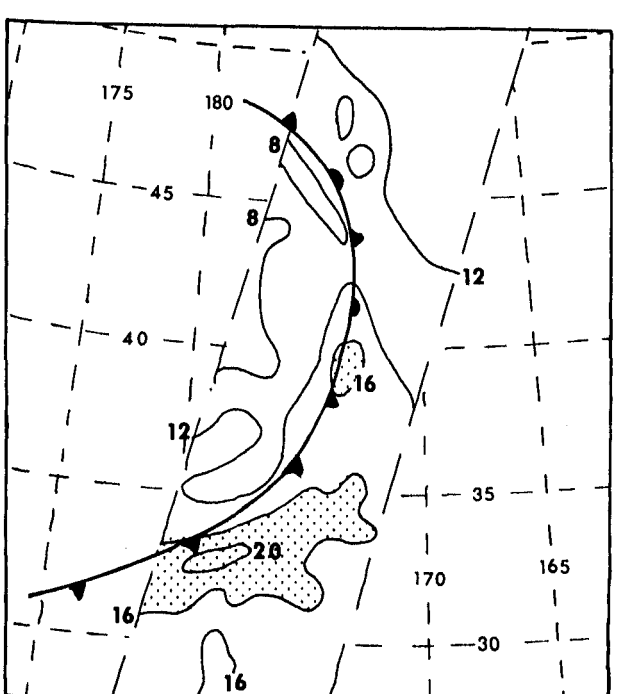

Fig. 1: Integrated water vapor from SMMR orbit number 1081 at 12 GMT 10 January, 1979. The field is contoured every 4 kg m^{-2} and the NMC 12 GMT frontal analysis is superimposed.

The vertical velocity and divergence of Q fields at the 700 mb level are shown in figs. 2a and 2b. The vertical motion is fairly weak in the vicinity of the cold fronts, 1.4 x 10^{-3}mb s^{-1}, and there is downward motion near the northern portion of the cold front. The divergence of Q field shows weak forcing (negative numbers indicate

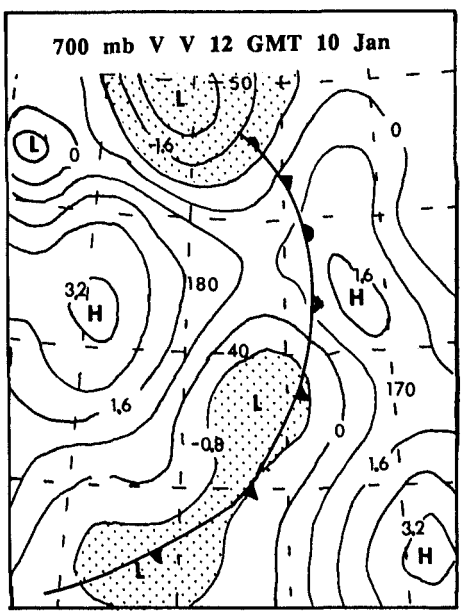

Fig 2a: Vertical velocity at the 700 mb level for 12 GMT 10 January 1979. The field is contoured every 0.8 x 10^{-3} mb s^{-1} and maxima and minima are indicated. Regions of negative values indicate upward motion and significant regions are shaded.

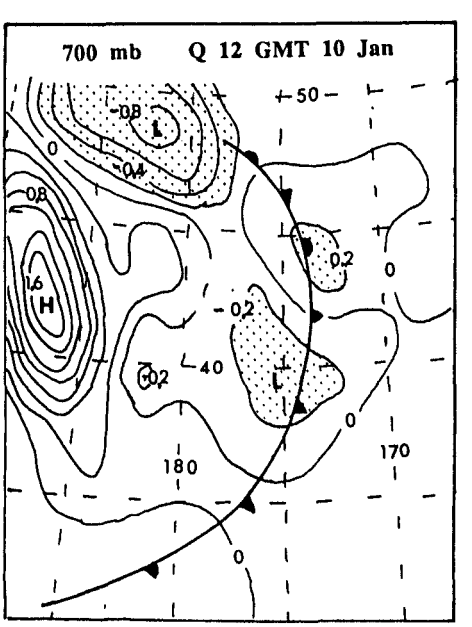

Fig 2b: The divergence of Q for 12 GMT 10 January, 1979 at the 700 mb level. The field is contoured every 0.2 x 10^{-17} m kg^{-1} s^{-1} and maxima and minima are indicated. Regions of negative values indicate positive forcing and upward motion and significant regions are shaded.

positive forcing of upward motion) at 40°N, otherwise the dominant features include forcing of downward motion west of the system, and upward motion to the northwest. The region of weak updrafts and quasi-geostrophic forcing coincide with the local maxima of water vapor ahead of the front at 32°N 178°W and 40°N 173°W. The vertical velocity and divergence of Q fields at the 500 mb level, not shown, are very similar to the ones at the 700 mb level showing weak upward motion and weak quasi-geostrophic forcing in the vicinity of the surface fronts.

The next SMMR overpass of this system, orbit number 1114, 2042 GMT 12 January, along with the 21 GMT NMC analysis is given in fig. 3. The integrated water vapor pattern at this time shows that the maximum in the vicinity of the cold front has increased slightly to 21 kg m^{-2} and to the north, 49°N, it has increased substantially from 11 to 17 kg m^{-2}. There is a sharp gradient behind the front to a minimum in the range 8 - 10 kg m^{-2}. The high water vapor values south of the system near 30°N are associated with an independent stationary front.

The 700 mb vertical velocity and Q-divergence fields are given in figs. 4a and 4b. At this time the vertical velocity is much larger than previously, with values of approximately 5.0 to 7.0 $x10^{-3}$ mb s^{-1} at 40°N ahead of the front. The Q-divergence field has also increased from the previous stage to 0.6 - 0.9 $x10^{-17}$ m kg^{-1} s^{-1}. In addition, the largest updraft and strong forcing at 700 mb coincides with the local maximum in water vapor at 40°N and 142°W in fig. 3. The corresponding diagnostic fields at the 500 mb level are given in

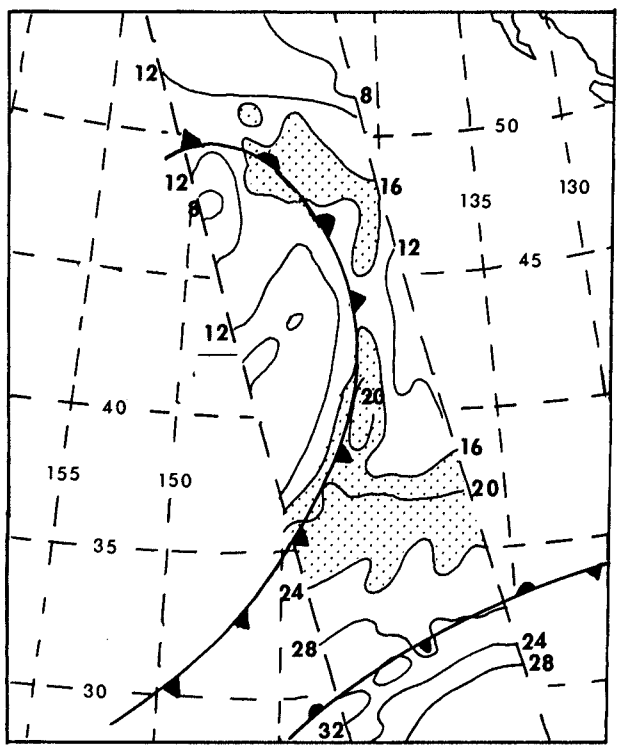

Fig 3: Integrated water vapor for orbit number 1114 at 21 GMT 12 January and the NMC 21 GMT frontal analysis.

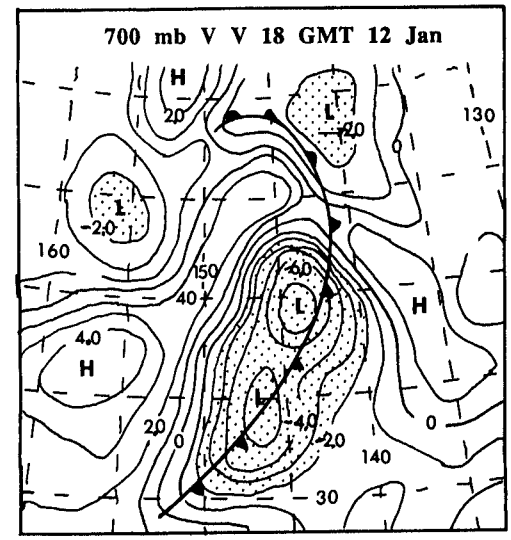

Fig 4a: Vertical velocity at the 700 mb level for 18 GMT 12 January 1979. The field is contoured every 1.0 x 10^{-3} mb s^{-1}.

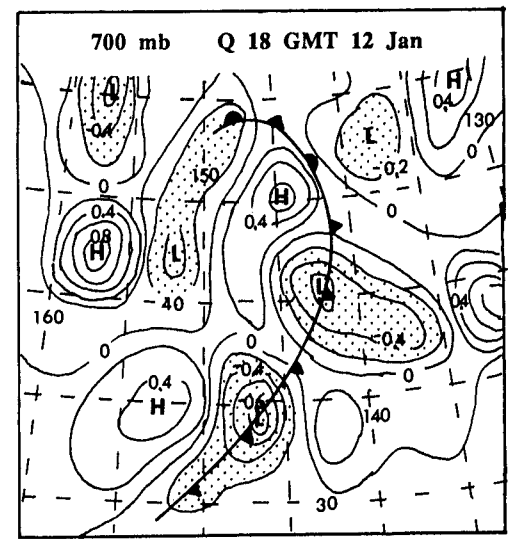

Fig 4b: The divergence of Q for 18 GMT 12 January, 1979 at the 700 mb level. The field is contoured every 0.2 x 10^{-17} m kg^{-1} s^{-1}.

figs. 5a and 5b. At this level, the vertical velocity is still strong, at 4 - 5 $x10^{-3}$ mb s^{-1}, but it is less than the vertical velocity at 700 mb. Whereas the divergence of Q is substantially larger at the 500 mb level, at a maximum of 3.5 x 10^{-17} m kg^{-1} s^{-1}.

4. DISCUSSION

When the upward vertical motion was weak and the quasi-geostrophic forcing implied by the divergence of Q was also weak, the SMMR pattern had maximum integrated water amounts that were less than normal and a weak gradient towards the cold air (figs. 1 and 2). When the upward motion was greater and the forcing greater, as in figs. 4 and 5, the SMMR vapor pattern had more structure, higher maximum values and a strong gradient towards the cold air (fig. 3). We have examined the development of two other storms and found the same relationships to apply.

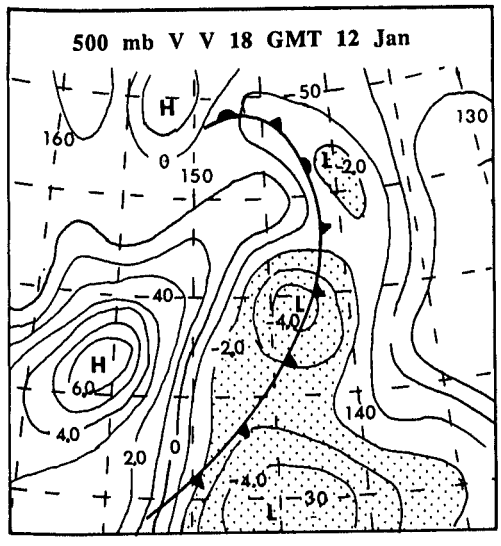

Fig 5a: Vertical velocity at the 500 mb level for 18 GMT 12 January 1979. The field is contoured every 1.0 x 10^{-3} mb s^{-1}.

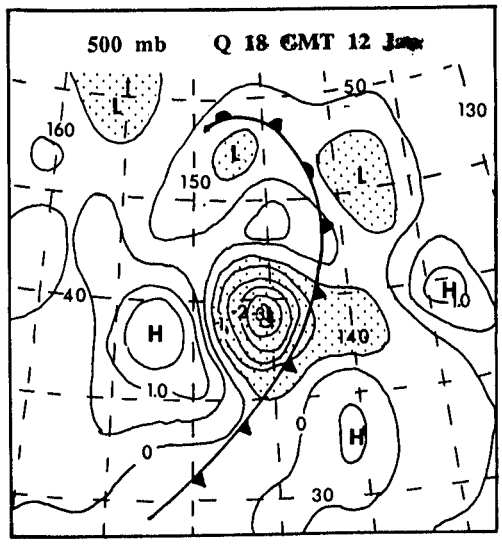

Fig 5b: The divergence of Q for 18 GMT 12 January, 1979 at the 500 mb level. The field is contoured every 0.5 x 10^{-17} m kg^{-1} s^{-1}.

In the second case, 18 GMT 12 January, the vertical velocity was greater at the 700 mb level, but the divergence of Q was greater at the 500 mb level. Rough estimates of the terms in eq. 2 suggest that the diabatic heating term ($\nabla^2 H$) is of the same magnitude as the $\nabla^2\omega$ term and could have contributed to the vertical motion field twice as much as the quasi-geostrophic forcing term ($\nabla \cdot Q$). In addition, the increase of water vapor in the vicinity of the fronts and the increase of cloudiness at this time support the possibility that the diabatic heating term could be significant. However, at the 500 mb level, quasi-geostropic forcing appears to be important.

In summary, we have demonstrated that variations in the SMMR derived integrated water vapor pattern from one stage of storm development to another can be related to the large scale vertical motion and quasi-geostrophic forcing in the midlatitude cyclone. Other case studies have verified this general conclusion; however, more cases should be examined in order to obtain quantitative relationships and a better statistical base. Our aim is to provide the background necessary to develop forecast and post-analysis techniques where satellite derived vapor fields, from instruments like SMMR or the current Special Sensor Microwave Imager (SSM/I), could help in the diagnosis of oceanic midlatitude cylones.

Acknowledgements: The SMMR data were provided by Dr. Per Gloersen of the National Space Science Data Center, Greenbelt, Maryland. This work was performed under NASA contract NAS8-36473.

5. REFERENCES

Anderson, R. K., J. P. Ashman, F. Bittner, G. R. Farr, E. W. Ferguson, V. J. Oliver, and A. H. Smith, 1969: Applications of meteorological satellite data in analysis and forecasting. ESSA Tech. Rep. NESC 51 (Available from Govt. Printing Office, Washington).

Bengtsson, L. M. Kanamitsu, P. Kallberg, and S. Uppala, 1982: FGGE 4-Dimensional data assimilation of ECMWF. *Bull. Amer. Met. Soc., 63*, 29-43.

Chang, H. D., P. H. Hwang, T. T. Wilheit, A. T. C. Chang, D. H. Staelin, and P. W. Rosenkranz, 1984: Monthly distributions of precipitable water from the NIMBUS 7 SMMR data. *J. Geophys. Res., 89*, 5328-5334.

Gloersen, P., D. J. Cavalieri, A. T. C. Chang, T. T. Wilheit, W. J. Campbell, O. M. Johannessen, K. B. Katsaros, K. F. Kunzi, D. B. Ross, D. Staelin, E. P. L. Windsor, F. T. Barath, P. Gudmandsen, E. Langham and R. O. Ransseier, 1984: A summary of results from the first NIMBUS 7 SMMR observations. *J. Geophys. Res., 89*, 5335-5344.

Hoskins, B. J., I. Draghici, and H. C. Davies, 1978: A new look at the omega-equation. *Quart. J. R. Met. Soc., 104*, 31-38.

Hoskins, B. J. and M. A. Pedder, 1980: The diagnosis of midlatitude synoptic development. *Quart. J. R. Met. Soc., 106*, 707-719.

Katsaros, K. B., P. K. Taylor, J. C. Alishouse, R. J. Lipes, 1981: Quality of Seasat Scanning Multichannel Microwave Radiometer (SMMR) atmospheric water determinations. In J. F. R. Gower (ed.), *Oceanography from Space*, Plenum Publishing Corp., 691-706.

Katsaros, K. B. and R. M. Lewis, 1986: Mesoscale and synoptic scale features of North Pacific weather systems observed with the Scanning Multichannel Microwave Radiometer on Nimbus 7. *J. Geophys. Res., 91*, 2321-2330.

McMurdie, L. A. and K. B. Katsaros, 1985: Atmospheric water distribution in a midlatitude cyclone observed by the Seasat Scanning Multichannel Microwave Radiometer. *Mon. Wea. Rev., 113*, 584-598.

McMurdie, L. A., G. Levy, and K. B. Katsaros, 1986: On the relationship between scatterometer derived convergences and atmospheric moisture. *Mon. Wea. Rev., 115*, 1281-1294.

2.2

PRECIPITABLE WATER DERIVED FROM NIMBUS-7 SMMR MEASUREMENTS AND ITS COMPARISON TO FGGE III-B DATA DURING JANUARY 10-FEBRUARY 13, 1979

Huo-Jin (Alex) Huang

Atmospheric Sciences Program
University of North Carolina at
Asheville, Asheville, NC 28804

Dayton G. Vincent

Dept. of Earth and Atmospheric
Sciences, Purdue University
West Lafayette, IN 470907

Franklin R. Robertson

Earth Science and Applications Division
NASA/Marshall Space Flight Center
Huntsville, AL 35812

1. INRODUCTION

In order to closely monitor the global variations of water vapor, remote sensing measurements and techniques become essential and dominant. Various passive microwave methods and algorithms have been proposed and applied to estimate the total precipitable water by utilizing different radiation sensors on different satellites, such as Staelin et al., 1976; Rosenkranz et al., 1978; Grody et al., 1980; Wilheit and Chang, 1980; Katsaros et al., 1981; Prabhakara et al., 1982; Wentz, 1983; Taylor, 1984; and McMurdie and Katsaros, 1985. The algorithm proposed by Prabhakara et al. (1982), which seems to be appropriate and physically complete, is applied in the present study to estimate total precipitable water from Nimbus-7 Scanning Multichannel Microwave Radiometer (SMMR) brightness temperature difference between 21 and 18 GHz channels in the horizontal polarization over the tropical oceans during part of FGGE SOP-1, more specifically, January 10-February 13, 1979. During this period, the South Pacific Convergence Zone (SPCZ) over the South Pacific and the South Atlantic Convergence Zone (SACZ) over South America and adjacent Atlantic Ocean were two dominant features in the global circulation. The SPCZ was quasi-stationary and convectively active for the first 15 days. Subsequent to January 24, the SPCZ shifted westward and weakened, the diagonal (northwest to southeast) portion of the SPCZ was essentially nonexistent. On the other hand, the SACZ maintained its location and intensity throughout the 35-day period. In order to compare total precipitable water from SMMR with the best available analyses, revised ECMWF (European Centre for Medium-range Weather Forecasts) and GLA (Goddard Laboratory for Atmospheres /NASA) FGGE Level III-b data sets are also processed to compute total precipitable water from surface up to 300 mb. The results from Nimbus-7 SMMR, ECMWF and GLA are very comparable and will be discussed in Section 3.

In summary, the objectives of the present study are:

(1) To utilize Nimbus-7 SMMR measurements to estimate total precipitable water in the atmosphere over the tropical oceans; and

(2) To make intercomparison of the total precipitable water derived from Nimbus-7 SMMR, ECMWF and GLA.

2. DATA AND METHODOLOGY

Nimbus-7 SMMR brightness temperature measurements at 5 channels (6.63, 10.69, 18, 21 and 37 GHz) in TCT-tape format are obtained from NASA/Goddard Space Flight Center. Each channel has both horizontal and vertical polarization. Only brightness temperatures at 21 and 18 GHz in the horizontal polarization are examined. These two channels are closely spaced and located on one side of the weak water vapor line centered at 22.235 GHz. The difference between the brightness temperatures in these two channels yields a measure of the absorption strength of this weak water vapor line, and therefore, related to total precipitable water in the atmosphere. The SMMR observations are only taken at local noon and midnight every other day; the swath width is about 800 km and the resolution for 21 and 18 GHz is about 50 km (Gloersen and Barath, 1977, and Njoku et al., 1980). The brightness temperature measurements are processed from magnetic tapes and converted into images on NASA/Marshall Space Flight Center's Man-Computer Interactive Data Access System (McIDAS, Suomi et al., 1983) and focused on the tropical oceans bounded by 30°N and 30°S, and the ascending node of the swath is used. The estimate of total precipitable water over lands is not usable due to the large emissivity of land (~0.9). Because of limitation of swath width (~800 km) and temporal resolution (available every other day) of SMMR data, the mosaic is composed over three data days (six calendar days).

The transient features of weather phenomena will be recognized by the discontinuity of systems, and the persistency of weather systems (such as ITCZ, SPCZ, and SACZ) is clearly identified from composited mosaic.

The algorithm to estimate total precipitable water based on brightness temperature difference between 21 GHz and 18 GHz in the horizontal polarization (Prabhakara et al., 1982) is

$$(T_{B21} - T_{B18})_H = 6.1 + 2572.1 * (e^{-k_{21}Wx} - e^{-k_{18}Wx}) \quad (1)$$

where T_{B21}, T_{B18} = brightness temperatures at 21 and 18 GHz, respectively,
$(\ )_H$ = horizontal polarization,
k_{21} , k_{18} = effective absorption coefficients for vapor at 21 and 18 GHz, respectively,
W = total precipitable water,
x = sec θ, where θ = 50° corresponding to the viewing geometry of SMMR on Nimbus-7.

ECMWF Level III-b data set is based on Level II-b data and processed by the European Centre for Medium-range Weather Forecasts (ECMWF). The recently revised ECMWF data have both uninitialized and initialized data sets available. For the diagnostic purpose, the uninitialized data set, which include mean sea level pressure, geopotential height and east-west and north-south wind components at mandatory levels, and precipitable water content for lowest five layers, is applied. The precipitable water contents are summed up at each grid point for these five layers to get total precipitable water. The grid intervals are 1.875° x 1.875° latitude/longitude and the time intervals are six hours.

The GLA analyses consist of objectively-analyzed values of geopotential height, temperature, relative humidity, horizontal wind components, vertical motions and many other derived variables at mandatory pressure levels at increments of 4° latitude by 5° longitude. The analyses were derived from the assimilation cycle of the GLA General Circulation Model (Baker, 1983). The model is the global fourth-order version described in detail by Kalnay-Rivas et al. (1977), Kalnay-Rivas and Hoitsma (1979), and Kalnay et al (1983). The model is based on an energy-conserving scheme with all horizontal differences computed with fourth-order accuracy. A two-dimensional (latitude and longitude), 16th order Shapiro (1970) filter is applied every 2 hours to the sea level pressure, wind and potential temperature fields. There are nine vertical layers, equal in sigma, with a uniform non-staggered horizontal grid (4° latitude by 5° longitude). With the exception of the computation of longwave radiation (Wu, 1980) the parameterization of the physical processes in the fourth-order model is substantially the same as in the second-order model of Somerville et al. (1974). Only temperature and relative humidity are used here to estimate the specific humidity and then sum it up vertically from 1000 mb to 300 mb to obtain total precipitable water at each grid point for each observation time (00, 06, 12, and 18 UTC).

3. Results and Discussion

Large areas containing convective cloud bands are known to exist in the tropics and have been identified from satellite imagery (e.g., Kornfield et al., 1967; Miller and Freddes, 1971; Gruber, 1972; Streten, 1973; Gruber et al., 1986). Tropical convections can also be recognized by low values of outgoing longwave radiation (OLR) or cold cloud top temperatures in infrared imagery. The present study applies the total precipitable water derived from Nimbus-7 SMMR data, ECMWF and GLA analyses, respectively. As another useful indicator of tropical convections during part of SOP-1, January 10 - February 13, 1979. During this period, the SPCZ and its accompanying cloud band underwent a dramatic change in location and intensity. During 10-24 January, both the SPCZ and SACZ cloud bands dominated the convective activity in the Southern Hemisphere. They were observed to be quasi-stationary, semi-permanent features of the circulation (Huang and Vincent, 1985). Subsequent to 24 January, the SPCZ shifted westward, weakened considerably, and appeared to become part of the Australian monsoon circulation. The diagonal (northwest to southeast) portion of the SPCZ, which was very active convectively in mid-January, was essentially nonexistent from late January until at least mid-February. The SACZ appeared to maintain its location and intensity during late January, but weakened slightly in the first half of February. Figure 1 shows the monthly mean distributions of OLR for January and February 1979 which were extracted from the Atlas of OLR by Gruber et al.(1986). It verifies the discussion which was just presented, in particular that the SPCZ was a dominant heat source in most of January, but not in February.

The daily variations of tropical convections can also be monitored in the Hovmöller diagrams of total precipitable water for a specific latitudinal band, e.g., 22°- 26°S for GLA analyses (Figure 2a) and 22.5°-26.25°S for ECMWF analyses (Figure 2b). It is noted that

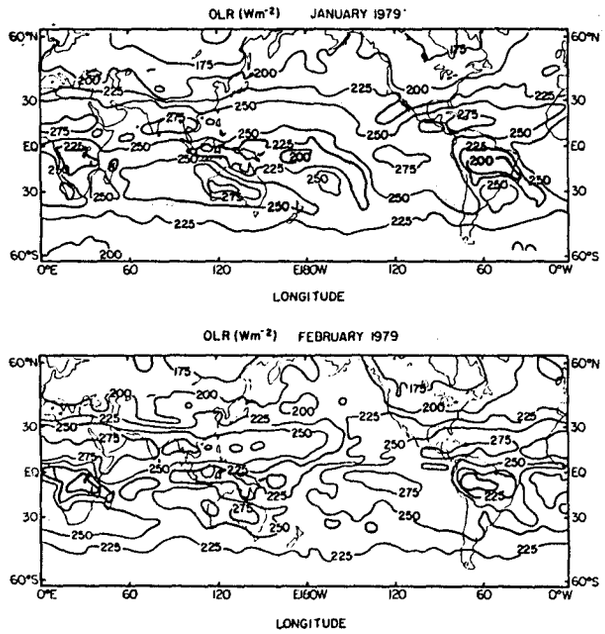

Fig. 1. Monthly mean distributions of outgoing longwave radiation (W m-2) for January and February 1979. Shaded regions are for OLR ≤ 225 W m-2 in the tropics and represent areas where deep convective activity most likely occurred.

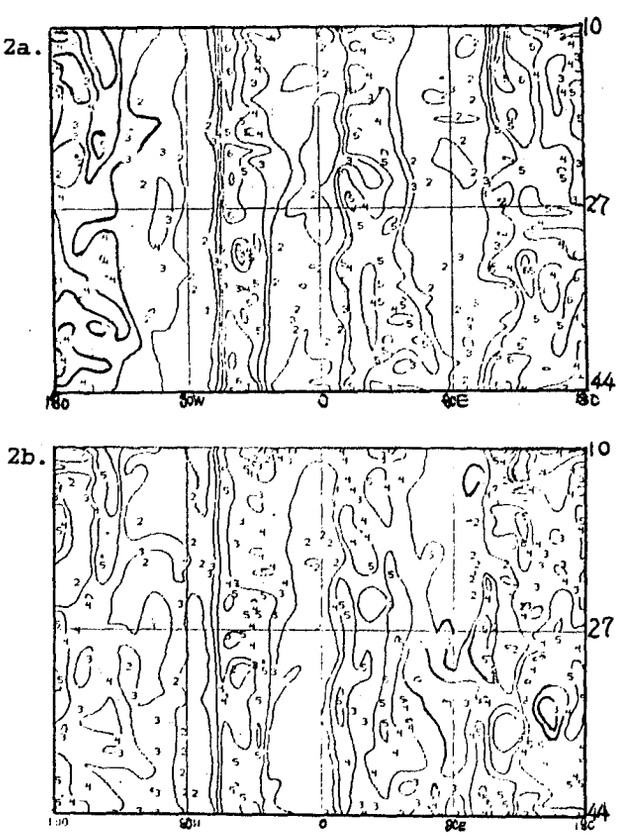

Fig. 2. Hovmoller diagrams of total precipitable water (g cm-2) derived from (a) GLA analyses for 22°-26°S and (b) ECMWF analyses for 22.5°-26.25°S during January 10 - February 13, 1979.

both analyses have similar patterns and comparable magnitudes; however, the GLA data set appears to be a little larger than that of ECMWF. Precipitable water maxima are found at or near the strong and organized convections, such as the SPCZ (~150°W), SACZ (~60°W), and convections over Southern Africa (~10°-45°E) and Eastern Indiana Ocean (~100°-130°E). All these maxima vary with time except the SACZ, which more or less maintains its location and strength throughout the study period. The SPCZ shifted westward and dissipated on around January 24 as expected; while the convections over the African and Indian Oceans started to become more active. This relationship between the convections over the Pacific and Indian Oceans has been suggested and related to 40-50 day oscillations (Lau and Chen, 1985; and Weickman et al, 1985). Huang and Vincent (1985) used the values of OLR lower than 225 W m-2 to locate the regions of active tropical convections. The Hovmöller diagram of OLR for 15°-20°S in their Figure 1 shows a similar pattern as in Figure 2 for the areas bounded by total precipitable water values of 4 g cm-2.

The comparisons of total precipitable water derived from SMMR, ECMWF, and GLA data are depicted in Figure 3. The enhanced mosaic of brightness temperature differences between 21 and 18 GHz measured by Nimbus-7 SMMR during January 10, 12 and 14 of 1979 is presented in the upper panel and identically reproduced in the lower panel of Figure 3a. The white regions show the continents and islands where the algorithm to estimate the total precipitable water fails. Dark grey areas show that total precipitable water values are more than 4.6 g cm-2, black areas for total precipitable water values between 3.1 and 4.6 g cm-2. The persistent feature, such as ITCZ and SPCZ are identified in the mosaic where the brightness temperature difference (total precipitable water) is greater.

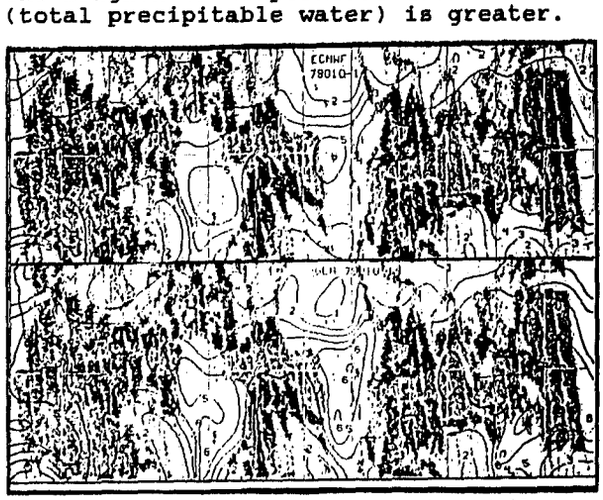

Fig. 3a. Enhanced brightness temperature difference between 21 and 18 GHz from Nimbus-7 SMMR data during January 10, 12 and 14, 1979 (upper and lower panels). Contours on the upper (lower) panel are the total precipitable water (g cm-2) derived from ECMWF (GLA) analyses averaged over January 10, 12 and 14, 1979.

The mosaic is composed of three SMMR data days, namely, January 10, 12 and 14, but elapses over six calendar days (January 10-15), since SMMR data are only available every other day. Contours of total precipitable water based on ECMWF are presented in the upper panel after averaged over January 10, 12 and 14. Contours of lower panel are the same as those of upper panel but based on GLA analyses. It is noted that all three data sets show a similar pattern and are quantitatively comparable in magnitudes. GLA seems to have larger values and are tighter in contours than those from ECMWF and SMMR, however. The general features of large-scale systems are well presented. The SPCZ, ITCZ, and convections over the Southern Africa and maritime continent are identified. Figure 3b is the same as in Figure 3a, except for January 16, 18 and 20 of 1979. A moisture burst from the SPCZ into the Northeastern Pacific Ocean and the development of convection over the Indian Ocean are noted. Figures 3c and 3d, which are for January 22-26 and January 28-February 1, respectively, clearly show the dissipation of the diagonal portion of SPCZ and the extension of convections over the Indian Ocean and maritime continent. The SACZ more or less remains unchanged.

Fig. 3b. Same as in Fig. 3a, except for January 16, 18, and 20, 1979.

Fig. 3c. Same as in Fig. 3a, except for January 20, 24, and 26, 1979.

Fig. 3d. Same as in Fig. 3a, except for January 28, 30, and February 1, 1979.

In order to assess quantitatively the total precipitable water derived from SMMR, ECMWF and GLA, one hundred and sixty (160) grid points over the oceans are selected randomly from Figure 3a as samples for statistical and linear regression analyses. Algorithm of Prabhakara et al. (1982) is applied to the brightness temperature differences between 21 and 18 GHz of SMMR to estimate total precipitable water at these selected points. Total precipitable water values from ECMWF and GLA at these points are also determined correspondingly. Table 1 shows that SMMR appears to have larger mean value and smaller standard deviation, presumably due to the truncation of real numbers into integer numbers while using McIDAS; however, they are very comparable to ECMWF values, and to some extent to GLA values. The largest standard deviation of GLA may be attributed to the stronger vertical motion field generated by GLA model (Huang and Vincent, 1986). The ratios of standard deviation to mean in the present study, however, are very compatible to previous studies which were based on different algorithms and rawinsonde observations.

Table 1. Basic statistics of total precipitable water (g cm-2) derived from SMMR, ECMWF and GLA based on 160 selected points during January 10, 12 and 14, 1979. The comparisons with previous studies based on Seasat SMMR data are also given (from Katsaros et al., 1981).

	MEAN(g cm-2)	STANDARD DEVIATION(g cm-2)	S.D. Mean(%)
Present study (160 points):			
SMMR	3.86	.82	21
ECMWF	3.70	.90	24
GLA	3.73	1.23	33
GOASEX[1] (7 samples):			
RAOB	1.50	.37	25
SMMR[3]	1.44	.45	31
SMMR[4]	1.76	.45	26
JASIN[2] (19 samples):			
RAOB	2.03	.59	29
SMMR[3]	2.14	.58	27
Tropical Stations (7 samples):			
RAOB	5.10	1.05	21
SMMR[3]	6.25	1.19	19
SMMR[4]	5.99	1.01	17

[1] GOASEX: The Gulf of Alaska - Seasat Experiment.
[2] JASIN: The Joint Air Sea Interaction Experiment.
[3] Based on Wentz algorithm (GOASEX Report, 1979).
[4] Based on Wilheit and Chang algorithm (1979).

Table 2. Correlation coefficients and F-values (in parenthesis) of total precipitable water between SMMR, ECMWF, and GLA based on 160 selected points during January 10, 12 and 14, 1979.

	SMMR	ECMWF	GLA
SMMR	1	.8325 (357)	.8120 (306)
ECMWF		1	.8672 (479)
GLA			1

F(1,158; 1%) = 6.80

The correlation coefficients between SMMR, ECMWF and GLA data sets based on the selected points are all greater than .80 and significant as shown in Table 2. Also in Figure 4, the linear relationship is found in total precipitable water derived from these data sets. It is believed that SMMR, ECMWF and GLA yield a confident estimation of total precipitable water. Furthmore, SMMR measurements could independently provide a data base of precipitable water to monitor the long-term variation of atmospheric moisture, since the global coverage of rawinsonde stations and another extensive field experiment such as FGGE are not likely to occur in the near future. Nevertheless, the absolute accuracy of total precipitable water estimated by passive microwave method needs further investigation and needs to be determined by comparing more rawinsonde observations to remote sensing measurements.

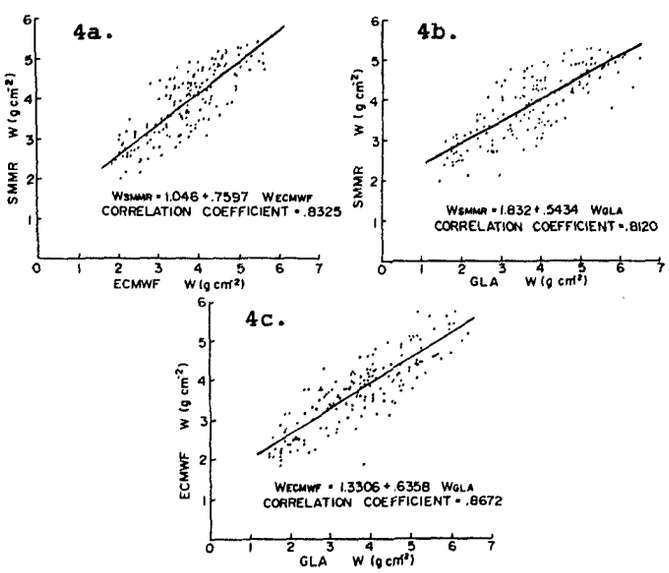

Fig. 4. Scatter diagrams of total precipitable water (g cm-2) at 160 selected points in Fig. 3 derived from (a) SMMR and ECMWF (b) SMMR and ECMWF and (c) ECMWF and GLA.

4. CONCLUDING REMARKS

It is found that passive microwave measurements with appropriate and realistic algorithm can provide a data base of global total precipitable water, which serves as a good indicator of convection. Also, total precipiable water from remote sensing, which is totally independent of rawinsonde observations, can be a consistency check on General Circulation Model outputs. The long-term variations of outgoing longwave radiation in the tropics demonstrate a close relationship between tropical convections and 40-50 day oscillations (Lau and Chan, 1985). It is believed that the variability of total precipitable water will also be able to show this trend, more importantly, the quantitative measurements of total precipitable water can provide an estimate of rainfall over the oceans. For the purpose of numerical modelling, the vertical profile of water vapor may be determined by combining both infrared and microwave measurements, as suggested by Viezee et al. (1979). The remote sensing measurements of total precipitable water can help provide a better understanding of atmospheric processes and improve the numerical modelling on general circulation.

However, some problems and limitations should also be addressed as follows:

(1) Due to large emissivity of land (~0.9), total precipitable water can only be estimated over the oceans;

(2) Sea surface emissivity varies with the surface roughness which caused by near-surface winds; nevertheless, the algorithm will still be valid if the wind speed is less than 10 m s-1 (Prabhakara et al., 1982);

(3) Cloud liquid water and heavy precipitation may contaminate the brightness temperature difference between 21 and 18 GHz, but not very seriously on the global-scale;

(4) The spatial and temporal resolutions of SMMR may not be adequate for synoptic-scale research, but Special Sensor Microwave/Imager (SSM/I) on Denfense Meteorological Satellite programme will alleviate this problem by providing a swath width of 1394 km and observations every 12 hours over most of the earth's surface; and

(5) In situ rawinsonde observations are needed to determine the absolute accuracy of total precipitable water. Some upcoming field experiments may provide necessary data to check on the total precipitable water measurements from SSM/I (Tayler, 1984).

ACKNOWLEDGEMENTS

The first author (HJH) is very grateful to many friends at NASA/Marshall Space Flight Center (NASA/MSFC) and Universities Space Research Association (USRA) for their kindest help and genuine support during his visit in the summer of 1987. Our special thanks go to Dr. Mike Kalb for handling administrative work; to Mike Goodman for requesting Nimbus-7 SMMR data and providing programs to run these data on McIDAS; to Paul Meyer for invaluable assistance with McIDAS; to Dr. Roy Spencer for scientific discussion; to Dr. Ned Reynolds for assisting on GLA data; and to Karen Parker and Karen Payne for program consultion. SMMR, ECMWF and GLA data tapes are provided by Per Gloersen and Ralph Post at NASA/Goddard Space Flight Center, Bob Williams at National Climatic Data Center, and Dr. Wayman Baker at NASA/GLA, respectively. All of them are greatly acknowledged. We thank the Earth Science and Applications Division of NASA/MSFC for providing all the supports throughout the research. This study was co-sponsored by the 1987 Summer Intern Program of NASA/MSFC through USRA under contracts NAS 8-34767 and NAS 8-36464.

REFERENCES

Baker, W.E., 1983: Objective analysis and assimulation of observational data from FGGE. Mon. Wea. Rev., 111, 328-342.

Gloersen, P., and F. T. Barath, 1977: A scanning multichannel microwave radiometer for Nimbus-G and Seasat-A. IEEE, J. Oceanic Eng., OE2, 172-178.

GOASEX Report, 1979: SEASAT Gulf of Alaska Workshop. Report vol. I and II, JPL-622-101-NASA, Jet Propulsion Laboratory, California Institute of Technology, Pasadena, California.

Grody, N. C., A. Gruber and W. C. Shen, 1980: Atmospheric water content over the tropical Pacific derived from the Nimbus-6 Scanning Microwave Spectrometer. J. Appl. Meteor., 19, 986-996.

Gruber, A., 1972: Fluctuations in the positions of the ITCZ in the Atlantic and Pacific Oceans. J. Atmos. Sci., 29, 193-197.

Gruber, A., M. Varnadore, P.A. Arkin and J.S. Winston, 1986: Monthly and seasonal mean outgoing longwave radiation and anomalies. NOAA Tech. Rep. NESDIS 26, U.S. Dept. of Commerce, NOAA/NESDIS, Washington, D.C. 20233. 7 pp and atlas of maps.

Huang, H.-J. and D. G. Vincent, 1985: Significance of the SPCZ in energy conversions of the Southern Hemisphere during FGGE, 10-27 January 1979. Mon. Wea. Rev., 113, 1359-1371.

Huang, H.-J. and D. G. Vincent, 1986: A comparison of global FGGE analyses and energetics (GLA vs ECMWF) for January 1979. Preprint of National Conference on the Scientific Results of the First GARP Global Experiment. January 14-17, 1986, Miami, Florida.

Kalney, E., R. Balgovind, W. Chao, D. Edelmann, J. Pfaendtner, L. Takacs, and K. Takano, 1983: Documentation of the GLAS fourth-order general circulation model. NASA Tech. Memo 86065, (NTIS N824-2813. Goddard Space Flight Center, NASA, Greenbelt, MD 20771.

Kalney-Rivas, E., A. Bayliss, and J. Storch, 1977: The 4th order GISS model of the global atmosphere. Beitr. Phys. Atmos., 50, 299-311.

Kalney-Rivas, E. and D. Hoitsma, 1979: The effect of accuracy, conservation and filtering on numerical weather forecasting. Preprints Fourth Conf. Numerical Weather Prediction, Silver Springs, MD, Amer. Meteor. Soc., Boston, MA, 02198, 302-312.

Katsaros, K. B., P. K. Taylor, J. C. Alishouse and R. G. Lipes, 1981: Quality of SEASAT SMMR (Scanning Multichannel Microwave Radiometer) atmospheric water determinations. Oceanography from Space, J. F. R. Gower ed., Plenum, 691-706.

Kornfield, J.A., A.F. Hasler, K. J. Hanson and V.E. Suomi, 1967: Photographic cloud climatology from ESSA III and V computer produced mosaics. Bull. Amer. Meteor. Soc., 48, 878-883.

Lau, K.M. and P.H. Chan, 1985: Aspects of the 40-50 day oscillation during the northern winter as inferred from outgoing longwave radiation. Mon. Wea. Rev., 113, 1889-1909.

McMurdie, L. A. and K. B. Katsaros, 1985: Atmospheric water distribution in a midlatitude cyclone observed by the SEASAT Scanning Multichannel Microwave Radiometer. Mon. Wea. Rev., 113, 584-598.

Miller, D.B., and R.G. Feddes, 1971: Global atlas of relative cloud cover. U.S. National Environmental Satellite Service and USAF Environmental Technical Applications Center, AD739434 Rep. No. 1, Washington, DC, 20233, 14 pp. and charts.

Njoku, E.G., E.J. Christensen and R.E. Cofield, 1980: The Seasat Scanning Multichannel Microwave Radiometer (SMMR) antenna pattern correction development and implementation. IEEE J. Oceanic Eng., OE 5, 125-137.

Prabhakara, C., H. Chang and A.T.C. Chang, 1982: Remote Sensing of precipitable water over the oceans from Nimbus 7 Microwave Measurements. J. Appl. Meteor., 21, 59-68.

Rosenkrantz, P.W., and D.H. Staelin, 1978: Typhoon June (1975) viewed by a Scanning Microwave Spectrometer. J. Geophys. Res., 83, 1858-1868.

Shapiro, R., 1970: Smoothing, filtering and boundary effects. Rev. Geophys. Space Phys., 8, 359-387.

Somerville, R.C.J., P.H. Stone, M. Halem, J.E. Hansen, J.S. Hogan, L.M. Druyan, G. Russell, A.A. Lacis, W.J. Quirk and J. Tennebaum, 1974: The GISS model of the global atmosphere. J. Atmos. Sci., 31, 84-117.

Staelin, D.H., K.F. Kunzi, R.L. Pettyjohn, R.K.L. Poon, R.W. Wilcox, and J.W. Waters, 1976: Remote sensing of atmospheric water vapor and liquid water with the Nimbus 5 Microwave Spectrometer. J. Appl. Meteor., 15, 1204-1214.

Streten, N.A., 1973: Some characteristics of satellite-observed bands of persistent cloudiness over the Southern Hemisphere. Mon. Wea. Rev., 101, 486-495.

Suomi, V.R., R. Fox, S.S. Limaye and W. L. Smith, 1983: McIDAS III: A modern interactive data access and analysis system. J. Climate Appl. Meteor., 22, 766-778.

Taylor, P.K., 1984: The determination of surface flukes of heat and water by satellite microwave radiometry and in situ measurements. Large-scale Experiments and Satellites, C. Gautier and M. Fieux, eds., D. Reidel, 223-246.

Viezee, W., P.A. Davis and D.E. Wolf, 1978: Technique to use satellite microwave spectrometer data in moisture budget studies of cyclones. Mon. Wea. Rev., 106, 1627-1633.

Weickmann, K.M., G.R. Lussky and J.E. Kutzbach, 1985: Intraseasonal (30-60 day) fluctuations of outgoing longwave radiation and 250 mb streamfunction during northern winter. Mon. Wea. Rev., 113, 941-961.

Wentz, F.J., 1983: A model function for ocean microwave brightness temperatures. J. Geophy. Res., 88, 1892-1908.

Wilheit, T. T. and A.T.C. Chang, 1979: An algorithm for retrieval of ocean surface and atmospheric parameters from the observations of the Scanning Multichannel Microwave Radiometer (SMMR). NASA Tech. Mem., 80277, Goddard Space Flight Center, Greenbelt, MD.

Wilheit, T. T. and A. T. C. Chang, 1980: An algorithm for retrieval of ocean surface and atmospheric parameters from the observations of the Scanning Multichannel Microwave Radiometer. Radio Sci., 15, 525-544.

Wu, M.-L.C., 1980: The exchange of infrared radiative energy in the troposphere. J. Geophys. Res., 85, 4084-4090.

2.3

AN EXAMPLE OF ESTIMATES OF PRECIPITABLE WATER DERIVED FROM NIMBUS-7 SMMR SATELLITE MEASUREMENTS AND FGGE UPPER AIR DATA

Douglas K. Miller
Department of Atmospheric Sciences AK-40
University of Washington
Seattle, WA 98195

Dayton G. Vincent
Department of Earth and Atmospheric Sciences
Purdue University
West Lafayette, IN 47907

1. INTRODUCTION

Moisture is an important constituent of the atmosphere and plays a vital role in determining cloud cover, precipitation, air masses, stability, etc.; therefore, it is important that accurate measurements of this variable be made. The vast oceans of our Earth's surface provide a large source of moisture that can modify the thermodynamics of the atmosphere through latent energy transfer and condensational heating. Unfortunately, it is over these water surfaces that observations of moisture variables are often quite sparse. In the last two decades, technological advances and the resultant increase in remotely-sensed observations associated with worldwide satellite deployment have provided an excellent data base which can help to alleviate the present spatial limitations of moisture variable measurements. The purpose of the present paper is to compare a sample of results of precipitable water estimates derived from the Scanning Multichannel Microwave Radiometer (SMMR) instrument aboard the NIMBUS-7 polar-orbiting satellite to those obtained from analyses of FGGE Level III-b data.

The paper utilizes satellite and FGGE data collected during the 10-18 January 1979 period over the South Pacific Ocean. During this period the South Pacific Convergence Zone (SPCZ) and its accompanying cloud band were quasi-stationary features of the circulation in the South Pacific. As seen in Fig. 1, the SPCZ cloud band had a zonal orientation along 5°-10°S from about 170°E to 160°W, then extended southeastward to about 40°S, 130°W. Latent heat appeared to play an important role in maintaining the zonal portion of the band while both latent heat and baroclinic processes seemed to be important in maintaining the diagonal portion for this period, (Vincent, 1982) Therefore, an examination of the moisture content of the SPCZ area during this period seems highly appropriate.

The SMMR instrument aboard NIMBUS-7 was the first microwave sensor to use multiple frequencies and has five frequency channels (6.6, 10.7, 18.0, 21.0 and 37.0 GHz), each having a vertical and horizontal polarization. The spatial resolution of SMMR data was improved over that from prior instruments, to 50 km x 50 km for the 18.0 and 21.0 GHz channels and 27 km x 27 km for the 37.0 GHz channel (Gloersen and Barath, 1977). Total integrated water vapor in a column (precipitable water), integrated liquid water and rainrate can each be estimated from SMMR data over oceans on a spatial scale not resolved by previous microwave instruments. The SMMR integrated water vapor data have been shown to be as accurate as those obtained from

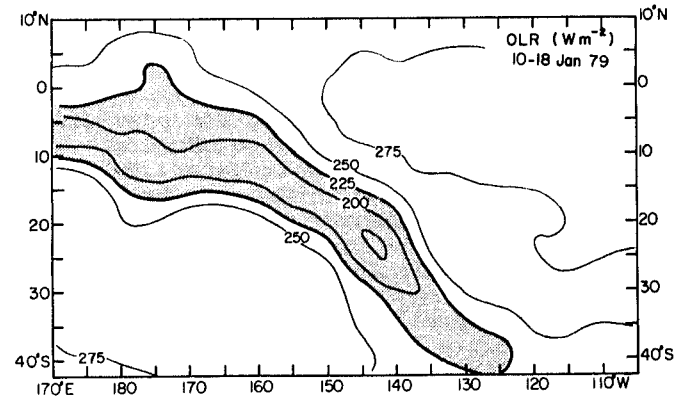

Fig. 1. Average outgoing longwave radiation (Wm^{-2}) for period 10-18 January 1979. Area shaded is OLR $\leq$ 225 Wm^{-2} and represents area occupied by deep convection.

radiosondes over the tropics and mid-latitudes (Lipes et al., 1979; Katsaros et al., 1981; Alishouse, 1983). The integrated water vapor over the oceans can be derived from SMMR with an accuracy of ~ 0.3 g cm^{-2} (Prabhakara et al., 1982, 1983; Prabhakara and Short, 1984), while the accuracy of liquid water estimates is about 10 mg cm^{-2} (Wilheit, 1979). Each overpass by the SMMR instrument covers an east-west swath width of about 600 km, and its orbit takes it approximately 30° longitude west of the previous pass, relative to the rotating earth below.

In the spectral region from 6.6 to 37 GHz, water vapor absorption in the atmosphere produces a dominant signal associated with the absorption line centered at 22.235 GHz. As described in section 2, the vertically-integrated water vapor content in the atmosphere is best sensed through the brightness temperature difference between the 21 and 18 GHz channels. That is, the differential absorption due to water vapor between these two channels provides, in general, a much stronger signal of precipitable water than other geophysical parameters.

The FGGE data set utilized in this study is the Goddard Laboratory for Atmospheres (GLA) Level III-b analyses. These analyses were derived from the assimilation cycle of the GLA General Circulation Model (GCM) and consist of objectively-analyzed values of geopotential height, temperature, relative humidity, horizontal wind components and vertical motions at mandatory pressure levels with the first-guess field provided by the model 6-h forecast. The GCM is the fourth-

order global atmospheric model described by Kalnay-Rivas et al., (1977) and Kalnay-Rivas and Hoitsma (1979), and more recently by Kalnay et al. (1983). There are nine vertical layers, each equal in sigma, with a uniform non-staggered horizontal grid (4° latitude by 5° longitude). The fourth-order version of the model is essentially the same as in the second-order model of Somerville et al. (1974).

2. METHODOLOGY

Values of the temperature, T (in degrees Kelvin), and relative humidity, RH (in percent), were extracted for each gridpoint within the study area (bounded by 10°N, 110°W, 46°S and 180°) at the 1000, 850, 700, 500, 400 and 300 mb levels. These were then converted to specific humidity, q. The q values at each of the six levels were used to calculate precipitable water, according to the definition:

$$W = \frac{1}{g} \int_{300}^{1000} q \, dp$$

where g is the acceleration due to gravity. This equation gives precipitable water in units of g cm^{-2}. Values of W were computed for each gridpoint within the 180-110°W and 10°N-46°S domain (15 x 15 array) and at 6-h interval from 0000 GMT 10 January to 1800 GMT 18 January 1979. Maps were then plotted and analyzed at 1 g cm^{-2} increments.

The orbit of the SMMR satellite yields about three passes (swaths) over the study area in approximately a 3.5-h time interval. The orientation of each pass depends upon the orbital phase of the satellite. For the passes in which the satellite is moving from north to south (descending node), the swaths have a northeast-southwest curved orientation relative to the Earth's surface, whereas they have a southeast-northwest curved orientation for a south to north pass (ascending node). Within each swath the SMMR instrument is able to resolve and retrieve a brightness temperature in a 50 km x 50 km area for the 18 and 21 GHz microwave channels. The brightness temperatures retrieved by SMMR and used in this study have been calibrated and corrected for instrument error by the National Space Science Data Center (NSSDC) at GLA in Greenbelt, Maryland.

The brightness temperatures were converted to two types of images through algorithms developed at the Marshall Space Flight Center (MSFC), NASA. One image type displays enhanced SMMR data retrieved by the 21 GHz channel (horizontally polarized), while the other displays an enhancement of the brightness temperature difference between 21 and 18 GHz. Both channels are sensitive to water vapor, liquid water and sea surface temperature (SST). The 21 GHz channel, being closer to the 22.235 GHz peak in the water vapor absorption band, is more sensitive to precipitable water (W). However, since the sensitivity of liquid water increases with frequency, the 21 GHz channel is also more sensitive to liquid water content in the air. Therefore, if the liquid water content is not too great, the difference between the 21 and 18 GHz channels is a good indicator of W, since the effect of SST is removed. On the other hand, if the liquid water content is high, as in the deep convective areas of the SPCZ, then the 21 GHz channel must be used, in conjunction with the difference (21-18 GHz), to accurately detect W. Within these convective regions, the liquid water signal between 18 and 21 GHz dominates over the water vapor signal. The resulting brightness temperature differences are considerably less than they would be in regions with no atmospheric liquid water present. Thus, the estimates of precipitable water values are too small and must be corrected. For these cases, the enhanced 21 GHz channel images were used to identify the strong convection areas and difference values at these grid points were adjusted upward to be compatible with the pattern shown on the 21 GHz image. A single image consists of the approximate three-swath coverage over the study area. Thusfar, we have processed the imagery for three days, 10, 12 and 14 January. Each day contains ascending, as well as descending nodes. The 21 and 18 GHz brightness temperature difference values were obtained from the computer-enhanced image at 4° latitude increments along each swath. Averages were computed for 4° latitude/longitude areas, since this spatial averaging corresponded most favorably to the grid increment of the GLA analyses.

The swath outlines of each of the three ascending node and descending node images were traced onto maps of GLA-analyzed precipitable water which corresponded to the nearest analysis (6-h) time. On each of the maps, precipitable water values were extracted from the analyses at increments of 4° latitude at grid points which were co-located with the previously-obtained SMMR values. The swath covered by some of the SMMR passes moved out of the study domain and, therefore, included less than the 15 latitudinal grid points. If the SMMR passes occurred near the middle of the GLA 6-h analyses interval, 6-h time averages of the GLA values of W were taken. For each swath a graph comparing the latitudinal trace of GLA precipitable water versus SMMR brightness temperature difference was plotted.

3. RESULTS AND DISCUSSION

Some examples of the location of SMMR passes relative to the GLA analyses of W for 10-11 January are shown in Fig. 2. It is important to note that any comparison between the GLA results and the SMMR observations will disagree slightly due to the different analysis times of the SMMR passes and the GLA field. For example, the eastern-most complete pass (centered at 115°W) will relate best with the same pass of the GLA field in the top panel, whereas the westernmost pass (centered at 170°W) will best compare with the same pass of the GLA field in the bottom panel.

The results plotted in Fig. 3 represent an example of the comparison between SMMR and GLA results for the descending and ascending nodes of the swaths for 10 January. The GLA values (plotted with the symbol "o") are area-averaged within the pass outlines at 4° latitude increments, as discussed previously. The set of GLA values in Fig. 3b have been time-averaged in order to best fit the SMMR pass times. This is an average of the 1800 GMT 10 January - 0000 GMT 11 January GLA values. The first set of values (Fig. 3a) were not time-averaged since the pass times were sufficiently close to a GLA analysis time. Comparing Fig. 3b to Fig. 2, it is seen that each

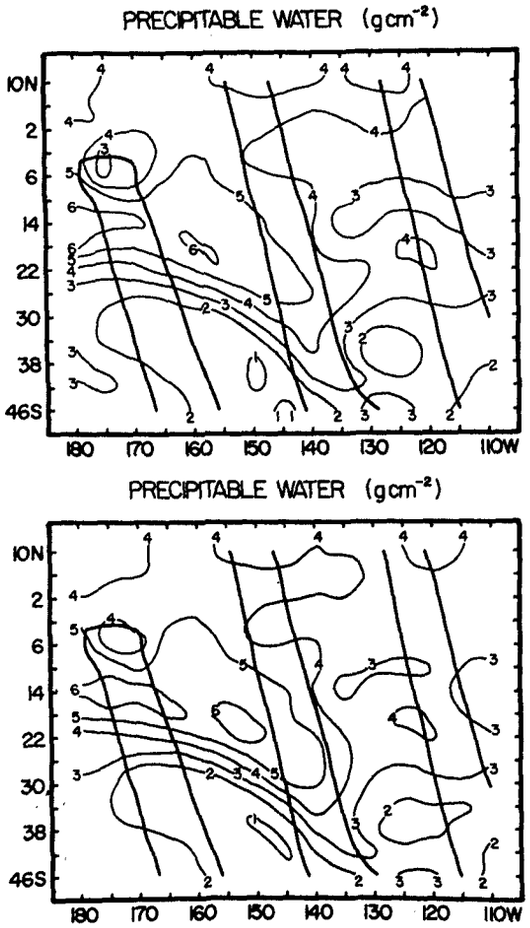

Fig. 2. SMMR passes superimposed on the precipitable water field derived from GLA analyses for the period 1800 GMT 10 January 1979 (upper panel) and 0000 GMT 11 January 1979 (lower panel). Equatorward crossing times of SMMR are 2320 GMT (left), 2145 GMT (middle), and 2000 GMT (right).

frame in Fig. 3b corresponds to a pass in Fig. 2 with the central longitude given in the lower right corner. The SMMR values (plotted with the symbol "+") in Fig. 3 have also been area-averaged as discussed in the previous section. The times given for each of the frames represent the equator crossing time of the SMMR instrument.

Figure 3 shows that the patterns of GLA precipitable water values compare well with the patterns of the SMMR brightness temperature differences. The most notable discrepancy occurs for GLA W values greater than 4 g cm^{-2} where the SMMR instrument consistently underestimates W. It is important to note that the scales of the vertical axes in Fig. 3 were chosen so that some gap would occur between the GLA and SMMR values. This makes it easier to identify relative similarities and differences in the patterns of the two schemes. In general, the SMMR patterns have a smoother appearance with lower peaks and less extreme minimum values than the GLA precipitable water patterns. This is most probably a result of the higher resolution (more data points) involved in the area averaging of the SMMR data compared to the more coarse resolution of data and area averaging of the GLA precipitable water data.

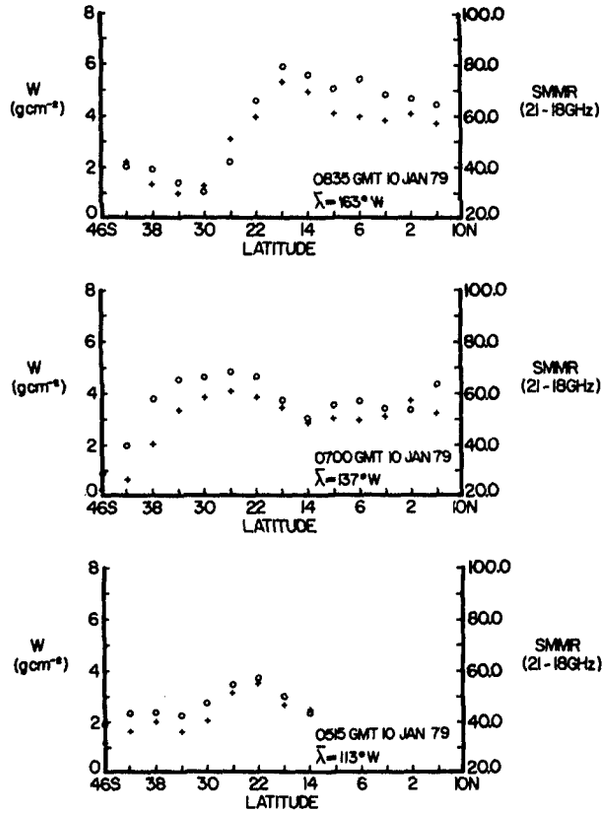

Fig. 3a. Comparison between precipitable water values (represented by "o" derived from GLA analyses and SMMR 21-18 GHz brightness temperature difference values (represented by "+"). Times given correspond to the equator crossing time of the SMMR instrument for each descending node on 10 January. The mean longitude location of each SMMR pass, $\bar{\lambda}$, is also given.

Although there is not sufficient space to show and discuss each of the GLA precipitable water fields analyzed in this study, they were found to be in good agreement with synoptic-scale features and various circulation patterns discussed in our previous South Pacific studies (Vincent, 1982, 1985; Miller and Vincent, 1987). For example, the orientation of the axis of maximum precipitable water values and higher modulations along this axis, corresponded well with the warm sectors of surface cyclones. Also, the orientation of the precipitable water minimum regions matched the position of the South Pacific subtropical high pressure region throughout the study period. Each of these observations supports the conclusion that the GLA precipitable water analyses for the area and time considered in this study were capable of depicting the horizontal variability of moisture with reasonable accuracy.

The research contained within this paper is only a small fraction of the possible research applications of the available GLA and SMMR data sets. At the time of this writing, SMMR images and brightness temperature difference values are being extended to include longer time and space scales. The results of that study are in progress by Huang et al. and should appear elsewhere in these conference proceedings.

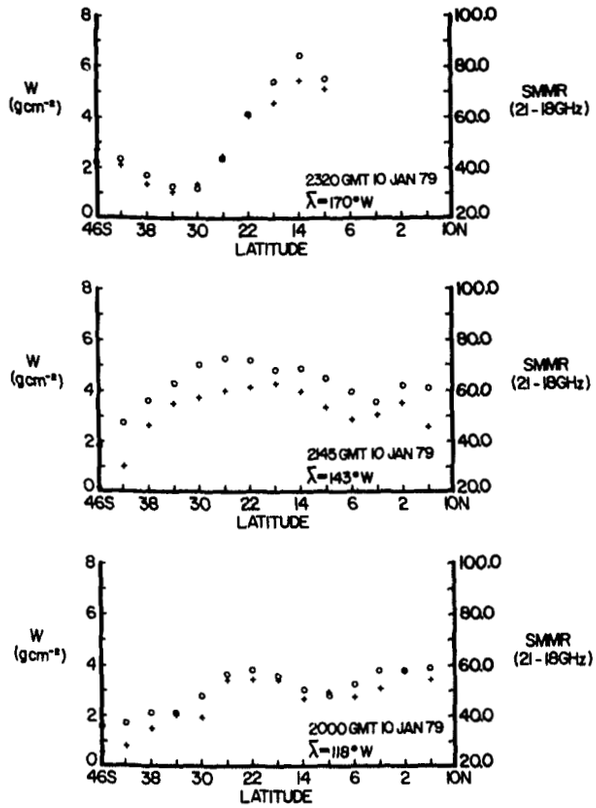

Fig. 3b. As in Fig. 3a, except for ascending node.

ACKNOWLEDGEMENTS

The authors thank the Marshall Space Flight Center for providing SMMR images and the Goddard Laboratory for Atmospheres, NASA, for supplying the data. They also thank Dr. Franklin R. Robertson of MSFC/NASA for his invaluable assistance, both technically and scientifically. In addition, the authors wish to express their appreciation to Ms. Helen Henry for typing the manuscript. The research within this report was sponsored by the National Aeronautics and Space Administration under Contract Numbers NAS8-35187 and NAS8-37127, issued to Purdue University.

REFERENCES

Alishouse, J.C., 1983: Total precipitable water and rainfall determinations from the Seasat Scanning Multichannel Microwave Radiometer (SMMR). J. Geophys. Res., 88, 1929-1935.

Gloersen, P., and F.T. Barath, 1977: A Scanning Multichannel Microwave Radiometer for Nimbus-G and Seasat-A. IEEE J. Ocean Eng., OE-2, 172-178.

Kalnay-Rivas, E., A. Bayliss, and J. Storch, 1977: The 4th order GISS model of the global atmosphere. Beitr. Phys. Atmos., 50, 299-311.

_____, and D. Hoitsma, 1979: The effect of accuracy, conservation and filtering on numerical weather forecasting. Preprints, Fourth Conf. Numerical Weather Prediction, Silver Spring, MD, Amer. Meteor. Soc., Boston, MA 02108, 302-312.

_____, R. Balgovind, W. Chao, D. Edelmann, J. Phaendtner, L. Takacs, and K. Takano, 1983: Documentation of the GLAS fourth order general circulation model. NASA Tech. Memo 96064 [NTIS N8424-28]. Goddard Space Flight Center, Greenbelt, MD 20771.

Katsaros, K.B., P.K. Taylor, J.C. Alishouse and R.J. Lipes, 1981: Quality of Seasat Scanning Multichannel Microwave Radiometer (SMMR) atmospheric water determinations. Oceanography from Space, J.F.R. Gower, Ed., Plenum, 691-706.

Lipes, R.G., R.L. Bernstein, V.J. Cardone, K.B. Katsaros, E.G. Mjoku, A.L. Riley, D.B. Ross, C.T. Swift and F.J. Wentz, 1979: Seasat Scanning Multichannel Microwave Radiometer, results of the Gulf of Alaska workshop. Science, 204, 1415-1417.

Miller, B.L. and D.G. Vincent, 1987: Convective heating and precipitation estimates for the tropical South Pacific during FGGE, 10-18 January 1979. Quart. J. Roy. Meteor. Soc., 113, 189-212.

Prabhakara, C., H.D. Chang and A.T.C. Chang, 1982: Remote sensing of precipitable water over the oceans from Nimbus 7 microwave measurements. J. Appl. Meteor., 21, 59-68.

_____, I. Wang, A.T.C. Chang and P. Gloersen, 1983: A statistical examination of Nimbus 7 SMMR data and remote sensing of sea surface temperature, liquid water content in atmosphere and surface wind speed. J. Clim. Appl. Meteor., 22, 2023-2037.

_____, and D.A. Short, 1984: Nimbus 7 SMMR derived seasonal variations in the water vapor, liquid water and surface winds over the global oceans. NASA Tech. Mem. 86080, Goddard Space Flight Center, Greenbelt, MD, 20771, 21 pp.

Somerville, R.C.J., P.H. Store, M. Halem, J.E. Hansen, J.S. Hogan, L.M. Druyan, G. Russell, A.A. Lacis, W.J. Quirk and J. Tenebaum, 1974: The GISS model of the global atmosphere. J. Atmos. Sci., 31, 84-117.

Vincent, D.G., 1982: Circulation features over the South Pacific during 10-18 January 1979. Mon. Wea. Rev., 110, 981-993.

_____, 1985: Cyclone development in the South Pacific convergence zone during FGGE, 10-17 January 1979. Quart. J. Roy. Meteor. Soc., 111, 155-172.

Wilheit, T.T., 1979: A model for the microwave emissivity of the ocean's surface as a function of wind speed. IEEE Trans. Geosci. Electron., GE4, 244-249.

TOTAL PRECIPITABLE WATER MEASUREMENTS FROM THE SSM/I

John C. Alishouse

National Oceanic and Atmospheric Administration
National Environmental Satellite, Data, and Information Service
Satellite Research Laboratory
Washington, D.C.

and

Jennifer Vongsathorn

S.M. Systems and Research Corporation
Lanham, Maryland

1. THE SSM/I

1.1 Channels

The SSM/I is a four frequency, seven channel microwave radiometer. The SSMI's frequencies are 19.35, 22.235, 37, and 85.5 GHz. All frequencies, except 22.235, are dual polarization. The 22.235 GHz channel is vertical polarization only. The 22.235 GHz channel is at the center of a weak water vapor absorption band. This channel when combined with the 19.35 and 37 GHz channels permit the retrieval of the total precipitable water and total cloud liquid water content of the atmosphere.

The instrument employs a conical scan with a cone angle of 45 degrees and an earth incidence angle of 53.1 degrees. The swath width is 1394 kilometers. The radiometers are total power, balanced mixer, superheterodyne receivers. Calibration is provided on-board by a hot absorber reference and a sky reference reflector. The data is digitized to 12 bits.

1.2 IFOVS

The satellite has an orbital height of 833 km and the SSMI has an antenna 60 x 66 cm. These factors combine with the view angle to give the channels IFOVs of 14 x 16-, 30 x 38-, 40 x 60-, and 45 x 70 km for the 85.5, 37, 22.2, and 19.35 GHz channels respectively.

1.3 Goals

This complement of frequencies and polarizations was selected to derive a number of geophysical parameters. The SSM/I will determine sea ice concentration and age (first or multi-year), surface wind speed over the ocean, total water vapor and cloud liquid water content over the ocean. Additionally the SSM/I will determine rain rates, surface moisture, snow cover, and ice edge location.

The present SSM/I is the first of an operational series. Therefore, it is very important to establish the accuracy of the brightness temperatures and geophysical parameters.

2. THE ALGORITHMS

2.1 Type

The algorithms used to derive the geophysical parameters are linear algorithms. A particular parameter is derived from the sum of products of coefficients and brightness temperatures and a constant term. This array of coefficients can be represented as a matrix; hence, this approach is sometimes called the D-matrix approach. The coefficients are derived by regression by comparing radiometric brightness temperatures with coincident surface measurements. Algorithms so derived are sometimes called regression algorithms.

2.2 Segments

The algorithms used to retrieve geophysical parameters for the SSM/I are specific to certain latitude zones and seasons. The latitudinal bands are: 0-20 (tropical), 20-25 (transition), 25-55 (mid-latitude), 55-60 (transition), and 60-90 (polar). There are three seasonal algorithms in the mid-latitudes and two seasonal algorithms in the tropical, transition, and polar regions. Each seasonal, latitudinal zone is called a climate code. There are eleven climate codes in all. There is no transition zone at the equator and the same seasonal algorithms are used in the same latitudinal zones in the Southern Hemisphere as in the Northern Hemisphere. Pre-launch simulations suggested the need for segmenting the algorithms to meet the accuracy goals. These simulations indicated that for the total precipitable water retrievals just three algorithms would be required. One algorithm is used for the warm equatorial and warm lower latitude transition zone. Another is used for both polar climate codes, the cold upper latitude transition zone, and the winter mid-latitude zone. The third is used in the remaining zones. The actual coefficients are given in Hollinger et al (1987).

2.3 Validation Strategies

The validation strategy for total preci-

pitable water is to compare satellite determinations with surface measurements. Most of the surface measurements are from radiosonde observations (raobs). There are some upward looking radiometer measurements. When comparing satellite measurements with surface measurements, sometimes called "ground truth", a number of conditions must be satisfied. Water vapor is highly variable on both spatial and temporal scales, therefore, it is important that the satellite and surface measurements be nearly coincident in space and time. For this investigation it is required that the observations be coincident to 2 degrees of latitude and longitude and 2 hours in time. The emissivity of land and water are quite different for the SSM/I frequencies. It should be noted that total precipitable water is retrieved only over the ocean. Therefore, it is important to insure that the observing platform be small enough not to perturb the satellite measurements. This restricts the number of sites for radiosonde launches or places for basing an upward looking microwave radiometer. The candidates are islands whose areas are less than 16% of the 19.35 GHz channel's IFOV and the remaining weather ships. A comprehensive list of about 50 stations was prepared to provide a wide sampling of latitudinal zones. The satellite orbit and other factors combine to limit actual data to about 20 stations.

3. RESULTS

3.1 Global Statistics

The results to be presented come from July and August, the boreal summer and austral winter seasons. The number of samples in the set is 83. The bias is the difference between the SSM/I and raob means.

MEANS	
RAOB	SSMI
2.96	3.06
STD DEV	
RAOB	SSMI
1.77	2.09
BIAS	RMS
0.10	0.62

The std dev is the natural variance and the rms is the rms difference between the raob and the corresponding SSM/I value. The units are in gm/cm^2.

3.2 Zonal Statistics

It is instructive to look at the statistics of the different algorithms on a zonal and seasonal (i.e., a climate code) basis. The following table shows the statistics for those climate codes having a significant number of samples.

ZONAL STATISTICS

ZONE	N	MEAN SSMI	MEAN RAOB	STD DEV SSMI	STD DEV RAOB	BIAS	RMS	CC
60-90N	32	1.17	1.39	0.35	0.46	-0.22	0.38	7
0 -20	23	5.72	4.88	0.60	0.60	0.88	0.94	1
0 -20S	11	4.10	4.43	0.81	0.84	-0.33	0.55	2
25-55	10	1.32	1.44	0.32	0.37	-0.12	0.40	7

Climate Code 1 is the tropical warm algorithm. Climate Code 2 is the tropical cool algorithm. Climate Code 7 is the mid-latitude winter algorithm and is also used in the upper latitude transition zone and the polar latitude zone.

None of the algorithms meet the accuracy goal of 0.2 gm/cm^2. CC1 shows a very significant tendency to overestimate the amount of water vapor. The other two algorithms show a tendency to underestimate the amount of water vapor. The errors produced by CC7 are comparable in the northern polar region and the southern mid-latitude region.

3.3 Improvements

When dealing with linear algorithms, there are two basic adjustments that can be made. One is the intercept or bias and the other is the slope. In the zonal statistics there is evidence to suggest that slope adjustments are required: however, these have not been implemented at this time. A bias or intercept change is more easily affected. The "before and after" of a simple bias removal are presented in the following table. The percentages are the percent that the rms differences are of the raob mean.

CLIMATE CODE	BEFORE RMS		AFTER RMS	
7	0.38	27%	0.31	22%
1	0.94	19%	0.33	6.8%
2	0.55	12%	0.33	7.4%
7	0.40	28%	0.38	26%

When adjustments for the slope are made as well, rms errors of about 0.2 gm/cm^2 are possible. Errors of 0.21 gm/cm^2 were achieved globally with the Nimbus 7 SMMR (Chang et al, 1984) and 0.24 gm/cm^2 with the Seasat SMMR (Alishouse, 1983).

4. REFERENCES

Alishouse, J.C., 1983: Total Precipitable Water and Rainfall Determination From the Seasat Scanning Multichannel Microwave Radiometer. J. Geophys. Res., 88, 1929-1935.

Chang, H.D., P.H. Hwang, T.T. Wilheit, A.T.C. Chang, D.H. Staelin, and P.W. Rosenkranz, 1984: Monthly Distributions of Precipitable Water from Nimbus 7 SMMR Data. J. Geophys. Res. 89, 5328-5334.

Hollinger, J., R. Lo, G. Poe, R. Savage, and J. Peirce, 1987: Special Sensor Microwave/ /Imager User's Guide. Naval Research Laboratory, Wash., DC, 177 pp.

MOISTURE PROFILE ESTIMATES IN CLOUDY LAYERS UTILIZING GEOSTATIONARY SATELLITE DATA

Jacques Hallé

Canadian Meteorological Centre
Atmospheric Environment Service
Dorval, Quebec, Canada H9P 1J3

1. INTRODUCTION

Numerical weather prediction models are sensitive to the analysis of moisture (Hallé and Benoit, 1985). Current operational moisture analysis schemes assimilate mainly conventional radiosonde data and TOVS and/or VAS water vapour retrievals.

Both data types have advantages and drawbacks. On one hand, radiosonde measurements are accurate but sparse over unpopulated and ocean areas. On the other hand, satellite TOVS/VAS retrievals have extended geographical coverage but are limited to clear and partly cloudy conditions and are much less accurate. There is also a definite lack of satellite moisture data in cloudy conditions.

This paper describes a simple procedure which uses cloud information as seen from GOES imagery to produce water vapour estimates in cloudy conditions, henceforth referred to as SATNEB (SATellite NEBulosity). The goal of the technique developed here is to produce moisture estimates to fill the gap left by other data sources, i.e. for cloudy systems over data sparse areas. The technique is based on the fact that clouds are an excellent indicator of the degree of saturation of the atmosphere. A similar method by Baba (1987) uses a cloud classification technique to estimate moisture in all cloud conditions.

Our proposed method requires an a-priori knowledge of the atmospheric state of temperature and snow cover, which is used in combination with GOES satellite radiances in the visible (6 microns) and infrared (11 microns) channels. The resulting product is a SATNEB, i.e. a statistically derived moisture profile of collocated radiosonde and GOES data over North America.

2. SATNEB PROCEDURE

The procedure delineates cloud/overcast areas (approx. 120 km x 120 km), estimates their vertical extent and degree of saturation. Cloud visible reflectance is dependent on many factors (Kaveney et al., 1977), two of which are cloud thickness and liquid water content. In this version of the procedure, the cloud thickness is assumed to be only a function of the visible reflectance. Within this layer, a statistically derived pressure-dependent relative humidity is assumed.

Processing is performed on a box of 15 x 15 pixels of 8 km resolution. No processing is attempted,

a) in areas where the satellite image is too distorted (satellite zenith angle ≥ 70°),
b) in areas lacking sunlight (sun zenith angle ≥ 80°),
c) over snow covered areas (obtained from an analysis of surface observing network snow cover data).

For each pixel a cloud albedo is computed using the visible digital count, the sun zenith angle and the visible calibration parameters. Each pixel is either classified as cloudy (albedo ≥ 35%) or clear (albedo < 35%). This very conservative threshold was chosen in order to make sure of the cloudiness of the pixel. Over cloudy or overcast boxes (i.e. 85% or more of the pixels in the box are cloudy), a cloud thickness is estimated assuming a linear function of albedo (Fig. 1). The mean visible albedo (averaged over cloudy pixels only) in the box is used.

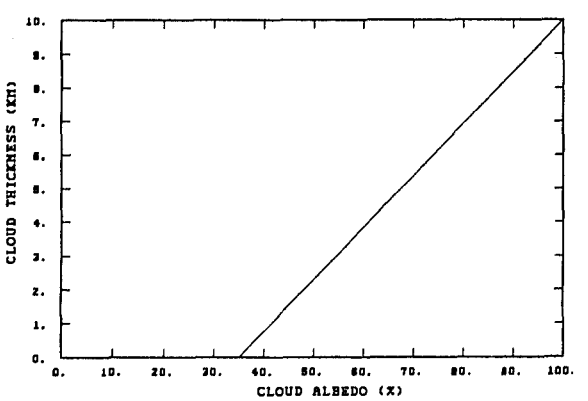

Fig. 1 Cloud thickness from cloud albedo.

At this stage in the procedure, a cloudy layer has been delineated with an estimated thickness. We compare the mean infrared temperature of the cloudy pixels in the box with the atmospheric temperature profile obtained from the Canadian Meteorological Centre's objective analysis. This leads to the determination of the cloud top and base of the cloud layer.

Within this cloudy layer, a statistically derived moisture profile is assumed. Currently, fixed relative humidity values are assigned at various pressure levels.

3. DATA

The procedure was developed and tested using GOES visible and IR (11 microns) data and radiosonde data over North America during a 10 week period from June 12th 1987 to August 20th 1987.

The radiosonde data consisted of 0000 GMT data and fell between latitudes 30N to 60N and longitudes 70W and 130W.

The first 6 weeks were used to derive mean relative humidity profiles in a SATNEB defined cloud layer. This is dataset A. During the following 4 weeks, the procedure was tested. This is dataset B. GOES satellite data were collected at 2100 GMT and SATNEB cloud boxes of 15 pixels by 15 pixels were processed. Each pixel is an 8 km x 8 km average visible and infrared value.

SATNEB and radiosonde data were collocated within 100 km and a 3-hour time log.

4. MEAN RELATIVE HUMIDITY PROFILE

The development sample (dataset A) was used to obtain mean relative humidities (RH) in the SATNEB defined cloudy layers. An analysis of the development sample of collocated SATNEB and radiosonde data (Table 1 and Fig. 2) shows very high mean RH values in the lower troposphere (85% to 91%) with fairly low standard deviations (8% to 17%). This shows that the cloudy layers as determined by the SATNEB technique are on average at or close to saturation at low levels. At 500 mb and higher, the mean RH values drop significantly and generally show more variations with standard deviations ranging from 15% to 26%.

Table 1. Collocation of radiosonde and SATNEB data. Development Sample (dataset A).

Pressure (mb)	Number of Collocations	R.H. (%) Mean	R.H. (%) Std. Dev.	Mixing Ratio (g/kg) Mean	Mixing Ratio (g/kg) Std. Dev.
1000	46	91.2	7.9	11.83	3.21
850	71	89.4	13.6	9.36	2.71
700	94	84.5	17.0	6.13	1.82
500	160	73.6	26.0	2.90	1.24
400	113	64.5	25.4	1.49	0.65
300	53	57.8	15.3	0.49	0.14

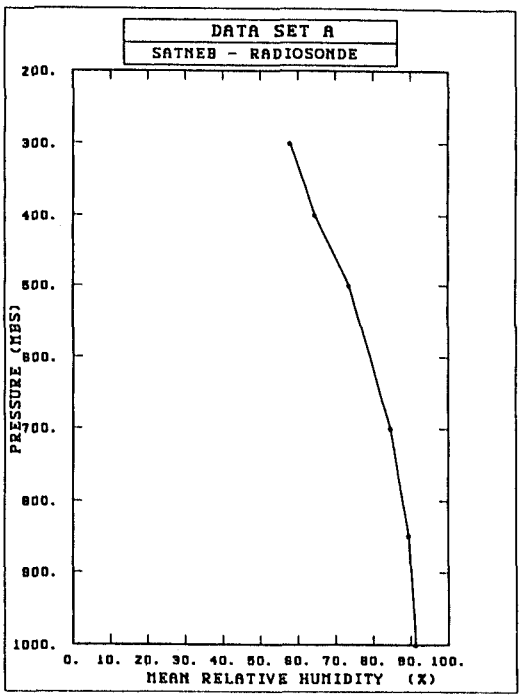

Fig. 2 Mean Relative Humidity profile. Development sample

5. RESULTS

SATNEBs were generated on the test sample (dataset B) using the mean RH profile from the development sample (dataset A) and collocated radiosonde and SATNEB data were compared. The results are shown in Table 2 and Fig. 3. RH biases are small and range from -3.7% to 3.9%. The root mean square (rms) difference between radiosonde and SATNEB data is very small at 1000 mb (9.2%) and at 850 mb (13.8%) and generally increase at higher levels, the highest being 26.3% at 400 mb.

Table 2. Collocation of radiosonde and SATNEB data. Test sample (dataset B).

Pressure (mb)	Number of Collocations	R.H. (%) Bias	R.H. (%) R.M.S.	Mixing Ratio (g/kg) Bias	Mixing Ratio (g/kg) R.M.S.
1000	44	3.9	9.2	0.52	1.24
850	72	-3.6	13.8	-0.25	1.30
700	78	1.2	22.1	0.14	1.66
500	124	-3.7	21.4	-0.19	0.95
400	89	1.1	26.3	-0.03	0.63
300	37	2.6	17.7	0.01	0.17

The agreement between the radiosonde and SATNEB data at 1000 and 850 mb is remarkable considering the 3-hour time lag between the two types of data and the fact that no vertical averaging was performed on the radiosonde data. The high number of collocations at mid levels may indicate a difficulty in recognizing multilayered cloud systems, e.g. a combination of cumulus and cirrus clouds. The high RH rms differences between 700 and 400 mb may be a reflection of this problem.

The results were also examined using another moisture variable, i.e. mixing ratio. These are shown in Table 2 and Fig. 4. Note that rms mixing ratio differences at 1000 and

850 mb are respectively 1.24 and 1.30 g/kg. Although no direct comparison between SATNEB and TOVS data is possible, these results suggest that moisture can be estimated in cloudy/overcast conditions with an accuracy which compares favourably with that of TOVS retrievals in clear or partly cloudy conditions (Golberg et al., 1986; Timchalk, 1986).

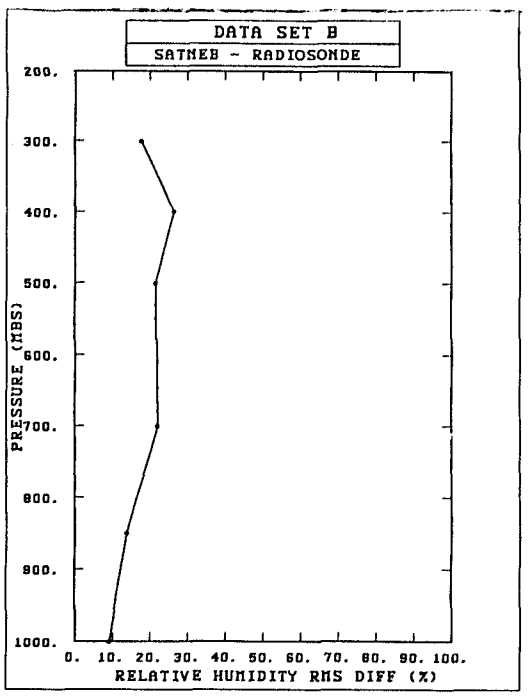

Fig. 3 Root mean square differences of Relative Humidity between SATNEB and radiosonde data. Test sample.

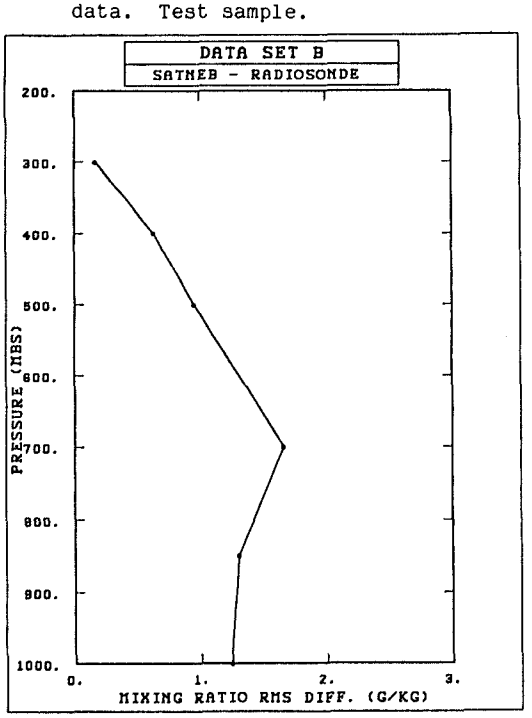

Fig. 4 Root mean square differences of mixing ratio between SATNEB and radiosonde data. Test sample.

It should be remembered though that a SATNEB profile is not a complete sounding but rather an estimated moisture profile of limited vertical extent in cloudy conditions, which is based on a statistically derived fixed relative humidity profile.

6. FUTURE PLANS

Plans for improving the SATNEB procedure include the statistical derivation of the relationship between cloud thickness and cloud albedo using collocated radiosonde data. Also planned is the use of cloud or air mass classification techniques to allow for variable mean relative humidity profiles.

7. CONCLUSIONS

A simple procedure has been described which uses cloud information from GOES (visible and infrared 11 micron channels) to produce three-dimensional moisture estimates in cloudy conditions (SATNEB).

Collocation with radiosonde data shows that moisture can be estimated with a reasonable degree of accuracy, especially in the low levels of the atmosphere.

SATNEB data has been used operationally in CMC's data assimilation scheme and NWP models for the past year.

8. REFERENCES

Baba, A., 1987: Improvement of the estimation method of moisture data from satellite cloud soundings, JMA/NDP Technical Report No. 16, Tokyo, Japan.

Golberg, M.D., A. Swaroop, H.E. Fleming and A. Reale, 1986: An analysis of temperature and water vapor retrievals using a minimum variance simultaneous method, Preprints of Second Conference on Satellite Meteorology/Remote Sensing and Applications, May 13-16, 1986, Williamsburgh, Va., AMS pp. 24-29.

Hallé J. and R. Benoit, 1985: Prévisions numériques utilisant les données satellite GOES, 19e Congrès Annuel CMOS, 12-14 juin, Programme et Résumés, pp. 41.

Kaveney, W.J., R.G. Feddes and K.N. Liou, 1977: Statistical inference of cloud thickness from NOAA 4 scanning radiometer data, Mon. Wea. Rev., 105, pp. 99-107.

Timchalk, A., 1986: Satellite derived moisture profiles, Preprints of Second Conference on Satellite Meteorology/Remote Sensing and Applications, May 13-16, 1986, Williamsburgh, Va., AMS, app. 64-66.

Blank page retained for pagination

PROFS QUANTITATIVE PRECIPITABLE WATER PRODUCT

Daniel Birkenheuer*

NOAA Environmental Research Laboratories
Environmental Science Group
Program for Regional Observing and Forecasting Services
Boulder, Colorado

1. INTRODUCTION

The Program for Regional Observing and Forecasting Services (PROFS) has incorporated Visible and Infrared Spin Scan Radiometer (VISSR) Atmospheric Sounder (VAS) data into its repertoire of data products since 1984. Initially, a low- to mid-level total precipitable water image developed after Chesters et al., 1983 (referred to here as the "split window" image) was used to qualitatively delineate water vapor concentration. The product showed utility during the summer forecast exercise conducted by PROFS in 1985. An assessment of VAS products made during and following the exercise indicated that water vapor imagery would be more useful if it were quantitative rather than merely qualitative (Birkenheuer and Snook, 1985). More recently Robinson et al., (1986) have compared various retrieval methods using a variety of VAS channel and surface data for computing precipitable water. The VAS "split window" algorithm demonstrated the highest rms error of the techniques studied. A 12-channel VAS-only regression was shown to be superior to all other methods independent of additional surface data. Smith et al., (1985) have also shown a linear combination of VAS channel data to be useful in quantitatively imaging precipitable water and other meteorological fields. The coefficients used by Smith et al. were a by-product of sounding retrieval computation. Regardless of the source, it is evident that a multilinear relationship can be effective in computing a precipitable water field from VAS channel data.

In 1986, PROFS adapted the physical retrieval algorithm developed at the University of Wisconsin - Madison (Smith, 1983) for its own in-house use. PROFS maintains real-time VAS data acquisition so, once the retrieval software became operational, real-time VAS soundings began to be produced routinely. With real-time soundings now available, PROFS is using linear regression to generate an image of precipitable water from VAS channel data which has a quantitative interpretation. This product replaces the qualitative "split window" product in the PROFS workstation. This paper documents the new precipitable water algorithm and illustrates its utility by example and observation.

2. PRODUCT DESCRIPTION

The coefficients for the multiple regression equation relating the 12-channel VAS brightness temperatures to precipitable water are computed from an ensemble of soundings within the region of interest, in this case, the western Great Plains and central Rocky Mountain states (Fig. 1). Both moisture and thermal VAS soundings are produced (clear skies allowing) at gridpoints spaced at roughly 110-km intervals in both N-S and E-W directions (Fig. 1). The dew point temperature soundings are integrated for total precipitable water, and following this, a multilinear regression is performed from which coefficients relating the brightness temperatures to precipitable water are determined for the entire region at each unique time.

The image is computed by applying the derived coefficients to each VAS pixel and determining a precipitable water value from the set of VAS IR brightness temperatures corresponding to the VAS pixel. A test of the IR window (band 8) brightness temperature is used to detect clouds. For summertime operation, 273 kelvins or colder has been successfully used as the criterion for flagging cloudy pixels.

Because of scanning constraints, the VAS IR data have either 8 or 16 km pixel resolution (nominal at 40 degrees north), and some bands skip scan lines at regular intervals ("Venetian blinding"). To compensate, all data are rep-

---

* on contract with the Cooperative Institute for Research in the Atmosphere and the CSU Research Foundation, Ft. Collins, Colorado.

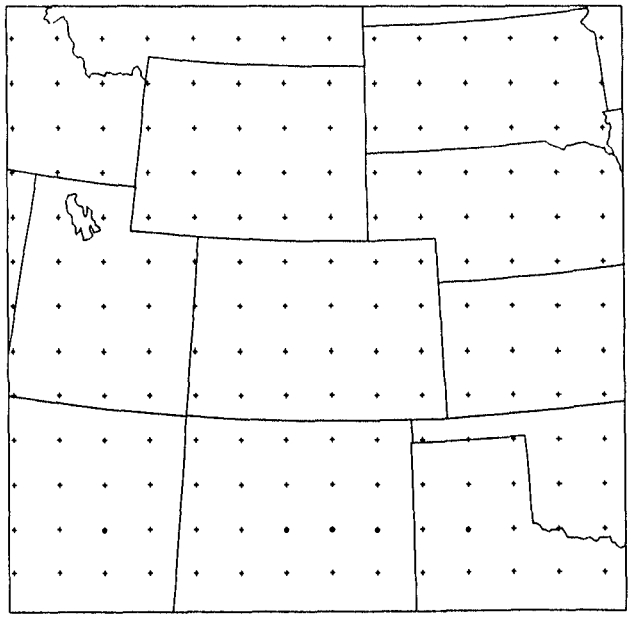

Fig 1. PROFS regional scale with crosses indicating operational VAS sounding retrieval coordinates. Soundings are produced for each location provided sky conditions are clear.

licated to 8 km resolution. This may seem dangerous, but the next step in the product's generation removes high frequency irregularities introduced by the replication procedure.

A smoothed image (PW^*) is produced by convolving the precipitable water pixel array (PW) with a shift invariant function (wt). In this case the 11 x 11 centrally weighted function is given by:

$$wt(m,n) = \cos\left[\pi\sqrt{m^2+n^2}/(2\sqrt{50})\right], \qquad (1)$$

where wt is the weight and m and n range from -5 to +5 including 0. The spatial extent of the weighting function was determined by examining Fourier transformations of typical scenes produced after the replication procedure and detecting characteristic periodic wavelengths likely to be related to the replication step. The discrete weighting function (Table 1) was found to be an optimal low pass filter for the image. The convolution is performed by calculating

$$PW^*(k,l) = \frac{\sum_{i=k-5}^{k+5}\sum_{j=l-5}^{l+5} wt(i-k,j-l)\,PW(i,j)}{\sum_{i=k-5}^{k+5}\sum_{j=l-5}^{l+5} wt(i-k,j-l)} \qquad (2)$$

with the requirements that pixel PW(k,l) is clear to begin with (otherwise $PW^*(k,l)$ immediately denoted cloudy) and the summed terms included in equation 2 are only clear pixels. By excluding cloud-flagged pixels, aliasing at cloud edges is eliminated. The computation can also extend to the array boundary by treating exterior points (for which data are not available) as cloud. Normalization is required with each application of the weighting function since the cloud amount and distribution constantly varies.

Table 1

The symmetric shift invariant function is tabulated below. Indices m and n each range from -5 to +5 as computed from equation (1). Normalization is performed with each application since the distribution of clear pixels keeps changing.

		±n					
		0	1	2	3	4	5
	0	1.00	.975	.903	.786	.631	.444
	1	.975	.951	.879	.763	.609	.424
	2	.903	.897	.809	.696	.546	.366
±m	3	.786	.763	.696	.588	.444	.272
	4	.631	.609	.546	.444	.309	.148
	5	.444	.424	.366	.272	.148	0.00

The color table enhancement used with the image is designed to contour levels of precipitable water with color intensity diminishing linearly between contour levels. For example, red will begin at zero intensity at 0 cm and increase to full at 1 cm, at which point the next color, yellow, begins at lowest intensity. The colors used include red (0-1cm), yellow (1-2cm), green (2-3cm), light blue (3-4cm), dark blue (4-5cm), violet (5-6cm), and neutral grey (clouds). The advantage of such a color table enhancement is that it both contours the field and images the field between contours. Clouds receive a neutral grey shade; initially they were colored white, but that proved to be distracting. It is also important to choose a color for clouds that is not confused with intermediate shades between contours.

An important feature of the product is that each image is computed from a new set of coefficients derived for that particular scene and unique time. Whether this is necessary is not known and is a subject receiving further study. However, if coefficients unique to each image are used, diurnal, thermal, and air mass variations do not cause fluctuations in the quantitative aspect of the image. Thus, the continuity and reliability of the final product are assured. Images can be confidently animated to show migration of moist or dry regions as well as overall trends such as moistening due to transpiration.

3. EVALUATION

The product was tested during the 1987 PROFS forecast exercise. Early impressions are described first; these are followed by a specific example.

Moist "pockets" or small islands of moist air are evident over the clear eastern plains of

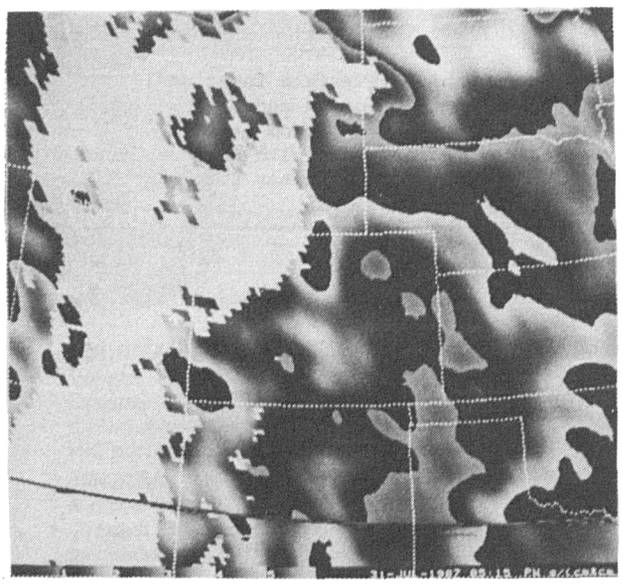

Fig. 2a. A black and white rendition of the VAS quantitative precipitable water product for 31 July 1987 0515 UTC. The grey shades delineate the breaks in the color enhancement. Amounts above 2 cm exist over the foothills and in SE Wyoming, while dryer conditions exist over SE and eastern Colorado. The structure of the water vapor distribution is evident in the partly cloudy skies in central Wyoming.

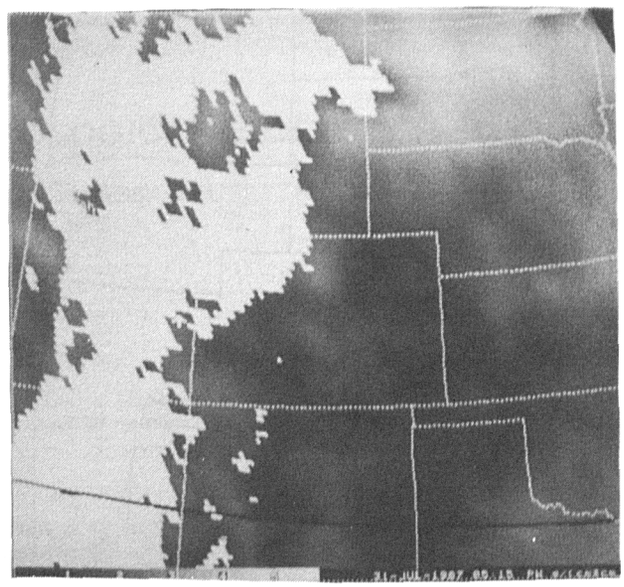

Fig. 2b. The same image as Figure 2a except the color enhancement has been replaced with a linear grey scale. Thus, it is possible to relate the imaged intensity with the quantitative amount of precipitable water in a black and white media.

Colorado. These often develop clouds on their down wind side showing their function as a moisture "fetch" feeding into the cloud. This is definitely a mesoscale feature and can possibly be used in generating local forecasts/nowcasts.

Breaks in cloudy areas reveal structure in moisture gradients possessing good continuity with similar structure in surrounding clear regions. These features demonstrate that cloudy pixels are being handled effectively since precipitable water values at cloud edges show little or no dry or moist bias. The cloud detection also seems effective because visible and infrared cloud imagery agree with the cloud structure in the precipitable water image.

When the product is overlayed with discrete values of precipitable water obtained from the soundings, a direct comparison can be made showing the agreement between the field and values that were used to produce the coefficients. Deviations occasionally exist at the extreme northern and southern parts of the region. These may be due to the zenith angle differences which varies predominantly in the north-south direction. In any case, the deviations appear to be tolerable for the summer season on this scale. Effects of the high terrain in the region's central portion have yet to be detected.

4. CASE STUDY: 30 - 31 JULY 1987

The days of 30 and 31 July 1987 were characterized by thunderstorms in the foothill and mountain regions of Colorado. Ample heating over the eastern plains of the state resulted in temperatures of low- to upper-30 degrees C (mid-90 to 100 degrees F). Thunderstorms did not develop over the plains even though dew points were high. Convection did occur over the foothills. There are many reasons for the preferred convection in the foothills on such days. Greater instability at higher altitudes is one factor. However, this does not explain why storms were not sustained over the plains and did form to the north over the Cheyenne, Wyoming area. One explanation may be available water vapor. VAS precipitable water imagery shows the moisture concentrated along the foothills and to the north (Fig. 2). The surface dewpoints decline slightly in the dry region to the east of Denver (Fig. 3), corresponding to the image to a limited degree. But because the total precipitable water is much less to the east of Denver, the moist layer is shallow over the plains, hence a lack of latent energy for fueling storms. A cumulus cloud field formed, but convection was lacking over the region. In fact, a storm did develop south of Denver over the Palmer Lake Divide. After moving northward it dissipated in the shallow moist air.

Precipitable water data from four ground-based radiometric profilers, two near the front range and two in the eastern plains, support the VAS imagery. Plots comparing the ground-based radiometer trends are shown in Figure 4. It is unusual to see drier conditions over the plains but this is supported by the profiler data, VAS imagery, and ensuing weather.

When used in conjunction with other data, the VAS precipitable water product was useful in locating deeper moisture in the region. Surface dew point observations of similar magnitude to those in the foothills did not reflect the extent of the water vapor. As with all meteoro-

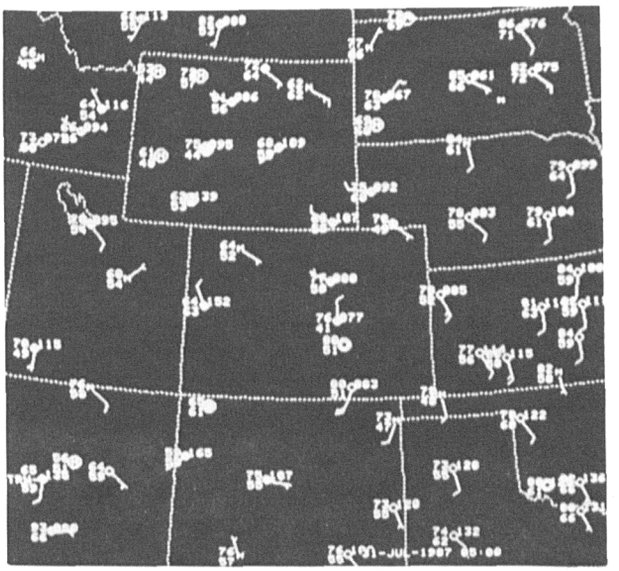

Fig. 3. Surface observations for 31 July 1987 at 0500 UTC. Dew points are slightly lower in eastern Colorado with weak corellation to the VAS moisture field in Figure 2.

logical data, no one data source will ever relate the entire picture. The importance of integrating VAS data with other data cannot be overemphasized.

5. CONCLUSIONS

The regression precipitable water product works quite well on the regional scale for convective season applications. Some discrepancies, possibly due to the variation of zenith angle over the scene, can perhaps be corrected by including zenith angle as an additional term in the regression equation. A national scale image will obviously have greater deviations due to this and other effects (e.g., variation in solar reflection in the near-IR bands during daylight hours, terrain effects, and a probable increase in the amount and complexity of cloud contamination with decreasing pixel resolution) and is one reason the regional scale was initially selected for the image.

The regression technique has great applicability to other meteorological parameters. Future plans are to produce images of lifted index and bulk thermal parameters such as positive buoyant energy. Finally, the coefficients generated during the routine operation of this product have been archived for study. It may be possible to identify specific sets of coefficients that have long-term applicability, thereby eliminating the necessity to perform regressions for each scene. This approach would make the product available much sooner since sounding production would not be a requirement for each image.

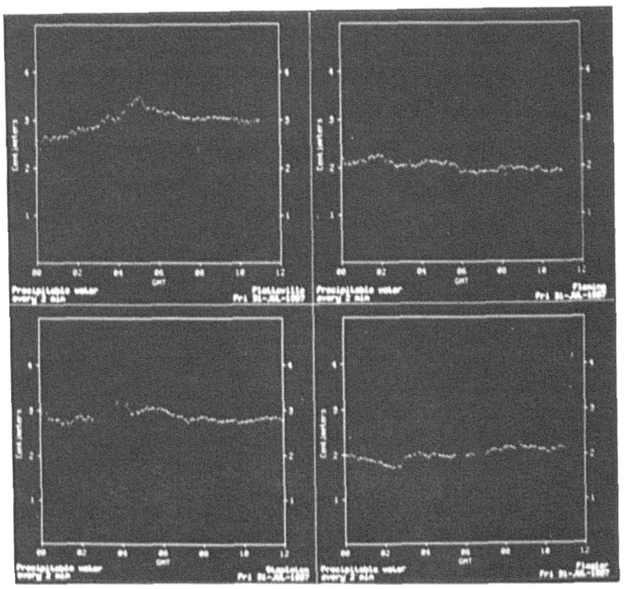

Fig. 4. A 12-hour time history plot of total precipitable water from 4 ground based, active microwave profilers. The two sites on the left, Stapleton and Platteville, are near the foothills. Flagler and Fleming show lower amounts of water vapor over the eastern plains of Colorado agreeing (in trend) with VAS imagery.

Since the product demonstrates an ability to detect mesoscale moisture features, it is a likely candidate to be used for small (local) scale analyses with grid spacing on the order of 10 to 30 km.

6. REFERENCES

Birkenheuer, D. and J. S. Snook, 1985: A revieiw of the VAS assessment during the 1985 PROFS summer exercise, NOAA Technical Memorandum, ERL ESG-19.

Chesters, D. C., L. W. Uccellini, and W. D. Robinson, 1983: Low-level water vapor fields from the VISSR Atomspheric Sounder (VAS) "split window" channels. J. Climate Appl. Meteor., 22, 725-743.

Robinson, W. D., D. Chesters, and L. W. Uccellini, 1986: Optimized retrievals of precipitable water fields from combinations of VAS satellite and conventional surface observations. J. of Geophysical Research, 91, 5305-5318.

Smith, W. L., 1983: The retrieval of atmospheric profiles from VAS geostationary radiance observation. J. Atmos. Sci., 40, 2025-2035.

Smith, W. L., G. W. Wade, and H. M. Wolf, 1985: Combined atmospheric sounding/cloud imagery - a new forecasting tool. Bull. Amer. Meteor. Soc., 66, 138-141.

An Extension of the Split Window Technique for the Retrieval of Precipitable Water: Experimental Verification

Thomas J. Kleespies
Air Force Geophysics Laboratory/LYS
Hanscom AFB, Bedford MA 01731

Larry M. McMillin
National Oceanic and Atmospheric Administration
National Environmental Satellite, Data, and Information Service
Washington D.C. 20233

1.0 Introduction

The "split window" technique was originally derived for the determination of surface skin temperature, specifically sea surface temperature (Anding and Kauth, 1969). The technique makes use of two differentially absorbing channels in the 11-12 μm region to remove the contaminating effect of water vapor and thus arrives at an improved estimate of the skin temperature. See McMillin and Crosby(1984) for a detailed discussion of the split window technique and an extensive review of the literature.

More recently the channels used for the split window have been applied to the retrieval of precipitable water (Chesters, et al, 1983, Chesters et al, 1987). Whereas these methods seemed to produce internally consistent fields of "low level water vapor", they required *a priori* knowledge of the mean air temperature and empirical adjustment of the absorption coefficients in order to bring the results in agreement with in situ observations.

In this paper we present the results of an extension to the split window technique such that precipitable water can be retrieved with a minimum of *a priori* information.

2.0 Theoretical Discussion

Kleespies and McMillin (1984,1986) have presented a theoretical discussion of this extension to the split window technique. Summarized briefly, this technique assumes that the upwelling longwave infrared radiance is emitted from a plane parallel, non scattering atmosphere in local thermodynamic equilibrium, and that the atmospheric contribution to the upwelling radiance can be described by an effective atmospheric temperature and transmittance. Then if observations are made in the two channels of the split window under two different conditions where the atmospheric contribution to the outgoing radiance is invariant but the surface contribution changes markedly, then a set of four simultaneous equations can be written and solved for the ratio of the transmittance in the split window (see Kleespies and McMillin (1986) for details). These conditions fall under two general categories; that of variation in time, and that of variation in space. Consecutive observations of a land surface from a geosynchronous satellite during the heating cycle of the day would be one example. Another would be observations from either a geosynchronous or polar orbiting satellite of immediately adjacent land and water surfaces with contrasting skin temperatures. The resultant relationship under these conditions is

$$\frac{\tau_{11}}{\tau_{12}} = \frac{T_{11}^{1} - T_{11}^{2}}{T_{12}^{1} - T_{12}^{2}} , \qquad (1)$$

where the superscripts refer to the different viewing conditions and the subscripts refer to the nominal 11 and 12μm channels of the split window. It has been shown that this ratio can be related to "low level water vapor" i.e., precipitable water (Chesters, et al, 1983).

Kleespies and McMillin (1984) discuss the theoretical application of this extension to the Visible Infrared Spin Scan Radiometer (VISSR) Atmospheric Sounder (VAS), and in their 1986 paper describe, again in theoretical terms, its application to Advanced Very High Resolution Radiometer (AVHRR) split IR window data. In ensuing sections, application of this technique to these two instruments is demonstrated with real data.

3.0 Application to Satellite Radiometer Data

The real test of a retrieval algorithm is to apply it to real data and to somehow verify it with ground truth. However this is fraught with difficulties, including cloud contamination, aerosol problems, collocation inaccuracies, and errors in the satellite instrument and the in situ measurements. In the following sections we apply this technique to measurements made with the VAS and the AVHRR. In all cases of comparison with radiosonde transmittance ratio, the transmittance ratio was computed from collocated radiosondes using the wide-band radiative transfer model described by Weinreb and Hill (1980).

3.1 Application to the VISSR Atmospheric Sounder

Observations were made with the VAS channels 7 and 8 (12.7 and 11.2 μm respectively) over North America on 25 August 1987. Multispectral imagery were acquired on the AFGL Interactive Meteorological System (AIMS) (Gustafson et al, 1987) at hourly intervals from 11:30 UT to 17:30 UT. This works out approximately from just before local sunrise in the mid-United States to just after local noon on the east coast. In order to achieve the contrasting surface contribution to the outgoing radiance, while minimizing the effects of surface obscuration due to convective cloudiness in the local late morning and early afternoon, a variety of time intervals were tested with the optimal interval subjectively selected to be from 1130-1530 UT. Typical brightness temperature increases due to diurnal heating of the surface during this interval were 5-10 K. Since the VAS oversamples along the scan line by a factor of 2:1 for band 8 and 4:1 for band 7, and the band 7 detector linear dimensions are twice that of band 8, a total of 6 pixels from band 7 were averaged to make one band 7 "retrieval spot" and 6 pixels from each of two lines of band 8 (a total of 12 pixels) were averaged to make one band 8 "retrieval spot". If the average brightness temperature in either channel were less than 273 K at either of the two times, the retrieval spot was assumed to be cloudy and was discarded. Furthermore, if the standard deviation of the brightness temperatures that went in to making the retrieval spot were greater than about 1.5 K for either time, the spot was assumed to be partly cloudy and was discarded.

The transmission ratio was computed for each non-discarded retrieval spot using Eq. (1). Examination of pseudo-imagery of this transmission ratio revealed that while interesting mesoscale features were apparent in this imagery, further spatial averaging was required before quantitative comparisons could be attempted.

Collocations were performed on launch sites of the 1200 UT radiosondes on 25 Aug 1987. Statistics were computed on the non-discarded transmittance ratios from a 9x9 box of transmittance ratios centered on the radiosonde site. Those transmittances outside of one standard deviation from the mean of the ratios were discarded and the mean was recomputed. This filtered mean was compared with the radiosonde only if the the resulting number of retrieval spots exceeded ten. The comparison between the transmittance ratio derived from the VAS and that derived from the radiosonde is presented in Figure 1.

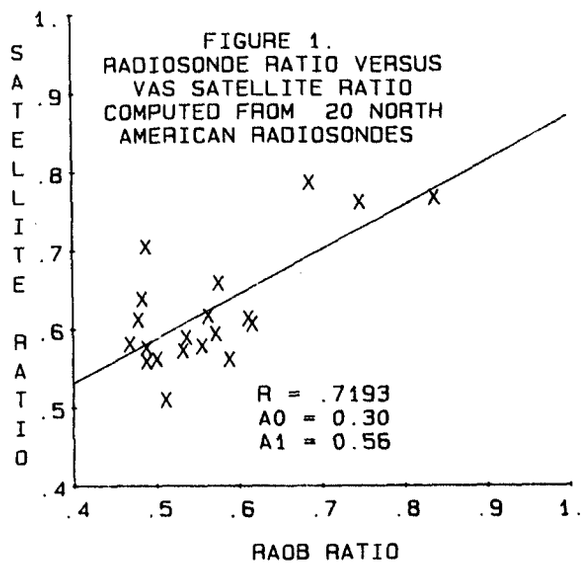

Precipitable water was computed from the mean ratio by adapting the method of Chesters et al (1987) to this problem

$$PW = 1/\Delta\alpha \left\{ 1/sec\ \theta \ \ln[\tau_{11}/\tau_{12}] - \Delta\kappa \right\} \qquad 2)$$

where $\Delta\kappa = 0.051$ and $\Delta\alpha = .136$ are differential absorption coefficients, θ is the local zenith angle and the τ's are the transmittances. The comparison between the precipitable water derived from Eq. (2) and the radiosonde precipitable water is given in Figure 2.

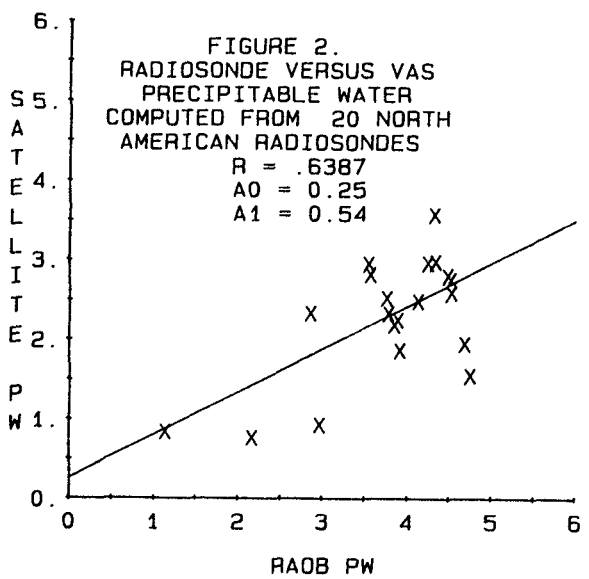

3.2 Application to the AVHRR

Global Area Coverage (GAC) data from the AVHRR were collected from NOAA-7 for 11 June 1982. GAC data has a nominal resolution of 4 km and is distinguished from the nominal AVHRR sensor 1 km resolution by the fact that four pixels are averaged along scan and four scans are skipped to make a GAC scan line. Bands 4 and 5 have the nominal wavelength of 10.7 and 11.8 μm respectively which correspond only approximately to those of the VAS (see Fig. 3). Nighttime data over North America was used in order to be as close as possible to radiosonde launch time and in order to avoid convective cloudiness. The orbits were from four hours to one hour prior to synoptic time. Cloud free areas were selected at the AIMS workstation by examining 24-bit multispectral imagery created from AVHRR bands 3, 4 and 5 (d'Entremont and Thomason, 1987). In this imagery opaque clouds appear white, low clouds and fog appear bright red against a brown background, and thin cirrus appears cyan, yielding a fairly unambiguous rendition of clear/cloudy regions. Contrasting surface temperatures were determined by selecting a body of water (lake, river, coastline) which at nighttime was relatively warm compared to the surrounding countryside. A 3×3 array of GAC spots were selected for both the warm water surface and the cooler countryside surrounding it. Since many of these water surfaces did not fill the 3×3 array of GAC pixels, a method was developed to determine the "best" combination of warm and cold brightness temperatures. Typical brightness temperature differences were about 5 K. A comparison of two ensembles of 3×3 arrays yields 81 possible combinations. The brightness temperature differences between these 81 combinations were sorted for each of the two channels. The sum of the rank order of the pixel pairs between the two scenes and the two channels was used as a quality measure, the idea being to maximize the brightness temperature difference between the warm and the cold scenes for both channels. Since there is a danger that sub-pixel cloudiness in one scene but not the other which would contribute to an excessively high quality measure, the transmission ratios computed from Eq. (1) were averaged for the top 10 quality measures.

The method presented by Chesters (1983) for computing precipitable water from transmission ratio applies only to the VAS instrument. Whereas it can be adapted to the AVHRR, time limitations for publication in these preprints allow only an indirect comparison with in situ measurements. Rather than compare the radiosonde precipitable water with AVHRR precipitable water using an untested relationship between precipitable water and transmission ratio, it was deemed most prudent to compare directly between the satellite and the radiosonde transmission ratios.

Radiosondes from 1200 UT on 11 June 1982 over North America were collected from the AFGL McIDAS upper air archive. Collocations were made to the closest radiosonde within 300 km of the satellite observation. The comparison between the modeled transmittance ratio and that computed from Eq. (1) for the AVHRR is given in Fig. 4.

FIGURE 3.
RELATIVE INSTRUMENT RESPONSE
FOR VAS AND AVHRR
SPLIT WINDOW CHANNELS

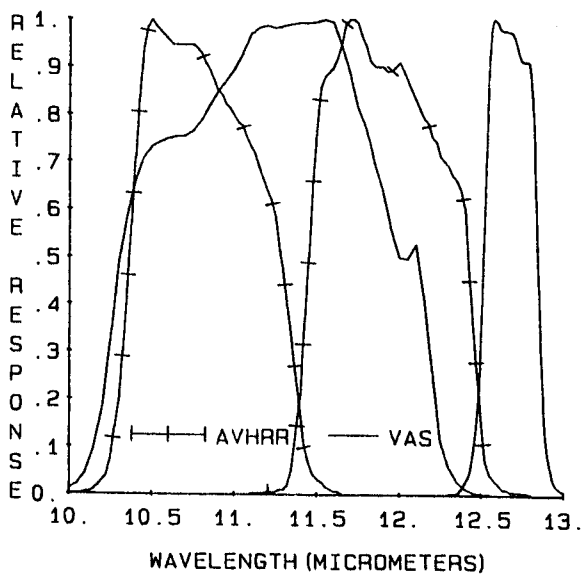

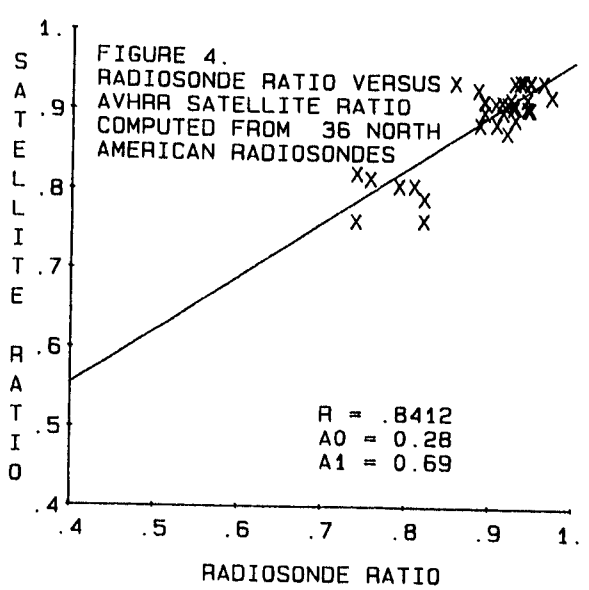

4.0 Discussion

The correlation between the VAS transmittance ratio and that computed from collocated radiosondes is about 0.72 . The correlation between the AVHRR ratio and the radiosonde ratio is an even more respectable 0.84 . The precipitable water computed from the VAS transmittance ratio had a correlation coefficient of about 0.64 when compared with the radiosonde precipitable water. Chesters et al (1983) reported a lesser correlation with their initial study, (r=0.43), even though they used ancillary information in the form of the atmospheric temperature averaged over a number of radiosonde sites. In their 1987 paper they substantially improved on this figure by using empirical adjustments to the absorption coefficients and by modifying the atmospheric temperature used in their algorithm. The method presented here requires no ancillary information. However, examination of Figures 1, 2 and 4 indicate that the line of best fit in each figure does not have a zero intercept or a slope of unity. It is clear that empirical adjustments are warrented to help remove the systematic bias which is evident in these figures.

Perhaps the greatest uncertainty in retrieving precipitable water from satellite observations lies in determination of the atmospheric absorption coefficients for these channels. Since these channels are quite broad and water vapor is a significant absorber in this region (the water vapor continuum is poorly characterized), absorption uncertainties dominate errors in the retrieval process. The focus of Chesters et al (1987) is the empirical adjustment of the absorption coefficients to optimize the precipitable water retrievals. Barton (1985) reports similar problems with his sea surface temperature determination.

Another major source of concern in application of this technique has to do with instrument noise. Since Eq. (1) deals with the ratio of a difference in the brightness temperatures, this method is quite sensitive to errors in the measurements. The VAS has a nominal NEΔT of 0.25 for these channels. The AVHRR has a NEΔT of 0.12 for its split window channels. Just on this figure of merit, the AVHRR would seem to be better suited for this purpose since a smaller brightness temperature difference would be required for Eq. (1) in order to minimize the effect of instrumental noise. However, it is much easier to

obtain the desired change in scene brightness temperature by observing diurnal temperature changes from geosynchronous orbit than searching for contrasting skin temperatures from polar orbit.

There is a further problem with the VAS instrument. We have noticed "streaking" in the band 7 imagery. Analysis of these streaks indicate that the brightness temperature from scan line to scan line can jump by as much as ± 4 deg K compared to surrounding scan lines. Menzel (1987, private communication) indicates that one of the two large HgCdTe detectors on the VAS instrument is not well calibrated, but it is not known which. This type of calibration problem will probably preclude operational use of the algorithm presented in this paper. However, the imager to be flown on GOES NEXT is very similar to the AVHRR, with planned NEΔT even better than the present AVHRR (Koenig, 1987). It is anticipated that with the launch of GOES NEXT, a thorough evaluation of this method can be made.

5.0 Acknowledgements

The authors wish to thank Mssrs. Mike Weinreb and Mike Hill of NOAA/NESDIS for providing the radiative transfer code used in this study, and Dr. Dennis Chesters for providing a pre-publication copy of his 1987 article. The authors also express their appreciation to Mr. Robert d'Entremont of AFGL Satellite Meteorology Branch for his assistance with the AVHRR GAC data.

6.0 References

Anding, D., and R. Kauff, Atmospheric Modeling in the Infrared Spectral Region: Atmospheric Effects on Multispectral Sensing of Sea Surface Temperature from Space, *Rep 2676-1-P, Willow Run Lab., Inst. Sci. Technol.*, Univ. Mich. Ann Arbor, Mich., 1969.

Barton, I. J., 1985: Transmission Model and Ground-Truth Investigation of Satellite-Derived Sea Surface Temperatures, *J. Clim. Appl. Met.*, Vol. 24, pp. 508-516.

Chesters, Dennis, Louis W. Uccellini and Wayne D. Robinson, 1983: Low Level Water Vapor Fields from the VISSR Atmospheric Sounder (VAS) "Split window" Channels. *J. Clim. Appl. Met.*, Vol 22, No. 5. pp 725-743.

Chesters, Dennis, Wayne D. Robinson and Louis W. Uccellini, 1987: A Note on Optimized Retrievals of Precipitable Water from the VAS "Split Window", *J. Clim. Appl. Met.*, Vol 26, No. 8. pp 1059-1066.

d'Entremont, Robert P. and Larry W. Thomason, 1987: Interpreting Meteorological Satellite Images Using a Color-Composite Technique, *Bull. Am. Met Soc.*, Vol 68, No.7, pp762-768.

Gustafson, G., D. Roberts, C. Ivaldi, R. Schechter, T. Kleespies, K. Hardy, R. d'Entremont, G. Felde and R. Lynch, 1987, The AFGL Interactive Meteorological System, *Preprints, Third International Conference of Interactive Information and Processing Systems for Meteorology, Oceanography, and Hydrology,* 12-16 January 1987, New Orleans, LA.

Kleespies, Thomas J. and Larry M. McMillin, 1984: Physical Retrieval of Precipitable Water Using the Split Window Technique, *Preprints, Conference on Satellite Meteorology/ Remote Sensing and Applications,* Clearwater Beach FL, Am. Met. Soc.

Kleespies, Thomas J. and Larry M. McMillin, 1986: An Extension of the Split Window Technique for the Retrieval of Precipitable Water. *Preprints, Second Conference of Satellite Meteorology/ Remote Sensing and Applications,* Williamsburg VA., Am. Met. Soc.

Koenig, E. W., 1987: GOES I Series Imager and Sounder, ITT Aerospace/Optical Division, 11pp.

McMillin, L. M. and D.S. Crosby, 1984: Theory and Validation of the Multiple Window Sea Surface Temperature Technique, *J. Geoph. Rsch.* Vol 89, No. C3, pp 3655-3661.

Weinreb, Michael P. and Michael L. Hill, 1980: Calculation of Atmospheric Radiance and Brightness Temperatures in Infrared Window Channels of Satellite Radiometers, *NOAA Technical Report NESS 80*, 40 pp.

2.8

DETERMINATION OF LOW-LEVEL PRECIPITABLE WATER VARIABILITY FROM SPLIT WINDOW CHANNEL RADIANCE DATA

Gary J. Jedlovec

NASA-Marshall Space Flight Center
Earth Science and Applications Division
Remote Sensing Branch, ED43
Huntsville, Alabama 35812

1.0 INTRODUCTION

The retrieval of moisture profiles from satellites has steadily improved since the first sounder back in the 1970's. This improvement in retrieval accuracy has been due to the refinement mathematical techniques and better instrumentation. Case study investigations and operational usage of these techniques have yielded improved understanding of atmospheric moisture variability (e.g., Hillger and Vonder Haar, 1981). Physical limitations on the vertical resolution and coarse spacing of moisture retrievals, even with the VISSR Atmospheric Sounder (VAS), have forced the use of imagery itself to infer moisture variations (Smith *et al*, 1985; Chesters *et al*, 1983; Robinson *et al*, 1986). While these products help investigate mesoscale moisture variability, they do not provide the resolution needed for many mesoscale studies.

Some studies have indicated that the natural variability and structure of atmosheric moisture and its associated environmental processes may not be well observed with conventional ground based and satellite measurements. Fuelberg *et al.* (1986), Barnes and Lilly (1975), and Gandin (1963) have indicated that the variation in atmospheric moisture is large on the lower end of the mesoscale (features with wavelengths of a few tens of kilometers). Phenomena at this scale are not currently diagnosed operationally with satellite remote sensing techniques. Jedlovec (1987), Menzel *et al.* (1986), and Jedlovec *et al.* (1986a), using high resolution aircraft radiometer data, have shown that mesoscale moisture variability exists at fine scales in both the middle and lower troposphere. This paper aims to document the capability of high resolution infrared radiance data to detect mesoscale moisture variability and to show the application of a new technique to describe mesoscale moisture variability from these measurements. Application of the technique to current and future satellite sensors is discussed.

2.0 BACKGROUND

2.1 The Multispectral Atmospheric Mapping Sensor (MAMS)

The data used in this research to derive high resolution moisture data is from the airborne Multispectral Atmospheric Mapping Sensor (MAMS) (Jedlovec *et al.*, 1986b). The MAMS is a multispectral scanner which measures reflected radiation from the earth's surface and clouds in eight visible bands and thermal emission from the earth's surface, clouds, and atmospheric water vapor in three infrared bands. From a high altitude aircraft flying at 20 km, the horizontal ground resolution of each field-of-view from MAMS is 100 m (Fig. 1). From this altitude, the width of the entire cross path field-of-view scanned by

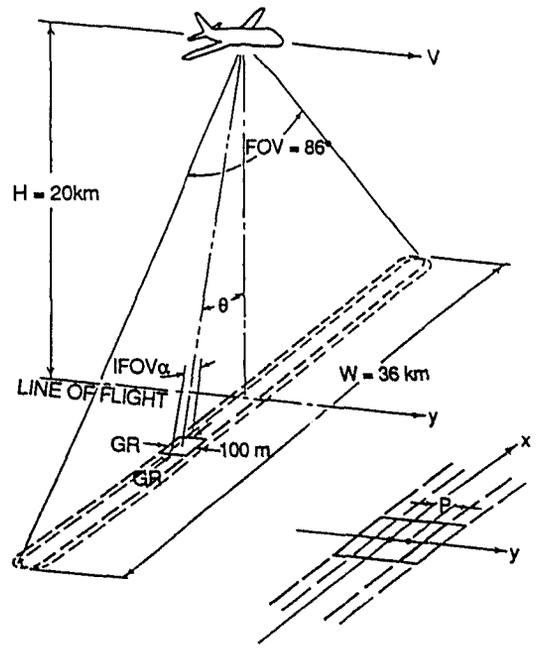

Figure 1. MAMS scan geometry from a high altitude aircraft platform.

the sensor is roughly 36 km, thereby providing detailed resolution over an area of considerable size.

The infrared channels from MAMS are similar to those from the AVHRR and VAS sensors on the existing weather satellites. Spectral response functions for these instruments in the pertainent channels are displayed in Fig. 2. The 11 micrometer channel of MAMS and VAS are similar while that of the AVHRR is narrower and shifted towards shorter wavelengths. The 12 micrometer channel of AVHRR is positioned near 11.8 micrometers with a band width about twice that of MAMS and VAS (and are positioned at longer wavelengths). These latter channels measure upwelling radiation where absorption by atmospheric water vapor is more significant. Further information about MAMS, including calibration techniques, can be found in Jedlovec *et al.* (1986b).

2.2 The split window channels

The 11 and 12 micrometer bands on these instruments make up what is referred to as the "split window" channels. While the 11 micrometer region of the spectrum is relatively transparent, increasing moisture absorption occurs at longer wavelengths. Thus, the 12 micrometer channels on AVHRR, MAMS, and VAS represent the increasing effects of low-level atmospheric water vapor. Table 1 indicates this effect by displaying the split window channel brightness temperature differences ($TBB_{11} - TBB_{12}$) for representative profiles. For the moist profile (39.6mm of precipitable water), the MAMS and VAS show large differences due to the increased absorption at longer wavelengths. The small split window difference for AVHRR occurs because of a shift of the 12 micrometer channel away from the strong absorption. The split window differences are reduced for drier conditions. Data from these channels have been used to derive low-level moisture information as discussed below.

Table 1

Split window channel brightness temperature differences for MAMS, VAS, and AVHRR. Units are degrees Kelvin.

	warm/moist pw = 39.6mm	warm/dry pw = 26.0mm
MAMS	9.8	8.3
VAS	10.2	8.1
AVHRR	2.8	0.9

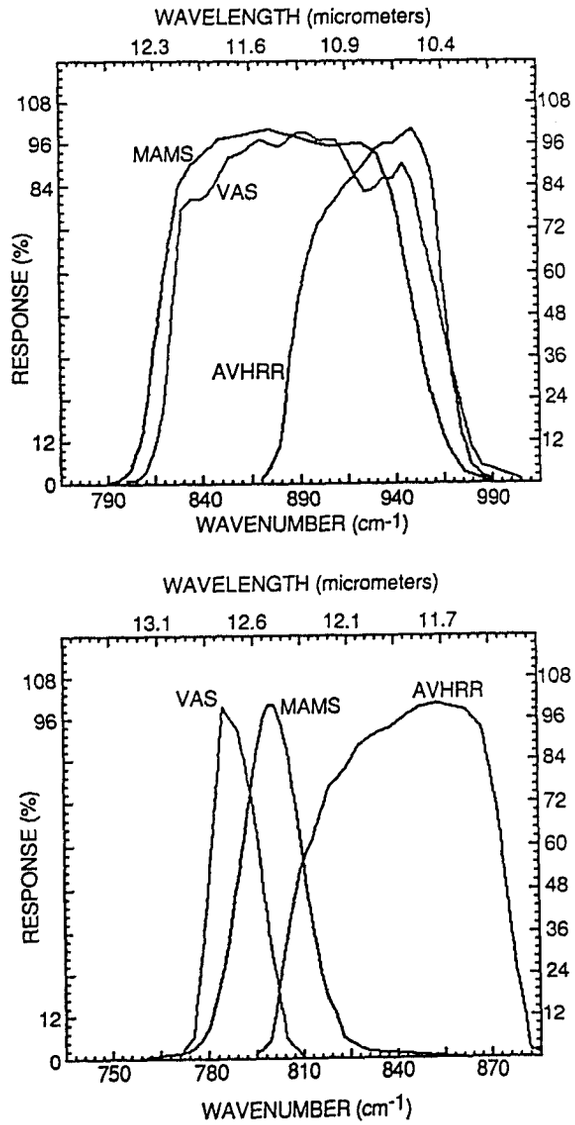

Figure 2. Spectral response functions for the MAMS, VAS, and AVHRR split window bands.

2.3 Past methods for precipitable water determination

Several techniques have been proposed to derive precipitable water estimates from split window imagery. Kleespies and McMillin (1984; 1986) discuss a method and apply it to simulated VAS and AVHRR radiance data. Their technique involves estimating atmospheric transmittance from split window measurements under varying surface "skin" (radiating) temperature conditions. The estimates are based on the ratio of split window channel brightness temperature differences. It is assumed that the atmospheric conditions are invariant for adjacent regions or over a short time interval (during which the skin

temperature changes and brightness temperature differences are calculated). The estimates are related to precipitable water by regression. Application of this technique to real data was not presented.

Chesters *et al.* (1983) and Robinson *et al.* (1986) have developed a technique to derive precipitable water data from VAS split window channel radiance measurements. Their technique parameterizes the channel transmittances using average absorption coefficients and observed brightness temperatures in a single layer radiative transfer model. Local soundings are used to develop the coefficients for the model. An advantage of this technique lies in the ability to derive precipitable water vapor imagery at a high temporal resolution from VAS. Adjacent measurements are averaged to reduce noise but the method retains sufficient horizontal resolution to describe larger mesoscale moisture variability. The weakness of the scheme lies in the need to formulate a radiating temperature of the atmosphere in their model which is derived from conventional rawinsonde data.

Another approach taken to produce precipitable water vapor imagery uses all twelve channels of VAS in a full retrieval procedure (Smith *et al.*, 1985). A simulataneous physical inversion is used to produce a set of coefficients based on a spatial average of VAS radiance data. These coefficients are then applied to individual fields-of-view in order to produce single pixel soundings. Precipitable water is calculated from these soundings using conventional methods. Although single pixel precipitable water data is produced, these values depend on retrieval coefficients derived on the larger mesoscale. Thus, only larger scale features (wavelengths greater than 100km) seem resolvable.

3.0 APPROACH

3.1 Split Window Variance Ratio

The technique used in this study to derive precipitable water estimates takes advantage of the fine spatial resolution of MAMS to derive precipitable water estimates. The "Split Window Variance Ratio" (SWVR) technique is an extension of the concepts put forth by Kleespies and McMillin (1984; 1986). They have shown that split window channel transmittances (τ_{11}/τ_{12}) can be related to the channel brightness temperature differences (ΔTbb) by

$$\frac{\tau_1}{\tau_2}=\frac{\Delta T_1}{\Delta T_2}. \qquad (1)$$

where the imply a difference in observed brightness temperatures due only to changing skin temperature. The subscripts denote the 11 and 12 micrometer split window channels, respectivily. Re-writing (1) as

$$\tau_2 \Delta T_{b1}=\tau_1 \Delta T_{b2} \qquad (2)$$

squaring both sides of (2), and taking the sum over adjacent ifov's, (2) becomes

$$\frac{\Sigma \tau_2^2 \delta T_{b1}^2}{N}=\frac{\Sigma \tau_1^2 \delta T_{b2}^2}{N} \qquad (3)$$

where N is the number of adjacent cloud-free ifovs used to calculate the variance. Assuming that atmospheric transmittance does not vary over neighboring points, it can be remove from the summation. If ΔTbb represents the difference between each individual ifov and the spatial mean (Tbb), then

$$\frac{\Sigma \delta T_b^2}{N}=\sigma^2, \qquad (4)$$

where σ^2 is the sample variance. Substituting (4) into (3) yields an expression for the square of the split window transmittance ratio as a function of the observed brightness temperature variance ratio

$$\frac{\tau_2^2}{\tau_1^2}=\frac{\sigma_2^2}{\sigma_1^2}. \qquad (5)$$

To correct this expression for random noise, the estimated error variance for MAMS (Menzel *et al.*, 1986) is subtracted from the scene calculated value and is given by

$$\frac{\tau_2^2}{\tau_1^2}=\frac{\sigma_2^2-\sigma_{\epsilon_2}^2}{\sigma_1^2-\sigma_{\epsilon_1}^2}. \qquad (6)$$

This equation can be applied to MAMS or any other split window channel data to produce relative horizontal variations in precipitable water. For MAMS, the mean used to compute the variance in (4) can be calculated over a large number of points and still provide high spatial resolution.

3.2 Relation of transmittance ratio to precipitable water

The ratio of the square of the split window transmittances, either simulated or estimated, provide a relative measure of column precipitable water. Thus, a spatial distribution of the split window channel variance ratio gives an estimate of the relative horizontal variability in precipitable water. In order to quantify this variability, it is necessary to form a relationship between column precipitable water and the square of the estimated transmittance ratio (i.e., the variance ratio). Kleespies and McMillin (1986), using rawinsonde data, have shown that the

simulated AVHRR split window transmittance ratio is nicely related to the total precipitable water. Likewise, total precipitable water can be related to the MAMS estimated square transmittance ratio via linear regression. Figure 3 presents the square transmittance ratio plotted as a function of precipitable water for 19 June 1986 rawinsonde data. Channel transmittances were simultated using the MAMS spectral response functions (Fig. 2) and the appropriate transmittance profiles (McMillin and Fleming, 1976). While extremely dry values were not measured in the rawinsonde data, the observations are representitive of the precipitable water variability of a summertime convective environment.

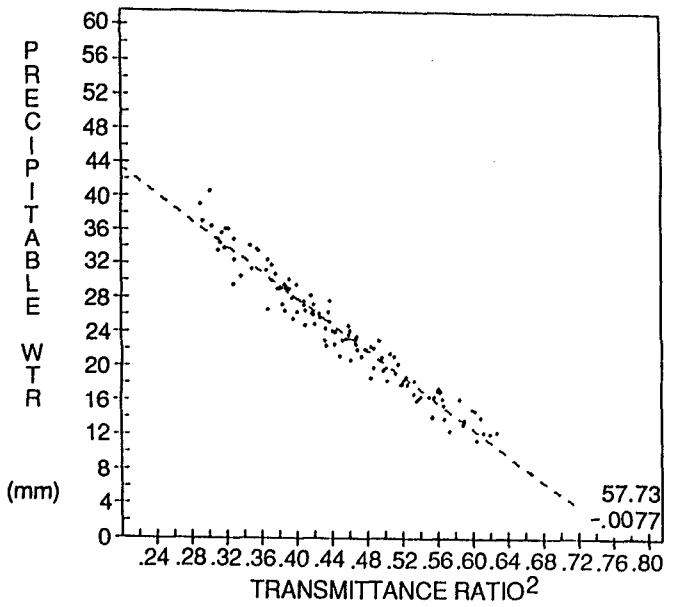

Figure 3. Precipitable water versus the square of the transmittance ratio for 19 June 1986 rawinsonde data.

3.3 Application of SWVR technique

The application of this technique to observed data is quite simple. At each image point, a search area or template is employed over which the mean channel brightness temperature and channel variance is calculated. Error variances are applied and the ratio of the split window channel values is made as in (6). Data checking procedures and cloud filtering are performed for each template area. Cloud filtering is based on a simple infrared threshold. Threshold values are subjectively determined for each image based upon MAMS visible and infrared data.

The choice of a template size is somewhat arbitrary. As shown in Fig. 4, the calculated image variance increases in

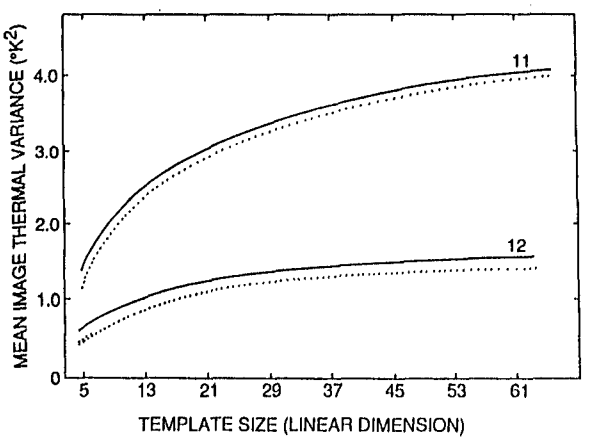

Figure 4. Split window channel image variance as a function of template dimension.

---

the MAMS split window channels as the template size increases. The increase slows beyond about the 27 x 27 size as computer CPU time steadly increases (not shown). A tradeoff between template size (spatial resolution) and computer time (practical efficiency) is necessary.

4.0 EVALUATION OF TECHNIQUE

To evaluate the performance of the SWVR technique, the method was applied to MAMS data on 19 June 1986. A visible image (channel 7) from MAMS over northeastern Alabama, just southwest of Chattanooga, Tennessee, is presented in Fig. 5. Clouds are represented as bright white with land and water features significantly darker in tone. Spatial resolution of each picture element (pixel) is about 100m. Image variances where calculated from the split window channel brightness temperatures using a 37 x 37 square template. The variance values were ratioed on a pixel by pixel basis, calibrated using data from Fig. 3, and assigned an 8 bit value based on their precipitable water amount. The resulting image is displayed in Fig. 6. Cloudy regions remain as white features in this image while values of precipitable water increase from dark to light. Regions with little or no 11 micrometer channel variance are also denoted with white. The black graphics display the county outline.

Several interesting features are noticeable in Fig. 6. First, precipitable water vapor variations are observed throughout the image at scales larger than the template size. Values range from 24 to 37mm of precipitable water. Second, there is a tendency for higher (brighter values) to appear towards the edges of the image. This is expected since the increased scan angle away from nadir

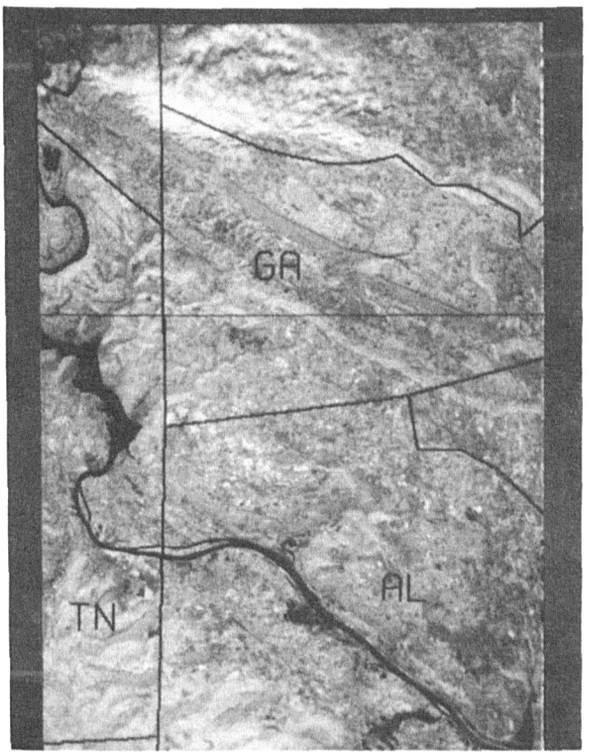

Figure 5. MAMS visible channel image for a region southwest of Chattanooga, Tennessee.

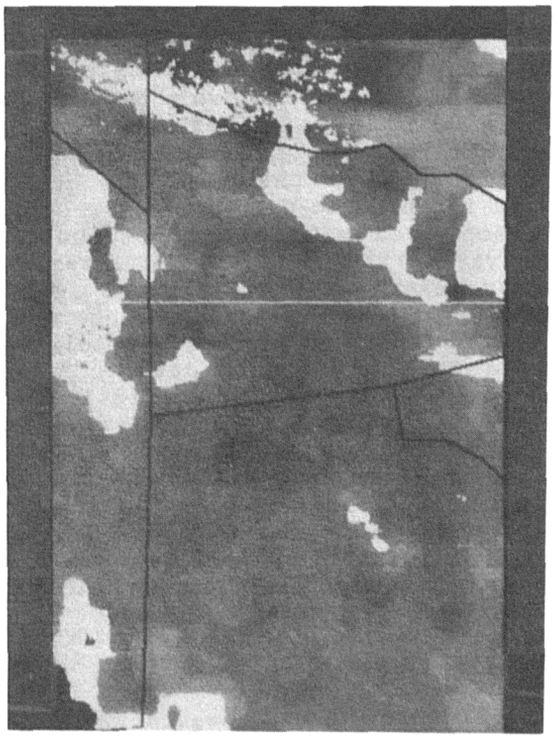

Figure 6. MAMS derived precipitable water vapor image for the scene displayed in Fig. 5.

provides an increased water vapor path length. This result in itself shows that the SWVR technique can discern changes in "line of sight" values of precipitable water.

In order to further investigate the accuracy and sensitivity of measurements and retrieval method to determining precipitable water vapor variations, the change in values with scan angle were further considered. Table 2 presents angle averaged variance ratio values for the data in Fig. 6. This shows that the variance ratio decreases (moisture increases) with increasing scan angle. There also seems to be a natural gradient superposed on this angle effect. From a special rawinsonde observation for Athens, Alabama at 1415 GMT, precipitable water was determined to be 28.5mm. Using the secant of the scan angle to simulate the MAMS viewing geometry, an increase in precipitable water of about 20% (5.7 mm) occur out on the edge of the MAMS scan. Thus for a variance ratio change of .039, an increse of 5.7mm in precipitable water occur should occur. This ratio change (.0069/mm) is similar to the slope of the calibration curve presented in Fig. 3. Therefore, these observations confirm the results from the simulated transmittances. It also indicates the sensitivity of the technique to small changes in precipitable water. Further evidence and applications of this technique will be presented at the conference.

5.0 DISCUSSION

The above example indicates that split window channel radiance measurements can be used to quantitatively define low-level precipitable water variability. The SWVR technique is useful for mesoscale investigations when high spatial resolution measurements are available. The technique is perfectly applicable to AVHRR and VAS split window channel radiances. Although the 12 micrometer channel of AVHRR is not as sensitive to atmospheric moisture, its relatively high spatial resolution (1 km at nadir) and excellant data quality (NEdT value of 0.1°K with 10 bit data) should provide a good data base for the application of the technique. The VAS, on the other hand, is much more sensitive to atmospheric moisture at 12 micrometers than MAMS or AVHRR (Table 1) but suffers in spatial resolution and data quality (see Menzel *et al* (1986) for comparison of data quality from these instruments in the split window channels). Although the channel error variance is explicity considered in the technique (equation (6)), it is handled only in a statistical sense. Infrequent but large data errors are not fully accounted for in this application.

6.0 SUMMARY

A technique has been described and demonstrated to quantitatively define low-level precipitable water vapor from radiance measurements. High resolution measurements from the airborne Multispectral Atmospheric Mapping Sensor (MAMS) have been used with this technique to define variability down to the lower end of the mesoscale. The technique is applicable to existing satellite sensors but will not provide the mesoscale resolution provided by the aircraft data. Future satellite instrumentation should include split window channel measurement capabilities with very high spatial resolution. This will not only allow for a better delineation of clouds and surface features, but with the addition of mid-tropospheric water vapor channels, will allow for better atmospheric moisture investigations at the mesoscale.

Acknowledgements

Portions of this research were performed while the author was affiliated with several organizations. Support by the Universities Space Research Association (USRA), the Cooperative Institute for Meteorological Satellite Studies (CIMSS) at the University of Wisconsin-Madison, and NASA's Cooperative Education Program at Marshall Space Flight Center is appreciated.

References

Barnes, S. L., and D. K. Lilly, 1975: Covariance analysis of severe storm environments. Preprints Ninth Conference on Severe Local Storms, AMS, Boston, 301-306.

Chesters, D., L. W. Uccellini, and W. B. Robinson, 1983: Low-level water vapor fields from the VISSR Atmospheric Sounder (VAS) "split window" channels. *J. Climo. Appl. Meteor.*, *22*, 725-743.

Fuelberg, H. E., Y. Lin, and H. Chang, 1986: A moisture analysis of the meso-β-scale thunderstorm environment during AVE-SESAME V (20-21 May 1979). *Mon. Wea. Rev.*, *114*, 534-545.

Gandin, L. S., 1963: Objective analysis of meteorological fields. Translated from Russian. Isreal Program for Scientific Translations, 1965, 242pp, (available NTIS TT-65-50007).

Hillger, D. W., and T. H. Vonder Haar, 1981: Retrieval and use of high-resolution moisture and stability fields from Nimbus 6 HIRS radiances in pre-convective situations. *Mon. Wea. Rev.*, *109*, 1788-1806.

Jedlovec, G. J., 1987: Determination of atmospheric moisture structure from high resolution MAMS radiance data. Ph.D. Disertation, University of Wisconsin-Madison, (available University Microfilms International, P.O. Box 1764, Ann Arbor, MI 48106), 173pg.

Jedlovec, G. J., W. P. Menzel, G. S. Wilson, and R. J. Atkinson, 1986a: Detection of mountain induced mesoscale wave structures with high resolution moisture imagery. Second Conference on Satellite Meteorology/Remote Sensing and Applications, AMS, Boston, 365-369.

Jedlovec, G. J., W. P. Menzel, R. J. Atkinson, and G. S. Wilson, 1986b: The Multispectral Atmospheric Mapping Sensor (MAMS): Instrument Description, Calibration, and Data Quality. NASA TM-86565, Marshall Space Flight Center, Huntsville, Alabama, 37 pg.

Jedlovec, G. J., 1985: An evaluation and comparison of vertical profile data from the VISSR Atmospheric Sounder (VAS). *J. Atmos. Ocean. Tech.*, *2*, 559-581.

Kleespies, T. J., and L. M. McMillin, 1986: An extension of the split window technique for the retrieval of precipitable water. Preprints Second Conf. on Satellite Meteorology/Remote Sensing and Applications, AMS, Boston, 42-45.

Kleespies, T. J., and L. M. McMillin, 1984: Physical retrieval of precipitable water using the split window technique. Preprints Conf. on Satellite Meteorology/Remote Sensing and Applications, AMS, Boston, 55-57.

McMillin, L. M., and H. E. Fleming, 1976: Atmospheric transmittance of an absorbing gas: A computationally fast and accurate transmittance model for absorbing gases with constant mixing ratios in inhomogeneous atmospheres. *Appl. Opt.*, *15*, 358-363.

Menzel, W. P., G. J. Jedlovec, and G. S. Wilson, 1986: Verification of small scale features in VAS imagery using high resolution MAMS imagery. Second Conference on Satellite Meteorology/Remote Sensing and Applications, AMS, Boston, 108-111.

Robinson, W. D., D. Chesters, and L. Uccellini, 1986: Optimized retrievals of precipitable water fields from combinations of VAS satellite and conventional surface observations. *J. Geophy. Res.*, *91*, 5305-5318.

Smith, W. L., G. S. Wade, and H. M. Woolf, 1985: Combined atmospheric sounding/cloud imagery -- A new forecast tool. *Bull. Amer. Meteor. Soc.*, *66*, 138-141.

Table 2

MAMS observed brightness temperature variance ratio averaged over different scan angles.

SCAN ANGLE								
-35	-30	-20	-10	0	10	20	30	35
.296	.294	.315	.322	.335	.324	.321	.311	.304

REMOTE SENSING OF SURFACE AIR TEMPERATURE AND HUMIDITY OVER OCEANIC AREAS WITH APPLICATION TO CLIMATOLOGY AND WEATHER PREDICTION

Louis Garand

Recherche en prévision numérique (RPN)
Atmospheric Environment Service, Dorval, Québec, CANADA H9P 1J3

1. INTRODUCTION

This paper investigates the potential of cloud classification as a basis of remote sensing or surface air temperature and humidity over oceans. The basic assumption is that to a given class may be associated a significant systematic deviation of the variable from climatology. Dew point depression is used as humidity variable.

Garand (1986, 1988) has presented an automated procedure to classify cloud fields in twenty classes. This is the main tool to be used in this study, along with collocated observations of air temperature and humidity obtained from ships and buoys. The names of the classes are listed in Table 1. A major asset of the classifier is its capability to recognize mesoscale cellular patterns (MCC, classes 7 to 10) known to be often associated with large negative (cold) temperature anomalies. We also hope to get from the classification classes where the surface humidity is particularly dry, or moist. The reader is referred to Garand et al. (1988) for a detailed version of this paper.

Table 1. List of the cloud classes

1. Clear
2. Stratus
3. Scattered cumulus
4. Broken cumulus
5. Scattered stratocumulus
6. Broken stratocumulus
7. Cloud streets
8. Rolls
9. Polygonal open cells
10. Strongly convective open cells
11. Bright closed cells
12. Nimbostratus
13. Altocumulus
14. Altocumulus with cumulus
15. Altocumulus with stratocumulus
16. Thin cirrus
17. Multilayers with cirrus
18. Multilayers with cumulonimbus
19. Dense cirrostratus
20. Overcast cumulonimbus

2. CLIMATOLOGY

The region of interest is between 25-50 N and 55-80 W. We studied the winter season. Marine data for January-February 1984 and January to March 1986 were used to get climatological maps. The raw fields, obtained from 91235 observations of temperature and 42250 observations of dew point depression, were smoothed by applying two passes of median filtering. We show in Fig. 1 the mean temperature, $\overline{T}$, and the standard deviation of the observations about that mean, S(T). Fig. 2 shows the similar maps for dew point depression, $\overline{DD} = \overline{T - TD}$, and for S(DD). These maps are devided from data at all hours. For application at 18 GMT, the time of satellite observations, we found that a positive bias of 0.8 K should be added to the temperature map of Fig. 1 a.

3. SATELLITE IMAGES

Over the domain of interest, we had almost all images at 18 GMT for January and February 1984. The cloud fields were classified at the scale of 128 x 128 km. The center of the cloud fields and the surface observations were collocated with accuracy better than 10 km.

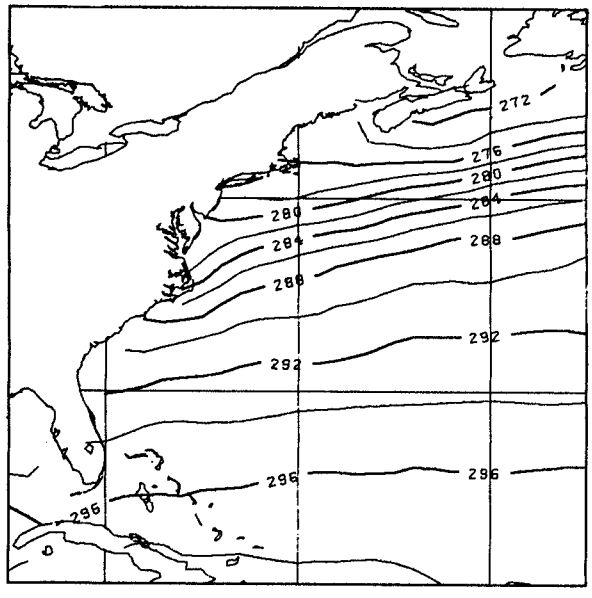

a) $\overline{T}$

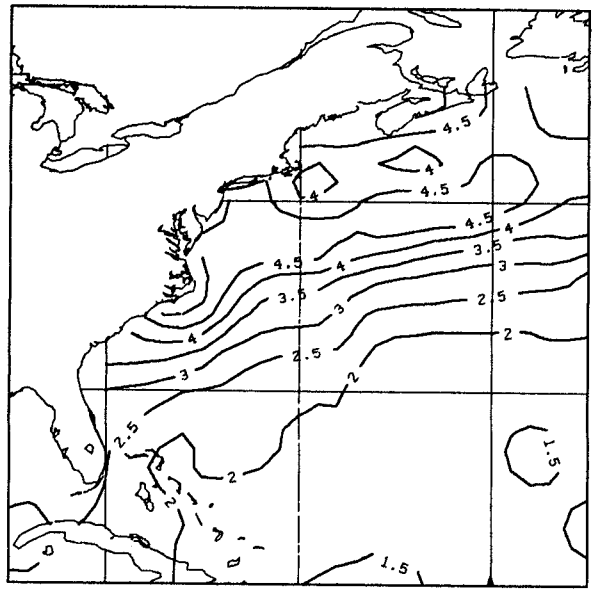

b) S(T)

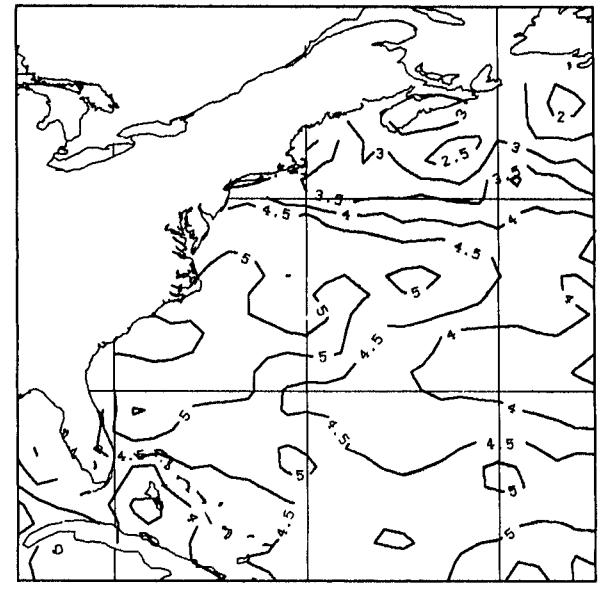

a) $\overline{DD}$

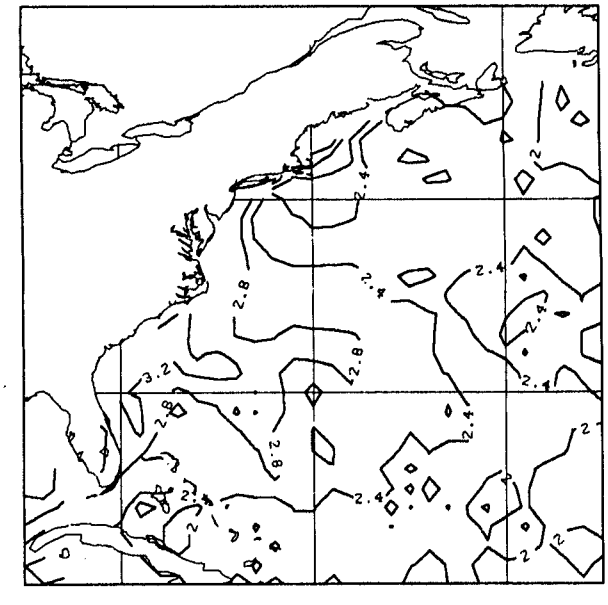

b) S(DD)

Fig. 1 a) Mean air temperature (K) in winter;

b) Natural standard deviation (K) of air temperature about the local mean.

Fig. 2 a) Mean dew point depression (K) in winter;

b) Natural standard deviation of dew point depression (K) about the local mean.

4. RESULTS

Using the subscript r to indicate a retrieval and c to indicate the local climatology, the retrievals are simply of the form:

$$T_r = aT_c + b \quad (1)$$

$$DD_r = DD_c + d \quad (2)$$

with a, b and d varying with cloud class; these parameters are listed in Table 2. The mean air-sea temperature difference is also listed, a quantity of interest since it is directly proportional to be sensible heat flux. The average sensible heat flux over the domain was about 40 W/m^2, but four times larger in classes 8 and 10 (Garand, 1986). The retrieval and climatological statistics are shown in Table 3 for the air temperature and in Table 4 for dew point depression. The mean relative humidity, $\bar{H}$, is also listed.

Table 2 shows that for most classes, the retrieval simply consists in removing a class climatological bias since the slope is unity. For classes 7, 8 and 10 however, T_r is best obtained with a slope different than unity. Fig. 3 shows the observations T as a function of T_c for classes 7 and 8. The plot implies that stronger anomalies are found with decreasing T_c i.e. north of the domain. We note that cloud streets are observed in the subtropics even with T equal or even warmer than T_c. The streets in these cases seem to be the result of mechanical alignment of the small cumuli with the ambient wind speed direction. Rolls, on the contrary (and the strongly convective open cells of class 10 as well) occur almost exclusively in major cold air outbreaks. It is the first time that results such as those of Fig. 3 are reported from machine classification.

The values of $S(T_c)$ and $S(DD_c)$ in Tables 3-4 represent the rms error that would be encountered from using a climatological estimate. The usefulness of the retrievals can be appreciated from comparing these values with those $S(T_r)$ and $S(DD_r)$. We propose the following criteria of usefulness:

a) For T: $S(T_c) - S(T_r) \geq 0.5$ K or $S(T_r) < 2.5$ K.
b) For DD: $S(DD_c) - S(DD_r) \geq 0.2$ K and $S(DD_r) < 2.4$ K.

Accepting these criteria, quality temperature retrievals are expected from the recognition of classes 4, 6-10, about 11% of the total data. The temperature retrievals are successful mostly for MCC patterns because these fields are associated with a large negative temperature anomaly. In the case of class 6, the classification is useful not because a large anomaly is found, but because a low natural variance is found (provided this would hold true with a larger data set). For DD_r, success is obtained for classes 2, 7, 9, 12, 18-20 or 39% of the time. The retrievals are successful for classes associated with H < 68% or H > 80%. Direct methods of remote sensing of surface humidity, such as the split-window technique of Chesters et al. (1984), work only in clear air. The proposed method, although indirect, significantly increases the areal coverage of quality retrievals.

Table 2. Parameters of Eqs. (1) and (2) and mean air-sea temperature difference for each class.

Class	$a(K^{-1})$	b(K)	$\overline{T - Ts}$(K)	d(K)
1	1.0	0.0	-1.7	1.3
2	1.0	0.9	-0.4	-0.9
3	1.0	0.5	-1.2	1.0
4	1.0	-3.1	-5.2	0.0
5	1.0	0.2	-1.3	0.7
6	1.0	-0.2	-1.8	1.1
7	1.250	-75.0	-4.5	2.0
8	1.140	-44.4	-7.3	0.8
9	1.0	-2.5	-4.1	1.5
10	1.143	-46.3	-8.0	0.6
11	1.0	-0.6	-3.0	0.5
12	1.0	-1.4	-4.1	-0.7
13	1.0	-0.8	-3.1	1.3
14	1.0	0.2	-1.8	-0.2
15	1.0	-0.1	-2.3	0.3
16	1.0	1.2	-0.8	0.8
17	1.0	1.1	-1.1	0.3
18	1.0	0.0	-2.5	-1.1
19	1.0	1.3	-1.0	-1.3
20	1.0	0.8	-1.9	-1.9

Table 3. Air temperature retrieval and climatological rms error (K) for each cloud class. N: number of samples.

Class	N	$S(T_r)$	$S(T_c)$
1	108	2.9	2.9
2	54	3.3	3.5
3	213	2.9	2.9
4	6	1.8	4.0
5	103	3.1	3.1
6	22	1.9	1.9
7	71	2.8	3.9
8	64	2.8	5.2
9	28	2.4	3.6
10	29	2.4	5.7
11	114	3.7	3.8
12	130	3.7	3.8
13	76	3.7	3.7
14	64	3.6	3.6
15	59	3.5	3.5
16	125	2.7	3.1
17	224	3.3	3.6
18	290	3.7	3.7
19	57	2.9	3.3
20	180	4.0	4.1

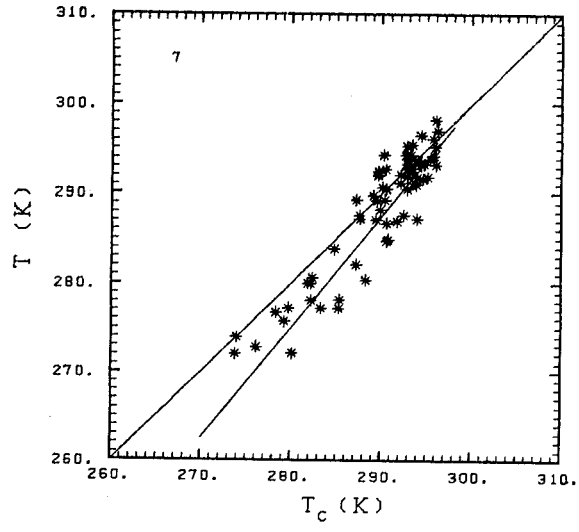

Fig. 3 a)

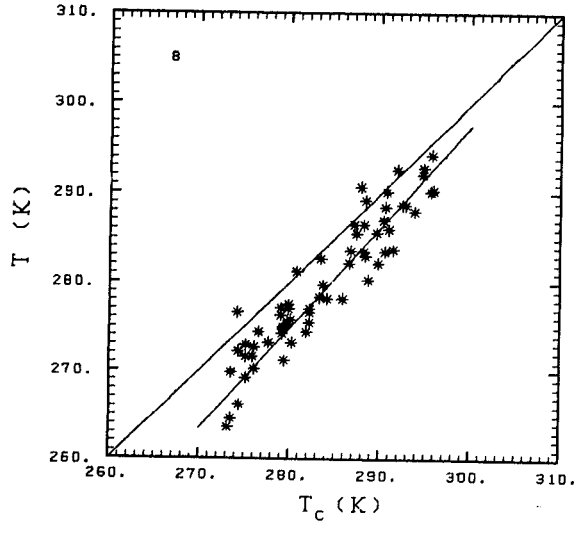

Fig. 3 b)

Fig. 3 Observed air temperature, T, as a function of local climatological temperature, T_c, for class 7 (a) and for class 8 (b). The regression line of Eq. (1) and the line $T = T_c$ are drawn.

Table 4. Dew point depression retrieval and climatological statistics (K) for each cloud class. $\bar{H}$: mean relative humidity (%).

Class	N	$\bar{H}$	$\overline{DD}$	$S(DD_c)$	$S(DD_r)$
1	72	69.0	5.9	2.9	2.5
2	32	85.4	2.5	2.5	2.3
3	148	72.4	5.3	2.7	2.6
4	5	75.7	4.0	2.1	2.1
5	76	72.6	5.1	2.3	2.2
6	20	71.7	5.4	2.7	2.5
7	47	64.5	6.8	3.3	2.3
8	38	71.7	5.1	2.7	2.5
9	24	67.8	6.1	2.5	2.1
10	23	71.0	5.3	2.4	2.2
11	86	73.5	4.7	2.4	2.3
12	88	81.7	3.1	2.0	1.8
13	56	70.9	5.4	2.7	2.4
14	46	77.2	4.3	2.5	2.5
15	42	73.9	4.8	2.7	2.6
16	92	74.1	4.9	2.8	2.7
17	176	76.0	4.5	2.6	2.6
18	189	83.5	2.9	2.6	2.3
19	44	82.8	3.1	2.5	2.1
20	130	86.4	2.5	2.5	1.9

Table 5. Retrieval, and trial fields statistics of surface air temperature and dew point depression (K) near Sable Island. Retrieval statistics shown for all cloud classes and for the selected classes for which retrievals are known to be most successful.

	Retreivals		Trial
	**********		*****
Classes	all	select	all
N (T)	204	17	180
$\bar{T}$	275.5	271.0	271.9
S(T)	4.4	5.4	3.9
$S(T_r)$, $S(T_f)$	4.2	2.8	1.4
Bias T_r, T_f	-0.4	-0.9	-0.6
N (DD)	176	80	180
$\overline{DD}$	2.6	1.7	2.9
S(DD)	2.0	1.6	1.7
$S(DD_r)$, $S(DD_f)$	1.8	1.2	2.3
Bias DD_r, DD_f	-0.1	0.0	-0.7

5. IMPACT ON NUMERICAL WEATHER PREDICTION

The analysis scheme (Rutherford, 1974) of the Canadian Meteorological Center (CMC) is based on a "trial" field which is a 6-hour forecast to be modified by new data where available. In order to evaluate the potential impact on operational analyses for weather prediction, we have compared the error statistics of the trial fields with those of the retrievals at Sable Island. The trial fields of T and DD at 1000 mb were compared with the observations (twice daily radiosondes) for the three-month period December 1986 to February 1987. The year is different than that of our satellite data but the season is again winter. The satellite retrieval statistics were collected up to 300 km away from Sable Island in order to get a similar number of cases. The results are shown in Table 5. The subscript f refers to the 6-hour forecasts trial fields. Over all classes, the error reduction of the retrievals is, as expected, modest, ~0.2 K rms, but for the selected classes where retrievals are most successful, the reduction is significant, 2.6 K rms for $[S(T_c) - S(T_r)]$ and 0.4 K rms for $[S(DD_c) - S(DD_r)]$. It appears clear that the trial fields were excellent for the air temperature, with $S(T_f) = 1.4$ K, but they were of marginal quality for dew point depression, with $S(DD_f) = 2.3$ K. Because of that and because the percentage of useful retrievals is higher for DD_r than for T_r, we conclude that a positive impact on NWP is more likely to result from humidity retrievals than from the temperature retrievals. This result should hold elsewhere as well because it is related to the fact that the autocorrelation of humidity decreases with horizontal distance much faster than the autocorrelation of temperature.

6. CONCLUSION

We have evaluated the potential of objective cloud classification as a means to infer surface air temperature and humidity. The temperature retrievals are useful mostly for mesoscale cellular patterns because a large temperature anomaly is associated with these cloud patterns. This is the first time that this known phenomenon is assessed from machine classification. The humidity retrievals are found useful for cloud classes associated with a mean relative humidity lower than 68% or higher than 80%. Because the frequency of useful retrievals is higher for the humidity variable than for the air temperature and because the trial fields of air temperature obtained from conventional data are already quite good, a significant impact on numerical weather prediction is more likely to result from the humidity retrievals than from the temperature retrievals. A logical next step would be to get mean observed humidity profiles associated with each class, thus extending to the entire column the applicability of the technique. These profiles could be used as such, for the appropriate classes, or serve to constrain the solution of physical methods of sounding based on the inversion of the radiative transfer equation.

REFERENCES

Chesters, D., Ucellini, W.L. and W.D. Robinson, 1984: Low-level water vapor fields from the VISSR atmospheric sounder (VAS) "split-window" channels, J. Climate Appl. Meteor, 22, 725-743.

Garand, L., 1986: Automated recognition of oceanic cloud patterns and its application to remote sensing of meteorological parameters, Ph. D. thesis, U. of Wisconsin-Madison, 231 pp.

Garand, L., 1988: Automated recognition of oceanic cloud patterns. Part 1: methodology and application to cloud climatology, J. Climate, 1, in press.

Garand, L., J.A. Weinman and C.C. Moeller, 1988: Automated recognition of oceanic cloud patterns. Part 2: application to remote sensing of surface air temperature and humidity, submitted to J. Climate.

Rutherford, I.D., 1972: Data assimilation by statistical interpolation of forecast error fields, J. Atmos. Sci., 29, 809-815.

DETERMINATION OF SURFACE AND ATMOSPHERIC PARAMETERS USING THE ADVANCED MICROWAVE SOUNDING UNIT

Norman C. Grody

National Oceanic and Atmospheric Administration
National Environmental Satellite, Data, and Information Service
Satellite Research Laboratory
Washington, D.C. 20233

1. INTRODUCTION

In recent years there has been an increased emphasis by the National Oceanic and Atmospheric Administration (NOAA) in the use of microwave sensors for providing atmospheric soundings of temperature and water vapor as well as surface products from polar orbiting satellites. As part of this new initiative a large development effort is underway to improve the current operational sounding system called the Tiros Operational Vertical Sounder (TOVS) which consists of three separate instruments: (1) the High Resolution Sounder (HIRS), a 20-channel infrared radiometer; (2) the Microwave Sounding Unit (MSU), a 4-channel passive radiometer in the 50 - 58 GHz region; and (3) the Stratospheric Sounding Unit (SSU), a 3-channel infrared instrument designed to sense the highest part of the atmosphere. The SSU was developed by the British Meteorological Office as part of an international, cooperative program.

A major deficiency of the TOVS system is the relatively poor quality temperature soundings produced in cloudy areas. In the clear areas, major emphasis is placed on the HIRS instrument, which contains the most channels and has a spatial resolution of about 10 km compared to the 110 km resolution of the MSU at nadir. However, temperature soundings in cloudy conditions are based primarily on the MSU, which has insufficient channels and poor spatial resolution. This can result in less accurate retrievals by as much as 20 percent near the surface compared to the clear soundings. The degradations in accuracy and spatial resolution are of immediate concern by the user community since the quality is reduced in the most meteorologically significant (cloudy) areas.

The four channel 110 km resolution MSU instrument is based on our initial understanding of the last decade and shall be upgraded with more channels and higher spatial resolution to gain the full advantage of microwaves for providing accurate soundings throughout cloud-shielded areas. In a concerted effort over the last few years individuals from both the scientific and user community have conferred in arriving at a specification for an Advanced Microwave Sounding Unit (AMSU) to replace the MSU as well as the SSU for NOAA-K and beyond. Of greatest significance will be the accurate, high resolution temperature soundings derived in critical meteorological areas. To meet the present and future needs of an expanded community this instrument will also provide precipitation measurements, humidity data and surface observations.

The Advanced Microwave Sounding Unit (AMSU) instrument is a 20-channel total power power radiometer system divided into two components, a 15-channel unit provided by the United States (AMSU-A) and a 5-channel unit to be provided by the British Meteorological Office (AMSU-B). Tables 1 and 2 list the channel specifications for the two modules. Both units contain antennas which scan across the satellite track by ± 47.8 degrees. For each module the different channels are obtained using polarization separation as well as various stages of filtering. Although the polarization vector rotates with scan angle, the most transparent channels (1-4, 15-17, 20) which sense the surface, are chosen to have the same polarization components. From an orbital altitude of 825 km the spatial resolution (half power) is 50 km at nadir for AMSU-A and 15 km for the B module.

Table 1: AMSU-A Channel Specifications

Channel Number	Center Frequency (GHz)	Number of Pass Bands	Bandwidth (MHz)	Center Frequency Stability (MHz)	NEDT (K)
1	23.80	1	270	10	0.30
2	31.40	1	180	10	0.30
3	50.30	1	180	10	0.40
4	52.80	1	400	5	0.25
5	53.59 ± 0.115	2	170	5	0.25
6	54.40	1	400	5	0.25
7	54.94	1	400	10	0.25
8	55.50	1	330	0.5	0.25
9	57.29 = fo	1	330	0.5	0.25
10	fo ± 0.217	2	78	0.5	0.40
11	fo ± 0.322 ± 0.048	4	36	0.5	0.40
12	fo ± 0.322 ± 0.022	4	16	0.5	0.60
13	fo ± 0.322 ± 0.010	4	8	0.5	0.80
14	fo ± 0.322 ± 0.004	4	3	0.5	1.20
15	89.00	1	6000	50	0.50

Table 2: AMSU-B Channel Specifications

Channel Number	Center Frequency (GHz)	Number of Pass Bands	Bandwidth (MHz)	Center Frequency Stability (MHz)	NEDT (K)
16	89.00	1	5000	50	2.00
17	157.00	1	4000	50	2.00
18	183.31 ± 1.0	2	1000	30	2.00
19	183.31 ± 3.0	2	2000	30	2.00
20	183.31 ± 7.0	2	4000	30	2.00

Note that many of the channels contain more than one pass band. The pass bands for channels 11 through 14 are symmetrically displaced about the 11^- and 13^- oxygen lines and channels 18 through 20 are centered about the 183.31 GHz water vapor line. This is done to improve the thermal noise (NEDT) as well as the frequency stability of the measurements. The location of these frequencies relative to the atmospheric absorption spectrum is shown in fig. 1. This figure was reproduced from a NASA Earth Observing System Report (Vol. IIe) which describes the AMSU instrument. Shown is the opacity due to oxygen and water vapor, where the total absorption is given by the sum of the two constituents for clear atmospheres. The oxygen channels (3-14) are used for deriving temperature profiles (soundings) while the water vapor channels (1, 17-20) provide humidity profiles. Surface information and precipitation data is obtained using the "window" channels 2, 15 and 16 which lie in the valleys between the oxygen and water vapor regions.

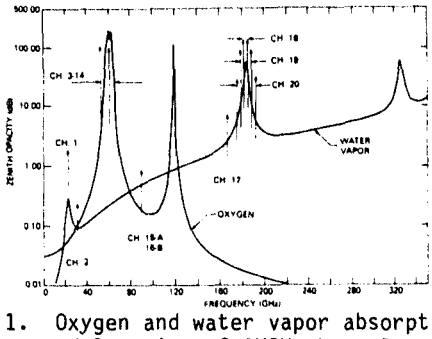

Fig. 1. Oxygen and water vapor absorption spectra and location of AMSU channels.

This description is somewhat oversimplified in that it is often necessary to combine channels from different spectral regions in determining the various geophysical parameters. As discussed below, in obtaining temperature profiles the window channels are used to correct the oxygen channel measurements for surface effects. Also, in obtaining humidity profiles using the water vapor channels, the oxygen channels are used to remove the temperature contribution in the water vapor channel measurements (Kakar and Lambrigsten, 1984). The interrelationship among the various channels is summarized in Table 3. Listed are the various geophysical parameters and the AMSU channels which are important in deriving the parameters. The most important channels are indicated by the letter "I", while the supportive channels are denoted by the symbol "*".

Table 3. AMSU Channel Characteristics

GEOPHYSICAL PARAMETERS	AMSU-A CHANNELS				AMSU-B CHANNELS		
	1	2	3-14	15	16	17	18-20
Temperature Profile	*	*	I	*			
Humidity Profile (Ocean)	I	I	I		*	*	I
Humidity Profile (Land)			I		I	I	I
Cloud Water (Ocean)	I	I					
Water Vapor (Ocean)	I	I					
Rain (Ocean)	*	I	*	I	I		
Rain (Land)	I	I	*	I	I		
Snow Cover	I	I	*	*	I		
Sea Ice Extent and Type	I	I	*	*	I		

In this short paper it is not possible to adequately describe the algorithms used in deriving all the geopohysical quantities. However, as an example of how the various channels are used, the procedures for obtaining temperature profiles and surface products are outlined below.

2. TEMPERATURE SOUNDING APPLICATION

The AMSU-A module was primarily designed to provide global temperature soundings as inputs to numerical analysis and forecast models. As such it contains twelve channels within the 50 - 60 GHz oxygen band whose brightness temperature measurements, $T_b(\nu)$, represent the vertically integrated temperature profile, T(p). Based on the radiative transfer equation for a scatter free atmosphere above a specular surface, the relationship becomes:

$$T_b(\nu) = \int_{\ln P_s}^{-\infty} T(p) \frac{dS_\nu(p)}{d\ln p} d\ln p + S_\nu(P_s) T_s \qquad (1a)$$

where

$$S_\nu(p) = \left[1 - (1-\epsilon_s)\left(\frac{\tau_\nu(P_s)}{\tau_\nu(p)}\right)^{2\sec\phi}\right]\tau_\nu(p)^{\sec\phi}. \qquad (1b)$$

The derivative term, $-dS_\nu(p)/d\ln p$, in eq.(1a) is called the temperature weighting function. For the oxygen channels the weighting functions have a unique distribution with pressure depending on the channel frequency, ν, and local zenith angle, ϕ. The frequency dependence of the weighting function is defined by the transmittance function, $\tau_\nu(p)$, in eq.(1b) which is the exponential absorption (mainly due to oxygen) along the vertical path beginning at the satellite level and terminating at pressure p. Figure 2 shows the gaussian shaped weighting functions for channels 3 through 14. The calculations were performed for the nadir viewing position and a surface emissivity, ϵ_s, of unity (representing dry land). For off-nadir viewing the weighting functions are elevated. The pressure level where the weighting functions peak is reduced by an amount nearly equal to $\sqrt{\cos\phi}$. Since the zenith angles are known for the different beam positions the "limb effect" is readily accounted for when processing the data.

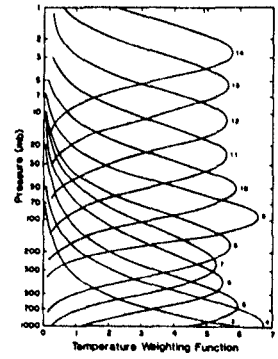

Fig. 2. Weighting functions for AMSU oxygen channels.

The largest uncertainty in the weighting functions occur for the lower sensing channels 3, 4, and 5, whose measurements are affected by the variations in the surface emissivity and surface pressure, Ps, over land. This is in contrast to the more uniform sea surface whose emissivity (≈ 0.5) is usually considered to be a known function of surface temperature, Ts, and local zenith angle. Procedures for obtaining surface corrections over land have been developed for the Special Sensor Microwave Temperature (SSM/T) sounder on the Block 5D DMSP (Defense Meteorological Satellite Program) satellites and are applicable to the AMSU channels. The algorithm shall be described in the next section.

Based on the radiative transfer equation (1a), a pseudoinverse relationship exists between T(p) and $T_b(\nu)$. The solution is obtained by correlating the temperature at different pressure levels with brightness temperatures at different frequencies. Using a least squares error criteria the solution can be written as

$$\hat{T}(p) = \overline{T}(p) + \sum_{n=1}^{N} a_n(p)[T_b(\nu_n) - \overline{T}_b(\nu_n)] \qquad (2)$$

where $\hat{T}(p)$ is the estimated (retrieved) temperature, and a_n are the regression coefficients based on the statistical correlation between temperatures and the "N" brightness temperature measurements. The coefficents can be obtained from simulations using an historical data base consisting of radiosonde profiles and brightness temperatures computed using (1). The data sample also provides the a-priori mean temperature $\overline{T}(p)$ and mean brightness temperatures $\overline{T}_b(\nu)$. Alternatively, the coefficients and a-priori mean values can be obtained using actual brightness temperature measurements and coincident radiosonde data. Both techniques have been tested using SSM/T data and show similar results.

2.1 Surface Corrections

As mentioned above, in using the oxygen channels for deriving temperature profiles it is necessary to correct the more transparent channels (ν <54 GHz) for surface emissivity and elevation effects. For channel 3, the surface contribution is about 70 percent (i.e., τ_ν (Ps)$\approx$0.7), so that it is considered a "window" channel and not used as a temperature predictor in (2). The two lower sounding channels 4 and 5 receive about 30 percent and 10 percent of its signal from the surface, respectively, and can be approximately corrected for. Also, except for areas of high elevation (>3 km) channel 6 contains a negligible surface contribution.

The brightness temperature measurements, T_b, can be adjusted to sea level pressure with an emissivity of zero, T_b', using an algorithm developed originally for the SSM/T sounder (Rigone and Stogryn, 1977; Grody et al., 1985);

$$T_b' = T_b + G(h) + [H(h) + K]\,\varepsilon s Ts. \qquad (3)$$

where the elevation dependence is contained in the G and H terms which are quadratic functions of elevation height, h. The surface emissivity correction is given by the term $K \cdot \varepsilon s Ts$ where K is approximately $\tau_\nu(Ps)^{2 Sec\phi}$. All three quantities (G, H, K) are obtained from simulations and depend on the channel frequency and local zenith angle. In applying (3), the elevation information is obtained from a fixed data base while the surface emission at 50 GHz is determined using the most transparent channels 1 and 2, and possibly channel 3. However, most of the surface information is obtained from the two lowest frequency channels since they are least affected by the atmosphere, i.e.,

$$\varepsilon s Ts = b_0 + b_1 T_b(23) + b_2 T_b(31) \qquad (4)$$

where the coefficients, b_n, are obtained from simulations. Equation (4) is based on the fact that for many surfaces the emissivity varies monotonically with frequency so that the emissivity at 50 GHz can be derived from the two lower frequency measurements. This emissivity characteristic is illustated in Figure 3, where the curves are based on measurements for snow and ice surfaces and model calculations for water and wet land. The application of the window channels to correct the oxygen channels will be tested using data from the SSM/T and SSM/I instruments aboard the recently launched DMSP satellite.

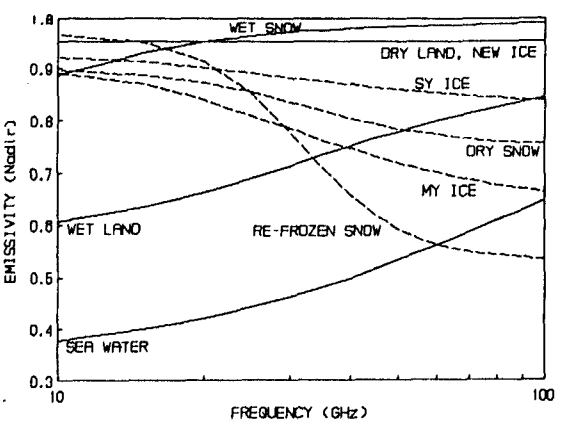

Fig. 3. Surface emissivity at nadir as a function of frequency for water, wet and dry land, snow (melting, dry and refrozen) and sea ice (new, second year (SY), multiyear (MY)).

2.2 Precipitation Editing

It has been demonstrated that the sounding channels appear unaffected by non-precipitating clouds (e.g., Grody, 1983). However, precipitation is composed of large water droplets and ice particles which attenuate and scatter the upwelling microwave radiation. The lower sounding channels 4, 5 and 6 require adjustments for these effects. Two different methods are available.

2.2.1 Median Filter Approach

Over land, sharp decreases in the horizontal brightness temperature field for channels 4, 5 and 6 are used to locate rainfall. This is accomplished using a "median filter" technique (Nappi et al., 1986). The median values are computed at each observation point using a minimum

of eight surrounding measurements. Difference values (observed minus median) exceeding 1K identify precipitation. Observations affected by precipitation can then be replaced by an interpolated value. In applying the median filter it is necessary for the brightness temperatures to be angle corrected. Emissivity corrections may also be necessary for channel 4 although the effects of emissivity on the filter technique are most pronounced over oceans.

Unlike land, the lower emissivity for water can cause the brightness temperature in precipitating regions to be greater than in rain free areas. This only occurs for channel 4, which is transparent enough to result in an increase in the measurements for low level stratiform rain, whereas convective precipitation results in a decrease in brightness temperature. Channels 5 and 6 are nearly opaque to the surface and therefore, respond to precipitation as in the case of land. As such, the median filter technique is mainly applicable to channels 5 and 6 over oceans.

2.2.2 Dual Frequency Approach

The above method will be compared with the use of the window channels 2 and 15 for detecting precipitation over land and oceans. As discussed below, the 89 GHz measurements are generally greater than the 37 GHz observations for rain free conditions, with the reverse being true for precipitating clouds. The "positive" difference between the two brightness temperature measurements, is used to identify precipitation over land and oceans. These window channels can provide a more direct and more sensitive indication of precipitation than the oxygen channels. Based on evaluations using actual measurements, either or both methods shall be used to identify and edit the sounding channels for precipitation effects.

Over oceans the higher emissivity, as well as the increased atmospheric absorption due to water vapor and clouds, results in a higher brightness temperature at 89 than at 31 GHz. This is in contrast to precipitating regions where scattering by large ice particles results in a lower brightness temperature at the higher frequency. As an additional test over oceans, comparisons will be made using the 23 and 31 GHz channels. These channels provide a measurement of cloud liquid water (also water vapor), which is an indicator of precipitation when the liquid water exceeds about 1 mm (Grody et al., 1980).

For land, the emissivity either increases with frequency or is nearly constant for open water, wet and dry land, and new sea ice (see Fig. 3). As such, the brightness temperature difference, $T_b(31) - T_b(89)$, is generally "negative". This difference is reversed due to scattering effects by precipitation sized ice particles. Unfortunately, this reversal in the difference measurements also occurs for scattering surfaces such as snow and multiyear sea ice (see Fig. 3). These surfaces shall be identified using appropriate threshold values for the 31 and 89 GHz channels, or through the use of sequential (spatial and temporal) measurements to remove the large scale surface features from that of precipitation.

3. SURFACE PRODUCTS

The AMSU shall also be used to derive surface quantities such as snow coverage and sea ice concentration. As illustrated in figure 3, the identification of surfaces can be obtained based on their different spectral signatures, where much of the information is contained in the emissivity value and its slope with frequency. Although the resolution at nadir is only 50 km for AMSU-A, the lower frequency channels, 1 and 2, are best suited for obtaining these emissivity parameters, leading to surface identification. Figure 4 shows an example of the use of the 18 and 37 GHz (vertical polarization) measurements from the Nimbus 7 Scanning Multichannel Microwave Radiometer (SMMR) for identifying different surfaces, as well as precipitation (Ferraro et al., 1986). The scatter plot shows the average and difference of the two brightness temperature measurements for a SMMR pass over the central U.S. for January 1979. This data contains areas of open water, wet and dry land, lake ice, rainfall and snow cover and is discussed in detail in the above mentioned paper. The diagram shows six "clusters" corresponding to the various surface and atmospheric features. Those observations which do not fall into a specific cluster are "mixed pixels" and correspond to more than one geophysical parameter within the field of view.

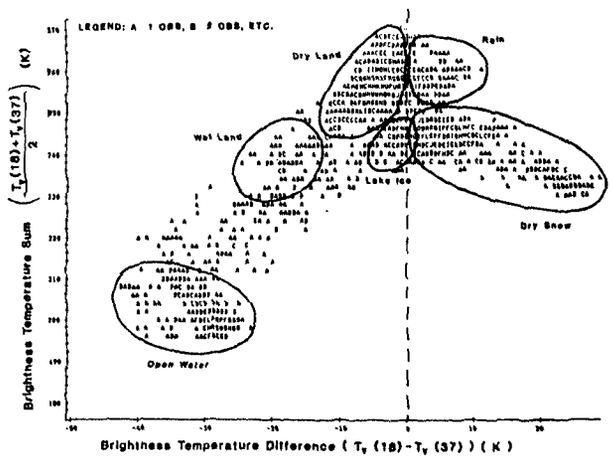

Fig. 4. Scatter plot of the average brightness temperature versus the difference using the 18 and 37 GHz vertically polarized SMMR channels. Data obtained over the central U.S. for latitudes between 25 and 60 North on January, 20, 1979 (See Ferraro et al., 1986).

A simple example of a mixed pixel occurs around coastlines where part of the field of view contains water and the remainder contains land. A more interesting case occurs for sea ice when there exists multiyear ice, first year ice and open water within a footprint. Based on a-priori knowlege of the different surface emissivities (see fig. 3), the fractional amount of the three surface types within the viewing area can be obtained using dual frequency measurements (e.g., Swift and Cavaleri, 1985).

Although affected more by clouds than the 23 and 31 GHz measurements, the higher resolution 89 GHz channel on AMSU-B shall be used to provide images of the surface and obtain a more accurate location of the ice edge and snow line than the lower frequency channels. This high resolution channel is also important for determining precipitation over land and ocean, particularly for the case of light precipitation which is difficult to detect over land using the lower frequency window channels. Many of these issues concerning the use of the various window channels for obtaining surface and precipitation quantities will be more fully established after analyzing data from the recently launched SSM/I sensor on the DMSP satellite.

4. REFERENCES

Ferraro, R.R., Grody, N.C. and Kogut, J.A. 1986: "Classification of geophysical parameters using passive microwave satellite measurements," IEEE Trans. Geosci. Remote Sensing, Vol. GE-24, 1008-1013.

Grody, N.C., Gray, D.G., Novak, C.S., Prasad, J.S., Piepgrass, M. and Dean, C.A., 1985: "Temperature soundings from the DMSP microwave sounder," Advances in Remote Sensing Retrieval Methods, A. Deepak Publishing, Hampton, Va., 249-265.

Grody, N.C., 1983: "Severe storm observations using the Microwave Sounding Unit," Jour. Clim. Appl. Meteor., 22, 609-625.

Grody, N.C., Gruber, A., and Shen, W.C., 1980: "Atmospheric water content derived from the Nimbus-6 Scanning Microwave Spectrometer over the tropical pacific," Jour. Appl. Meteor., 19, 986-996.

Kakar, R.K., and B.H. Lambrigsten, 1984: "A statistical correlation method for the retrieval of atmospheric moisture profiles by microwave radiometry," Jour. Clim. Appl. Meteor., 23, 1110-1114.

Nappi, A., Swaroop, A., Grody, N.C., and J. Weinman, 1986: "Precipitation effects on Microwave Sounding Unit data," 2nd AMS Conference On Satellite Meteorology/Remote Sensing and Applications, Williamsburg, Va., 114-117.

Rigone, J.L., and A.P. Stogryn, 1977: "Data processing for the DMSP microwave radiometer system," Proc. 11th Int. Symp. Remote Sensing of the Environment, University of Michigan, 1599-1608.

Swift, C.T., and D.J. Cavalieri, 1985: Passive microwave remote sensing for sea ice research," EOS Trans. American Geophys. Union, Vol. 66, No. 9, 1985.

ENHANCED IMAGE PRODUCTS BY LIMB-CORRECTION AND SMOOTHING OF VAS RADIANCE MEASUREMENTS

Andrew S. Jones[1,2]
Donald W. Hillger[2,3]
James F. W. Purdom[2,3]
Thomas H. Vonder Haar[1,2]

[1]U.S. Army Center for Geosciences
[2]Cooperative Institute for Research in the Atmosphere (CIRA)
[3]Regional and Mesoscale Meteorology Branch
Satellite Applications Laboratory, NOAA/NESDIS

Colorado State University
Fort Collins, CO 80523-0033

1. INTRODUCTION

GOES VISSR Atmospheric Sounder (VAS) imagery is subject to two undesirable characteristics: limb darkening or brightening effects due to varying satellite viewing (zenith) angles, and instrument noise. Limb effects are associated with a vertical shift of a wavelength's characteristic weighting function. As an example, the weighting function in Figure 1 responds to a larger zenith angle by shifting upward, since the larger zenith angle creates a longer optical path which increases absorption at higher levels. To counteract this effect the radiances in an image can be in effect "normalized" to a reference zenith angle by limb-correcting the image. The result is an image with a minimal limb-related gradient, so the atmospheric gradients of interest become more obvious. The second undesirable feature, instrument noise, varies depending on the channel characteristics, with greater noise for channels sensitive to the upper atmosphere. The statistical structure function analysis method of Hillger *et al.* (1987) was used to determine noise levels and optimal spatial averaging distances. The averaging domain size from the statistical structure function analysis was then used to produce smoothed images using a running average technique.

2. THEORETICAL BACKGROUND

The upwelling radiance measured by the satellite radiometer can be expressed mathematically as,

$$L_m(\nu_j) = B(\nu_j, T_s)\tau(\nu_j, \theta, p_s) + \int_{p_s}^{0} B[\nu_j, T(p)]\frac{\partial\tau(\nu_j,\theta,p)}{\partial(\ln p)}\frac{dp}{p}. \quad (1)$$

L_m is the spectral radiance measured in a channel whose effective wavenumber is ν_j. The first right-hand term in (1) is the spectral surface radiation contribution assuming the surface emittance to be unity. B is the Planck function associated with wavenumber ν and temperature T. τ is the transmittance of the atmosphere above a pressure p, and the subscript s denotes surface values. The zenith angle, θ, is defined as the angle between the measured upwelling radiance and the normal of the earth's surface. The atmospheric contribution to the measured radiance is given by the second right-hand term in (1). The measured upwelling radiance given by (1) can be written more compactly as,

$$L_m = L_{sfc}(\theta) + L_{atm}(\theta), \quad (2)$$

where the wavenumber dependence is understood. Likewise, the desired limb-corrected radiance referenced to zenith angle θ_0 can be written as,

$$L_c = L_{sfc}(\theta_0) + L_{atm}(\theta_0). \quad (3)$$

A ratio of (2) and (3) yields

$$L_c = L_m\left[\frac{L_{sfc}(\theta_0) + L_{atm}(\theta_0)}{L_{sfc}(\theta) + L_{atm}(\theta)}\right], \quad (4)$$

which relates the limb-corrected radiance to the measured radiance. Estimates of the atmospheric temperature and water vapor profiles can be used to compute $\tau(\nu_j, \theta, p_s)$, and L_{atm}. The surface temperature, T_s, can be determined by solving (1) for VAS channel 8, as,

$$T_s = B^{-1}\left[\frac{L_m - L_{atm}(\theta)}{\tau(\theta, p_s)}\right]. \quad (5)$$

3. PROCEDURE

3.1 Limb-correction

The case studied was 18 UTC 22 July 1981 over central North America and included zenith angles ranging from approximately 20 to 90 degrees. Several of the VAS channels

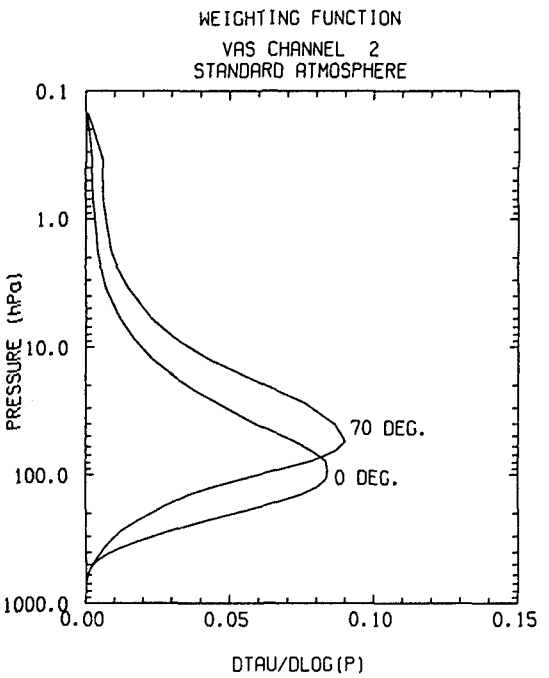

FIG. 1: Weighting functions of VAS channel 2 for zenith angles of 0 and 70 degrees assuming a standard atmospheric profile.

Table 1

VAS channel	Wave-length (μm)	W.F. Peak* (hPa)	Absorbing Gas	Averaging Domain Size line (km)	Averaging Domain Size elem. (km)	Number of FOVs line	Number of FOVs elem.
1	14.7	40	CO_2	> 400	280	> 30	13
2	14.5	70	CO_2	> 400	420	> 30	19
3	14.3	150	CO_2	> 400	> 670	> 30	> 30
4	14.0	450	CO_2	167	210	12	10
5	13.3	950	CO_2	16	27	2	2
6	4.5	850	CO_2	20	27	2	2
7	12.7	sfc	H_2O	< 14	< 23	1	1
8	11.2	sfc	window	< 14	< 23	1	1
9	7.3	600	H_2O	20	56	2	3
10	6.8	400	H_2O	15	26	2	2
11	4.4	500	CO_2	> 400	> 670	> 30	> 30
12	3.9	sfc	window	< 14	26	1	2

(* nadir viewing angle)

were considered. Selected characteristics of all the VAS channels are listed in Table 1. To simplify the limb-correction process, several assumptions were made:

a) fixed temperature and water vapor profiles (standard atmosphere),

b) fixed surface pressure (1000 hPa),

c) clear sky radiances (no clouds), and

d) radiative transfer computation could account for the effects of zenith angle changes, for the angles considered here.

The reference zenith angle chosen was zero degrees.

The limb-correction process consisted of:

1) compute $L_{atm}(\nu_8, \theta)$,

2) determine the surface temperature, T_s, using (5),

3) calculate the surface and atmospheric contributions given in (1) for the local zenith angle and the reference zenith angle using the assumed profile, and

4) compute the ratio term in (4) and multiply by the measured radiance to find the limb-corrected radiance.

The amount of limb-correction, denoted by asterisks for VAS channel 2 in Figure 2, shows that the radiances in the stratospheric channels decrease when corrected to a smaller reference zenith angle. This is due to a shift to the zero degree zenith weighting function in Figure 1, weighting the colder tropopause region more heavily. For tropospheric channels such as channel 9 in Figure 3, the limb-correction is positive due to shifting of the weighting functions downward into warmer temperatures as the zenith angle decreases. A combination of effects can occur for channels whose weighting functions peak above the tropopause for higher zenith angles, but below the tropopause for zero zenith angle. In these cases, the limb-correction is positive for smaller zenith angles and negative for larger zenith angles due to the temperature profile gradient's change in sign at the tropopause.

Examples of uncorrected and limb-corrected images for VAS channel 6 are shown in Figure 4. Figure 4 is displayed in image count values which vary inversely to brightness temperature. For example, white areas, which are high image count values, correspond to low brightness temperatures and are therefore cold. Likewise dark areas are warm. Limb-correction eliminated a large part of the limb darkening effect in Figure 4, so the image appears approximately as it would if the satellite were in a nadir viewing position for each pixel. Note the more uniform appearance of the limb-corrected image.

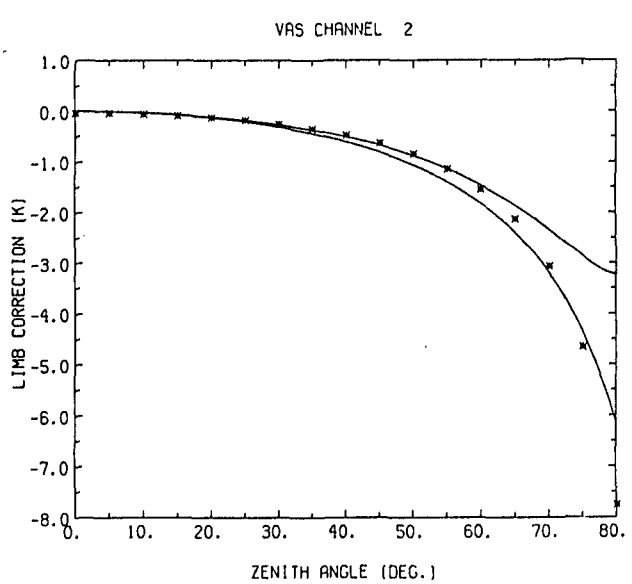

FIG. 2: Limb-correction as a function of zenith angle for VAS channel 2, given in terms of brightness temperature difference. (Asterisks denote values based on assumption of a standard atmospheric profile. Lines denote one standard deviation from the mean of the 15 verification profiles.)

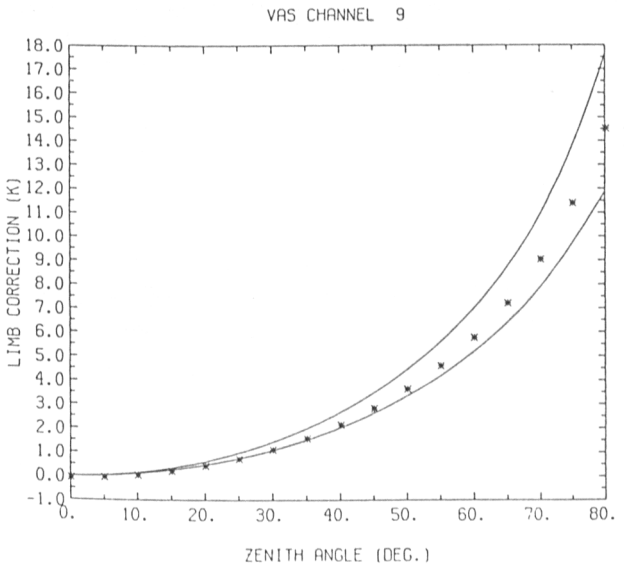

FIG. 3: As in Fig. 2, but for channel 9.

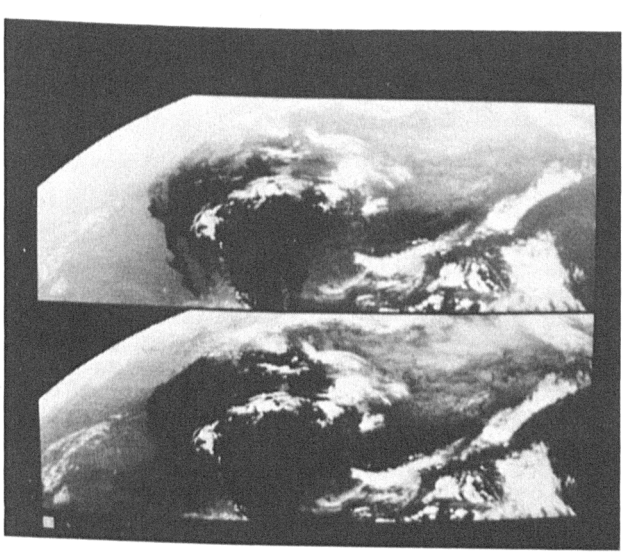

FIG. 4: Imagery from VAS channel 6; Top: original image, Bottom: limb-corrected image.

3.2 Possible Errors in Limb-correction

We randomly selected 15 soundings from across the U.S. and Canada as a basis for testing the limb-correction assumptions. These soundings and surface pressures were used to calculate verification limb-corrections to determine the mean error and standard deviation due to assumptions (a) and (b). For most channels the assumptions of a standard atmosphere and fixed surface pressure lead to results that were close to the mean results of the verification atmospheres, except at large zenith angles (>70 degrees). For large zenith angles, a noticeable problem with assumption (d) was evident for VAS channel 6 in Figure 5. The transmittance software produced unrealistic weighting functions at large zenith angles leading to erroneous results.

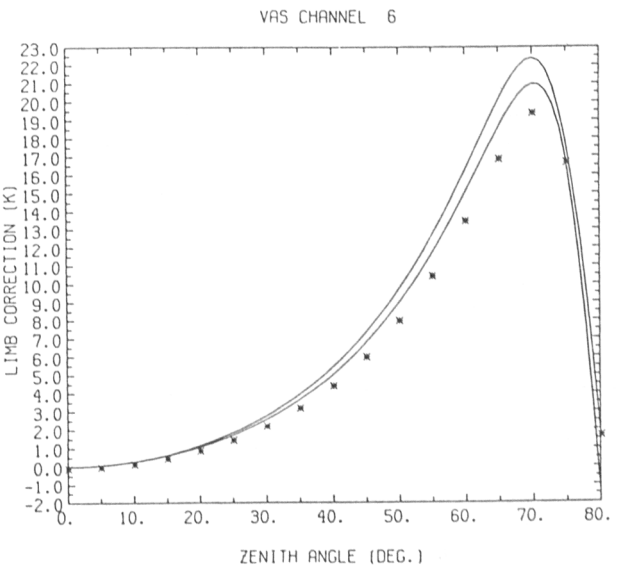

FIG. 5: As in Fig. 2, but for channel 6.

The bias error in the limb-correction was caused by two characteristics of the standard atmosphere, a cooler troposphere and a lower and warmer tropopause than was typical of the 15 soundings. The verification profiles generally had colder temperatures near the tropopause, and the limb-corrected radiances which assumed a standard atmosphere were therefore overcorrected; the tropopause discrepancy had little effect on low-level channels. The effect of the generally cooler temperatures in the troposphere of the standard atmosphere was to undercorrect the image. For example, in Figure 5 the bias errors for channel 6 were approximately 12 percent. To do a more exact correction, in-situ measurements or a full sounding retrieval would have to be used.

The variability of the verification limb-corrections, shown by the spread between the solid lines in the figures, generally increased with increasing zenith angle, since the weighting functions were shifted more with larger zenith angle increasing the radiance errors introduced by assuming a fixed atmospheric profile. An example was channel 9 in Figure 3, which had an equivalent brightness temperature standard deviation of 0.5 K at a zenith angle of 50 degrees and 1.5 K at 70 degrees. The CO_2 channels had less variability since they were not influenced by the water vapor profile assumption.

While we applied the limb-correction scheme presented here on an image which included clouds, the formulation of the atmospheric contribution assumed no clouds were present. For the blackbody cloud case, the surface pressure becomes in effect the cloud top pressure. The resulting error was to over correct the cloudy areas making the cloud/land contrast slightly smaller for the lower atmospheric channels. This effect could be accounted for by using one of several cloud top height estimates available, which would allow the surface pressure to be fixed at the cloud top level. Other concerns would be cloud emittance and fractional cloudiness. Emittance of cirrus and stratocumulus may remain less than unity and fractional cloudiness is an ever present problem. A technique for determining these cloud parameters would then have to be applied (*e.g.* Yeh and Vonder Haar, 1985).

3.3 Noise Reduction

The VAS radiance measurements were smoothed by applying a running average. The extent of averaging was influenced by a desire to average out the noise without destroying mesoscale information. The maximum averaging resolution was determined by statistically comparing the gradient information to the random noise in a selected sample area. Since the two spatial orientations, along lines and along elements, can yield different averaging resolutions, an elliptically shaped domain was chosen with the major and minor axes along the two orientations. Each pixel inside the averaging domain was weighted equally since the instrument noise was assumed to be random. Statistical analysis results for VAS are given in Table 1 (Hillger *et al.*, 1987). For the upper atmospheric channels, the size of the domain was relatively large, while little or no averaging was needed for the lower atmospheric channels. Results of smoothing applied to VAS channel 2 are shown in Figure 6. The noise in the original image obscures recognizable patterns, but stratospheric planetary waves become more evident with smoothing.

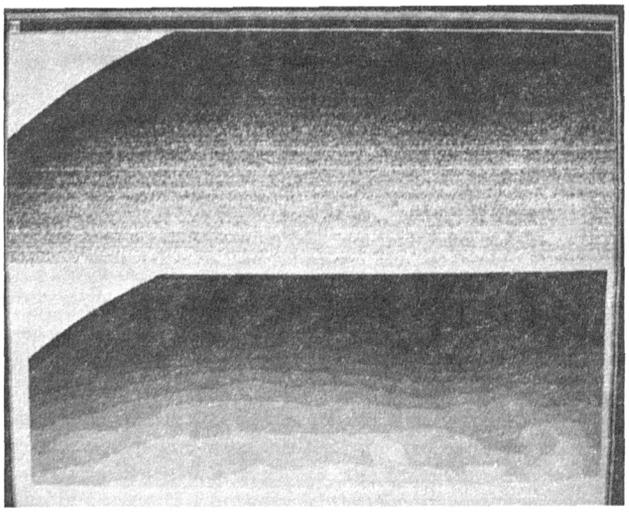

FIG. 6: Imagery from VAS channel 2; Top: original image, Bottom: limb-corrected and smoothed image using 30 by 19 pixel averaging domain.

4. CONCLUSION

Limb-correction and smoothing can produce a final image product with improved visual information content by minimizing the undesirable features of the uncorrected image. It holds promise as a way to objectively enhance VAS imagery by reducing noise and limb effects, while maintaining mesoscale information. The method is computationally fast compared to a full temperature/moisture profile retrieval using the VAS radiances. While assuming a standard atmospheric profile produces reasonable results, further improvements to this procedure could be made by inputing local soundings and/or cloud parameter estimates which would reduce the errors introduced by the imposed assumptions.

Acknowledgements. We would like to thank Mr. Alan Lipton for his suggestions in review of this paper. This research was jointly funded by NOVA Grant NA85RAH05045, NASA Contract NAS8-36472, and ARO Grant DAAL03-86-G-0190.

REFERENCES

Hillger, D. W., A. S. Jones, J. F. W. Purdom, T. H. Vonder Haar, and R. N. Green, 1987: Mesoscale applications of spatially-averaged VAS radiance measurements based on statistical structure function analysis. Third Conference on Mesoscale Processes, 21-26 August, Vancouver, BC, Canada, AMS, 122-123.

Yeh, H. Y., and T. H. Vonder Haar, 1985: Cloud parameters and temperature profile retrieval from infrared sounder data. *J. Atmos. Sci.*, **42**, 2360-2370.

3.4

ESTIMATION OF METEOROLOGICAL PARAMETERS OVER MESOSCALE REGIONS FROM SATELLITE AND *IN SITU* DATA

Jan L. Behunek

METSAT, Inc.
Fort Collins, Colorado

Chi-Fan Shih

METSAT, Inc.
Fort Collins, Colorado

Thomas H. Vonder Haar

Colorado State University
Fort Collins, Colorado

1. INTRODUCTION

The advent of multispectral data from geostationary satellites has provided a wealth of detailed information on the mesoscale state of the atmosphere, as have innovative instrument systems such as surface mesonetworks and vertical profilers. Satellite-based observations of the atmosphere are characterized by excellent spatial and temporal coverage, whereas measurements from ground-based sensors typically have more limited spatial coverage and greater accuracy than the satellite observations. The work summarized here examined methods of combining satellite sounding and image data from the Geostationary Operational Environmental Satellite (GOES) with *in situ* surface and upper-air measurements to obtain an optimum analysis of atmospheric conditions throughout a mesoscale region that was not uniformly covered by *in situ* observations. This effort was consistent with the current interest in mesoscale atmospheric processes and measurement techniques.

The meteorological quantities examined include cloud cover descriptors (cloud covered locations, cloud base heights, cloud top heights), surface temperature, surface wind, visibility and precipitation. Those quantities that could not be measured directly by the satellite were parameterized by observable quantities. The *in situ* observations were used to adjust the magnitude of the satellite analysis where available, maintaining the best characteristics of each platform. Development and testing of the method was accomplished using mesoscale data from sixteen case studies. Application of the methods developed are anticipated in the civilian sector at the boundary of densely-instrumented surface mesonet and profiler networks on land and at sea coasts and in the military sector within battlefield regions.

2. DATA SETS

Development and validation of the analysis methods for this study required the availability of mesoscale data sets describing meteorological conditions at the earth's surface and aloft. The data sets that were used were collected during several field programs specializing in the study of mesoscale weather because data collected by operational networks did not provide the necessary spatial and temporal resolution to meet the objectives of the study. A total of sixteen cases were examined, each with a minimum duration of six hours. The cases were evenly divided between those representing midlatitude summer and winter conditions, and two cases from each season were reserved for validation of the analyses. The primary area studied had dimensions of 200 km by 200 km, although data surrounding the primary area contributed to the analysis of boundary conditions.

The digital satellite data that were essential to the study of conditions outside of dense in situ instrument networks were collected from GOES because of the high temporal resolution of those data relative to data from polar-orbitting satellites. The multispectral satellite data originated from the Visible and Infrared Spin Scan Radiometer Atmospheric Sounder (VAS) instrument aboard GOES. All eleven of the available spectral channels were used for the retrieval of vertical soundings, which contributed to the analysis of some of the atmospheric parameters as discussed below. Other parts of the analysis were executed using data from individual channels formatted as images. The frequency of satellite data transmissions ranged from 90 minutes to three hours for the full multispectral data and was as little as 30 minutes for certain useful single channel data.

Surface observations were supplied by the standard surface observing sites maintained by the National Weather Service and the Federal Aviation Administration and by automated surface mesonetworks. The atmospheric quantities typically measured by the mesonet stations were surface air temperature, humidity, wind speed and direction, station pressure, and precipitation accumulation. The standard surface observations provided measurements of all of those quantities plus cloud cover and base height descriptors and surface visibility. Upper-air observations were obtained from rawinsonde networks, which often took measurements during the field experiments at higher temporal and spatial scales than the synoptic rawinsonde network.

The special field programs from which data were drawn and the dates of those cases were as follows:

A. The Cooperative Convective Precipitation Experiment (CCOPE) conducted over eastern Montana during the summer of 1981 (Knight, 1982). The cases analyzed were 13 July, 23 July, 24 July, and 27 July, 1981.

B. The Preliminary Regional Experiment - Stormscale Operational and Research Meteorology (PRE-STORM) which occurred over Kansas and Oklahoma during the summer of 1985 (Cunning, 1986). The PRE-STORM cases used were 28 May, 14 June, and 21 June, 1985.

C. The Genesis of Atlantic Lows Experiment (GALE) conducted over and offshore of the Midatlantic part of the United States during the winter of 1986. The 25 January, 9 February, 22 February, 24 February, 27 February, and 9 March, 1986 GALE cases were analyzed.

Additional data were collected for this study during the winter and summer of 1986 over Colorado. The surface data over Colorado included automated measurements made by the Program for Regional Observing and Forecasting Services (PROFS) mesonetwork (Reynolds, 1983).

3. ANALYSIS METHOD AND RESULTS

The analysis method required an initial estimate of each meteorological field from the satellite data alone. Some of those fields were estimated directly from satellite observations, such as the calculation of surface temperatures from the 11 μm infrared window channel. After the initial satellite estimate of a directly estimated quantity was obtained, the available in situ observations were used to adjust the magnitude of the entire satellite-derived field such that the final analysis incorporated the excellent spatial coverage of the satellite analysis and the high accuracy of the in situ observations. A polynomial curve fitting procedure was used to accomplish that adjustment. Other fields could not be estimated directly from the satellite data and were parameterized from quantities that were more easily measured by satellite. Parameterization was accomplished by calculating the statistical regression relationship between the quantities observable by satellite and the quantities for which final estimates were needed. The regression analysis took advantage of the in situ data available over part of the region of interest by obtaining the dependent variable in the regression from those data while the satellite provided estimates of the independent variables. Surface visibility is an example of a field that was parameterized by satellite estimates of surface wind and relative humidity. For the case of surface visibility, the regression equation was calculated from the satellite-derived estimates of the independent wind and humidity variables and the dependent in situ measurements of surface visibility. Once the regression relation had been formed for a given location and time, it was possible to use the satellite estimates of the independent variables and the regression equation to predict values of the dependent variable in areas where no in situ data were available. Completion of the regression analysis effectively accomplished the adjustment of satellite estimates to a best fit with the in situ observations that was performed by curve fitting for the fields estimated directly from the satellite data.

The analysis of individual meteorological variables to be discussed in the following paragraphs all were executed on gridded data, which made the use of objective analysis techniques possible. The objective analysis was

accomplished by use of the Barnes (1964) objective analysis method. In addition to its function of interpolating irregularly spaced observations to a regularly spaced grid, the objective analysis procedure helped alleviate the effects of cloud cover on the the satellite estimates of atmospheric conditions. It was not possible to make satellite estimates of weather near the surface in cloudy areas because of the reliance of the method on infrared spectral measurements, which are attenuated by clouds. The objective analysis interpolated the satellite-derived fields from clear regions into cloudy regions.

The retrieval of vertical profiles of atmospheric temperature and moisture was a necessary precursor to the completion of many of the analysis tasks. Although most of the meteorological quantities of interest were surface quantities, execution of the sounding retrieval process supplied fields of thermodynamic parameters, such as the pressure field, that could not be derived from individual spectral channel measurements. A physical retrieval technique based on inversion of the radiative transfer equation was utilized to compute profiles from the multi-spectral VAS data. The technique was similar to that described by Smith (1983).

The three cloud field descriptors analyzed were cloud presence at a particular point, cloud base height and cloud top height. Cloud presence was diagnosed from satellite data from a single spectral channel. The visible channel data were used when available because of their high spatial resolution (1 km at nadir) and the infrared window channel data were employed at other times. The automated cloud detection algorithm relied on the analysis of a histogram of the brightness values contained in the corresponding image. A sample histogram is depicted in Figure 1. The relative maxima in Figure 1 represent the two most significant objects in the image (Rosenfeld and Kak, 1976) - the earth's surface and cloud. The relative minimum between those two peaks represents the edge between the corresponding objects. Therefore, that minimum indicates the brightness threshold that separates cloud and ground in the image. All locations within the satellite image with brightness values higher than that threshold were diagnosed as cloudy.

Cloud top heights were estimated from a combination of the 11 µm IR window channel image from GOES, rawinsonde-derived atmospheric temperature profiles, and vertical soundings from GOES-VAS data. The radiance from the 11 µm image was converted to an equivalent blackbody temperature of the emitting surface by application of the Planck function. The equivalent blackbody temperature provided an estimate of the cloud top temperature where cloud was present. The cloud top temperature was used to compute a corresponding cloud top height by referring to a vertical profile of atmospheric temperature derived from rawinsonde or satellite sounding data. The rawinsonde-generated profile was used when it matched the cloud top temperature analysis closely in space and time, whereas the VAS-generated profile was used otherwise.

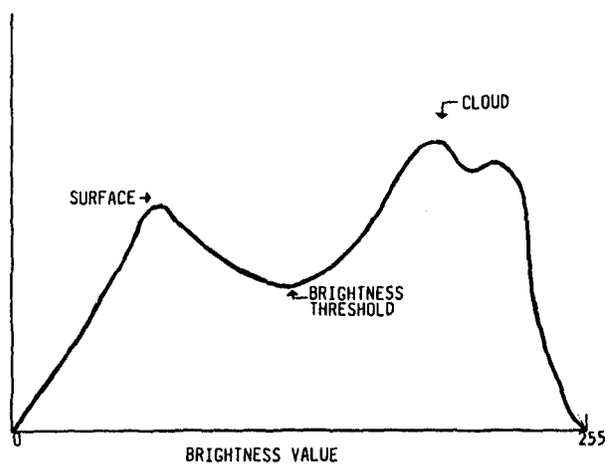

Fig. 1. Brightness histogram for cloud detection. This idealized histogram shows frequencies of satellite brightness values along with the objects they represent.

It was not possible to make direct measurements of cloud base height from satellite data because of the perspective of the satellite from above the clouds. The best estimate analysis of cloud base height was based on locating the level of transition from saturated to unsaturated atmospheric conditions that occurs below cloud top. Once cloud top was located by the process described above utilizing the 11 µm IR data and the sounding data, cloud base was assigned at the next unsaturated level below. The condition of the atmosphere with regard to saturation was determined from the rawinsonde data and retrieved VAS soundings. Surface observations of cloud base height from those sites where manual observations were taken were used to control the quality of the cloud base height estimates.

Surface temperature was estimated in a similar manner to that used to estimate cloud top temperature. Radiances from the 11 µm channel were converted to equivalent blackbody temperatures in clear parts of the analysis region. The resulting initial satellite estimate of the surface temperature field was interpolated into cloudy areas by the Barnes objective analysis algorithm. Adjustment of the

satellite estimate to a best fit with the available in situ data decreased the effect of errors introduced by emission from lower tropospheric water vapor, the difference between the skin temperature of the earth measured by the satellite the desired surface air temperature and cloud effects. Although more sophisticated methods exist for removing those error sources individually, they would require the use of satellite sounding data, which were not available at the same high temporal resolution as the single channel IR data.

Sample analyses of the surface temperature field are contained in Figures 2, 3, and 4. These analyses were generated from data collected on 27 August 1986 over Colorado. Figure 2 depicts the surface temperature field resulting from the Barnes objective analysis of observations from the PROFS surface mesonet and the hourly surface reporting stations. The lack of observations over the eastern part of the domain results in a large area where the surface temperature conditions are unknown. Figure 3 shows the raw satellite estimate of the surface temperature field throughout the domain. Although the data void region has been filled in by the satellite data, significant discrepancies in the magnitude of surface temperature exist between the satellite estimate and the in situ observations. Figure 4 depicts the satellite estimate adjusted to a best fit with the in situ observations. The adjustment procedure has performed well in adjusting the magnitudes of the satellite estimate to a closer agreement with the available in situ data while maintaining the added information supplied by the satellite data.

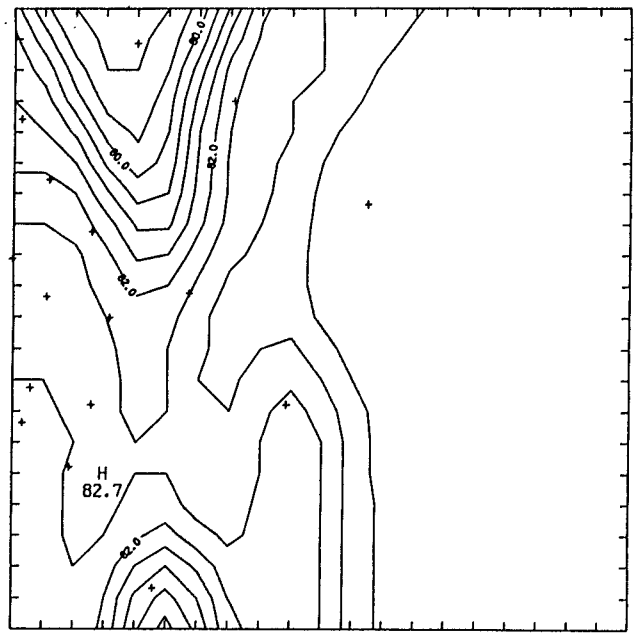

Fig. 2. Surface temperature analysis from in situ data. 27 Aug 1986 at 2000 GMT. Contours are at 0.5 deg. F intervals.

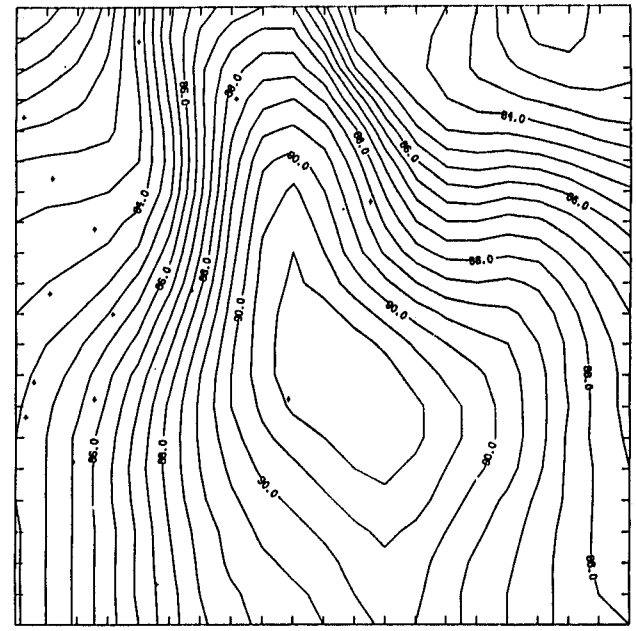

Fig. 3. Raw satellite estimate of surface temperature. Same date, time and units as Fig. 2.

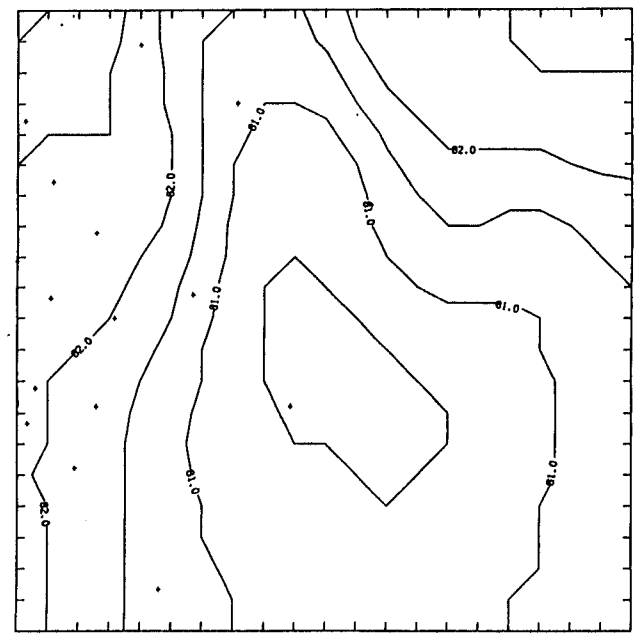

Fig. 4. Adjusted satellite estimate of surface temperature. Same date, time and units as Fig. 2.

The satellite wind estimation scheme designed for this study utilized the pressure and temperature fields near the earth's surface derived from the retrieved VAS profile. The availability of those fields allowed the computation of the u and v components of the geostrophic wind. The initial estimate of surface wind given by the geostrophic wind then was adjusted to a best fit with the observed surface wind where in situ data were available using the polynomial curve fitting method. That adjustment

diminished errors in the final satellite estimate of the wind field due to friction and inaccuracies in the satellite-derived pressure and temperature fields.

Full implementation of the surface wind estimation from satellite data has not yet occurred. Preliminary results from the 20 March 1986 Colorado case showing the adjustment of u-component geostrophic wind approximations to the observed surface u-component are depicted in Figure 5. The geostrophic wind fields shown in Figure 5 were computed from in situ measurements of the surface pressure and temperature rather than estimates of those quantities near the surface retrieved from GOES-VAS data. Figure 5 demonstrates considerable adjustment of the geostrophic approximation of the u-component toward better agreement with the observed u-component. The correlation coefficient between the adjusted estimate of the u-component shown in Figure 5b and the observed u-component was 0.86.

The satellite precipitation estimation scheme devised for this study was simple relative to many of the methods that have been attempted previously because it had to be capable of being automated and applied over various geographic areas. This precipitation estimation scheme used satellite observations of the coldest cloud top temperature, the time rate of change of that quantity, and the rate of change of cloud top area for a particular cloud or cloud system. Those variables were selected because they are related to physical processes associated with precipitation generation. Each of the parameters gave an indication of the strength of upward motion in the cloud. The cloud top temperature supplied additional information about the microphysics of the cloud - whether or not the cloud penetrated to sufficiently cold temperatures to allow efficient precipitation production. Measurement of the time rate of change quantities from satellite data required the tracking of clouds or cloud systems over a sequence of images. The satellite precipitation estimation technique made use of the regression relation between observed precipitation and the predictors described above. This built-in calibration of the satellite precipitation analysis sets this method apart from most other satellite-based methods, and it is an important factor in allowing the method to be applied over varying seasons and geographic locales.

The technique designed to estimate visibility from satellite data as part of this study relied on analyses of relative humidity and wind speed near the earth's surface derived from satellite data as justified by the studies of Renard and Thompson (1984) and Hanel (1971).

Fig. 5. Surface wind estimates from geostrophic approximations. Data were from 27 Aug 1986 at 2000 GMT. Analyses are of:

(A) Geostrophic U-Component

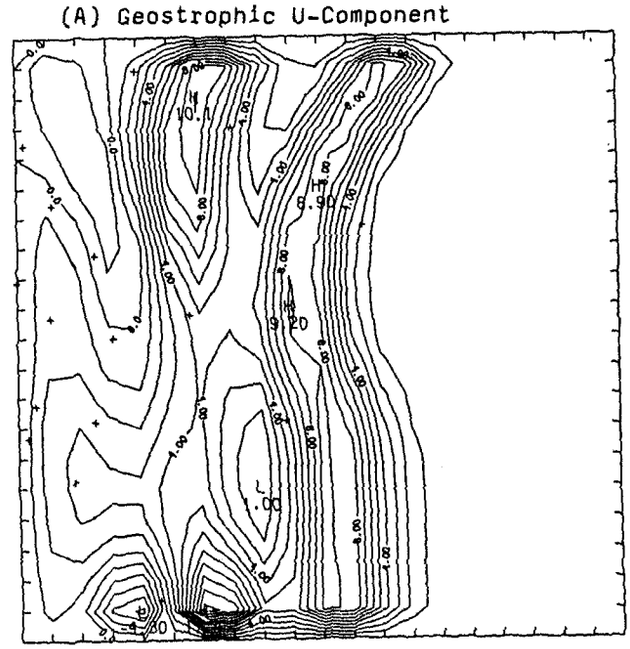

(A)

(B) Adjusted U-Component

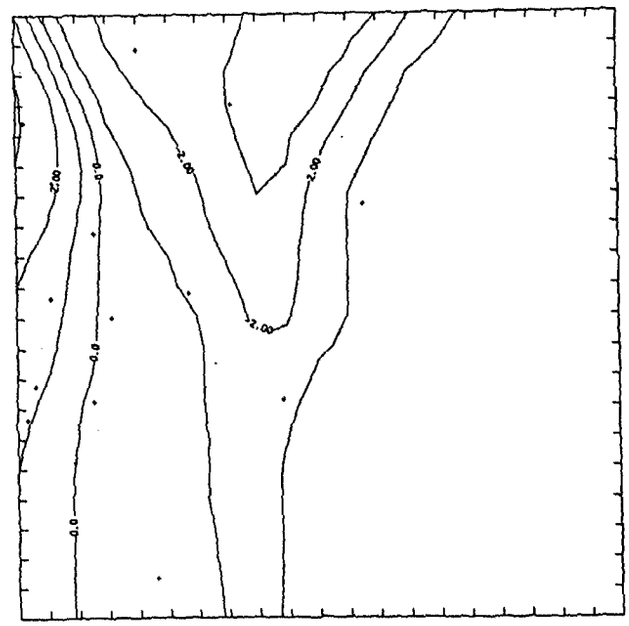

(B)

Relative humidity was expected to influence visibility by its effect on haze generation, and wind speed was thought to affect aerosol loading in the atmosphere. Additional parameters that are being tested for their ability to estimate visibility are precipitation and latent heat flux. Statistical evaluations of covariates to atmospheric visibility have been hampered by the

sparsity of reliable visibility measurements. None of the data sets gathered from the surface mesonetworks used in this study included visibility observations because of the difficulty of maintaining well-calibrated instruments capable of making automated measurements of that quantity. Compositing of data sets is being investigated as an interim method to obtain statistically significant results until in situ observations of visibility can be collected at appropriate spatial scales.

4. CONCLUSION

This study sought methods for combining multispectral satellite data with in situ observations at the surface and aloft to create an optimum analysis of mesoscale meteorological conditions. The raw satellite estimates of important meteorological fields were characterized by excellent spatial coverage, but they lacked the high degree of accuracy of the measurements from in situ sensors. The in situ data were used to calibrate the satellite analysis such that the accuracy of the satellite estimate also was improved outside the area covered by in situ data.

Results obtained so far are encouraging in that the satellite data yield estimates of the desired fields where no other information is available. The adjusted satellite-derived fields also fit the in situ observations better than the raw satellite estimates. Additional validation of the techniques that were developed remains to be done. The validation work will be accomplished by comparing the adjusted satellite estimates of particular fields against analyses from in situ data that will be withheld from the analysis procedure prior to the validation phase and that cover the region initially considered void of in situ data.

5. ACKNOWLEDGEMENTS

This paper is supported primarily by Contract # 2015 from the Army Research Office through Battelle Laboratories and, in part, by ONR Contract # N00014-86-C-0463.

6. REFERENCES

Barnes, S. L., 1964: A technique for maximizing details in numerical weather map analysis. J. Appl. Meteor., 3, 396-409.

Cunning, J., 1986: The Oklahoma - Kansas preliminary regional experiment for STORM-Central. Bull. Amer. Meteor. Soc., 67(12), 1478-1486.

Hanel, G., 1971: New results concerning the dependence of visibility on relative humidity and their significance in a model for visibility forecast. Beitr. Phys. Atmos., 44, 137-167.

Knight, C. A., 1982: The Cooperative Convective Precipitation Experiment (CCOPE), 18 May - 7 August 1981, Bull. Amer. Meteor. Soc.,63(4), 386-398.

Renard, R. J., and W. J. Thompson, 1984: Estimating visibility over the North Pacific Ocean using model output statistics. Nat. Wea. Dig., 9(2), 18-25.

Reynolds, D. W., 1983: Prototype work station for mesoscale forecasting. Bull. Amer. Meteor. Soc., 64, 264-273.

Rosenfeld, A. and A. C. Kak, 1976: Digital Picture Processing. Academic Press, N.Y., 457 pp.

Smith, W. L., 1983: The retrieval of atmospheric profiles from VAS geostationary radiance observations. J. Atmos. Sci., 40, 2025-2035.

3.5

TEMPORAL AND SPATIAL VARIABILITY AND CONTAMINATION OF 6.7 AND 7.3 MICROMETER WATER VAPOR RADIANCES

Keith G. Blackwell, James P. McGuirk and Aylmer H. Thompson

Department of Meteorology
Texas A&M University
College Station, TX 77843-3146 (409-845-4431)

1. INTRODUCTION

Accurate evaluation of the spatial and temporal distribution of atmospheric water vapor (WV) remains a problem over data-sparse areas. Rawinsonde measurements are by far the most reliable (Timchalk, 1986); yet rawinsonde information is virtually nonexistent over oceanic areas. Similarly, the eastern tropical Pacific Ocean is plagued by a scarcity of data; however, this data limitation became less of a problem during the FGGE year of 1979. FGGE's Special Observing Period 1 (SOP 1) provided an increase of meteorological observational data including additional land/ship launched rawinsondes reports and satellite-measured radiances.

Of the various wave bands sensed by the satellite-borne radiometers, the 6.7 μm and 7.3 μm wavelengths are very close and moderately close, respectively, to the wavelength which experiences the maximum absorption by (water vapor) WV in the troposphere. Therefore, 6.7 μm radiances (channel 12) are highly moisture sensitive, and the 7.3 μm band (channel 11) is moderately sensitive to moisture content of the troposphere. As a result of this sensitivity, these two wavelengths are used widely to detect variations of atmospheric moisture in time and space.

2. OBJECTIVE

The objective of this research is to evaluate the accuracy and synoptic information content of quantitative WV radiance data in a tropical area bounded by latitudes 10°S and 30°N and longitudes 90°W and 180°. The period of study is 21-29 January, 1979. Special attention is focused on the relationship between the moisture-sensitive radiances (6.7 μm and 7.3 μm channels) and the changes in the topography of a moist layer as measured by conventional "ground truth" rawinsondes.

3. BACKGROUND

Several studies (Chesters et al., 1982, Stout et al., 1984, Weldon and Holmes,[1] and Stewart et al., 1985) have focused on the vertical resolution of moisture sensitive satellite channels, especially the 6.7 μm band. Most of these studies indicate a potential relationship between the variation in the height of mid- or upper-tropospheric moist layers and the changes observed in WV brightness temperatures (BTs). In addition, Ramond et al. (1981), Stewart et al. (1985), Stewart and Fuelberg (1986) and Peterson et al. (1984), among others, associate high BTs with deep subsidence in the middle and/or upper troposphere. Roulleau (1978), Rodgers et al. (1976) and Steranka et al. (1973) concluded that WV imagery may be used as a tracer to delineate tropospheric dynamics, including mid-tropospheric vertical motions.

4. DATA

The data from FGGE SOP 1 consist of traditional observations, satellite information, and computer-generated analyses based on these data. The data set includes aircraft dropsondes, ship- and surface-launched rawinsondes, and satellite-derived BTs. The BTs used in this investigation were the moisture-sensitive channel 11 and 12 infrared (IR) radiances from the TIROS-N polar orbiting satellite.

The computer-derived ECMWF analyses are labeled FGGE IIIb. They include pressure surface wind fields which are available on a 1 7/8° by 1 7/8° gridded field, modified to a 3 3/4° by 3 3/4° gridded field of zonal (u) and meridional (v) components for 21-29 January 1979.

In addition to the FGGE data sets, infrared satellite imagery was used. This imagery was obtained from the GOES West satellite located above the equator near 130°W.

Dropsondes were not used because of their inaccuracy in measuring mid-tropospheric moisture (Velden et al., 1984). Dropsondes examined within the area of interest for this study possessed errors similar to those found by Velden, et al.

5. OBSERVED BRIGHTNESS TEMPERATURE SIGNATURES

The satellite BTs available within the analysis area over the 9-day period of study were located over the ocean and the adjacent land over the southwest United States, Mexico and Central America. Possible adverse terrain

[1]From a manuscript titled: "Characteristics of Water Vapor Imagery." Manuscript available from NOAA/NESDIS, Washington, D.C. 20233.

influences on the WV imagery were checked by testing the mean of 145 "continental" BTs from each channel with the mean of 180 adjacent "oceanic" BTs from each channel. Statistical tests detected no significant difference in BT means between ocean and land in either channel; therefore, high terrain was not significantly influencing the BTs over Mexico and the southwest United States. This conclusion was anticipated because both IR satellite imagery and rawinsondes indicated an extensive layer of mid- and upper-tropospheric moisture associated with an active synoptic cloud system blanketing this region. For drier conditions, topography may be a problem in this region.

A distribution of frequency of occurrence of channel 12 BTs as a function of observed temperatures is shown in Fig. 1. Constructed from 3330 TIROS-N 6.7 μm BTs recorded during the 9-day study period over the eastern Pacific, this distribution shows a skewed pattern in the direction of larger BTs. This skewness was nearly 10 times larger than the expected standard deviation of the skewness for a typical sample of this size taken from a true normal distribution. This pattern suggests a bimodal distribution in frequency of occurrence of BTs. Most BTs approximate a normal distribution about a mode of -17°C; a smaller group of higher BTs is clustered around -12.5°C.

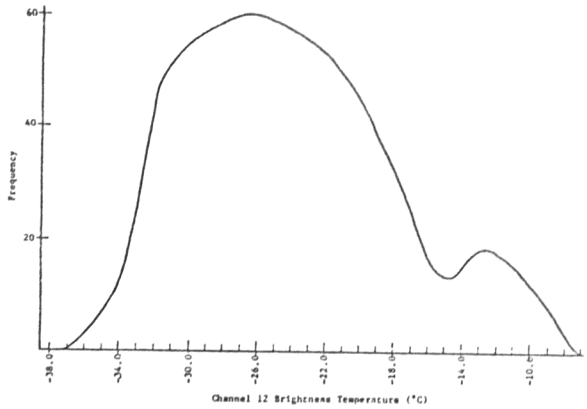

Fig. 1. Channel 12 brightness temperature (BT) frequency distribution. Frequency is given as the number of occurrences per 0.3°C interval out of 3330 observations.

The majority of the BTs in the frequency distribution were lower than -15°C. Although these lower BTs are distributed nearly normally, the peak was broad between -20°C and -32°C. The smaller group of BTs higher than -15°C appeared to show evidence of another frequency maximum between -11°C and -13°C.

Unlike the channel 12 BTs, the frequency distribution for 3330 TIROS-N 7.3 μm channel 11 BTs during the same period of time showed a pattern approximating a normal distribution with very little evidence of skewness toward higher BTs.

Evidence of a secondary frequency maximum in channel 12 BTs and the apparent absence of a secondary maximum in the frequency of occurrence of channel 11 BTs may be significant. Since the peak weighting of channel 12 typically occurs near the 500 mb level (Fig. 2), this secondary maximum of high BTs observed in Fig. 1 may be the signature of a synoptic feature in the upper troposphere.

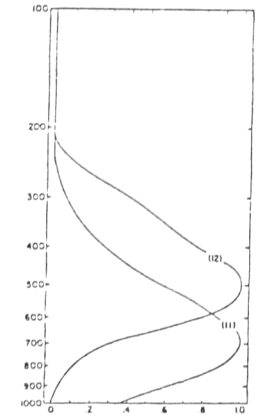

Fig. 2. TOVS weighting functions (normalized) for channel 11 (7.3 μm) and channel 12 (6.7 μm). After Smith et al. (1979).

Figure 3 shows the unenhanced window channel GOES West IR satellite imagery of the eastern Pacific at 0615 UTC 24 January 1979; the hatched region southwest of Hawaii displays the corresponding geographical distribution of channel 12 BTs observed on 24 January which were higher than -15°C. All of the BTs observed in this persistent cluster (hatched region in Fig. 3) fell within the smaller frequency maximum in Fig. 1, and also fell within a near cloud-free region southwest of Hawaii in Fig. 3. Without exception, this same pattern was observed each day throughout the period. From the 21st through 25th, these high BTs were clustered south and west of Hawaii and corresponded to large, mostly clear regions in the window channel imagery. Especially interesting was the location of these BTs directly adjacent to the western flank of a developing moisture burst (McGuirk et al., 1987). The region of high BTs elongated eastward and diminished during the last few days of the period as the moisture burst moved toward the east and weakened (Schaefer, 1985).

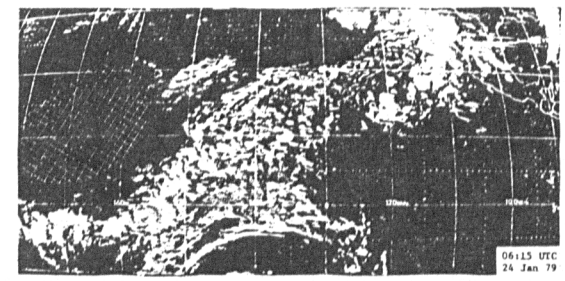

Fig. 3. Unenhanced window channel GOES West satellite image for 0615 UTC 24 January 1987. Hatched region southwest of Hawaii represents the geographical distribution of channel 12 BTs higher than -15°C for 24 January 1979.

The region southwest of Mexico (known as the Pacific dry zone) looked very similar in GOES West window channel imagery to the high BT region southwest of Hawaii; however, there was a noticeable lack of high BTs within this dry zone. This region south of Mexico remained free of any synoptic cloud systems throughout the

entire 9-day period and also remained virtually free of any BTs higher than -15°C which would be contained within the smaller channel 12 BT frequency maximum (see Fig. 1).

These findings suggest that the broad peak of the bimodal distribution in Fig. 1 may be related to the typical occurrence of low BTs associated with a normal to very wet mid and upper troposphere in the tropics; the smaller frequency peak of high BTs may be associated with an extremely dry mid- and upper-tropical troposphere. These extremely dry mid- and upper-tropospheric regions have been verified below 300 mb by rawinsondes. Moisture profiles above this level were generally not available from conventional rawinsonde soundings. This small set of high BTs seems to be related exclusively to certain synoptic disturbances over the eastern Pacific.

Similar to the sounding profiles southwest of Hawaii, rawinsonde soundings south of Mexico in the Pacific dry zone indicated very dry mid-tropospheres. However, the upper tropospheric profiles near the 300 mb level in the dry zone were moister.

It is hypothesized that the large area of extremely high channel 12 BTs observed near and south of Hawaii may be associated with deep tropospheric subsidence as previously suggested by several researchers. Furthermore, it is hypothesized that the movement and concentrated nature of these large channel 12 BTs relative to the active convection associated with a moisture burst may denote the subsidence branch of an intense, direct synoptic-scale circulation. This hypothesis is further substantiated by the observed shrinking of this BT area as the moisture burst weakens. Since channel 11 is more sensitive to moisture in the lower troposphere (see Fig. 2), the absence of a small secondary frequency peak in the higher BT region of the channel 11 distribution suggests that phenomena producing the secondary channel 12 peak may be an anomaly restricted to the upper troposphere. This absence of a secondary channel 11 peak also suggests that the subsidence of dry air does not extend into the tropical boundary layer. This lack of subsidence into the boundary layer was further evidenced by numerous soundings within the high BT region which indicated a moist surface layer overlain by dry air, separated by a pronounced inversion.

6. ESTIMATING TROPICAL SYNOPTIC VERTICAL MOTIONS

Initially, a procedure described by Stout et al. (1984) was used to estimate vertical motion; however, results were extremely discouraging. A relationship was developed between mid-tropospheric precipitable water (PW) thicknesses calculated from over 100 soundings, and collocated 6.7 μm and 7.3 μm water vapor BTs sensed by satellite.

The distribution of the upper 5 mm of PW for each sounding was calculated as a function of pressure by integrating the specific humidity downward from 300 mb at each reported sounding level. The pressure level associated with each 0.1 mm PW increment was referred to as a PW thickness pressure (PWTP). Although strong correlations (0.81 at the 0.6 mm PW thickness and 0.84 at the 0.9 mm PW thickness for channels 12 and 11, respectively) were obtained between these PWTPs and BTs (essentially a correlation between pressure and BT), a large root mean square (RMS) error was also observed.

Comparison of estimated vertical motions with adiabatically derived estimates, with velocity potential fields, and with outgoing longwave radiation fields demonstrated the failure of the technique in its current configuration. Therefore, the correspondence between mid- to upper-tropospheric moisture measured directly by rawinsonde with that sensed indirectly by satellite is questioned. It is hypothesized that the two moisture-sensitive satellite channels used in this study may have sensed moisture undetectable by conventional rawinsondes.

7. MOISTURE SAMPLING ERRORS

7.1 Comparisons of PWTP, BT and Sounding Profiles

If rawinsonde and satellite were actually sensing the same moist layers, then the rawinsonde/satellite plots of PWTP versus BT for each sounding location should fit closely to the composite linear regression curve for all sounding locations. Fig. 4 shows the 0.6 mm PWTP/channel 12 BT scatter plot for Johnston Island. Points marked "B" in this figure represent very dry soundings with most having less than 0.6 mm of PW above the 550 mb surface. Also shown is the distribution of "Bs" with respect to the linear regression curve for all the data shown in Fig. 9. The slope of the best fit curve for the data represented by the "B"s is different from the slope of the composite regression line. The nearly horizontal orientation of a best-fit line through this data plot suggests that the moisture profiles, as determined by rawinsonde for all 12 Johnston Island soundings, were very closely related. The 0.6 mm PWTPs for all the Johnston Island soundings varied by only 41 mb in range (12% of the total PWTP range shown in Fig. 9); however, the collocated channel 12 BTs differed up to 14°C (56% of the total BT range in Fig. 9).

Results for channel 11 are similar, but with less variation than in channel 12 BTs. This reduced variation suggests that the Johnston Island soundings may have closely resembled one another in channel 11 imagery. In contrast to channel 12 data, this smaller variation of channel 11 BTs also implied that channel 11 BTs may have recognized mean-profile similarities in soundings better than channel 12.

Similar Johnston Island soundings are shown for 0000 UTC on 23 January 1979 (Fig. 5a) and for 1200 UTC on 28 January 1979 (Fig. 5b). The 24°C wet-bulb potential temperature curve is shown on both soundings as a reference. On the 23rd, a strong inversion existed near 700 mb; on the 28th the inversion appeared near 800 mb. Both soundings were moist below and very dry (dew point depression defaulted to 30°C) above the inversion. Due to instrument limitations,

dew point depressions, as measured by rawinsonde, which were greater than or equal to 30°C were recorded as 30°C. Therefore, actual dew point depressions likely were greater than 30°C. More evidence of sounding similarity was shown by the rather insignificant 4 mb difference between their 0.6 mm PWTPs of 578 mb and 582 mb. Given these nearly identical rawinsonde soundings, one would expect only a small difference in collocated channel 12 BTs. Rather, the channel 12 BT difference between soundings was 12°C (46% of the BT range observed in Fig. 10). Although the sounding on the 28th was colder in the 400-300 mb layer, the absence of detectable moisture in this layer significantly lessened the layer's influence on the collocated channel 12 BT. Smaller, but significant, discrepancies were detected with channel 11 BTs as well.

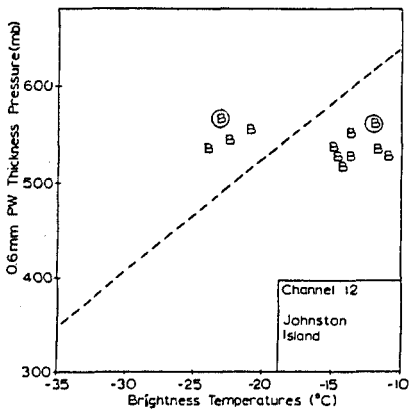

Fig. 4. Scatter plot of 0.6 mm PWTPs versus channel 12 BTs for Johnston Island (B = 91275). Circled letters correspond to the two soundings discussed.

7.2 Calculated versus Observed BTs

The potential of PW in the cold upper troposphere to affect channel 12 and 11 BTs was explored by comparing observed BTs to model-derived BTs. BTs were calculated from actual soundings by means of the GLAS Physical Inversion radiative transfer model (RTM) (Susskind et al., 1982). The RTM produced channel 12 weighting function curves from the Johnston Island soundings shown in Fig. 5. These weighting function curves are shown in Fig. 6. In layers where the sounding dew point depression defaulted to 30°C and moisture was systematically overestimated. This overestimation occurred between 750 mb and 300 mb in the two Johnston Island soundings. Moisture at pressures less than 300 mb was set to zero since rawinsonde moisture readings terminated at heights just above this level. Analogous to the soundings, the weighting function curves were similar, with both curves peaking near 500 mb. The collocated RTM and observed BTs at 0000 UTC on the 23rd were -10°C and -11°C, respectively; thus the correlation was excellent. However, the comparison at 1200 UTC on the 28th was extremely poor. As expected due to sounding similarity, the RTM BT remained high (-9°C) while the observed BT was -23°C, suggesting significant moisture in the atmosphere above 300 mb.

A more conclusive BT/sounding test was constructed using the detailed moisture information available from a limited number of special rawinsondes launched from scientific ships in the eastern Pacific. RTM channel 12 and channel 11 BTs were first computed from 1000-300 mb moisture profiles obtained from the ship-launched rawinsondes and these RTM BTs were compared to observed BTs. BTs also were calculated from the 1000-100 mb moisture profile available from the special soundings.

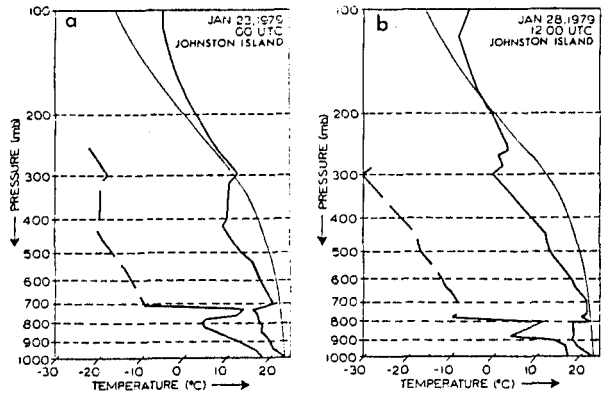

Fig. 5. Johnston Island Soundings for 0000 UTC 23 January 1979 (a) and 1200 UTC 28 January 1979 (b). The smooth curve in this skew-T log p plot represents the 24°C wet-bulb potential temperature. The jagged line on the right represents the temperature. The jagged line on the left represents the dew point. Dashed regions on the dew point curve represent dew point depressions ≥ 30°C.

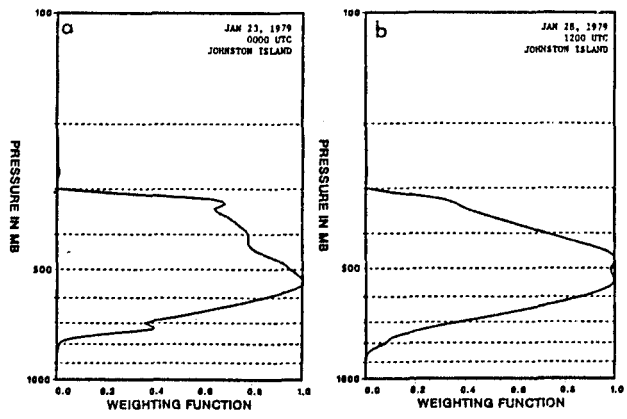

Fig. 6. RTM channel 12 weighting function profiles for the Johnston Island soundings at 0000 UTC 23 January 1979 (a) and 1200 UTC 28 January 1979 (b). Moisture has been deleted at heights above 300 mb. The slight weighting above 300 mb is not due to the influence of moisture on the RTM.

The Matamoros sounding from 2100 UTC on 26 January (Fig. 7a) is given as an example. For channel 12, the observed BT was -10°C; the RTM-calculated BT for moisture between 1000 and 300 mb was -8°C; and the RTM estimate including moisture between 300 and 100 mb (equivalent to 0.038 mm of PW) was -15°C.

The special sounding from 2100 UTC on 26 January (Fig. 7b) from the ship Pariz provides a second graphic example. Although the total PW contained in the 300-100 mb layer was only 0.187 mm, the channel 12 weighting function curves for the 1000-300 mb (Fig. 8a) and 1000-100 mb (Fig.

8b) moisture profiles were extremely different. The profile with moisture extending to the 100 mb level indicated nearly half the total area encompassed by this weighting curve occurred at heights above the 300-mb level. This large discrepancy in weighting function profiles produced correspondingly large differences in the RTM BTs: -15°C for the RTM computation, dry above 300 mb; -31°C for the RTM computation with moisture to 100 mb; and -35°C observed by the satellite over Pariz.

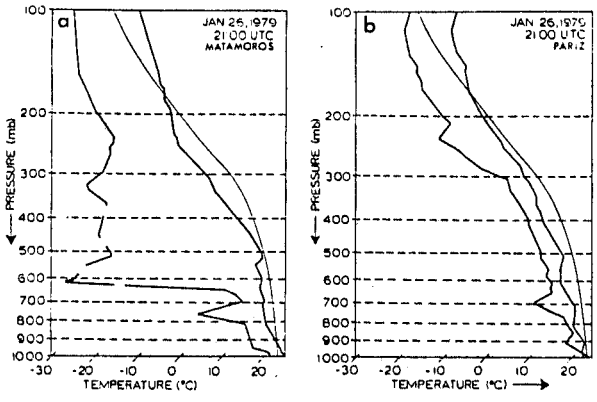

Fig. 7. As in Figure 5, except for 2100 UTC 26 January 1979 soundings for Matamoros ship at 7°N/91°W (a) and Pariz ship at 1°N/150°W (b).

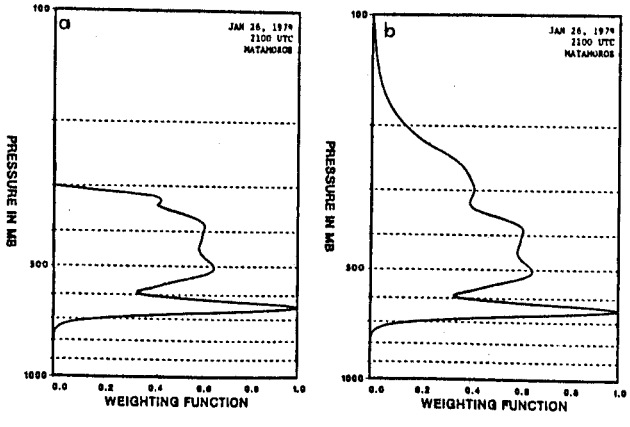

Fig. 8. RTM channel 12 weighting function profiles for the Matamoros ship sounding at 2100 UTC 26 January 1979. Moisture deleted at heights above the 300 mb level (a) and moisture deleted at heights above the 100 mb level (b). The slight weighting above 300 mb in (a) is not due to the influence of moisture on the RTM.

Finally, RTM BTs were calculated from all 111 rawinsondes, with moisture above 300 mb not included. These RTM BTs were compared to the collocated observed BTs and the discrepancies were analyzed on the scatter plot shown in Fig. 9. The drier soundings, associated with higher channel 12 BTs, produced better agreement with the RTM; the wetter soundings, coupled with lower BTs, produced poorer agreement. Special significance was given to the BTs in the upper right corner of the plot. Without exception, BTs higher than -14°C closely matched the BTs produced by the RTM. These were the same BTs encompassed within the very high channel 12 BT region observed in the subtropical Pacific to the northwest of the moisture bursts (see Fig. 3) and falling within the secondary frequency maximum observed in channel 12 BTs (see Fig. 1).

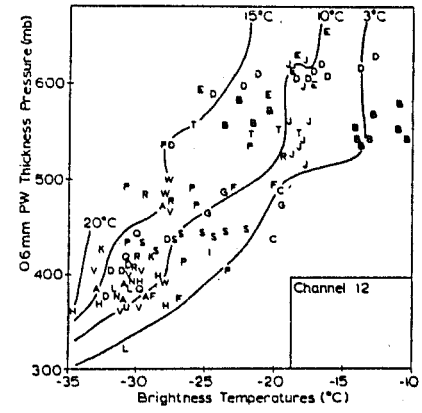

Fig. 9. Scatter plot of 0.6 mm PWTPs versus channel 12 BTs with overlaid observed-BT/RTM-BT difference contours. Each rawinsonde station is represented by a letter (A = 91700, B = 91275, C = 91066, D = 91165, E = 91285, F = 91487, G = CROMW, H = PARIZ, I = DISCO, J = MATAM, K = 76723, L = 76225, M = 76612, N = 72261, O = 76394, P = 76679, Q = 72255, R = 72250, S = 76692, T = 78641, U = 76256, V = 76458, W = 76654).

A less defined pattern was displayed in the channel 11 analysis (Fig. 10). In addition, the magnitudes of the differences between observed BTs and RTM BTs for channel 11 were significantly smaller than those for channel 12. Channel 11 seemed to be much less sensitive to the contaminating influence of upper tropospheric moisture than channel 12.

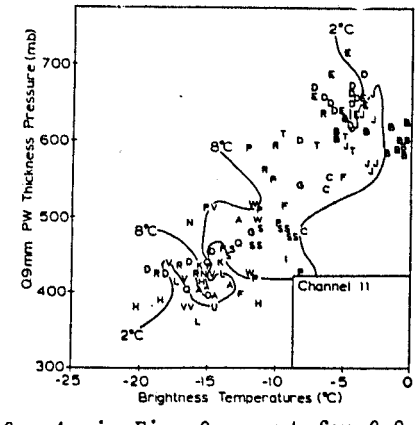

Fig. 10. As in Fig. 9 except for 0.9 mm PWTPs versus channel 11 BTs.

8. SUMMARY AND DISCUSSION

Initially, the high correlations obtained between moisture sensitive BTs (derived by satellite) and the upper few tenths of a millimeter of PW (derived from rawinsonde) measured at heights below the 300-mb level implied that the moist layers sensed by satellite were nearly identical to the ones measured by rawinsonde. However, the large RMS errors obtained when linear and polynomial curves were fitted to the satellite/rawinsonde comparisons suggested a more complex relationship. Minute quantities of upper tropospheric moisture, not detectable by conventional rawinsondes, significantly modulate the radiation signature emanat-

ing from lower levels. This upper moisture acts to mask the moisture profile in the middle and lower troposphere. Channel 11 was less affected by this upper tropospheric moisture than channel 12; yet, both channels were significantly influenced. Thus, evidence in this study indicates that satellites significantly sense the upper moist layer in the tropical troposphere while, in most situations, rawinsondes do not.

This discrepancy in sensing capability was observed over the vast majority of the eastern Pacific Ocean; therefore, an extensive layer of high tropospheric moisture, possibly concentrated just beneath the tropical tropopause, may be the rule rather than the exception. Indeed, all measurements reported by Kley et al. (1982) indicated saturated conditions in the vicinity of the tropical tropopause.

The concentrated area of very high BTs in the subtropical Pacific appears to have been the only region observed during this study where both satellite and rawinsonde consistently and correctly evaluated the top layer of tropospheric moisture actually present. Therefore, through some process, this upper moist layer must have been eliminated. As mentioned in several studies, very high channel 12 BTs have been associated with deep tropospheric subsidence; yet, these high BTs occurred in the tropical eastern Pacific only in a localized, nearly cloudless region south of Hawaii. From IR satellite pictures, a subsidence-dominated troposphere is also expected in the cloudless eastern Pacific dry zone to the south of Mexico; however, very few of the high channel 12 BTs were found there, and certainly not the highest. This discrepancy appears to be associated with the presence of upper tropospheric moisture over the eastern Pacific dry zone.

Finally, the observed closeness of the high BT region to the western flank of a moisture burst, the eastward movement of this BT region as the moisture burst moved eastward, and the areal shrinking of these high BTs concurrent with the weakening of the moisture burst indicate these BTs may be the descending branch of an intense, direct, synoptic-scale circulation. Furthermore, this deep subsidence may originate in the stratosphere and extend into the mid or lower troposphere.

9. REFERENCES

Chesters, D., L. W. Uccellini, and A. Mostek, 1982: VISSR Atmospheric Sounder (VAS) simulation experiment for a severe storm environment. Mon. Wea. Rev., 110, 198-216.

Kley, D., A. L. Schmeltekoph, K. Kelly, R. H. Winkler, T. L. Thompson, and M. McFarland, 1982: Transport of water through the tropical tropopause. Geophys. Res. Lett., 9, 617-620.

McGuirk, J. P., A. H. Thompson, and N. R. Smith, 1987: Moisture bursts over the tropical Pacific Ocean. Mon. Wea. Rev., 115, 787-798.

Petersen, R. A., L. W. Uccellini, A. Mostek, and D. A. Keyser, 1984: Delineating mid- and low-level water vapor patterns in pre-convective environments using VAS moisture channels. Mon. Wea. Rev., 112, 2178-2198.

Ramond, D., H. Corbin, M. Desbois, G. Szejwach, and P. Waldteufel, 1981: The dynamics of polar jet streams as depicted by the Meteosat WV channel radiance field. Mon. Wea. Rev., 109, 2164-2176.

Rodgers, E. B., V. V. Salmonson, and H. L. Kyle, 1976: Upper tropospheric dynamics as reflected in Nimbus 4 THIR 6.7 μm data. J. Geophys. Res., 81, 5749-5758.

Roulleau, M., 1978: Remote Sensing of the Atmosphere: Inversion Methods and Applications. Elsevier, 149-159.

Schaefer, J. R., 1985: Observing the synoptic structure of two moisture bursts. Masters Thesis, Texas A&M University, College Station, TX, 145 pp. (see pp. 38-66).

Smith, W. L., H. M. Woolf, C. M. Hayden, D. Q. Wark, and L. M. McMillin, 1979: The TIROS-N Operational Vertical Sounder. Bull. Amer. Meteor. Soc., 60, 1177-1187.

Steranka, J., L. J. Allison, and V. V. Salmonson, 1973: Applications of Nimbus-4 THIR 6.7 μm observations to regional and global moisture and wind field analysis. J. Appl. Meteor., 12, 386-395.

Stewart, M. R., and H. E. Fuelberg, 1986: Relationships between 6.7 micrometer imagery and radiosonde-derived parameters. Preprints, Second Conference on Satellite Meteorology/Remote Sensing and Applications, Amer. Meteor. Soc., Williamsburg, VA, May 13-16, 1986, 67-72.

Stewart, T. R., C. M. Hayden, and W. L. Smith, 1985: A note on water-vapor wind tracking using VAS data on McIDAS. Bull. Amer. Meteor. Soc., 66, 1111-1115.

Stout, J., J. Steranka, and R. A. Petersen, 1984: Vertical displacements of the mid-tropospheric water vapor boundary in the tropics derived from the VISSR Atmospheric Sounder (VAS) 6.7 μm channel. Preprints, Conference on Satellite/Remote Sensing and Applications, Amer. Meteor. Soc., Clearwater Beach, FL, Jun. 25-29, 1984, 86-89.

Susskind, J., J. Rosenfield, D. Reuter, and M. T. Chahine, 1982: The GLAS physical inversion method for analysis of HIRS2/MSU sounding data. Tech. Memo. No. 84936, NASA, Goddard Space Flight Center, Greenbelt, Maryland 29771.

Timchalk, A., 1986: Satellite derived moisture profiles. Preprints, Second Conference on Satellite Meteorology/Remote Sensing and Applications, Amer. Meteor. Soc., Williamsburg, VA, May 13-16, 1986, 64-66.

Velden, C. S., W. L. Smith, and M. Mayfield, 1984: Application of VAS and TOVS to tropical cyclones. Bull. Amer. Meteor. Soc., 65, 1059-1067.

3.6

IDENTIFICATION AND RECOVERY OF DISCONTINUOUS SYNOPTIC FEATURES IN SATELLITE-RETRIEVED BRIGHTNESS TEMPERATURES USING A RADIATIVE TRANSFER MODEL

G. A. White, III, J. P. McGuirk and A. H. Thompson

Department of Meteorology
Texas A&M University
College Station, Texas 77843-3146

1. INTRODUCTION

Meteorological analysis over critically data sparse areas, such as tropical oceans, is dependent, in part, on remotely sensed data from satellites. In the classic retrieval method, a portion of the satellite channel brightness temperature data and a knowledge of the climatological conditions of the region and season are used in algorithms to reconstruct atmospheric vertical temperature profiles. Despite the success of conventional retrieval methods, additional unused information may be present in the satellite channel data.

McGuirk et al. (1985, 1986) used empirical orthogonal function (EOF) analysis of satellite data to explore the structural detail of the atmosphere. They found that individual channel brightness temperatures may be preferable to reconstructed temperature and moisture profiles because the reconstructions are smoothed both horizontally and vertically.

The objective of this study is to recover and identify discontinuous synoptic features directly from satellite-retrieved brightness temperatures. Of special interest are the meteorologically important elements of an atmospheric sounding; namely, the near discontinuities in temperature and moisture found typically in fronts and inversions. The techniques used to create conventional reconstructed temperature and moisture profiles from satellite data unavoidably smear these discontinuities and contaminate their signatures. In pursuit of the objective, this study poses two main questions: can vectors of satellite channel brightness temperatures be classified by synoptic source (e.g., fronts, inversions, etc.), and can these sources be quantified?

To answer these questions, a synthetic climatology of atmospheric temperature and moisture soundings was chosen, containing well-defined synoptic features representative of those found over the tropical eastern Pacific Ocean. The temperature and water vapor variables in each of a set of "seed soundings" were perturbed randomly, within narrow limits, to create a statistically meaningful training data set of 50 soundings for each seed sounding. Each sounding was transformed by a non-linear radiative transfer model (RTM) to a vector of 22 of the 24 individual satellite channel brightness temperatures which would have been observed had TIROS N satellite sensors viewed that vertical section of the atmosphere. (Two channels were omitted because they contain no relevant information for this study.)

The brightness temperature vectors arising from the training data sounding groups were classified and labeled as to their known synoptic features using two methods: (1) *a priori* through knowledge of the initial seed sounding and (2) objectively through cluster analysis (Johnson and Wichern, 1982). Both methods led to nearly identical results.

Finally, to test the ability of the system to associate unknown soundings with recognizable synoptic features, temperature and dewpoint temperature profiles containing synoptic features not originally part of the sounding climatology were evaluated by the RTM. The resulting satellite channel brightness temperature vectors were added to the sounding climatology which was then evaluated by canonical discriminant analysis (CDA).

CDA serves three purposes: first, it confirms (or refutes) the initial classifications of the sounding climatology; second, it quantifies the basis for synoptic classification (Johnson and Wichern, 1982); and finally, it places the unknown brightness temperature vectors in the physically most similar family in the sounding climatology. Identification of the synoptic features found in brightness temperature vectors is accomplished in a relative sense by comparison rather than by iterative solution of the radiative transfer equation.

2. METHOD

2.1 Radiative transfer model

As in similar studies, the need for collocated satellite observations and upper air data was evident. However, since this work focuses on the development of statistical techniques, the use of synthetic atmospheric temperature and moisture soundings and a RTM to produce satellite channel brightness temperature vectors provided a simplified approach. The combination of soundings and RTM posed two distinct advantages: first, it allowed the flexibility to study any synoptic feature for which atmospheric vertical profiles could be drawn, and second, the complex signals found in real soundings were eliminated.

The RTM was developed at NASA Space Flight Center's Laboratory for the Atmospheres

and is documented by Susskind et al. (1982). It is a non-linear 66-layer (surface to 1 mb) rapid transmission algorithm which directly calculates brightness temperatures for HIRS and MSU channels on board TIROS N. Because of its non-linearity, the model slightly increases the variability of the atmospheric temperature and dewpoint temperature information.

2.2 Sounding classification

Vertical soundings of temperature and dewpoint temperature were created to represent typical synoptic conditions found over the tropical eastern Pacific Ocean. The soundings were coded according to their synoptic origin. Natural variation in the soundings was introduced by modifying randomly the seed sounding temperature and mixing ratio by as much as ± 2 percent in each of the 66 layers of the RTM. The variability was distributed as white noise. Fifty perturbation iterations were calculated from each seed to create a statistically meaningful sounding climatology each containing a synoptic signature.

2.3 Retrieval vs classification

Direct reconstruction of vertical atmospheric profiles from satellite sounding data is not possible (Chahine, 1970). The retrieval of blackbody radiation requires inversion of the radiative transfer equation. No stable solution can be obtained by simultaneous integral equations for each satellite channel because of the redundancy resulting from overlap of channel weighting functions. A stable solution normally is obtained by introducing another condition—an average observed temperature profile appropriate to the location and season. The brightness temperatures are used to find small deviations from the climatological mean profile. There is some bias toward the mean sounding, and the method works best for small deviations from the main sounding. Further, this successive approximation method produces a profile of temperature only; moisture retrievals rely on other approaches.

The method described here is similar to conventional temperature retrieval techniques in that it requires statistical comparison of satellite data products to known soundings. However, there are two distinct advantages: (1) moisture, as well as temperature, retrieval is possible; and (2) smoothing that takes place in the conventional retrieval process is minimized.

2.4 Canonical discriminant analysis (CDA)

Canonical correlation analysis is a generalization of regressing one variable on another; i.e., regressing one vector on another vector. CDA extends this concept by regressing the random variables of satellite channel brightness temperatures on dummy variables (class of atmospheric sounding, in this case). CDA is related to EOF analysis; the main difference is that EOF analysis seeks to interpret total variance while CDA attempts to explain primarily between-class variance. Thus CDA accounts for within-class means and serves to discriminate among groups by responding to between-class variance.

Analyzing the satellite channel brightness temperature vectors with CDA has two purposes. The first is to confirm the classification of individual soundings by noting clustering of canonical variates. The second is to find sets of linear combinations of variables that best describe the physical differences of the synoptic features as represented by the various clusters (Smith and Woolf, 1976).

2.5 Physical interpretation of CDA

The brightness temperature vectors resulting from RTM analysis of the perturbations of the original seed soundings and their synoptic classifications constitute a training data set. When evaluated by CDA, the training data become separated according to between-sounding-class variance. The greatest variance is explained by the first canonical variable and successively smaller amounts of variance are explained by additional canonical variables. In this fashion, CDA reveals a physical basis for the sounding group separation and thus suggests synoptic signatures which are present in the channel brightness temperature vectors.

A physical representation of the canonical variables is seen in the correlation coefficients of satellite channel brightness temperatures. A large coefficient (absolute value) indicates that a channel is a significant contributor to the variance for a given canonical variable. With a knowledge of the atmospheric variables to which a channel is sensitive (Smith et al., 1979) and a summary of between-class canonical correlation coefficients, each brightness temperature channel is assigned membership in appropriate canonical variables. Since most of the between class variance is associated with the first canonical variable (CAN 1), the greatest separation of sounding groups is revealed by the amplitude of this canonical variable. Lesser variance is carried by, and hence lesser separation is shown by, subsequent canonical variables. Normally, the first three canonical variables account for most of the variance. For example, if HIRS channels 10 and 11 (the water vapor channels) constitute the major contribution to the first canonical variable, then CAN 1 derives the variance it represents from lower tropospheric water vapor fluctuations. Similar inferences may be drawn from interpretation of the correlation matrices and assignment of additional TIROS N channels to the remaining canonical variables.

3. DATA

A small data base was constructed using seven seed soundings representative of conditions often found over the tropical Pacific Ocean. The soundings were perturbed randomly to create the training data set as described above. Two additional test soundings, depicting similar but distinctly different synoptic features than contained in the training data set were introduced in the analysis procedure.

3.1 Training data set

While seven soundings are not a complete representation of conditions found over the tropical Pacific Ocean, they present an adequate group for testing the method described here. The seed soundings are shown in Fig. 1. The envelope of perturbed temperature and moisture soundings for sounding class 1 is shown in Fig. 2.

The synoptic conditions in the lower troposphere are of most interest, and oftentimes upper tropospheric moisture shields the lower troposphere from satellite view especially in the moisture channel wavelengths. Therefore, temperatures and dewpoint temperatures above 600 mb were kept constant at values consistent with the tropical eastern Pacific atmosphere in an attempt to stabilize RTM performance at upper levels.

3.2 Test soundings

Two real soundings, distinctly different from, but typical of the tropical eastern Pacific Ocean, were introduced to test the sounding identification and classification method. These soundings were not perturbed. They are shown in Fig. 3.

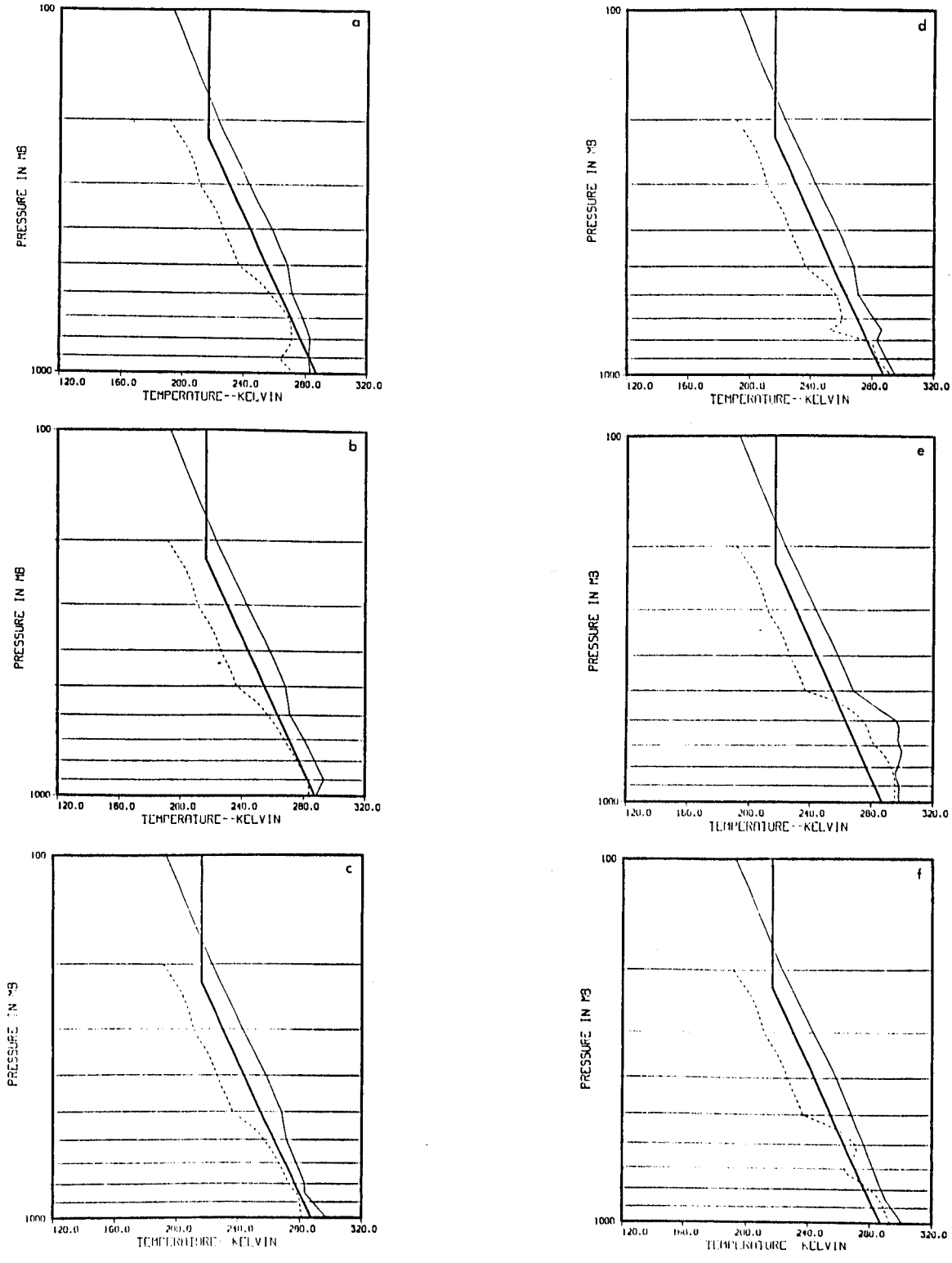

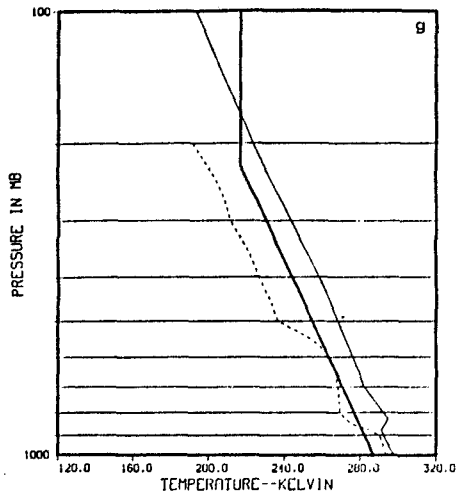

Fig. 1. Seed soundings for training data. Heavy line is tropical standard atmosphere, for reference. a) Sounding #1. Frontal inversion, surface to 850 mb. Cool surface temperature, dry throughout. b) Sounding #2. Radiation inversion, surface to 900 mb. Moist at surface, drying at inversion and remaining dry aloft. c) Sounding #3. Turbulence inversion resulting from well-mixed layer. Very dry at surface, turning moist at 850 mb. Inversion from 850 to 800 mb. Top of inversion starts dry layer to 600 mb. d) Sounding #4. Trade wind inversion, 800 to 750 mb. Moist surface layer, drying slightly at 900 mb, becoming moist again at 800 mb, then drying significantly at 750 mb. e) Sounding #5. Tropical cyclone. Warm and moist at surface, saturation at 850 mb, strong drying and significant warming aloft. Inversion, 850 to 650 mb. f) Sounding #6. Carrizal (9.5 °N, 67 °W). July. Warm surface, moist layer at 850 mb, with pronounced dryness at 700 mb, converging to moist layer at 600 mb. g) Sounding #7. Subsidence inversion in warm anticyclone. Warm and moist, surface to 850 mb. Inversion 850 to 800 mb with pronounced dry layer at 800 mb.

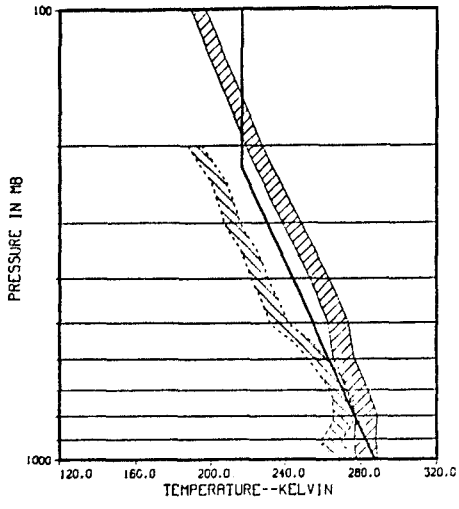

Fig. 2. As in Fig. 1a, with perturbation envelope shown. Random perturbation is ± 2%, distributed as white noise. Seed sounding makes vertical ascent through center of envelope.

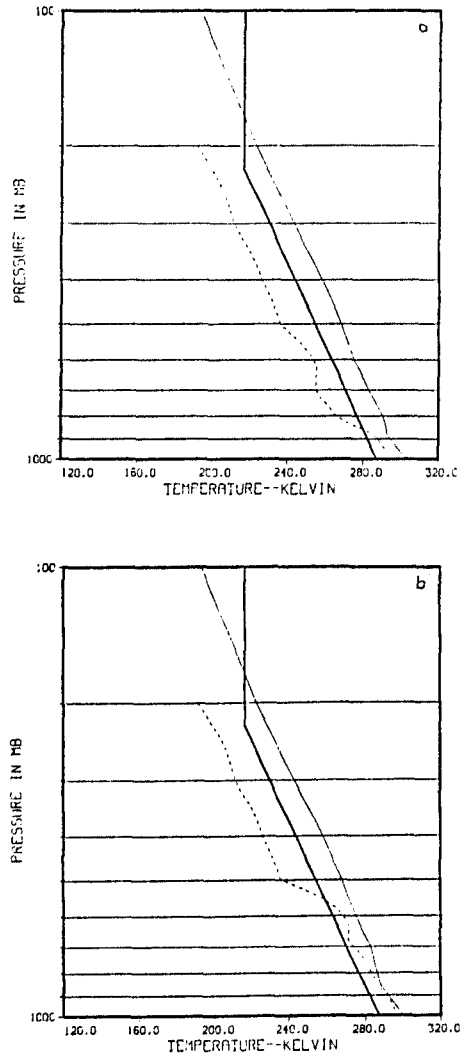

Fig. 3. Test soundings A and B, both 11 July 1957, 0000 UTC. a) Test sounding A. Kwajalein Island. b) Test sounding B. Majuro Island.

3.3 Brightness temperature vectors vs soundings

It should be remembered that the analysis procedure acts on brightness temperature vectors created for each sounding by the radiative transfer model. Conventional temperature and moisture sounding plots are shown for the seed and test soundings as a convenience in interpretation.

4. RESULTS

4.1 Cluster analysis

After evaluation by the RTM, the training data set brightness temperature vectors were classified and labeled according to their synoptic origins. The classifications were made two ways: (1) *a priori* through knowledge of the generating seed sounding, and (2) objectively through cluster analysis. In this study, both methods led essentially to the same results, i.e., cluster analysis reproduced almost the same sounding groupings as did the generating procedure.

4.2 Canonical discriminant analysis (CDA)

The linear combinations, or canonical variables of the channel brightness temperatures derived by CDA, explain between-sounding-class variance. The first canonical variable, CAN 1, carries nearly 90 percent of the variance. The second canonical variable, CAN 2, accounts for nearly 9 percent of the variance, and CAN 3 reveals slightly less than 1 percent. Cumulatively, the first three canonical variables account for nearly 99 percent of the between sounding class variance. These canonical variables may be accepted with confidence according to the results of Wilks' Lambda and associated T^2 tests.

4.3 Physical interpretation of CDA

Table 1 summarizes the interpretation of individual satellite channel membership in the first three canonical variables. CAN 1 is comprised of surface window and channels sensitive to lower-tropospheric temperature variations. The near surface water vapor channel, channel 10, is included in CAN 1.

CAN 2 is dominated by the mid-tropospheric moisture channels, 11 and 12, and most tropospheric temperature channels. One stratospheric channel makes a minor contribution.

Table 1. Satellite channel assignment to canonical variables.

CAN 1		
HIRS/MSU Channel	Level of peak Energy (mb)	Purpose of the radiance observation
7	900	Temperature sounding
8	Surface	Window
10	900	Water vapor sounding
13	1000	Temperature sounding
14	950	Temperature sounding
18	Surface	Window
19	Surface	Window
MSU 1	Surface	Surface emissivity

CAN 2		
HIRS/MSU Channel	Level of peak Energy (mb)	Purpose of the radiance observation
1	30	Temperature sounding
4	400	Temperature sounding
5	600	Temperature sounding
6	800	Temperature sounding
11	700	Water vapor sounding
12	500	Water vapor sounding
15	700	Temperature sounding
16	400	Temperature sounding
MSU 2	700	Temperature sounding
MSU 3	300	Temperature sounding

CAN 3		
HIRS/MSU Channel	Level of peak Energy (mb)	Purpose of the radiance observation
2	60	Temperature sounding
3	100	Temperature sounding
MSU 4	90	Temperature sounding

CAN 3 represents only about 1 percent of the between sounding group variance and is derived exclusively from stratospheric channels at or above 100 mb. No variation in channels sensitive to upper level radiation was expected, because temperature and dewpoint temperature in the original seed and test soundings were kept constant above 600 mb. A possible explanation of the variation is absorption from below and re-radiation at higher levels within the RTM.

4.4 Canonical variable plots

The canonical variables define sounding group separation as shown in Fig. 4. Plots of CAN 2 vs CAN 1 and CAN 3 vs CAN 1 depict sounding clusters and illustrate the between-group variance exhibited by the three canonical variables.

When plotted, the three canonical variables may be thought of as a three-dimensional representation of the variance of the sounding groups. Based on the physical interpretation of the canonical variables, the CAN 1 axis represents sounding group separation due to surface and near-surface temperature and moisture variability. The CAN 2 axis displays tropospheric temperature and moisture variability, and the CAN 3 axis describes minor variations of stratospheric temperature.

It is significant to note that the physical interpretation of variance groups revealed by this study is unique to this sounding climatology. Indeed, close examination of the seed soundings in Fig. 1 confirms that the greatest difference occurs in surface and near surface temperature in accordance with CDA results. Successive and thus lesser sounding differences are beyond the resolution of the seed sounding plots.

4.5 Identification of test brightness temperature vectors

The two test soundings introduced into the training data set and evaluated by the RTM appear as points A and B in Fig. 4. The points seem closest to seed sounding 6. The assignment is confirmed by the Mahalanobis distance calculations (a measure of cluster spacing) in Table 2.

Table 2. Mahalanobis distances between sounding classes.

Sound	A	B	1	2	3	4	5	6	7
A	.	25.91	88.00	67.30	29.44	36.27	35.01	19.19	26.26
B	25.91	.	70.19	49.89	18.60	22.13	20.90	8.98	12.25
1	88.00	70.19	.	21.76	59.73	52.13	68.46	75.12	63.71
2	67.30	49.89	21.76	.	39.51	31.43	48.16	54.52	42.70
3	29.44	18.60	59.73	39.51	.	9.18	28.21	18.70	9.62
4	36.27	22.13	52.13	31.43	9.18	.	27.22	24.83	13.14
5	35.01	20.90	68.46	48.16	28.21	27.22	.	23.52	20.01
6	19.19	8.93	75.12	54.52	18.70	24.83	23.52	.	12.74
7	26.26	12.25	63.71	42.70	9.62	13.14	20.01	12.74	.

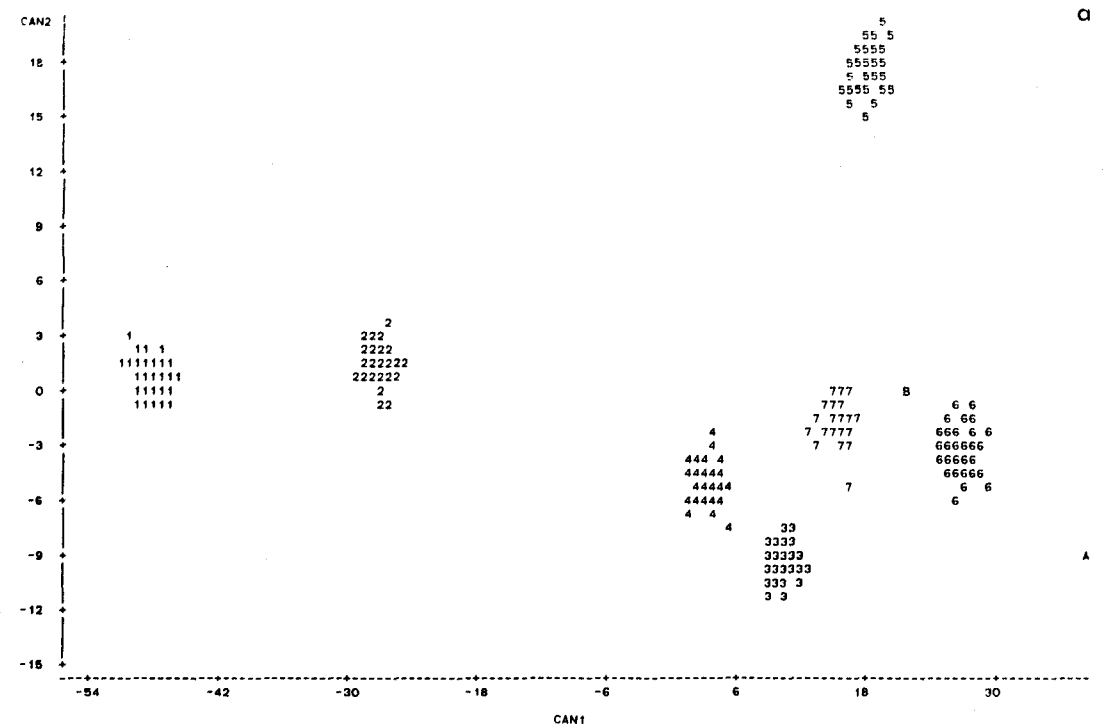

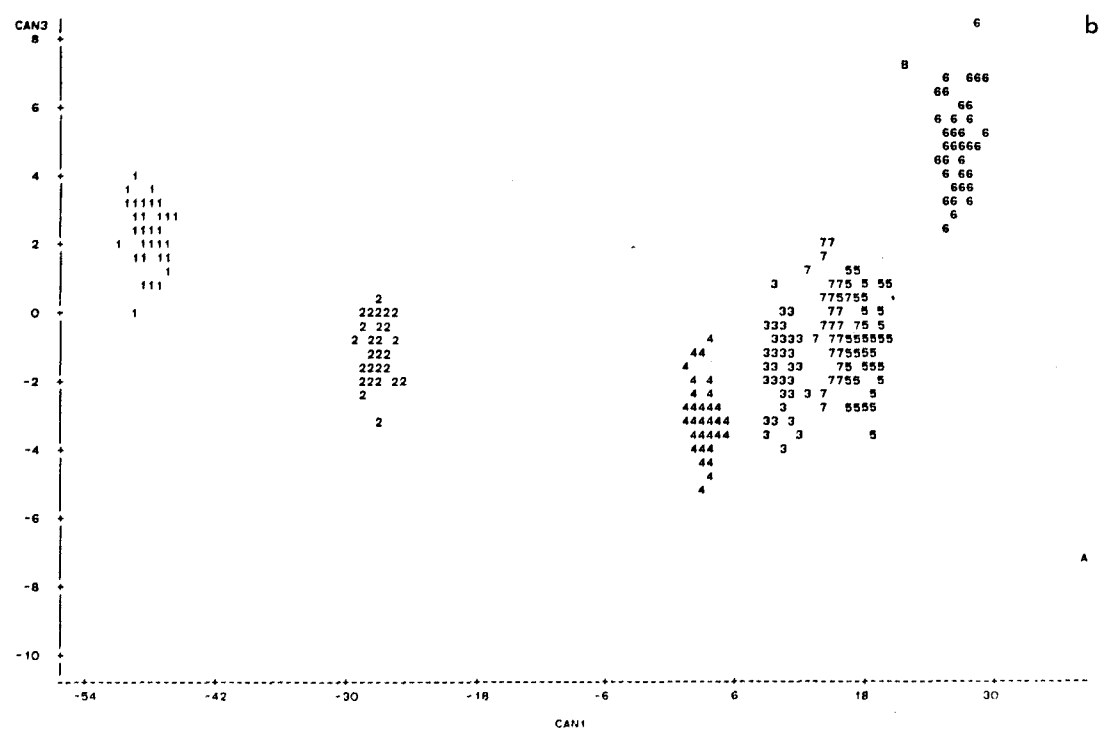

Fig. 4. Canonical discriminant analysis plots. Distribution of all synthetic soundings (1-7) and real soundings (A and B). For amplitudes of a) CAN 2 vs CAN 1, and b) CAN 3 vs CAN 1. Canonical variables are described in the text and in Table 1.

The physical characteristics of the two test soundings indeed are similar to seed sounding 6 (Fig. 1 f). Test sounding A is taken from Kwajalein (July) and test sounding B is taken from Majuro (July). Seed sounding 6 is based on Carrizal (July). All are warm at the surface. Carrizal and Majuro show increasing saturation from the surface to about 850 mb while a constant dewpoint depression is maintained from the surface to 850 mb at Kwajalein. From 850 mb to 700 mb, all three soundings present a layer of pronounced dryness which lapses into another moist layer at approximately 600 mb.

The Mahalanobis distance table confirms the next seed sounding with similar characteristics is 7 (Fig. 1 g). It is a composite sounding created to represent a warm anticyclone subsidence inversion. While not as warm at the surface, there is increasing moisture to about 850 mb, a layer of pronounced dryness at 800 mb (vice 700 mb), and a gradual increase in moisture from 800 mb to 600 mb. In general, the conditions are similar to seed sounding 6.

5. CONCLUSIONS

It has been shown that is it is possible to associate TIROS N channel brightness temperature vectors with synoptic features. The success of this approach is dependent entirely on the judicious choice of seed soundings, the allowable spread of soundings about the seed, and the quality of the radiative transfer model which produces the brightness temperatures from atmospheric variables.

The method is not without difficulties. Most of the variance is carried in the first canonical variable. Unfortunately, in this study, the channels appearing in CAN 1 are sensitive primarily to surface or near surface conditions. The atmospheric conditions of greatest interest—mid- to lower tropospheric temperature and moisture variations—appear in the second canonical variable, CAN 2, which carries a smaller percentage of the variance. The third canonical variable carries variance of little use in sounding identification.

One is reminded that canonical discriminant analysis focuses on the between-class variance. Within-class variances are an important, but often overlooked, byproduct of CDA. Evaluated properly, within-class variances may reveal how soundings within a given cluster differ and may lead to quantification of synoptic signatures directly from satellite channel brightness temperatures.

6. ACKNOWLEDGEMENTS

The research reported here is supported by NASA's George C. Marshall Space Flight Center, under Contract No. NAS8-37284. The radiative transfer model was provided by J. Susskind and D. Reuter of the NASA Goddard Laboratory for Atmospheres. R. Liles provided computational support. N. Streetman prepared figures and assembled the manuscript.

7. REFERENCES

Chahine, M. T., 1970: Inverse problems in radiative transfer: Determination of atmospheric parameters. *J. Atmos. Sci.*, 27, 960-967.

Johnson, R. A. and D. W. Wichern, 1982: *Applied Multivariate Statistical Analysis.* Prentice Hall, 594 pp.

McGuirk, J. P., L. L. Anderson and A. H. Thompson, 1985: Satellite-derived synoptic climatology in data-sparse regions. *Adv. Space Res.*, 5(6), 45-48.

———, A. H. Thompson and L. L. Anderson, 1986: Wintertime disturbances in the tropical Pacific: FGGE IIIb and satellite comparisons. Preprint from National Conference on Scientific Results of the First GARP Global Experiment, Miami, Jan. 1986, 4 pp.

Smith, W. L. and H. M. Woolf, 1976: The use of eigenvectors of statistical covariance matrices for interpreting satellite sounding radiometer observations. *J. Atmos. Sci.*, 66, 1127-1150.

———, H. M. Woolf, C. M. Hayden, D. Q. Wark and L. M. McMillin, 1979: The TIROS-N operational vertical sounder. *Bull. Am. Meteor. Soc.*, 58, 1177-1187.

Susskind, J., J. Rosenfield, D. Reuter and M. T. Chahine, 1982: The GLAS physical inversion method for analysis of HIRS2/MSU sounding data. NASA Tech. Memo. 84936, Goddard Space Flight Center, Greenbelt, MD, 101 pp.

SPATIAL SCALE OF RADIATION TO SPACE: A SPECTRAL AND STRUCTURE FUNCTION ANALYSIS OF SATELLITE IMAGERY

G.G. Campbell and T.H. Vonder Haar

CIRA/CSU
Ft. Collins, CO 80523

1. Introduction

A visual qualitative look at satellite imagery seems to show different characteristic spatial scales. We have prepared a spectral analysis of several different maps of emitted radiance to examine this scaling. Using high resolution (10 km) data from GOES one sees a red spectrum over regions on the order of 1000 km. Cahalan et al. (1982) looked at similar statistics from lower resolution data to infer effects of cloud fluctuations. Our hypothesis is that smaller scale fluctuations separate from the large scale weather phenomina and thus subgrid scale parameterization is a reasonable idea. Of course the primary source of smaller scale changes are cause by the presence or absence of clouds.

2. Data

We will present results primarily from observations from the 11 um window channel instruments on geosynchronous satellites. As a Sector Processing Center for the International Satellite Cloud Climatology Project (ISCCP) we have access to a large body of observations from GOES 6 at 10 km resolution. For GOES 6 we have analysed the region for 40 north to 40 south latitude and 65 west to 145 west longitude (a region centered on the satellite sub point). In addition we have looked at some preliminary results from the global analysis of ISCCP which is a composite of 4 geosynchronous satellites and AVHRR, again from 40 north to 40 south but for the whole latitude belt. The orginal satellite counts were converted to spectral radiance by the Plank function evaluated at 11 um. Subtle details of the spectral response functions and varing absorption characterists of the atmosphere should have no impact on our results.

2. Analysis

A spectral analysis is an easy way to summarize the spatial distribution of the radiance field. One can transform a spatial function, f, into spectral coefficients, C, as a function of wave number, $\underline{k}$, via a Fourier transform, eq 1.

Eq 1. $f(\underline{r}) = \sum C(\underline{k})\exp(-i\underline{k}\cdot\underline{r})$

The two dimensional spectra are nearly axially symmetric so it is reasonable to average for all equal wavelengths giving a one dimensional spectra. As we will discuss below these spectra are very red, fig 1.

In addition one can construct the spatial covariance directly from the spectra via equation 2.

Eq 2.
$\mathrm{Cov} = \langle f(\underline{r})\ f(\underline{r}+\underline{d})\rangle = \sum C^{*}C\ \exp(-i\underline{k}\cdot\underline{d})$

where < > denotes the average value. This can also be transformed to the spatial structure function, $S(\underline{d})=(1-\mathrm{Cov}(\underline{d})/\mathrm{Variance})$. Again this is nearly axially symmetric, fig 2, so an average over equal distance will be a good measure of the one dimensional structure function or the correlation function.

3. Results

Several images from April, 1985 were processed. Each pixel had resolution of 10 km and were separated by about 32 km. These times were selected without regard to the synoptic situation and represent a very small random sample of the weather. Figure 1 shows a superposition of the spectra from the many images. The fact that these all look the same implies that the spectra have the same shape irrespective of the synoptic situation. Figure 2 shows the two dimensional structure function of one image. This is very much like the spatial correlation functions shown by Cahalan et al. (1982) or Charlock et al. (1988) where 2.5 degree regional averages were used for each grid point. Figure 3 shows the superposition of several one dimensional structure functions again showing the uniformity of the statistics. The structure follows closely a log-log relation to distance up to about 1500 km.

To expand the study we processed some 2.5 degree (about 280 km) average data from the global analysis of ISCCP. This data data was a composite of GOES 6, GOES 5, METEOSAT, GMS and AVHRR. The

use of the geosynchronous data allows an instantaneous view of the whole globe rather than a composite over 24 hours as used by Cahalan or Charlock. Figure 4 shows the structure function of several global images superimposed on those from the smaller regions and higher resolution data shown in figure 3. The break in the structure lines occurs in both these data at about 1500 km.

4. Discussion

The spectral and structure analysis of data from 10 km to global scale shown above shows that the radiation field is highly correlated up to 1500 km. This supports the analysis schemes of several large experiments like ISCCP and the Earth Radiation Budget Experiment which collect averages on a 2.5 degree grids. This 280 km resolution is quite adequate to detect changes in the mean weather and climate. If the subgrid scale processes are adequately modeled then the grid spacing of most general circulation modeling at about 1000 km is adequate. For instance the Community Climate Model at NCAR has a resolution of 800 km by 500 km (Washington, 1982).

Charlock and Smith (1987) have discussed the fact that the variance of long wave radiance as calculated by a GCM is larger than the variance seen in satellite observations. The spatial correlation function may give clue to explain this difference. Leith (1973) discussed the suppresion of variance of standard deviation because of too frequent time sampling of a long time series. Because of the time autocorrelation between real geophysical fields variance measurements will be affected by the frequency of measurement. A similar problem arises in the estimation of variance of a geophysical field with different resolution measurement pixels. One would expect that the time variance of a radiation field measured with 280 km resolution would be smaller than one at 10 km. With the spatial correlations derived above one can calculate some estimate of the ratio of the variances. In analogy with Leith, one comes up with eq 3, as the ratio of the variance for two different pixel sizes, assuming a one dimensional covariance.

$$\text{Eq 3.} \quad r(a,b) = \frac{\int_c^a [1-(x/a)]\mathrm{Cov}(x)dx \,/a}{\int_c^b [1-(x/b)]\mathrm{Cov}(x)dx \,/b}$$

For the distributions of covariance shown above, one comes up with 1.25 for the ratio of variance comparing 10 km pixels with 280 km pixels.

To look at this empirically we processed a months worth of GOES 6 data recording the variance of all individual pixels in 2.5 degree regions as well as the variance of the individual regional averages. Figure 5 shows a plot of the ratio of the variances. This is substantially larger than the theory shown in equation 3 predicted, but in the right direction.

The empirical evidence as well as the theory show that the variance for small pixels is substantially larger than that of regional averages. If the model results are more a representation of points, than regional averages, then one would expect that the model variance would be higher than corresponding satellite data which are definitely regional averages.

5. Conclusions

The recording of climatologies of radiation fields on 2.5 degree grids is sufficient to record most of the relevant information. The modeling on a 500 km analysis grid is adequate for radiation analysis with parameterization of smaller scales. The spatial correlation of the radiance fields show that the variance of 280 km fields will be smaller than 10 km pixel variance. This may explain some of the difference seen in variance statistics from GCMs and variances from satellite observed radiation fields.

6. Acknowledgements.

This research was supported by NOAA under project NA85 RAH 05045 and NSF under project ATM 8401229.

7. References

Cahalan, R.F., D.A. Short and G.R. North, 1982: Cloud fluctuation statistics. Mon. Wea. Rev., 110, 26-43.

Charlock, T.P., Cattany-Carnes K.M. and F. Rose, 1988: Short time and space scale fluctuation statistics of outgoing infrared radiation in a general circulation model and satellite data. Mon. Wea. Rev. in press.

Leith, C.E. 1973: The standard error of time average estimates of climatic means. J. Appl. Meteor., 12, 1066-1069.

Smith, L.D. 1987, personal communication.

Washington, W., Ed., 1982: Documentation for the Community Climate Model, Climate Section, NCAR, Boulder, CO 80307.

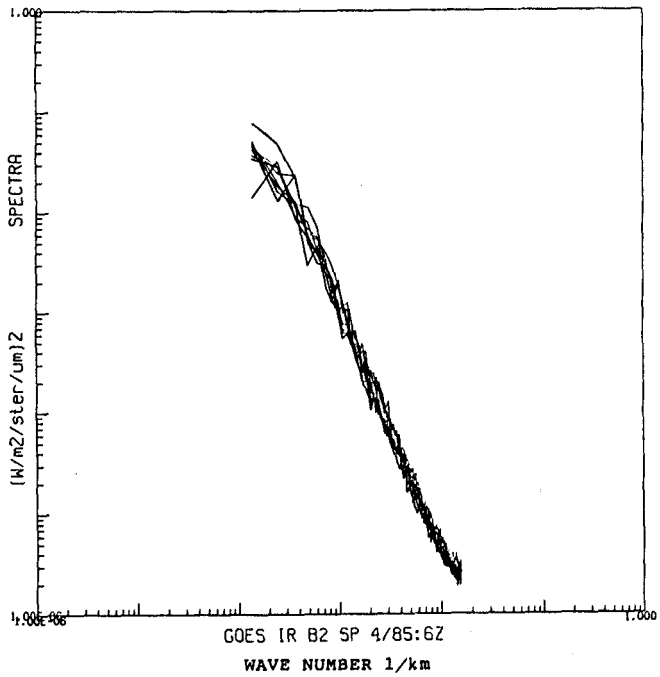

Figure 1, Spectra of several GOES 6 images from several different day of April 1985 for the region 40 north to 40 south latitude and 65 west to 165 west longitude.

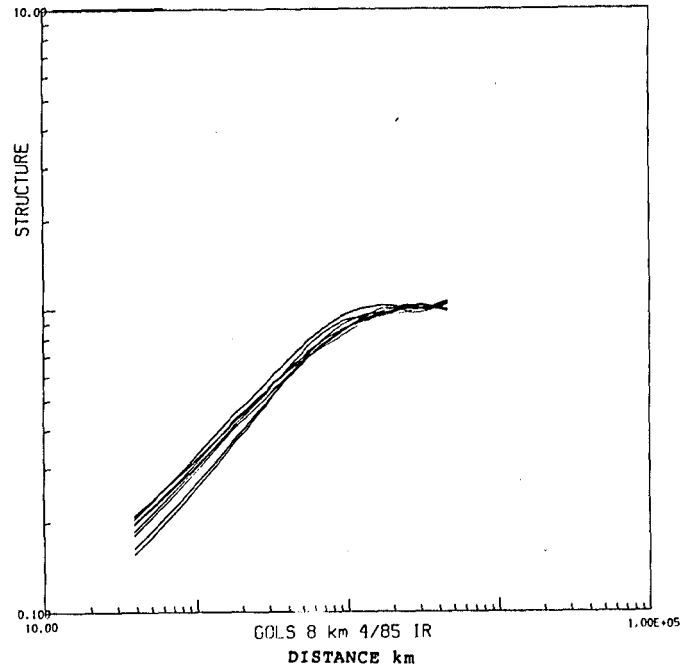

Figure 3, Structure function of several GOES 6 IR images from several different days of April 1985 for the region 40 north to 40 south latitude and 65 west to 165 west longitude.

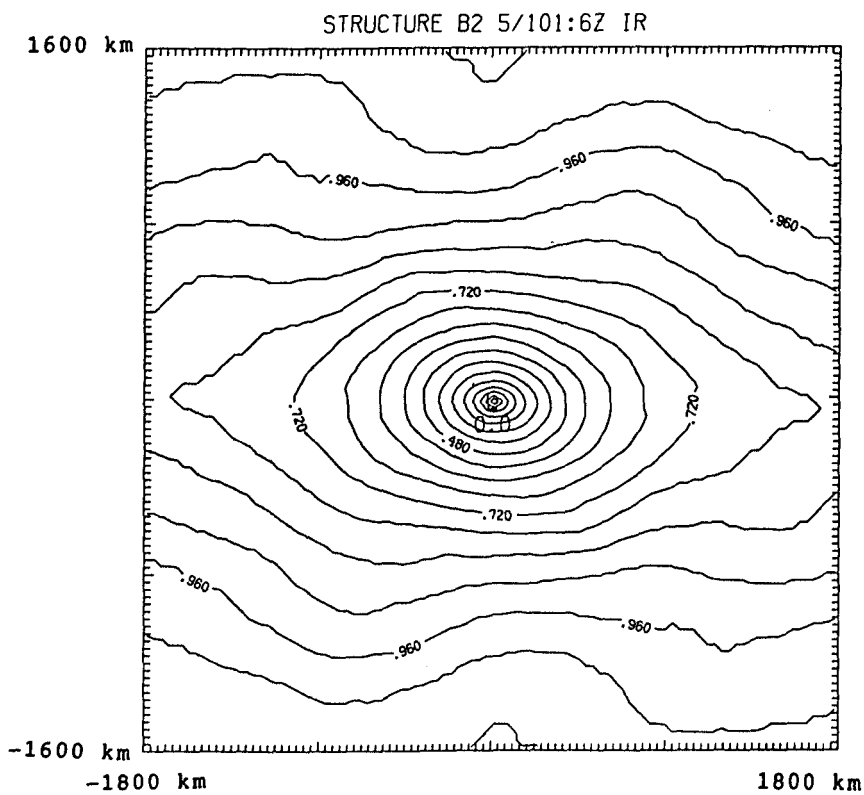

Figure 2, Two dimensional structure function of a single image from GOES 6, day 101, 1985 at 6Z.

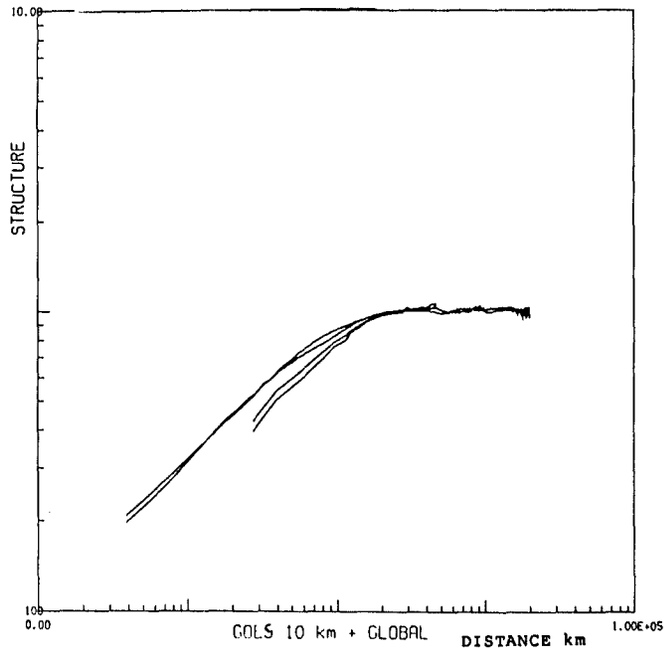

Figure 4, Structure functions of GOES 10 km data and structure functions of 2.5 degree regional averages from global analysis (40 north to 40 south). Notice that they line up very well.

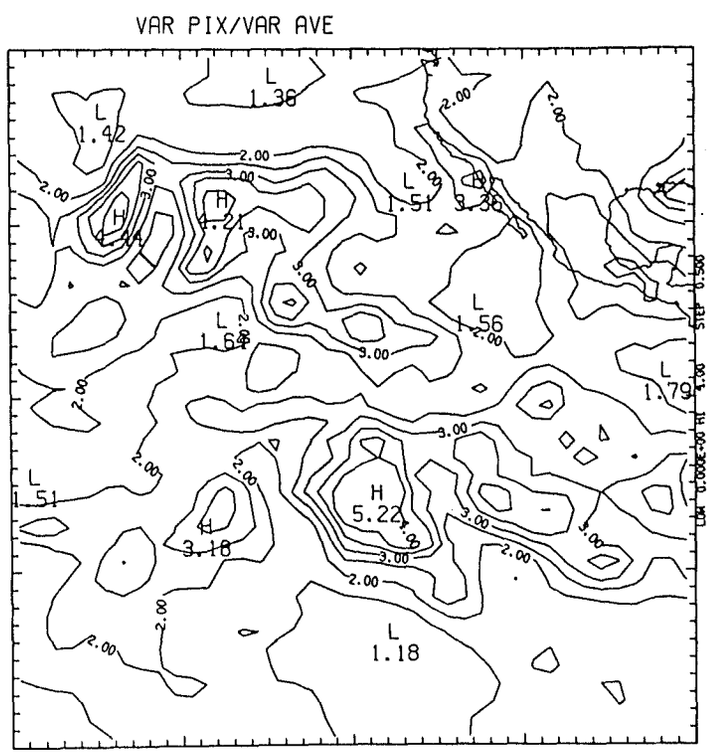

Figure 5, Variance of 10 km pixel data divided by the variance of 2.5 degree regional averages for the month of April, 1985. Data was recorded every 3 hours.

DECONVOLUTION RESULTS FOR WIDE FIELD-OF-VIEW RADIOMETER MEASUREMENTS OF REFLECTED SOLAR RADIATION

by

G. Louis Smith

Atmospheric Sciences Division
NASA, Langley Research Center, Hampton, Virginia

and

David Rutan

PRC Kentron, Inc., Hampton, Virginia

1. INTRODUCTION

Wide field-of-view (WFOV) radiometers have been used for the Earth Radiation Budget (ERB) instruments which flew on the Nimbus 6 and Nimbus 7 spacecraft (W. L. Smith et al, 1977; Jacobowitz et al, 1979) and for the Earth Radiation Budget Experiment (ERBE) instruments which flew on the NOAA 9 and NOAA 10 operational meteorological spacecraft and on a dedicated ERBE spacecraft (Barkstrom and Smith, 1986). Thus, a nearly unbroken high quality set of WFOV Earth radiation budget measurements has continued since 1975. G. L. Smith and Green (1981) developed an analysis procedure for WFOV measurements which applies to the case of Earth emitted radiation, and this method has been applied to a 1-year set of Nimbus 6 ERB data by Bess et al. (1981) and more recently to a 10-year set of Nimbus 6 and 7 ERB data by Bess and Smith (1987a and b).

The problem of analyzing reflected solar radiation was formulated by Smith (1981). This case is more difficult than that of the Earth-emitted radiation, for which there is an analytic solution. The measurement is an integral over the entire field of view of the radiometer (see Figure 1) weighted by the directional response of the radiometer. The equations for the reflected solar radiation case can be discretized, resulting in a set of matrix equations. Smith (1987) recommended the solution of these equations by the method of singular decomposition because the problem is ill-posed. In the present paper, this method is demonstrated by applying it to data from the Nimbus 7 spacecraft for December 1978.

2. THEORY

The measurement equation for reflected solar radiation is (Smith, 1981):

$$m(\theta_S,\Phi_S,\theta_H,\Phi_H) = \frac{1}{\pi} H \int_{FOV} R(\theta_T,\Phi_T,\theta,\phi-\phi_H,\xi) \times \cos^{*}\xi G(\alpha) A(\theta_T,\Phi_T) d\Omega \quad (1)$$

where m is the measurement in $W\text{-}m^{-2}$ at the sensor, whose colatitude and longitude are θ_S and Φ_S. The colatitude and longitude of the sub-solar point are θ_H and Φ_H and the solar incidence at the Earth's position is H. The sensor directional response is $G(\alpha)$, and for a flat-plate response $G(\alpha) = \cos\alpha$. The albedo A at a point at the top of the atmosphere is a function of colatitude θ_T and longitude Φ_T, and is assumed to be constant with local time. The bidirectional model R is a factor which expresses the anisotropy of the reflected radiation. With the constraints imposed by the orbit, equation (1) may be rewritten as:

$$m(\eta,\Phi_S) = \int_{FOV} K(\eta,\Phi_S,\theta_T,\Phi_T)\, A(\theta_T,\Phi_T)\, d\Omega \quad (2)$$

where the kernel function K includes all the terms in the integrand of equation (1) except for the reduced albedo A. The orbit angle η is the angular distance from the Equator to the spacecraft.

The measurement equation (2) is an integral equation which can be solved for the albedo by separation of variables under certain conditions: $A(\theta_T,\Phi_T) = \sum_{n=0}^{N} \exp(in\Phi_T)\, f_n(\theta_T)$ (3) thereby affording a considerable theoretical and computational simplification. The resulting equations are discretized with respect to a grid system, resulting in:

$$B_n \underline{f}_n = \underline{g}_n \quad (4)$$

where $g_n(\eta)$ is the complex Fourier transform in longitude of the measurement map:

$$g_n(\eta) = (2\pi)^{-1} \int_{\Phi=0}^{2\pi} m(\eta,\Phi)\, e^{-in\Phi}\, d\Phi. \quad (5)$$

The behavior of the B_n matrices is discussed by Smith (1981).

The resolution with which the albedo A can be described by data from a WFOV instrument is limited, causing the B_n matrices to be singular. Smith (1987) presented the use of singular value decomposition for this system. This approach delineates the parts of the solution which are retrievable and those which are not. The solution of equation (4) may be written as (Twomey, 1965; 1977):

$$f_n = \sum_{j=1}^{M} \lambda_{nj}^{-1} (v_{nj} g_n)\, u_{nj} + \sum_{j=M+1}^{J} \sigma_{nj}\, u_{nj} \quad (6)$$

where M is the number of non-zero singular values and the σ_{nj} are the coefficients of the singular vectors which have zero singular values. The σ_{nj} cannot be determined from the solution of equation (3). This is explained as follows.

The vector f_n is an element of a J-dimensional space F, and the vector g_n is an element of a P-dimensional space G. The u_{nj} provide an orthogonal basis set which spans F, and the v_{nj} likewise span G. The B_n matrix maps F onto a J-dimensional subspace of G, denoted as the image of F in G. This is indicated schematically in Figure 2. There is a subspace of F which is mapped onto zero. These albedo distributions will produce no signal in the measurement and are thus said to be unobservable

with the WFOV radiometer. They are expressed by the second term of equation (6). Points in G outside the image of F are inconsistent; i.e., there are "measurement" vectors g_n which cannot be produced by any albedo vectors f_n. In application, inconsistency may arise due to errors in B_n or in g_n.

Because of the error arising when λ_{nj} is small or zero it is necessary to consider the terms associated with these singular values, in the first summation of equation (6), as being unobservable. These terms include those components with high wave numbers, which results in a limitation of resolution in the final results. In addition, there are unobservable vectors due to low solar illumination near the terminator.

3. APPLICATION

The preceding theory is now applied to data from the Nimbus 7 Earth Radiation Budget (ERB) shortwave wide field-of-view radiometer for the December case. For the Nimbus 7 spacecraft, the orbit is circular with an altitude of 955 km, an inclination of 99.2°, and an Equator crossing time of 11:55 a.m. local time.

3.1 Singular Values and Singular Vectors of Observation Matrix

The singular values for the ERB WFOV radiometers on Nimbus 7 for December are shown in Figure 3. The singular values decrease exponentially with the latitudinal wavenumber, showing that the effect of the corresponding singular vector components on the measurements decreases. These slopes will increase with increasing spacecraft altitude. Likewise, the singular values also decrease with increasing longitudinal wavenumber.

A few singular vectors are shown in Figure 4 for December. As the order of the singular vector increases, these waves tend to cancel each other out in the measurement, resulting in decreasing singular values as the wavenumber increases. The singular vectors corresponding to the low order singular values all vanish at the high latitudes, as shown in Figures 4a and 4b. Only high-order singular vectors, corresponding to very small singular values, have significant values at high latitudes, as shown in Figure 4c for wavenumbers 33 and 34. This is because albedo variations near the terminator, but still in the sunlit portion of the Earth, are practically unobservable. This problem of unobservability is inherent in the measurement itself. Another important aspect of the wavenumber 33 and 34 singular vectors is that they are each highly localized, so that singular vector 33 has significant magnitude only south of 55°S and singular vector 34 has significant magnitude only north of 50°N. The components of these singular vectors in the solution will have large errors due to division by the singular values in equation (6). However, Figure 4c shows that the effects of these errors will be restricted to the neighborhood of the terminator.

3.2 Construction of the Albedo Field

The measurements from the Nimbus 7 ERB shortwave WFOV radiometer were compiled using a 5° x 5° grid to produce a monthly average measurement. The next step of the inversion process is to compute the complex Fourier components $g_n(\eta)$ by use of equation (5), after which the terms in the first summation of equation (6) are computed.

Because of the errors in the $v_{0j}g_{0j}$ terms, which are magnified by λ_{0j}^{-1}, the series must be terminated in order to obtain a meaningful result. This is a characteristic of inversion problems of integral equations resulting from remote sensing. Most of the errors are due to the fact that the grid box value is not a true average, but is the average of a sample whose selection is governed by the orbital overflights of the grid system. Longitudinally adjacent grid boxes will be sampled on different days, thereby aliasing time variations of the field into variations of the spatial average.

One effect of truncating the series is to limit the resolution. The other effect is to limit the latitudinal coverage of the solution. The solutions with various numbers of terms included are shown in Figure 5 for December. It is seen that as the number of terms increases, the summation converges in the low and mid latitudes. However, near the terminator and at high latitudes, the summation has large changes with the inclusion of additional terms. For terms of high order, the information content of the measurements, as described by the $v_{0j}g_{0j}$ components, is very small. Figure 5 shows the g_0 as computed using a number of terms from 16 through 24. It is seen that 18 terms reproduce the measurement profile g_0 quite closely. The remainder are unobservable. The vanishing of the retrieved albedo at both ends of the domain requires treating.

The terms which describe the albedo in the polar regions have small or zero singular values and are unobservable; thus, they are in the second summation of equation (6). In order to produce a realistic albedo solution, a priori data are needed to provide an estimate for the coefficients σ_{nj} in the unobservable summation. The zonal profiles of Ellis and Vonder Haar (1976) are used for the a priori values.

The truncation point of the series M is important in the retrieval. The M values for the various Fourier components are listed in Table 1. The rapid decrease of M with n is attributed to the decrease of amplitude of the g_n with n. For M = 18, the unobservable part of the solution is localized, providing the albedo value very near the terminator and pole and damping out away from these regions.

The information content depends on the orbit altitude and inclination. For increasing orbit altitude, the first singular value will decrease and the slope of the line for singular values as a function of order will increase, corresponding to loss of retrievable resolution. Also, if the orbital inclination is changed so as to cover a smaller latitude range, the singular values will decrease more rapidly and the corresponding singular vectors will describe the unobserved latitude range.

The observed albedo and the a priori estimate for the unobservable part of the solution are combined as shown in Figure 6 to produce the mean albedo profiles. The resulting total profiles are more realistic than the observable part alone because of the behavior of

the profiles at the high latitudes.

3.3 Variation of Information Content With Latitude

Figure 6 shows that the albedo is defined by the measurements in the low and midlatitudes, but that information in the polar regions is inadequate for reasonable albedo results. This situation is depicted in Figure 7, where the case of December for the Nimbus 7 orbit is shown. From 40°N to 70°S (region IV), the albedo can be retrieved with no significant contribution from the unobservable part of the albedo distribution. In this region, the albedo is defined by the WFOV measurements. In latitudes 67°N to 50°N (region II) and 80°S to 90°S (region VI), the WFOV measurements provide very little information. In latitudes 50°N to 40°N (region III) and 70°S to 80°S (region V), the WFOV measurements provide significant information, but the part of the distribution which is unobservable in the WFOV measurements is also significant. These are transition regions between region IV and regions II and VI, respectively. The albedo is physically undefined for latitudes poleward of 67°N (region I). The boundaries for these regions move with the solar declination. Also, these boundaries are a function of the orbit characteristics of the spacecraft.

3.4 Albedo Results

Albedo is computed using equation (3), and the results are shown in Figures 8 and 9 for December 1978 and September 1981, respectively. In the low latitudes, there is much longitudinal variation of albedo. Regions are seen where the patterns roughly correspond to continent shapes. From 60° to the poles in both hemispheres, the albedo is very strongly zonal, but the Antarctic does produce a noticeable high in the longitudinal direction. The oceans show low albedo regions, which are assumed to be regions of low cloudiness, with albedos on the order of 9 to 12%. The Indonesia-New Guinea region has an albedo in the range 25 to 30%, which indicates high cloudiness. The Tibet-Western China region shows a high albedo of 37%, again this is associated with the high cloudiness of the region. The high albedo of Greenland causes the 40% albedo line to move in a wide arc around the island. This is a measure of the resolution available from the WFOV measurements at this latitude.

For December, the results are quite similar. Note the illumination of Greenland is so low that it is not resolvable for this month. In the Tropics, the deep convective centers over the Amazon, Southern Africa, and the Indonesia-New Guinea regions are apparent. This matches well with the WFOV results for Earth-emitted radiation, in which these centers are notable due to the low Earth-emitted radiation from the cold high cloud tops (Smith and Bess, 1983). Thus, the reflected and absorbed solar radiation exhibits a strong three wave pattern as does the Earth-emitted radiation near the Equator.

3.5 Absorbed Solar Radiation

The primary purpose of determining albedo is to determine the amount of solar radiation absorbed by the Earth-atmosphere system. For computing the absorbed solar radiation, the albedo was assumed to be constant for the diurnal cycle. The zonal mean absorbed solar radiation is shown in Figure 10 for December 1978. The incident solar radiation is shown for comparison. Because the unobservable part of the albedo is a source of error, the absorbed radiation which is based on this term is shown also. Except for the South Pole, this part is very small. The reason for this is simply that this part is unobservable because, for the Nimbus 7 orbit, the radiant incidence is small in these regions. At the South Pole, the error in absorbed radiation is large because the albedo error and incident radiation are large. The albedo error is large because the region corresponding to this 5° latitude band is very small and the satellite only goes to a latitude of 81°S.

4. CONCLUDING REMARKS

A technique has been demonstrated by which the deconvolution of WFOV measurements of solar radiation reflected from Earth is reduced from the solution of a two-dimensional integral equation to the solution of a set of one-dimensional integral equations. The theoretical operational difficulties associated with the solution of ill-posed problems are thus greatly simplified by working with one-dimensional integral equations rather than with two-dimensional integral equations. The solution is given by the method of singular value decomposition, which permits the partitioning of the albedo field into an observable part and an unobservable part. This unobservability is due to limitations in the nature of the wide field-of-view measurement and is present in any analysis technique. The present study delineates the unobservability. The unobservable part includes high spatial frequency components, regions of low solar illumination and near the poles. The unobservability of the high spatial frequencies limits the resolution which is obtainable from the wide field-of-view radiometer. The albedo field is observable in the low and mid latitudes. The error near the terminator due to the unobservable part causes only small errors in absorbed solar radiation.

5. REFERENCES

Barkstrom, B. R. and G. L. Smith, 1986: The earth radiation budget experiment: Science and implementation. Reviews of Geophysics, 24, 379-390.

Bess, T. D., R. N. Green and G. L. Smith, 1981: Deconvolution of wide-field-of-view radiometer measurements of Earth-emitted radiation. Part II: Analysis of first year of Nimbus 6 ERB data, J. Atmos. Sci, 38, 474-488.

Bess, T. D. and G. L. Smith, 1987a: Atlas of wide-field-of-view outgoing longwave radiation derived from Nimbus 6 Earth radiation budget data set - July 1975 - June 1978. NASA RP-1185

Bess, T. D. and G. L. Smith, 1987b: Atlas of wide-field-of-view outgoing longwave radiation derived from Nimbus 7 Earth radiation budget data set - November 1978 - October 1985. NASA RP-1186

Ellis, J. S. and T. H. Vonder Haar, 1976: Zonal average earth radiation budget measurements from satellites for climate studies.

Atmospheric Science paper 240, Colorado State University.
Jacobowitz, H.; Smith, W. L.; Howell, H. B.; Nagle, F. W.; and Hickey, J. R., 1979: The first 18 months of planetary radiation budget measurements from the Nimbus 6 ERB experiment. J. Atmos. Sci., 36, No. 3, 501-507.
Smith, G. L., 1981: Deconvolution of wide-field-of-view satellite radiometer measurements of reflected solar radiation. Proceedings, Fourth Conference on Atmospheric Radiation, Amer. Meteor. Soc., June 16-18, 1981, Toronto, Canada.
Smith, G. L., 1987: Deconvolution of wide-field-of-view measurements of reflected solar radiation. Proceedings, Sixth Symposium Meteorological Observations and Instrumentation, Amer. Meteor. Soc., Jan. 12-16, 1987, New Orleans, La.
Smith, G. L.; and Bess, T. D., 1983: Annual cycle and spatial spectra of earth-emitted radiation at large scales. J. Atmos. Sci., 40, 998-1015.
Smith, G. L.; and Green, R. N., 1981: Deconvolution of wide-field-of-view radiometer measurements of earth-emitted radiation. Part I. Theory. J. Atmos. Sci., 38, 461-473.
Smith, W. L.; Hickey, J.; Howell, H. B.; Jacobowitz, H.; Hilleary, D. T.; and Drummond, A. J., 1977: Nimbus 6 earth radiation budget experiment. Appl. Opt., 16, No. 2, 306-318.
Twomey, S., 1965: The application of numerical filtering to the solution of integral equations encountered in indirect sensing measurements. J. of Franklin Institute, 269, No. 2, 95-109.
Twomey, S., 1977: Introduction to the Mathematics of Inversion in Remote Sensing and Indirect Measurement. Elsevier Scientific Publishing Co.

Table 1. Number of terms retrieved for each wavenumber

wavenumber	M, order of last term retained	
	September	December
0	18	18
1	12	14
2	11	13
3	3	6
4	2	1
5	2	1
6	1	1
7	1	1
8	1	1
9	1	1
10	1	1
11	1	1

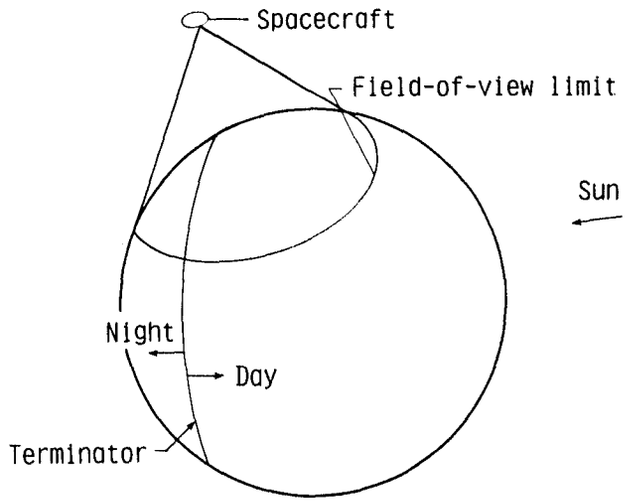

Fig. 1. Wide-field-of-view analysis problem.

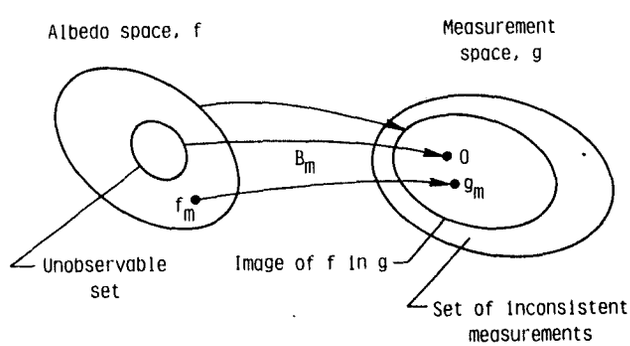

Fig. 2. Schematic of function space relations for inversion problem.

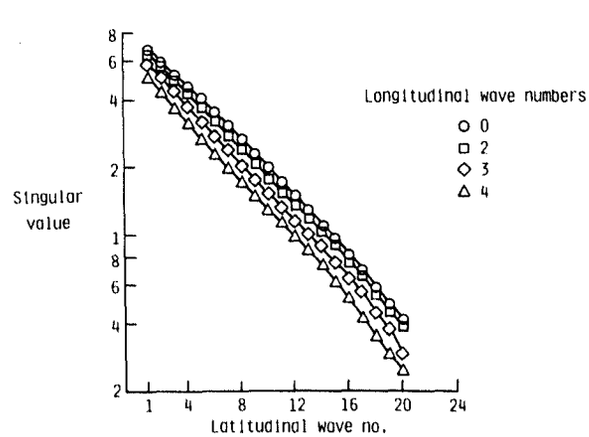

Fig. 3. Singular values of measurement matrices for Nimbus 7 WFOV for December 1978.

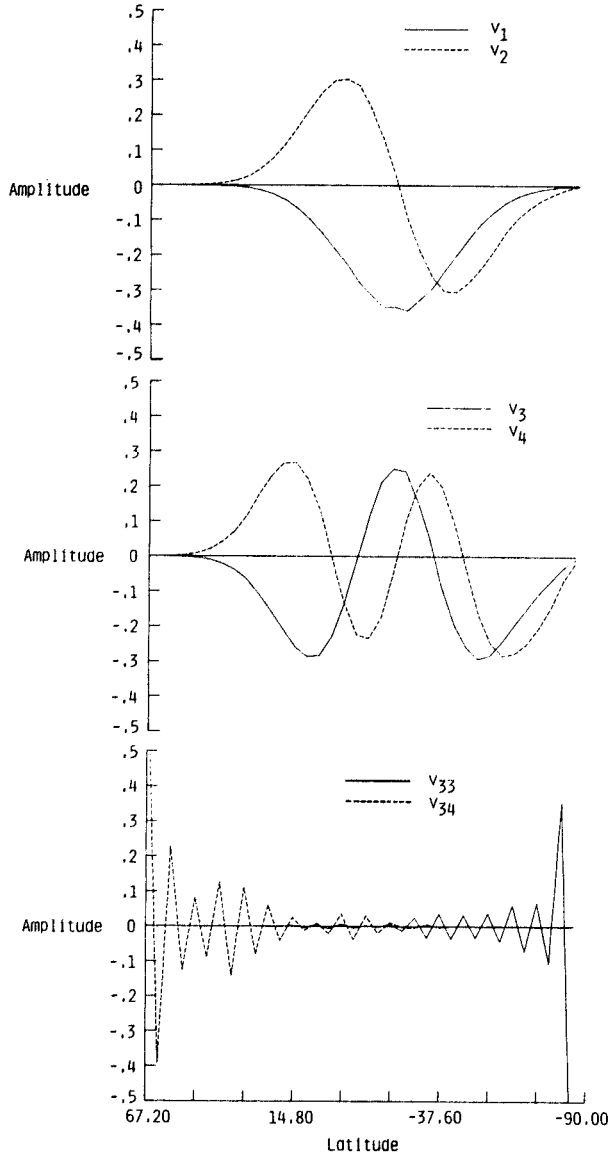

Fig. 4. Singular vectors of measurement matrices for Nimbus 7 WFOV for December 1978.

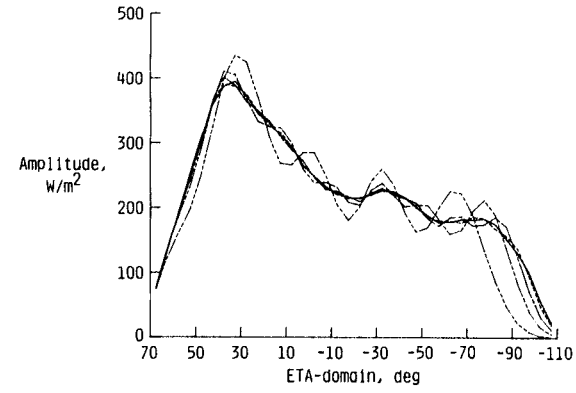

Fig. 5. Profiles of measurement map Fourier components $g_0(\eta)$ for December 1978 and combining of terms to build g_0.

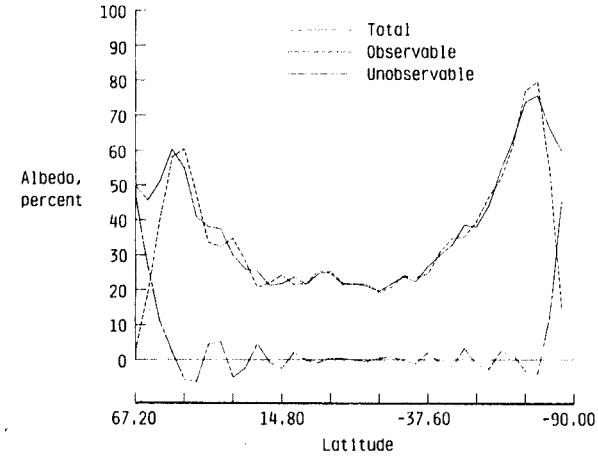

Fig. 6. Zonal profiles with and without a priori data used for unobservable part of albedo for December 1978.

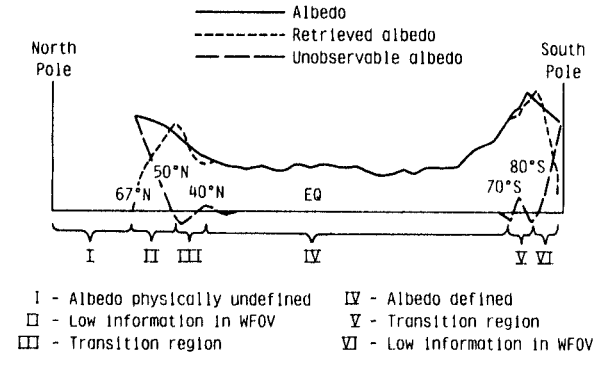

Fig. 7. Observability regions.

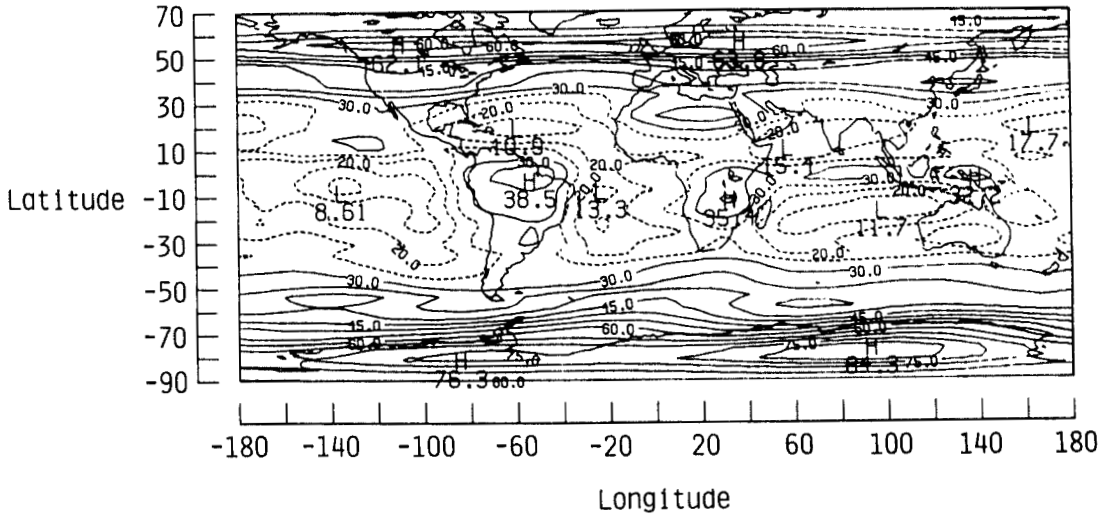

Fig. 8. Albedo map with a priori information for December 1978.

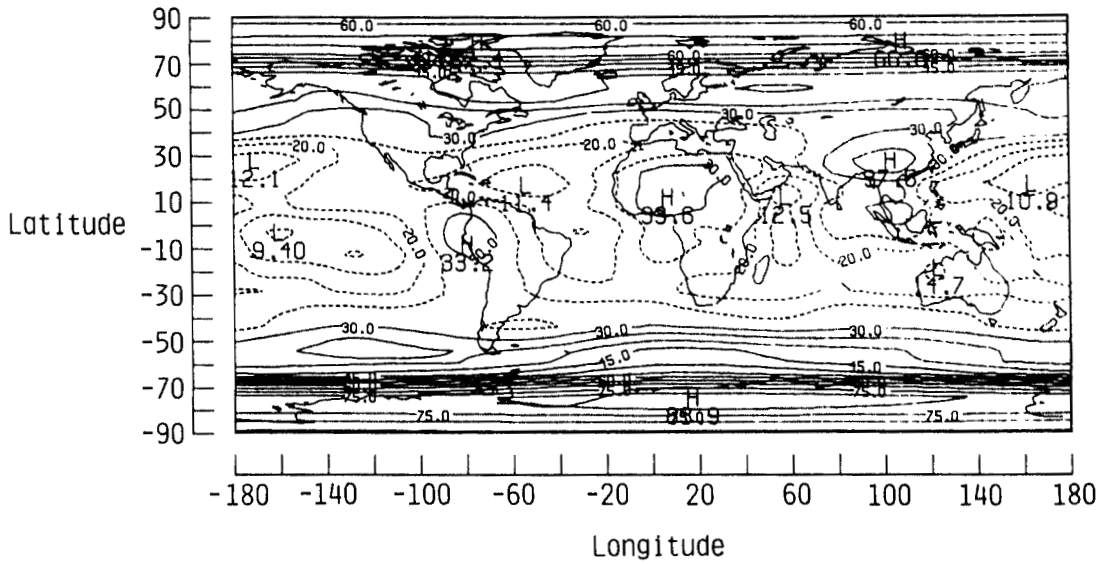

Fig. 9. Albedo map with a priori information for September 1981.

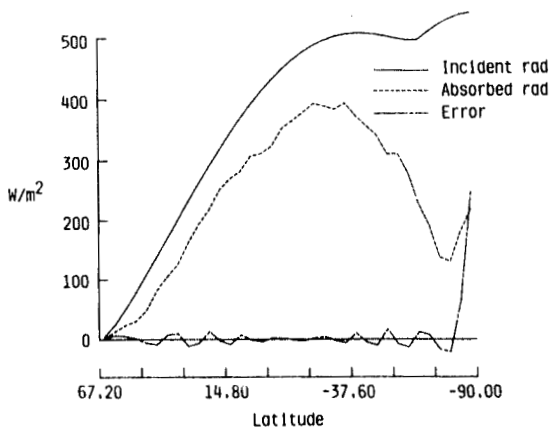

Fig. 10. Zonal average profile of absorbed solar energy for December 1978.

Intercomparison of Outgoing Longwave Radiation Obtained from ERBE and NOAA Operational Satellite: A Preliminary Result

Shi-Keng Yang*, Arnold Gruber**, Brant Liebmann* and Alvin J. Miller***

* CICS, Dept. of Meteorology, University of Maryland
** SRL/NESDIS National Oceanic and Atmospheric Administration
*** CAC/NMC National Oceanic and Atmospheric Administration

INTRODUCTION

The NASA Earth Radiation Budget Experiment (ERBE) (Barkstrom, 1984) is designed to measure the planetary radiation budget with broadband instruments onboard three satellites. The accuracy of the instruments and the spatial-temporal resolution of the observing system surpasses those of previous attempts. Two instruments are on-board the sun-synchroneous NOAA 9 and NOAA 10 satellites, the third is in a highly retrograde orbit (Earth Radiation Budget Satellite) to provide diurnal coverage.

On the other hand, NOAA has been providing earth outgoing longwave radiation (OLR) derived from the narrow band AVHRR measurement onboard the operational satellite series (Gruber and Krueger, 1984) for more than thirteen years, the longest OLR data set available.

The purpose of this paper is to present results from a preliminary study comparing OLR measured by the broadband and estimated by narrow band instruments. Although we tend to find a slight non-linearity in the comparison over the ocean region, overall the standard deviation of the data is within 2%. The study also suggests that to fine tune the AVHRR OLR, we might need different regression algorithms for different surface geographies.

DATA

The AVHRR outgoing OLR used in this study are those from the NOAA 9 satellite and analyzed by Climate Analysis Center, NMC (Janowiak, 1985). The analyses are monthly means derived from the daily mean which, in turn, is the average of the daytime and nighttime observations. The satellite equator crossing time are 0230 and 1430 local time.

ERBE OLR data are observed by the scanning radiometer onboard the ERBE satellite (ERBS). The satellite is inclined at 57 degrees and precesses about 5 degrees a day. The monthly mean used in this study is derived from the daily mean which takes into account the diurnal cycle, either through the compositing over the various local hours observed during the month or through use of an explicit diurnal model. Due to satellite coverage, only those data between 60° degree North and South are considered in this study.

Although both the data of ERBE and AVHRR are specified on 2.5 x 2.5 deg. lat./long. boxes, the centers of ERBE grid boxes are offset from the AVHRR grid points by 1.25 degrees in both latitude and longitude. For compatability, the AVHRR data were converted to the ERBE grid by averaging over the surrounding four grid points.

While we have examined several time periods of both ERBE and AVHRR data, we will focus in this paper on the one month of April 1985 as these data have now been finalized for the ERBE and are scheduled to go into the public archive.

Results

Figure 1, which depicts the April 1985 monthly average maps of OLR as well as the difference (ERBE minus AVHRR), we see that for the contour of 250 W/M**2, AVHRR is very close to ERBE. However, for the contour of 275 W/M**2, ERBE has much larger area than that of AVHRR, especially over the ocean regions. One of the possible reasons for such difference is that the inferred OLR from AVHRR measurements is derived from a regression process (Ohring et. al., 1984), thus, it is expected that when compared to ERBE broad-band measurement, AVHRR OLR would be more conservative.

Yet, there are regions where ERBE underestimates AVHRR. Particularly over desert area, such as western Sahara, central Australia, and, some regions over land, such as Central Asia, northern China, Mexico and Rocky Mountains area. Although there are also some small regions over the ocean where ERBE underestimates AVHRR, the area is much smaller than that of land-desert and not well organized.

The zonally averaged OLR as a function of latitude are presented in Figure 2. We see that the two data sets agree very well in the latitudinal distribution with ERBE over-estimating AVHRR for all of the latitudes. This is also shown in Table 1. ERBE has a higher global mean (60° North and South with area weighting) than that of AVHRR by 2.84 W/M**2. The largest differeces are in the subtropical subsidence regions with 2.7% difference for the Southern Hemisphere and 1.6% difference for the Northern Hemisphere.

Figure 3 is a scatter plot of the actual grid point data and shows that the relationship between AVHRR and ERBE can fit fairly well with a least square regression of slope 1.11. The

slope, which is larger than unity, agrees with the argument that AVHRR is in general conservative when compared to ERBE. Caution has to be taken as this argument does not apply to specific regions as we shall see later. More careful examination shows the center cohesive portion of the scatter plot has some non-linear curvature. Stratification of the scatter plot by surface geographical types segregates this region as ocean, Fig. 4. Also, indicated in Table 1. is that the vast ocean area dominates the slope of the least square fit. Nevertheless, the ocean has larger standard error of estimate than when all surface types are considered, 7.29 W/M**2 vs. 6.22 W/M**2, regardless of the high correlation coefficient.

Examination of the relationship between AVHRR and ERBE over land and desert are depicted in Figures 5 and 6, respectively, and we see that their overall slope is rather close to 1.0 (Table 1). The desert has a higher standard error than that of land, 4.59 W/M**2 vs. 3.91 W/M**2. This could be due to the effect of the strong diurnal cycle on the different satellite sampling times. Also, very notablely, desert is the only surface type that AVHRR has higher global mean than that of the ERBE by 2.1W/M**2.

Snow regions are mostly located in the Northern Hemisphere at this time of the year and the scatter plot of this region, Fig. 7, shows the relationship has the lowest slope compared to other types of geography. However, the OLR over snow has a very small range, 185 to 215 W/M**2, so that the confidence interval for the slope is less.

Remarks

Due to the varying satellite sampling times, ERBS OLR probably is closer to the true monthly mean than AVHRR OLR, which is based on sun-synchroneous observations. The larger standard error of desert and land could be due to this sampling differece in that the diurnal cycle is large. This, however, does not explain the essentially non-linear relationship between the two over the ocean areas.

A more selective comparison is underway by choosing space-time colocated regions for comparison. Also, the data from the two different instrument, broadband from ERBE and narrow band from AVHRR, but onboard the same satellite, NOAA9, will be available soon for further analysis. This data set will eliminate the questions arising from the different sampling times.

REFERENCES

Barkstrom, B. B., 1984: The Earth Radiation Budget Experiment (ERBE). Bull. Am. Meteor. Soc. V.65, p1170

Gruber, A. and A. F. Krueger, 1984: The Status of the NOAA Outgoing Longwave Radiation Data Set Bull. Am. Meteor. Soc. V.65, p958

Janowiak, J.E., A.F. Krueger, P.A. Arkin and A. Gruber, 1985: Atlas of Outgoing Longwave Radiation Derived from NOAA Satellite Data. NOAA Atlas No.6 Dept. of Commerce. NTIS PB85-155455

Ohring, G., A. Gruber, R.G. Ellingson, 1984: Satellite Determination of the Relationship between Total Longwave Radiation Flux and Infrared Window Radiance. J. Clim. & Applied Meteor., V.23, p416

	total	Ocean	Land	Snow	Desert
No. Grid box	7056	4935	1189	172	434
Slope	1.11	1.11	1.00	.88	.97
Corr. Coef.	.98	.99	.98	.88	.97
Std error	6.22	7.29	4.59	1.72	3.91
RMS Diff.	5.44	5.48	5.22	4.43	6.3
AVHRR Mean	238.7	239.6	230.3	196.2	261.5
ERBE Mean	241.5	243.4	231.2	199.8	259.4
Mean Diff.	-2.8	-3.8	-.9	-3.6	+2.1

Table 1. Statistics from least square fit. Std error is the standard error of the estimate. RMS Diff is the root mean square difference between AVHRR and ERBE. The Means are global means between 60° North and South.

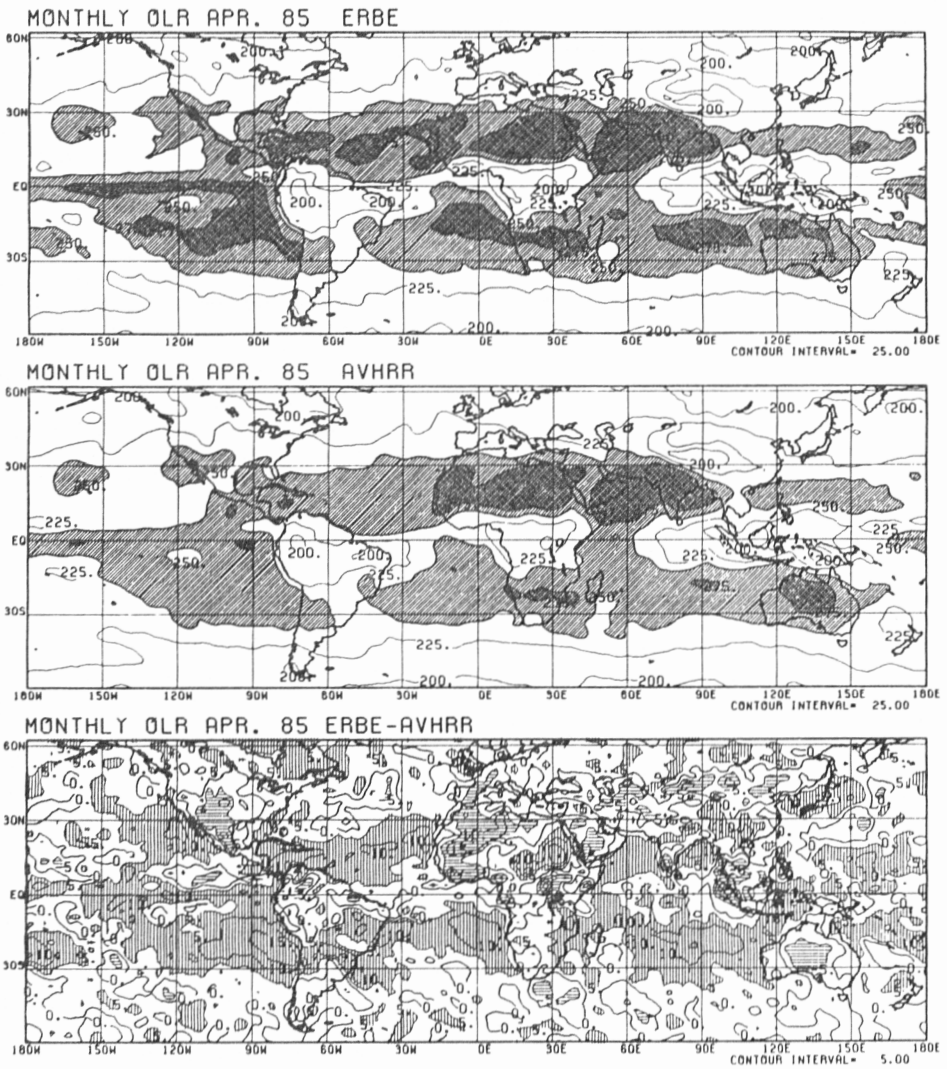

Fig. 1 Monthly Average OLR for April 1985 from (a) ERBE, (b) AVHRR and (c) Difference between ERBE and AVHRR. For (a) and (b), single shaded areas are larger than 250 W/M**2; double shanded areas are larger than 275 W/M**2. For (c) '|' is larger than 5 W/M**2 and '-' is smaller than -5 W/M**2.

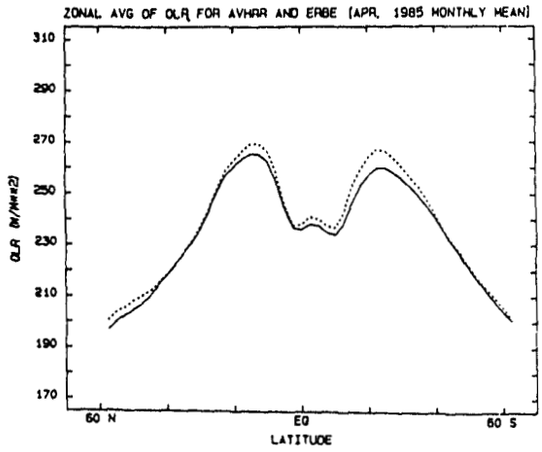

Fig. 2 Zonal averages of OLR for ERBE, dashed line, and AVHRR, solid line.

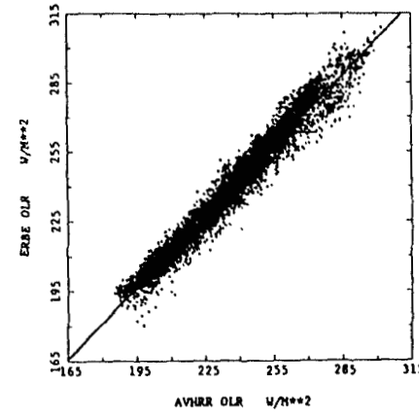

Fig. 3 Scatter plot for ERBE vs. AVHRR between 60° North and South. The solid line is the slope of the least square fit.

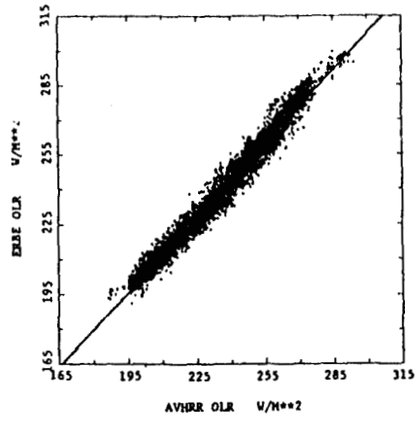

Fig. 4 Same as Fig. 3, except for ocean.

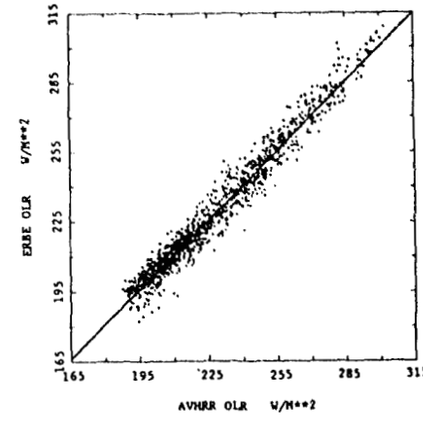

Fig. 5 Same as Fig. 3, except for land.

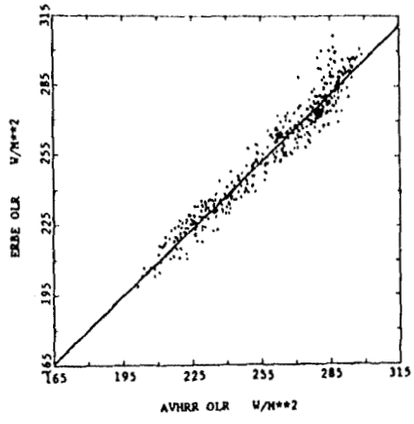

Fig. 6 Same as Fig. 3, except for desert.

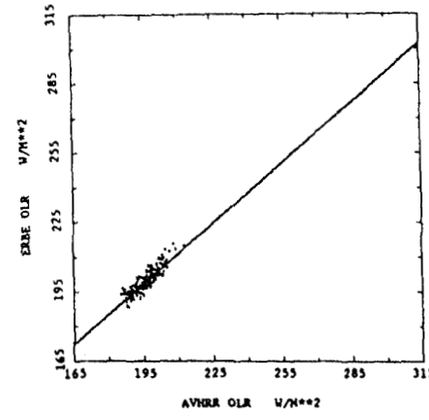

Fig. 7 Same as Fig. 3, except for snow.

4.4

TEMPORAL VARIABILITY OF THE OUTGOING INFRARED FLUX FROM NFOV DAILY DATA: COMPARISON BETWEEN NOAA AND NIMBUS-7 POLAR ORBITING SATELLITES.

Laura D. Smith and Thomas H. Vonder Haar

Department of Atmospheric Sciences
Colorado State University
Fort Collins, Colorado

1. INTRODUCTION

Daily observations of the shortwave and longwave components of the Earth Radiation Budget (ERB) from polar orbiting satellites are currently being used for validation of the radiation balance obtained from long term climate simulations with three dimensional atmospheric general circulation models (GCM's). Climate modelers are focusing their research on the ability of GCM's to reproduce the first and higher order statistics of the key climate variables driving the atmospheric general circulation of the Earth Atmosphere system. Measurements of the ERB at the top of the atmosphere from satellites, which are uniquely defined and highly calibrated quantities, available on various time scales and space resolutions over the whole globe constitute one of the best tool to help validate the parameterization of shortwave and longwave radiative transfer processes and improve cloud generation schemes.

Measurements of the longwave radiation emitted by the various atmospheric constituents and by the earth's surface are available from two different series of polar orbiting satellites over the time period between June 1979 and February 1980. Although primary designed for imaging and estimates of surface temperatures, scanner radiometers on board the successive NOAA spacecrafts have been providing a continuous record of spectral narrowband longwave radiances since June 1974. On the other hand, the primary goal of the NIMBUS-7 ERB experiment was to accurately measure narrow angle of view (NFOV) spectral broadband emitted longwave flux. However, due to a mechanical failure in the scanning mechanism, only twenty months of data are available between November 1978 and June 1980. Different orbital characteristics ,temporal and spatial samplings between both satellites, and more important different spectral wavelength intervals of the infrared channels lead to measurable differences between both data sets.

In this study, daily mean observations from both satellite experiments are used to compute seasonal average and standard deviation of the outgoing longwave radiation over the time periods DECEMBER 79-JANUARY 80-FEBRUARY 80 and JUNE 79-JULY 79-AUGUST 79 (respectively referred as winter and summer in the following sections). Its primary goal is to infer if, on a global scale and for a specific spatial resolution, estimates of the temporal variability of climate are affected when either spectral narrowband converted to broadband, or spectral broadband measurements of the longwave component of the radiation balance are used. In the last section, we used daily observations from the NOAA satellite over the period JUNE 79-JULY 79- AUGUST 79 to compute time lagged autocorrelation coefficients of the outgoing infrared flux. Zonal averages and global maps are presented to point out the effect of the diurnal cycle of the cloud top and earth 's surface temperatures.

2. SATELLITE DATA SETS

2.1 NIMBUS-7

The NIMBUS-7 satellite was launched in October 1978 into a sun synchronous near polar orbit with equatorial crossing times close to the local noon in its ascending node and the local midnight in its descending node. However, because of a mechanical failure in the scanning mechanism, only twenty months of NFOV shortwave and longwave observations are available between November 1978 and June 1980. Characteristics of the NFOV infrared channels are summarized in Table 1 (from Gruber and Jacobowitz, 1985). Additional information on the scanning mechanism and on the performances of the scanner radiometers can be found in Jacobowitz et al (1984). NFOV spectral broadband infrared radiance data were recorded on a 3 days "ON", 1 day "OFF" cycle, and converted into irradiances using angular dependence models developed by Taylor and Stowe (1984). They were further averaged into daily mean values stored on the so called "MATRIX" tapes into 2070 target grids of approximately equal surface area of 500 km by 500 km. The daily averaged data were then streched into a rectangular grid of 4.5° latitude-longitude resolution, and missing grid points were filled in with a weighting interpolation scheme. Because of the 3 days "ON", 1 day "OFF" cycle, only 67 and 69 days are respectively available over the time periods DECEMBER 79-JANUARY 80-FEBRUARY 80 and JUNE 79-JULY 79-AUGUST 79.

2.2 NOAA

Daily observations of the planetary outgoing longwave radiation were obtained from two different series of NOAA operational polar spacecrafts between June 79 and February 80, as indicated in Table 1. Gruber and Jacobowitz (1985) discuss how monthly averaged observations from the TIROS-N satellite compare to the NOOA-6 data, to assess the compatibility of both IR time series. Empirical regression relationships developed from NIMBUS-7 ERB observations are used to convert radiances measured in the window region ($10.5 - 11.5\mu m$) into spectral broadband values (Ohring et al, 1984). Measurements of the outgoing IR for the ascending and descending nodes are available on a rectangular grid of 2.5° latitude-longitude resolution. The missing grid points were also filled in and flagged as negative values for each

map. In order to match as closely as possible the NIMBUS–7 IR time series, each daily averaged field was further streched into a 4.5° latitude-longitude rectangular grid. Daily observations which were missing in the NIMBUS–7 IR time series were also omitted in the NOAA IR data in order to come up with two "look alike" data sets for both northern hemisphere winter and summer seasons.

Table 1: Characteristics of the NIMBUS–7 and NOAA satellites (from Gruber and Jacobowitz, 1985).

SATELLITE	TIROS–N	NOAA–6	NIMBUS–7
INFRARED WINDOW (μm)	10.5-11.5	10.5-11.5	4.5-50.0
PERIOD OF RECORD	01-79;01-80	02-80;07-81	11-78;06-80*
EQUATOR CROSSING (LT)	0300-1500	0730-1930	1200-2400
RESOLUTION	4 km	4 km	90 km

* Normal duty cycle was 3 days "ON" followed by 1 day "OFF".
* January 4, 1979 - February 6, 1979: No scanning in descending portion of orbit down to a subsatellite position of 27°S.
* December 10, 1978 - May 22, 1979: No scanning during first of the 3 "ON" days.

3. TIME AVERAGE, STANDARD DEVIATION

In this section, the seasonal average (IR) and the standard deviation computed from and normalized by the seasonal average ($\sigma(IR)$) obtained from the NOAA time series are compared to these from NIMBUS–7 spectral broadband measurements. Prior to this comparison (but not shown in this paper), the NOAA IR data were used with and without missing days to show that missing daily observations had a small effect on the actual statistics. Figure 1 presents global maps of IR from NIMBUS–7 (A) and NOAA (B) data for the period DEC 79-JAN 80-FEB 80. The geographical distribution of IR is very well known from earlier satellite observations. Extended areas of high infrared emission are located above the relatively "cloud-free" subtropical oceans and desertic zones above the continents, and areas of low infrared emission are found along the Intertropical Convergence Zone above the oceans, and regions characterized by heavy rainfall and cumulus activity above the continents.

NIMBUS–7 IR systematically shows higher (lower) values above regions of high (low) outgoing longwave radiation than NOAA IR, as seen above the monsoon region for which the difference reaches 11 $W.m^{-2}$. This also indicates that there is a sharper gradient of IR between areas of low and high infrared emission for NIMBUS–7 than for NOAA. This difference is observed on Figure 2 where the zonal averages of NIMBUS–7 and NOAA IR are plotted for northern hemisphere winter (A) and summer (B) conditions. As for the horizontal projection, the agreement is fairly good in the middle and high latitudes, but for the summer hemisphere south of 40° , as seen on Figure 2.A. At low latitudes, the absolute difference is less than 8 $W.m^{-2}$ for both seasons. Although daily mean observations were used to minimize the effect of the diurnal cycle, we expect different time samplings to have the greatest influence at low latitudes, especially above the continents. However, this difference is within the range of incertitude expected on the measurements of the daily outgoing IR, w hich may result from:

(i) different calibration of the NFOV infrared channels on the NIMBUS–7 and NOAA scanner radiometers.

(ii) narrowband to spectral broadband conversion of the NOAA radiances.

(iii) radiance to irradiance conversion using angular dependence models.

Figure 3 presents global maps of $\sigma(IR)$ from NIMBUS–7 (A) and NOAA (B) data over the period DEC 79-JAN80-FEB 80. The global distribution of $\sigma(IR)$ is discussed in Smith and Vonder Haar (1987) for both northern hemisphere winter and summer conditions using NIMBUS–7 NFOV outgoing infrared daily data. At low latitudes, as shown on Figure 1.A and 3.A (or on Figures 1.B and 3.B), there is a direct relationship between areas of low (respectively high) seasonal average and high (respectively low) standard deviation. $\sigma(IR)$ shows a sharp gradient at the boundaries between clear and cloudy regions, which indicates that the variability of outgoing infrared emission at the top of the atmosphere is primarily driven by day to day fluctuations of high convective clouds. In addition, Figure 4 shows zonal averages of $\sigma(IR)$ for northern hemisphere winter (A) and summer (B) seasons. Between 40°N and 40°S, the NIMBUS–7 IR time series present a slightly higher day to day variability than the NOAA time series. However, the difference between the two does not exceed 4 $W.m^{-2}$ on Figure 4.A and the agreement is remarkably good for summer conditions, as seen on Figure 4.B. A larger difference is seen in the zonal averages at higher latitudes where NOAA $\sigma(IR)$ systematically shows greater values than NIMBUS–7 $\sigma(IR)$. Although the NOAA observations were streched into a 4.5° grid size as NIMBUS–7 data, a smaller spatial resolution of the NFOV scanners on board the NOAA satellite may partially explain this greater variability seen in the middle latitudes. At these latitudes, day to day fluctuations in the outgoing IR mainly arise from horizontal advection of the large scale humidity and frontal systems. Because the infrared signal, measured at the top of the atmosphere, is not as strong as at low latitudes, a smaller spatial averaging is needed to distinguish between cloudy and cloud free areas. As an example, along the north east coast of the United States, characterized as a cyclogenetic area, $\sigma(IR)$ reaches 14.1 $W.m^{-2}$ on Figure 3.B and is less than 8 $W.m^{-2}$ for the NIMBUS–7 IR data.

This study shows that both data sets are in very good agreement and that the use of spectral broadband, or spectral narrowband converted to broadband irradiances does not affect the time average and standard deviation at that specific time scale and spatial resolution.

4. AUTOCORRELATION COEFFICIENT

The previous section showed that NIMBUS–7 and NOAA data could be indifferently used to study the first order variability of the outgoing longwave radiation at the top of the atmosphere. However, the NIMBUS–7 IR time series present important limitations to compute time lagged autocorrelation coefficients. The 3 days "ON", 1 day "OFF" cycle reduces the length of the time series by one third on a seasonal basis and the spatial averaging of the irradiance field into 4.5° side gridbox limits studies on a regional scale of cloudy versus clear sky conditions. In this section, NOAA IR data combining ascending and descending nodes for the 2.5° latitude-longitude grid resolution are used to compute autocorrelation coefficients for successive 12 hour time lags over the time period JUN 79-JUL 79-AUG 79.

Figure 5.A shows zonal averages of the autocorrelation coefficients computed every 24 hour lag for the first five days of the time series. After 24 hours, the correlation of the outgoing infrared flux has dropped by 50% over the whole globe with the largest decrease occuring in the middle latitudes in the southern hemisphere. Minima above the equatorial and middle latitudes mainly result from day to day fluctuations in the water vapor field and in the cloud cover distribution. Two maxima coincide with the subtropical latitudes, where relatively clear sky conditions prevail over the whole season. The correlation keeps decreasing between 24 and 48 hours, but stays about constant at higher time lags. This indicates that the outgoing infrared radiation is very sensitive to fluctuations in the atmosphere from one day to the next, but that on a longer time scale, the generation, advection and dissipation of clouds, as well as the advection of the temperature and water vapor fields tend to keep the infrared signal relatively constant on a seasonal basis. Figure 5.B shows the global distribution of the autocorrelation coefficient for a 24 hour lag. As already pointed out for Figure 5.A, a strong correlation is found above the major desertic regions, as the Sahara desert, and areas of low (or even negative) correlation are located along the Intertropical Convergence Zone above the oceans.

Figure 6.A and 6.B are presented to highlight the impact of the diurnal cycle of the cloud top and earth 's surface temperatures on the computation of the time lagged autocorrelation coefficients. On Figure 6.A, the zonal averages of the 12 hour lag (1) and 24 hour lag (2) autocorrelation coefficients show that the day–night "blinking" of the equivalent blackbody temperature of the Earth Atmosphere system is mostly felt in the subtropics. The radiative cooling of the earth 's surface during the night above desertic regions leads to a decrease in the terrestrial emission and therefore to a negative correlation with day time conditions. On the other hand, the correlation strongly increases for a 24 hour lag for which only daytime (nightime) conditions are respectively coupled. On a zonal average, this effect is not seen along the equator or at higher latitudes. However, analyses of individual 2.5° gridbox allow to pick up the diurnal signal of the convective clouds along the Intertropical Convergence Zone. Figure 6.B represents the global distribution of the 12 hour lag correlation coefficient and can be compare with Figure 5.B. The diurnal signal of the surface temperature is clearly observed above the major desertic regions. As an example, above the Sahara desert, the correlation coefficient is equal to -92.3 % and +94.3 % for a time lag of respectively 12 and 24 hours. On the other hand, above a convective region the correlation coefficient decreases but stays positive for a 12 and 24 hour lag. The use of daily averaged values , as in section 3 allows to smooth out the diurnal cycle and the zonal average of the autocorrelation coefficient every 24 hour lags resembles this shown on Figure 5.A. In addition, although the seasonal cycle of the outgoing infrared flux is small over a 90 day period, it was not substracted to the daily field in this study.

5. CONCLUSION

The comparison, on a global scale, of the seasonal average and standard deviation of the outgoing longwave flux obtained from NIMBUS–7 and NOAA NFOV daily data has shown that both data sets can be indifferently used for studies of short term variations in climate. In addition, the computation of time lagged autocorrelation coefficients using the NOAA IR time series allowed to highlight the importance of the diurnal cycle, especially above desertic regions. Validation of long term climate simulations with a general circulation model is currently being done using both satellite data sets for northern hemisphere winter and summer conditions. We plan, in the near future to focus our research on the study of specific regional areas.

REFERENCES

GRUBER, A., and H. JACOBOWITZ, 1985: The longwave radiation estimated from NOAA polar orbiting satellites: An update and comparison with NIMBUS–7 ERB results.
Adv. Space Res., **5**, 111–120.

JACOBOWITZ, H., H.V. SOULE, H.L. KYLE, F. HOUSE, and the NIMBUS–7 ERB Experiment Team, 1984: The Earth Radiation Budget (ERB) Experiment. An overview.
J. Geophys. Res., **89**, 5021–5038.

OHRING, G., A. GRUBER, and R. ELLINGSON, 1984: Satellite determination of the relationship between total longwave radiation flux and infrared window radiance.
J. Clim. Appl. Meteor., **22**, 416–425.

SMITH, L.D., and T.H. VONDER HARR, 1987: Temporal variability of the Earth Radiation Budget from NIMBUS–7 NFOV data.
Submitted to J. Clim. Appl. Meteor.

TAYLOR, V.R., and L.L. STOWE, 1984: Reflectance characteristics of uniform earth and cloud surfaces derived from NIMBUS–7 ERB.
J. Geophys. Res., **89**, 4987–4996.

ACKNOWLEDGMENTS

This research was supported under NASA Grant NAS1-16465.

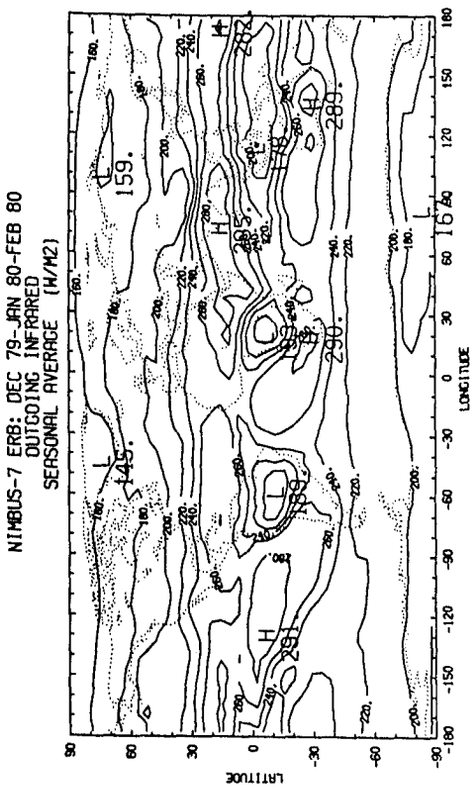

FIGURE 1.A: Horizontal projection of outgoing infrared from NIMBUS–7 data. Contour interval every 20 $W.m^{-2}$.

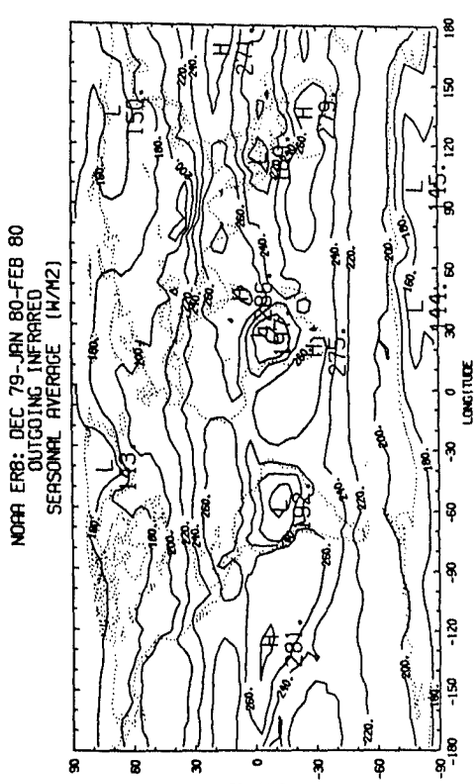

FIGURE 1.B: As FIGURE 1.A from NOAA data.

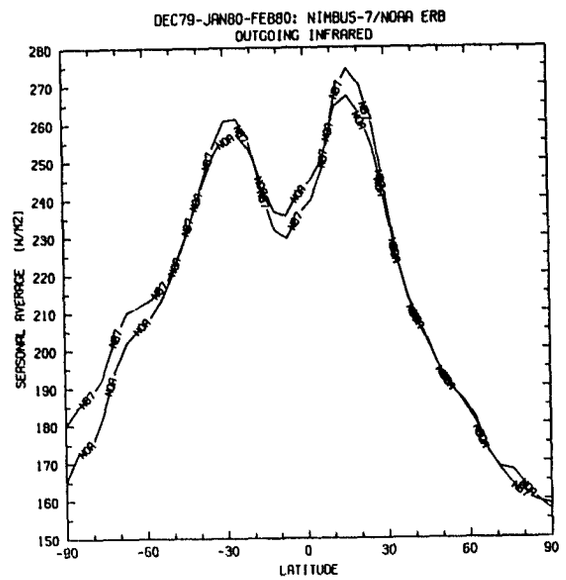

FIGURE 2.A: Zonal average of outgoing infrared ($W.m^{-2}$). Comparison between NIMBUS–7 (NB7) and NOAA (NOA) data for DEC 79-JAN 80-FEB 80.

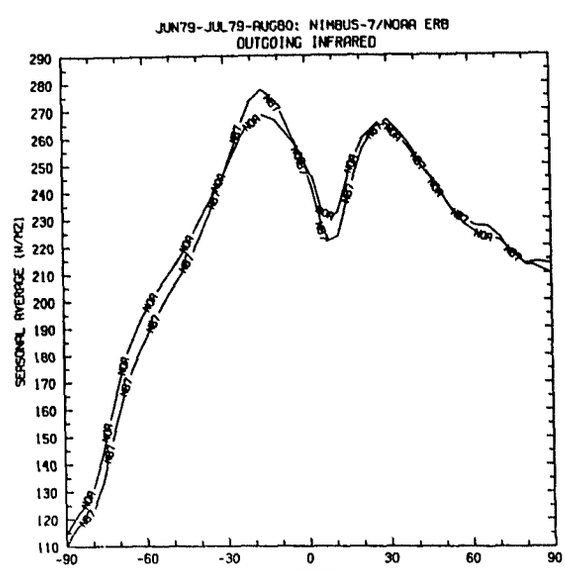

FIGURE 2.B: As FIGURE 2.A for JUN 79-JUL 79-AUG 79.

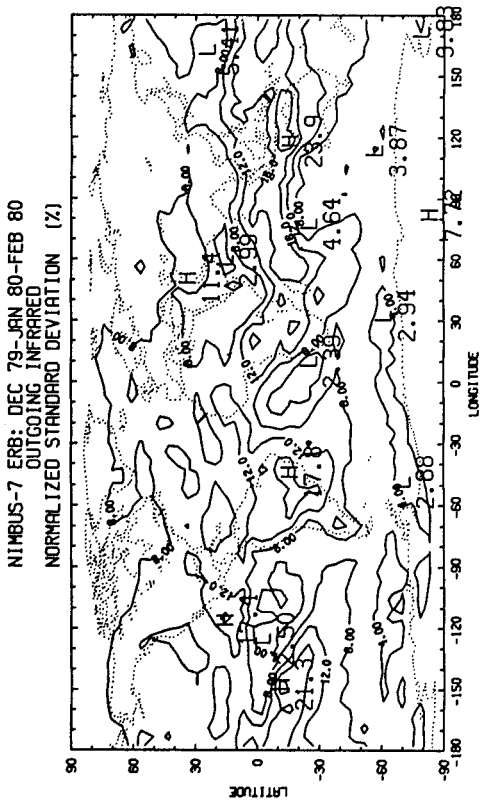

FIGURE 3.A: Horizontal projection of the normalized standard deviation of outgoing infrared from NIMBUS-7 data. Contour interval every 4%.

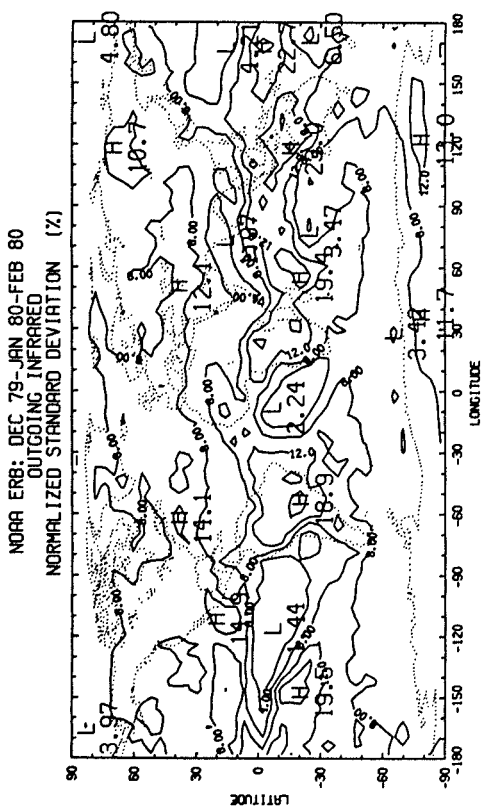

FIGURE 3.B: As FIGURE 3.A from NOAA data.

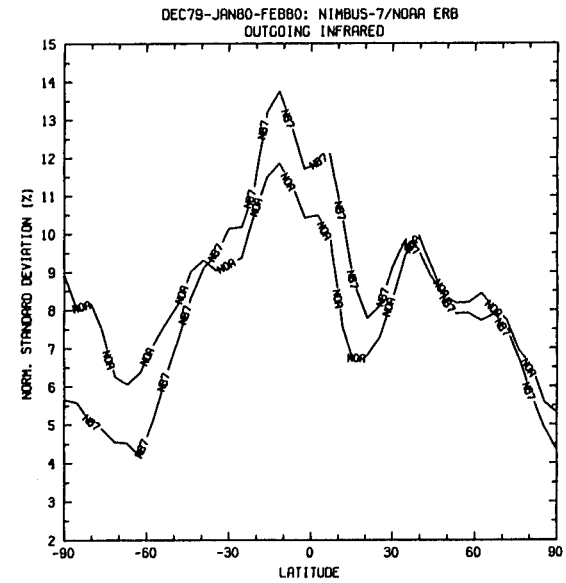

FIGURE 4.A: Zonal average of the normalized standard deviation (%) of outgoing infrared. Comparison between NIMBUS–7 (NB7) and NOAA (NOA) data for DEC 79-JAN 80-FEB 80.

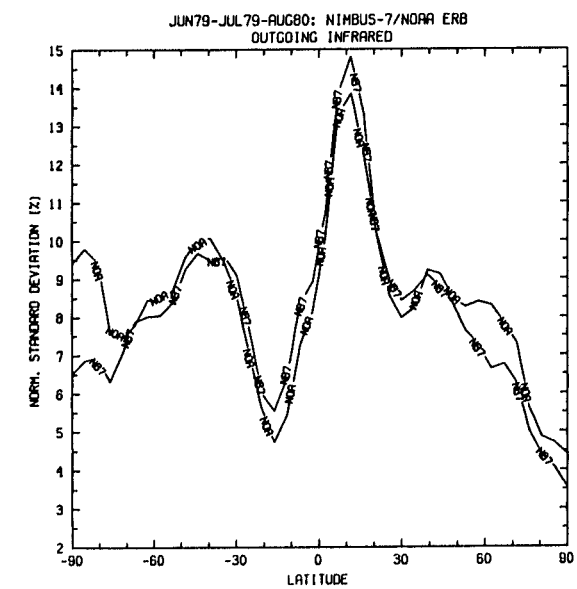

FIGURE 4.B: As FIGURE 4.A for JUN 79-JUL 79-AUG 79.

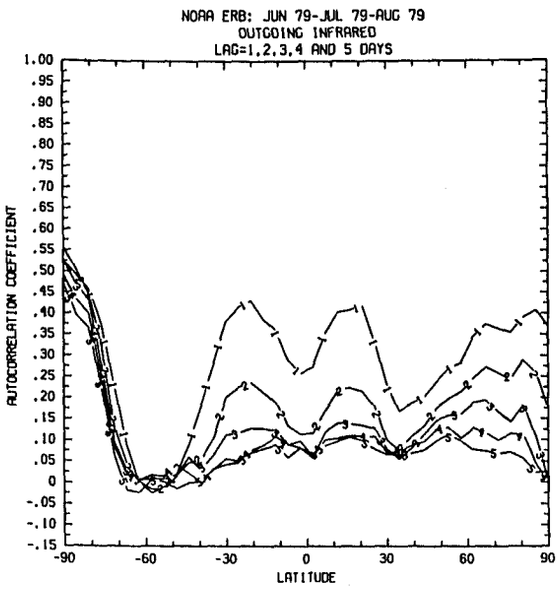

FIGURE 5.A: Zonal average of the autocorrelation coefficients of outgoing infrared every 24 hour time lag.

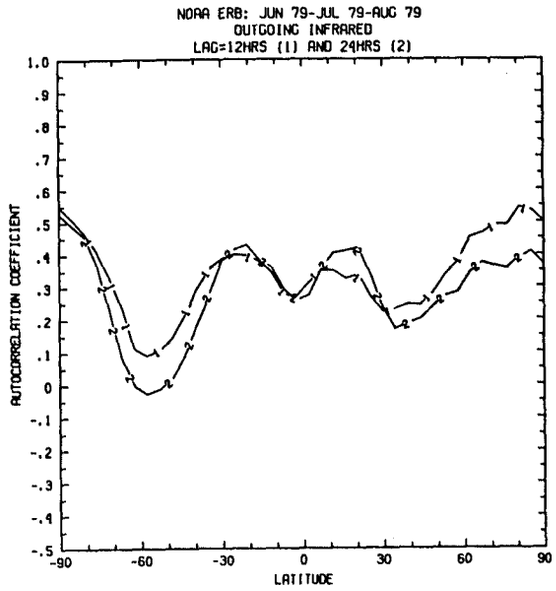

FIGURE 6.A: Zonal average of the autocorrelation coefficients of outgoing infrared (%) for a 12 hour (1) and 24 hour (2) time lag.

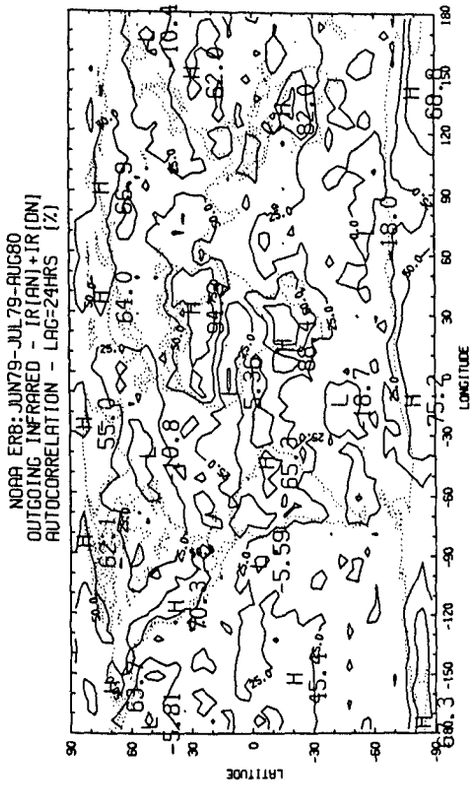

FIGURE 5.B: Horizontal projection of the autocorrelation coefficients of outgoing infrared for a 12 hour time lag. Contour interval every 25 %.

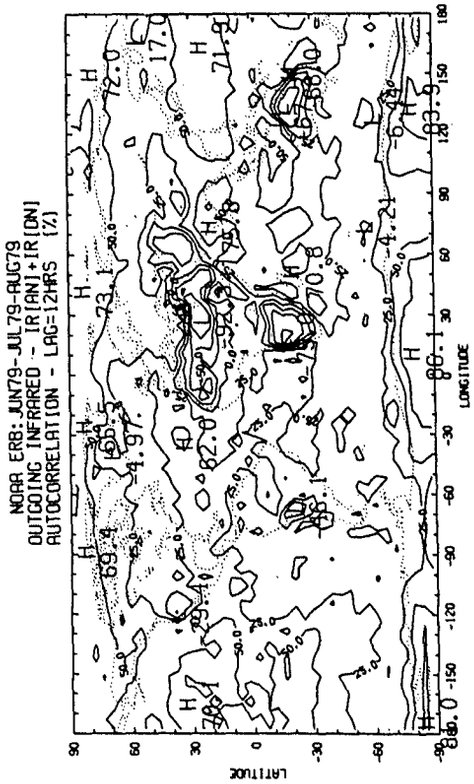

FIGURE 6.B: As FIGURE 5.B for a 24 hour time lag.

NIMBUS-7 EARTH RADIATION BUDGET MEASUREMENTS AND THEIR RELATIONSHIP TO THE ENERGETICS OF THE GENERAL CIRCULATION

David L. Randel and Thomas H. Vonder Haar

Cooperative Institute for Research in the Atmosphere (CIRA)
Colorado State University, Fort Collins, Colorado 80523

1. INTRODUCTION

Upon examination of the operation of the Earth-Atmosphere system, it becomes apparent that it's the variation of energy both temporally and spatially that drives the general circulation. Differences in the incoming shortwave radiation, and outgoing longwave radiation between the equator to poles provide the energy source for the atmospheric heat engine which drives the mid-latitude winds and eventually the mid-latitude cyclones. It is the purpose of this work to use the Nimbus-7 Earth Radiation Budget (ERB) observations to examine how changes in these equator to pole energy gradients effect northern hemisphere mid-latitude energetics.

Important to this work is the ability to examine ERB measurements over a number of years to define the ERB "climate". The Nimbus-7 ERB experiment makes this ideal due to its long term data set (over 8 years). A complete description is presented by Kyle et al. (1985). Equally important is the ability to use the ERB data on a weekly time scale instead of monthly, as has been used in previously reported results. It was shown (Randel, 1986) that data from the ERB WFOV instrument can be averaged to form a composite image with minimum time frequency near one week. Ellis (1972) made the same energetic calculations on a monthly average time scale using NMC gridpoint data from 1963 to 1971 and compared these to the NET radiation gradient measurements from a variety of satellites. Found were relationships between ERB gradients and energetics during times of strong interannual anomalies, and significant lag/lead correlations.

Calculations of kinetic energy, both mean and eddy, available potential energy, both mean and eddy, thermal wind, and average 700 millibar U wind component (zonal index) were made as possible describers of the mid-latitude circulation. Presented here will be results using just the kinetic energy calculations compared to the gradients of infrared (IR) flux and NET radiation.

2. DATA SETS

2.1 NIMBUS-7 ERB

The NIMBUS-7 ERB instruments included both scanning and fixed hemispheric radiometers. This study focuses on data from the fixed Wide-Field-Of-View (WFOV) instruments due to the long time series of that is available. Data started in November 1978, with data collection continuing through 1987, although only the first 7 years, until October 1985, was used. It was decided that only the northern hemisphere winters would be examined, therefore only the months of November through April are used. Due to the design of the WFOV instruments the data coverage during each day is poor. Therefore it was needed to construct a "composite" of 6 data time periods to achieve full global coverage. This inserts some error into the final weekly "composite" but is within the value of the total instrument error. In the first 5 years the instruments ran on a cycle of three days on, one day off. Therefore to get 6 data time periods we must take 8 actual calender days. In the last two years the instrument ran almost everyday, but for continuity the same 8 day period was used in the composite, only more data was available. This tended to decrease the error in the composite. For the six calender months in this study this led to a sample of 23 periods for each year in the time series.

The gradients of NET radiation and infrared flux were calculated by simple differencing of the zonal averages at 20 degrees and 70 degrees north latitude. Anomalies for each year were calculated by differencing the individual annual averages with the 7 year mean for each of the 23 periods.

2.2 Circulation Data

Due to its global extent the circulation data chosen was the NMC gridpoint analysis on the 2.5 X 2.5 latitude/longitude grid. Originally the U and V wind components were used in the kinetic energy (KE) calculations, but these proved to be too noisy due to the filling of missing data areas (Figure 1). Instead the geostrophic wind components were calculated from the geopotential heights and used in the kinetic energy equations. These equations are described in Oort (1964), and are simplified by using just the space domain. Eddy and zonal kinetic energy were calculated for each available time including the 00 and 12 UST for each day. Then these were averaged to create a concurrent data set with the ERB gradient data. Yearly anomalies were computed as with the ERB data.

The final circulation data set thus included: eddy and zonal kinetic energy for 7 northern hemisphere winters. Each year (November–April) contained the same 23 time periods as the ERB data. Levels used in the

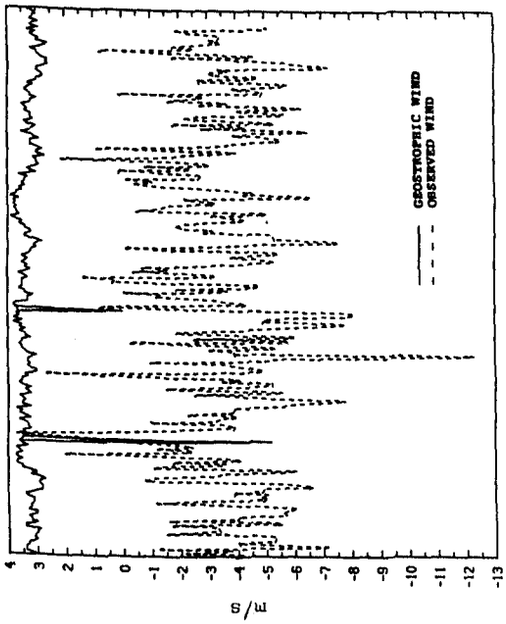

Figure 1. Time series of the daily global average U component observed wind and geostrophic wind.

kinetic energy calculations included the mandatory reporting levels with the exception of 250mb (1000, 850, 700, 500, 300, 200mb). Latitudinal extent was the same as the ERB gradients: 20 degrees to 70 degrees north.

3. RESULTS

3.1 Seasonal Cycle Net Radiation Gradient

The 7 years of ERB gradient and KE data were averaged over the entire data set to produce a mean state. The winter time series (23 periods) of the zonal KE and the NET radiation gradient are shown in Figure 2. A strong annual cycle is evident with the zonal KE leading by 5 time periods (40 days) in the early and mid-winter, but only by 15-20 days in March and April. Lag and Lead correlation coefficients are presented along with the figure, and maximum correlation is shown at -5 periods (ERB lagging). Figure 3 shows the identical plot except the with eddy KE instead of zonal KE. Again we see a strong annual cycle, and in this case a 6-7 time period ERB lag (Maximum correlation at -6 periods). The change in the NET radiation gradient is due to variation at both 20 and 70 degrees. Figure 4 shows the cycle of NET radiation at 20 and 70 degrees and the difference of the two for year 2. The NET radiation at 20 degree starts increasing much sooner (time period 8 vs. 14) than at 70 degrees. This is due to 20 degrees "seeing" the increase in solar radiation sooner as the sun moves out of the southern hemisphere. It is this complicated difference in each plot at 20 and 70 degrees that creates the lagged NET radiation. The difference starts increasing around January 1st and is greatest around March 1st. Between 5-7 weeks before the increase starts the zonal wind speeds and eddy activity are already increasing. Finally with winter over, the decrease in the ERB gradients and winds happens much closer together.

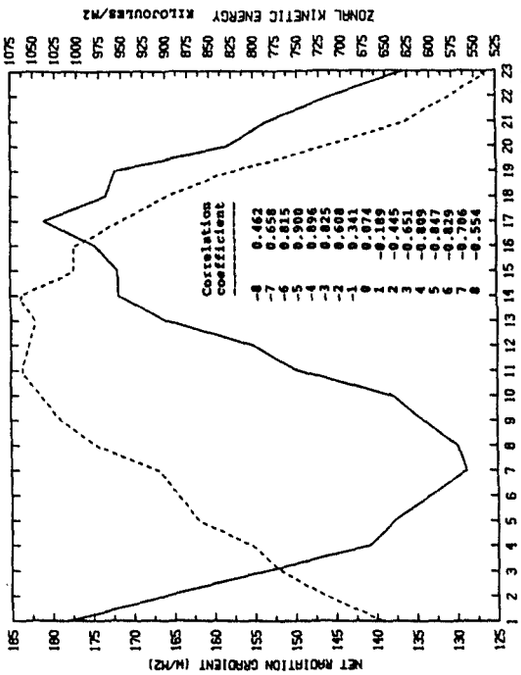

Figure 2. Time series of 7 year average NET radiation gradient and zonal kinetic energy from 20°N to 70°N latitude. The 23 time periods are approximately 8 days each from April. November to Correlation coefficients are included.

3.2 Seasonal Cycle Infrared Flux Gradient

Figures 5 and 6 compare the IR flux gradients with the zonal and eddy KE. As with the NET radiation gradient the latitudinal extent is from 20 to 70 degrees north. No large time lag in the seasonal cycle is apparent as was the case the the NET gradient. The zonal KE show maximum correlation with no time lag. Out of the seven years, the IR flux lead by 2 weeks 1 year, lagged 3 years, and was concurrent 2 years. The eddy KE over the 7 year average shows a 1 week lag by the IR flux, but this again varied from year to year (-3 weeks to +2 weeks). The maximum ERB gradient values and KE values occur in January. The close relationship between these parameters is to be expected as the IR flux measurements are an excellent describer of the overall temperature change at each latitude. As the temperature gradient increases so does the zonal wind speed and with slight delay the eddy winds.

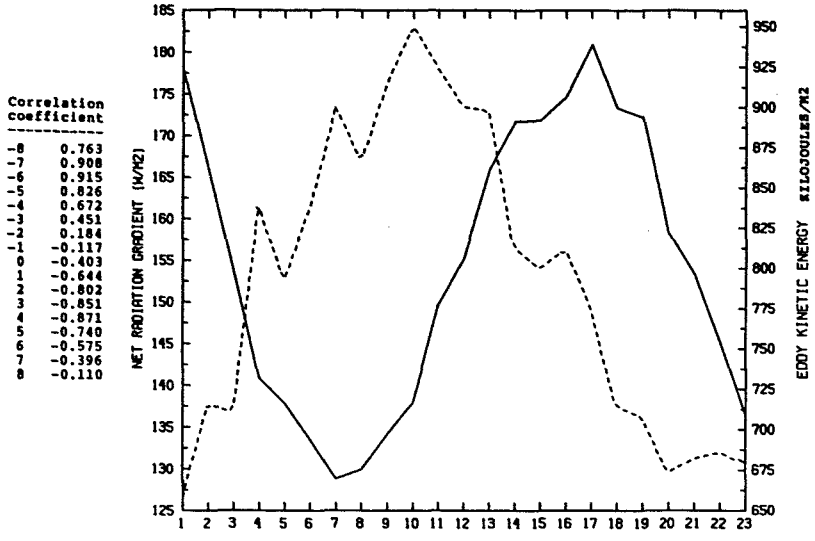

Figure 3. Same as Figure 2 except with the eddy kinteic energy.

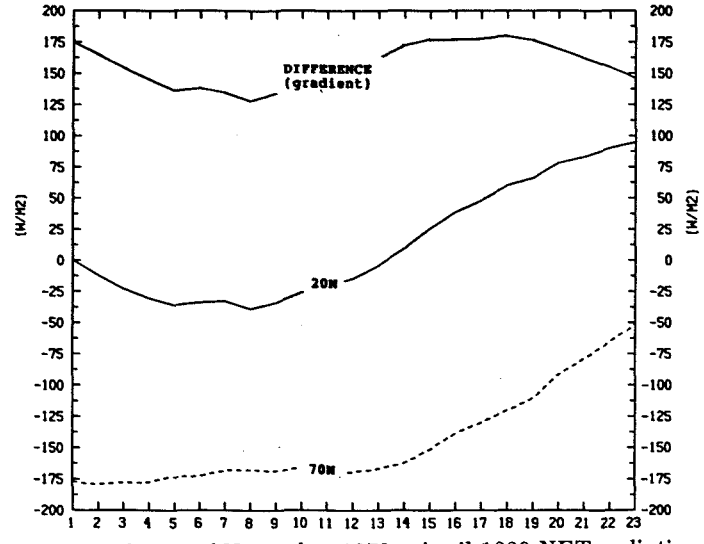

Figure 4. Time Series of November 1979 - April 1980 NET radiation. Zonal average values at 20 and 70 degrees north are plotted as well as their difference (NET gradient).

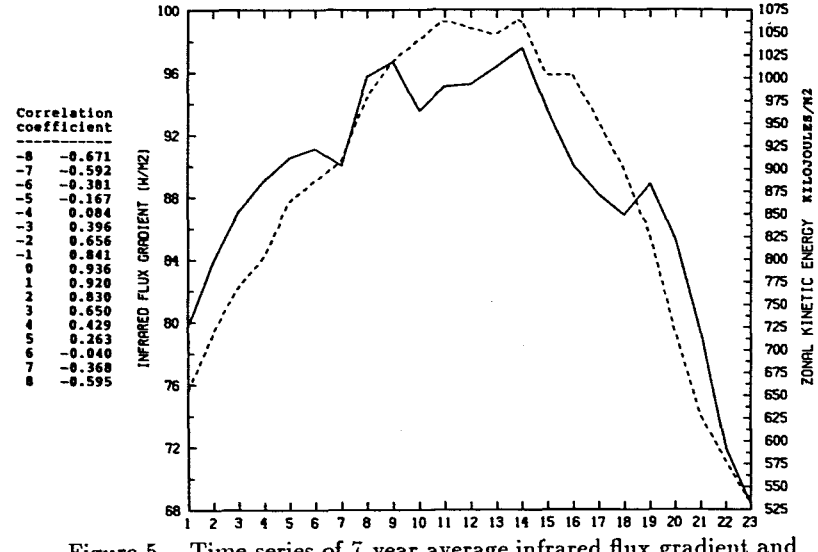

Figure 5. Time series of 7 year average infrared flux gradient and zonal kinetic energy from 20°N to 70°N latitude. The 23 time periods are approximately 8 days each from November to April. Correlation coefficients are included.

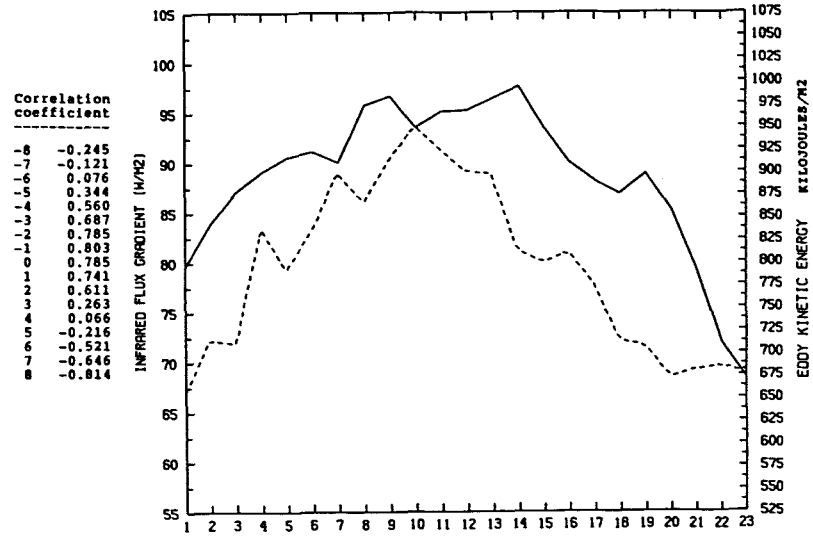

Figure 6. Same as Figure 5 except with the eddy kinteic energy.

3.3 Seasonal Cycle Removed

Using the 7 year averages as a mean state, allows for the removal of the annual cycle from the NET and IR flux gradients and from the eddy and zonal KE. Time correlations were then computed on the residual or anomaly for each year. Ellis (1972) found strong correlations between the zonal KE and the NET radiation anomalies with a 2 month radiation lag. Due to the limited number of sample periods (23), correlations of less than 2 months were examined. Over this time scale no consistent year to year lag/lead correlations were found between the anomalies of eddy KE and zonal KE when compared with the gradients of NET and IR flux. Certain years show acceptable levels of lag/lead correlation coefficient but these relationships aren't consistent over the whole data set. Examples are shown in Figures 7 and 8. Figure 7 compares the 1984-1985 NET gradient anomaly to the zonal KE anomaly. A high correlation of .745 was found with a KE lag of 1 week. However in Figure 8 (the same parameters but for 1979-1980), only small correlations were found. No definitive statement can be made at this time on the ability to use the ERB measurements to "predict" changes in the mid-latitude eddy of zonal kinetic energy.

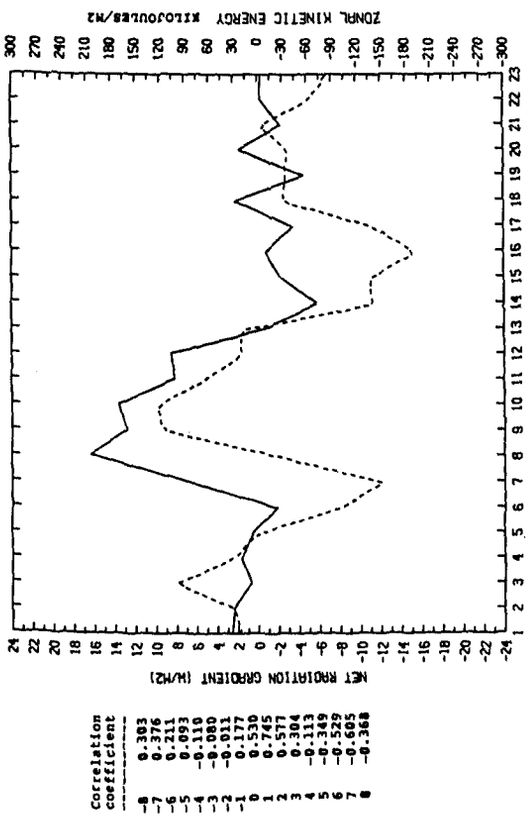

Figure 7. Time series of November 1984 - April 1985 NET radiation gradient and zonal kinetic energy anomalies from 20°N to 70°N latitude. Anomalies were created by removing 7 year average from individual years. Correlation coefficients as in Figure 5 are included.

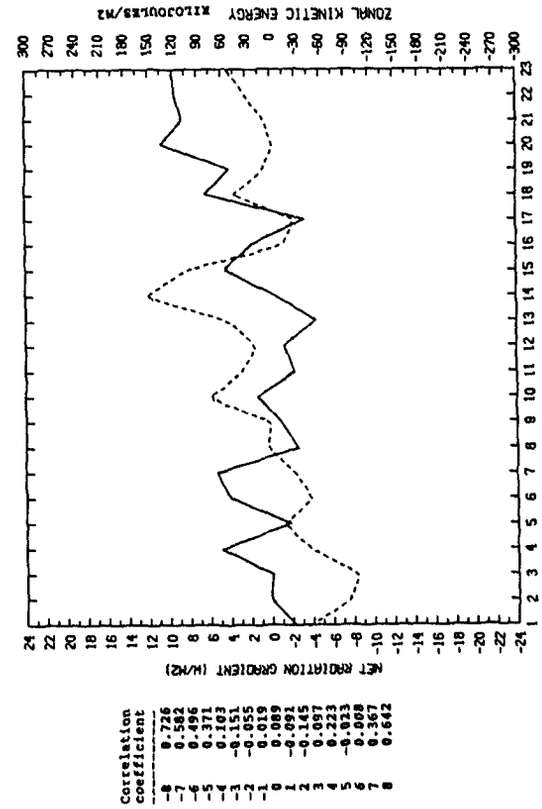

Figure 8. Same as Figure 7 except with November 1979 - April 1980.

4.0 ACKNOWLEDGEMENTS

Thanks to Roy Barnes at the National Center for Atmospheric Research (NCAR) Data Support Section for quick delivery of the NMC grid point data, and to Loretta Wilson for help in preparing this manuscript. This research was supported under NASA grants NAG-1-661.

5.0 REFERENCES

Ellis, J.S., 1972: Interannual variation in the Earth's Radiation Budget and the General Circulation. Masters thesis, Department of Atmospheric Science, Colorado State University, 59 pp.

Krueger, A.F., J.W. Winston, and D.A. Haines, 1965: Computations of atmospheric energy and its transformation for the Northern Hemisphere for a recent five-year period. *Mon. Wea. Rev.*, **93**, 227–238.

Kyle, H.L., P. Ardanuy, and E.J. Hurley,1985: The status of the NIMBUS-7 Earth-Radiation-Budget data set. *Bull. Amer. Meteor. Soc.*, **66**, 1378–1388.

Oort, A.H., 1964: On estimates of the atmospheric energy cycle. *Mon. Wea. Rev.*, **92**, 483–489.

Randel, D.L., G.G. Campbell, T.H. VonderHaar, and L. Smith, 1986: Defining the minimum temporal and spatial scales available from a new 72-month Nimbus-7 Earth Radiation Budget climate data set. Extended Abstracts, 6th Conference on Atmospheric Radiation, Williamsburg, VA, p. 280 (AMS).

SATELLITE INTERPRETATION TECHNIQUES INVOLVING THUNDERSTORMS

Ernest H. Goetsch
National Weather Service Forecast Office
Louisville, Kentucky 40213

1. INTRODUCTION

Severe weather warnings over the Continental U.S. have traditionally been based mainly on radar data and spotter information. Very little operational input to field office forecasts has resulted from satellite imagery, because of the relatively late receipt of the data and lack of looping capability. But with the addition of SWIS (Satellite Weather Information System) to weather offices across the United States, real-time "nowcasting" of convective activity is now possible using satellite imagery.

The goal of this paper is to make field forecasters aware of how important satellite interpretation can be to operational forecasting of severe weather and heavy rain. Techniques are listed that provide the forecaster with a brief description of the most significant convective signatures and their meaning. Throughout the text, important signatures are highlighted by <u>underlined</u> type with a limited number of examples.

2. BACKGROUND

This study examines over 200 individual case studies covering the period of 1978 to 1987. Listed techniques have been collected from numerous authors, and expanded into this comprehensive summary. This paper is the nucleus of a much larger training presentation at the Louisville WSFO.

3. STORM CHARACTERISTICS

3.1 <u>Texture Signatures</u>

The texture of a storm can define whether severe weather and/or heavy rain is possible. The <u>Hard Cell Signature</u> (Hedges, 1980) identifies storms in which a high speed updraft is present. These storms have a very sharp (well defined) outer cloud anvil edge in the visible imagery. A tight temperature gradient is present on the outer cloud edge in the infrared (IR) data (Cells 1 and 2, Figure 1 and 2). As the storm grows, anvil cirrus is carried downwind, often making the downstream cloud edge appear fuzzy or less defined. Even though this occurs, severe potential will continue as long as

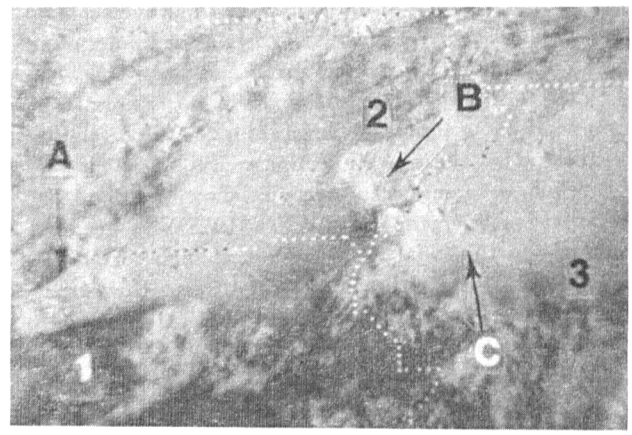

Figure 1. 1 mile-2 km Visible, 2200z, 13 April 1981

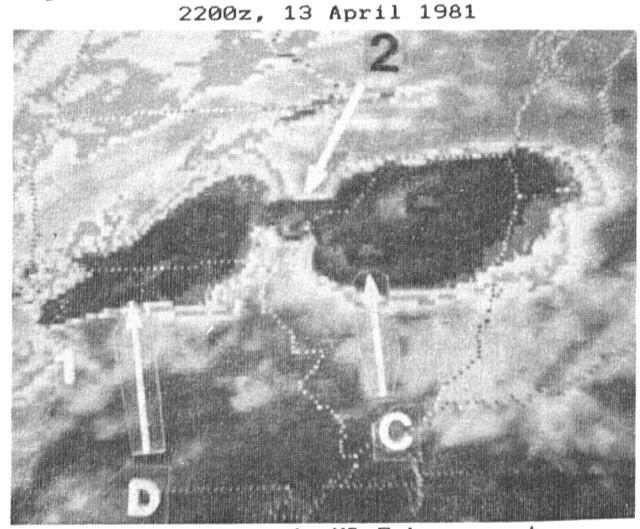

Figure 2. Infrared, MB Enhancement Curve, 2200z, 13 April 1981

the upwind edge remains sharp. Later in the cell's life cycle, the storm will become less defined, taking on the <u>Fuzzy Signature</u>. This signifies the storm's decaying stage and the end of severe potential.

The <u>Overshooting Top Signature</u> is illustrated by a storm's strong updraft penetrating through it's cirrus canopy (Point B and C, Figure 1). The updraft core is located beneath the overshooting top. Lemon and Doswell (1979) stated that the surface mesolow forms directly under or slightly south or southeast of the updraft, frequently the best area for tornadic development. In the infrared

data, the overshooting top is often seen as a small pimple of colder cloud top temperatures on the cell's cirrus canopy.

The Enhanced-V Signature (McCann 1981) in the IR imagery is formed by a storm's updraft blocking the environmental wind and diverting flow around it (Point C and D, Figure 2). A "V" shaped cold IR temperature area results. An induced "wake" of warmer temperatures appears just downstream of the overshooting top and the crest of the "V". For severe weather to occur, the storm must be growing: IR contours expanding and cloud top temperatures cooling. Once the "V" is detected, a storm will remain severe as long as the storm grows, even if the "V" disappears. Severe weather will occur 5-25 km south or southeast of the coldest top and about thirty minutes after the V-notch appears (McCann, 1981).

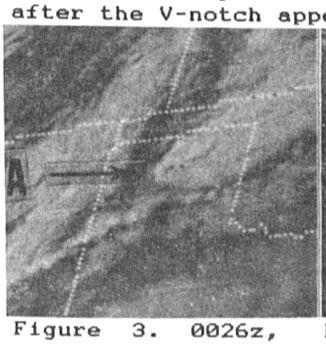

Figure 3. 0026z, 29 June 1979

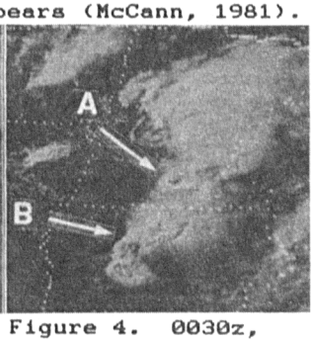

Figure 4. 0030z, 6 June 1982

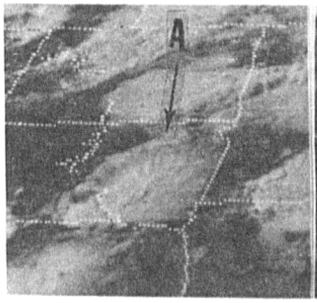

Figure 5. 0001z, 24 June 1981

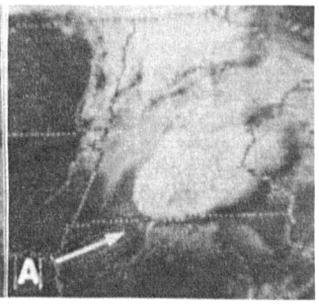

Figure 6. 0030z, 27 June 1980

Another potential severe weather producer is the Collapsing Top Signature (Point A, Figure 3). The collapse of a supercell storm is often the stage at which a tornado forms (Lemon and Doswell, 1979). Fujita (1978) also stated that some downbursts are caused by the collapse of the updraft.

Many storm complexes go through numerous phases of development. Some build, collapse, then rebuild, etc. With all of these variations in the normal development and dissipation cycle, a thunderstorm complex will sometimes have numerous pits and overshooting tops, not just one. The Pimpled and Pitted Signature on a cirrus canopy represents the presence of such a storm complex (Area B, Figure 4). These storms may not be of the supercell type, but may be very severe, with heavy rain also possible.

Striations in the Cirrus Canopy appear as numerous ripples or waves in a cell's cirrus top (Point A, Figure 5). This is a signal that the storm complex is beginning to weaken. The cirrus outflow will continue to expand and the once hard cell usually becomes fuzzy and dissipates.

3.2 Flanking Lines

The Flanking Line Signature is sometimes called a "cell with a tail" (Point A, Figure 6). A flanking line (Lemon, 1976) is a line of CB's building into the middle of a supercell storm. This signature develops in the low level convergent area between the rear flank downdraft and the inflow region. A mature flanking line will increase in size as it approaches the parent storm, building into the storm core where the strong updraft and overshooting top are located. This same area is where mesolow formation and tornado generation are possible.

Other storms become strong enough to change the surrounding low level environment, without developing a flanking line. Lines of cumulus clouds often appear to "feed" into a storm cell. These CU Feeder Lines represent a strong low level inflow of moist air. Storms with feeder lines are usually not as severe as flanking line storms. CU feeder lines can later strengthen into flanking lines, signifying supercell development.

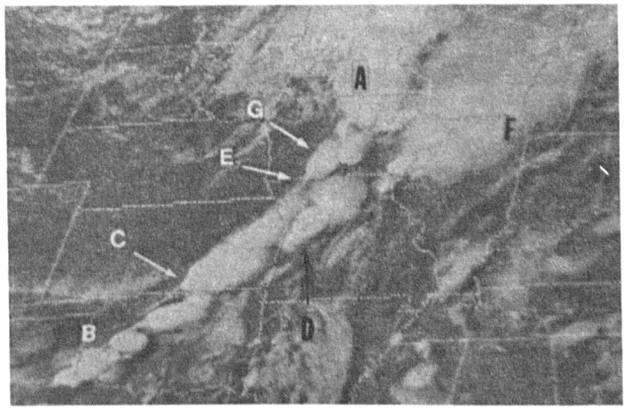

Figure 7. 2330z, 6 July 1982

3.3 Storm Orientation

The way individual cells are oriented can aid in defining the severe potential of a particular storm. A broken line (Point B-C, Figure 7) will usually be more severe than a solid line because each storm is able to draw upon its own undisturbed moist airmass. In a solid line (Point C-E), a gust front will develop that may interfere with the other cells in the line. Fewer supercells will therefore develop in a solid line, with the most severe cell forming on the southern end of the line (Point C). This is where the strongest low level inflow of undisturbed moisture is located.

A cell that develops south or upwind of another will usually be more severe. The southern cell may cut off the low level fuel source to the storm north of it. The northern cell will either dissipate, or may never develop (Cell D and Area E, Figure 7).

When a major surface boundary is present, cumulus will often develop down the boundary apparently feeding into the southern storm. The result will be a tail on the left rear side of the southern cell (Point C, Figure 7). This is not a flanking line. This tail forms in response to frontal convergence, not in response to a supercell's rear flank downdraft. This storm may still be severe, but usually not as strong as the flanking line.

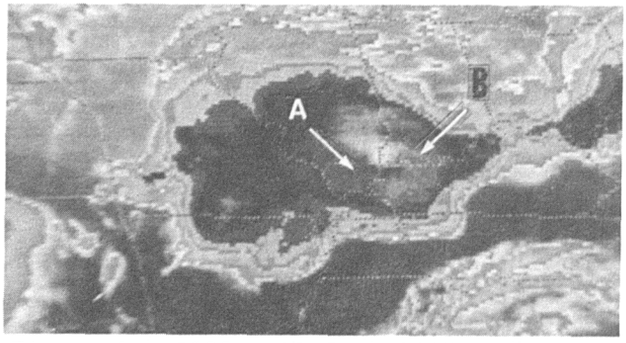

Figure 8. 0330z, 10 June 1985

3.4 Storm Clusters

Downburst signatures in satellite imagery are depicted as the occurrence of rapid warming within the anvil top of a thunderstorm cluster. Two types of cloud top warming occur. The first is rapid warming near the core of a storm cluster with an oval-shaped anvil (Point A, Figure 8). Wind flow at anvil level is relatively weak with the warming area just upwind from the coldest infrared tops (Point B). The downburst is located beneath the coldest tops, ahead of the corresponding warming (Fujita, 1978). The second type occurs when the anvils are wedge-shaped. This shape is produced by the presence of strong anvil level winds and strong vertical shear. Rapid cloud top warming occurs downwind from the downburst, in an elongated band or trench (Ellrod, 1985).

Numerical guidance can be modified using satellite data to accurately track Mesoscale Convective Complexes (MCC's) (Maddox, 1983) throughout their life cycles. MCC's (Point A, Figure 9) produce large areas of heavy rain and flash flooding, plus tornado and downburst occurrences. A minor jet max usually develops on the north side of an MCC, visible as an anticyclonically curved cirrus streak (Point B-C, Figure 10). After the complex has dissipated, a low to middle level vorticity maximum will usually remain behind (Point A), acting as a trigger for new convection during

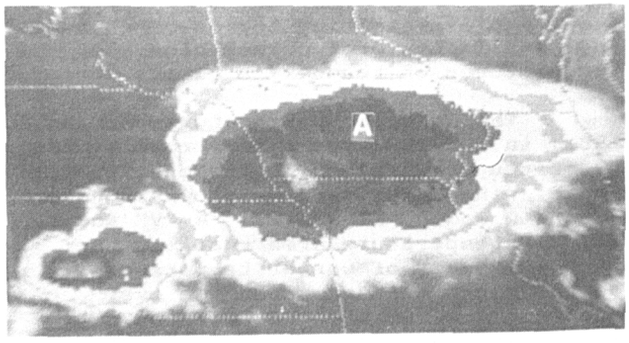

Figure 9. 0230z, 24 June 1985

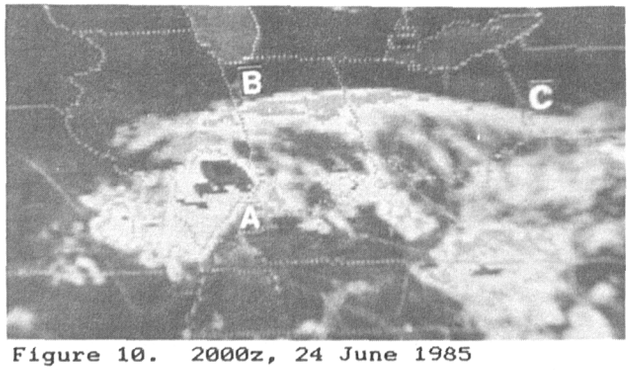

Figure 10. 2000z, 24 June 1985

the next diurnal heating period (Johnston, 1982).

3.5 Heavy Rain Characteristics

Many of the signatures important for severe weather are also highly significant in determining heavy rain development. Heavy rain occurs in the active portion of a storm system, where the strong updrafts are located. Overshooting tops, Enhanced-V signatures, bright anvils, and textured anvil tops (such as pits or pimples) identify this portion of the storm. For thunderstorms embedded in strong vertical wind shear, the heaviest rainfall will occur along the upwind edge of the anvil. For storms in weak wind shear, the heaviest rain will fall near the anvil center (Scofield, 1984).

The merger of two thunderstorms dramatically increases rainfall amounts by combining two updrafts into one strong convective system. The merger of a storm with a low level boundary produces a similiar rainfall increase.

Rainfall estimates can be calculated based on cold cloud top temperatures and growth, plus divergence aloft. Strong divergence is depicted by the upwind anvil edge forming a wedge shape. An anvil wedge angle of 50 to 90 degrees pointing upwind is highly significant (Scofield, 1984).

Storm continuity can be monitored by animated satellite imagery. Stationary storms, plus a series of storms following one after another over the same area (Train Echo Effect) can produce severe flash flooding.

4. ENVIRONMENTAL CHARACTERISTICS

4.1 Moisture Patterns

Moist, unstable air is identified in satellite imagery by fields of cumulus and towering cumulus clouds. These clouds usually develop in deep moisture pockets and along axes of deep low level moisture (Point E-D, Figure 11). These features trigger new convection or intensify previously developed storms when intersected (Purdom, 1979).

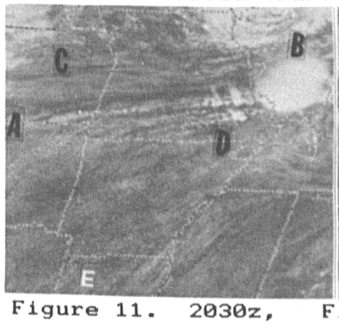

Figure 11. 2030z, 29 May 1982

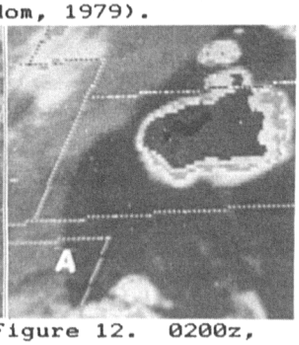

Figure 12. 0200z, 15 April 1982

Low level moisture can be identified in the IR imagery when a significant temperature contrast between moist and dry air occurs. A dryline at night is illustrated in Figure 12 (Point A).

4.2 Wind Patterns

Cumulus clouds will frequently become aligned parallel to the low level wind field, in a cloud pattern called Cumulus Streets (Point E-D, Figure 11). From the cumulus defined wind field (from E to D and C to B), convergence zones can be identified that may trigger convection (Point A to Cell B).

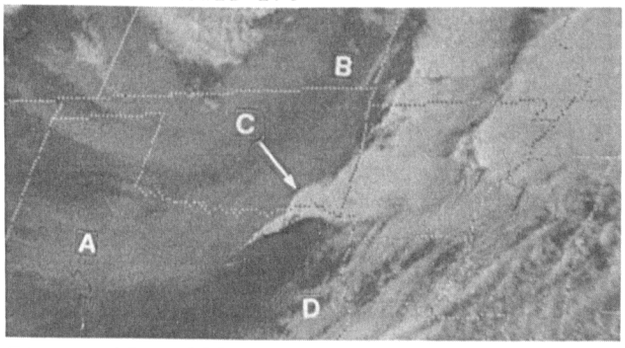

Figure 13. 2230z, 2 April 1982

Wind flow can also be defined by the presence of dust. Dust will appear as a diffuse, hazy area. A strong low level jet axis is often present parallel to the dust streak (A to B, Figure 13). Convergent flow of the jet into a moisture axis can produce severe convection.

4.3 Low Level Boundaries

The severe thunderstorm environment will usually have an additional characteristic that a non-severe, airmass situation is missing. That feature is some type of low level discontinuity or "boundary" that triggers the initial lifting needed for thunderstorm development. Low level boundaries can be major synoptic scale fronts and drylines, or mesoscale systems. Satellite data is essential for locating boundaries between surface observation sites.

Diurnal heating can be a very efficient producer of mesoscale boundaries. In a seemingly homogenous airmass, differential heating caused by morning clouds in one area and clear skies in another will allow a temperature discontinuity to develop. These cloud induced fronts may trigger afternoon thunderstorm development under unstable conditions. Such features may also trigger severe weather when intersection occurs with another line of storms.

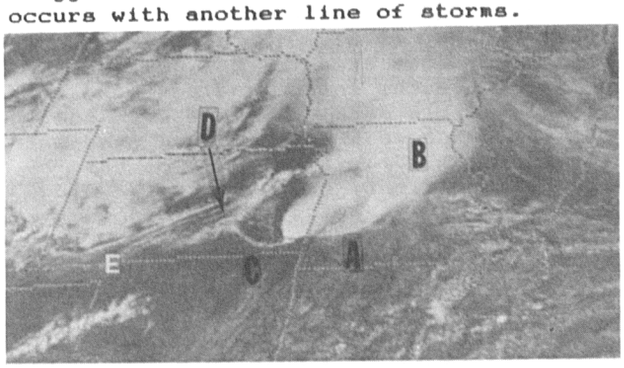

Figure 14. 1830z, 30 May 1982

The Thunderstorm Outflow Boundary or Gust Front is a feature that forms when rain-cooled thunderstorm air makes contact with warm, moist environmental air. Strong horizontal shear and turbulence, gusty winds, plus very strong vertical motion will usually accompany the passage of a gust frontal boundary. A thin line of cumulus clouds, called an arc cloud, will frequently develop on the boundary in response to vertical motion at the frontal surface. Two types of gust fronts exist. The active type (Gurka, 1976) (Point A, Figure 14) moves rapidly, being reinforced by convective downdrafts. Extensive cumulus development exists between the front and the parent storm. Maximum wind gusts with frontal passage will usually be twice the forward frontal speed. The inactive type (Gurka, 1976) (Point C) involves stratiform clouds along the front and clear air behind it. This front moves slower with no additional convection developing along it. Gusty surface winds are no longer produced with frontal passage.

Storm complexes frequently produce such large amounts of rain-cooled air that a mesoscale high pressure area forms, called a "Bubble High" (Miller, 1975). Strong bubble highs can trigger squall line development on the forward bubble edge where extense low level convergence of moist, unstable air is

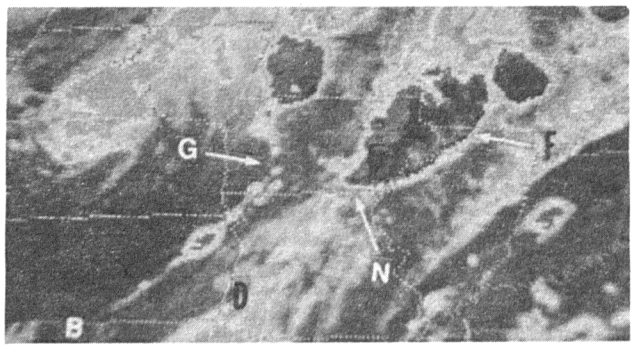

Figure 15. 2000z, 6 July 1982

located. These Bubble Squall Lines (Miller, 1975) usually have an oval shape with a curved, sharp leading edge, bulging in the direction of movement (Point N-F, Figure 15). The forward anvil edge will have a tight IR gradient indicating strong winds with storm passage (Hedges, 1980) (Gurka, 1976). The strongest winds will occur just ahead of the most active cells, where the sharp leading cloud edge in the visible data coincides with the maximum enhanced IR temperature gradient (McCarthy, 1985). A relaxing of the tight IR gradient, or cloud top warming will signify weakening of the complex.

All thunderstorm systems leave behind a rain-cooled, stable airmass, frequently clear of most cumulus clouds (Figure 15, Central Iowa). A discontinuity exists between this rain-cooled air and the moist, undisturbed air to the south (D). This old outflow boundary (Point N-G) may later trigger new storms.

4.4 Intersections

When two or more boundaries meet or intersect, vorticity and vertical motion are enhanced and concentrated into a confined region (Miller, 1975). This makes intersection areas prime for severe convection and heavy rain (Purdom, 1979). Intersections can occur between any type of boundary; including fronts, squall lines, and/or thunderstorm outflow boundaries. The merging of two separate cells will also produce the same result--rapid convective development in the intersection area. Figure 15 depicts the intersection of a weak front (Point A-B) with an old outflow boundary (Point N-G). Convection develops at intersection Area G, also shown in Figure 7 at G.

Figure 14 illustrates a second example. A bubble high remains over Missouri, produced by Storm B. Outflow boundary A-C-D is intersecting an old front (E-D) at Point D. Severe storms form later at D.

Intersection areas are frequently seen in radar data as Line Echo Wave Patterns (LEWP). Some strong LEWP's or frontal bends can also be detected in satellite imagery (Point C, Figure 13).

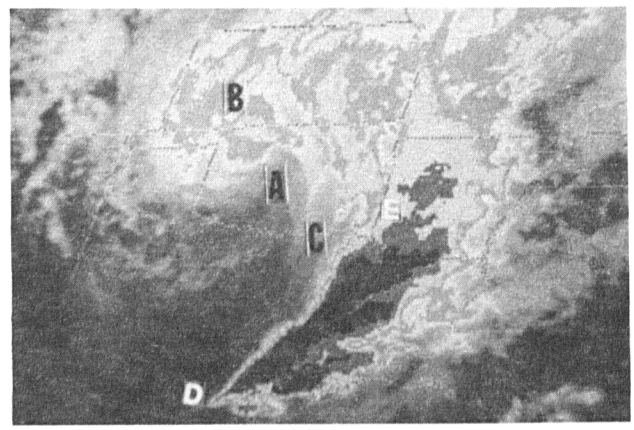

Figure 16. 2200z, 9 May 1981

5. SYNOPTIC SCALE FEATURES

5.1 Comma Clouds

The Comma Cloud (Weldon, 1979) is the classic pattern in which a short wave will appear in satellite data. The cloud itself is an area of upward motion and positive vorticity advection (PVA) with downward motion in the upwind clear air. A vorticity trough can be analyzed along the cloud edge (Point A-C-D, Figure 16). A second vorticity trough is associated with the main upper trough axis and usually extends south behind the tail of the cloud (Point B to D). The vorticity maximum (Point A) is located just outside the comma cloud head (Point B), near the cloud edge inflection point and north of the jet maximum position (Point C). The surface front can be approximated along the comma tail (Point E-D).

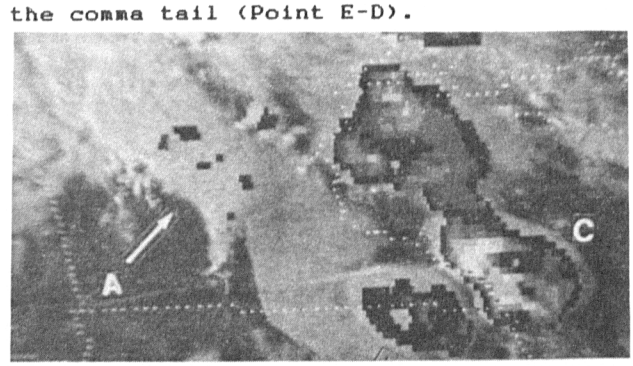

Figure 17. 1C3 Enhancement Curve, 2300z, 25 April 1986

Individual thunderstorm clusters can frequently take on a comma cloud shape. These Mini-Comma Cloud systems (Point A, Figure 17) will usually be very severe, due to highly concentrated mesoscale vorticity.

5.2 Upper Level Wind Flow

The upper level streamline flow over an area can be estimated from cirrus clouds. Divergent wind flow patterns and jet maximum can also be tracked (Weldon, 1979).

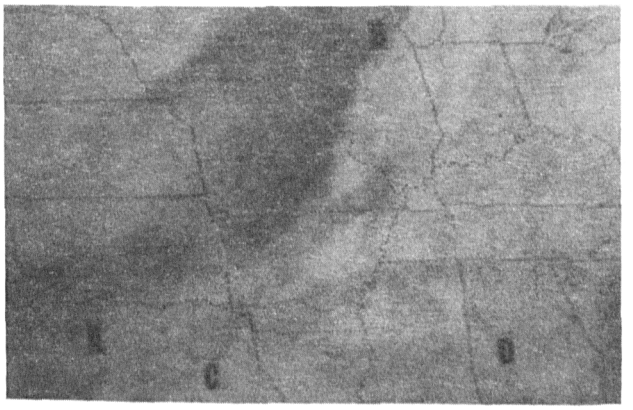

Figure 18. 0530z, 10 November 1984

Moisture Channel Imagery (VAS) on board present GOES satellites can define upper level wind patterns (Gurka, 1985). Operational verification of how numerical models are performing can be accomplished, in addition to defining upper level circulation systems. In Figure 18, the streamline flow is from A-B and C-D, triggering storms in the divergence over Arkansas.

6. CONCLUSION

Satellite imagery can be an extremely valuable tool in thunderstorm forecasting. When added to radar and conventional data, the techniques listed result in a "birds-eye" view of the total storm environment and cell structure. Though much research remains, operational forecasters can now effectively add satellite data to the forecast routine, helping to more accurately warn the public.

7. ACKNOWLEDGEMENTS

Capt. Jeffrey R. Hedges deserves special credit for development of many of the described techniques in a satellite interpretation school taught in Omaha in 1980. The author would also like to thank Fred Keyes and Dan Houser from the Ann Arbor, Mi. WSFO for all their encouragement and support. Special thanks go to my wife Becky for her continuous support and frequent paper review!

8. REFERENCES

Ellrod, G., 1985: Dramatic Examples of Thunderstorm Top Warming Related to Downbursts. National Weather Digest, 10, No. 2, 7-13.

Fujita, T. J., 1978: Manual of Downburst Identification for Project Nimrod. SMRP Research Paper No. 156, University of Chicago, 104 pages.

Gurka, J. J., 1976: Satellite and Surface Observations of Strong Wind Zones Accompanying Thunderstorms. Preprints, 6th Conference on Weather Forecasting and Analysis, May 10-13, AMS, Boston, 499-502.

Gurka, J. J., 1985: The Use of 6.7 Micron Water Vapor Imagery for Improving Precipitation Forecasts. Proceeding of the 6th Conference on Hydrometeorology, Oct. 29-Nov. 1, AMS, Boston, 260-265.

Hedges, Capt. J. R., 1980: Severe Weather Unit Satellite School Seminar. AFGWC Severe Weather Unit, Omaha, Neb., unpublished.

Johnston, N. 1982: Mesoscale Vorticity Centers Induced by Mesoscale Convective Complexes. Preprints, 9th Conference on Weather Forecasting and Analysis, June 28-July 1, AMS, Boston, 206-213.

Lemon, L. R., 1976: The Flanking Line, A Severe Thunderstorm Intensification Source. Journal of Atmospheric Science, 33, 686-694.

Lemon, L. R., and Doswell, C., 1979: Severe Thunderstorm Evolution and Mesocyclone Structure as Related to Tornadogenesis. Monthly Weather Review, 107, 1184-1197.

McCann, D. W., 1981: The Enhanced-V, A Satellite Observable Severe Storm Signature. NOAA Technical Memorandum NWS NSSFC-4, NSSFC, Kansas City, Mo., 31 pages.

Maddox, R. A., 1983: Large-scale meteorological conditions associated with mid-latitude, mesoscale convective complexes. Monthly Weather Review, 111, 1475-1493.

Miller, R. C., 1975: Notes on Analysis and Severe Storm Forecasting Procedures of the Air Force Global Weather Central. AWSTR 200 (Rev.), HQ Air Weather Service, Scott AFB, Ill., 190 pages.

Purdom, J. F. W., 1979: The Development and Evolution of Deep Convection. Proceedings of the 11th conference on Severe Local Storms, October 2-5, AMS, Boston, 143-150.

Scofield, R. A., 1984: The NESDIS Operational Convective Precipitation Estimation Technique. Proceedings of the 10th Conference on Weather Forecasting and Analysis, June 25-29, AMS, Boston, 171-180.

Weldon, R, B., 1979: Part IV - Cloud Patterns and the Upper Air Wind Field. Satellite Training Course Notes, NOAA/NESS, Application Laboratory, WWB, Suitland, Md., 80 pages.

STORM DIAGNOSTIC/PREDICTIVE IMAGES DERIVED FROM A COMBINATION OF LIGHTNING AND SATELLITE IMAGERY

Steven J. Goodman[1], Dennis E. Buechler[1], and Paul J. Meyer

[1]Universities Space Research Association
NASA/Marshall Space Flight Center
Huntsville, Alabama 35812

1. INTRODUCTION

Weather satellites and radars are the most widely used tools for short-term forecasting and warning of thunderstorm hazards such as tornadoes, hail, flooding, and microbursts. Until recently, the lightning hazard could only be inferred from radar reflectivity displays. With the advent of lightning detection technology, it is now possible to directly measure the existence and frequency of lightning activity in storms over large areas in real-time. The recent deployment of regional and national networks using magnetic direction finding (Krider et al, 1976) and time-of-arrival (Bent and Lyons, 1984) techniques provides a new opportunity for merging lightning data with radar and satellite data for thunderstorm nowcasting.

Computers are routinely processing a wealth of meteorological data acquired from a number of sensors having a broad range of spatial and temporal resolutions. There will be an increased need for, and a greater emphasis placed on extracting and displaying the relevant information contained in these multiple data sets. We still tend to focus our attention on displays of single sensor measurements (e.g., black-body cloud-top temperatures, radar reflectivities or rain rates, lightning locations). Yet, with McIDAS or PROFS workstations, for example (and the future AWIPS-90 meteorological display system), it is (will be) possible to overlay radar and lightning data with satellite imagery, surface, and upper air data. But sooner or later the analyst or forecaster will find the relevant information buried under a mass of contours, dots, shapes, and numbers. If we are to improve on the human factors aspects of meteorological displays (i.e., the man-machine interaction), there must be a effort aimed at reducing the number of products we have to look at in order to form a conceptual picture of what is going on in the atmosphere.

In this paper we present a technique for generating trend or convective tendency images using a combination of GOES satellite imagery and cloud-to-ground lightning observations made with a ground-based lightning detection network operated by NASA/Marshall Space Flight Center. The intent of such imagery is two-fold. On the one hand, the lightning data provides an X-ray, if you will, on the location, growth, and decay of the convection that is obscurred in satellite imagery by cirrus clouds. This problem is generally a serious one when storms are embedded in mesoscale convective systems. We show that the lightning flash rate trend provides different diagnostic information from the time-rate-of-change of cloud top black-body temperatures. A second objective is to combine the life-cycle characteristics into a single derived product that provides information on past, present, and future storm development.

2. A CONCEPTUAL MODEL OF CLOUD ELECTRICAL DEVELOPMENT

In order to understand the additional usefulness of the lightning measurement, we need to consider the lightning activity in the context of thunderstorm evolution. Figure 1 shows a simplified conceptual model of the growth and decay of a typical thunderstorm and its associated lightning activity. The temporal evolution of the lightning activity is in-phase with the development of the storm updraft and is strongly coupled to the life-cycle of the thunderstorm as described by Byers and Braham (1949), Workman and Reynolds (1949), and others. The electrical development of the cloud is intimately connected to its dynamical and microphysical development. The total amount of lightning and peak flash rates associated with a storm will be a non-linear function of its size, height, duration, and environment (Grosh, 1978; Williams, 1985; Cherna and Stansbury, 1986; Goodman and MacGorman, 1986; and Buechler et al, 1988).

Once a storm electrifies, the initial discharge will almost always be intracloud. The discharge occurs 5-10 minutes after initial electrification, which itself begins 5-10 minutes after the onset of strong convection and the detection of a 35-40 dbZ radar echo aloft. The stage is now set for the active lightning-producing phase. As the storm continues to develop, the active electrical phase may have a duration lasting from a few minutes to hours depending on the storm variables described above. On average, the first cloud-to-ground discharge will occur 15-20 minutes after the initial radar echo is observed in a vertically growing

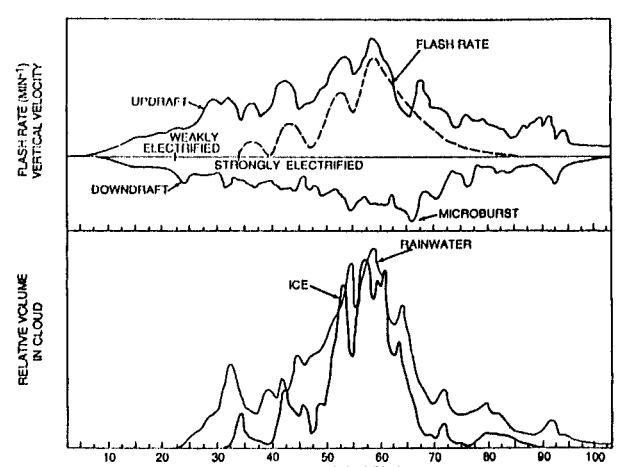

Figure 1. Conceptual model of the temporal evolution of cloud electrical, kinematic, and microphysical development.

cloud. As a general rule, the longer a storm takes to reach its maximum intensity, the longer it takes to decay. A rapidly growing storm is often a rapidly dying storm. The evolutionary history will generally follow an exponential growth and decay life-cycle (Goodman and MacGorman, 1986). This relationship appears to to be true for the ensemble convection embedded in mesoscale convective systems as well. Thus, the time-rate-of-change of flash rates is in step with the growth and decay of the thunderstorm.

3. RESULTS

The methodology used to generate lightning/satellite convective tendency imagery is explained by example. We use the evolution of the June 11, 1986 mesoscale convective system observed during the Cooperative Huntsville Meteorological Experiment (COHMEX) as a test case for the technique. COHMEX was an interagency field program conducted in the Huntsville, Alabama area during the summer of 1986 directed towards the study of microburst producing storms and small mesoscale weather systems (Dodge et al, 1986). Lightning strike locations and intermittent rapid scan imagery were analyzed from 2245-0000 GMT to generate the illustrative examples.

The June 11 storm system proved to be an attractive test case because of the availability of rapid scan satellite imagery and some radar data collected by the Lincoln Laboratory 10-cm Doppler radar (FL2). The convective storms consolidated into an intense squall line at 2300 GMT with a trailing region of stratiform rain. The northernmost cell in the line produced an F1 tornado at Killen, AL just as the radar began its surveillance that evening at 2320 GMT (Figure 2). Radar reflectivity patterns of the squall line show the classical appearance of a bow echo at the time of the tornado. New cells formed at the southern end of the line during the next hour and moved rapidly to the northeast to merge with the pre-existing and decaying convection.

3.1 Lightning Data Sets

The first step in the analysis involved correcting the lightning bearing measurements for the systematic errors which are common with these magnetic direction finding systems (Mach et al, 1986). Optimal solutions were computed with the corrected bearing data using a technique described by Wangsness (1973). The detection efficiency and location accuracy of the lightning network have been briefly examined. The flash detection efficiency is on the order of 80 percent within 100 km of the radars (Figure 3). This estimate is based on a comparison with ground truth collected by an instrumented mobile laboratory operated by the National Severe Storms Laboratory (Williams et al, 1987). The average semi-major axis of the 50 percent error ellipse is on the order of 1 km.

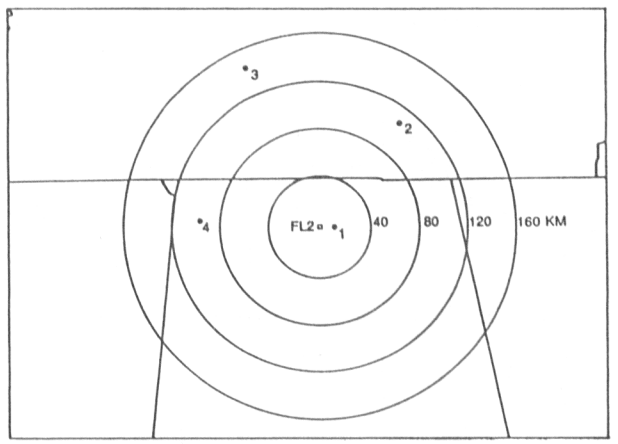

Figure 3. Map of the COHMEX region. Range rings are relative to the FL2 radar. The four magnetic direction finder sites comprising the lightning location network are indicated by the dots numbered 1-4.

The analyzed lightning locations are stored in a file on the NASA/MSFC McIDAS system where they can be further processed in conjunction with the radar and satellite imagery. After the locations have been computed, the location data are clustered into groups having a cell dimension measuring 0.1° latitude by 0.1° longitude. These groups are representative of individual and multi-cellular storms. The progression of these storm clusters over 5 minute intervals (comparable in time to the temporal resolution of the satellite and radar imagery) is shown in Figure 4.

Cells A-G can be clearly identified and tracked during their eastward progression. Cell B is the tornadic storm. The small storm to the east of Cell B during the period 2320-2330 GMT can also be seen in the radar displays in Figure 2. At 2335 GMT the small storm begins to rain out and is no longer separable as an individual lightning cluster (using the 0.1 degree lightning cell dimensions

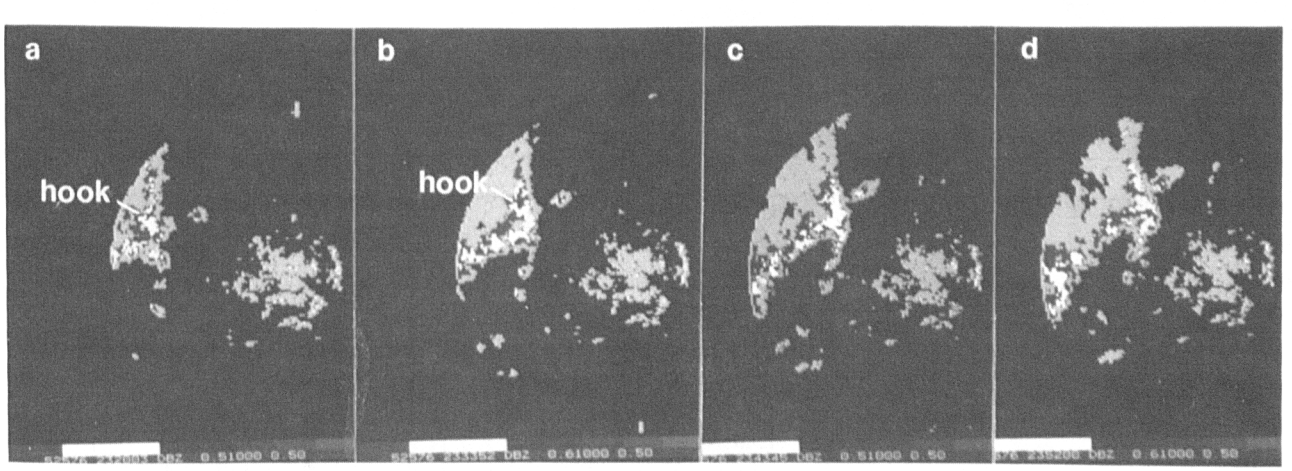

Figure 2. Radar reflectivity displays at 0.5-0.6 degree elevation to a range of 90 km taken at (a) 2320 GMT; (b) 2333 GMT; (c) 2343 GMT; (d) 2352 GMT. The intensity scale is as follows: 10-30 dBZ (gray); 30-45 dBZ (black); >45 dBZ (white). The hook echoes are associated with the Killen, AL tornado.

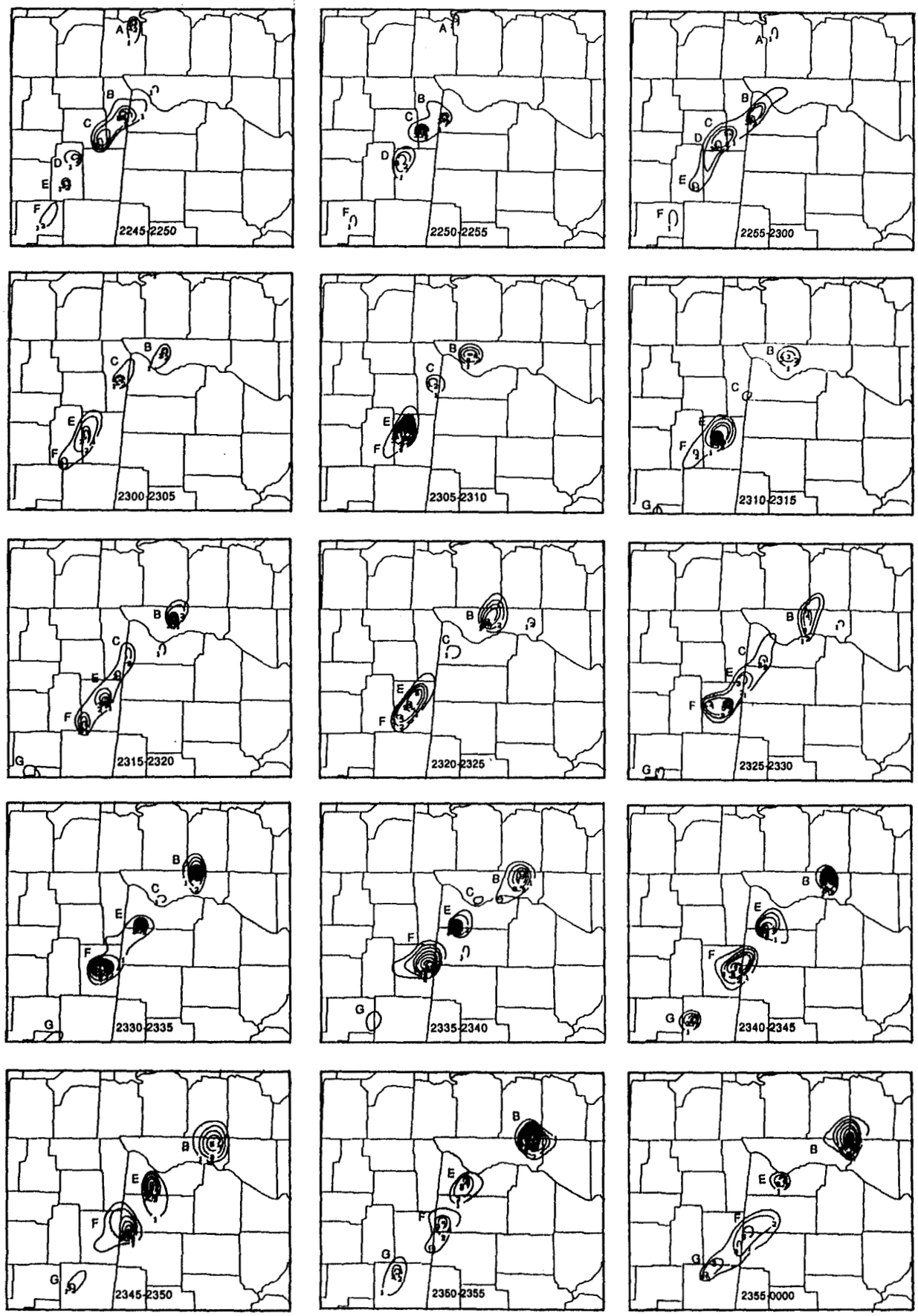

Figure 4. Cloud-to-ground lightning contour maps of the storm clusters embedded within the June 11, 1986 mesoscale convective weather system. Time in GMT.

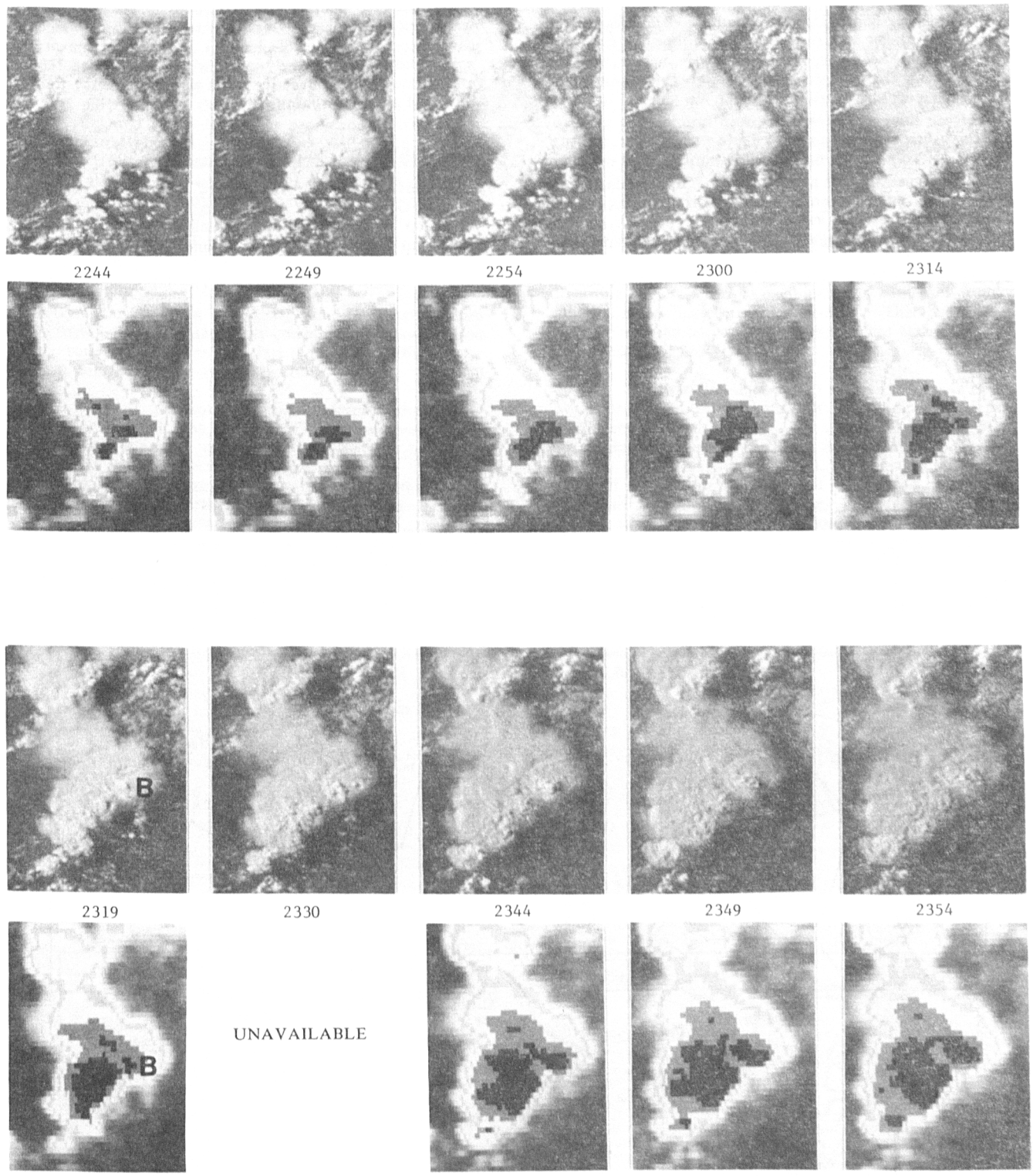

Figure 5. Sequence of GOES rapid scan visible and infrared (MB enhancement curve) imagery of the June 11, 1986 mesoscale convective weather system. Dark gray represents black-body temperatures colder than 220 K and black represents black-body temperatures colder than 215 K. Time in GMT.

employed in Figure 4). However, the small storm is still separable until 2345 GMT if we use a 0.05 degree cell dimension instead (not shown). At this time the flash rate of cell B increases in association with its merger with the small storm. This scenario is consistent with the conceptual life-cycle model proposed in Figure 1.

3.2 Satellite Data Sets

Figure 5 shows a sequence of GOES visible and infrared (MB enhancement) imagery corresponding to the lightning clusters and radar reflectivity displays, where available. Missing images are not uncommon on an operational basis. The longest gap in infrared satellite imagery occurs between 2319 and 2344 GMT. Cell B at the time of the tornado is identified in the 2319 images. A gravity wave feature propagating outward from the turret of cell B can be seen in the visible image. A large fraction of the cold cloud top (black-body temperatures colder than 220 K) encompassing the convective cores also contains the trailing region of stratiform rain (see Figure 2).

3.3 Convective Trends

Convective trends for the six long-lasting storms (B through G) are plotted in Figure 6. Minimum black-body cloud top temperatures, T_{min}, associated with each storm s (T_s), and 5-minute cloud-to-ground lightning flash rates (L_s), show a mixture of growing and decaying cells embedded within the squall line. The minimum cloud-top

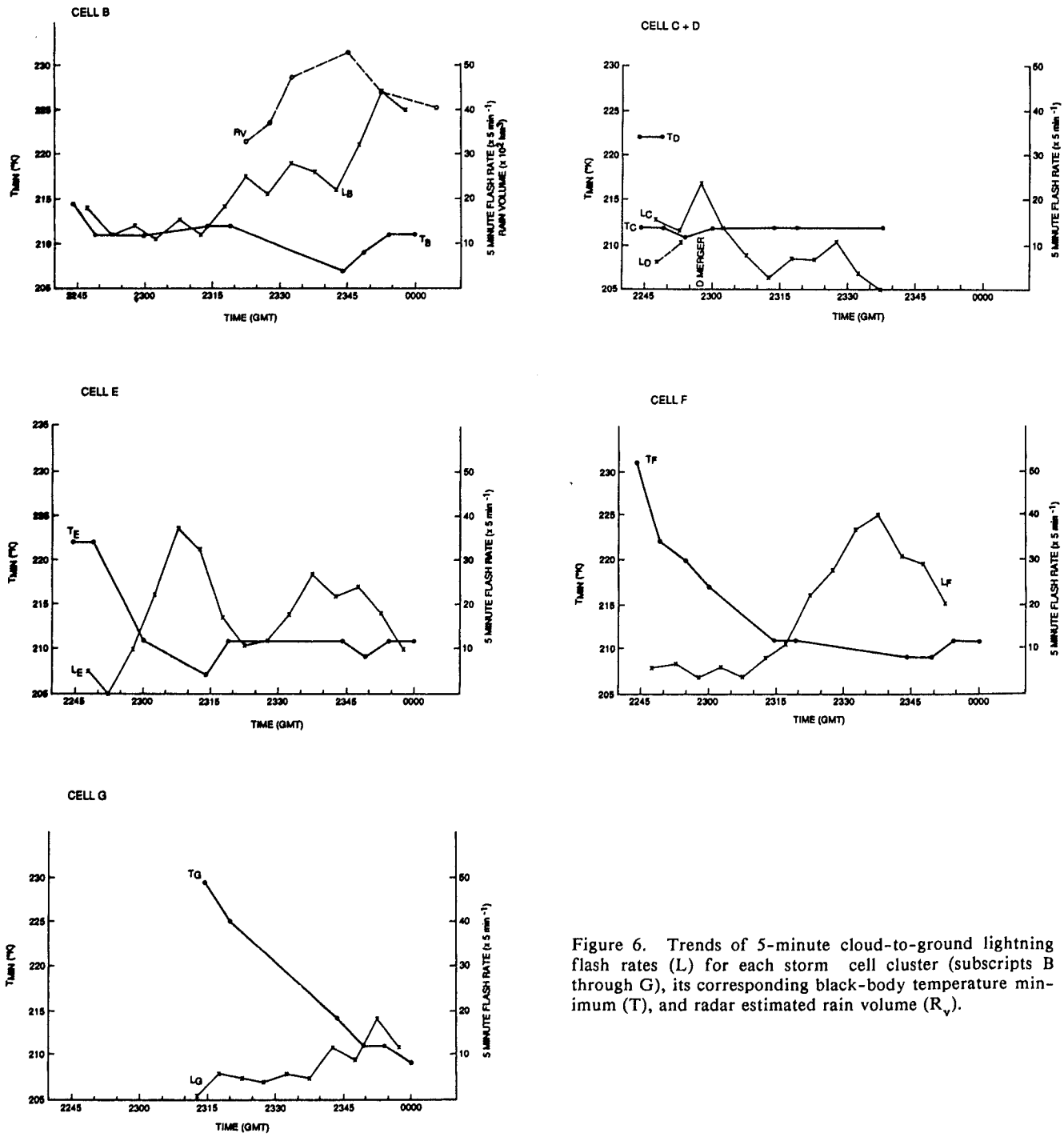

Figure 6. Trends of 5-minute cloud-to-ground lightning flash rates (L) for each storm cell cluster (subscripts B through G), its corresponding black-body temperature minimum (T), and radar estimated rain volume (R_v).

temperature is determined by interactively identifying and tracking each storm cell by its cloud-top features in the visible image, and then by locating the minimum temperature in close proximity to that feature.

Griffith et al (1978), Adler et al (1985), Doneaud et al (1987), and others discuss the problems associated with feature extraction and tracking using visible and infrared images. The cirrus debris is probably the most serious problem affecting feature extraction, especially in determining the end of convective activity. The relatively poor spatial resolution of the infrared pixel (on the order of 5 km) may cause gross errors in associating the coldest tops with the tallest clouds. Relative black-body temperature minima are not always indicative of underlying thunderstorms and not all thunderstorms produce temperature minima. By overlaying and looping the radar, lightning, and satellite data together, we can iteratively converge to a classification that better allows us to associate a given lightning cluster with a minimum cloud-top temperature.

Cell B, the isolated tornadic storm at the leading edge of the squall line, and the first convective impulse labelled cell E are the only two storms that exhibit strong convective intensification where the decreasing cloud top temperature minima correspond to rapidly increasing flash rates. The precipitation-filled (>30 dBZ) rain volume growth of cell B, estimated from the radar data, also corresponds to the lightning and temperature minima trends. This result agrees with that of Negri and Adler (1981) who showed a good correlation between changes in T_{min} and radar rain volume rain rates. However, the remaining storms give us a different picture.

Both cells F and G show rapid initial cooling of the cloud top, yet there is only a gradual increase in flash rates. A flash rate increase and decrease is associated with the latter part of the life-cycle of storms C,E, and F, yet there are no significant changes in cloud-top temperature minima due to the presence of cirrus debris from pre-existing convection. Thus, the lightning trends provide information on storm growth and decay that cannot always be inferred from changes in cloud-top temperatures.

4. CREATION OF CONVECTIVE TENDENCY IMAGES

Figure 7 shows an example of how the satellite and lightning data sets can be combined into a derived product which depicts convective tendencies. This example is drawn from the successive infrared images and trends between 2345 and 2350 GMT.

The lightning data in two successive time intervals are gridded and clustered into cells. The 5-minute flash rate during the previous time $L(t_{i-1})$ is subtracted from the most recent data at time t_i to produce a derivative image (Figures 7a-c). The derivative image ($\Delta L(t_i)$) contains the present shape of the cell while the current flash rate is replaced by the value of the derivative or slope. For example, the flash rate of cell B increases by 10 flashes in 5 minutes while cell G decreases by 3 flashes. The cells with increasing flash rates (growing storms B and E) can be easily distinguished from the decaying storms (F and G) having decreasing flash rates. This image product is useful in its own right.

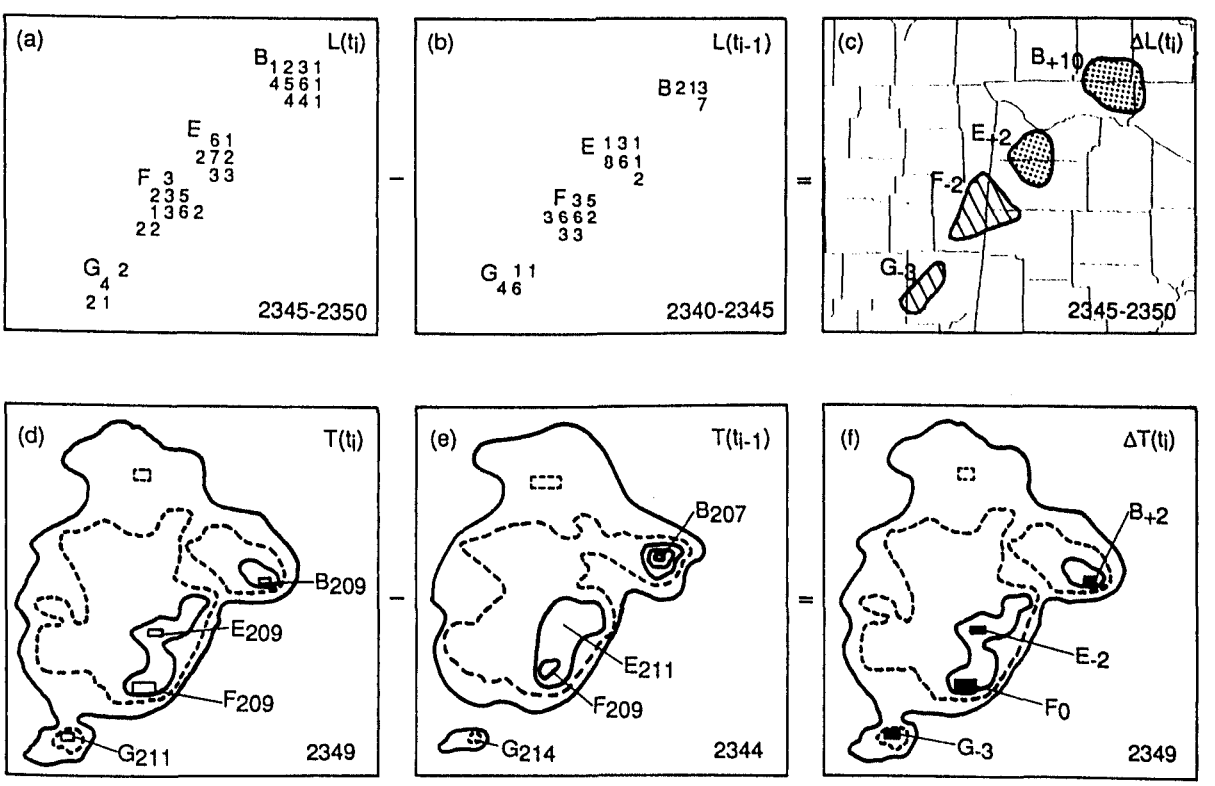

Figure 7. Total lightning flashes (L) at each grid point during two successive time intervals (a) t_i=2345-2350 GMT, (b) t_{i-1}=2340-2345 GMT matching the contours in Figure 4. The rate-of-change (ΔL) image (c) shows growing cells as stippled clusters and decaying cells as hatched clusters. The black-body cloud top temperatures at two successive times (2349 and 2344 GMT) in (d) and (e) show each cell and its minimum temperature (°K). The rate-of-change (ΔT) image (e) identifies each cell with its corresponding temperature change. Temperature contours are 207 K, 209 K, 211 K, 214 K (dashed), and 218 K.

The same procedure is performed on the infrared temperature field. The derivative temperature product $\Delta T(t_i)$ is generated by subtracting the previous cloud top relative minima ($T(t_{i-1})$) from the present black-body temperature minima ($T(t_i)$). The derivative information replaces the temperature minima in the most recently available infrared satellite image (Figure 7d). The derivative product (Figure 7f) shows cell B becomes 2 degrees warmer, cells E and G get colder, and no change at all for cell F. The derivative image properly reflects the growth of cell E with a decreasing T_{min} associated with an increasing flash rate. However, the T_{min} derivative provides misleading or no trend information for the other cells. The radar derived precipitation-filled rain volume of cell B in this time interval increases (by 800 km^3) as does the flash rate, yet the minimum temperature shows the cloud top warming.

The final step in the process is to substitute the derivative information from Figure 7c for the trends in Figure 7f to produce the integrated diagnostic/predictive or convective tendency image in Figure 8 ($\Delta T(L)$). This one image shows the location of the cloud-to-ground lightning activity and convective cores, the spatial distribution of convective rainfall, the extent of the remaining cloudy and stratiform rain areas, and the growing and decaying storms.

5. CLOSING REMARKS

A technique has been proposed for merging satellite imagery and lightning data to produce a convective tendency image for the short-term forecasting of storm development. Successive convective tendency images can be looped or animated to show the previous growth or decay of thunderstorms and their associated lightning activity. The rapid convective information updates available from the lightning observations are not only a useful adjunct to the conventional rapid scan satellite imagery, but perhaps are even more valuable in the context of the normal operational availability of 15 or 30 minute images.

Once the peak lightning rate has been reached (and the flash rate derivative changes sign), the flash rates will decrease exponentially (Goodman and MacGorman, 1986) to the end of the storm. This observation is further supported by the time series plots and emphasized in the conceptual model.

Buechler et al (1988) show that the decreasing flash rates are a precursor signature to the decay or collapse of storms that produce wet microbursts in the southeast U.S. These storms are a serious hazard to aviation and have been linked to seven major airplane crashes in the United States since 1970 resulting in nearly 600 fatalities. The decreasing flash rates provide a 3-5 minute lead time to the onset of the microburst event. In addition, the mere presence of lightning activity in a microburst environment (dry adiabatic sub-cloud layer with a dry, potentially colder layer of air aloft) signals the potential for strong downdrafts during storm demise. Therefore, we propose that the convective tendency image can be used to indicate potential microburst producing storms as well.

Acknowledgements

This study was partially supported by NASA Contract NAS8-34748. We also wish to thank M.I.T. Lincoln Laboratory for the use of their FL2 Doppler radar data.

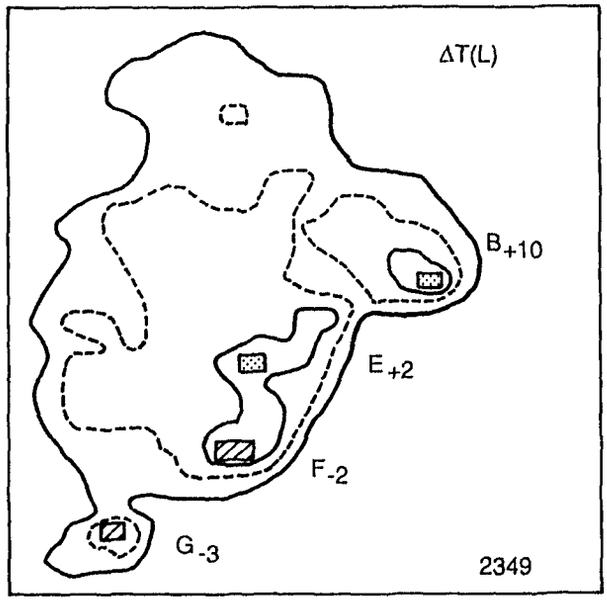

Figure 8. Diagnostic/Predictive satellite image representing the integration of the trend information from Figure 7c with the infrared black-body temperature field (in °K) from Figure 7f. The stippled clusters represent growing storms and the hatched clusters represent the decaying storms.

6. REFERENCES

Adler, R. F., M. J. Markus, and D. D. Fenn, 1985. Detection of severe Midwest thunderstorms using geosynchronous satellite data, Mon. Wea. Rev., 113, 769-781.

Bent, R. B., W. H. Highlands, and W. A. Lyons, 1984. Description and theoretical evaluation of LPATS (Lightning Position and Tracking System) to monitor lightning ground strikes using a Time-of-Arrival (TOA) technique, Preprints, 9th International Aero. and Ground Conf. on Lightning and Static Elect., Orlando, FL, FAA Technical Ctr., Atlantic City Airport, New Jersey.

Buechler, D. E., S. J. Goodman, and M. E. Weber, 1988. Cloud-to-ground lightning activity in microburst producing storms, Preprints, 15th Conf. on Severe Local Storms, Baltimore, MD, Am. Meteor. Soc., Boston, MA.

Byers, H. R., and R. R. Braham, Jr., 1949. The Thunderstorm, U. S. Govt. Printing Office, Washington, DC.

Cherna, E. V., and E. J. Stansbury, 1986. Sferics rate in relation to thunderstorm dimensions, J. Geophys. Res., 91, 8701-8707.

Dodge, J., J. Arnold, G. Wilson, J. Evans, and T. Fujita, 1986. The Cooperative Huntsville Meteorological Experiment (COHMEX), Bull. Am. Meteor. Soc., 67, 417-419.

Doneaud, A. A., J. R. Miller, L. R. Johnson, T. H. Vonder Haar, and P. Laybe, 1987. The area-time-integral technique to estimate convective rain volumes over areas applied to satellite data-A preliminary investigation, J. of Clim. and Appl. Meteor., 26, 156-169.

Goodman, S. J., and D. R. MacGorman, 1986. Cloud-to-ground lightning activity in mesoscale convective complexes, Mon. Wea. Rev., 114, 2320-2328.

Griffith, C. G., W. L. Woodley, P. G. Grube, D. W. Martin, J. Stout, and D. N. Sikdar, 1978. Rain estimation from geostationary satellite imagery-visible and infrared studies, Mon. Wea. Rev.,106, 1153-1171.

Grosh, R., 1978. Lightning and precipitation-the life history of isolated thunderstorms, Preprints, Conf. on Cloud Physics and Atmos. Elec., Issaquah, WA, Am. Meteor. Soc., Boston, MA, 617-624.

Krider, E. P., R. C. Noggle, and M. A. Uman, 1976. A gated, wideband magnetic direction finder for lightning return strokes, J. Appl. Meteor., 15, 301-306.

Mach, D. M., D.R. MacGorman, and W. D. Rust, 1986. Site errors and lightning detection efficiency in a magnetic direction finder for locating lightning strikes to ground, J. Atmos. Oceanic Tech.,3, 67-74.

Negri, A. J., and R. F. Adler, 1981. Relation of satellite-based thunderstorm intensity to radar-estimated rainfall, J. Appl. Meteor.,20, 288-300.

Wangsness, D. L., 1973. A new method of position estimation using bearing measurements, IEEE Trans. Aero. and Elec. Sys., November, 959-960.

Williams, E., 1985. Large-scale charge separation in thunderstorms, J. Geophys. Res., 90, 6013-6025.

Williams, S. F., H. M. Goodman, K. R. Knupp, and J. E. Arnold, 1987. SPACE/COHMEX Data Inventory Document, NASA TM-4006, NTIS, Springfield, VA,22161.

Workman, E. J., and S. E. Reynolds, 1949, Electrical activity as related to thunderstorm cell growth, Bull. Am. Meteor. Soc., 30, 142-144.

5.4

USING SATELLITE DATA TO AID IN DIAGNOSING AND FORECASTING CONVECTIVE DEVELOPMENT AND INTENSITY ALONG ARC CLOUD LINES

James F.W. Purdom

Regional and Mesoscale Meteorology Branch
Applications Laboratory
NOAA/NESDIS

and

Peter C. Sinclair

Department of Atmospheric Science
Colorado State University
Fort Collins, Colorado

Cooperative Institute for Research in the Atmosphere
Colorado State University
Fort Collins, Colorado

1. INTRODUCTION

Convective storms play an important role across many scales in meteorology. For example, convective storms are important contributors to the total energy budget of the global circulation as well as summertime tropical regions through their release of latent heat, radiational properties and the convective cluster scale up-moist/down-dry vertical circulations they induce (Gray, 1973). Locally, the convective storm lies at the heart of many weather-related events that affect everyday life. During the spring and summer months, tornadoes, hail, flash floods, downbursts and lightning pose serious threats to life and property. While wreaking havoc in one area, the same convective storm may be providing much needed water for another. While thunderstorms are providing much needed moisture to one area, other areas need summertime precipitation augmentation to improve water resources for human consumption, for power generation and for agricultural purposes. For such local scale convective weather events, more precise very-short range forecasting is badly needed. Before precise thunderstorm nowcasting becomes a reality, an improvement in understanding convective storm genesis and development is required. This paper will briefly investigate one of the dominant mechanisms responsible for thunderstorm development: the arc cloud line and convective scale interactions associated with it.

2. SATELLITE DATA AND MESOSCALE METEOROLOGY

Prior to the high resolution geostationary satellite there existed a lack of routine meteorological information concerning the mesoscale evolution of deep convective clouds and their local environment. The mesoscale was a "data sparce" region. For example, over the continental United States, approximately 1000 hourly surface observing sites and 126 upper air sounding sites cover an area of about 8×10^6 sq km, forcing meteorologists to make inferences about mesoscale meteorological phenomena from macroscale observations. With GOES imagery (and to some extent polar orbiting satellite imagery), meteorological phenomena that are frequently detected at fixed observing sites are routinely observed: a "reporting station" exists every 1 km using information implicit in the visible data, and every 8 km (1 km polar) for the infrared. The clouds and cloud patterns observed in satellite imagery represent the ongoing effect of dynamic and thermodynamic processes in the atmosphere - they provide the meteorologist with a visualization of mesoscale meteorological processes. Effective use of satellite imagery requires that we understand that imagery in terms of those processes - both subjectively and quantitatively.

Similar to satellite image data, satellite sounding data provides information concerning the mesoscale structure of the atmosphere on spatial (and temporal with GOES) scales never before possible. Satellite sounding data are able to depict small and significant spatial (and temporal with GOES) variations in atmospheric temperature and moisture structure. From satellite soundings we have: 1) near instantaneous observations through a column in the atmosphere; 2) high spatial resolution (in the absence of clouds); 3) moderate vertical resolution; and 4) one uniformly calibrated sensor making all of the measurements. With the GOES-VAS, soundings may be taken over an area the size of the United States as frequently as once every hour. How to best use satellite sounding data for nowcasting is currently an area of intense investigation.

3. CONVECTIVE SCALE INTERACTION

Movies made from high resolution geostationary satellite data, Bohan (1981), show that convective scale interaction, Purdom (1979), is of primary importance in determining the development and evolution of deep convection. Convective scale interaction is directly associated with outflow boundaries produced by precipitating convective storms. This interaction manifests itself as the merger and intersection of those outflow boundaries (arc cloud lines, Purdom (1973)) with other convective ares, lines and boundaries, Figure 1. Under the proper atmospheric conditions, this interaction has been observed to precede tornadic storm development, Purdom (1984, 1986). The process of convective scale interaction is fundamental to the evolution and maintenance of deep convection; it is complex because of the continuously evolving nature of the convective environment. Until recently (Wilson and Carbone, 1984), convective scale interaction had only been observed using satellite imagery. Purdom (1979) has identified several basic properties of convective scale interaction:

1) Thunderstorm outflow boundaries may maintain their identity as arc cloud lines for several hours after they have moved away from their parent source.

2) The arc cloud line outflow boundary can, and often does, cause deep convection to develop along it at distances well over 150 km from its point of generation.

3) Deep convective development along an outflow boundary is a selective process - it is most favored where the arc cloud line merges with a cumulus region or intersects another boundary.

4. As the cumulus regime evolves on a given day, and much of the cumulus field dies away, the majority of new thunderstorms are confined to arc cloud line intersection points.

Sinclair and Purdom (1984) have made a series of research aircraft flights into arc cloud lines order to bring into sharper focus their dynamic and thermodynamic features. The aircraft observations, when analyzed with the satellite data, helped define the arc cloud line's life cycle as three evolving stages. In its formative stage, Figure 2, the arc cloud line may be thought of as an extension of the parent storm's highly channeled outflow. Convergence of a strong cool outflow jet into the rear of the density ;surge line (DSL) coupled with a solenoidal circulation in that region contributes to a mixed updraft region beneath the arc cloud line. As the formative stage evolves into the mature stage, the DSL begins to move as a density current. Convergence in the warm environmental air due to the outwardly moving DSL results in a warm and positively buoyant updraft along the arc cloud line whose intensity is a function of both the strength of the DSL (convergence along the DSL in depth) and the stability of the environment into which it is moving. The dissipating stage is marked by a shallow and slow moving DSL above which weak overshooting thermals may cause cumulus cloud development. Figure 3 is a schematic of the

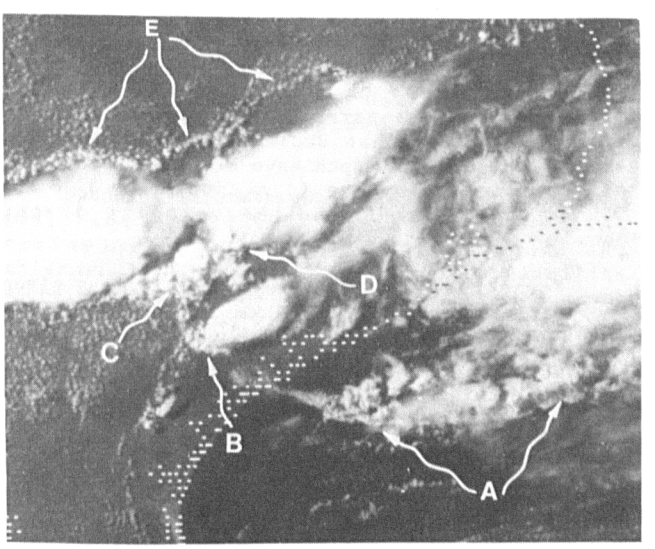

Figure 1. GOES-East, 1 km visible image at 4 pm CST, July 28, 1980. Arc cloud from dissipated MCS triggers new thunderstorms over the Gulf of Mexico (A), at intersection points with sea breeze (B), and stationary front (C & D). New arcs move into dry air behind front at E.

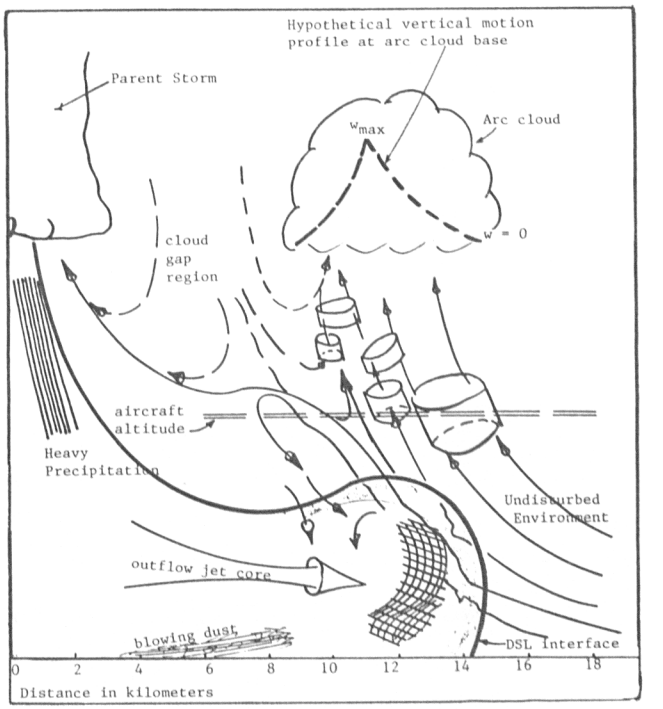

Figure 2. Several of a number of possible trajectories for air entering updraft region of arc cloud during formative stage. Shaded region is area of intense mixing along DSL interface, while hatched region is possible area of precipitation roll. Convergence in the warm air due to the advancing DSL interface is on the order of 10^{-2} sec^{-1}. Based on aircraft observations of Sinclair and Purdom (1984).

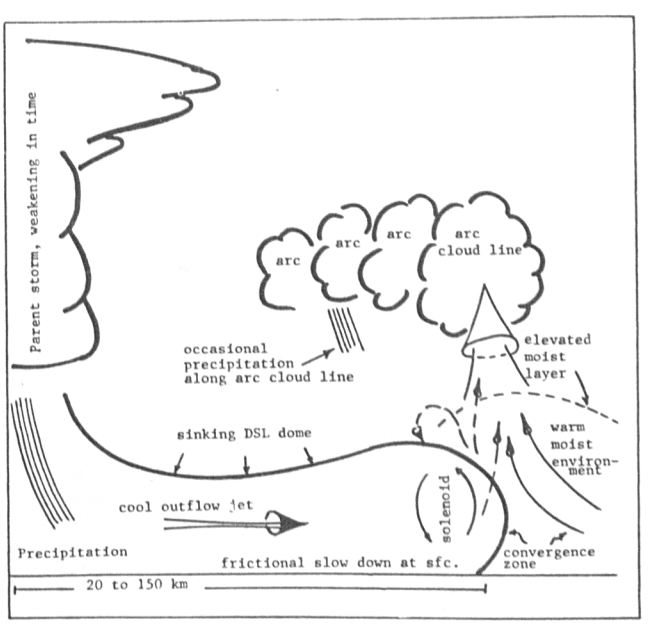

Figure 3. Schematic of mature stage. The arc cloud line is formed above the leading edge of the density surge line. The parent cold air source weakens as does the strength of the cool outflow jet. Occasional precipitation of moderate intensity falls from some of the convection along the DSL, locally strengthening the cold pool. The DSL is moving as a density current, forcing up the warm and potentially unstable environmental air along the DSL interface.

mature stage: note that occasional precipitation of moderate intensity falls from some of the clouds along the arc, thus locally strengthening the cold pool.

Figure 4a shows an arc cloud line over the Gulf of Mexico that is approaching Boothville, (BVE), Louisiana, while Figure 4b is a time comoposite image that shows that arc cloud line's evolution over several hours. Notice how the amount of convection along the arc decreases the further its distance from its source region. Why?

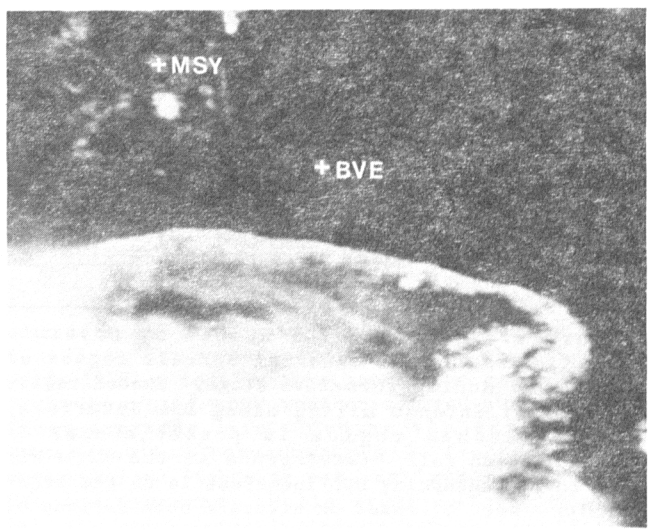

Figure 4a. Goes-East 1 km resolution visible image for July 28, 1986. The arc cloud line in the image has been produced by a large thunderstorm system that is moving slowly westward across the southern Gulf Coastal States. The arc cloud line is moving from south to north toward the Louisiana Coast.

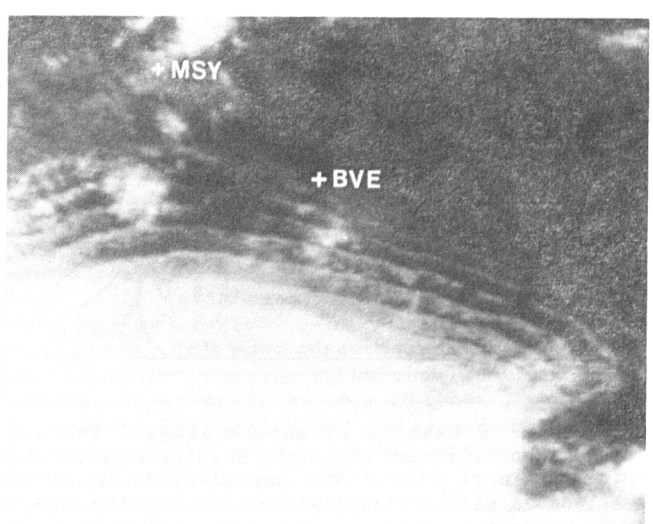

Figure 4b. GOES-East 1 km resolution visible image time composite from noon to 4 pm CST. When the arc cloud line passed Boothville (BVE), winds shifted from light northerly to south by southwesterly at 5 to 7 m/s.

Fujita (1959) showed that the excess mass in the cold dome of a mesoscale high was a function of the evaporation of rain inside the boundary. Fujita further showed that the total excess pressure within a cold dome whose source had dissipated, integrated over the area covered by the dome, remained virtually unchanged by subsidene as the dome spread out seeking hyrostatic equilibrium with its environment. Thus, as the arc cloud line's cold dome sinks and spreads out, the excess pressure driving the density current decreases proportionally as does the convergence along the arc as well as the depth over which that convergence occurs. For example, assume an initial cold source with an excess pressure of 4.1 mb exists over a circular area of 50 km in radius and 1.5 km in depth. In the case of no new air being provided by an active cold air source (i.e., the parent storm has dissipated), initially the boundary will move outward at 16 m/s. When the dome area has doubled, the excess pressure and dome depth will have decreased by a factor of 2 (i.e., p (mb) = 2.05 and DSL depth = 0.75 km), and the velocity of the boundary will be 11.3 m/s. This gives an average velocity of 13.65 m/s which means for the dome's radius to spread from 50 km to 70.7 km requires an elapsed time of 25.3 minutes. Furthermore, the velocity of the boundary will have a value of approximately 35% its initial value after almost three hours. Thus, after the active cold air source has dissipated, the arc cloud line will maintain a substantial velocity for a considerable period of time. However, the depth of the DSL will decrease in time as the arc cloud line spreads out.

When considering the velocity of an arc cloud line during its mature stage, it should be remembered that this stage is one in which the arc cloud line's cold air source is still active. Furthermore, precipitating clouds are often found along the outflow arc. Both of those factors will contribute to a larger pressure pertubation within the cold air than for a similar situation in which the cold air source has totally dissipated. For example, rather than have the source totally dissipate at the initial time, let the excess pressure in the cold dome uniformly decrease by 20% by the time the dome area has doubled in size. This corresponds to a decrease in cold air production by the parent source of 40%. By the time the cold dome has doubled in area both its excess pressure and depth have a value that is 80% of their initial value (i.e., p(mb) = 3.28 and DSL depth = 1.2 km), and the velocity of the boundary will be 15.2 m/s.

For comparison purposes, both examples given above attain a radius of 100 km in approximately one hour, however, the active source's DSL has a velocity 1.6 times as great as that for the dissipated source, and its dome is slightly over 2.5 times as deep. Such a marked differences, due to a cold source staying active, have a profound influence on the vertical motions capable of being generated in depth at the leading edge of the DSL due to forced convergence. Thus there is hope that by knowing the intensity of the arc cloud line's parent source and how that intensity is changing in time, coupled with direct measurements of the arc cloud line's velocity, one could define the strength of the vertical motion field being generated in the convergence zone along the leading edge of the arc cloud line.

Both satellite image and sounding observations show that marked variations in the atmosphere's ability to support deep convection exist within a mesoscale environment. In a satellite image, organized convective and clear regions in the air in advance of the arc cloud line reflect certain dynamic and themodynamic features of that airmass. Pre-existing convergence and vertical motion coupled with deep layer moistening in the cumulus regions, versus gradual subsidence in the clear regions, makes the cumulus regions more favorable for deep convective development if vertical forcing takes place. Based on consideration of parcel buoyant energy, one may calculate a variety of parameters related to thunderstorm development and intensity. For example:

1) Positive buoyant energy (PBE) - positive area between a local sounding's level of free convection (LFC) and equilibrium temperature;

2) Negative buoyant energy, surface to lifting condensation level, LCL (NBE1) - amount of energy input required to lift a mixed parcel from the surface layer to condensation; and

3) Negative buoyant energy, LCL to LFC (NBE2) - amount of energy input required to lift a parcel from its LCL to its LFC.

One may assume that air in a convective region reflects the local scale dynamics of that region, and consequently that convective air has already had sufficient energy input to reach its LCL. Furthermore, depending on the amount of cumulus development (cumulus to towering cumulus) some portion of the input energy required to attain free convection beyond the LCL has also been realized. In the clear regions, on the other hand, energy input is still required for the first stages of cumulus development. Upon local vertical forcing, different convective responses should be expected for cumulus regions versus adjacent clear regions. "How may such image data be quantified over mesoscale areas?" Present technology does not allow the direct measurement of convergence and vertical motion on local scales over large areas. However, certain information concerning the atmosphere's ability to utilize local scale forcing for the development of deep convection may be inferred using satellite sounding data.

Sounding information from GOES/VAS can detect small and significant spatial and temporal variations in atmospheric temperature and moisture. Purdom, (1985) has used satellite sounding data to show that the difference of input energy required to overcome the amount of negatively buoyant air and attain free convection between adjacent clear and cumulus filled regions may be substantial. Furthermore, bassed on analysis of VAS satellite soundings, Zehr (1986) has been able to show striking differences between airmasses on the mesoscale. To determine the potential for new storm development, one should evaluate the convective potential (PBE) and forcing requirements (NBE 1 & 2) on the mesoscale using VAS soundings. Next, using coincident image data, the amount of energy input from the environment already provided (by whatever means) to overcome NBE 1 and NBE 2 as depicted by the state of cumulus development is determined. Thus, through the combined use of satellite image and sounding data it is possible to assess the convective potential of different portions of a mesoscale airmass, and estimate the amount of vertical forcing that must be applied locally to attain free convection.

4. *CONCLUSIONS*

From the above considerations certain pieces of the convective scale interaction phenomena may be understood better from both a qualitative and quantitative point of view. Merger occurs when an arc cloud moves into a region of pre-existing cumulus and cumulus congestus cloudiness and triggers new deep convective storms, Figure 5. The ability of an arc cloud line to trigger new vigorous convection is a function of both the strength of the vertical motion along the leading edge of the DSL, as well as the stability of the environmment into which the DSL is advancing. The DSL/outflow boundary moves into the environment with a relatively narrow and concentrated band of vertical motion occurring along its leading edge. The strength of this organized band of vertical motion generally decreases in time. Furthermore, the air mass into which an arc cloud line moves is in no way uniform in its ability to support new deep convection. As the arc cloud line moves into a cumulus filled region, it provides a band of

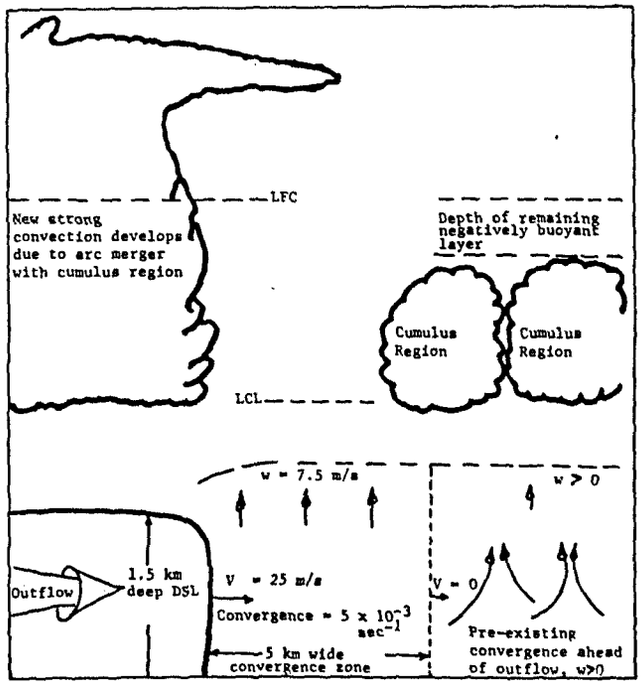

Figure 5. Schematic of strong convective development along an arc cloud line due to merger with a pre-existing cumulus region. Due to convergence in the environment ahead of the arc cloud line, a region of organized cumulus convection develops. Those cumulus represent a region where some of the vertical motion required to overcome the negative buoyancy in the environment between the lifting condensation level (LCL) and level of free convection (LFC) has already been realized. Therefore, the vertical motion generated along the narrow convergence zone in advance of the arc cloud line's DSL is able to force the less stable air in the cumulus region to deep convection.

organized vertical motion to a relatively moist and locally unstable airmass. Thus convective scale interaction due to merger with pre-existing convection often leads to the development of a new cumulonimbus which in turn reinforces the cold pool which is driving the arc cloud line's DSL. On the other hand, as the arc cloud line's DSL moves into a clear region, it encounters air that is stable with respect to that in a cumulus region. When the arc cloud line's DSL interacts with that air, it produces cumulus cloudiness along its leading edge. Taking into account the normal diurnal heating cycle and its influence on convective development helps explain the strong influence merger imposes on new deep convective development and its associated rainfall in the noon to 4 pm. time frame (see Figures 6 and 7).

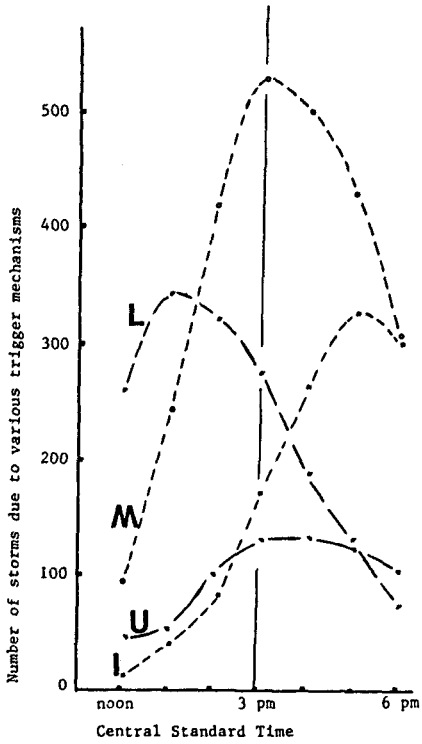

Figure 6. Distribution of number of storms for each hour by generation mechanism. L = Local Forcing, M = Merger, I = Intersection, U = Indeterminable.

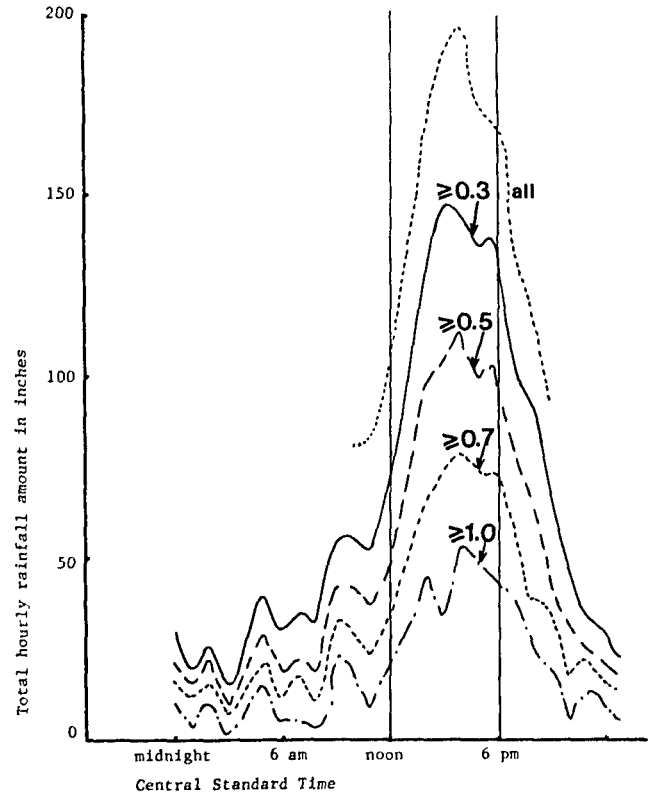

Figure 7. Total hourly rainfall measured over the same study area as was used for Figure 6 and for the days included in the study period for Figure 6.

ACKNOWLEDGMENTS

Portions of this work were supported by NSF ATM-8420980, NASA NAS8-36472, and NOAA NA85RAH 05045. The author wishes to thank Mrs. Debbie Eckdahl for help in preparation of the manuscript.

REFERENCES

Bohan, W.A., 1981: The importance of thunderstorm outflow boundaries in the development of deep convection. WAB 456, 16mm color sound movie, The Walter A. Bohan Co., 2026 Oakton Street, Park Ridge, IL, 29 minutes.

Fugita, T.T., 1959: Precipitation and cold air production in mesoscale thunderstorm systems. J. Meteorol., 16, 454-466.

Gray, W.M., 1973: Cumulus convection and larger scale circulations I. Broadscale and mesoscale considerations. Mon. Wea. Rev., 101, 839-855.

Purdom, J.F.W., 1973: Meso-highs and satellite imagery. Mon. Wea. Rev., 101, 180-181.

Purdom, J.F.W., 1979: The development and evolution of deep convection. Preprints, 11th Conf. on Severe Local Storms, Kansas City, Amer. Meteor. Soc., 143-150.

Purdom, J.F.W., 1984: Use of satellite soundings and imagery for nowcasting and very-short-range forecasting, Nowcasting II Proceedings of the Second International Symposium on Nowcasting, Norrkoping, Sweden, European Space Agency, 99-111.

Purdom, J.F.W., 1985: The application of satellite sounding and image data to the Carolina tornado outbreak of 28 March 1984. Preprints, 14th Conf. on Severe Local Storms, Indianapolis, Amer. Meteor. Soc.

Purdom, J.F.W., 1986: Satellite contributions to convective scale weather analysis and forecasting, Eleventh Conference on Weather Forecasting and Analysis, Kansas City, Mo., American Meteorological Society, 295-314.

Sinclair, P.C. and J.F.W. Purdom, 1984: The genesis and development of deep convective storms: A new approach to their prediction and possible modification. CIRA, Cooperative Institute for Research in the Atmosphere, Colorado State University, Ft. Collins, CO, 47 pp.

Wilson, J. and R. Carbone, 1984: Nowcasting with Doppler radar: forecaster-computer relationship. Preprints Nowcasting II Symposium, Norrkoping, Sweden, European Space Agency, 177-186.

Zehr, R.M., 1986: Analysis of mesoscale air masses with VAS retrievals. Preprints, 2nd Conference on Satellite/Remote Sensing and Applications, Clearwater Beach, Amer. Meteor. Soc., 94-98.

ASSIMILATION OF SATELLITE SURFACE WIND SPEED DATA USING THE GLA ANALYSIS/FORECAST SYSTEM

S. C. Bloom and R. Atlas

Laboratory for Atmospheres, Code 611
Goddard Space Flight Center
Greenbelt, Maryland 20771

1. INTRODUCTION

The description and modeling of the formation, movement, and modification of water and air masses as well as the development and intensification of storms near coasts and over the open ocean all require adequate descriptions of the surface fluxes of heat, moisture, and momentum. However, obtaining these fluxes is severely hampered by the lack of adequate observations of pertinent meteorological quantities over oceans; for example, surface wind observations from ships are notoriously variable in quality and areal as well as temporal coverage. Thus, in areas of poor data coverage, analyses become dominated by errors in the first guess (forecast) fields, which result in poorly computed surface fluxes. The research reported in this paper is a continuation of work at the Goddard Laboratory for Atmospheres (GLA) which seeks to augment analyses of conventional surface oceanic observations with remotely-sensed data (cf. Atlas et al., 1987).

Surface wind speed measurements are available from a number of satellites (e.g. Seasat, Nimbus-7 and Geosat). Such data have the great virtue of day-to-day widespread global coverage, in stark contrast to the nature of the ship wind data. Nevertheless, both operational and research models and data assimilation schemes are in general not designed to use speed observations alone, and these data have not been used except in very limited studies. Atmospheric models do not predict wind speeds directly; they require initial states which contain the full vector wind. In addition, most analysis systems (especially ones based on Optimal Interpolation methods) analyze wind components, not speed and direction. It is thus evident that the use of these wind speed data requires the development of a procedure to assign a direction to these speeds, i.e. to turn them into wind vectors.

In this paper, we describe four possible techniques to assign directions to surface wind speed data, and the methodology we plan to use in evaluating these methods with respect to both simulated and real data. Some preliminary results comparing the first two methods using simulated data are presented in this preprint article.

2. ELEMENTS OF THE GLA ANALYSIS/FORECAST SYSTEM

The preliminary results presented in this article were generated with an analysis/forecast system very similar to the one used by Atlas et al. (1987). Only a very brief summary of the GLA Fourth-Order General Circulation Model is given here; a detailed description of the model can be found in Kalnay et al. (1983). The GLA GCM has 6 prognostic variables (surface pressure, ground temperature, u and v wind components, temperature, and specific humidity) which are integrated on a 4 deg latitude by 5 deg longitude horizontal mesh and on a 9 sigma layer grid in the vertical. The model employs a 7.5 min time step using Euler-backward (Matsuno) time differencing. The governing equations for the prognostic variables are written in flux form using fourth-order finite differencing. The model contains a full range of subgrid scale physical parameterizations: longwave and shortwave radiation, surface physics, large-scale and convective precipitation.

A successive corrections method (SCM; see Baker, 1983) was used for the objective analysis of data to model grid points for the preliminary results presented here. We plan to have results using a multivariate Optimum Interpolation scheme (Baker et al., 1987) by the time of the conference. In either case, the objective analysis is used as part of a 6h assimilation process, where the data have been 'binned' +/- 3h of the analysis time.

3. METHODS TO ASSIGN DIRECTIONS TO WIND SPEEDS

Previous work at GLA has been involved with removing the directional ambiguity in Seasat Scatterometer (SASS) winds (Baker et al., 1984; Atlas et al. 1987). The research reported here is an extension of the previous work in the use of GCM fields in algorithms to assign rather than select wind directions. We are testing the following methods for this purpose:

Method 1: Use Model "First Guess" Wind Directions

In this approach, the 6h GCM forecast winds are interpolated bilinearly to the wind speed datum location; the direction of the resultant wind is then assigned to the wind speed observation. The new wind vector is then assimilated in a regular analysis. For these preliminary

results, we approximate "surface winds" by using 1000 mb winds; in this way the assimilation process then employs a standard 1000 mb analysis step. We plan to have a more realistic treatment of the surface winds (by means of an extrapolation into the planetary boundary layer) by the time of the conference.

This method clearly places a heavy reliance on the quality of the GCM forecast. In areas where the model is in serious error, the assignment of bad directions to the wind speeds would not lead to the generation of a useful product.

Method 2: Use Analyzed Wind Directions

This is a multi-pass approach. The first step involves performing a surface analysis incorporating all conventional (buoys, ships, etc.) surface data. Then one proceeds as in Method 1, except the analyzed surface winds are used instead of the model first guess winds.

There is less reliance placed on the quality of the GCM forecast in this case, although this method devolves to Method 1 in regions with very sparse surface data.

Method 3: Use Surface Pressures with a Balance Relation

This method is largely the one developed by T. Yu (1987). Briefly, the method works as follows. First perform a conventional surface analysis, as done in Method 2. Next, estimate a value of the surface drag, Cd, by combining the observed wind speeds and the gradients of the analyzed surface pressure with an Ekman Balance relation:

$$C_D^2 S^4 = \frac{1}{\rho^2} |\nabla p|^2 - S^2 f^2$$

where S = wind speed, ρ = density, and f = Coriolis parameter. Finally, put Cd, S and surface pressure into the Ekman Balance relations to obtain directly the wind components u and v. Once the wind components have been obtained, these data are assimilated along with the rest of the conventional data in the same manner as the previous two methods.

Unlike the previous two methods, Method 3 concentrates on the mass field (surface pressure) and a balance relation to obtain the desired directions. Any flaws in the underlying assumptions of the balance relation will be transferred directly to the assigned directions. For example, Ekman balance is probably not really applicable in the Tropics; other terms in the momentum equations (advection, even time-tendency) could play important roles in the overall tropical wind balance. In middle latitudes where there are regions of strong curvature in the flow, a gradient-wind type of modification would appear to be needed to model adequately the wind balance.

Method 4: Use a Variational Analysis Method (VAM)

This method differs substantially from the previous three, in that it combines the direction assignment and subsequent analysis steps. It employs a formalism which incorporates constraints on smoothness, closeness of fit to a first guess, and dynamical balance. VAM's can take into account both the accuracy of the data (through the use of metric weights describing the fit of the analysis to the data) and the level of confidence to be ascribed to the applied constraints (through the use of "weak" constraints; Sasaki, 1970).

We plan to use an algorithm based on the VAM developed by Hoffman (1982, 1984) for use in objectively dealiasing Seasat data.

4. PRELIMINARY RESULTS

At the time of this writing, we have run a prototypical example, comparing Methods 1 and 2 in a simulation experiment of the wind speed direction assignment methods. In this experiment, a reference atmosphere or "Nature" is taken from a 20 day integration of the 1.875 deg x 1.875 deg x 15 level ECMWF model from 0000 GMT 10 November to 0000 GMT 30 November 1979. We make use of two kinds of "observations" in this study: simulated FGGE conventional and satellite observations, and simulated satellite surface wind speeds. The FGGE data were generated at the National Meteorological Center (NMC) by interpolating the Nature fields to representative observation locations, and then adding primarily random noise in accordance with the observation error characteristics (details are given by Dey et al., 1985, and Atlas et al. 1985). The satellite surface wind speeds with no errors added were simulated by interpolating the Nature values to typical Seasat tracks. As mentioned earlier the oceanic surface wind data in this preliminary run were assumed to be at 1000 mb.

The second component of the experiment is an assimilation run with the GLA GCM, which has been "spun-up" by assimilating GLA real conventional data every 6 h for 5 days prior to the start of the simulation experiment. The simulated data were analyzed using a SCM every 6h and then assimilated into the GLA GCM; the assimilation period lasted 4.5 days, from 0000 GMT 10 Nov 1979 through 1200 GMT 14 Nov 1979. Three sets of assimilations were performed: using (1) Method 1 or (2) Method 2 to assign wind directions, or (3) using the surface direction and speed specified by the Nature run (i.e. "Perfect"). A fourth assimilation run without any satellite surface wind data is planned but has not yet been completed. Table 1 shows the average global direction differences (in degrees) for all speeds among these three cases over the 4.5 day assimilation period. Each of these averages contain 104400 wind vector direction differences, which were computed and averaged at the data locations. Table 1 demonstrates that Method 2 is closer to the perfect simulated data than Method 1. The global mean difference of 22.1 degrees for Method 2 is close to the design goal of 20 degrees for the Seasat Scatterometer (which was designed to measure the vector surface wind).

Table 1

Average Global Wind Direction Difference

Method 1 - Perfect	26.1
Method 2 - Perfect	22.1
Method 1 - Method 2	11.0

Table 2 shows how the directional difference averages vary as a function of speed. Again, Method 2 is superior to Method 1 for all wind speeds. Note that the largest differences occur at small wind speeds, and that the size of the directional differences decrease for larger wind speeds.

Table 2

Global Direction Difference Averages as a Function of Speed

	0-5	5-10	10-15	15+
Meth 1 - Perf	43.3	20.7	18.7	13.4
Meth 2 - Perf	37.7	17.1	15.4	11.4
Meth 1 - Meth 2	18.6	9.2	7.1	4.2
Number	28641	49619	20631	5509

In order to assess the regional variability of the differences averaged in the above tables, we now show selected plots of the differences of the gridded fields. There are four sets of gridded fields to intercompare: 1) Nature run , 2) Perfect , 3) Method 1 , and 4) Method 2. Figures 1a-b show plots of the vector magnitude of the surface wind differences between the Nature and the Perfect wind assimilation at the beginning and the end of the assimilation period. The large differences in Fig 1a reflect the large differences between the ECMWF model's state and the GLA model's estimate of that state. As the simulated FGGE and satellite surface wind data from the Nature run are assimilated, the GLA analyses are drawn ever closer to the Nature run; after 4.5 days, the two runs are very similar, as shown in Fig 1b. The significant departures over land are due to different extrapolations below ground to 1000 mb.

Figure 2 shows the difference between Methods 1 and 2 after one day of assimilation. Note that overall, the two surface fields are similar, except for significant differences in widely separated areas. An examination of the differences between the two methods at other times revealed a consistent trend; the differences were very small initially, they grew to magnitudes comparable to those shown in Figure 2, and then they diminished gradually in size (but not to zero) as the assimilation proceeded to 4.5 days. Small differences between Method 1 and Method 2 imply one of two causes. First, there is no conventional data in the area, or the analysis did not draw to that data; then Method 2 becomes Method 1. Second, the assimilating analysis/forecast system is doing sufficiently "well" that the conventional data from the Nature run adds no useful information to the direction algorithm. It appears that the initial small differences are due to the first reason, while the second explanation appears to be operating (note the small differences in Fig. 1b) later in the assimilation run.

Finally, we show in Figures 3a-b how the two methods compare with the assimilation which used the correct wind directions. The very large difference between the two methods off the west coast of South America appears to be largely due to the presence of a ship report near 38 deg South and 80 degrees West. It is likely that the presence of isolated conventional data will have similarly large impacts in other regions. If an isolated piece of conventional data is erroneous, it could thus have a very deleterious effect on Method 2 in those areas, unless it is corrected by the objective analysis.

5. SUMMARY

As shown in Tables 1 and 2, as well as Figure 3, our preliminary test finds Method 2 with its use of conventional data to give better estimates of the direction for the surface wind speeds. The most dramatic differences occur in regions with sparse conventional data, where the model first guess is poor. As larger amounts of data are assimilated, and the model first guess improves, the differences between Methods 1 and 2 diminish.

Several extensions of this work are underway, and we plan to present the results of a number of them at the conference. One important modification of the work reported here is the replacement of the SCM analysis scheme with a multivariate OI analysis, so that we can make the best use of the conventional data (whether real or simulated). Another important procedural change is the implementing of a more realistic specification of the surface winds. With those changes we will then perform an intercomparison of all four methods using the simulation methodology. We also plan to do some real data (Geosat and Nimbus-7) forecast impact tests using the more promising methods found in the simulation studies.

6. ACKNOWLEDGEMENT

The authors would like to thank J. Ardizzone, R. Rosenberg, J. Terry, and J. Woollen for providing computing support for this project.

7. REFERENCES

Atlas, R., E. Kalnay, W. E. Baker, J. Susskind, D. Reuter, M. Halem, 1985: Simulation studies of the impact of future observing systems on weather prediction. Proceedings of the 7th Conference on Numerical Weather Prediction, June 17-20, Montreal P.Q. Canada, 145-151.

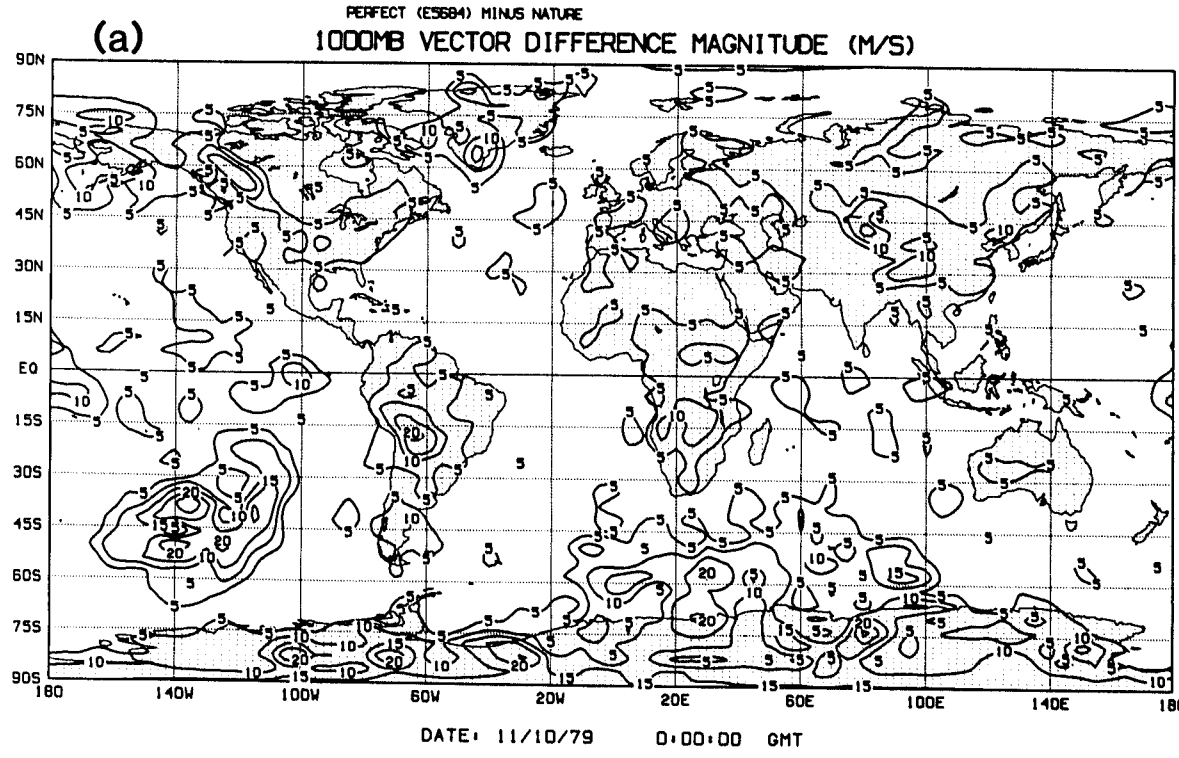

Fig. 1a Vector magnitude of the surface wind differences perfect - Nature at 0000- GMT 10 Nov. 1979

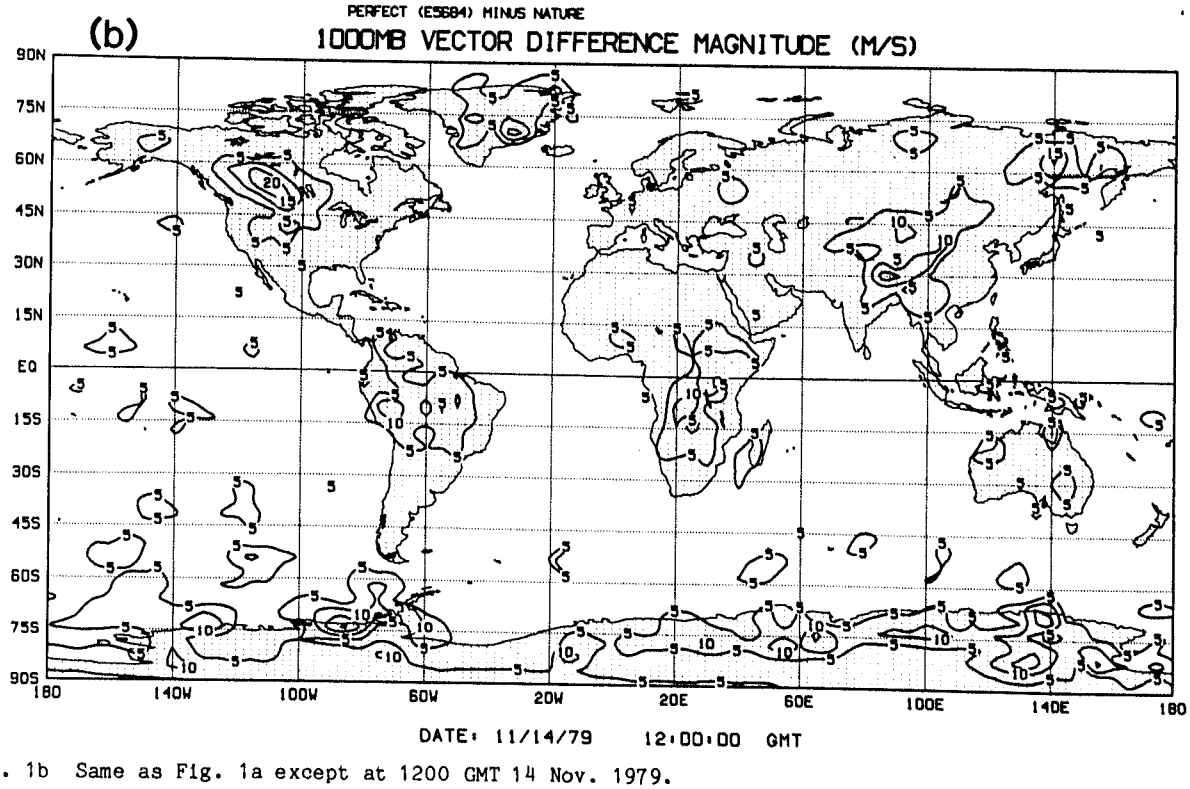

Fig. 1b Same as Fig. 1a except at 1200 GMT 14 Nov. 1979.

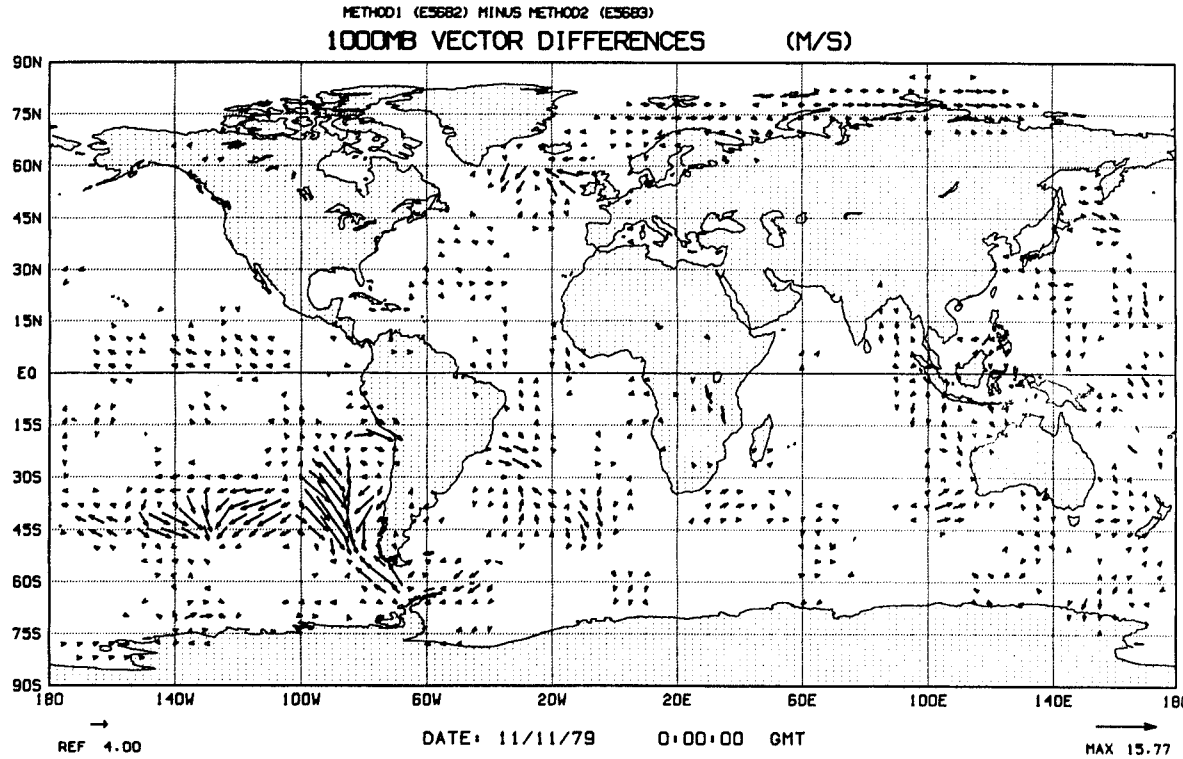

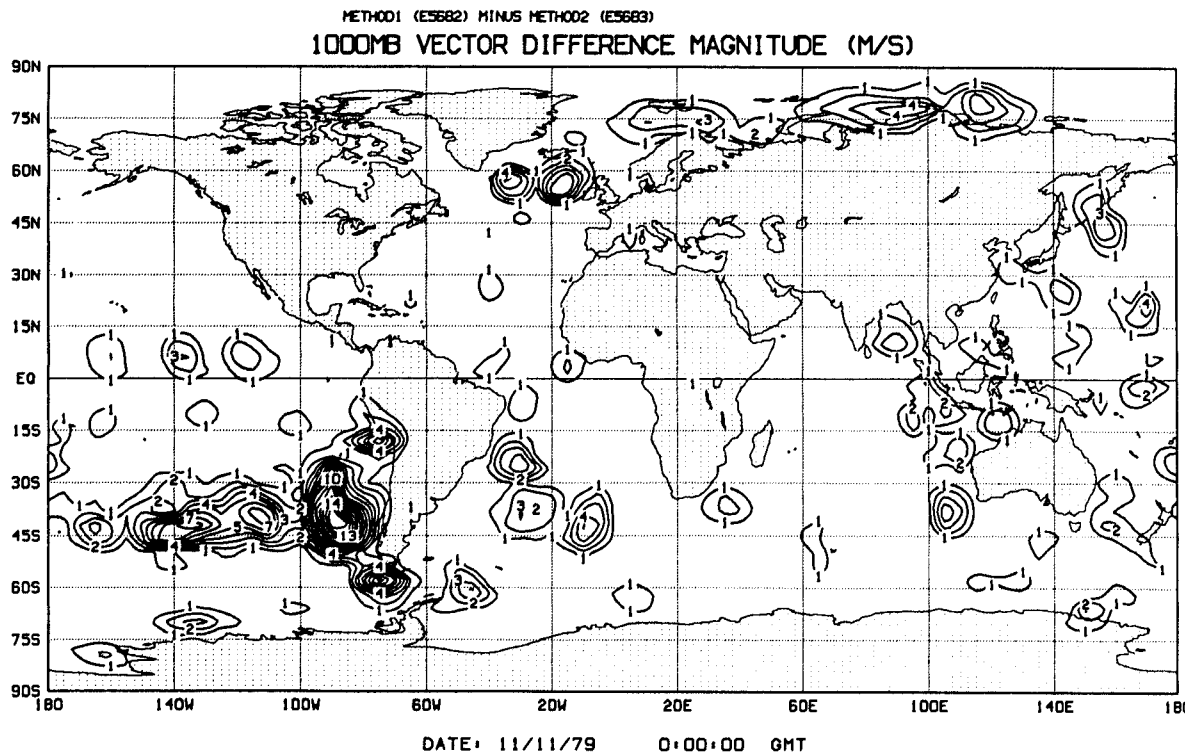

Fig. 2 Surface wind differences Method 1 - Method 2 at 0000 GMT 11 Nov. 1979.

_____, A. J. Busalacchi, M. Ghil, S. Bloom, E. Kalnay, 1987: Global Surface Wind and Flux Fields From Model Assimilation of Seasat Data. J. Geophys. Res., 92C, 6477-6487.

Baker, W. E., 1983: Objective analysis and assimilation of observational data from FGGE. J. Atmos. Sci., 111, 328-342.

_____, R. Atlas, E. Kalnay, M. Halem, P. M. Woiceshyn, S. Peteherych, D. Edelman, 1984: Large-Scale Analysis and Forecast Experiments With Wind Data From the Seasat A Scatterometer. J. Geophys. Res., 89D, 4927-4936.

_____, S. C. Bloom, J. S. Woollen, M. S. Nestler, E. Brin, T. W. Schlatter, G. W. Branstator, 1987: Experiments with a three-dimensional statistical objective analysis scheme using FGGE data. Mon. Wea. Rev., 115, 272-296.

Dey, C. H., W. J. Bostelman, C. P. Arnold Jr., 1985: Design of a Windsat Observing System Simulation Experiment. Proceedings of the NASA Symposium on Global Wind Measurements, W. E. Baker and R. J. Curran eds. 73-79.

Hoffman, R. N., 1982: SASS wind ambiguity removal by direct minimization. Mon. Wea. Rev., 110, 434-445.

_____, 1984: SASS wind ambiguity removal by direct minimization. Part II: use of smoothness and dynamical constraints. Mon. Wea. Rev., 112, 1829-1852.

Kalnay, E., R. Balgovind, W. Chou, D. Edelman, J. Pfaendtner, L. Takacs, K. Takano, 1983: Documentation of the GLAS Fourth Order General Circulation Model. NASA Tech. 86064.

Sasaki, Y., 1970: Some basic formalisms in numerical variational analysis. Mon. Wea. Rev., 98, 875-883.

Yu, T., 1987: A technique for deducing wind direction from satellite microwave measurements of wind speed. Mon. Wea. Rev., in press.

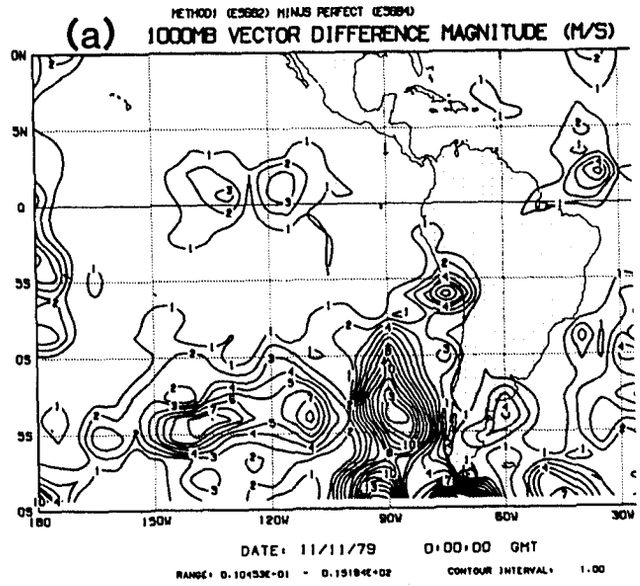

Fig. 3a Vector magnitude of the surface wind differences Method 1 - Perfect at 0000 GMT 11 Nov. 1979.

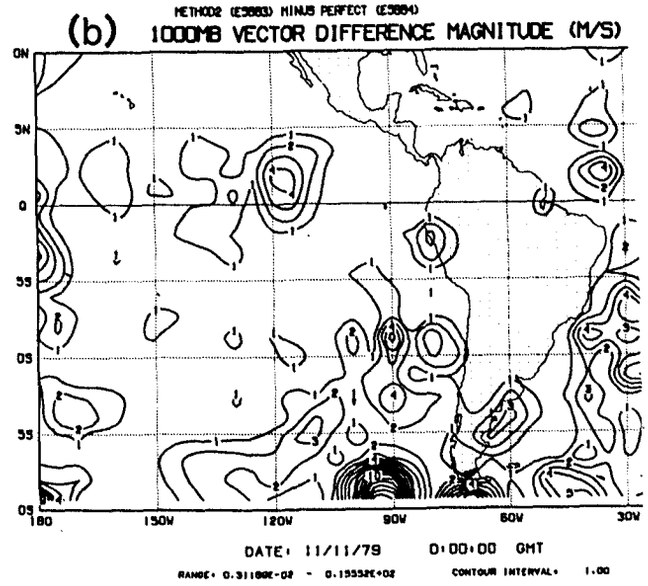

Fig. 3b Same as Fig. 3a except Method 2 - Perfect.

INTEGRATION OF SATELLITE SCATTEROMETER AND RADIOMETER MEASUREMENTS

Marie C. Colton
Allan B. Caughey

Naval Environmental Prediction Research Facility
Monterey, CA

1. INTRODUCTION

1.1 Background

Recent research in satellite meteorology and oceanography has demonstrated the benefits of a multisensor approach to the development of new applications of remotely sensed data. For example, McMurdie et.al. (1987) used the Seasat scatterometer (SASS) and radiometer (SMMR) data in conjunction with conventional data to aid in the diagnosis of midlatitude storms. They showed that fronts in the radiometer integrated water vapor fields are closely aligned with pressure fronts located by conventional analyses. In addition, patterns in the divergence of the wind field, as computed from the scatterometer wind vectors, are physically consistent with the patterns of atmospheric water (vapor and rain) (Figure 1).

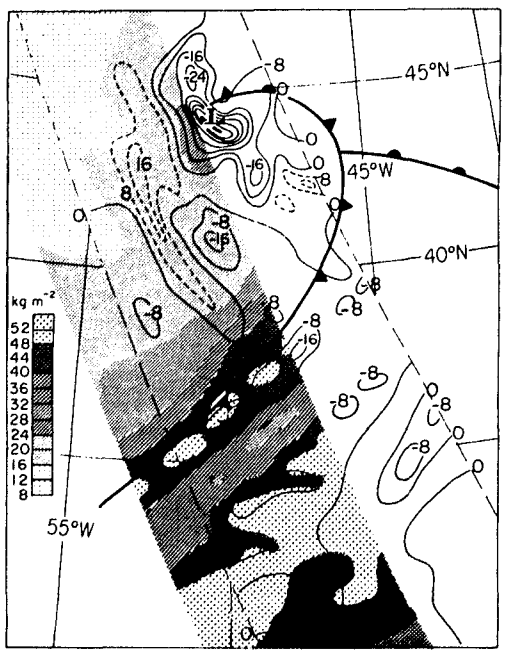

Fig. 1. Scatterometer divergence contoured every 8.E-05 s^{-1} (solid lines, convergence; dashed lines, divergence); SMMR integrated water vapor and surface pressure fronts (from McMurdie et.al., 1987)

In preparation for the above type of analysis, there is a substantial investment of the researcher's time devoted to the subjective analysis of the combined (voluminous) satellite data sets. If these new applications are to be used in near real-time then the data preparation sequence needs to be automated to the maximum extent possible, using objective techniques (Levy and Brown, 1986). Further, the satellite data need to be assimilated into current analysis products (Sasaki and Goerss, 1984).

At the Naval Environmental Prediction Research Facility (NEPRF), the Satellite Processing and Display System (SPADS) provides a convenient tool to develop, evaluate, and implement new applications of satellite data (Schramm, et.al, 1980). The SPADS consists of a catalogue of programs which provide the user with a standard toolset for the analysis of satellite data in image or swath format. Especially useful is the capability to access directly the meteorological fields produced at the Fleet Numerical Oceanography Center and to overlay them on the satellite fields.

1.2 Scope of the Study

For the present study, a component program of the SPADS was modified to address the following questions:

(1) *Multisensor Analysis*

Can the satellite derived fields of integrated water vapor and divergence, and conventional pressure analysis be objectively analyzed on a common grid in such a way as to preserve the alignment of the fronts and convergence patterns as demonstrated by McMurdie et.al.?

(2) *Automation of Procedures*

Can this procedure be automated to yield a nowcasting tool for storms analysis? Could this be a data product of the recently launched DMSP SSM/I?

(3) *Analysis Updates*

Can the scatterometer and radiometer wind *speeds* be incorporated into a forecast (analysis) field to provide an improved first guess (updated analysis)?

2. DATA

2.1 Satellite Data

The Seasat scatterometer and radiometer data as recently reprocessed and described by Wentz et.al (1986) were used in this study. The reprocessing was performed using a revised normalized radar

cross-section (NRCS) algorithm which was derived to correct systematic polarization and incidence angle errors in winds retrieved from the scatterometer. Also, to uncouple the NRCS algorithm coefficients from any *in situ* data, Wentz et.al. assumed a Rayleigh distribution of wind speeds to compute new coefficients. With regard to the SMMR, a new brightness temperature, T_B, algorithm was used to eliminate the artificial dependence of T_B on sea surface temperature and atmospheric liquid water as produced in the original algorithm. Biases, temporal drifts and position dependence errors in T_B were also corrected with the new algorithm.

For comparison of the objectively analyzed results with those of McMurdie et.al. the test case chosen for study is the familiar QEII storm which occurred in the North Atlantic near the Gulf Stream during 9 to 11 September 1978. The corresponding scatterometer wind vectors and radiometer integrated water vapor data are from an orbit which passed over the storm at about 1200 GMT on 9 September.

2.2 Conventional Data

The global, polar stereographic surface pressure analysis field for the area of the QEII storm was retrieved from the FNOC archives. These analyses are produced at six-hour synoptic time intervals from a combination of all the current surface observations available to the analyst and the previously analyzed field.

2.3 Model Output

To address question (3) above, the forecast wind at 19.5 m in the QEII area produced by the Navy Operational Global Atmospheric Prediction System (NOGAPS) was retrieved from the FNOC archives.

3. MULTISENSOR SURFACE WIND ACQUISITION SYSTEM (MUSSWAS)

3.1 Original Intent

The original purpose of MUSSWAS was to provide a wind direction for radiometer derived wind speed using NOGAPS forecast winds at 925 mb, GOES cloud track winds and sea surface temperature (Clark, 1984). The cloud track winds were veered to the surface using the other two fields and then interpolated to the SMMR data points. In this formulation of the program the radiometer rain-rates were also gridded using a Barnes-type objective analysis and contoured.

3.2 Modifications Required

The MUSSWAS program is highly modular so that adaptation of it for this new application amounted mostly to rearranging the modules, reformatting certain data sets and substituting new input files for some of the originals; i.e., scatterometer multiple solution wind vectors vice cloud track winds, wind speed at 19.5 m from NOGAPS vice 925 mb and surface pressure vice suface temperature analyses. New programming was required to choose the correct scatterometer wind direction, to compute the divergence of the scatterometer wind field using an improved numerical scheme (Boggs, 1986), to overlay the surface pressure analysis on the satellite fields and to update the scatterometer files.

3.3 Functional Description

In the initialization phase of the program, the geographic subarea and all input data files are defined by the user. The program then proceeds into the analysis update mode as described in Fig. 2.

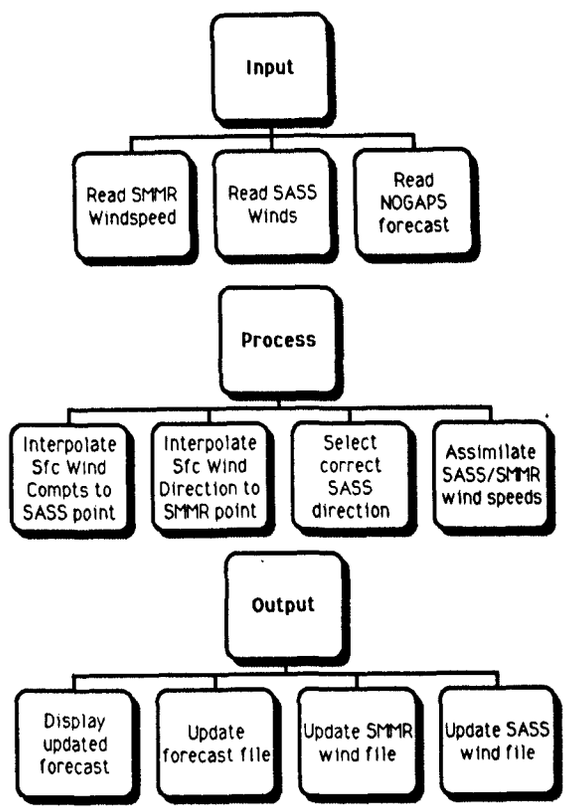

Fig. 2. Functional Description of the MUSSWAS Analysis Update mode.

The SMMR windspeed, SASS multiple solution wind vectors and NOGAPS forecast wind field are read first. In the processing sequence a bilinear interpolation of the u and v wind components is used to compute a first guess wind direction at the SASS and SMMR data points. This estimated direction is used to determine the correct scatterometer direction in the manner of Levy and Brown (1986). That is, the correct solution, D_{nc}^{s}, corresponds to the minimum over m of

$$1 - \cos(D_n - D_{nc}^{s}) = \min[1 - \cos(D_n - D_{nm}^{s})] \quad (1)$$

where D_n is the direction of the first guess and D_{nm}^{s} are the m scatterometer directions.

The final step is to assimilate the SASS wind vector and SMMR windspeed into the original first guess field. This is achieved by a Barnes objective analysis of the u and v components from the combined scatterometer, radiometer and forecast fields. The updated field is displayed and stored, the scatterometer file is updated with the correct wind direction and the radiometer file is updated with the first guess directions.

The construction of the wind, water vapor and surface pressure composite figure is illustrated in Fig. 3. The input files consist of the SASS correct wind vectors (from the analysis update mode or an independent source), the SMMR integrated water vapor field and the surface pressure field. The SASS/SMMR data are first transformed to a Mercator grid via the Barnes objective analysis subroutine. The divergence of the wind is computed using a numerical scheme devised by Boggs (1986). In this scheme the partial derivatives u_x and v_y at a grid point are computed one grid row or column at a time using a central difference formula with a fourth-degree interpolating polynomial. The divergence is then computed in pseudo-spherical coordinates as the sum of u_x, v_y and a term which corrects for the convergence of the meridians at the poles. The divergence and water vapor fields are contoured and the pressure field overlayed. The output is the final composite figure.

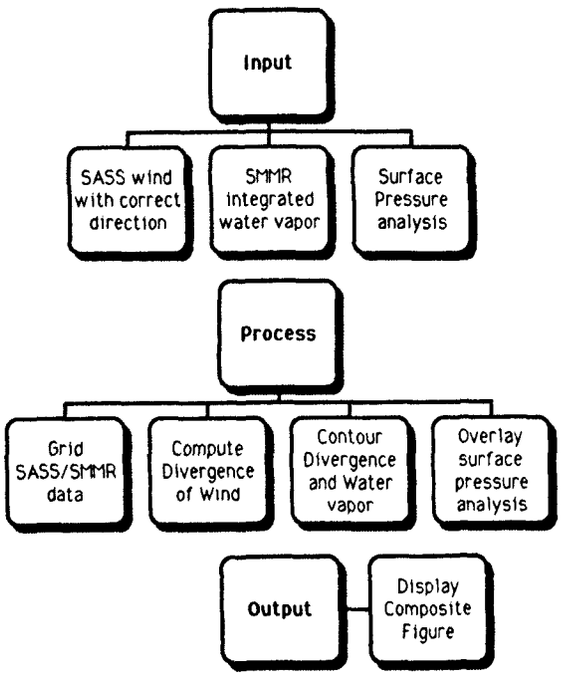

Fig. 3. Functional Description of the MUSSWAS SASS/SMMR/Pressure Composite Figure mode.

3.4 Current Objective

The objective now is to exercise both the analysis update and composite figure modes of the MUSSWAS program using the QEII storm as a test case. The results of the test runs will be reported at the AMS proceedings.

4. SUMMARY

Recent applications of satellite data to geophysical problems have been derived using a multisensor approach in which complementary data types are combined to produce improved diagnostic aids. In this study Seasat scatterometer wind vector and radiometer windspeed data were combined with a forecast wind field to compute an improved wind analysis and to determine the correct wind direction from the scatterometer multiple solutions and an estimated wind direction for the radiometer wind speed. Further, an objective method, patterned after a subjective analysis by McMurdie (1987), was developed to construct a wind divergence, water vapor, surface pressure composite analysis from the scatterometer wind vectors, radiometer integrated water vapor, and FNOC surface pressure analysis.

5. REFERENCES

Boggs, D.B., 1986: Internal Report, dB Systems, Ltd.,LaCanada, CA.

Clark, J.R.,1984:Multi-Sensor Surface Wind Acquisition System Functional Description,NEPRF Document No. W0253/FD13.

Levy, G.A.,and Brown, R.A.,1986:A Simple, Objective Analysis Scheme for Scatterometer Data, *J.Geophys.Res*, **91**, 5153-5158.

McMurdie, L.A., Levy, G.A., and Katsaros, K.B.,1987: On the Relationship between Scatterometer Derived Convergences and Atmospheric Moisture, *Mon.Wea.Rev.*,1281-1294.

Sasaki, Y.K. and Goerss, J.S.,1984: Four-Dimensional Satellite Data Assimilation, Contractor Report, N00014-79-C-0758.

Shramm, W., Zeleny, P., Nagle, R.E., and Weinstein, A.I.,1982: The Navy SPADS, A Second Generation Environmental Display System, Ninth Conf. Weather Forecasting and Analysis, Seattle,WA.

Wentz, F.J., and Mattox, L.A.,1986:New Algorithms for Microwave Measurement of Ocean Winds: Applications to Seasat and the Special Sensor Microwave Imager, *J.Geophys.Res*, **91**, 2289-2307.

5.7

ERROR ANALYSIS OF AUTOMATED WINDS DERIVED FROM GOES MULTISPECTRAL IMAGERY

Steven D. Swadley

Naval Environmental Prediction Research Facility
Monterey, California 93943-5006

1. INTRODUCTION

Cloud motion vectors (CMV's) have been derived from sequences of geostationary satellite images since the late 1960's. Operational use of CMV's in global and regional analyses quickly became routine in the 1970's despite the many inherent problems of both the manual and automated CMV derivation techniques. Hubert (1979) gives a thorough review of many aspects of CMV derivation methods as they evolved during the 1970's.

With the implementation of Optimum Interpolation (OI) schemes at many operational meteorological data processing centers, there exists a need for a priori knowledge of the inherent random errors and spatial covariance functions of the various observation types utilized in the analysis. Statistical structure and correlation functions can provide an accurate determination of the covariance structure of the various meteorological fields (Gandin, 1963). By-products of these functions have been quantitative estimates of the inherent random error of a given observation type. The purpose of this paper is to compare the accuracy of two automated CMV generating systems via structure and correlation function analysis.

2. THE AUTOMATED CLOUD MOTION VECTOR SYSTEMS

2.1 SAWEGS

SAWEGS, the System for Automatic Wind Extraction from Geostationary Satellite-Data, is based upon the computation of a cross-covariance (XCOV) between two precisely aligned satellite image subareas. Displacement information about the original images is related to a Fast Fourier Transform (FFT) produced cross-covariance function directly. The maximum value of the XCOV matrix defines the cloud displacement relative to the two image subareas. In the XCOV method the displacement is the direct result of a single XCOV calculation, and a single vector is determined for each subarea. If two or more different cloud layers are moving in different directions within the subarea, the XCOV operation tends to cancel these motions against each other and to produce a displacement that does not accurately represent any motion.

Automatic Quality Control (QC) is performed as a final processing step of SAWEGS. The SAWEGS QC procedure consists of four passes through a basic two-step configuration. The analysis step averages the observations to produce a smooth wind field. The discard step compares the observations with the smoothed wind field and flags inconsistent vectors. No subjective manual editing was performed. SAWEGS currently runs on a Data General Eclipse S/250 16-bit mini-computer equipped with an integral array processor, and produces a maximum 961 CMV's from a 512 by 512 image. Lee and Nagle (1980), give a complete description of SAWEGS and the XCOV method.

2.2 NASA/MSFC's Automated Wind System

Wilson (1984) introduced a new multispectral technique for deriving mesoscale CMV's from geostationary satellites. The system was designed to produce mesoscale CMV's (approx. 10 km spacing) from 1 km resolution GOES rapid scan imagery. The Naval Environmental Prediction Research Facility (NEPRF) has utilized this system with standard GOES imagery at 4 and 8 km resolutions. This provides a much greater areal coverage with nominal CMV spacings of about 40 and 80 km respectively.

The NASA/MSFC system utilizes "template matching" numbers to determine the relative similarity between an image template and the corresponding image search area (Barnea and Silverman, 1972). This technique, known as the Sequential Similarity Detection Algorithm (SSDA), involves the simple calculation of an absolute value difference between the pixel values in the template and the corresponding pixels in the search area for a given displacement. The NASA/MSFC system and SAWEGS both employ a simple IR black-body temperature approach for height assignment of the CMV's.

Automatic QC for the NASA/MSFC system utilizes three objective image processing QC parameters. The first involve the elimination of all CMV's with SSDA minima that fall on the search area boundaries. Template match quality parameter one is defined as:

$$TMQ1 = \frac{\text{SSDA MEAN}}{\text{SSDA MIN}} \geq 1.6, \qquad (1)$$

where the SSDA mean is computed over the entire search area. Template match quality parameter two is defined as:

$$TMQ2 = \frac{\text{SSDA SECONDARY MIN}}{\text{SSDA MIN}} \geq 1.14, \qquad (2)$$

where the secondary min is outside the 3 by 3 area surrounding the primary SSDA min. Utilization of these values has allowed a confidence stratification of the resulting CMV's.

The NASA/SSDA Cloud Tracking System is currently running on NEPRF's 32-bit Concurrent 3260-MPS mini-computer. Generation of a CMV set requires over two hours of processing time. A maximum of 1800 CMV's are produced from a 512 by 512 image.

3. THE STRUCTURE AND CORRELATION FUNCTION METHOD

Many researchers have used statistical structure and correlation functions to determine the inherent random error associated with a specific observation type and to reveal details of the observed scales of atmospheric variability (Barnes and Lily, 1975; Hillger and Vonder Haar, 1979; Maddox and Vonder Haar, 1979; Fuelberg and Meyer, 1984; Morone, 1986).

The structure function suitable for meteorological variables (Gandin, 1963) is defined as:

$$STR(R) = \frac{1}{N} \Sigma [f'(\mathbf{r}_i)-f'(\mathbf{r}_j)]^2 \qquad (3)$$

where $\mathbf{r}_i$ and $\mathbf{r}_j$ are the position vectors of the observation sites. The separation interval R was defined to be a specific distance interval, e.g. 25 km < R ≤ 50 km. N is the number of data pairs $f'(\mathbf{r}_i)$, $f'(\mathbf{r}_j)$ whose separation radius, $|\mathbf{r}_i-\mathbf{r}_j|$, falls within the interval R. We also define $f'(\mathbf{r}_i) = f(\mathbf{r}_i) - \bar{f}$, with $\bar{f}$ being the mean value defined over a specific distance interval R. The correlation function is defined as

$$COR(R) = \frac{\frac{1}{N} \Sigma f'(\mathbf{r}_i)\ f'(\mathbf{r}_j)}{\frac{1}{K} \Sigma f'^2(\mathbf{r}_j)} \qquad (4)$$

with notation the same as in (3). The denominator in (4) is the variance computed with observations within a separation interval used only once for a total of K times.

The approach used in this study for computing structure and correlation functions is that of Maddox and Vonder Haar (1979). The implicit assumptions of homogeneity and isotropy were validated by examining plots of the structure and correlation functions as a function of bearing and distance to determine the distance at which the functions become strongly dependent upon bearing (Morone,1986).

The inherent random error can be estimated by extrapolating the structure function to zero distance separation, and is defined as:

$$E = [STR(0)/2]^{1/2} \qquad (5)$$

The extrapolation procedure was a least-squares fit of an exponential function to the structure values of the form:

$$STR(X) = B * EXP(AX), \qquad (6)$$

where X is the separation distance, A is the curvature coefficient and B the intercept (Fuelberg and Meyer, 1984). Structure values with separation distances less than 500 km and at least 50 data points within the interval were used for the curve fitting.

The correlation functions as computed by (4) contain the effect of random observational errors, which leads to values of less than 1.0 at zero separation. Hillger and Vonder Haar (1979) describe a method for adjusting the correlation functions for this effect. Correlation functions in the present study were adjusted using the above method. In this way the correlation function describes the meteorological variability, without the additional effect of random noise. The correlation values were then fit to an exponential function of the form:

$$COR(X) = B * EXP(-AX^2), \qquad (7)$$

where X is the separation distance, A the coefficient of curvature and B the intercept.

4. DATA AND RESULTS

Cloud motion vector fields were generated by both SAWEGS and the NASA/SSDA automated systems for three separate cases. The CMV's for each case were divided into four layers in the vertical: 1000-900 mb, 899-700 mb, 699-400 mb and less than 399 mb.

4.1 Case I: May 21, 1986 Results

The SAWEGS derived CMV's, all pressure levels included, for 2300 GMT is shown in Figure 1. Only the CMV's which have passed SAWEGS QC criterion are plotted. The SAWEGS CMV's depict the low level anticyclonic flow off the west coast. The upper level ridge axis is marginally depicted. The upper level low centered over eastern Oregon is not well defined by SAWEGS CMV's. The subtropical jet, south of Baja California, is indicated by SAWEGS as a small group of southwest winds of up to 33 m/sec.

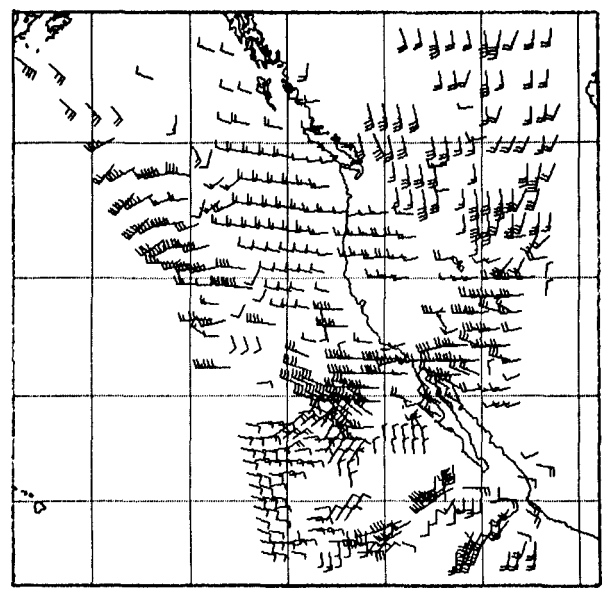

Fig. 1. SAWEGS derived CMV's for 21 May 1986 at 2300 GMT. All levels plotted.

Figure 2 shows the structure functions for the u and v components and the best fit exponential curve for SAWEGS derived winds in the 699-400 mb layer. The adjusted correlation functions for the SAWEGS u and v components of the same layer are shown in Figure 3.

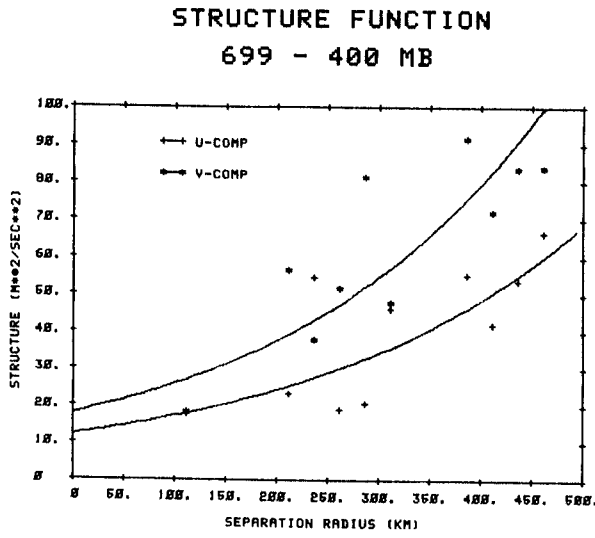

Fig. 2. Structure functions for SAWEGS derived u and v components of the 699-400 mb layer for 21 May 1986.

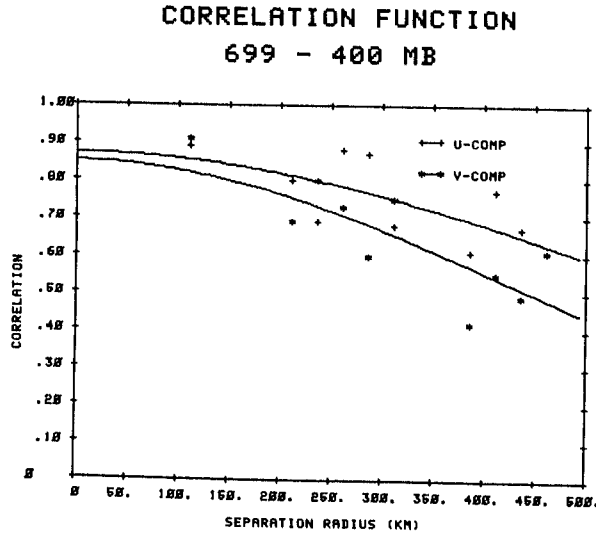

Fig. 3. Corrected coorelation function for SAWEGS derived u and v components of the 699-400 mb layer for 21 May 1986.

The NASA/SSDA derived CMV's, with all pressure levels plotted, for 2300 GMT are shown in Figure 4. Only CMV's which have met at least one of the TMQ1 or TMQ2 QC parameters are plotted. The NASA/SSDA CMV's define the low level anticyclonic flow as well as the center of the high. The upper level ridge pattern is quite well defined and the CMV's display a high degree of uniformity. The subtropical jet is observed by about 30 CMV's with maximum speeds of 40 m/sec. Figure 5 shows the structure functions

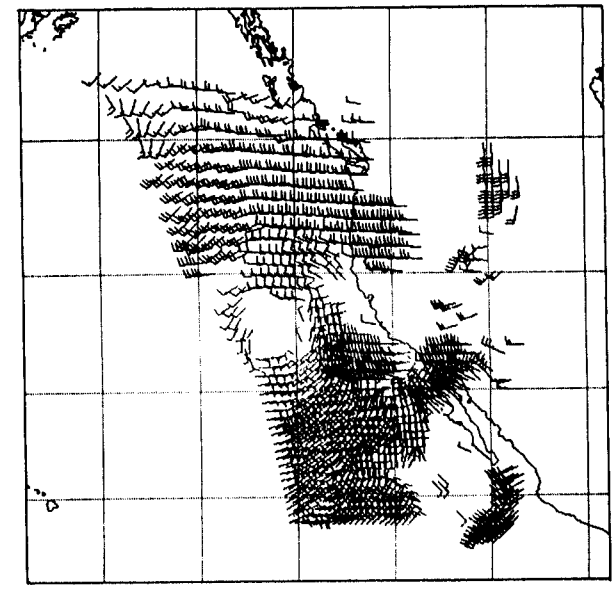

Fig. 4. NASA/SSDA derived CMV's for 21 May 1986 at 2300 GMT. All levels plotted.

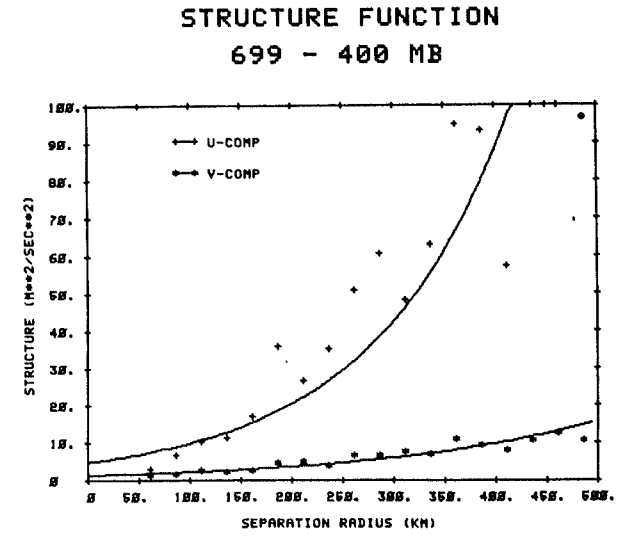

Fig. 5. Structure function for the NASA/SSDA derived u and v components of the 699-400 mb layer for 21 May 1986.

for the NASA/SSDA u and v components and best fit exponential curve for the 699-400 mb layer. Figure 6 shows the associated correlation functions for the same layer.

Table 1 compares the means of the u and v components and wind speeds derived by SAWEGS and NASA/SSDA for Case I. Table 2 compares the random CMV measurement error of the two systems as derived by the method of extrapolating the structure function to zero separation.

4.2 Case II: March 24, 1987

The case II synoptic pattern for the northeastern Pacific is dominated by a large low level anticyclone and an approaching frontal system

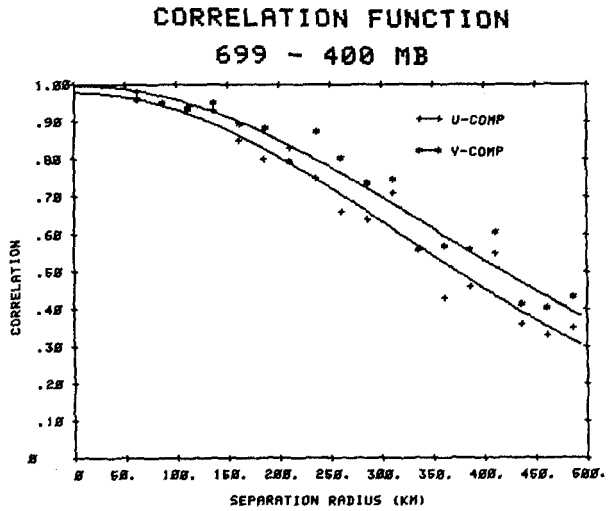

Fig. 6. Corrected coorelation function for NASA/SSDA derived u and v components of the 699-400 mb layer for 21 May 1986.

Table 1. NASA/SSDA vs. SAWEGS mean values for the u and v components and wind speed for 21 May, 1986.

	NO. OBSV.	MEANS (M/SEC)			SYSTEM
LEVEL (MB)	N	u	v	Speed	
1000-900	141	3.8	-2.0	6.9	NASA
	137	4.2	0.7	8.7	SAWEGS
899-700	299	1.0	-2.3	6.8	NASA
	163	3.1	0.5	8.2	SAWEGS
699-400	431	3.5	-1.1	9.4	NASA
	105	5.4	5.4	13.8	SAWEGS
< 399	117	13.7	4.1	17.4	NASA
	95	9.8	6.2	15.3	SAWEGS

Table 2. NASA/SSDA vs. SAWEGS random error comparison values for the u and v components and vector wind for 21 May, 1986.

	NO. OBSV.	ERRORS (M/SEC)			SYSTEM
LEVEL (MB)	N	u	v	V	
1000-900	141	0.49	0.41	0.64	NASA
	137	7.94	11.36	13.86	SAWEGS
899-700	299	0.75	0.59	0.95	NASA
	163	3.38	1.91	3.88	SAWEGS
699-400	431	1.54	0.83	1.75	NASA
	105	2.47	2.98	3.87	SAWEGS
< 399	117	1.60	1.18	1.79	NASA
	95	5.22	4.00	6.57	SAWEGS

with an extensive cirrus leaf. The subtropical jet is very pronounced and appears to have a double jet streak configuration.

The SAWEGS derived CMV set for 1930 GMT on 24 March, 1987, is shown in Figure 7. The depiction of the subtropical jet displays a typical problem with the cross-covariance method, in that, when multiple cloud layers (jet stream cirrus and stratocumulus) are moving in different directions, the resulting CMV depicts motion unrepresentative of either level. SAWEGS also depicts the progression of the frontal band rather than the movement of the high clouds along the front, which is another common problem with the XCOV method.

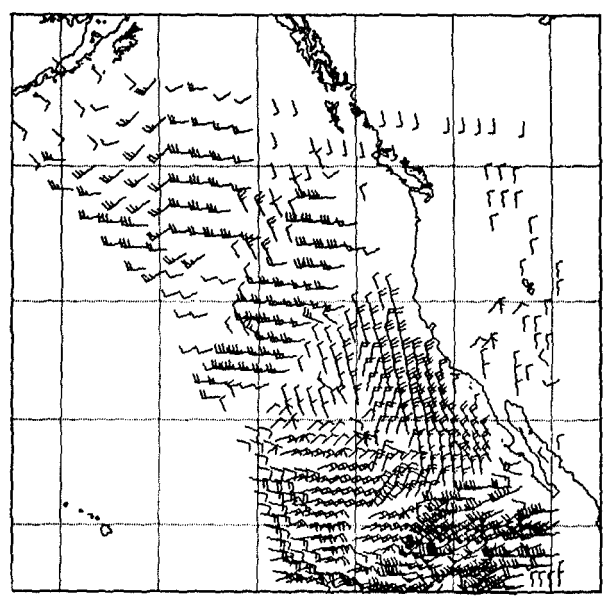

Fig. 7. SAWEGS derived CMV's for 24 March 1987 at 1930 GMT. All levels plotted.

The NASA/SSDA derived CMV set for 1930 GMT on 24 March, 1987, is shown in Figure 8. To keep the Figure 8 from appearing cluttered, only half of the original 1184 CMV's are plotted. The subtropical jet feature is depicted as a broad region of high winds with maximum speeds of 42 m/sec. The mid level winds within the cold air region behind the frontal band are more uniform than the SAWEGS CMV's for that region. The CMV's within the frontal band did not meet the NASA/SSDA QC criterion and and were automatically flagged as low quality winds. Table 3 compares the random CMV measurement errors for case II.

4.3 Case III: October 1, 1986

Case III presents a rather complex synoptic pattern for cloud tracking. Hurricane Paine, which attained maximum surface winds of 80 kts near 0000 GMT on 2 October, lies just south of Baja California.

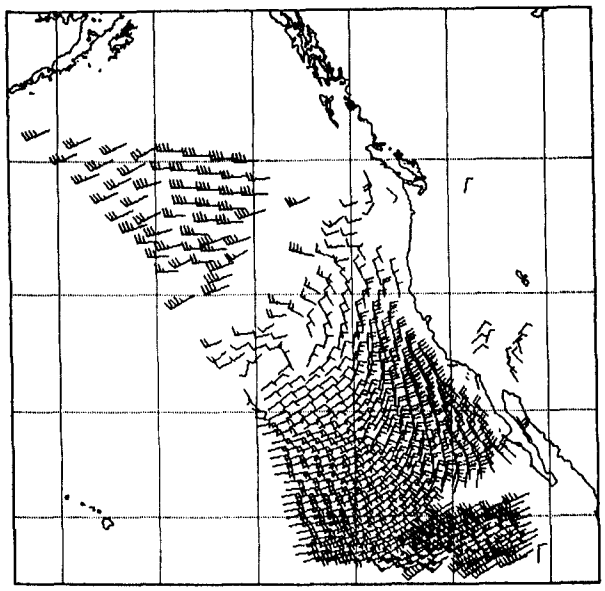

Fig. 8. NASA/SSDA derived CMV's for 24 March 1987 at 1930 GMT. All levels with every other CMV plotted.

Table 3. NASA/SSDA vs. SAWEGS random error comparison values for the u and v components and vector wind for 24 Mar, 1987.

	NO. OBSV.	ERRORS (M/SEC)			SYSTEM
LEVEL (MB)	N	u	v	V	
1000-900	34	-	-	-	NASA
	144	4.48	3.66	5.78	SAWEGS
899-700	792	0.55	0.53	0.76	NASA
	139	1.44	1.66	2.20	SAWEGS
699-400	209	2.02	1.26	2.38	NASA
	318	5.04	3.25	6.00	SAWEGS
< 399	149	1.19	1.01	1.57	NASA
	64	-	-	-	SAWEGS

The SAWEGS derived CMV set for 1630 GMT on 1 October, 1986, is shown in Figure 9. The NASA/SSDA derived CMV set is shown in Figure 10. Both sets of CMV's depict the northerly flow over Mexico and in the maritime stratus west of Paine. The cyclonic low level circulation is clearly marked by the NASA/SSDA CMV's and the upper level outflow is also depicted. SAWEGS CMV's depict the outflow but show little indication of low level cyclonic circulation. The NASA/SSDA QC scheme flagged numerous CMV's near the central dense overcast (CDO) region of the storm, while SAWEGS QC scheme failed to remove many ambiguous CMV's near the CDO. The random observational errors for the two systems are shown in Table 4.

5. SUMMARY AND CONCLUSIONS

The accuracy of two automated cloud motion vector generating systems has been investigated via the structure and correlation function

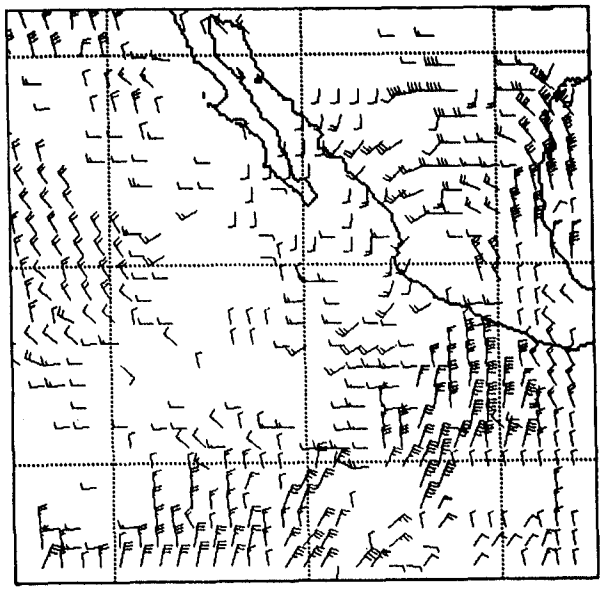

Fig. 9. SAWEGS derived CMV's for 1 October 1986, 1630 GMT. All levels plotted.

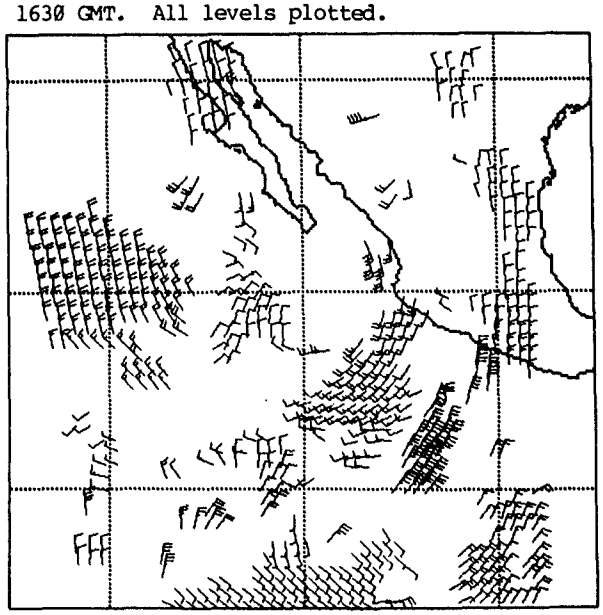

Fig. 10. NASA/SSDA derived CMV's for 1 October 1986, 1620 GMT. All levels plotted.

Table 4. NASA/SSDA vs. SAWEGS random error comparison values for the u and v components and vectors wind for 1 October, 1986.

	NO. OBSV.	ERRORS (M/SEC)			SYSTEM
LEVEL (MB)	N	u	v	V	
1000-900	0	-	-	-	NASA
	338	3.16	5.13	6.02	SAWEGS
899-700	141	0.84	0.67	1.08	NASA
	137	2.38	4.80	5.36	SAWEGS
699-400	290	1.24	1.49	1.94	NASA
	69	3.08	2.70	4.10	SAWEGS
< 399	180	0.85	0.81	1.17	NASA
	53	-	-	-	SAWEGS

analysis approach of Maddox and Vonder Haar (1979). CMV data sets for three separate cases, depicting various synoptic situations, were analyzed for each automated system. Extrapolation of the structure functions to zero distance produces a random observational error estimate for each wind component. The NASA/SSDA vector errors for the lower layers ranged from 0.6 to 1.1 m/sec, while the mid and upper layer vector errors ranged from 1.2 to 2.4 m/sec. The SAWEGS vector errors for the lower layers ranged from 2.2 to 13.9 m/sec, while the mid and upper layer vector errors ranged from 3.9 to 6.6 m/sec. However, these estimates assume that spatially correlated errors (which would decrease the magnitude of these errors) were not present and the actual random errors would be slightly larger.

Height assignment errors contributed to the random errors of both systems, but SAWEGS low level winds often contained winds depicting flow at upper levels which partially explains the large random errors for SAWEGS low level winds.

The primary goal of this study was to compare the accuracy of the two automated cloud motion vector systems currently in use at NEPRF. The CMV's generated by SAWEGS require significant amounts of manual subjective editing to lower the random observational errors, which results in degraded spatial coverage. The NASA/SSDA generated CMV's require little or no manual editing and the spatial coverage is clearly superior to the SAWEGS CMV's.

Experiments are now being designed and conducted to determine the most effective way to assimilate the NASA/SSDA generated CMV's into the global and regional multi-variate optimum interpolation schemes now in use at FNOC.

6. ACKNOWLEDGMENTS

Special thanks go to Dr. Greg Wilson and Dr. Bob Atkinson for developing and adapting the NASA/SSDA system for use at NEPRF. Thanks is also extended to Dr. Ed Barker and Dr. Ted Tsui for providing helpful suggestions concerning structure and correlation function analysis and interpretation.

7. REFERENCES

Barnea, D.I., and H.F. Silverman, 1972: A Class of algorithms for fast digital image registration. IEEE Transactions on Computers. C-21, 179-186.

Barnes, S.L., and D.K. Lilly, 1975: Covariance analysis of severe storm environments. Preprints, Ninth Conf. Severe Local Storms, Norman, Ok., Amer. Meteor. Soc., 301-306.

Fuelberg, H.E., and P.J. Meyer, 1984: An analysis of the AVE-SESAME I period using statistical structure and correlations functions. Mon. Wea. Rev., **112**, 1562-1566.

Gandin, L.S., 1963: Objective analysis of meteorological fields. Translated from Russian, Israel Program for Scientific Translations, Jerusalem, 242pp. [NTIS TT-65-50007.]

Hillger, D.W., and T.H. Vonder Haar, 1979: An analysis of satellite infrared soundings at the mesoscale using statistical structure and correlation functions. J. Atmos. Sci., **36**, 287-305.

Hubert, L.F., 1979: Wind derivation from geostationary satellites. In Quantitative Meteorological Data from Satellites, WMO Tech. Note 66., edited by J. Winston, 33-59.

Lee D.H., and Nagle R.E., 1980: An automatic cloud tracking system based on the cross-covariance method. NAVENVPREDRSCHFAC Tech. Rept. TR 80-08, 64 pp.

Maddox, R.A., and T.H. Vonder Haar, 1979: Covariance analysis of satellite-derived mesoscale wind fields. J. Appl. Meteor., **18**, 1327-1334.

Morone, L.L., 1986: The observational error of automated wind reports from aircraft. Bull. Amer. Meteor. Soc., **67**, 177-185.

AUTOMATIC ANALYSIS OF STEREOSCOPIC IMAGE PAIRS FROM GOES SATELLITES

A. F. Hasler
Laboratory for Atmospheres

J. Strong
Space Data & Computing Division
NASA/Goddard Space Flight Center
Greenbelt, MD 20771

R. Morris & H. Pierce
General Sciences Corporation
Laurel, MD 20707

1. INTRODUCTION

It has been demonstrated that making cloud height measurements from stereoscopic weather satellite images is a very useful analysis technique with a broad spectrum of applications. Measurements have been made which have added to our understanding of the structure and dynamics of hurricanes and severe local thunderstorms. The heights of satellite cloud winds have been also determined. In Hasler (1981), (1987) stereoscopic observations from meteorological satellites are presented using simultaneous GOES-EAST and GOES-WEST images. It was also demonstrated that the cloud top structure could be determined by stereoscopic measurements with vertical accuracy of approximately 0.5 km. Detailed contours of hurricanes were presented by Rodgers *et al.* (1983) and Hasler and Morris (1986) and of severe thunderstorms (Mack *et al.* 1983). Work by Hasler *et al.* (1983) shows that stereoscopic measurements can be made not only by identical geosynchronous satellites (GEOs), but also by combination of GEOs with Low Earth Orbiters (LEOs). Using their techniques it is possible to observe cloud tops stereoscopically for research studies in most areas of the world. Operational stereo imaging is likely in the near future.

Perhaps the primary obstacle to operational use of stereo measurements has been the lack of an automatic technique to determine cloud heights. Automatic analysis of stereo pairs is now being intensively investigated at many institutions for making of topographical maps from aerial and satellite photographs. The automatic analysis requires a very powerful computer because of the many cross-correlations which must be performed. The advent of parallel architectures such as that of the Massively Parallel Processor (MPP), described by Batcher (1980), has made it possible to apply computationally intensive cross correlation techniques to obtain high resolution results in the detection of local differences between pairs of large images. At Goddard Space Flight Center the MPP was initially used to study automatic analysis of stereo pairs from the Shuttle Imaging Radar B (SIRB). The algorithm developed for this work has been applied to stereo pairs of severe local storms and hurricanes observed by two GOES satellites. The automatically derived height fields have been compared with manual analyses. The automatic analysis produces much more detailed structure in much less time than the manual analysis and is qualitatively the same. However in areas where the features are very small the manual analysis appears to be superior. Quantitative comparisons are given in the following sections.

2. TECHNIQUES

In the stereo technique, two satellites simultaneously scan the same geographical area from different view angles, and the parallax between the two images of an observed feature is proportional to its height. Cloud height becomes a direct measurement based on geometrical relationships and is nearly independent of cloud characteristics. For both the manual and automatic techniques it is critical that one image is remapped into the coordinate system of the other so that feature matching can be done with a minimum of distortion.

2.1 Manual Stereo Analysis

Conventional manual stereo analysis generally involves looking at a stereo image pair through a binocular viewer and measuring the parallax by floating a dot until it appears to touch the terrain surface. At NASA/GSFC analysis tools have been developed to improve the quality of the stereo analysis and the display of combined data sets from various observing systems. The stereo analyses presented in this paper were made using enhancements of techniques developed by Hasler (1981) and reported by Mack *et al.* (1983). All image preprocessing and stereo analysis is performed on the Atmospheric and Oceanographic Information Processing System/2 (AOIPS/2) at GSFC as described by Hasler *et al.* (1986). In addition to normal destriping, and noise removal a "local area enhance" algorithm is used to enhance the contrast for improved feature matching between the two images. The stereo analysis is then done on the enhanced image using image alternation, interpolated zoomed images, and an on-screen graphics display technique described by Mack *et al.* (1983).

2.2 Automatic Stereo Analysis

2.2.1 Background

The advent of parallel architectures such as that of the Massively Parallel Processor (MPP) has made it possible to apply computationally intensive cross correlation techniques to obtain high resolution results from large images in the automatic detection of local differences between pairs of images. For this reason it was necessary to develop an algorithm for the automated analysis of stereo image pairs to determine elevation information, (Strong and Ramapriyan, 1987),

Stereo analysis requires the determination of local displacements in image location between images caused by cloud-top elevation. Local correlation techniques are used to do this job. With local correlation it is necessary to match a reference or template neighborhood in one image with various candidate matching neighborhoods within a search area in the other. Once the relative locations of matching neighborhoods in the two images ("disparity" in stereo analysis) are known, elevation maps can easily be computed. The number of calculations for local correlation operations is proportional to the product of the area of the neighborhoods, the number of candidate neighborhoods, and the number of points in the image where the matching is to be performed (or the required resolution). As will be discussed in later sections, it is required that all pixels in the two images be matched. With images of 512 x 512 pixels, one has on the order of 100 billion calculations. The resulting computation load can be handled in a reasonable amount of time only with very high-speed computers. The massively parallel architecture of the MPP is ideally suited to solving the above problem.

2.2.2 Difficulties in Stereo Matching:

The major difficulties in matching corresponding pixels in the two images are:

a) Different brightness levels in the two images.
b) Local distortions of the image.
c) Low contrast areas and noise.

The first difficulty is often obviated by the use of normalized correlation functions for matching gray level or edge images. The second is inherent in stereo analysis because of the different viewing angles. It occurs most severely in regions of rapidly changing elevation and creates a horizontally stretched or compressed area surrounding corresponding pixels in one image relative to the other. Because of the large off-nadir viewing angles and difference in viewing angles required to achieve reasonable elevation accuracy, this problem is particularly acute in GOES satellite images. Thus, the basic clue used to determine the elevation also makes its determination more difficult.

Any techniques for correcting local distortions must take into account the fact that the distortion function can have a broad band of wave lengths. For example, the distortion function for a large thunderstorm cloud would have low frequencies, but added to these would be high frequencies caused by small scale cloud features making up the surface. When a human observer fuses two images seen through a viewer, the low frequency information is used to obtain an initial fusion in which the eyes are brought into alignment (a technique used for automatic focusing of some cameras) and then high frequency information brings out a detailed perception of depth. The progression from low to high frequency suggests that a hierarchical approach for detecting matching pixels would be appropriate. With this approach, an initial match is performed on low frequency information in an image and then increasingly higher frequencies are incorporated to obtain the final matching of corresponding pixels.

Even with no local distortion, errors can occur due to noise, spatial periodicities and low contrast in the image. One way of reducing errors in general is to provide redundancy by computing matches at nearly every pixel in the image. Then, surface continuity constraints on cloud tops can be used to correct for local elevation discontinuities due to noise. Matching at nearly every pixel is a formidable task on standard serial computers. However, the architecture of the MPP is well suited to the local neighborhood operations required for matching pixels. The following sections discuss the matching technique developed for the MPP and results obtained using the MPP algorithm. To aid in the discussion, one image is labeled the "reference" image and the other the "test" image. All operations are performed on the test image.

The matching algorithm implemented on the MPP is an example of what has been termed the Hierarchical Warp Stereo technique explored initially by Marr and Poggio (1979) and pursued later by Quam (1984). Both techniques are iterative, starting with low resolution and increasing resolution with each iteration. The MPP algorithm consists of the following steps.

a) Preprocessing of the test image,
b) Determination of matches,
c) Removal of "bad match" areas in the disparity function,
d) Smoothing the resulting disparity function,
e) Warping the test image.

The steps b) through e)are repeated for each iteration. The following subsections discuss each of these steps in detail.

2.2.3 Preprocessing of the Test Image:

Because of the viewing geometry, the resolutions of the two GOES images are different in the stereopsis direction. Thus, the test image is remapped into the coordinate system of the reference image as described by Hasler (1981) so that their resolutions are the same.

2.2.4 Determination of Matches:

For each reference image pixel, a match is performed between a neighborhood surrounding that pixel (the "template") and neighborhoods within a search area in the test image. At each iteration of the algorithm the size of all neighborhoods are reduced allowing higher resolution matches at each step. The location of the center pixel within each neighborhood in the test image relative to the location of the reference pixel is the disparity value associated with that neighborhood.

The measure used for matching neighborhoods is the normalized mean and variance correlation given by:

$$Match\ Score(k) = \frac{\sum(x_i - \overline{x}) \times (y_{i-k} - \overline{y_k})}{\sqrt{\sum(x_i - \overline{x})^2} \times \sqrt{\sum(y_{i-k} - \overline{y_k})^2}}$$

Where x_i and y_{i-k} are grey levels of the ith pixels within the template neighborhood and the k-th in the search area respectively. The values $\overline{x}$ and $\overline{y}_k$ are the mean values computed over the template and k-th search area neighborhoods.

For each pixel in the reference image, the match score for all neighborhoods within the search area is computed. The pixel at the center of the neighborhood with the highest correlation value or match score is selected as the matching pixel. The resulting disparity function is, therefore, made up of integer values.

2.2.5 Removal of "Bad Match" areas in the Disparity Function

If it is assumed that cloud top surfaces are continuous when viewed from the positions of the two GOES satellites, the disparity function must also be continuous. Therefore sudden jumps in disparity are assumed to be produced by bad matches. Typically in the algorithm implemented on the MPP, jumps of disparity greater than + or -1 pixel between neighboring pixels are considered to define bad matches. Precipitous cloud edges ar lack of texture would cause this problem.

The human visual system appears to have the capability of interpolating surfaces over areas where bad matches occur. This process is emulated in the MPP algorithm by interpolating the disparity function across all areas where a bad match has been detected. Interpolation is performed using an iterative solution to partial differential equations similar to those used in heat flow problems (with disparities in the place of temperatures). To perform the interpolation, two dimensional partial differential equations are applied to solve for the disparity in the bad match regions. The bordering pixels surrounding the bad match area constitute the boundary values which are held constant.

2.2.6 Smoothing the Resulting Disparity Function

After interpolation, the disparity function is smoothed to obtain a more continuous warping function with fractional pixel values rather than integer values. Smoothing is performed on the MPP by averaging over a neighborhood proportional in size to the neighborhood used to obtain the disparity function.

2.2.7 Warping the Test Image:

The smoothed disparity function is used as a one dimensional distortion function to "geometrically correct" the test image in the stereopsis direction. The warped image values are obtained by resampling the test image using linear interpolation.

2.3 Perspective Display techniques

The perspective techniques used to display the stereo analyses in this paper are described by Hasler *et al.* (1985) and the hardware used to display these images is the AOIPS/2 using the International Imaging Systems (IIS) Corporation #75 terminal (see Hasler *et al.* 1986). The program requires two data arrays: 1) a height field which defines the three dimensional surface to be portrayed and 2) a shading or coloration image which supplies the information to produce the proper texture for the image. The manual stereo contours or MPP disparity image are used as the height field and the corresponding visible image gives the information necessary to produce the shadows and bright areas of the final image. The program combines the two images into a single perspective image. The process of producing the perspective images is also computationally intensive, requiring about 20 min to do a typical 512 X 512 image on a MicroVAX. The perspective program also requires 1) the location from which the array is to be viewed (eye-point) and 2) the location of the point being viewed (view-point). The algorithm then constructs the image of the hurricane as it would be seen from that eye-point looking towards the given view-point.

3. RESULTS

3.1 Comparison of Manual and Automatic Analyses

The automatic stereo analysis has been tested on two types of weather phenomena. For severe thunderstorms, the tornadic thunderstorm cloud tops at 0048 GMT on 3 May 1979 were chosen as a test case. At this time the low sun angle gives excellent contrast to the cloud top features and the automatic analysis was very successful as described below. For hurricanes a low sun angle example of Hurricane Frederic on 12 September 1979 was chosen for analysis. In this hurricane case (not shown here) the automatic analysis produced good results near the over shooting tops in the middle of the central dense overcast. In the cirrus outflow, fairly large areas had so little structure that the automatic cross-correlations failed. However, it was also impossible to make accurate height measurements by manual techniques in these regions.

Fig. 1a. shows a perspective display of manual stereo analysis of tornadic thunderstorm cloud tops at 0048 GMT on 3 May 1979 from GOES East and GOES West images as reported by Hasler (1981) and with a more precise height analysis on AOIPS by Mack *et al.* (1973). A new analysis was made of the tallest towers for this comparison on the new AOIPS/2 system (Hasler *et al.* 1986). The contour interval is 0.5 km with heights ranging from 13.0-17.0 km. A tornado occurred on the ground directly beneath the tallest tower on the right at the time of this image. An analysis of this complexity takes two or three days of careful work by an expert analyst.

In Fig. 1b. the automatic stereo analysis produced in about 20 seconds using the MPP from the same GOES image pair used in Fig. 1a is presented. The MPP height field is artificially illuminated using a standard Laplacian algorithm.

As you can observe the major features are represented by both the manual and automatic analysis. However note the difference in detail between Fig. 1a and 1b. The automatic analysis from the MPP is able to detect much more structure in most locations than the human operator can in a reasonable amount of time. However the expert operator is able to recognize certain single pixel features on top of the tallest towers which are missed by the smoother automatic analysis.

Fig. 1c. presents a perspective display of height field from Fig. 1b combined with the visible GOES image instead of the Laplacian illumination image. Note the additional structure which is apparent from the bright westward- or sun-facing slopes contrasted with the dark shadows on the easterly slopes. Contours at 0.5 km height intervals have also been added.

The problem with making quantitative comparisons between Figs. 1a and 1b is that the MPP analysis shows so much more structure on the sloping surfaces while the manual analysis shows only plateaus. For this reason both the MPP analysis and the manual analysis are presented with the same 1.0 km interval contours as shown in Fig. 2. Again here we see general agreement on the major features. However it is still difficult to compare the details because a slight difference in where the contour falls can make a big difference in the ap-

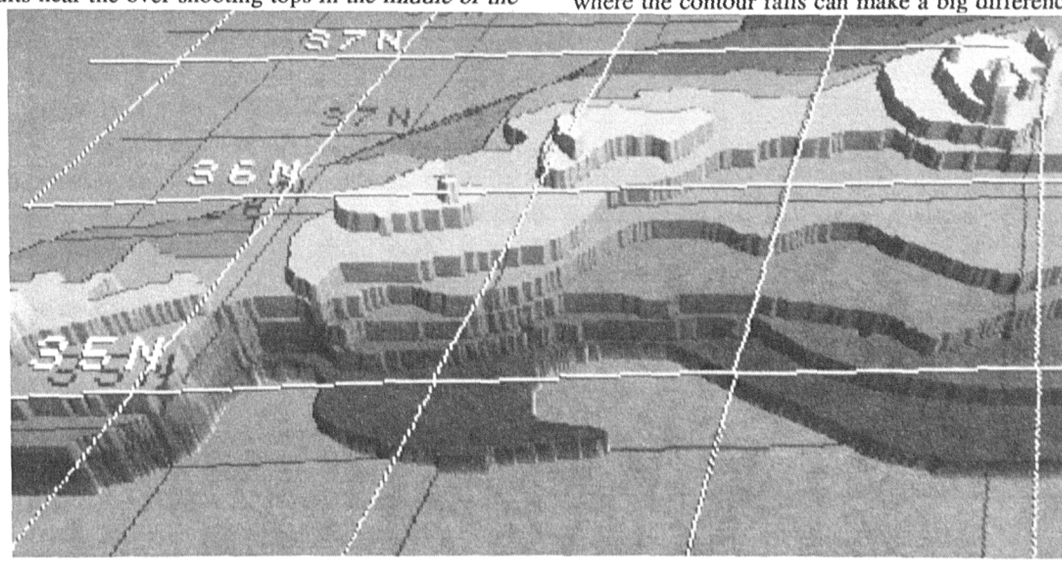

Fig. 1a. Perspective display of manual stereo analysis of tornadic thunderstorm cloud tops from 3 May 1979 from GOES East and GOES West images as reported by Mack *et al.* 1973. The contour interval is 0.5 km with heights ranging from 13.0-17.0 km.

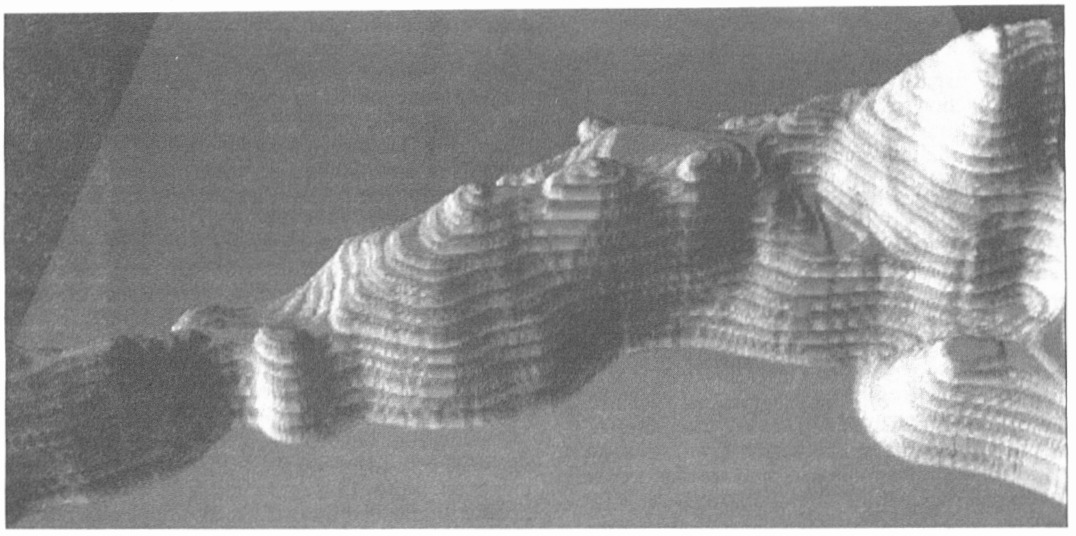

Fig. 1b. Automatic Massive Parallel Processor (MPP) stereo analysis corresponding to Fig. 1a.

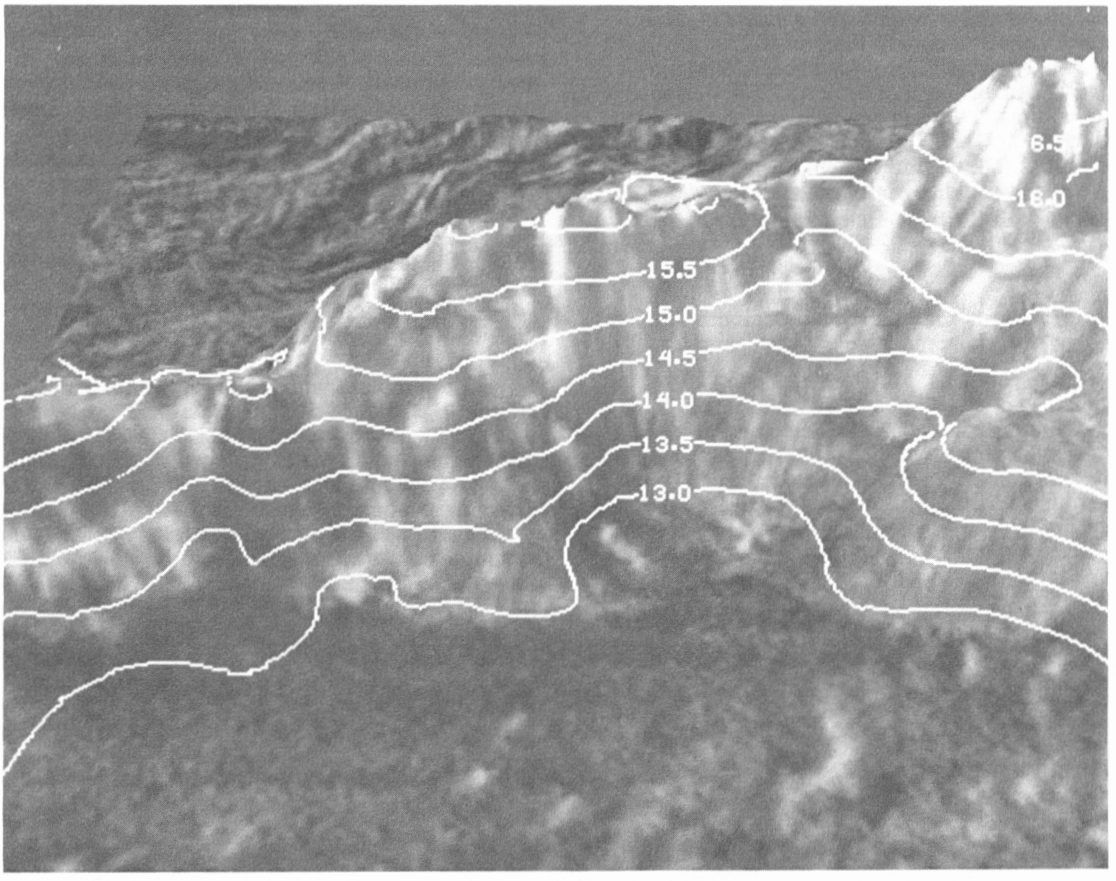

Fig. 1c. Perspective display of height field from Fig. 1b combined with the visible GOES image with 0.5 km interval height contours.

pearance of the plateaus at the 1.0 contour interval. It must also be kept in mind that there is a degree of subjectivity in the manual analysis.

3.2 Comparison of Automatic Analysis with Original Stereo Pairs

There are two methods of testing the accuracy of the automatic analysis by comparison with the original data. The first is to warp the test image using the disparity function (as describe in section 2.2.7) and compare it with the reference image. In other words you would warp the GOES West image to match the GOES East image using the MPP derived parallax or height field. Any horizontal displacements observed while alternating these images indicate errors in the stereo analysis. The second is to compare the original stereo pair viewed in binocular stereo with the computed stereo pair (test image and warped test image). These pairs appear to the operator as three dimensional surfaces and errors in the automatic analysis appear as differences in height.

By these methods of testing it is easy to detect areas

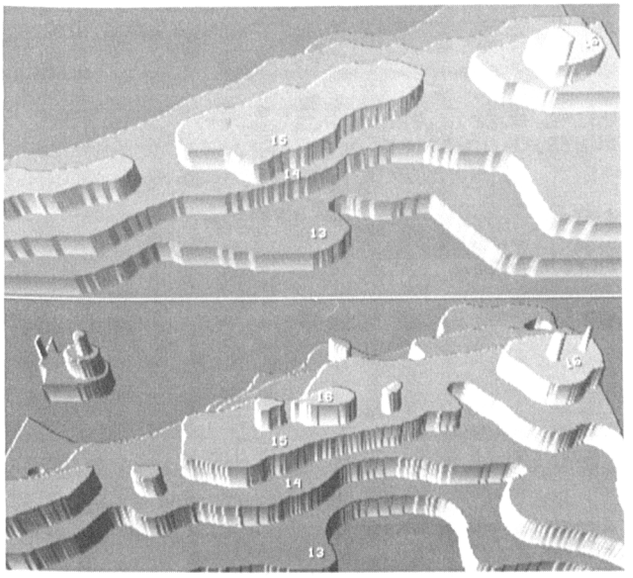

Fig. 2 Comparison of manual & automatic stereo analyses. 3 May 1979 tornadic thunderstorm case from Fig. 1. displayed with 1.0 km contour interval. The top image (2a) is the manual analysis while the bottom image (2b) is derived from the MPP automatic stereo analysis.

where the automatic analysis has failed. This method of quality control indicates that the automatic stereo is very accurate in the parts of the image where well defined structure exists. Furthermore, the stereo pairs derived from the automatic analysis give a much more dramatic three dimensional impression than the original pairs. This is due to the wide angular separation of the two satellites which makes fusion of the stereo pair more difficult.

4. CONCLUSIONS AND FUTURE WORK

It has been demonstrated that stereo measurement of cloud height can be accomplished automatically. Severe thunderstorm and hurricane cloud top topography have been automatically analyzed. using a prototype super computer with the novel Massively Parallel Processing (MPP) architecture. The automatic analysis is of equivalent quality to, and much more detailed than manual analyses while taking several orders of magnitude less time. A typical 512 X 512 pixel image is processed in 20 sec by the MPP. In the future powerful, but small and economical, workstations such as the PIXAR developed by Lucas Films will be used to do this kind of analysis. Stereo height measurements are possible in regions with sufficiently high contrast features in the large overlap regions between the operational geosynchronous satellites (Hasler *et al.* 1983) Under large solar elevations (low contrast) or featureless cirrus regions the automatic techniques will probably fail and manual techniques become less accurate. However, the most important over shooting towers which indicate intense convection below are easily detected and measured using the stereo technique.

With the capability of routine stereo imaging which should be available in the GOES NEXT time frame and the automatic processing demonstrated in this paper, the major impediments to operational stereo cloud height measurement will have been removed. It is proposed to demonstrate real-time stereo using the GOES data ingest system being developed for AOIPS/2 at Goddard and a PIXAR type workstation.

5. ACKNOWLEDGEMENTS

The assistance of Lafayette Long with the photographic processing and lay-up of this paper is greatly appreciated.

6. REFERENCES

Batcher, K. E., 1980: Design of a Massively Parallel Processor. *IEEE Transactions on computers,* pp. 836-840.

Hasler, A. F., 1981: Stereographic observations from satellites: An important new tool for the atmospheric sciences. *Bull. Amer. Meteor. Soc.*, **62,** 194-212.

———, R. Mack, and A. Negri 1983: Stereoscopic observations from meteorological satellites, *Adv. Space Res.* **2**, No.6, pp. 105-113, 1983, Pergamon Press.

———, H. Pierce and J. Dodge 1985: Meteorological data fields "in perspective". *Bull, Amer. Meteor. Soc.* **66,** pp. 795-801.

———, A. J. Negri, and T. S. Piper, 1986: AOIPS/2: An interactive system to analyze and display integrated remotely sensed and in situ meteorological data sets. *Second International Conference on Interactive Information and Processing Systems for Meteorology Oceanography, and Hydrology*, Jan. 14-17. 1986 Miami Florida. AMS. Boston Mass.

———, and K. R. Morris, 1986: Hurricane structure and wind fields from stereoscopic and infrared satellite observations and radar data. *J. Climate Appl. Meteor.*, 25, 709-727.

———, 1987: Stereo measurements. *Silver Anniversary Book on Weather Satellites*, Section VII-4, NOAA. (in press)

Mack, R. A., A. F. Hasler, and R. F. Adler 1983: Thunderstorm cloud top observations using satellite stereoscopy, *Mon. Wea. Rev.*, **111**, 1949-1964.

Marr, D. and Poggio, T. 1979: A Computational Theory of Human Stereo Vision ,.*Proceedings, Royal Society of London,* , pp. 301-328.

Quam, L. 1984: "Heirarchical Warp Stereo", *Proceedings, Image Understanding Workshop*, pp. 149-155.

Rodgers, E., R. Mack, and A. F. Hasler 1983: A satellite stereoscopic technique to estimate tropical cyclone intensity, *Mon. Wea. Rev.*, **111**, pp. 1599-1610.

Strong, J. P. and H. K. Ramapriyan 1987: Massively Parallel Correlation Techniques to Determine Local Differences. *Proceedings 2nd International Conference on Supercomputing,* June 1987, Santa Barbara CA, International Supercomputer Institute.

FORECASTING CYCLOGENESIS USING GOES WATER VAPOR SATELLITE IMAGERY AND NUMERICAL MODELS

LeRoy E. Spayd Jr.
Forecast Branch
National Meteorological Center
NWS/NOAA
Camp Springs, Maryland

1. INTRODUCTION

This paper presents a signature in GOES water vapor imagery which is used operationally by meteorologists and oceanographers to modify numerical model forecasts in areas of surface cyclogenesis. Errors in objective predictions of surface cyclogenesis have major impacts to surface wind and wave conditions. GOES water vapor images are available on a half-hourly basis to National Weather Service meteorologists via communication lines to hardcopy machines or to a video display on the new SWIS (Satellite Weather Information System) computer. By subjectively interpreting areas of relative darkening or warming and the movement of these areas on successive images, the synoptic scale atmospheric dynamic patterns can be inferred and related to surface cyclogenesis.

2. GOES 6.7 um WATER VAPOR IMAGERY

The GOES 6.7 um channel is sensitive to absorption by atmospheric airborne water vapor. Smith (1983) states that the vertical profile of the sensitivity of the 6.7 um channel peaks approximately at 400mb according to theoretical studies. Weldon (1986) compared extensively digital water vapor data to atmospheric radiosonde profiles. Weldon concluded that both the thermal and water vapor vertical profile of the atmosphere is critical in determining the radiance values the 6.7 um channel observes. Areas with large amounts of water vapor aloft in the form of aerosols or condensed into clouds will be sensed and appear as cold temperatures and white shades on the 6.7 um imagery. In areas of rapid subsidence aloft the air is warmed and dried and the 6.7 um channel senses moisture at a lower level and warmer temperature in the atmosphere. This appears as a warm temperature and a dark shade on the water vapor image. Therefore by observing consecutive water vapor images with respect to an atmospheric circulation system, darkening with time can directly be related to subsidence aloft. The rate of warming with time is an indicator of the intensity and the change of intensity of the subsidence.

Weldon (1979) states that the developing dry slot region during cyclogenesis is an area of vertically deep subsidence. Figure 1 shows Weldon's schematics of cyclogenesis as seen in infrared satellite images. Note the surge region becomes the dry slot as cyclogenesis occurs and the comma cloud develops. According to Weldon the strongest surface pressure falls occur as the dry slot surges east then north of the developing surface low or as the dry slot curves just north of the tip of the comma head on the water vapor images.

3. OCEANIC CYCLOGENESIS

On 10 May 1987 surface cyclogenesis occurred near forty degrees north latitude and sixty one degrees west longitude southeast of Cape Cod, Mass. The synoptic situation consisted of a strong polar vortex in northern Canada and a strong zonal westerly jet across southern Canada. A short wave trof was embedded in this jet and progressed south of Hudson's Bay and into eastern Canada. A lingering slow moving trof just offshore of the mid-atlantic states was forced eastward by the short wave and stronger flow in southeastern Canada. The twelve hour surface pressure and 1000-500 mb thickness forecasts of the Nested Grid Model (NGM), Limited Fine Mesh (LFM), and Medium Range Forecast (MRF) numerical models valid for 1200 GMT 10 May 1987 are shown in figure 2. Note that all

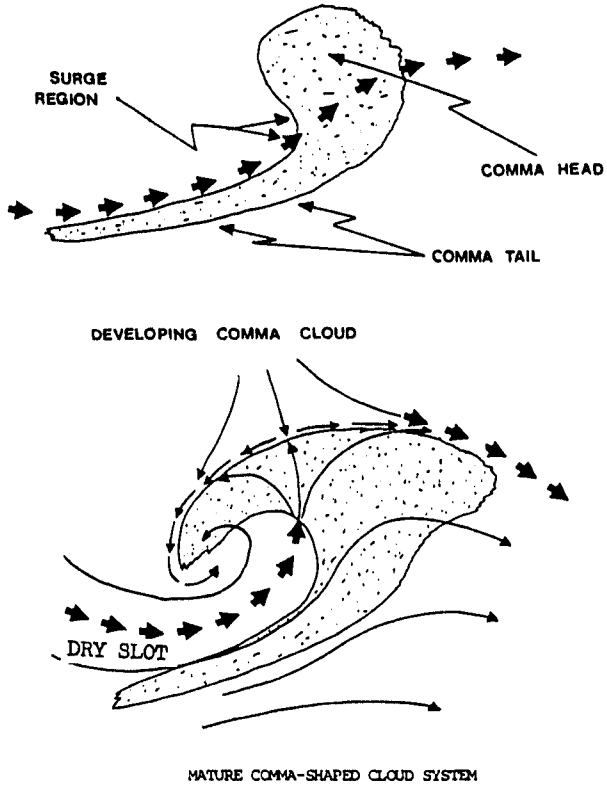

Figure 1. Schematic of cloud top patterns of cyclogenesis from infrared satellite images (Weldon 1979).

three models forecast a pressure trof just east of sixty degrees longitude and the MRF forecasts a 1007 mb surface low near coordinates 43 N and 61 W.

GOES water vapor images at 0200 GMT and 1000 GMT 10 May 1987 are shown in figure 3. The most prominent feature on the images is the large dark area extending from the southeastern United States eastward into the western Atlantic. The letter (A) points to the eastern extent of this dark area as it darkens with time and forms the developing dry slot as cyclogenesis occurs. Although the numerical models were not indicating cyclogenesis this developing dry slot as seen on the water vapor images was interpreted by the operational meteorologists at the National Meteorological Center (NMC) of the NWS as a clear signature that cyclogenesis was occurring. They subsequently made modifications to the surface sea level pressure analysis and forecasts. The official NMC 1200 GMT North American surface analysis chart in figure 4 shows a 1000 mb occluded low based on this satellite signature. A late reporting ship from just south of this low reported a 1001 mb pressure and a ten knot westerly wind confirming the intensity of the analyzed signature. The visible image at 1230 GMT clearly shows the comma cloud and the pronounced

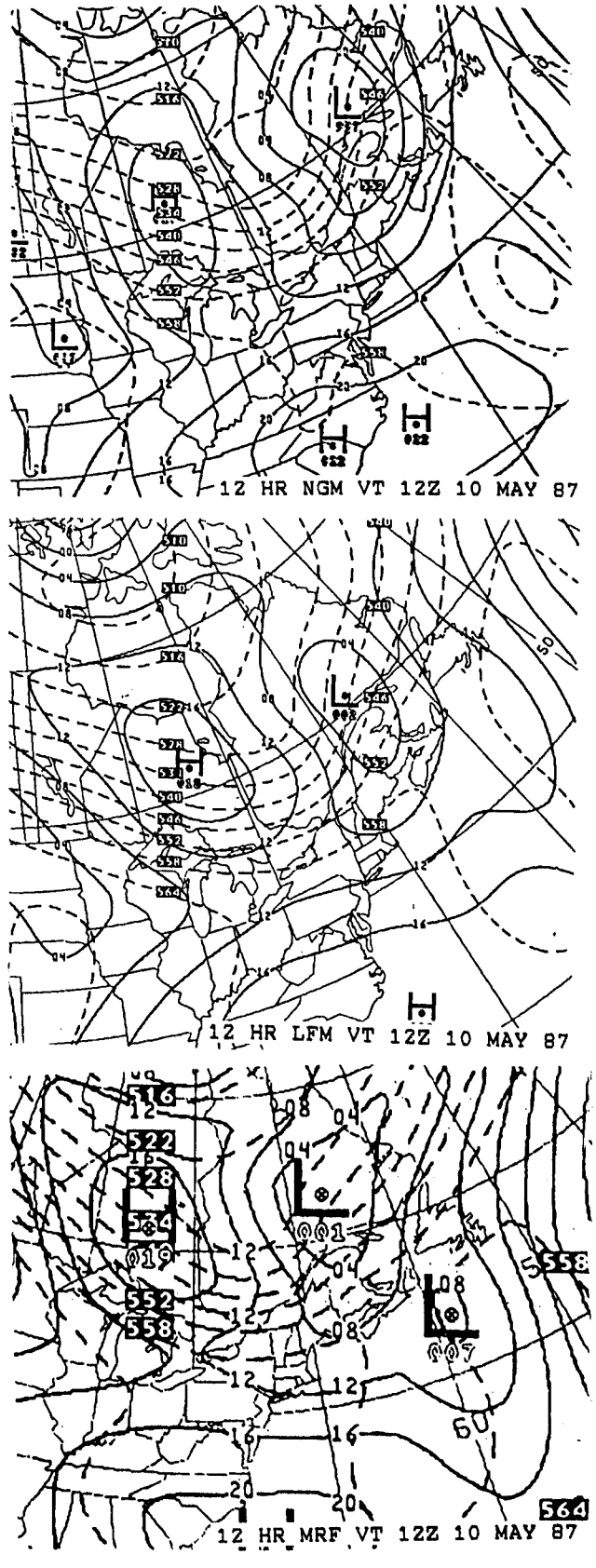

Figure 2. NGM, LFM, and MRF 12 hour surface pressure and 1000-500 mb thickness forecast for 1200 GMT 10 May 1987.

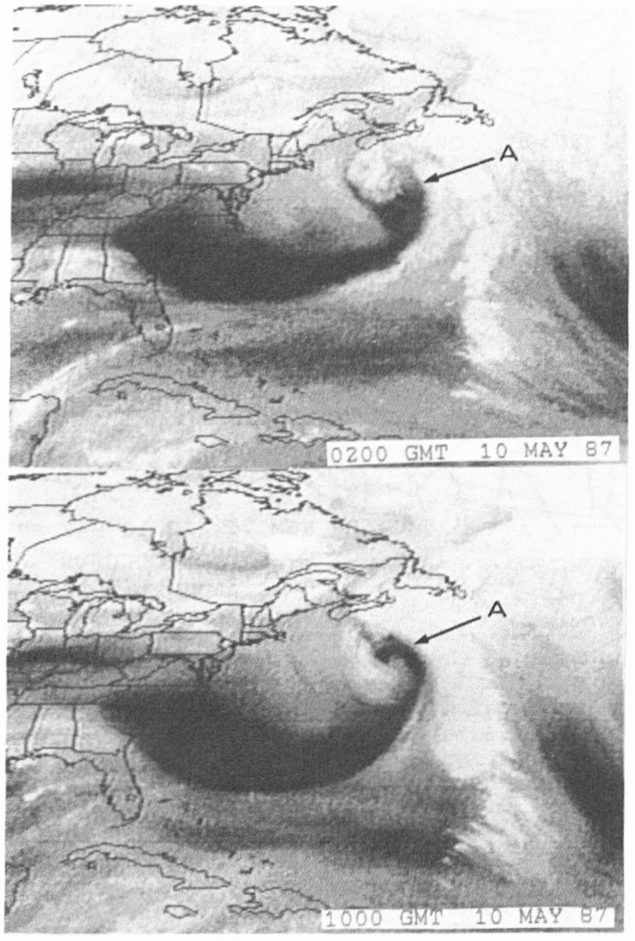

Figure 3. GOES water vapor images at 0200 and 1000 GMT 10 May 1987. The letter A points to the developing dry slot region which darkens with time on the images.

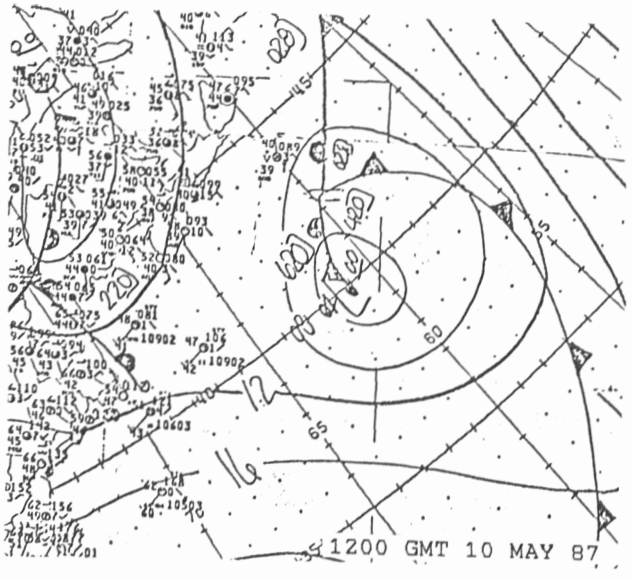

Figure 4. NMC surface analysis at 1200 GMT 10 May 1987.

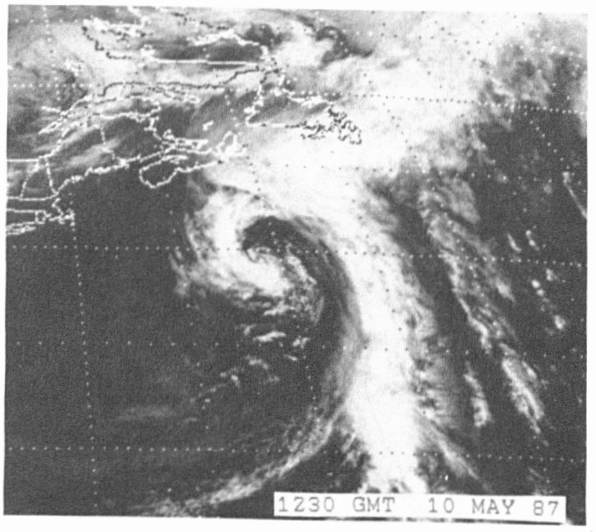

Figure 5. Visible satellite image at 1230 GMT 10 May 1987.

dry slot (Figure 5). Both the LFM and MRF were approximately 11 mb too high with the NGM nearly 15 mb too high at the center of the low on their 12 hour forecast.

4. CYCLOGENESIS IN SOUTHERN CANADA

On 27 April 1987 cyclogenesis occurred in southern Canada between Lake Superior and Hudson's Bay. A sharp short wave trof dropped southeastwards over a strong upper level ridge in western Canada into the upper level longwave trof position along the east coast. Both the NGM and LFM models forecasted cyclogenesis with this trof. The twelve hour forecasts of the LFM and NGM models verifying at 1200 GMT on 27 April 1987 is shown in figure 6. The model twelve hour forecasts are very consistent with each other in both the magnitude and placement of the surface low with the NGM and LFM forecasting 1007 and 1008 mb pressures respectively.

A sequence of water vapor images at 2330, 0530, and 1130 GMT on 26-27 April 87 is shown on figure 7. The developing comma cloud appears as a white shade on the water vapor images. The letter (B) points to the dark dry slot that darkens with time between 2330 and 0530 GMT. Note how the dry slot spirals into the comma cloud at 1130 GMT indicating a mature cyclone according to Weldon (1979). The most rapid surface pressure falls occurred as the dry slot spiraled around the east to the north of the surface low pressure center. A visible image at 1230 GMT (Figure 8) shows a classic comma cloud with a cloud circulation center which was coincident with the surface pressure center. The NMC surface analysis at 1200 GMT 27 April 87 indicates the surface low was analysed as a 1002 mb center (Figure 9).

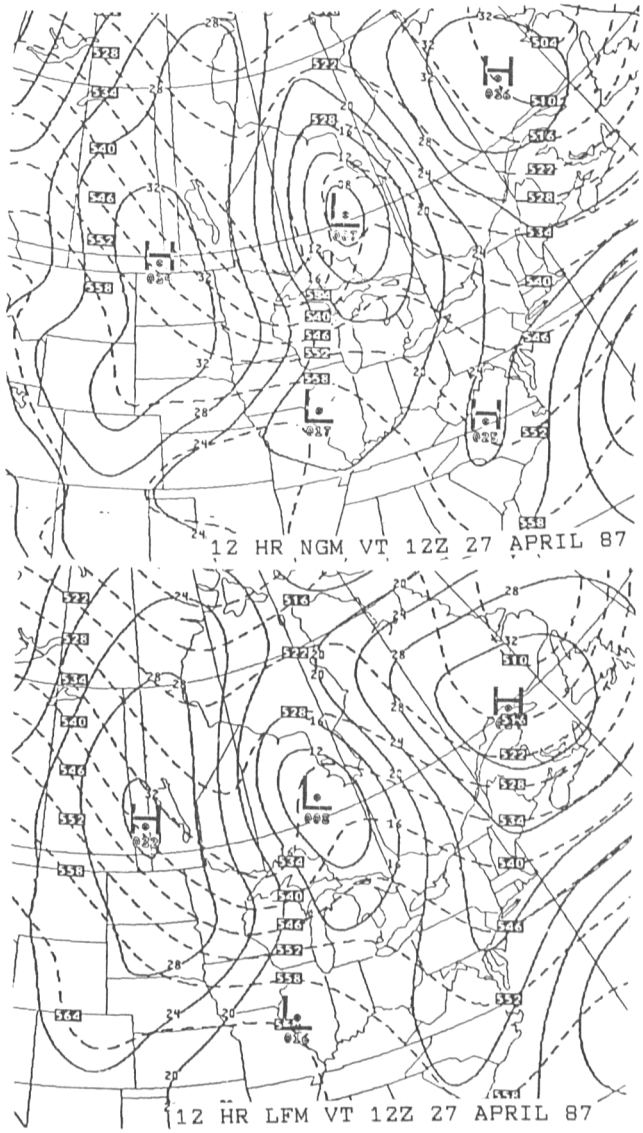

Figure 6. NGM and LFM 12 hour surface pressure and 1000-500 mb thickness forecast for 1200 GMT 27 April 87.

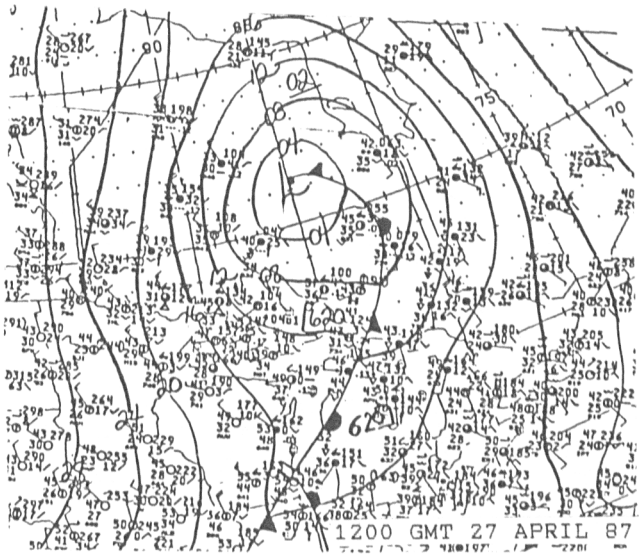

Figure 9. NMC surface analysis at 1200 GMT 27 April 1987.

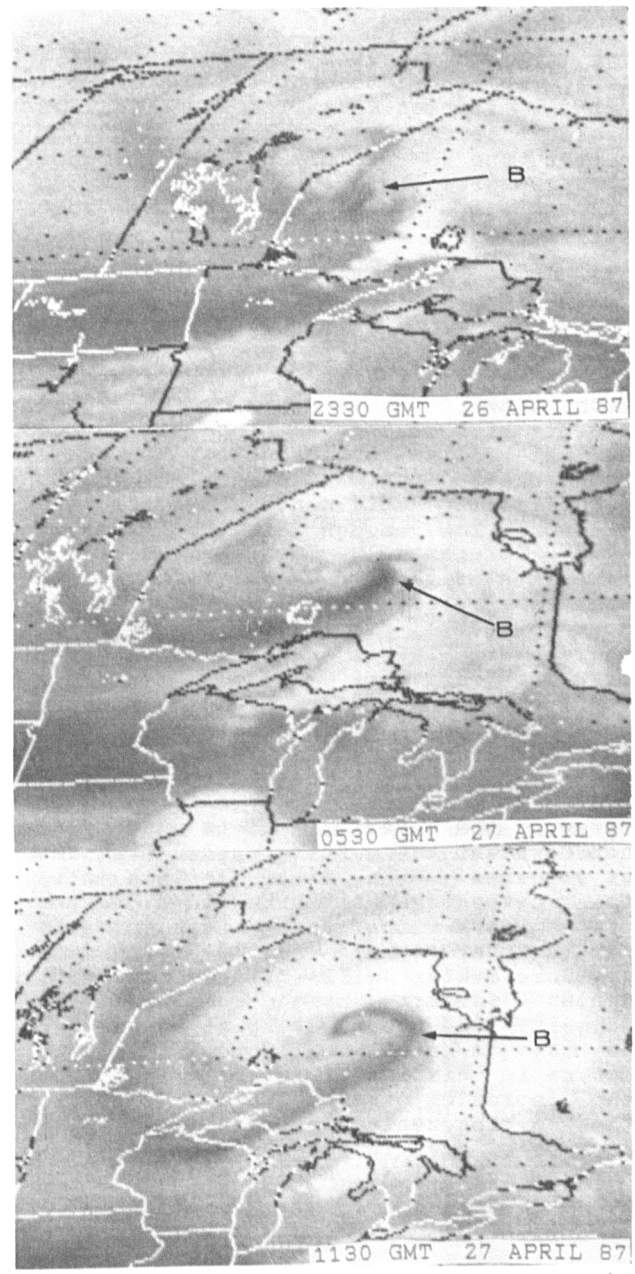

Figure 7. GOES water vapor images at 2330, 0530, and 1130 GMT 26-27 April 87. The letter B points to the developing dry slot region.

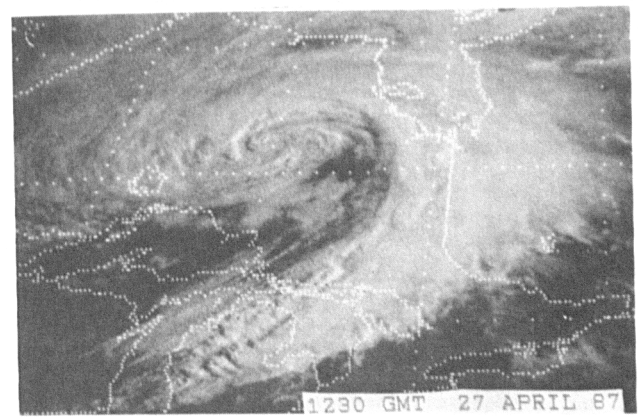

Figure 8. Visible satellite image at 1230 GMT 27 April 1987.

The nearest reporting observation was a 1004.7 mb report to the west of the low with a fifteen knot wind and a falling pressure tendency. Using the 1002 mb center the NGM and LFM did not forecast the pressures low enough by 5 and 6 mb respectively on their twelve hour forecasts.

5. CONCLUSION

This paper showed how darkening with time in the water vapor imagery of the dry slot of a developing cyclone can be related to cyclogenesis. In these two cases the numerical models significantly did not forecast the pressures low enough on their twelve hour forecasts. Twenty four hour forecasts of the models verifying at the same time verified worse than the twelve hour forecasts. In the two cases shown there were larger errors as expected over the "data poor" oceanic areas as compared to the "data rich" continent. This darkening with time of the dry slot in the water vapor images is not observed with all deepening surface pressure systems. However when it is observed the numerical models usually do not forecast the surface pressure as low as observed. When meteorologists note this darkening with time and extension of the dark zone into the dry slot region they should assume the surface pressure center will deepen and will deepen faster than model forecasts suggest. One possible explaination may be that a small scale tropopause fold occurs in this intense sinking zone and the intrusion of stratospheric air into the cyclogenesis process is not accounted for in the numerical models. Further investigation is needed however to substantiate this hypothesis.

6. REFERENCES

Smith, W. L., 1983: The Retrieval of Atmospheric Profiles from VAS Geostationary Radiance Observations. Journal of Atmospheric Sciences, Vol. 40, No. 8, 2025-2035.

Weldon, R.W., 1979: Part IV, cloud patterns and the upper air wind field. In-house publication: Satellite Training Course, Applications Laboratory, NESS, Wash. D.C.

Weldon, R.W., 1986: Unpublished set of Department of Defense Training notes and personal communications.

TROPOPAUSE ADJUSTMENT TO TROPICAL CYCLONES AS INFERRED FROM SATELLITE OZONE OBSERVATIONS

Edward B. Rodgers
Laboratory for Atmospheres
NASA/Goddard Space Flight Center
Greenbelt, MD 20771

John Stout and Joseph Steranka
General Sciences Corporation
Laurel, MD 20707

Simon Chang
Naval Research Laboratory
Department of the Navy
Washington, DC 20375

1. INTRODUCTION

With the advent of the Nimbus-7-flown Total Ozone Mapping Spectrometer (TOMS), it is now possible to map the distribution of the vertically integrated total ozone within and surrounding tropical cyclones. The TOMS data may help to improve the understanding of: (1) how the lower stratosphere and upper troposphere cause or respond to tropical cyclone structure changes and (2) why mature tropical cyclones intensify.

The purpose of this work is to: (1) use a tropical cyclone numerical model to interpret these total ozone patterns and (2) develop climatological total ozone maps to diagnose storm intensity and to differentiate intensifying from weakening tropical cyclones.

2. NIMBUS-7 TOMS

TOMS, which was flown on Nimbus-7 and launched in October 1978 into a sun-synchronous polar orbit, uses six wavelengths from 312.5 to 380.0 nm to separate the effects of ozone absorptions, molecular scattering, and surface (including cloud) reflection. From these wavelengths, total ozone in a column is determined from TOMS data to within 2% relative to ground-based observations (Shapiro et al., 1982). Total ozone is corrected in cloudy regions assuming a climatological profile of ozone mixing ratio below the cloud top and a climatological estimation of cloud-top height.

The TOMS instantaneous-field-of-view at the Earth's surface is at nadir a circle with a diameter of 50 km and at 50 degrees of nadir an ellipse whose minor and major axes are approximately 75 and 150 km, respectively. Since the sensor uses the backscatter ultraviolet radiation and because TOMS is onboard a polar-orbiting satellite, total ozone observations are obtained only at local noon. Additional information about Nimbus-7 TOMS and the TOMS total ozone algorithm can be found in the Nimbus-7 User Guide (Nimbus Project, 1975) and in the TOMS User Guide (Fleig et al., 1982), respectively.

3. THE INTERPRETATION OF THE TOTAL OZONE DISTRIBUTION

Based on the premises that stratospheric air is rich in both potential vorticity and ozone (Danielsen, 1968) and that the tropospause can be defined both statistically and in the local synoptic sense by a fixed potential vorticity value (~1.0 x 10^{-5} km^2 Kg^{-1} s^{-1}) from the pole to 5 degrees latitude (Reed and Danielsen, 1959), upper-tropospheric/lower-stratospheric potential vorticity patterns simulated for a tropical cyclone will be used to interpret the TOMS-observed total ozone patterns associated with a tropical cyclone. A tropical cyclone (central pressure ~ 984 mb) was simulated by initiating the limited-area, three-dimensional hydrostatic primitive equation Naval Research Laboratory (NRL) tropical cyclone model (Chang and Madala, 1980) with a 20 m s^{-1} cyclonic vortex and sea-surface temperatures (SST's) of 302.5 K and integrating the model for 96 h. Figure 1 shows the potential vorticity in isobaric coordinates (2 x 10^{-6} s^{-1} mb^{-1} interval) and total wind (vector length proportion to strength) at the 150-mb level (i.e., V_{max} ~ 34 m s^{-1}). The shaded area depicts negative values of potential vorticity and the region with the longest vectors depicts the outflow jet. Points of interest are: (1) the elliptical donut-shaped area of negative potential vorticity that appears on the anticyclonic side of the outflow jet; (2) a narrow region of high potential vorticity on the cyclonic side of the jet; and (3) the high potential vorticity associated with the cyclonic circulation that is found within the center of the system. A cross-sectional analysis (r-z plane perpendicular to the outflow jet axis) showed that the secondary circulation associated with the outflow jet contributed to the strong gradients in potential vorticity found along the jet axis (figure not shown). For example, in the entrance region of the jet (north and east of the center), it was found that the greatest potential vorticity was associated with the descending branch of the thermally direct circulation on the cyclonic side of the outflow jet while the least amount of potential vorticity was found with the ascending branch of the direct circulation of the outflow jet. This analysis suggests that ozone-rich stratospheric (ozone-poor tropospheric) air is intruding into the upper troposphere (lower stratosphere) on

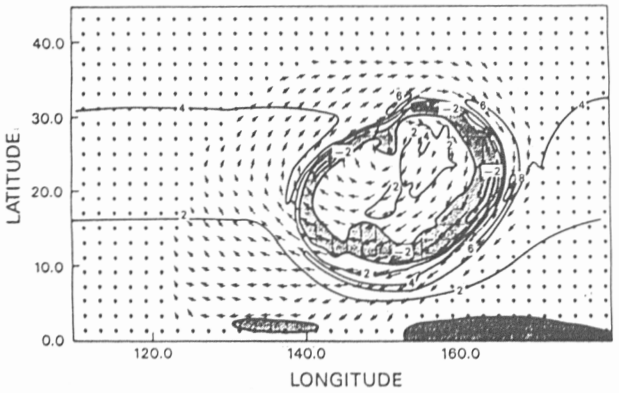

Fig. 1. *Plan view of the simulated 150-mb winds (vector length proportioned to strength) and potential vorticity (2×10^{-6} s^{-1} mb^{-1} interval) for a tropical cyclone (P_{min} ~ 984 mb) that was generated from the NRL tropical model. Integration time is 96 h. Shaded area is negative potential vorticity.*

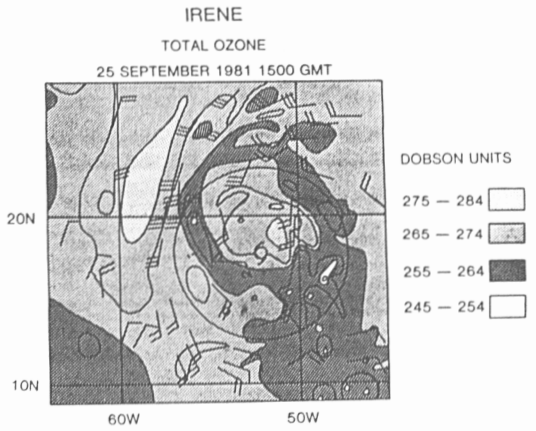

Fig. 2. *Nimbus-7 TOMS-measured total ozone (DU) and the satellite-derived winds ($m\ s^{-1}$) at the cirrus level for hurricane Irene (P_{min} ~ 979 mb) ~ 1500 GMT 25 September 1981. Hurricane symbol locates Irene's center.*

the cyclonic (anticyclonic) side of the entrance region of the jet. However, in the jet maximum region where the secondary circulation is minimum and in the exit region of the jet where the thermally indirect secondary circulation was opposite to what was found in the entrance region, but considerably weaker, potential vorticity was mainly distributed by horizontal transport from the entrance region of the jet.

To compare the simulated 150-mb level potential vorticity patterns with observed total ozone, Fig. 2 is shown. The figure shows the TOMS-measured total ozone for tropical cyclone Irene at ~1500 GMT 25 September 1981 together with the cirrus-level satellite-derived winds ($m\ s^{-1}$). At the time of the observation, Irene's central pressure of ~979 mb was 5 mb less than the simulated tropical cyclone. By comparing the two figures, it is observed that the TOMS-measured total ozone pattern and the simulated potential vorticity patterns are quite similar. For example, the region of ozone-rich air near the center of Irene and within the cyclonic side of the outflow jet (particularly in the entrance region found northwest of the center along 20 degrees latitude) corresponds, respectively, to the region of high potential vorticity found at the center of the simulated tropical cyclone and on the cyclonic side of the simulated tropical cyclone outflow jet. Also, the elliptical donut-shaped region of low total ozone corresponds to the elliptical donut-shaped region of low potential vorticity found on the anticyclonic side of the simulated tropical cyclone outflow jet. Thus, the total ozone/potential vorticity relationship observed with the entrance region of the tropical cyclone outflow jet is similar to what was found by Sechrist et al. (1986) in the entrance region of a polar jet. Also, the total ozone/potential vorticity relationship observed near the tropical cyclone center suggests that stratospheric air is intruding into the storm's inner circulation.

The strong total ozone/potential vorticity relationship found within the tropical cyclone system cannot be verified outside Irene's circulation due to the limitations of the NRL tropical cyclone model. However, the maximum total ozone found in the trough west of Irene (delineated by the cyclonic shear) can best be explained using the concepts developed by Reed (1955). In that paper, he suggested that the distribution of ozone comes from the influence of advection and vertical motion at the tropopause level, since ozone may be considered a passive tracer at that level. Thus, in the case of the trough west of Irene, the accumulation of ozone-rich air in the base of the trough was most likely caused by the combination of advection of air from higher latitudes where the ozone is more abundant and subsidence of ozone-rich stratospheric air in the descending branch of the direct circulation located in the entrance region of the outflow jet. From these results, it appears that the concepts developed by Reed (1955) relating the distribution of total ozone to the upper-tropospheric/tropopause heights of the higher latitudes can also be applied to the tropical cyclone and its subtropical environment.

This relationship is encouraging, since TOMS data will greatly improve the analysis of the storms' upper-tropospheric/tropopause topography as compared to other satellite infrared/microwave profiling methods. This is based on the following reasons. First, the TOMS measurements are less affected by cloud cover than infrared methods and, second, TOMS will be able to resolve better the small horizontal gradients of heights usually found with tropical upper-tropospheric troughs (TUTT's), since TOMS total ozone values are related closely to tropopause height rather than a thickness layer. TOMS also will be able to better delineate subtropical and the tropical cyclone outflow jets, since the transverse circulation associated with these jets produces strong gradients in the total ozone distribution.

4. TROPICAL CYCLONE TOTAL OZONE CLIMATOLOGY

Because of the advantages of using TOMS data, climatological total ozone maps were developed in order to diagnose storm intensity and to aid in differentiating intensifying tropical cyclones from weakening tropical cyclones. To produce these maps, TOMS-measured total ozone anomalies (TOA's) were used (e.g., difference between the observed and the daily time mean total ozone) rather than total ozone in order to avoid the longitudinal, and especially the latitudinal, seasonal gradients. The TOA were than sampled and composited by placing the center of the tropical cyclone at the center of the stereographic horizon map projection (Shenk et al., 1971) and rotating the tropical cyclones so that the direction of motion of each storm was at a common azimuth. The stereographic horizon map projection extended out to 2222 km from the tropical cyclone center.

The name and observation time of the western Atlantic tropical cyclones used for this climatological study are seen in Table 1.

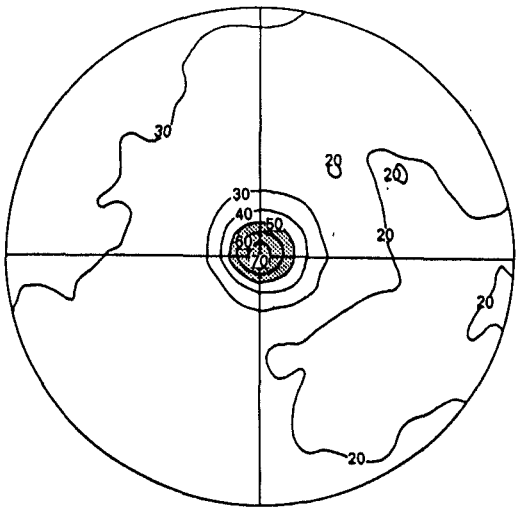

Fig. 3. *Mean Nimbus-7 TOMS-measured reflectivity (10% interval) for 80 western Atlantic tropical cyclone observations (see Table 1). Shaded area has reflectivity > 50%. Outer radius is 2222km. The storm's motion is toward the top of the page.*

TABLE 1

1979		1980	
DAVID	26-28 AND 30 AUGUST	ALLEN	2-8 AUGUST
FREDERIC	31 AUGUST-3 SEPTEMBER	BONNIE	14-18 AUGUST
	11 AND 12 SEPTEMBER	EARL	5-8 SEPTEMBER
GLORIA	6-13 SEPTEMBER	FRANCES	7-17 SEPTEMBER
1981		**1982**	
DENNIS	8-10 AUGUST	BERYL	29 AUGUST-2 SEPTEMBER
EMILY	1-3 SEPTEMBER	DEBBY	14-16 SEPTEMBER
FLOYD	5-10 SEPTEMBER		
GERT	8-12 SEPTEMBER		
HARVEY	13-16 SEPTEMBER		
IRENE	23-28 SEPTEMBER		

The total sample consisted of 80 total ozone observations of 15 named tropical cyclones during the period from 1979-1982. To eliminate the effects that cold SST and landfall have on tropical cyclone intensity and intensity change, only tropical cyclones located over open-ocean regions at latitudes no greater than 35°N and occurring only in the months of July-September were chosen.

4.1 Mean Tropical Cyclone TOA Distribution

From this sample, a mean cloud reflectivity and TOA maps were generated from the TOMS and are shown in Figs. 3 and 4, respectively. The shaded region of high reflectivity (above 50%) observed near the center of the grid and extending ~333 km radius from the center (Fig. 3) are the cloudy regions associated with the averaged tropical cyclones' central dense overcast (CDO) (Hwang et al., 1987).

All storms in this sample were moving toward the top of the figure.

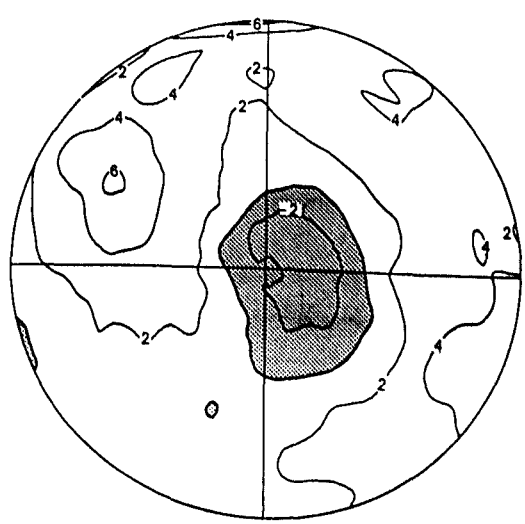

Fig. 4. *Same as Fig. 3 except the figure contains the mean Nimbus-7 TOMS-measured TOA (2 DU interval) for 80 western Atlantic tropical cyclone observations (see Table 1). Shaded areas have negative TOA.*

The mean TOA map (Fig. 4) for the same storms depicts a region of minimum TOA at ~555 km to the right of the storms' CDO with maximum TOA outside the radius of ~1111 km from the center of the grid in the forward-left quadrant and the rear-right quadrant. By assuming the relationship between tropopause height and total ozone discussed earlier, the mean TOA pattern suggests that the region of low total ozone delineates the area of high tropopause associated with the transverse circulation of the outflow jet, while the regions of high total ozone delineate the area of low tropopause associated with the upper-tropospheric troughs. The results from the NRL tropical cyclone model also suggest that the transverse circulation of the outflow jet should produce strong gradients in the total ozone. Examining Fig. 4, it is seen that the large TOA gradients within ~555 km of the center in the forward-left quadrant may delineate the mean location of the entrance region of the outflow jet. Finally, the region of slightly larger values of total ozone over the center of tropical cyclone Irene (Fig. 2) also appears to be a common feature of these tropical cyclones.

4.2 Tropical Cyclone Intensity vs. TOA Distribution

To examine the effects of intensity on the ozone distribution, tropical cyclones were stratified into two intensity groups. The first group contained depressions and tropical storms ($V_{max} < 32$ m s^{-1}), while the second group contained hurricanes ($V_{max} \geq 32$ m s^{-1}). The TOA maps for the two groups are seen in Figs. 5 and 6, respectively. The main difference between the two TOA patterns is that the more intense systems have: (1) greater total ozone in a region within 1111 km to the left of the center of the grid, (2) stronger TOA gradients within 555 km of the center in the forward-left quadrant, and (3) larger TOA over the center. The greater TOA left of the center that has been suggested to be associated with the upper-tropospheric troughs and the stronger TOA gradients in the forward-left quadrant that appear to be associated with the stronger transverse circulation found in the entrance region of the outflow jet suggest that stronger systems have greater mutual adjustment between the storm and its upper-tropospheric environment. Storms that come into juxtaposition with upper-tropospheric troughs and enhance their outflow jet through down-gradient acceleration appear to be more intense. Also, the larger values of TOA found over the CDO of intense storms suggest that stratospheric intrusion is more prevalent for stronger systems.

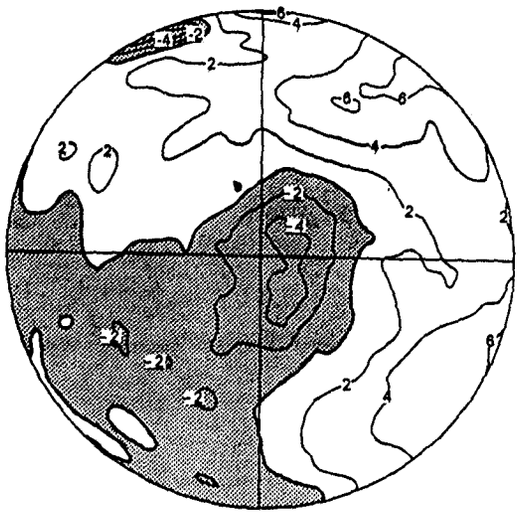

Fig. 5. *Same as Fig. 3 except the figure contains the mean Nimbus-7 TOMS-measured TOA (2 DU interval) for the western Atlantic tropical cyclones (see Table 1) that were less than hurricane strength. Shaded areas have negative TOA.*

Fig. 6. *Same as Fig. 5 except for tropical cyclones of hurricane strength.*

4.3 TOA Distribution vs. Tropical Cyclone Intensity Change

Considering the hypothesis that intensity changes in mature tropical cyclones located over open oceans with SST > 26°C are linked to upper-tropospheric forcing by means of the outflow channel (Holland and Merrill, 1984; Chen and Gray, 1984) and that the upper-tropospheric circulation associated with the tropical cyclone and its environment can be delineated from the total ozone distribution, TOA's were examined for the potential to differentiate intensifying tropical cyclones from weakening ones. From the original TOA sample, tropical cyclones were stratified into intensifying systems (e.g., > 2.5 m s^{-1} in 12 h during observation time) and weakening systems (e.g., < 0.0 m s^{-1} in 12 h during observation time). The average intensity and intensity change for the non-intensifying and intensifying composites are, respectively, 32.3 m s^{-1} - 1.2 m s^{-1}/12h and 31.9 m s^{-1} + 4.6 m s^{-1}/12h. The TOA maps for non-intensifying and intensifying tropical cyclones are seen in Figs. 7 and 8, respectively. Figure 9 shows the difference between the two TOA maps (i.e., Fig. 8 - Fig. 7). It can be seen from these figures that intensifying tropical cyclones have the following TOA characteristics: (1) the maximum TOA in the forward-left quadrant are closer to the storms' center, (2) TOA gradients within 555 km from the center in the forward-left quadrant are stronger, (3) TOA outside 555 km to the right of the center are lower, and (4) TOA within the center of the storms are slightly higher. The TOA maps, therefore, for at least these cases, showed that intensifying tropical cyclones: (1) are closer to upper-tropospheric troughs; (2) have stronger outflow jets and, therefore, stronger transverse circulation and TOA gradients in the forward-left quadrant and lower TOA right of the center; and (3) have greater stratospheric intrusion near the center.

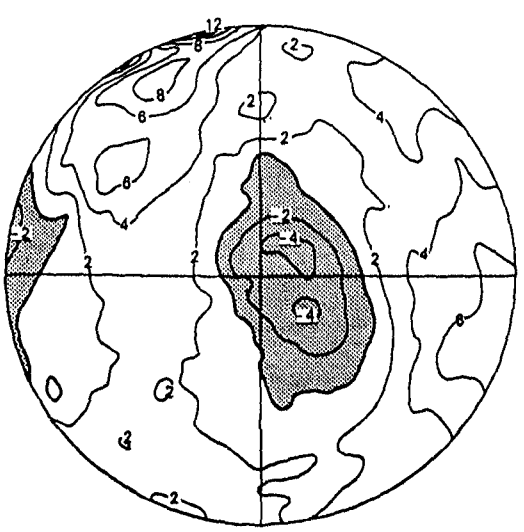

Fig. 7. *Same as Fig. 5 except for non-intensifying tropical cyclones.*

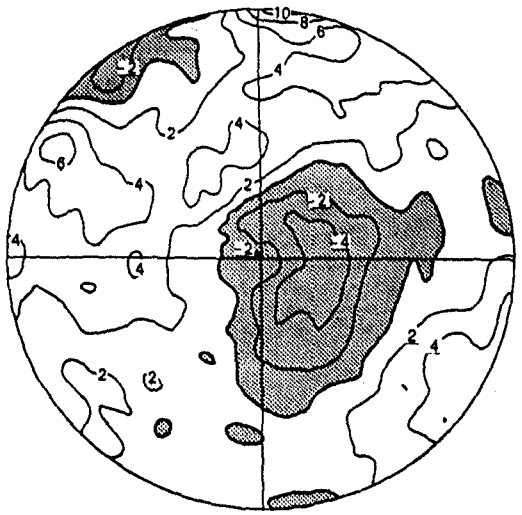

Fig. 8. *Same as Fig. 5 except for intensifying tropical cyclones.*

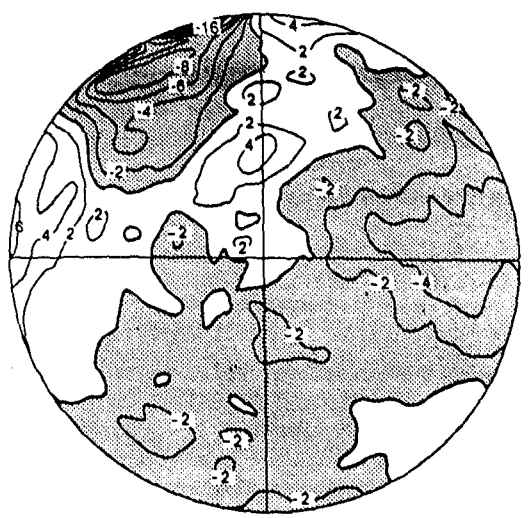

Fig. 9. *Difference in the mean Nimbus-7 TOMS-measured TOA (2 DU interval) between intensifying and non-intensifying tropical cyclones. Shaded areas have negative TOA.*

5. CONCLUSIONS

The TOMS-measured total ozone may present important information concerning the mutual adjustment between a tropical cyclone and its upper-tropospheric environment. This information may lead to a better understanding of the upper-tropospheric forcing that causes tropical cyclone intensity changes. The tropical cyclone numerical model simulations demonstrate that the total ozone distribution within a tropical cyclone is mainly dictated by the strong transverse circulation associated with the outflow jet. The wind and total ozone data confirmed Reed's (1955) study showing that the distribution of total ozone can best be explained by the three-dimensional transport near the tropopause. Because of these relationships and the advantages of using TOMS, total ozone data was composited within and surrounding tropical cyclones to diagnose storm intensity and to differentiate intensifying from non-intensifying systems. The composited maps showed that more intense systems had greater ozone intrusion within the center and stronger total ozone gradients within the entrance region of the jet, which implies a stronger transverse circulation and, therefore, a stronger outflow jet. Intensifying systems showed greater total ozone nearer to the center in the forward-left quadrant. This implies a closer positioning of the upper-tropospheric trough with the tropical cyclone.

6. REFERENCES

Chang, S. W., and R. V. Madalla, 1980: Numerical simulation of the influence of sea surface temperature on translating tropical cyclones. J. Atmos. Sci., 37, 2617-2630.

Chen, L., and W. M. Gray, 1984: Global view of the upper level outflow patterns associated with tropical cyclone intensity changes during FGGE. Preprints, 15th Conf. on Hurricanes and Tropical Meteorology, Amer. Meteor. Soc., 238-242.

Danielsen, E. F., 1968: Stratoshperic-tropospheric exchange based on radioactivity, ozone, and potential vorticity. J. Atmos. Sci., 25, 502-518.

Fleig, A. J., K. F. Klenk, P. K. Bhartia, and D. Gordon, 1982: User's guide for the Total Ozone Mapping Spectrometer (TOMS) instrument first year ozone-T data set. NASA Ref. Pub. 1096, 50 pp.

Holland, G. L., and R. T. Merrill, 1984: On the dynamics of tropical cyclone structure change. Quart. J. Roy. Meteor. Soc., 110, 722-745.

Hwang, P. H., L. L. Stowe, and H. Y. M. Yeh, 1987: An overview of the Nimbus-7 global cloud climatology data archive. Bull. Amer. Meteor. Soc. (accepted).

Nimbus Project, 1978: Nimbus-7 User Guide. Nimbus Project, National Space Science Data Center, Goddard Space Flight Center, Greenbelt, MD 20771, 263 pp.

Reed, R. J., 1955: A study of a characteristic type of upper-level frontogenesis. J. Meteor., 12, 226-237.

_____, and E. F. Danielsen, 1959: Fronts in the vicinity of the tropopause. Arch. Meteor. Geophys. Bioklim., A11, 1-11.

Sechrist, F. S., R. A. Petersen, K. F. Brill, A. J. Krueger, and L. W. Uccellini, 1987: Ozone, jet streaks and severe weather. Preprints, 2nd Conf. on Satellite Meteorology/Remote Sensing and Applications, Amer. Meteor. Soc., 388-392.

Shapiro, M. A., A. J. Krueger, and P. J. Kennedy, 1982: Nowcasting. K. A. Browning, Ed., Academic Press, London, 256 pp.

Shenk, W. E., H. Powell, V. V. Salomonson, and W. R. Bandeen, 1971: Meteorological uses of the stereographic horizon map projection. J. Appl. Meteor., 110, 582-589.

5.12

RELATIONS BETWEEN WATER VAPOR IMAGERY, VERTICAL MOTION, AND TROPOPAUSE FOLDS

Steven R. Moore
Henry E. Fuelberg

Department of Meteorology
Florida State University
Tallahassee, FL 32306

1. INTRODUCTION

Water vapor imagery has been available from geostationary satellites for nearly ten years. The 6.7 μm channel reflects the distribution of middle tropospheric water vapor where dark shades customarily represent warm brightness temperatures, i.e., dry conditions, and light shades represent moist areas. Past studies have employed water vapor imagery to diagnose winds and circulation patterns, enhance water vapor analyses, infer jet stream dynamics, and investigate tropopause folds. This paper examines the atmospheric processes associated with the movement and further development of a pronounced dry feature in a series of 6.7 μm images on 6-7 March 1982. It is an extension of work by Stewart and Fuelberg (1986).

2. METEOROLOGICAL CONDITIONS

Figure 1 presents surface analyses, 500 mb heights and temperatures, and 300 mb isotachs subjectively analyzed from radiosonde data. At the surface (left column) at 0000 GMT 6 March 1982, a stationary front extended from the lower Rio Grande River Valley through the Gulf of Mexico and Southeast States into the Atlantic Ocean. Several weak low pressure waves were located along this front. A moderate area of high pressure was centered over Nebraska, and a secondary cold front stretched along the Canadian border. By 0000 GMT 7 March, the stationary front remained over the Southeast, extending into the Gulf of Mexico as a cold front. The secondary cold front advanced southward into Kansas. The high centered over Nebraska at the inital time moved south and diminished, while another anticyclone followed the secondary front.

Middle tropospheric (500 mb) analyses (Fig. 1, center column) at 0000 GMT 6 March show a longwave trough extending from the Desert Southwest northeastward into the western Great Lakes. The trough propagated into the Southcentral States during the period, extending from Texas to Manitoba at the final time when a longwave ridge was evident over the West Coast. Two weak shortwaves were embedded in the trough at 0000 GMT 6 March. The one located over Oklahoma, just east of the base, intensified slightly while moving slowly downstream. The second shortwave initially was over Arizona, slightly upstream of the trough axis, but then moved into the base and amplified considerably. A shortwave ridge located over Idaho at 0000 GMT 6 March amplified and moved southeastward during the next 12 h; however, by 0000 GMT 7 March, it was near the longwave trough and smaller in amplitude.

Middle tropospheric temperature patterns at 0000 GMT 6 March (Fig. 1, center column) include a baroclinic zone over the Desert Southwest and a cold dome over the central Great Plains and Intermountain States. By 0000 GMT 7 March, the baroclinic zone had intensified to 16°C/ 5°Lat., both narrowing in width and increasing in length, and stretching from southwest Texas to Arkansas. As the cold dome moved southeastward, it diminished in area and exhibited warming, thereby suggesting subsidence.

At 300 mb on 0000 GMT 6 March (Fig. 1, right column), the axis of the polar jet stream extended from the Pacific Northwest through the Desert Southwest and Southcentral States into the Ohio River Valley. The axis sharpened during the study period, and by 0000 GMT 7 March stretched from the Pacific Northwest southeastward to the lower Rio Grande River Valley, then northward into the Midwest. Two jet streaks were embedded in the polar axis. One remained quasi-stationary over the Ohio River Valley, having a peak value of 81 m/s. The other, centered over the Desert Southwest at 0000 GMT 6 March, propagated to southern Texas by 0000 GMT 7 March. Its greatest speed was approximately 67 m/s. A subtropical jet stream was evident at 200 mb (not shown). It generally was parallel to, but somewhat south of its polar counterpart.

Water vapor (6.7 μm) imagery for the study period is presented in schematic form in Fig. 2. Patterns indicate that a pre-existing "dark band" and a developing "dark band" combined into one large image feature by the end of the period. Specifically, at 0000 GMT 6 March, a dark band of relatively warm brightness temperatures stretched from the Pacific Northwest into the Desert Southwest, with darkest shades over the California-Nevada border. This apparent center propagated at a nearly constant speed of 18 m/s and will be denoted as the "advective band".

Development of a new dark (warm) feature and enhancement of the older advective band are both apparent at 1200 GMT 6 March (Fig. 2). The advective component now over Nevada and Arizona had darkened, partly attributable to the decreasing zenith angle, i. e., the so-

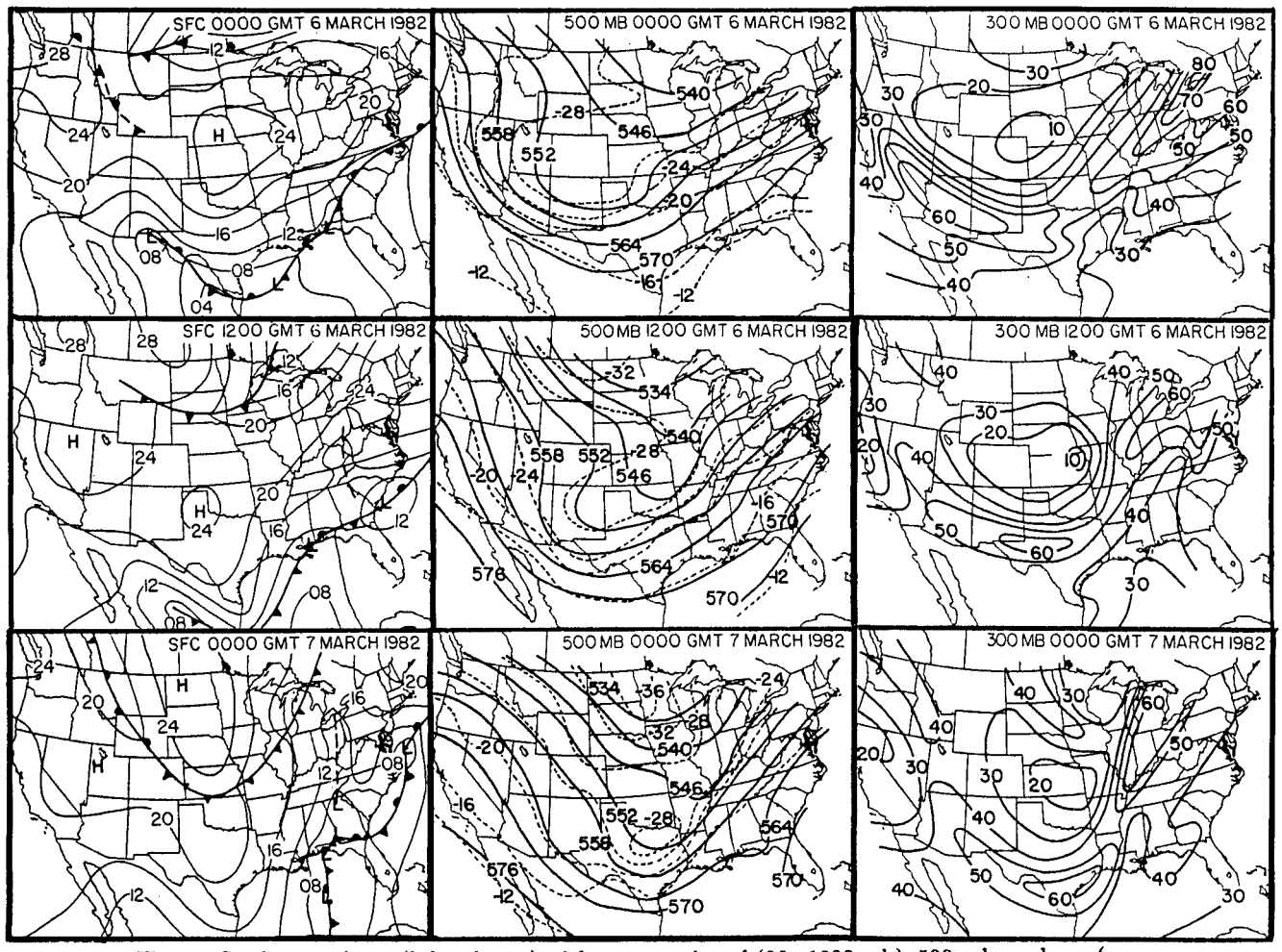

Fig. 1. Surface analyses (left column) with pressure in mb(20=1020 mb), 500 mb analyses (center column) with heights (540=5540 gpm, thick solid) and temperatures in °C (dashed), and isotachs at 300 mb in m/s (right column).

called "limb effect". In addition, a new area, the "development band", extended from Kansas through Iowa into Wisconsin, with a less distinct band bisecting Oklahoma. These features over the Great Plains were only faintly evident 12 h earlier.

The advective and development sections combined into one large, dark feature by 0000 GMT 7 March, although both preceeding components were still distinguishable. The development portion darkened (warmed) to the shade of the advective section, extending from central Texas, northeastward into Illinois. The advective section over southern New Mexico and western Texas did not change its appearance.

3. RESULTS

Before considering the processes responsible for 6.7 μm image features, we examined moisture patterns to confirm their role in creating the observed imagery. Radiosonde-derived dew point analyses at 500 mb (not shown) support the accepted relation that the images primarily reflect middle tropospheric water vapor distributions. Time sections (not shown) constructed to diagnose vertical and temporal humidity structures also support this conclusion.

To facilitate the calculation of other parameters, radiosonde data at the surface and every 50 mb from

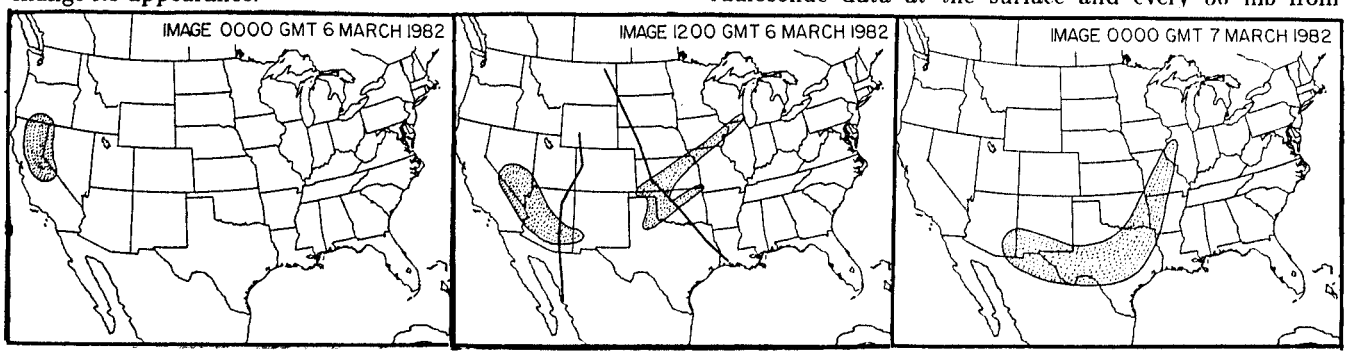

Fig. 2. Schematics of 6.7 μm warm, dark image features. Axes of cross sections in Fig. 6 at 1200 GMT 6 March are shown in center.

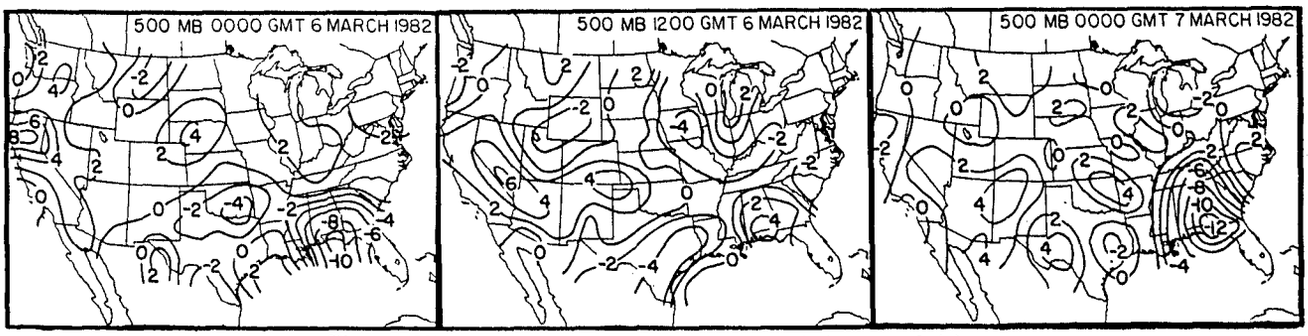

Fig. 3. Kinematic vertical motion at 500 mb (2=2.0 μb/s).

900 mb to 50 mb were objectively analyzed using the Barnes (1973) procedure. The response function was selected to retain a conservative 50 percent of the amplitude of 800 km wavelengths (twice the data spacing). Divergence (not shown) was computed using centered finite differences, and kinematic vertical motions computed therefrom were adjusted to zero at 100 mb based on the O'Brien (1970) method. The vertical motion patterns shown at 500 mb (Fig. 3) are similar to those at other levels.

Concerning the advective component of the image, the large area of subsidence (8.8 μb/s, Fig. 3) over northern California at 0000 GMT 6 March coincides with the darkest region (Fig. 2). This subsidence is associated with the entrance region of the polar jet streak (Fig. 1). Both the center of subsidence (6.3 μb/s) and the image feature propagate to Nevada and Arizona by 1200 GMT 6 March, and two centers of descending motion are associated with the dark band at 0000 GMT 7 March. The one over New Mexico (5.6 μb/s) is associated with the polar jet, while the other, over west Texas (4.9 μb/s), appears to result from confluence north of the polar jet.

The development section of the image (Fig. 2) also is associated with subsidence (Fig. 3). At 0000 GMT 6 March, there is descent (4.2 μb/s) over Nebraska, where the development component is only faintly detectable. This subsidence is located between the shortwave ridge and trough discussed in Section 2 (Fig. 1). The descent strengthens to 5.0 μb/s at 1200 GMT 6 March while translating to the southwestern edge of the image feature (i.e., southeastern Colorado). Both the image band and its associated subsidence are over the Ozark Plateau at 0000 GMT 7 March. The descent over southwestern Texas may also contribute to formation of the development band.

To summarize, the isobaric analyses relate both the advective and development components of the dark image feature to subsidence. Isentropic analyses are the most advantageous way to confirm and examine in greater detail the processes at work in producing the image patterns.

An isentropic data set was created from the isobaric version using a transformation procedure similar to that outlined in Reiter (1972). Isentropic levels were at 2 K intervals from 270 to 424 K. Potential absolute vorticity (PAV) was used to diagnose tropopause folding (i.e., air of recent stratospheric origin in middle and upper tropospheric fronts). PAV is the product of absolute vorticity (AV) and static stability (SS) on isentropic surfaces. Shapiro (1976) stated that PAV greater than 10×10^{-6} K/(mb s) represents stratospheric conditions. Thus, a tropopause fold is denoted by these values being extended into the mid-troposphere (i.e., approximately 500 mb).

Figure 4 contains pressures of the National Weather Service (NWS) reported tropopause based on the standard definition involving temperature lapse rate. Also shown are pressures of the 304 K surface where PAV indicates stratospheric values. Other surfaces that were examined exhibited patterns similar to those on 304 K. At 0000 GMT 6 March, the axis of stratospheric PAV is oriented northeast-southwest, which, as expected, is coincident with the axis of the cold dome (Fig. 1). Stratospheric PAV corresponds to both the cold dome and baroclinic zone through the remainder of the period. One should especially note the correspondence between PAV and the development section of the image band over the Great Plains (Fig. 2).

The pressure distribution of stratospheric PAV on 304 K at the first time (Fig. 4) indicates that stratospheric values reaching approximately 350 mb still are near

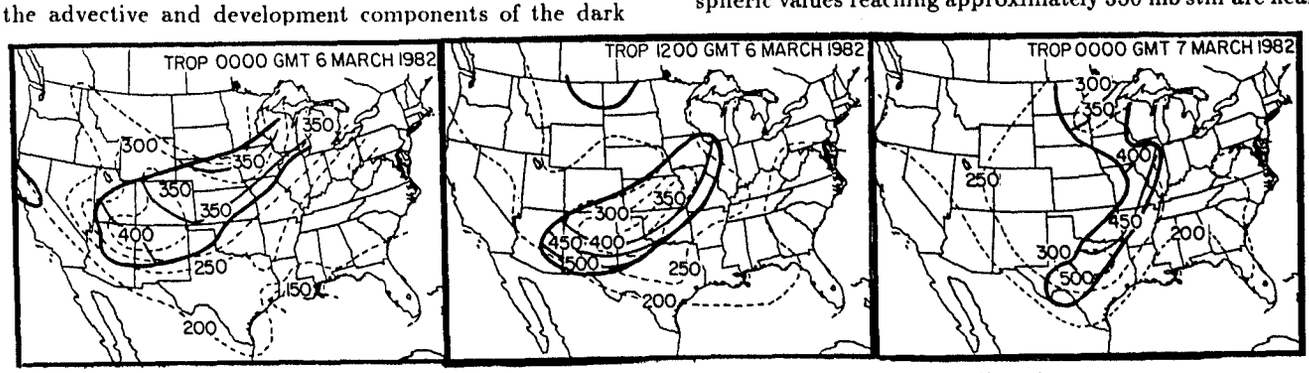

Fig. 4. Tropopauses reported by the National Weather Service in mb (dashed) and pressure topography (mb, thin solid) of the 304 K surface within the 10×10^{-6} K/(mb s) isoline of potential absolute vorticity (heavy solid).

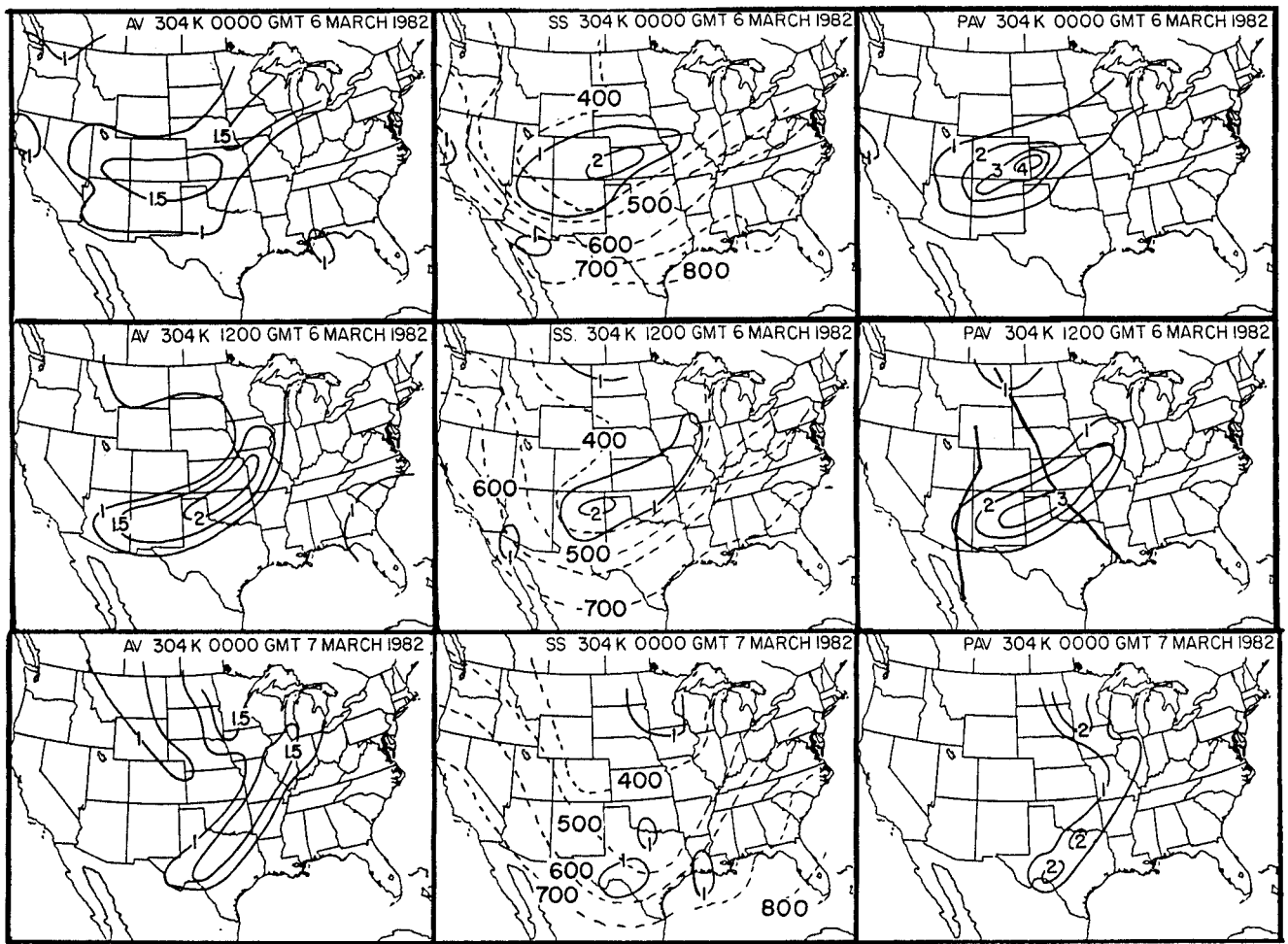

Fig. 5. Isentropic analyses on 304 K of absolute vorticity (AV, left column, $1.5 = 1.5 \times 10^{-4} s^{-1}$), static stability (SS, center, $2 = 20 \times 10^{-2}$ K/(mb)), and potential absolute vorticity (PAV, right column, $1 = 10 \times 10^{-6}$K/(mb s)). Pressures of the 304 K surface are given in the center panels as dashed lines. Axes of cross sections in Fig. 6 at 1200 GMT 6 March are shown in right column.

the traditionally reported tropopause level (350 mb). The only exception is the extreme southern section of the enclosed region where the 430 mb PAV altitude is lower than that of the standard tropopause. An evolution over the southern region is apparent by 1200 GMT 6 March, when stratospheric values now extending to 500 mb are well below the standard tropopause (250 mb). On the other hand, values over the northern portion of the enclosure still are near the standard tropopause (360 mb). At 0000 GMT 7 March, stratospheric PAV continues to reach beyond 500 mb, extending at least 100 mb below the NWS tropopause. It is important to note that this delineation of the tropopause fold extending from Texas northeastward to Illinois is coincident with the dark, dry band of the 6.7 μm image (Fig. 2). The implication of Fig. 4 is that air now in the troposphere is of recent stratospheric origin, and should have the stratospheric properties of large PAV, high ozone concentration and low water vapor content (Danielsen, 1968).

Magnitudes of PAV on 304 K (Fig. 5, right column) were observed to steadily diminish through the 24 h period. This decrease is due to a reduction in static stability (Fig. 5, center column) coupled with near constant absolute vorticity (Fig. 5, left column). A decrease in SS should be offset by increasing AV (Uccellini *et al.*, 1985). In our case, however, the response function of the objective analysis may be partly responsible for the constant, not increasing, AV. Specifically, observed horizontal wind gradients strengthened during the period, whereas the analyzed versions sometimes were not increased to the values observed. Unfortunately, the response function could not be altered to better resolve these gradients without introducing noise into the remainder of the analyses. Uccellini *et al.* (1985) also noted that analysis deficiencies may produce non-conservative PAV, and it has been observed below the level of maximum wind in frontal zones (Gidel and Shapiro, 1979), and resulting from diabatic processes (Staley, 1960).

Figure 6 contains cross sections through the advective and development components of the image. The cross section through the advective feature at 1200 GMT 6 March is similar to those at other times. The extension of stratospheric PAV penetrates to 520 mb between Winslow (INW) and Tuscon (TUS), Arizona, signifying a tropopause fold that is coincident with the image (Fig. 2). The conventional NWS tropopause is located near 200 mb (Fig. 4) over this region.

Cross sections through the development feature at 0000 GMT 6 March (not shown) indicate a zone of

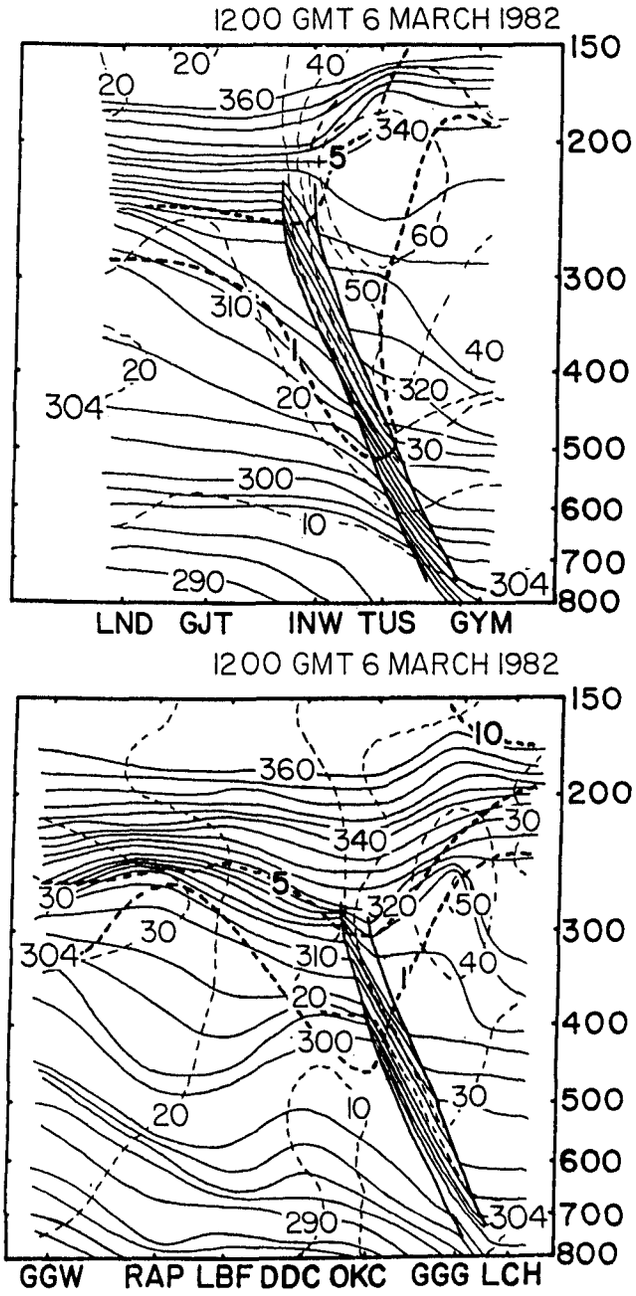

Fig. 6. Cross sections through the advective (top) and development (bottom) image bands of potential temperature (K, solid), wind speed (m/s, thin dashed) and potential absolute vorticity (1 = 10×10^{-6} K/(mb s), thick dashed) for 1200 GMT 6 March.

enhanced horizontal wind shear, but no strong temperature gradient. Stratospheric PAV exhibits only a slight depression in the shear zone, remaining above 400 mb. By 1200 GMT 6 March (Fig. 6), on the other hand, the tropopause folding process is well underway over Oklahoma City (OKC), Oklahoma, near the development section of the image band. Strong temperature gradients and wind shear are both quite apparent between OKC and Longview (GGG), Texas, producing an extension of stratospheric PAV down to 470 mb. The fold is fully developed at 0000 GMT 7 March (not shown), and is coincident with the development image band.

Ozone measurements have been related to tropopause folding in several previous studies (e.g., Danielsen, 1968). Uccellini *et al.* (1985) noted that TOMS (Total Ozone Mapping Spectrometer) data can be useful "in that maximum ozone concentrations indicate a relatively thick stratosphere and correspondingly thinner troposphere." At 1700 GMT 6 March (Fig. 7), the TOMS data indicate a deep stratosphere over northeastern Texas (410 Dobson Units), with the axis of maximum concentration extending from Texas northeastward to Illinois. It is significant that this location is coincident with the area of stratospheric PAV on the 304 K surface (Fig. 4) and the development image component (Fig. 2) between 1200 GMT 6 March and 0000 GMT 7 March. This is further evidence of a tropopause fold over the central United States.

To obtain a three-dimensional representation of processes responsible for the image feature, isentropic backward trajectories were constructed using the implicit technique of Danielsen (1961). Figure 8 presents a sample of trajectories for both the advective and development image bands on the 304 K surface.

The trajectories terminating in the advective image feature were constructed between 1200 GMT 6 March and 0000 GMT 6 March. Figure 8 indicates that air ending over central Arizona at 544 mb originated near Ely, Nevada at 412 mb. This descent of 132 mb over 12 h corresponds to an average vertical motion of 3.1 μb/s. Results for other trajectories in the advective band are similar. These parcels conserve their potential absolute vorticity, having values characteristic of tropospheric air.

Similar to results just described, backward trajectories between 0000 GMT 7 March and 1200 GMT 6 March (Fig. 8) reveal considerable descent near the development image band. For example, air at 447 mb near Monett, Missouri, at 0000 GMT 7 March originated 12 h earlier at 370 mb near Dodge City, Kansas. Corresponding subsidence also is evident in other nearby trajectories. Although PAV is not conserved, decreasing from 16 to 11×10^{-6} K/(mb s), stratospheric values are maintained (i.e., $\geq 10 \times 10^{-6}$ K/(mb s). It should be noted that nonconservation of PAV is not unusual and has been encountered by many investigators (e.g., Danielsen, 1968). In the current work, it may result from the objective analysis

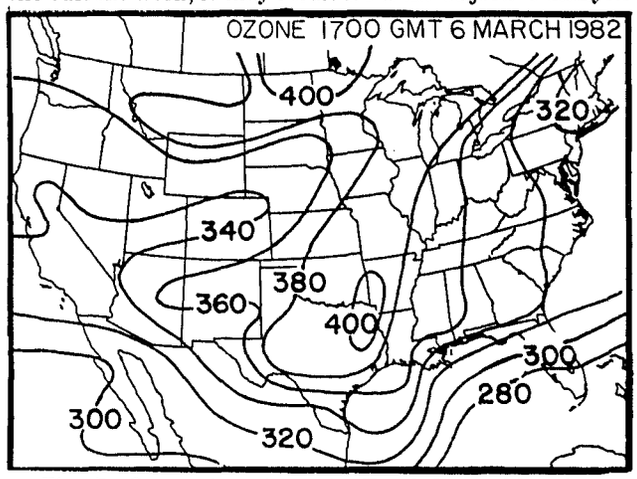

Fig. 7. Ozone data from the Total Ozone Mapping Spectrometer (TOMS) in Dobson units for 1700 GMT 6 March. Data are courtesy of NASA's Goddard Space Flight Center.

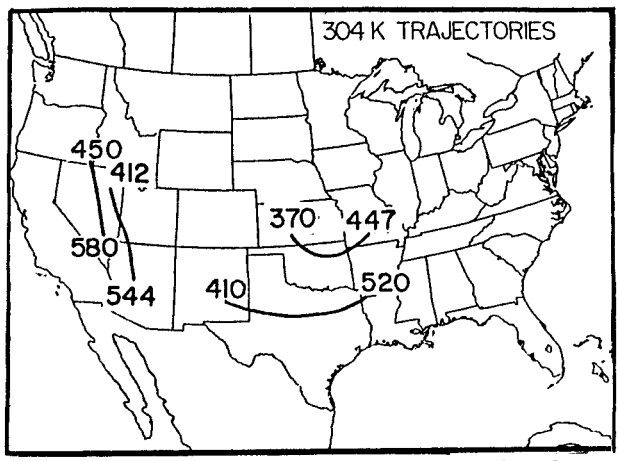

Fig. 8. Backward trajectories on 304 K for the advective image band from 1200 to 0000 GMT 6 March (left), and development band from 0000 GMT 7 March to 1200 GMT 6 March (right). Heavy numbers denote beginning and ending pressures (mb).

deficiencies noted earlier.

4. SUMMARY AND CONCLUSIONS

The dark, warm image bands in 6.7 μm water vapor imagery on 6-7 March 1982 are due to subsidence. Specifically, the advective band is produced by descent associated with the entrance region of a polar jet streak. On the other hand, the evolution of the development image component is coincident with a tropopause fold and associated intrusion of dry stratospheric air into the middle troposphere. Although space limitations do not permit a complete discussion, we have successfully simulated these increasing brightness temperatures by altering upwind soundings based on trajectory-determined vertical motion, and then using both the original and altered profiles as input to a radiative transfer model.

Water vapor imagery is a powerful tool for diagnosing middle tropospheric humidity distributions, and constitutes a true mesoscale data source of global proportions. Case studies such as this help explain the processes responsible for image fluctuations.

ACKNOWLEDGEMENTS

We appreciate the help of several persons during this investigation. TOMS data were provided by Drs. Louis Uccellini and Dennis Chesters of the NASA Goddard Space Flight Center. Dr. Thomas Carney of Florida State provided assistance in preparing the trajectories. Ms. Asha Nayak was very helpful preparing the cross sections. The manuscript was expertly prepared by Ms. Cynthia Wheatley-Lovoy.

Finally, the authors gratefully acknowledge the support of NASA through Grant NAG8-033, under the auspices of the Remote Sensing Branch of the Marshall Space Flight Center.

REFERENCES

Barnes, S. L., 1973: Mesoscale objective map analysis using weighted time-series observations. *NOAA Tech. Memo. ERL NSSL-62, U. S. Dept. of Comm.*, 48 pp.

Danielsen, E. F., 1961: Trajectories: Isobaric, isentropic, and actual. *J. Meteor.*, **18**, 479-486.

_____, 1968: Stratospheric-tropospheric exchange based on radioactivity, ozone and potential vorticity. *J. Atmos. Sci.*, **25**, 502-518.

Gidel, L. T., and M. A. Shapiro, 1979: The role of clear air turbulence in the production of potential vorticity in the vicinity of upper tropospheric jet stream-frontal systems. *J. Atmos. Sci.*, **36**, 2125-2138.

O'Brien, J. J., 1970: Alternative solutions to the classical vertical velocity problem. *J. Appl. Meteor.*, **9**, 197-203.

Reiter, E. R., 1972: *Atmospheric Transport Processes, Part 3: Hydrodynamic Tracers.* U. S. Atomic Energy Commission, 212 pp.

Staley, D. O., 1960: Evaluation of potential-vorticity changes near the tropopause and the related vertical motions, vertical advection of vorticity, and transfer of radioactive debris from stratosphere to troposphere. *J. Meteor.*, **17**, 591-620.

Shapiro, M. A., 1976: The role of turbulent heat flux in the generation of potential vorticity in the vicinity of upper-level jet stream systems. *Mon. Wea. Rev.*, **104**, 892-906.

Stewart, M. R., and H. E. Fuelberg, 1986: Relationships between 6.7 micrometer imagery and radiosonde-derived parameters. *Preprints, Second Conf. Satellite Meteor./Remote Sensing and Applications*, Williamsburg, Amer. Meteor. Soc., 67-72.

Uccellini, L. W., D. Keyser, K. Brill and C. H. Wash, 1985: The President's Day cyclone of 18-19 February 1979: Influence of upstream trough amplification and associated tropopause folding on rapid cyclogenesis. *Mon. Wea. Rev.*, **113**, 962-988.

THE USE OF POLAR ORBITER DATA IN TROPICAL WEATHER SYSTEM ANALYSIS

Debra A. Lubich[1]
Raymond M. Zehr[2]

[1]Cooperative Institute for Research in the Atmosphere (CIRA)
Colorado State University, Fort Collins, CO 80523-0033

[2]Regional and Mesoscale Meteorology Branch
Satellite Applications Laboratory
NOAA/NESDIS, Fort Collins, CO 80523-0033

1.0 INTRODUCTION

The Equatorial Mesoscale Experiment (EMEX) was conducted in Northern Australia from January 8 to February 18, 1987. EMEX ran concurrently in cooperation with Phase II of the Australian Monsoon Experiment (AMEX) and the Stratospheric-Tropospheric Exchange Project (STEP). The objective of EMEX was to study heating mechanisms within mesoscale tropical cloud clusters and the vertical profile of large-scale heating through the troposphere. Several research aircraft were used to collect Doppler radar data, conventional flight level information, microphysical data, and radiation measurements. A surface network of radars and radiosonde stations provided data in addition to the conventional synoptic observations (Holland et al, 1986). In addition, supplemental satellite data were obtained from the National Environmental Satellite, Data and Information Service (NESDIS).

This paper describes satellite data which are available from NESDIS for remote locations (areas outside of GOES coverage) and gives a review of the processing and application of a data set covering the development of a tropical storm in light of the research objectives of AMEX/EMEX/STEP.

2.0 AVAILABLE SATELLITE DATA

The NOAA polar orbiting satellites operate in a near polar, sun-synchronus orbit at approximately 870 km above the earth. Digital visible and infrared Advanced Very High Resolution Radiometer (AVHRR) data from both NOAA-9 and NOAA-10 were archived. AVHRR Local Area Coverage (LAC) data at 1 km resolution is generally available for a region only through special data collection requests submitted to NESDIS. The Regional and Mesoscale Meteorology (RAMM) Branch of NESDIS arranged for collection of LAC data during EMEX. In addition, the AVHRR Global Area Coverage (GAC) visible and infrared imagery at 4 km resolution were archived. Satellite sounding data from NOAA-9 and NOAA-10 were also archived. The soundings were collected by two sensors on board the TIROS Operational Vertical Sounder (TOVS): the Microwave Sounding Unit (MSU) and the High Resolution Infrared Radiation Sounder/2 (HIRS/2). The MSU is a passive scanning microwave spectrometer with 4 channels in the 5.5 micrometer oxygen region. The 124 km resolution at subpoint creates an underlap of approximately 115 km between scan lines. The HIRS/2 measures incident radiation in the infrared region of the spectrum, including both longwave and shortwave radiation. The instrument has 20 channels with a horizontal resolution of 17.4 km in diameter at nadir (Smith et al, 1979). NOAA-9 passed over the EMEX study region at approximately 0630 and 1830 UTC daily, while NOAA-10 passed over at 1030 and 2230 UTC. This provided two late afternoon and two early morning data sets. Figure 1 shows the channel characteristics and weighting functions of the various instruments. (See NASA Goddard Space Flight Center, 1987, for further details.)

In addition to the polar orbiter data, digital visible and infrared imagery were available from the Geostationary Meteorological Satellite (GMS) which is operated by the Japan Meteorological Agency. The GMS satellite has a subpoint of 0 degrees latitude, 140 degrees E longitude. The GMS data is archived at NESDIS at a resolution of 10 km as full disk images every 3 hours as part of the International Satellite Cloud Climatology Project (ISCCP) (World Climate Programme, 1985).

3.0 IMAGERY AND PRODUCT DEVELOPMENT

Software to extract, calibrate, and grid the different data sets was developed at the Cooperative Institute for Research in the Atmosphere (CIRA) at

Colorado State University. Additional software used to correct the HIRS/2 and MSU soundings for the limb effect and for emissivity was supplied by the University of Wisconsin in Madison. In lower resolution data such as HIRS/2 and MSU, the resolution degrades near the scan edges, therefore only data centered on the area of study were examined.

Additional software was developed to create various products from the different data sets which could then be viewed on an image processing system, separately and in conjunction with each other. A VAX 11/780 and a COMTAL Vision One image processing system were used to process and display the data.

Advanced Very High Resolution Radiometer (AVHRR/2)
1.1-km resolution; >2600-km swath width

Channels	Wavelengths (μm)	Primary Uses
1	0.58 - 0.68	Daytime cloud/surface mapping
2	0.725 - 1.10	Surface water delineation, ice and snow melt
3	3.55 - 3.93	Sea surface temperature, nighttime cloud mapping
4	10.30 - 11.30	Sea surface temperature, day and night cloud mapping
5	11.50 - 12.50	Sea surface temperature, day and night cloud mapping

TIROS Operational Vertical Sounder (TOVS):
A 3-sensor atmospheric sounding system

High Resolution Infrared Radiation Sounder (HIRS/2): 17.4-km resolution

Channels	Wavelengths (μm)	Primary Uses
1 - 5	14.95 - 13.97	Temperature profiles, clouds
6 - 7	13.64 - 13.35	Carbon dioxide & water vapor bands
8	11.11	Surface temperature, clouds
9	9.71	Total O_3 concentration
10 - 12	8.16 - 6.72	Humidity profiles, detection of thin cirrus clouds
13 - 17	4.57 - 4.24	Temperature profiles
18 - 20	4.00 - 0.69	Clouds, surface temperatures under partly cloudy skies

Microwave Sounding Unit (MSU): 105-km resolution

Channels	Frequencies	Primary Uses
1	50.31 GHz	Temperature soundings through clouds
2	53.73 GHz	
3	54.96 GHz	
4	57.95 GHz	

Figure 1a. Characteristics of instruments on board NOAA polar orbiting satellites.

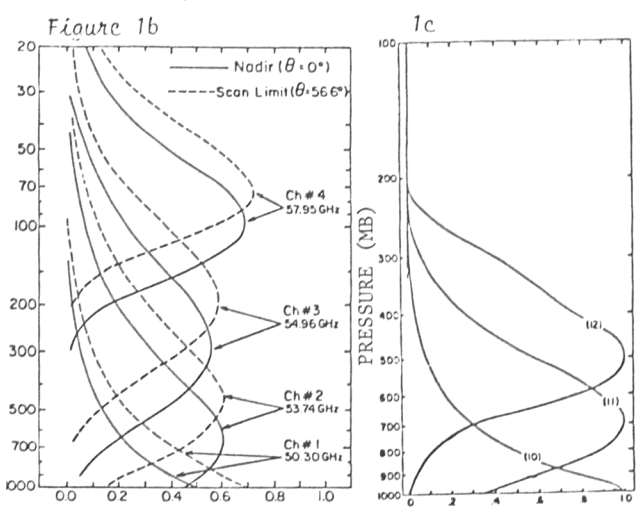

Figure 1. Weighting functions b) calculated for nadir and scan limit of MSU instrument, and c) for HIRS/2 water vapor channels.

The AVHRR raw data consist of radiance measurements. The radiances were converted to eight bit (0-255) brightness temperatures such that each digital value in the imagery represented a 1.0 degree C interval. The high resolution LAC imagery provides excellent visual information about cloud top structures as well as high resolution thermal information, but the size of one full image for each channel (over 2.5 million bytes) made working with the imagery very time consuming and cumbersome. Figure 2 shows the detail available in a visible full resolution LAC image. Note the distinct overshooting tops of the deep convection.

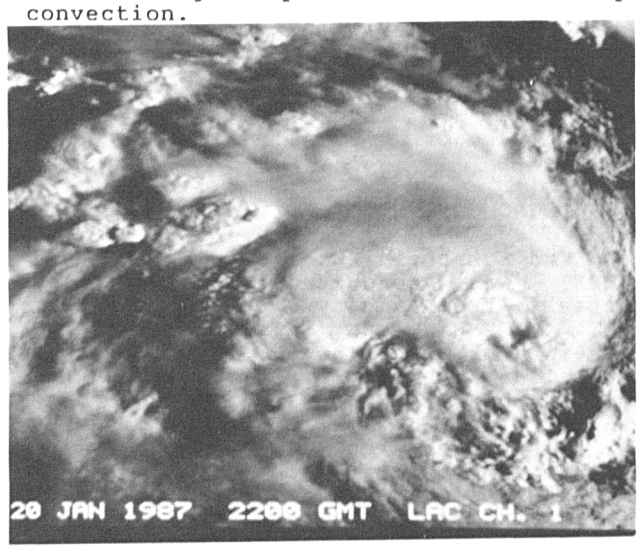

Figure 2. Full resolution visible image from 20 January, 1987 at 2200 UTC. (NOAA-10 AVHRR LAC).

The 3-hour interval GMS data provides time continuity not available with the polar orbiter data. GMS data have been used to describe diurnal variation of deep convective clouds observed with West Pacific tropical cyclones (Zehr, 1987). Animation of the GMS imagery allowed accurate determination of development and movement of weather systems. In addition, the GMS data were used to locate features of interest which were then studied in the higher resolution AVHRR data sets.

The sounding data were also converted from radiance values to brightness temperature. The brightness temperature data were then corrected for limb and emissivity effects, (Smith et al, 1974) and converted to displayable imagery. The lower resolution of both instruments produces a blocky image which is difficult to interpret, therefore the data were smoothed and expanded via a trend analysis interpolation scheme (Purdom et al, 1984) which then made it possible to overlay the imagery onto the AVHRR imagery.

The HIRS/2 6.7μ channels 10, 11 and 12 measure atmospheric water vapor.

The weighting function for channel 10 peaks almost at the surface, while channels 11 and 12 cover the mid-level atmosphere, peaking at approximately 700 and 500 mb respectively (see Figure 1c). Channels 11 and 12 were used to examine mid-level moist and dry regions in the study area.

The four MSU channels measure microwave radiation at 4 levels of the atmosphere. Channel 1 (50.30 GHz) measures the surface, while channel 2 (53.74 GHz) senses the lower troposphere with little surface influence. The upper troposphere is measured by channel 3 (54.96 GHz) and the tropical tropopause by channel 4 (57.95 GHz). The cloud penetrating properties of microwave radiation allow for temperature measurement in areas covered by heavy clouds. However, tropical storms contain areas with high amounts of liquid water, causing increased absorption at the lower levels of the atmosphere and preventing accurate temperature calculation from channels 1 and 2. Therefore, MSU channel 2 was used to determine areas of precipitating clouds (Grody et al, 1982), while channel 1 was used to examine surface characteristics. Channels 3 and 4 were used to display temperature gradients in the upper atmosphere. Channel 3 was also reviewed for any evidence of storm influence. Due to the small temperature variation in the tropics, imagery from channels 2, 3 and 4 were also contoured at .1 degree C intervals to examine small scale temperature gradients not visible when the raw temperature data was converted to integer values for image display.

4.0 TROPICAL CYCLONE IRMA

During the period of 16-19 January, 1987, the monsoon trough was very well defined, extending WNW-ESE across northern Australia. The monsoon trough is characterized by deep westerlies to the north and deep easterlies to the south with extensive cloudiness and heavy rainfall accompanying numerous mesoscale convective systems. Tropical Cyclone Irma developed during this time over the Gulf of Carpentaria. EMEX/AMEX conducted research flight missions into the region, with mid-point times of the flights at approximately 0000 UTC on 19-20 January. Tropical Cyclone Irma attained minimal hurricane intensity just before landfall as it tracked southwestward and eventually dissipated over the Northern Australian interior. The best track and minimal sea-level pressure observations are shown in Figure 3.

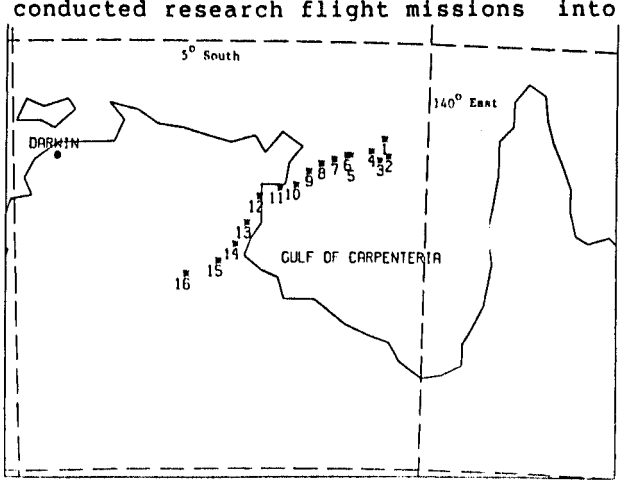

Figure 3a. Path of TC Irma.

4.1 Analysis of Archived Data for Tropical Cyclone Irma

The GMS data were used to study early storm genesis and later deep convection. Figure 4a shows the variation in cold cloud top temperatures (< - 65 degrees C) at a 0-4 degree radius from the tropical cyclone center obtained by the best track information. These results agree favorably with recent findings described by Zehr (1988) regarding the time series of objective satellite-derived quantities and their relation to tropical cyclone evolution. The deep convection during 15-16 January coincides with the tropical cyclone genesis stage and is followed by 1-2 days of suppressed convection. A large increase in the extent of cold cloudiness is again seen during intensification to a mature tropical cyclone (18-19 January). The maximum in deep convection precedes maximum intensity by 12-24 hours. A large majority of tropical cyclones in the western North Pacific have exhibited very similar features for infrared cloud areas less than -65 degrees C out to 4 degrees latitude radius (Zehr, 1988). Figure 4a also shows a large diurnal variation. The deep convection within the monsoon trough has a pronounced tendency for intensification over land in the afternoon hours and over large bodies of water in the early morning hours (Williams and Houze, 1987). This tendency for a double diurnal maximum can be seen in Figure 4b for the area out to 8 degrees latitude. Large continental and oceanic regions are covered by this area.

POS	DATE/TIME	LAT	LON	CENTRAL PRESSURE
1	19/0300	12.2	138.9	998
2	0600	12.6	139.0	996
3	0900	12.7	138.8	994
4	1200	12.5	138.6	994
5	1500	12.6	138.1	992
6	1800	12.6	138.0	990
7	2100	12.7	137.7	988
8	20/0000	12.8	137.4	987
9	0300	13.0	137.1	987
10	0600	13.3	136.8	984
11	0900	13.4	136.4	984
12	1200	13.6	135.9	984
13	1500	14.2	135.6	984
14	1800	14.7	135.3	984
15	2100	15.1	134.9	984
16	21/0000	15.4	134.1	984

Figure 3b. Best track and minimal sea-level observations for TC Irma.

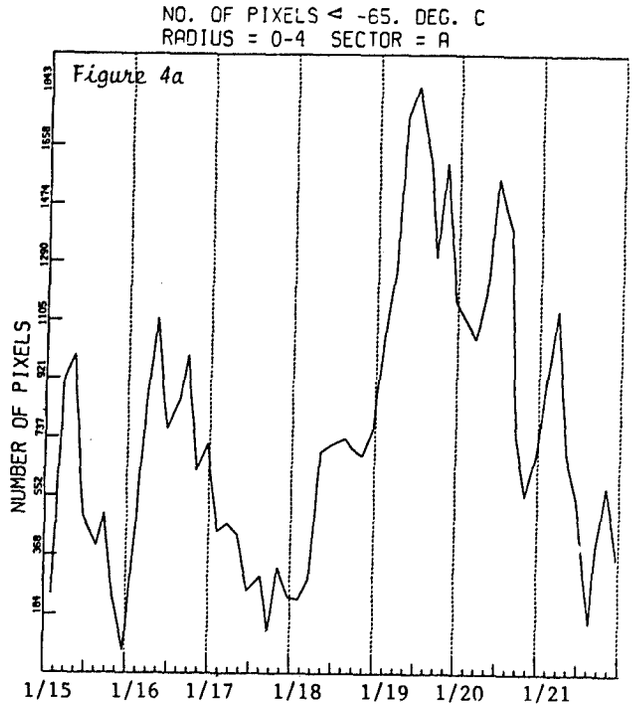

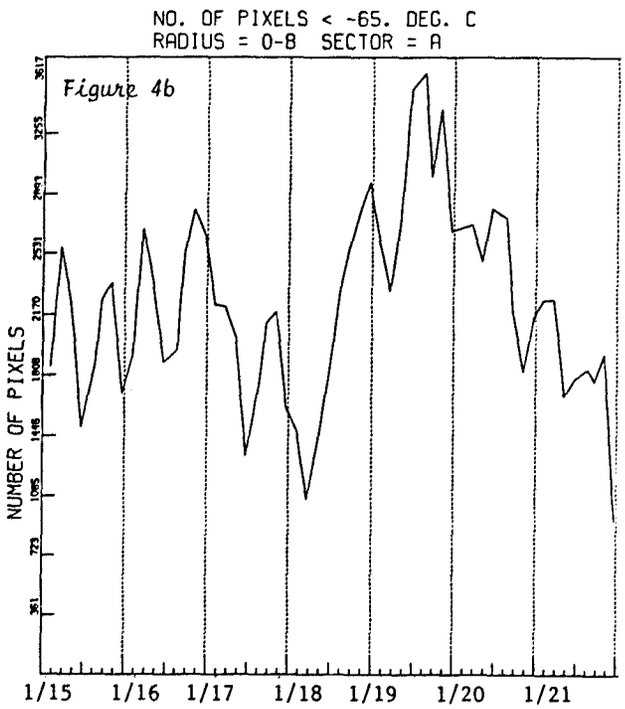

Figure 4. Variation in cold cloud top temperatures and area for a) 0-4° radius from storm center and b) 0-8° radius from storm center.

The coldest cloud top temperatures were compiled for AVHRR and GMS imagery (Figure 5). The coldest temperature measured occurred on both GAC and GMS data at approximately 0900 UTC on 19 January. The GMS instrument measured a temperature of -97.3 degrees C, while the GAC radiometer measured -98.17 degrees C. The GMS data also showed a minimum temperature of -97.3 degrees C on 16 January at 1500 UTC, during the storm genesis. LAC IR imagery for 16 January at 2200 UTC displayed at minimum temperature of -96.0 degrees C. Figure 6 is a plot of a radiosonde observation from Gove, Australia at 1000 UTC on 19 January. Gove is located at approximately 12 degrees south latitude on the western shore of the Gulf of Carpentaria. Note the very cold tropopause temperature of -94 degrees C. (More typical tropopause temperatures are -80 to -85 degrees C.) Surface parcel ascent based on the sounding in Figure 6 indicates that the overshooting cloud top parcels to a pressure level near 80 mb at -100 degrees C are indeed possible.

	GMS temp (C)		AVHRR temp (C)		
1/18	0200	-91.62	1/18		
	0500	-91.58		0700	-85.71
	0800	-91.58		0900	-90.17
	1100	-94.33			
	1500	-97.30			
	1700	-97.30			
	2000	-94.33			
	2300	-94.33			
1/19	0200	-91.58	1/19		
	0500	-91.58			
	0800	-97.30		0900	-98.17
	1100	-94.33			
	1500	-94.33			
	1700	-94.33			
	2000	-94.33			
	2300	-91.58		2200	-88.75
1/20	0500	-89.02			
	0800	-94.33			
	1100	-94.33			
	1500	-91.58			
	1700	-91.58			
	2000	-94.33			
	2300	-89.02			

Figure 5. Coldest cloud top temperatures measured by GMS and AVHRR.

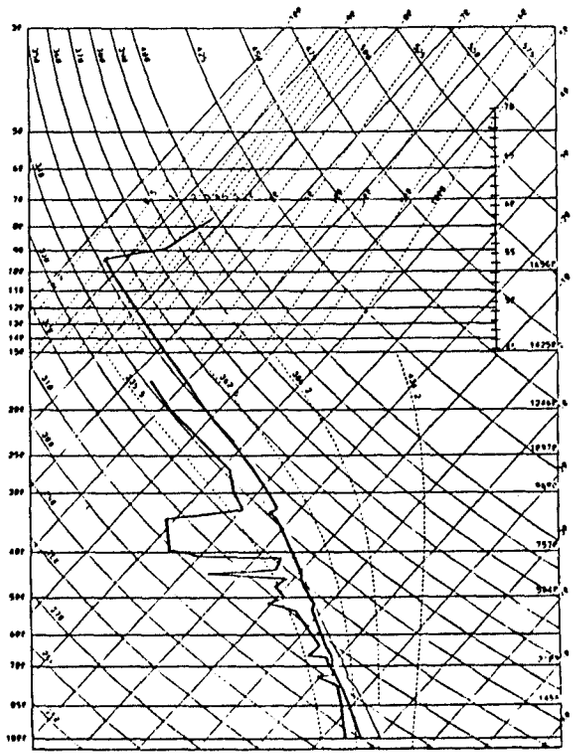

Figure 6. The thin line temperature plot is dry-bulb temperature. The bold lines are (left) dewpoint temperature and (right) wet bulb temperature.

The GAC data channels were combined for display as truecolor imagery to help distinguish cloud levels and cloud top features. While searching for any satellite observed eye development in the storm, it was discovered that a warm core which appeared in the channel 4 and 5 imagery for 0400 UTC on 19 January was actually, when viewed in the visible imagery, an overshooting top. Cloud matter that remains in the stratosphere due to a persistent overshooting convective tower occasionally emits a relatively warm signal in infrared satellite data because it acquires the temperature of the warmer environment. Weak eye development was observed on 20 January at 2200 UTC (Figure 2).

The most useful information obtained from the MSU data pertained to upper temperature gradients, and to the visibility of areas of heavy moisture and/or rainfall. The liquid water attenuation (Grody et al, 1982) appeared to increase in conjunction with the deepening convection of the storm. This is supported by the decreasing central pressure reported by the best track information. Areas of heaviest attenuation appeared in channels 1 and 2 from 0400-0900 UTC on January 19, which corresponded with the coldest, highest areas of cloud cover in the AVHRR and GMS imagery (Figure 7). The attenuation could also be observed over land as the storm moved inland, and in the aftermath of the storm, possibly due to the effect of wet ground on the surface channel measurements. Previous studies have shown that the upper-tropospheric microwave channel (54.96 GHz) can detect the upper-level warm core of tropical cyclones, thus allowing an estimate of storm intensity (Kidder et al, 1978; Grody et al, 1979; Grody and Shen, 1982). The 54.96 GHz channel data, when contoured at .1 degree, detected a possible slight warm core signature, along with a colder area that could correspond to heavy precipitation influence, or to the reflection of precipitation in the 53.74 GHz channel (Grody et al, 1979). Considering the relatively small size and weak intensity of Irma and the relatively large field of view of the MSU sensor, the weak warm core signature was not unexpected.

The most difficult information to interpret was the HIRS/2 water vapor measurements. In the tropics, there are generally no strong horizontal temperature gradients to be observed by the temperature sounding channels. The extreme cloud cover present in the area of the storm prohibited any delineation of strong moist and dry boundaries, although the imagery did show the dry areas of the central continent gradually becoming more moist southwest of the Gulf of Carpentaria prior to the storm's turn inland. HIRS/2 water vapor soundings from several days after the storm passage also indicated a general drying out of the mid-level atmosphere. Several days of suppressed convective activity in northern Australia followed Tropical Cyclone Irma.

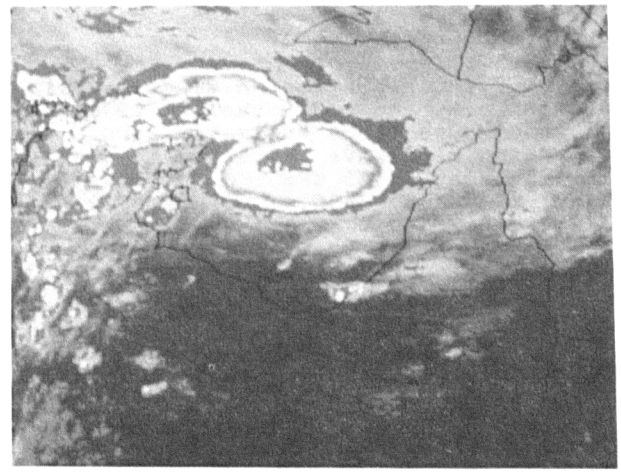

Figure 7a. AVHRR GAC IR image at 0900 UTC on 19 January, 1987 at TC Irma peak intensity. The dark cloud top areas indicate coldest temperatures.

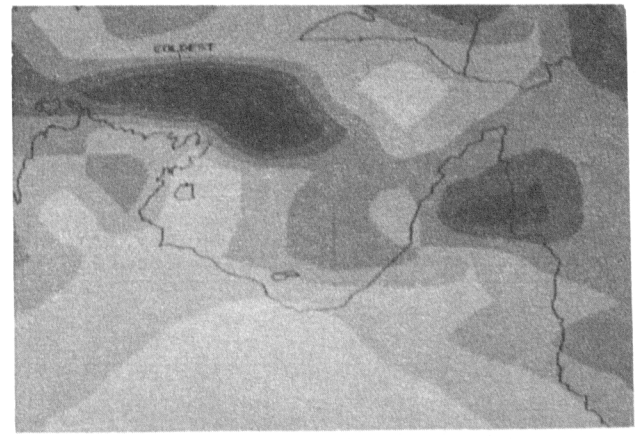

Figure 7b. Corresponding MSU 53.74 GHz channel image. Darkest areas are those of heaviest rain attenuation.

5.0 SUMMARY

The extensive satellite data set compiled during EMEX offers a unique opportunity to study coincident measurements from geostationary and polar orbiting satellites in conjunction with surface and flight level information collected over Northern Australia during the experiment. The low spatial but high temporal resolution of the GMS data offers excellent large scale circulation and weather pattern information. The higher resolution polar orbiter data offers more detailed temperature and cloud structure information from a variety of instruments, but with little time continuity. The use of these data sets in combination provides much satellite information about tropical weather systems in the western North Pacific area studied by EMEX.

6.0 ACKNOWLEDGEMENTS

This work was supported by NOAA NA85RAH05045.

7.0 REFERENCES

Grody, N.C., C.M. Hayden, W.C. Shen, P.W. Rosenkranz, and D.H. Staelin, 1979: Typhoon June winds estimated from scanning microwave spectrometer measurements at 55.45 GHz. J. Geophys. Res., 84, 3684-3695.

Grody, N.C. and W.C. Shen, 1982: Observations of Hurricane David (1979) using the microwave sounding unit. NOAA Technical Report NESS 88, 52 pp.

Holland, G.J., J.L. McBride, R.K. Smith, D Jasper, and T.D. Keenan, 1986: The BMRC Australian Monsoon Experiment: AMEX. Bul. Amer. Meteor. Soc., 67, 1466-1472.

Kidder, S.Q., W.M. Gray, and T.H. VonderHaar, 1978: Estimating tropical cyclone central pressure and outer winds from satellite microwave data. Mon. Wea. Rev., 106, 1458-1464.

NASA Goddard Spaceflight Center, 1987: Advanced TIROS-N. NASA Goddard Spaceflight Center, Greenbelt, Md.

Purdom, J.F.W., T.H. VonderHaar, R.N. Green, J.F. Weaver, R.M. Zehr, M. Kruidenier, and M. Eddy, 1984: Enhancing GOES infrared imagery for nowcast applications. CIRA report, 21 pp.

Smith, W.L., H.M. Woolf, C.M. Hayden, D.Q. Wark and L.M. McMillin, 1979: The TIROS operational vertical sounder. Bull. Amer. Meteor. Soc., 58, 1177-1187.

Williams, M., and R.A. Houze, Jr., 1987: Satellite-observed characteristics of winter monsoon cloud clusters. Mon. Wea. Rev., 115, 505-519.

World climate Programme, 1985: International satellite cloud climatology project - description of reduced resolution radiance data, July, 1985, WMO/T.D. - No. 58, Geneva.

Zehr, R.M., 1987: The Diurnal Variation of Deep Convective Clouds and Cirrus with Tropical Cyclones. Preprints 17th Conf. on Hurricanes and Tropical Meteorology, Miami, Amer. Meteor. Soc., 276-xxx.

Zehr, R.M., 1988: Satellite diagnosis of tropical cyclones, 3rd Conf. on Satellite Meteorology and Oceanography, Anaheim, Amer. Meteor. Soc.

USING THE VAS DATA UTILIZATION CENTER (VDUC) FOR THE ANALYSIS AND FORECASTING OF HEAVY RAINFALL PRODUCING MESOSCALE CONVECTIVE SYSTEMS (MCSs)

Roderick A. Scofield

NOAA/NESDIS/Satellite Applications Laboratory
Washington, DC 20233

1. Introduction

The "short-fuse" and devastating characteristics of flash floods make it essential that "state-of-the-art" technology be used to produce timely special weather statements and warnings. Most of the "short-fused" heavy rain events come from Mesoscale Convective Systems (MCSs). A MCS is a thunderstorm system that ranges in scale from the largest Mesoscale Convective Complex (MCC) (Maddox, 1980) down to the smallest single cluster (Jiang and Scofield, 1987). Today, VAS Data Utilization Centers (VDUCs) are the newest systems available for weather analysis and forecasting. The VDUC system allows the meteorologists to identify and timely analyze MCSs that may produce flash flooding. VDUC systems are currently located at NMC, National Hurricane Center, National Severe Storms Forecast Center, U. of Wisconsin and Colorado State University. Information available on VDUC include: conventional surface and upper air data, NMC analysis/forecasts/guidance products, radar data, VAS imagery and derived fields (divergence, vorticity, surface moisture divergence, 850-300 mb thickness, equivalent potential temperature (θ_e), stability, etc.) from conventional, model, and VAS data. VAS data includes: visible (VIS), infrared (IR) and 6.7 um water vapor imagery, 12 channel dwell sounding data and meteorological parameters (mentioned above) derived from the sounding data. VDUC is a digitally based system that can be used to: color enhance the data, superimpose data fields, add and subtract data fields and animate the data (length of loops can be a day or longer).

The VDUC capabilities cited above would vastly improve satellite-derived precipitation estimates and forecasts as compared to those estimates and forecasts computed on the current Interactive Flash Flood Analyzer (IFFA) (Clark, et al., 1985) system. IFFA has a limited capability but can be used to: animate imagery (length of loop limited to 3 hours), enhance the imagery, superimpose some data fields on the imagery and can automatically add up the estimates and produce isohyetal analyses.

This paper presents a four stage analysis and forecast methodology for heavy convective rainfall; the methodology would be applicable to those centers that possess VDUC systems. The methodology is a refinement of the short-range forecasting technique presented by Spayd and Scofield, 1984. The emphasis in this paper will be discussing VDUC-derived products for accomplishing Stages 1-4.

2. The Chicago Flash Flood, 14 August 1987

The enhanced IR imagery in Figure 1 show deep convection over Illinois, Missouri, and along the Gulf Coast from the Florida Panhandle to extreme southern Mississippi. The MCS along the Gulf Coast was associated with an active surface trough and was producing heavy rainfall. Due to the significant satellite signature and plenty of available moisture, Synoptic Analysis Branch meteorologists (of NESDIS) were concentrating their efforts on analyzing and computing estimates for the MCS along the Gulf Coast. However, during this same period, several small MCSs passed over the Chicago area. As a result, devastating flash floods occurred in Chicago, Illinois. Plotted six hour rainfall amounts are shown in Figure 2. Chicago O'Hara International Airport received 9.21 inches of rain within an 18 hour period. The Chicago flash flood occurred because four MCSs transversed the same location within an 18 hour period. A sequence of enhanced IR imagery for the heavy rain period (0300 to 1800 GMT) is shown in Figure 3. Each individual MCS may not have produced enough rainfall to cause flash flooding itself; however, the cumulative effect of several MCSs passing over Chicago was devastating. The animation capabilities of VDUC allow meteorologists to keep a cumulative record of the paths of previous convective systems to properly assess the flash flood potential of current or future convective systems. Important surface and upper air features for 0000 and 1200 GMT, 14 August are depicted in Figures 4a and 4b, respectively. Features noted are: a persistent maximum 850 mb flow of the most unstable air into the Chicago area and weak 500 mb positive vorticity advection centers oriented NE-SW over the Chicago area. Chicago is located: south of an east to west thickness pattern with a moderate gradient and is

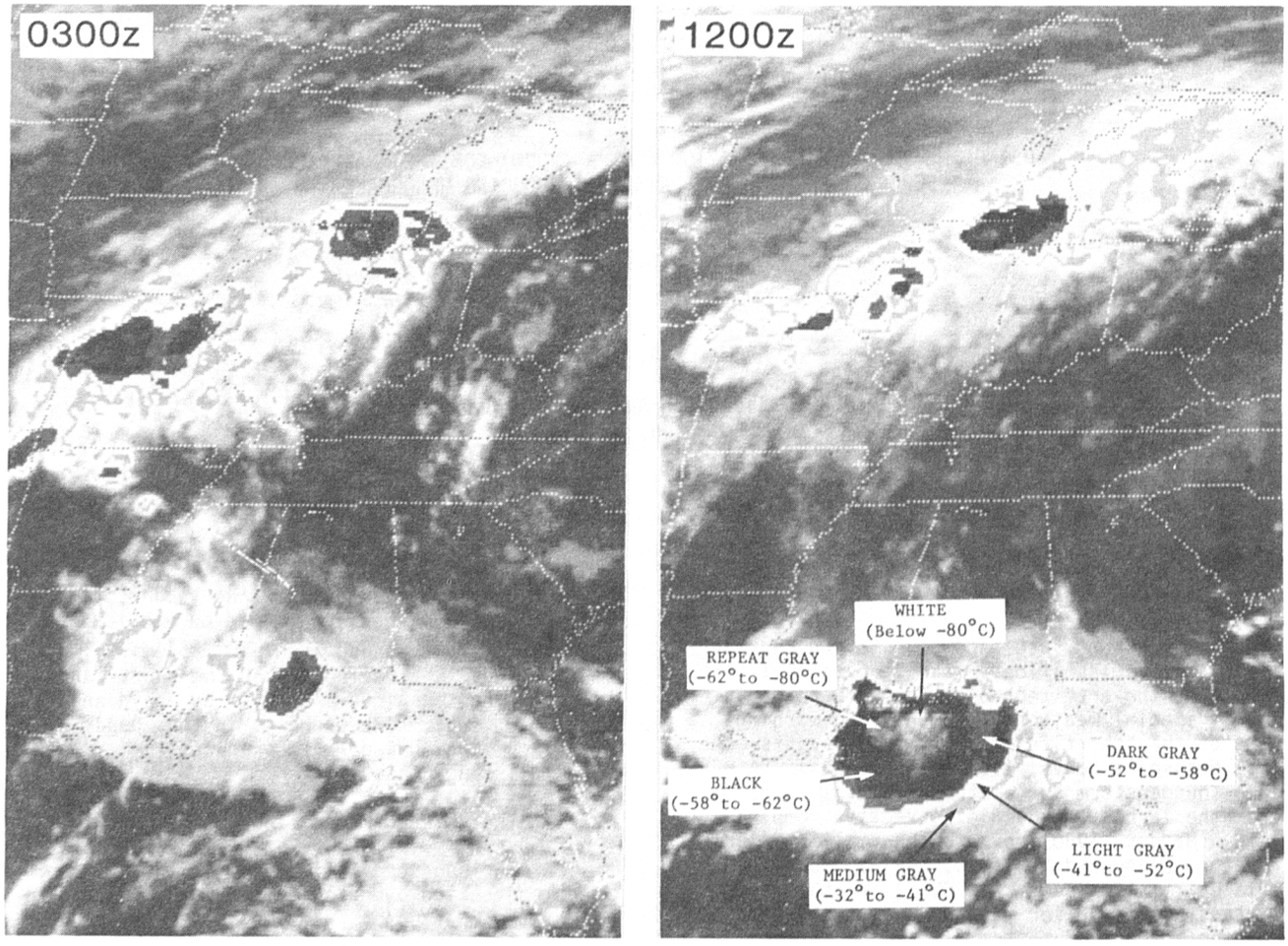

Fig. 1 Enhanced infrared imagery (Mb Curve), 14 August 1987.

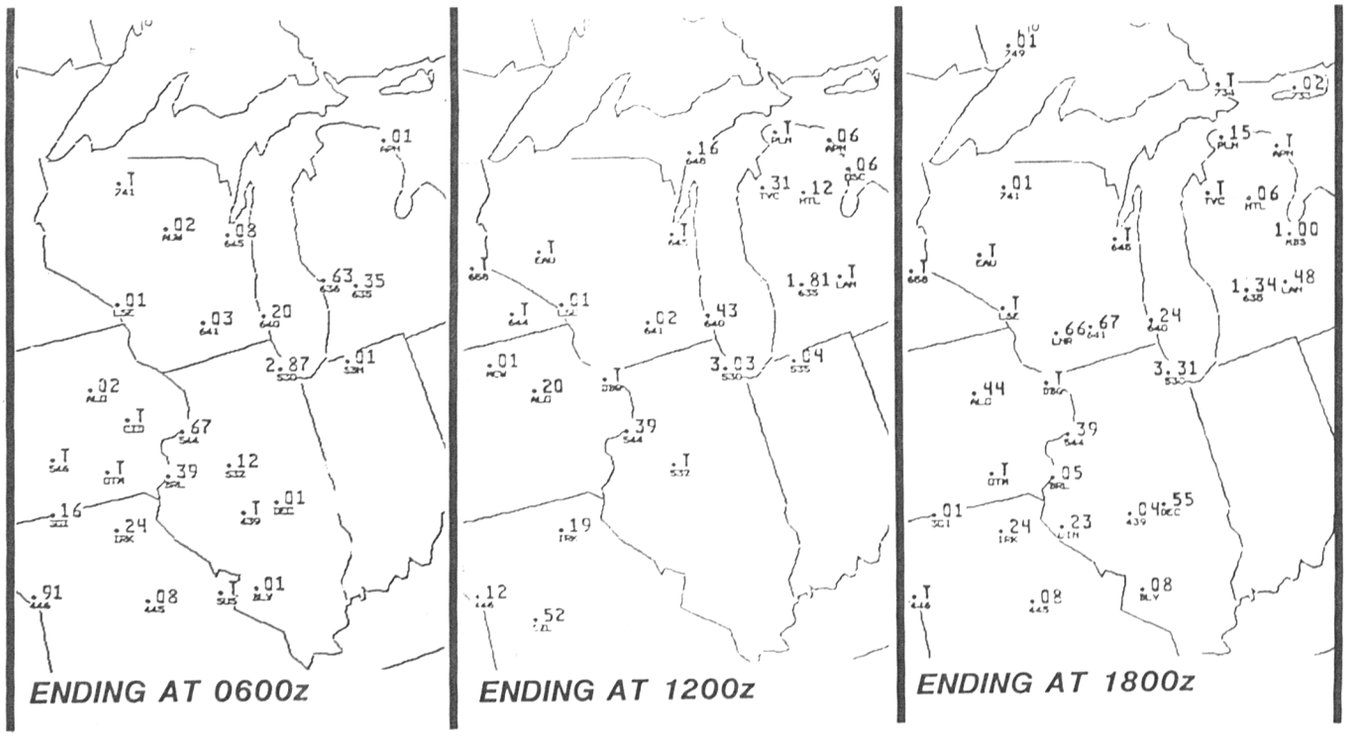

Fig. 2 Six hour rainfall observations, 14 August 1987.

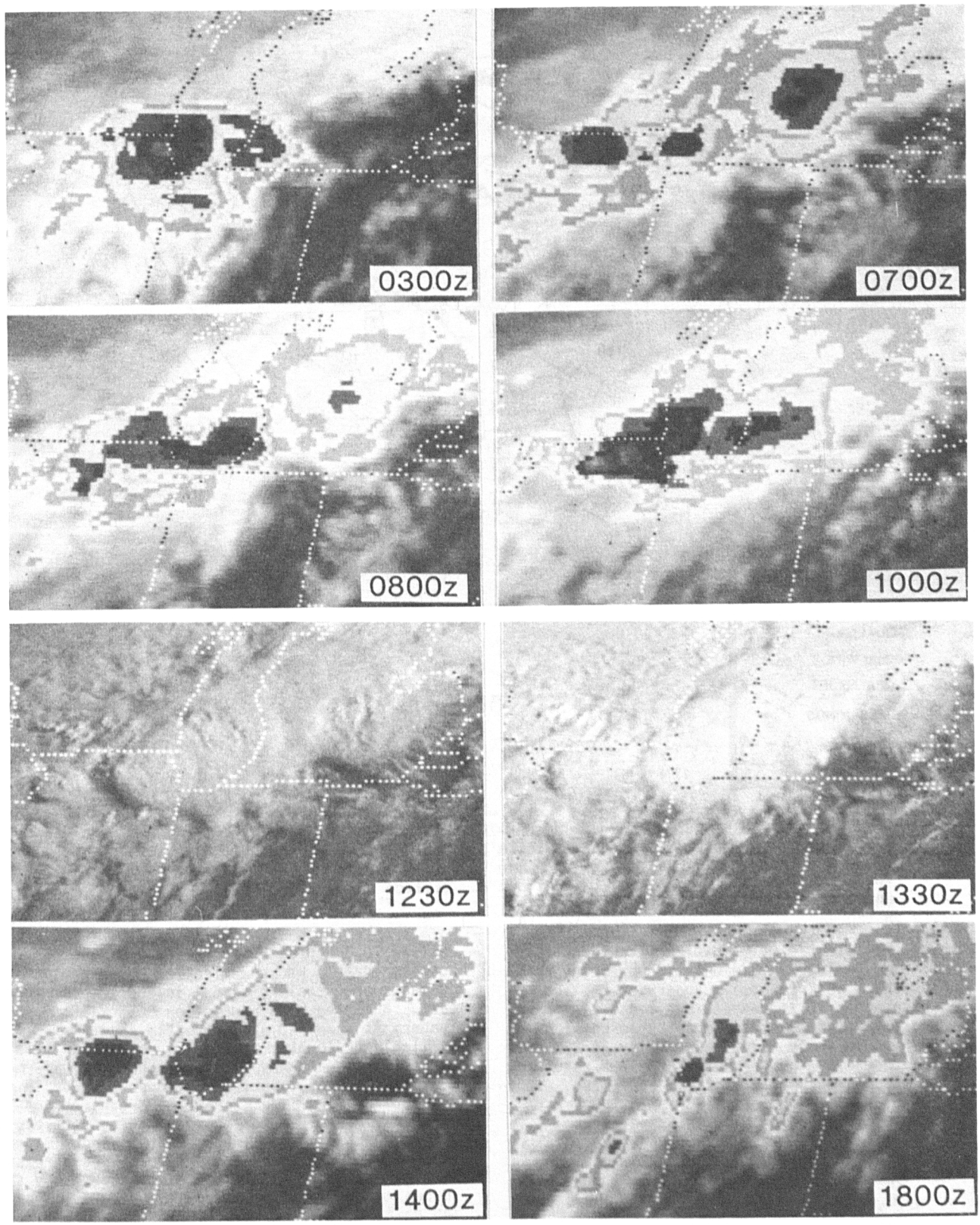

Fig. 3 Enhanced infrared imagery (Mb Curve) and visible imagery (at 1230 and 1330 GMT), 14 August 1987.

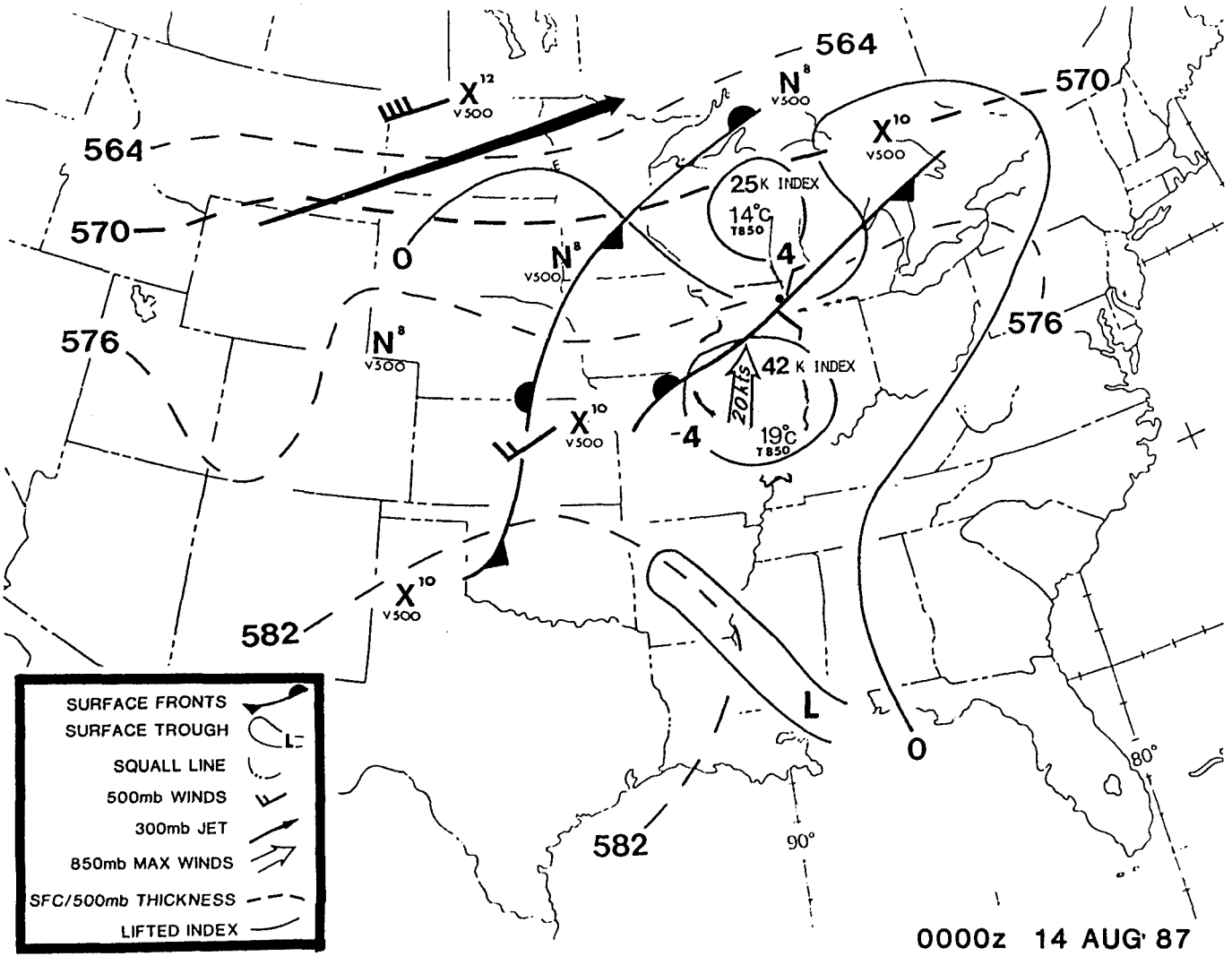

Fig. 4a Surface and upper air features for August 14, 1987, 0000 GMT; T850 indicates 850 mb temperatures in that area and V500 locates either a 500 mb max vorticity center (X) or a min vorticity center (N). Vorticity values are indicated in 10^{-5} sec^{-1}. Surface winds are indicated near the Chicago area.

south of the jet stream. Additional features over Chicago include weak middle to upper level SW winds and a weak frontal boundary at the surface; also moisture is readily available as measured by the sfc-500 mb precipitable water of around 2 inches and a relative humidity of 85%. These features fit the characteristics of regenerating MCSs discussed in Scofield and Jiang, 1987 and Jiang and Scofield, 1987. The VDUC allows a meteorologists to superimpose, keep track of various features and evaluate the local change of stability with respect to time using the hourly VAS-derived stability fields.

3. The Analysis and Forecasting of MCS

Stage 1: 0-6 and 6-12 Hour Forecast of Favorable Synoptic and Mesoscale Conditions for the Development of MCSs

In this step the meteorologist uses the VDUC system to identify and locate features in the conventional and satellite data that may initiate or focus heavy convective rainfall. Nowcasting (0-3 hours) weighs heavily in the 0-6 hour forecast. NMC numerical model forecasts and guidance products are useful in the 12 hour forecast. Animated high resolution GOES VIS and IR imagery is examined as frequently as it is available to locate: thunderstorm outflow boundaries, mesoscale boundaries produced by differential heating, mergers of convective cells or convective cloud lines, areas of organized convection versus areas of unorganized convection, boundary intersections, etc. Water vapor imagery (6.7 um) is used to locate and track jet streaks, vorticity centers and lobes, middle-level dry air surges and deformation zones. Hourly VAS sounding data is used to monitor areas of increasing low level moisture and instability. The ability to locate synoptic and mesoscale lifting mechanisms and to compute the convective available potential energy and the local change of stability with respect to time will help pin point areas of potential MCS development. Meteorological assessment of VAS sounding derived products in monitoring the pre-convective environment and for nowcasting convection is presented in the VAS

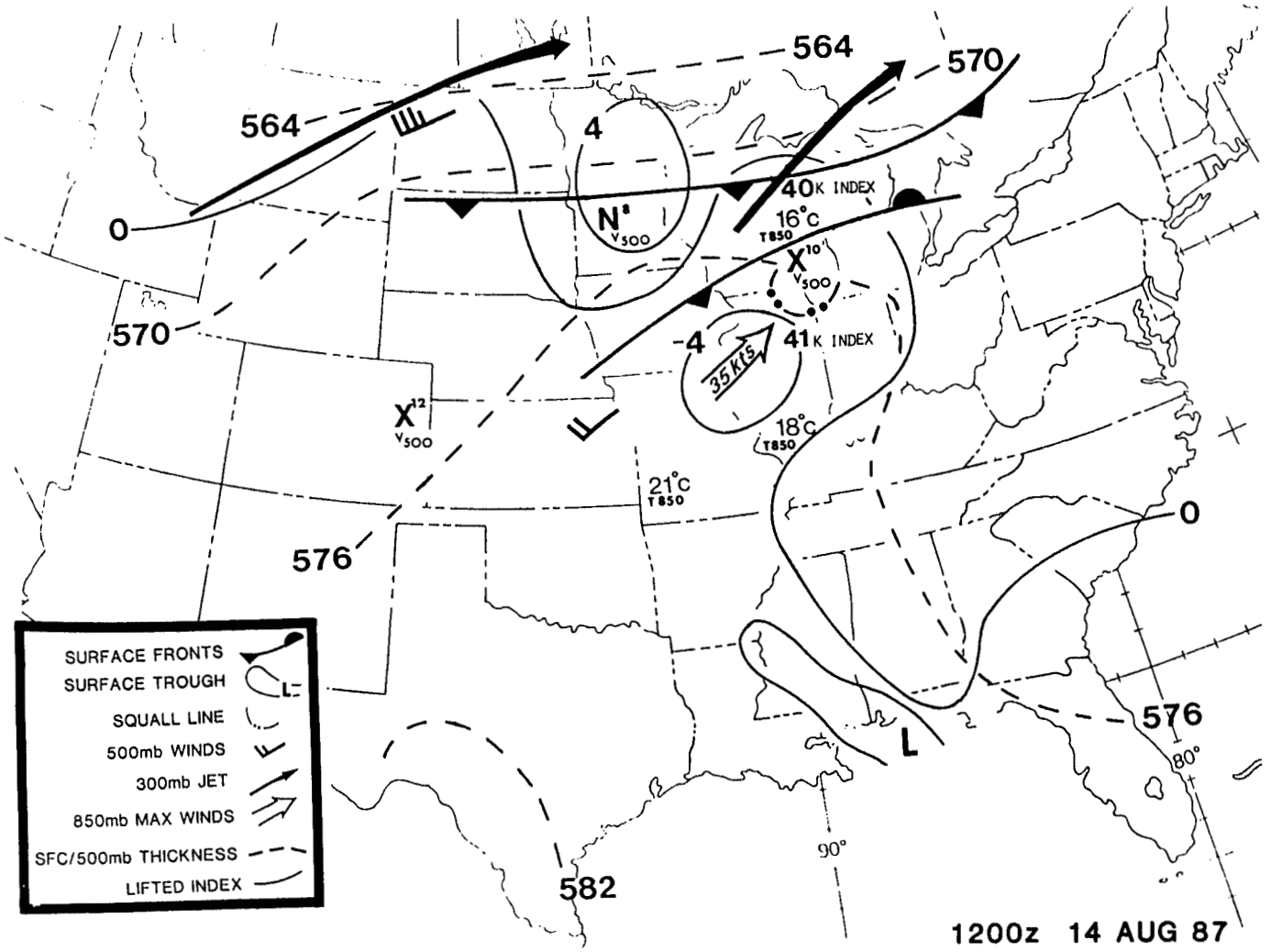

Fig. 4b Surface and upper air features for August 14, 1987, 1200 GMT; T850 indicates 850 mb temperatures in that area and V500 locates either a 500 mb max vorticity center (X) or a min vorticity center (N). Vorticity values are indicated in 10^{-5} sec^{-1}.

demonstration: description and final report (1985). One of the more interesting products in this final report which this heavy precipitation forecasting technique intends to test is the split window, low level moisture product. The split window product combined with the 6.7 um imagery can be used to detect convectively unstable air masses as exhibited by mid-level dry air intrusions overlying areas of maximum low level moisture. In the conventional data, the meteorologist analyzes: the equilibrium level (EL) and areas of high surface to 500 mb precipitable water, mean relative humidity, and surface dewpoints, and reanalyzes the latest NMC charts.

The conventional, VAS sounding derived, and satellite imagery features mentioned above can be plotted as a composite chart on the VDUC TV screen. The composite chart may be superimposed directly on the satellite imagery. The composite chart is then evaluated. The larger the number of favorable interactions between potential triggering mechanisms at one location, the greater the chance that heavy convective rainfall will develop at that location. The composite chart is evaluated with respect to heavy rainfall/flash flood event models such as frontal, synoptic, mesohigh models (Maddox, et al., 1979), regional models such as South Texas (Grice, et al., 1982), and types of convective systems (Spayd, 1982; Fleming, et al., 1984 and Fleming, et al., 1986). Recently, Scofield (1987b) proposed a short range heavy precipitation index forecasting technique. A data tablet based on the parameters of that heavy precipitation index is being developed for the VDUC system. Data tablets are used to simplify the entering of commands. The data tablet is being programmed so that a specific location selected by a pointer performs a specific function (e.g. computes convective available potential energy and its advection). The data tablet is an efficient means of manipulating complex data in an operational environment.

Stage 2: Monitoring the Propagation and Stability Characteristics of Developing MCSs

In this stage, the meteorologists monitor areas of growing towering cumuli, growing MCSs and MCSs that have been in existence for some time but are moving too fast to produce flash

floods. The temperature of the thunderstorm cloud tops as observed in the satellite imagery is compared with the calculated EL from the nearest RAOB sounding. If the cloud top temperatures are equal to or colder than the EL, the MCS has reached its potential to produce heavy rainfall. Of course, other factors have to be considered such as: available moisture (see Stage 1) and the speed and movement of MCSs. Predicting accurately the speed and movement of an existing MCS can be quite difficult. In most cases, propagation is the controlling influence on the movement of the MCS. The type of propagation (backward and forward) often determines the amount of rainfall that occurs from MCSs. Backward propagating MCSs are usually associated with heavier rainfall than those exhibiting forward propagation. The type of propagation (Scofield and Jiang, 1987 and Jiang and Scofield, 1988) is determined by the stability, low level windflow, equivalent potential temperature patterns, low to mid level moisture and temperature advection, thickness patterns, mid to upper level windflow, vertical wind shear and the existence of synoptic scale and mesoscale upward vertical motion areas.

The heavy rainfall areas in forward propagating MCSs often move in the direction of the mean cloud layer shear vector, coincident with the 850-300 mb thickness contours (Merritt and Fritsch, 1984). Backward propagating MCSs often move along the ridge axis of maximum θ_e toward higher values. Many of the above mentioned meteorological parameters (e.g. thickness and θ_e) can be derived from VAS sounding data. Hourly VAS-derived products aid in determining the propagation and stability characteristics of MCSs.

Stage 3: Estimating Flash Flood Rainfall Potentials of MCSs

Rainfall estimates are computed for those MCSs that exhibit the following characteristics:

- backward propagation
- slow forward propagation
- regeneration

Rainfall estimates are sent to WSFOs and River Forecast Centers if they approach or exceed flash flood guidance. The current rainfall estimation program is discussed in a paper by Clark and Borneman, 1984). An interactive flash flood technique (Scofield, 1987a) is used to compute these estimates. Currently, it is difficult for a meteorologist to compute rainfall estimates for more than three MCSs at a time; sometimes even monitoring two or three MCSs are extremely taxing. A reliable objective, automatic estimation technique could be useful as a "first guess" estimate for every MCS occurring anywhere in the US. It could provide half-hourly and accumulated estimates that would help a meteorologist "zero in" on potential flash flood producing MCSs. Once the potential flood-producing MCS is located, more detailed estimates would be produced using the interactive flash flood technique. Adler and Negri (1987) have developed such an automatic technique which is currently being installed for use on the VDUC system.

Stage 4: 0-3 Hour Estimation Outlook of How Much More Rain is Expected

This stage is a NOWCAST that uses persistence, extrapolation, trend and expectancy guidelines. The speed and direction of movement of the coldest portions of the satellite-observed MCSs are measured on the VDUC system. The speed and direction are used to extrapolate the current rainfall rates out to 3 hours. Propagation effects (Stage 2) are also considered. Trend and expectancy guidelines and satellite-observed characteristics of heavy convective rainfall systems are used to anticipate the evolution of the MCS within the next 3 hours. The values of the above extrapolated rainfall estimates are adjusted and relocated, if necessary, based on the guidelines presented in the short-range forecasting technique (Spayd and Scofield, 1984 and Scofield, 1987a).

Flash flooding often results when two or more unrelated MCSs transverse the same location within a 24 hour period (e.g. the Chicago flash flood in Section 2). Each individual thunderstorm system may not produce enough rainfall to cause flash flooding by itself. It is essential that the operational meteorologist keep a record of the paths of previous MCSs within the last 24 hours in order to properly assess the flash flood potential of current or future convective systems. The VDUC system allows the meteorologist to do this function and keep track of previous MCS events.

4. Summary and Outlook

The VDUC system represents a technology that is ideal for timely analyses and forecasts of flash flood producing MCSs. The VDUC's animation, enhancing, overlaying and current data (all types) capabilities allow the meteorologist to analyze the vital characteristics of flash flood producing MCSs.

Applications of VAS data to precipitation estimates is in the early stages of assessment. Many important VAS data applications are anticipated over the next several years to improve precipitation estimates and the general understanding mesoscale meteorological features. This should especially be important to short range forecasting of precipitation related meteorological features. In the future, precipitation estimates will be computed using 15 minute satellite data; this may be an automatic technique. An automatic estimation technique will enable meteorologists to concentrate more effort on the improvement of NOWCASTS and short range forecasts - a major goal for the current satellite precipitation estimation program. As an aid to making NOWCASTS, a short-range forecasting algorithm that uses GOES VAS data to predict thunderstorm trends and precipitation is needed.

The methodology presented in this paper will also be applied, tested and modified to identify precipitation from extratropical and tropical cyclones.

5. Acknowledgments

The author thanks Fran Holt for reviewing this paper, Tina Cashman for typing and John Shadid and Gene Dunlap for the final draft of the figures and illustrations.

6. References

Adler, R. F. and A. J. Negri, 1986: A satellite infrared technique to estimate tropical convective and stratiform rainfall. Lab for Atmospheres, NASA/Goddard, submitted for publication in Journal of Climate and Applied Meteorology.

Clark, D. and R. Borneman, 1984: Satellite precipitation estimation program of the Synoptic Analysis Branch. Proceedings of the Tenth Conference on Weather Forecasting and Analysis, June 25-29, 1984, Clearwater Beach, FL, AMS, 392-399.

Clark, D. and M. Perkins, 1985: The NOAA Interactive Flash Flood Analyzer. Proceedings of the International Conference on Interactive Information and Processing Systems for Meteorology, Oceanography, and Hydrology, January 7-11, 1985, Los Angeles, CA, AMS, 255-259.

Fleming, E., L. E. Spayd, Jr., R. A. Scofield, 1984: Characteristics of east coast convective flash flood events in GOES imagery. Proceedings of the Tenth Conference on Weather Forecasting and Analysis, June 25-29, 1984, Clearwater Beach, FL, AMS, 409-417.

Fleming, E. L. and L. E. Spayd, Jr., 1986: Characteristics of western region flash flood events in GOES imagery and conventional data. NOAA Tech Memo NESDIS 13, Washington, DC.

Grice, G. K. and R. A. Maddox, 1982: Synoptic aspects of heavy rain events in south Texas associated with the westerlies. NOAA Tech Memo NWS-106, Fort Worth, TX.

Jiang, Shi and R. A. Scofield, 1987: Mesoscale convective system propagation characteristics in satellite pictures. Submitted for publication as a NOAA/NESDIS Tech Memo.

Maddox, R. A., 1980: Mesoscale convective complexes. Bulletin of the American Meteorological Society, 61, 1374-1387.

Maddox, R. A., C. F. Chapell, and L. R. Hoxit, 1979: Synoptic and mesoscale aspects of flash flood events. Bulletin of the American Meteorological Society, Vol. 60, No. 2, February 1979, 115-123.

Merritt, H. and J. Fritsch, 1984: On the movement of the heavy precipitation areas of mid-latitude mesoscale convective complexes. Proceedings of the Tenth Conference on Weather Forecasting and Analysis, Clearwater Beach, FL, AMS, 529-536.

Scofield, R. A. and Jiang Shi, 1987: Evolutionary characteristics of mesoscale convective systems and extratropical cyclones observed through satellite animation and conventional data. Proceedings of the Workshop on Satellite (and Radar) Imagery Interpretation, Bracknell, UK, 395-414.

Scofield, R. A., 1987a: The NESDIS operational convective precipitation estimation technique. Monthly Weather Review, 115, 1773-1792.

Scofield, R. A., 1987b: Ingredients for a short range forecasting heavy precipitation index. Proceedings of the Seventh Conference on Hydrometeorology, Edmonton, CA, AMS.

Spayd, L. E., Jr., 1982: Estimating rainfall using satellite imagery from warm-top thunderstorms embedded in a synoptic scale cyclonic circulation. Proceedings of the International Symposium on Hydrometeorology, June 13-17, 1982, Denver, CO, AWRA, 139-146.

Spayd, L. E., Jr. and R. A. Scofield, 1984: An experimental satellite-derived heavy convective rainfall short-range forecasting technique. Proceedings of the Tenth Conference on Weather Forecasting and Analysis, June 25-28, 1984, Clearwater Beach, FL, 400-408.

VAS Demonstration: Description and Final Report, 1985. Edited by H. E. Montgomery and L. W. Uccellini, Goddard Space Flight Center, Greenbelt, MD, 198 pp.

VAS Model Impact Studies at NMC

Anthony Mostek and Anthony Siebers
NMC, Techniques Development Group

Ralph Petersen and Dennis Keyser
NMC, Short-Range Modeling Branch

Christopher Hayden and W. P. Menzel
NESDIS, System Design and Applications Branch

1. INTRODUCTION

In the winter season of 1981-82, the National Meteorological Center (NMC), in cooperation with the National Environmental Satellite Data and Information Service (NESDIS), conducted the Eastern Pacific (EPAC) studies. During EPAC, VISSR Atmospheric Sounder (VAS) retrievals were generated over the eastern Pacific for inclusion in the NMC forecast and analysis system. The assumption was made that the increased number of observations available over this data sparse region would yield a comparable improvement in subsequent NMC model forecasts. Unfortunately, the results of these studies have been inconclusive due to a series of problems addressed in Section 2.

NMC has now developed a completely new experimental design which should better exploit the positive aspects of the VAS observations. The short term goal of these studies, called the VAS model impact studies (VMIS), is to establish the impact of VAS retrievals upon NMC's operational analyses and short-term numerical guidance.

Initially, VMIS plans will examine only moisture information gleaned from the VAS retrievals and will focus on a single case of 3 September 1986. The impact of these moisture retrievals will be compared against that obtained from the current operational procedure which is a subjective satellite moisture "bogus" (Smigielski et al., 1982; Timchalk, 1986). Currently, these satellite moisture profiles are the only source of upper-air moisture information over oceanic regions. In a parallel effort, NMC has begun evaluating the quality of TOVS (TIROS Operational Vertical Sounder) moisture retrievals, and will eventually determine the impact upon operational analyses. In the long term, the goal of VMIS is to demonstrate the utility of satellite sounding data within the framework of a 4-dimensional assimilation process.

2. BACKGROUND

The early EPAC studies at NMC were based on the insertion of VAS retrievals into the Limited Fine Mesh (LFM) analysis system by converting a profile of heights at specific levels to various thickness layers. An attempt was then made to interpret the subsequent impact upon the model analyses and forecasts. VAS retrievals were inserted only over the data-sparse eastern Pacific, and only at 1200 GMT, when TOVS soundings were not available in this region. The EPAC study was conducted during the winter season, since the models sometimes have a difficult time forecasting the strong features that can develop over the Pacific at this time of year.

The result of the EPAC experiment's attempts to use VAS data in the LFM model was that no significant or reliable positive impact was achieved. Results obtained from the EPAC studies (Mostek and Olson, 1986 and O'Lenic, 1984 and 1986) were found to be limited by several major factors:

- Being retricted by the LFM model with its coarse resolution.

- Processing VAS data into a radiosonde profile, which smeared any available information.

- Converting specific level height data to thickness; this may not be the correct procedure for using the vertically smooth observations from VAS.

- Bias problems were apparent in the VAS retrievals; these may be seasonally and instrumentally dependent. Some retrievals over the Pacific were done at large zenith angles, which reduce the effectiveness of the soundings.

- Areal coverage was limited to the eastern Pacific and coastal regions only, thus the impact on the initial analysis could not be verified due to the lack of conventional data.

- No microwave channels are available on VAS, so that retrievals are limited to cloud free areas.

- VAS moisture information was not addressed.

- A single insertion of data does not exploit the temporal strength of VAS.

The VMIS effort will attempt to address many of these deficiencies, by beginning with the VAS moisture data. In addition, the findings from other VAS model impact studies (Gal-Chen et al. 1986; Cram and Kaplan, 1985; Douglas, 1986, Hayden and Schreiner, 1984; Thomasell et al. 1986, and Aune et al. 1986) will be incorporated in these studies by NMC.

The inclusion of statistical-based TOVS temperature soundings in NMC models has yielded positive results (Phillips et al. 1979, Tracton et al. 1980). However, a study by (Hirano, 1977 and 1978) indicated that TOVS moisture retrievals were of poor quality and should not be inserted in NMC operational analyses. A more recent study by Timchalk (1986) shows that oceanic TOVS moisture retrievals are at least as good if not better than the moiture "bogus" profiles now used operationally. NESDIS has begun producing experimental physical-based TOVS soundings, which are now being evaluated by NMC. First indications are that temperature, and especially, moisture information is of higher quality than from statistical-based TOVS retrievals. VMIS, along with the parallel effort examining the physical-based TOVS moisture, will establish the relative quality of satellite moisture bogus profiles. The bogus reports contain large deficiencies in clear and undefined oceanic regions, where a default moisture profile category must be assigned (see Timchalk). It is hoped that the VAS, and to some extent TOVS, moisture soundings can eventually replace the bogus reports <u>in clear regions</u>.

3. VMIS PLAN

The goal of VMIS is to assess the potential for including VAS derived information in the operational NMC analysis and forecast system. As a result of the inconclusive results that were obtained when using VAS temperature soundings in earlier studies, the current effort will focus exclusively on VAS moisture information. The VAS instrument contains three channels selected for their sensitivity to water vapor in the atmosphere. The channels (or bands) are numbered 7, 9 and 10 and are centered at 6.7, 7.3 and 12.7 microns, respectively (see Fig. 1). Channel 7's weighting function peaks near the surface, channel 9 between 400 and 600 mb, and channel 10 between 250 and 500 mb. It is hoped that these channels contain enough sensitivity to moisture to provide a vertically smoothed signal of the low, middle and upper level moisture content in the atmosphere with enough horizontal detail to help fill in between the radiosondes. Several studies have shown that VAS does provide a useful moisture signal (Chesters et al., 1983, Robinson et al., 1986). The short-term goal of VMIS is to incorporate these findings into the operational NMC analyses.

The VMIS effort will investigate the use of VAS data to provide the horizontal variations of the gross vertical moisture structures. The model first guess along with radiosonde observations will then be used to fill in the details in the vertical moisture structure. In addition, it should be possible to use the 6.7 micron water vapor channel to monitor the pressure level at which the first millimeter of moisture (or moisture "cap") is present (Stout et al., 1984, 1988). Thus, VAS can provide measurements of both the precipitable water and upper level moisture "cap". Other procedures will be examined, including those used by the European Center for Medium Range Weather Forecasts (ECMWF). This technique converts the one water vapor channel (at 6.3 microns) available on METEOSAT into a single layer of mean relative humidity at mid-levels (Schmetz, 1986). The initial VMIS effort will be restricted to the current VAS processing system as available on the McIDAS (Suomi et al., 1983) and VDUC systems. The thrust of VMIS will be to evaluate the VAS moisture retrieval procedures and to measure the impact of the retrievals on NMC's regional forecast and analysis system.

4. 3 SEPTEMBER 1986 CASE STUDY

A. EXPERIMENT DESIGN

The first phase of this experiment concentrates on an evaluation of the physical retrieval algorithm developed by the NESDIS team on the McIDAS system, rather than immediately inserting VAS moisture data into the NMC models without a thorough understanding of the retrieval characteristics.
Specifically, the VMIS effort has focused on the following:

1) Verification of the access and use of the first guess.

2) Establish dependency of the algorithm on the first guess.

3) Establish where optimal moisture signal is being generated.

4) Establish impact of retrievals on NMC analysis system.

5) Establish impact on NMC Nested Grid Model (NGM) forecasts.

6) Establish impact of moisture bogus data.

To verify the use of the first guess in the <u>V</u>AS <u>R</u>etrieval <u>A</u>lgorithm (VRA), a thorough analysis was conducted

on the impact of the first guess fields upon the resulting retrievals. The VRA requires a first guess for both temperature and dewpoint temperature at all the levels for which a retrieval will be generated (see Smith 1983 for a description of the VAS retrieval algorithm). The first change to the VRA required for VMIS was to use higher resolution forecasts available from NMC's Nested Grid Model (NGM), rather than the LFM or global model fields which were previously used. The original guess fields were compared to the reformatted data used by the VRA. Several deficiencies were discovered. Analyses were being done to the NGM forecast grids prior to insertion into the VRA to convert from polar stereographic projection of the model to a latitude/longitude grid at two degree intervals as required by the VRA. Modifications were then made to produce a higher density grid at one degree intervals to more accurately reflect the higher analysis resolution available from the NGM. The transfer of the NGM forecast grids to McIDAS and VDUC was also modified to include the additional levels available at the low levels between 700 and 1000 mb. Having completed this review, the access and use of the NGM forecasts for a first guess in the VRA is now being done accurately. While it is desirable to access the NGM forecasts directly, without interpolating the grids into a latitude/longitude grid, this will require extensive modifications to the VRA software, which was not feasible at present.

Once the mechanics in the first guess procedures were modified, a thorough evaluation of the sensitivity of the VRA to variations in the guess was begun to test the ability of the VAS retrievals to correct deficiencies in the first guess. To investigate this sensitivity, VAS retrievals were generated using the same radiance dataset but three different first guesses (an analysis and two forecasts from the NGM) all valid at the same time, 1200 GMT 3 September 1986.

The NGM, initialized at this time, forecast a band of heavy precipitation (greater than 75 mm accumulation over 12 hours) extending across the Texas panhandle for the 24 hour forecast (Fig. 2). By 48 hours into the forecast (Fig. 3), the band of heavy precipitation had moved northeastward across central Oklahoma, with precipitation amounts in excess of 80 mm in 12 hours. The band of precipitation actually verified approximately 300 km to the south of the predicted location across the Red River Valley region of Texas and Olkahoma. Although the NGM displaced the precipitation too far to the south, the forecast accumulation amounts were quite good.

Examination of the 1200 GMT 3 September RAFS analyses of850, 700 and 500 mb relative humidity superimposed over radiosonde and satellite moisture observations of relative humidity (Figs. 4,5 and 6) reveals the probable cause of the poor NGM precipitation forecasts. At all three levels, the moisture bogus data contribute to an unrealistically low analysis of relative humidity over the Gulf of Mexico. Most of these bogus reports are the default category relative humidity profile, which assigns low humidity values to the lower troposphere. When the bogus moisture values are compared with the corresponding radiosonde relative humidity values along the Gulf Coast, the unrealistically low bogus values are quite apparent. The flow pattern at these levels transported this dry air over Texas by 24 hours into the forecast and was responsible for preventing the precipitation from developing over the northern part of Texas at this time in the forecast.

VAS moisture data from the VAS retrievals over the Gulf of Mexico for this case have the potential for improving the analyses and short-range forecasts. The VAS retrieval area of coverage extends from 20 to 45 degrees north latitude and 70 to 100 degrees west longitude, which was specifically selected to provide data both over the continental U.S. and over the Gulf of Mexico. This coverage will allow for comparisons in both data rich and data sparse areas.

Three separate first guesses were acquired for the 3 September case: a 00-hour analysis, a 12-hour and a 24-hour NGM forecast all valid at 1200 GMT. These three guesses were then used by the VRA to generate three sets of VAS retrievals. With these three sets of retrievals, a series of comparisons (both qualitative and quantitative) were conducted.

B) RESULTS

The findings of VMIS to this point have entailed evaluating these three sets of retrievals. Figure 7 presents a qualitative display of the large variations that occur with the 700 mb dewpoint fields. The largest variations occur over the Gulf of Mexico where values vary in the model forecasts (Fig. 7-A,-C, -E) from -12 degrees C (00-hour) to -4 degrees C (12-hour) to -15 degrees C (24-hour). These fluctuations in the model analysis and forecasts are quite significant. The VAS retrievals (Fig. 7-B, -D, -F) display the same large variations from -12 degrees C (00-hour) to -5 degrees C (12-hour) to -16 degrees C (24-hour). An example of a large change produced by the VAS retrievals is seen across southern Texas and northern

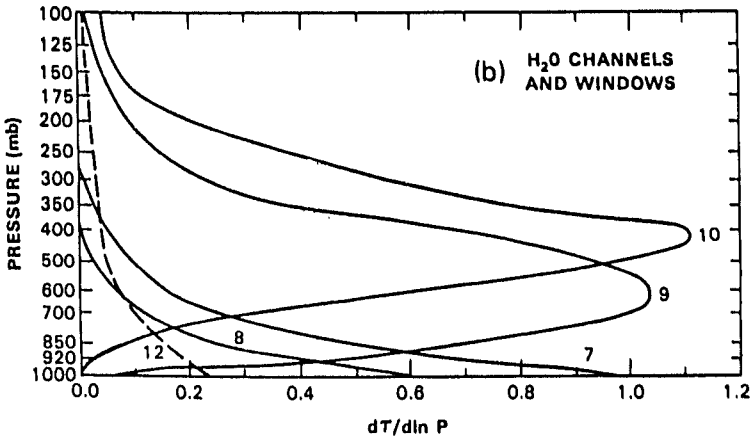

Fig. 1. The VAS weighting functions for U.S. Standard Atmosphere for three water vapor channels (7 at 12.7 microns; 9 at 7.3 microns; 10 at 6.7 microns) and two window channels (8 at 11.2 microns and 12 at 3.9 microns).

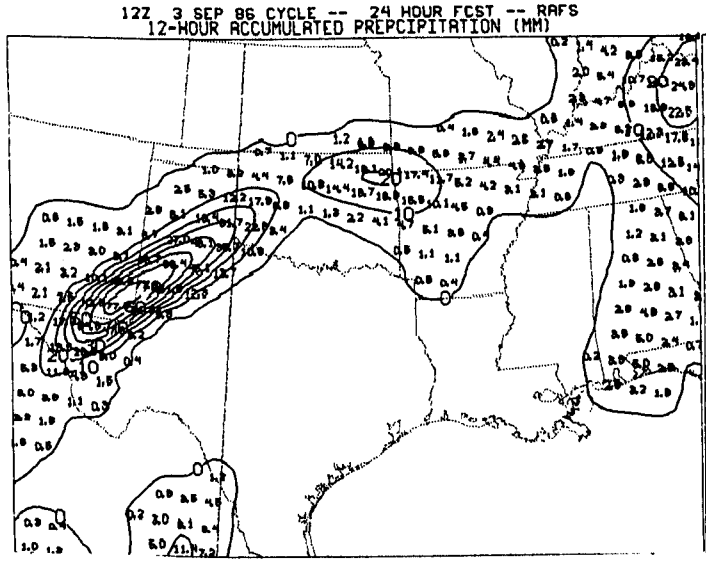

Fig. 2. NGM 12-hour accumulated precipitation 24-hour forecast (in MM) valid at 1200 GMT 4 September 1986.

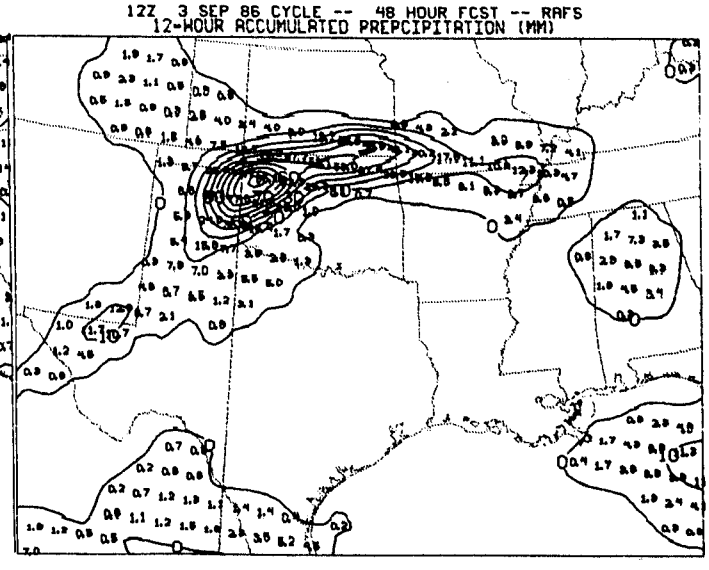

Fig. 3. NGM 48-hour accumulated precipitation 48-hour forecast (in MM) valid at 1200 GMT 4 September 1986.

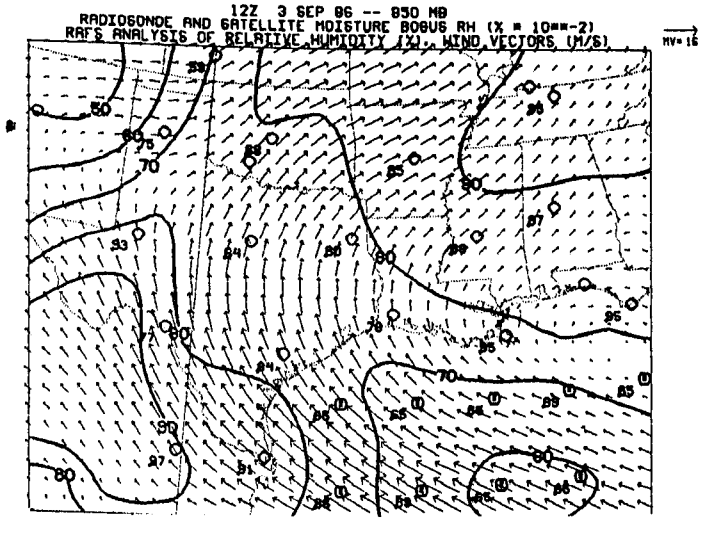

Fig. 4. Radiosonde and satellite bogus relative humidity (%) 850 mb analysis at 1200 GMT 3 September 1986.

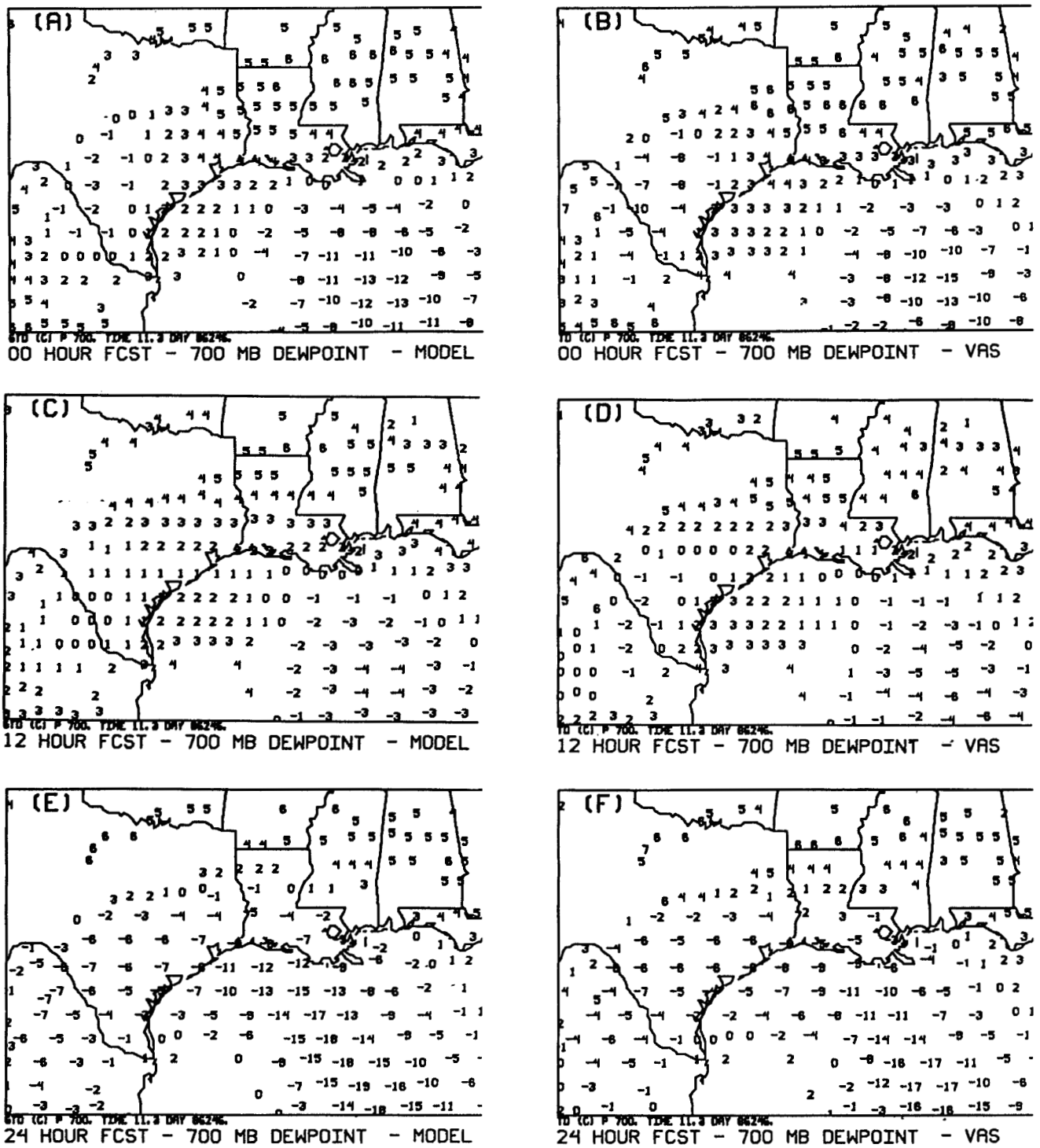

Fig. 7. 700 mb dewpoint temperature plots (degrees C) valid at 1200 GMT 3 September 1986 for (A) 00-hour NGM analysis, (B) 00-hour VAS retrievals, (C) 12-hour NGM forecast, (D) 12-hour VAS retrievals, (E) 24-hour NGM forecast and (F) 24-hour VAS retrievals.

Mexico where the dewpoint values drop by as much as 8 degrees C (compare Fig. 7-A and -B). The 6.7 moisture channel shows a distinct dry band across this area, which may indicate that this channel's effect at 700 mb is too strong. However, using the other two guesses, the impact of VAS over this area is not nearly as strong with modifications to the guess generally limited to 2 degrees C or less.

For a quantitative analysis, RMS statistics are shown in Figs. 8 to 11. Figure 8 shows the three RMS differences between the first guess and VAS retrieval dewpoints for each of the different first guesses, providing an indication of the change made to the first guess by the VAS data. The differences show that below 500 the effect from VAS is small (less than 2 degrees), and above 500 the effect from VAS doubles to almost 5 degrees. This increase shows that the VAS data have a much greater impact on the first guess at these higher levels. This effect should be a direct influence of the two water vapor channels (Fig. 1) at 6.7 and 7.3 microns. The surprising result is the lack of effect at low levels, since the 12.7 micron channel should contribute a stronger signal here.

To look at this finding from another perspective, figures 9 to 11 show the differences among the first guesses (striped) versus the VAS retrievals (solid black). The differences between the guess fields (black) provide a measure of the variability between these fields, while the differences between the retrieved data (striped) give an indication of how the VAS retrieval information is helping to bring the original guess fields towards a common solution. In almost every case, the VAS retrievals reduce the differences between the guesses, which is good news. Again, the reduction in RMS is most noticeable above 700 mb. The important differences in an absolute sense (if the 00-hour analysis is used as a benchmark) are between the 00-hour and the 12- and 24-hour fields (Figs. 9 and 10). At 850 mb and below, the impact is small and even in the wrong sense in a couple of cases. The charts may indicate a problem with the analysis and use of surface moisture data.

In summary, the differences between the guess and the retrievals at 850 mb and above are generally larger than the differences amongst the guesses. The VAS retrievals are reducing the differences between the guesses, in other words, the retrievals are going towards a statistically similar solution. However, at 850 and especially at 700 mb, more variability is still present between the retrieval sets than the modification made to the first guess by the VAS. Another potential pitfall is shown at 850 mb in figures 10 and 11, when the guess deteriorates the VAS data may or may not nudge the guess in the right direction.

The overall findings indicate that:

- The VRA is quite sensitive to the first guess for both temperature (not shown) and dewpoint temperature at all levels reviewed (to 100 mb for temperature and to 300 mb for dewpoint). Variations in the first guess cause a comparable change in the retrievals, although the retrievals tend to converge toward a common solution.

- By comparing the statistics between the VAS retrievals with the same statistics between the first guess fields, the RMS and differences are almost all smaller for the VAS retrievals. In other words, the VAS signal usually applies the same correction to the guess, regardless of the guess. This results in a smaller difference between the VAS retrievals. Without having an absolute correct field (the analysis should be rather accurate over the U.S. area but may still not be too representative over the Gulf of Mexico region - see Fig. 6), the improvement of the VAS retrievals can not be judged in an absolute sense. However, the small reduction in the variance between the sets of the VAS retrievals does indicate a positive result.

Therefore, the overall effect of the VAS data is to modify the first guess fields in a consistent manner, but the changes are only about half that of the difference already present in the first guess in an RMS sense. The VAS data are adjusting the guess in the proper direction, but the adjustment is too small.

5. FUTURE PLANS

Having established that the contribution of the first guess to the VRA is quite significant, the next phase of VMIS will still be to insert the three sets of VAS retrievals into the NMC's regional analysis (Dimego, 1987) used to provide initial conditions for the NGM. The optimum interpolation technique used by the RAFS requires a set of error characteristics for the VAS retrievals before they can be used. These error statistics have been derived and four sets of analyses will be generated for 1200 GMT 3 September 1986. These four analyses (a benchmark analysis based on the current configuration of the RAFS, plus 3 individual analyses based on each first guess) will be compared with a focus on the impact upon the moisture fields. Corresponding NGM forecasts will also be generated from each analysis to

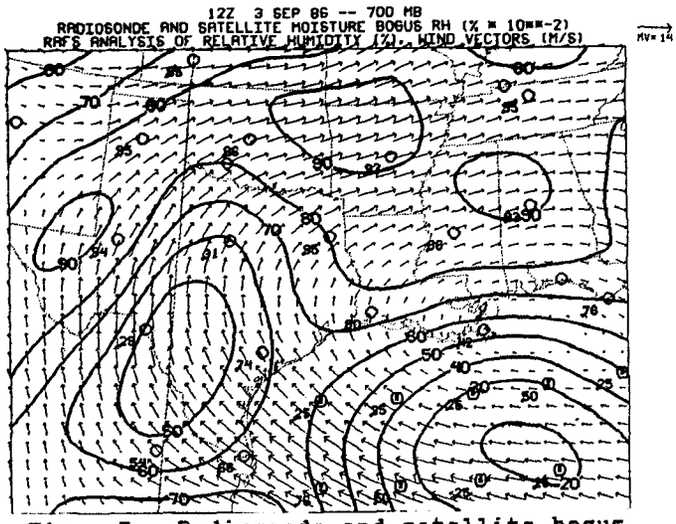

Fig. 5. Radiosonde and satellite bogus relative humidity (%) 700 mb analysis at 1200 GMT 3 September 1986.

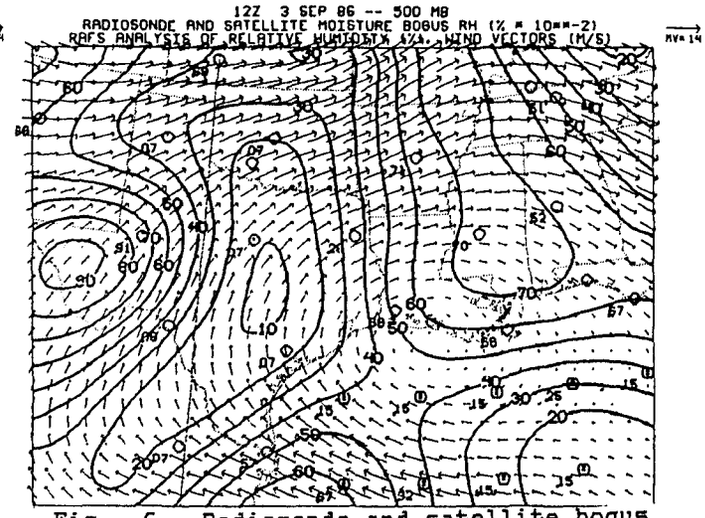

Fig. 6. Radiosonde and satellite bogus relative humidity (%) 500 mb analysis at 1200 GMT 3 September 1986.

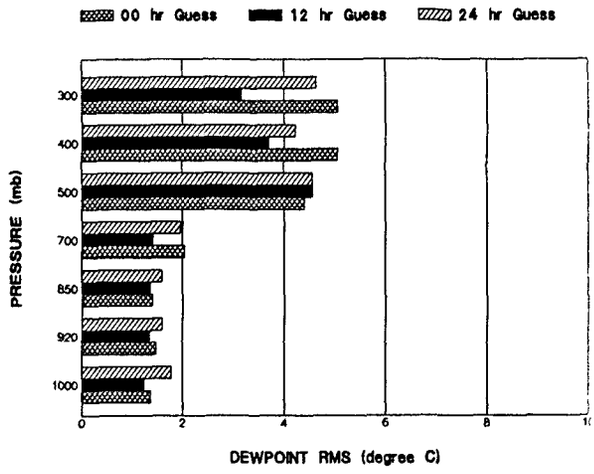

Fig. 8. RMS 700 mb dewpoint temperature differences between NGM guesses and VAS retrievals valid at 1200 GMT 3 September 1986 for 00-hour analysis (cross-hatch), 12-hour forecast (black) and 24-hour forecast (striping).

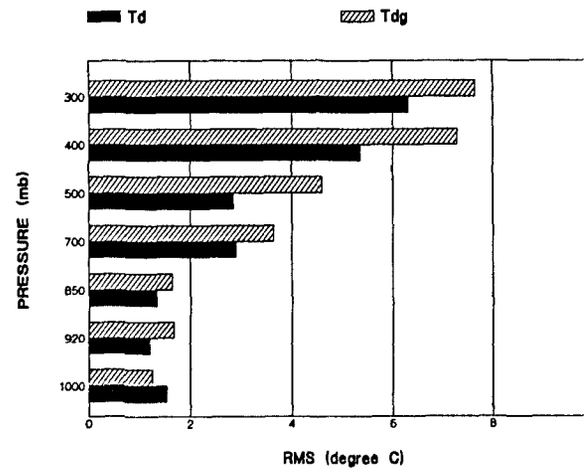

Fig. 9. RMS 700 mb dewpoint temperature differences (degrees C) between 00-hour analysis and 12-hour forecast valid at 1200 GMT 3 September 1986 for NGM guess (striping) and VAS retrievals (black).

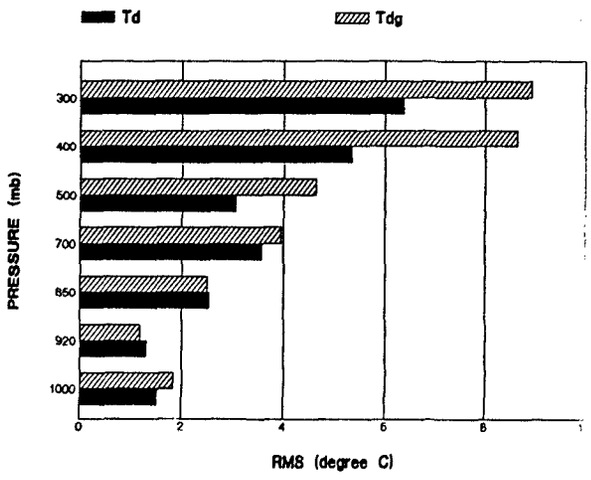

Fig. 10. As in Fig. 9, except between 00-hour analysis and 24-hour forecast.

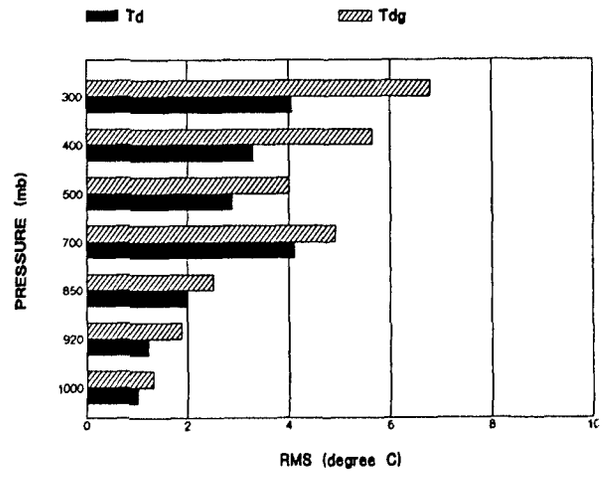

Fig. 11. As in Fig. 9, except between 12-hour and 24-hour forecast.

establish the impact of the VAS data upon the precipitation guidance.

Another effort will be to isolate the effect of the moisture bogus information within the analyses and guess fields. As previously discussed, these data appear to be responsible for the poor NGM precipitation forecasts for the 3 September case. The analysis will be rerun without any moisture bogus information at 1200 GMT 3 September 1986. In addition, the effects of poor moisture bogus data at earlier times on the 1200 GMT 3 September first guess will be removed by eliminating the bogus profiles from the earlier analyses. Then, the RAFS and NGM can be run to produce a "no bogus case", a "no bogus case with VAS", a "no default bogus case" and a "no default bogus case with VAS". These new NGM forecasts may be available by the time of the conference.

A review of the VAS physical retrieval algorithm will be conducted in an effort to tune the algorithm to the moisture signal. The goal here will be to derive only one or two parameters such as precipitable water and mid-level relative humudity. This phase of VMIS will continue to use the data from 3 September 1986.

While this case study continues, the Synoptic Analysis Branch (SAB) of NESDIS will begin generating VAS retrievals for VMIS in real time on the VDUC system beginning in November 1987. These retrieval sets will cover the same geographic area (20 to 45 degrees north latitude and 70 to 100 degrees west longitude). A daily review of the retrieval sets will be conducted and selected sets will be stored for eventual case study. As new techniques are uncovered by the VMIS effort, they will be developed on McIDAS and then implemented on the VDUC for evaluation as part of the cooperative NESDIS/NWS VAS program. One of the first exercises will be to deploy a "split window" technique following the procedure decribed by Robinson et al. 1986 in an attempt to derive a low-level precipitable water product. The next effort will be to develop a mid-level moisture product similar to the process now used at ECMWF. The ultimate goal will be to incorporate VAS derived moisture products within NMC's operational anlysis and forecast system.

6. REFERENCES

Aune, R.M., L.W. Uccellini, R.A. Petersen and J.J. Tuccillo; 1987: A VAS-Numerical model impact study using the Gal-Chen variational approach. Mon. Wea. Rev., 115, 1009-1035.

Chesters,D., L.W. Uccellini and W.D. Robinson; 1983: Low-level water vapor fields from the VISSR Atmospheric Sounder (VAS) "split window" channels. J. Climate Appl. Meteor., 22, 725-743.

Cram, J.M. and M.L. Kaplan; 1985: Variational assimilation of VAS data into a mesoscale model; Assimilation method and sensitivity experiments. Mon. Wea. Rev., 113, 467-484.

Dimego, G.J., 1987: The National Meteorological Center regional analysis system. Accepted in Mon. Wea. Rev., 117, December.

Douglas, S.G.; 1986: Incorporation of VAS satellite data in the initialization of a mesoscale model: An oceanic-cyclogenesis simulation. M.S. Thesis, Pennsylvania State University, 145 pgs.

Gal-Chen, Tzvi; B.D. Schmidt and L.W. Uccellini; 1986: Simulation experiments for testing the assimilation of geostationary satellite temperature retrievals into a numerical prediction model. Mon. Wea. Rev., 114, 1213-1230.

Hayden, C.M. and A.J. Schreiner; 1984: Real time meteorological application of the geostationary satellite sounder on GOES-6: Battling the computer, code and clock. Proc. SPIE Tech. Symp. East, Vol. 481, Arlington, 100-107.

Hirano, R., 1978: Satellite relative humidity bogus using a fixed lat-lon network: The first two weeks. NMC Office Note, March 1978. [Available from the National Meteorological Center, NOAA, Washington DC 20233]

Mostek, Anthony and David A. Olson; 1986:Eastern pacific model impact study (EPAC) at the National Meteorological Center. 2nd Conf. on Satellite Meteorology/Remote Sensing and Applications, Williamsburg, VA, Amer. Meteor. Soc., 164-166.

O'Lenic, Edward A.; 1986: The effect of VISSR Atmospheric Sounder (VAS) data on some LFM analyses and forecasts. Mon. Wea. Rev., 114, 1832-1846.

O'Lenic, Edward A.; 1984: Results of experimental numerical forecasts using temperature profiles from geostationary satellite. Proceedings of SPIE Symposium East, April 29 - May 9, 1984, Crystal City, Va.

Phillips,N., L. McMillin,A. Gruber and D. Wark, 1979: An evaluation of early operational temperature soundings from TIROS-N. Bull. Amer. Meteor. Soc., 60, 1188-1197.

Robinson, W.D., D. Chesters and L.W. Uccellini; 1986: Optimized retrievals of precipitable water fields from combinations of VAS satellite and conventional surface observations. J. Geophysical Res., 91, 5305-5318.

Schmetz, J., 1986: An atmospheric-correction scheme for operational application to METEOSAT infrared measurements. European Space Agency Journal, 10, 145-159.

Smigielski, F., T. Burtt, and S. Hirsch; 1982: Moisture bogus program. NOAA/NESS/SAB Office Operations Note (Chapter 225), February 1982, 22 pgs.

Smith, W.L.; 1983: The retrieval of atmospheric profiles from VAS Geostationary radiance observations. J. Atmos. Sci., 49, 2025-2035.

Stout, J., J. Steranka and R.A. Petersen, 1984: Vertical displacements of the mid-tropospheric water vapor boundary in the tropics derived from the VISSR Atmospheric Sounder (VAS) 6.7 micron channel. Preprints, Conf. on Satellite Meteorology/Remote Sensing and Applications, Clearwater Beach, FL, Amer. Meteor. Soc., 86-89.

Stout, J., J. Steranka, E. Rodgers and R. A. Petersen; 1988: Vertical motion as inferred by the VAS 6.7 micron water vapor channel. 3rd Conf. on Satellite Meteorology/Remote Sensing and Applications, Anaheim, CA, Amer. Meteor. Soc.

Suomi, V.E., R. Fox, S.S. Limaye and W.L. Smith; 1983: McIDAS III: A modern data access and analysis system. J. Clim. and Appl. Met., 22, 766.

Thomasell, A.Jr.,A. Gruber, H. Brodrick, N. Wolfson, Z. Alperson; 1986: The impact of satellite soundings on the numerical forecasts of the Israel meteorological service. Mon. Wea. Rev., 114, 1251-1262.

Timchalk, A.; 1986: Satellite-derived moisture profiles. NOAA Tech. Report NESDIS 24.

Tracton,M.S., A.J. Desmarais, R.Y. van Haaran and R.D. McPherson, 1980: The impact of satellite soundings on the National Meteorological Center's analysis and forecast system - The data system and test results. Mon. Wea. Rev., 108, 543-586.

VERTICAL MOTION AS INFERRED BY THE VAS 6.7 μm WATER VAPOR CHANNEL

John Stout and Joseph Steranka

General Sciences Corporation
Laurel, MD 20707

Edward Rodgers and Ralph Petersen*

Goddard Space Flight Center
Greenbelt, MD 20771

1. INTRODUCTION

Since vertical motions play a role in many theories concerning tropical cyclone intensification and the interaction between tropical cyclones and their upper and middle tropospheric environment, there is a need to measure vertical motion near these storm systems. For example: 1) Riehl (1950) proposed that sinking cold domes adjacent to tropical cyclones release potential energy necessary for tropical cyclone intensification, 2) Arnold (1977) theorized that tropical cyclone formation and intensification may occur when a small region (radius 200 km) of dynamically forced upper tropospheric subsidence is superimposed over a lower tropospheric cyclonic vortex, and 3) Merrill (1984) proposed that the secondary circulation in the entrance region of a jet streak acts to intensify a tropical cyclone by increasing the upper-tropospheric vertical motion in the convective regions of the cyclone.

Vertical motions in the atmosphere are difficult to measure directly. Consequently the most commonly used methods, the quasi-geostrophic omega equation and the kinematic and adiabatic methods, are indirect. Over the subtropical oceans, however, where most tropical cyclones occur, even these techniques are hampered by insufficient measurements of pressure, wind, or temperature.

Satellite measurement in the 6.7 μm infrared band offers an alternative means to detect vertical motion. Several investigators have linked patterns of 6–7 μm brightness temperature (T*) to patterns of presumed vertical motion (e.g., Martin and Salomonson (1970), Ramond, et al. (1981), Petersen, et al. (1983), and Weldon (personal communication)). Shenk and Rodgers (1978) found subsidence in a clear column region computed by the quasi-geostrophic omega equation to correspond to high brightness temperature in the Nimbus 3 6.7 μm channel around hurricane Camille.

In the absence of mid- and upper-level clouds, the 6.7 μm band receives radiation emitted almost completely by water vapor in the mid-troposphere (Chesters, personal communication). The intensity of radiation, indicated by T*, depends on the temperature of the emitting water vapor, which in turn depends on the height of the top of the significant tropospheric water vapor region and the ambient lapse rate. Thus, for example, increasing T* at an individual location indicates either the presence of vertical motion at that point or the lateral transport of air which has previously subsided at another location.

This paper uses the change of topography of the upper-most water vapor layer as a tracer to directly estimate vertical motion in subtropical atmospheres. An equation for vertical motion is derived using the relationship between 6.7 μm T* and the altitude of the upper layer of water vapor. Vertical motion is estimated, from this equation, over the southeastern United States in July, 1984 and then compared to vertical motion derived kinematically from radiosondes.

2. METHOD

The prerequisite to the equation for vertical mo-

* Current affiliation: NOAA/NWS/NMC, Washington, DC 20233

tion is the relationship derived by Stout et al. (1984) between the air pressure of the upper layer of water vapor and the 6.7 μm T*. First, they defined precipitable water depth (D) as the amount of precipitable water integrated downward from the top of the atmosphere. For example, exactly 1 mm of precipitable water exists between the D=1 mm level and the top of the atmosphere. Second, they collected 100 pairs of VAS and radiosonde measurements over the Gulf of Mexico and Caribbean Sea. The use of this subtropical area minimizes the horizontal and temporal variation of temperature so that the temperature variation of the upper layer of water vapor is mostly due to altitude change. Third, they found a linear relationship between pressure (P) at the D=1 mm level and the 6.7 μm T*:

$$P = (11\ mb\,K^{-1})\ T^* + \text{constant} \tag{1}$$

The correlation was 0.70, but the true relationship may be stronger since radiosondes do not accurately measure low amounts of water vapor and water vapor at low temperatures. P was calculated by assigning a dewpoint depression of 30 K to levels that were too dry to measure accurately. If P is instead calculated by assigning zero moisture to those levels, the results would be a correlation of 0.65 and a slope of 22 mb K^{-1}.

We now wish to use this relationship to estimate vertical motion over subtropical oceans, where there is a lack of conventional data, and at a level that may be above dropsondes, which are normally released near 400 mb. Since water vapor is essentially conserved in the mid-troposphere in the absence of clouds, it is a tracer which can be used to follow air motions. Letting P be the pressure at D=1 mm, ω the vertical motion in pressure coordinates, t the time, V the horizontal wind, and ∇ the horizontal gradient,

$$\omega = \frac{\partial P}{\partial t} + V \cdot \nabla P \tag{2}$$

In order to test this method in a simple situation, the advecting term can be eliminated in a maximum of P. Since the gradient of P is zero, (2) can be simplified to

$$\omega = \frac{\partial P}{\partial t} \tag{3}$$

The time difference is taken over a 6 hr period. Combining (3) with (1) gives

$$\omega = 11\ mb\,K^{-1}\ \frac{\partial T^*}{\partial t} \tag{4}$$

In applying the equation to estimate vertical motion the following conditions must be met. 1) No clouds are present except at a low-level. 2) The vertical eddy diffusion of water vapor is small. 3) Horizontal temperature advection is small, which will generally be true in the subtropics. 4) The vertical distribution of water vapor contains no upper thin (about 1 mm) layer of water vapor above a dry layer. If such a moist layer were to become even thinner, due to divergence, it would transmit more radiance from below and falsely appear to be descending. 5) Moisture anomalies at different levels are not becoming superimposed with time due to vertical shear of speed or direction. This condition is also generally met in the subtropics.

3. RESULTS

On 0000 GMT, 20 July 1984, a weak upper- and mid-level trough lay from Ohio south to Mississippi, then west to Texas. The 6.7 μm images on 2030 GMT, 19 July 1984 (Fig. 1), 2330 GMT, 19 July 1984 (Fig. 2), and 0230 GMT, 20 July 1984 (Fig. 3) show a cloud free region with a T* maximum (shown in white) located over Arkansas and northern Mississippi. Subsidence suggested by increasing T* (about 2 K in 6 hr) at the T* maximum is consistent with subsidence expected by quasi-geostrophic theory behind a trough.

At the location of maximum T*, vertical motion was estimated to be 1 $\mu b\,s^{-1}$ near the 650 mb level. For comparison, vertical motion was estimated with a kinematic technique which uses three-dimensional isentropic analysis (Petersen, 1986) and the O'Brien (1970) correction. Fig. 4 shows this estimate interpolated to the D=1 mm surface. At the location of the T* maximum, the kinematic method estimates subsidence at about 2 $\mu b\,s^{-1}$, although considering the large gradient, the subsidence could be anywhere in the range 1–3 $\mu b\,s^{-1}$. If one uses the alternate calculations of P discussed in section 2 (with zero moisture assigned to levels too dry for the radiosonde to measure), the satellite estimate of vertical motion becomes 2 $\mu b\,s^{-1}$ at 800 mb and matches the kinematic estimate. Considering the inaccuracies of vertical motion estimation, agreement within a factor of two is reasonable.

Let us examine the five assumptions listed in section 2 to see that each is satisfied at the location of maximum T*. 1) Images in both the 11 μm window channel and the 6.7 μm channel were examined and found to be free of clouds other than low level clouds. 2) Diffusive processes are thought to be of secondary importance above the boundary layer (Holton, 1979). 3) Horizontal temperature advection was calculated from the radiosonde data and found to be less than $2 \times 10^{-5}\,K\,s^{-1}$ for each of the levels 400, 500, 600, 700 mb. Horizontal advection equal to $2 \times 10^{-5}\,K\,s^{-1}$ at all levels would result in an error in estimating vertical motion of only 0.2 $\mu b\,s^{-1}$, which is smaller than typical values of vertical motion (Holton, 1979). 4) There is no evidence of a thin moist layer, which would most likely have formed from the evaporation of cirrus clouds or strong advection in a thin layer. The 6.7 μm images of six hours prior to the synoptic time were examined and showed no cirrus. In addition, the radiosonde data does not show a thin moist layer within the area in which we will calculate vertical motion. 5) Superpositioning of dry anomalies at different levels would appear in the 6.7 μm images as an elongated maximum of T* which is contracting and brightening with time. However, the observed T* maximum expands with time. Also, horizontal advection of moisture was calculated from the radiosonde data at 400, 500, 600, and 700 mb and showed zero ad-

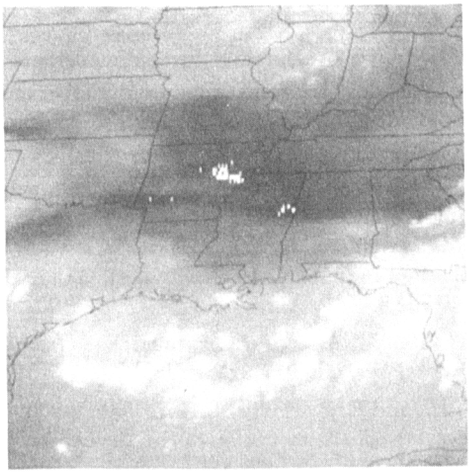

Figure 1. *The VAS 6.7 μm image on 2030 GMT, 19 July 1984. Warmer brightness temperatures are darker, except for temperatures above 258 K which are colored white.*

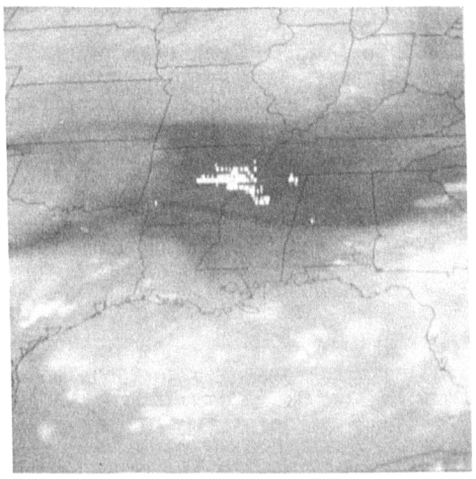

Figure 2. *Same as Fig. 1, but for 2330 GMT, 19 July 1984.*

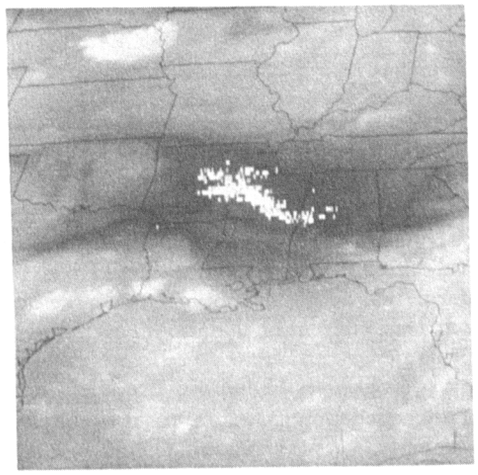

Figure 3. *Same as Fig. 1, but for 0230 GMT, 20 July 1984.*

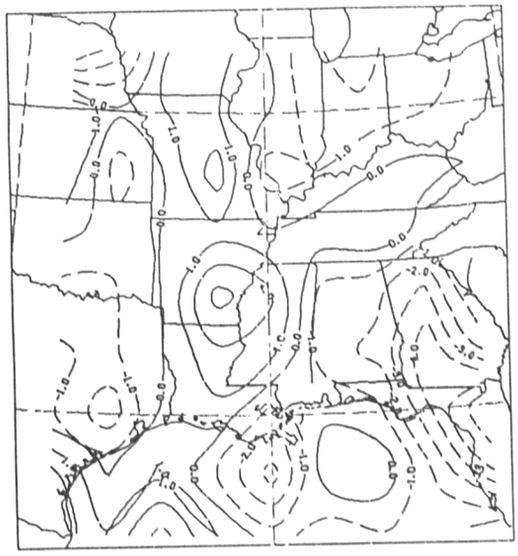

Figure 4. *Vertical motion for 0000 GMT, 20 July 1984, calculated by the kinematic method using the O'Brien correction and three-dimensional isentropic analysis, interpolated to the D=1 mm surface. Contour interval is 1 $\mu b\, s^{-1}$*

vection within 100 km of the T* advection. Finally, wind shear over the 500 to 700 mb layer was less than 5 m s^{-1} at the three stations nearest to the T* maximum. From the observations we conclude that all five assumptions are satisfied.

4. CONCLUSIONS

A method to estimate vertical motion in subtropical atmospheres from the local change of the VAS 6.7 μm channel alone has been successfully demonstrated with one case, although further testing should be done for more complete validation. This technique should add to the store of information about air motions over large oceanic areas, which lack conventional data. The method described in this paper can only be used in regions where the gradient of brightness temperature is small, but calculation of advection using satellite based wind measurement, for example, "water vapor winds," may extend the area of coverage. With advection, vertical motion could be estimated by satellite alone in any region meeting the following criteria: 1) the horizontal temperature advection is small, making this technique useful mainly in the sub-tropics, 2) middle or high level clouds are not and have not recently been present, and 3) moisture anomalies at different levels are not becoming superimposed with time. The authors expect to present two more validation cases: 0000 GMT, 19 July 1984 and 1200 GMT, 20 July 1984. The authors also expect to present estimates of vertical motion in the environment of hurricane Irene of September, 1981 and compare them to Irene's intensity and convection.

REFERENCES

Arnold, C. P., 1977: *Tropical Cyclone Cloud and Intensity Relationship.* Colorado State University, Department of Atmospheric Science, Paper No. 277, 154pp.

Holton, J. R., 1979: *An Introduction to Dynamic Meteorology.* Academic Press, New York, San Francisco, and London, 391 pp.

Martin, F. L., and V. V. Salomonson, 1970: Statistical characteristics of subtropical jet-stream features in terms of MRIR observations from Nimbus II. *J. Appl. Meteor.*, **9**, 508-520.

Merrill, R. T.,1984: Structure of the tropical cyclone outflow layer. *Preprints, Conf. Satellite/ Remote Sensing and Applications*, June 25-29, 1984, Clearwater, FL. Amer. Meteor. Soc., Boston, MA, 421-426.

O'Brien, J. J., 1970: Alternative solutions to the classical vertical velocity problem. *J. Appl. Meteor.*, **9**, 197-203.

Petersen, R. A., D. A. Keyser, A. Mostek, and L. W. Uccellini, 1983: Techniques for diagnosing mesoscale phenomena affecting aviation using VAS satellite data. *Preprints Ninth Conf. on Aero. and Aeron. Meteor.,* Omaha, Amer. Meteor. Soc., 12-17.

Petersen, R. A., 1986: Detailed three-dimensional isentropic isentropic analysis using an objective cross-sectional procedure. *Mon. Wea. Rev.* ,**114**, 719-735.

Ramond, D., H. Corbin, M. Desbois, G. Szejwach and P. Waldteufel, 1981: The dynamics of polar jet streams as depicted by the METEOSAT water vapor channel radiance field. *Mon. Wea. Rev.* , **109**, 2164-2176.

Riehl, H., 1950: A model of hurricane formation. *J. Appl. Phys.*,**21**, 917-925.

Shenk, W. E., and E. B. Rodgers, 1978: Nimbus 3/ATS 3 observations of the evolution of Hurricane Camille. *J. Appl. Meteor.*, **17**, 458-476.

Stout, J., J. Steranka and R. A. Petersen, 1984: Vertical displacements of the mid-tropospheric water vapor boundary in the tropics derived from the VISSR Atmospheric Sounder (VAS) 6.7 μm channel. *Preprints, Conf. Satellite/Remote Sensing and Applications*, June 25-29, 1984, Clearwater, FL. Amer. Meteor. Soc., Boston, MA, 86-89.

TROPICAL SYNOPTIC SIGNATURES IN COMPOSITED 6.7 MICROMETER WATER VAPOR IMAGERY

A. H. Thompson, J. P. McGuirk and D. J. Ulsh

Department of Meteorology
Texas A&M University
College Station, TX 77843-3146

1. INTRODUCTION AND OBJECTIVE

Long plumes or bands of air with above-average moisture content, indicated by extensive cirrus and mixed high and middle clouds, frequently develop near the intertropical convergence zone (ITCZ). These plumes, which we call "moisture bursts," grow rapidly poleward and eastward. These moisture bursts are clearly evident in satellite-derived visual (VIS) and window channel infrared (IR) imagery. The high moisture content of the bursts probably extends beyond the boundaries of the visible cloud mass and provides early indications of the developments.

The objective of this study is to determine the signature and behavior of the moisture bursts as presented in satellite-derived imagery of the 6.7 micrometer water vapor channel (WV) imagery of the GOES system. This is accomplished by constructing composite models from a large number of individual cases of the distribution of 6.7 micrometer brightness temperature from about 48 h before to some 24 h after definition of the burst. The characteristics revealed in these composites are discussed and compared with the signatures of the moisture bursts as seen in VIS and IR imagery.

2. PREVIOUS WORK

Plumes of high clouds originating in the equatorial regions over the eastern and central Pacific Ocean and extending to and across the coasts of Baja California and California were noted frequently in the satellite imagery of the 1960s (Anderson and Oliver, 1970). The first systematic investigation, by Thepenier and Cruette (1981), showed that these tongues of cloud were quite frequent and occurred over other oceans as well.

McGuirk et al. (1987) coined the expression "moisture burst" for these cloud bands. They also carried out an extensive investigation of the frequency and distribution of occurrence over the North Pacific Ocean east of longitude 180°. They define a moisture burst as a band of high clouds or high and middle clouds (oriented roughly NE-SW) at least 2000 km long and extending across latitude 15°N. Their definition also included criteria on beginning and ending times. This definition is objective, but moisture bursts are defined only in terms of the cloud appearance in unenhanced IR imagery from GOES. The studies show that the bursts tend to be phenomena of the northern hemisphere cool season, with about ten bursts occurring each month. Frequency is significantly less during summer and apparently during years of El Niño.

Thepenier and Cruette mention frequent midlatitude cyclogenesis downstream of the moisture bursts. McGuirk et al. also mention such events, while Schroeder (1983) found that about three quarters of the local severe weather outbreaks over North America were related to the interaction of a moisture burst with an extratropical system.

3. DATA AND ANALYSIS TECHNIQUE

The primary satellite data consist of 6.7 micrometer WV imagery from GOES-West and the paired IR imagery, both sets usually available at 6-h intervals. The data period covers 200 days beginning 15 October 1983, thus for the Northern Hemisphere winter season. Use of the 6.7 micrometer data from GOES-West restricts the area of analysis to the eastern Pacific.

Selection of events was based on the tabulation of moisture bursts prepared as part of the study reported by McGuirk et al. These events were defined in terms of their IR signature. Thirty-five events were identified and used in preparation of the composite model. For each event, a "zero time" was established as the time of the satellite imagery nearest the time when the moisture burst first attained a length of 2000 km while extending across latitude 15°N. At this time, the system satisfied the moisture burst definition; for purposes of compositing, this time is termed "definition" time. Additional reference times were established at 48 h and 24 h before, and 24 h after, the definition time. Composite models were synthesized for each of the four reference times. The intent of the earliest composite is to identify the water vapor structure that exists prior to development of the clouds associated with the moisture burst; the -48 h composite is designated "precursor." The composite at -24 h depicts early development moisture structure. Cloud development and initial poleward progression typically commence within a few hours of this composite; it is thus designated as "initiation" time. The +24-h composite is designated as the "mature" stage, and is nominally associated with maximum length of the cloud band.

Another 35 cases without occurrence of a

moisture burst were used to construct a "quiescent" composite model. These cases were selected from the same 200-day period as were the moisture burst cases.

A grid with dimensions of 35° latitude by 60° longitude was used to develop the composites. This grid was divided into squares 5° on a side. Each square was further divided by a NE-SW diagonal, roughly parallel to the axis of the moisture burst; thus, the resulting data appear, effectively, on a staggered grid. The grid is movable, with the origin located with respect to the main cloud mass of the moisture burst. The specific origin, fixed objectively for each individual case, was the northwest "corner" of the main cloud mass as seen in the IR imagery at definition time (the zero time). The origin point of the grid is not the origin point of the moisture burst as defined by McGuirk et al., but rather it was chosen to minimize smoothing of the frequently-seen strong gradient of brightness temperature (in both IR and WV imagery) along the northwest boundary of the burst. The grid's latitude lines were always placed parallel to actual latitude. Once the grid origin was fixed at definition time of a given case, it remained at that point for the other three times of that case.

The grid used for the quiescent cases also was movable, but only with respect to latitude. The zero of relative latitude was positioned at the instantaneous zonal mean latitude of the ITCZ cloud band through the longitudinal extent (165°W to 105°W) of the grid domain.

The displayed gray shades located above the water vapor image were grouped into four gray-shade categories or "brightness temperature indices" (BTI), roughly equally divided across the range of possible gray shades. Category 1, the lowest brightness temperatures, represents deep convective cloudiness. Category 2 is associated with thin or multi-layered cloudiness in the middle or upper troposphere. Categories 3 and 4 are associated with increasing dryness of the middle and upper troposphere. These last two categories represent regions devoid of middle and upper clouds.

Gridding was performed by selecting for each example at the definition time the category (1 through 4) which best matches the gray shade of the small triangular area represented by each grid point. This was repeated for each of the 35 events. Composites were constructed by averaging the BTI at each grid point. Averaged gridded data were contoured. The BTI varies between values of 1 (convective cloud at a gridpoint for nearly every case) and 4 (nearly dry above the boundary layer for nearly every case). Composites were constructed for each of the other times (-48 h, -24 h, and +24 h, and for the quiescent events). The resulting set of five maps represents the composite pattern of the developmental stages of a moisture burst, as seen in WV imagery, and a composite of quiescent conditions in the same imagery. These composite mappings of the WV structure of a moisture burst as shown by the BTI pattern are discussed in the next section.

4. THE WATER VAPOR STRUCTURE OF MOISTURE BURSTS

McGuirk et al. discussed the limitations of describing moisture bursts solely in terms of the appearance in IR imagery. The resulting picture and understanding of moisture bursts is preconditioned by, and limited to, the cloud patterns viewed by IR pictures. Significant modification to our understanding results when moisture bursts are seen from a different point of view -- WV imagery. Weaker systems, precursor signals developing before the clouds appear, and lower tropospheric features are all important examples.

4.1 Quiescent Composite

The quiescent composite represents the water vapor field when there is no defined moisture burst active in the eastern North Pacific area for at least 24 h both before and after the time of each of the 35 cases used in construction. The intent of the quiescent composite is to provide a means for evaluation of the uniqueness and relative strengths of the moisture burst as seen in the four WV composite charts, especially in the water vapor precursor pattern when patterns are not prominent. Note that this composite is "quiet" only in the sense that there are no identifiable moisture bursts occurring in the grid domain within a period of about two days.

The pattern of BTI in the WV channel for the quiescent composite is shown in Fig. 1. In general, the BTI pattern shows a nearly E-W orientation. The general features are of alternating zonal bands of warmer, drier (higher BTI) and colder, wetter features. The moist feature near 0° relative latitude represents the mean position of the ITCZ. It is more moist (lower BTI, suggesting a more active ITCZ in this area) and displaced slightly poleward on the east side of the domain. The dry features north and south appear to be evidence of the mean location of the subsiding branch of the Hadley Cell circulation. On the northern side, the Hadley circulation appears asymmetric, with the ascending branch stronger to the east and the descending branch stronger to the west; of course, this is not a closed circulation. The moist feature on the northern edge of the composite is likely the southern edge of the climatological position of an upper-level, difluent trough in the westerlies (Palmén and Newton, 1969), and the generally more moist

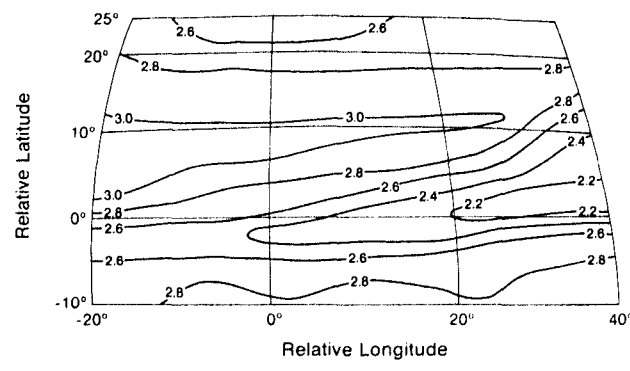

Fig. 1. Composite water vapor mapping for the quiescent (non-moisture burst) events. Isopleths are brightness temperature index, with low being moist.

atmosphere to the north of the subtropical highs of the northern hemisphere.

4.2 Precursor Composite (48 h before definition)

McGuirk et al. (1987) state that the first distinct poleward advance, seen in VIS and/or IR imagery, of the clouds of a developing moisture burst begin some 12 to 24 h before the burst reaches initial maturity. Figure 2, a composite of the distribution of BTI 48 h before the burst reaches maturity, suggests that WV imagery provides useful information much earlier. Three features are worthy of note. The ITCZ contains two active, or moist, regions separated by a drier region between relative longitudes +5° and +20°. A line drawn along the axis of the low BTI region suggests a wave pattern along the ITCZ with a crest near relative latitude +1° and relative longitude +6°. The distribution of variance of the BTI suggests that the dry (high BTI values) region is a realistic and statistically significant feature, as is the wave-like pattern.

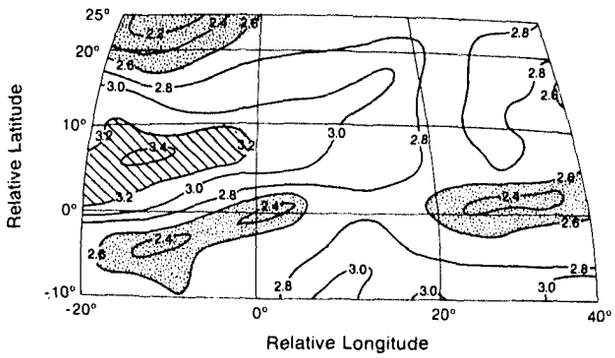

Fig. 2. As in Fig. 1, except for precursor composite, 48 h before moisture burst definition. In this and later diagrams, stippled areas are relatively moist; hatched areas are dry.

The second feature is the ENE-WSW axis of high BTIs parallel to, and some 1300 km to the NNW of, the moist belt. A similar, but weaker, feature is seen south of the ITCZ band. The gradient of BTI is a maximum between the ITCZ and the high BTIs to the NNW.

The third feature is the region of low BITs in the northwest corner of the grid to the north of the dry center. It has the appearance and position suggesting a middle-latitude wave in the polar westerlies (the absolute latitude of the northern boundary of the composite chart is near 35°N). A check of individual cases shows that over three-fourths have a cloud mass in this position which fits the description of a cold-frontal band in IR imagery.

A graphical subtraction (Fig. 3) of the quiescent composite from the composite of 48 h before moisture burst maturity emphasizes the features and anomalies in the precursor composite. Note for example the increase of BTI east of the grid origin and the decrease near and southwest of the origin. Also, note the indication of strengthening of the BTI gradient north

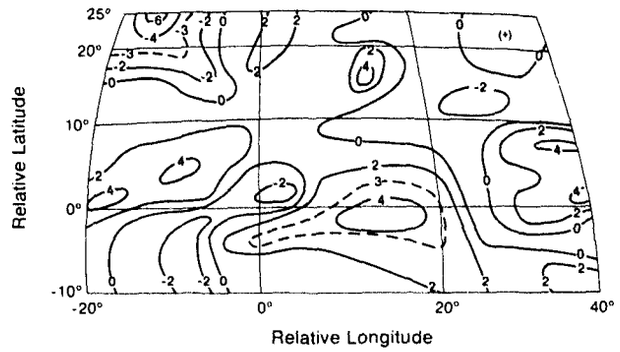

Fig. 3. Graphical subtraction of the quiescent composite (Fig. 1) from the precursor composite (Fig. 2). Contours are BTI values multiplied by 10, with positive signifying drier than quiescent.

of the ITCZ west of the origin and the large drop in BTI in the NW corner of the chart. The spacing of anomaly centers along the ITCZ suggests a wave of length near 4000 km.

4.3 Initiation Composite (24 h before definition)

The composite constructed for 24 h before burst definition (Fig. 4) reveals features similar to those of Fig. 2, though with significant differences. The moist area along the ITCZ is no longer split, and the BTI values indicate that there is less convective activity than earlier west of the grid origin, while the BTI values east of the grid origin have decreased (moistened); the 2.6 BTI contour has expanded significantly meridionally. The maximum decrease occurs about 1500 km east of the origin, suggesting the probability of maximum convective activity there. However, there is little evidence of a moist axis developing extensively to the NE in advance of the developing moisture burst; northeastward cloud progression commences within 12 h after the initiation composite of Fig. 4. Both the dry region to the NW of the origin and the strong gradient of BTI continue as dominant features;

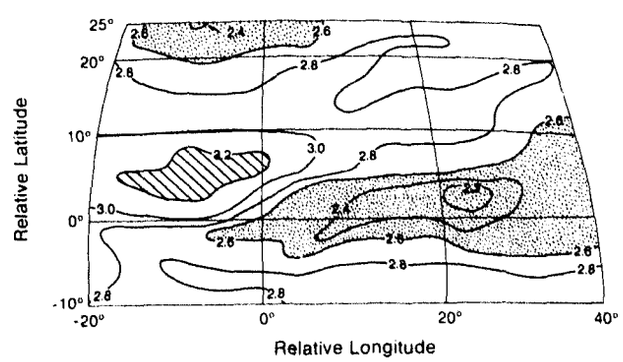

Fig. 4. As in Fig. 1, except for initiation composite 24 h before definition.

the counterclockwise turning of the strong-gradient axis is the principal indicator of the evolving burst. The axis has extended all the way to the northeast corner of the domain, although the strong gradient is confined to within about 5° of the ITCZ. The moist middle latitude feature in the NW portion of the composite shows significant drying (increase in BTI) and spreading with decreasing gradient of BTI during the 24-h interval before Fig. 4. This indicates either a weakening of the dynamic mechanism associated with this feature or a rapid movement or both. Recall that the origin of the composite is effectively fixed in position, so eastward propagation of the feature nearer the westerly belt is expected. 24-h changes from precursor to initiation composite are shown quantitatively in Fig. 5, which is the graphical subtraction of the pattern of Fig. 2 from that of Fig. 4. The pattern reflects intensification of the ITCZ wave, a narrow warming/drying band on the north side of the ITCZ, a broader moistening band further north, and another drying band on the northern border of the domain.

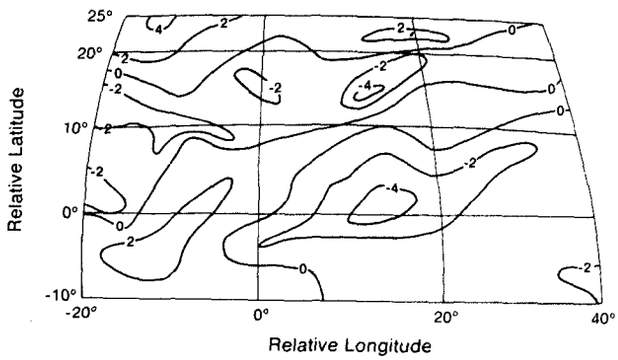

Fig. 5. 24-h BTI change from the composites 48 h and 24 h before definition computed by graphically subtracting Fig. 2 from Fig. 4. Contours as in Fig. 3.

4.4 Definition Composite (zero time)

During the 24 h following initiation (Fig. 4), the moisture burst grows from no indication in VIS or window channel imagery to an extensive plume of visible cloud at least 2000 km in length and crossing 15°N (absolute latitude). By this burst definition time ("zero time"), the corresponding WV composite (Fig. 6) presents a very distinct pattern of a mature burst:

* An elliptical area of low BTI oriented NE-SW and centered some 1600 km to the ENE of the origin point.
* A region of quite high BTI with long axis E-W centered some 800 km NW of the origin point.
* A strong gradient of BTI on the south side and especially on the west side of the burst.

In addition, indications of the ITCZ extend both east and west along 0° relative latitude, with an indication that the western part is slightly south of and considerably weaker than, the eastern part. As in the earlier composites, a

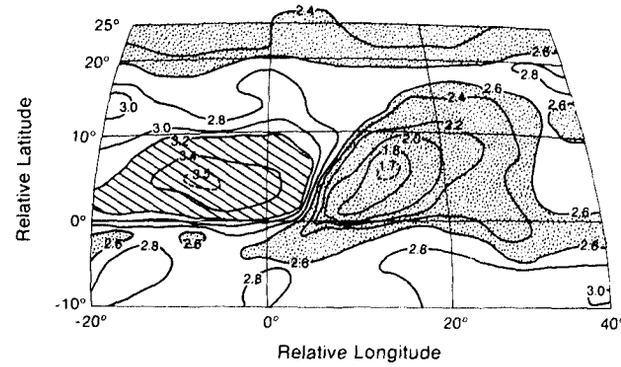

Fig. 6. As in Fig. 1, except for definition time.

wave pattern along the ITCZ is visible, and appears to have amplified. The northern edge of the composite shows weak indications of two moist pockets spaced about 3000 km apart.

The extent of the moisture burst cloud band at this time exceeded 4000 km from the 2.6 BTI line near the grid origin to the same line at the leading edge of the burst. The minimum value of BTI of 1.7 suggests significant deep convection. The signature for the definition stage of the burst as displayed in the WV channel data is very like that displayed in window channel and/or visible imagery.

The 24-h change chart for the period ending at definition time (Fig. 7) supports the concept of the near explosive development of the moist area northeast of the grid origin, and continued wave intensification. Note the drop of BTI of a full unit some 1400 km ENE of the origin and the significant rise of BTI north and northwest of the origin. Along with the cloud generation along the moisture burst axis there was significant drying immediately west of the moisture burst. However, this dry area seems to develop well before definition time; the BTI increases in this area appear to be associated mainly with eastward movement of the moisture burst system through the grid.

Comparison (not pictured) of the quiescent stage (Fig. 1) with the definition composite (Fig. 6) shows that the moisture burst exhibits a coherent pattern of anomalies over a

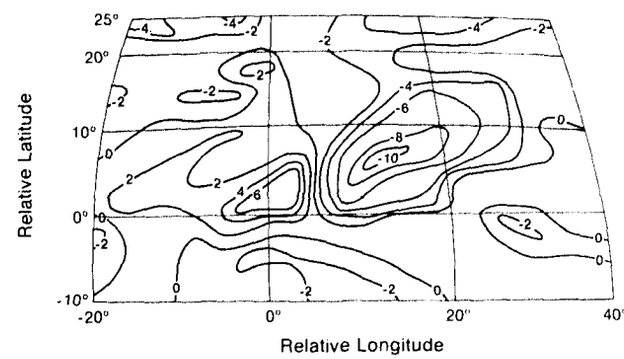

Fig. 7. As in Fig. 5, except for the composites 24 h before and at the definition time.

significant portion of the eastern Pacific environment.

4.5 Mature Composite (24 h after definition)

The final moisture burst composite in Fig. 8, constructed for 24 h after the initial maturity time, shows features similar to those at definition (Fig. 6) except that the burst has had time to spread further NE and gradients and sharpness of the features have decreased. The low BTI center associated with the burst also has shown a significant increase in value (a drying). This drying is probably a combination of weakening of the moisture burst dynamics and variation in the orientation of the burst from case to case. The variation is likely the less significant of these factors since the area of the 2.6 BTI isoline has shown little change from the definition composite.

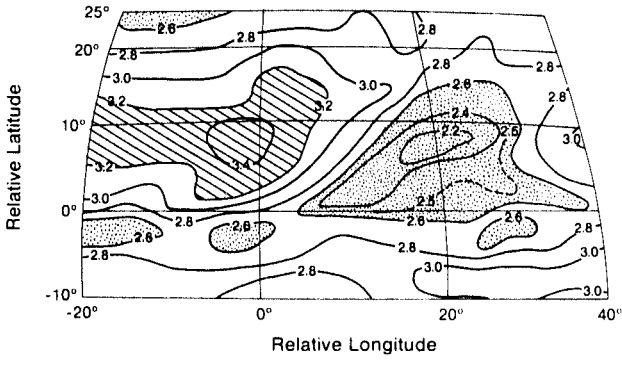

Fig. 8. As in Fig. 1, except mature composite, 24 h after definition.

The dry area to the west of the burst has shown only slight weakening (moistening) as contrasted with the pronounced change in the moist area. There also is slight indication of rejuvenation of convective activity along the ITCZ, away from the moisture burst.

5. A MODEL OF DEVELOPMENT IN WATER VAPOR IMAGERY

The composites described in the preceding section contain sufficient consistency and continuity to allow construction of a model describing the development of the synoptic entity which we call a "moisture burst" in terms of its characteristics in 6.7 micrometer imagery. The model contains four stages, based on the four composites:

a) Precursor: about 48 h before definition.
b) Initiation: about 24 h before definition.
c) Definition stage: Identified moisture burst.
d) Mature stage: 24 h after definition.

In some cases, the system may not begin actual dissipation until much longer than 24 h after initially reaching maturity -- bursts have lasted as long as 10 d.

Examination of the composites, of the water vapor imagery themselves, and of the corresponding window channel imagery, indicated a relationship between the BTI contours and the existence of middle and upper tropospheric clouds on window channel imagery. The 2.6 BTI contour seems to be the average cloud/no cloud cutoff value for middle/upper troposphere. Similarly, the 3.2 BTI contour is assumed to be the boundary of the region of enhanced subsidence to the west of the (incipient) burst region. This value represents an area that is somewhat drier than the normal background signal of the quiescent composite.

Three separate signals are recognizable in the composites and are transferred to the model (Fig. 9). The first is the wetter (lower BTI) values of the ITCZ, labelled A in the model. This signal later becomes the moisture burst. The signal labelled B is the encroaching mid-latitude trough to the NW. C is the region of enhanced dryness associated with subsidence west of the burst origin region. These signals are represented by the appropriately-labelled stippled areas in Fig. 9.

Fig. 9a represents the precursor stage, when the ITCZ (with its axis represented by the dashed line) has a section of relative minimum convective activity a short distance downstream from the origin of the burst-to-be and between the two active areas A. The approaching middle-latitude trough (B) and the dry region of suppressed activity (C) are shown at the upper left and left center, respectively. The solid lines with directional indications suggest the upper tropospheric flow pattern of the precursor stage: the intensifying middle latitude trough in the northwest and the cross-equatorial flow into a speed maximum immediately west of the burst origin and thus directly over the region of maximum gradient of BTI. These wind fields were determined by use of the individual wind analyses of the European Centre for Medium Range Weather Forecasting.

Fig. 9b represents the initiation stage some 24 h before burst definition, and usually shortly before the burst is apparent in window channel imagery. By this time, convective activity, signal A, has decreased along the western portion of the ITCZ and increased in the central section where the wave crest is located. Signal B shows some spreading eastward, while signal C also moves to the east. The flow from northwest associated with signal B has moved equatorward and shows strong confluence and an associated speed maximum near the burst origin in association with the cross-equatorial flow. The visual manifestations of the moisture burst are not yet present. Nonetheless, the indications of burst development are definite in terms of evolving wind pattern.

Fig. 9c shows signal C near maximum extent and signal A showing extensive development to the NE as the winds east of the origin back, and the ITCZ wave continues to intensify.

The continued maintenance or gradual dissipation of the burst is shown in Fig. 9d, with the upper trough retreating poleward and the convection of the ITCZ reestablishing itself. The gradient between signals A and C shows distinct weakening by this time.

6. CONCLUSIONS

A model of the signatures of a synoptic development as seen in 6.7 micrometer water

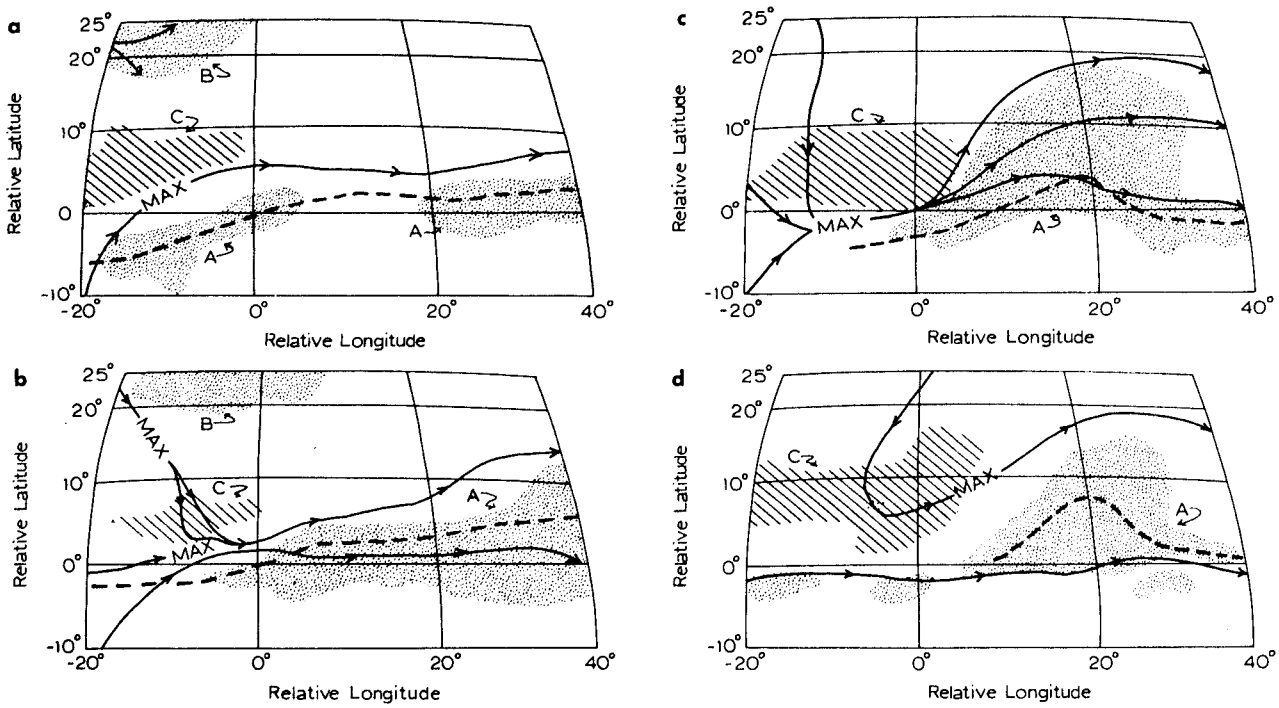

Fig. 9. A model of moisture burst development as seen in 6.7 micrometer water vapor imagery. a. Precursor stage. b. Initiation stage. c. Definition stage. d. Mature stage. Symbols are explained in text.

vapor channel imagery is constructed easily from a composite of cases, in this example a moisture burst over the eastern Pacific Ocean. Some of the signatures appear in the water vapor imagery before appearance in the window channel or visible imagery.

One of the advantages, not previously discussed, of using this form of satellite imagery is that it uniquely clarifies the role of the tropics in the evolution of moisture bursts. Previous studies (Anderson and Oliver, 1970) focus on the important mid-latitude aspects to the near exclusion of any active tropical role. The WV imagery, particularly the 24-h change maps, focus on important tropical development, almost to the exclusion of mid-latitude features. This emphasis has been an unexpected benefit of WV images.

Finally, a test of the forecast capability of the model was performed on 120 consecutive days including 29 moisture bursts. A meteorologist given 2 h of training with the models was able successfully to forecast 19 (65%) of the bursts at least 24 h in advance of definition. In only 6 cases were bursts forecast when none occurred. Forecast failures were dominated by situations of multiple synoptic systems in the Pacific domain. This preliminary test suggests that the precursor signals in 6.7 micrometer water vapor imagery are sufficiently robust to allow significant forecasting skill over 24 to 48 h.

Acknowledgements. This study was supported partially by the Marshall Space Flight Center, NASA, under Contracts NAS8-35182 and NAS8-37284. Conclusions are those of the authors.

References

Anderson, R., and V. Oliver, 1970: Some examples of the use of synchronous satellite pictures for studying changes in tropical cloudiness. Proc. Symposium on Tropical Meteorology, Honolulu, Amer. Meteor. Soc., E XII 1-6.

McGuirk, J., A. Thompson and N. Smith, 1987: Moisture bursts over the tropical Pacific Ocean. Mon. Wea. Rev., 115, 787-798.

Palmén, E., and C. Newton, 1969: Atmospheric Circulation Systems, Academic Press, 603 pp.

Schroeder, T., 1983: The subtropical jet stream and severe local storms - a view from the tropics. Preprints 13th Conf. on Severe Local Storms, Tulsa, OK, Amer. Meteor. Soc., 161-162.

Thepenier, R., and D. Cruette, 1981: Formation of cloud bands associated with the American subtropical jet stream and their interaction with midlatitude synoptic disturbances reaching Europe. Mon. Wea. Rev., 109, 2209-2220.

SATELLITE DIAGNOSIS OF TROPICAL CYCLONES

Raymond M. Zehr

Regional and Mesoscale Meteorology Branch, NOAA/NESDIS
Cooperative Instiute for Research in the Atmosphere (CIRA)
Colorado State University, Fort Collins, Colorado

1. INTRODUCTION

Satellite images have historically played an important role in analysis and forecasting of tropical cyclones. This has been mainly a result of detection and tracking. In fact, it is only since the advent of satellites that an accurate global climatology of tropical cyclones has been possible. More recently, with the availability digital satellite data from geostationary satellites, and computer-based image display systems and workstations; quantitative satellite-derived information has been used by researchers and operational forecasters. The most useful quantitative data has been the equivalent blackbody temperatures from the infrared image data. The infrared temperatures provide estimates of the extent and intensity of deep convective clouds which grow to near or above tropopause height. A large portion of the tropical cyclone cloud shield consists of thin, non-precipitating cirrus clouds. For example, the familiar infrared cloud image of a tropical cyclone (often shown without image enhancement) typically includes infrared temperatures ranging from -10°C to -85°C. It is important to use a sufficiently cold temperature threshold to differentiate the active deep convective regions from the total cloud shield.

Previous studies (Adler and Rodgers, 1977; Gentry, et al., 1980; Steranka, et al., 1986) have shown relationships between satellite infrared cloud measurements and tropical cyclone intensity changes. Dvorak (1984) has developed a technique to estimate tropical cyclone intensity based on subjective identification of features in the visible and infrared images. His method also includes an objective algorithm for mature tropical cyclones computed from the infrared cloud top temperature field. Dvorak's technique has been used operationally for several years.

This paper reports on some preliminary results of an extensive project to not only improve intensity estimates of tropical cyclones, but also extend satellite diagnosis to other attributes such as outer core wind distribution and tropical cyclone genesis. One of the drawbacks of tropical cyclone research with satellite data has been the lack of high quality data sets to verify the satellite diagnosis. An extensive data set has been compiled from U.S. Air Force reconnaissance flights in the West Pacific. This aircraft data set is used along with the satellite data for the findings presented in this paper. Three-hourly GMS (geostationary at 140°E) satellite data at 10 km resolution have been extensively analyzed for 48 tropical storms and typhoons during 1983-1984. This is a unique data combination which is suitable for research addressing a wide variety of topics including tropical cyclone motion and genesis.

2. GMS SATELLITE DATA

The GMS data sets used for this study were extracted from the ISCCP (International Satellite Cloud Climatology Project) archive, which is comprised of full disk image files at 10 km resolution for both visible and infrared at three-hour intervals (World Climate Research Programme, 1985). Each 10 km by 10 km data point (pixel) has a count value, calibrated to radiance. For infrared image data, this can be converted to a brightness temperature (T_B), which is often referred to as equivalent blackbody temperature. Since infrared image data is sensed at the 11.2 micrometer wavelength (the window region), the clear atmosphere is nearly transparent and T_B measures the radiative temperature of the cloud, the surface, or combinations of the two within the 10 km square field. The range of T_B associated with each count value varies from about 0.5°C to 2.0°C. Therefore, the infrared image data can be color enhanced, shaded, etc., to a resolution of approximately 1.5°C at typical cloud top temperature.

3. RECONNAISSANCE DATA

Observations from the U.S. Air Force storm reconnaissance missions during 1977 through 1984 have been compiled at Colorado State University by Dr. William M. Gray and staff. These data have been used for previous studies of typhoon wind profile variability (Weatherford, 1985, 1987) and tropical cyclone genesis (Lunney, 1987; Middlebrooke, 1987). The observations were taken aboard WC-130 aircraft at 15-minute intervals. They include measurements of sea surface temperature, flight level temperature and dewpoint, flight level wind direction and speed, and sea-level pressure extrapolated to the surface from a flight level D-value (Henderson, 1978). Two kinds of flight missions are tasked by the Joint Typhoon Warning Center (JTWC) at Guam: investigative missions (invests) and fix missions. The invests are flown at low-level (1500 feet) to determine whether or not a low-level circulation center exists in a suspect area. Fix missions are flown at 700 mb to pinpoint the location of a tropical cyclone already known to exist.

4. PRELIMINARY RESULTS BASED ON 1983-1984 WEST PACIFIC TROPICAL CYCLONES

Time series plots of cloud areas derived from the infrared GMS data were produced for the entire life cycle of each tropical cyclone including at least two days prior to classification as a tropical depression. Cloud areas were defined by circular cyclone-centered areas ranging from one to eight degrees latitude radius, and infrared temperature thresholds ranging from -55°C to -85°C. Time series of observations from each aircraft mission were also plotted. Analyses for a variety of combinations of cloud area definitions have been plotted as time series for most of the West Pacific tropical cyclones during 1983-1984.

A few of these plots have been selected to illustrate some important points regarding objective satellite diagnosis for three different topics: 1) tropical cyclone intensity changes, 2) tropical cyclone size and outer core winds, and 3) tropical cyclone genesis.

a. Intensity

Tropical cyclone intensity is generally expressed as either maximum sustained wind speed or minimum sea-level pressure. Figure 1 shows plots of area of infrared temperature less than -65° C within 6 degrees radius for three typhoons. The minimum sea-level pressure for each typhoon is plotted in Figure 2. A very large diurnal variation with an early morning local time maximum is noted. This diurnal variation is described in detail by Zehr (1987). A 24-hour running mean of the satellite observations effectively removes the diurnal variation and allows the changes in deep convection to be more readily related to intensity changes.

Figures 3, 4, and 5 are plots of the 24-hour running mean of infrared cloud areas less than -75°c, for radius out to 4, 2, and 1 degrees latitude respectively. Each figure includes notation of the time the cyclone attained tropical storm intensity (35-knot sustained winds), typhoon intensity (64 kt) and maximum intensity. The maximum cold cloud areas are associated with deepening typhoons while filling systems show rapidly decreasing convective cloudiness. Note that for each typhoon, the peak in cold cloud area precedes maximum intensity. In addition, the deep convective cloud areas located near cyclone center (Figs. 4 and 5) relate better to intensity change than the cold cloud areas for the larger areas (Figs. 1 and 3). The observation that a maximum in satellite-derived cold cloudiness precedes maximum tropical cyclone intensity has been shown by several previous studies (Gentry, et al., 1980; Motoki and Shimada, 1986; Steranka, et al., 1986; Zehr, 1987). It has not yet been determined whether an objective satellite-derived quantity can consistently and accurately estimate intensity change for a large sample of tropical cyclones.

When one compares cold cloud area extent to intensity for a number of different storms, three main conclusions become apparent regarding the relationship between satellite estimates of deep convection and tropical cyclone intensities. 1. Deep convection intensity and extent correlate better with intensity change than with absolute

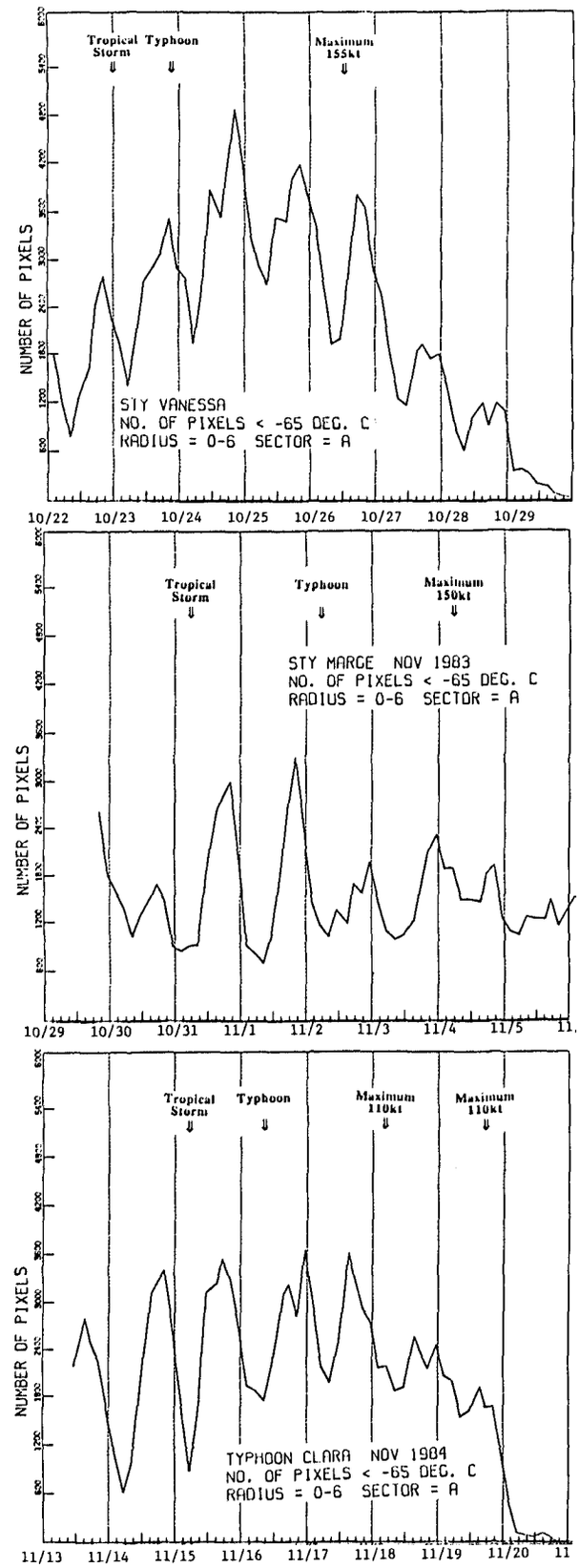

Fig. 1. Area of infrared temperature less than -65°C, within 6 degrees latitude of cyclone center. Each pixel equals approximately 100 km^2. Date and time are given in GMT. The dashed vertical lines are 00 GMT. a. Supertyphoon Vanessa. b. Supertyphoon Marge. c. Typhoon Clara.

intensity. 2. Convective cloudiness close to the cyclone center relates better to intensity changes, as opposed to convection over a large area which includes the entire cyclone circulation. 3. Intensity estimates should be based on cold cloud areas which are circularly symmetric around the cyclone center. This conclusion follows from the observation that some tropical cyclones in a strongly sheared environment may have extensive cold cloud areas, but their intensity is inhibited due to the low-level center being displaced from the deep convection.

These conclusions illustrate why the subjective, empirical rules included in the intensity estimate technique developed by Dvorak (1984) have shown more success in than any simple quantitative satellite-derived measure of intensity. This is particularly true for early stages of development.

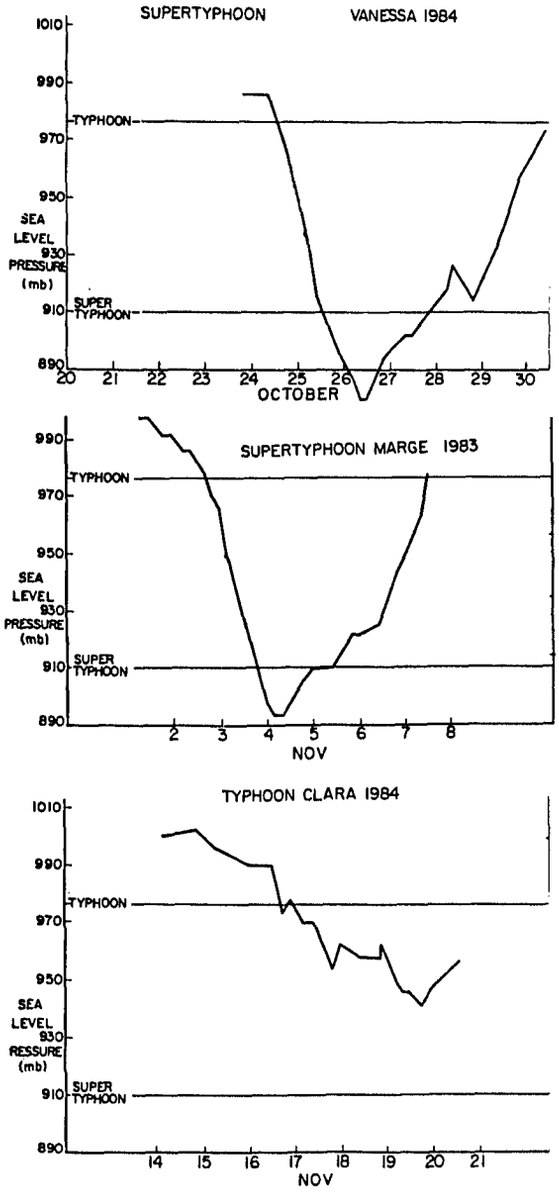

Fig. 2. Time series of minimum sea-level pressure (from Weatherford, 1985). a. Supertyphoon Vanessa. b. Supertyphoon Marge. c. Typhoon Clara.

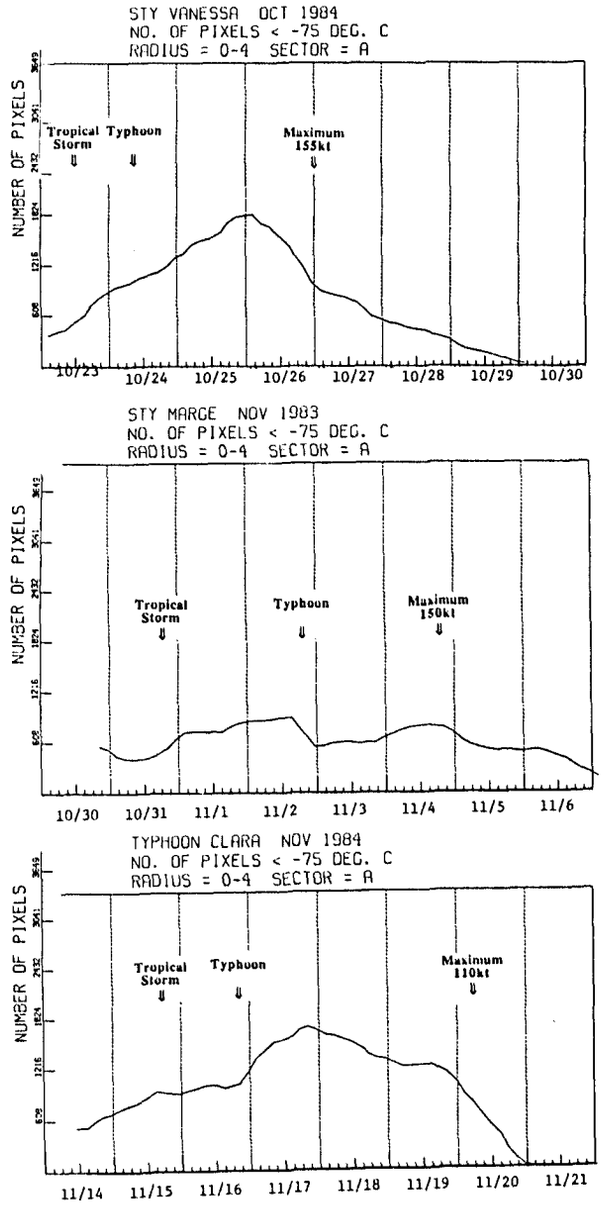

Fig. 3. 24-hour running mean of infrared cloud areas with temperature less than -75°C, within 4 degrees latitude of cyclone center (R=0-4°). Data is plotted centered on the period of each 24-hour mean. Times of first tropical storm, typhoon, and maximum intensities are indicated. a. Supertyphoon Vanessa. b. Supertyphoon Marge. c. Typhoon Clara.

b. Size and outer core winds

As shown by Merrill (1984) and Weatherford (1985) the size of a tropical cyclone circulation and the wind speeds outside the radius of maximum winds are attributes which are somewhat independent of intensity. The size can be defined by the "outer closed isobar" or radius of 30-knot winds. For practical, operational purposes, the radius of 50-knot winds is also an important parameter. Weatherford and Gray (1987) have defined a quantity termed outer-core wind strength

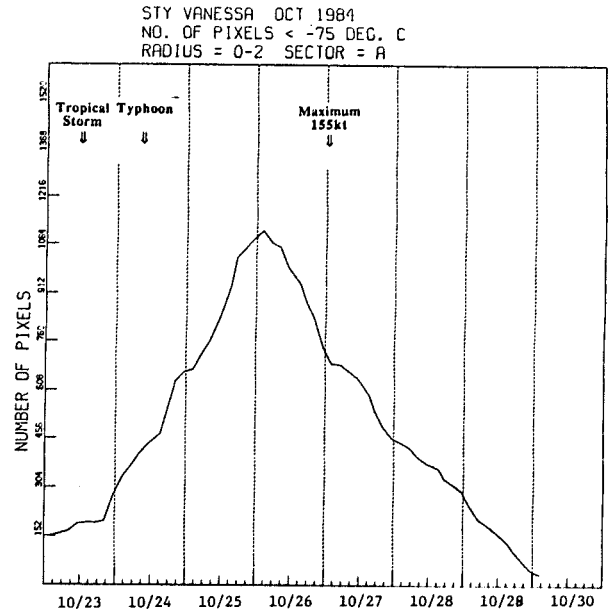

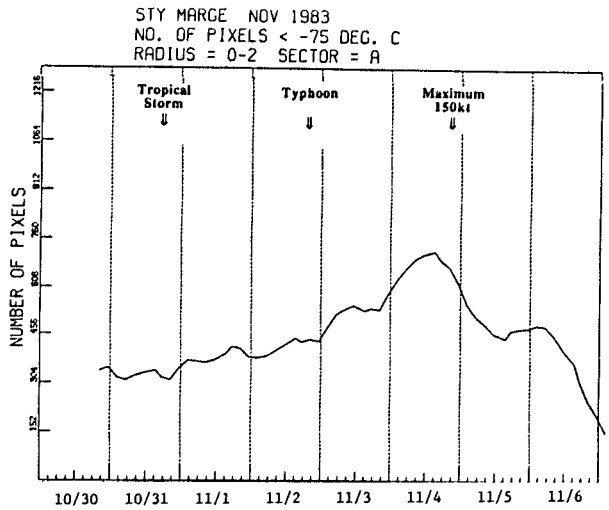

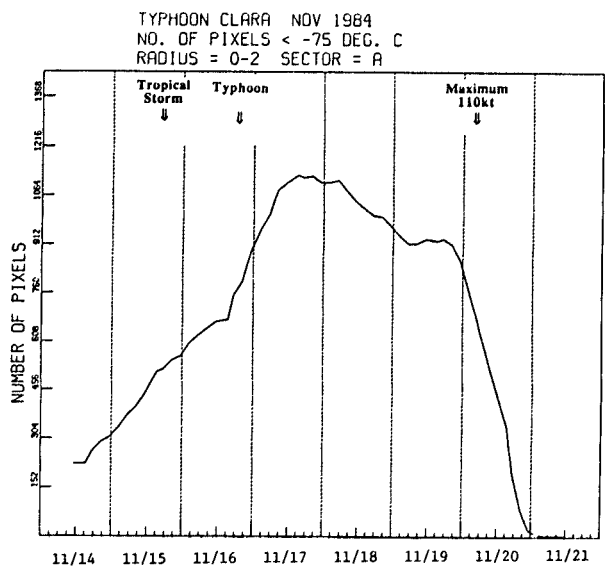

Fig. 4. Same as Fig. 3 for R=0-2°.

Fig. 5. Same as Fig. 3 for R=0-1°. (OMITTED)

(OCS) as the average observed flight level wind at 1-2.5 degrees latitude radius from cyclone center for a particular reconnaissance cyclone fix mission. The average OCS were computed for the entire life cycle of several typhoons. Figure 4 shows the OCS values along with the time series of areas with infrared temperature less than -65°C at 2-6 degrees latitude radius from center, for three pairs of typhoons. Each pair was chosen as two typhoons with comparable maximum intensities, but largely different outer core winds. Note that each typhoon with the stronger outer core winds also has significantly more deep convective clouds (as measured by cloud area with infrared temperature less than -65° C). Weatherford (1985) showed that radius of 50-knot winds, radius of 30-knot wind, and outer core mean wind speeds are all correlated fairly well to each other. Therefore, there appears to be a relationship between convective cloudiness outside the central core region, and the outer tropical cyclone circulation wind profile. This relationship was proposed in a study by Wei and Gray (1985), but they did not have access to digital satellite data to give an accurate quantitative measure of convective cloudiness.

Figure 6 also indicates that additional research is needed before satellite data can provide a good estimate of size or outer core winds for a given time period. This is because the convective cloud amounts even at outer radii are not independent of intensity. In addition, there is a tendency for outer core winds to continue to increase after maximum tropical cyclone intensity has been reached. Weatherford (1985) also showed a relationship between latitude and outer core winds, with cyclones further north having a greater tendency for strong outer wind speeds.

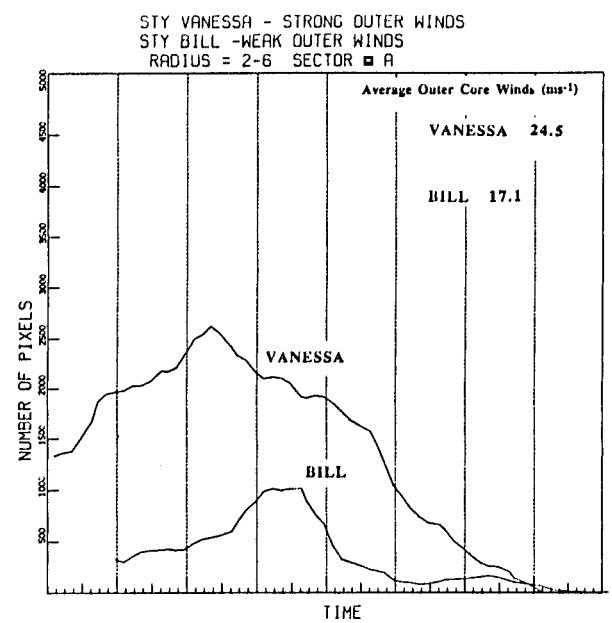

Fig. 6. Pairs of areas with infrared temperatures areas less than -65°C at 2 to 6 degrees radius, during the active convective portions of each typhoon. The average outer core winds during this period are shown. a. Supertyphoons Vanessa and Bill. b. Typhoons Orchid and Agnes. c. Supertyphoons Forrest and Marge.

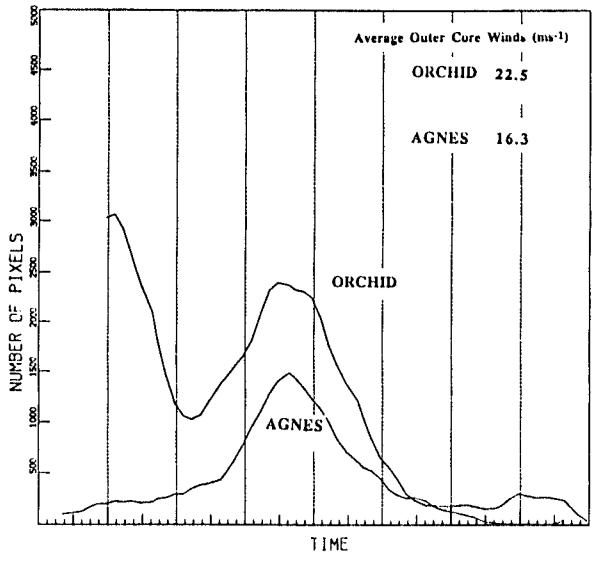

Figure 6b.

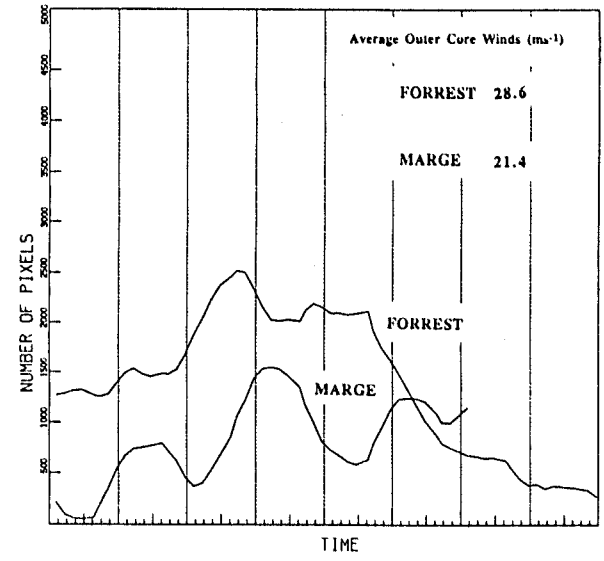

Figure 6c.

c. Genesis

The large-scale environmental conditions in which tropical cyclones develop have been well known for many years (Gray, 1968, 1975). More recently, research studies based on conventional data analyses, rawinsonde composites, and low-level investigative aircraft flight data have identified additional characteristics which differentiate tropical disturbances which undergo cyclogenesis from those that do not (McBride and Zehr, 1981; Lee, 1986; Lunney, 1987; Middlebrooke, 1987). However, forecasting tropical cyclone genesis remains a difficult problem and the physical mechanisms which form the initial cyclone vortex are poorly understood. Several case studies have identified low-level large-scale wind surges which advect into the region of a tropical disturbance and appear to initiate tropical cyclone genesis (Molinari and Skubis, 1985; Lee, 1986).

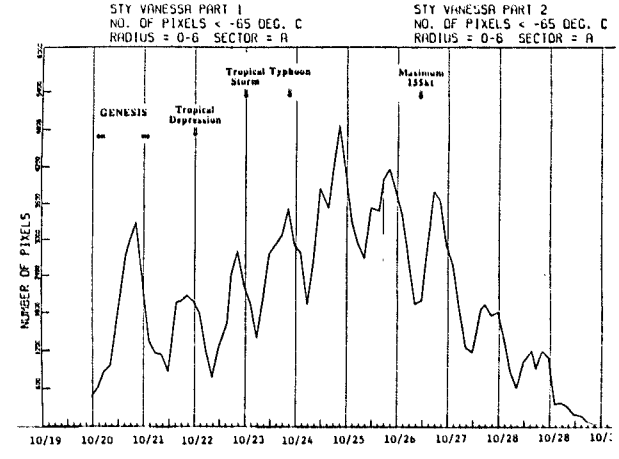

Fig. 7. Infrared cloud areas with temperature less than -65°C, including several days before tropical depression stage. a. Supertyphoon Vanessa. b. Typhoon Agnes. c. Typhoon Doyle .

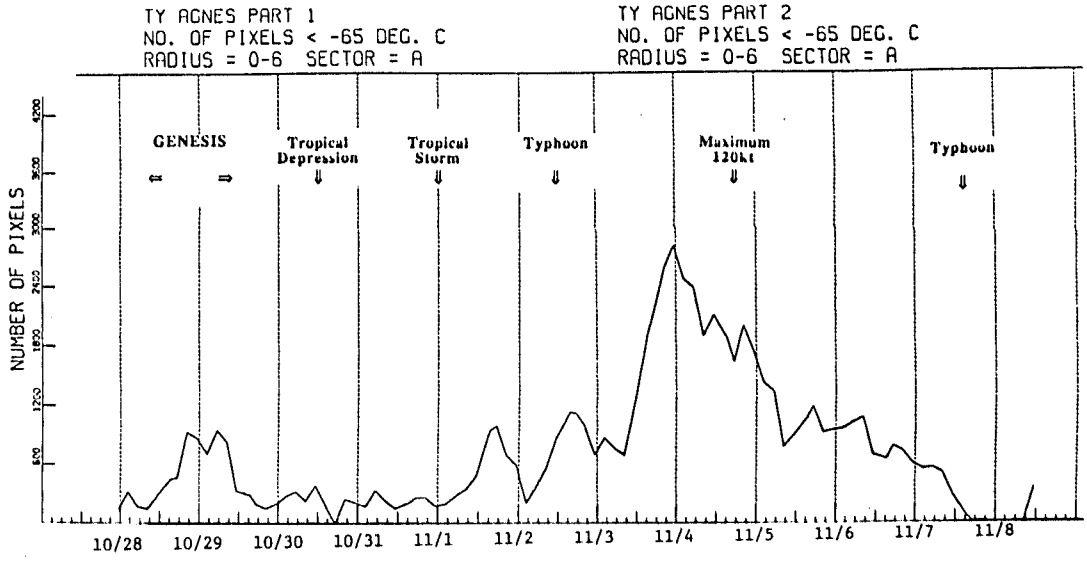

Figure 7b.

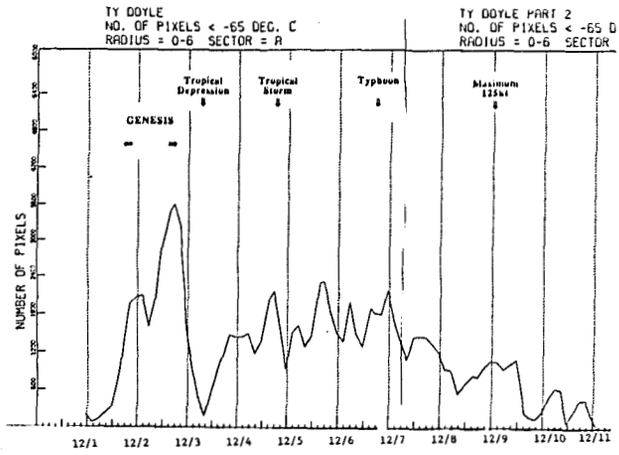

Figure 7c.

The time series of cold infrared cloud areas derived from GMS data are shown in Figure 7 for three different typhoons (Vanessa, Agnes, and Doyle). The plots include the period two to four days before the pre-typhoon disturbance was classified as a tropical depression. Note that there is a very distinct maximum in convective cloudiness coinciding with the genesis period for each example shown. This maximum is quite large compared with cloud areas during the mature stages. Results from 1983-1984 indicate that a large majority of West Pacific tropical cyclones are preceded by a 12-36 hour period of extensive deep convection which is followed by a 1 to 3 day period of suppressed convection. After this inactive period the extent and intensity of deep convection increases once again as the cyclone undergoes intensification and attains typhoon intensity.

5. CONCLUDING REMARKS

This paper presents preliminary results which are very encouraging with regard to satellite diagnosis of tropical cyclones. The availability of the GMS digital infrared data allows the time evolution of a tropical cyclone's deep convection to be monitored quantitatively. The aircraft flight data provides an independent evaluation of the tropical cyclone wind and pressure distribution, intensity changes, motion, etc. The two data sources together, processed for the large number of tropical cyclones which occur in the West Pacific (approximately 25 per year), represent a wealth of valuable information for ongoing and future tropical cyclone research. The data set, utilized in this paper, is to be completed soon for the four year period 1983-1986, which will include nearly 100 tropical cyclones.

6. ACKNOWLEDGMENTS

Portions of this research were supported by NOAA Grants NA85RA-H-05045, NA84AA-H-00020, and NA84AA-D-00017. Dr. William M. Gray and project provided many helpful suggestions. NOAA/NESDIS and ISCCP are acknowledged for supplying the satellite data. Debra Lubich, CIRA, developed most of the computer programs for analysis and plotting. The author also thanks Mrs. Debbie Eckdahl, CIRA, for manuscript preparation.

7. REFERENCES

Adler, R.F., and E.B. Rodgers, 1977: Satellite-observed latent heat release in a tropical cyclone. Mon. Wea. Rev., 105, 956-963.

Dvorak, V.F., 1984: Tropical cyclone intensity analysis using satellite data, NOAA Technical Report NESDIS 11, 47 pp.

Gentry, R.C., E. Rodgers, J. Steranka and W. Shenk, 1980: Predicting tropical storm intensity using satellite measured equivalent blackbody temperature of cloud tops. Mon. Wea. Rev., 108, 445-455.

Gray, W.M., 1968: Global view of the origin of tropical disturbances and storms. Mon. Wea. Rev., 96, 55-73.

Gray, W.M., 1975: Tropical cyclone genesis. Atmos. Sci. Paper No. 234, Colo. State Univ., Ft. Collins, CO, 121 pp.

Henderson, R.S., 1978: USAF Aerial Weather Reconnaissance using the Lockheed WC-130 Aircraft. Bull. Amer. Meteor. Soc., 59, 1136-1143.

Lee, C.-S., 1986: An observational study of tropical cloud cluster evolution and cyclogenesis in the western North Pacific. Dept. of Atmos. Sci. Paper No. 403, Colo. State Univ., Ft. Collins, CO, 250 pp.

Lunney, P.A., 1987: Environmental and convective influence on tropical cyclone development vs. non-development. Dept. of Atmos. Sci. M.S. Thesis, Colo. State Univ., Ft. Collins, CO, 95 pp.

McBride, J.L. and R. Zehr, 1981: Observational analysis of tropical cyclone formation, Part II: Comparison of non-developing versus developing systems. J. Atmos. Sci., 38, 1132-1151.

Merrill, R.T., 1984: Comparisons of large and small tropical cyclones. Mon. Wea. Rev., 112, 1408-1418.

Middlebrooke, M., 1987: Investigation of tropical cyclone genesis and development using low-level aircraft flight data. Dept. of Atmos. Sci. M.S. Thesis, Colo. State Univ., Ft. Collins, CO, 88 pp.

Molinari, J., and S. Skubis, 1985: Evolution of the surface wind field in an intensifying tropical cyclone. J. Atmos. Sci., 42, 2865-2879.

Motoki, T., and K. Shimada, 1986: Variations in the transition process from the tropical depression to the tropical storm observed by the GMS. Geophys. Mag., 42, 19-38.

Steranka, J., E.B. Rodgers, and R.C. Gentry, 1986: The relationship between satellite measured convective bursts and tropical cyclone intensification. Mon. Wea. Rev., 114, 1539-1546.

Weatherford, C.L., 1985: Typhoon structural variability. Dept. of Atmos. Sci. Paper 391, Colo. State Univ., Ft. Collins, CO, 80523, 75 pp.

Weatherford, C.L., and W.M. Gray, 1987: Typhoon structural evolution. Dept. of Atmos. Sci. Paper (forthcoming), Colo. State Univ., Ft. Collins, CO, 80523.

Wei, D.W. and W.M. Gray, 1985: Estimation of typhoon outer wind strength from satellite imagery. Dept. of Atmos. Sci., Colo. State Univ., Ft. Collins, CO, 80523.

World Climate Programme, 1985: International Satellite Cloud Climatology Project - Description of reduced resolution radiance data, July, 1985, WMO/T.D. - No. 58, Geneva.

Zehr, R.M., 1987: The diurnal variation of deep convective clouds and cirrus with tropical cyclones. Preprints, 17th Conf. on Hurricanes and Tropical Meteorology, AMS. April 7-10, Miami, FL.

6.1 Suggested GOES I-M Satellite Operational Scenarios

William E. Shenk[1], W. Paul Menzel[2], Fredrick Mosher[3], and Robert T. Merrill[4]

[1]Laboratory for Atmospheres, NASA/Goddard Space Flight Center, Greenbelt, MD

[2]Advanced Satellite Products Project, Madison, WI

[3]NOAA/National Severe Storms Forecast Center, Kansas City, MO

[4]Cooperative Institute for Meteorological Satellite Studies, Madison, WI

1. INTRODUCTION

The combination of a flexible and quantitative GOES I-M satellite system with more powerful and interactive ground facilities during the 1990's should lead to large advances in the utilization of GOES data in severe local storm and tropical cyclone analysis and forecasting. How the GOES satellites are operated, where they are located, and what products are derived is critical for success. Hopefully, by considering these issues now, we can properly prepare ourselves to realize the full value of these valuable data. Two suggested operating scenarios for the GOES I-M satellite are presented. One is for severe local storm situations and the other is for tropical cyclones.

2. GOES I-M CAPABILITIES

The GOES I-M spacecraft will be a three-axis, body-stabilized platform with separate imaging and sounding instruments. Unlike the present GOES where the VAS (VISSR Atmospheric Sounder) is time-shared to perform the imaging and sounding functions, the GOES I-M imager and sounder operate completely independent of each other. The GOES I-M radiometers offer improved sensitivity, scan flexibility, pointing accuracy, signal quantization, and spatial resolution when compared to the current VAS. These characteristics are briefly summarized (see Juarez and Koenig, 1986 for additional details).

The imager on GOES I-M is capable of multi-spectral observations at intervals less than 30 sec over areas of about 1000x1000 km and can scan the full disk in under 30 minutes. The resolution will range from 1 km to 8 km depending on spectral interval. The sensitivity in the thermal bands will be better than 0.25 K at nominal scene temperatures. The absolute pointing accuracy will be within 2 km, a considerable improvement over the current 10 to 20 km (Juarez and Koenig, 1986). These capabilities offer the opportunity for better atmospheric monitoring and wind field depection through tracking clouds and moisture features in image sequences.

The GOES I-M sounder is a 19 channel filter radiometer that has a small instantaneous geometric field of view (8 km), a high sampling rate providing rapid areal coverage (soundings over the contiguous United States require roughly 40 minutes and soundings over a 1000x1000 km area require about 10 minutes), and an increased thermal sensitivity for each field of view (e.g. better than the sounding requirement of .25 mW/ster/m**2/cm^{-1} in the 15 µm CO_2 band). While the vertical resolution of the soundings has not been significantly changed from the VAS, the improved calibration of these radiances with an external blackbody is expected to yield high quality soundings of temperature and moisture.

3. SEVERE LOCAL STORM SCENARIO

a. Introduction

The GOES I-M observations that are taken during a day of intense convection in the midwestern U.S. will be expected to place the greatest demands on the satellite and ground facilities. This is due to the space and timescale of the meteorological features and the rapid perishability of the products. All other mesoscale phenomena observing scenarios could be variations on the one for severe local storms, and no increase in overall capability will be needed.

b. Severe Local Storm Phases

There are three basic phases of activity on a severe local storm day. The first is to define the atmospheric conditions which are favorable for storm development. This will involve the use of regional scale and possibly mesoscale models which will need satellite data as part of the total data base. Also, the progress of key atmospheric circulation features (e.g., jet streams, areas of low level convergence) and indices (e.g., stability) will have to be monitored during the day, especially in the morning through early afternoon before any strong convection has started to develop. This is also when the modelling results are the most useful.

The second phase is when the convection begins to grow beyond the cumulus phase. Two important activities being. One is the monitoring of the convection growth rates, and the other is the localizing of some of the quantities that were measured in phase one. Whereas phase one is the current outlook and watch process, phase two is the updating of watches and the beginning of the warnings.

Phase three is when there are areas of mature strong convection in progress. The same monitoring of favorable atmospheric conditions continues but its importance is lessened since convection has already appeared in most of the places that can support it. The emphasis has now shifted primarily to the monitoring of the rapid fluctuations of the convective cores to ascertain their present and anticipated (within an hour) severity. Very high imaging rates are now required because updraft speeds are near their maximum, and the air can rise, often nearly undiluted, to at or above tropopause levels.

Another important area of observation in phase three is the interactions between the storms and their immediate environment. This exchange of heat and momentum often results in circulations which can act to modulate convection intensity and strongly influence the enviornmental structure both upstream and downstream from the storms. The measurements associated with phase three can primarily concentrate on the most active areas.

The required measurements associated with the phases have considerably overlap in time and space. There are gradual transitions between phases. One portion of the total surveyed area could be in phase one, while another portion is in phase three.

c. GOES I-M Observations

In designing the severe local storm scenario, there were three different types of requirements that were considered. In addition to the special observations for severe local storms, there are simultaneous requirements for full disk imaging and higher frequency regional scale imagery to satisfy local needs over the U.S. and nearby areas away from the severe storm regions.

It would be difficult to make quantitative calculations east of the Mississippi river from GOES-West at its current location (135°W). This, plus other considerations, has led to the suggestion that the GOES I-M satellites be positioned at 70°W and 120°W. The coverages shown in this severe local storm scenario are based on the 70°W and 120°W locations. The scenarios would still work with the satellites at their current locations but there would be a greater dependence on GOES-East.

(1) Sounder Coverage Scenarios

There are two types of suggested sounder coverage. Fig. 1 shows the sounder coverages for GOES-East and GOES-West during the first two phases of severe local storm development. This coverage could also be used for any regional scale requirements that were centered over the U.S. The overlap area between the satellites can be used for profile comparisons. The practical profiling limit for each sounder is shown, which will reduce the effective area for profiling slightly below the scanned areas. There is a slight bias in the combined coverage towards the west to detect systems moving from the west that could influence severe weather conditions in 24-48 hours in the central U.S. Areas of this size can be covered by each sounder in less than an hour. The size of each area is about

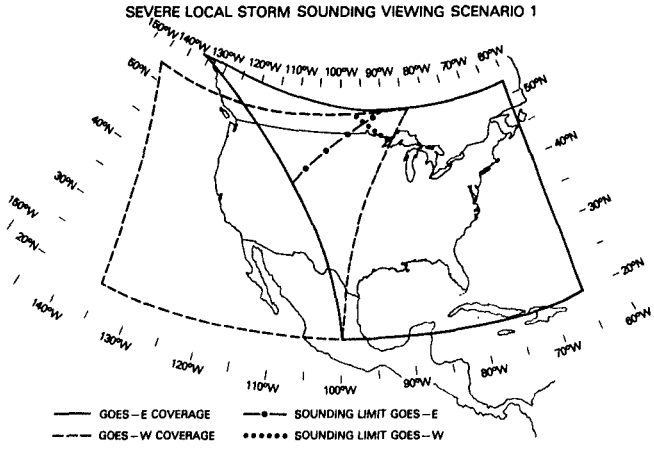

Fig. 1 - First GOES I-M severe local storm sounding viewing scenario coverage with the GOES-East subsatellite point at 70°W and the GOES-West subsatellite point at 120°W.

the same, thus the sounder scans can be synchronized.

Once the storms have reached the mature state (phase three) then a scenario change is suggested. Fig. 2 shows a typical case where GOES-West still covers the same sized regional area as before (shifted 10° of longitude further east than in Fig. 1) while GOES-East is focussed on a local area. This local area is where strong storm environment interactions should be occurring and/or is an important area for future storm development where clouds are more numerous and the higher observation frequency will yield enough profiles for adequate coverage. The small area is scanned in less than 10 minutes.

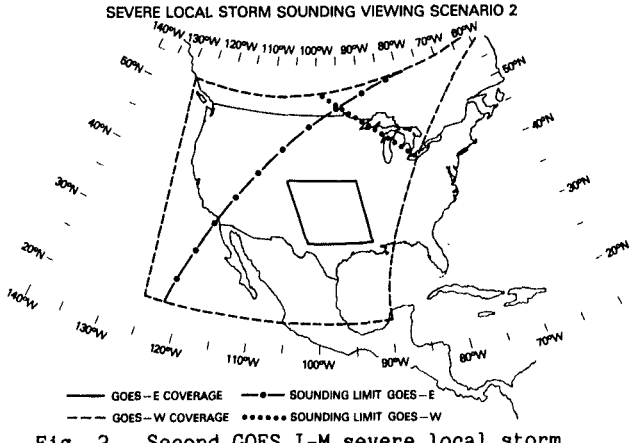

Fig. 2 - Second GOES I-M severe local storm sounding viewing scenario coverage. The GOES-East and GOES-West subsatellite locations are the same as Fig. 1.

(2) Imaging Coverage Scenarios

The imaging scenarios are a little more complicated than the ones for the sounders because there is a need for full-time imagery to support U.S. and international users, and to produce winds from cloud motions every 6 hours. Fig. 3 shows the suggested imagery coverage from both satellites to support phases one and two of the severe local storm development cycle. Each satellite covers most of the U.S. and nearby

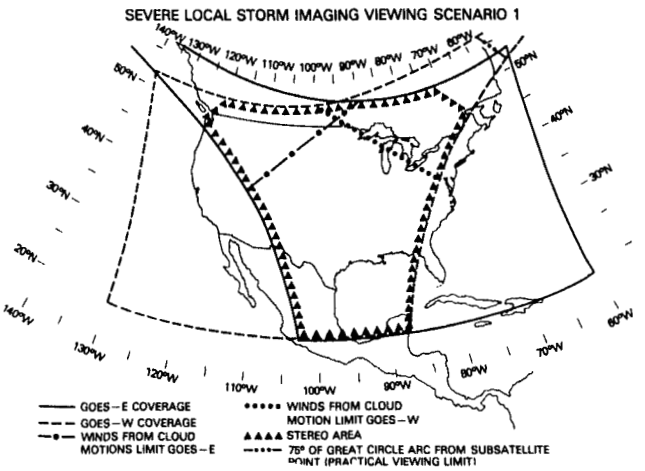

Fig. 3 - First GOES I-M severe local storm imaging viewing scenario coverage. Same subsatellite points as in Fig. 1.

adjacent states, covering about the same area as Fig. 1. There is larger overlap in the center of the U.S. for stereo coverage which will be important for cloud height measurements that will be used to support winds from cloud motions and convective growth calculations. The practical limits for winds from cloud motions, stereo, and imagery from a general user's perspective (75° of great circle arc from the subsatellite point) are all shown in Fig. 3. It will take about 3 minutes to take each image. There are the same size. The 3 minute interval will be needed for mesoscale low level winds from cloud motions and convective growth in the early stages. Time compositing can be used to obtain surface temperature and low level moisture information at longer intervals with reduced cloud effects due to the high image frequency. Once the storms have reached the mature stage, a second type of image scenario is suggested. Fig. 4 shows the coverage for two types of image scanning. The larger area is done from either satellite and provides the routine coverage of the U.S. and adjacent waters every 3.5 minutes. These images would be used for the same purpose as the ones shown in Fig. 3. The much smaller area, which could be done by either satellite, is designed for intensive convection monitoring, and covers the approximately 1000x1000 km area in about 25 secs. This high frequency allows the proper determination of convective vertical rise rates for even the most intense cells. While slower image rates would still capture most of the rise rates correctly, the most intense convection would not be properly measured. Since it is the extremes that are the most important, the scenarios should be designed to measure them. The small images can be combined with the larger ones to generate useful stereo in the small image areas at the frequency of the larger images since the greatest time separation between two would be 12 sec. The high frequency in the small areas would provide the best low level cloud motion winds since cumulus continuity would be outstanding. Experiments should be performed with both satellites scanning the same small area to see if the high frequency stereo (which would also be more precise than the stereo done between the small and large images) would substantially benefit the intense convection analysis.

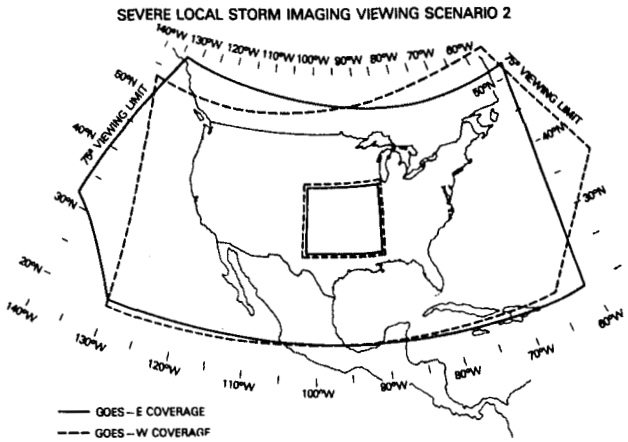

Fig. 4 - Second GOES I-M severe local storm imaging viewing scenario viewing coverage. Same subsatellite points as in Fig. 1.

The final imaging scenario is when full disk imaging is required. During the winds determination period, both satellties will probably be simultaneously operated in the full disk mode (every 6 hours). In between, it is suggested that any full disk imaging be staggered in time. Thus, one satellite would take one of the large areas in Fig. 4, while the other would cover the full disk (Imaging Scenario 3).

(3) Scenario Timetables

Since these sounding and imaging coverage scenarios change during the day as the meteorological situation evolves, a timetable for their use was developed. Fig. 5 shows the timetable for a typical midwestern U.S. severe local storm day. The general operational requirements are interleaved with the special requirements for a storm event. It is assumed that the significant convective onset (i.e. storms reaching the mature stage) begins at 1400 CST.

The timetable is subdivided for the imagers and sounders and the GOES-West and GOES-East imager timetables are individually depicted. The numbers above each of the horizontal bars refer to a particular sounder or imager coverage scenario and temporal resolution, and correlate with the scenario numbers shown in Figs. 1-4. The total special observation period extends from 0500 CST (1100) GMT on one day to 0100 CST (0700 GMT) on the next.

The first sounder coverage scenario is used up to 1400 CST to determine the atmospheric state prior to and during the early stages of the convection. Later, this scenaro is employeed again for an hour each to support dynamic model initialization at the times when the full disk images are being used for cloud motion winds. All of the other times, the second sounding scenario is used during the intense convection periods.

The imager timetable is similar to the sounding timetable in that the switch is made at 1400 CST to the more intensive coverage from one or both of the satellites. The severe local storm coverage is interleaved with the full disk requirements through the period. The image boundaries can be flexible to cover the incipient storm development with stereo. The

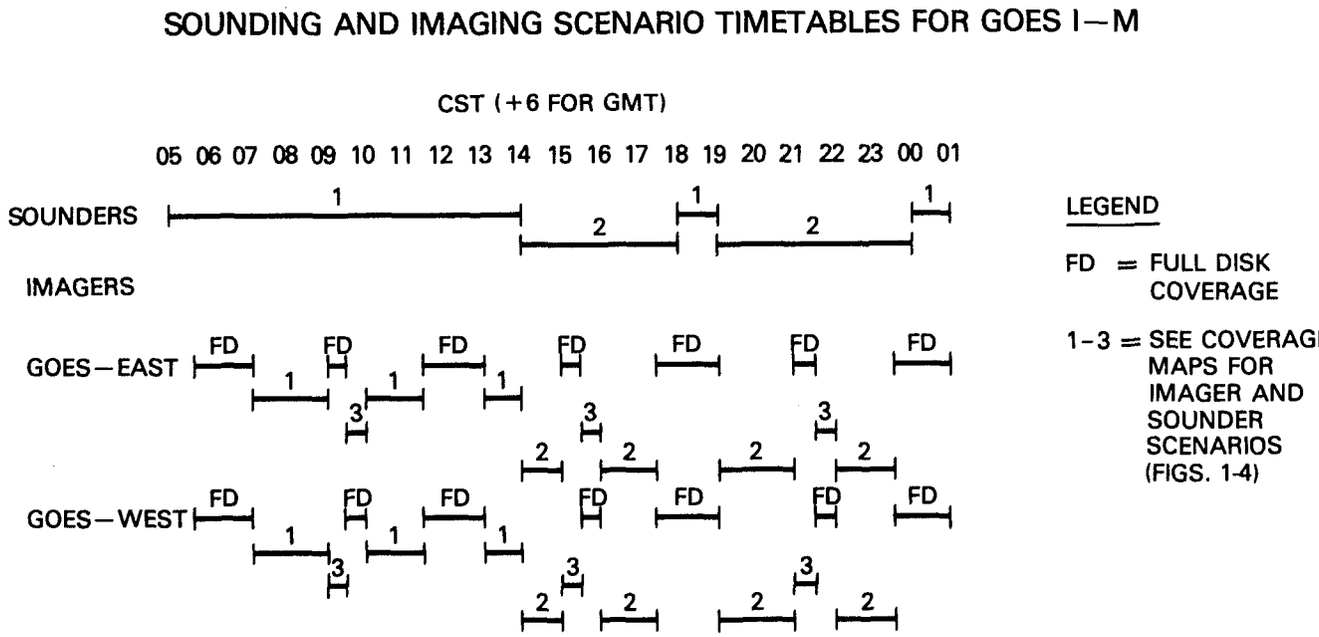

Fig. 5 - GOES I-M sounding and imaging timetables for a typical severe local storm event. Assume the onset of severe convection at 1400 CST.

full disk requirements not associated with cloud motion winds are staggered such that regional imaging scenario 3 can continue the regional coverage uninterrupted during the time in between the cloud motion wind periods.

4. TROPICAL CYCLONE SCENARIO

a. Tropical cyclone detection, analysis and prediction and the role of the GOES satellites

The GOES satellites have been an important part of the hurricane warning system for over a decade. Although the GOES satellites alone cannot meet the needs of operations, they are recognized as being an indispensible tool for hurricane prediction.

Hurricane forecasting is a subtle problem since the significant flow is weaker and mass gradients are far smaller than in the mid-latitudes. Thus, the remote sensing of a tropical disturbance and its surrounding circulations is more difficult due to a poorer signal-to-noise ratio for the necessary observations.

Well over 50 areas of disturbed weather occur each hurricane season in the tropics or subtropics, and these must be monitored for signs of development. Although aircraft are used to confirm cyclogenesis, the decision to commit them to flight is made primarily from the visible and infrared imagery from the GOES satellites.

The low level circulation is identified forming within a cloud mass. Infrared imagery loops are generally less useful than the visible loops because of their lower resolution (8 km versus 1 km) of low level features, but they are still essential at night.

Once a tropical cyclone forms, it must be located accurately and frequently. For hurricanes nearing land, aircraft reconnaissance and land-based radar are used extensively, but limited resources require that many hurricanes at sea are tracked using satellite information alone. In 1987, aircraft reconnaissance has been eliminated in the western Pacific. Finding the center is even more difficult at night, as the center of a weak or moderate cyclone is often apparent only in small low cloud features which are difficult to discern in the reduced resolution infrared imagery. The increased infrared resolution of GOES I-M is expected to help with this problem.

The maximum winds and area of damaging winds must also be monitored as part of the tracking responsibility. In the absence of reconnaissance aircraft, intensity must be estimated from satellite images. Intensity is estimated from single images every 3 to 6 hours (Dvorak, 1984) with emphasis on using the enhanced infrared images. The area of damaging winds can sometimes be measured from low level cloud motions determined from high frequency (e.g., 7 1/2 minutes) images (Rodgers, et al., 1979).

Warnings are the core of hurricane forecasting. The nature, extent, and seriousness of the threat must be communicated quickly and evoke an appropriate response. Here is where the satellite images, with suitable enhancements and graphic annotation, are extremely valuable. It is also essential that the display devices in the field offices allow access by the new media without interfering with the detection, tracking, and analyses functions.

b. Goes I-M Observations

The hurricane scenario for GOES I-M satisfies the traditional requirements for full disk imaging every 3 hours and regional scale imaging every half hour and attempts to schedule sufficient hurricane imaging and sounding so that the needs of the hurricane forecaster are met. Table 1 shows the 6-hour duty cycle that either

Table 1

GOES-Next Hurricane Schedule

Time	Imager	Sounder
0-1	15,15[a] full disc	US[d] eye, eye[e]
1-2	15,15[a] 7½, 7½, 7½, 7½[b]	US[d] eye, eye[e]
2-3	7½, 7½, 7½, 7½[b] 15, 15[c]	hurricane[f] eye, eye[e]
3-4	15, 15[c] full disc	US[d] eye, eye[e]
4-5	15, 15[c] 7½, 7½, 7½, 7½[b]	US[d] eye, eye[e]
5-6	7½, 7½, 7½, 7½[b] 15, 15[c]	hurricane[f] eye, eye[e]

a initial 90 minutes of imaging enables global winds every 6 hours, three 15-minute scans of northern hemisphere followed by the same in the southern hemisphere

b rapid scan imaging over hurricane covering a 4200x4200 km area (to be synchronized with other GOES for stereo coverage when possible)

c 15-minute interval imaging to monitor convergence/divergence

d US sounding coverage takes 40 minutes for continued NSSFC support; in a landfalling hurricane situation, US coverage will be replaced by hurricane coverage to provide hourly sounding updates (US coverage must then be accomplished from the other GOES)

e attempts for eye sounding in 1000x1000 km area takes 5 minutes

f hurricane sounding coverage of 3000x3000 km area takes 40 minutes and is used for model initialization every 6 hours and for monitoring major thermal and moisture gradients (including SST, 500-700 mb moisture) every 3 hours

GOES-East or GOES-West could use, depending on whether the storm is in the Pacific or the Atlantic basin.

(1) Imager Scenario

The imager is first scheduled for three 15-minute scans of the northern hemisphere followed by three 15-minute scans of the southern hemisphere to enable determination of global winds. Currently, global winds are produced from half-hour interval image loops. It has been suggested that reducing the time interval to 15 minutes will greatly improve the calculation of wind from cloud motions for the global winds.

The next phase is rapid scan imaging over the hurricane area. This imaging occurs at 7.5-minute intervals for 1 hour. Rodgers, et al., 1979, showed that up to ten times as many low level winds were derived from 7.5-interval images as from those at 30-minute intervals. The higher temporal resolution also increased the number of traceable upper tropospheric cloud elements. Thus, these short interval images make it possible to produce better wind data between 200 and 1100 km from the tropical cyclone center which will help define the area of winds greater than 15 m/sec knots and improve the initial fields necessary for numerical forecasts. Attempts will be made to synchronize some of the rapid scan imaging from both GOES so that stereo coverage is possible. Hasler (1981) showed that the three-dimensional cloud geometry available from stereo imagery improves the altitude assignment for the cloud motion winds and reveals changes in the structure in the central dense overcast region as a function of time.

Fifteen-minute imaging over the northern hemisphere follows. This allows simultaneous support of all the national weather centers through the monitoring of cloud and water vapor motions over the continent as well as over the oceans.

The next 3 hours are a repeat of the previous 3 without the southern hemisphere wind coverage.

(2) Sounder Scenario

Sounding coverage over the hurricane region (3000x3000 km) takes about 40 minutes and is scheduled to occur every 3 hours. The profile retrievals from this coverage can be used for model initializations and for monitoring the major atmospheric thermal and moisture gradients. The soundings are synchronized with the rapid scan imaging (7.5 minutes) from the imager so that wind fields and retrievals are available simultaneously. In addition, the radiances observed in the infrared window channels will provide sea surface temperatures (SST) in cloud-free areas.

Attempts to sound in the eye of the hurricane, if one has formed, are scheduled to occur twice every hour. Sounding in the 1000x1000 km area surrounding the hurricane center (which takes 5 minutes) occupies the last 10 minutes of each hour. While the likelihood of a successful sounding in the eye is not high, the value of an accurate determination of eye characteristics warrants the attempt.

In between the three hourly hurricane sounding coverage, the sounder is programmed to scan the contiguous United States for the first 40 minutes of each hour. This enables continued support for the National Severe Storm Forecast Center (NSSFC). In a landfalling situation U.S. coverage would be replaced by hurricane coverage to provide hourly sounding updates (U.S. sounding coverage would then be accomplished from the other GOES).

5. CONCLUSIONS

The opportunity for improved support to the National Severe Storm Forecast Center and the National Hurricane Center is coming with the GOES I-M launches, scheduled start in the spring of 1990. The satellite scenarios suggested here make the relevant data available in the appropriate time interval. The processing system that will convert the data into information must be designed so that winds and soundings can be processed within an hour. The forecasting and analysis teams at the center must have sufficient training and familiarity with the satellite-derived products to make correct meteorological inferences.

6. REFERENCES

Dvorak, V. F., 1984: "Tropical cyclone intensity analysis using satellite data," NOAA Tech. Rep. NESDIS 11, p. 47.

Hasler, A. F., 1981: "Stereographic observations from geosnychronous satellites: an important new tool for the atmospheric sciences, " Bull. Amer. Met. Soc., Vol. 62, No. 2, 1984.

Juarez, D. J. and E. W. Koenig, 1986: "Infrared imaging and sounding from a geostationary body stabilized spacecraft," Second Conference on Satellite Meteorology/Remote Sensing and Applications, May 13-16, 1986, AMS Preprints, 503.

Rodgers, E., R. C. Gentry, W. Shenk, and V. Oliver, 1979: "The benefits of using short-interval satellite images to derive winds for tropical cyclones," Mon. Wea. Rev., 107, 575.

THE DETECTION AND LOCATION OF LIGHTNING FROM GEOSTATIONARY ORBIT

H.J. Christian
Structures and Dynamics Laboratory
NASA/Marshall Space Flight Center, AL

1. Introduction

A lightning mapper sensor as presently conceived will detect and locate lightning over large areas of the earth's surface, mark the time of occurrence and measure the radiant energy. It will basically be a calibrated lightning imager. Scientific importance of these measurements include the fact that this type of information is not presently available on a large scale basis. With a mapper, scientists will be able to study the electrosphere from scales on the order of the earth's diameter down to the size of individual storms (10 km). They will be able to study both the spatial and temporal evolution of lightning activity on a continuous basis and relate the lightning measurements to other observables such as cloud images, radar returns, and the standard meteorological variables on both the synoptic and mesoscale. The ability to study lightning activity in continental storms will be improved because a lightning mapper will detect all types of lightning, will provide near uniform spatial coverage and detection efficiency and will disseminate the information in a readily usable form. On the larger scale, a lightning mapper will provide information that can only be obtained with a space-based instrument. Lightning detection in data sparse regions such as the tropics and ocean areas will be possible. Lightning activity could be studied on a nearly global basis. The evolution of storms as they develop and propagate will be compared on a regional basis. Lightning climatology will change from its present thunderstorm day based on audible thunder to a true measure of lightning activity based on flash density as measured in time and space.

Table 1, a summary from Davis, et al. (1983), shows a partial list of scientific activities that would be possible if a lightning mapper possessing the basic attributes of continuous large area coverage, storm system spatial resolution, high detection efficiency, high temporal resolution and a measurement of flash intensity were available. Figure 1 compares the proposed lightning mapper sensor capabilities with earlier satellite measurements. Of particular importance is (1) the capability for detecting lightning on a continuous basis rather than during very limited periods; (2) the ability to detect nearly all lightnings within the sensor field of view (90%) rather than poor detection efficiencies; and (3) a spatial resolution on the order of 10x10 km rather than the hundreds of km that were typical of the pioneering lightning sensors.

These orders of magnitude improve-

SCIENTIFIC OPPORTUNITIES POSSIBLE WITH MAPPER IN GEOSTATIONARY ORBIT

- MAGNETOSPHERIC AND IONOSPHERIC RESEARCH
  - RELATIONSHIP BETWEEN LIGHTNING AND WHISTLERS
  - VLF-ELF ELECTROMAGNETIC NOISE
  - VLF WAVES
  - SCHUMANN RESONANCES
- EARTH'S ELECTRIC CIRCUIT
  - FAIR WEATHER ELECTRICITY
  - IONOSPHERIC CURRENTS
  - ATMOSPHERIC CURRENTS
- ATMOSPHERIC CHEMISTRY
  - NITROGEN FIXATION
  - OZONE REACTIONS
  - RADICAL AND OXIDANT FORMATION
  - HCN FORMATION
  - STRATOSPHERIC CHEMISTRY
- STORM PHYSICS
  - LIGHTNING ACTIVITY/STORM INTENSITY
  - OCEAN LAND LIGHTNING RATIO
  - HURRICANE ELECTRIFICATION
  - LIGHTNING/TORNADIC ACTIVITY
  - INITIAL ELECTRIFICATION
  - SYMPATHETIC LIGHTNING
  - WARM CLOUD LIGHTNING
- SOLAR-TROPOSPHERIC EFFECTS
  - SOLAR VARIABILITY/LIGHTNING RATES
  - ELECTRICAL CONNECTION

Table 1. Examples of scientific disciplines that require lightning mapper data.

SATELLITE LIGHTNING EXPERIMENTS

SATELLITE	SENSOR	ORBIT	PERIOD	LIGHTNING POWER SENSITIVITY (WATTS)	FOOTPRINT
OSO	PHOTOMETERS		MOONLESS NIGHT	$\sim 10^{8}$*	
VELA V	PHOTODIODES	1.1×10^{5} km	DAY - NIGHT	$10^{11} - 10^{13}$	VERY WIDE FIELD OF VIEW
DMSP	SCANNING RADIOMETER	830 km	LOCAL MIDNIGHT	SENSITIVE*	100 km
DMSP-SSL	12 PHOTODIODE ARRAY	830 km	LOCAL MIDNIGHT	$10^{8} - 10^{10}$	750 x 750 km
DMSP-PBE-2, 3	0.1° PHOTODIODE		DAWN/DUSK	$4 \times 10^{8} - 10^{12}$	1300 km DIA.
ISS	4 NARROW BAND RECEIVERS		DAY/NIGHT	RF	IONOSPHERE DEPENDENT (TYPICALLY-HUNDREDS OF km)
SHUTTLE-NOSL	PHOTOCELL PLUS FILM	150 km	SHUTTLE OPERATIONS	NA	VARIABLE
LIGHTNING MAPPER (PROPOSED)	CCD ARRAY	GEO-STATIONARY	CONTINUOUS COVERAGE	$10^{8} - 10^{11}$	10 km

Figure 1. Characteristics of previous satellite lightning experiments.

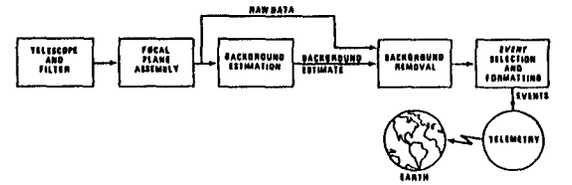

TELESCOPE	POWER	WEIGHT	VOLUME	DATA RATE
F/1.0 10 cm APERATURE	~ 40 WATTS	~ 35 KG	~ 0.1 m^3	~ 64 KB/S

Figure 2. Block diagram of lightning mapper sensor components.

ments in overall sensor performance are rather difficult to achieve. The major difficulty in the detection and location of lightning from geostationary orbit, given the detection efficiency and resolution specified in Figure 1, is caused by the strong background illuminated produced by sunlight reflecting from the tops of clouds. The high cloud albedo makes this background much brighter than the illumination produced by lightning. Because the lightning signal tends to be buried in the "background noise," the only way to detect lightning during daytime is to implement techniques that increase the lightning signal relative to the cloud signal. Fortunately, the character of the two signals is much different. While the lightning pulse duration is on the order of 0.5 msec, the background illumination tends to be constant on a time scale of seconds; thus one could use temporal filtering to attenuate the background "noise" relative to the lightning signal.

Another difference between the signals is that the lightning signal is composed of predominately discrete emission lines, while the background illumination closely follows the blackbody-like continuum of the sun; thus the requirement for an optimized spectral filter. Finally, the lightning tends to illuminate a smaller area than the background and this illuminated area tends to change with each event. A form of spatial filtering can be used which matches the field of view of each detector to the typical cloud top area illuminated by a lightning stroke.

Even after using these three filtering techniques, the ratio of background illumination to lightning signal may still exceed 50 to 1 at the focal plane. For this reason, post-detection filtering must be implemented. Feasibility studies performed by Hughes (V. Norwood, 1983), and TRW (Eaton, et al. 1983) reviewed a number of post-detection background removal techniques. They both selected analog background subtraction schemes similar to the one illustrated in Figure 3. This approach utilizes a modified frame-to-frame subtraction or adaptive filter approach. An important point to understand is that the power of any post-detection technique is totally limited by the lightning signal to background noise ratio coming off the focal plane.

2. Sensor Components

The design of the required filtering methods is conceptionally straightforward. However, the actual implementation can be quite complex. Figure 2 is a block diagram of probably sensor components. The optics system is expected to consist of a fairly fast lens using refractive elements and a narrow band filter, both of conventional design. The emission line centered filter performs the previously described spectral filtering. The lens must be fast to provide high throughput because of the weak signals arriving at geostationary altitude.

The focal plane assembly (FPA) is the heart of the lightning mapper. This is the component that detects an incident photon flux and outputs an electrical signal. Together, the lens and the focal plane array determine the spatial resolution of the mapper. The temporal filtering performance is determined by the focal plane integration time and readout rate.

The focal plane assembly will consist of a large mosaic array of either photodiodes or charge coupled devices (CCD). If the FPA is operated in the charge integration mode, then each individual sensor (or pixel) must be sufficiently large to store the charge produced by both the background and lightning signals. In addition, a physically large pixel is required to produce a big signal so that an adequate signal to noise ratio can be achieved. The requirement for large pixel size, a large number of pixels for wide area, 8 km resolution coverage, and fast readout times, may be mutually exclusive. Hence, either multiple focal plane as-

semblies, each with its own lens system, or multiple mosaic array chips butted together to form a single large assembly may be required.

Independent of the specific focal plane geometry that is implemented, the major challenge in the focal plane design is the development of a high speed readout technique. As discussed previously, the background signal can be attenuated relative to the lightning signal if one takes advantage of the temporal behavior of the signals. In an integrating sensor, the only means to control this parameter is the frame integration time. The integration time specifies how long a particular pixel accumulates a signal between readouts. The lightning signal to noise ratio improves as the integration period approaches the pulse duration. However, if the integration period becomes too short, the lightning signal tends to be split between successive frames. Frame splitting actually decreases the signal to noise ratio. Instrumented U-2 measurements indicate that the median optical lightning pulse width, when viewed from above, is 400 usec, (Christian, et al., 1983). Based on this pulse width, a TRW analyst (Eaton, et al., 1983) suggests that a one msec frame time is appropriate for minimal pulse splitting and high lightning detectability.

One thousand frames per second is extremely fast for an imaging sensor. If the focal plane array contained 500,000 pixels, the total data rate coming off the focal plane would be 5×10^8 pixels per second. No commercially available mosaic array detector is capable of clocking data out at this rate. Thus, an important technological development for a lightning mapper sensor will be a custom focal plan array that can be accessed at the required rates and a data processor capable of compressing the data to rates that can be handled by conventional telemetry systems.

Since FPA maximum clocking rates are presently limited to between 5 and 20 MHz, multiple output lines will be required. The data coming off the focal plane will have to be processed in parallel. If the total data rate were 5×10^8 pixels per second, then a minimum of 25 parallel output lines and data processors would be required. Since presently available solid state arrays have only one output line, any array used in the lightning mapper will require modification to include the multiple readout lines. This type of circuit modification is technically straight forward and is well within the present state-of-the-art.

Figure 3 shows a possible configuration for the data processor. This

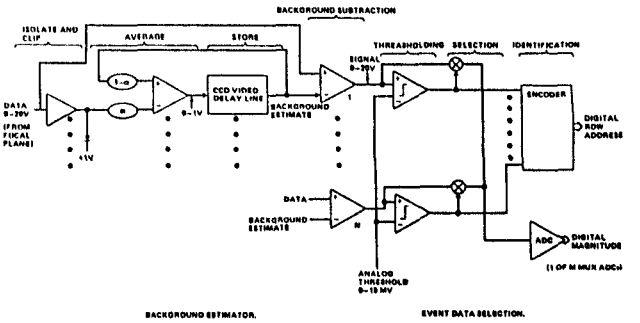

Figure 3. Lightning data processing circuit.

SENSOR PARAMETERS AND PERFORMANCE

LENS f/#	~ 1.0
DIAMETER	~ 10cm
SPACIAL RESOLUTION	~ 10 km (@ 30°N LAT)
FILTER WAVELENGTH	~ 7774Å
FILTER BANDWIDTH	~ SMALL AS POSSIBLE, COMPATIBLE WITH FOV RESTRICTIONS
FRAME TIME	≥ 1 m sec
FOCAL PLANE ARRAY	
NUMBER OF PIXEL	~ 800 X 800
PIXEL SIZE	≥ 20μm
FULL LEVEL CAPACITY	> 10^5 ELECTRONICS
BACKGROUND REMOVAL	~ ANALOG TIME DOMAIN FILTERING
SIGNAL TO NOISE RATIO	~ 6 (OR EQUIVALENT)
LIGHTNING DETECTOR EFFICIENCY	≈ 90% (GOAL)
DATA RATE	~ 64 k bits/sec (BUFFERED)

Figure 4. Example of possible sensor parameters.

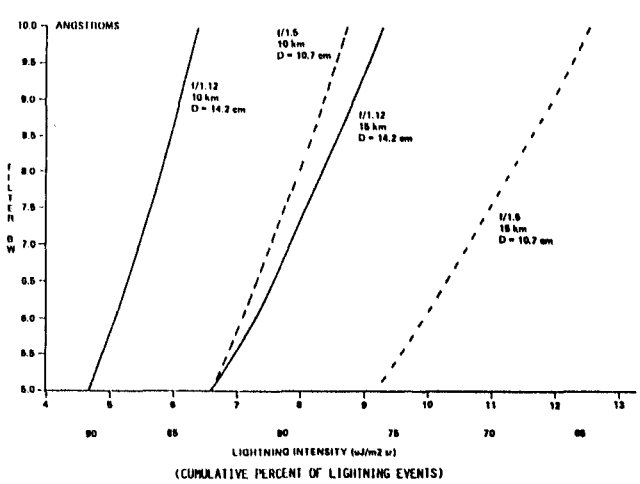

Figure 5. Lightning intensity versus filter bandwidth for constant SNR.

circuit, by subtracting the background and digitizing only lightning events, would reduce the transmission data rate by a factor 10^6 to a rate on the order of 20 kbits/sec. Background subtraction is performed by first generating a pixel by pixel background estimate. That is, an independent running average of the background signal of each pixel is stored. This background estimate for a particular pixel is subtracted, using a difference amplifier, from the signal of the same pixel as it is clocked off the focal plane. If the output from the difference amplifier is greater than a predetermined threshold, then the output is accepted as a lightning signal. The amplitude of the lightning signal is then digitized and a digital word that represents the X-Y position of the specific pixel is determined.

The final signal processing requires the multiplexing of the digital lightning signal, the event address, a time stamp and housekeeping information into an event queue. Queuing is needed to smooth the events, which may occur in burst, into a data rate which is consistent with a larger term average. From the event buffer, the data can be formatted into a serial bit stream and transmitted to ground stations.

3. Sensor Performance

The overall performance of the lightning mapper will be determined by a number of parametric tradeoffs. The major factors that will determine the ability of the lightning mapper to detect lightning during daytime will be the overall sensor throughput and the ratio of lightning signal to background noise ratio and total signal throughputs are determined by many sensor parameters including lens speed, detector quantum efficiency, filter bandwidth, frame time, spatial resolution, etc. Figure 4 lists some of the sensor parameters that extensive radiometric analyses indicate might be reasonable.

The major objective of all the tradeoff analyses is to maximize the sensor lightning detection efficiency. The goal is to detect 90% of all lightnings that occur within the sensor field of view. Figure 5 shows how changes in certain sensor parameters effect the detection efficiency which is directly related to the strength of the lightning signal. For example, a sensor with the values listed in Figure 4 should detect approximately 80% of all lightnings within its field of view. If the filter bandwidth were changed to from 8A to 5A and the lens speed were changed from F/1.5 to F/1.12, then the detection efficiency would improve to 90%. Obviously, there are many variables such as weight, power, cost, filter bandpass shifts, etc. that effect the overall system design in such a way that maximum sensor performance may not be desirable.

The lightning mapper design should be completed over the next year or so and it is expected that the instrument will be developed on a time schedule that is compatible for inclusion of the sensor on the GOES M satellite. Once on orbit, it is expected that the lightning mapper will provide unique and valuable data both for basic scientific research and real time hazard warnings. In addition, it will demonstrate that the combination of modern solid state mosaic focal plan arrays with extensive onboard signal processing provides a powerful technique for the detection of weak, background contaminated signals. The technology being applied to the lightning mapper problem should be easily adaptable for other atmospheric remote sensing applications. The resulting steering sensors would have significant advantages over present scanning systems.

References

Christian, H.J., R.L. Frost and S.J. Goodman, 1984: "Optical Characteristics of Lightning as Measuring from Above Cloud Tops." Preprint Volume, VII International Conference on Atmospheric Electricity, Albany, NY.

Davis, M.H., M. Brook, H. Christian, B.G. Heckes, R.E. Orville, C.G. Park, R.G. Roble and B. Vonnegut, 1983: "Some Scientific Objectives of a Satellite-Borne Lightning Mapper." Bull. Am. Meteor. Soc., Vol 64, 114-119.

Eaton, L.R., C.W. Poon, J.C. Shelton, N.P. Loverty and R.D. Cook, 1983: "Lightning Mapper Sensor Design Study." NASA Contractor Report, NASA CR-170909, Marshall Space Flight Center, AL.

Norwood, V., 1983: "Lightning Mapping Sensor Study." NASA Contractor Report, NASA CR-170908, Marshall Space Flight Center, AL.

CONCEPT FOR GEOSTATIONARY EXPERIMENTAL TEMPERATURE AND MOISTURE SOUNDER (GETMS)

J. B. Kumer, L. W. Sterrit, B. C. Steakley, L. A. Springer,
A. E. Roche, W. J. Rosenberg, T. C. James, J. F. Potter, A. R. Ostling,
D. O. Murray, L. G. Naes, T. C. Nast, and G. A. Perscheid

Lockheed Research & Development Division
3251 Hanover Street
Palo Alto, CA 94304

E. W. Koenig

ITT Aerospace Optical Division
3700 East Pontiac Street
Fort Wayne, IN

W. E. Shenk, J. Susskind, and D. Chesters

Laboratory for Atmospheres
NASA/Goddard Space Flight Center
Greenbelt, MD 20771

1. INTRODUCTION AND SUMMARY

The concept for a Geostationary Experimental Temperature and Moisture Sounder (GETMS) addresses a previously reported requirement (Shenk et al., 1987, 1986) for an advanced sounder that can achieve spectral resolution of the order 0.2 cm^{-1} in the 4.2-μm region with signal/noise sufficient to achieve temperature profile retrievals with vertical resolution of the order 1 to 2 km and accuracy to 1 K or less. The sounder must also be able to obtain high spectral resolution measurements (for H_2O profiling) in the 5- to 5.5-μm range as well as broadband (tens of cm^{-1}) measurements in a number of bands from 3.74 to 14.7 μm to characterize cloudiness and surface conditions.

The concept supports operation in a high-resolution 'nominal experimental mode' that would achieve the performance cited above for 1800 soundings of 10-km^2 pixels in 1 h. By using an interactively programmable capability to selectively sample clear-air areas, the effective areal coverage in a 1-h period might be a factor 2 to 10 times 180,000 km^2.

In the nominal experimental mode, soundings would be obtained: (1) in 13 channels near 4.18 μm at 0.2 cm^{-1} as recommended by Kaplan et al. (1977) to achieve enhanced vertical temperature resolution; and (2) in 8 channels (four each near 5.19 and 5.43 μm) at 0.3 cm^{-1} to achieve enhanced vertical H_2O vapor resolution. For comparison, additional soundings would be obtained in the 18 broadband infrared channels utilized by the GOES IJK.

The tropospheric nadir temperature sounding weighting functions for the 0.2-cm^{-1} channels near 4.18 μm provide the ultimate vertical resolution. This is due to a combination of three effects.

The 4.3-μm region has two advantages compared to the 15-μm region. The logarithmic derivative (dB/dT)/B of the blackbody function B near 4.3 μm changes approximately 3 times faster with temperature, which leads to narrower weighting functions in the troposphere where temperature increases as altitude decreases. The 4.18-μm wing absorption coefficient has additional strong temperature dependence, e.g., ~ exp(-2250/T) for channel 8, since it is dominated by high J value lines. Another advantage of the 4.3-μm region is its relative insensitivity to the water vapor continuum.

Finally, the 0.2-cm^{-1} resolution allows for sounding channels between the tightly packed (~ 0.7 cm^{-1} spacing) R-branch lines. Thus, optical depth and top side emissivity vary directly as pressure squared, much faster than for broader band channels (that include line centers), which vary directly as the pressure at best. The R-branch is free of complications, e.g., non-LTE, due to CO_2 hot-band or isotope lines. The only other significantly contributing specie in the region is N_2 via the pressure-induced continuum, which shares the pressure squared advantage.

The concept is versatile enough to support more experimental modes than the nominal described above. One mode would use more high-resolution channels near 4.18 μm than the 13 recommended by Kaplan et al. The Kaplan et al. channels 6 through 11 have weighting function peaks that span the altitude region 0 to 9 km with ~1.8-km spacing. Central spectral positions for these channels are located at the "holes" between lines in the 4.18-μm CO_2 band wing. Every other hole is used by Kaplan et al. for channels 6 through 11. An experimental mode that used all the holes in this region would produce a set of 11 weighting functions with 0.9-km spacing between the peaks on the range 0 to 9 km. Comparison of vertical resolution against ground truth for retrievals obtained in this mode versus the nominal experimental mode would be very interesting and useful. It is expected that better vertical resolution might be obtained by using more channels.

A second possibility would emphasize soundings from the mid troposphere to the lower strato-

sphere. This mode might be employed to develop cross sections of the jet stream, for example. In this mode, areal coverage would be sacrificed for precision.

A third possibility would involve the use of special high-resolution channels for sounding troposhperic chemistry and/or pollutants. An example would be measurement of the long-term structure and dynamics of the CO plume off the east coast of the United States.

Finally, the instrument could also be run in a purely operational mode utilizing only the GOES IJK channels and could achieve 1,080,000 km^2 coverage per hour in this mode.

Cryogenic cooling of the focal plane to achieve the necessary sensitivity for the 0.2 cm^{-1} 4.18-μm channels is required. The concept design calculated lifetime for a system compatible with a GOES experimental satellite that is launched by the STS is 2 years. Better than 18-month operation might be expected with such a system. Relaxation of the experimental sounder volume envelope from the one set by the STS launch scenario could improve the lifetime to 5 years or more, and maintain reasonable weight. These issues are discussed below.

2. SYSTEM CONSTRAINTS AND OVERVIEW

The baseline concept emphasized in this paper is constrained by compatibility with deployment on an experimental satellite that would be a sixth or seventh member of the GOES IJKLM series and would be limited to the STS launch envelope. Under this constraint, a baseline concept that can provide timely and valuable scientific data as described above is possible.

Where appropriate, we will point out advantages of an optimized concept that is essentially free of the STS launch envelope and weight constraints. The optimized concept is not necessarily incompatible with deploymaent on an experimental satellite that would be a sixth or seventh member of the GOES IJKLM series.

Figure 1 shows a functional schematic of the baseline experimental concept. The concept uses a modification of the operational temperature and moisture sounder that is to be deployed on the GOES series IJK (Jaurez and Koenig, 1986 and Koenig, 1987). The GOES IJK sounder has mass ~116 kg, focal plane radiatively cooled to 102 K, 220-K broadband filter wheel, and 295-K front-end optics with 12-in. primary and dual-axis interactively programmable scanning mirror.

The baseline experimental concept is constrained to retain the 295-K front end. A new module containing spectrometer, focal plane assembly (FPA), and solid CH_4 cryogenics would be interfaced with the front end of the present GOES IJK sounder at the position of the primary mirror. A multistage radiative cooler similar to the current design would be used to cool the spectrometer and to guard band the solid CH_4. The solid CH_4 would be used exclusively to cool the FPA to < 60 K. The new module would accept a convergent beam from the present front end. The entire system is constrained to fit in the position on the GOES satellite now occupied by the GOES IJK sounder, with volume increase constrained to permit launch by the STS.

The experimental concept spectrometer employs two filter wheels. The filter wheels are placed on either side of a first focus. The first of these contains 18 filters with the spectral

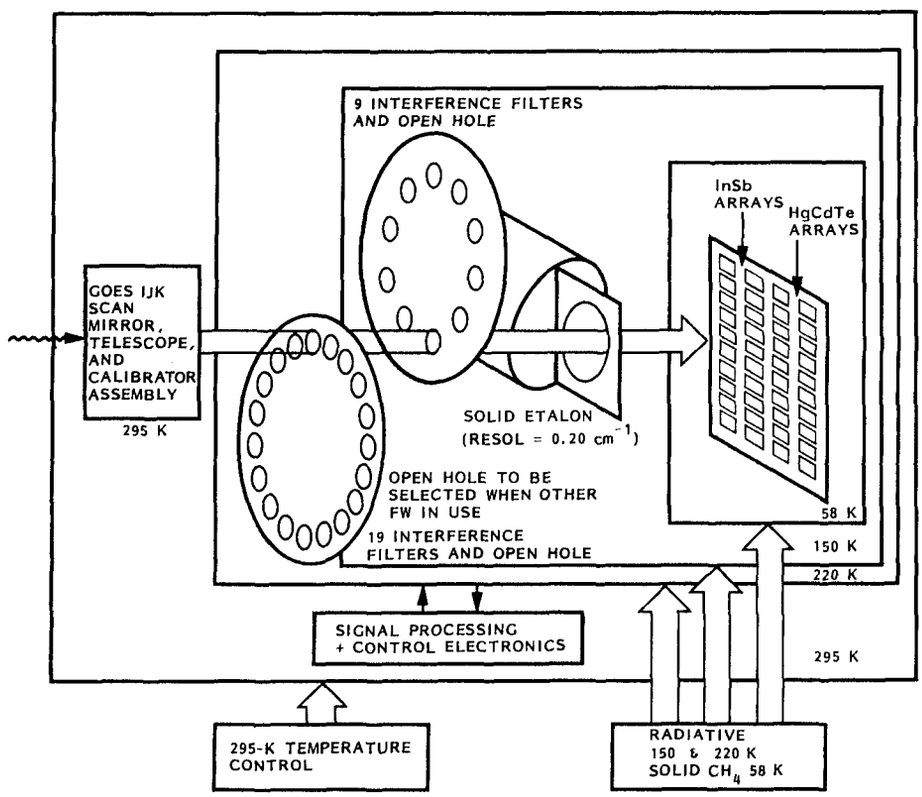

Fig. 1 GETMS Functional Diagram

characteristics of the GOES IJK sounder filters, an open hole, and a spare position. This filter wheel is radiatively cooled to 220 K. The second wheel is the first element of a an etalon spectrometer modeled after the one used by the Cryogenic Limb Array Etalon Spectrometer (CLAES). CLAES will be deployed on the NASA Upper Atmosphere Research Satellite (UARS) and is currently in assembly (Roche, 1985). The etalon spectrometer is cooled to 150 K by the next stage of the radiator.

When high-resolution measurements are in progress, the 220-K filter wheel is set so that the beam passes through the open hole. The etalon spectrometer is used to obtain the high-resolution measurements. It consists of the second wheel with nine broadband filters and an open hole. After passing through the broadband filter, the beam is collimated and passed through a narrowband solid (sapphire spacer) etalon. For example, for the 4.18-μm measurements, the broadband filter is ~10 cm^{-1} FWHM, and the etalon is 0.2 cm^{-1} FWHM, with finesse ~50. The etalon transmission channel can be tuned to any position within the broad filter band width by tilting 10 deg or less.

When the broadband measurements are in progress, the beam passes through a filter on the 220-K wheel, then through the hole in the 150-K wheel. The etalon is stowed parallel to the collimated beam. Positioning the etalon like this causes some obscuration but supports use of a low power draw etalon drive mechanism.

A 2-in. f1.5 optic focuses the beam on to the FPA (Fig. 2). There are 4 arrays of 10 detectors on the FPA. The center-to-center detector spacing is 0.12 mm. Active areas are (0.1 mm)* (0.1 mm). This corresponds to an active field of view (FOV) ~8 km*8 km at the ground, and 10-km center-to-center spacing.

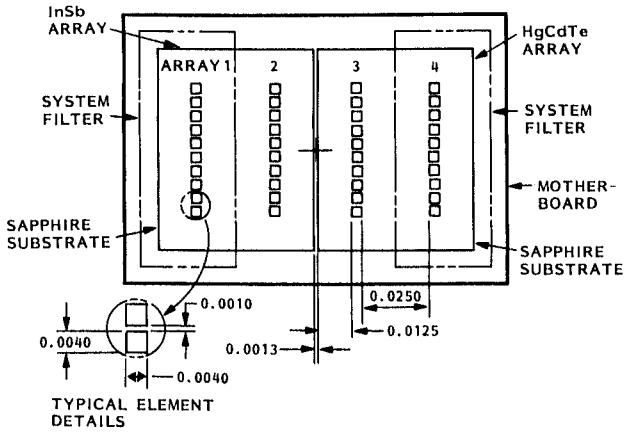

Fig. 2 GETMS Focal Plane

Array 1 will be used exclusively for temperature sounding near 4.18 μm. A system filter of ~100 cm^{-1} width is attached to the FPA over this array to reduce noise from the 150-K spectrometer cavity photons. Array 2 is used for sounding H_2O at high resolution, for high-resolution sounding for other tropospheric constituents such as the CO possibility cited above, and for the GOES IJK SWIR bands. (Spectral characteristics are listed in Jaurez and Koenig, 1986.) Arrays 1 and 2 will be In:Sb. Arrays 3 and 4 will be used for the GOES IJK MW and LW bands. The latter two arrays will be HgCdTe PC tuned to their respective spectral regions of application and will be chopped by a 500-Hz first-focus chopper at 150 K.

During a measurement in any given channel, only the data obtained on one of the four arrays will have meaning. A complete sounding in the nominal experimental mode described above will require that data be taken sequentially on all four arrays, i.e., 13 channels on array 1, 8 narrow channels on array 2, followed by six SW broadband channels on array 2, then five MW broadband channels on array 3, and finally six LW on array 4. While the filters are switched to move from one spectral region to the next, the scanning mirror must be used to register that array on the same area. This motion will be 7 x 280 μrad at most, and at least 0.1 s is budgeted for it. This is consistent with current GOES IJK scan mirror capability. Table 1 shows the timing for moving the two filter wheels, tilting the etalon, and moving the scan mirror to implement the nominal experimental mode described above. Cold space and blackbody calibration operations will be similar to those of the GOES IJK sounder.

The < 60-K, 0.1-mm In:Sb detectors will use JFET and charge integrating amplifiers similar to those described by Hartill et al. (1986) or Low (1984). This scheme takes advantage of the large resistance (~4 x 10^{12} Ω) of these diodes at 60 K and effectively eliminates Johnson noise to the extent that noise is dominated by signal and/or front-end optics photon fluctuations and, for relatively short integration times, read noise.

The HgCdTe photoconductive detectors have nominal impedance of 50 Ω; hence, bipolar amplifiers that are not on the focal plane may be used. These devices have total input noise values of the order 0.5 nV per root Hz. Power dissipation is not critical, since they are not located on the focal plane.

The HgCdTe detectors will be operated at approximately 0.1-V bias to limit power dissipation on the focal plane to less than 5 mW. Based on the Kinch et al. (1977) measurements, we estimate that this will degrade zero background detectivity by about 40 percent. This should not impact GETMS performance, since the relatively long integration time will ensure that sensitivity is equal to or exceeds that of the GOES IJK operational sounder.

3. PERFORMANCE

3.1 Baseline System Performance Analysis for the 4.18-μm Sounding

The system area times solid angle product for the active area of a detector is 3.69E-5 cm^2-sr. The GETMS concept design (Fig. 3) shows four mirrors in the spectrometer. Total system transmission exclusive of the blocker filter, system filter, and etalon is estimated by assuming 0.97 specular reflectivity for each of the seven mirrors in the system, 0.9 transmittance for the window, and 0.8 obscuration factor due to the secondary mirror. Resulting optics and window transmittance equal 0.654. System filter, blocker filter at one-half maximum, and etalon at maximum transmittances are taken to be 0.85, 0.25, and 0.55, respectively. Thus, total system transmittance is 0.068. The spectral bandwidth is $(FWHM/2)\pi = 0.314$ cm^{-1}, where FWHM refers to the etalon. Thus, the spectral throughput T_{put} = 7.84E-7 cm^2-sr-cm^{-1}.

Table 1 PROPOSED TIMING FOR GETMS NOMINAL EXPERIMENTAL MODE

Array No.	150-K BFW Blocker No.	Channel No.	Integration Time (τ)	Move Time (s)		
				150-K BFW	Etalon	220 K-BFW
1	→1, 4.18 μm			0.5		
		1	0.5		0.125	
1	→2, 4.18 μm			0.5		
		2	0.5		0.125	
1	→3, 4.18 μm			0.5		
		3→7	5*0.5		5*0.125	
1	→4, 4.18 μm			0.5		
		8→13	6*0.25		6*0.125	
2	→5, H_2O 1			0.5		
		1→4	4*0.125		4*0.125	
2	→6, H_2O 2			0.5		
		5→8	4*0.125		4*0.125	
2	→7, hole			0.5		
2		SW*6	6*0.1			6*0.1
3		MW*5	5*0.1			5*0.1
4		LW*7	7*0.1			7*0.1
Timing Totals =			7.8	3.5	2.63	1.8

Total operational period = 15.73 s
Several seconds per cycle for calibration activities must be alotted; hence, ≈ 20 s per cycle implies 30 soundings/min or 1800 soundings/h

The cold-space viewing noise equivalent spectral radiance (NESR) can be broken into contributions that vary as τ^{-1} and $\tau^{-0.5}$, where τ is the integration time. The first of these components is the read noise, referred to as the "series noise" by Hartill et al., who calculated 150 read noise electrons for their system. Their experiment indicated that read noise might be as high as 180. Low has reported experimental read noises on the order of 10 electrons. Infrared Laboratories, Inc. of Tucson, Arizona, advertises less than 50 read noise electrons for 1- to 64-s integration times for their Frank Low design JF77 JFET integrating amplifier. The Hartill et al. formula for noise electrons scaled as the inverse square root of T_{RD} the correlated double sample and hold read time. They used a 1-ms T_{RD}. Going to 10 ms then would presumably give approximately 50 noise electrons, which approaches the Low results. Low did not report a read time. Both sets of results were reported for integration times on the order of 1 s. In both cases, the number of read noise electrons was independent of integration time to first order.

For our baseline system noise analysis, we conservatively assume a read noise of about 200 electrons. This corresponds to NEP = 1.4E-17 W/Root Hz, and the read noise component NESR-RD is given by NESR-RD = 1.79E-11/τ in units W/(cm^2-sr-cm^{-1}).

The contributions to NESR-ROOT, the component of noise that scales like $\tau^{-0.5}$, are from fluctuations of photons emitted by the 295-K front-end mirrors and window and fluctuations of photons emitted in the 150-K spectrometer cavity, and fluctuations due to detector thermal generation, i.e., Johnson noise. For τ = 1 s, the contribution from each of these is 4.65E-11, 0.69E-11, and 1.27E-11 W/(cm^2-sr-cm^{-1}), respectively. The RMS sum NESR-ROOT = 4.87E-11.

For arbitrary τ, the cold-space view NESR COLD = SQRT[(1.79E-11/τ)^2 + (4.87E-11/$\tau^{0.5}$)^2] and NESR-COLD = 5.19E-11 W/(cm^2-sr-cm^{-1}) for τ = 1 s. Note 1 mW/(m^2-sr-cm^{-1}) = 1.E-7 W/(cm^2-sr-cm^{-1}).

For the baseline system, the 1-s integration time, 4.18-μm NESR-COLD is dominated by emission from the 295-K front-end mirrors and window. On nadir viewing, we would expect the noise to be dominated by signal photon fluctuations for channels that see deep into the troposphere, and by the cold-space NESR for channels that see down to the vicinity of the tropopause.

This point is illustrated by the data listed in Table 2. These include the NESR-COLD for values of the integration time τ = 0.25 and 0.5 s for the baseline system, and τ = 0.25 s for an optimized system (defined in section 3.3). The contributions from signal photon fluctuations NESR-SIG, and NESR-TOT, the RMS sum of NESR-SIG and NESR-COLD, are also listed in Table 2 as a function of the temperature T of the viewed scene, with T ranging from 180 to 340 K for the three cases cited above.

The noise equivalent temperature (NET) corresponding to NESR-TOT is also listed in Table 2. NET is less than 0.20 K for sounding in the mid to low troposphere for all three cases. The optimized case obtains highest performance in the shortest time over the widest range of scene temperatures.

3.2 Requirement for Cryogenic FPA

The thermal generation noise varies as $(T/RA)^{0.5}$ where RA and T are the detector resistance area product and temperature. From data published by Wimmers et al. (1982), the near zero bias RA varies directly as exp(1267/T), where T is the detector temperature. For τ = 0.5 s and T = 70 K, the detector thermal generation noise would be equal to the sum of all other noises cited above; for T = 79 K, it would be 4.65 times greater. It is this fast variation in Johnson noise with temperature that sets the requirement

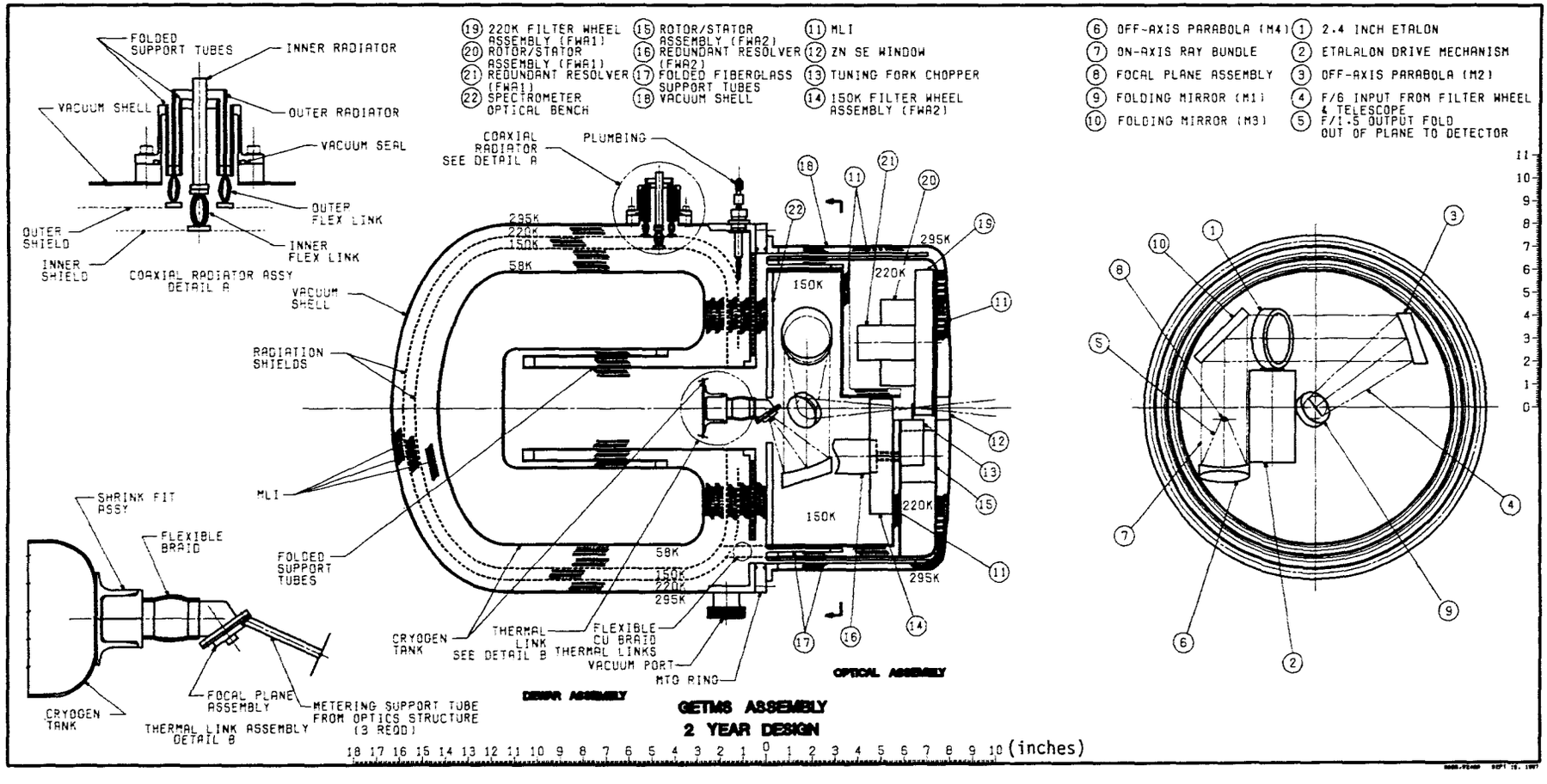

Fig. 3 GETMS Spectrometer and Cryogenics (SC) Module Design Concept

Table 2 NOISE VERSUS VIEWING SCENE TEMPERATURE*

Scene Temp. (K)	Baseline System τ = 0.25 s NESR-COLD =0.121E-09			Baseline System τ = 0.50 s NESR-COLD =0.776E-10			Optimized System τ = 0.25 s NESR-COLD = 0.157E-10		
	NESR-SIG	NESR-TOT	NET (K)	NESR-SIG	NESR-TOT	NET (K)	NESR-SIG	NESR-TOT	NET (K)
340.0	0.675E-09	0.685E-09	0.03	0.477E-09	0.483E-09	0.02	0.675E-09	0.675E-09	0.03
330.0	0.579E-09	0.591E-09	0.04	0.409E-09	0.417E-09	0.03	0.579E-09	0.579E-09	0.04
320.0	0.492E-09	0.506E-09	0.04	0.348E-09	0.356E-09	0.03	0.492E-09	0.492E-09	0.04
310.0	0.414E-09	0.431E-09	0.05	0.292E-09	0.303E-09	0.03	0.414E-09	0.414E-09	0.05
300.0	0.344E-09	0.364E-09	0.06	0.243E-09	0.255E-09	0.04	0.344E-09	0.344E-09	0.05
290.0	0.282E-09	0.307E-09	0.07	0.199E-09	0.214E-09	0.05	0.282E-09	0.283E-09	0.06
280.0	0.228E-09	0.258E-09	0.08	0.161E-09	0.179E-09	0.05	0.228E-09	0.229E-09	0.07
270.0	0.182E-09	0.218E-09	0.10	0.129E-09	0.150E-09	0.07	0.182E-09	0.182E-09	0.08
260.0	0.142E-09	0.187E-09	0.13	0.101E-09	0.127E-09	0.09	0.142E-09	0.143E-09	0.10
250.0	0.109E-09	0.163E-09	0.17	0.772E-10	0.110E-09	0.12	0.109E-09	0.110E-09	0.12
240.0	0.820E-10	0.146E-09	0.25	0.580E-10	0.969E-10	0.17	0.820E-10	0.835E-10	0.14
230.0	0.601E-10	0.135E-09	0.40	0.425E-10	0.885E-10	0.26	0.601E-10	0.621E-10	0.18
220.0	0.428E-10	0.128E-09	0.68	0.302E-10	0.833E-10	0.44	0.428E-10	0.455E-10	0.24
210.0	0.295E-10	0.124E-09	1.27	0.208E-10	0.804E-10	0.82	0.295E-10	0.334E-10	0.34
200.0	0.196E-10	0.122E-09	2.56	0.138E-10	0.788E-10	1.65	0.196E-10	0.251E-10	0.53
190.0	0.124E-10	0.122E-09	5.67	0.880E-11	0.781E-10	3.65	0.124E-10	0.200E-10	0.93
180.0	0.753E-11	0.121E-09	13.87	0.532E-11	0.778E-10	8.91	0.753E-11	0.174E-10	1.99

*NESR-SIG, the signal photon fluctuations noise contribution; NESR-TOT, the RMS of NESR-COLD and NESR-SIG; and the corresponding noise equivalent temperature (NET) are listed versus scene temperature. NESR units are $W/(cm^2\text{-}sr\text{-}cm^{-1})$.

for cryogenic rather than radiative cooling of the FPA. For example, since the solar mast is in the field of view of the GOES IJK FPA radiative cooler, this cooler could achieve no lower temperature than 77 K, even if the heat load on it were zero.

3.3 Baseline Versus Optimized System Performance Results

The solid-CH_4 cryogen (T = 58 K) selected for the baseline sets the Johnson noise well below the baseline instrument photon fluctuations noise floor. These fluctuations are driven by the requirement to make observations at local midnight, which in turn drives the front-end optics long-term temperature to 295 K.

For an optimized system, one might consider closing the front-end aperture for ~1 h before and after local midnight. In this case, if the front-end optics temperature could be kept stable at ~200 K and the spectrometer temperature reduced slightly from baseline, then instrument photon noise would never be greater than signal photon noise. In the optimized case, solid-Ar cryogen would reduce detector temperature to ~48 K, so again Johnson noise would not be a factor. Finally, based on the results of Hartill et al. and Low, we believe that 30 to 50 read noise electrons per integration is a realistic goal.

Table 3 compares baseline and optimized system parameters. Table 4 shows the NET expected to be achieved by the baseline, and optimized systems for integration times of 0.25 and 0.5 s, for a standard midlatitude summer atmosphere, and for channels 1 through 11 of the 13 recommended by Kaplan et al. The NET for channels 12 and 13 is expected to be slightly better than for channel 11.

3.4 Performance for Arrays 2, 3, and 4

The narrowband H_2O measurements are to be made on array 2, which will use charge amplifiers similar to array 1. Broadband SW measurements will also be made on array 2. The broadband MW and LW measurements will be made on arrays 3 and 4, respectively. Table 5 summarizes performance of these measurements.

4. BASELINE DESIGN CONCEPT

4.1 System Design, Weight, Power, and Envelope

Figure 3 shows the GETMS spectrometer and cryogenics (SC) module design concept. The GETMS accepts an f/6 beam from the GOES IJK front-end optical assembly. This assembly includes the GOES two-axis scan mirror system, classic Cassegrain telescope, and calibrator assembly.

The GETMS design concepts are based on CLAES technology. The GETMS spectrometer support structure is based on the fiberglass tube structure used in the CLAES sensor. The tube thicknessess were estimated from CLAES guidelines that provide sufficient strength to withstand launch loads while still providing minimal thermal conductance between temperature zones. The optical/ mechanical packaging and drive mechanism envelopes were also drawn from the CLAES design. The various spectrometer component weights were scaled from similar CLAES component weights.

The design of radiator interface (detail A) with the vacuum shell and inner and outer shields has been developed and tested over the past 5 years for application to the Long-Life Cooler Program solid CH_4/NH_4 cooler. The flexible copper links as well as the shield to spectrometer connections are shrink-fit mechanisms which are assembled with clearance at room temperature and sieze on cooldown to provide a high-conductance thermal joint. These have been used in several flight

Table 3 CHARACTERISTICS OF BASELINE VERSUS OPTIMIZED SYSTEM PARAMETERS AND PERFORMANCE FOR SOUNDING AT 4.18 μm IN 13 0.2-cm^{-1} CHANNELS (KAPLAN et al.)

Parameters	Baseline	Optimized
Cryogen	CH_4 (T = 60K)	Ar (T = 48K)
Front-End Temp. (K)	295	200
Calculated Lifetime (years)	2	6
Spectrometer Temp. (K)	150	130
Length (in.)	23.5	33.8
Diameter (in.)	16.0	23.5
Weight (lb)	139.2	278.6
NESR (τ = 1 s) Contributions W/(cm^2-sr-cm^{-1}):		
Front-End Photons	4.65E-11	2.92E-12
Spectrometer	0.69E-11	1.18E-12
Johnson Noise	1.27E-11	1.01E-12
NESR-ROOT	4.87E-11	3.31E-12
Read Noise	1.79E-11 (200 e)	3.58E-12 (40 e)
NESR-COLD	5.19E-11	4.88E-12

Table 4 NET FOR THE BASELINE AND OPTIMIZED SYSTEMS FOR A STANDARD MIDLATITUDE SUMMER ATMOSPHERE AND FOR CHANNELS 1 THROUGH 11 RECOMMENDED BY KAPLAN, et al.*

Channel No.	Pressure (mbar)	Temperature (K)	Altitude (km)	Noise Equ. Temp. (K) Dwell Times (s)			
				0.25	0.50	0.25	0.50
				Baseline		Optimized	
11	1013.0	300.0	0.0	0.060	0.040	0.050	0.040
10	847.0	291.0	1.6	0.069	0.049	0.059	0.040
9	678.0	281.0	3.4	0.079	0.049	0.069	0.049
8	548.0	269.0	5.2	0.103	0.072	0.082	0.061
7	421.0	256.0	7.2	0.145	0.101	0.108	0.074
6	330.0	244.0	9.0	0.210	0.145	0.130	0.091
5	162.0	213.0	13.7	1.020	0.659	0.301	0.207
4	110.0	200.0	16.0	2.560	1.650	0.530	0.340
3	77.0	199.0	18.2	2.789	1.797	0.561	0.358
2	35.0	215.0	23.1	0.887	0.574	0.279	0.194
1	18.0	227.0	27.6	0.470	0.305	0.196	0.141

*Pressure, temperature, and altitude refer to the weighting function maximum for each channel

hardware programs (Naes and Nast, 1987) to facilitate ease of assembly and attain high reliability.

The design concept provides a basis to estimate system weight and heat flow through support tubes, multilayer insulation (MLI), lead wires, and plumbing. The heat flow estimates are required to size the radiator cooling capacities and to set requirements on temperature control heat inputs.

Total SC module weight estimate is 63.3 kg, 20.55 for cooler, 29.18 for spectrometer, and 13.64 for electronics. This is interfaced with the GOES IJK sounder front-end of mass 106 kg. The total GETMS mass is estimated to be approximately 170 kg. The total SC module electrical power requirement is estimated to be 30 W. Since the electrical power requirement of the GOES IJK sounder system is 108 W, we expect the GETMS total requirement to be less than 138 W. The baseline 2-year GETMS, comprised of the GETMS SC module integrated with the GOES IJK front end, will extend 5.5 in. longer in the direction of the input optical beam than does the current GOES IJK sounder. This just fits into the GOES STS launch envelope. A 5-year calculated lifetime CH_4 system would weigh only 46 lb more, but would be 7.5 in. longer and 5 in. wider.

4.2 Cryogenics

The CRYOP computer code was used to size the cryostat. This code was initially developed in 1973 and has been continously upgraded and refined since then. Its features include (a) temperature-dependent properties, (b) user choice of MLI materials, (c) vapor-cooled shield, and (d) user choice of nine cryogens. Normally, the CRYOP inputs are the required cryogen lifetime, the experiment heat load, and a geometric parameter (either the system diameter or the length-to-diameter ratio). CRYOP

Table 5 PERFORMANCE OF THE BROADBAND CHANNELS AND NARROWBAND H_2O CHANNELS FOR THE INTEGRATION TIMES GIVEN IN TABLE 1

Channel Assignment	NESR-COLD	NESR-200	NESR-300
	(1.E-12 W/cm^2-sr-cm^{-1})		
Narrowband H_2O 5.19 μm	1111.0	1118.0	1707.0
Narrowband H_2O 5.42 μm	1342.0	1354.0	2101.0
GOES IJK LW channel 1	864.4	887.0	978.2
channel 2	884.0	905.6	997.0
channel 3	902.3	923.0	1014.
channel 4	758.7	778.0	867.5
channel 5	773.5	792.0	881.2
channel 6	443.3	459.0	541.1
channel 7	285.9	299.1	373.6
GOES IJK MW channel 8	150.2	170.1	281.5
channel 9	291.0	305.6	434.3
channel 10	169.2	172.7	242.5
channel 11	124.3	126.7	182.4
channel 12	170.3	171.7	218.7
GOES IJK SW channel 13	29.57	29.96	72.86
channel 14	28.89	29.25	70.62
channel 15	27.88	28.19	67.20
channel 16	16.39	16.50	39.02
channel 17	15.05	15.13	34.06
channel 18	6.969	6.995	16.49

outputs the overall system dimensions, tank sizes, cryogen weight and total cryostat dry weight, optimized MLI thicknesses, and heat loads to external radiators.

CRYOP calculations were used to size 58-K CH_4 systems and performance-optimized 48-K Ar systems for calculated lifetimes ranging from 2 to 6 years. The baseline 2-year CH_4 baseline system is an example that fits into the STS launch envelope.

4.3 Heat Load Summary

The first stage of each InSb detector integrating amplifier will be a JFET with characteristics similar to the Infrared Laboratories JF77 which dissipates less than 40 μW. The total InSb preamp dissipation on the focal plane will be less than 0.8 mW. The InSb detectors will be operated near zero bias, so there will be no detector dissipation contribution. The 50-Ω HgCdTe PC detectors will be operated at 0.1-V bias and will dissipate a total of 4 mW on the focal plane. As mentioned above, the bipolar amplifiers for these detectors will not be located on the focal plane. Total focal plane dissipation is estimated to be less than 5 mW.

Table 6 summarizes the heat loads to the solid CH_4 and the 150- and 220-K radiators. Temperature control in the 150- and 220-K areas is implemented via heaters, PRT sensors, and electronic feedback control. Temperature control is required to maintain spectral stability and to compensate for MLI degradation.

4.4 ETALON SPECTROMETER

The optics are required to collimate the incoming beam to pass it through the etalon. The

Table 6 HEAT LOAD SUMMARY FOR BASELINE GETMS

FPA and Structure to Cryogen:

Source	Heat Load (mW)
Dissipation on focal plane	5.0
Lead wires to focal plane	1.0
150-K radiation into FPA	4.0
Support structure to 150-K optic	8.0
Margin	7.0
Parasitics	49.0
Total	73.0

Heat Flow into 150-K Radiator:

Source	Head Load (mW)
Chopper Dissipation	100
EDM Drive Dissipation	182
Mechanisms Lead Wire Conduction	100
Parasitics	695
Temperature Control	400
Total	1477

Heat Flow into 220-K Radiator:

Source	Heat Load (mW)
150-K BFW Motor Dissipation	200
220-K BFW Motor Dissipation	500
Mechanisms Lead Wires	400
Parasitics	990
Temperature Control	1000
Total	3090

fastest possible practical optic is required to focus the beam onto the FPA to optimize signal/noise. The FPA is supported off the spectrometer structure to facilitate alignment. Move times, weights, and electrical power requirements of the spectrometer mechanisms are determined from CLAES experience and test data with analogous brassboard and flight units.

The spectral characteristics of the blocking filters in the 150-K blocking filter wheel (BFW) are consistent with actuals for the CLAES blocking filter set. A 2-in. clear-aperture etalon comprised of a 300-μm thick sapphire substrate, and mirrors consisting of 5 1/4 wave (4.5 μm) high-low Ge:ZnSe pairs with the ZnSe adjacent to the sapphire, will exceed the etalon performance requirements cited in Section 2, provided that parallelism of the substrate faces of better than 6328A/24 is achieved and that loss on reflection due to scattering and/or absorption less than 0.5 percent is achieved. Based on CLAES and previous experience, these are benign requirements. Since sapphire is slightly birefringent, the substrate must be cut and mounted so that the optic axis and propagation direction are coincident at normal incidence. The splitting will be less than 0.06 cm^{-1} at maximum tilt angle.

4.5 GETMS Versus CLAES Weight Comparison

The fully charged CLAES cryostat weighs 2197 lb, and the fully charged GETMS cryostat weighs 45.2 lb. Both have 2-year calculated lifetimes. Differences in system requirements determine the relative weights. For GETMS, only the FPA requires cryogenic cooling. CLAES requires high sensitivity at long wavelength. This requires cryogenic cooling of the telescope and spectrometer in addition to the FPA. CLAES uses solid Ne to cool the spectrometer and FPA to less than 19 and 15 K, respectively. The Ne-cooled region is guard banded by a solid CO_2-cooled region. The solid CO_2 is also used to cool the telescope. Table 7 follows through this comparison quantitatively.

5.0 REFERENCES

Hartill, D., F. Lisi, and A. Bettarini, Applied Optics, Vol. 25, No. 10, 1701, 1986.

Jaurez, D. J., and E. W. Koenig, Paper 10.6, Proc. AMS-sponsored Second Conference on Satellite Meteorology/Remote Sensing and Applications, Williamsburg, VA, May 1986.

Kaplan, D. K., M. T. Chahine, J. Susskind, and J. E. Searl, Applied Optics, Vol. 16, No. 2, 322, 1977.

Koenig, E. W., ITT Electro-Optical Systems Report, Sep 1987.

Kinch, M. A., S. R. Borrello, and A. Simmons, Infrared Physics, Vol. 17, 127, 1977.

Low, F. J., Applied Optics, Vol. 23, No. 9, 1308, 1984.

Naes, L. G., and T. C. Nast, Advances in Cryogenic Engineering, Vol. 31, 295, Plenum Press, 1987.

Roche, A. E., IAGA Symposium on Radiation in the Middle Atmosphere, Prague, Czechoslovakia, 1985.

Shenk, W. E., F. Von Bun, V. S. Suomi, W. Esais, and M. Maxwell, Paper 10.7, Proc. AMS-sponsored Second Conference on Satellite Meteorology/Remote Sensing and Applications, Williamsburg, VA, May 1986.

Shenk, W. E., T. H. Vonder Haar, and W. L. Smith, Bulletin of American Meteorological Society, 21, 1987.

Wimmers J. T., and D. S. Smith, Proc. SPIE, Vol. 364, 123, 1982.

Table 7 COMPARISON OF GETMS VERSUS CLAES WEIGHTS

Characteristics	GETMS	CLAES
Heat load (mW) to cryogen:		
FPA and parasitics to CH_4	73	
FPA, spectrometer, and parasitics to Ne	-	710
Aperture and parasitics to CO_2	-	2130
Enthalpy of sublimation (J/g)	615 for CH_4	
	-	105 for Ne
	-	607 for CO_2
Calculated lifetimes (years)	2	2
Weight of cryogens (lb)	16.7 CH_4	988 Ne
	-	484 CO_2
Dry cryostat (lb)	28.5	707
Total cryostat weight (lb)	45.2	2197

HIGH RESOLUTION INTERFEROMETER SOUNDER - THE RETRIEVAL OF ATMOSPHERIC TEMPERATURE AND WATER VAPOR PROFILES

W. L. Smith[1], H. M. Woolf[2], H. B. Howell[2], H. E. Revercomb[1], and H.-L. Huang[1]

[1]Space Science and Engineering Center
[2]NOAA/NESDIS Systems Design and Applications Branch
Cooperative Institute for Meteorological Satellite Studies
Madison, Wisconsin 53706

1. INTRODUCTION

The High resolution Interferometer Sounder (HIS) is the first of a new generation of passive remote sensors for achieving high vertical resolution sounding information. An aircraft version of HIS is a Michelson Interferometer with a spectral resolving power ($\lambda/\Delta\lambda$) of approximately 2000 covering a spectral range from 3.7-16.7μm. A spacecraft version of the instrument is under development for operational geostationary applications beginning around 1995. In this paper, a technique is described for retrieving atmospheric profiles from the 3000 spectral radiance observations provided by the HIS. Results achieved from spectral radiances observed from the NASA ER2 aircraft are compared with radiosondes and soundings obtained by the VISSR Atmospheric Sounder (VAS) to demonstrate the improved sounding performance achieved with the HIS.

The use of high spectral resolution interferometry will enable the achievement of optimal performance of passive remote sounders. To approach the ultimate limit of vertical resolving power of passive radiometers, the sounding instrument must achieve a spectral resolution better than 0.1%. With this resolution, one avoids smearing contributions to the upwelling radiances from relatively opaque line centers with radiances from much more transparent regions in between the absorption lines.

For examples, Figs. 1 and 2 show the effect of spectral resolution on radiance smearing. The radiance spectrum was achieved with the airborne version of the High resolution Interferometer Sounder (HIS) (Smith et al., 1986) from the NASA U2 aircraft overflying Huntsville, Alabama on June 15, 1986. The HIS spectra are achieved at a resolution of about 0.5 cm^{-1} from 600-1100 cm^{-1} (9.1-16.7μm), and 1.0 cm^{-1} resolution from 1100-2700 cm^{-1} (3.7-9.1μm). The ground resolution and spacing of the HIS observations is 2 km from the U2 altitude of 65,000 feet. The noise equivalent temperature and calibration accuracy are both about 0.1-0.2°C over much of the spectrum (Revercomb et al., 1987). In Fig. 1, blackened portion of the bars representing the half power spectral bandwidths of the current GOES VISSR Atmospheric Sounder, VAS, (Smith et al., 1981) are shown for comparison. In Fig. 2, the brightness temperature spectrum of a small portion of the R-branch of the 15 μm CO_2 band is shown at the HIS resolution and at the nominal 15 cm^{-1} resolution of the filter radiometers such as the VAS. It can be seen that brightness temperature smearing of the order of 30°K occurs as a result of the inability of the filter radiometer to resolve the CO_2 lines which have a typical spacing of 1.7 cm^{-1} (0.03μm) in this spectral region. A 30°K brightness temperature smearing corresponds to a typical vertical temperature gradient over a 5 km depth of the atmosphere. Considering that the width of a monochromatic weighting function is 8 km, the added 5 km smearing due to inadequate spectral resolution causes an additional 60% degradation of vertical resolving power in spectral regions where all the absorption lines are of equal strength. Because the line strengths will vary considerably over a 15 cm^{-1} interval (see Fig. 2), additional vertical resolving power degradation occurs.

Figure 3 shows typical Planck radiance weighting functions for a VAS and HIS spectral channel. One can see that there is a 50 percent greater resolving power in a single HIS channel than in a single VAS channel. The ultimate vertical resolution of atmospheric profiles derived from a set of spectral radiances depends

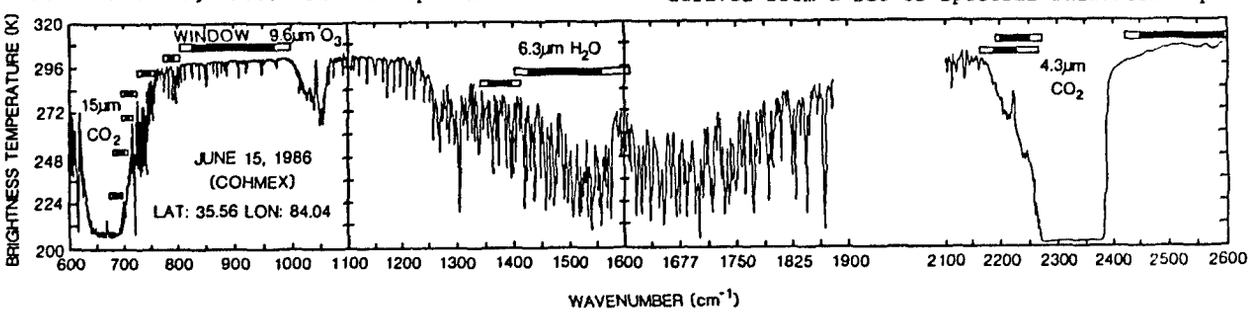

Fig. 1. HIS observed spectrum with VAS spectral bandwidths superimposed.

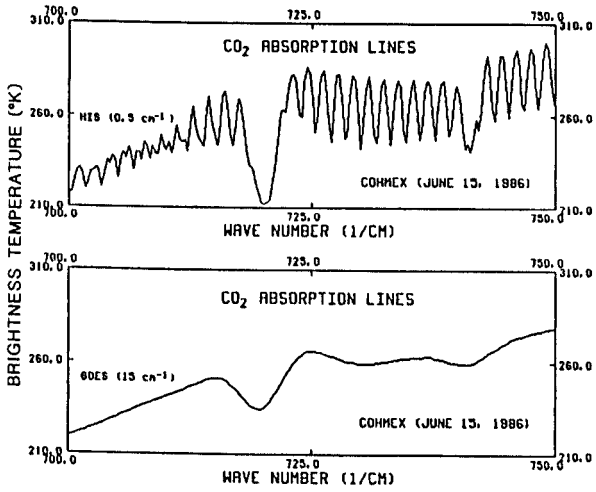

Fig. 2. CO_2 emission spectrum at HIS (0.5 cm^{-1}) resolution (top) and VAS (15.0 cm^{-1}) resolution (bottom).

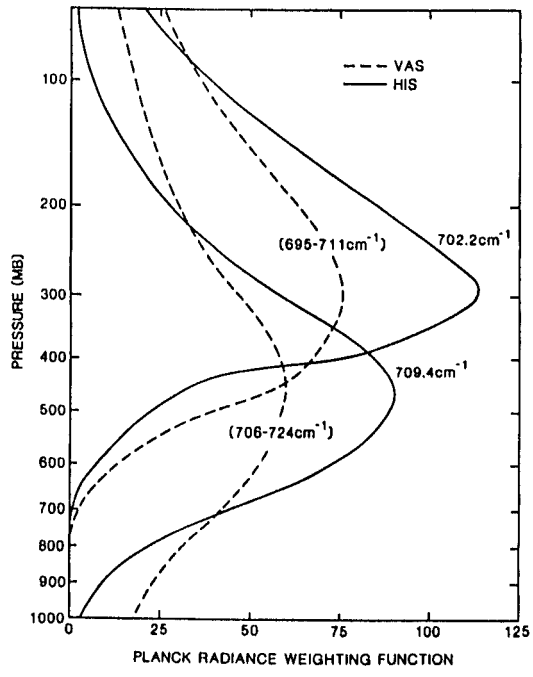

Fig. 3. Plank radiance weighting functions ($d\tau/d\ln p$) at HIS and VAS spectral resolutions.

on the number of spectral channels, their positions, and the noise level of the radiances. The expected vertical resolution of HIS soundings has been determined from theoretical analyses to degrade from 0.7 km near the surface to 3 km at 100 mb with further degradation to 6 km at 10 mb and above. This resolution is a factor of two to three better than that achievable with filter radiometers and will provide significantly improved profiles for weather analysis and forecast models.

2. SOUNDING RETRIEVAL PROCEDURE

The perturbation form of the radiative transfer equation has been shown by Smith et al. (1984) to be

$$\delta T_B = \delta T_s f_s \hat{\tau}_s - \int_0^{P_s} \delta T f \frac{d\hat{\tau}}{dp} dp + \int_0^{P_s} \delta\tau f \frac{dT}{dp} dp \quad (1)$$

where δT_B is the deviation of the observed brightness temperature, T_B, for a given wavelength, from that corresponding to a reference or guess atmospheric temperature and water vapor profile condition, δT_s is the deviation of the actual surface skin temperature from the reference condition, δT is the deviation of the true atmospheric temperature, T, from its reference, T, $\delta\tau$ is the deviation of the true spectral transmittance profile from that corresponding to the reference water vapor profile condition, $\hat{\tau}$, and f is the ratio $(\partial B/\partial T_B)/(\partial B/\partial T)$ where B is Planck radiance.

With the HIS, we have 3000 spectral channels sensitive to the surface temperature and the temperature and water vapor profile. The sensitivity of the radiances to temperature and water vapor varies greatly across the spectrum due to the degree of overlap between water vapor absorption lines and lines due to uniformly mixed gases such as CO_2 and N_2O. Also, the Planck function dependence upon wavelength and temperature contributes to the spectrally varying sensitivity. Because of the mutual dependence of radiance on temperature and water vapor, it is desirable to solve for the temperature and water vapor profile simultaneously from the complete set of spectral observations. A simultaneous solution is achieved by noting that for the very high HIS spectral resolution, the atmospheric transmittance can be represented as the product of those for water vapor and dry air. Thus,

$$\hat{\tau} = \tau_d \hat{\tau}_w \quad (2)$$

In (2), τ_d is the transmittance of the "dry" atmosphere which is a function of the uniformly mixed gases whose concentrations are known and $\hat{\tau}_w$ is the spectral transmittance due to water vapor alone. (Ozone is included in τ_d.) Using (2) in (1) yields

$$\delta T_B = f_s \delta T_s \hat{\tau}_s - \int_0^{P_s} f \delta T \hat{\tau}_w \frac{d\tau_d}{dp} dp - \int_0^{P_s} f \delta T \tau_d \frac{d\hat{\tau}_w}{dp} dp + \int_0^{P_s} f \tau_d \delta\tau \frac{dT}{dp} dp \quad (3)$$

In order to solve (3) for the water vapor profile, let

$$\delta\tau_w \cong \frac{d\hat{\tau}_w}{d\hat{U}} \delta U \quad (4)$$

where U is the precipitable water vapor profile. Furthermore we note that

$$\delta U = \frac{d\hat{U}}{dT} (T - T_w) \quad (5)$$

where T_w is the temperature profile as a function of the true precipitable water vapor profile U whereas T is the temperature profile as a function of the reference precipitable water vapor profile $\hat{U}$. Substituting (5) and (4) into (3) yields

$$\delta T_B = f_s \delta T_s \hat{\tau}_s - \int_0^{P_s} f \delta T \hat{\tau}_w \frac{d\tau_d}{dp} dp - \int_0^{\hat{U}_s} f \delta T_w \tau_d \frac{d\hat{\tau}_w}{d\hat{U}} d\hat{U} \quad (6)$$

where $\delta T = T - \hat{T}$ and $\delta T_w = T_w - \hat{T}$. Equation (6) describes the perturbation of the observed brightness temperature spectrum from a reference condition in terms of three variables: the deviation of the true surface skin temperature from the reference, the deviation of the atmospheric temperature profile from the reference profile as a function of pressure and the deviation of the atmospheric temperature profile from the reference profile as a function of atmospheric precipitable water vapor content. Note that if the reference precipitable water vapor concentration as a function of pressure is correct then $\tau_w = \tau_w$, $\delta T_w = \delta T$ so that the two integrals combine to yield the normal form of the radiative transfer equation ($f\delta T_s \tau_s - \int_0^{P_s} f\delta T(d\tau/dp)dp$). Otherwise, $\delta T_w \neq \delta T$ so that the T and T_w profiles resulting from the solution of (6) will differ from each other depending upon the error in the presumed water vapor condition.

The numerical solution of (6) is achieved by using a basis function representation of δT and δT_w; namely,

$$\begin{matrix}\delta T(p) \\ \text{and} \\ \delta T_w(p)\end{matrix} = \sum_{i=1}^{N} C_i \phi_i(p) \qquad (7)$$

where $\phi_i(p) = (p/p_i^*) \operatorname{Exp}(-p/p_i^*)$ where p is atmospheric pressure and p_i^* is the pressure of the "standard" atmospheric pressure levels (1000, 850, 700, 500, 400, 300, 250, 200, 150, 100, 70, 50 mb). The functions $\phi_i(p)$ can be shown to be equivalent to Planck radiance weighting functions ($d\tau/d\ln p$) of a uniformly mixed absorbing constituent peaking at the pressure p_i^*. Substituting (7) into (6) gives the system of equations

$$\delta T_{Bj} = \sum_{i=0}^{M} C_i A_{ij} \qquad j = 1, 2,,,K \qquad (8)$$

where K is the number of spectral channels and

$$C_0 = \delta T_s \ , \ A_0 = f_{sj}\hat{\tau}_{sj}$$

$$A_{ij} = \int_0^{P_s} \phi_i(p) f_j \hat{\tau}_{wj}(p) d\tau_{dj}(p) \qquad i = 1, 2,,,M/2$$

$$A_{ij} = \int_0^{P_s} \phi_i(p) f_j \hat{\tau}_{dj}(p) d\hat{\tau}_{wj}(p) \qquad i = \frac{M}{2} + 1, \frac{M}{2} + 2,,,M$$

where M/2 is the number of "standard" atmospheric pressure levels. In the case of the aircraft HIS experiment, K is approximately 2500 and M is 24. Thus, (8) represents a system of 2500 equations with 25 unknowns.

The solution of (8) is achieved using the conditioned least squares inverse solution

$$\vec{C} = (A^T A + \gamma I)^{-1} A^T \vec{t}_b = A^* \vec{t} \qquad (9)$$

where $\vec{t}$ is the vector of brightness temperature observations (δT_B), A^* is the solution matrix, I is the identity matrix, and γ is a Lagrangian multiplier ($=10^{-2}$) used to condition the matrix $A^T A$ for inversion. The superscript T denotes matrix transposition.

When utilizing brightness temperature observations it is proper to account for the errors in δT_B due to measurement errors and to uncertainties in the atmospheric transmittance observations used to calculate $\hat{T}_B$ from $\hat{T}(p)$ and U(p). This error can be defined as

$$\varepsilon_j = \sqrt{\rho_j^2 + \eta_j^2} \qquad (10)$$

where $\rho = r/(\partial B/\partial T_B)$ is the expected random brightness temperature measurement error (r_j being the radiance error) specified from the observations when viewing a constant calibration source, and η_j is the difference between the observed and calculated brightness temperature for known atmospheric conditions. In order to account for the spectral dependence of ε_j, both sides of equation (8) are scaled by ε_j (i.e., $\delta T_{Bj} = \delta T_{Bj}/\varepsilon_j$ and $A_{ij} = A_{ij}/\varepsilon_j$). Thus, the spectral regions whose observation error and atmospheric transmittance uncertainties are smallest carry the greatest weight in the solution for the atmospheric profiles.

Having determined the coefficient vector $\vec{C}$, the atmospheric profiles T(p) and $T_w(p)$ are obtained from (7). The water vapor concentration profile U(p) is then obtained using (5) in the form

$$U(p) = \hat{U}(p) + \frac{d\hat{U}(p)}{dT(p)} [T(p) - T_w(p)] \qquad (11)$$

or

$$U(p) = \hat{U}(p) \left[1 + \frac{T(p) - T_w(p)}{dT/d\ln\hat{U}}\right] \qquad (12)$$

The mixing ratio profile is then calculated using the relation

$$q(p) = \hat{q}(p) \frac{dU(p)/dp}{d\hat{U}(p)/dp} = \hat{g}(p) \frac{dU(p)}{d\hat{U}(p)} \qquad (13)$$

where all the vertical derivations are computed as centered finite differences.

3. ATMOSPHERIC TRANSMITTANCES AND CALCULATED RADIANCE SPECTRA

The atmospheric transmittance functions for water vapor, $\tau_w(p)$, and $\tau_d(p)$ are calculated using the line-by-line transmittance model "FASCODE" (Clough et al., 1986). For the calculation of the radiance corresponding to the reference sounding condition, the total transmittance is calculated considering all optically active constituents (H_2O, CO_2, N_2O, CH_4, O_3, N_2, SO_2, NO, CO, etc.) simultaneously. In order to represent the HIS spectra, the transmittances are calculated at high spectral resolution ($\sim$0.06 cm^{-1}) and then transformed to an interferogram incorporating the spectral response and finite field of view properties of the airborne HIS instrument. The interferogram is

$$\tau_x(p) = \int_0^\infty \tau_\nu(p)\phi_\nu \frac{\sin 2\pi\nu x\alpha^2/4}{2\pi\nu x\alpha^2/4} \cos(2\pi\nu x)d\nu \quad (14)$$

where x is delay, $\tau_\nu(p)$ is the spectral transmittance as a function of wavenumber, ν, α is the half angle field of view of the HIS and ϕ_ν is the spectral response function due primarily to the interference filter used to limit the incoming radiation. Then $\tau_\nu(p)$ for the HIS resolution is achieved using a cosine transform of $\tau_x(p)$ using precisely the same delay cutoff and interferogram apodization function used to process the HIS interferogram radiance observations.

$$\tau_\nu(p) = 2\int_0^{X_m} \tau_x(p)\Psi_x \cos(2\pi\nu x)dx \quad (15)$$

where X_m=1.4 for band 1 (600-1100 cm^{-1}), X_m=0.9 for band 2 (1100-1900 cm^{-1}), and band 3 (2000-2700 cm^{-1}). In the processing of the HIS spectra, the apodization is

$$\Psi_x = (1 - x^2/X_m^2)^2 \quad (16)$$

Figure 4 shows spectra of radiance computed from the average of two special radiosonde observations taken at 17 GMT near Huntsville, Alabama on June 15, 1986. The radiosonde observations were taken in support of the COoperative Huntsville Meteorological EXperiment (COHMEX) to study convective weather. Also shown is an average of HIS spectra observed in the vicinity of the two radiosonde observations. The differences generally exceed the single sample observation errors of 0.2 mw/m^2-cm^{-1}-sr for band 1, 0.1 mw/m^2-cm^{-1}-sr for band 2, and 0.01 mw/m^2-cm^{-1}-sr for band 3. These differences are due to errors in simulating the spectral characteristics of the HIS observations in the radiance computations, errors in the radiosonde observations, errors in the FASCODE transmittance computations, and errors due to quadrature in the radiative transfer computations. These discrepancies are accounted for in the retrieval algorithm through their inclusion in the estimation of the forward radiance computation error spectrum defined by Eq. (10). Furthermore, we attempt to correct the calculated spectra for their discrepancy with observations using the approximation

$$\hat{T}_B^c(\nu) = \hat{T}_B(\nu) + \eta(\nu) \quad (17)$$

where $\hat{T}_B^c(\nu)$ is the corrected radiative transfer computation of the brightness temperature spectrum and $\eta(\nu)$ is an expected difference between observed and calculated brightness temperature spectra for known atmospheric conditions as previously defined by Eq. (10).

4. AN EXAMPLE OF ATMOSPHERIC PROFILE RETRIEVALS FROM AIRBORNE HIS SPECTRA

On June 15, 1986, the HIS flew aboard the NASA U2 from Wallops Island, Virginia to the COHMEX observation area over northern Alabama and Tennessee. Figure 5 shows the flight track of the U2 over a GOES visible channel cloud image at 18 GMT, the central time of the U2 flight. As can be seen, the COHMEX area was covered with low

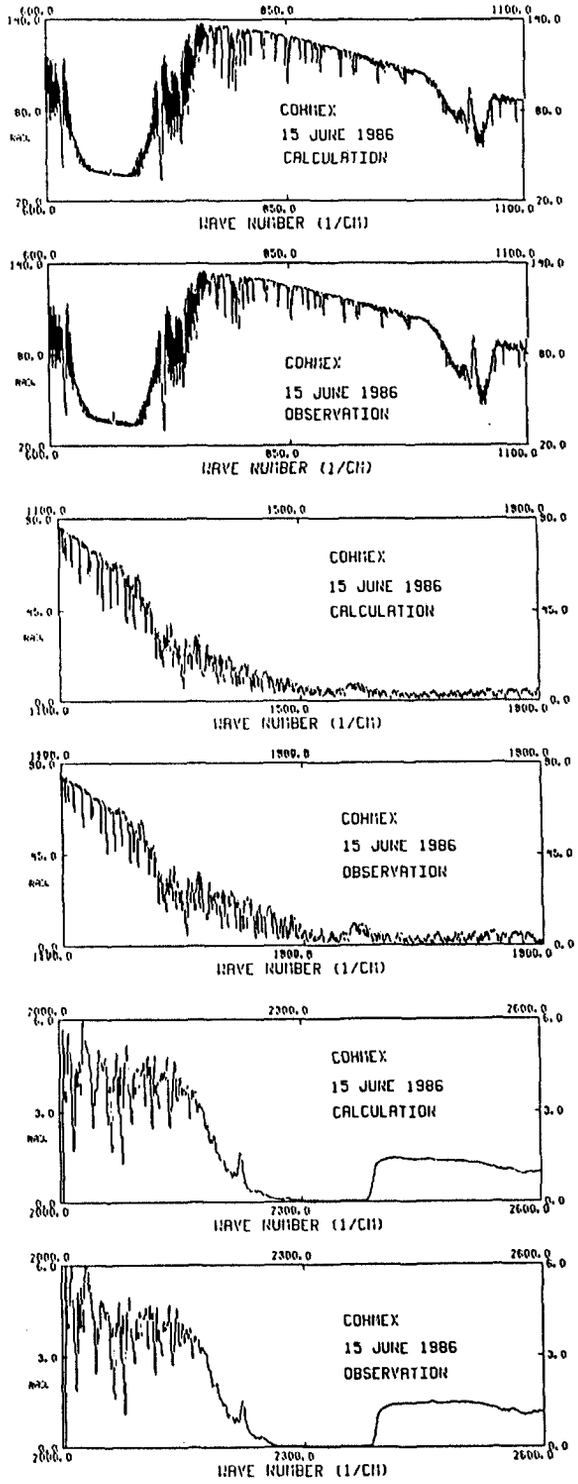

Fig. 4. Calculated and observed radiance for COHMEX region on June 15, 1986.

scattered cumulus clouds whose tops are estimated from radiosonde and HIS window channel brightness temperature data to be at a pressure altitude of 850 mb. In these initial retrievals conducted from the HIS data, no attempt was made to account for the cloud effects on the HIS spectra (i.e., all spectra were handled as if they were observed for cloud-free sky conditions). An NMC forecast temperature and water vapor profile for Huntsville, Alabama was used as the guess profile for all the retrievals to be shown (i.e., the solu-

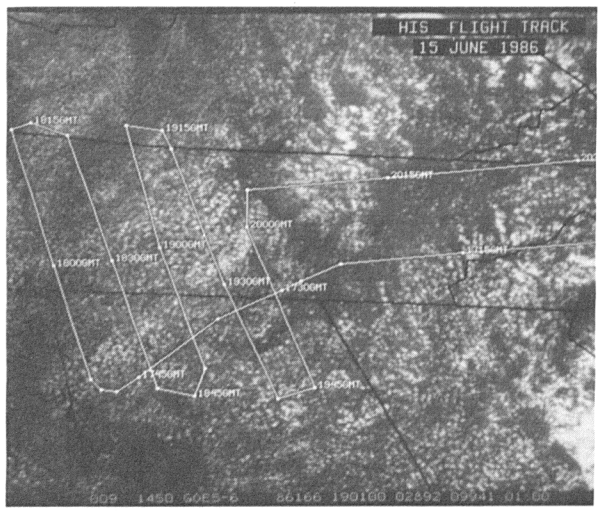

Fig. 5. Flight track of the NASA U2 aircraft overlaying a GOES visible image.

tion matrix, A* of Eq. (9), was computed once and held constant for all the retrievals).

Figure 6 shows a plot of HIS retrieved dewpoint at 300 mb overlaying a VAS 6.7μm water vapor image. Also shown are the few special radiosonde observations conducted in this area. As can be seen, there is a systematic difference between the HIS and radiosonde dewpoints at 300 mb, the radiosonde being warmer by 4.0°C. However, the horizontal gradient is in excellent agreement (i.e., within 1°C). Also, there is excellent agreement between the small scale horizontal features of the retrieved dewpoints and the moisture gradients revealed in the VAS moisture channel image.

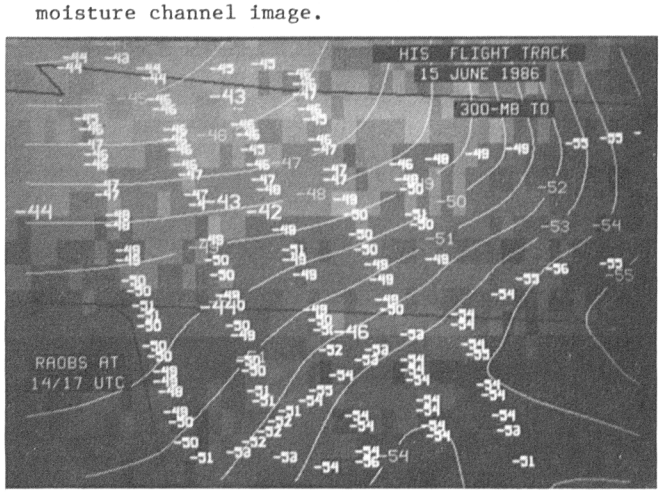

Fig. 6. HIS 300 mb dewpoint temperatures observed along the U2 flight track. The image is from the VAS 6.7μm water vapor channel. Dark regions correspond to high radiance (i.e., low values of water vapor concentration). Radiosonde values are shown as the large numbers.

Figure 7 shows an example skew T-log P diagram comparing a HIS profile retrieval with a radiosonde and the NMC guess, and VAS profile retrieval with the same radiosonde. The NMC first guess profile was used for both the HIS and VAS profile retrieval. The ability of the HIS to resolve the fine scale vertical structure of atmospheric moisture, in particular, is remark-

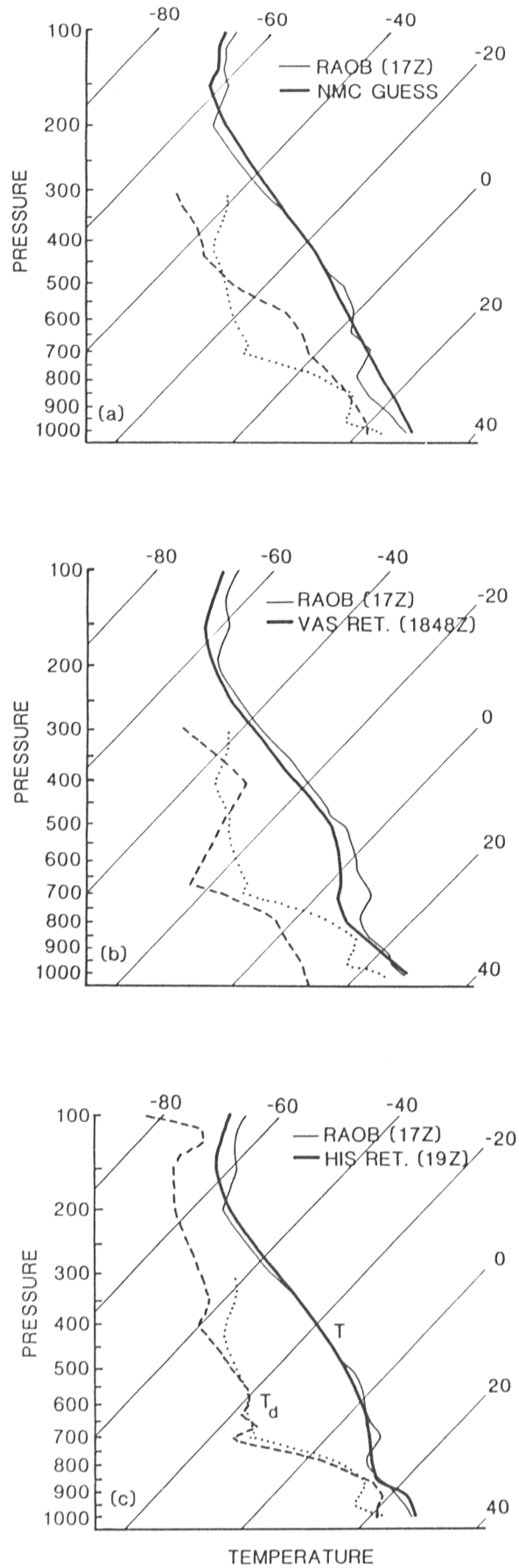

Fig. 7. An example comparison of NMC first guess, VAS retrieval, and HIS retrieval with a nearly coincident radiosonde observation.

able. The HIS temperature profile retrievals are superior to those achieved with the VAS, but still rather disappointing in that much of the fine scale structure is not resolved. This deficiency is due to the rather large uncertainties in the forward computation radiative transfer model (i.e., transmittances, numerical quadrature, etc.). As future studies lead to improvements in the radiative transfer model, thereby reducing the expected error estimates, much greater weight will be given to the observations for retrieving finer scale vertical structures.

5. REFERENCES

Clough, S. A., F. X. Kneizys, E. P. Shettle, G. P. Anderson, 1986: 6th Conf. on Atmospheric Radiation, AMS, Boston, MA, p. 141.

Revercomb, H. E., D. D. LaPorte, W. L. Smith, H. Buijs, D. G. Murcray, F. J. Murcray, and L. A. Sromovsky, 1987: High-altitude aircraft measurements of upwelling radiance: prelude to FTIR from geosynchronous satellite, 6th Intl. Conf. on Fourier Transform Spectroscopy, Vienna, Austria, 24-28 August, in press.

Rosenkranz, P. W., M. J. Komichak and D. H. Staelin, 1982: A method for estimation of atmospheric water vapor profiles by microwave radiometry. J. Appl. Meteor., 21, 1364-1370.

Smith, W. L., V. E. Suomi, W. P. Menzel, H. M. Woolf, L. A. Sromovsky, H. E. Revercomb, C. M. Hayden, D. N. Erickson, and F. R. Mosher, 1981: First sounding results from VAS-D. Bull. Amer. Meteor. Soc., Vol. 62, No. 2, pp. 232-236.

Smith, W. L. and H. M. Woolf, 1984: Improved vertical soundings from an amalgamation of polar and geostationary radiance observations. Conf. on Satellite/Remote Sensing and Applications, Clearwater Beach, FL, June 25-29.

Smith, W. L., H. E. Revercomb, H. B. Howell, H. M. Woolf, and D. D. LaPorte, 1986: The High resolution Interferometer Sounder (HIS). CIMSS View, Vol. II, No. 3, Fall.

Acknowledgments

The authors express the sincere appreciation to James Fischer (NOAA/NESDIS) and numerous staff members of NASA Headquarters and the NASA Ames aircraft flight facility for their support of HIS instrument development and successful aircraft demonstration. We are grateful to numerous personnel at the University of Wisconsin, University of Denver, Bomem, Inc., and Santa Barbara Research Center for their participation in the construction and testing of the HIS. The expert preparation of this manuscript by Laura Beckett is greatly appreciated.

6.5

NASA's Earth Science Geostationary Platform

Gregory S. Wilson

NASA Marshall Space Flight Center
Huntsville, Alabama 35812

and

Robert J. Curran and Dixon M. Butler

NASA Headquarters
Washington, DC 20546

1. INTRODUCTION

During early 1987, NASA began to formally define the science and mission requirements for an earth science geostationary flight program for the late 1990's. The Geostationary Platform Earth Science Steering Committee was formed from members representing NASA, NOAA, USGS, universities, and the international space community of Europe and Japan. The steering committee was tasked with the following objective:

> Define and articulate the scientific measurement requirements, from the full spectrum of Earth Science disciplines, that should be made from geostationary orbit to study the entire Earth System, including requirements for supporting information systems and instrument concepts.

In parallel with this activity, NASA is supporting preliminary mission definition concept studies that will establish several earth science geostationary platform mission approaches using the output from the science steering committee. This paper will present a summary status report of these activities since the final study is not to be completed until late in 1988.

2. BACKGROUND

While NASA has been conducting its highly visible efforts of manned space flight and planetary exploration, it has also pioneered the remote sensing of the Earth from space. It is now time for NASA to expand these efforts and provide revolutionary new capabilities to characterize our home planet and its global environment. The science community has pointed out that the Planet Earth is already in a process of global change in which virtually all aspects of the Earth interact as part of an integrated system and the impact of human activity is significant. With over five (5) billion people on our planet, the evidence that human-induced global change is occurring including carbon dioxide increase, deforestation and desert growth, stratospheric ozone depletion, and environmental pollution (i.e., acid rain) is incontrovertible.

Today, we lack the ability to adequately foresee the direction of these changes and their effects on the global physical, economic, and social climate. Both our nation and the world now require the understanding to reliably predict the future course of our environment on time scales of decades to centuries in response to both human activities and natural forces. The long-term quantitative measurement of the atmosphere, land surface, oceans, and solid Earth, using the global perspective of space, is essential as the foundation of a new integrated approach to the study of Planet Earth called Earth System Science.

Earth System Science has the following goal and challenge:

EARTH SYSTEM SCIENCE

- **THE GOAL:**
  TO OBTAIN A SCIENTIFIC UNDERSTANDING OF THE ENTIRE EARTH SYSTEM ON A GLOBAL SCALE BY DESCRIBING HOW ITS COMPONENT PARTS AND THEIR INTERACTIONS HAVE EVOLVED, HOW THEY FUNCTION, AND HOW THEY MAY BE EXPECTED TO CONTINUE TO EVOLVE ON ALL TIME SCALES.
- **THE CHALLENGE:**
  TO DEVELOP THE CAPABILITY TO PREDICT THOSE CHANGES THAT WILL OCCUR IN THE NEXT DECADE TO CENTURY, BOTH NATURALLY AND IN RESPONSE TO HUMAN ACTIVITY.

Figure 1 shows a very simplified "wiring diagram" of the major components of the Earth System with three major multidisciplinary process cycles (Physical Climate or Energy cycle, Biogeochemical cycles, and Global Moisture or Hydrologic cycle) functioning under external forcing and internal human influences shown on the left and right of the chart, respectively. NASA is committed to pursue the Earth System Science goal through implementation of new Earth observing systems in orbit, information systems on the ground, and by stimulating others to contribute to this effort.

3. MISSION TO PLANET EARTH

The Apollo mission provided mankind with a

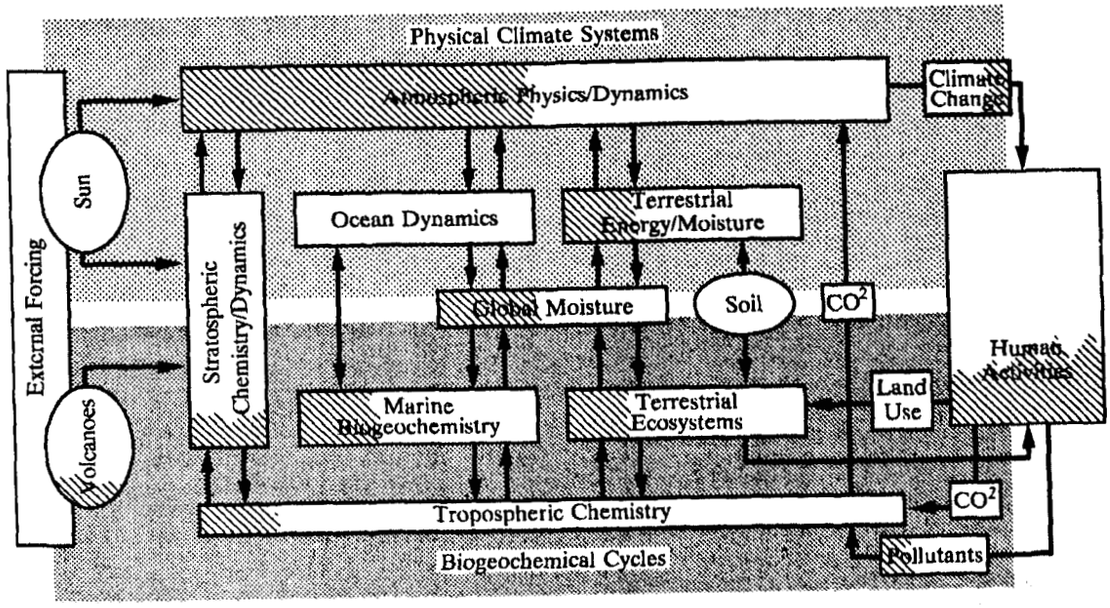

Figure 1. Simplified Earth System Wiring Diagram. Hatched areas denote some of the Earth System processes that must be observed from geostationary orbit due to their short time and space scale.

new perspective of the Earth showing a gleaming blue and white ball floating in the blackness of space. This dramatically reshaped our view of ourselves and triggered an awareness of our planet as a life support system. More quantitative remote sensing of the Earth from orbit has become a part of modern life with all of us viewing geostationary satellite cloud pictures and data as the basis for nightly explanations of the weather and seeing multispectral Landsat photographs of many land areas. The use of space observations along with vast improvements in computer power have enable the development of global scale models of the atmosphere and long-range weather prediction. Extensions of this modeling approach to the stratosphere, the oceans, and the solid Earth is underway and the need to take this approach to large scale terrestrial ecosystems is recognized. The science community is now able to foresee the development of a model for the coupled global system and the Earth System Sciences committee of the NASA advisory council has advanced this systems approach to the study of the Earth as the key to future efforts in Earth science and applications both for NASA and for other agencies including NOAA and NSF. NSF has already initiated its global geosciences program.

An integrated model of the Earth offers the potential for predicting the future course of the global environment as well as for understanding the global change already taking place. The development of this capability requires long-term, consistent observations of the Earth and the global perspective offered by remote sensing instruments in Earth orbit is uniquely suited to providing these data. The ultimate accomplishment of this goal will require many contributions from government agencies, the international space and research communities, and others. It is NASA's role to lead the development of revolutionary new Earth observing systems, their reliable long-term deployment on orbit, and the integration of the resulting data into the study and modeling of the Earth as a system. NASA views this activity as part of its responsibility to both our nation and mankind and is committed to expanding its current Earth observations activities to carry out what may be best described as a Mission to Planet Earth. Spaceflight is not just a means to stimulate the mind and imagination of humanity; it also provides the basis for improvements in our day to day lives on Earth both now and in the future.

NASA has developed the orbiting capabilities which today form the basis of the NOAA and GOES operational weather satellites and the Landsat commercial land remote sensing satellites. These pioneering developments by the U.S. have been emulated abroad with the geostationary weather satellites GMS, Meteosat, and Insat being launched by Japan, Europe, and India respectively and by the SPOT commercial land remote sensing satellite program of France. NASA is currently orbiting the Nimbus 7 and ERBS research satellites which are providing global data on stratospheric ozone, sea surface and sea ice variables, and the balance of radiation input and output between the Earth and space which is key to improving our understanding of climate. Approved future programs at NASA in Earth science and applications include the Upper Atmospheric Research Satellite (UARS) and the TOPEX/Posiedon mission. UARS will provide the first comprehensive measurements of the interplay among dynamic, radiative, and chemical processes in the stratosphere and mesosphere which determine the extent and durability of the

MISSION TO PLANET EARTH

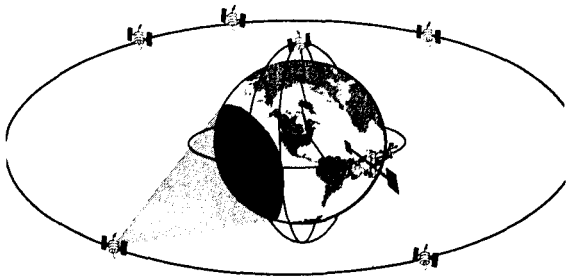

Figure 2. Complimentary orbiting satellite system required to completely observe the Earth System. Shown are the Polar Orbiting Platforms, the low-inclination Manned Space Station and several Geostationary Platforms.

ozone layer. TOPEX will provide the first detailed measurements of the global circulation patterns of the ocean including the manner in which strong poleward currents such as the Gulf Stream are balanced by equatorward flow. These missions are both building blocks of a comprehensive understanding of the Earth as a system. Each mission addresses a key aspect of the system and a particular environmental region.

The comprehensive approach to observing the full spectrum of processes which comprise the Earth system requires enlarged concentrations of orbiting remote sensing instrumentation and mission lifetimes of a decade or more (see Figure 2). The characteristics of the complimentary orbital views in Figure 2 are shown below:

MISSION TO PLANET EARTH

COMPLIMENTARY ORBITAL VIEWS

SUN-SYNCHRONOUS POLAR ORBITS: AM & PM CROSSING TIMES
- GLOBAL COVERAGE
- SAMPLING AT 6 HOUR TO 3 DAY INTERVALS
- LASER, RADAR, & PASSIVE REMOTE SENSING

LOW-INCLINATION, LOW-ALTITUDE ORBITS
- TROPICAL COVERAGE
- SAMPLING ALL LOCAL TIMES
- RADAR AND PASSIVE REMOTE SENSING

GEOSTATIONARY ORBITS
- LIMITED AREA COVERAGE
- CONTINUOUS TEMPORAL COVERAGE
- PASSIVE REMOTE SENSING ONLY

The key piece of new space infrastructure to enable such an effort is the Polar Platform which NASA is developing as part of the Space Station program. NASA is working with the Earth observations offices of our Space Station partners (ESA, Japan, and Canada) and with NOAA as well as with the Earth science community to define and implement the Earth Observing System (EOS) which will provide the instruments and data systems to capitalize on the polar platform capability. NASA is also examining smaller missions such as the Tropical Rainfall Measurement Mission and the Geopotential Research Mission which require unique orbits different from those planned for polar platforms and which contribute to pursuit of Earth System Science. Of particular interest in this paper is an expanded geostationary observing system, following the same general approach being taken for EOS in low altitude, sun-synchronous Earth orbit, called the Earth Science Geostationary Platform Missions.

Summarized below are primary elements of NASA's Mission to Planet Earth approach including three (3) GEO-EOS geostationary platforms:

MISSION TO PLANET EARTH

NASA PROGRAM ELEMENTS

- EARTH SCIENCE & APPLICATIONS INFORMATION SYSTEM
- EOS WITH 2 POLAR PLATFORMS
- TROPICAL RAINFALL MEASUREMENT MISSION (TRMM)
- GEO-EOS WITH 3 GEOSTATIONARY PLATFORMS
- TECHNOLOGY DEVELOPMENT
- SUPPORTING INFRASTRUCTURE:
  LAUNCH, ASSEMBLY, SERVICING, DATA RELAY

Commitments by NASA in each of these areas are already stimulating and catalyzing corresponding commitments in Europe and Japan which will make this effort truly international.

4. EARTH SCIENCE GEOSTATIONARY PLATFORM SCIENCE AND MISSION REQUIREMENTS

The Earth Science Geostationary Platform (ESGP) Science and Mission Requirements are being developed around the essential elements of the Mission to Planet Earth concept shown below:

MISSION TO PLANET EARTH

ESSENTIAL ELEMENTS OF THE CONCEPT

- CENTERPIECE OF EARTH SYSTEM SCIENCE PROGRAM IMPLEMENTATION
- INFORMATION SYSTEM APPROACH – UNDERSTANDING IS THE DELIVERABLE
- RESEARCH AND OPERATIONAL PAYLOADS / DATA SYSTEMS DEVELOPED & IMPLEMENTED TOGETHER
- LONG-TERM, CONSISTENT DATA SETS ESSENTIAL
- INTERNATIONAL SCOPE IN SYSTEM PROVISION, USE, BENEFIT
- ICSU GLOBAL CHANGE / IGBP COORDINATED GROUND OBSERVATIONS CONTEXT

These guidelines dictate that all earth science disciplines are considered as integral to the Earth System Science approach and that the measurement and understanding of Global Change Processes provide the centerpiece of the mission development philosophy. This approach parallels the development strategy for the Space Station Polar Platforms in many respects including the desire to fly together research and operational payloads using jointly developed and implemented data systems that would provide international participation and crucial data sets for studying longer term earth system processes.

However, the ESGP will make a unique and program-critical contribution to the Earth System measurement program due to its continuous temporal sampling and integrating capability. Figure 3 shows a time/space earth science

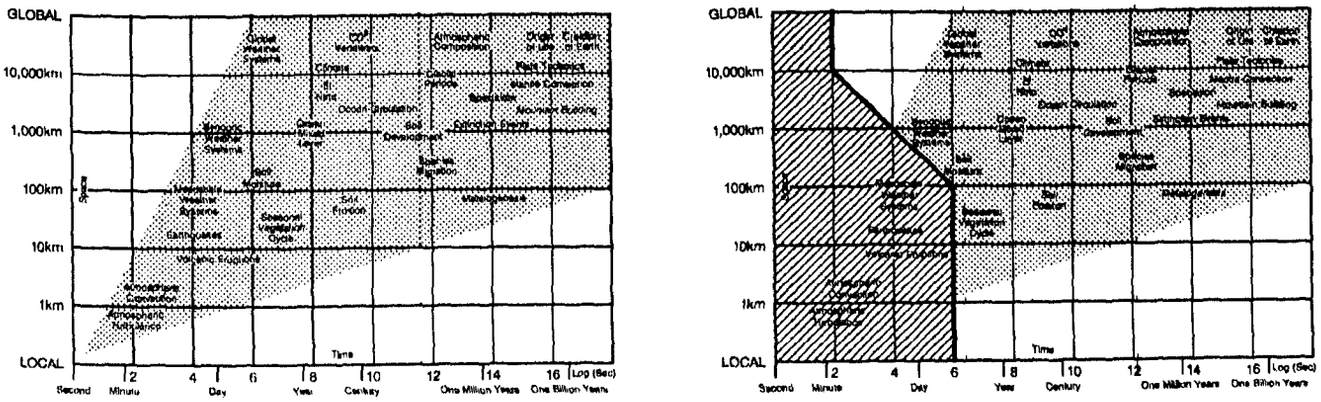

Figure 3. Space/time diagrams for earth science phenomena. Hatched area on the right-hand diagram shows processes of unique interest to the Earth Science Geostationary Platform Mission.

phenomena diagram and depicts (hatched) those processes whose time and space scale are of particular interest to the ESGP. Phenomena whose time scales ranged from <1 second (i.e., lightning) to daily (i.e., diurnal heating and tides) over nearly global regions can be monitored uniquely from this mission. The ability to dwell over a specific region of the world to study a particular multidisciplinary process (i.e., the southern oscillation) makes the ESGP particularly important in providing a dynamical understanding of the physical processes that control natural and man-influenced global changes.

Referring back to Figure 1, the hatched areas in the earth system "wiring diagram" depict some of the discipline processes that require the measurement capabilities of the ESGP. The ESGP Science Steering Committee has already identified some of the specific processes within these discipline areas that demand measurement from the geostationary orbit. A small sample of these phenomena are listed below:

- o precipitation and lightning
- o mesoscale atmospheric/oceanic circulations
- o coastal processes including tides
- o environmental pollution
- o volcanoes and earthquakes
- o oceanic phytoplankton blooms
- o water vapor sources/sinks and structure
- o solar flux and constant
- o atmospheric trace gases
- o diurnal terrestrial ecosystem processes
- o cloud evolution and severe storms
- o earth system radiation balance

Many others will be identified as the ESGP Steering Committee completes its work in 1988.

In order to provide a broad and cross-discipline approach to defining the ESGP Science and Mission Requirements, three subpanels have been created around the three fundamental cycles shown in Figure 1.

- o Physical Climate (Energy Cycle)
- o Global Moisture (Hydrologic Cycle)
- o Biosphere Chemistry (Biogeochemical Cycle)

These subpanels, in addition to identifying specific measurement requirement for the ESGP, must establish sensor concepts and advanced technology needed to accomplish the mission. Shown below is a generic list of new sensor technologies that would be needed for the ESGP candidate payloads.

- **Large Aperature antenna design studies for high-resolution microwave radiometry**
- **Sub-millimeter techniques for imaging and sounding**
- **Design studies of one and two dimensional array detectors which operate in narrow spectral intervals in the visible and infrared**
- **Design studies for very high spectral resolution spectroradiometers for improved atmospheric sounding**
- **Programmable on-board processing and data compression**
- **Serviceability considerations**

Utilizing these new technologies and some very preliminary instrument concepts, several conceptual mission designs have been established that use various launch capabilities and space transportation options. Figure 4 shows only one of the concepts and identifies specific strawman instruments. However, the concepts will undergo serious review and modification as the ESGP Steering Committee completes its job.

GEOSTATIONARY PLATFORM ON ORBIT CONFIGURATION

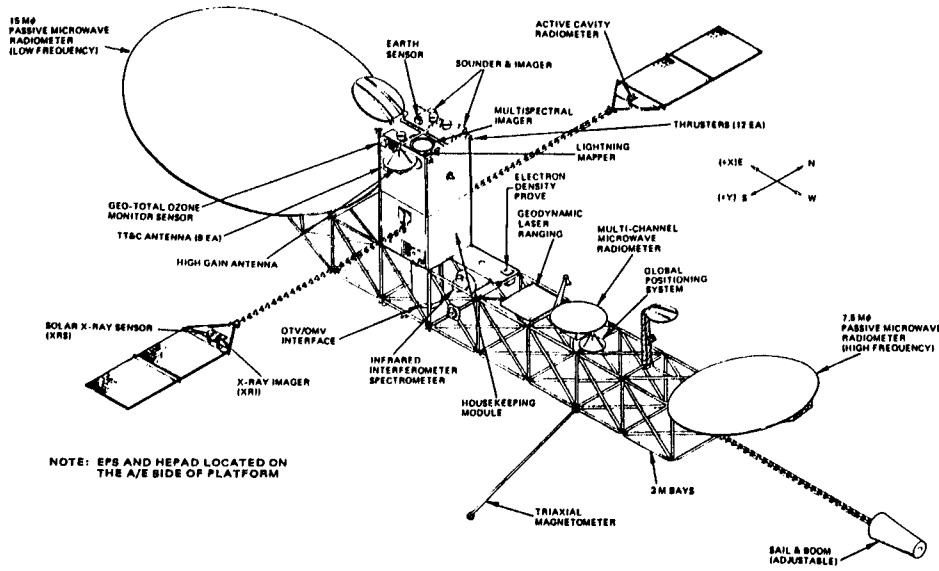

Figure 4. One of several Earth Science Geostationary Platform preliminary mission concepts.

GEOSTATIONARY PLATFORM PROGRAM SCHEDULE OPTIONS

SUMMARY

CANDIDATE PLATFORM BUS	CY										
	1988	1989	1990	1991	1992	1993	1994	1995	1996	1997	1998
GOES I-M BUS*			PHASE B		PHASE C/D				LAUNCH △		
MILSTAR BUS			PHASE B		PHASE C/D				LAUNCH △		
NEW BUS			PHASE B			PHASE C/D					LAUNCH △

* PRECURSOR MISSION

Figure 5. Earth Science Geostationary Platform Schedule Options.

Figure 5 shows a summary schedule for three fundamental options for the ESGP Program. They include:

1) a research GOES mission
2) an ESGP using an existing bus (i.e., Milstar)
3) an ESGP with new bus plus payload

NASA has officially decided to remove option 1) from consideration and pursue option 2) or 3) with an expected launch date in the late 1990's.

5. CONCLUSIONS

NASA will continue its support of efforts by the U.S. Earth science community to pursue the study of Global Change and shape a comprehensive national contribution to the International Congress of Scientific Unions International Geosphere Biosphere program. NSF will play a major role in ground based observations and fundamental research through its Global Geosciences initiative, and NOAA will be an invaluable source of data from its ground based and space based operational measurement systems. The other substantive contributions from the full range of US agencies involved in Earth science can be coordinated to ensure US leadership in this international arena. The development of the Earth Science Geostationary Platform Measurement System will provide the final and crucial element of the Mission to Planet Earth Program needed to provide a full spectrum of global measurements of the earth system to monitor and dynamically understand/predict Global Change of our Planet Earth.

6.7

DOPPLER LIDAR WIND MEASUREMENTS ON THE EOS: LAWS

Daniel E. Fitzjarrald

NASA Marshall Space Flight Center
Huntsville, AL

1. INTRODUCTION

It is possible to make wind profiles from space using current technology. These wind profiles are essential for investigating many of the interdisciplinary scientific questions of the Earth Observing System (Eos). A spaceborne wind sounder, the Laser Atmospheric Wind Sounder (LAWS) has been chosen as a facility instrument on the Eos. This paper discusses the efforts currently underway to prepare for the deployment of the LAWS instrument on an Eos polar orbiter and on the Manned Space Station. The measurement technique heritage, which includes groundbased and airborne measurements in the atmosphere, is discussed, along with the scientific and technical issues that are being addressed. Whether obtained globally from the Eos polar platform or in the tropics from an Space Station, wind profiles from space will provide essential information for advancing the skill of numerical weather prediction, furthering our knowledge of the large-scale atmospheric circulation and climate dynamics, and improving our understanding of the global biogeochemical and hydrologic cycles. These scientific issues are also briefly discussed.

2. HERITAGE OF THE TECHNIQUE

Measurement of wind using pulsed, CO_2 Doppler lidars has received considerable attention since the first research data were obtained in 1979. Groundbased units have progressed from the first breadboard constructions to van mounted instruments that can routinely be transported to remote research sites and used in mesoscale scientific investigations. The latest of these groundbased instruments belongs to NOAA/ERL and has a pulse energy nearly that needed from the low earth orbit of Space Station or Eos. Real-time signal processors and computer controlled beam scanners allow flexibility in the planning and execution of experiments.

Airborne Doppler lidars have been tested since 1971. The latest of these instruments uses a computer controlled scanner and dedicated inertial navigation system to point the beam in a known direction and subtract the aircraft motion. Since the measurement platform moves much faster than changes occur in the airflow pattern, line of sight measurements into the test region from different angles can be used to compute the horizontal motion of the air, ie., the wind. A similar technique can be used from space, allowing one instrument to determine the wind around the globe by making line of sight measurements from a moving platform.

3. SPACE APPLICATIONS

A number of studies have been done to determine the feasibility of using Doppler lidar from a platform in space to measure the wind globally. These studies have shown the general feasibility of the technique and have identified a number of technological and scientific issues that need to be resolved before such an instrument can be built.

The lidar system must be designed, tested, and qualified for space operation. While a transmitter of this size is not large compared to some other possible space applications of lasers, its size is unprecedented for remote observation of the earth. This instrument, along with others of the Eos facility instruments, will usher in a new era of active measurements of the earth that will need relatively large platforms with their large payload capacity and high power availability.

Lidar systems for use in space fall into two general categories: 1) those that use coherent detection of the signal, and 2) those that use incoherent detection. In the former, a reference beam is put on the detector along with the returning Doppler shifted radiation, and the resulting beat frequency is the signal. In the latter technique, a Fabry-Perot

interferometer is used to extract the signal from the returning radiation. The coherent detection technique has been used in the past and is currently in use in the field using CO_2 lasers as radiation sources. Recent advances in solid state laser technology using diode pumped lasers show good promise for lidar design. All of these technologies are being evaluated by NASA.

At the present time CO_2 coherent detection lidar is the baseline for wind measurement from space. This technique currently, or in the near future with some development work will satisfy the requirements for space flight, namely: 1) efficiency, 2) longevity, 3) weight. But most importantly, this technique has the experience base upon which to make confident predictions that the instrument will work, so that we can proceed directly to its design and implementation.

As the initial feasibility study and subsequent ones have pointed out, more data must be obtained concerning the global distribution of naturally occurring atmospheric aerosols that provide signal return at the wavelengths used by all the techniques described above. A comprehensive research program, the Global Backscatter Experiment (GLOBE) has been formed by NASA to accomplish this crucial research. The research program will include an extensive airborne experiment in the remote Pacific using the NASA DC8 research aircraft outfitted with a variety of lidars and aerosol instruments, a shipboard lidar instrument, and surface measurements by lidars and aerosol sampling networks. Data from these sources and others, including research data from NOAA, researchers in the UK, France, Germany, and Japan will be synthesized into a model to be used in feasibility assessments and performance analyses of a space borne Doppler lidar.

4. SCIENCE BENEFITS

The experience of operational weather prediction centers and the considerable recent research has indicated that wind profiles are the single most important data source with the potential to effect dramatic improvement in numerical weather prediction. This improvement will occur through the enhancement of the coverage and data quality in areas already served by conventional radiosondes, and through the extension of the coverage of high quality wind profiles to the sparsely instrumented oceanic, tropical, and southern hemisphere areas. Simulation experiments indicate that weather forecasts would improve to the point that weather in the southern hemisphere and the tropics could be predicted with as much skill as the northern hemisphere. Moreover, even in the much better observed northern hemisphere, specific cases of very significant forecast improvement have been noted using simulated wind profiles.

In the tropics, wind observations are even more important than in mid-latitudes, since pressure patterns cannot be used to calculate atmospheric motion, and since there are few observing stations. The tropics are of particular interest, since much of the global energy input to the atmosphere occurs there. Less understood, but potentially very important, are the teleconnections between large scale atmospheric phenomena in the mid-latitudes and anomalies in the tropics as evidenced in the recent El Nino episode.

Globally obtained wind data will also be of great use in the understanding and prediction of transient atmospheric phenomena such as tropical cyclones. Global wind profiles obtained by the LAWS instrument will be ideal to determine the mid-troposphere steering currents that are important in hurricane track forecasts.

Obtaining a better understanding of the atmosphere, oceans, cryosphere, and biota as a coupled system is the essence of the Eos concept. Atmospheric dynamics plays a central role in coupling the elements of the entire system through the transport of heat, water vapor, momentum, and trace gases. Wind observations and models are needed to provide a better definition of the hydrologic cycle and the long-range transport of trace gases and aerosols. The measurements made by the Doppler lidar LAWS instrument on the Eos polar orbiter or from the Manned Space Station will be an important part of a revolutionary new study of the system earth.

AEROSOL BACKSCATTER VARIABILITY AT 10.6 MICRONS OVER COLORADO HIGH PLAINS DURING JAWS EXPERIMENT

Jeffry Rothermel

Universities Space Research Association
Earth Science and Application Division
NASA/Marshall Space Flight Center
Huntsville, Alabama 35812

David A. Bowdle

Johnson Research Center
University of Alabama, Huntsville
Huntsville, Alabama 35899

J. Michael Vaughan

Royal Signals and Radar Establishment
Great Malvern, United Kingdom WR14 3PS

1. INTRODUCTION

Recent years have seen increased interest in the physical, chemical, and optical properties of micrometer-sized particles naturally present in low concentrations in the free troposphere. Such knowledge is essential to design and performance studies of proposed space-based lidar systems that use aerosols as passive backscatterers to measure some primary atmospheric quantity, such as global tropospheric winds or trace species concentrations.

Since 1981 the Royal Signals and Radar Establishment and Royal Aircraft Establishment, United Kingdom, have operated an airborne continuous-wave (CW) focused CO_2 Doppler lidar, the Laser True Airspeed System (LATAS), obtaining vertical and horizontal sounding measurements of aerosol backscatter cross-section. A detailed description of the design, calibration, and operation of the LATAS, which is mounted on an HS-125 aircraft, is found in Foord et al. (1983) and Vaughan et al. (1987). Biasing by occasional regions of high aerosol concentration is prevented by high spatial and temporal resolution, which is obtained through a high volume sampling rate at high sensitivity. Because most conventional aerosol instruments cannot easily achieve these qualities using the available sampling platforms (e.g., balloons, aircraft, high-altitude ground sites), comparatively little detailed information is available on free tropospheric aerosols.

During the summer of 1982 the Joint Airport Weather Studies (JAWS) field experiment was held in the vicinity of Denver, Colorado to study severe thunderstorm downdrafts and resulting outflows near the surface. The LATAS participated in JAWS with a two-fold purpose: (1) to measure wind shears potentially hazardous to aviation operations, and (2) to obtain profiles of aerosol backscatter. This presentation describes LATAS backscatter profile measurements from JAWS, which were obtained primarily in the absence of deep convection and strong shears. Ancillary data is described to consider qualitative relationships between backscatter and the vertical distribution of temperature and water vapor. It is noted in passing that a pulsed, ground-based CO_2 Doppler lidar, operated by the Wave Propagation Laboratory (WPL) of the National Oceanic and Atmospheric Administration (NOAA), also participated in JAWS, with similar objectives. A future publication describes an intercomparison between the two lidars (Bowdle et al., 1987).

2. EXPERIMENT AND DATA

The backscatter sounding flights were made in the lee of the front range of the Colorado Rocky Mountains, in the vicinity of Denver's Stapleton International Airport. Area elevations are roughly 1650 m above mean sea level. Land usage in the surrounding area is primarily agricultural, except for the Denver metropolitan area and scattered, smaller towns. The climate is characterized by low humidity, frequent cloud-free days, low precipitation, and a large diurnal temperature range. Diurnal development during the summer typically leads to a deep, dust-laden planetary boundary layer (PBL), and occasional, severe thunderstorm activity in the afternoon and evening. Backscatter flights were typically made during periods when the region was dominated by an upper air high pressure ridge.

Typical flights were made during 0900-1100 local

time (1500-1700 GMT), lasted for 30-40 min, and extended to 13 km. Resolution was 20-25 m near the surface, and decreased steadily as the aircraft approached maximum altitude. Nine profiles were obtained during participation in JAWS. High resolution temperature measurements were also made by the LATAS, however water vapor measurements were not made. National Weather Service special rawinsonde data, obtained within 2 hr of the flights, were used for interpretation of backscatter features. In all cases, agreement between LATAS and sounding temperatures was better than 1.0 C throughout most of the profile, and less than 2.0 C throughout the entire profile.

Backscatter measurements obtained with no electrical attenuation were processed using the algorithm described by Rothermel et al. (1987), which is based on the theoretical formulation of Vaughan et al. (1987). Non-zero attenuation was usually applied in the PBL, to prevent detector saturation due to strong signal. Data obtained under these conditions have been eliminated in the present study. Measurements affected by LATAS system malfunctions were also removed from the data set. Potential temperature profiles were derived to evaluate the likelihood of vertical mixing during the measurement period, to identify aerosol source regions (e.g., the planetary boundary layer, PBL), and to locate layers that had already been affected by vertical mixing from these source regions. An amplitude-weighted velocity variance of the return signal was computed as a rough indicator of atmospheric turbulence.

3. RESULTS

3.1 Synoptic Scale Structure

The JAWS profile measurements contain three persistent features: a strong backscatter layer associated with the PBL, a mid-tropospheric "clean background," and a stratospheric aerosol layer. Some variation in the layer thicknesses and altitudes occurs.

Fig. 1 (Flight 772) shows representative backscatter and potential temperature profiles. Typically, the layer of enhanced backscatter associated with the PBL extends to 6 km or less, with values of 10^{-8} $m^{-1}sr^{-1}$ or more. The neutrally-stable portion of the potential temperature profile confirms that the layer is well-mixed, suggesting a surface-derived aerosol source. Highest humidities are found typically in the PBL. In other soundings, occasional backscatter enhancement occurs at the top of the PBL, indicative of deliquescence and growth in a higher humidity environment preceding cloud formation.

A layer of minimum backscatter, or clean background, typically extends from above the PBL to 1-2 km below the tropopause. Occasional backscatter enhancements, considered in section 3.2, are found in this layer. In Flight 772, the clean background is evident between 7-12 km, with a layer of enhanced backscatter near 10 km. The clean background layer shows uniformity from day to day, with backscatter values of approximately 10^{-10} $m^{-1}sr^{-1}$. Minimum backscatter usually occurs between 7-11 km. Variations in layer position and thickness may be explained by variations in PBL depth and synoptic scale forcing. A clean background condition, described by Bowdle (1986), is assumed to be produced by nearly complete removal of moisture and aerosols from rising air masses in large-scale storm systems, i.e., "scrubbing."

At 1-2 km below the tropopause, backscatter values begin to increase above the clean background through the remainder of the troposphere and into the stratosphere. For Flight 772, the tropopause height (determined from the rawinsonde sounding made within 2 hr of the flight) was roughly 14 km. Since the enhancement generally begins well below the tropopause, the stratosphere apparently acts as an aerosol source, probably due to residual material from the Mt. Saint Helens volcanic eruption of May 18, 1980, or the initial influence of the El Chichon, Mexico eruption in April 1982, or both.

The general features described above are also evident in soundings made during descent.

3.2 Microscale Structure

In addition to the persistent structure described above, microscale features and variations are occasionally superimposed.

Fig. 2 (Flight 787) contains another example of backscatter enhancement, at 11 km, as well as the general features noted above. This sounding was obtained on ascent. An enhancement at the same level is absent on descent, indicating that the scattering layer had limited horizontal extent. Such an enhancement is usually associated with visible cirrus; however, on this occasion none was observed. The backscatter enhancement is associated with a thin, nearly isentropic layer and increased velocity variance (not shown), indicative of light turbulence. Approximately two hours later, at 1330 local time, cirrus was detected visually and with the WPL lidar, with peak scattering at roughly 11.5 km. These middle and upper tropospheric layers are attributed to incipient, active, or residual cirrus. Water vapor measurements from rawinsondes are generally unavailable above heights of roughly 10 km. Below this level, the rawinsonde water vapor data show positive correlation only with deep layers of backscatter enhancement on the order of several km thick, i.e.. the PBL and relatively deep cloud layers. The lack of complete correlation may be explained in terms of insufficient sensitivity and vertical resolution of the rawinsonde, differences in spatial and temporal location between the LATAS and rawinsonde, and the evolution and decay of cloud features.

Considerably detailed structure is evident upon closer examination of the profiles. An enlargement of Flight 772 is shown in Fig. 3, showing backscatter and potential temperature. There are numerous examples of negative correlation between backscatter and potential temperature fluctuations, e.g., at 4.1, 4.5, 5.0, 5.8, and 5.9 km. No satisfactory explanation has yet been found for this relationship.

A third example of microscale structure is the abrupt transition between the PBL backscatter values and those of the free troposphere, e.g., Flight 787 (Fig. 2a). Backscatter values may vary by as much as three orders of magnitude over as little as 200-300 m.

4. CONCLUDING REMARKS

Aerosol measurements are important as inputs to design and simulation studies of prospective satellite-based lidars that will use aerosols as backscattering targets. It is noted that several data bases of direct CO_2 backscatter measurements exist and are being expanded. The RSRE/RAE have made extensive measurements with the LATAS in varied locations, including a five year climatology of profiles over the

United Kingdom. These are currently being analyzed. The WPL/NOAA group has made backscatter measurements from a fixed location in Boulder, Colorado over a three year period (Post, 1984). Measurements have been made in Pasadena, California at multiple CO_2 wavelengths (Menzies et al., 1984).

The National Aeronautics and Space Administration (NASA) has recently initiated a research program, the Global Backscatter Experiment (GLOBE), to provide a comprehensive global scale aerosol data base, and ultimately a global-scale model of aerosol backscatter (Bowdle, 1986; Bowdle and Fitzjarrald, 1987). GLOBE activities include, but are not limited to, review of existing aerosol measurements, a program of direct CO_2 backscatter measurements, use of satellite-based measurements of aerosols or aerosol surrogates (tracers), measurements of aerosol physicochemical properties, and calibration issues. This model will be used in design and simulation studies for NASA's prospective Laser Atmospheric Wind Sounder (LAWS) (Baker and Curran, 1985). The performance of a device such as LAWS depends critically upon the signal-to-noise ratio of the received signal, which is primarily a function of the concentration and backscatter efficiency of aerosols in the sample volume. LAWS is planned for deployment to low earth orbit in the mid 1990's.

5. ACKNOWLEDGMENTS

We gratefully acknowledge the assistance of many colleagues and the enthusiastic cooperation of the air and ground crews. Analysis of the JAWS data was supported, in part, by the Universities Space Research Association, under NASA contract NAS8-36474, and by the University of Alabama, Huntsville, under NASA contract NAS8-36279. The support of Dr. Robert J. Curran, Director of the Global Scale Processes Research Program at NASA Headquarters, is gratefully acknowledged.

6. REFERENCES

Baker, W.E. and R.J. Curran, 1985: Report of the NASA Workshop on Global Wind Measurements, Columbia, Md., 29 July-1 August, sponsored by NASA Global Scale Atmospheric Processes Research Program. A. Deepak Publ., Hampton, Va., 70 pp.

Bowdle, D.A., 1986: A global-scale model of aerosol backscatter at CO_2 wavelengths for satellite-based lidar sensors. Preprints, Second Conf. Satellite Meteor./Remote Sensing, Williamsburg, Va., 13-16 May, Amer. Meteor. Soc., 303-306.

Bowdle, D.A. and D.E. Fitzjarrald, 1987: The Global Backscatter Experiment (GLOBE) program. Optical Soc. of Amer. Topical Meeting on Coherent Laser Radar: Technology and Applications, Aspen, CO, July 27-30, pp. 108-111.

Bowdle, D.A., J. Rothermel, J.M. Vaughan, M.J. Post, A.A. Woodfield, and D.W. Brown, 1987: Aerosol backscatter intercomparison with airborne and ground-based CO_2 Doppler lidars. J. Geophys. Res., in preparation.

Menzies, R.T., M.J. Kavaya, P.H. Flamant, and D.A. Haner, 1984: Atmospheric aerosol backscatter measurements using a tuneable coherent CO_2 lidar. Appl. Optics, 23, 2510-2517.

Post, M.J., 1984: Aerosol backscattering profiles at CO_2 wavelengths: the NOAA data base. Appl. Optics, 23, 2507-2509.

Rothermel, J., J.M. Vaughan, and D.A. Bowdle, 1987: Algorithm to calculate aerosol backscatter from airborne CW focused CO_2 Doppler lidar measurements. Optical Soc. of Amer. Topical Meeting on Coherent Laser Radar: Technology and Applications, Aspen, CO, July 27-30, pp. 73-76.

Vaughan, J.M., R. Callan, D.A. Bowdle, and J. Rothermel, 1987: Spectral analysis, digital integration and measurement of low backscatter in coherent laser radar. Appl. Optics, in preparation.

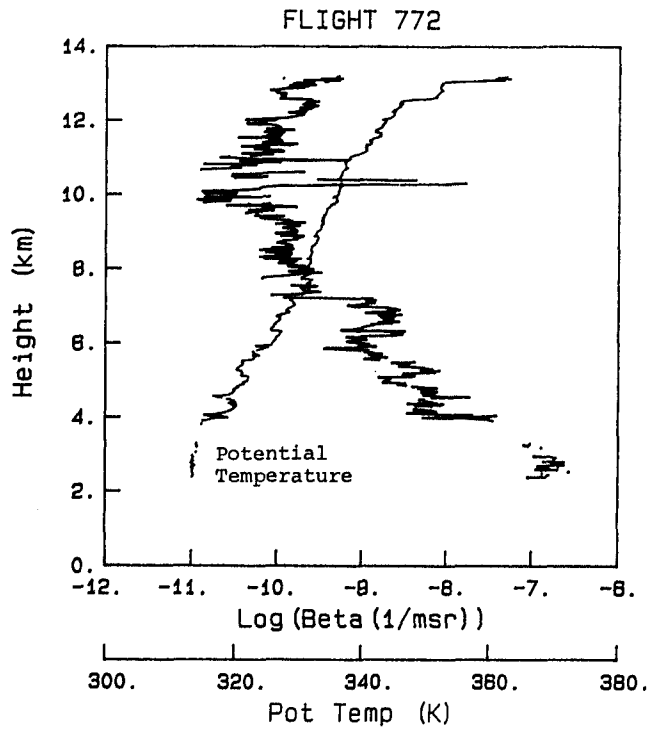

Figure 1. Soundings of potential temperature (K) and log of aerosol backscatter coefficient (denoted by "beta," in units of $m^{-1}sr^{-1}$) for Flight 772 on 2 July 1982 near Denver, Colorado.

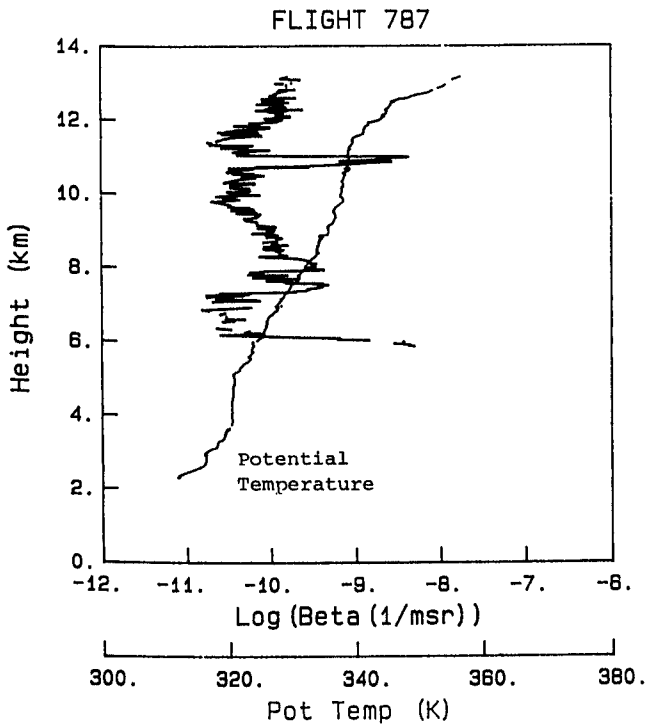

Figure 2. Soundings of potential temperature and log of aerosol backscatter coefficient for Flight 787 on 13 July 1982 near Denver, Colorado. Note enhancement at 11 km, probably due to incipient or residual cirrus cloud layer.

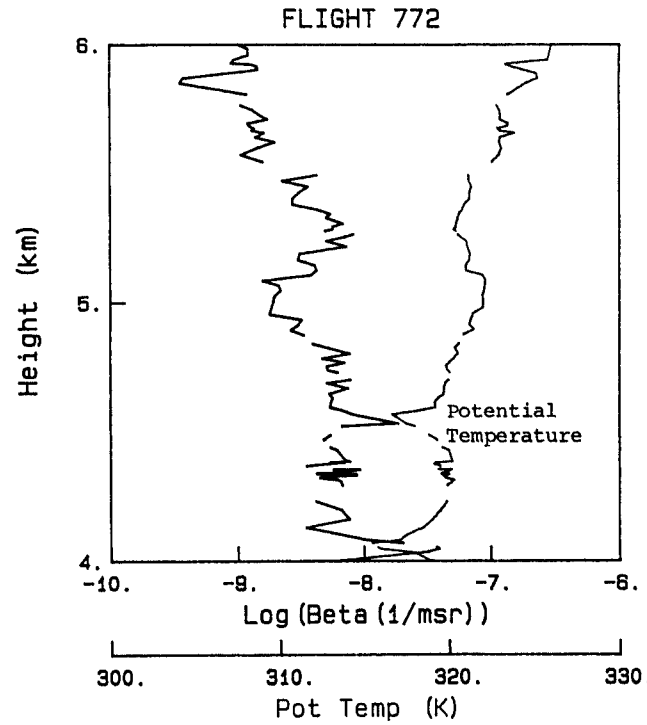

Figure 3. Enlargement of Fig. 1, illustrating negative correlation between potential temperature and backscatter fluctuations.

DIRECT MEASUREMENT OF BOUNDARY LAYER WINDS OVER THE OCEANS USING A SPACE-BASED DOPPLER LIDAR WIND SOUNDER

G. D. Emmitt

Simpson Weather Associates, Inc.
Charlottesville, Virginia

1. INTRODUCTION

Winds play a major role in regulating the transfer of heat, moisture, and momentum between the atmosphere and the underlying oceans. Currently the measurement of surface winds over 70% of the globe is limited to a sparse network of buoys, island stations, and inaccurate reports from merchant ships.

In 1978 the Seasat-A Satellite Scatterometer (SASS) was flown for 5 months and obtained indirect measurements of the surface winds over the oceans with 50 km spatial resolution and every-other-day coverage. Although σ_o (scattering cross section per unit area) may be better correlated with the surface stress than a wind measured some height above the sea surface, there are ambiguities or aliases in wind direction. Objective dealiasing schemes (Baker, et al., 1984) were developed and used in model data assimilation studies (Atlas, et al., 1987), producing encouraging results in resolving global fields of momentum, sensible heat, and latent heat fluxes.

After SASS's short lived flight, there were plans to launch another scatterometer. However, this multiagency program has since been cancelled. New initiatives are underway by both NASA[1] and DOD[2] to place pulsed lasers on orbiting space platforms to obtain direct measurements of tropospheric winds. Although limited to areas that provide CLOS's[3] and sufficient aerosols, the space-based Doppler lidar promises a totally new perspective on global circulations and a new data base for atmospheric and oceanographic modelling.

2. DESCRIPTION OF LAWS

NASA's version of a space-based Doppler Lidar Atmospheric Wind Sounder (LAWS) could fly on either a polar orbiter or Space Station. Currently the lidar is configured as a 10.6 µm or 9.11 µm CO_2 laser whose pulsed energy is directed with a conically scanned 1 meter diameter telescope. Primary lidar and scanner parameters are listed in Table 1.

The lidar measures a line of sight (LOS) component of the air motion by emitting energy at a known frequency and detecting the Doppler shifts in the energy reflected from aerosols. The resulting Doppler frequency spectrum is broadened by the turbulent motions and velocity gradients within the cylindrical sample volume.

The measurement accuracy of the LOS wind component depends upon the strength of return signal above the random noise level and the signal processing used to find the mean speed of the air motion. In general, the error or uncertainty in the estimate of the wind along the LOS is mostly a function of the signal to noise ratio (SNR) which, in turn, is a function of factors such as laser power, detector sensitivity, or aerosol concentrations. Consequently, the accuracy of the LOS wind can be expressed in terms of plus or minus a few meters per second. For example, in the lowest 1 km of the earth's atmosphere over the continents, a reasonable LOS uncertainty would be a RMS speed of $\pm$ 1-2 m s^{-1}.

The LOS measurements are taken in a spatial pattern dictated by the conical scanner parameters (Table 1) and the earth-relative motion of the space platform (Figs. 1 and 2). Variations in the shot pattern can be achieved by modulating some of the LAWS parameters such as PRF or scanner slew rate (Emmitt, 1985).

Table 1
Lidar/Scanner Parameters for LAWS

Laser wavelength (µm)	10.6 or 9.11
Laser power (joules)	10
Laser pulse repetition frequency (Hz)	8
Scan angle (° from nadir)	45-55
Scan rate (deg/sec)	18-36
Sample volume dimensions	
length (m)	150-2000
diameter[1] (m)	10-20
Ground Swath width[2] (km)	2500-3000
Average shot density (km^{-2})	2500-3000
Average shot pair density (km^{-2})	5000-6000

Given the LAWS configuration described in Table 1, we can expect, on the average, a 50-60 km spacing between LOS measurements. These LOS components could be used in a regression with predicted or modelled wind fields without any further processing. However, more information is available by combining the LOS measurements to obtain estimates of the u and v components of the wind field.

[1] National Aeronautics and Space Administration
[2] Department of Defense
[3] Clear Line of Sight

SATELLITE BASED DOPPLER LIDAR SIMULATION

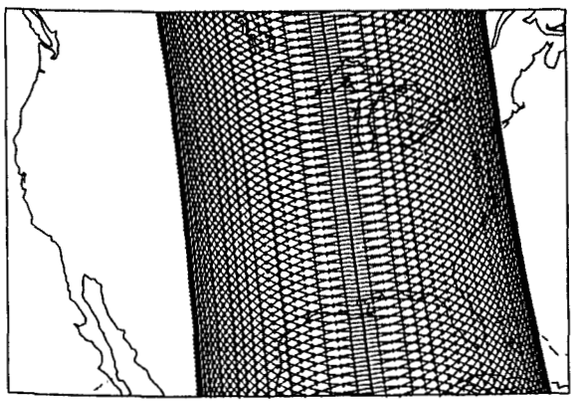

Fig. 1. Cycloidal pattern traced out by a conically scanning space-based lidar in a 800 km polar orbit with a 45° scanning angle.

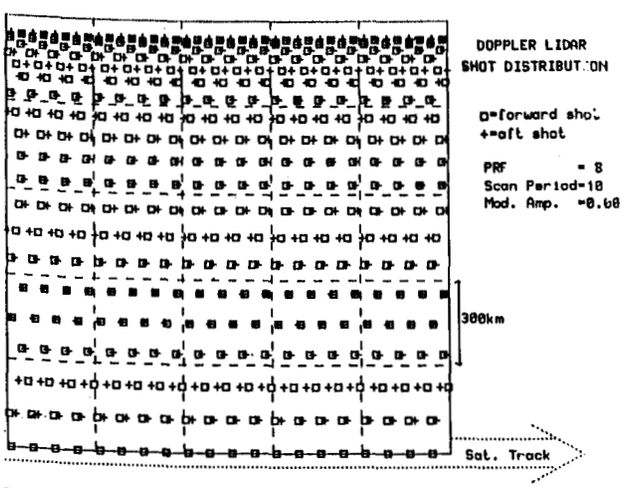

Fig. 2. Enlargement of a portion of the scan domain illustrated in Figure 1. Shot management studies seek scanner controls that optimize the coincidence of fore and aft shots.

3. WIND VECTOR COMPUTATIONS

The LOS data can be combined in several ways to obtain estimates of the u and v components of the wind. A weighted least squares approach can be used as long as there is no spatial correlation of the variance in the wind field within the resolution volume. With an average spacing of 50-60 km, the assumption of incoherent varience is weak and is clearly violated in the presence of mesoscale wind structures such as jet streaks, convective storms or oragraphic flows. Emmitt (1982) developed a more general approach using shot pairs and an adaptive algorithm for achieving a prescribed accuracy and/or representativeness. This multi-paired algorithm (MPA) is currently undergoing testing and modification to meet changing hardware configurations. The MPA is used throughout the remainder of this paper.

Whereas the uncertainty in the LOS velocity estimate was, in general, independent of location relative to the satellite ground track, the uncertainties in the computed u and v components are directly related to location within the LAWS scan domain. The reason for this is that the velocity information within a specific resolution volume (e.g. 300 x 300 x 1 km³) is usually composed of two subsets of LOS winds--those LOS's with a forward perspective and those LOS's with an aft perspective. The potential error in the u,v computation will depend upon the angle between these two general perspectives--the less orthogonal, the greater the error. In general, the expected uncertainty in speed will be on the order of 3-8% and 5-15 degrees in direction.

There are two major consequences of the above:

1) Resolution of structures with wavelength ≈ 100 km will depend upon relative location to satellite ground track; and
2) Coherent features with wavelength ≈ 1000 km will appear as coherent finer scale features in the wind field. This problem can be minimized with proper shot management.

4.0 LAWS POTENTIAL IMPACT ON OCEANOGRAPHY

Winds are the largest single input of momentum to the oceans. Wind stress on the sea surface plays a critical role in a number of oceanographic phenomena (O'Brian, 1982):

1) ocean mixing layer, the depth of which governs the sea surface temperature (SST) which in turn plays a primary role in the earth's climate:
2) wind waves which are important to most marine activities;
3) ocean currents which vary in response to changes in the wind stress or more specifically the wind stress curl;
4) inertial gravity waves which may be generated by mesoscale wind structures;
5) up welling, e.g. the El Nino phenomena off the western coast of South America;
6) planetary boundary layer (PBL), which is directly related to the sea surface conditions and whose structure controls much of the energy transfer from ocean to atmosphere and vice versa.

Our understanding and modelling of each of the phenomena listed above will be enhanced by the wind measurements obtained with a space-based Doppler lidar. With the current hardware configuration we can expect, in cloud free regions, spatial coverage similar to that illustrated in Figures 3 and 4. The observational data base for the winds in the regions of major ocean currents such as the Antarctic Circumpolar Current, Gulf Stream (Figure 3) or Kuroshio Current (Figure 4) will be updated at least every 12 hours from a polar orbiting platform.

The stress on the sea surface would be computed using the first lidar sample volume above the sea surface. The length of this volume may be on the order of 200-500 meters which, given a 45° scan angle, would mean a vertical resolution depth of 150-350 meters. In most cases, this means that winds will be obtained for several heights within the PBL. The stress would then be computed using the profile method.

Additional information on the sea surface may be available from the lidar sample volume that intersects the ocean. The return from the water surface will dominate the frequency spectrum and provide some estimate of the average motion of the sea surface. However, since the zero motion "ground" return will be used to calibrate the lidar velocity information, there may be the need to process the winds in the oceanic regions in a different manner than those obtained over land.

Fig. 3. Four orbits of simulated maximum resolution (no averaging) boundary layer winds over the U.S. including a portion of the east coast Gulf Stream. Blank regions denote cloud cover or the band of suppressed data near the satellite ground track.

Fig. 4. Similar to Figure 3 except for eastern Asia, including a portion of the Kuroshio Current region.

5. CONCLUSIONS

The technical feasibilty of placing a Doppler lidar in space to measure winds is currently being assessed. The potential impact of that capability has been briefly discussed in reference to some specific oceanographic phenomena. In general, the 50-300 km resolution and twice per day coverage will mean a major increase in global wind data available for both the atmospheric/oceanographic research and operations communities.

6. REFERENCES

Atlas, R., A. J. Busalacchi, M. Ghil, S. Bloom, and E. Kalnay, 1987: Global surface wind and flux fields from model assimilation on Seasat data. J. Geophys. Research, 92, C6, 6477-6487.

Baker, W. E., R. Atlas, E. Kalnay, M. Halem, P. M. Woiceshyn, and D. Edelmann, 1984: Large-scale analysis and forecast experiments with wind data from the Seasat-A scatterometer. J. Geophys. Res., 89, 4927-4936.

Baker, W. E. and R. J. Curran, 1985: Report on the NASA Workshop on Global Wind Measurements, A. Deepak Publishing, Hampton, Virginia.

Emmitt, G. D., 1982: Conical lidar scanning from low earth orbit--the effects of meso α and convective scale atmospheric phenomena. Paper presented at 11th International Laser Radar Conference, July 1982, Madison, Wisconsin.

Emmitt, G. D., 1985: Doppler lidar sampling strategies and accuracies-regional scale. Paper presented at the Symposium and Workshop on Global Wind Measurements, July 29-August 1, Columbia, Maryland.

Emmitt, G. D., 1987: Error analysis for total wind vector computations using one component measurements from a space-based Doppler lidar. Fourth Conf. on Coherent Laser Radar: Technology and Applications, July 1987, Aspen, Colorado.

Emmitt, G. D. and S. H. Houston, 1986: Constraints on resolving meso-alpha and meso-beta phenomena using a space-based Doppler lidar wind profiler. Preprints of the 2nd Conf. on Satellite Meteorology, May 1986, Williamsburg, Virginia.

Freilich, M. H., 1985: Science Opportunities Using the NASA Scatterometer on N-ROSS. JPL Publication 84-57, JPL, California Institute of Technology, Pasadena, California.

O'Brien, J. J., Ed., 1982: Scientific Opportunities Using Satellite Wind Stress Measurements over the Ocean, NOVA University/NYIT Press, Fort Lauderdale, FL.

THE TROPICAL RAINFALL MEASURING MISSION (TRMM)

John S. Theon

NASA Headquarters
Washington, DC 20546

1. INTRODUCTION

Precipitation is certainly one of the most significant meteorological phenomena in determining climate and the utility of the Earth's land surfaces. The occurrence of precipitation is highly variable in time and place and, to make the climate a productive one, its frequency of occurrence must be within a relatively narrow band and its total accumulation must be within a limited range.

However, it is not only the life-sustaining properties of precipitation that should interest us. Precipitation plays an important role in redistributing the solar energy which is incident on the Earth's surface. It does this by releasing the latent heat of condensation which was absorbed in the transformation of liquid water into water vapor as cloud droplets grow to precipitable sizes. The water vapor is readily transported by the circulations of many scales by the atmosphere. In the processes of evaporation (and transpiration), condensation and precipitation, energy is absorbed, transported, and released, thus interacting with the atmospheric dynamics and generating circulations and components of flows which would not occur in a dry atmosphere.

While a rain gauge is one of the simplest of instruments, merely requiring a container whose volume is somehow quantified, the highly variable nature of rainfall requires more than merely point sampling to provide a realistic estimate of the distribution. In addition, only a few countries in the world have dense rain gauge networks which are read and reported reliably. In developing nations, in sparsely inhabited regions of the world, and over the nearly three-quarters of the Earth's surface covered by oceans, rainfall data are virtually non-existent. Island and coastal station reports are not necessarily representative of the rain distributions which occur over the open oceans, and gauges aboard ships are notoriously unreliable because of the orientation and location problems as well as the opportunity for contamination by sea spray. Thus, knowledge of rainfall over even a large portion of the globe is not known to better than a factor of two.

Most of the precipitation occurs in the tropical and subtropical regions of the globe, i.e., between the latitudes of 30°S and 30°N where air and surface temperatures are highest and where convection occurs readily, carrying water vapor to levels where it is condensed and precipitated out easily. This process is organized in a band where circulation and latent heating reinforce each other in the intertropical convergence zone. Hadley was the first to recognize the cellular nature of the flow during the 18th century. Riehl and Simpson (1979) recognized and confirmed the importance of convective "hot towers" in sustaining this meridional circulation.

The importance of tropical rainfall goes beyond the organized convection which interacts with the Hadley circulation. The Walker circulation and its quasi-periodic breakdown are now known to effect the El Nino-Southern Oscillation (ENSO) which not only causes major redistributions of the rainfall in the southwestern Pacific Ocean, but also, by forcing a change in the normal position of large-scale atmospheric waves, affects the circulation at middle latitudes virtually around the planet. Although a rudimentary understanding of these phenomena is now emerging, we are not yet able to verify and improve upon the theory because we do not have an adequate quantitative estimate of the latent heating nor its vertical distribution. Measurements of the latent heating, its vertical distribution, as well as a reliable estimate of the ratio of convective to stratiform rainfall that occurs in the tropics, are required to address these questions (Houze, 1987).

2. TRMM SCIENCE GOALS

The Tropical Rainfall Measuring Mission (TRMM), a satellite mission first proposed by North, Wilheit, and Thiele in 1984, is designed to provide the kind of measurements which will address the issues raised above. By combining high spatial resolution capability, a low altitude, non-sun-synchronous orbit, passive and active microwave sensors together with visible and infrared sensors, TRMM overcomes all of the shortcomings of previous attempts to estimate rainfall from satellite measurements. The TRMM Science Steering Group, a panel first

convened in 1985 to establish the science goals and develop the scientific requirements for such a mission, has been working toward the completion of their report, due in the spring of 1988. Their current draft report (1987) lists the following goals for the mission:

I. To advance the Earth system science objective of understanding the global energy and water cycle by means of providing distributions of rainfall and heating over the global tropics;

II. To understand the mechanisms through which changes in tropical rainfall influence global circulation, and to improve our ability to model these processes in order to predict global circulation and rainfall variability at monthly and longer time scales;

III. To evaluate a space-based system for rainfall measurement;

and, a secondary goal which must be pursued in order to achieve the main goals is to better model and understand convectively driven precipitating cloud systems in the tropics, their organization on the mesoscale, and their interactions with the oceans and the atmosphere.

3. MISSION STUDIES

TRMM has been under study by the Advanced Missions Analysis Office at the NASA Goddard Space Flight Center since 1985. Concurrently, a number of researchers have been studying various aspects of the mission including the physics and radiative transfer of remotely sensing rain from space, the wavelengths and instrumentation required for TRMM, sampling statistics of rainfall and the sampling characteristics of the TRMM orbit and sensors, error analyses of TRMM observations, TRMM ground truth (validation) requirements and how they can be met, etc.

The instrument complement required for TRMM is listed below in Table 1.

Table 1 - TRMM Sensors - Required

Microwave Radiometers	Radar	Visible/Infrared Radiometer
19, 37, 90 GHz at 10km resolution 600km swath width	14 and 24 GHz at 4km resolution 150km swath width 250m range resolution	visible, 10um at 1km resolution 600km swath width
	Desired	
10 GHz at 20 km res.	600km swath	Moonlight visible 1.6 um
5 GHz at 40km res.		6.7um split window

The salient features of a TRMM spacecraft are:

Table 2 - TRMM Spacecraft (Keating 1987)

Mass:	2,500 kg (3,500 at launch)
Fuel Mass:	1,000 kg
Fuel:	hydrazine
Attitude Control:	+ 0.2 degree (3 axis-stabilized)
Power:	800W total
Command and Data Handling:	
- Frequency:	S-Band
- Command:	1 Kbps
- Telemetry:	4 Kbps (TDRSS multiple access mode) realtime; 32 Kbps playback; OR 32 Kbps (TDRSS single access mode) realtime; 512 Kbps playback

(TDRSS is the NASA Communication Satellite Tracking and Data Relay Satellite System)

The TRMM orbit will be 300 km (nominal) circular, at 28.5° inclination, the mission requires a 3-year lifetime, and the launch is desired by 1994 in order to overlap with the Tropical Ocean-Global Atmosphere Experiment (TOGA).

4. U.S. - JAPAN COOPERATION ON TRMM

The mission and the research supporting it are being studied jointly by NASA and several agencies in Japan. Since 1984, the Radio Research Laboratory of Japan and NASA Goddard Space Flight Center have been conducting research on the remote sensing of rain using microwave techniques. Presently, the Radio Research Laboratory and the National Space Development Agency of Japan are assessing the feasibility of the TRMM and are expected to issue a decision in early 1988 on whether to join NASA in developing the TRMM jointly. Under such an agreement, NASA would furnish the spacecraft, the passive microwave radiometer(s) and the vis/IR radiometer, while Japan would provide the radar and the launch on an H-II rocket. Both countries would collect data (primary tracking and data acquisition by NASA), conduct the ground truth experiments, analyze the data, and conduct scientific research and applications with it.

5. EXPECTED SCIENTIFIC ADVANCES

Simpson (1987) lists the following advances expected by the TRMM Science Steering Group to accrue from the mission:

- Validation of global atmospheric circulation models
- Vertically integrated latent heat release and its vertical distribution for model initialization
- Calibration of satellite infrared rainfall estimation techniques
- Direct oceanic precipitation measurements to validate models of thermohaline circulations

- Biomass relationships, diagnostic studies, drought and/or anomalous rainfall

- Climate variations - predictability studies and improved models.

6. REFERENCES

1. Houze, R.A., Jr., 1987: Convective and stratiform precipitation in the tropics. Proc. International Symposium on Tropical Rainfall, Oct. 28-31, Tokyo.

2. Keating, Thomas, 1987: Tropical Rainfall Measuring Mission. EASCON Conference, October, Washington, DC

3. Riehl, H. and J. Simpson, 1979: The heat balance of the equatorial trough zone, revisited. Contr. to Atmos. Phys., 52, 287-305.

4. Simpson, Joanne, 1987: Tropical Rainfall from Space. Proc. International Symposium on Tropical Rainfall, Oct. 28-31, Tokyo.

5. TRMM Science Steering Group, 1987: Draft TRMM Science Report, NASA Goddard Space Flight Center, Greenbelt, MD.

SATELLITE MICROWAVE RAINFALL SIMULATIONS WITH A THREE-DIMENSIONAL DYNAMICAL CLOUD MODEL

Robert F. Adler[1], Wei-Kuo Tao[2], N. Prasad[2], Joanne Simpson[1], and Hwa-Young Yeh[3]

[1]Laboratory for Atmospheres, NASA/Goddard Space Flight Center, Greenbelt, MD 20771.

[2]General Sciences Corporation, Laurel, MD 20707.

[3]CAELUM Research Corporation, Silver Spring, MD.

1. INTRODUCTION

In this paper, a three-dimensional, multi-cloud model (Tao and Soong, 1986) is used to generate the three-dimensional distribution of pertinent microphysical and state parameters which are used as input into a microwave radiative transfer model. The radiative transfer model is used to calculate upwelling radiance (brightness temperature, T_B) at various microwave frequencies from 10 to 183 GHz with an ocean background. This model combination is then used to study the relationship between simulated upwelling brightness temperature and cloud-model-generated rain rate at the surface. By calculating area averages of the calculated T_B's and rain rates, simulations of satellite-observed T_B values and associated area-averaged rain rates can be made.

2. *CLOUD MODEL AND RADIATIVE TRANSFER MODEL*

The cloud model used in this study is a three-dimensional, multi-cloud model developed by one of the authors, Wei-Kuo Tao, and described by Tao and Soong (1986) and Tao et al. (1987). The main features of the model are outlined in Table 1.

Table 1
Tao Cumulus Population Model
Main Features

1. Anelastic system (two- or three-dimensional)
2. Forcing by large-scale lifting
3. Includes:
   - o radiative cooling
   - o sea-surface fluxes
4. Initialized by a horizontal random disturbance on the temperature field in the subcloud layer
5. Parameterized subgrid-scale turbulence
6. Microphysical parameterization:
   - o liquid water - Kessler-type treatment
   - o ice phase - two or three classes

This model can be run in two or three dimensions, although present available computing capacity permits only a rather restricted domain for the three-dimensional runs. It can also be run with two or three classes of ice. With two ice classes, the bulk parameterization is similar to that for water droplets, with small "cloud ice" particles having little or no terminal velocity and the larger-sized graupel or hail category falling relative to the air. The third, or intermediate-size, class of ice (snow) proves to be essential in capturing key features of tropical clouds. It has a finite terminal velocity, but one which is much less than that of graupel.

A comparison of the substantial differences between the ice parameterizations in use has been made by McCumber et al. (1987). So far, the scheme by Rutledge and Hobbs (1984) appears to give the most realistic bright melting band and anvil precipitation in tropical cases. The reason appears to be that the terminal velocity of the graupel is comparatively slow (2 to 4 m s^{-1}). The radiative transfer model used here is an improved version by Szejwach et al. (1986) of the plane-parallel model by Wilheit et al. (1982). The improvements include a mixed phase layer, 19 layers in the vertical, and updated scattering coefficients.

3. RESULTS

Figure 1 shows rain rate results from a three-dimensional Tao cloud model run with the Rutledge-Hobbs ice parameterization, using the same environment observed for fast-moving squall lines in the GATE. At the present stage, the radiative model uses a substantial amount of computer time. Therefore, so far only the outlined 18 x 18 km box (12 x 12 grid elements) has been selected for the purpose of linkage with the radiative model.

In this example, frequencies of 10, 18, and 90 GHz have been used in the radiative model. Results for 10 GHz are shown first. Figure 2a shows an enlargement of the rain rates from the dynamic model. The resulting field of brightness temperatures at 10 GHz (horizontal polarization) is shown in Fig. 2b, with contours of T_B drawn every 10 K. Figure 3 comprises two

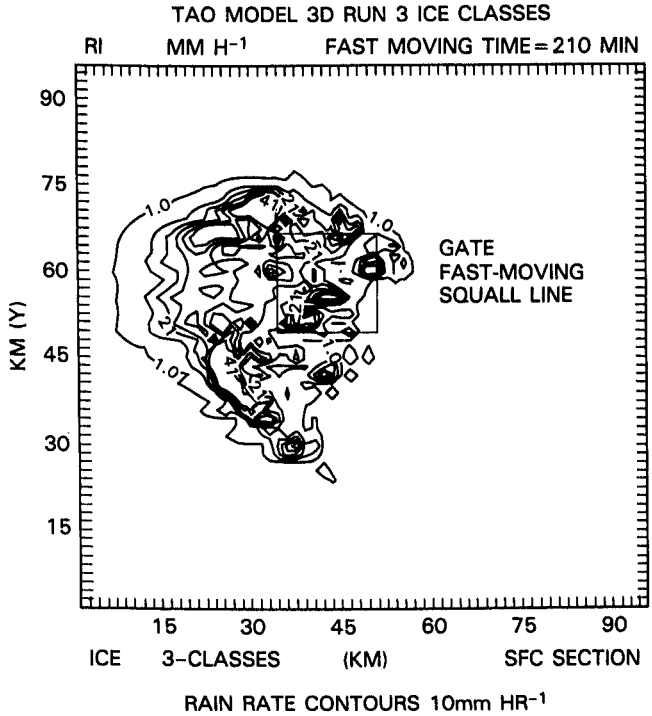

Fig. 1. *Runs from a three-dimensional cumulus population model by Tao containing three classes of ice. The environmental conditions are those of a fast-moving oceanic tropical squall line in GATE. Surface section of rain rates in mm h^{-1}. Horizontal resolution of the model is 1.5 x 1.5 km. The y axis is parallel to the squall line, while the x axis is perpendicular to it. Rain contours are for 10 mm h^{-1}, beginning at 1 mm h^{-1}, so that maximum values exceed 31 mm h^{-1}. The small black-outlined box is the 18 x 18 km region where the radiative model was applied.*

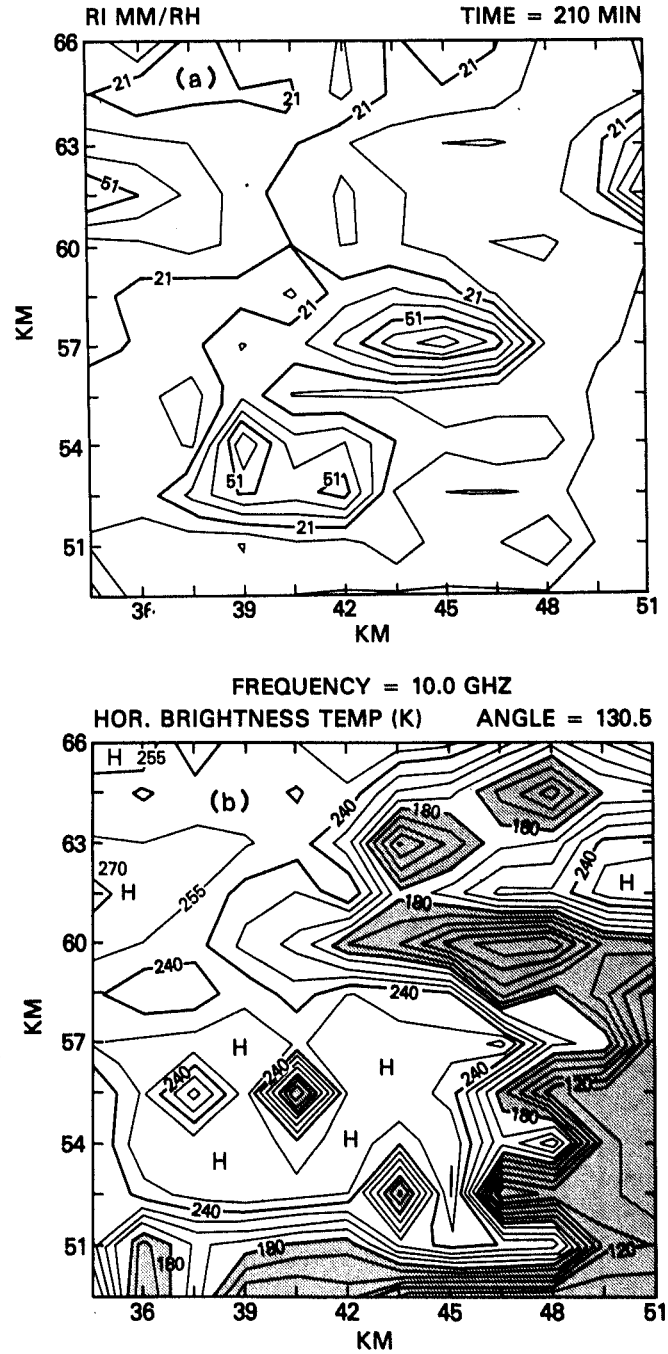

Fig. 2. *a) Contours of rain rate at 10 mm h^{-1} interval from 18 x 18 km box (outlined in Fig. 1) in the Tao model. The grid intervals in this box are 1.5 x 1.5 km. b) Contours every 15 K of T_B for 10 GHz (horizontal polarization) calculated with the radiative model from the water substance hydrometeor profiles given by Tao's microphysical/dynamical model in the black-outlined box shown in Fig. 1. Compare the high values of T_B in the center and upper right with the high rain rates (> 66 mm h^{-1}) in the same position in Fig. 1.*

plots for all 144 values of T_B, one for the vertical hydrometeor profile at each point on the grid. Figure 3a shows the T_B's plotted against integrated water content. The points have little scatter, as expected. In Fig. 3b, the plot of T_B's against rain rate, there is considerable scatter, traceable to several causes. In Tao's model, as in real clouds, the rain may fall at the same rate from different height clouds, and from clouds with and without the bright melting band. Additional scatter occurs because rain reaching the ocean surface is not perfectly vertically aligned with hydrometeors aloft, neither in the multi-cloud dynamical/microphysical model nor in real clouds in the atmosphere. The solid line is the relationship of Wu and Weinman (1984) derived from an assumed hydrometeor profile for tropical clouds in a plane-parallel radiative model for convective cores (see their Fig. 2). Their conceptual cloud has a mixed-phase transition layer between the freezing level and -35°C (about 9 km). The dashed line is from the radiative model of Wilheit et al. (1977), which does not contain a mixed phase layer. The best-fit curve to the points, using second- to fifth-order polynomials, was virtually indistinguishable from the Wu-Weinman curve (the curve fitting was cut off at 30 mm h^{-1}).

To investigate the problem of cloud contamination at low rain rates, the hydrometeor profiles were examined for three classes of points in the rain rate range 5 to 15 mm h^{-1}, namely those points with T_B's 10°C or more above the line, those within 10°C of the line, and those the same amount below the line. The proportion of the total liquid content contributed by cloud water in the model cloud decreased from about 37% to 23% with decreasing T_B, indicating that a large fraction of non-raining clouds with substantial water contents might cause small overestimates of the low rain rates at this frequency.

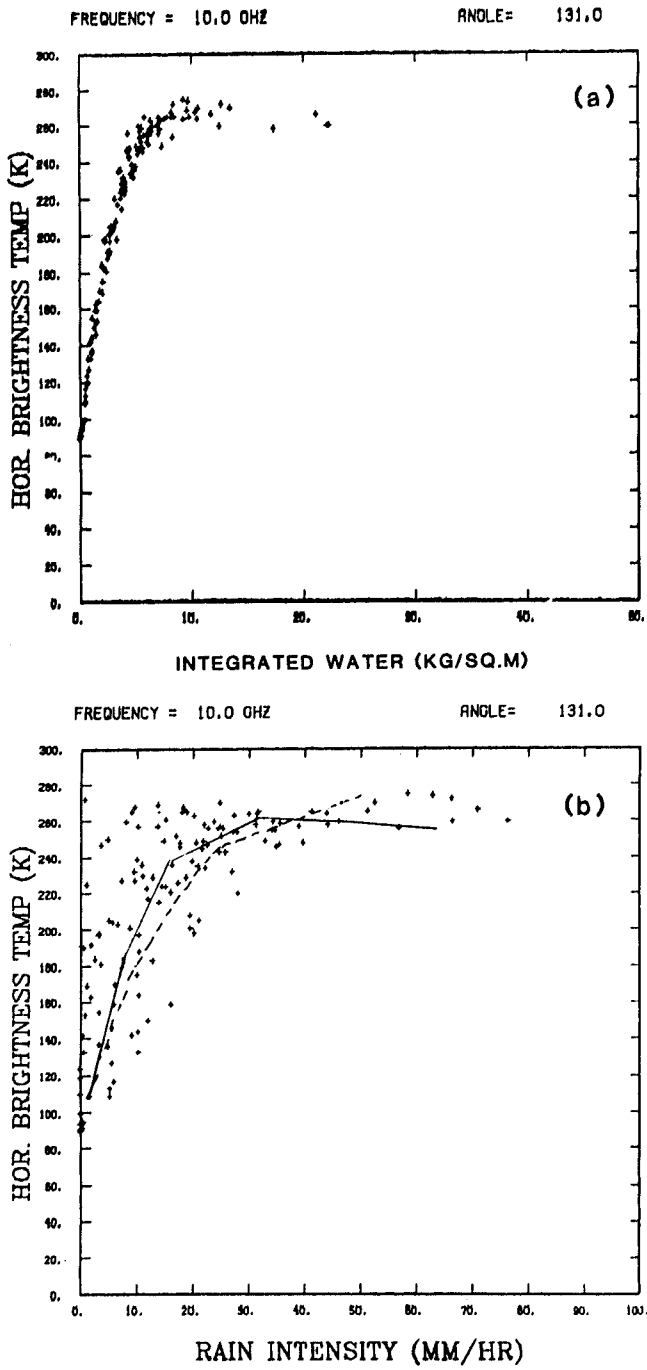

Fig. 3. *Coupled radiative model with Tao model results for 10 GHz (horizontal polarization): a) T_B plotted against integrated water content in kg m^{-2}; b) T_B plotted against rain intensity in mm h^{-1} showing all the 144 profile points, with the Wu and Weinman (1984) relationship the superimposed solid line and the Wilheit et al. (1977) relationship the dashed line.*

Next, each variable was averaged over boxes of increasing size. Figure 4 shows the T_B versus rain rate relationships when each variable is averaged over 9 x 9 km boxes. As the averaging areas are increased, scatter is reduced and the relationship becomes more linear. It is worth noting, however, that the line slope is increased by 37% relative to the linear portion of Fig. 3b, indicating that plane-parallel model algorithms will give some underestimation due to beam filling, even at this low frequency.

Figure 5 gives the corresponding T_B versus rain rate for 18 GHz (horizontal polarization). Figure 5a shows the relationships of both Wu and Weinman (solid line) and Wilheit et al. (dashed line) superimposed on the model plot for all 144 profiles in the grid, while Fig. 5b shows results when the variables are averaged over 9 x 9 km boxes. Both the Wu-Weinman and Wilheit curves now significantly underestimate the rain rate. This result brings home the impact of the beam-filling problem. The plane-parallel model curves are constructed for horizontally uniform hydrometeor profiles. When horizontal variability occurs within the averaging area, the rain rate derived by the plane-parallel model curve is biased, the more so the greater the departure from linearity. The bias is an underestimate when the curve is concave downward. If, in Fig. 5b, a T_B of 235 K is selected, the Wu-Weinman curve underestimates the rain rate by about 43%. This bias is undoubtedly due to the fact that many of the

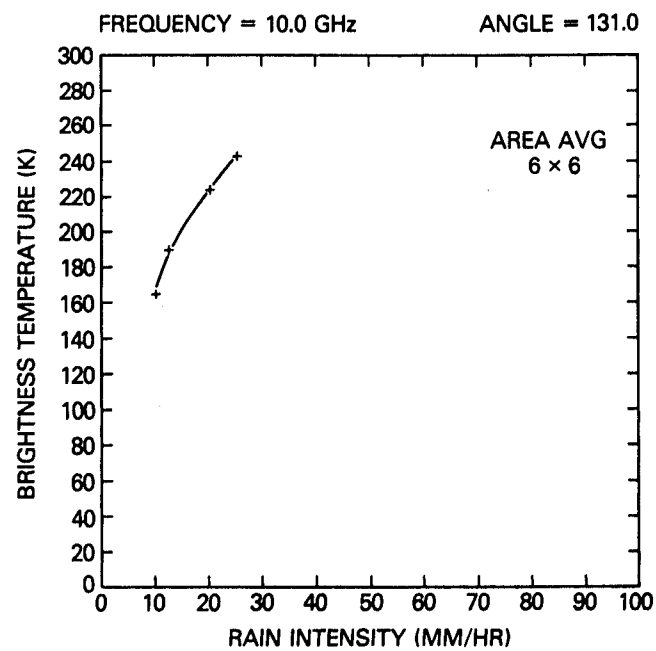

Fig. 4. *Coupled radiative model with Tao model results for 10 GHz, with each variable averaged over 9 x 9 km squares (6 x 6 grid points).*

footprints were not totally filled. When partially filled footprint effects are accounted for (Kummerow, 1987), the bias is removed and agreement becomes quite good. The much better behavior of the plane-parallel models with the 10 GHz channel would appear to be due to the more linear response at that frequency, although many more tests need to be made to establish these relationships and to really understand the effects of different hydrometeor structures and different averaging areas for varying types of convective systems.

From Figs. 5a and 5b, it is not clear what the "real" relation is between 18-GHz T_B (horizontal polarization) and surface rain rate. When the calculations at full model resolution (1.5 km in the horizontal direction) are examined (Fig. 5a), the large scatter suggests that the complexity of the convection when viewed on a small spatial scale renders the T_B-rain rate relations almost meaningless on that scale. When spatial averaging is carried out, the scatter is reduced and a curve shape like that of the theoretical curve emerges. However, the bias related to the non-linear response also appears. The simple, smooth theoretical curve does not exist in the real world at the small scale because of the complexity of the convection and does not exist in the spatially averaged data because of the non-linear response.

The quite different relationship between T_B and rain rate for the ice-scattering frequencies is illustrated here for 90 GHz (vertical polarization) in Fig. 6. The reason for the rapid decrease in brightness temperature with increasing rain rate is believed to be caused by the association of deeper layers of large graupel with heavier rain rates in convective clouds. In Fig. 6a, all 144 data points from the multi-cloud model appear, with the Wu and Weinman relationship for convective cores shown by the solid line. Even with the large scatter, the line is a fair fit to the data, except for about six points with very high rain rates and warm brightness temperatures. These are probably due to horizontal offsets or tilts in rain cores, so that the heavy rain at the surface is offset horizontally from the location of high ice concentrations in the middle and upper parts of the cells.

However, when the multi-cloud model data are averaged over 6 x 6 km boxes, the scatter decreases dramatically, with the resulting slope being somewhat steeper than determined by Wu and Weinman. The lower T_B's at the same rain rate (as compared to Wu and Weinman) are due to significantly more ice in the upper parts of the Tao model clouds as compared to the schematic cloud profiles of Wu and Weinman. The nearly linear T_B-rain rate relation at 90 GHz indicates that "beam-filling" problems will be muted at this wavelength. The strong correlation of T_B (90 GHz) with rain rate in Fig. 6b clearly indicates the usefulness of this frequency in estimating rain rate and agrees with findings by Hakkarinen and Adler (1987), who compared 92-GHz aircraft data with ground-based radar data.

4. CONCLUSIONS AND FUTURE WORK

The results of the calculations in this paper indicate, first of all, that there is a great complexity in the relationships between rain rate at the ocean surface and upwelling brightness temperature at all frequencies when considered on this small spatial scale (1.5 km). At all frequencies, there was significant scatter in the rain rate-T_B relations. However, on the average, the relations agreed favorably

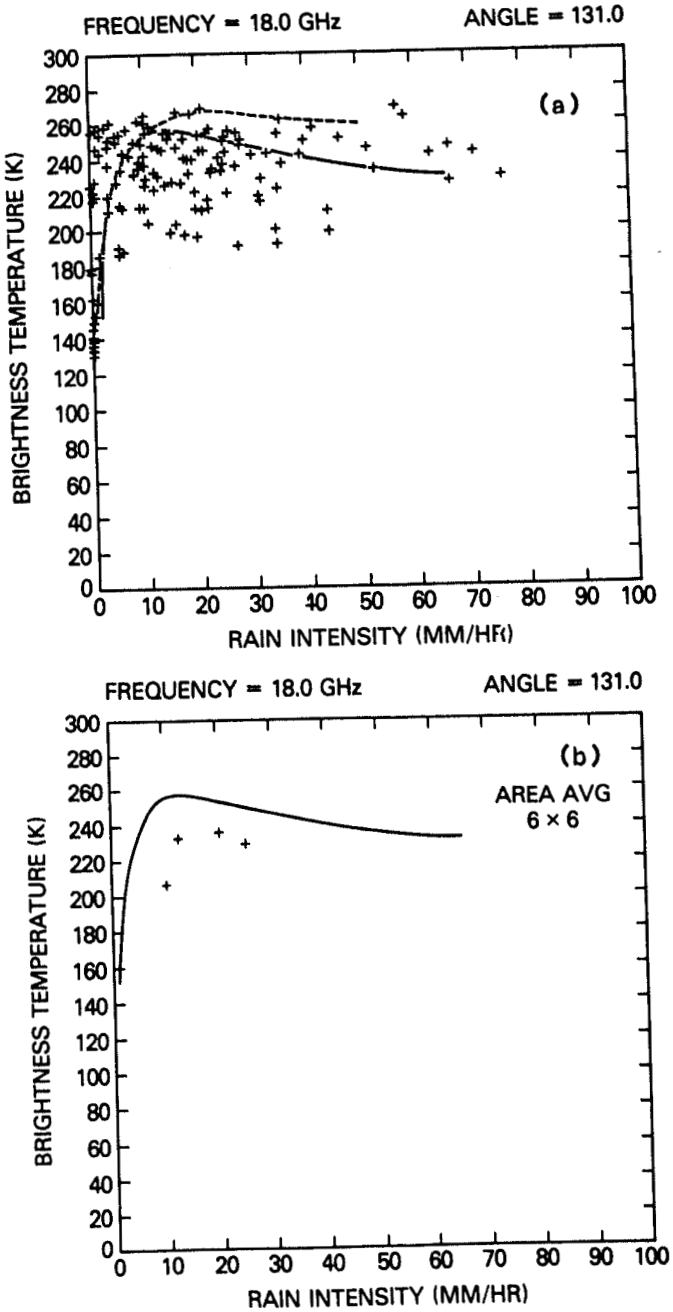

Fig. 5. *Coupled radiative model with Tao model results for 18 GHz (horizontal polarization): a) T_B plotted against rain rate showing all 144 profile points with Wu and Weinman (1984) curve the superimposed solid line and the Wilheit et al. (1977) curve dashed; b) T_B plotted against rain rate for 18 GHz when both variables are averaged over 9 x 9 km squares (6 x 6 grid points), with the Wu and Weinman curve the superimposed solid line.*

with those calculated by Wu and Weinman (1984). The distribution of ice was also shown to be a critical factor in determining the relations.

Analysis of the calculations also indicate that at 10 GHz non-precipitating cloud water may cause small overestimates of low rain rates at this frequency.

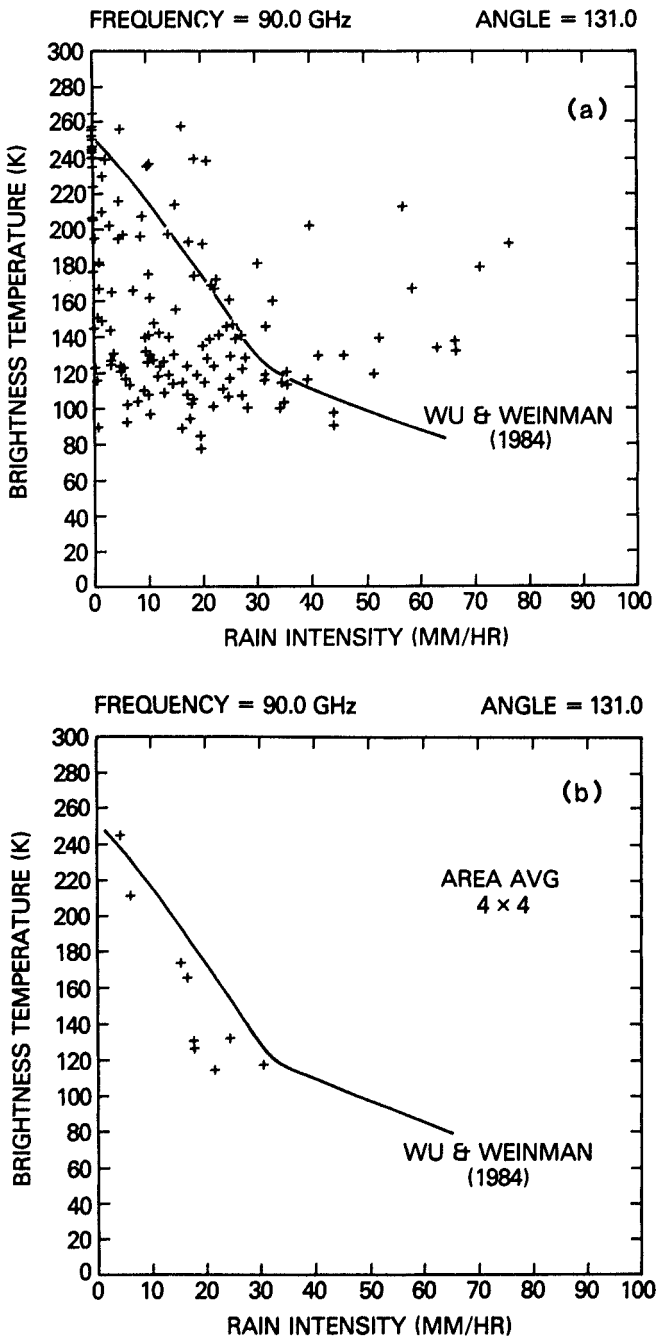

Fig. 6. *Coupled radiative model with Tao model results for 90 GHz (vertical polarization): a) T_B plotted against rain rate showing all 144 profile points. The Wu and Weinman (1984) curve for 85.6 GHz is the superimposed solid line. b) T_B plotted against rain rate for 90 GHz when both variables are averaged over 6 x 6 km squares (4 x 4 grid points), with the Wu and Weinman curve the superimposed solid line.*

In order to simulate satellite brightness temperature-rainfall relations, spatial averaging of the calculated brightness temperatures and model-generated rain rates was carried out. In this initial exercise, the averaging remained over a relatively small area (total area = 18 km square). The averaging process on varying scales going from 1.5 to 9 km clearly indicates that the spatial averaging removes a significant portion of the scatter in the brightness temperature-rain relationships due to the complexity of the convective phenomenon. At low frequencies (10 and 18 GHz), the large scatter in the T_B-rain relations is replaced by the usual bias caused by the non-linear relation when area averaging is performed for footprints up to 9 km on a side. At the higher frequencies, little correlation between the small-scale brightness temperature and rainfall rate calculations was evident, but spatial averaging clearly results in a negative correlation between, for example, the 90-GHz brightness temperature and the rainfall rate.

The domain of these calculations will soon be expanded so that this approach can be used to simulate past, present, and future satellite passive microwave observations and can be used to analyze the relationships between brightness temperature and rainfall rate at satellite-observable scales.

5. REFERENCES

Hakkarinen, I. M., and R. F. Adler, 1987: Observations of convective precipitation at 92 and 183 GHz: Aircraft results. Meteor. and Atmos. Phys. (accepted).

Kummerow, C. D., 1987: Microwave radiances from horizontally finite, vertically structured precipitating clouds. Ph.D. Dissertation, University of Minnesota, 146 pp. [Portions submitted to J. Geophys. Res.]

McCumber, M. C., W.-K. Tao, J. Simpson, R. Penc, and S.-T. Soong, 1987: Comparison of ice-phase microphysical parameterization schemes in tropical, fast-moving convective line simulations. Preprints, 17th Conference on Hurricanes and Tropical Meteorology, Amer. Meteor. Soc., Miami, FL.

Rutledge, S. A., and P. V. Hobbs, 1984: The mesoscale and microscale structure and organization of clouds and precipitation in midlatitude clouds. XII: A diagnostic modeling study of precipitation development in narrow cold frontal bands. J. Atmos. Sci., 41, 2949-2972.

Szejwach, G., R. F. Adler, I. Jobard, and R. A. Mack, 1986: A cloud model-radiative model combination for determining microwave T_B-rain rate relations. Preprints, 2nd Conference on Satellite Meteorology/Remote Sensing and Applications, Amer. Meteor. Soc., Williamsburg, VA, 444-449.

Tao, W.-K., and S.-T. Soong, 1986: The study of the response of deep tropical clouds to mesoscale processes: Three-dimensional numerical experiments. J. Atmos. Sci., 43, 2653-2676.

Tao, W.-K., J. Simpson, and S.-T. Soong, 1987: The statistical properties of a cloud ensemble: A numerical study. J. Atmos. Sci., 44 (in press).

Wilheit, T. T., A. T. C. Chang, M. S. V. Rao, E. B. Rodgers, and J. S. Theon, 1977: A satellite technique for quantitatively mapping rainfall rates over the oceans. J. Appl. Meteor., 16, 551-560.

Wilheit, T. T., J. L. King, E. B. Rodgers, R. A. Nieman, B. M. Krupp, A. S. Milman, J. S. Stratigos, and H. Siddalingaiah, 1982: Microwave radiometric observations near 19.35, 35, 92 and 183 GHz of precipitation in tropical storm Cora. J. Appl. Meteor., 21, 1137-1145.

Wu, R., and J. A. Weinman, 1984: Microwave radiances from precipitating clouds containing aspherical ice, combined phase, and liquid hydrometeors. J. Geophys. Res., 89, 7170-7178.

THE 1982-83 ENSO GLOBAL CONVECTIVE PRECIPITATION ANOMALY DERIVED FROM NIMBUS-7 SMMR 37 GHZ SCATTERING MEASUREMENTS

Roy W. Spencer
NASA/Marshall Space Flight Center
Huntsville, Alabama 35812

H. Michael Goodman
Johnson Research Center
University of Alabama in Huntsville
Huntsville, Alabama 35899

1. INTRODUCTION

The 1982-83 El Nino/Southern Oscillation (ENSO) caused global changes in precipitation patterns (Rasmusson and Wallace, 1983). Because these changes were persistent for several months over regional areas, it is possible to observe them with the relatively infrequent sampling of polar orbiting satellites. Infrared observations from these platforms have allowed documentation of high level cloudiness variations associated with deep convective activity variations during this ENSO event (e.g. Kyle et al., 1986).

Even the narrow swath width (780 km) and alternate day operation of the Nimbus-7 Scanning Multichannel Microwave Radiometer (SMMR) has been sufficient to observe the ENSO oceanic precipitation anomalies. Prabhakara et al. (1986) measured atmospheric liquid water-induced brightness temperature (T_B) increases over the radiometrically cold oceans at 6.6 and 10.7 GHz, related them to monthly rain gauge totals, and then determined fields of rainfall surpluses and deficits during the ENSO.

Unfortunately, these low frequency observations can only be used to obtain oceanic rain rates because the thermal emission from the rain does not contrast with a radiometrically warm land surface. At the highest SMMR frequency of 37 GHz, however, the relatively unpolarized T_B depressions due to scattering by precipitation size ice within convective storms allow precipitation observation over both land (Spencer et al., 1983) and ocean (Spencer, 1986).

Here we will apply these scattering algorithms to the 1981-84 December through May (DJFMAM) periods to obtain the 1982-83 DJFMAM convective precipitation anomaly patterns associated with the ENSO. It is not our purpose to derive quantitative fields of precipitation anomaly, but to demonstrate the ability to map precipitation surplus and deficit patterns that qualitatively match known regions of anomalies. To the extent that the precipitation anomaly fields can be derived, despite poor sampling in both space and time and at a frequency where the scattering signature is often weak (37 GHz), this demonstration foreshadows more successful future quantitative studies based upon the new Defense Meteorological Satellite Program (DMSP) Special Sensor Microwave / Imager (SSM/I). A single copy of the SSM/I is currently providing four times as much earth coverage as the Nimbus-7 SMMR, and its 85 GHz channels will provide much improved sensitivity to light rain over the 37 GHz channels used here (see Hood and Spencer, this volume).

2. METHOD

The passive microwave detection of precipitation over the earth requires a significant T_B contrast between the rain and the surrounding background. Over land, differencing two frequencies having markedly different sensitivities to volume scattering induced by precipitation size ice will isolate the volume scattering signal while greatly reducing the effects of background thermometric temperature variations (Spencer, 1984). Over the oceans, polarization information is necessary at frequencies where both volume scattering and low surface emissivities can produce low T_B (e.g. 37 GHz). This allows one to distinguish between T_B depressions due to the cold ocean background and those due to volume scattering by ice (Spencer, 1986).

In both land and ocean cases, the quantity that we will use as a surrogate for precipitation intensity is ΔT_B. Over land, this difference is between frequencies (here, 21 and 37 GHz), while over the ocean it is between individual footprint and area-averaged effective radiating temperatures (ERT, see Spencer, 1986) computed from horizontal (H) and vertical (V) polarization 37 GHz T_B's.

A decision diagram of the specific steps involved in the identification of precipitation from the SMMR measurements is shown in Fig. 1. Decisions based upon the radiative effects of the earth are in bold boxes, while fine boxes contain steps that are required to reduce sampling and measurement errors from variable calibration, noise in the T_B data, footprint misalignment between channels, and large footprint size.

Because there is a one-quarter footprint offset between the H37 and V37 footprints, the first step is to correct this with a weighted average of chronologically adjacent footprints. Next, small scan-angle dependent changes in the V37 T_B resulting from insufficient polarization rotation corrections (up to 2.5° at the scan extremes) are taken into account. This effect is a function of both the distance from the swath center and the magnitude of the T_B. After this, a ten scan cycle average ERT is computed from an average of all oceanic H37 and V37 data. The nearest H10.7 T_B is then checked to determine if the location is over land (warm T_B) or ocean (cold T_B).

If over land, small lakes are screened out which can look like rain by causing the (smaller footprint) 37 GHz T_B to be depressed more than the (larger footprint) 21 GHz T_B. This polarization screening omits the footprint if it is highly polarized at 37 GHz, indicating a water surface. If this test is passed, then the average of two chronologically adjacent

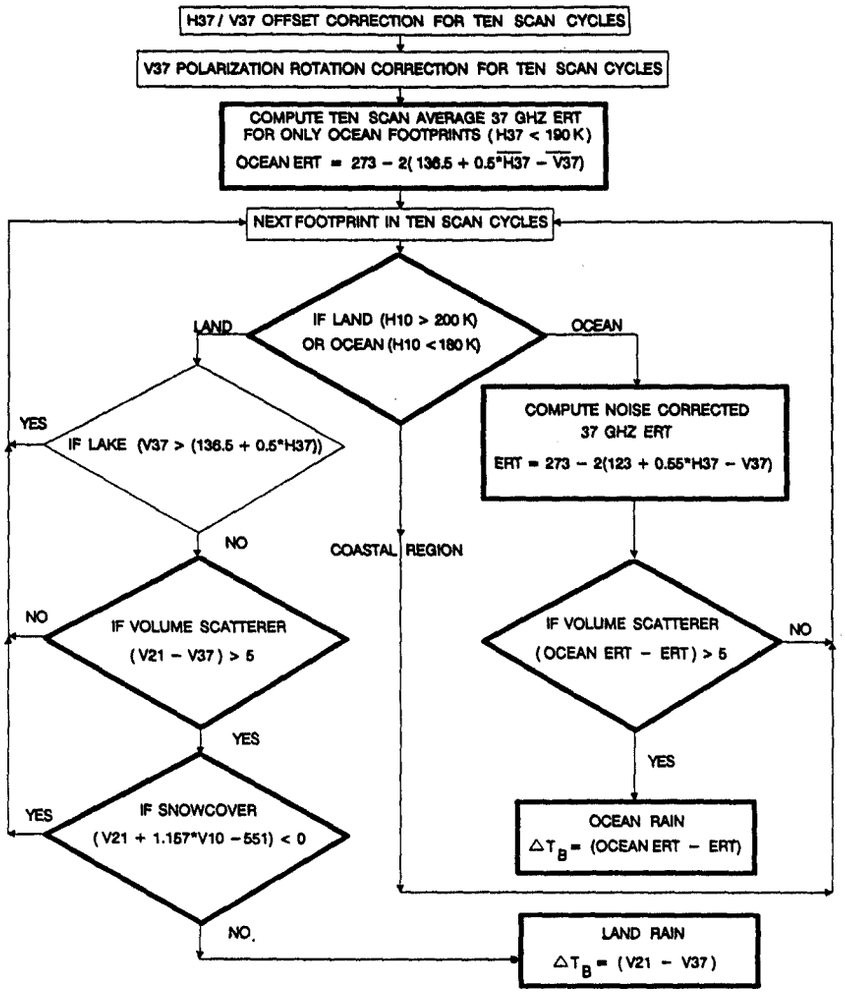

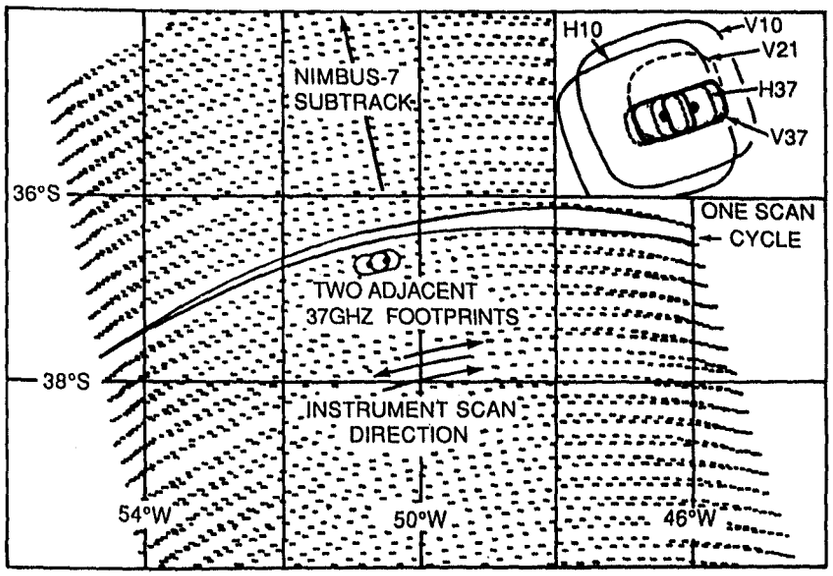

Fig. 1 Flowchart (above) of the steps involved in retrieving precipitation events from measurements of scattering at 37 GHz from the Nimbus-7 SMMR; and (below) the scanning geometry of the Nimbus-7 SMMR showing individual 37 GHz footprint locations, their approximate size (30 km for 3 dB beamwidth), and an example of the relative size and positioning of several of the SMMR footprints. The flowchart process is repeated for each ten scan cycle subset of data (about 150 subsets per orbit). For precipitation to be diagnosed, all 37 GHz conditions must be met for the average of two chronologically adjacent footprints.

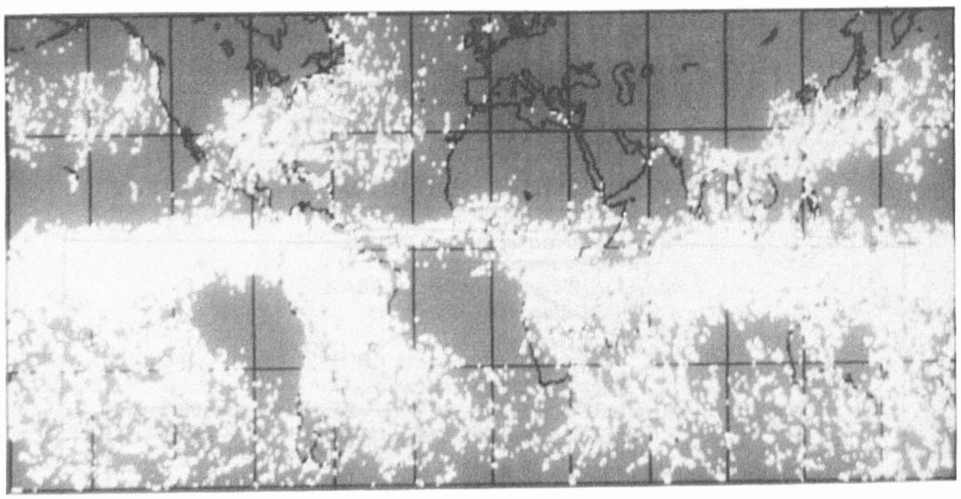

Fig. 2 Locations of SMMR scattering-diagnosed precipitation ($\Delta T_B > 5°$) during DJFMAM of 1982-83. Each dot represents two chronologically adjacent 37 GHz footprints satisfying the criteria in Fig. 1. The total number of events is approximately 140,000.

V37 T_B is compared to the nearest V21 T_B to see if the former is at least 5° colder than the latter, indicating a volume scatterer. Because snowcover is also a volume scatterer of microwave energy, it must be discriminated from precipitation. Different combinations of SMMR channels have been found to be useful for this purpose (Spencer and Santek, 1985), and for simplicity we have here chosen a weighted difference between the V21 and V10.7 measurements. This allows separation between those volume scatterers in a cold environment (snowcover) from those in a warm environment (convective precipitation cells). If the precipitation test is passed, then T_B from all 10 channels are stored in a file, and the next footprint is checked.

If the H10.7 T_B is less than 180 K, then an ocean location is indicated. The polarization corrected 37 GHz T_B is then computed for two chronologically adjacent footprints and compared to the corresponding ten scan cycle (up to about 1000 footprints) average of the same quantity. If the two-footprint value is at least 5° colder than the background (ten scan cycle average) value, then precipitation is assumed. As in the land case, all channels are stored, along with the polarization corrected 37 GHz T_B.

The 5° threshold is considerably less than the 19° used by Spencer and Santek (1985) for a global survey of intense convective precipitation over land. Values much less than 5° result in false alarms that soon outnumber the rainfall events, especially from snowfields. Vegetated land typically has ΔT_B values close to 0° C.

Large scale overrunning (stratiform) precipitation, unless heavy, was generally not discriminated at 37 GHz. This is probably due to a combination of (1) smaller rain rates, (2) shallower ice layers above the freezing level, and (3) (in the case of land) cooler land surfaces below warm overrunning air causing the more penetrative 18 GHz radiation to be depressed at the same time the 37 GHz T_B is depressed by weak volume scattering. These effects result in our classification of the diagnosed precipitation signals as almost universally deep convective in origin.

3. CHARACTERISTICS OF THE SCATTERING EVENTS

The locations of the individual scattering events (each representative of a 1000 km^2 area) for DJFMAM of 1982-83 are shown in Fig. 2. It can be seen that even with six months of SMMR data, some areas exist without diagnosed precipitation even in climatologically active zones. The total number of events in this figure amounts to about 140,000.

A scatter plot of the 37 GHz ocean background ERT for all December 1981 oceanic rain events is shown in Fig. 3 as a function of latitude. The ERT values (set by the constants in the equation at the top of Fig. 1) are the same as a typical theoretical value resulting from any amount of the footprint being covered by deep convective non-precipitating cloud having drop sizes small enough to neglect scattering (Spencer, 1986). Note that the values decrease away from the equator, indicating a cooling of the atmosphere. T_B falling at least 5° below these values are then classified as precipitation induced.

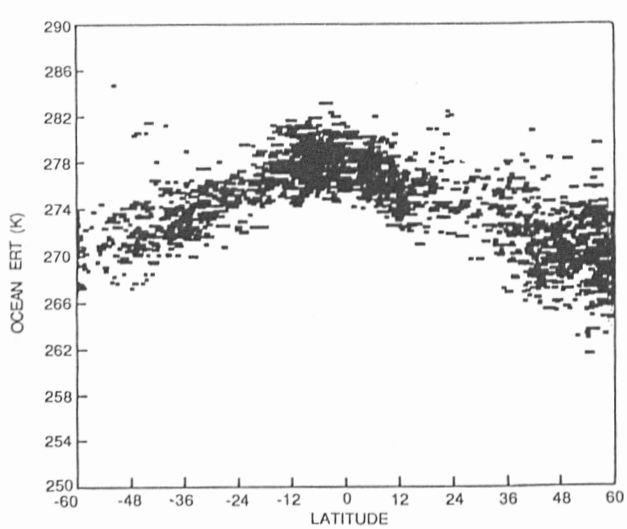

Fig. 3 Relationship between ocean background ERT and latitude for all diagnosed oceanic rain events during December, 1981.

A frequency histogram of the ΔT_B for December 1981 oceanic precipitation (Fig. 4a) reveals a logarithmic behavior that we would expect for a quantity that is related to precipitation intensity. Based upon previous comparisons with radar derived rain rates (e.g. Spencer et al., 1983, Spencer, 1986) we can expect that each degree change in T_B corresponds to about 1 mm h^{-1} change in rain rate. However, our confidence in the accuracy or stability of this relationship for various climatic regimes is quite low due to our still meager understanding of how storm core microphysics above the freezing level vary regionally. Thus, our 5° threshold in this study corresponds to approximately 5 mm h^{-1}, but could easily have a factor of two bias depending upon the microphysical character of the storms. The land storms (Fig. 4b) are relatively more intense in their ice scattering characteristics, as evidenced by the greater proportion of high values of ΔT_B compared to the ocean.

4. THE ENSO PRECIPITATION ANOMALY

All precipitation events classified by the algorithms represented by Fig. 1 were assigned to 5° x 5° latitude-longitude bins. The sum of all events' ΔT_B intensities within each bin were converted into image intensities. The sums for DJFMAM 1981-82 (Fig. 5 top) and 1983-84 (Fig. 5 middle) show similar patterns which contrast with some dramatic changes during the middle (ENSO) year (1982-83, Fig. 5 bottom). These changes are more noticeable when the two bracket years are averaged and subtracted from the ENSO year (Fig. 6). The major features are surpluses in the central and eastern tropical Pacific (where the anomalously high sea surface temperatures were observed), central Indian Ocean, and extreme southern Brazil. Major deficit areas occur in the usual location of the South Pacific Convergence Zone (SPCZ), over much of Amazonia, the tropical Atlantic, much of the Sahel, and the extreme southwestern North Pacific. Most of these features contribute to a broken band of precipitation deficits of varying magnitude appearing to circle the earth between the equator and 10° N.

The spatial coherence of the surplus and deficit patterns is quite good considering the poor sampling characteristics of the Nimbus-7 SMMR. Most of the individual strong signals are not isolated, but are part of a widespread (though noisy) region of similar response. Many isolated weaker deficits and surpluses occur, as would be expected.

5. CONCLUSIONS

The ability to map semi-annual convective precipitation patterns over global land and ocean regions has been demonstrated based upon the volume scattering effect that precipitation-size ice has on Nimbus-7 SMMR 37 GHz brightness temperatures. This suggests that the new DMSP SSM/I 85 GHz data (in combination with 37 and 19 GHz data) will be very valuable in global surveys of precipitation patterns. This conclusion is based upon (1) much greater sensitivity of the 85 GHz T_B to light precipitation compared to 37 GHz (see Hood and Spencer, this volume), and (2) the ability of a single DMSP SSM/I to observe almost four times as much area as the Nimbus-7 SMMR. The eventual quantification of these precipitation signals in terms of rain rate is currently being worked on by various investigators. Assuming the existence of a fairly complete SSM/I archive, future studies requiring global rainfall distributions and anomalies should benefit greatly.

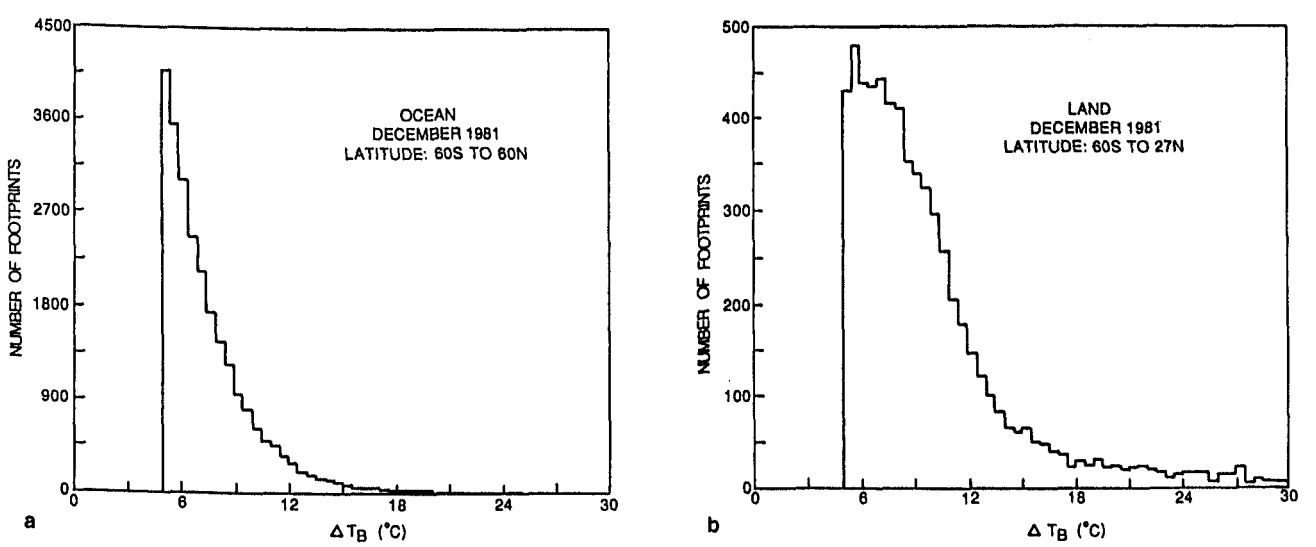

Fig. 4 Frequency histogram of T_B for (a) the oceans, and (b) land during December 1981, showing the logarithmic behavior of the precipitation signal intensities.

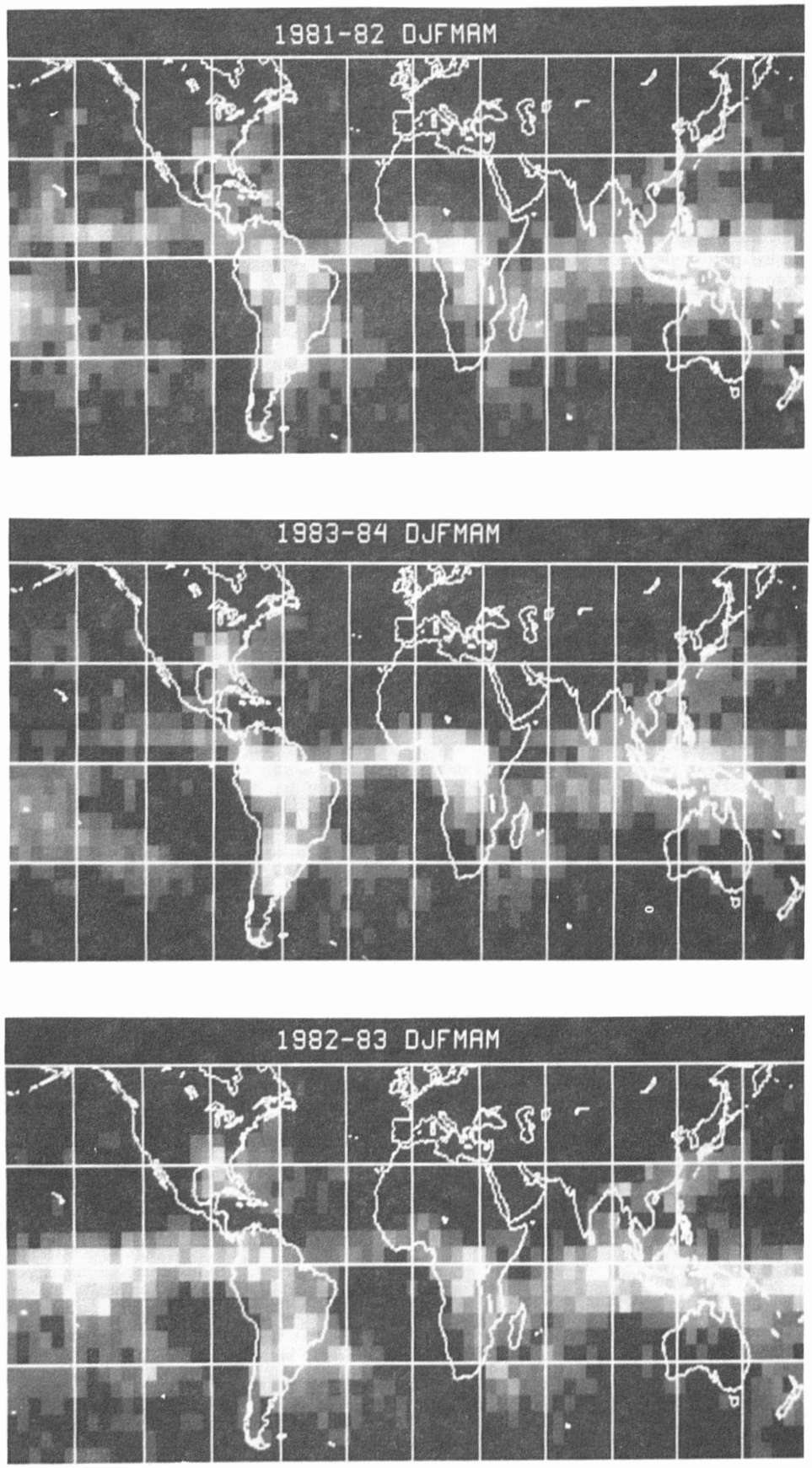

Fig. 5 Images of the total scattering-induced 37 GHz ΔT_B during DJFMAM of 1981-82 (top); during 1983-84 (middle); and the 1982-83 ENSO period (bottom). The brightest 5° x 5° cells correspond to a sum of 800 ΔT_B's exceeding 10,000 °C.

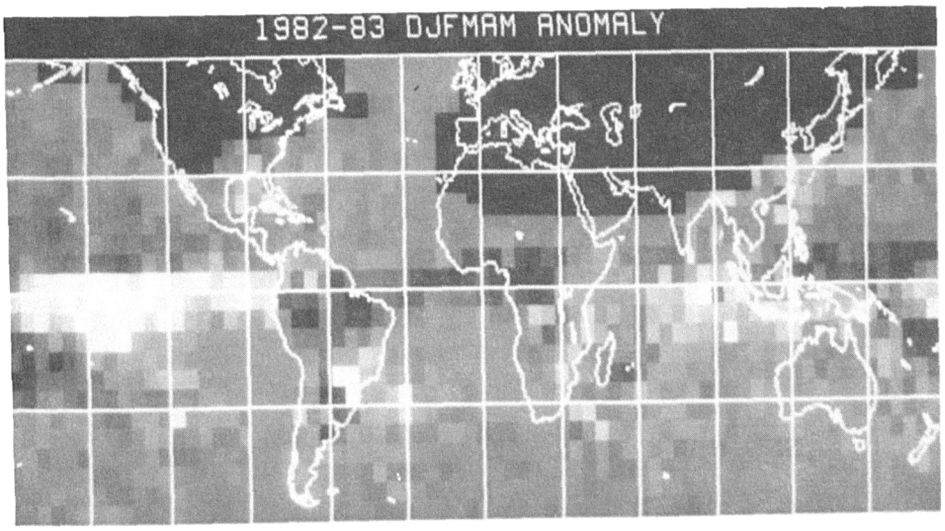

Fig. 6 Images of the DJFMAM 1982-83 ENSO deep convective precipitation anomalies. Areas brighter than the background are precipitation surplus, while darker areas are deficits. Blacked-out areas in the Northern Hemisphere were dominated by unscreened false alarms from snow cover, and a few from geologic features in the Sahara Desert.

6. ACKNOWLEDGMENTS

We would like to thank Homer Rice and Fred Calhoun for archiving the SMMR data from tape to online cartridges. The SMMR data were provided to us by the National Space Science Data Center. David Santek (Space Science and Engineering Center, Madison, Wisconsin) provided programming advice. This work was supported by the NASA Headquarters Mesoscale Processes Research Program.

7. REFERENCES

Kyle, H. L., P.E. Ardanuy, and R.R. Hucek, 1986: *El Nino and Outgoing Longwave Radiation: An Atlas of Nimbus-7 Earth Radiation Budget Observations*. NASA Ref. Pub. 1163, Scientific and Technical Information Branch, NASA, Washington D.C. 20233.

Prabhakara, C., D.A. Short, W. Wiscombe, R.S. Fraser, and B.E. Vollmer, 1986: Rainfall over oceans inferred from Nimbus 7 SMMR: Application to 1982-83 El Nino. *J. Climate Appl. Meteor.*, **25**, 1464-1474.

Rasmusson, E.M., and J.M. Wallace, 1983: Meteorological aspects of the El Nino/Southern Oscillation. *Science*, **222**, 1195-1202.

Spencer, R.W., D.W. Martin, B.B. Hinton, and J.A. Weinman, 1983: Satellite microwave radiances correlated with radar rain rates over land. *Nature*, **304**, 141-143.

Spencer, R.W., 1984: Satellite passive microwave rain rate measurement over croplands during spring, summer, and fall. *J. Climate Appl. Meteor.*, **23**, 1553-1562.

Spencer, R.W., and D.A. Santek, 1985: Measuring the global distribution of intense convection over land with passive microwave radiometry. *J. Climate Appl. Meteor.*, **24**, 860-864.

Spencer, R.W., 1986: A satellite passive 37 GHz scattering based method for measuring oceanic rain rates. *J. Climate Appl. Meteor.*, 25, 754-766.

Blank page retained for pagination

THUNDERSTORM ICE INDUCED BRIGHTNESS TEMPERATURE DEPRESSIONS AT 18, 37, and 92 GHz DURING COHMEX AND THEIR IMPLICATIONS FOR SATELLITE PRECIPITATION RETRIEVALS

Robbie E. Hood and Roy W. Spencer

NASA/ED43
Marshall Space Flight Center, AL 35812

1. BACKGROUND

The retrieval of rainfall rates over radiometrically warm backgrounds from spaceborne passive microwave radiometers has become a topic of increasingly active study. The possibility of a correlation between precipitation rates and microwave radiation has been demonstrated theoretically by Wu and Weinman (1984), with aircraft data by Wilheit et al. (1982), and Hakkarinen and Adler (1986), and with satellite data by Spencer et al. (1983) and Spencer (1986) among others. The nature of these findings have shown that precipitation scattering signatures measured in the microwave present a striking contrast to many earth surface features. In particular, precipitation over land which is the focus of this paper tends to depress the brightness temperature (T_B) measured by a downward viewing radiometer to a value much lower than that of the radiometrically warm land background.

The reason for this may be demonstrated with Mie theory. The volume extinction properties, which include scattering and absorption, of both water and ice hydrometeors are correlated to the size and number density of the hydrometeors as well as the frequency of the upwelling passive microwave radiation. Figure 1 shows the relationship of volume extinction coefficient (km^{-1}) to rainfall rate ($mm\ h^{-1}$) for water spheres at -10°C and ice spheres at 0°C assuming the particle size distribution defined by Marshall and Palmer (1948). In general, for a rainfall rate between 0 and 30 $mm\ h^{-1}$, the higher the frequency or greater the rainfall rate the larger the extinction coefficient becomes. Of considerable importance in this study is that the extinction coefficients for ice are so much larger at 92 GHz than at 37 or 18 GHz.

Figure 2 displays the relationship of rainfall rate to single scattering albedo which is the ratio of the scattering coefficient to the extinction coefficient. Scattering is the primary extinction mechanism for ice particles. Liquid hydrometeors, however, are predominantly absorbers and thus, emitters of microwave radiation. Therefore in a thunderstorm situation, the upwelling microwave radiation emitted by the land background and liquid raindrops will be backscattered by the upper ice layer of the storm causing the observed T_B to decrease. Because the extinction coefficients vary so much between frequencies (Fig. 1), the altitude of response for all but the weakest storms will vary significantly between frequencies. Wu and Weinman (1984) have demonstrated with their plots of weighting functions that for a given rain rate the lower the frequency, the lower the height of the peak scattering response.

2. COHMEX ER-2 MISSIONS

The COoperative Huntsville Meteorological EXperiment (COHMEX) provided an unique opportunity to measure simultaneously this ice scattering effect with several frequencies and with higher spatial and temporal resolution than in previous satellite studies. COHMEX which took place in the Northern Alabama/Central Tennessee region during June and July, 1986 was an extensive ground-based, airborne, and satellite atmospheric science field project sponsored by NASA, NOAA, NSF, and FAA and coordinated at Marshall Space Flight Center.

The window frequency microwave instrumentation consisted of the Microwave Precipitation Radiometer (MPR) measuring 18 and 37 GHz and the Advanced Microwave Moisture Sounder (AMMS) which sampled at 92 and 183 GHz. The instruments, which were used in cooperation with Goddard Space Flight Center, were mounted aboard a NASA ER-2 high altitude aircraft. The AMMS scanned directly below the aircraft across nadir while the MPR stared ahead of the aircraft about 45° from nadir as pictured in Fig. 3. At an aircraft altitude of 20 km, the viewing geometry provided a ground resolution of about 3 km for the 18 and 37 GHz channels, 0.7 km for the 92 GHz channel, and 0.35 km for the 183 GHz channel.

The NCAR CP-2 dual-wavelength, dual-polarization radar was also in operation during COHMEX as part of a Doppler radar network. The CP-2 radar was able to collect data out to a range of 150 km, but the more accurate information was measured within an 80 km ring. The ER-2 was deployed from Wallops Island, VA with instructions to sample any convective activity along the flight path to Huntsville. Once in the COHMEX area, thunderstorms within range of CP-2 were given highest priority for overflight by the ER-2. If this criterion was not met then the ER-2 was directed to other precipitation regions preferably in the vicinity of a National Weather Service radar. Air time for the ER-2 in the COHMEX region was approximately 3 hours.

3. TIME SERIES OF STORM RESPONSES

The microwave frequencies of primary interest in this paper are 18, 37, and 92 GHz. The AMMS data were spatially averaged to the same resolution as the MPR data, and the three frequencies were studied in time series format. Examination of these time series plots has revealed several interesting features of the COHMEX data set. One significant feature, which is consistent with the ice extinction

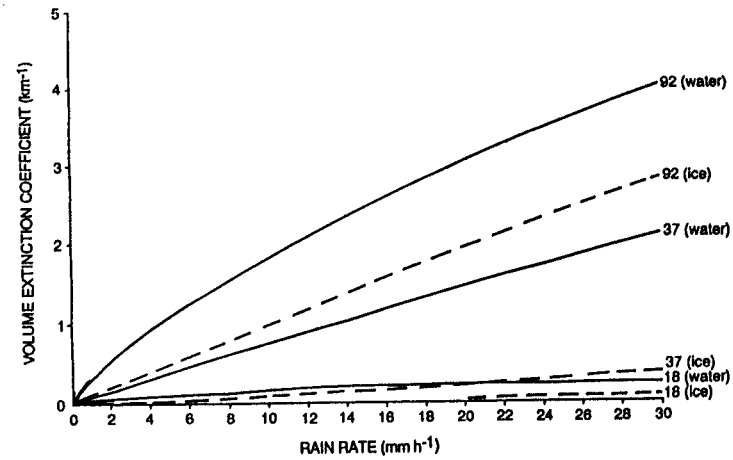

Fig. 1. Mie theory volume extinction coefficient as a function of Marshall-Palmer rain rate for water spheres at -10°C and ice spheres at 0°C.

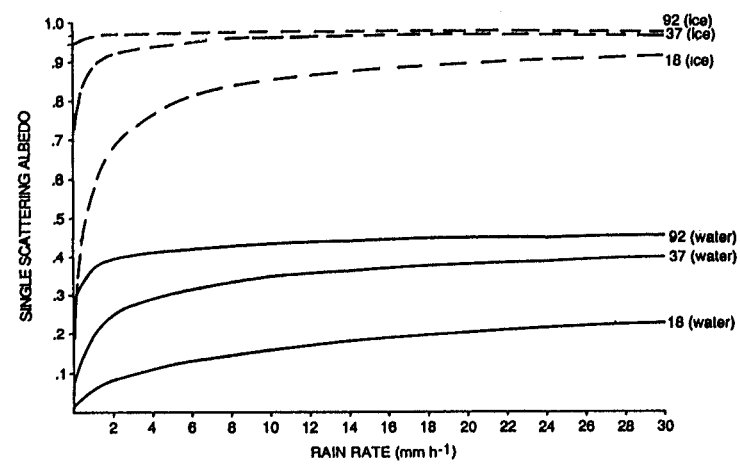

Fig. 2. Mie theory single scattering albedo as a function of Marshall-Palmer rain rate for water spheres at -10°C and ice at 0°C.

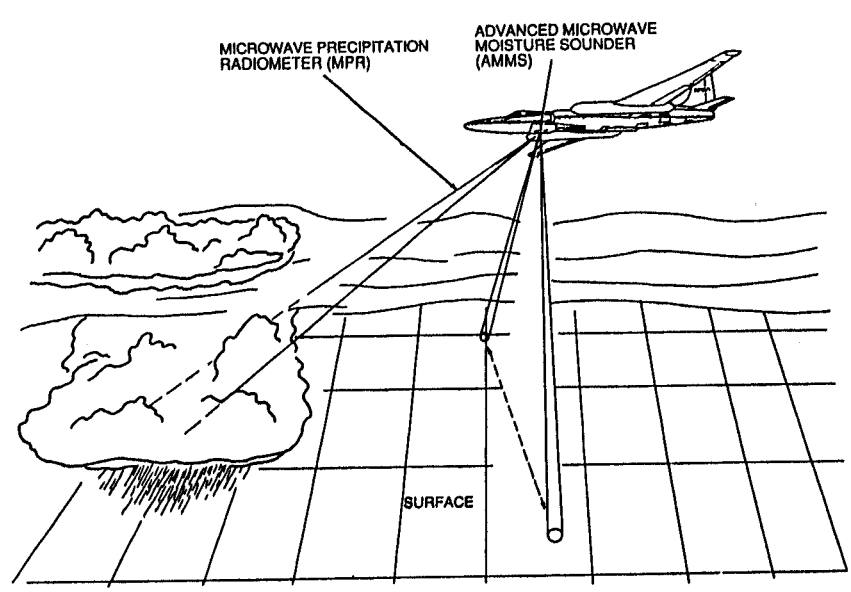

Fig. 3. The viewing geometry of the MPR and the AMMS aboard the NASA ER-2.

coefficients in Fig. 1, is the great sensitivity of the 92 GHz to very light rain. The weakest scattering events of the COHMEX data had 92 GHz T_B depressions three to five times as large as those at 37 GHz (see Fig. 8). Figure 4 displays two of these cases. This great sensitivity of 92 GHz to light precipitation will lead to footprint averaging biases when satellite (e.g. the Special Sensor Microwave/Imager, SSM/I) data are interpreted. Thus, a small intense storm might produce a T_B measurement the same as a large lightly precipitating area, even though the footprint averaged rain rate for the storm is larger. This nonlinearity effect is analogous to that of the 19 GHz emission algorithms for oceanic rain retrieval (e.g. Wilheit et al., 1977).

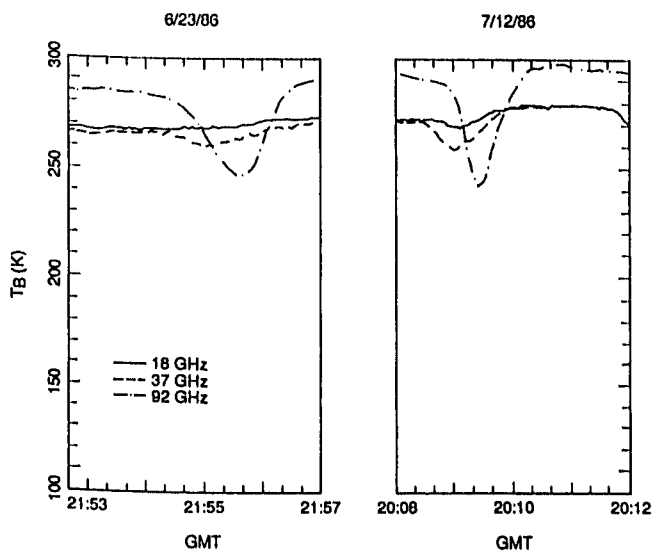

Fig. 4. COHMEX examples of the sensitivity of 92 GHz T_B to light rain.

Another feature of the data is the variation of the 18/37/92 GHz T_B interrelationship. As had been expected, the brightness temperature depressions associated with precipitation were enhanced with increasing frequency so that the 37 GHz T_B depressions were always stronger than the 18 GHz depressions, and the 92 GHz response drops much stronger still. Figure 5 displays two cases of convective precipitation observed on different days. The response of the 92 GHz frequency is roughly the same in each case, but the magnitude of the 18 GHz depression varies greatly from one case to another. This suggests two possibilities. One is the 18 and 92 GHz frequencies are responding to an ice layer so dense that their altitudes of response are significantly overlapping and a difference in particle size between storms is being observed. Another, more probable possibility is that the different channels are responding to quite different altitudes so that the 18 GHz channel is sensitive to ice size and/or number density differences at a level deeper than the 92 GHz channel can see. Unfortunately, radar data were not available to investigate these storms together. Nevertheless, the hope does exist that the dissimilarities in response between frequencies may someday be able to provide information concerning the vertical structure of precipitation within a storm. This approach would be similar to, but admittedly more complex and uncertain than, the method used to perform temperature soundings today.

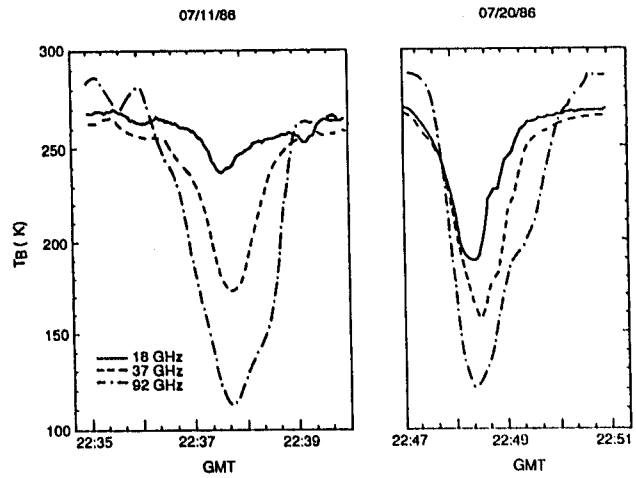

Fig. 5. COHMEX examples of 18, 37, and 92 GHz T_B responses to convective precipitation. Note the similar 92 GHz T_B depressions in relation to the dissimilar 18 GHz signatures.

Finally, a third feature of the COHMEX time series data is the opportunity to assign an approximate height to the scattering events assuming the 37 and 92 GHz channels are viewing features at roughly the same height. As seen in Fig. 3, the viewing geometries of the two instruments are such that a surface feature observed by the AMMS will lag the MPR observation of the same feature. This lag is about 100 seconds for a surface feature and around 50 seconds for a feature at a 10 km height (half way between the ground and the ER-2 flight level). For plotting purposes, all AMMS data were shifted forward in time by 1 minute which roughly lines up the 37 and 92 GHz T_B depressions for a scattering feature located 8 km above the surface. The height of a scattering event was then estimated by attributing each additional 20 second time separation between the 37 and 92 GHz depressions to a 4 km height shift above or below the 8 km height level. Using this method, the overall height range of all the scattering events from nine COHMEX days was found to be between 4 and 11 km. Yet since the 37 GHz response will actually be from a lower level than the 92 GHz response, these altitude assignments will have a low bias.

4. COMPARISON WITH CP-2 RADAR RAIN RATES

A comparison of CP-2 radar-derived rainfall rates to the AMMS and MPR radiometric responses was performed for data collected on 11 July 1986 between 21:53 and 21:57 GMT. However, defining the height within the storm to obtain a radar rain rate for this comparison was not an obvious procedure. Surface rainfall rates are important products to be eventually derived from satellite data, but a precipitation rate derived from the upper levels of the storm would better characterize the processes affecting the radiometric responses. For this study a weighted path-averaged precipitation rate was used based upon assumed phase and particle size distributions applied to the CP-2 10 cm reflectivity measurements.

This quantity was computed by first assuming a Marshall-Palmer size distribution within the storm which consisted of only water spheres below 4 km, only ice spheres above 8 km, and a linear combination of the two between 4 and 8 km. The Marshall, et al. (1955) relationship between radar reflectivity (Z) and rain rate (R):

$$Z = 200R^{1.6}$$

(where Z is in $mm^6\ m^{-3}$ and R is in $mm\ h^{-1}$) was adjusted for the presence of ice above the freezing level. The original

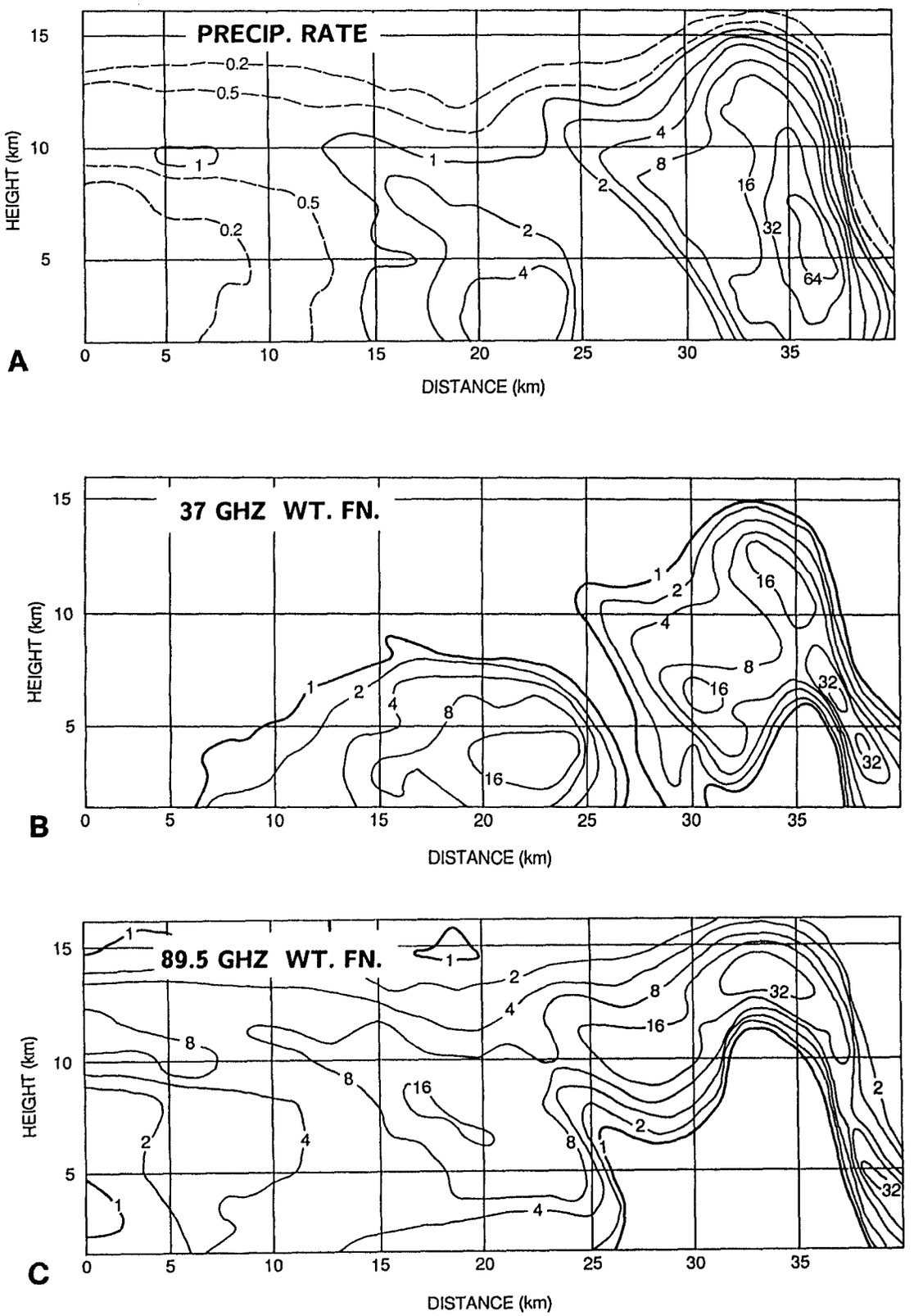

Fig. 6. Vertical cross sections of (a) radar-derived precipitation rates (mm h^{-1}), (b) 37 GHz weighting function (km^{-1}), and (c) 89.5 GHz weighting function (km^{-1}) along the flight track at a nadir viewing angle on 11 July 1986 between 21:53 and 21:57 GMT. The vertical axis represents height in kilometers above the surface starting at 1.5 km. The horizontal axis represents relative distance in kilometers. (1 horizontal kilometer = 5 seconds of aircraft flight time)

CP-2 radar reflectivities considered only the liquid phase, but were modified for this work to account for the combined influence of ice and liquid hydrometeors. The adjusted CP-2 10 cm reflectivities were then used to derive a vertical distribution of precipitation rate. This modification to account for the effect of ice increases the radar derived precipitation rates by a factor of 2.7 for heights above 8 km, and by a smaller factor between 4 and 8 km. A vertical cross section of radar-derived precipitation rates along the flight track of the aircraft for a nadir viewing angle may be seen in Fig. 6a. Both a weak and a strong area of convection are distinguishable.

Next the radar-derived precipitation rates were used to obtain a vertical distribution of volume extinction coefficient. For ease of computation the parameterizations relating rain rate to extinction coefficient calculated by Savage (1976) using Mie theory were employed for water spheres at -10°C and ice spheres at 0°C. Although the Savage parameterizations consider 19.35 and 89.5 GHz instead of 18 and 92 GHz, the slight difference in frequencies results in only small differences in extinction coefficients. Deviations from the assumed temperatures will have only a very small effect. Weighting functions were then calculated using the extinction coefficients and the following expression:

$$w = k_p(z) * \exp[- \int_z^{20km} k_p(z')dz'/\cos \Theta]$$

where w is the weighting function (km^{-1}), $k_p(z)$ is the extinction coefficient (km^{-1}) at height z (km) and Θ represents viewing angle. Figures 6b and 6c show the vertical cross sections of weighting function for 37 and 89.5 GHz, respectively, along the flight track assuming a nadir viewing angle. These figures demonstrate the sensitivity of a higher frequency such as 92 GHz to upper levels of the convective activity. When the rain rate is very low then the 92 GHz channel will observe a thick layer, but as the precipitation rate increases, 92 GHz responds only to the upper levels. The 37 GHz channel, in comparison, responds to lower levels due to its smaller extinction coefficients (Fig. 1).

Finally, the weighting function values and rain rates at each level were multiplied together and divided by the total sum of the weighting function values for a given column, assuming a nadir viewing angle, to produce a weighted path-averaged precipitation rate. These precipitation rates along with the corresponding radiometric responses are displayed in Fig. 7. At this point, a comparison may only be made in a qualitative sense because the sensitivity to errors resulting from the assumptions made during this procedure have yet to be studied. The Marshall-Palmer distribution probably contains particles which are too large leading to weighting functions peaking too high in the storm. Also, the radar-derived precipitation rates might be too great. However, the peaks of weak and strong convection do appear to occur at about the same times in both the T_B and rain rate plots in Fig. 7. Both the 37 and the 89.5 GHz channels detect similar precipitation rate values for the weak convection which is relatively shallow and transparent. As for the intense convection, the 89.5 GHz channel does not sense deeply enough to respond to the greater precipitation rates the 37 GHz channel senses.

Despite the differences in sensitivity between 37 and 92 GHz suggested by the theory, a survey of all the 11 July radiometer measured storm core responses at 37 and 92 GHz (Fig. 8) reveals a high degree of correlation. Thus, either the two channels are observing significantly different heights and precipitation intensities that are highly correlated, or they are observing more nearly the same level and intensities, implying some error in our assumptions. Other case studies will hopefully shed light on this problem.

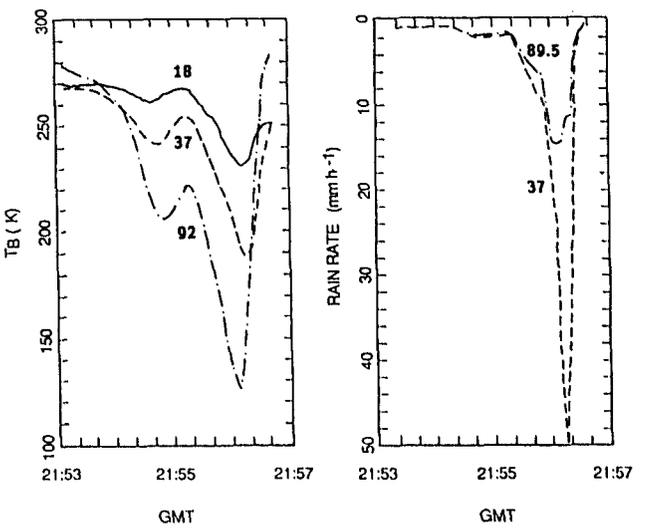

Fig. 7. 37 and 92 GHz T_B and 37 and 89.5 GHz weighted path-averaged rain rates on 11 July 1986 between 21:53 and 21:57 GMT.

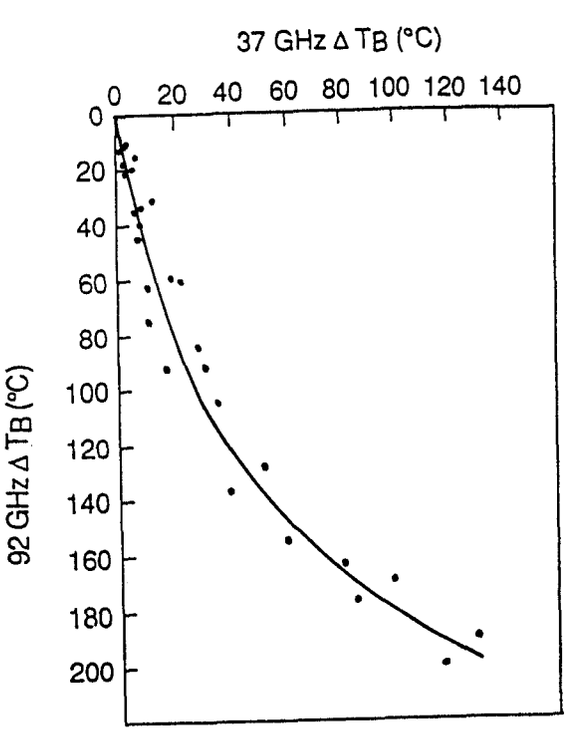

Fig. 8. Comparison of 37 and 92 GHz convective core T_B depressions for COHMEX 11 July 1986 data.

5. IMPLICATIONS FOR SATELLITE RETRIEVALS

Analysis of the MPR and AMMS data from COHMEX have demonstrated several useful implications for future satellite retrievals. The 92 GHz frequency has been found to be very sensitive to low rain rates as long as the ice phase is present. This should also hold true for the 85 GHz channel of the SSM/I. The 37 GHz channel should provide better estimate of intense precipitation due to greater linearity of response than at the higher frequencies. However, a high correlation between 37 and 92 GHz during 11 July of COHMEX does suggest that there may be little independent information between these two channels and that the 92 GHz could provide a good indirect estimate of stronger precipitation. Also, the occasionally large dissimilarities between the 18 GHz responses compared to similar 92 GHz responses do offer hope for precipitation soundings, even though the method would be much more uncertain than temperature soundings due to sensitivity to changes in ice particle size and number density.

6. ACKNOWLEDGMENTS

This work was supported by the NASA Headquarters Mesoscale Processes Research Program. The authors are grateful to Dr. V.N. Bringi and Dr. J. Vivekanandan of Colorado State University for providing copies of the COHMEX CP-2 radar data. Appreciation is also extended to Carl Mohr and L. Jay Miller of NCAR for the development of the SPRINT/CEDRIC software used to process the radar data.

7. REFERENCES

Hakkarinen, I.M. and R.F. Adler, 1986: Precipitation estimation using passive microwave radiometry at 92 and 183 GHz. *Preprints Second Conf. on Satellite Meteorology/Remote Sensing and Applications*, Williamsburg, VA, Amer. Meteor. Soc., 237 - 242.

Marshall, J.S., Hitschfeld, W., and Gunn, K.L.S., 1955: Advances in radar weather. *Adv. Geophys.*, **2**, 1 - 56.

Marshall, J.S., and Palmer, W., 1948: The distribution of raindrops with size. *J. Meteor.*, **5**, 165 - 166.

Savage, R.C., 1976: the transfer of thermal microwaves through hydrometeors. Ph.D thesis, University of Wisconsin, 143 pp.

Spencer, R.W., 1986: A satellite passive 37-GHz scattering-based method for measuring oceanic rain rates. *J. Climate Appl. Meteor.*, **25**, 754 - 766.

Spencer, R.W., D.W. Martin, B.B. Hinton, and J.A. Weinman, 1983: Satellite microwave radiances correlated with radar rain rates over land. *Nature*, **304**, 141 - 143.

Wilheit, T.T., A.T.C. Chang, J.L. King, E.B. Rodgers, R.A. Nieman, B.M. Krupp, A.S. Milman, J.S. Stratigos, and H. Siddalingaiah, 1982: Microwave radiometric observations near 19.35, 92, and 183 GHz of Precipitation in tropical storm Cora. *J. Appl. Meteor.*, **21**, 1137 - 1145.

Wilheit, T.T., A.T.C. Chang, M.S.V. Rao, E.B. Rodgers and J.S. Theon, 1977: A satellite technique for quantitatively mapping rainfall rates over the oceans. *J. Appl. Meteor.*, **16**, 551 - 560.

Wu, R. and J.A. Weinman, 1984: Microwave Radiances from precipitation clouds containing aspherical ice, combined phase, and liquid hydrometeors., *J. Geophys. Res.*, **89**, 7170 - 7178.

Comparison of Weather Radar and Satellite-Based Passive Microwave Observations of Rainfall Over Land and Oceans

Ralph R. Ferraro
Research and Data Systems, Corporation
10300 Greenbelt Road
Lanham, MD 20706

John C. Alishouse
NOAA/NESDIS
Washington, DC 20233

Joseph V. Fiore
Research and Data Systems, Corporation

1. INTRODUCTION

The determination of global rainfall amount and areal extent is essential in scientific disciplines such as hydrology, climatology, and agriculture. Over land, the only continuous information comes from worldwide synoptic station reports and weather radar observations. However, the reliability of these records as well as their lack of global coverage make the determination of rainfall coverage and amount a very difficult task, especially on a real-time basis. Over the oceans, the task becomes extremely difficult since there is virtually no ground truth except from those few reports from ships and island stations. To meet this demand for global rainfall information, scientists have attempted to utilize the continuous measurements from satellites. The purpose of this study is to develop algorithms for the retrieval of rainrates over land and ocean via matchups between weather radar observations and coincident passive microwave measurements.

The advantage of a microwave technique as opposed to one based upon the visible and infrared (IR) is that the microwave measurements respond directly to the column of rain, while the visible and IR can only indirectly determine the presence and intensity of rain. The present disadvantages of microwave techniques are the poor spatial resolution (25 km versus 1 km) and lack of global coverage. Future technology will undoubtedly improve the resolution of the microwave instruments and future satellite missions will provide near global coverage. For example, the recently launched (June 1987) Special Sensor Microwave Imager (SSM/I) with its 1392-km swath width and near sun-synchronous polar orbit can provide twice daily coverage over a large portion of the Earth.

2. BACKGROUND

Much work has ensued over the past several years in developing rainrate retrieval algorithms from passive microwave measurements. Aside from those investigations involving aircraft measurements, the majority of these studies have focused their attention on measurements from the Nimbus-5 and -6 Electrically Scanning Microwave Radiometer (ESMR) and from the Nimbus-7 Scanning Multichannel Microwave Radiometer (SMMR), the latter of which is used in this investigation.

2.1 Basic Microwave Theory

The ratio of the brightness temperature of a medium (TB) to its physical temperature (TS) is called the emissivity (ϵ) of the medium. Simply written, it is

$$\epsilon = TB/TS$$

The emissivity is a highly variable quantity and is primarily a function of the surface type, microwave frequency, view angle, and polarization. For a given surface type, second order variations of emissivity are caused by surface roughness and texture effects, thickness of the emitting medium, etc. Since many of these controlling variables are known when using passive microwave measurements (i.e., frequency, view angle, and polarization), much of the brightness temperature variations measured by satellite radiometers are due to changes in surface type and any perturbations within those surfaces.

2.2 The Microwave Response to Rain

The microwave response to rain is vastly different over land than over the oceans. Because of this, the retrieval of such information must be approached differently over these two surfaces.

2.2.1 Rain Over Land

Over land, the emissivity has a value very close to one over drier soils and vegetated land. The emissivity decreases as the soil moisture content increases and approaches that of open water for the barest and wettest soils. The primary effect of rain over land is to scatter the upwelling radiation since the rain droplets and ice particles in the rain layer are comparable to the wavelength of the microwave emission. This scattering effect increases with rain intensity and with observation frequency. However, due to the relatively small change in the TB caused by this scattering effect, the TB decreases associated with rain cannot be distinguished from TB variations due to varying surface conditions (i.e., soil moisture content, surface temperature variations, etc.) when looking at a single channel. One notable exception occurs in severe convective storms, as was first described by Spencer, et al (1983a). Here, the presence of highly scattering precipitation size ice particles can cause a significant decrease in the observed microwave temperatures at 37 GHz and lesser of a decrease at 18 GHz. In these instances, the heavy rain areas can easily be separated from the surrounding land.

Recent work by Grody (1984) and Ferraro, et al. (1986) have utilized a dual-channel approach to identify areas of rain over land. The former uses dual-polarization measurements at 37 GHz while the latter uses observations at 18 and 37 GHz. Both of these approaches are investigated in this study. Finally, quantitative relationships have been formulated by Spencer, et al. (1983b) and Spencer (1984) to retrieve SMMR derived rain rates with rather good success.

2.2.2 Rain Over the Ocean

Over the oceans, the identification of rain is much different than that over land since the background signature is that of the radiometrically cold ocean surface (i.e., low emissivity of water). The presence of clouds (i.e., water vapor and cloud liquid water) tend to obscure the ocean surface beneath it, causing a greater re-emission at cloud height. Clouds producing precipitation tend to contain more liquid water than those that do not produce rain, and thus, emit at an even warmer TB. The presence of precipitation also reduces the polarization (vertical TB minus the horizontal TB at a given frequency). As the rain rate increases, the rain layer will act as a scattering medium, reducing the TB. The rain rate where the TB saturates is inversely proportional to the frequency.

One problem which has been observed when developing oceanic rainrate retrieval algorithms from microwave radiometers is related to the fraction of the radiometer field of view (FOV) filled with rain. This phenomenon, commonly referred to as "beam filling", arises since the radiometer FOV is generally less than 100% covered by rain cells (the SMMR 37 GHz FOV is on the order of 400 km^2). This effect worsens as the observation frequency decreases (i.e., FOV increases). However, it is believed that passive microwave measurements still respond to a FOV average rainrate. Investigations correlating SMMR measurements with coastal radar observations have been performed by Spencer, et al. (1983c), Spencer (1986), and Ferraro, et al. (1987).

3. DATA SOURCES

The source of microwave data comes from the Scanning Multichannel Microwave Radiometer (SMMR) aboard the Nimbus-7 satellite. The SMMR has been observing earth emitted radiation at five frequencies (6.6, 10.7, 18, 21, and 37 GHz) and dual-polarization since launch in November 1978 and at this writing, is still in limited operation. As such, an invaluable data set of nearly nine years is available. More details about SMMR are presented by Gloersen and Barath (1977). In this study, we focus our attention on the dual-polarization measurements at 18 and 37 GHz, which have approximate footprints of 50 and 25 km, respectively.

Over land, data in the form of Manually Digitized Radar (MDR) were used as a measure of rain rate to match-up with nearly coincident SMMR measurements. The MDR data give the maximum reflectivity value which occurred within a 40 km grid cell across the WSR-57 radar network operated by the National Weather Service (NOAA, 1980). Six different Digital Video Integrator and Processing (DVIP) levels are designated based upon a Z-R relationship and are summarized in Table 1. The MDR gridding procedure will place the maximum VIP level in a cell regardless of areal extent. The only exception is for VIP level 1, which requires that the 40 km cell be at least 20% covered. This gridding method, although it identifies the areas of maximum precipitation, does not give any FOV coverage information. This makes a comparison with SMMR a difficult task since the FOV is highly sensitive to the areal coverage of rain. However, the availability of the MDR data in computer-compatible tapes made it a logical choice for our initial investigations.

Over the oceans, we have focused our attention on data in the form of Radar Data Processor-2 (RADAP-2). The RADAP-2 automatically digitizes radar data using a minicomputer (Nova-1200) located at selected NWS WSR-57 radar sites. RADAP-2 was designed as an interim radar data processor until the implementation of the Next Generation Weather Radar (NEXRAD). Archived RADAP-2 data are available from

the Techniques Development Laboratory (TDL) of the NWS from spring 1985 to summer 1986. The characteristics of the RADAP-2 data include two degree azimuthal spacing by 1 nautical mile (nm) range bins (from 11 nm to 125 nm). The first 10 nm of the data are not archived due to ground clutter present at close ranges. The scans are taken every 10 minutes and include information on scan time and date, radar elevation angle, and DVIP values (see Table 1). In addition, complete scan sequences (from 0.5 to 16.0 degree elevation angle in two degree increments) are included in the archive when available. The three major advantages of the RADAP-2 over the MDR is the increased spatial resolution, 15 versus 6 DVIP levels, and routine quality control.

Table 1. Values of reflectivity and rainfall rate for MDR and RADAP-2 reflectivity intensity categories.

RADAP-2 DVIP Value	MDR DVIP Value	Operational Threshold dbz	Mid-Point Rainrate (mm/hr)	
1	1	18.5	2.0*	1.0**
2		24.5	4.1	2.0
3	2	29.5	9.9	4.3
4		35.5	17.0	7.6
5		38.5	24.6	11.2
6	3	40.5	33.5	15.0
7		42.5	39.9	17.8
8		43.5	49.3	22.1
9	4	45.5	66.8	30.0
10		47.5	85.3	38.1
11		49.0	104.4	46.7
12	5	50.5	143.3	64.0
13		53.0	199.6	89.2
14		55.0	199.6+	115.6
15	6	56.5	199.6+	>127.0

* Based upon $Z = 55\ R^{1.6}$
**Based upon $Z = 200\ R^{1.6}$
+ Lower values used to minimize effects of hail.

4. METHODOLOGY

Case studies where the SMMR instrument made measurements over areas of rain were examined. Since the SMMR instrument operates on an alternate day duty cycle, overpasses an area at local noon and local midnight, and has a swath width of 822 km, many potential cases were identified but could not be matched with the radar data because one of these three factors contributed to missing the rain region. For the rain over land investigation, we chose the central United States as a test site due to its rather homogeneous terrain. We matched SMMR observations at 18 and 37 GHz (dual-polarization) with the MDR data for case studies during 1979 and gridded all the data to a common projection. A grid cell size of approximately 25 km was used for the MDR and SMMR 37 GHz data, while a cell size of 50 km was used for the 18 GHz observations. When comparing the 18 GHz, 37 GHz, and MDR data, the higher resolution data were spatially averaged to match the 18 GHz cell size.

For the rain over oceans investigation, we matched the SMMR 37 GHz and RADAP-2 data from Tampa Bay, Florida in a similar manner. At the present time, RADAP-2 data from Tampa Bay, Florida are only available for July, August, and September 1985. Tampa Bay is the only coastal RADAP-2 site. Due to the limited range of the radar (125 nm in all directions) and the SMMR instrument characteristics previously mentioned, we were extremely limited to the number of SMMR and RADAP-2 matchups. However, due to the high spatial resolution of these data, we were able to compute the average DVIP values and the percentage of the grid cell covered by rain at the SMMR 37 GHz footprint size.

The analyses were initially performed on an image processing system where the colocated data were examined via interactive analysis. The data were then transferred to a mainframe computer where the statistical analysis was performed.

5. RESULTS

The approach taken in the analysis was to find a relationship between radar reflectivity (i.e., DVIP levels) and SMMR brightness temperatures. No attempt was made to convert the DVIP values to rain rate due to the uncertainties in Z-R relationships with varying rain events.

5.1 Rain over Land

SMMR and MDR matchups from eight descending Nimbus-7 orbits over the central United States were obtained during 1979. The time between SMMR and MDR observations was at worst 30 minutes. The cases selected included a wide range of synoptic weather situations ranging from widespread stratiform rains to severe convective storms. Coincident 11.5 micron Nimbus-7 Temperature and Humidity IR Radiometer (THIR) observations were used to categorize the storms and to screen the data used in the analysis. Any SMMR observation where the 11.5 micron TB was greater than 273 K was removed from the data set. This assured us of being over a potential precipitation producing cloud and helped to remove some of the possible SMMR/MDR temporal matchup problems. Table 2 summarizes each of the case studies.

The initial analysis of the SMMR/MDR matchups was very disappointing. Tremendous scatter was evident in the data, as there was a wide range in TB for each DVIP value. We attributed this to the beam-filling problem and the fact that the MDR data has no areal coverage requirements (except DVIP 1); it simply indicates the most intense reflectivity within each cell. In order to overcome

Table 2. Characteristics of the 1979 SMMR/MDR rain over land data set

Date	SMMR Time (GMT)	Storm Type	No. of 25 km Points	No. of 50 km Points
1/20	0620	S	314	77
2/5	0615	S	274	75
4/4	0610	S	105	28
5/4	0645	SV	169	44
5/10	0655	C	89	26
7/5	0705	C	181	55
7/9	0635	SV	317	77
7/15	0645	SV	209	52

S = Stratiform
C = Convection
SV = Severe Convection

this problem, all of the SMMR measurements were binned by DVIP level. These mean TB's then represent the "average" microwave response to DVIP level at the "average" FOV coverage (still an unknown).

As was previously mentioned, dual-channel techniques have shown promise in identifying precipitation. We have chosen two commonly used parameters, namely the polarization ratio (PR) and the gradient ratio (GR), defined here as:

$$PR = \frac{TB(37V) - TB(37H)}{TB(37V) + TB(37H)}$$

$$GR = \frac{TB^*(18) - TB^*(37)}{TB^*(18) + TB^*(37)}$$

where $TB^*(i) = 0.5(TB(iV) + TB(iH))$

Figures 1 and 2 show the PR and GR as a function of DVIP level. Breakdowns by season are also indicated. In theory, the PR should increase over a given region with the presence of rain. However, the polarization is highly sensitive to soil moisture and vegetation. Note how the PR is much greater in winter than in summer at low DVIP levels, most likely due to the lack of vegetation. From the results shown in Figure 1, it appears that on the average, the PR is responding to rain somewhere between DVIP levels 2 and 3.

In Figure 2, the GR shows an increase in value with DVIP level. Again, a jump from DVIP 2 to DVIP 3 is seen. Also, the change from a negative GR to a positive GR is a strong indicator of rain, as scattering is being detected by the SMMR measurements. The differences between winter and summer are probably due to vegetative effects and precipitation intensities (i.e., stratiform vs. convective).

Although the results presented in Figures 1 and 2 are not very conclusive, examination of color-enhanced imagery (to be presented during the oral presentation) of the original SMMR TB's compared to the GR and PR qualitatively show the success in using these algorithms.

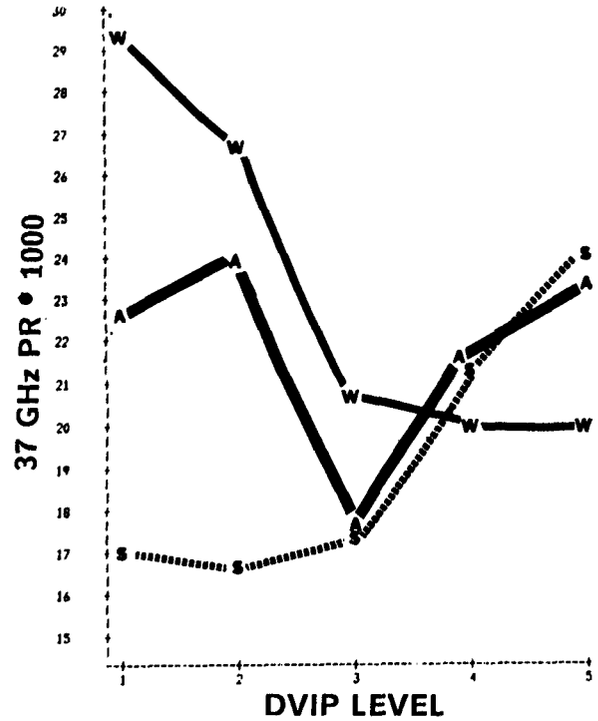

Figure 1. Plot of the 37 GHz polarization ratio (times 1000) as a function of the MDR DVIP level. Also shown are the values for winter (W), summer (S), and all (A) cases.

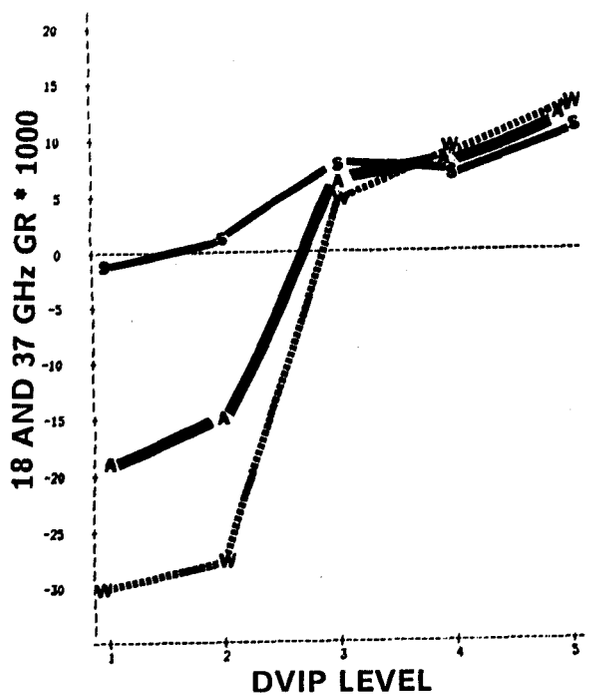

Figure 2. Plot of the 18 and 37 GHz gradient ratio (times 1000) as a function of MDR DVIP level and season.

5.2 Rain over Ocean

Again, the approach taken was to derive a relationship between DVIP level and SMMR measurements. However, due to the very high spatial resolution of the RADAP-2 data, the SMMR FOV coverage was computed and 15 DVIP levels were available to compute a mean DVIP level for each grid cell. On the average about 40 RADAP-2 observations fell within one SMMR FOV.

At the time of this writing, we were only able to find three worthwhile matchups between the SMMR and RADAP-2 during the summer of 1985. These are summarized in Table 3.

Table 3. Characteristics of the 1985 SMMR/Tampa Bay RADAP-2 rain over oceans data set

Date	SMMR Time (GMT)	RADAP-2 Time (GMT)	Storm Type	No. of 25 km Points
8/4	0544	0548	Convection	32
8/10	0545	0548	Convection	15
9/1	1656	1610	Hurricane Elena	65

The RADAP-2 and SMMR observations were within 2 minutes of each other for the two August cases. Unfortunately, the nearest RADAP-2 data for Hurricane Elena was approximately 45 minutes after the SMMR observations. Despite the large time mismatch, we still included some of this data in the analysis since the two August cases had predominantly low DVIP values while Elena had many DVIP values greater than 10. Average DVIP values less than two were omitted from the Elena case to account for temporal mismatches in the data.

Several linear regression models were fit between the SMMR 37 GHz TB, FOV and RADAP-2 data. These are summarized in Table 4. It should be noted that the DVIP values of 0-15 were multiplied by 10 and then averaged over the SMMR FOV, yielding possible values of 0 to 150. These were used in the regressions.

Table 4. Regression models, correlation coefficient (R), and explained variance (R^2) for the SMMR/RADAP-2 rain over oceans analysis

Model	R	R^2
(1) DVIP = a T37H + b	0.47	0.22
(2) DVIP = a T37V + b	0.47	0.22
(3) DVIP = a ΔT + b	0.45	0.20
(4) DVIP = a $\bar{T}$ + b ΔT + c	0.46	0.22
(5) FOV = a T37H + b	0.72	0.52
(6) FOV = a T37V + b	0.70	0.49
(7) FOV = a ΔT + b	0.72	0.52
(8) FOV = a $\bar{T}$ + b ΔT + c	0.72	0.52
(9) DVIP = a FOV + b	0.76	0.57

ΔT = T37V - T37H
$\bar{T}$ = (T37V + T37H)/2

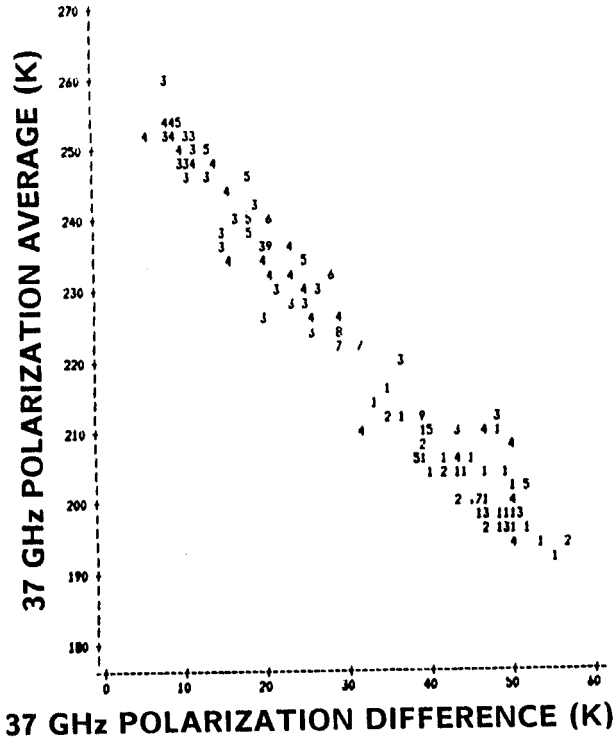

Figure 3. VIP value as a function of the 37 GHz polarization average and difference. The values plotted represent average VIP values times 10 in the following ranges: 1 = 1-10, 2 = 11-20, ..., 9 = 81-90.

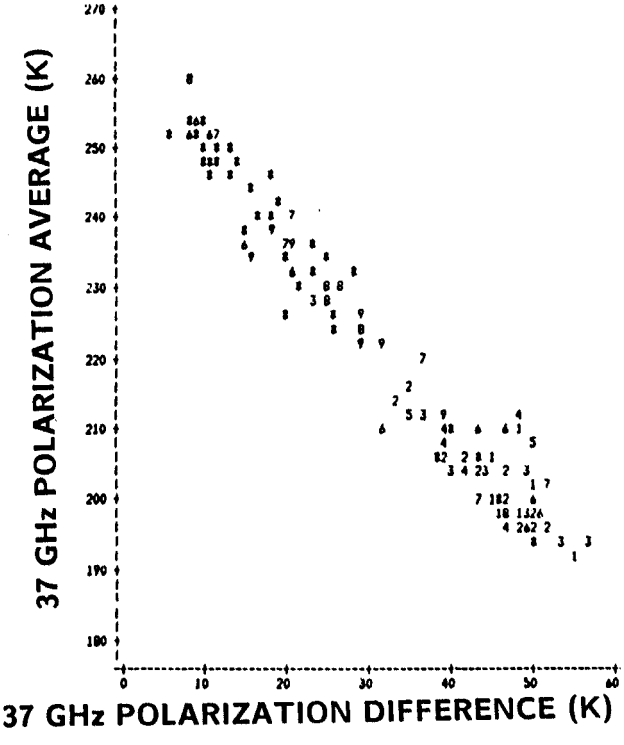

Figure 4. As in Figure 3, but for the percentage of the SMMR FOV covered by rain. The values plotted represent the FOV coverage in the following ranges: 1 = 1-10%, 2 = 11-20%, ..., * = 90-100%.

Figures 3 and 4 show plots of the data used in models 4 and 8, respectively. Several interesting features are indicated in the regression results. In general, all the different predictors perform the same. The most significant result is that the FOV percentage correlates better with SMMR 37 GHz measurements than the actual DVIP value. However, we are cautiously optimistic of this result since our sample size was rather small (112 observations). Also, it may be more appropriate to perform a logorithmic average of DVIP value over the SMMR FOV rather than a straight linear average. Further case study matchups are needed to further assess these models.

One final point to note is the correlation between DVIP and FOV percent covered by rain (Model 9). The fact that the DVIP value increases as FOV coverage increases is not surprising. However, if in fact nature is as variable as this relationship indicates (~57% variance explained), then the relationships found between SMMR, FOV coverage, and DVIP value should not be expected to perform better than this value.

6. SUMMARY

In our investigation, we have examined the passive microwave response to rain over land and ocean. Near-coincident weather radar data (MDR over land; RADAP-2 over ocean) was colocated with the 18 and 37 GHz dual-polarization measurements from the Nimbus-7 SMMR. The test sites were the central United States and the coastal waters off Tampa Bay, FL.

Although the usefulness of the MDR data was somewhat limited in the rain over land investigation (i.e., no areal coverage information), it appears that the SMMR measurements at 18 and 37 GHz can detect the presence of rain somewhere between DVIP levels 2 and 3. It also appears that the use of dual-frequency measurements at 18 and 37 GHz performs better than the dual-polarization measurements at 37 GHz.

The rain over the oceans study was much more successful due to the use of the higher resolution and quality RADAP-2 data. Despite only a very small data set, we found linear relationships between the RADAP-2 DVIP values and the SMMR 37 GHz data. In addition, we found that the percent of SMMR FOV covered by rain was more strongly correlated to the SMMR measurements.

We plan to continue the investigations over the oceans by obtaining more RADAP-2/SMMR matchups. In addition, we plan to perform similar studies using RADAP-2 data from Oklahoma City, OK. This should improve our results over land. Finally, SSM/I data will be obtained and the usefulness of the 85 GHz channel will be investigated.

7. REFERENCES

Ferraro, R. R., N. C. Grody, and J. A. Kogut, 1986: Classification of Geophysical Parameters Using Passive Microwave Satellite Measurements. IEEE Trans. Geosci. Remote Sensing, GE-24, 1008-1013.

Ferraro, R. R., J. C. Alishouse, N. C. Grody, and J. D. Tarpley, 1987: Observations of Surface and Atmospheric Features from Passive Microwave Satellite Measurements. In Volume I Proceedings of the ASPRS/ACSM Annual Convention, Baltimore, MD, 166-175.

Gloersen, P., and F. Barath, 1977: A Scanning Multichannel Microwave Radiometer for Nimbus-7 and Seasat-A. IEEE J. Oceanic Eng., OE-2, 172-178.

Grody, N. C., 1984: Precipitation Monitoring Over Land from Satellites Using Microwave Radiometry. In Proceedings of the International Geoscience and Remote Sensing Symposium (IGARSS '84), Strasbourg, France, 417-423.

NOAA, 1980: National Weather Service Radar Code User's Guide. Department of Commerce, NOAA, Silver Spring, MD, 179 pp.

Spencer, R. W., W. S. Olson, W. Rongzhang, D. Martin, J. A. Weinman, and D. A. Santek, 1983a: Heavy Thunderstorms Observed Over Land by the Nimbus-7 Scanning Multichannel Microwave Radiometer. J. Climate Appl. Meteor., 22, 1041-1046.

Spencer, R. W., D. W. Martin, B. B. Hinton, and J. A. Weinman, 1983b: Satellite Microwave Radiances Correlated with Rain Rates over Land. Nature, 304, 141-143.

Spencer, R. W., B. B. Hinton, and W. S. Olson, 1983c: Nimbus-7 37 GHz Radiances Correlated with Radar Rain Rates over the Gulf of Mexico. J. Climate and Appl. Meteor., 22, 2095-2099.

Spencer, R. W., 1984: Satellite Passive Microwave Rain Rate Measurement over Croplands during Spring, Summer, and Fall. J. Climate Appl. Meteor., 23, 1553-1562.

Spencer, R. W., 1986: A Satellite Passive 37 GHz Scattering-Based Method for Measuring Oceanic Rain Rates. J. Climate Appl. Meteor., 25, 754-766.

7.5

A PILOT STUDY TO DETERMINE RELATIONSHIPS BETWEEN NORTH PACIFIC PRECIPITATION FROM NIMBUS-7 SCANNING MULTICHANNEL MICROWAVE RADIOMETER DATA AND ASSOCIATED ATMOSPHERIC CONDITIONS

Mark R. Anderson

Climatology Program, Dept. of Geography
University of Nebraska
Lincoln, NE 68588-0135

John O. Roads

Climate Group
Scripps Institution of Oceanography
University of California, San Diego
La Jolla, CA 92093

1. INTRODUCTION

The frequency and distribution of winter precipitation over the west coast can be related to the eastward moving mid-latitude storms which form and move over the western and central North Pacific Ocean. These storm tracks and associated precipitation are generally directed by large-scale atmospheric circulation (e.g Klein, 1965; Namais 1979; and Cayan and Roads, 1984).

In the past, determining the climatological position of the storm tracks in the North Pacific Ocean has been accomplished by examining, analyzing and comparing daily surface pressure charts (e.g. Klein, 1956; Petterssen, 1956 and more recently Zishka and Smith, 1980; Wittaker and Horn, 1981; 1984). Remote sensing techniques using visible and infrared images have also been generated to better pin down the cyclone development and movement (e.g. Streten and Troup, 1973; Carleton, 1982). Passive microwave data have also been associated with the position of cold fronts (McMurdie and Katsaros, 1985).

The major reason for the interest in the cyclone tracks is that they provide information about precipitation and the large scale atmospheric field. This paper uses a reversed approached, that is, by determining precipitation areas, relationships with the large scale field and the location of cyclone tracks can be determined. This is accomplished by deriving precipitation locations from the NIMBUS-7 Scanning Multichannel Microwave Radiometer (SMMR) data for two winter seasons, December 1978 thru February 1979 and 1979-1980. These locations are then compared to the large scale atmospheric conditions. Understanding the relationships between precipitation and cyclone tracks could then help improve both short and long term forecasts.

2. DATA

The precipitation locations are obtained by the Katsaros and Lewis (1986) experimental algorithm which uses a linear interpretation of the 37 GHz vertically polarized brightness temperature. Other precipitation algorithms (Wilheit and Chang, 1980; and Spencer, 1986) also produce similar regions, however the rainrates differed. The Spencer algorithm, developed for convective processes, calculates the largest rainrates, between 14 and 35 mm/hr for the test case, while the Katsaros and Lewis algorithm, developed for precipitation along the west coast, calculates rainrates between 1.0 and 12 mm/hr. The Wilheit and Chang algorithm produced similar results to the Katsaros and Lewis algorithm.

To produce daily precipitation locations, the orbital 30 km resolution SMMR CELL-ALL data are obtained for the 37 GHz channel and rainrates are calculated. Each pixel with a rainrate of at least 1 mm/hr is then binned into a 0.5 latitude by 0.5 longitude grid. This is produced for the alternating days of the SMMR data for the two winter seasons studied. An example of the daily coverage is given in figure 1, illustrating the poor spatial resolution of the SMMR data.

Once the daily locations are determined, five day composites (three data days and two non-data days) were produced by summing the number of observations for the period. Using five day composites, complete coverage is obtained for the study area (figure 2a and 2b). Monthly composites are then produced from five day composites in the same manner (figures 3 and 4). 1000 mb height fields were obtained from the German Weather Service archives of the twice daily T 15 spherical harmonic analyses by Speth and Kirk (1981). These data were made

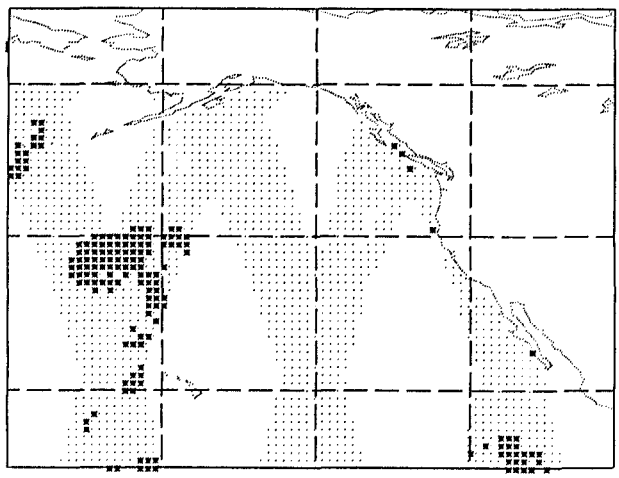

Figure 1. Precipitation locations derived from SMMR data, asterisks, for December 8, 1979. The daily coverage is represented by the small dots.

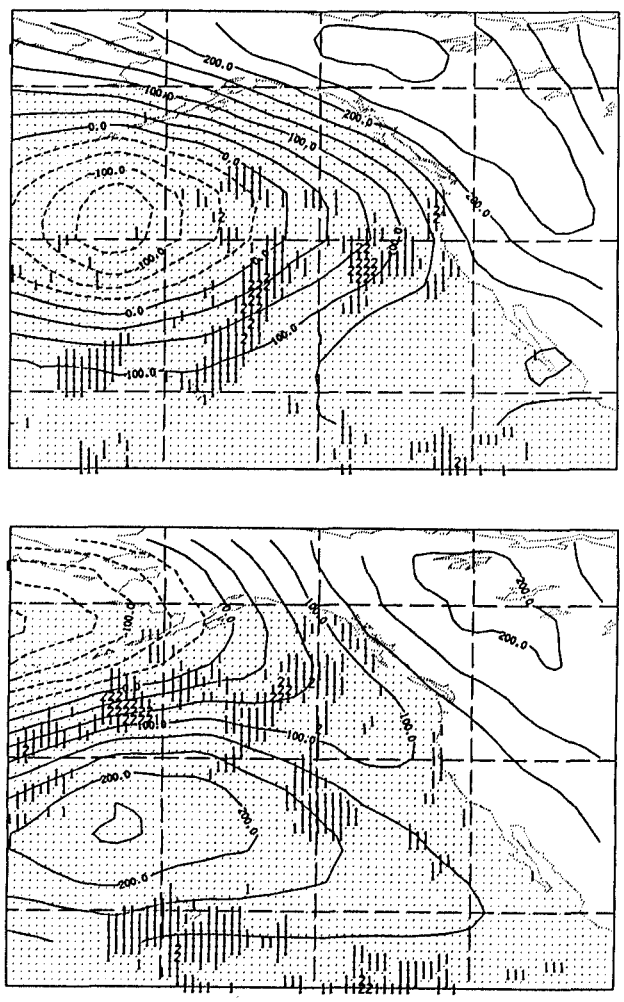

Figure 2. Five day composites of the SMMR-derived precipitation locations and the corresponding 1000 mb height field for a) January 6-10, 1979 and b) January 12-16, 1979.

available by the Max Plank Institut fur Meteorologie. Storm track locations were collected from the Mariners Weather Log.

3. RESULTS

Initial comparisons are very promising for the 5 day and monthly results of precipitation locations and mean 1000 mb heights. For example, two contrasting 5 day periods, January 6-10, 1979 (figure 2a) and January 12-16, 1979 (figure 2b) show precipitation associated with southwesterly winds in advance of the low pressure system. These are thought to be regions of positive vorticity advection and moreover correspond well to coastal relations. In addition, a poleward shift in the location of the precipitation can be observed between the two periods.

The monthly analyses show strong differences between the two winter seasons. Comparing for example the December 1978 and 1979 cases (figures 3a and 4a), the area of intense precipitation during 1978 is found south of the Aleutian Islands well off the west coast with the mean position of the surface low in the Bering Sea. In contrast, 1979 shows the surface low much further eastward in the Gulf of Alaska and the region of precipitation has shifted southeastward into the west coast. In addition, the precipitation locations associated with the ITCZ are also shifted further to the south in December 1979.

The southward shift in the precipitation locations is also found during January 1980 (figure 4b) with the mean position of the 1000 mb low located 10 degress south of the Bering Sea compared to the mean positions in January 1979 (figure 3a). Cyclone tracks obtained from the Mariner's Weather Log and averaged over the two January periods (figure 5) also exhibit the shift. The precipitation locations showed similiar results for the two months in February (figures 3c and 4c).

In comparing the SMMR-derived precipitation locations to the mean cyclone tracks, the mean cyclone position is the approximate northern boundary of the precipitation locations. Therefore, as would be expected the precipitation locations can give an estimate of the mean position of the cyclone track.

4. SUMMARY

It has been shown that monthly precipitation positions in the North Pacific derived from passive microwave data can give an estimate of the cyclone position on a monthly time scale. A more comprehensive understanding of the relationships between precipitation and storm tracks using passive microwave data can be expected with further analysis with the complete SMMR data set (1978 through 1987). In addition, the successful launch of the DMSP SSM/I will produce a more complete spatial and

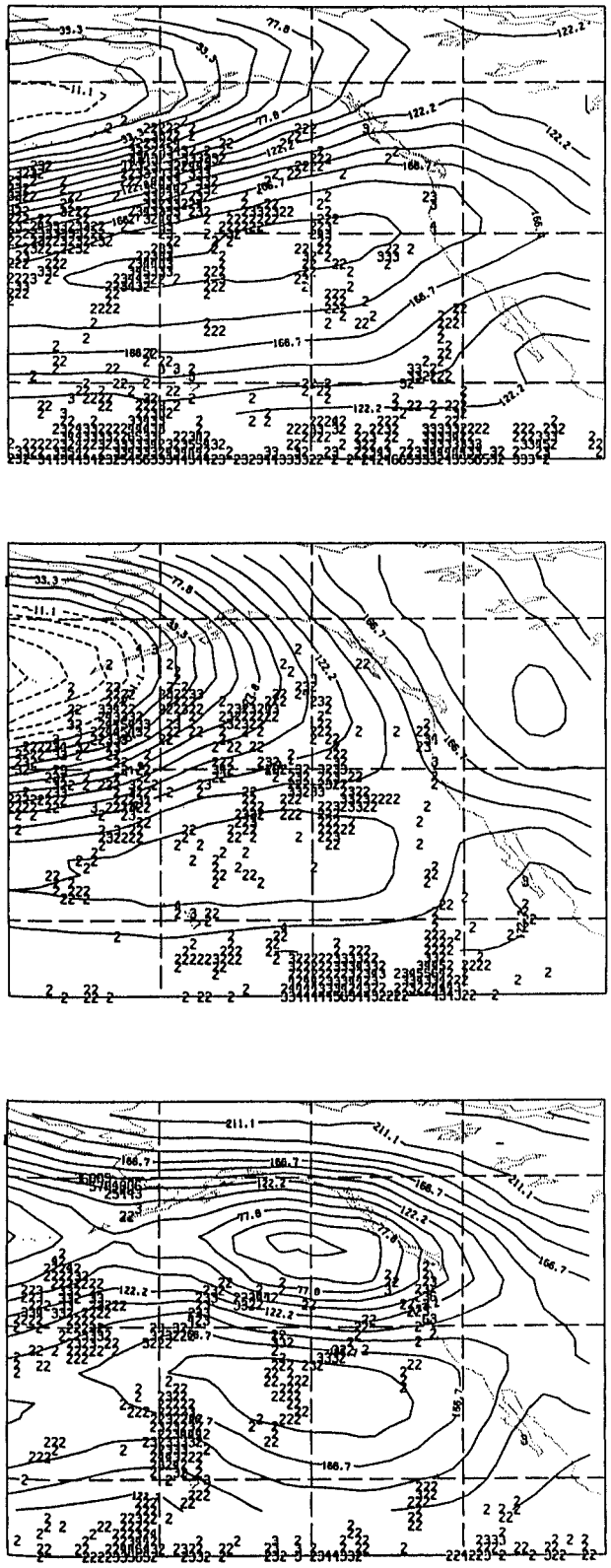

Figure 3. Monthly composites of the SMMR-derived precipitation locations and the corresponding 1000 mb height field for a) December 1978, b) January 1979 and February 1979.

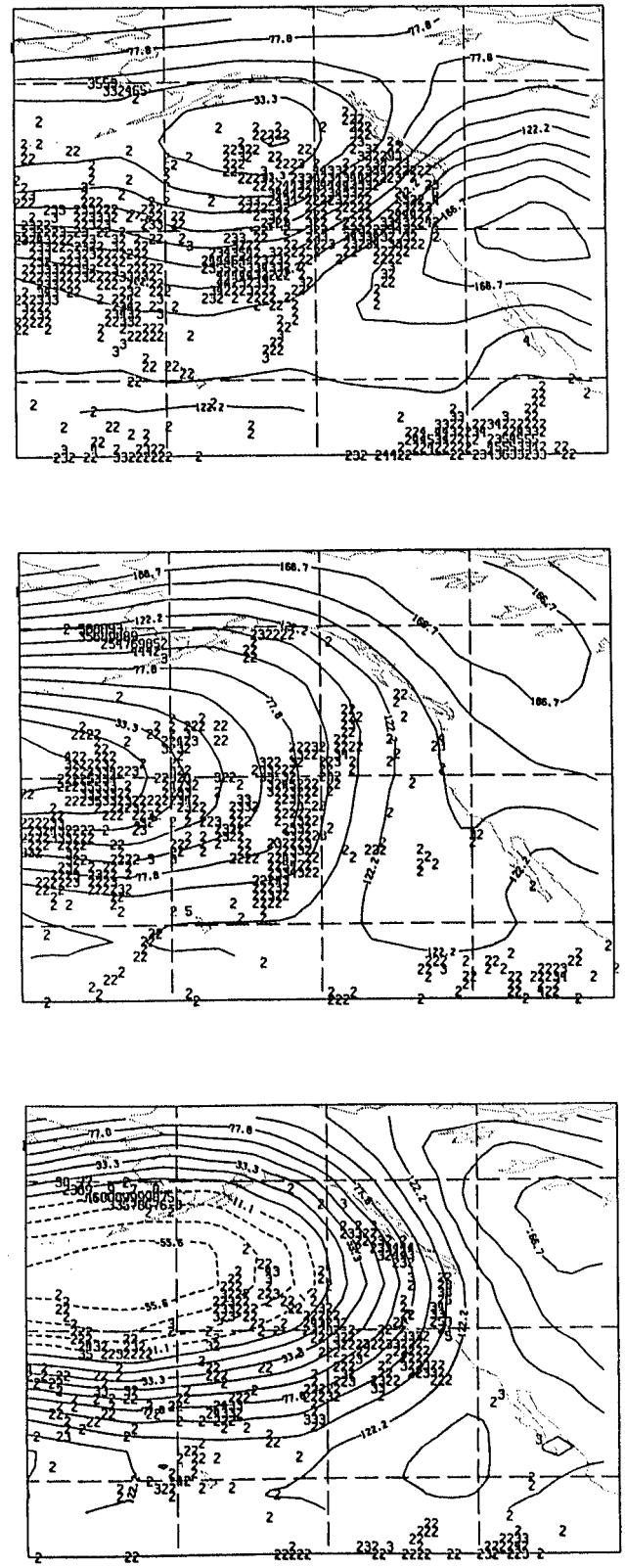

Figure 4. Monthly composites of the SMMR-derived precipitation locations and the corresponding 1000 mb height field for a) December 1979, b) January 1980 and February 1980.

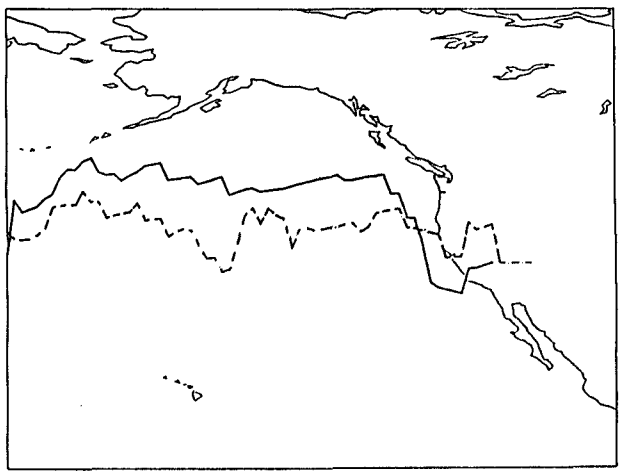

Figure 5. Average position of the cyclone tracks for January 1979 (solid line) and January 1980 (dashed line).

temporal coverage. The results presented here are preliminary and further work will continue to take place to quantify the location of the precipitation and the atmospheric conditions.

5. ACKNOWLEDGMENTS

This work was supported by the California Space Institute Mini-Grant Program and NASA grant NAG-236. The SMMR data were obtained from the National Space Science Data Center.

6. REFERENCES

Carleton, M.A. (1979): Monthly variability of satellite-observed extratropical cyclone activity for the Southern Hemisphere winter, J. of Climatology, 21-38

Cayan, D.R. and J.O. Roads (1984): Local relationships between United States West Coast precipitation and monthly mean circualtion parameters, Mon. Wea. Rev., 112, 1276-1282.

Katsaros, K.B. and R.M. Lewis (1986): Mesoscale and synoptic scale features of North Pacific weather systems observed with Scanning Multichannel Microwave Radiometer on Nimbus 7, J. Geophys. Rev., 91(C2), 2321-2330.

Klein, W.M. (1957): Principal tracks and mean frequencies of cyclones and anticyclones in the Northern Hemisphere, Res. Pap. No. 40, U.S. Weather Bureau, U.S. Government Printing Office, Washington D.C., 60 pp.

Klein, W.M. (1965): Application of synoptic climatology and short-range numerical prediction to five-day forecasting,Res. Pap. No 46, U.S. Weather Bureau, Washington D.C.20233, 109 pp.

McMurdie, L.A. and K.B. Katsaros (1985): Atmospheric water distribution in a midlatitude cyclone observed by Seasat Scanning Multichannel Microwave Radiometer, Mon. Wea. Rev., 113(4), 584-598.

Mariner's Weather Log (1973-1980): National Environmental Satellite Data Information Service, NOAA, Washington, D.C. 20235.

Namais, J., (1979): Premonitory signs of the 1978 break in the West Coast drought, Mon. Wea. Rev., 107, 1675-1681.

Petterssen, S (1956): Weather Analysis and Forecasting, Vol 1, 2nd ed., McGraw-Hill.

Spencer, R.W., B.B. Hinton and W.S. Olsen (1983): Nimbus-7 GHz radiances correlated with radar rain rates over the Gulf of Mexico, J. Clim. Appl. Met., 22(12), 2095-2099.

Speth, P. and E. Kirk (1981): Representation of meteorological fields by spatial harmonics., Meteor. Rundsch., 34, 5-10.

Streten, N.A. and A.J. Troup (1973): A synoptic climatology of satellite-observed cloud vortices over the Southern Hemisphere, Quart. J.R. Met. Soc., 99, 56-65.

Whittaker, L.M. and L.H.Horn (1981): Geographical and seasonal distribution of North American cyclogensis, 1957-1977,Mon. Wea. Rev., 109(11), 2312-2322.

Whittaker, L.M. and L.H. Horn (1984): Northern Hemisphere extra-tropical cyclone activity for four mid-season months, J. of Climatology, 4, 297-310.

Wilheit, T.T. and A.T.C. Chang (1980): An algorithm for retrieval of ocean surface and atmospheric parameters from observations of the Scanning Multichannel Microwave Radiometer, Radio Sci., 15(3), 525-544.

Zishka, K.M. and P.J. Smith (1980): The climatology of cyclones and anticyclones over North America and surrounding environs for January and July 1950-77, Mon. Wea. Rev., 108(4),387-401.

Precipitation Estimation Using Visible and Infrared Satellite and Surface Data

C.E. MOTELL AND C.H. WASH

Department of Meteorology
Naval Postgraduate School
Monterey, CA

1. Introduction

Visible and infrared data from Geostationary Operational Environmental Satellites (GOES) have been used frequently to estimate rainfall for periods ranging from 30 minutes to 24 hours (Atlas and Thiele, 1982).

Others have used the GOES data to obtain areal estimates of instantaneous rainfall (Lovejoy and Austin, 1979; Tsonis and Isaac, 1985). Further work has been performed to class instantaneous areal rainfall estimates by rainfall intensity and type: either convective or continuous (Tsonis, 1987; Lee, Chin and Martin, 1985).

The previously mentioned studies have concentrated on using radar data to provide "ground truth" for calibrating and verifying satellite estimates of instantaneous rainfall. However, rainfall estimates, made with schemes calibrated using radar data, may be invalid when extrapolated beyond the radar range (Lovejoy and Austin, 1979).

In this study, hourly weather reports from Service-A surface stations (SVC-A) are examined as an alternative to radar data in providing ground truth to synoptic scale satellite rainfall estimates. Reports from 137 stations located in the southeastern United States were examined for a 30 day period in August 1979 for a statistical relationship between GOES VIS and IR data. Emphasis is placed on examining statistical properties of the satellite data, and how these properties may be related to surface reports of (1) precipitation or no-precipitation during overcast and broken skies, (2) light or moderate-to-heavy precipitation, and (3) convective or continuous precipitation. The purpose of this analysis is to reveal which of the previously mentioned surface reported weather conditions may be identified in single image pairs. An application of the GOES data to precipitation and no-precipitation classification is also presented.

2. Data

The data used in this study consist of colocated GOES hourly digital data and SVC-A reports for August 1979 from stations located in southeastern United States. Only observations from 1200-2000 GMT were included to avoid distortion of the visual data due to low solar zenith angle.

The satellite measurements were obtained from the Visible and Infrared Spin Scan Radiometer (VISSR) mounted on the GOES-3 (GOES-East). The IR channel measurements (10.5-12.5 microns) have a nadar point resolution of ~7 km with 8 bit resolution of the intensity. The VIS channel measurements (0.55-0.75 microns) have a nadir point resolution of ~1 km with 6 bit intensity resolution. VIS measurements were averaged to 7 km resolution for consistency with the IR data.

The data set, prepared by the University of Wisconsin (UW), consists of 10x10 pixel matrices of hourly VIS and IR data centered over each of the 137 surface stations (Fig. 1). These matrices cover an area of 45 nmi x 45 nmi at 30°N (60 nmi x 60 nmi at 42°N). The matrices were earth-located to an accuracy of 1-2 km by the Man-computer Interactive Data Access System (McIDAS) at UW. Also available from the UW tape are the SVC-A hourly weather reports.

The VIS pixel elements were converted to "adjusted" albedos (A_0) using an algorithm by Muench and Keegan (1979) which corrects for varying zenith angle and anisotropic scattering as related to the zenith angle. The IR pixel elements were converted to brightness temperatures using the standard GOES IR calibration table.

Only pertinent information from the surface weather reports was retained. That is, a total of 70,623 colocated satellite and surface reports were examined, but only those reports indicating at least broken cloud cover or precipitation were used. The number of reports of each surface weather category used is given in Table 1.

Table 1. Definition of class types and number of observations for each class.

Class	SVC-A report	Reports
R	"R"[1]	538
ROVC	"R"/overcast skies	329
ROVCB	"R"/overcast-broken skies	534
RCONT	R-, R, R+[2]	112
RCONV	RW-, RW, RW+, TRW-,[3] TRW, TRW+, TR-, TR, TR+	426
RL	R-, RW-, TRW-, TR-	464
RMH	R, R+, RW, RW+, TRW, TRW+, TR, TR+	74
NROVC	R/overcast skies	1976
NROVCB	R/overcast-broken skies	7358

[1]"R" indicates any type of rain.
[2]The "R" codes "+" ," " or "-" indicate either heavy, moderate or light continuous rain, respectively.
[3]RW, TR, and TRW codes represent convective rain.

3. Satellite and Surface Rainfall Statistics

a. Methodology

In judging the sensitivity of the satellite data to surface weather, the data were first compared to surface reports of rain, including reports of rain/overcast skies (ROVC), rain/overcast and broken skies (ROVCB), and the no-rain/overcast class (NROVC).

The rain and no-rain/overcast statistical analysis that follows discusses in detail the parameters examined in this study. These parameters are then examined for usefulness in separating continuous rain (RCONT) from convective rain (RCONV), and light rain (RL) from moderate-to-heavy rain (RMH) classes.

The summer satellite data, consisting of the GOES 10 x 10 pixel matrices (hereafter referred to as 10^2 windows), from August 1979 were used to compare the rain and no-rain/overcast data sets.

The effect of data resolution in identifying weather categories was studied by varying the number of pixels per window. Additional window sizes of 8^2, 6^2 and 4^2 pixels, centered over the surface stations, were examined. Smaller windows were avoided due to relatively increasing navigation errors.

The preliminary statistical analysis consisted of the following procedures:

1) Examination of the frequency distributions of VIS and IR observations as a function of rain and overcast frequency.

2) Examination of the window statistics.

3) Examination of Co-spectral plots which indicate the ability of VIS and IR based window statistics to delineate rain occurrence, intensity and type.

b. Rain class data (P)

Fig. 3a shows the frequency of rain occurrences versus mean 10^2 window values of VIS (albedo) and IR derived brightness temperatures or simply temperatures. The data generally cluster in elliptical patterns which indicate some relationship between albedo/temperature measurements and rain.

The bivariate distribution presented in Fig. 3a appears roughly bimodal with a maximum located in the 250-260k and 0.5-0.6 temperature/albedo interval. Fig. 3b is identical to 2a but for the 4^2 window size. For the 2-3% relative frequency isopleths these figures and those for the 8^2 and 6^2 windows (not shown) show a discernible shift toward higher albedos and lower temperatures (colder cloud top temperatures), with decreasing window size.

A quantitative description of the data shown in Figs. 3a-3b is obtained by first calculating the arithmetic mean, w_k, of each VIS and IR window (ie, 10^2, 8^2, 6^2 or 4^2 pixel windows), and then calculating the mean w_k value by averaging over all 137 stations. This statistic is called the mean of the means (W) and is calculated by

$$W = N^{-1} \times \sum_{k=1}^{137} w_k \qquad (1)$$

Textural properties of the satellite images based on pixel to pixel intensity changes can also be quantified by calculating the mean of the standard deviations of each window. The mean of the standard deviations is referred to hereafter as the mean Window Spatial Deviation (WSD) statistic to emphasize its use in estimating the spatial variability of the data. Mean WSDs are calculated by

$$WSD = [N^{-1} \cdot SIZE^{-1} (\sum_{k=1}^{137} \sum_{i=1}^{size} (p_i - w_k)^2]^{1/2}, \qquad (2)$$

where p_i represents the ith pixel for the kth window, with i varying from 1 to the total window SIZE, i.e., 10^2, 8^2, 6^2, or 4^2. Values for W and WSD are given in Table 2 along with the standard deviation of W (W_s) and WSD (WSD_s).

Table 2. Window statistics from the Rain class data (both ROVC and ROVCB) for four window sizes. VIS units are in percent of adjusted albedo, and IR units are in degrees K.

window statistic	10^2	8^2	6^2	4^2
W (VIS)	0.579	0.591	0.603	0.614
W_S(VIS)	0.211	0.214	0.219	0.227
WSD(VIS)	0.173	0.161	0.144	0.124
WSD_S(VIS)	0.078	0.078	0.075	0.072
W(IR)	253.0	252.2	251.4	250.8
W_S(IR)	20.7	21.0	21.3	21.7
WSD(IR)	10.4	9.1	7.6	5.6
WSD_S(IR)	7.0	6.7	6.0	4.9

The standard deviations give only a qualitative estimate of the variability in the W and WSD statistics because the distributions of W and WSD are non-normal. Therefore, no statistical significance can be assigned from the standard deviation.

As seen in Figs. 3a-3b, mean albedos monotonically increase from 0.579 to 0.614, while mean temperatures decrease from 253.0K to 250.8K with decreasing window size. Both albedo and temperature spatial deviation monotonically decrease with decreasing size from 0.173 to 0.124 and 10.4K to 5.6K, respectively. Decreases in spatial deviation with window size are expected, since adjacent pixels should have similar characteristics. Also as the window size is decreased, the probability of dissimilar pixels is also decreased.

Because the means and spatial deviations either increase or decrease monotonically with size, it is sufficient to consider only the two extreme sizes: the 10^2 and 4^2 windows.

c. No-rain/overcast (NROVC) class

The frequency distribution of the no-rain/overcast observations (not shown) is shifted toward warmer, less reflective clouds relative to the rain data.

The mean and spatial deviation statistics for the no-rain/overcast reports are given in Table 3. The 8^2 and 6^2 window sizes statistics are also included.

Table 3. Same as in Table 2 but for no-rain/overcast (NROVC) data.

window statistic	10^2	8^2	6^2	4^2
W(VIS)	0.407	0.411	0.415	0.418
W_S(VIS)	0.205	0.208	0.213	0.219
WSD(VIS)	0.122	0.113	0.102	0.087
WSD_S(VIS)	0.056	0.054	0.052	0.049
W(IR)	272.6	272.5	272.4	272.3
W_S(IR)	17.8	18.1	18.3	18.6
WSD(IR)	5.4	4.7	3.9	2.9
WSD_S(IR)	4.8	4.4	3.9	3.1

Table 3 shows that the mean albedos increase from 0.407 to 0.418 while the temperatures values decrease from 272.6k to 272.3k, for the 10^2 and 4^2 windows, respectively. Although the absolute changes may appear trivial, it is significant that they are clearly monotonic.

d. Rain and no-rain comparison

The differences in the observed bivariate frequency distributions for the rain and no-rain/overcast classes suggest that the preceding statistics can be used to separate these two classes using only single image pairs of VIS and IR data.

Toward this end, co-spectral plots were used to subjectively evaluate the ability of the VIS and IR statistics to identify whether a particular satellite window observation is associated with precipitating or non-precipitating surface weather. Examples of co-

Toward this end, co-spectral plots were used to subjectively evaluate the ability of the VIS and IR statistics to identify whether a particular satellite window observation is associated with precipitating or non-precipitating surface weather. Examples of co-spectral plots are given for the mean statistic in Fig. 3c and for the spatial deviation statistic in Fig. 3d. In these plots, the mean value of a window statistic, either the mean of the means or the mean of the spatial deviations, is denoted by a closed circle and the variation by the width of the error bar containing the mean (here ±1 standard deviation). Co-spectral plots indicate the potential overlap between class spectral or statistical response and show which combination of spectral bands and/or statistics might be best for discrimination. Ideally, the bands with the least amount of overlap will be best for classifying rain and no-rain cloud systems.

From Figs. 3c and d the following observations are made concerning the statistics of the rain and no-rain/overcast data sets:

1) The temperature means (Fig. 3c) show slightly less overlapping of the two classes responses than do the albedo means.

2) The temperature spatial deviation statistics show slightly more separation than do the albedo spatial deviation statistics; and, in contrast to the mean statistics, there is slightly more separation of the no-rain data using the 10^2 window.

3) The degree of separation does not appear to be dependent on window size.

4) The spread of the rain spatial deviations is larger than the spread of the no-rain spatial deviations for both spectral bands.

The co-spectral plots for the rain and no-rain/overcast data show substantial overlapping in all spectral bands. This is not surprising given that the no-rain reports are included only when accompanied by overcast conditions. However, for both spectral bands the rain means are separated by approximately one standard deviation, suggesting that the possibility of successful discrimination via a linear or non-linear combination of VIS and IR statistics.

e. Comparison of rain classes

In addition to comparing SVC-A reports of rain versus no-rain/overcast, comparison are made of reports of convective (RCONT) versus continuous rain (RCONT), and light rain (RL) versus moderate-to-heavy rain (RMH) (see Table 1). This section summarizes the use of 10^2 window statistics in separating these classes.

1) CONVECTIVE (RCONV) VERSUS CONTINUOUS (RCONT) RAIN

The physical processes involved in convective rain, or showers, are different from those involved in continuous rain. These differences in the processes might result in a statistical separation between the two types of rain.

However, the co-spectral plot in Fig. 3e shows that there is almost complete overlapping of the mean albedo bands for the two rain classes, and only slightly more separation between mean temperature bands. Furthermore, the spatial deviation bands from both the albedo and temperature bands again show extensive overlapping, although to a lesser degree than do the mean statistics.

Thus, use of the mean and spatial deviation statistics for classifying rain events as continuous or convective may not feasible using the statistics and summer-time data set presented in this paper.

2) LIGHT (RL) VERSUS MODERATE-TO-HEAVY RAIN (RMH)

The co-spectral plot in Fig. 3f shows the statistical responses of the mean and spatial deviation statistics for the light and moderate-to-heavy rain data sets. The differences observed in the responses of the spatial deviation statistics are relatively small, and only the VIS means of the means show any significant amount of separation (approximately 1/2 standard deviation). Again, as in the case of the convective and continuous rain data sets, the separation of light from moderate-to-heavy rain appears infeasible using the statistics shown here.

4. Summary and Conclusions

The SVC-A weather reports, including reports of instantaneous rainfall type and intensity, can be used with GOES VIS and IR data to develop a scheme to estimate instantaneous rainfall area. Furthermore, these schemes can employ simple statistics, computer efficient schemes, like mean VIS and IR window values to separate precipitating areas from non-precipitating ones.

Like Lovejoy and Austin (1979) we found that simple statistics derived from the GOES data were sufficient to separate raining areas from non-raining cloudy areas. These statistics failed, however, to indicate a sufficiently large response difference between the convective and continuous rain classes or the light and moderate-to-heavy rain classes. Separation of these latter two classes might be obtained using more sophisticated statistical techniques, such as those used by Wu et al. (1985) or Tsonis (1987).

Only small differences were observed in predictive abilities between the 10^2 and 4^2 window. However, if both window sizes are available then the smaller window size offers the advantage of computational simplicity while the larger window offers the advantage of greater versatility in the number of statistical parameters that can be derived from the window data.

5. Acknowledgments

The authors would like to acknowledge the work of two NPS graduates, LCDR Linda Paul, USN and CAPT David Rust, whose work contributed to this preprint. This study has been supported by the Naval Environmental Prediction Research Facility, Monterey, California.

6. References

D. Atlas and O. Thiele, 1982: Precipitation measurements from space: Workshop summary. Bull. Amer. Meteorol. Soc., vol. 63, 53-63.

Lee, B.G., R.T. Chin and D.W. Martin, 1985: Automated rain-rate classification of satellite images using statistical pattern recognition. IEEE Trans. Geos. Remote. Sens., vol. ge-23, 315-323.

Lovejoy, S., and Austin, G.L., 1979: The delineation of rain areas from visible and IR satellite data for GATE and midlatitudes. Atmos.-Ocean, 17, 77-92.

Paul, L.S., 1983: A study of precipitation occurence using visual and infrared satellite data. Masters Thesis, Naval Postgraduate School, Monterey, California, 114 pp.

Tsonis, A.A., and Isaac, G.A., 1985: On a new approach for instantaneous rain area delineation in the midlatitudes using GOES data. J. Climate Appl. Meteorol., 24, 1208-1218.

Tsonis, A.A., 1987: Determining rainfall intensity and type from GOES imagery in the midlatitudes. Remote Sens. Environ., 21, 29-36.

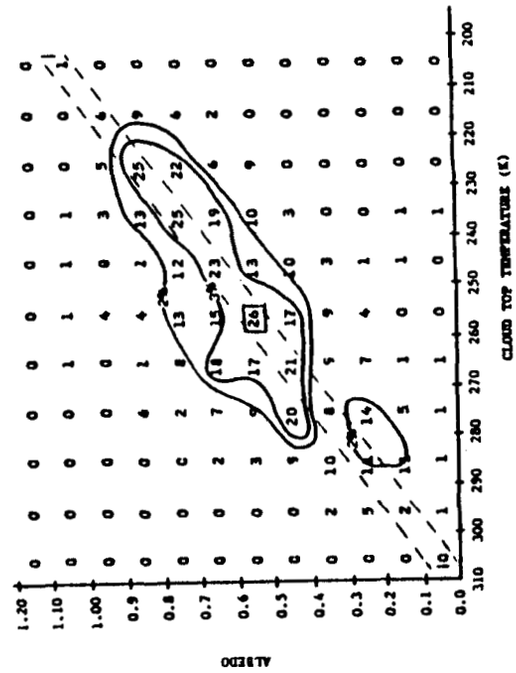

Fig. 3a. Rain data for the 10^2 windows. The mean, 0.579 and 253.0K, interval is boxed (From Paul, 1983).

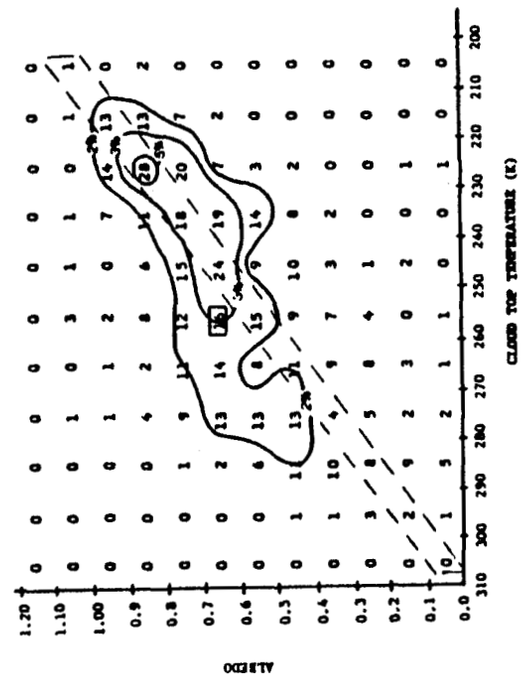

Fig. 3b. Same as 3b but for 4^2 windows.

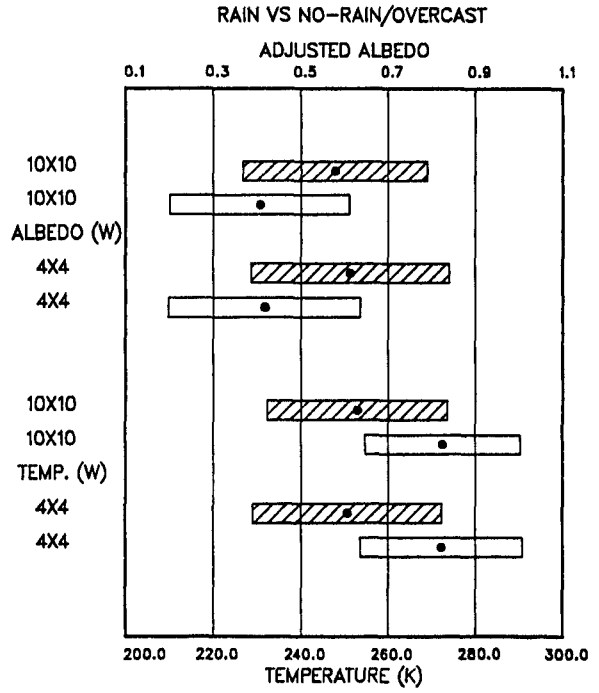

Fig. 3c. Co-spectral plot for the mean window statistic (W). Spread of the data is indicated by the width of the bars (2 standard deviations) and the mean by the closed circle. Shaded bars indicate rain, unshaded indicate no-rain.

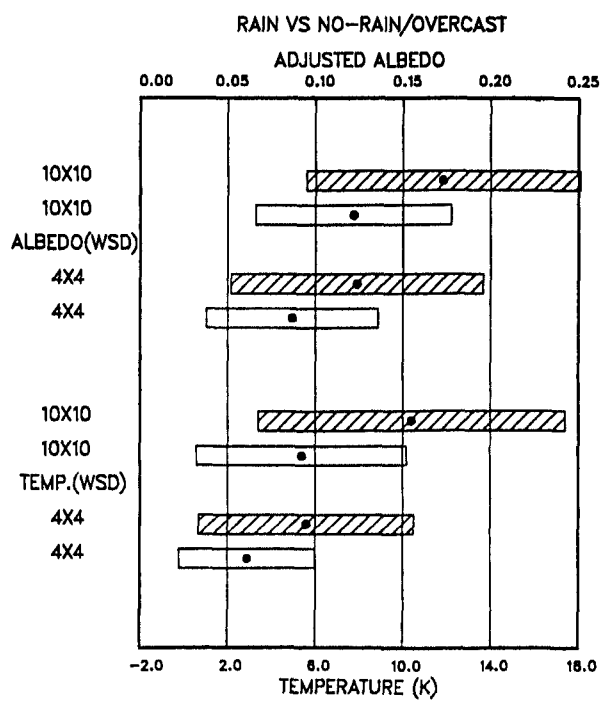

Fig. 3d. Same as 3c but for the spatial deviation statistic (WSD).

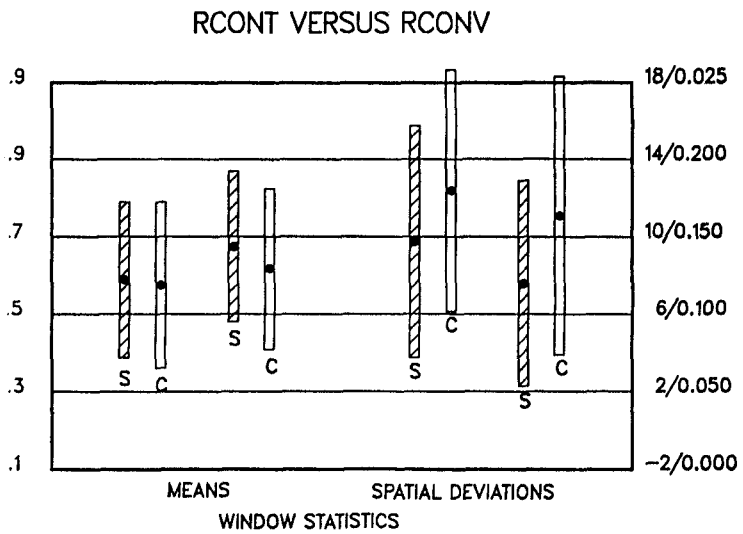

Fig.3e. Co-spectral plot comparing convective rain (unshaded bars) to continuous rain (shaded bars). The albedo statistics are labeled A, and the temperature statistics are labeled T.

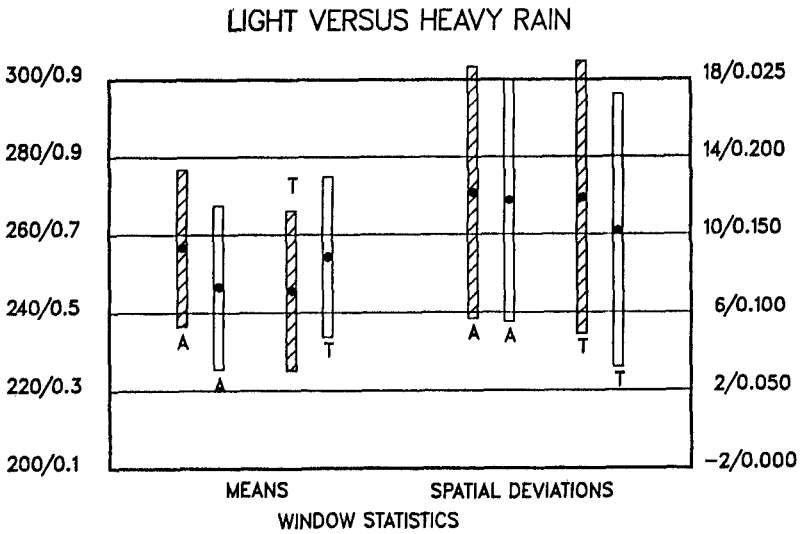

Fig. 3f. Same as 3e but comparing light rain (unshaded bars) to moderate-to-heavy rain (shaded bars).

7.7

THE ADDITION OF VISIBLE CHANNEL DATA TO SATELLITE INFRARED RAIN ESTIMATION SCHEMES

Andrew J. Negri
Robert F. Adler

Laboratory for Atmospheres
NASA/Goddard Space Flight Center
Greenbelt, MD 20771

1. INTRODUCTION

There has recently been renewed interest in the use of the visible channel (VIS) data (both radiance and structure) in satellite rain estimation schemes that traditionally used only infrared (IR) wavelengths. Tsonis (1987) and Tsonis and Isaac (1985) used clustering analysis to separate raining and non-raining clouds. Bellon and Austin (1986) [henceforth BA] found empirical relations between VIS and/or IR data useful in delineating rain areas above a low-rain threshold. Wu et al. (1985) found that the addition of textural features raised skill scores in rain detection from 56 to 83%.

This study examines the ability of three satellite threshold schemes to estimate convective precipitation: VIS, IR, AND VIS/IR (bi-spectral). Following the methodology of BA, empirical relationships between the satellite and radar data (4 km grid) were determined. The independent data were a subset of the dependent data in order to 1) assess the validity of derived aggregate relationships on individual days and 2) the impact of the VIS data (on IR schemes) unencumbered by other factors.

Results are presented for two areas: the FACE (Florida Area Cumulus Experiment) area (~1.4×10^4 km^2) and an area ~250 km on a side centered on 26°N, 81°W, which is inclusive of the FACE area but exclusive of points within 50 km or greater than 170 km of the Miami WSR-57 radar. This south Florida area is ~6.4×10^4 km^2. Estimated volume rainrate is separated into areal and rate components, and results are presented on four days.

2. DATA AND METHODOLOGY

The data set used has been described by Negri and Adler (1987a,b) and by Adler and Negri (1987). It consists of five days (51 images) of VIS, IR and radar data collected during the FACE. Visible data (4 km averages of 1 km data) were normalized for solar zenith angle and recalibrated to account for differences between satellites. Infrared data were oversampled to match the VIS resolution, and were calibrated in terms of blackbody temperature. Digital reflectivity data from Miami were converted to rainrate via $Z=300R^{1.4}$ and averaged to 4 km. Analysis was done from 1800-2200 UTC each day, with 30 min interval data.

Following the methodology of BA, rainrate and other rain parameters were derived as a function of VIS and IR data, both individually and bidimensionally. The IR data was divided into 5 K intervals, the VIS data (0-64), into 2-count intervals. The relationships among VIS, IR and radar data for the five days of dependent data are displayed in Fig. 1, in VIS/IR space. Fig. 1a portrays the average rain rate per VIS/IR cell. While a VIS threshold of 32 counts delineates rain/no-rain, discrimination of higher rainrates begins at lower IR temperatures. The percent contribution (of each VIS/IR cell) to the total volume rainrate, accumulated over the south Florida area on each of the 51 images, is shown in Fig. 1b. Contours of cumulative volume rainrate, accumulated from the warm, dark end, are displayed in Fig. 1c. The mean rainrates in each division are determined, and (in EXP 1) reapplied as a rain estimation technique on four of the five days. Fig. 1d presents contours of cumulative percent rain area (1 mm/h as determined by the radar data). The line in VIS/IR space which represents 50% of the raining VIS/IR cells delineates the rain/no-rain boundary in EXP 2. Fig. 1e displays the contours of cumulative number of VIS/IR points, expressed as a percent of the total number of points. The line in VIS/IR space which represents the coldest and brightest 8% area (the fraction of total area with rainrates > 1 mm/h) delineates the rain/no-rain boundary in experiment 3.

A summary of the three experiments and three rain estimation schemes is presented in Table 1. In EXP 1, the divisions of cumulative percent volume rainrate (% VRR) determine the range (VIS counts, IR temperature, or region in VIS/IR space) in which the radar-determined mean rainrate (R_c) is calculated. The adjusted mean rainrate (R_a) is calculated by setting the lowest category to zero, and adjusting the remaining rates to conserve the total VRR. In experiment 2 the thresholds that define 50% of the cumulative rain area are used as the rain/no-rain boundaries. The mean rainrate in the raining area is computed, then adjusted to conserve the total VRR. Experiment 3 is an equal area method. It is identical to experiment 2 except that the rain/no-rain thresholds are set such that only the coldest (brightest) 8% of the satellite pixels receive rain. This is the percent of the total area determined (by the radar data) to be raining, and includes several images with little or no rain.

3. RESULTS

Statistics to be presented include the bias, (the mean difference between the estimated and observed values), and the normalized root mean square error (NRMSE),which expresses the absolute difference (estimated - observed) as a fraction of the observation, and is expressed as a percent. Estimates were made on 41 of the 51 images (4 of 5 days). When both the estimate and the observed values for the FACE area were less than 0.10 mm (0.05 for the South Florida area), the pair was not included in the statistics. This had no significant effect on the results.

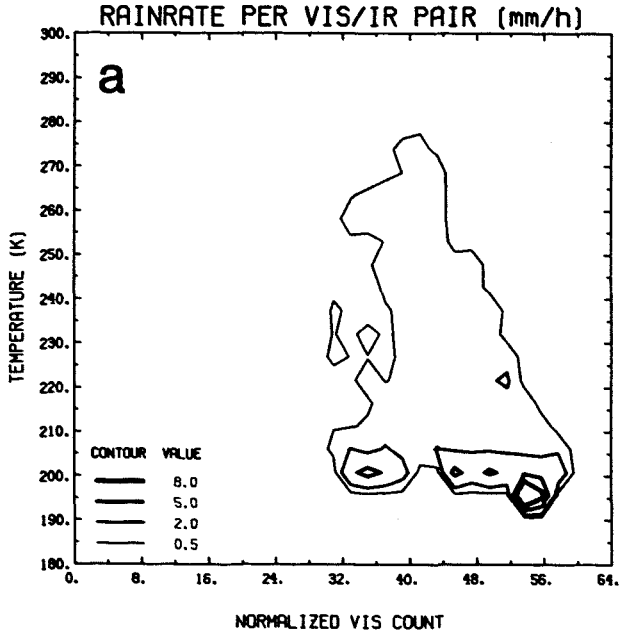

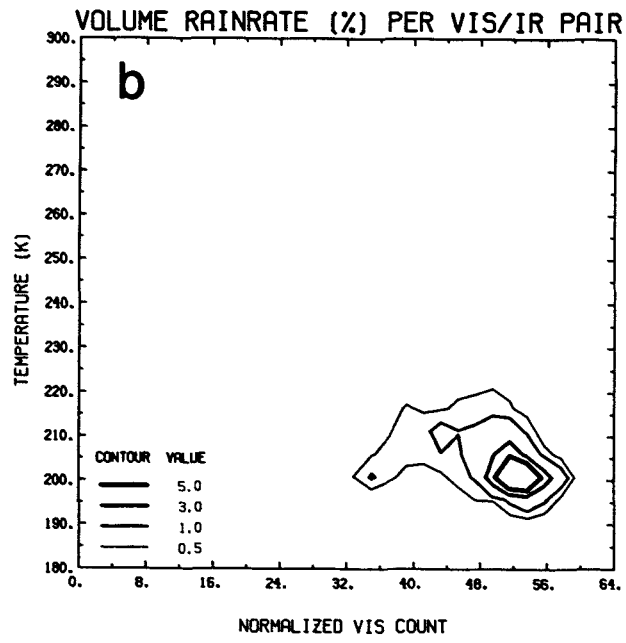

Figure 1. Relationships among VIS, IR and radar data for the five days of dependent data, displayed in VIS/IR space (5 K, 2 count intervals).

a) The average rainrate per VIS/IR cell. A visible threshold of 32 counts delineates rain/no-rain, and discrimination of higher rainrates is better effected by the infrared.

b) Percent contribution to the total volume rainrate, accumulated over space and time, by each 5 K and 2 count cell.

c) Contours of cumulative volume rainrate, accumulated from the warm, dark end. The mean rainrates in each division are determined, then reapplied as a rain estimation technique to the individual days (Experiment 1).

d) Contours of cumulative percent rain area (1 mm/h threshold). The line in VIS/IR space which represents the 50% of the raining VIS/IR pixels delineates rain/no-rain (Experiment 2).

e) Contours of cumulative number of VIS/IR points, expressed as a percent of the total points. The line in VIS/IR space which represents the coldest and brightest 8% area (the fraction of total area with rainrates > 1 mm/h) delineates rain/no-rain (Experiment 3).

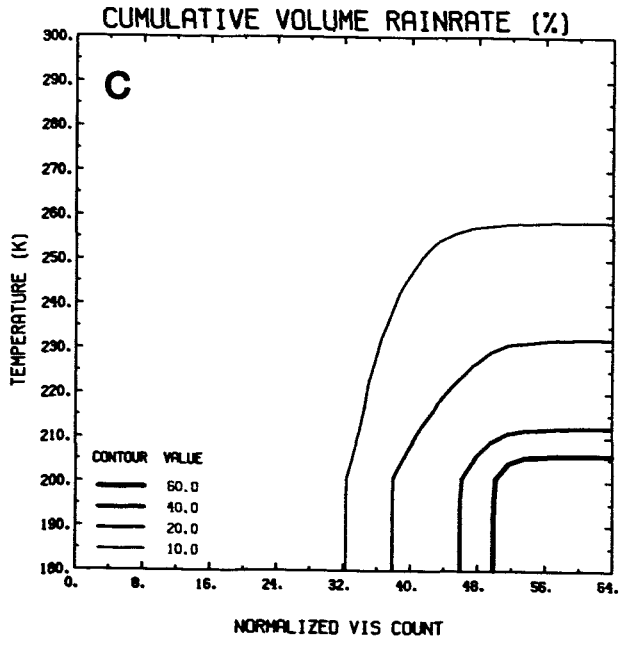

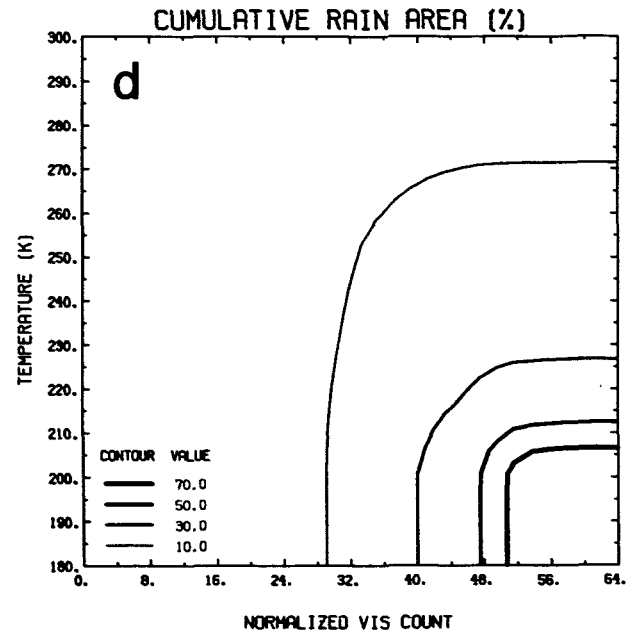

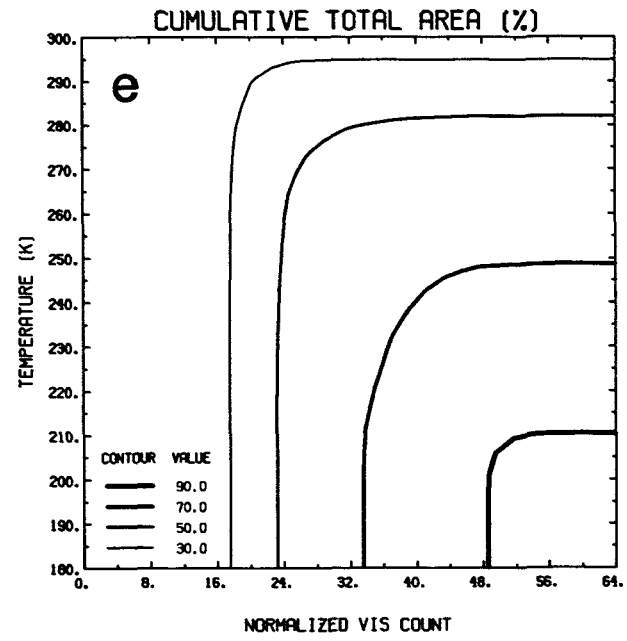

TABLE 1

Three rain estimation experiments involving VIS and IR data. In experiment 1 the divisions of cumulative percent volume rainrate (% VRR) determine the range (VIS counts, IR temperature, or region in VIS/IR space) in which the radar-determined mean rainrate (R_c) is calculated. The adjusted mean rainrate (R_a) is calculated by setting the lowest category to zero, and adjusting the remaining rates to conserve the total VRR. In experiment 2 the threshold in VIS or IR space, or the contour in VIS/IR space, that defines 50% of the cumulative rain area is used as a rain/no-rain boundary. The mean rainrate in the raining area is computed, then adjusted to conserve the total VRR. Experiment 3 is an equal area method. It is identical to experiment 2 except that the rain/no-rain threshold is set such that only the coldest (brightest) 8% of the satellite pixels receive rain. This is the percent of the total area determined (by the radar data) to be raining, and includes several images in which little or no rain occurred.

EXPERIMENT #	VIS ONLY RANGE (counts)	VIS ONLY R_c (mm/h)	VIS ONLY R_a (mm/h)	IR ONLY RANGE (K)	IR ONLY R_c (mm/h)	IR ONLY R_a (mm/h)	VIS & IR RANGE	VIS & IR R_c (mm/h)	VIS & IR R_a (mm/h)	VRR (%)
1	0-37	0.1	0.0	231-330	0.1	0.0		0.2	0.0	0- 20
	38-45	1.1	1.3	216-230	0.8	1.0	see	1.6	2.0	20- 40
	46-49	2.0	2.5	206-215	1.5	1.8	Fig. 1c	2.1	2.6	40- 60
	49-64	2.8	3.5	198-205	4.8	6.0		4.6	5.8	60-100
2	0-47	0.3	0.0	211-330	0.3	0.0	see	0.3	0.0	0- X^1
	48-64	2.7	4.9	198-210	3.0	5.2	Fig. 1d	3.1	6.7	X^1-100
3	0-49	0.4	0.0	211-330	0.3	0.0	see	0.4	0.0	0- Y^2
	50-64	2.8	4.9	198-210	3.0	5.2	Fig. 1e	3.2	8.5	Y^2-100

[1] Percent varies: 45% for VIS only, 42% for IR only, 53% for VIS & IR.
[2] Percent varies: 57% for VIS only, 42% for IR only, 62% for VIS & IR.

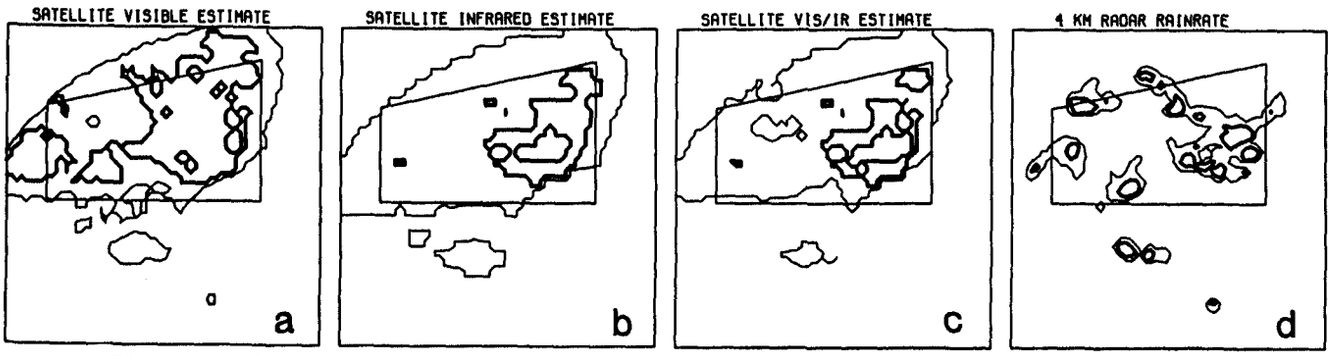

Figure 2. (a-c) Estimates of rainrate on 2000 UTC 12 Aug 1978 from EXP 1. Lowest and highest rainrates for each scheme have been contoured (see Table 1). Apparent third (inner) contour represents lower rainrates. (d) The 4 km-averaged rainrate from the Miami radar, with contours of 1 and 10 mm/h displayed.

3.1 Results of EXP 1

When estimates of the mean rain depth in the south Florida area made every 30 min for four days were compared to observations, there was virtually no bias, nor were there differences in bias among the three methods. This is not surprising given that each method was "trained" using virtually the same data set. In considering the individual days, each technique overestimated on two days and underestimated on two days. There was also a tendency to underestimate the early (lower amount) rainfall and overestimate the rainfall later in the day. This tendency has been shown to be typical of threshold techniques by Adler and Negri (1987).

The statistics for the smaller FACE area reveal, on average, a slight negative bias (-0.04 to -0.08) with little difference among the three methods. The underestimate-early/overestimate-late bias was more pronounced. The major drawback with the approach in EXP 1 was the estimated area of precipation: such areas were 2-4 times larger than the radar determined area. An example in shown in Fig. 2 (a-c), the estimates of rainrate on 2000 UTC 12 Aug 1978. The lowest and highest rainrates have been contoured (see Table 1). The innermost contours actually represents lower rainrates (holes). In Fig. 2d, the 4 km-averaged rainrate from the Miami radar provided the verification of the rain area. One can see that not all cold/bright clouds contain precipitation. This technique conserves the volume rain rate in an area by imposing lower per-pixel rates than the radar but applys them over much larger areas. These poor areal results provided the motivation for EXP's 2 and 3.

3.2 Results of EXP 2

Experiment 2 attempted to find the contour in VIS/IR space that represented the 50% probability of rain as determined by radar data. That is, only the VIS/IR cells known to be raining were evaluated, an approach not unlike that of Doneaud et al. (1987). The cumulative frequency of raining points was determined, and the 50% contour was chosen to delineate rain from no-rain (Fig. 1d). All VIS/IR points falling to the right of the 50% contour were assigned a rainrate of 6.7 mm/h. This is comparable to the 7.0 mm/h rate determined by Bellon and Austin

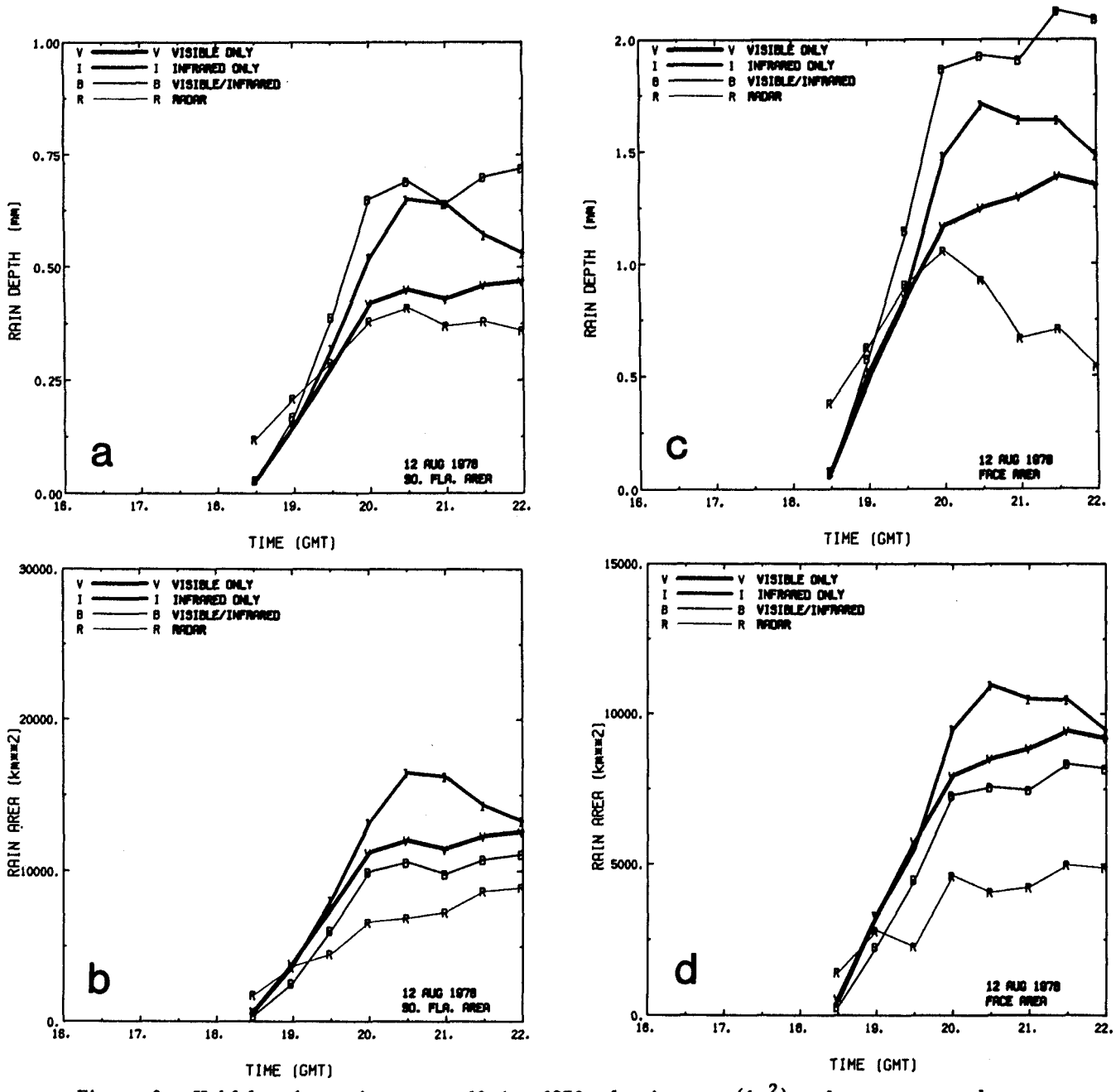

Figure 3. Half-hourly estimates on 12 Aug 1978 of rain area (km^2) and area-averaged rain depth (mm) from the VIS, IR and VIS/IR satellite techniques. The equal area method (EXP 3) has been used, and comparisons are made to the radar-estimated area and depth.

South Florida area (~6.4 x 10^4 km^2)
a) rain depth
b) rain area

FACE area (~1.4 x 10^4 km^2)
c) rain depth
d) rain area

(1986) for the Montreal area in their method 2. For the schemes that used only VIS or IR data, a single threshold is determined. The VIS threshold (47) was close to the value of 44 found by BA, however the IR threshold of 211 K (-62° C) is considerably lower than the 256 K (-17° C) in BA, due most likely to the higher tropical tropopause in Florida.

The bias (in mm) of the three satellite estimation schemes, compared to the FACE area-averaged rain depth determined by 4 km-averaged digital radar data is shown in Table 2. Results are stratified by cumulative (radar) rainfall. While the aggregate (4 day) biases are small (-0.03 to +0.11), two days had large negative bias and two days had large positive bias, which tended to cancel (part a). When stratified into first half/second half estimates, (parts b and c) all three techniques, (in the 4-day aggregate) displayed an underestimate (early)/overestimate (late) problem as in EXP 1. The addition of the VIS data to the IR introduced a small positive bias that did not exist with either wavelength alone. This was particularly apparent in the estimates made later in each day, though the sample sizes are small.

3.3 Results of EXP 3

EXP 3 is an equal area method, identical to EXP 2 except that the rain/no-rain threshold is set so that only the coldest (brightest) 8% of the pixels receive rain. This is the percent of the total area determined (by the radar data) to be raining, and includes several images with little or no rain.

TABLE 2
Bias (in mm) of three satellite estimation schemes (in EXP 1) compared to the area-averaged rain depth determined by 4 km-averaged digital radar data.

a) South Florida area

	29 JUL 1978	12 AUG 1978	16 AUG 1978	18 AUG 1980	ALL
VIS ONLY	-0.05	+0.05	-0.07	+0.09	+0.01
IR ONLY	-0.00	+0.04	-0.06	+0.08	+0.02
VIS & IR	-0.03	+0.03	-0.10	+0.02	-0.02
NUMBER	(7)	(8)	(9)	(10)	(34)

b) FACE area

	29 JUL 1978	12 AUG 1978	16 AUG 1978	18 AUG 1980	ALL
VIS ONLY	-0.30	+0.26	-0.21	+0.08	-0.05
IR ONLY	-0.27	+0.20	-0.18	+0.11	-0.04
VIS & IR	-0.28	+0.23	-0.25	+0.02	-0.08
NUMBER	(8)	(8)	(9)	(8)	(33)

TABLE 3
Bias (in mm) of three satellite estimation schemes (in EXP 2) compared to the FACE area-averaged rain depth determined by 4 km-averaged radar data. Results are stratified by cumulative radar rainfall.

a) ALL ESTIMATES

	29 JUL 1978	12 AUG 1978	16 AUG 1978	18 AUG 1980	ALL
VIS ONLY	-0.12	+0.52	-0.22	+0.15	+0.07
IR ONLY	-0.26	+0.45	-0.18	+0.10	+0.02
VIS & IR	-0.13	+0.68	-0.21	+0.23	+0.13
NUMBER	(8)	(8)	(9)	(8)	(33)

b) 1ST HALF ESTIMATES

	29 JUL 1978	12 AUG 1978	16 AUG 1978	18 AUG 1980	ALL
VIS ONLY	-0.11	+0.12	-0.18	-0.26	-0.11
IR ONLY	-0.22	-0.01	-0.22	-0.48	-0.23
VIS & IR	-0.19	+0.13	-0.22	-0.34	-0.16
NUMBER	(6)	(4)	(6)	(4)	(20)

c) 2ND HALF ESTIMATES

	29 JUL 1978	12 AUG 1978	16 AUG 1978	18 AUG 1980	ALL
VIS ONLY	-0.18	+0.93	-0.30	+0.56	+0.36
IR ONLY	-0.39	+0.91	-0.12	+0.68	+0.40
VIS & IR	+0.06	+1.24	-0.19	+0.81	+0.59
NUMBER	(2)	(4)	(3)	(4)	(13)

Results of half-hourly estimates of rain depth and area for one day (12 Aug 1978) are shown in Fig. 3(a-d), while statistical summaries for all days are displayed in Tables 4-6. This day was a typical example of a convective rain event in south Florida. Both rain depth and rain area in the south Florida were overestimated by all three schemes (Fig. 3a,b), despite being part of the sample to which the schemes were "tuned". Rain area, despite being confined to only the top 8% of the data was also overestimated (by about a factor of 2). Differences among the schemes were more apparent in the rate (as opposed to the area) estimate, with the bi-spectral method actually overestimating the depth more than either VIS or IR alone. Results tabulated for the smaller FACE area (Fig. 3c,d) displayed a greater deviation from the radar ground truth, with all satellite estimates nearly doubling the observed values of both rain area and depth.

TABLE 4
Bias (in mm) of three satellite estimation schemes (in EXP 3) compared to the area-averaged rain depth determined by 4 km-averaged digital radar data.

a) South Florida area

	29 JUL 1978	12 AUG 1978	16 AUG 1978	18 AUG 1980	ALL
VIS ONLY	-0.02	+0.02	-0.12	+0.04	-0.04
IR ONLY	+0.01	+0.11	-0.06	+0.06	+0.03
VIS & IR	+0.11	+0.18	-0.09	+0.00	+0.04
NUMBER	(7)	(8)	(9)	(10)	(34)

b) FACE area

	29 JUL 1978	12 AUG 1978	16 AUG 1978	18 AUG 1980	ALL
VIS ONLY	-0.25	+0.26	-0.31	+0.07	-0.07
IR ONLY	-0.26	+0.45	-0.18	+0.10	+0.02
VIS & IR	-0.07	+0.74	-0.22	+0.21	+0.15
NUMBER	(8)	(8)	(9)	(8)	(33)

TABLE 5
Normalized root mean square error (percent) of three satellite estimation schemes (in EXP 3) compared to the area-averaged rain depth determined by 4 km-average radar data. This statistic expresses the absolute difference (estimated - observed) as a fraction of the observed rainfall.

a) South Florida region

	29 JUL 1978	12 AUG 1978	16 AUG 1978	18 AUG 1980	ALL
VIS ONLY	32	32	72	78	60
IR ONLY	22	52	69	101	71
VIS & IR	39	70	71	119	83
NUMBER	(7)	(8)	(9)	(10)	(34)

b) FACE region

	29 JUL 1978	12 AUG 1978	16 AUG 1978	18 AUG 1980	ALL
VIS ONLY	49	78	72	121	84
IR ONLY	45	102	69	111	85
VIS & IR	46	151	73	159	117
NUMBER	(8)	(8)	(9)	(8)	(33)

TABLE 6
Normalized root mean square error (percent) of three satellite estimation schemes compared to the rain area (> 1 mm/h) determined by 4 km-average radar data. This statistic expresses the absolute difference (estimated - observed) as a fraction of the observed rain area.

a) South Florida region

	29 JUL 1978	12 AUG 1978	16 AUG 1978	18 AUG 1980	ALL
VIS ONLY	50	56	64	68	61
IR ONLY	48	87	83	92	81
VIS & IR	37	44	73	74	61
NUMBER	(7)	(8)	(9)	(10)	(34)

b) FACE region

	29 JUL 1978	12 AUG 1978	16 AUG 1978	18 AUG 1980	ALL
VIS ONLY	52	95	65	90	77
IR ONLY	48	116	77	121	95
VIS & IR	53	72	72	79	70
NUMBER	(8)	(8)	(9)	(8)	(33)

Table 3 (depth) and Table 4 (area) present the NRMSE of the three satellite estimation schemes compared to the area-averaged rain depth (or rain area > 1 mm/h) determined by the radar data in both the South Florida (a) and the FACE region (b). The NRMSE expresses (as a percent) the absolute difference (estimated - observed) as a fraction of the observed rainfall. Results were similar for both rain parameters, depth and area. NRMSE for a daily series of 30 min estimates of rain depth ranged from 22 to 119% in the south Florida area. Four-day aggregates were 60, 71 and 83% for the VIS, IR and VIS/IR respectively. For the FACE region, these increased to 84, 85 and 117%. When the error associated with the rain area is examined (Table 6), similar percent errors were recorded for this parameter in both the FACE and south Florida area. This experiment is similar to that of Arkin (1979), who correlated the fractional coverage of cold cloud with precipitation. While the 211 K threshold found here is lower than the 235K threshold found by Arkin, the overestimate of rain area appears to be common to threshold techniques that have been calibrated by rain rate or amount.

4. COMMENTS AND CONCLUSIONS

In this study we attempted to show the impact of the VIS data on IR-threshold rain estimation. In addition, we presented some of the limitations and error statistics of both mono- and bi-spectral methods of satellite rain estimation. The methodology of Bellon and Austin (1986) was employed, but our results are less optimistic in regard to the role VIS data may play. BA found that their VIS/IR method had the lowest absolute difference compared to raingage measurements, and that the VIS data alone had a higher Critical Success Index at lower rainrates. They determined that the IR only method overestimated the rain at point locations, but presented no statistics on rain areal extent.

Previous studies have acknowledged that significant biases and mean square errors can result when a technique is applied to areas other than those of its derivation. This study has extended that further in that:

a) application of three satellite techniques trained with south Florida data resulted in a slight bias and significant percentage errors when applied to a smaller area than the training area.

b) while no net bias existed for the 4-day sample taken together, the rainfall was underestimated on two days and overestimated on two others.

c) all the threshold techniques tended to underestimate the rainfall early in the day, and overestimate late, as a consequence of setting the threshold to an intermediate value.

d) despite deriving each method in terms of the contour in VIS, IR or VIS/IR space in which the probability of rain was 50%, area estimates of rainfall had associated errors of 50 to 100%.

e) When the VIS/IR threshold was set to equalize the satellite and radar area (8% for the total sample), overestimation of rain area still occurred. This was because many images received no rain while late in the day, cold cloud anvils were over-compensated.

f) the problems that thin (non-precipitating) cirrus clouds might have on satellite rain estimation were not readily apparent in this study for two reasons:

1) there was very little thin cirrus (as opposed to thick anvil cirrus) in this data set and

2) the relatively cold and bright thresholds used in this study effectively eliminated thin cirrus.

It was observed however, (in EXP 1) that cirrus debris from early morning convection outside the Florida area would be erroneously identified as precipitation. The methodology of Arkin (1979) might be particularly prone to this cirrus debris problem due to a warmer (235 K) IR threshold, and it is here that the addition of the VIS data may help reduce the errors and overestimation on IR schemes.

5. REFERENCES

Adler, R. F., and A. J. Negri, 1987: A satellite infrared technique to estimate tropical convective and stratiform rainfall. J. Climate Appl. Meteor., 26, (in press).

Arkin, P. A., 1979: The relationship between fractional coverage of high cloud and rainfall accumulations during GATE over the B-scale array. Mon. Wea. Rev., 107, 1382-1387.

Bellon, A. and G. L. Austin, 1986: On the relative accuracy of satellite and raingage rainfall measurements over middle latitudes during daylight hours. J. Climate Appl. Meteor., 25, 1712-1724.

Doneaud, A. A., J. R. Miller and L. R. Johnson, 1987: The area-time-integral technique to estimate convective rain volumes over areas applied to satellite data - a preliminary investigation. J. Climate Appl. Meteor., 26, 156-169.

Negri, A. J. and R. F. Adler, 1987a: Infrared and visible satellite rain estimation. I: A grid cell approach. J. Climate Appl. Meteor., 26, (in press).

Negri, A. J. and R. F. Adler, 1987b: Infrared and visible satellite rain estimation. II: A cloud definition approach. J. Climate Appl. Meteor., 26, (in press).

Tsonis, A. A., 1987: Determining rainfall intensity and type from GOES imagery in the midlatitudes. Remote Sens. Environ., 21, 29-36.

Tsonis, A. A., and G. A. Isaac, 1985: On a new approach for instantaneous rain area delineation in the midlatitudes using GOES data. J. Climate Appl. Meteor., 24, 1208-1218.

Wu, R., J. A. Weinman, and R. T. Chin, 1985: Determination of rainfall rates from GOES satellite images by a pattern recognition technique. J. Atmos. Ocean. Tech., 2, 314-330.

GLOBAL PRECIPITATION DERIVED FROM HIRS2/MSU SOUNDINGS

Man-Li C. Wu and Joel Susskind
Laboratory for Atmospheres
NASA/Goddard Space Flight Center

1. INTRODUCTION

Atmospheric and surface soundings for the FGGE year have been produced by Susskind et al. (1987) from analysis of HIRS2/MSU sounding data. We have used these soundings to compute fields of total outgoing longwave radiation (OLR) for the FGGE year with a modified version of the radiation code used in the Goddard Laboratory for Atmospheres (GLA) fourth order General Circulation Model (GCM). The input geophysical parameters to the radiation code are the soundings of the atmospheric temperature-humidity profiles, sea/land surface temperature, and cloud top pressure and radiatively effective cloud cover. Comparison of OLR computed from the soundings with other measures of OLR can serve as a validation for both the soundings and the radiation code. In addition, computing OLR rather than observing it provides the capability of attributing spatial and temporal variations of OLR to variations in other geophysical parameters. It also allows for computation of hypothetical fluxes, such as the OLR which would have been observed if clouds were not present. This is not the same as OLR observed under clear conditions because the temperature-humidity soundings used are averages over all conditions, rather than just cloud free areas, which might be biased.

The OLR computed using all of the geophysical parameters (i.e. including effective cloud cover and cloud top pressure) will be referred to as cloudy OLR in the following discussion and the OLR computed by assuming no clouds will be referred to as clear OLR. The difference field of clear OLR minus cloudy OLR, ΔOLR, is a measure of longwave cloud radiative forcing. This is related to the strength of convection, which is associated with precipitation. Thus, we might expect a relationship between ΔOLR and precipitation. Precipitation is inhibited over land when the surface temperature is high during the day because this phenomenon raises the cloud base. An indicator of ground heating, and possibly cloud base height, can be constructed by using the difference of clear daytime OLR and clear nighttime OLR, ΔCLR. This difference is also a measure of soil moisture when one accounts for the amount of solar radiation reaching the ground. An algorithm has been developed to estimate global precipitation from ΔOLR and ΔCLR. These fields have been derived using average soundings for every 10 days of the FGGE year.

2. DESCRIPTION OF THE RADIATION ROUTINE

The GLA fourth order GCM uses a radiative transfer program which was parameterized by Wu and Kaplan and documented by Kirshnamurti (1982). In order to calculate OLR at the top of the atmosphere, the program was modified to calculate the OLR at 1 mb, rather than 10 mb, which is the top of the model. In addition, the radiation code was modified to treat the retrieved radiatively effective fractional cloud cover which can be at any of the standard 66 pressure levels of the retrieval system (Susskind et al., 1984), rather than the model levels. The total calculation of longwave (LW) radiation is divided into 11 spectral bands. The water vapor transmittance in each band is calculated as a function of temperature and humidity according to the statistical band model, with Godson's version of the Curtis-Godson approximation in non-homogeneous atmospheres, as was described by Rodgers and Walshaw (1966). The mean transmittance of CO_2 in the 15 μm band and mean transmittance of O_3 in the 9.6 μm band are parameterized based on transmittances computed using detailed line-by-line calculations for a number of profiles. The CO_2 mean transmittance is parameterized as a function of surface pressure and atmospheric temperature profile. The ozone transmittances uses values which vary as a function of latitude based on climatological ozone profiles.

The parameterizations have been tested by comparison of fluxes computed for the McClatchey mid-latitude summer temperature humidity profile using the Wu-Kaplan radiation code on the one hand, with fluxes computed by other groups using potentially more accurate but more computer intensive line-by-line calculations for the same profile. These results are shown in Table I. Agreement of all calculations is of the order 1 Wm^{-2}.

3. OUTGOING LONGWAVE RADIATION COMPUTED FROM THE SOUNDINGS

The input parameters to the radiation code are the soundings of the atmospheric temperature-humidity profiles, sea/land surface temperature, and cloud top pressure and effective cloud cover, as derived from analysis of the HIRS2/MSU data for the FGGE year by using the GLA physical retrieval system developed by Susskind et al. (1984). For purpose of discussion, the monthly mean values of July 1979 have been chosen. In the tropics, where thermal variations are rela-

tively low, the parameters which have the largest effect on the OLR are the cloud top pressure and effective cloud fraction (which is the product of cloud emissivity and cloud fraction). High effective cloud fractions with low cloud top pressure (high altitude) are found over areas associated with the ITCZ and the monsoon. These same features show up as low values in the OLR field. High values of OLR are generally found immediately to the north and south of the convective areas in regions of subsidence, which are either relatively clear or have stratus clouds at low altitudes. In the extra-tropics, OLR generally decreases with decreasing temperature and is more correlated with temperature.

The OLR computed using products retrieved from the HIRS2/MSU, which will be referred to as HIRS OLR, has been compared to two other determinations of OLR, the OLR derived for the narrow band (~ 11μm) measurements of AVHRR, which will be referred to as AVHRR OLR, and to the OLR derived from ERB broad-band (5-50 μm) narrow field of view observations (NFOV) of Nimbus 7, which will be referred to as ERB OLR.

In general, there is excellent agreement between the computed HIRS OLR field and those derived from the observations, both in patterns as well as magnitude. High OLR (>275 Wm^{-2}) is found in areas associated with oceanic trade wind systems, low level stratocumulus, and deserts and semi-arid areas, and low OLR (<225 Wm^{-2}) is found in areas associated with major convective cloud systems such as the ITCZ and monsoon, or regions having low temperatures such as the polar regions.

Statistical comparisons of OLR determined from the three sources are shown in Table II for July 1979. Values given are mean and standard deviation of the global OLR for each system as well as corresponding values for the difference fields. It is shown in Table II that the July 1979 global mean values of OLR computed from HIRS soundings and determined from AVHRR observations differ by 1.1 Wm^{-2} while HIRS differs in the mean from ERB by 11.3 Wm^{-2} and AVHRR from ERB by 12.4 Wm^{-2}. The HIRS-ERB difference shows a global standard deviation of 6.2 Wm^{-2}, HIRS-AVHRR is 7.5 Wm^{-2} and AVHRR-ERB is 10.0 Wm^{-2}, all taken on the 4° x 5° latitude-longitude grid. While all the differences are small, the patterns of the differences are systematic and indicate that the differences are related to the values of OLR themselves, with ERB showing the biggest dynamic range, HIRS a close second, and AVHRR being the most damped. This is consistent with the values of the standard deviations of the measurements themselves, with ERB being largest and AVHRR smallest.

The reasonable agreement between the computed OLR and OLR derived from measurements serves as validation of the individual geophysical parameters retrieved from the HIRS2/MSU soundings as well as the radiative transfer code used in the GLA GCM. Most significantly, the agreements are in magnitude as well as in patterns. This indicates that the GLA physical retrieval system derived relatively accurate soundings and the radiative transfer code properly takes the cloud radiative properties, surface conditions, humidity and temperature variations into account. This gives us the ability to relate variations in space and time of OLR to variations in other geophysical parameters. In addition it allows for computation of fields such as ΔOLR which depicts cloud forcing but cannot be measured directly.

4. ESTIMATE OF PRECIPITATION

Fields of OLR have been used as estimates of precipitation over the tropics because low values of OLR correspond to areas of large amounts of high cloudiness. In the extratropics, and even the tropics, cloud effects are distorted in the OLR field because of temperature variations in the fields. These temperature effects are removed to first order in ΔOLR, which appears to be more closely associated with precipitation than the OLR field itself. Large values occur in July over areas associated with the high level convective clouds of the ITCZ, the monsoon area, and also in the South Pacific Convergence Zone (SPCZ), which is not apparent in the OLR field. Moderate values appear over mid-latitude areas as well. Small values are found in areas associated with tradewind cumulus, low level stratocumulus, deserts and semi-arid areas, and polar regions. Moderate values of clear OLR minus cloudy OLR also sometimes appear over semi-arid land areas, which do not have significant precipitation. This occurs in areas which are characterized by large day-night surface temperature differences. This may be indicative of high cloud base, a factor inhibiting rainfall.

The global precipitation field is reasonably well depicted by a linear combination of the two difference fields, the clear OLR minus the cloudy OLR, and the clear daytime OLR minus the clear nighttime OLR. Coefficients, appliable for the entire year, were derived by relating the global difference fields for each month of the FGGE year, 1979, to precipitation derived from rainguage measurements for the FGGE year, provided by Walker and Mintz (1987).

EOF analyses have been applied to ten day mean precipitation maps in different locations and seasons. The seasonal cycle, the 30 to 60 day oscillations, the monsoon trough over the Indian area, the Mei-Yu and Bai-Yu fronts over the East-China and Japan are well depicted in the first three EOFs and their principal components.

In conclusion, this study indicates that precipitation is derivable from space on a global scale. This technique is flexible and can be applied to other satellite observations of OLR used together with HIRS2/MSU soundings. It is useful for studying intraseasonal variability and atmospheric oscillations. When a long term record is available, it will be useful for studying intraannual and interannual varibility.

Table I

Downward flux at surface (Wm^{-2})

	LMD[1]	GLAS[2]	GFDL[3]	Wu-Kaplan
H_2O lines only	---	265.24	267.29	268.1
$H_2O + CO_2 + O_3$ (No Continuum)	300.69	300.69	302.06	301.1
Total with continuum	341.8	341.3	----	342.3

Upward Flux (Wm^{-2})

Total with continuum	284.	283.3		283.6

LMD[1]: Laboratorie de Meteorologie Dynamique
GLAS[2]: Goddard Laboratory for Atmospheric Sciences
GFLD[3]: Geophysical Fluid Dynamic Laboratory

Table II

Statistics of Global OLR Fields (Wm^{-2}) July 1979

FIELD	MEAN	STD DEV
HIRS	248.3	46.3
ERB	237.0	48.5
AVHRR	249.4	43.4
HIRS-ERB	11.3	6.2
HIRS-AVHRR	-1.1	7.5
AVHRR-ERB	12.4	10.0

5. REFERENCES

Gruber, A., and A. F. Krueger, 1984: The status of the NOAA outgoing longwave radiation data set. Bull. Am. Meteorol. Soc., 65, 958-972.

Janowiak, J. E., A. F. Krueger, P. A. Arkin, and A. Gruber, 1985: Atlas of outgoing longwave radiation derived from NOAA satellite data. NOAA Atlas No. 6, NOAA National Environmental Satellite Data and Information Service, Silver Spring, MD 44 pp.

Krishnamarti, V., 1982: The Documentation of the Wu-Kaplan radiation parameterization. NASA Tech. Memo 83926, NASA/Goddard Space Flight Center, Greenbelt, MD 93 pp.

Kyle, H. L. and K. L. Vasanth, 1986: Some characteristic differences of the earth's radiative budget over land and ocean derived from the Nimbus-7 ERB experiment. J. Climate Appl. Meteoro., 25, 959-981.

Ohring, G., A. Gruber, R. G. Ellingson, 1984: Satellite determination of the relationship between total longwave radiative flux and infrared window radiance. J. Climate Appl. Meteoro., 23, 416-425.

Rodgers, C. D., and D. C. Walshaw, 1966: The computation of infrared cooling rate in planetary atmospheres. Quart. J. Roy. Meteoro. Soc., 92, 67-92.

Susskind, J., J. Rosenfield, D. Reuter, and M. T. Chahine, 1984: Remote sensing of weather and climate parameterization HIRS2/MSU on TIROS-N. J. Geophys. Res., 89D, 11602-11608.

Susskind, J., D. Reuter, W. Baker, J. Pfaendtner, and T. Aro, 1987: The GLA Interactive Forecast-Retrieval-Analysis Cycle for the FGGE year. FGGE Hydrological Cycle Workshop, National Academy of Sciences, E. White editor, Airlie, VA, April 27-30, pp 98-112.

VERTICAL PROFILES OF HEATING DERIVED FROM IR-BASED PRECIPITATION ESTIMATES DURING FGGE SOP-1

Franklin R. Robertson
Earth Science and Applications Division
NASA Marshall Space Flight Center
Huntsville, AL 35812

Dayton G. Vincent
Department of Earth and Atmospheric Sciences
Purdue University
West Lafayette, IN 47907

1. INTRODUCTION

An adequate description of diabatic forcing by deep convection is fundamental to understanding many dynamical processes of interest in atmospheric science. Most researchers have approached the problem of estimating distributions of latent heating through analyses of the residuals Q1 and Q2 in the heat and moisture budgets (Yanai et al, 1973). Physical interpretation of the residuals places stringent requirements on data collection and analysis since observational and computational errors reside in these terms by definition.

This paper examines a methodology to provide an additional, complementary evaluation of moist diabatic processes using geostationary infrared (IR) data. Digital GOES West IR imagery is used to obtain precipitation fields which are independent of those inferred from residuals in heat budget analyses based on the the FGGE (First GARP Global Experiment) level III-b data sets. Vertical distributions of the associated heating are then obtained using the thermodynamic data from the level III-b analyses, one-dimensional cloud models and the satellite-estimated precipitation.

A discussion of the methodology is contained in section 2. Application of the technique to infer heating in the South Pacific Convergence Zone (SPCZ) during a portion of FGGE SOP-1 is considered in section 3 along with a comparison to heat budget calculations made using the ECMWF analyses. Sensitivity of the results to the rainfall spectrum and the assumed properties of the one-dimensional cloud models is considered in section 4.

2. METHODOLOGY

In estimating the diabatic heating field from satellite, we approach the problem in two steps. The first requirement is to obtain the vertically integrated net heating, or, equivalently, the precipitation that falls in association with the cloud field. This quantity is obtained by an empirical relationship between the cloud-top equivalent black-body temperature, T_b, and rainrate (Robertson, 1987). The problem then reduces to finding the resulting vertical distribution of this heating and the associated vertical eddy heat flux convergence. Adopting the procedure of Austin and Houze (1973) and Houze et al, (1980), we use large-scale temperature and moisture analyses to infer the thermodynamic characteristics of a population of clouds described by one-dimensional parcel theory. The mass fluxes of the clouds are then constrained to be those which reproduce the satellite-estimated precipitation. Subsequently, the cloud mass fluxes and the thermodynamic properties are used in calculating the heating profiles. Austin and Houze and Houze et al have relied upon radar data to obtain the precipitation and cloud top heights, referring to this approach as the "radar method" in contrast to the "synoptic method" of using heat and moisture budget residuals as constraints on the heating profile (Yanai et al, 1973; Ogura and Cho, 1973; Johnson, 1976). The present study differs from the "radar method" in that satellite imagery is the source for the precipitation and cloud top height information.

2.1 Precipitation estimates from GOES infrared imagery

Use of IR or visible imagery to estimate rainfall can be classified as an "indirect" approach since the satellite sensors respond primarily to suspended hydrometeors which mask any precipitation which may be present. The physical basis for indirect schemes lies mainly in the fact that, for deep convection and for sufficient spatial and temporal averaging, cold high clouds are well-correlated with precipitation and are signatures of upward motion in a locally saturated atmosphere. This relationship degrades significantly in middle latitudes where cold high clouds are not always associated with deep convection.

The particular algorithm was developed using raingauge data along the southeast coastal U.S. The algorithm expresses rainfall as a simple quadratic function of IR cloud top effective black-body temperature, T_b. Since the developmental data set relates pixel T_b's to hourly, point rainfall measurements, the correlation is quite low (-.36). However, averaging the pixel-size rain estimates over areas approximately 10^5 square kilometers and periods of 12h improves the correlation markedly since life-cycle effects have a substantial random component (Richards and Arkin, 1981). In testing the algorithm over the GATE B-Scale Array during a portion of Phase III a correlation of .85 was found between radar and satellite estimates. In using the algorithm one must address the possible sources of error introduced by transferring the algorithm from its developmental region to a new locale. Since raingauge measurements in the South Pacific are quite sparse it is clearly impossible to evaluate the area-averaged accuracy directly. Still, some measure of performance can be obtained by comparing single pixel estimates of rainfall to island gauge measurements. Using raingauge measurements at 43

locations for the period 10-18 January 1979, it was found that use of the original algorithm results in about a twenty percent over-estimate of the rainfall observed at the gauges. Therefore, in this study the original algorithm for rain rate,

$$R(\mathrm{mmh}^{-1}) = 7.04 + 11.10T^* - 4.26T^*, \qquad (1)$$

where

$$T^* = (T_b - 200)/50, \qquad (2)$$

is scaled by this factor.

Application of the algorithm to a digital IR image of T_b yields a corresponding image of estimated rainfall rate. Temporal averaging is accomplished by using 3h sequences of imagery and integrating over time to produce a 12h mean image. Spatial smoothing to a 2.5 degree lat x lon grid covering the region 10N to 42.5S and 110W to 170E is done by simple averaging within the 2.5 degree box centered on each ECMWF gridpoint.

In addition to the total rainfall rate the contribution by clouds with tops in a given temperature interval is obtained using the large-scale temperature field and assuming that the clouds are in thermal equilibrium with the environment. The area-averaged rain rate, R, is expressed as

$$R = \sum_{i=1}^{n} r_i, \qquad (3)$$

where

$$r_i = \frac{1}{M} \sum_{j=1}^{m} rr(T_{bj}), \qquad \text{for } T_b(p_{ti}) < T_{bj} < T_b(p_{bi}), \qquad (4)$$

and where n is the number of class intervals of cloud tops, M is the total number of pixels in a 2.5 degree lat x lon box, m is the number of pixels in the box within the temperature interval $T_b(p_{ti}) < T_b < T_b(p_{bi})$ and p_{ti} and p_{bi} are the top and bottom pressure levels bounding the ith cloud top class. The r_i are the the contributions to the area-average instantaneous rain rate, R, by each sub-ensemble. This rain rate spectrum derived from GOES IR imagery is employed as a constraint on the one-dimensional cloud processes and, thus, on the vertically integrated heating due to condensation.

2.2 Recovering vertical heating distributions via the cloud mass flux approach

Diagnostic studies of large-scale heat budgets commonly express the dry static energy equation in the form

$$Q1 - QR = \frac{\partial \bar{s}}{\partial t} + \nabla\, \overline{s\bar{V}} + \frac{\partial}{\partial p}\overline{\omega s} = L(\bar{c} - \bar{e}) - \frac{\partial}{\partial p}\overline{\omega' s'}, \qquad (5)$$

where ($\bar{}$) denotes a grid-scale quantity, ( )′ is a subgrid-scale departure, $\bar{s} = c_p\bar{T} + g\bar{z}$ is dry static energy, Q1 is the apparent heat source (Yanai et al, 1973), QR is radiative forcing, $\bar{c}$ and $\bar{e}$ are condensation and evaporation, respectively, and the remaining symbols have their conventional meteorological meaning. Many investigators (Ogura and Cho, 1973; Arakawa and Schubert, 1974; Johnson, 1976,) have used one-dimensional cloud models of varying complexity, along with their inherent assumptions, to express the right-hand side of (5) as

$$L(\bar{c} - \bar{e}) - \frac{\partial}{\partial p}\overline{\omega' s'} = \underset{(a)}{-M_c \frac{\partial \tilde{s}}{\partial p}} + \underset{(b)}{\int_0^{\lambda_o} \delta(s_u - \tilde{s})\, d\lambda} + \underset{(c)}{\delta^*(s^* - \tilde{s})} \underset{(d)}{- LE_e} \qquad (6)$$

M_c represents the net cloud mass flux which is the sum of convective updrafts (Arakawa and Schubert, 1974) and convective downdrafts (Johnson, 1976). The environmental dry static energy, $\tilde{s}$, is generally approximated by $\bar{s}$ which is derived through observed $\bar{T}$ and $\bar{z}$ fields. The entrainment parameter, λ, characterizes convergence of mass into the clouds and, by diluting their excess moist static energy ($c_pT + gz + Lq$), provides for a population of possible cloud heights. Discrete values of λ are found which result in updraft buoyancy vanishing at the level of mean cloud top pressure corresponding to each of the cloud ensembles. Lateral detrainment of cloud mass, δ, and cloud top detrainment of mass, δ^*, are the other two parameters which along with λ determine the shape of the cloud mass flux profiles. s_u^* corresponds to dry static energy at the top of the updrafts. LE_e is the evaporation of cloud condensate into the environment as a result of the mass detrainment process. The net heating associated with the convective condensation in (6) is thus represented by environmental subsidence effects accompanying the net cumulus mass flux,(a); lateral and cloud top detrainment of excess dry static energy,(b) and (c), respectively; and evaporation of condensate detrained into the environment, (d). Given additional information provided by the precipitation spectrum discussed in the previous section and assumed cloud scale water budget characteristics, M_c and E_e can also be diagnosed. Net condensational heating of the environment as given by (6) can then be evaluated.

Recent studies by Cheng and Houze (1979), Johnson and Young (1983) and Gamache and Houze (1983) have pointed to the importance of of mesoscale updrafts and downdrafts as components of convective systems active in accomplishing condensation, evaporation and vertical transport of energy. Including these components would provide additional terms in (6) involving mesoscale mass fluxes and their thermodynamic transports. Since their formulation would involve additional assumptions about poorly known parameters, we will account for these components only in an indirect fashion as described in section 2.4.

2.3 Cloud scale properties

Cloudscale properties are determined from 1-D equations of the form

$$\frac{\partial I(\lambda,p)}{\partial p} = \lambda(\tilde{I}(p) - I(\lambda,p)) + S(\lambda,p) \qquad (7)$$

where I is any cloud property, ($\tilde{}$) is the environmental value and S is a source or sink of $I(\lambda,p)$. In this study five possible cloud sub-ensembles corresponding to five discrete value of λ are recognized with cloud tops in the intervals 100-200mb, 200-300mb,...500-600mb. The updraft mass flux profile is given by

$$m_u(\lambda,p) = m_b n_u(\lambda,p) = \begin{cases} m_b \exp(\lambda(p-p_b)) & p_b \geq p \geq p^* \\ m_b \exp(\lambda(p^*-p_b)) \dfrac{(p-p_b)}{(p^*-p_b)} & p^* \geq p \geq p_t \end{cases} \quad (8)$$

where m_u is updraft mass flux, m_b is cloudbase mass flux, p_b and p_t are updraft cloudbase and cloud top pressures, respectively, and p^* is the pressure level above which entrainment ceases and only detrainment occurs. The resulting mass flux profiles increase exponentially with height to the level p^* and then decrease linearly to zero at the level of zero buoyancy. Early studies with spectral cloud models (Ogura and Cho, 1973) retained pure exponential profiles which put all mass detrainment in an infinitely thin layer at cloud top. Three-dimensional cloud model results suggest it is more realistic to expect detrainment to occur over an appreciable depth of the cloud (e.g. Klemp and Wilhelmson, 1978). We adopt such a profile in this study by setting $p^*=p_t+150$mb.

In a similar fashion downdrafts are modeled as inverted plumes with λ being opposite in sign to that used in the updrafts (Johnson, 1976):

$$m_d(\lambda,p) = m_o n_d = m_o \exp(-\lambda(p-p_o)) \quad (9)$$

where m_o is the mass flux at the top of the downdraft, p_o. Downdraft initial conditions are saturation at the ambient wet-bulb temperature T_w. The depth of the downdraft, p_b-p_o, is assumed to be three-quarters of the pressure depth of the updraft.

To obtain s_u and q_u, we substitute moist static energy, $h_m = s_u + Lq_u$ into (7) in which case $S(\lambda,p)=0$. Assumed cloud base conditions are zero virtual temperature excess and saturation specific humidity. If we further assume clouds are saturated and that pressure perturbation effects can be neglected, s_u and q_u can be retrieved (Arakawa and Schubert, 1974). With the thermodynamic characteristics and vertical mass flux profile shape determined as a function of λ, the updraft condensation (downdraft evaporation) is proportional to the initial updraft (downdraft) mass flux for each sub-ensemble. The equation for vertically integrated condensation is written

$$C_u(\lambda) = m_b(\lambda) \int_{p_t}^{p_b} n_u(\lambda,p) \left[\frac{\partial q_u(\lambda,p)}{\partial p} - \lambda(\tilde{q}(p) - q_u(\lambda,p) \right] dp \quad (10)$$

where $m_b(\lambda)$ is the cloud base mass flux, $\tilde{q}(p)$ is the environmental specific humidity [assumed equal to $\bar{q}(p)$], n_u is the normalized updraft mass flux profile defined by (8), and p_t and p_b are the cloud top and cloud base pressures. Profiles of h_d, q_d and s_d are retrieved in a similar fashion to the updrafts and the expression for vertically-integrated evaporation rate in the downdrafts is

$$E_d(\lambda) = m_o(\lambda) \int_{p_t}^{p_o} n_d(\lambda,p) \left[\frac{\partial q_d(\lambda,p)}{\partial p} + \lambda(\tilde{q}(p) - q_d(\lambda,p) \right] dp \quad (11)$$

where p_o is the starting pressure level of the downdraft, $m_o(\lambda)$ is the initial downdraft mass flux and n_d is the normalized downdraft mass flux profile. Downdrafts are assumed to detrain only below cloud base. Equations (10) and (11) can be solved for m_b and m_o if $C_u(\lambda)$ and $E_d(\lambda)$ are known. We determine $C_u(\lambda)$ and $E_d(\lambda)$ via the satellite estimated rainfall of each sub-ensemble and the cloud scale water budget.

2.4 Cloud scale water budget

We adopt a cloud scale water budget of the form

$$C_u(\lambda)d\lambda = [R(\lambda) + E_d(\lambda) + E_e(\lambda)]d\lambda. \quad (12)$$

Houze et al (1980) note that, in general, both convective and mesoscale processes should be treated as distinct components. Mesoscale components analogous to those above must be evaluated along with a term allowing condensate flux between convective entities and the mesoscale anvil. Recent investigations suggest that while almost fifty percent of total mesoscale convective system rainfall may actually fall from accompanying stratiform clouds, more than half of the condensate in these clouds may originate in convective updrafts (Gamache and Houze, 1983). Evidence from a number of studies suggests that precipitation efficiency for convective cells lies typically in the range of .2 to .6 (Fritsch and Chappell, 1981). Part of this low efficiency is due to the export of condensate from convective cells to mesoscale anvils (Houze et al, 1980) where it falls as rain or is evaporated in mesoscale downdrafts. Since we are forcing the model clouds to account for all rainfall and since the convective efficiencies do not account for the convectively generated rain that falls from mesoscale anvils, we adopt a precipitation efficiency value $R(\lambda)/C_u(\lambda)=.60$ as being representative for total cloud efficiency.

In determining values for $E_e(\lambda)$, a maximum upper bound for the evaporation of detrained condensate can be obtained from

$$E_e(\lambda)d\lambda|_{max} = \delta q_l(\lambda,p) \quad (13)$$

where q_l is cloud water content. q_l is estimated from a cloud condensate equation (Yanai et al, 1973),

$$\frac{\partial m_u(\lambda,p) q_l(\lambda,p)}{\partial p} = \delta q_l(\lambda,p) - C_u(\lambda,p) + c_o q_l(\lambda,p), \quad (14)$$

where c_o is an autoconversion parameter and $C_u(\lambda,p)$ is condensation derived by the non-integrated form of (10). However, detrained condensate is obviously required to provide a source for mesoscale rain falling outside of updrafts and force downdrafts. These effects are crudely modeled by assuming that some small fraction (one-fourth) of the detrained water is re-evaporated into the environment. With $C_u(\lambda)$, $R(\lambda)$ and $E_e(\lambda)$ known, $E_d(\lambda)$ is determined as a residual in (12) and $m_b(\lambda)$ and $m_o(\lambda)$ can be determined from (10) and (11).

2.5 Grid-scale stratiform precipitation

In addition to stratiform precipitation accompanying mature mesoscale convective systems, saturated ascent can occur in the atmosphere where potentially instablity is absent. In this situation, many researchers (e.g. Edmon and Vincent, 1976) have used an approximation of the form

$$Q1-QR = -L\bar{\omega}\frac{\partial \bar{q}_s}{\partial p} \qquad \text{for } \bar{q}_{th}(p) < \bar{q}(p) < \bar{q}_s(p) \quad (15)$$

where $\bar{q}_s$ is saturation specific humidity and $\bar{q}_{th}$ is some threshold value; typically $\bar{q}_{th}/\bar{q}_s$ is specified as 80 percent. Equation (15) constitutes a special case of (5) in which vertical eddy transports vanish by definition and evaporation of condensate produced by grid-resolvable upward motion in saturated air is assumed negligible. For application in the present study, the vertical integral of (15) is simply the satellite-estimated precipitation. Each gridpoint having satellite-estimated precipitation is examined to determine whether sufficient potential instability exists to insure that the vertical mean cloud scale temperature perturbation is positive. If this is not the case, (15) is invoked. The vertical distribution of heating is obtained by first assuming that the profile $\bar{\omega}$ is a parabolic in shape and is zero both at the surface and the pressure level corresponding to the highest cloud top observed in the GOES imagery. It is further assumed that the region between 850 mb and the highest cloud top pressure is saturated. With the satellite-estimated precipitation as an integral constraint and using $\bar{q}_s$ derived from the large-scale temperature profiles, $\bar{\omega}$ and $\partial\bar{q}_s/\partial p$ are diagnosed at each level.

3. APPLICATION TO A TROPICAL ENVIRONMENT

An application of this technique to a convectively active maritime environment is now discussed. The region considered (10°N, 42.5°S, 110°W, 170°E) encloses the South Pacific Convergence Zone during 10-18 January, 1979. It is apparent when looking at the SPCZ with three-hourly GOES imagery that the cloud band is highly convective in nature. One would expect an IR method to perform reasonably well in deriving precipitation estimates consistent with global FGGE analyses (several degrees lat x lon, 6-12h intervals). The particular data set used in this study is the Level III-b analysis produced by ECMWF reinterpolated to a 2.5° lat / lon grid. For a more complete description of this data set see Vincent (1982).

Figure 1. compares vertically-integrated heating, Q1, to the satellite-estimated precipitation. Since Q1 is computed as a residual it contains also net radiative cooling and surface sensible heat flux. Positive values of Q1 clearly outline the convective region of the SPCZ. Negative values are all $\geq -.3$ mmh^{-1} and correspond to regions of radiative cooling. GOES W precipitation estimates are notably higher than Q1 in the equatorward portion of the cloud band. This disagreement could be due in part to weak tropical vertical motions and divergent winds which were characteristic of the original FGGE III-b ECMWF analysis (Lin and Mock, 1986).

The precipitation spectrum as determined from the GOES data and (4) is shown in Fig. 2. The shape of this distribution is similar to the GATE results derived from radar (Cheng and Houze, 1980). The large contribution to total precipitation by high clouds also requires that these model clouds contain a large fraction of the upward mass flux. Profiles of diabatic heating from the satellite-estimated precipitation have been derived by evaluating (6) and are shown in Fig. 3. The dominant forcing comes from the compensating mass flux term. Detrainment of excess dry static energy also contributes significantly in upper levels where, due to the shape of the updraft mass flux profiles dictated by (8), detrainment of relatively warm air from updrafts is occuring. Opposing this

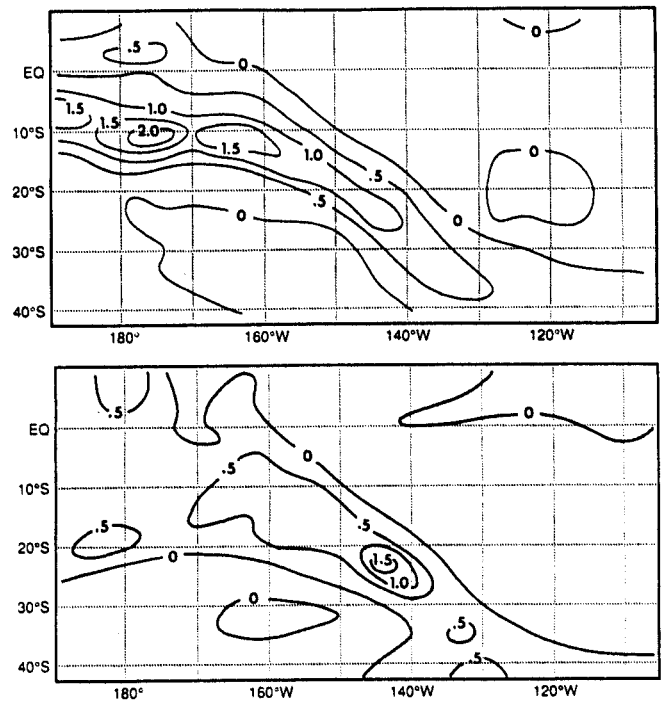

Figure 1. (Top) Satellite-estimated precipitation rate (mm h^{-1}) for 10-18 January 1979. (Bottom) Vertically-integrated heat budget residual, Q1, determined from ECMWF data for same period. Units are equivalent precipitation rate (mm h^{-1}).

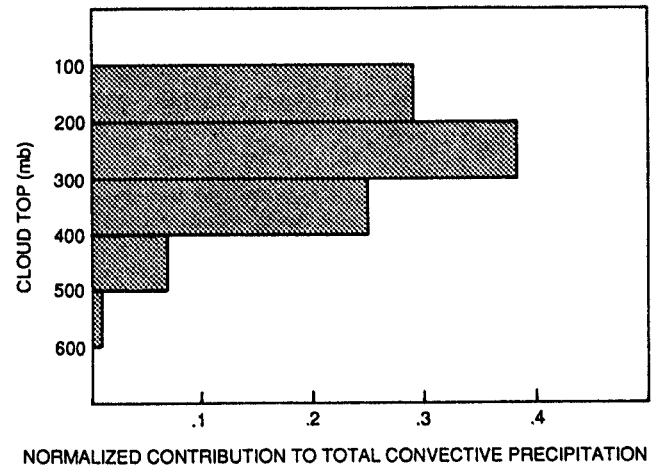

Figure 2. Contribution to total convective precipitation by each cloud top category. Amounts are normalized by total amount.

heating effect is cooling due to evaporation of detrained condensate. Net heating from these processes yields a maximum near 450 mb. This profile can be compared to that derived from the heat budget calculations using the ECMWF analyses in Fig. 4. Net radiative cooling was computed as follows: In regions of the computational area where 12h mean vertical motion was downward, QR was assumed to equal Q1. In regions of upward motion, radiative calculations from Cox and Griffith (1979) for the A/B ship array during disturbed periods of GATE Phase III were used. The two calculations were then areally weighted. The shapes of both

satellite-estimated and budget-determined heating profiles are quite similar with the satellite-diagnosed profile maximizing slightly higher.

4. SENSITIVITY ANALYSIS

Uncertainties in the vertical distribution of heating are examined by considering the water budget parameters in (12) and the satellite-derived precipitation spectrum. The results of a sensitivity analysis using data during the period 0000 to 1200 GMT 14 January 1979 are shown in Fig. 5. Precipitation efficiency values of .3 and .9 are considered extreme bounds since we are considering the efficiency of the entire precipitating cloud ensemble– convective and mesoscale. From (12) it is seen that increasing (decreasing) the efficiency requires a decrease (increase) in the sum of E_e and E_d if R is to remain fixed. The results in Fig. 5 suggest a rather large impact for assumed low precipitation efficiency. Low efficiency results in stronger (weaker) diagnosed heating above (below) 550 mb since proportionately larger downdraft mass fluxes are required to evaporate the unrealistically large amount of condensate via downdrafts in the lower portion of the cloud. The M_c profile thus maximizes higher in the troposphere. However the pronounced lower tropospheric cooling departs substantially from that indicated by the residual method and cannot be regarded as very likely in the present study. The partitioning of condensate evaporation between downdrafts and the environment is tested by arbitrarily increasing the cloud liquid water content by a factor of 3. This forces the largest portion of the evaporation to occur in the cloud top environment and consequently yields weaker downdrafts. This situation also appears unlikely since it requires cloud water contents to average near 5.0 g Kg^{-1} in the upper portion of the clouds and reduces upper tropospheric heating to an unrealistically small amount in comparison to the budget results.

Uncertainties in the precipitation spectrum can produce errors in the net cloud mass flux profile via (10) and (11). This effect was examined in two tests by arbitrarily specifying two different precipitation spectra. In the first test, clouds in the topmost two layers (100-200 mb and 200-300 mb) were assumed to produce all the precipitation. The level of maximum heating was shifted upward slightly to 400 mb and intensified while heating was reduced below about 500 mb. A second test specified that precipitation was produced equally by the top four layers. This resulted in a lowering of the maximum heating level to 550 mb and produced more (less) heating below (above) the level of maximum heating. Each of these specified precipitation spectra is quite different from that estimated GOES data and that determined from radar data by Cheng and Houze (1979).

5. CONCLUDING REMARKS

This study has examined a method to retrieve vertical profiles of heating and cooling due to moist diabatic processes. GOES IR imagery was used first to estimate the column-integrated heating and then to constrain mass flux profiles in one-dimensional cloud models. This substantial degree of independence from heating obtained via the residual method is a valuable attribute which can be used to establish more confidence in quantitative estimates of condensational heating. It is

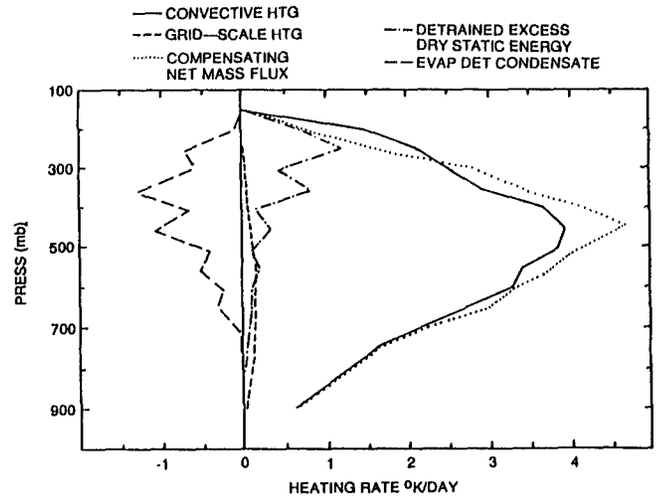

Figure 3. Contributions to area-averaged, time-mean heating rate as diagnosed by satellite-estimated precipitation and equations (6) and (14).

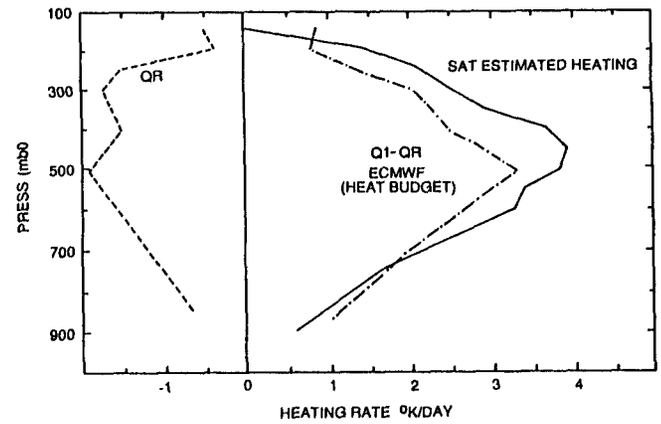

Figure 4. Comparison of satellite-estimated heating versus ECMWF heat budget estimates of Q1-QR.

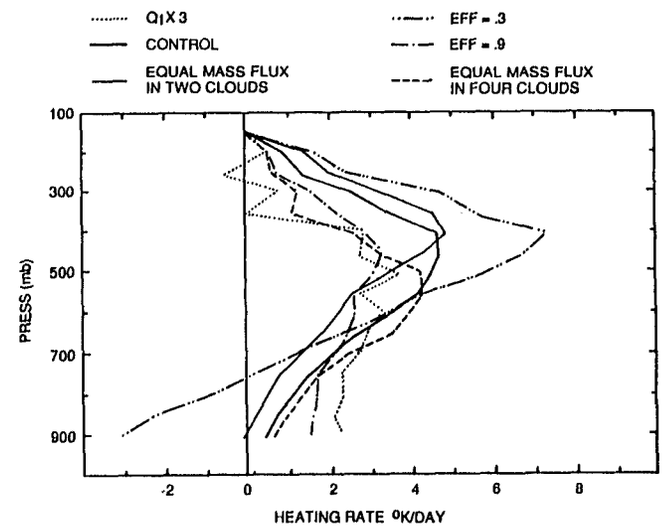

Figure 5. Results of sensitivity analysis of satellite-derived heating using data from 0000-1200 GMT 14 January 1979. See text in section 4. for explanation of experiments.

likely that atmospheric observations over oceanic regions will rely upon remote sensing methods for the forseeable future. Techniques to utilize satellite measurements more effectively in defining the variability of tropical forcing need to be formulated and tested.

7. ACKNOWLEDGEMENTS

This research was conducted as part of a joint project between Marshall Space Flight Center and Purdue University under contract NAS8-35187 and the auspices of the NASA Global Scale Atmospheric Processes Research Program, Dr. Robert Curran, Program Manager.

8. REFERENCES

Arakawa, A. and W.H. Schubert, 1974: Interaction of a cumulus cloud ensemble with the large-scale environment, Part I. J. Atmos. Sci., 31, 674-701.

Austin, P.M. and R.A. Houze, 1973: A technique for computing vertical transports by precipitating cumuli. J. Atmos. Sci.,30, 1100-1111.

Cheng, C.-P. and R.A. Houze, Jr., 1979: The distribution of convective and mesoscale precipitation in GATE Radar Echo Patterns, Mon. Wea. Rev., 107, 1370-1381.

Cox, S.K. and K.T. Griffith, 1979. Estimates of radiative divergence during Phase III of the GARP Atlantic Tropical Experiment: Part II. analysis of Phase III results. J. Atmos. Sci.,36,586-601.

Edmon, H.J., Jr. and D.G. Vincent, 1976: An application of two tropical parameterization schemes of convective latent heat release in midlatitudes. Mon. Wea. Rev.,104,1141-1153.

Fritsch, J.M. and C.F. Chappell, 1980: Numerical prediction of convectively driven mesoscale pressure systems. Part I: Convective parameterization. J. Atmos. Sci., 37, 1722-1733.

Gamache, J.F. and R.A. Houze, Jr., 1983: Water budget of a mesoscale convective system in the tropics. J. Atmos. Sci.,40, 1835-1850.

Houze, R.A., Jr., C.-P. Cheng, C.A. Leary and J.F. Gamache, 1980: Diagnosis of cloud mass and heat fluxes from radar and synoptic data. J. Atmos. Sci., 37, 754-773.

Johnson, R.H., 1976: The role of convective-scale precipitation downdrafts in cumulus and synoptic-scale interactions,J. Atmos. Sci., 33, 1890-1910.

Johnson, R.H. and G.S. Young, 1983: Heat and moisture budgets of tropical mesoscale anvil clouds. J. Atmos. Sci.,40, 2138-2147.

Klemp, J.B. and R.B. Wilhelmson, 1978: The simulation of three-dimensional convective storm dynamics. J. Atmos. Sci.,35,1070-1096.

Lin, R.-Q. and D.R. Mock, 1986: A test of the ECMWF model in tropical synoptic-scale diagnosis. Mon. Wea. Rev.,114,1519-1538.

Ogura, Y. and H.-R. Cho, 1973: Diagnostic determination of cumulus cloud populations from observed large-scale variables, J. Atmos. Sci.,30,1276-1286.

Richards, F. and P. Arkin, 1981: On the relationship between satellite-observed cloud cover and precipitation. Mon. Wea. Rev., 109, 1081-1093.

Robertson. F.R., 1987: Use of GOES IR data in estimating Synoptic-scale rainfall: algorithm development and transferability. Submitted to J. Clim. and Appl. Met.

Yanai, M., S. Esbensen, and J.-H. Chu, 1973: Determination of bulk properties of tropical cloud clusters from large-scale heat and moisture budgets, J. Atmos. Sci., 30, 611-627.

7.10

THE EVALUATION OF SIMPLE APPROACHES FOR THE DELINEATION OF RAIN AREA FROM SATELLITE IMAGERY

Anastasios A. Tsonis

Department of Geological and Geophysical Sciences
University of Wisconsin-Milwaukee
Milwaukee, WI 53201

1. INTRODUCTION

The delineation of rainfall from satellite visible and/or infrared imagery has received well deserved attention in the past 10 years. As a result many techniques have been developed which produce maps of the rainfall extent using visible and/or infrared information. Those techniques can be divided into three major categories: 1) the indexing techniques, 2) the life history methods and 3) the bispectral methods. According to the indexing techniques (for a review see Barrett and Martin, 1981 rainfall depends on the cloud type. The rainfall area is found after the cloud shave been classified to various types according to their spectral properties. The life history methods make use of information provided by at least two preceding half-hour GOES infrared images in order to estimate point rainfall rates (Scofield and Oliver, 1977 and Griffith et al, 1978) and volumetric rainrates (Stout et al. 1979). These techniques are based on the observed growth of the clouds and have provided very useful results especially in cases of strong convection. According to the bispectral methods the rain area is determined using information from both images (Lovejoy and Austin, 1979 and Bellon et al, 1980). Basically, these techniques define an optimum "boundary" in the visible/infrared domain which is used to discriminate between rain and no-rain. This optimum boundary is defined using a pattern recognition technique involving satellite and coextensive radar data. Apparently, these methods depend on radar data and therefore their applicability is limited to only areas over which adequate radar coverage is available. Lately Tsonis and Isaac (1985) developed a technique according to which the above mentioned optimum boundary is determined without the need of coextensive radar data. Their technique makes use of the bivariate frequency distribution in the visible/infrared domain. It has been shown (Tsonis, 1984a) that the observed peaks of such distribution correspond to different classes. Tsonis and Isaac (1985) showed that the peaks that correspond to raining clouds tend to cluster in a well defined region of the visible/infrared domain thus allowing their discrimination from the other classes (clear skies, nonraining clouds, etc.). After that the delineation of the rain area from the raining clouds is based on an optimum visible threshold which depends on the day, time and type of precipitation. Lately, Wu et al. (1985) and Tsonis (1987) presented pattern recognition approaches for classification of the satellite derived rain area into light moderate and heavy rainrate subareas.

All the above mentioned and other techniques have reported good results and have added to our knowledge of rainfall estimation from satellite imagery. The very well recognized problem however, is the fact that all the above techniques are more or less "localized". This means that some methods are adequate for the tropics, some for the midlatitudes, some for instantaneous delineation of rain area, some for rainfall mapping over a long time, some for severe weather, etc. Even though each one of the above techniques satisfies a need for the region for which it was developed, it is not certain that it will work in some other region of the world. Part of the problem may be that most of these methods exhibit a high degree of sophistication which is usually coupled with the climatology of the region. This combination on one hand results in good rainfall estimation in a specific region but on the other hand makes the scheme "rigid" and "localized". This may be the reason that in practice much simpler approaches are employed (Martin and Howland, 1986 and Arkin and Meisner, 1987, for example). Undoubtedly, simpler approaches are more flexible and, therefore, are more easily applied over different regions and in larger time and space scales. Simple approaches can result in realistic convective rainfall estimates (Arkin and Meisner, 1987) but a detailed evaluation of their performance has not yet been given. Partly, this is due to the lack of adequate ground truth systems.

In view of the foregoing facts a very interesting question arises: What is the price paid by employing simple approaches? What is the accuracy loss

due to simplicity? The purpose of this work is to evaluate in detail the skills of simple approaches in estimating mesoscale instantaneous rainfall and to compare the results with results obtained by more elaborate techniques on the same and on different data sets.

2. DATA

The data set used in Tsonis and Isaac (1985) will be used to achieve the objectives of this work. This data set consist of coextensive satellite and radar data.

The satellite data used in this work are GOES East visible (0.54 - 0.70 μm wavelength) and infrared (10.5 - 12.6 μm wavelength) images. The temporal resolution of the satellite data is 30 minutes and the spatial resolution is 4 X 4 km. It should be noted at this point that the true resolution of the sensed infrared images is 8 X 8 km. From these images, 4 X 4 km resolution images have been constructed for a better resolution equivalence between the infrared and visible data (Bellon, 1979). The intensity range of the visible image is 0 - 63 and that of the infrared is 0 - 255.

The visible count is taken to be an indication of cloud thickness while the infrared count refers to cloud or land temperature. The infrared count C_{IR} is an approximation to the temperature T of the emitting cloud or land by the conversion formula

$$T = 330^\circ K - \frac{C_{IR}}{2} \text{ for } C_{IR} \leq 176,$$

$$T = 418^\circ K - C_{IR}, \text{ for } C_{IR} \geq 176,$$

The relation between visible count C_{VIS} and cloud thickness is more intricate and uncertain. The three dimensional cloud structure, its composition and solar zenith angle are the main factors influencing the computed thickness. Normalization, taking into account the sun's elevation angle from the horizon (z), has been applied to the visible data. The normalization factor is simply taken equal to $1/\sin^{1/2}(z)$. More information on the normalization of the visible data can be found in Bellon et al 1982. The data were tested for relative shifts between the visible and infrared images according to Tsonis (1984b). No such shifts were observed.

The analysis of the data was restricted to the area in Ontario, Canada, which is covered by the C-band Woodbridge weather radar (Crozier and Scott, 1981), indicated by the dark circle in Fig. 1. Table 1 gives a summary of the satellite and radar data used in this study. The radar data used in this study are echo top maps. The echo top maps show the maximum height above the ground of the observed radar echoes. Therefore, an echo top map will indicate the areal extent of the rain, independent of altitude. The echo top maps do not carry an rainfall rate information but they give a better indication of the actual areal extent of the rain over a given area (Tsonis and Isaac, 1985).

3. APPROACH

A method which delineates the rain area by using a single threshold from a single image (visible or infrared) is apparently the simplest possible. Since the purpose of this work is to evaluate the skills of very simple approaches. The accuracy of single thresholding is evaluated in detail next.

The evaluation of the rain area delineation techniques is usually based on the following variables.

N_N number of points correctly classified no-rain
N_R number of points incorrectly classified no-rain (misses)
R_N number of points incorrectly classified rain (false alarms)
R_R number of points correctly classified rain (hits).

Accordingly, the satellite delineated rain area can be expressed as:

$$\hat{A}_R = R_N + R_R$$

For the following formulations, A_R will denote the radar rain area as indicated by the radar echo top maps. From the above notation, many statistics have been devised in order to evaluate a rain area estimation method using satellite data. The most commonly used are:

1) the probability of detection (POD) defined as

$$POD = R_R/A_R;$$

2) the false alarm ratio (FAR) defined as

$$FAR = 1 - (R_R/\hat{A}_R);$$

3) the percent error f defined as

$$f = (N_R + R_N)/(R + N),$$

where

$$R = R_N + R_R,$$
$$N = N_N + N_R.$$

A perfect method will give POD = 1, FAR = 0 and f = 0. However, none of these statistics can be considered as more representative of the success of the method. Each statistic gives additional

information about the success of the rain area delineation from the satellite data. For example, the POD gives an idea of the ability of the scheme to "find" the rain. However, a scheme could create five or ten times larger rain area than the actual and still give a POD of one. Therefore, high POD should be accompanied by a small FAR in order to be meaningful. The percent error is representative of the error in rain area delineation with respect to the total area over which the method is applied. The percent error could be small even when POD is low and FAR is high, especially when we are dealing with small precipitation areas. The reverse could be the case as well. For direct comparison between different techniques more than one statistic could be used.

4. RESULTS AND COMPARISON WITH OTHER METHODS.

Figure 2 shows the average values for POD, FAR and the percent error as a function of the visible threshold. Selective error bars indicate observed standard deviations. Figure 3 is similar to Fig. 2 but for the infrared threshold. The general shape of these curves is justified. For very low threshold (visible or infrared) too much rain area is usually delineated. This means that R --> A_R and $R_R/\hat{A}_R << 1$. Thus, POD -->1 and FAR --> 1. At the same time N_R --> 0 and thus $f = R_N/A$ where $A = R + N$ (the radar covered area). Thus, for very small thresholds the average percent error will be proportional to the average R_N which should be close to $A - \bar{A}_R$ ($\bar{A}_R$ is the average rain area for the cases studied). As we increase the threshold we obviously delineate smaller rain areas (FAR --> 0) but at the same time we may miss some rain (POD will decrease). Because by this method we "approach" some optimum threshold we should expect that the percent error will decrease as well. For very high threshold values we delineate very small rain areas. Therefore, in this case $R_R \approx \hat{A}_R$ --> 0. Thus POD$\approx$FAR --> 0. At the same time R_N --> 0 and thus $f = N_R/A$. Thus, for very high thresholds the average percent error will be proportional to the average N_R which will be close to $\bar{A}_R$. Therefore, POD and FAR should decrease monotonically as a function of the threshold (visible or infrared). The percent error should decrease up to some threshold and then it may increase for high thresholds. In addition, for very low thresholds one always delineates too much rain with the consequence that one always obtains POD$\approx$ 1. Similarly for very high thresholds one always delineates very little rain thus obtaining always POD $\approx$ 0.0. Because of that one will expect a smaller standard deviation for very low and very high thresholds. Similar arguments can be extended for FAR.

Unfortunately the above statistics can not be unified in order to quantitatively evaluate a technique. The evaluation of the results is therefore let to the user and should be compared to results reported in a similar fashion from other methods.

As Figs 2 and 3 indicate,using a visible threshold of 50 the following mean (standard deviation) values are obtained: POD = 0.62 (0.13), FAR = 0.38 (0.16) and f = 0.22 (0.06). The corresponding values for a visible threshold of 52 are 0.53 (0.14), 0.34 (0.16) and 0.19 (0.06). In the infrared domain a threshold of 170 (-28°C) yields the following values: POD = 0.60 (0.14), FAR = 0.40 (0.18) and f = 0.30 (0.07). These values change to 0.48 (0.14), 0.30 (0.17) and 0.26 (0.08) respectively if an infrared threshold of 180 (-35°C) is used. In general, it seems that "an optimum" threshold in the visible will be more efficient than an optimum threshold in the infrared. This is consistent with previous findings of Tsonis and Isaac (1985), Lovejoy and Austin (1979) and many others that the visible images are about 10% - 15% more efficient than the infrared images in delineating the rain area. It is interesting to note that the sum between the average values of the percent error for very low and very high thresholds should be approximately equal to $A/A - \bar{A}_R/A + \bar{A}_R/A = 1$. As it can be seen in Figs 2 and 3 this is true for this analysis.

The above noted values are very comparable to those reported in Tsonis and Isaac (1985) for the same data set obtained according to a much more elaborate technique. Tsonis and Isaac (1985) reported the following average statistic values: POD = 0.66 (0.12), FAR = 0.37 (0.14) and f = 0.20 (0.055) These values are only slightly different than those obtained by using, for example, a visible threshold of 50 (mean accuracies decrease by approximately 5%) or by using an infrared threshold of 175 (mean accuracies decrease by approximately 20%). The above noted results are also comparable to those reported by Lovejoy and Austin (1979). According to their approach the rain area is obtained by pattern recognition between visible, infrared and coextensive radar data. For a specific area (over which coverage by a training radar is available), the probability of rain is derived by considering the bivariate frequency distributions in the visible/infrared domain of the raining and of the nonraining points. The derived probability of rain is then applied outside the area covered by the training radar. The success of the method outside the training area is usually evaluated by another radar (verifying radar). The above techniques show good skills in

delineating the rain area over the range of the training radar but the accuracy decreases with distance outside that range. In their analysis over the area covered by the radar they report an average value for the POD of 0.55 (0.14) and an average value for the percent error of 0.13 (0.04). Both the above techniques are highly sophisticated and have reported high accuracies. Despite, however, their sophistication they result in only slightly better estimation of rain area compared to very simple single thresholding. Direct comparison with other techniques is rather difficult mainly because 1) the purpose for which they have been developed is somewhat different, 2) detail evaluation of the accuracy of many schemes has not been performed and 3) the statistics used to evaluate their performance are different. In general, everybody will agree that very few techniques dealing with estimation of rainfall from satellite imagery result in success of the order of 60-70% and/or are often accurate within a factor of two of what actually happened.

The above reported analysis considered convective and non-convective cases together. The results do not change significantly when they are considered separately but in general single thresholding works somewhat better in convective cases. A classic example and support of the finding reported here is the work by Negri et al (1984), where the evaluation in detail of the Griffith-Woodley Technique (GWT) (Griffith et al, 1978) was performed. The GWT technique is a life-history technique and it calculates rain amounts using an elaborate technique which involves the past history of the clouds. Their analysis suggests an average percent error of about 130%. They then went on to simplify the GWT by effectively eliminating the need of cloud life history. The result was a much lower estimate for the percent error of about 40%. They then concluded that "...the GWT rain volume calculation and the GWT apportionment algorithm are unnecessarily complicated..." This is the point that I am trying to make in this report as well.

5. CONCLUSIONS AND REMARKS

The need for rain estimation on a larger or a global scale has been lately not only recognized but it seems to be a necessity if we were to improve our understanding about climate and its changes in time scales longer than a month or so. Towards this goal a "unified" scheme for rainfall estimation from satellite imagery should be developed. Apparently, such a scheme if it were to be applied on a global scale it should be accurate and as simple as possible. Thus some assessment of the accuracy of simple approaches and some investigation of the accuracy loss when results obtained by simple methods are compared to results obtained by more elaborate techniques should be made.

This assessment was made here in terms of single thresholding and instantaneous rain area delineation at a spatial resolution of 4 X 4 km. It was found that in general very little loss of accuracy will be lost if simple approaches will be considered. This loss of accuracy will be compensated by less time for processing the data, more flexibility (and therefore applicability of the results), and less cost. The results reported here deal specifically with instantaneous rain area delineation and they do not imply that more elaborate techniques are useless. They suggest, however, that accuracy requirements should be critically addressed and investigated before a scheme is employed. The results reported here may have implications for the large scale and long time-scale estimates of rain which are results of averaging of many sequences of smaller scale estimates. The link or interaction between smaller and larger scales is not very well understood. Nonlinearities in the atmosphere may result in large fluctuations in the large scale from a small deviation in a smaller scale. In such a case if the error in estimating some variable (such as rain) in a smaller scale is significant should a large scale mean be considered as adequate? From the results reported here the loss of accuracy is rather small and therefore simple techniques may be our hope for a "unified" but adequate scheme for an effective estimation of rain from satellite imagery over large scales (space and time).

And why simple approaches should perform as satisfactory as more complicated approaches? Delineation of rain from visible and infrared imagery is based on the fact that thick (high visible responses) and tall (high infrared responses) clouds will most likely precipitate. That is all the physics that enter this problem. Rainfall, however, is not that simple. Rainfall exhibits an extreme variability and complicated physics. When the sources of detecting precipitation are based on one or two parameters which may not even be directly related to precipitation, I believe that simple approaches have as good a chance of success as the very complicated ones.

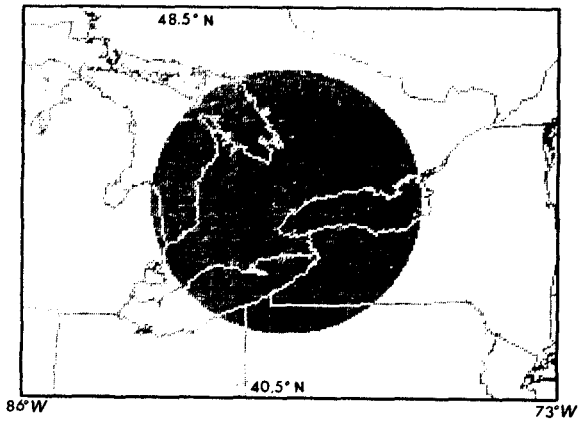

Fig. 1: The geographical area considered in this study. The satellite data analysis is restricted inside the dark circle which represents the area covered by the Woodbridge weather radar.

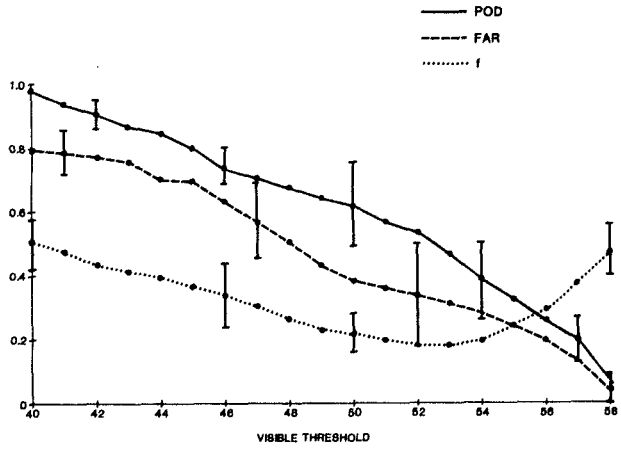

Fig. 2: Average probability of detection (POD), false alarms ratio (FAR) and percent error (f) as a function of the visible threshold. Selective error bars indicate observed standard deviations.

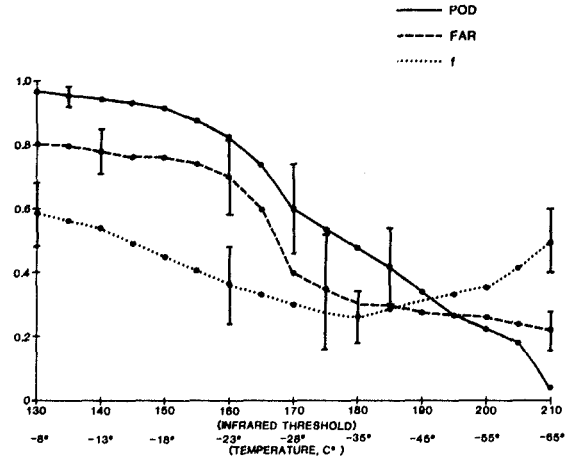

Fig. 3: As in Fig. 2 but for infrared thresholds.

Date	Time (GMT)	Type
4 July 1983	2030	Convective
	2230	Convective
21 July 1983	1730	Convective
	1930	Convective
	2130	Convective
29 July 1983	1400	Nonconvective
	1600	Nonconvective
	1800	Nonconvective
	2000	Nonconvective
	2200	Nonconvective
13 May 1984	1530	Nonconvective
	1730	Nonconvective
	1900	Nonconvective
23 May 1984	1300	Nonconvective
	1500	Nonconvective
	1700	Nonconvective
	1930	Convective
	2100	Convective

Table 1: Summary of the data used in this study

REFERENCES

Arkin, P.A. and B.N. Meisner, 1987: The relationship between large scale convective rainfall and cold cloud over the Western Hemisphere during 1982-1984. Mon. Wea. Rev., 115, 51-74.

Barrett, E.C. and D.W. Martin, 1981: The Use of Satellite Data Rainfall Monitoring. Academic Press, 340 pp.

Bellon, A., 1979: The development of a real-time automated system for short -range precipitation forecasting using combined radar and satellite data. Final report to AES (DSS) Contract OSU 78-0056, DSS File 01SU.KM601-8 -025 (available from Stormy Weather Group, McGill University), 92 pp.

Bellon, A., S. Lovejoy and G.L. Austin, 1980: Combining satellite and radar data for the short range forecasting of precipitation. Mon. Wea. Rev., 108, 1554-1566.

Bellon, A., A. Kilambi and G.L. Austin, 1982: Analysis of the navigational error and development of an automated visible normalization procedure and severe weather delineation technique using GOES satellite imagery. McGill Radar Weather Observatory Rep., 78 pp.

Crozier, C.L., and J.W. Scott, 1981: A C -band weather radar system with spherics to serve multiple diverse users in the Canadian climate. Reprints 20th Conf. on Radar Meteorology, Boston, Amer. Meteor. Soc., 749-756.

Griffith, C.G., W.L. Woodley, P.G. Grube, D.W. Martin, J. Stout and D.N. Sikdar, 1978: Rain estimation from geosynchronous satellite imagery - Visible and infrared studies. Mon. Wea. Rev., 106, 1153-1171.

Lovejoy, S. and G.L. Austin, 1979: The delineation of rain areas from visible and IR satellite data for GATE and mid -latitudes. Atmos-Ocean, 17, 77-92.

Martin, D.W. and M.R. Howland, 1986: Grid history: A geostationary satellite technique for estimating daily rainfall in the tropics. J. Climate Appl. Meteor. 25, 184-195.

Negri, A.J., R.F. Adler and P.J. Wetzel, 1984: Satellite rain estimation: An analysis of the Griffith-Woodley technique. J. Climate Appl. Meteor., 23, 102-116.

Scofield, R.A. and V.J. Oliver, 1977: A scheme for estimating convective rainfall from satellite imagery. NOAA Tech. Memo. NESS 86, 47 pp.

Stout, J.E., D.W. Martin and D.N. Sikdar, 1979: Estimating GATE rainfall with geosynchronous satellite images. Mon. Wea. Rev., 107, 585-598.

Tsonis, A.A., 1984a: Determination and correction of the relative shift between the visible and thermal infrared GOES sensor images, Int. J. Remote Sensing, 5, 975-979.

Tsonis, A.A., 1984b: On the separability of various classes from the GOES visible and infrared data. J. Climate Appl. Meteor., 23, 1393-1410.

Tsonis, A.A. and G.A. Isaac, 1985: On a new method for instantaneous rain area delineation in the midlatitudes using GOES data. J. Climate Appl. Meteor. 24, 1208-1218.

Tsonis, A.A., 1987: Determining rainfall intensity and type from GOES imagery in the midlatitudes, Remote Sensing of Environment, 21, 29-36.

Wu, R., J.A. Weinman and R.T. Chin, 1985: Determination of rainfall rates from GOES images by a pattern recognition technique, J. Atmos. Ocean. Technol., 2, 314-330.

VARIATION OF SATELLITE RAIN RELATIONSHIPS IN SPACE AND TIME

Patrick King Tsoi-ching Yip

Meteorological Services Research Branch
Atmospheric Environment Service
Downsview, Ontario, Canada

1. INTRODUCTION

From September 1984 to September 1987, the Aerospace Meteorology Research Division of the Atmospheric Environment Service (AES) ran a demonstration project called RAINSAT for estimating precipitation areas and forecasting their short term motion. The basic techniques were developed by Geoff Austin and his colleagues at McGill University (Bellon et al.,1980). The McGill system was modified and a realtime version was developed and implemented by AES. Reports dealing with the accuracy of the analyses and 3h forecasts generated by RAINSAT have been made elsewhere (King and Yip,1987a,b). In this paper we will concentrate on aspects of the characteristics of the probability of rain relationship (PoRR), which relates the probability of rain with the characteristics of the cloud as viewed in VIS and IR.

The purpose of this paper is to evaluate changes in PoRRs over different time periods and in different regions and to compare PoRRs generated using radar as ground truth with those using surface data. This information is needed for determining the best way of 'training' an operational precipitation estimation scheme of this type.

2. SEMI-OPERATIONAL RAINSAT

The RAINSAT algorithms are installed on a Data General Eclipse S-130 located at AES in Downsview,Ontario. AES operates a GOES VISSR ground station which sends digital GOES visible and infrared images to the RAINSAT computer each half hour. The visible data are averaged values for (nominally) 4x4km grids. The RAINSAT computer also receives radar data every 10min from the AES King radar (40km north of Toronto) which are used to calibrate the system.

RAINSAT uses navigation information included with the IR image to remap the VIS and IR data from the satellite projection to a Lambert conformal projection (pixel size 8x8km) for a 1500x2000km area in eastern North America (see Figure 1). The actual resolution of the data of course depends on the location of the area being remapped with respect to the satellite. During the summer of 1985 GOES-6 was at 98W and the estimated resolution for the visible data available to the system is 6km in the southwest part of the remapped region and 12km in the northeast corner. For the IR these figures will be about double.

Because the sun angle varies throughout the day the visible data must be normalized so that the same satellite/radar relationship may be used for all daylight hours. In RAINSAT all visible pixels are normalized by dividing by the sine of the solar elevation angle similar to Tsonis and Isaac,1985. If the sun is less than 10° above the horizon the visible datum for that pixel is not used; if the sun angle for the central pixel of the image is less than 10° none of the visible data for that half hour are used. At 45N the sun is more than 10° above the horizon for about 13h in midsummer, about 10h at the equinoxes and about 6h in midwinter. This limits the useful period of the visible data for RAINSAT to these periods of time.

The normalization did not perform well within 3h of sunrise and sunset probably due to the low satellite view angle (approximately 20°-30°). To minimise this problem daytime data from 1300 to 2100 UTC only are used in this study; this is approximately 4h either side of local noon. If data from GOES-E at 75W had been available these problems would have been less serious.

A probability of rain map is constructed from the VIS and IR images using a previously calculated probability of rain relationship (PoRR). Displacement vectors inferred from 2 consecutive probability of rain maps are used to construct a probability of rain forecast by extrapolation. All 4 maps are transmitted in real-time to the Centre Meteorologique du Quebec (CMQ) for use in the forecast program for the province of Quebec.

In the next section we will discuss in detail characteristics of the PoRR over time periods ranging from a few hours to a few months.

3. THE PROBABILITY OF RAIN RELATIONSHIP

3.1 Calculation of the Probability of Rain Relationships

The RAINSAT probability of rain relationship (matrix or vector) is calculated by comparing remapped GOES satellite data for a given half hour with the corresponding radar data. Visible and Infrared data are used to calculate a probability of rain relationship for daytime use and infrared data only are used to create a

probability of rain vector for use at night. Both the matrix and vector are created using daytime data to minimize problems due to spurious radar returns which are more common at night because of nocturnal temperature inversions.

The probability of rain matrix gives the probability that a given (VIS,IR) pair is associated with rain at the ground (or more precisely at the height of the radar CAPPI used). It is calculated by summing a large number of half-hourly 2 dimensional histograms of raining and non-raining points. The half-hourly histograms are determined as follows:

- for each point within radar range obtain the normalized VIS count and the IR count, say (VIS,IR). A mask is used to exclude points where data may be suspect
- if radar indicates rain, increment counter for the (VIS,IR) cell in the raining histogram; otherwise increment the corresponding cell in the non-raining histogram.

For that half-hour the probability of rain for a given (VIS,IR) pair is simply:

$$\text{prob(VIS,IR)} = \frac{\text{rain(VIS,IR)}}{\text{rain(VIS,IR)} + \text{norain(VIS,IR)}}$$

The radar data on which the PoRRs were based are 1.5km CAPPIs. The pixel size was 2x2km but this was reduced to 8x8km to match the RAINSAT grid by choosing the highest reflectivity falling within the larger area. The lowest rainfall rate (0.25mm/h) was used to decide if a pixel was raining in constructing the PoRR. A mask was used to eliminate data from areas which are subject to spurious echoes.

The PoRR used in a real-time system could range from a real-time PoRR to a long term average. Based on experience described later in this paper the real-time version of RAINSAT was modified in 1986 to use seasonal averages for the PoRR. This is done to reduce problems associated with the short-term variability of the characteristics of raining clouds.

Probability of rain relationships were also constructed using surface data as ground truth.

The surface data used were hourly accumulations of rain at 75 stations in eastern Canada indicated in Figure 1. Because rainfall may have occurred at any time within the hour prior to observation, we averaged the satellite data to 24x24km when constructing surface based PoRRs. To estimate spatial variability the surface stations were divided into 6 groups as shown in Figure 1. The groupings were chosen to agree with expected climatic characteristics and to be approximately equal in area.

3.2 Characteristics of Probability of Rain Relationships

The probability of rain relationships derived from King radar for each of 4 seasons are shown in Figure 2. March and September were omitted from the calculations because of missing data due to equipment problems.

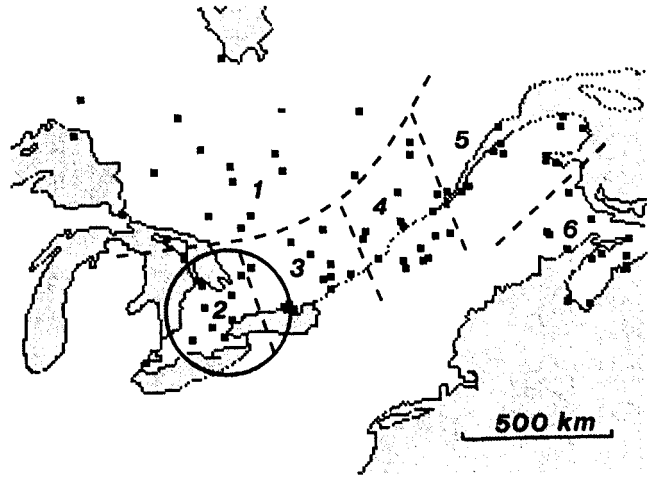

FIGURE 1. Lambert conformal projection used for remapped RAINSAT products. The large circle is the 200km range ring for King radar. The geographical areas shown are:

1. North
2. Southwestern Ontario
3. Upper St Lawrence
4. Middle St Lawrence
5. Lower St Lawrence
6. Maritimes

The frequency of occurrence of each combination of VIS count and IR count is shown by the solid lines and the probability of precipitation is shown by the dashed lines. The frequency of occurrence has been computed by accumulating the data into bins which are 2 VIS counts by 4K in IR brightness temperature and have been normalized to a total of 10000 observations. Thus all the bins inside the lines labelled 100 contain 1% or more of the total observations. The actual number of observations of 8x8km pixels ranged from 694566 in autumn to 1591528 in winter.

Features in the histograms may be associated with cloud types which have been visually identified in the images (as was done by Platt (1981) using GMS-1 data). We will make similar observations in this paper.

A number of features which persist from season to season are evident in the frequency plots. There is a large maximum at low VIS counts and warm IR temperatures corresponding to clear skies. This peak is most prominent in summer (Jun,Jul,Aug) and becomes less prominent in spring (Mar,Apr) and autumn (Oct,Nov). In the winter (Jan,Feb,Dec) the peak is reduced to a ridge of higher values and moves to temperatures below freezing and to higher VIS counts. The double peak in this area in spring is due to snow which occasionally persists to the lee of Georgian Bay in April. There is a weak ridge of higher frequencies with VIS counts in the high 20's extending from near 0C to -20C in summer and autumn. This feature can be more easily identified on daily average PoRRs. Examination of a number of individual cases showed this to be due to thin cirrus in otherwise clear skies.

In all seasons there is a ridge of maximum values with VIS counts in the mid to high 40's. In the summer there are individual peaks near 0C and -20C and a "plateau" near -40C. The 0C peak is associated with stratocumulus and fair weather cumulus while the plateau at -40C is associated with deep convection and thick layer clouds. It is more difficult to attribute the cause of the peak at -20C but it is likely due

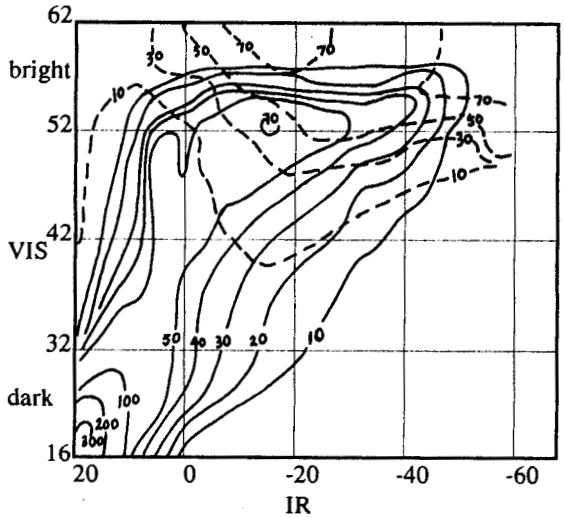

Figure 2(a). Histogram and PoRR Jun,Jul,Aug 1985

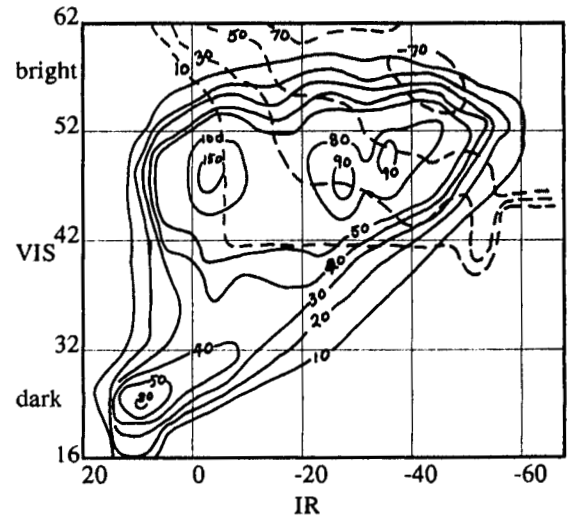

Figure 2(b). Histogram and PoRR Oct,Nov 1985

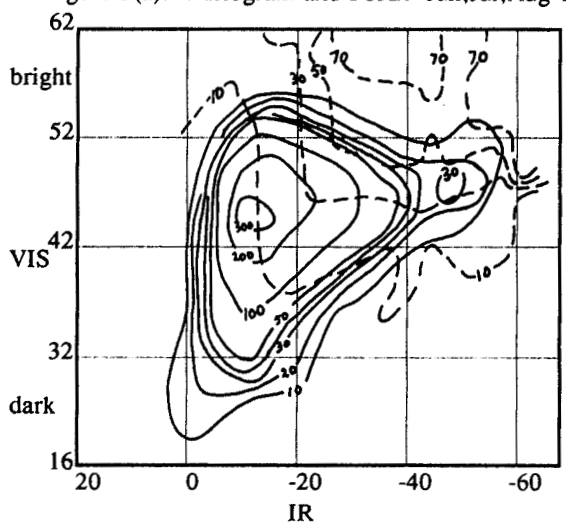

Figure 2(c). Histogram and PoRR Jan,Feb,Dec 1985

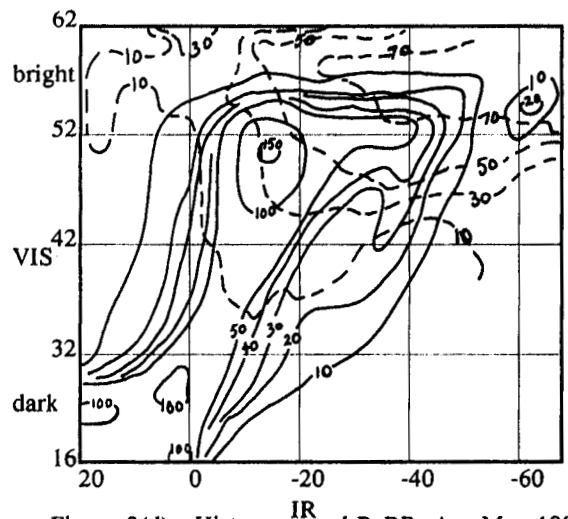

Figure 2(d). Histogram and PoRR Apr,May 1985

Figure 2. Histogram of VIS and IR values and probability of rain over area of King radar. Solid lines are frequency of occurrence. The total number of points has been normalized to 10000 so that dividing by 100 yields percent. Dashed lines are percent probability of precipitation lines.

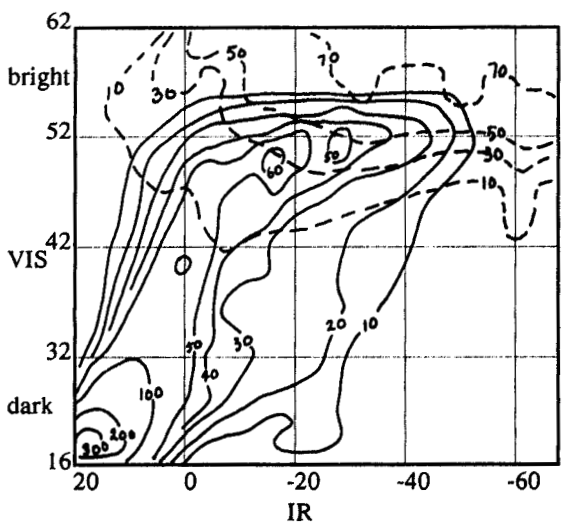

Figure 3. Histogram of VIS and IR values and probability of rain derived from 75 surface stations shown in Fig. 1. Lines have same meaning as in Figure 2.

to convective clouds which have not developed a cirrus shield. The 8x8km pixel size used in this analysis will result in the averaging of IR temperatures for convective clouds and neighbouring clear areas. This will result in higher apparent temperatures for such clouds. The 'stratocumulus' peak in summer is associated with near zero probability of precipitation while the other two peaks have near 50% probability of precipitation. The stratocumulus peak moves to lower temperatures and becomes the dominant peak in the autumn and winter but becomes almost insignificant in spring. The frequency of clouds colder than -50C is greatest in the autumn and winter.

The probability of rain relationship shows relatively little season to season variability in spite of the large variability in the cloud distributions. The positions of the 10%,30% and

50% lines move only slightly with season. The 70% line is more variable since it is based on much smaller numbers of observations.

It is clear from Figure 2 that below a cloud top temperature of -20C that the probability of precipitation has little dependency in any season on IR brightness temperature. This agrees with the conclusion of Tsonis and Isaac(1985) but not with Negri and Adler (1986). The reason for this is likely that Negri and Adler were concerned with convection in the subtropics whereas this paper deals with midlatitude regions where precipitation more often occurs from stratiform cloud and where convective clouds are often embedded in stratiform clouds. The probability of precipitation depends on both VIS and IR in the summer and autumn at brightness temperatures above -20C. In winter and spring there is little dependence on the VIS count for cloud top temperatures above -20C. In these seasons a double threshold classification technique would produce results similar to RAINSAT.

The probability of rain relationship and frequency diagram for Summer derived from the 75 surface stations is shown in Figure 3. There is a marked similarity between the frequencies shown in Figure 2(a). The principal difference is that the 'cloudy ridge' is displaced about 2 counts darker for the surface based frequencies. However when the southwestern Ontario region is compared with the King radar based frequency this discrepancy disappears. The main contribution to this difference is from lower apparent brightness of clouds in the two eastermost regions.

A clearer idea of the seasonal variation of the PoRRs can be obtained from Figure 4 in which the 30% probability of precipitation lines for each month are grouped by season. The winter and summer months show little within group variability. The lines for the summer months are within 1 or 2 VIS counts for the entire range below -10C. In winter months the 30% probability (of snow) line is relatively constant at a brightness temperature of -20C but is quite variable below that. Autumn shows the greatest apparent variability. September and October are similar to the summer months at colder temperatures and November is similar to winter months at warmer temperatures. This behaviour in autumn probably reflects periods of warmer and colder weather in which cloud populations are similar to summer or winter. However as noted before there was a good deal of data missing from September which might also increase the apparent variability. It is also noteworthy that non-zero probabilities of rain occur at higher temperatures in the summer than do non-zero probabilities of snow in the winter. This may be due to cloud shields being more extensive in winter than summer minimizing the probability that a precipitating cloud will be surrounded by a clear area at significantly higher temperature.

The 30% probability lines for each of the six regions are shown in Figure 5. They have been separated into 2 groups based on their similarities and to improve legibility; one group contains the 4 inland regions and the other the two coastal regions. The principal difference between the two groups is that the 30% line for the coastal regions is a few VIS counts darker from 0 to -20C. There is little difference between the regions at colder temperatures. This separation is the same as that indicated by the frequency plots. The difference between the two groups may be caused by the difference in cloud populations due to the maritime climate of the easternmost regions. The broad similarity between the regional PoRRs supports the use of data from one region to calibrate a system such as RAINSAT over a large area.

3.3 Comparison of Probability of Rain Maps

In a previous study (King and Yip,1987b) probability of rain maps generated using radar based PoRRs were evaluated using surface data from the same six regions as in this study. Variations in scores from region to region were found to be comparable in value with variations from month to month within a region. From this we concluded that one can apply a PoRR to a region at some distance from the training region.

To further test this conclusion we constructed a series of probability of rain maps for each region using a PoRR based on surface data from that region. We then compared the verification statistics with probability of rain maps which had been generated in real-time using King radar based PoRRs. The procedure followed in this study was to calculate a PoRR for each region from 1 months data, to construct a series of probability of rain maps from the next months data and finally to calculate verification scores which were then compared with the corresponding scores from the previous study. Because of space limitations details concerning the evaluation procedures in the previous paper are omitted here.

The 1 month PoRRs were very noisy and even 3 month PoRRs were somewhat noisy. To obviate this problem a 5 point smoother with double weight at the centre point was applied.

The results are summarized in Table 1.

TABLE 1

ANALYSIS - Brier scores - July

	King PoRR	Surface PoRR
North	0.076	0.077
Southwestern Ontario	0.031	0.033
Upper St Lawrence	0.049	0.053
Middle St Lawrence	0.045	0.049
Lower St Lawrence	0.049	0.048
Maritimes	0.039	0.039

The Brier scores shown here are a measure of the difference between RAINSAT probability categories and whether or not it is raining according to the surface observations. A perfect Brier score is zero. To give these figures some context, Brier scores ranged up to about 0.20 on analyses which were judged subjectively to be poor.

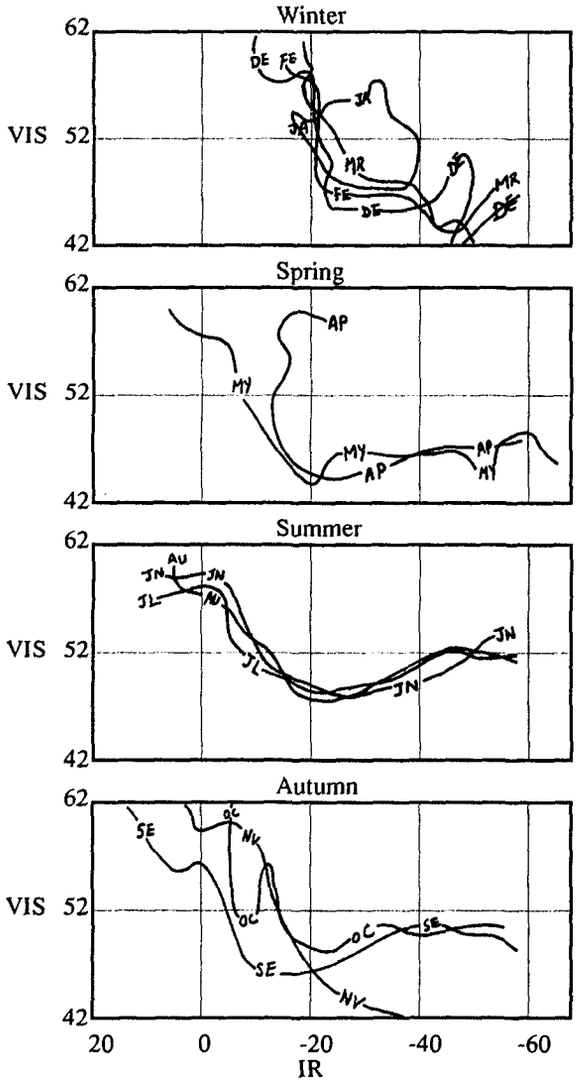

Figure 4. 30% probability of rain line for each month (grouped by season) derived from King radar data.

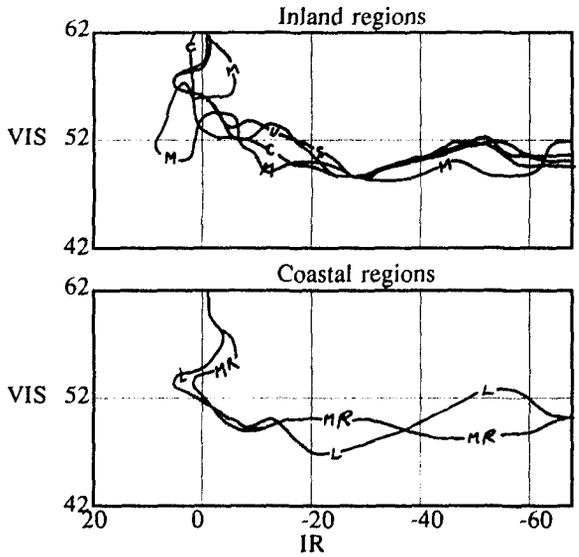

Figure 5. 30% probability of rain line derived from surface data for each of six regions in Fig. 1.

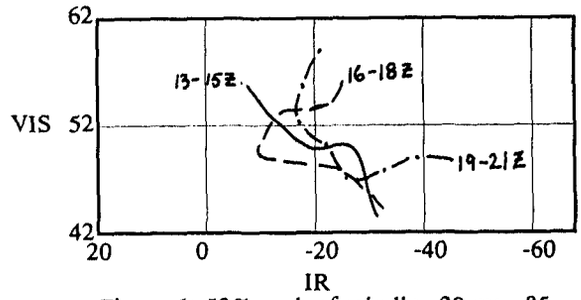

Figure 6: 50% prob of rain line 20 may 85

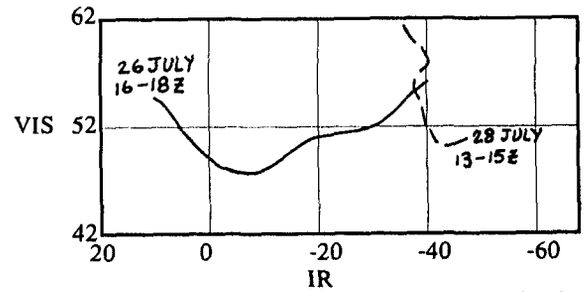

Figure 7: 70% prob of rain lines 26,28 jul 85

It appears that there is remarkably little difference in the error characteristics of the probability of rain maps whether or not one uses a PoRR based on local surface observations or a PoRR based on a remote radar. Obviously there must be limits to such a conclusion. In the previous study there appeared to relatively little variation in the east-west direction but more in the north-south.

3.4 Shorter term variability - some illustrations

Probability of rain relationships calculated over short time periods can vary markedly even though the synoptic situation has not changed. To illustrate this Figure 6 shows the 50% probability of rain line for 3 separate periods of 2.5h on 20 May 1987. During this time a cold front which stretched from central Quebec to southern Lake Michigan was crossing the area of the King radar. The cloud band was about 200km wide and had relatively sharp edges.

The frequency diagrams for all 3 time periods were relatively constant with a prominent peak in the warm dark region joined by a ridge to an equally prominent cold bright peak. The principal difference was the presence of significant numbers in a ridge of higher values parallel to the IR axis with VIS counts in the low 50's. Examination of a loop of images showed that a narrow band of cumuliform clouds ahead of the main band and clouds along the trailing edge of the main band contibuted to this ridge in the histogram. In spite of the relative constancy of the histograms the PoRRs change significantly as shown in Figure 6. The shift of the 50% line to warmer temperatures near VIS count 50 for the period 16-18 UTC is due in part to the cumulus clouds mentioned previously. However these cloud bands persisted beyond 19 UTC but the 50% line shifted back to lower temperatures.

Even greater differences can occur between PoRRs from different days. The 70% probability of rain lines from 2 days in July are shown in Figure 7. The July 26 case was a slow-moving cold front with indications of the development of a wave. The July 28 case was marked by deep convection in a line ahead of an approaching cold front. The areas in VIS/IR space corresponding to greater than 70% probability of rain are almost completely disjoint. There were almost no pixels in the cold front case with a temperature below -40C but these dominated the convective line. Examples such as these point to the possibility of calculating PoRRs corresponding to meteorological features such as cold fronts and warm fronts. We classified synoptic situations for a period of two months and compared the half-hourly PoRRs but found no consistent pattern among the PoRRs for each synoptic type. Nevertheless it might be possible to average an ensemble of half-hourly warm front PoRRs to get a mean PoRR which corresponds to the 'average' warm front.

4. CONCLUSIONS

We have examined the characteristics of probability of rain relationships derived from GOES satellite data and surface and radar data. PoRRs calculated from a month's worth of data were relatively constant within a given season. These PoRRs changed only slightly from season to season although the frequencies of cloud types changed considerably. Over periods of a few days the PoRRs were almost completely disjoint. However the variations from day to day were not consistent enough with synoptic type to allow the construction of PoRRs keyed to synoptic type. Over periods of a few hours there were significant changes in the PoRRs although the associated cloud frequencies had not changed much.

PoRRs derived from surface data were quite consistent with those derived from radar. This means that the RAINSAT technique could be used in regions where radar data are unavailable. The region to region variation was similar in magnitude to the month to month variation within a region. This results supports the assumption that systems such as RAINSAT can be calibrated in one region and used in another. However caution must be exercised in extrapolating in the north-south direction since the greatest region to region variation was found in that direction.

5. REFERENCES

Bellon A., S. Lovejoy and G.L. Austin,1980: Combining satellite and radar data for the short-range forecasting of precipitation. *Mon.Wea.Rev.*, 108,1554-1566.

King P. and T.-C. Yip,1987a: Evaluation of RAINSAT precipitation system in real-time use. *Proceedings of the Symposium on Mesoscale analysis and forecasting, Vancouver,Canada. 17-19 August 1987.*

King P. and T.-C. Yip,1987b: Evaluation of RAINSAT precipitation analyses and forecasts *Second Workshop on Operational Meteorology. Halifax, NS. 14-16 Oct,1987.*

Negri,A.J. and R.F.Adler,1986: Visible and Infrared structure of Florida convection and its implication for estimating rainfall. *Second Conference on Satellite Meteorology/Remote sensing and applications. May 13-16,1986. Williamsburg,VA.* 462-467.

Platt C.M.R.,1981: Two dimensional Histograms of GMS-1 satellite visible and infrared temperature for selected cloud systems. *Div.Atm.Phys. Tech paper 40 CSIRO Australia.*

Tsonis,A.A. and G.A.Isaac,1985: On a new approach for instantaneous Rain Area Delineation in the Midlatitudes using GOES data. *J.Clim. and Appl. Met.*,24,1208-1218

7.12

MID-LATITUDE EVALUATION OF SOME SATELLITE RAINFALL ESTIMATION TECHNIQUES

W.D. Hogg, A.J. Hanssen, A. Niitsoo and V.L. Polavarapu

Atmospheric Environment Service
Downsview, Ontario, CANADA

1. INTRODUCTION

Conceptually, the use of satellite data to estimate the areal distribution of precipitation is very appealing. From the geostationary satellite we can get frequent digital images of an area containing information on cloud height, thickness, and areal distribution with a resolution to a few kilometres. Since rainfall production is related to all of these parameters, numerous investigators have attempted to deduce rainfall rates from satellite information.

This ability to infer the occurrence and amount of precipitation from satellite data has important ramifications for the meteorological observing strategy adopted by large northern countries such as Canada. Yet many of the methods for estimating precipitation from satellite data were developed for convective cloud systems and have been widely applied in southern latitudes only. The objective of this study was to compare the ability of existing techniques to derive daily, weekly, and monthly precipitation estimates under Canadian conditions and ascertain the utility of these estimates to Canadian users. The intent is to ascertain if there are suitable precipitation estimation procedures that exhibit sufficient skill to warrant consideration of the development of a fully automated system to derive precipitation estimates for Canada from satellite data.

This study has been designed to provide a fair comparison of the capability of the techniques developed by Negri, Adler, and Wetzel (1984), Lovejoy and Austin (1979a), and Barrett (1970) to estimate precipitation totals for daily, weekly, and monthly periods over southern Canada. Two previous papers reported on the preliminary results of this study based upon less than a week of data. This paper reports on the results based upon a month of data.

The comparison has been carried out by remapping GOES, RADAR and gauge data to a common latitude longitude grid ranging from 42 to 47 degrees north and 72 to 84 degrees west with a grid spacing of 0.05 degrees (Figure 1). The three precipitation estimation techniques have been used to derive daily and weekly estimates from the remapped data and have been compared by examining the contoured fields and calculating a number of statistics. These statistics reflect the spatial correspondence of the occurrence of precipitation and the agreement of the magnitude of the precipitation estimates.

Furthermore, the comparisons have been carried out on daily and weekly estimates derived from satellite observations taken every hour, every three hours, and every six hours. These comparisons will indicate the adequacy of precipitation estimates derived from fewer observations (i.e. if the large volume of data processed is reduced). Because of the large volume of data involved, half-hourly satellite observations have not been used.

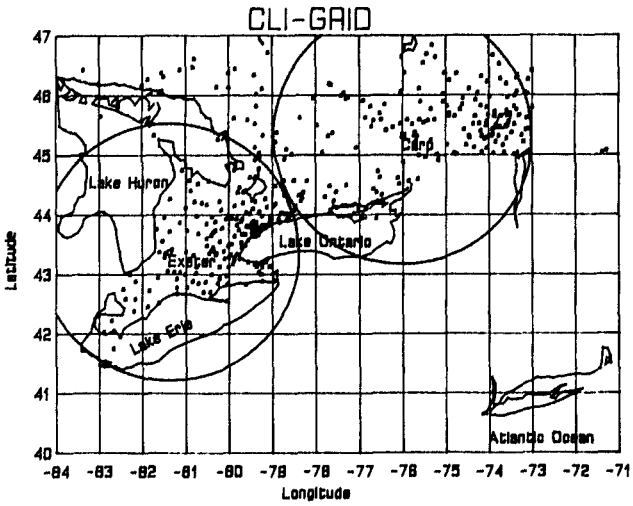

Fig. 1. Satellite Rainfall Evaluation Project Grid showing gauge and quantitative radar locations. Grid spacing is .05 degrees.

To examine the effect of increasing the scale of observation, precipitation estimates were calculated with average spatial resolutions of approximately $(5\text{-km})^2$, $(10\text{-km})^2$, $(23\text{-km})^2$, and $(94\text{-km})^2$ prior to the comparisons. The latter two resolutions roughly correspond to the spatial resolutions required for climate and research applications on continental and global scales respectively (Atlas and Thiele, 1981).

2. TECHNIQUES

The three techniques initially chosen for examination in this study were selected from the literature on the basis of their relative simplicity and suitability for automation. The techniques are typical of the methods in the three prominent types of procedures which

Barrett and Martin (1981) have classified as cloud indexing methods, life-history methods, and bi-spectral methods. All of the methods have the capability to measure the duration of cloud cover over southwestern Ontario and the Negri et al. (1984) procedure and RAINSAT (Lovejoy and Austin, 1979) methods can apportion precipitation at differing rates within the cloud area. At this time, no claim is made regarding the suitability of these procedures for the task at hand. The intent is to explore the suitability and capability of the methods for deriving precipitation estimates for weekly to monthly time periods.

The simplest method used in this study, and referred to as the Control technique, is based on the early work of Barrett (1970), Follansbee (1973), and the Cropcast system (Dismachek and Bohse, 1981). This procedure uses the satellite's capability to observe the spatial distribution and duration of cloud and assumes a climatological precipitation rate to derive precipitation estimates. The technique, quite simply, accumulates the climatological hourly precipitation rate al all locations determined to be cloudy from the satellite data. The skies over a grid point are considered to be cloudy when the satellite observed temperature is less than -20°C during the night. During daylight hours, a grid point is considered cloudy when the infrared temperature is less than -10°C and the GOES visible count is greater than 50. The assumed climatological precipitation rate is the ratio of the average monthly precipitation over southwestern Ontario to the average number of hours with overcast skies during the month of concern. This was adjusted to 0.6 mm/hr to reflect the observed April 1985 conditions.

The Negri, Adler, and Wetzel (1984) procedure is a simplification of the life-history procedure known as the Griffith-Woodley Technique (Griffith et al., 1976). In this simplified procedure, cloud entities are defined by the -20 degree celsius isotherm. For precipitation rate purposes, the cloud is partitioned into three areas. No precipitation is assigned to the warmest 50% of the cloud area. Fifty percent of the cloud's rain volume is assigned to the coldest 10% of the cloud area. The remaining 50% of the rain volume is assigned to the remaining 40% of cloud area. Using Florida data, Negri et al. (1984) selected rainfall rates of 9.0 mm/hour and 1.8 mm/hour for the coldest 10% and 40% of the cloud respectively. For this April, 1985, study, rates of 2.4 mm/hour and 0.6 mm/hour were used.

This simplified procedure is independent of the cloud life history, but is dependent on the definition of a cloud. This technique has been derived from a life-history method, but is essentially a more refined version of the control technique previously described. For the purposes of this study, clouds have been defined to be entities with temperatures less than -20°C.

The RAINSAT approach has been documented by Lovejoy and Austin (1979). The technique is essentially a supervised classification procedure that uses radar observations to train the technique to recognize precipitation clouds. The original procedure has been revised so that the probability of precipitation derived from the visible and infrared pairs is accumulated. The accumulated probabilities are then multiplied by a conversion factor based on mean hourly precipitation, given that it is raining, to derive the daily precipitation field. A value of 2.4 mm/hr was used for this study. Precipitation rates of zero were assigned to grid sqares with less than 10% probability of precipitation.

3. DATA AND PROCESSING

The visible (.55 to .75 m) and infrared (10-12.5 m) satellite data used in this study are from the GOES-E VISSR (Clark, 1983) located above the equator at approximately 74°W longitude. The data were received at Environment Canada's satellite data laboratory in Downsview, Ontario and stored on magnetic tape. Up to 72 of the visible and infra-red images can be loaded into the disk based database, thereby enabling the remapping of up to three days of hourly observations to the grid without operator intervention. The data were remapped using the navigational parameters in the VISSR data and the computer procedures provided by Hambrick and Phillips (1980).

Radar data were obtained from the 5-cm Sceptre radar systems located at Carp (45°18'N 75°59'W) and Exeter (43°21'N 81°29'W). The archived volume scans were processed to derive a 1.5 km Constant Altitude PPI (CAPPI) at ten minute intervals for each radar. These 240 km by 240 km CAPPIs, centred on the radar site, consisted of radar reflectivities in $(2\text{-km})^2$ bins that were transformed to ten minute rain accumulations using the Marshall-Palmer distribution (Battan, 1973). Hourly rain accumulations were obtained by accumulating six CAPPIs. Up to 72 hourly precipitation fields for each radar were loaded to the database. These precipitation fields were then remapped to the same grid as the GOES data.

Daily rain gauge data for up to 450 climate stations in southern Ontario were also loaded to the data base. An objective analysis technique based on a procedure by Shepard (1968) was used to assign daily precipitation totals to the grid points.

Following the remapping of the satellite, radar, and gauge data to the common grid, each of the three satellite precipitation estimation techniques was used to derive hourly precipitation estimates for each of the grid points. These sets of hourly precipitation fields were then sampled at equal intervals of 1, 3, and 6 hours to obtain daily precipitation totals. These daily totals were then spatially averaged to obtain estimates for the larger areas listed in the introduction.

The full and reduced resolution precipitation fields derived from each of the satellite, radar, and gauge data were then contoured and plotted on a graphics device. A number of statistics, selected to indicate the spatial correspondence of the precipitation fields and the correlation in the magnitudes of the precipitation estimates were also calculated.

This paper will concentrate on a discussion of correlation coefficients and mean squared errors. A paper by Willmott (1981) was particularly useful for clarifying the use of mean squared errors in the evaluation of model simulations of observations. The paper makes a

good case for the use of the root mean squared error (RMSE) as a measure of the performance of a model and further recommends the separation of the RMSE into systematic and unsystematic components. The systematic component includes contributions to the RMSE due to bias and errors in slope of the relationship. The unsystematic component contains the residual errors and is a measure of the totally random portion of the model predictions as compared with observations. Because bias existed in all 3 satellite techniques being evaluated and was strictly dependent upon the climatological rain rate selected, it was concluded that the unsystematic RMSE was the most appropriate measure of the potential of one of the techniques to successfully estimate rain. In all results discussed here, the individual grid estimates of rain amount by satellite technique were considered the model predictions and the estimates for the same grids obtained by objective analysis of the gauge data were considered to be the observations.

4. RESULTS

The remapping of these data, generation of rainfall estimates, and processing of the rainfall estimates to produce precipitation maps and comparative statistics is a large data processing task. For each 3-day event, these tasks require 4 to 5 hours of dedicated processing on a relatively large and fast minicomputer (MODCOMP Classic 7870) with graphics devices. In spite of the volume of data and computer time required, a significant dataset of 27 days (9 3-day events) for April, 1985, has now been completely analysed.

Satellite data for April 1 and April 5 were missing, so these days were subtracted from all datasets. For logistical reason, April 29 and 30, which had little or no rain, were excluded from the analysis, as well.

The weather during the test period was typical of spring conditions in Eastern Canada. Well developed cyclonic disturbances tracked from west to east across the region while three airmasses, with characteristics ranging from arctic to tropical, alternately dominated the local conditions. Widespread rain due to warm frontal lift and vertical motion within the low pressure system gave way to convective showers in the warm air and ahead of cold fronts. This in turn was replaced by wet snow and rain showers as the modifying cold air returned after the passage of the cyclonic system. This sequence was repeated nine times during the test period.

Rain amounts averaged over the portion of the grid covered by gauge data are shown in Figure 2. Plotted values represent the total rain during each of nine 3-day events. Daily values are also available but event statistics are presented throughout to reduce the clutter in figures by decreasing the number of data points.

Figure 3 depicts the correlation coefficient for each satellite technique and each of the nine 3-day events. As noted in the previous section, predictions and observations were obtained by using the satellite estimate of daily rain and gauge objective interpolation of grids within the area of overlapping gauge and satellite data. Correlation coefficients are all quite low and no single technique stands out.

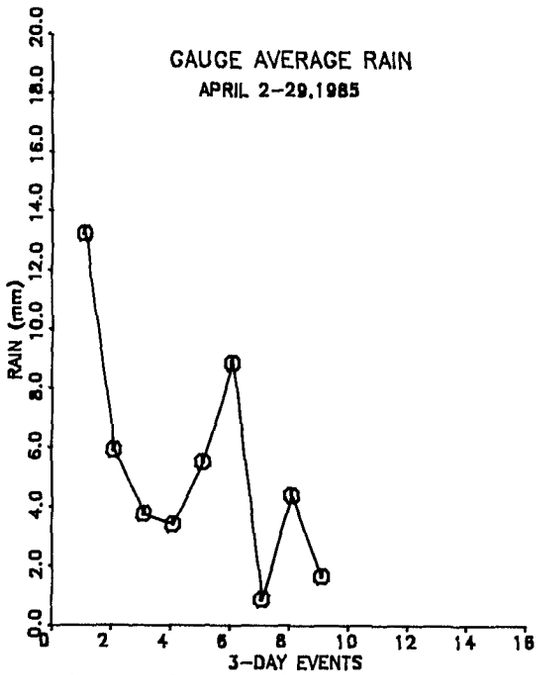

Fig. 2. Total rainfall for each of 9 3-day events during April 2-29, 1985, averaged over the Canadian portion of the project grid.

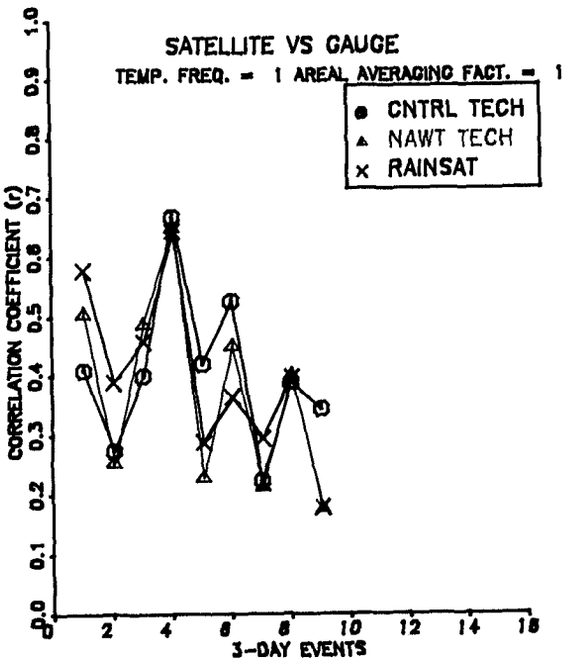

Fig. 3. Spatial correlation coefficients for satellite vs. gauge estimates of rain for 3-day events and for the Control, Negri-Adler-Wetzel and RAINSTAT techniques.

Figure 4 show two things: the RMS errors for all techniques are quite large compared to the event rain and the magitudes are similar for all techniques. The Negri-Adler-Wetzel technique produces consistently higher mean errors.

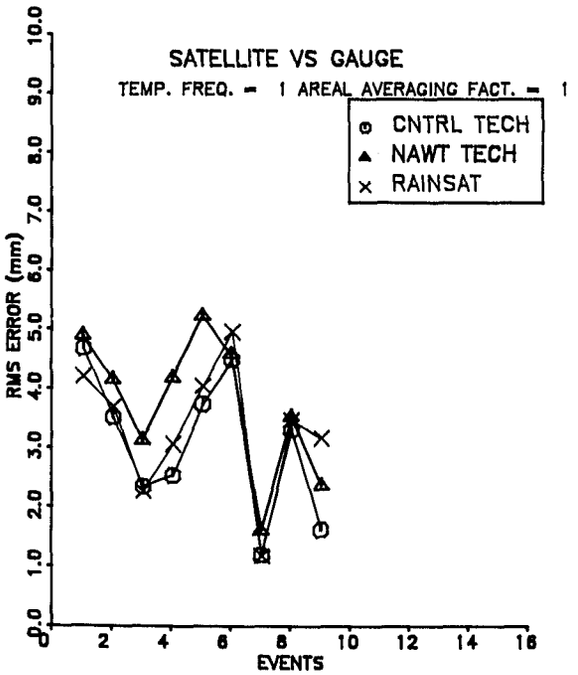

Fig. 4. Satellite vs. gauge root mean square error for 3-day events and 3 satellite techniques.

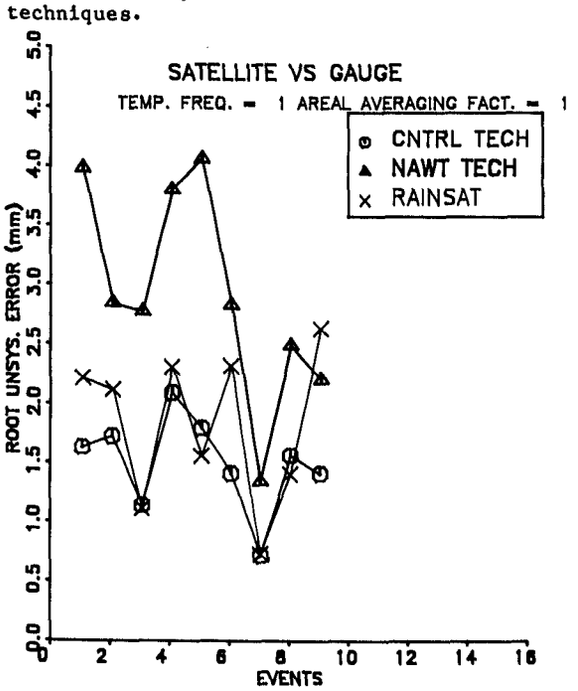

Fig. 5. Same as Figure 4 except for unsystematic portion of RMS error.

Figure 5 shows the unsystematic portion of the RMSE as defined by Willmott (1981). If the earlier premise concerning the unsystematic RMSE being the most appropriate measure of the skill of a technique is accepted, then figure 5 shows that the simplistic Control technique was at least as skillfull as the other two more complex techniques. The Negri-Adler-Wetzel technique was the least skillfull for estimating daily rain during this mid-latitude April case study. Since the Negri-Adler-Wetzel technique was developed for convective situations in the sub-tropics, this is not totally surprising.

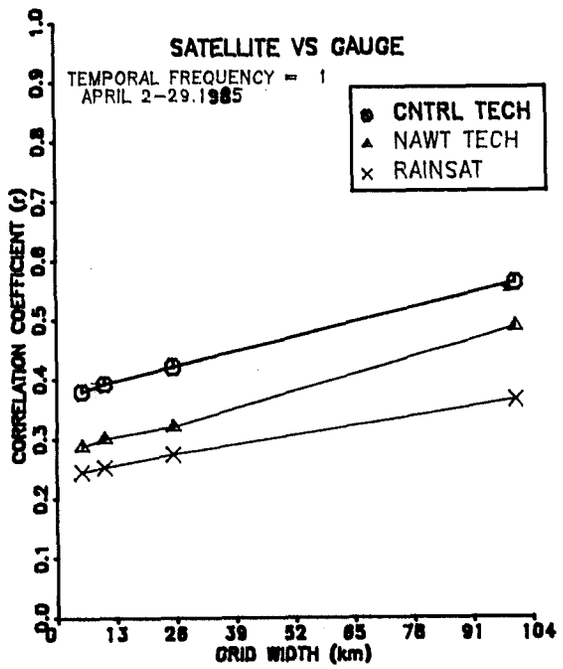

Fig. 6. Spatial correlation coefficients for satellite and gauge estimates of April 2-29 total rainfall field. Grid widths of 5, 10, 20 and 100 km indicate the areas of 25 to 10000 km² over which amounts were averaged prior to computation of statistics.

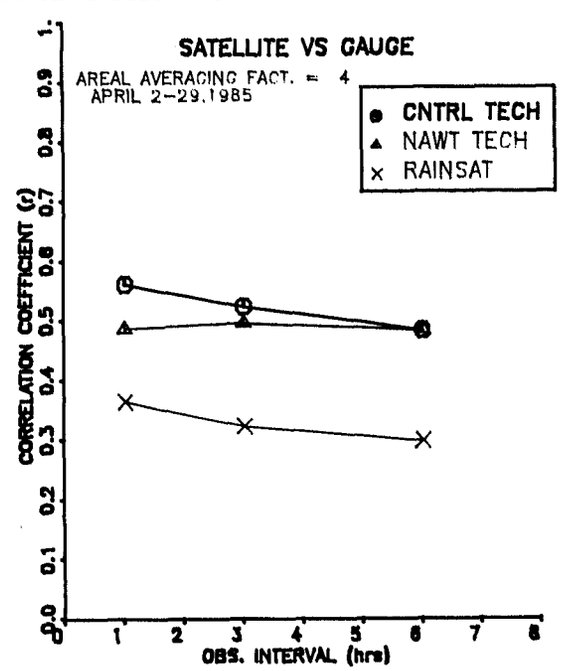

Fig. 7. Spatial correlation coefficients as in Figure 6 except satellite estimates were based on images every 1, 3 or 6 hours. All estimates were averaged over 10000 km² areas.

Still, there is no evidence that the more complex models of rain generated by the Negri-Adler-Wetzel technique or the RAINSTAT technique show any skill at all compared to the simplistic cloud/no-cloud model for daily rain during this April case.

Accumulation grids were prepared by summing the 27 daily grids to provide monthly

rainfall maps as generated by each technique and the gauge data. As a check, a separate objective analysis of individual gauge monthly totals was performed which produced a map virtually identical to the one produced by summing the daily maps. Again the statistics were generated by comparing individuals grid squares for each technique with gauge objectively interpolated grids. Throughout the analysis, separate maps were generated and accumulated for different frequencies of satellite observations and for a variety of grid sizes. Each combination of observation interval and grid size was mapped and accumulated independently so that comparison statistics could be generated separately for the various sampling intervals and grid or areal averaging sizes.

Figure 6 shows the correlation coefficients for the April 2-29 accumulation maps based on hourly satellite data. Coefficients for each technique are plotted for grids with approximate spacings of 5 km, 10 km, 20 km and 100 km and hence comparing rainfall estimates for areas ranging from 25 km² to 10,000 km². As expected, correlations improved as grid size increases. Variation of correlation coefficient with satellite data sampling interval for the 10000 km² grid size is shown in Figure 7. The decrease of correlation with increased sampling interval is not dramatic.

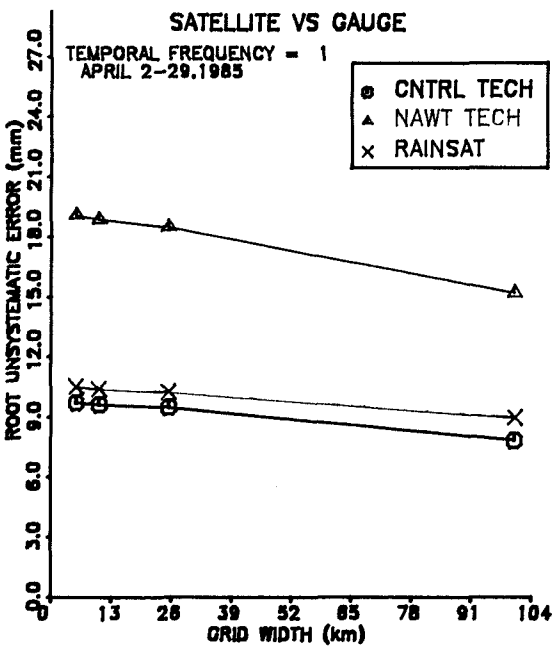

Fig. 8. Same as Figure 6 except data are for unsystematic RMS error vs. areal averaging size.

The variation of unsystematic RMSE with grid size for the 27 day accumulations is shown in Figure 8. Again, errors were least for the Control technique and improvement was slight for comparisons made with larger grid areas. The total RMSE for the 27 day accumulation of the Control technique was 16 mm while the average rain for the grid based on gauge accumulations was approximately 40 mm. Thus, the Control technique produced estimates of monthly rain with a scatter index (RMSE divided by the mean) of 40%. The bias for this application of the control technique was small but the bias is directly dependent upon the selection of the average rain rate. There could well be considerable variability in this parameter both seasonally and year to year.

It was postulated that the large errors and low correlations might have been due, in part, to the use of an objective analysis of gauge data as the ground truth field. In a separate experiment to reduce the dependence of comparisons on the interpolation procedure, the radius of influence of the observations in the objective analysis scheme was reduced until there were only about as many grids included in the comparison as there were stations. All other grids were considered as missing data. That is, only grids with observations in, or immediately adjacent to them, were included in the comparison with satellite estimates. No significant change in the results was observed.

5. CONCLUSIONS

This project has taken an important step towards evaluating the ability of visible/IR satellite techniques to estimate areal rainfall amounts. A month-long test, under spring conditions in Eastern Canada, has shown that a simple satellite cloud accounting technique has some skill for estimating daily and monthly rain with a scatter index value of 40% for monthly rain. However, more complex satellite models of rainfall do not generally improve the estimates. Data from a summer period will be analysed in the near future to investigate the bahaviour of the satellite techniques during periods when convective rainfall dominates.

6. REFERENCES

ATLAS, D. and THIELE, O.W. (eds). 1981. Precipitation Measurements from Space, Workshop Report. NASA, Goddard Space Flight Centre, Greenbelt, Maryland, 2-1 to 2-21.

BATTAN, L. 1973. Radar Observation of the Atmosphere. The University of Chicago Press, Chicago, 324 pp.

BARRET, E.C. 1970. The estimation of monthly rainfall from satellite data. Mon. Wea. Rev., 98, 322-327.

BARRET, E.C. and MARTIN, D.W. 1981. The Use of Satellite Data in Rainfall Monitoring. Academic Press, New York, 340 pp.

CLARK, D. (ed). 1983. The GOES User' Guide. NESDIS, NOAA, U.S. Dept. of Commerce, Washington, D.C.

DISMACHEK, D.C. and BOHSE, J.R. 1981. Verification of techniques for cropland precipitation analysis. Preprints of the 4th Conf. On Hydrometeorology, Oct. 7-9, 1981, Reno, Nevada, Amer. Meteorol. Soc., Boston, 129-133.

FOLLANSBEE, W.A. 1973. Estimation of average daily rainfall from satellite cloud photographs. NOAA Technical Memorandum NESS 44, Washington, D.C., 39 pp.

GRIFFITH, C.G. WOODLEY, W.L., BROWNER, S., TEIJEIRO, J., MAIER, M., MARTIN, D.W., STOUT, J., and SIKDAR, D.N. 1976. Rainfall estimation from geosynchronous satellite imagery during daylight hours. NOAA Tech. Rep. ERL 356-WMPO 7, Boulder, Colorado, 106 pp.

HAMBRICK, L. and PHILLIPS, D. 1980. Earth locating image data of spin-stabilized geosynchronous satellites. NOAA Technical Memorandum III, Washington, D.C.

LOVEJOY, S. and AUSTIN, G.L. 1979. The delineation of rain areas from visible and IR satellite data for GATE and mid-latitudes. Atmosphere-Ocean, 77-92.

NEGRI, A.J., ADLER, R.F. and WETZEL, P.J. 1984. Rain estimation from satellites: An examination of the Griffith-Woodley Technique. J. of Climate and Appl. Meteorol., 23, 102-116.

SHEPARD, D. 1968. A two-dimensional interpolation function for irregularly spaced data. Proc. of the 1968 ACM National Conference, 517-524.

WILLMOTT, C.J., 1981. On the validation of models. Physical Geography, 2, 184-194.

7.13

COMPARISON OF SATELLITE IR RAIN ESTIMATES WITH RADAR RAIN OBSERVATIONS IN HURRICANES

K. Robert Morris
General Sciences Corporation
Laurel, Maryland 20707

Andrew J. Negri and Robert F. Adler
NASA/Goddard Space Flight Center
Greenbelt, Maryland 20771

1. INTRODUCTION

Satellite IR and combined visible-IR rain estimation techniques have been developed to estimate rainfall globally or locally in regions lacking adequate surface rainfall measurements. Applications of satellite rain estimates include climatology, hydrology and agricultural forecasting, and real-time estimates of flash flood potential in severe local storms. Whether as part of a global estimate or as an independent exercise (Griffith et al., 1978), satellite rain estimation techniques have been applied to cases involving tropical cyclones, an application for which they were not originally developed. In this paper, radar data for times prior to and during the landfall of Hurricanes Frederic (1979), Alicia (1983) and Diana (1984) in conjunction with GOES IR data are used to infer the validity of IR rain estimation parameters and precipitation totals in the tropical cyclone environment for three IR techniques of varying complexity. These techniques are the Arkin method (Arkin, 1983), the Negri-Adler-Wetzel technique, denoted NAW (Negri et al., 1984), and the Convective-Stratiform technique, denoted CST (Adler and Negri, 1987). Results for Hurricane Alicia using the modified Scofield-Oliver manual technique, denoted MSO (Spayd and Scofield, 1984), are discussed in terms of the radar/satellite comparisons.

2. BRIEF DESCRIPTION OF IR TECHNIQUES

The Arkin IR rain estimation technique is the least sophisticated of the techniques applied in this comparison study. In the modified Arkin technique (Adler and Negri, 1987) a fixed rainrate of 3 mm/h is assigned to each pixel on the IR image with an equivalent blackbody temperature (TBB) less than or equal to 235K.

The NAW IR technique is the simplification of the Griffith-Woodley technique derived by Negri et al. (1984). NAW define a cloud area bounded by the 253K TBB isotherm, and within this area the total rain volume of the cloud is apportioned equally between the coldest 10% and the next coldest 40% of the cloud area. Thus the area of rainfall is entirely within the coldest 50% of the defined cloud area. NAW yields a rainrate of 8 mm/h in the coldest 10% area and 2 mm/h in the 40% area using the calibration based on observations of Florida convective precipitation.

The CST attempts to identify regions of stratiform and convective precipitation in GOES IR data. Convective precipitation areas are identified as local TBB minima in the data colder than 254K which pass a screening criteria, basically a 2-dimensional temperature gradient determination, in order to eliminate areas of non-precipitating cirrus. An empirical field of view correction is applied to qualifying TBB minima, and rainrates and areas are then assigned to each based on cloud model results using representative atmospheric profiles. A Florida summer profile was used in the hurricane CST calculations, and for the TBB minima identified in the hurricane IR data the average convective rainrate was near 20 mm/h. A threshold TBB for a stratiform rain area is calculated from the temperature field in which the minima is embedded. A fixed rainrate of 2mm/h is assigned to all points colder than the threshold and not previously assigned convective rain. This threshold is typically about 210K.

In contrast to the above techniques, MSO is a subjective manual technique and is dependent on the operator's ability to identify and interpret observed hurricane features. Its primary advantage for hurricane rain estimation is that it is partly based on observations of hurricane precipitation structure. Nominal rainrates are applied to the wall cloud (defined as 20 n mi either side of the eye or analyzed center), to the Central Dense Overcast (CDO, defined as outside the wall cloud and within 50 n mi of the center), to the Outer Banding Area (OBA), and to embedded cold convective cloud tops (ECT) in the OBA. Nominal values may be modified upwards in the presence of colder or more structured cloud tops (CDO area) or cloud tops which are growing or becoming colder (ECTs), or downwards for tops decreasing in area or becoming warmer. Hence, the MSO technique takes into account temporal changes in the observed clouds on consecutive GOES IR images and cannot be properly applied to single images. MSO nominal rainrates are 50 mm/h in the wall cloud, 25 mm/h in the CDO, 8 mm/h in the OBA, 25 mm/h, 12 mm/h and 5mm/h respectively for growing, decreasing and warming ECTs, and 25 mm/h for the onshore flow area of the first outer band from the CDO.

3. RADAR PRECIPITATION ESTIMATES

Digital radar data collected with the NOAA/HRD portable digitizer and used in this study are described in Dodge et al. (1987). The calibrated

radar data were remapped into GOES image coordinates (Hasler and Morris, 1986) for direct comparison with the output of the IR rain estimation techniques. Radar reflectivity values were converted to rainfall rates according to the relation derived for mature hurricanes by Jorgensen and Willis (1982). There are several limitations on the accuracy of radar rainfall estimates which result from the distribution of hurricane precipitation and the characteristics of the radars employed. In particular, the range of quantitative precipitation estimates from fixed, ground-based radar is limited by increasing beam height and volume at greater ranges combined with the lack of vertical extent of stratiform precipitation outside of the eyewall and outer band convective cores. Jorgensen and Willis show that the reflectivities in the stratiform region of hurricanes drop off significantly above the freezing level at approximately 5 km. Also noted in these regions is the occurrence of a bright band, 0.5 km below the freezing level, due to melting of frozen precipitation. The maximum quantitative range for the WSR-57 radar data in stratiform rain areas with minimal influence from the bright band is then ~175 km.

Because of the large horizontal extent and offshore distance of Hurricane Frederic during the time period presented here it was necessary to combine radar precipitation estimates from digital radar data collected at Slidell, Louisiana (SIL) with estimates from PPI VIP level photographic data taken at Pensacola, Florida (NPA). NPA PPI photos were digitized by a video technique using the AOIPS (Hasler and Morris, 1986), and data from both radars were remapped to GOES coordinates. The average rainrate for each VIP level of the NPA radar was estimated by calculating the average rainrate of the VIP level equivalent area from overlapping SIL digital data, restricting the computations to within the quantitative ranges of both radars. Rainrate images for the two radars were then digitally composited on the AOIPS. Compositing of the two radars approximately doubled the volume rainfall totals beneath the CDO in Hurricane Frederic.

4. COMPARISON OF RAINFALL ESTIMATES

a) Areal definitions

The areal distribution of estimated rainfall from the NAW and CST IR techniques are shown relative to the radar rainrate and GOES IR cloud observations in Figs. 1-3. The Arkin IR estimate areas (not shown) are almost identical to the NAW total areas. The IR techniques place the highest rainrates in the coldest cloud areas of the CDO and outer rainbands. On the 0000 GMT 18 August 1983 estimates for Hurricane Alicia (Fig. 1) the heavier satellite rain estimates occur in the gap between the eyewall and a broad inner rainband on the Galveston, Texas (GLS) radar. An outer band of precipitation to the east of the CDO is recognized by all three estimates but extends beyond the quantitative and maximum ranges of the radar data. Several areas of convective precipitation are identified by the CST in the central overcast in echo-free or stratiform precipitation areas on the radar. By 0400 GMT (Fig. 2) the rainfall patterns in the CDO for the satellite estimates remain almost unchanged, while at the same time the radar-observed pattern has become highly

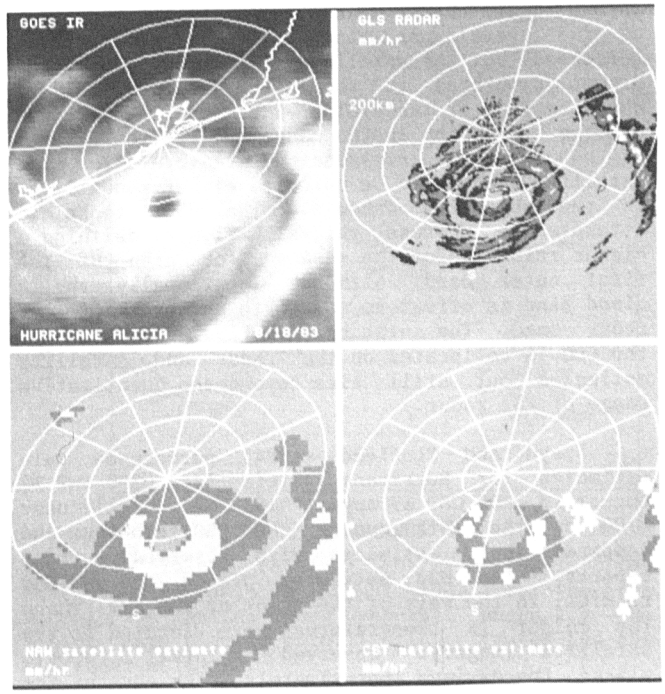

Fig. 1. Clockwise from upper left: GOES IR image, GLS radar rainrate PPI image, CST rainrate estimate, and NAW rainrate estimate for Hurricane Alicia at 0000 GMT, 18 August 1983. Gray scale for estimates is black, 1 mm/h; dark grey, 2-7 mm/h; light grey to white, 8-22 mm/h; repeat black, >22 mm/h. All estimates are displayed in GOES coordinates. Radar range circles in 50 km increments.

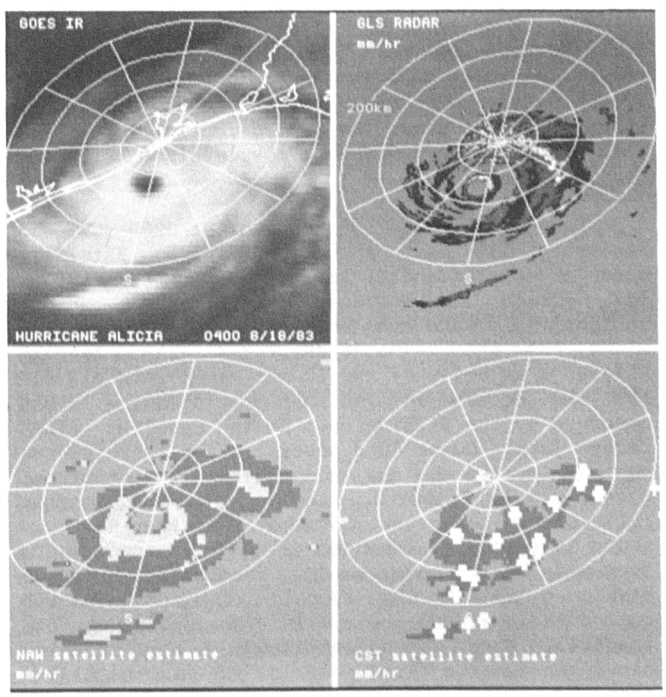

Fig. 2. Same as Fig. 1 except for Alicia at 0400 GMT.

asymmetrical. Radar rainrates in the north sides of the eyewall and broad inner band have greatly increased, yet the satellite estimates place the higher rainrates in the colder clouds on the opposite side of the cyclone. Whatever the cause of the asymmetry in the radar observations, there is no obvious corresponding feature in the satellite IR data to be detected either manually or in the objective schemes. The MSO technique attempts to address this situation by defining a higher rainrate for the onshore flow area of the first outer band, although locationally the IR cloud band is offset to the north and east of the radar band. The outer band in Fig. 2 now south of the CDO is co-located on the radar and satellite estimates but still lies beyond the quantitative range of the radar.

Spayd and Scofield (1984) performed rain estimates for Hurricane Alicia from 0300 GMT 18 August to 0900 GMT 19 August 1983 (landfall near 0700 on the 18th) using the MSO technique and compared their estimates with observed surface reports. The MSO estimates placed the maximum rainfall to the west of the track of the eye where the colder IR temperatures were located in the satellite imagery. Observed rainfall reports placed the maximum approximately 30 km east of the eye track and 65 km east of the satellite estimate maximum. It is apparent from the MSO landfall estimate that the difficulty in identifying areas of precipitation in the CDO can persist even after a hurricane has made landfall and is weakening. The ability of the MSO technique to define the eyewall location and assign to it the highest rainrate appears to be diminished by the analyst's interpretation of the IR imagery. Spayd and Scofield note that the meteorologist positions the maximum rainrate in MSO estimations near the coldest IR temperatures, whereas the Alicia estimate location would have been improved by placing the maximum in a concentric fashion about the eye and reducing or eliminating the rainfall contributions of cold CDO areas. An exception would have to be made in the presence of growing, overshooting convective tops in the CDO or eyewall which have been shown to be directly associated with a radar echo maximum at low levels (Hasler and Morris, 1986).

Estimates for Hurricane Diana at 0200 GMT 13 September 1984 are shown in Fig. 3. Satellite cloud cover area and IR temperatures were similar for Alicia and Diana, but maximum radar reflectivities and echo area were much lower for Diana (35 dBZ vs. 48 dBZ for Alicia). As with Alicia, a majority of the IR-estimated rainfall in the CDO occurs in the non-precipitating areas observed by the Wilmington, North Carolina (ILM) radar data. Outer band precipitation features are again colocated on the radar and IR estimates. Diana did not develop the persistent asymmetric reflectivity structure shown by Alicia, nor was there evidence of enhanced rainfall in the onshore flow area of the outer bands. Precipitation maxima developed within the eyewall of Diana and moved cyclonically around the eye in the period before landfall. There was no evidence of a corresponding cloud top feature observable in the IR satellite data.

A detailed comparison between radar and satellite IR and visible stereo data for Hurricane Frederic may be found in Hasler and Morris (1986). Frederic displayed the asymmetric radar

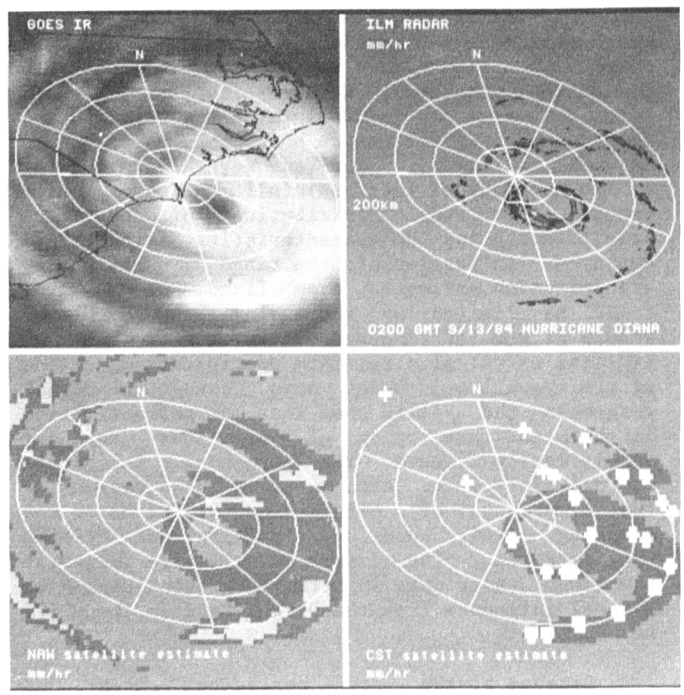

Fig. 3. Same as Fig. 1 except ILM radar for Hurricane Diana at 0200 GMT, 13 September 1984.

reflectivity structure of Alicia by having a broad inner band and higher eyewall reflectivities on the landward side of the eye. Overlying the inner band of stratiform precipitation was a warm trench in the CDO north and west of the eye so that as with Alicia, the higher satellite rainfall estimates occurred outside the region of high radar estimates. Frederic was unique among the three hurricanes studied by the presence of large overshooting convective tops or anvils in the eyewall. The development of an overshooting top would be accompanied by the appearance of a low-level radar reflectivity maximum roughly beneath. Other radar maxima of equal or greater intensity were present without overshooting cloud tops. These overshooting tops are the only cold IR feature in the CDO region for the 3 cases which can be positively correlated with a radar precipitation maximum.

The radar-satellite comparisons serve to point out the weaknesses of satellite IR techniques in locating active areas of precipitation, as defined by radar, in the tropical cyclone environment. Most satellite rain estimation techniques have been developed for use in convective rain situations, and inherent in the estimates is the assumption that areas of precipitation are directly associated with cold cloud tops observed in the IR data. This assumption breaks down in the highly sheared tropical cyclone center where there can be significant displacements of the cold cloud tops from the precipitation areas seen on low-level radar or as measured by surface raingages.

Comparison of the eyewall location with the cloud top topography reveals that the eyewall precipitation underlies not the coldest cloud tops but the sloping region of the eye on the satellite IR image. This is consistent with the outward

slope with height of the eyewall found by Jorgensen (1984) and others. Unless a satellite rainfall technique can identify the eye or center of a tropical cyclone and apply appropriate rainrates under the sloping cloud tops (or equivalent area if no eye is distinguishable), the location of the highest rainrates will be in error, and the most significant precipitation area (due to the high rainrate in the eyewall) will be missed. In addition, dense cirrus in the CDO masks underlying clouds of the stratiform precipitation areas, the latter characterized by relatively small vertical extent (as deduced by vertical scanning radar). The satellite rain estimation techniques have greater success locating the radar observed precipitation in the outer bands where the vertical wind shear is reduced (Hasler and Morris, 1986), and where overlying cirrus is not present.

b) Quantitative rainfall comparisons

Area rainfall totals for the IR and radar rain estimates were computed to assess the effectiveness of the IR techniques in estimating, if not the actual distribution, the total amount of precipitation and its temporal variability in a tropical cyclone. Volume rainrates were computed for the estimates within the area defined by the quantitative range of the given radar(s) and are plotted as a function of time in Figs. 4-6. Volume rainrate is the product of the hourly rainrate within an image pixel and the area of the pixel, summed over the precipitation area. For Alicia and Frederic (Figs. 4 and 6) the estimates were totaled for the entire CDO areas. Totals for Diana (Fig. 5) were restricted to within 150 km of the radar due to a higher elevation angle during radar data collection. MSO estimates were not included in the comparisons due to their subjective nature. Estimates for the outer bands could not be compared because of the quantitative range restriction. Satellite estimate areas for the CDO and OBA were generally distinct, allowing the CDO to be evaluated separately.

Alicia estimates shown in Fig. 4 show a general increase in volume rainfall during the hours prior to landfall. The CST is closest to the GLS radar estimate in terms of amount but is much more variable with time. The variability of the CST relative to the other methods is due to its sensitivity to IR temperature within the CDO and to the higher maximum rainrates assigned to identified convective features. The Arkin technique, a simple IR threshold, is the most similar to the GLS estimate in terms of temporal variation. The average overestimates of the IR schemes compared to radar are 86%, 62%, and 18% respectively for Arkin, NAW, and CST. IR rain estimation techniques were apparently able to discern the increase in radar volume rainrate in Alicia on the scale of the CDO.

Estimates for Diana are in marked contrast to the favorable Alicia comparisons. CDO area and temperature distribution for Diana were similar to Alicia, yet the rain totals for Diana were an order of magnitude less. Airborne radar data taken during reconnaissance flights of Diana corroborate the low radar reflectivities observed by the ILM radar (Black, 1987). The upward trend with time of the satellite estimates in Fig. 5 is not shared by the nearly constant ILM radar estimate. Total precipitable water (PW) from area soundings was computed in order to explain the radar-observed rainfall differences between Alicia and Diana. PW

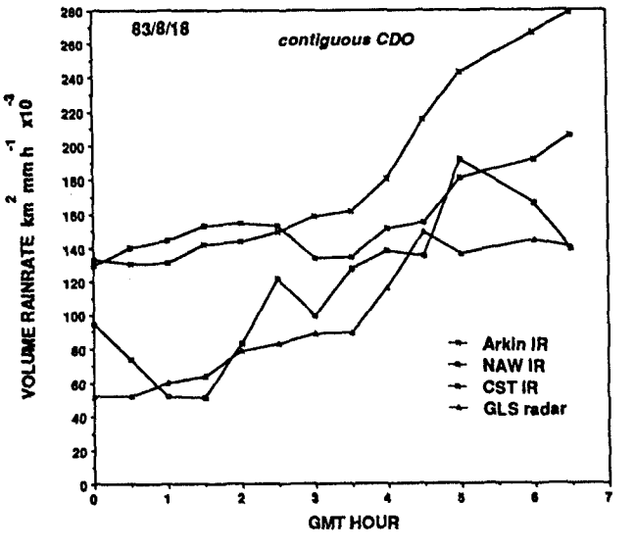

Fig. 4. Volume rainfall estimate totals for Hurricane Alicia, 18 August 1983 ,for the area beneath the Central Dense Overcast. Shown are the Arkin, NAW, and CST satellite IR estimates and the GLS radar estimate.

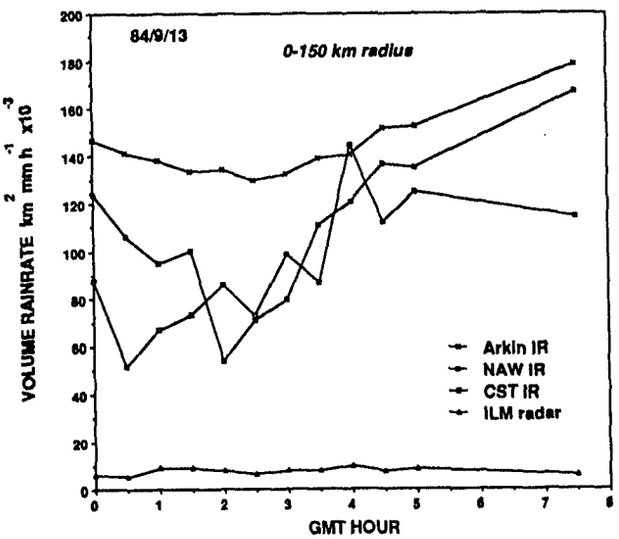

Fig. 5. Volume rainfall estimate totals for Hurricane Diana, 13 September 1984, for the area within 150 km of the ILM radar. Shown are the Arkin, NAW, and CST satellite IR estimates and the ILM radar estimate.

was not a discriminating factor and was actually 5% higher for Diana. Although other environmental factors cannot be ruled out in accounting for the rainfall disparity, a likelier explanation may lie in the structural differences of the hurricanes themselves. Assumping that the CDO cirrus canopy is produced mainly by vertical motion in the eyewall with outflow aloft, eyewall-only volume rainrates were calculated for Alicia and Diana by subjectively defining the eyewall on the radar data. Eyewall volume rainrates were only 56% greater for Alicia than Diana when averaged over the analyzed time periods. Diana did not have the broad inner precipitation band displayed by Alicia in Fig. 1. On the average, the eyewall accounted

for 70% of the rain in Diana within 150 km, but only 9% of the rainfall inside the CDO in Alicia. The IR rain estimation techniques may only be giving an estimate proportional to the amount of precipitation produced in the eyewall, and may not be able to discriminate important differences in precipitation structure elsewhere beneath the CDO.

Hurricane Frederic falls between Alicia and Diana in the degree of satellite overestimate relative to radar. Only a brief time period of data were available for the Frederic comparisons in Fig. 6, but the nearly steady-state nature of Frederic is reflected in the rain estimates. Frederic, like Alicia, possessed an inner band of stratiform precipitation within the radar data which would serve to lower the satellite overestimates. The radar compositing used for the Frederic rain estimations would reduce the accuracy of an eyewall-only radar estimate that could be used to compare with the findings for Alicia and Diana and an eyewall estimate for Frederic was not attempted.

5. SUMMARY AND CONCLUSIONS

Satellite IR rain estimation techniques were applied to 3 hurricane cases and resulting rainrate maps compared to radar-observed rainrates and areas. Success of the IR techniques in identifying areas of rainfall were dependent on the hurricane feature being addressed. Objective IR techniques were unable to identify the locations of radar-observed eyewall and inner band precipitation areas because of strong vertical wind shear in the eyewall and lack of vertical extent of stratiform precipitation beneath the Central Dense Overcast. Cold IR areas are assigned the highest rainrates by the satellite techniques but are displaced from major precipitation areas in the CDO. Precipitation areas in the outer bands were colocated in the satellite and radar estimates. Radar-satellite comparisons bear out the rules for identifying rain areas in the manual satellite rain estimation presented by Spayd and Scofield, with the exception of placing heavy rain estimates near the cold CDO regions.

Quantitative rain volumes are overestimated by the objective IR techniques relative to the radar estimates to a degree determined by the internal precipitation structure of the hurricane. IR estimates for Hurricane Alicia, which had a broad inner band of stratiform precipitation, were within a factor of 2 of the the radar estimate for the CDO area. Satellite overestimates for Diana, which was similar in IR-measured parameters to Alicia but had no inner stratiform band, were an order of magnitude greater than for Alicia. The ratio between satellite IR estimates for the CDO and radar estimates for the eyewall only was much closer for the two hurricanes and indicate that the IR rain estimates may only be monitoring amounts of precipitation produced in the eyewall. Current satellite IR rain estimation techniques were unable to identify structural differences beneath the CDO of hurricanes which are critical to locating precipitation areas and estimating total rainfall volumes.

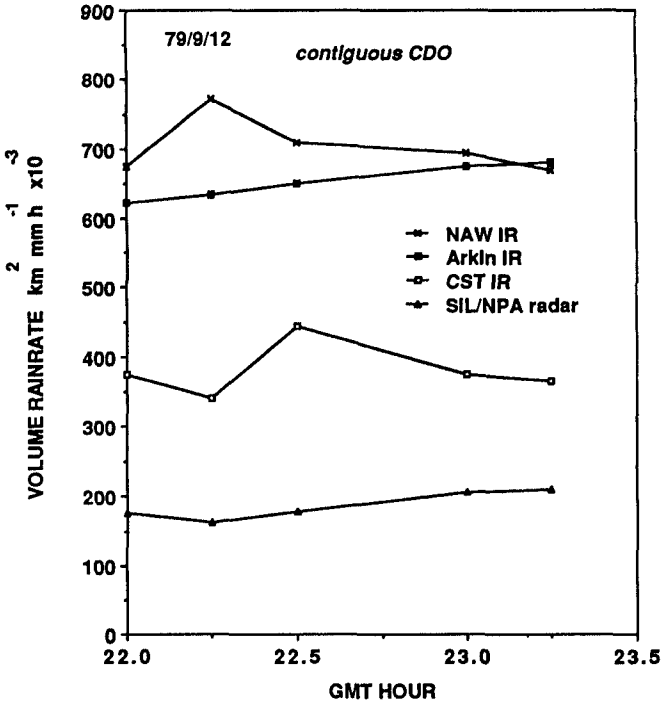

Fig. 6. Volume rainfall estimate totals for Hurricane Frederic, 12 September 1979, for the area beneath the Central Dense Overcast. Shown are the Arkin, NAW, and CST satellite IR estimates and the SIL/NPA composite radar estimate.

6. REFERENCES

Adler, R. F., and A.J. Negri, 1987: A satellite infrared technique to estimate tropical convective and stratiform rainfall. J. Climate Appl. Meteor. (In press).

Arkin, P.A., 1983: A diagnostic precipitation index from IR satellite imagery. Tropical Ocean-Atmosphere Newsletter, No. 17, 5-7. Available from JSIAO, U. of Washington, AK-40, Seattle, WA 98105.

Black, P.G., 1987: Personal communication.

Dodge, P., M. Black, R.W. Burpee, and F.D. Marks, Jr., 1987: Time lapse radar imagery from land-falling hurricanes. Preprints, 17th Conference on Hurricanes and Tropical Meteorology, Miami, AMS.

Griffith, C.G., P.G. Grube, D.W. Martin, J. Stout and D.N. Sikdar, 1978: Rain estimation from geosynchronous satellite imagery: visible and infrared studies. Mon. Wea. Rev., 106, 1153-1171.

Hasler, A.F., and K.R. Morris, 1986: Hurricane structure and wind fields from stereoscopic and infrared satellite observations and radar data. J. Climate Appl. Meteor., 25, 709-727.

Jorgensen, D.P., and P.T. Willis, 1982: A Z-R relationship for hurricanes. J. Appl. Meteor., 24, 356-366.

____, 1984: Mesoscale and convective-scale characteristics of mature hurricanes. Part 1: General observations by research aircraft. J. Atmos. Sci., 41, 1268-1285.

Negri, A.J, R.F. Adler and P. J. Wetzel, 1984: Rain estimation from satellites: An examination of the Griffith-Woodley technique. J. Climate Appl. Meteor., 23, 102-116.

Spayd, L. E., Jr. and R.A. Scofield, 1984: Preliminary operational results of a tropical cyclone precipitation estimation technique using GOES data. Preprints, 15th Conference on Hurricanes and Tropical Meteorology, Miami, FL, AMS, 207-216.

RAIN ESTIMATION FROM SATELLITES: AREAL RAINFALL-RAIN AREA RELATION

Long S. Chiu

Applied Research Corporation
8201 Corporate Drive, suite 920;
Landover Maryland 20785 U.S.A.

1. INTRODUCTION

Accurate measurements of global precipitation are vital to the advancement of our knowledge of the dynamics of the Atmosphere and oceans. The sparcity of rain gauges over the vast oceans and inherent measurement errors on board ships pointed to satellite observations as the ultimate mode by which global precipitation measurements can be made (Atlas and Thiele 1981; Austin and Geotis 1981).

Rainfall estimation techniques from satellite observations have been reviewed by Barrett and Martin (1981). Many of these techniques involved the estimation of cloud parameters from visible or infrared imageries. The underlying assumption is the association between precipitation and rain clouds. Arkin (1979) found that the fraction of high cloud coverage as derived from the GOES IR imageries correlates significantly with areal rainfall in GATE. An GPI (GOES precipitation index) which relates the rainfall amount to fractional high cloud is developed. This index of precipitation, which is calibrated to the GATE data, is found to worked remarkably well for tropical rainfall. Incorporating information from both IR and visible imageries, Lovejoy and Austin (1979) developed a statistical pattern recognition technique which discriminates high altitude highly reflective but non-raining clouds from the rain bearing clouds in an IR imagery. The rain amount is the product of the cloud area and a climatological rainrate constantly updated with radar measurements. The success of both techniques to estimate rainfall pointed to a tight relation between areal rainfall and cloud area.

From radar studies, it has been shown that the amount of rainfall associated with convective storms are related to the so called Area Time Integral (ATI) which is the integral of convective rainy areas integrated over the life time of storms (Lopez et al. 1983, Doneaud et al. 1981, 1984). If we consider sampling the rain field following the storm through a moving frame of reference, the distribution of all observations can be modeled by a mixed distribution. The mixed distribution consists of a discrete part of (1-p) at zero rainrate and a continuous distribution for the rainy observations whose integral is p. The probability of rain, p, can be interpreted as a measure of intermittency that describe events of moist instability in the rain field. The mean of the mixed distribution is p multiplied by a, where a is the average rainrate of the rainy pixels. If we associate p with the ATI, it becomes apparant that the most sensitive parameter in the mixed distribution in estimating total rainfall is the parameter p. Such sensitivity is also demonstrated from point rainrate measurements by Jackson (1986) who found that monthly rainfall in tropical weather stations is significantly correlated with the number of raindays but shows little relation to the average intensity of raindays. We shall demonstrate in this paper that the areal average rainfall rate is significantly correlated with the rain area if the area under consideration is large compared to the lagragian integral scale.

Satellites do not measure rainrates directly but provide covariate measurements such as radiances from different portions of the spectrum. The resolution of these measurements are different depending on the frequency bands over which they are measured. The parameters of the mixed distribution are dependent on the resolution of observation: if the field of view (FOV) of the satellite sensor is large, there is a greater chance of observing rain within the larger FOV, i.e. a larger p in the mixed distribution (Kedem and Chiu 1987). For GATE, p is about 10% for pixel size of 4 km and 50% for pixel size of 40 km (Chiu 1987). The detection of rainy areas also involves the choice of a threshold. Since the radiance measurements contain noise, a low threshold may include noise whereas a high threhold may weaken the signal and the statistics may be unstable. This paper examines the problem of resolution and threshold in the estimation of areal rainfall from rain areas.

2. THE GATE DATA

The data we used for this study is the radar-derived rainfall rate data collected in the so called B-scale during the first two phases of GATE. The data for the first two phases, each lasting about three weeks, are based mainly on the C-band radar observations on board the research vessel "the Oceanographer" located at the center of GATE. The center of the B-scale area is located at roughly 8.5N, 23.5W and encompasses a circle of about 200 km in diameter. Arkell and Hudlow (1977) composited the radar data from all ship observations at 15 minutes intervals.

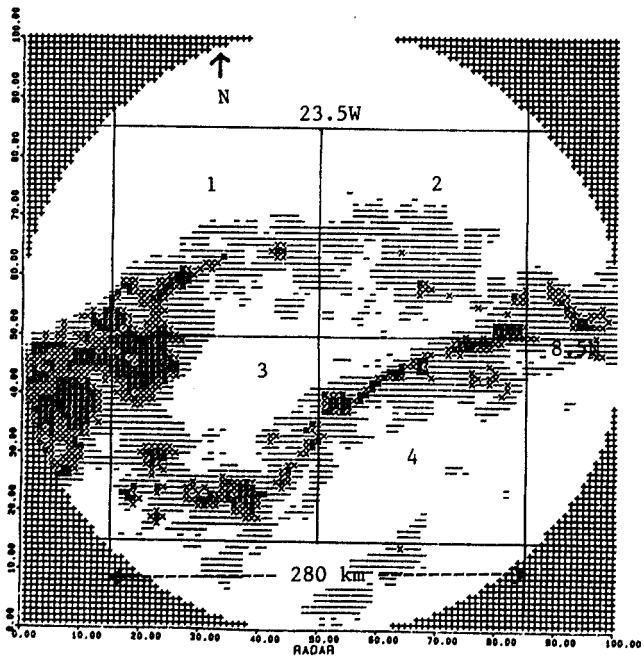

Figure 1. Schematic showing the GATE B-Scale Region and four sub-regions.

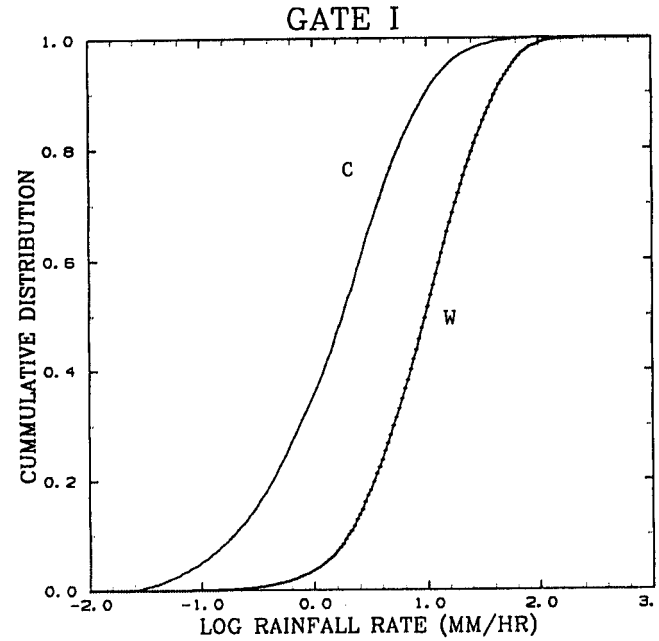

Figure 2. Cummulative distribution of rainrate observations C(R) and contribution to total rain volume W(R).

Patterson et al (1979) converted the radar data to rainrates and binned the data into 4 km pixels. The space-time scales in the basic data are therefore 4 km and 15 minutes. Not counting missing periods, there are altogether 1716 15-minute "snap shots" in phase I and 1512 in phase II of GATE. To minimize computer storage and increase computational efficiency, only data in a 280 km square (70 pixels on the side) centered in GATE. (see Fig. 1).

3. RAINRATE STATISTICS

We first present some rainrate statistics from GATE for resolutions of 4 km and 40 km. Fig. 2 shows the cummulative distribution (C) of 4 km pixel rainrate observations in GATE I and the contribution to the total rainfall amount by different rainrate categories (W) which are defined as

$$C(R) = \sum_{Ri=0}^{Ri=R} f(Ri)$$

$$W(R) = \sum_{Ri=0}^{Ri=R} Ri\ f(Ri) \Big/ \sum_{Ri=0}^{Ri=Rmax} Ri\ f(Ri)$$

where f(Ri) is the percent of rainy pixels with rainrate Ri and Rmax is the maximum observed rainrate. The normalization guarantees that

$$C(0) = 0 = W(0) \text{ and } C(Rmax) = 1 = W(Rmax)$$

The functions C(R) and W(R) for GATE II are very similar (see Table 1). In the range of 0-5 mm/hr is contained about 80% of the rainy observations but only about 30% of the total amount. About 90% of the total rain amount falls in the range 1 to 50 mm/hr which contains only about 60% of the rainy observations. At a resolution of 40 km, the statistics are different. About 30% of the total rain falls at a rate of less than 2-3 mm/hr and 90% of the rain falls in the range of .25-15 mm/hr which contains about 60% of the rainy observations also.

TABLE 1. CUMMULATIVE DISTRIBUTION AND CONTRIBUTION TO TOTAL RAINFALL

RESOLUTION	4 KM				40 KM			
GATE	PHASE I		PHASE II		PHASE I		PHASE II	
RAINRATE (mm/hr)	C	W	C	W	C	W	C	W
.25	.13	.00	.13	.00	.57	.04	.58	.05
.5	.23	.01	.24	.01	.67	.08	.70	.10
1	.36	.04	.38	.04	.77	.15	.80	.19
2	.54	.11	.55	.11	.86	.28	.89	.34
3	.66	.18	.67	.18	.91	.39	.93	.45
4	.74	.25	.74	.25	.93	.49	.95	.56
5	.78	.31	.80	.31	.95	.57	.96	.63
10	.91	.53	.91	.51	.987	.82	.99	.86
15	.95	.67	.95	.64	.997	.94	.99	.96
20	.97	.75	.97	.72	.999	.98	.999	.98
30	.987	.85	.98	.82	.999	.998	.999	.99
50	.997	.94	.99	.92	1.0	1.0	1.0	1.0
100	.999	.99	.99	.99	1.0	1.0	1.0	1.0

For each snap shot, the areal mean rainrate [R] and fractional rain area Pr is calculated. [.] denotes area averaging over the 280 X 280 km square. Pr is the fractional area of the square which is covered by rain with rain rates greater than a specified threshold value, r. Fig. 3 shows the cummulative distribution of the fractional rain area Pr with rainrate (r) greater than 0 mm/hr, i.e. Po, for GATE I and II. It can be seen that the median of Po is about 0.085 for

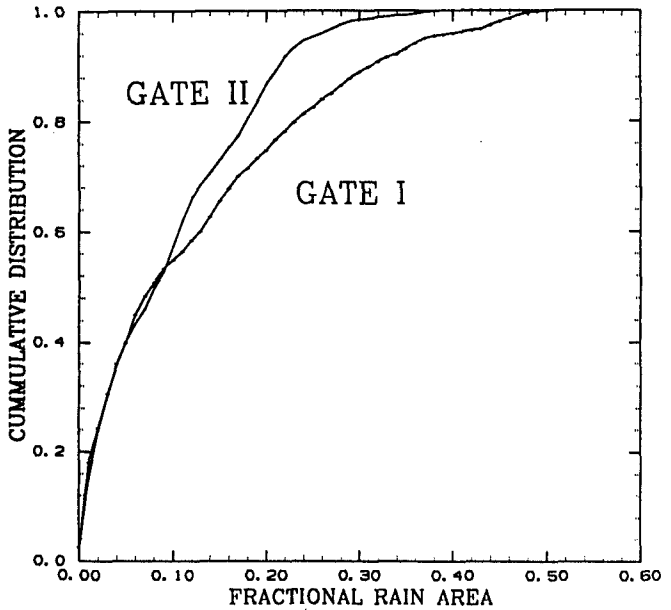

Figure 3. Cummulative distribution of fractional Rain Area, Po, in 280 km square.

both phases of GATE. However, GATE I is dominated by large values of Po. About 25% of the scans in GATE I have fractional rain area in excess of 0.2 of the 280 km square while in GATE II this is only about 15%.

4. AREAL RAINFALL-RAIN AREA RELATION

We examine the relation between areal average rainfall and rain area for GATE in this section. To study the sensitivity of the relation to the threshold used, indices of rain areas are obtained by choosing thresholds of 0, 1, 5, 10 and 20 mm/hr. These sensitivity tests are similar to Arkin's (1979) analysis who examines different cloud top heights to maximize his high cloud coverage- rainrate relationship. In practice, a high cutoff is preferred since this signal will be less contaminated by noise in the rain field. On the other hand, if a very high cutoff is set, the signal will be weak (i.e. Pr small).

Fig. 4 shows the scattergrams of [R] verses Pr for r=0, 1, 5, 10 and 20 mm/hr for GATE phase I (upper panel) and II (lower panel). The nature of the scattergrams are quite different. For the low cutoffs (r=0 and 1 mm/hr), the scattergrams show a slight upward curvature whereas at the higher cutoffs (r= 5 and 10 mm/hr), the scattergrams are linear and at the 20 mm/hr cutoff, they even show a slight downward curvature. At a threshold of 5 mm/hr, the scatters are small and the relation between [R] and Pr is almost linear.

Linear regression analyses of the form

$$[R] = b\,Pr + c + e$$

where b is the slope, c the intercept and e the error are performed. The regression procedure minimizes the mean square error (MSE) defined as:

$$MSE = \langle e^2 \rangle$$

where < > denote time averaging over the total number of snap shots.

The estimated slope b, intercept c, the percent of variance explained by the linear regression (square of coefficient of correlation) and the MSE for GATE I and II are summarized in table 2.

TABLE 2. REGRESSION COEFFICIENTS, MEAN SQUARE ERROR AND VARIANCES EXPLAINED

	GATE I				GATE II			
VARIANCE(mm/hr)	0.50				0.24			
r (mm/hr)	b	c	VAR (%)	MSE	b	c	VAR (%)	MSE
4 km PIXELS								
0	5.06	-0.13	77.6	0.113	4.94	-0.91	70.6	0.071
1	7.21	-0.01	88.6	0.057	7.52	-0.68	85.3	0.035
5	15.85	0.05	97.9	0.011	18.09	0.01	97.0	0.007
10	33.27	0.12	94.7	0.027	36.24	0.07	96.0	0.009
20	93.14	0.16	85.3	0.074	82.42	0.14	87.4	0.030
40 km PIXELS								
0	1.53	-0.27	30.7	0.350	0.98	-0.08	22.6	0.186
1	4.63	-0.04	84.5	0.078	4.28	-0.01	85.3	0.035
2	6.63	0.03	92.2	0.040	6.16	0.06	91.3	0.021
3	8.54	0.09	93.8	0.031	8.09	0.10	91.4	0.021
4	10.43	0.14	92.2	0.039	10.01	0.15	87.1	0.031
5	12.53	0.18	89.5	0.053	12.09	0.18	83.6	0.040

b and c are slope and intercept of the linear regression, VAR variance explained by the linear model and MSE mean square error.

It can be seen that the variance explained increases from .77 for a threshold of 0 mm/hr to a maximum of 0.97 for a threshold of 5 mm/hr. The best correlation (corr = 0.98) occurs at a cutoff rainrate of about 5 mm/hr, with MSE's of about 2 to 3% of the rainrate variance, var([R]). For a resoultion of 40 km the best regressor is rain area defined by a threshold of 3 mm/hr. The area defined by rainrates greater than 0 m/hr only explains about 30% of the variance.

The slopes of the regression equation are quite different between GATE I and II. At a threshold of 5 mm/hr, the slope is about 16 for GATE I and 18 for GATE II. It is difficult to assess the significance of the difference since the number of independent samples (degrees of freedom) is unknown.

To examine the spatial variablity of the regression, we partitioned the 280km square into 4 equal area 140 km squares (labelled 1, 2, 3 and 4 in Fig. 1) and perform similar regression analyses. The resolution and threshold are 4 km and 5 mm/hr respectively. The results are presented in Table 3.

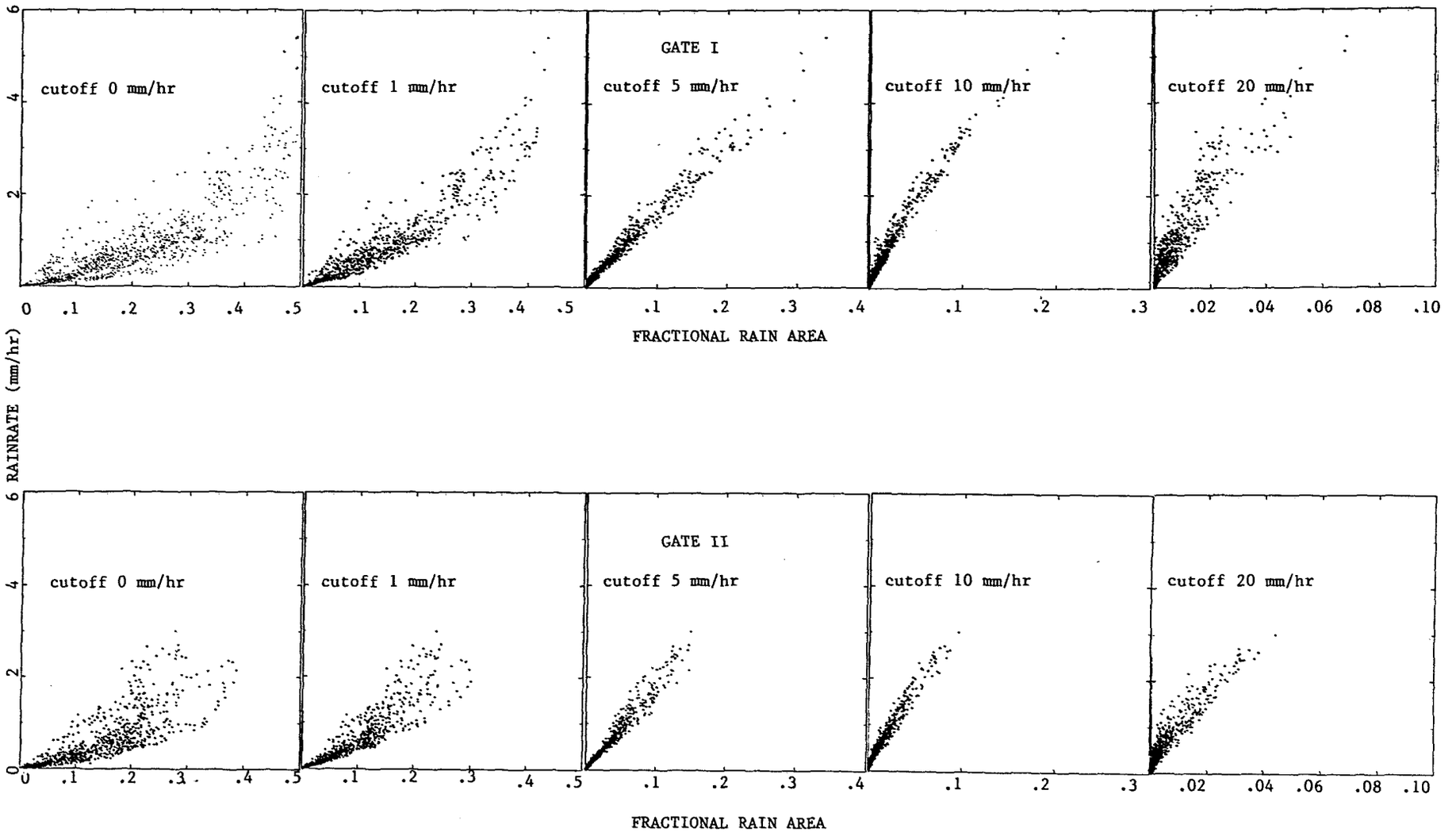

Figure 4. Scattergrams of areal average rainrate versus fractional area with rainrate above cutoff for GATE phase I(upper panel) and Phase II (lowe panel).

TABLE 3. REGRESSION PARAMETER FOR FOUR REGIONS IN GATE

GATE PHASE	REGION	f(%)	AVG RR	b	c	VAR(%)
I	1	54	.255	17.0	.025	96
	2	65	.501	15.4	.065	96
	3	58	.396	15.8	.046	96
	4	67	.815	15.6	.078	97
II	1	52	.323	16.5	.032	95
	2	62	.367	18.1	.023	95
	3	71	.317	18.3	.017	95
	4	65	.536	17.5	.023	97

f is the percent of scans with nonzero Pr's.
AVG RR is average rainrate in the 140km square
b and c are slope and intercept of the regression and VAR is the variance explained.

Region 4 has the highest rainrate in both phases of GATE. The slopes of the regression equations seem to be independent of f and the average rainrate. We show in the appendix that if an exact linear relation holds between areal average rainrate and rain area, the existence of a large number of zero of the rain area index does not appreciable change the estimate of the slope of the equation.

5. DISCUSSION

We showed that the fractional rain area in GATE accounts for a large part of the areal rainfall variance. The best index is the fractional rain area defined by a threshold of about 5 mm/hr at a resolution of 4 km and 3 mm/hr at a resolution of 40 km. The variance explained are about 97% and 93% respectively for the 4 km and 40 km resolution.

Why is the variance explained a maximum at a threshold of 5 mm/hr at the 4 km resolution? The answer lies in the dynamic structure of precipitation in GATE. Cheng and Houze (1979) estimated 30-40% of the GATE rainfall are stratiform precipitation associated with anvils of convective complexes. These anvil precipitation falls in the 2-4 mm/hr range (Leary and Houze 1979). From Table 1, we found that about 30% of the total rain volume falls at a rate of 5mm/hr and lower. Hence the 5 mm/hr threshold can be considered a boundary between convective and stratiform precipitation and the rain area index defines regions of convective precipitation. This is consistent with Arkin's cloud index which represents the fraction of deep convective clouds.

The high variance of areal rainfall explained by the rain area suggests that the rain area is a useful parameter in the estimation of tropical rainfall. This relation is especially encouraging in view of the simulation results of Adler and Mack (1986) who showed that the rain area within a NIMBUS 7 SMMR pixel is related to the polarization at 37 GHz. The regression parameters are however dependent on resolution and threshold and hence in applying the rain area index to satellite rain estimation, caution should be exercised in the calibration procedure. Other data sets should be examined to study the statistical stability of the relation.

APPENDIX: LINEAR REGRESSION WITH ZEROES

Consider a sequence of Y's which are linearly related to X's through the relation $Y_i = a X_i + b$, $i=1, \ldots, Nf$, $0<f<1$, where f is the ratio of the number of nonzero rain area index to the total number of snap shots (N), or the frequency of observing nonzero rain index. Define the sequence (of size N) Q and Z which contains N(1-f) zeroes and X's, $Q=\{0,\ldots,0,X\}$ and Y's, $Z=\{0,\ldots,0,Y\}$. Let [ ] and < > be defined as

$$[(\ )] = 1/Nf \sum^{Nf} (\ ) \quad \text{and} \quad \langle(\ )\rangle = 1/N \sum^{N} (\ )$$

then it can be shown that

$$[Y] = a\,[X] + b$$
$$\langle Q\rangle = f\,[X]$$
$$\langle Z\rangle = f\,[Y]$$
$$\langle ZQ\rangle = f\,[XY] = f(a\,[X^2] + b[X])$$
$$\langle Q^2\rangle = f\,[X^2]$$

If we perform a linear regression of the form

$Z = c\,Q + d + e$, then the minimumm error estimate for c is

$$c = (\langle ZQ\rangle - \langle Z\rangle\langle Q\rangle) / (\langle Q^2\rangle - \langle Q\rangle^2)$$

After substitution, we find

$$c = a + b(1-p)/([X^2]-p[X]^2)$$

If $b = 0$, then $c = a$ and it is easily shown that $d = 0$.

ACKNOWLEDGEMENTS

T. Bell, G. North and D. Short provided stimulating discussions. This work is supported by the National Aeronautics and Space Administration through contract NAS5-30083.

REFERENCES

Adler, R. F. and R. A. Mack, 1986: "Field of View Effects in Estimating Precipitation from Satellite Micrwoave Radiances", 2nd conf. Satellite Meteor. and Remote Sensing Appl., Williamsburg, VA, Amer. Meteor. Soc., Boston, MA.

Arkell, R. and M. Hudlow, 1977: GATE Internation Meteorological Radar Atlas, US Dept. of Commerce, NOAA, US government printing Office, Washington, D.C.

Arkin, P.A., 1979: "The Relationship between Fractional Coverage of High Cloud and Rainfall Accumulation during GATE over the B-Scale", Mon. Weath. Rev., 107, 1382-1387.

Atlas D. and O. Thiele, 1981: Precipitation Measurements from Space, Workshop Report, Oct 1981, NASA, Goddard Space Flight Center, Greenbelt, MD 20771.

Austin, P.M. and S. Geotis, 1980: "Precipitation Measurements over the Oceans", Air Sea Interaction, eds. F. Dobson, L. Hesse and R. Davis, Plenum pub. corp., 227 West 17th St., New York, NY, 10011.

Barrett, E. C. and D. M. Martin, 1981: The Use of Satellite Data in Rainfall Monitoring, Academic Press, New York, NY, 340pp.

Cheng, C-P, and R. A. Houze, Jr., 1979: "The Distribution of Convective and Mesoscale Precipitation in GATE Radar Echo Patterns", Mon. Weath. Rev., 107, 1370-1381.

Chiu, L. S., 1987: "Estimating Areal Rainfall From Rain Area", Conf. Tropical Precipitation Measurements, Oct. 28-30, Toyko, Japan, Science and Technology Corp., PO Box 7390, Hampton, VA 23666-0321.

Doneaud A.A., L. Smith, A.S. Dennis and S. Sengupta, 1981: "A Simple Method for Estimating Convective Rain Volume over an Area", Water Resour. Res., 17, 1676-1682.

Doneaud, A. A., S. Ionescu-Niscov, D. L. Priegnitz and P. L. Smith, 1984: "The Area-Time Integral as an Indicator for Convective Rain Volume", J. Clim. Appl. Meteor., 23, 555-561.

Jackson I.J., 1986: "Relationship between Raindays, Mean Daily Intensity and Monthly Rainfall in the Tropics", J. Climatology, 6, 117-134.

Kedem, B. and L. S. Chiu, 1987: "Are Rainrate Processes Self-similar?" Water Resour. Res.. (to appear)

Lopez, R. E., J. Thomas, D. O. Blanchard and R. L. Holle, 1983: "Estimation of Rainfall over an Extended Region using only Measurements of the Area Covered by Radar Echoes", Preprints, 21 st conf. Radar Meteor., Edmonton, Alberta, 681-686, Amer. Meteor. Soc., Boston, MA.

Lovejoy S. and G. L. Austin, 1979: "The Delineation of Rain Areas from visible and IR Satellite Data for GATE and Mid-Latitudes", Atmosphere-Ocean, 17(1), 77-92.

Patterson V.L., M.D. Hudlow, P.J. Pytlowany, F.P. Richards and J.D. Hoff, 1979: GATE Radar Rainfall Processing System, NOAA Technical Memorandum, EDIS 26, NOAA, Washington, D.C.

INTENSIVE OBSERVATIONS OF MARINE STRATOCUMULUS DURING FIRE

Bruce A. Albrecht

The Pennsylvania State University
University Park, Pennsylvania

1. INTRODUCTION

A major effort was made during the summer of 1987 to provide the observations needed to answer key questions concerning the formation, maintenance, and dissipation of marine stratocumulus clouds. A comprehensive set of measurements was obtained off the coast of California from 29 June - 19 July 1987 using aircraft, satellite, and surface-based instruments. These Intensive Field Observations (IFO) were part of the First ISCCP Regional Experiment (FIRE) and were intended to not only increase our physical understanding of marine stratocumulus, but to provide the in situ measurements needed to develop and test satellite cloud retrieval schemes. A key and unique aspect of the experiment was the coordinated use of several observing platforms to simultaneously make measurements in selected cloud areas off the coast of California.

The overall objectives and the basic plans for the FIRE marine stratocumulus IFO were outlined by Randall et al. (1984). A general description of FIRE and the associated IFO's is given by Cox et al (1987). In this paper we summarize the 1987 marine stratocumulus IFO, show samples of the data collected, and discuss the general plans for the analysis of this unique data set.

One element of the experiment that was an unqualified success was the weather. Extensive low-level clouds covered much of the eastern Pacific during the entire three weeks of the experiment. The extent of cloudiness that was observed during the IFO clearly illustrated why stratocumulus clouds are such an important element of the earth's climate system. Another striking feature revealed by the satellite images obtained during the IFO is the variability in the cloud structure over a wide spectrum of space scales. A challenge facing FIRE researchers will be to transform relatively complicated and detailed descriptions of this structure into generalizations (models) that can be of use for climate modeling and satellite retrieval.

Several key questions concerning our understanding of marine stratocumulus were raised by Randall et al (1984). A theme central to those questions concerns cloud structure - how various processes (e.g. entrainment and radiation) control the structure and how the cloud structure in turn affects those processes. Consequently , the experiment was designed to resolve and study cloud structure on time and space scales ranging from the micro to the large scale (10^{-6} to 10^{6} m). This was accomplished by using various observational platforms and strategies.

2. SURFACE-BASED MEASUREMENTS

A number of measurements were made from the northwest tip of San Nicolas Island, an island located approximately 60 miles southwest of Los Angeles. Continuous, high temporal resolution (at data rates of 1 minute or less) measurements were obtained during the marine stratocumulus IFO to describe the time evolution of the cloud and the related marine boundary layer structure. Continuous measurements of wind, temperature, humidity, and solar and longwave radiation were made from the surface and from a tower located at the tip of the island. In addition, several remote sensing devices were used to measure the time evolution of the boundary layer structure. A Doppler acoustic sounder was used to obtain wind profiles in the boundary layer (to height of approximately 1000 m). The reflectivity profiles from the acoustic sounder are being used to estimate the height of the inversion. A laser ceilometer simultaneously provided a continuous record of cloud-base height and was used to describe detailed variation in the cloud base height. A microwave radiometer was used to measure the vertically integrated liquid water and water vapor content. A continuous record of the winds above the inversion was obtained using a 400 MHz wind profiler. The instruments that were operated in the continuous mode worked very well during the entire experiment and will be used to describe the detailed temporal evolution of the structure of the boundary layer.

An advantage of the continuous ground-based measurements over those from other platforms is that they can define the evolution of the generation and dissipation of the clouds. This is illustrated in Fig. 1 where data from the ceilometer, acoustic sounder and a surface solar radiometer have been used to define the temporal evolution of a cloud deck from 12 Z, July 12 to 6 Z, July 15. These data show the breakup of the stratus at approximately 18 Z on July 12 and the reformation of the cloud approximately 12 hours later. The solar irradiance clearly reflects variations in the cloud depth. An important first step in the analysis of the island data will be to combine the data obtained from all the instruments that were used in a continuous data collection mode. This integrated data set will provide an unprecedented description of the time evolution

of the cloud-topped boundary layer. These data should be particularly useful in the evaluation of cloud retrievals from GOES data.

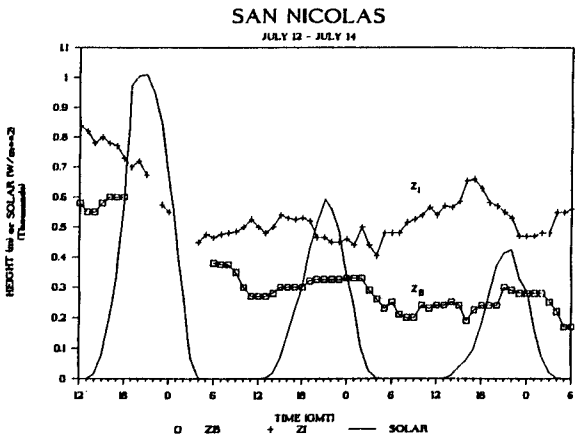

Fig. 1 Cloud base (z_B) and inversion heights (z_I) at one hour intervals determined subjectively from ceilometer and acoustic sounder data with downward solar irradiance from an Eppley pyranometer.

In addition to the continuous measurements, observations were made from two tethered balloons that were flown on a number of days during the experiment. The NASA Wallops balloon was used as a platform for turbulence, cloud microphysics, and radiation measurements. The balloon was used in either a fixed level or a profiling mode. Turbulence measurements were made with probes that were designed and operated by the British Meteorological Office. These probes were attached to the tether cable and measured wind, temperature and moisture fluctuations. Measurements were made by positioning the balloon above cloud such that probes attached at various intervals along the tether made measurements above, in, and below the cloud. These fixed level measurements will be used to define heat, moisture and momentum fluxes at several levels in the boundary layer.

In addition to the turbulence measurements, mean thermodynamic, cloud microphysical, and radiative flux measurements were made from instruments mounted on a pallet that was suspended from the balloon. During the fixed-level flights the measurements from this platform were used to define temporal variations in the cloud structure. In the profiling mode, observations taken from the pallet were used to give detailed profiles of temperature, water vapor, liquid water, cloud droplet spectra and radiative fluxes. The turbulence and profile measurements obtained from the tethered balloons will also be used to assist in the interpretation of the data collected from the instruments that were operating in a continuous mode during the experiment.

Although technical difficulties prevented flights with the Wallops balloon during the last few days of the experiment, a second tethered balloon operated by NRL was used to obtain profiles of temperature, moisture and aerosols during this period and for a week following the experiment.

Two to four rawindsonde launches per day were made from the island using a CLASS system. In addition, two radiosonde launches per day were made by personnel from the Pacific Missile Test Center.

The ship Point Sur, a research vessel owned by the National Science Foundation, was used by the Naval Postgraduate School to make measurements of atmospheric and sea conditions upstream from the island from July 8 to July 16. The ship was instrumented to make pressure, temperature, moisture, wind, radiation, aerosol and sea surface temperature measurements. Acoustic sounders were used to obtain boundary layer wind and reflectivity profiles. In addition, four rawindsonde launches per day were made from the ship. Measurements from the Point Sur will be used to determine how representative the island is of open ocean-conditions and to help estimate advective effects at the island.

A smaller ship, the Shanta Ray, was used to launch constant-level balloons (tetroons) to tag and follow the movement of air masses in the region of interest. High winds and seas, however, hampered these operations. Despite the adverse conditions, three balloons were launched and successfully tracked during an eight hour period. During the following day the tracking aircraft was unable to locate the balloons as they drifted into military restricted zones.

3. AIRCRAFT MEASUREMENTS

Several aircraft were used during the experiment. The UK C-130 and the NCAR Electra were used to make turbulence, radiation, cloud microphysics, and aerosol measurements in the boundary layer. In addition, the NCAR Electra was instrumented with a newly-developed lidar and with instruments for sampling chemical composition. The C-130 and Electra were used to gather data at a high rate for the purpose of calculating fluxes of energy, moisture, momentum, and ozone. Vertical profiles of these fluxes will be constructed and entrainment rates will be estimated from the fluxes at the base of the inversion. The high frequency data will also be analyzed using conditional sampling techniques. Since the C-130 and the Electra had comparable instrumentation and range they were used in a number of coordinated missions to study the temporal and spatial variability of the structure of marine stratocumulus. Most of the data collected from these aircraft were obtained by flying constant-level legs of 10 to 20 minute duration at levels below, in and above the cloud.

The NCAR Electra lidar provided a detailed description of cloud-top and cloud-base structure during many of the flights. Although the lidar is still under development, it worked well during a large part of the experiment. An example of the cloud-top structure obtained with the lidar is shown in Fig. 2 and shows considerable cloud-top structure at various scales.

The University of Washington (UW) C-131 was instrumented to make detailed cloud microphysics and radiation measurements and was equipped with a sophisticated scanning, spectral radiometer. It was principally used for in-cloud measurements and flew coordinated radiation missions with the C-130 and with the NASA ER-2.

The ER-2 was instrumented with a cloud lidar system, a multispectral cloud radiometer, and a Thematic Mapper Simulator, which simulates the spectral and spatial characteristics of a

similar instrument on Landsat-4 and also makes measurements in spectral bands similar to those of the Advanced Very High Resolution Radiometer (AVHRR) instruments on the NOAA-9 and NOAA-10 satellites. Since the boundary layer aircraft sample a relatively small area relative to that viewed by the satellites, a major role of the ER-2 was to serve as a bridge between the low-level aircraft and the satellites. Consequently, it was generally coordinated with the flight paths of the low-level aircraft.

Several coordinated and single-aircraft missions were flown during the experiment. They were designed to study the downstream evolution, diurnal variations and open-ocean structure of the cloud-topped boundary layer and to obtain measurements that could be compared with satellite and island measurements. Overall there were relatively few equipment failures on the aircraft and excellent cloud conditions were present during most of the experiment. Consequently, detailed descriptions of the structure of marine stratocumulus were obtained for a variety of cloud conditions. A total of 40 flights were made with the five aircraft involved in the experiment and twelve coordinated, multi-aircraft missions were flown.

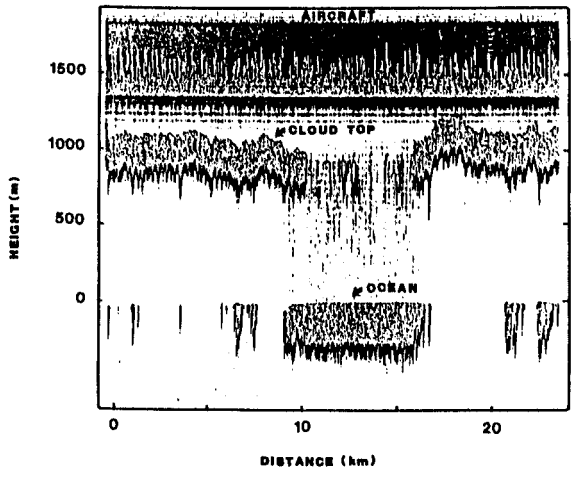

Fig. 2 Backscatter profiles obtained with an airborne lidar operating from the NCAR Electra for 14:04:53 GMT to 14:00:43 on 18 July.

4. SATELLITE MEASUREMENTS

GOES satellite images were used extensively for the planning of the aircraft missions. These images were obtained in near real time using a link to the University of Wisconsin with a UNIDATA/McIDAS workstation. When possible, aircraft operations were closely coordinated with the overpasses of various polar-orbiting satellites. On nearly every flight, the areas of interest were in the field of view of either the NOAA-9 or NOAA-10 AVHRR instruments. In addition, detailed multiple aircraft missions were flown in LANDSAT scenes on three different days. There were excellent cloud conditions on each of these three days. On July 7 a well-defined boundary between a clear and cloudy region was centered in the LANDSAT scene. This boundary was stationary during the day and the NCAR Electra made turbulence measurements across this boundary for approximately six hours. On July 14 and 16 coordinated missions involving the NCAR Electra, UK C-130, the NASA ER-2, and the UW C-131 were flown in LANDSAT scenes. Data from the European satellite SPOT were also collected for the FIRE region.

The satellites provided a description of the cloud structure on a much larger scale than that obtained from the aircraft measurements. A sample of the cloud structure information inferred from NOAA-9 and NOAA-10 AVHRR data using techniques described by Coakley and Bretherton (1982) is shown in Fig 3. These data are for a broken cloud field that was observed on 18 July for an area near 31.5 N and 122.5 W. The characteristic arch structure of the spatial variability of the radiances indicates the broken nature of the clouds (Coakley and Bretherton, 1982). In Fig. 3a each point represents a $(4km)^2$ portion of the region for a $(130\ km)^2$ area. The cloud-free 11 μm brightness temperature is 286.2 $\pm$ 0.4 K and the cloud brightness temperature is 278.4 $\pm$ 0.3 K. The mean cloud cover for $(30\ km)^2$ mesoscale regions is approximately 0.2. A similar analysis of data from NOAA-10 at 1605 Z (Fig 3b) for a $(250\ km)^2$ area indicates a cloud-free 11 μm brightness temperature of 287.7 $\pm$ 0.4 K and the cloud-top brightness temperature is 280.1 $\pm$ 0.6 K. The mean cloud cover at this time for $(60km)^2$ mesoscale regions is approximately 0.35. The characteristic arch structure of the spatial variability of the radiances indicates the broken nature of the clouds (Coakley and Bretherton, 1982). The Electra lidar data shown in Fig. 2 were obtained in this region at approximately 1400 Z (7000 LT).

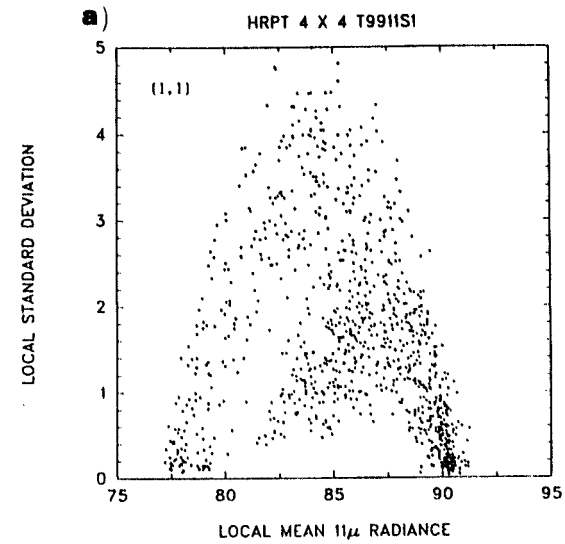

Fig. 3 Spatial coherence analysis for NOAA-9 and NOAA-10 AVHRR data obtained near 31.5 N and 122.5 W for a) 1103 Z NOAA-9 pass and b) 1605 Z NOAA-10 pass.

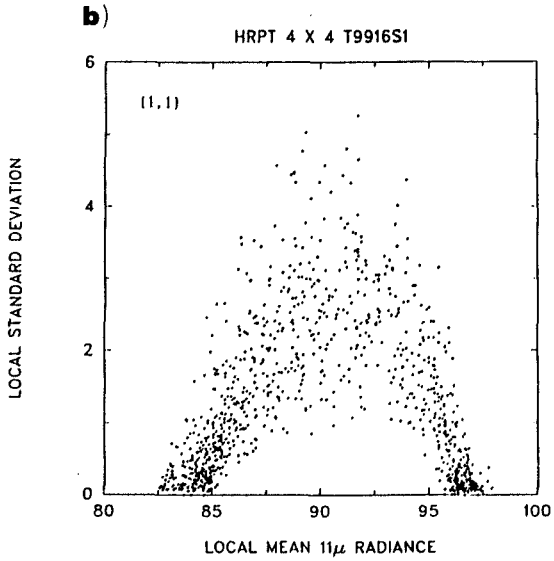

A potential temperature profile (from a preliminary data set) obtained in the same area is shown in Fig. 4. This profile indicates a two-layer vertical structure below the inversion with a stable layer near cloud base. The mixing ratio obtained from this sounding decreased by approximately 1 g/kg across the transition zone at cloud base and ozone increased across the layer. Although these results are preliminary, it would appear that the broken cloud structure observed in this region is related to the two-layered vertical structure. This structure is more like that associated with trade-cumuli (eg. Augstein et al. 1974) than the well-mixed structure assumed in the simple stratocumulus models.

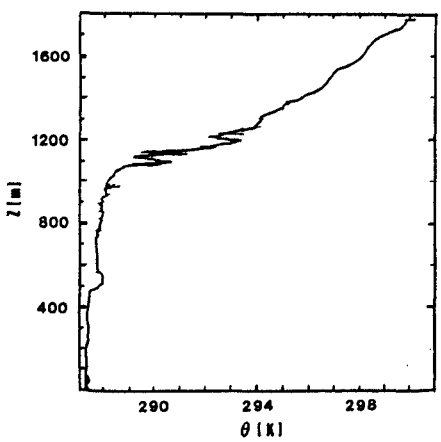

Fig. 4 Potential temperature profile obtained from the NCAR Electra at approximately 14:15:00 GMT on 18 July 1987.

The cloud-top temperature obtained from this sounding is approximately 279 K, which compares well with the cloud-top brightness temperatures of 278-280 K corresponding to the satellite data shown in Fig. 3. On this particular day the ER-2 made lidar and radiometer measurements in coordination with the NCAR Electra measurements. The early morning Electra flight was followed by a flight with the C-130 in the same region. Satellite measurements indicate that the clouds in this region became less broken during the 14 hours spanned by the Electra, C-130 and ER-2 flights. A complete analysis of the data collected during this day should provide a very useful documentation of the evolution of the mean, turbulence and cloud microphysical structure associated with variations in the cloud structure obtained from satellite observations. Several multiple aircraft missions with good satellite coverage were carried out during the IFO. A major effort will be made to combine the analyses obtained from aircraft and surface-based observations with the satellite observations.

5. CONCLUSIONS

An unprecedented set of aircraft, surface-based, and satellite measurements of the mean, turbulent, microphysical, radiative, and chemical characteristics of marine stratocumulus was obtained during the FIRE marine stratocumulus 1987 IFO. In general, the operational goals of the experiment were satisfied and preliminary results are very encouraging. Much of the success of this phase of FIRE can be attributed to nearly ideal cloud conditions. Significant analysis, however, will be required before the full impact of this unique data set can be realized. A major challenge will be to integrate and synthesize the analyses obtained from a variety of instruments and platforms to give the understanding needed to improve the parameterization of stratocumulus clouds in climate models and the methods for retrieving cloud properties from satellite observations.

6. ACKNOWLEDGEMENTS

I am grateful to James Coakley, Chris Fairall, Erik Miller, Wayne Schubert, Ronald Schwiesow, and Dennis Thomson for kindly supplying the preliminary data that were included in this paper. My participation in FIRE has been supported by the National Science Foundation (Grant ATM-8619854) and the U.S. Navy (Grant N000014-86-K-06880).

7. REFERENCES

Augstein, E., H. Schmidt, F. Ostapoff, 1974: The vertical structure of the atmospheric boundary layer in the undisturbed trade winds over the Atlantic Ocean. Bound. Layer Meteo., 6, 129-150.

Coakley, J. A., Jr., and F. P. Bretherton, 1982: Cloud cover from high resolution scanner data: Detecting and allowing for partially filled fields of view. J. Geophys. Res., 87, 4917-4932.

Cox, S.K., D. McDougal, D. Randall, R. Shiffer, 1987: FIRE - The First ISCCP Regional Experiment. Bull. Amer. Meteor.Soc.,67, 114-118.

Randall, D.A., J.A. Coakley, Jr., C.W. Fairall, R.A. Kropfli, and D.H. Lenschow, 1984: Outlook for research on subtropical marine stratiform clouds. Bull. Amer. Meteor. Soc., 65, 1290-1301.

CLOUD COVER STATISTICS FROM GOES/VAS

Donald P. Wylie, Peter Grimm

Space Science and Engineering Center
University of Wisconsin-Madison
Madison, Wisconsin

W. Paul Menzel

NOAA/NESDIS Advanced Satellite Products Project
Madison, Wisconsin

1. INTRODUCTION

The frequency of occurrence of cirrus clouds usually has been underestimated in cloud population studies. Satellite methods of analyzing cloud cover often mistake cirrus clouds for lower level clouds or completely miss them, because their infrared brightness temperatures are warmer than the temperature associated with their true altitudes. Thin cirrus are especially hard to identify on visible satellite images because they reflect little solar radiation and appear as dark or broken cloud fields. With the multi-spectral infrared sensor on the GOES-VAS satellite the identification of most cirrus is now possible.

A technique for deriving cloud top altitudes from the VAS infrared sensor was developed by Menzel (1983). It is also applicable to the polar orbiting High-resolution Infrared Radiometer Sounder (HIRS). The technique takes advantage of infrared channels with partial CO_2 absorption where the different channels are sensitive to different levels in the atmosphere. Thus, clouds appear on each channel in proportion to their level in the atmosphere. Low clouds will not appear at all on the high level channels, while high clouds appear on all channels. By modelling the upwelling infrared radiation from the earth atmosphere system in several VAS channels simultaneously, it is possible to infer the cloud top height independent of radiative transmissivity of the cloud. This gives the CO_2 technique the ability to distinguish thin cirrus clouds that would normally be missed by other techniques due to the transmission of terrestrial radiation through the cirrus.

The CO_2 technique has been installed on the Man-computer Interactive Data Access System (McIDAS) at the University of Wisconsin-Madison. It has been run operationally using the GOES-VAS imagery starting in October 1985. Statistics on cloud cover and especially cirrus cloud cover are being gathered for the continental United States and its bordering oceans. This paper describes the techniques and some of the first results of this program.

2. CO_2 TECHNIQUE DESCRIPTION

The VAS radiometer detects infrared radiation in twelve spectral bands that lie between 3.9 and 15 microns at 7 or 14 km resolution in addition to visible reflections at 1 km resolution. The 15 micron CO_2 band channels provide a good sensitivity to the temperature of relatively cold regions of the atmosphere. A demonstration of the vertical resolution of the three relevant CO_2 channels is given by the temperature profile weighting functions shown in Fig. 1. Each curve in the figure shows the sensitivity of the radiance observed in the spectral interval of the indicated channel to local variations in atmospheric temperature. As may be seen, only clouds above the 350 mb level will have strong contributions to the radiance to space observed by the 14.2 micron band (VAS channel 3), while the 14.0 micron band (VAS channel 4) senses down to 700 mb and the 13.3 micron band (VAS channel 5) senses down near the surface of the earth.

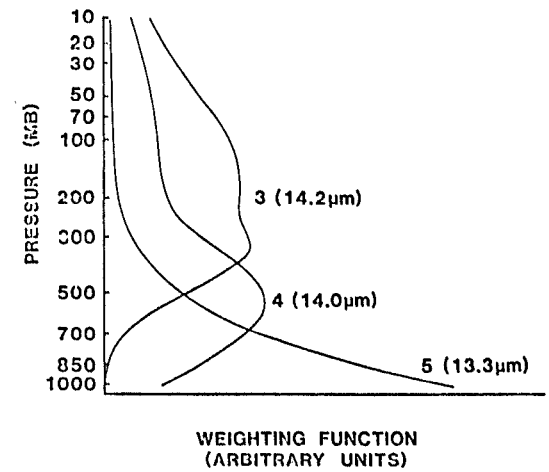

Fig. 1. The temperature profile weighting function of radiance to space as a function of emitting level for the VAS CO_2 spectral bands centered at 14.2, 14.0, and 13.3 microns.

To assign a cloud top pressure to a given cloud element, the ratio of the deviations in cloud produced radiances, $I(\nu)$, and the corresponding clear air radiances, $I_{cl}(\nu)$, for two spectral channels of frequency ν_1 and ν_2 viewing the same field-of-view is written as

$$\frac{I(\nu_1) - I_{cl}(\nu_1)}{I(\nu_2) - I_{cl}(\nu_2)} = \frac{\varepsilon_1 \int_{P_s}^{P_c} \tau(\nu_1, p) \frac{dB[\nu_1, T(p)]}{dp} dp}{\varepsilon_2 \int_{P_s}^{P_c} \tau(\nu_2, p) \frac{dB[\nu_2, T(p)]}{dp} dp}$$

In this equation ε is the cloud emittance, P_s the surface pressure, P_c the cloud pressure, $\tau(\nu, p)$ the fractional transmittance of radiation of frequency ν emitted from the atmospheric pressure level (p) arriving at the top of the atmosphere (p = 0), and $B[\nu, T(p)]$ is the Planck radiance of frequency ν for temperature T(p). If the frequencies are close enough together, then $\varepsilon_1 \cong \varepsilon_2$, and one has an expression by which the pressure of the cloud within the field-of-view (FOV) can be specified. The left side of equation (1) is determined from the VAS observed radiances and clear air radiances provided from spatial analyses of VAS clear-sky radiance observations. The right side of equation (1) is calculated from a temperature profile and the profiles of atmospheric transmittance for the spectral channels as a function of P_c, the cloud top pressure (discrete values at ~50 mb intervals spanning 1000 to 100 mb are used). In this study, global forecast temperature and moisture fields from the National Meteorological Center (NMC) are used. The optimum cloud top pressure is determined when the absolute difference $|\text{right}(\nu_1, \nu_2) - \text{left}(\nu_1, \nu_2, P_c)|$ is a minimum.

Once a cloud height has been determined, an effective cloud amount can be evaluated from the infrared window channel data using the relation

$$N\varepsilon = \frac{I(w) - I_{cl}(w)}{B[w, T(P_c)] - I_{cl}(w)}$$

Here N is the fractional cloud cover within the FOV, $N\varepsilon$ the effective cloud amount, w represents the window channel frequency, and $B[w, T(p_c)]$ is the opaque cloud radiance.

Using the ratios of radiances of the three CO_2 spectral channels, three separate cloud top pressures can be determined (14.2/14.0, 14.0/13.3, and 14.2/13.3). If $(I - I_{cl})$ is within the noise response of the instrument (~ 1 mW m^{-2} - sr^{-1} - cm^{-1}) the resulting P_c is rejected. Using the infrared window and the three cloud top pressures, three effective cloud amount determinations are made. As described by Menzel (1983), the most representative cloud height and amount are those that best satisfy the radiative transfer equation for the three CO_2 channels.

If no ratio of radiances can be reliably calculated because $(I - I_{cl})$ is within the instrument noise level, then a cloud top pressure is calculated directly from the VAS observed 11.2 micron infrared-window channel brightness temperature and the temperature profile. In this way all clouds are assigned a cloud top pressure either by CO_2 or infrared-window calculations.

The CO_2 technique is independent of the fractional cloud cover; heights and effective cloud amounts can be determined for partially cloudy FOVs. However, the CO_2 technique sees only the highest cloud and cannot resolve multi-layer clouds. Because the VAS FOV resolution is coarse (14 km for this work), very small element clouds are difficult to detect. Also, because the weighting functions for the VAS channels are broad, there is an inherent lack of vertical resolution in the measurements. Nonetheless, reliable cloud statistics can be calculated with appropriate application of the technique.

Since October 1985, the VAS instrument on board GOES-6 has been programmed to gather sounding data over the United States at least twice daily (near 1200 GMT and 0000 GMT) and as often as four times daily (near 00, 0600, 1200, and 1800 GMT). The CO_2 technique has been applied to these data routinely. In this study, radiances for three FOVs were averaged for cloud height and amount determinations (representing an area of 14 by 42 km at the satellite subpoint) at roughly 100 km spacing. Surface observations were used to adjust the global forecast temperature and moisture fields. No adjustments for topography were made. Transmittances were determined from line by line calculations with the spectral response functions for the appropriate VAS channels.

3. VALIDATION

Quantitative comparisons are shown in Fig. 2. The CO_2 (or infrared window where necessary for low clouds) cloud top pressures are shown with the determinations from radiosondes. Cloud-top pressures are estimated from 1200 or 0000 GMT radiosonde temperature and dew point temperature profiles by noting where the dew point temperature profile becomes much drier as it emerges from the cloud and hence indicates cloud-top pressure. Since the profile analysis is not always definitive, a reliable radiosonde cloud height determination is not always available, especially in cirrus clouds. VAS observations were usually within 30 minutes of the raobs and were gathered over a three month period. The range of VAS cloud top pressures is from the four FOVs nearest to the radiosonde location. The VAS

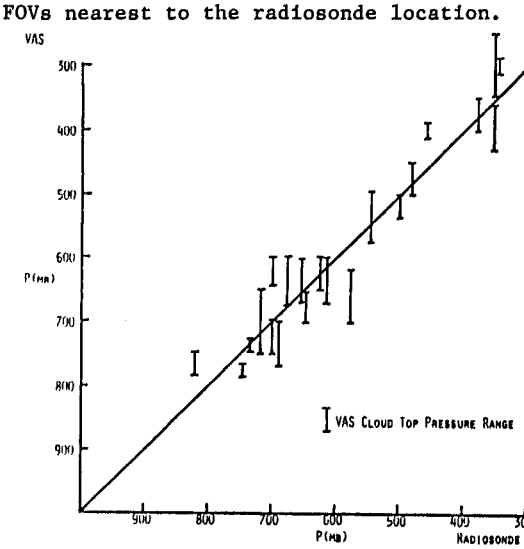

Fig. 2. VAS versus radiosonde cloud top pressures observed during winter 1985-86. RMS difference is 40 mb.

cloud top pressures compare extremely well with the radiosonde determinations; they are within 40 mb rms of each other. It should be noted that most of the height determinations below 600 mb are infrared window calculations. Validation of the cirrus heights will be accomplished with lidar determinations in future work.

4. EXAMPLE STATISTICS

Cloud cover is a highly variable phenomenon which depends heavily on the storm tracks and other weather conditions. Detailed statistics of the November 1985 cloud summary for two cities in the midwestern United States (shown in Table 1) provide an example of how cloud cover can vary over short distances. Madison, Wisconsin and Chicago, Illinois are separated by approximately 150 km. The statistics of the satellite cloud observations for local noon (1800 GMT) are given for ten intervals of cloud top altitude and for five intervals of effective cloud amount or emissivity. The left column gives the frequency of cloud reports by altitude regardless of the cloud amount/emissivity. The next five columns show the distribution of cloud reports for five intervals of cloud amount or emissivity. The low cloud amount/emissivities (center columns) indicate cirrus clouds which were partially transmitting infrared radiation, while the right column summarizes the reports of opaque clouds that did not transmit upwelling radiation. The sum of the five right columns should account for all of the cloud reports (100%).

Both cities experienced many days of deep opaque cloud cover. This is evident by the high frequency of reports from 400 to 200 mb in the left column. Clear sky conditions were indicated by the 1000 mb reports. Chicago had 29% clear reports, while Madison only had 12%. The frequency of cirrus cloud reports that partially transmitted upwelling infrared radiation (emissivities less than .8) were also higher in Madison (27% summed over columns 2 through 5) compared to Chicago (16%). The thicker opaque cloud cover (right column) was also higher at 61% in Madison compared to 54% in Chicago. These differences reflect the fact that the position of the polar front and cyclone tracks were north of Chicago during the month.

5. GEOGRAPHICAL COVERAGE

Statistical results for the entire United States plus coastal oceans for 13 months (October 1985 to October 86) are shown in Table 2 (coverage includes 27° to 51°N latitude and 55° to 157°W longitude). Cloud height determinations were made near 1800 GMT using the VAS radiances (the statistics reflect over 984,000 determinations). The most immediate finding is that 26% of the area was covered with thin or cirrus clouds. Approximately 45% of the United States was covered with thick opaque clouds and truly clear sky conditions occurred about 29% of the time. The cloud top pressures were distributed with 10% above 300 mb, 21% between 300 and 500 mb, 40% between 500 and 900 mb, and 29% at the surface (clear sky conditions). The thin clouds were mostly above 500 mb.

The geographical distribution of cloudy, cirrus and clear sky conditions for the year of October 1985 thru October 1986, is summarized in

TABLE 1. Cloud Statistics for Madison, Wisconsin 42°N 90°W November 1985. 483 Observations in a 2°x2° box over 19 days from 1500 to 1800 GMT.

	Cloud Emissivity				
Level(mb)	0.0-0.2	0.2-0.4	0.4-0.6	0.6-0.8	0.8-1.0
100-199	0%	0%	0%	0%	0%
200-299	0	1	2	2	6
300-399	0	2	3	4	13
400-499	0	3	3	2	12
500-599	0	1	1	1	6
600-699	0	0	1	1	11
700-799	0	0	0	0	9
800-899	0	0	0	0	3
900-999	0	0	0	0	1
1000-1099	12	0	0	0	0
Total	12%	7%	10%	10%	61%
	12% Clear		27% Cirrus		61% Cloudy

Cloud Statistics for Chicago, Illinois 42°N 88°W November 1985. 408 Observations in a 2°x2° box over 19 days from 1500 to 1800 GMT.

	Cloud Emissivity				
Level(mb)	0.0-0.2	0.2-0.4	0.4-0.6	0.6-0.8	0.8-1.0
100-199	0%	0%	0%	0%	0%
200-299	0	1	1	0	16
300-399	0	1	2	1	11
400-499	0	1	3	1	4
500-599	1	1	1	1	5
600-699	0	0	0	1	9
700-799	1	0	0	0	8
800-899	0	0	0	0	1
900-999	0	0	0	0	0
1000-1099	29	0	0	0	0
Total	31%	4%	7%	4%	54%
	29% Clear		17% Cirrus		54% Cloudy

TABLE 2. Cloud Statistics for United States, 27° to 51°N and 55° to 157°W for October 1985 thru October 1986 near 1800 GMT.

	Cloud Emissivity				
Level(mb)	0.0-0.2	0.2-0.4	0.4-0.6	0.6-0.95	0.95-1.0
100-199	0%	0%	0%	0%	0%
200-299	2	2	2	2	2
300-399	1	3	2	3	3
400-499	1	2	2	2	3
500-599	0	0	1	1	3
600-699	0	0	0	0	6
700-799	0	0	0	0	13
800-899	0	0	0	0	10
900-999	0	0	0	0	5
1000-1099	27	0	0	0	0
Total	31%	7%	7%	8%	45%
	29% Clear		26% Cirrus		45% Cloudy

Fig. 3. All reports inside 2° latitude by 2° longitude boxes for each day at 1800 GMT were averaged together to produce the cloud statistics. Cloudy indicates all reports with cloud amounts/ emissivities greater than 0.95 in Fig. 3a. Cloud reports with cloud amounts/ emissivities less than 0.95 were summarized as cirrus in Fig. 3b, and clear sky reports are summarized in Fig. 3c. A large change in cloud cover with latitude is apparent. The states of Arizona and New Mexico in the central southern United States has the lowest frequency of cloudy conditions and the highest frequency of clear conditions. The frequency of clear reports reinforces the descriptor "Sun Belt" associated with southern states bordering Mexico. Transmissive cirrus clouds (Fig. 3b) were found at all locations in frequencies of 10 to 30%. The highest occurrences were in the northwestern mountain states of Utah, Colorado, and Wyoming. An increase in cirrus reports with latitude also is apparent.

6. CONCLUSIONS

This is a preliminary report of an ongoing study of cloud cover. Definitive conclusions on cloud cover statistics must wait until more years of data are compiled. However, these statistics for one year show results which have been reasonably anticipated. The most obvious finding of this study is the high incidence of thin cirrus clouds. Cirrus clouds have been given little attention in the past because they do not yield precipitation or damaging weather. But they do have a large impact on the radiative balance of the earth. Thin cirrus allow solar heating yet at the same time trap upwelling terrestrial infrared radiation. Our cloud statistics indicate that thin cirrus (cloud amount/ emissivities less than 0.95) occur 15 to 40% of the time over the United States. Thus, they are very numerous and must have a large effect on the heat balance of the earth.

7. REFERENCES

Menzel, W. P., W. L. Smith, and T. R. Stewart, 1983: Improved cloud motion wind vector and altitude assignment using VAS. J. Clim. Appl. Meteor. 22, 377-384.

8. ACKNOWLEDGMENTS

The Authors gratefully acknowledge the efforts of Mr. William Smith, Jr. who performed most of the data processing presented here. This research was supported by grant N00014-87-K-0436 from the Office of Naval Research.

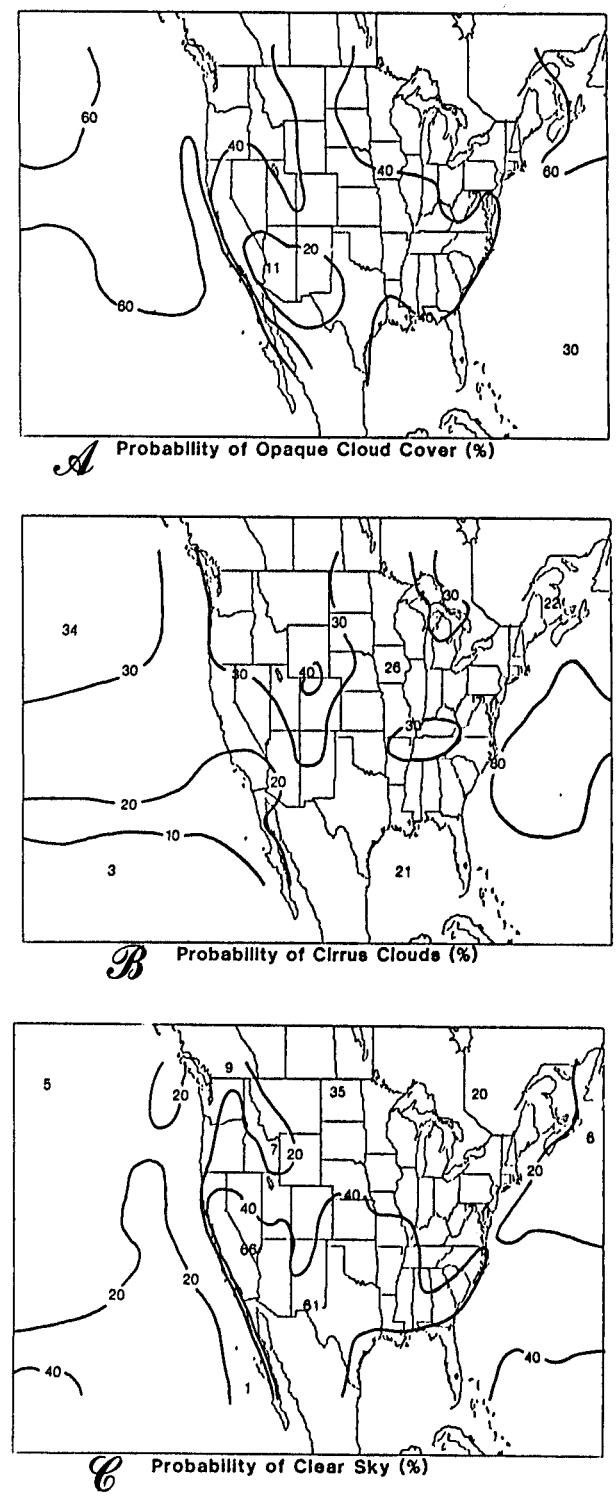

Fig. 3. Geographic distribution of VAS determinations of cloudy (a), cirrus (b), and clear (c) sky conditions for October 1985 thru October 1986.

8.5

ANNUAL AND INTERANNUAL VARIATIONS IN THE VERTICAL DISTRIBUTION OF COLD CLOUDINESS OVER THE EASTERN PACIFIC AND THE AMERICAS

Phillip A. Arkin

Climate Analysis Center
Washington, D.C. 20233

1. INTRODUCTION

Variations in the spatial and temporal distribution of clouds are of great significance to diagnostic and modeling studies of the climate system. Monitoring the annual and interannual variability of the climate requires the capacity to observe variations in cloudiness on time scales of weeks and horizontal space scales of about 200 km, and with some currently unspecifiable degree of vertical resolution. Geostationary satellite observations provide the potential to describe these variations in substantially greater detail than has been possible in the past. This is, in fact, one of the goals of the International Satellite Cloud Climatology Project (ISCCP).

In this paper we shall present results derived from a more limited data set than that used for the ISCCP. The details of the data and the processing will be discussed in Section 2, and the annual variability will be described in Section 3. In Section 4 we shall present some results regarding the interannual variability during the period, while the vertical coherence of the observed variations will be discussed in Section 5.

2. DATA

As a part of an effort to monitor variability in tropical rainfall (Arkin and Meisner, 1987), histograms of equivalent blackbody brightness temperature (EBBT) have been compiled for each month from December 1981-November 1986 for 2.5° latitude x 2.5° longitude areas visible to the U.S. geostationary meteorological satellites. Eight images, spaced at 3-hr intervals, were used each day, and no spatial sampling or averaging was performed. When two satellites were available, the dividing line between them was chosen to be 105°W.

The histograms were constructed by sorting the EBBTs for each pixel into the appropriate areal bin and incrementing the proper class for that image time. The class limits used are given in Table 1. The data are thus capable of describing the annual, interannual and diurnal variations in monthly cloudiness. Due to the frequent periods when one of the satellites was unavailable, the area for which 5 full years of data is available is between 50°N-47.5°S and about 130°W-65°W.

TABLE 1. Limits (in both degrees Kelvin and digital counts) of the classes of the histograms derived from GOES data used in this study.

Class	Temperature limits (K)	Digital count limits
1	>270	<119
2	266-270	119-128
3	261-265	129-138
4	256-260	139-148
5	251-255	149-158
6	246-250	159-168
7	241-245	169-177
8	236-240	178-182
9	231-235	183-187
10	226-230	188-192
11	221-225	193-197
12	216-220	198-202
13	211-215	203-207
14	201-210	208-217
15	191-200	218-227
16	<191	>227

3. ANNUAL VARIABILITY

The 5-year average percentage of the total pixels with an EBBT between 230-250 K for each of the calendar seasons is shown in figs. 1-4. Each season has a large region of very low cloudiness in this range in the eastern South Pacific. Other regions of low cloud cover are found in the Caribbean during December-February (DJF) and March-May (MAM), and west of Baja, California, during June-August (JJA) and September-November (SON).

A maximum, probably associated with the Intertropical Convergence Zone (ITCZ) is seen between 5°-15°N during each season, although it is quite weak during DJF and strongest during JJA. An increase with latitude in the percentage of cloud cover is seen in all seasons, and is clearest in the winter hemisphere.

4. INTERANNUAL VARIABILITY

The percentage coverage by cloud with EBBT in the 230-250 K range averaged from 80°-120°W for 20° latitude bands is shown for the 5-year period in fig. 5. The annual cycle is larger in the Northern Hemisphere than in the Southern, and is nearly absent in the band from 10°S-30°S. The annual peak in the highest latitude band occurs during the winter in both hemispheres.

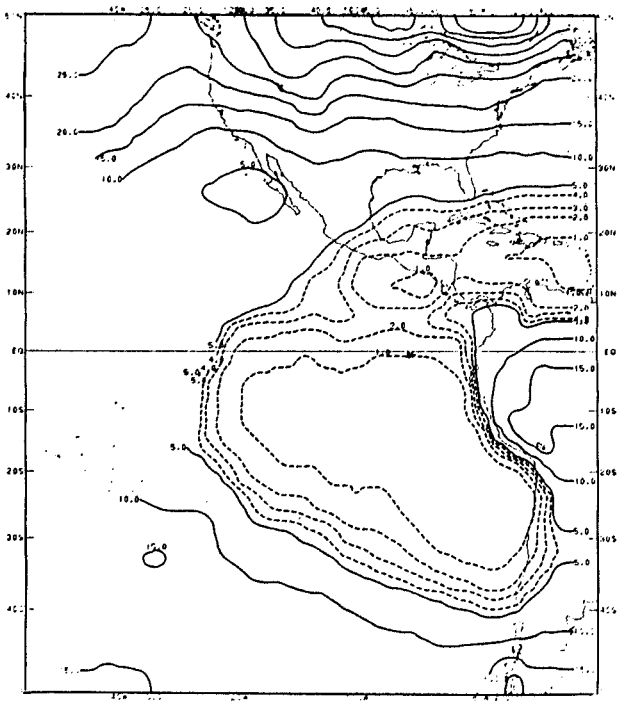

FIGURE 1. 5-year mean percentage coverage in the range 230-250 K for the December-February season. Solid contours at 5% intervals; dashed contours at 1% intervals below 5%.

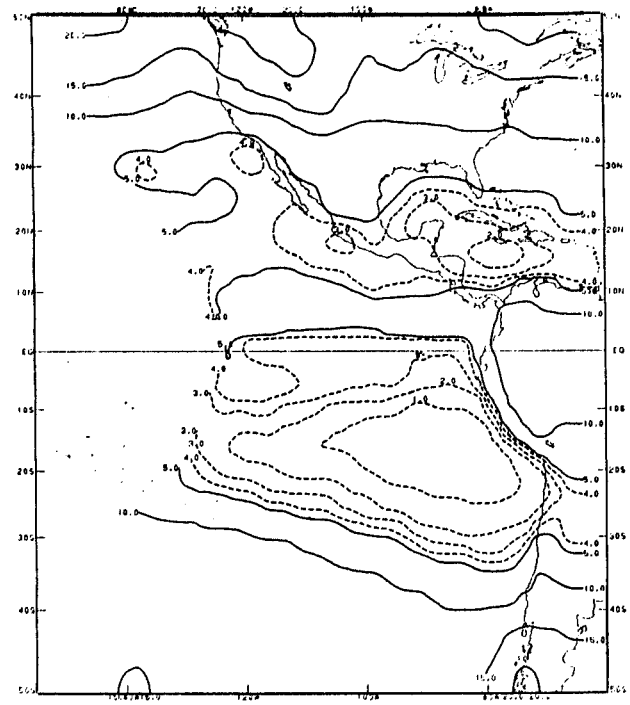

FIGURE 2. 5-year mean percentage coverage in the range 230-250 K for the March-May season. Solid contours at 5% intervals; dashed contours at 1% intervals below 5%.

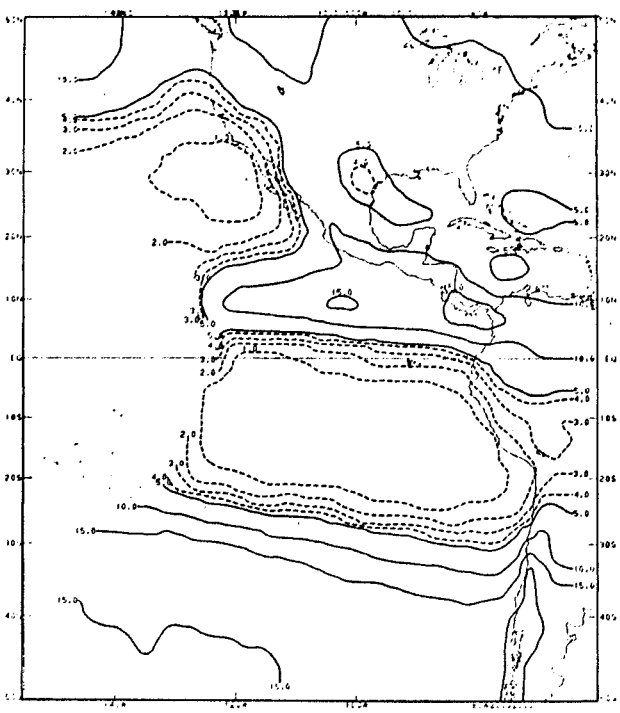

FIGURE 3. 5-year mean percentage coverage in the range 230-250 K for the June-August season. Solid contours at 5% intervals; dashed contours at 1% intervals below 5%.

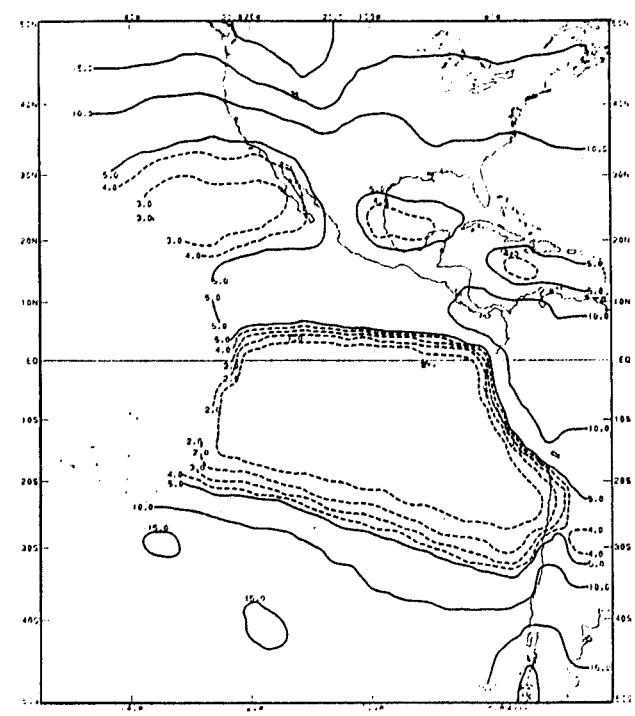

FIGURE 4. 5-year mean percentage coverage in the range 230-250 K for the September-November season. Solid contours at 5% intervals; dashed contours at 1% intervals below 5%.

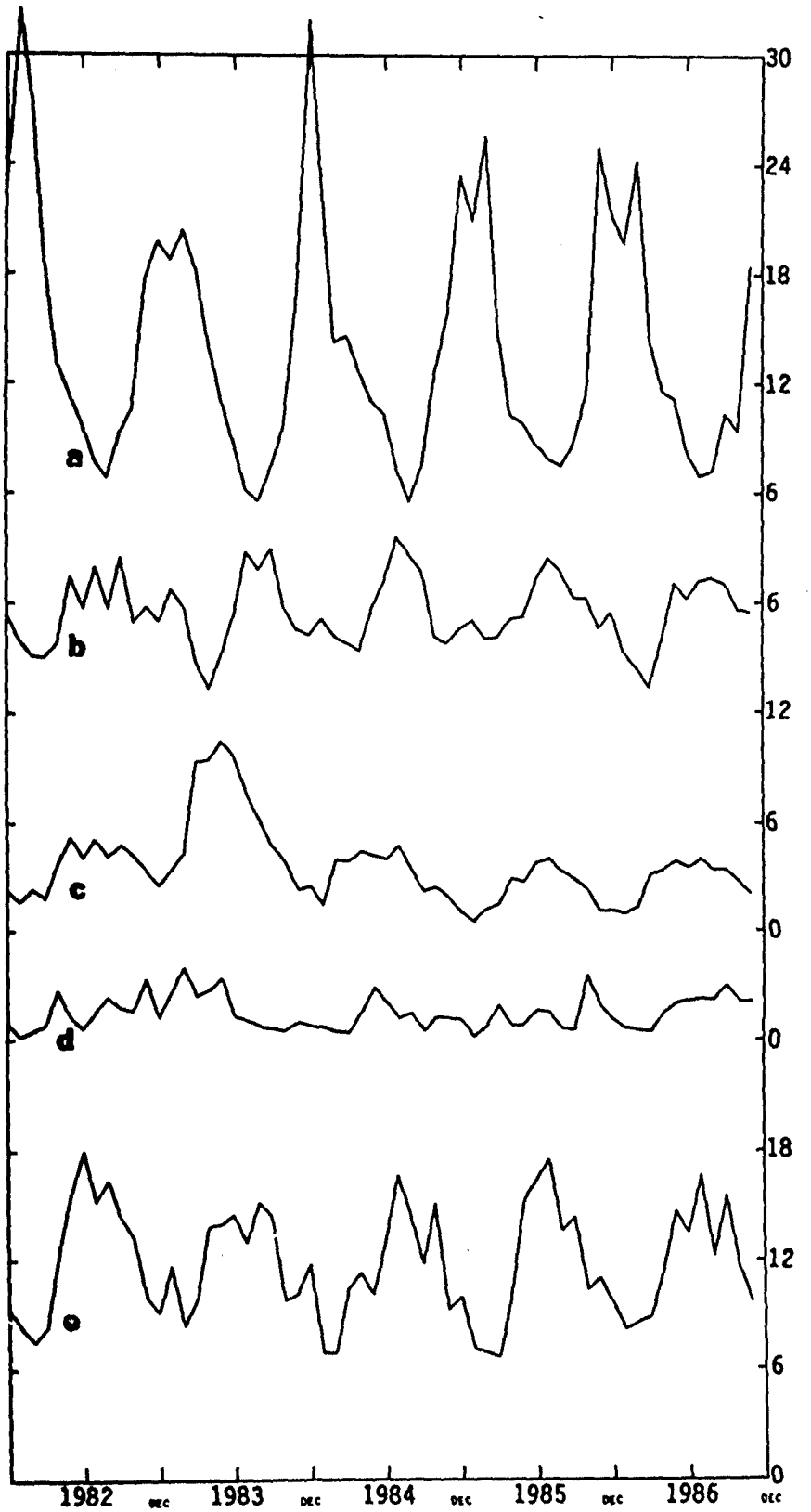

FIGURE 5. Time series of the percentage of pixels with EBBT in the range 230-250 K averaged over the longitudes 80°-120°W for 50°-30°N (a), 30°-10°N (b), 10°N-10°S (c), 10°-30°S (d), and 30°-50°S (e).

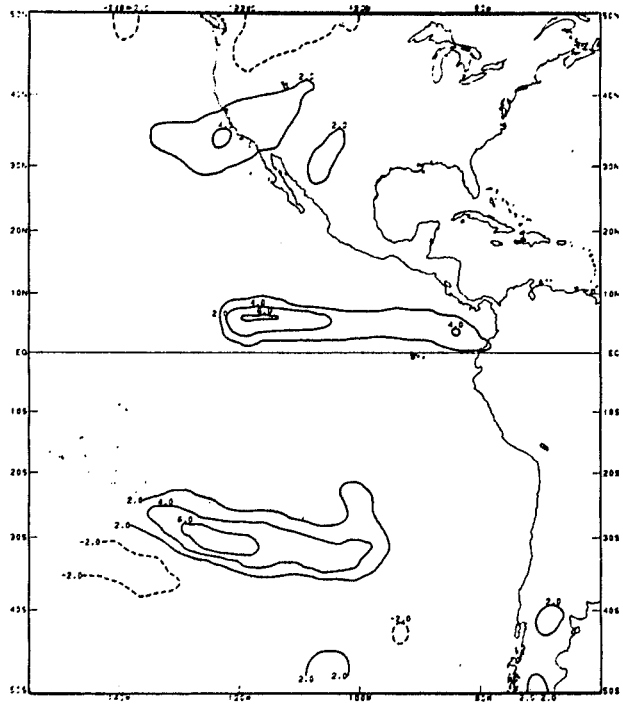

FIGURE 6. Departure from the 5-year mean percentage coverage of pixels with EBBT from 230-250 K for SON 1982. Contour interval 2% with negative contours dashed; no zero contour.

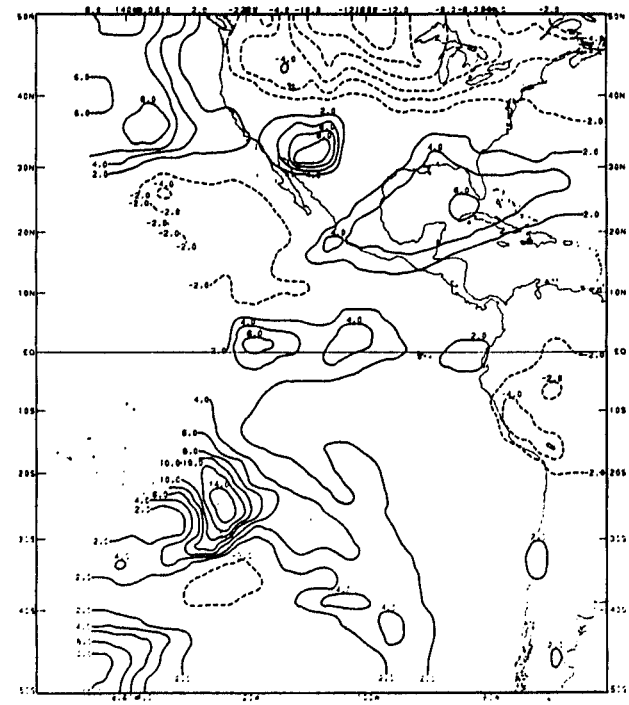

FIGURE 7. As in fig. 6 except for DJF 1982-83.

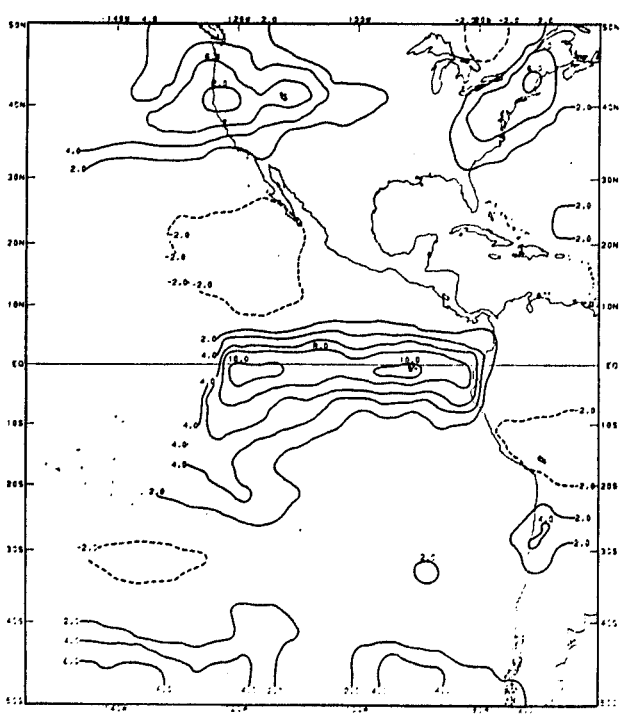

FIGURE 8. As in fig. 6 except for MAM 1983.

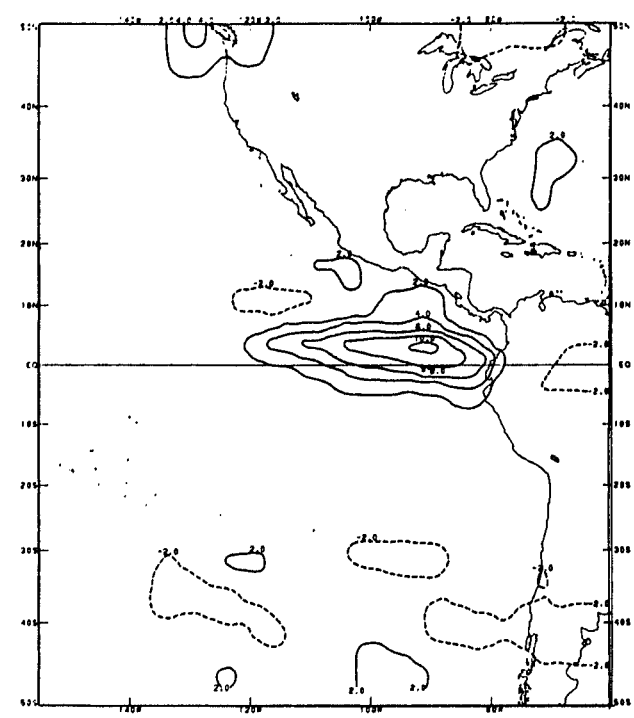

FIGURE 9. As in fig. 6 except for JJA 1983.

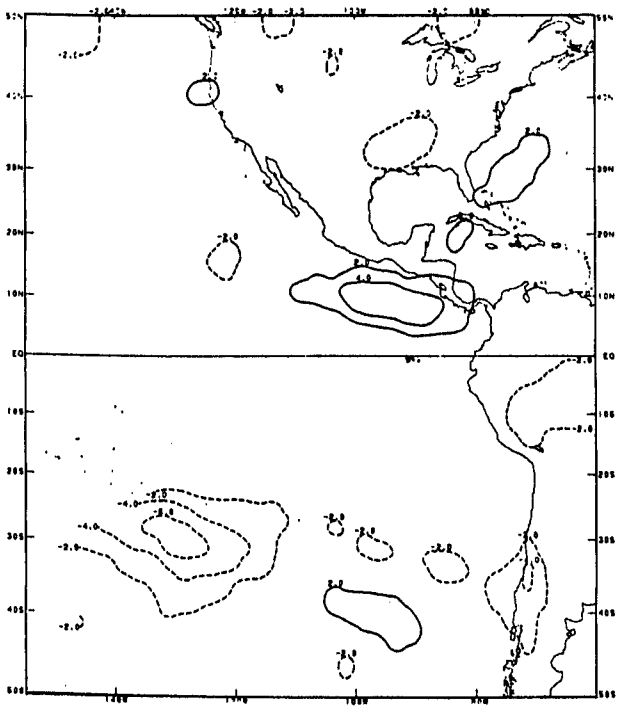

FIGURE 10. As in fig. 6 except for SON 1983.

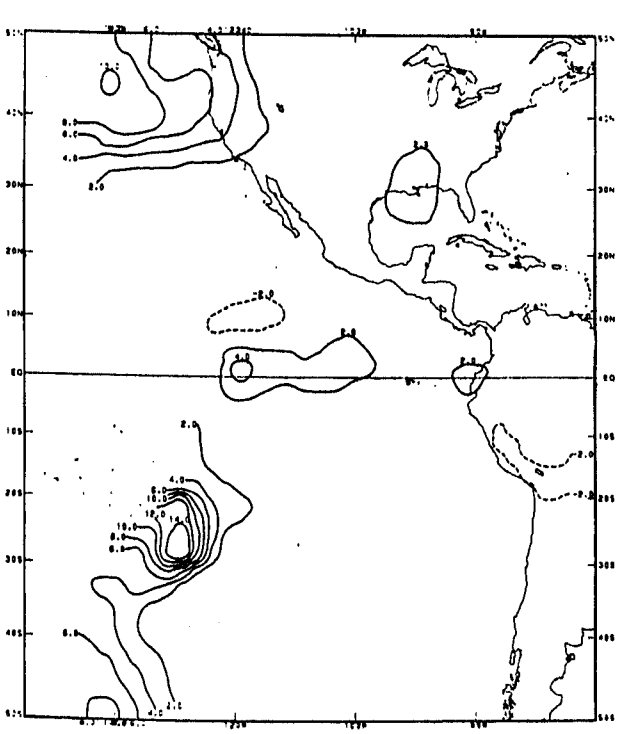

FIGURE 11. As in fig. 7 except for EBBT in the range 210-230 K.

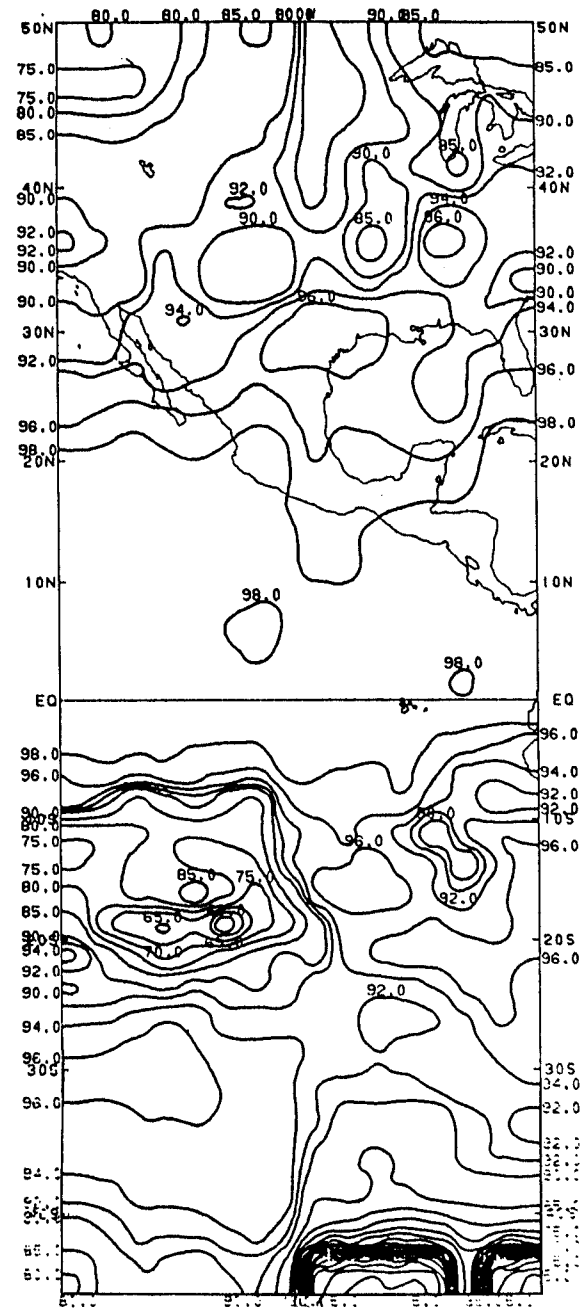

FIGURE 12. Linear correlation (multiplied by 100) between the monthly anomaly in the percentage of pixels in the ranges 235-240 K and 230-235 K. Contour interval 5 below 90 and 2 from 90-100.

Of the interannual changes apparent in these time series, the most impressive are those associated with the 1982-83 El Niño/Southern Oscillation (ENSO) warm episode (Rasmusson and Wallace, 1983). Near equatorial cloudiness was nearly double that observed during the remainder of the period, while the percentage coverage from 30°-50°N was substantially less than that observed during the other winters. The first is probably associated with the large amounts of rainfall observed in the eastern equatorial Pacific during the event (Arkin and Meisner, 1987), but the decrease in northern mid-latitudes is harder to understand.

Maps of the departure of the percentage coverage from the 5-year mean for the 5 seasons from SON 1982-SON 1983 (figs. 6-10) show the dominance of the equatorial positive anomaly during this period. It was elongated zonally, with an axis which began near 5°N in SON 1982, was slightly south of the equator during MAM 1983, and was back to near 7.5°N by SON 1983. The largest amplitude was observed during MAM 1983. Other positive anomalies of note were found off the west coast of the U.S. and over the Gulf of Mexico during DJF 1982-83 and near both coasts during MAM 1983.

The most intense negative anomaly (fig. 7) is that implied by the time series of cloud cover between 30°-50°N (fig. 5). Pixels with EBBT between 230-250 K were far below the 5-year mean over the north central U.S. Since no attempt was made in this analysis to screen out the effects of surface temperature, it is conceivable that the warmer than normal temperatures observed during this season (Quiroz, 1983) were involved in this anomaly.

5. VERTICAL COHERENCE

All the results shown here have been calculated for pixels with EBBT in the range 210-230 K, as well. The vertical coherence between the two layers is by and large impressive. In fact, the only strong difference tends to confirm that the negative anomaly in the north central U.S. was indeed associated with surface temperatures rather than cloudiness, since no similar feature is seen in the colder range (fig. 11).

The correlation between the anomaly time series for two temperature classes (fig. 12) shows that very high correlations (>0.9) are quite common. The cause for the observed spatial variations in the correlation is not obvious; it is certainly possible that in some regions the frequency of cloudiness at various heights is less vertically coherent than in others. This question is of significance not only for the monitoring of variations in cloudiness, but for the application of satellite rainfall estimation schemes which are based on observations of the cloud tops (Arkin and Meisner, 1987).

6. ACKNOWLEDGMENTS

The author wishes to thank Kathy Stevenson for her help in preparing the manuscript, and Diane Davidowicz and John Kopman for help with the figures.

7. REFERENCES

Arkin, P. A. and B. N. Meisner, 1987: The relationship between large-scale convective rainfall and cold cloud over the Western Hemisphere during 1982-84. Mon. Wea. Rev., 115, 51-74.

Quiroz, R. S., 1983: The climate of the "El Niño" winter of 1982-83--a season of extraordinary climate anomalies. Mon. Wea. Rev., 111, 1685-1706.

Rasmusson, E. M. and J. M. Wallace, 1983: Meteorological aspects of the El Niño/Southern Oscillation. Science, 222, 1195-1202.

8.6

Snow and Low-Cloud Discrimination from Multispectral Satellite Measurements

ROBERT C. ALLEN, PHILIP A. DURKEE AND CARLYLE H. WASH

Department of Meteorology
Naval Postgraduate School
Monterey, CA 93943

1. Introduction

A long standing problem in cloud and snow analysis from satellites is the discrimination of low clouds from snow cover. Middle and high clouds can be detected against snow cover due to the thermal contrast detectable at infrared wavelengths, but in the region of the electromagnetic spectrum used most often in satellite analysis, low clouds and snow cover have similar radiometric properties. In the visible portion of the spectrum both have high albedo, and in the infrared portion both have similar thermal properties. Thus there is little contrast in images at these spectral wavelengths.

This paper addresses the identification problem of low clouds over snow using multispectral imagery from the Advanced Very High Resolution Radiometer (AVHRR) utilized on the National Oceanic and Atmospheric administration (NOAA) polar-orbiting satellites. Specifically, channel 3 imagery centered at 3.7 μm will be utilized in conjunction with the standard visual and infrared channels (channel 1, centered at .68 μm and channel 4, centered at 11.0 μm) to improve the daylight detection of low clouds over snow.

Bunting et al. (1977) discussed the reflectance properties of snow and clouds at visible and near-infrared wavelengths, using data from the Earth Resources Experiment Package which flew aboard Skylab. They analyzed the imagery in pairs: one set in the visible spectrum and the other in the near-infrared spectrum (1.55 μm to 1.75 μm). The two sets showed high reflectance for snow, water clouds and ice clouds in the visible spectrum, but in the near-infrared the reflectance was high for water clouds, medium for ice clouds and very low for snow. They concluded that these differences could be the basis for an automated routine which makes an analysis decision based on the ratio of visible reflectance to near-infrared reflectance. Bunting and d'Entremont (1982) tested six automated classifiers on data from a special Defense Meteorological Satellite Program (DMSP) sensor in the wavelength band from 1.51 μm to 1.63 μm, along with visual and infrared data. They used the classifiers successfully to distinguish water clouds, ice clouds, snow cover and other cloud-free surfaces. Their technique was so successful that plans are now being made to add this sensor as an operational component of the DMSP satellite.

Kidder and Wu (1984) showed that there is a contrast in brightness temperature between snow and low clouds in daytime imagery of channel 3 (3.7 μm) of the National Oceanic and Atmospheric Administration (NOAA) polar-orbiting Advanced Very High Resolution Radiometer (AVHRR). They related this contrast to solar reflection, which is a substantial component of the channel 3 radiance measurement along with thermal emission. Since low clouds and snow have similar emission temperatures, this contrast is the result of a difference in their solar reflection at 3.7 μm which, in theory, is just a few percent for snow and about 20 percent for clouds. This results in a warmer brightness temperature for clouds (darker image) than for snow (whiter image).

The first objective of this study is to report calculations of solar reflectance in AVHRR channel 3 using a method that estimates the thermal emission from channel 4 and removes this portion from the channel 3 radiance measurement. Derived values will be compared to theoretical 3.7 μm reflectance for snow cover, land and clouds. During the 1990's both NOAA and the Department of Defense plan to launch satellites with a 1.6 μm sensor for daytime snow/cloud discrimination, and the NOAA satellite will have a 3.7 μm sensor for use at night. Even with this change, there are good reasons to pursue this work now. First, by the time the new sensor flies there will be over 10 years of archived daytime 3.7 μm imagery. Second, since snow and cloud reflectances are similar at 1.6 μm and 3.7 μm, a data set of reflectances from channel 3 would be very useful in testing software for the new sensor.

The second objective is to use calculated channel 3 reflectance to develop an automated cloud analysis routine that separates snow cover, clouds and snow-free land. It will be designed to handle various combinations of cloud and surface features, but the focus is on the separation of low clouds and snow. The routine will rely on basic physical principles of radiative transfer in the earth's atmosphere. In addition to similar visible reflective properties, low clouds and snow have nearly identical infrared thermal properties. Because of this and the results of the previously mentioned studies, the routine is based primarily on the reflective properties of these surfaces in AVHRR channel 3. A multispectral technique is developed using visible and infrared data along with channel 3 to process daytime AVHRR images. The technique is verified against the available surface observations using the standard categories of clear, scattered, broken and overcast.

2. Development of the Analysis Algorithm

Although the primary objective is the separation of low clouds and snow cover, the algorithms are developed to work in the presence of high-level clouds including cirrus and for cases when snow is not present. The procedure used was to calculate AVHRR observed reflectance and thermal emission for representative snow, bare land, ice and liquid cloud regions from several dependent data cases. The dependent data was taken from the 2000-2100 GMT NOAA 9 passes of 9-10 November 1986 over the upper midwestern United States. These passes, taken after the first major Midwest snowfall of the 1986-87 season, have a combination of clouds and clear skies over both bare land and over snow cover.

Care was taken to insure that all of the surfaces to be analyzed were sampled in nearly equal numbers, and also that the areas chosen were comprised only of either snow, snow-free land, ice clouds or liquid clouds. Uniformity of these areas was determined subjectively by evaluating the visible and infrared images along with plotted surface observations of the area. From both passes a total of 300 land pixels, 400 ice cloud pixels, 300 liquid cloud pixels, and 300 snow pixels were sampled and the following information calculated:

1. Channel 1 reflectance.
2. Channel 3 reflectance.
3. Channel 4 brightness temperature.

Channel 1 AVHRR Channel 1 data are preflight calibrated in terms of albedo (Lauritson et al., 1979). The measured directional reflectance was converted to isotropic reflectance by weighting the measurement by the cosine of the solar zenith angle and the anisotropic reflectance factor as discussed above. This reflectance is very similar for snow cover and clouds, but it can be used to separate land from clouds and snow cover.

Channel 3 During daytime the channel 3 AVHRR radiance measurement is comprised of both solar reflection and thermal emission. Bunting (1986, personal communication) suggested a method discussed here for removing the thermal emission in channel 3. There are two major assumptions involved in using this technique (Ruff and Gruber, 1983). First, atmospheric transmission effects are neglected. The most important absorbing constituent in the atmosphere in this portion of the spectrum is water vapor and in this study the data were taken from high latitude, cold air masses where there is little water vapor present. Second, it was assumed that the emissivity of a viewed scene is 1.0. Thermal emission for the scene was then determined directly from the channel 4 radiance measurement. Error results from this assumption due to the fact that the emissivity of any surface is variable between channels 3 and 4 and not equal to 1.0. It is impractical to try to determine the emissive properties of the viewed scene so this effect was not corrected. The error resulting from these assumptions should have the greatest effect when deriving the reflectance for snow cover, land, or ice clouds because the magnitude of thermal emission for these surfaces is comparable to that of solar reflection. The least effect from the resultant error should occur with liquid clouds since for these surfaces the magnitude of solar reflection is much greater than that of thermal emission.

Channel 4 A non-linear correction (Lauritson et al, 1979) must be added to Channel 4 AVHRR data when converting from radiance to temperature. A polynomial was fit to the published corrections for NOAA-9 for use in the computer program (Gerald and Wheatley, 1984). The polynomial derived for the NOAA-10 corrections was unstable so linear interpolation was used instead. For ease in computer processing all channel 4 temperatures were assumed to be in the range from 225 K to 275 K so that only one central wavenumber need be used in the calculations (Lauritson et al, 1979). This range of temperatures provides adequate separation of the various features to be analyzed. Temperatures less than or greater than these were set to 225 K and 275 K respectively. This assumption is valid for the images processed in this study since they were from the fall and winter, and it is unlikely that an emitting surface has a temperature outside this range at that time of year.

Channel 1 and 3 reflectance results are summarized by Fig. 1 and 2. These measured values agree quite well with those determined from various theoretical studies and summarized in Allen (1987). The importance of channel in this algorithm is evident from the Fig. 1 and 2 results. Whereas snow and liquid cloud reflectance overlap for Channel 1, there is a clear separation between snow and liquid clouds in the channel 3 reflectance (liquid clouds >.10 while snow <.04). Thin cirrus still presents a problem as shown by the reflectance overlap between snow, land and cirrus. Stephens (1981) showed that the channel 3 brightness temperature of cirrus is greater than in channel 4 because cirrus is more transparent to surface radiation in channel 3. A temperature factor was derived from the brightness temperature difference, and when cirrus and snow cover were indistinguishable based on channel 3 reflectance, the routine attempted to analyze the cirrus based on this factor.

3. Results

Six images were analyzed and the total cloud cover was verified against a total of 110 conventional surface observations using the standard categories of clear, scattered, broken and overcast. The algorithm was very successful and produced excellent results, even at very large solar zenith angles. Its main strength was in separating low clouds from snow cover, while its weakest point was the analysis of cirrus clouds.

To illustrate the results, one of six cases is summarized in this preprint. Allen (1987) discusses all six cases in detail. The visual (channel 1), Fig. 3, and infrared (channel 4), Fig. 4, AVHRR data for 23 January 1987 (1443 GMT) describes a complex cloud snow situation over Kansas and northern Oklahoma. The river valley and earth terrain patterns indicate a snow field from central Oklahoma northeastward to Missouri. Shadows in the visual data indicate several areas of low clouds over this snow cover southeastern Kansas. A more organized cloud system is present over northeast Kansas and northern Missouri while clear bare ground conditions are found to the northwest over northern Kansas and to the southeast over eastern Oklahoma. This is a typical visual image which requires manual interpretation of high resolution data to properly classify the cloud areas from visual data alone.

The infrared data (channel 4), Fig. 4, is even more difficult to analyze. The most distinct feature is the cloud band to the northeast. The low cloud, snow and bare ground region of central and northern Kansas is difficult to interpret from temperature data alone. The warm lakes are apparent but the low cloud areas appear actually warmer than the clear snow and bare ground areas.

The channel 3 AVHRR data, Fig. 5, clarifies the low cloud-snow classification considerably. Note the relatively dark appearance in Fig. 5 of the low cloud areas subjectively determined in Fig. 3. In fact, channel 3 reveals additional smaller cloud elements over snow cover which are difficult to find using the normal visual and infrared data alone. These darker regions result from the relatively stronger solar reflection at 3.7 μm from liquid clouds versus snow.

All three channels are utilized to classify objectively picture elements for this scene. The resultant analysis is given by Fig. 6. Note that the algorithm describes both the low cloud over snow, the extent of the snow cover, as well as high clouds such as the cirrus at the bottom of the scene.

This case, and five others, were verified using surface hourly airways observations. It was assumed that the ground observer can see approximately 30 km, so reporting stations were located on each image and each pixel with 30 km was sampled for cloud cover. All the cloud pixels from these samples were then tallied for each station and the cloud cover was determined by the ratio of the number of cloud pixels to the total number of pixels sampled. The percent coverage was converted to four categories as follows:

1. Clear - less than 2 percent coverage
2. Scattered - 2 to 50 coverage
3. Broken - 50 to 98 coverage
4. Overcast - greater than 98 percent coverage

Table 1 presents the overall evaluation results. The analyzed sky cover was within category for 55 percent of the stations, one category different for 33 percent, 2 categories different for 9 percent and 3 categories different for 3 percent of the stations. The most significant shortcoming of the algorithm is discrimination between snow cover and cirrus clouds due to their similar reflective properties in both channels 1 and 3. Unfortunately, the temperature factor did not improve the analysis significantly because in addition to the difference in transmissive properties, solar reflection contributes to the difference in brightness temperature. The reflectance was variable enough to make unambiguous separation of the two surfaces possible only for cirrus with a limited range of optical depths.

5. Summary

An algorithm is developed and evaluated for discriminating among clouds, snow cover and clear land. The multispectral technique uses daytime images of AVHRR channels 1 (0.63 μm), 3 (3.7 μm) and 4 (11.0 μm). Reflectance is derived for channel 3 by using the channel 4 emission temperature to estimate and remove the channel 3 thermal emission. Separation of clouds from snow and land is based primarily on this derived channel 3 reflectance. Using this technique, observed reflectance in channel 3 is 2 to 4 percent for snow, 3 to 10 percent for land, 2 to 27 percent for ice clouds and 8 to 36 percent for liquid clouds. These values overlap for thin cirrus and snow, so the routine then attempts analysis of cirrus based on its different transmissive properties between channels 3 and 4. Six images were analyzed and the total cloud cover was verified against a total of 110 conventional surface observations using the standard categories of clear, scattered, broken and overcast. The routine was quite successful, with analyzed sky cover being within category for 55 percent of the stations, one category different for 33 percent, 3 categories different for 9 percent and 3 categories different for 3 percent of the stations. A major remaining problem is discrimination between ice clouds and snow cover due to the great similarity of reflective properties of these two surfaces.

6. References

Allen, Robert C., 1987: Snow and low-cloud discrimination from multispectral satellite measurements. M.S. Thesis. Naval Postgraduate School, Monterey, CA 93943, 107 pp.

Bunting, James T., Francis R. Valovcin, and Thomas J. Keegan, 1977: Meteorological Satellite Measurements and Applications. Air Force Geophysics Laboratory Tech. Rep. 77-0035, 17 pp.

Bunting, James T. and Robert P. d'Entremont, 1982: Improved cloud detection utilizing Defense Meteorological Satellite Program near infrared measurements. Air Force Geophysics Laboratory Tech. Rep. 82-0027, 91 pp.

Gerald, Curtis F. and Patrick O. Wheatley, 1984: .us Applied Numerical Analysis (Third Edition). Addison-Wesley Publishing Co., Inc., Reading, MA, pp. 191-196.

Kidder, Stanley Q. and Huey-Tz'u Wu, 1984: Dramatic contrast between low clouds and snow cover in daytime 3.7&mu.m imagery. .us Mon. Wea. Rev., .bd;112 .ct , 2345-2346.

Lauritson, Levin, Gary J. Nelson, and Frank W. Porto, 1979: Data extraction and calibration of TIROS-N/NOAA radiometers. NOAA Technical Memorandum NESS 107, U.S. Dept. of Commerce, Washington, D.C., Appendix B.

Ruff, Irwin and Arnold Gruber, 1983: Multispectral identification of clouds and earth surfaces using AVHRR radiometric data. U.S Preprints Fifth Conf. on Atmospheric Radiation, American Meteorological Society, Baltimore, MD, 31 October - 4 November 1983.

7. Acknowledgements

The authors would like to thank Dr. James Bunting of the Air Force Geophysics Laboratory, Hanscom AFB, MA for his help and encouragement. Mr. Doug Burks of NPS was especially helpful with the computer system image processing. Ms. Ann Gilbert skillfully typed the manuscript. This study has been supported by Naval Environmental Prediction Research Facility, Monterey, CA.

Table 1

Verification statistics for all objective cloud analyses

Category	Count	Percentage
Correct	60/110	55
1 category difference	36/110	33
2 category difference	10/110	9
3 category difference	4/110	3

Table 1. Verification statistics for all objective cloud analyses.

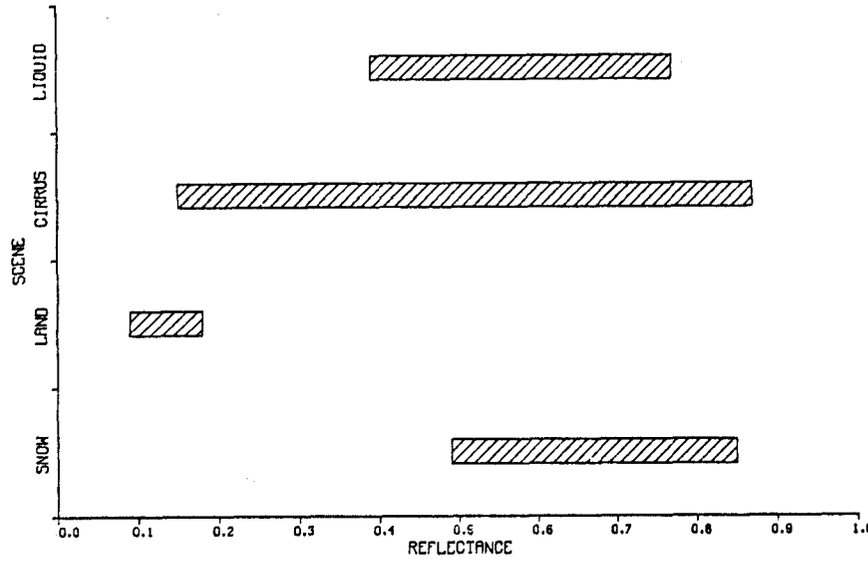

Fig. 1. Summary of NOAA-9 AVHRR observed channel 1 reflectance for 900 land pixels, 1600 ice cloud pixels, 1300 liquid cloud pixels, and 1000 snow pixels.

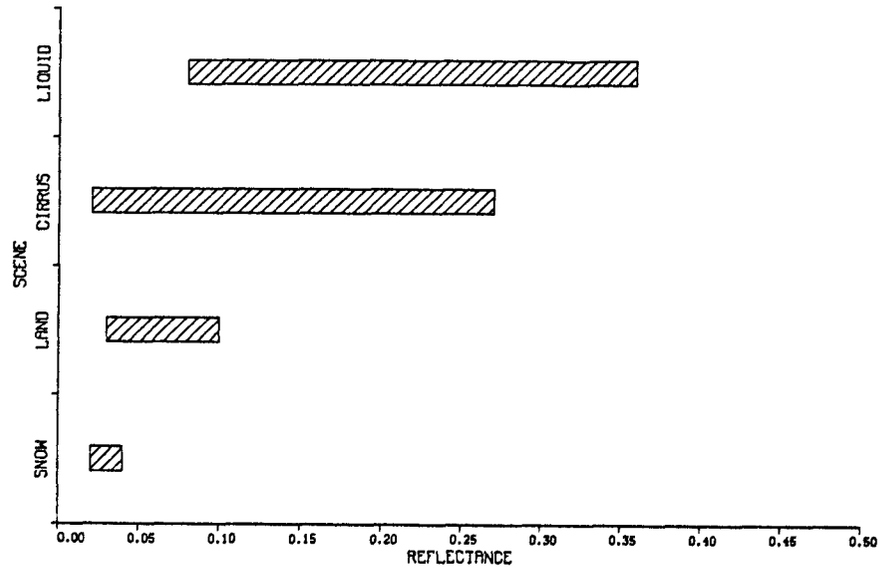

Fig. 2. Same as Fig. 1 except for derived channel 3 reflectance.

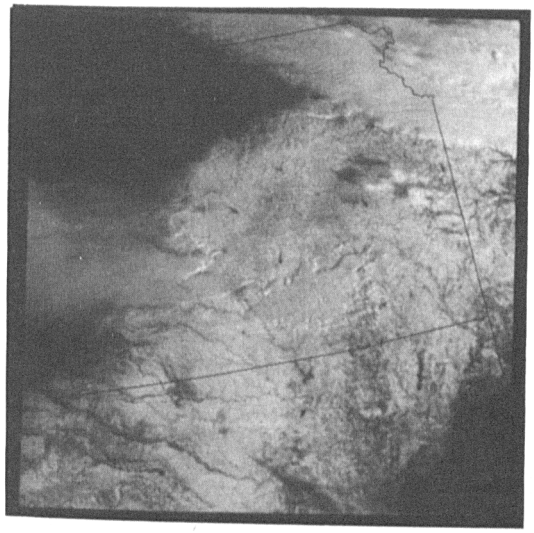

Fig. 3. 23 Jan. 1987 subscene, 1443 GMT. NOAA-9 AVHRR channel 1 reflectance.

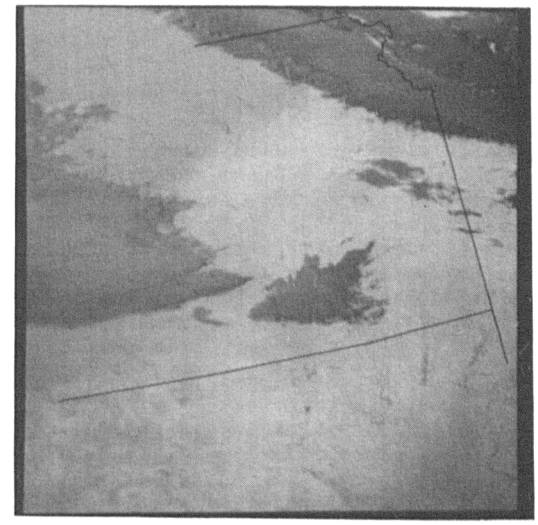

Fig. 4. 23 Jan. 1987 subscene, 1443 GMT. NOAA-9 AVHRR channel 4 brightness temperature.

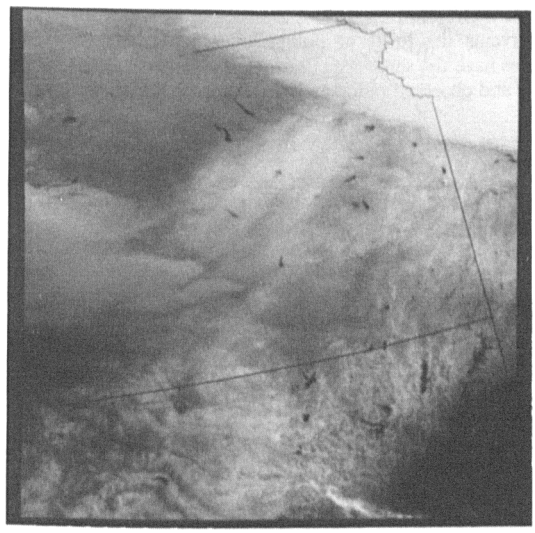

Fig. 5. 23 Jan. 1987 subscene, 1443 GMT. NOAA-9 AVHRR channel 3 brightness temperature.

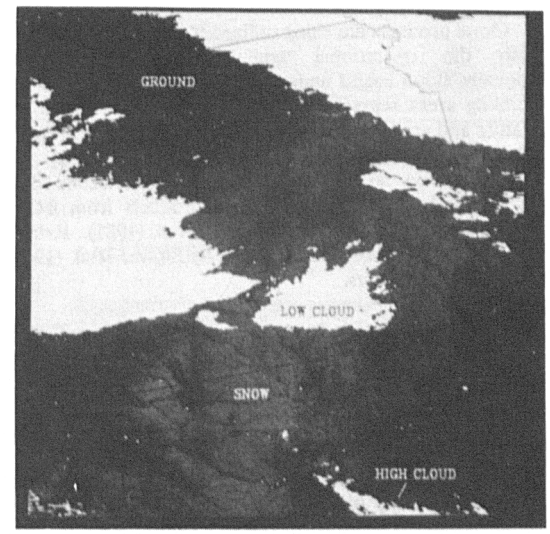

Fig. 6. 23 Jan. 1987 cloud and snow classification. Cloud white, snow gray, ground black.

AN IMPROVED METHOD FOR THE RETRIEVAL OF CLOUD HEIGHT AND AMOUNT FROM SATELLITE RADIANCE MEASUREMENTS

Andrew J. Nappi and Anand Swaroop

ST Systems Corporation (STX)
4400 Forbes Blvd., Lanham, MD 20706

Larry M. McMillin

NOAA/NESDIS
Washington, D.C. 20233

1. INTRODUCTION

Global satellite data products are produced from TIROS-N Operational Vertical Sounder (TOVS) radiance measurements by NOAA/NESDIS. The requirement of obtaining reasonably accurate retrievals of cloud height and amount was not met by the previous TOVS algorithm which was based on a regression scheme and intended more as quality check of radiances in partly cloudy areas than as a true estimation of cloud parameters. The algorithm was unable to produce cloud parameters in totally overcast regions. Interest in retrieving cloud amount and cloud height directly from the TOVS radiances has resulted in the development of a new algorithm based on a modification of the radiance-slope method (McCleese and Wilson, 1976). This algorithm utilizes radiances from selected channels of the High Resolution Infrared Radiation Sounder (HIRS/2) and the Microwave Sounding Unit (MSU) to retrieve cloud parameters for each field-of-view (FOV). This algorithm has been used at NOAA/NESDIS since 1984 to produce global cloud products.

Cloud products are being utilized for various applications in both the operational and research environments. Operationally, cloud height and amount information is produced for sounding areas represented by 9 FOVs each. Cloud top temperature and amount at the individual FOVs is utilized by the Operational Ozone Processing System (OOPS) at NOAA/NESDIS in an effort to retrieve global ozone data. Another method for retrieval of cloud products from TOVS radiances has been developed by Susskind, et al. (1987). Related work on this topic has been undertaken by Stowe, et al. (1984), Chahine (1982) and others.

2. METHODOLOGY

In the new method, the radiances for two channels for two or more FOVs which have different cloud amounts are used to derive a line. The overcast radiances are calculated prior to the retrieval step, during the cloud clearing procedure. This has the advantage of allowing some quality control of the radiances before the retrieval step is undertaken. The entire calculation of cloud amount and cloud top temperature is carried out in a single step as follows: The radiance of one channel is plotted versus the radiance of a second channel and a curve results which represents the locus of all points for which these 2 channel radiances give the same brightness temperature. The clear column radiances at individual FOVs, produced by the TOVS cloud-clearing procedure, McMillin and Dean (1982), are used with the observed radiances for the 2 channels to produce a straight line. Figure 1 represents the concept graphically. The point where the lower portion of the line intersects the curve is the radiance at the cloud top. Due to atmospheric attenuation of the radiances above the clouds, the overcast radiance is corrected slightly, effectively shifting the line relative to the curve.

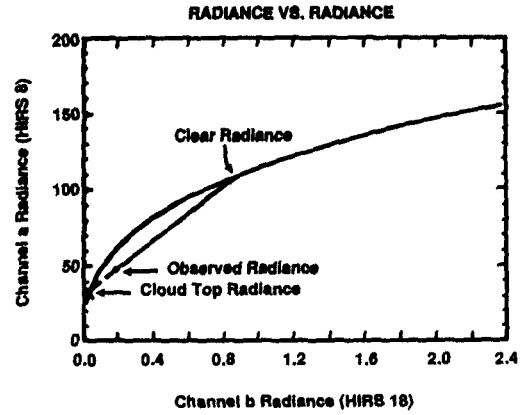

Figure 1. Graph of Channel a radiance vs. Channel b radiance. The curve is the locus of points for which channel a and b radiances have the same temperature. The straight line is formed by clear and observed radiances for the channels a and b.

In practice, the equation used to obtain the intersection of the straight line and the curve can be solved iteratively by the Newton-Raphson method and is of the form

$$X_{n+1} = X_n - \frac{f(X_n)}{f'(X_n)} \qquad (1)$$

where n = 0, 1, 2, 3 ...
X_o is the initial estimate of the quantity, x
X_n is the value of x at the nth iteration
$f'(X_n)$ is represented by $\frac{\Delta f(X_n)}{\Delta X_n}$

Once cloud top radiance is found, the cloud top temperature, cloud height and cloud amount can be easily obtained from known quantities as described in Section 3.

3. APPLICATION OF THE ALGORITHM

The application of the new algorithm to the TOVS radiance data is accomplished by the use of clear and observed radiances for a pair of channels to derive the necessary curve and straight line. This method assumes that each of the two channels

in the pair will sense the same temperature when a cloud is present. In practice, 4 distinct pairs of channels are used for different conditions of cloud cover, land/sea and day/night consideration. Optimally, radiances for HIRS channels 8 and 18 would be used for all the clear and observed radiances required to derive the curve and the line. Their use is limited, however, to partially cloudy FOVs at night due to serious cloud effects in totally overcast scenes and solar contamination of channel 18 during the day. For partly cloudy conditions during the day, channel 18 is replaced with channel 6 which senses the lower troposphere. In totally overcast conditions, the direct use of infrared radiances is precluded, requiring the use of the 3rd channel pair over oceans and the 4th over land. Over oceans, the sea-surface temperature is available and is converted to radiance as an estimate of the infrared channel 8 clear column radiance. The radiance from MSU channel 2 scaled to HIRS channel 6 is used as the second channel clear radiance. The observed radiances are from MSU channel 2 predicted from HIRS channels 5, 6, 7 and 8 and from regressed MSU channel 2 scaled to HIRS channel 6. The final channel pair is for overcast data over land where HIRS channel 6 and 7 are regressed from stratospheric HIRS channels 1, 2 and 3 and MSU channels 2, 3 and 4 to obtain the clear radiances required. The actual HIRS channels 6 and 7 are used as the observed radiances. Table 1 summarizes the channels used.

Table 1

Condition	Chan. a	Chan. b	Accuracy
Partly cloudy/night	HIRS 8	HIRS 18	Most
Partly cloudy/day	HIRS 8	HIRS 6	↓
Overcast/sea	MSU 2	SKIN TEMP	
Overcast/land	HIRS 6	HIRS 7	Least

Once the channel pairs are selected, the cloud top temperature is calculated via the iterative technique described in Section 2. The actual computation of cloud top temperature is from the following equation and use of the Planck relationship.

$$Tc_{n+1} = Tc_n - \frac{f(Tc_n) - m}{f(Tc_n) - f(Tc_n - \delta)} \qquad (2)$$

where Tc is the cloud top temperature

f(Tc) is a function given by $\dfrac{I_{(\nu_2)c} - I_{(\nu_2)o}}{I_{(\nu_1)c} - I_{(\nu_1)o}}$ (3)

n is the iteration number

δ is an incremental decrease, e.g. 1.0

and

m is the slope of the line formed by the 2 Channel radiances given by $\dfrac{I_{(\nu_2)c} - I_{(\nu_2)}}{I_{(\nu_1)c} - I_{(\nu_1)}}$ (4)

In equations 3 and 4

$I_{(\nu_1)c}$, $I_{(\nu_2)c}$ are the clear radiances for channels 1 and 2, respectively

$I_{(\nu_1)o}$, $I_{(\nu_2)o}$ are the overcast radiances for channels 1 and 2, respectively

$I_{(\nu_1)}$, $I_{(\nu_2)}$ are the observed radiances for channels 1 and 2, respectively

The initial value of Tc can be any temperature, but in practice, it is the observed temperature for the second channel of the pair, chosen to cause the iteration to converge more quickly to the solution.

Cloud height requires an atmospheric profile available in a subsequent retrieval step for comparison with cloud top temperature. The cloud amount is directly obtained via use of the radiance at the cloud top, the clear radiance, and the observed radiance for the given FOV. The quantities are related via the following equation:

$$\text{Amount} = 1 - \frac{I_{(\nu_2)} - I_{(\nu)o}}{I_{(\nu_2)c} - I_{(\nu)o}} \qquad (5)$$

where $I_{(\nu_2)}$ is the observed radiance for ch. 2 of the pair

$I_{(\nu_2)c}$ is the clear radiance for ch. 2 of the pair

$I_{(\nu)o}$ is the overcast radiance computed at cloud top

For operational purposes, the cloud amounts for all the FOVs are averaged for a sounding area (roughly 50-100 km) and a cloud amount in percent is produced for certain pressure levels.

Figure 2 illustrates a plot of these vertically interpolated cloud amounts averaged and plotted for individual sounding areas. Values are plotted in percent, with highest values representing the cloudiest regions. Only about 20% of the actual soundings are plotted for clarity. The large data gap over the ocean is due to rain contaminated MSU data which is discarded by the TOVS system.

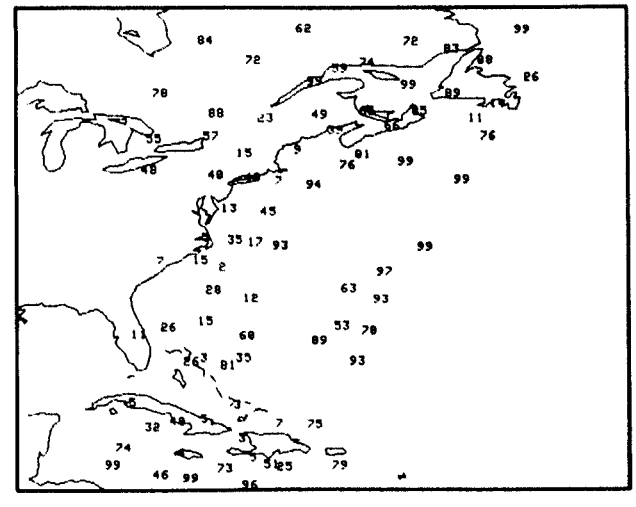

Figure 2. Cloud amount in percent at sounding locations

4. DATA VERIFICATION AND CASE STUDY

Cloud product data are especially difficult to verify as little or no quantitative measure of cloud amount or cloud top temperatures exists. Though a database can be constructed from the TOVS data for cloud top temperature, global statistics for this parameter are not readily available, therefore, no presentation of this data is attempted here. Comparison of cloud fields from visible or infrared satellite imagery with satellite derived cloud algorithm output is somewhat subjective, but does provide a general perspective of the performance of the algorithm. Most of the verification and evaluation of this algorithm therefore has taken the form of case study analyses of cloud amount, an example of which is presented here.

Cloud amount information from the TOVS cloud algorithm is compared to NOAA-10 AVHRR visible photographs over the east coast of the U.S. and a portion of the Atlantic ocean. The TOVS data shown represents the vertically integrated cloud amount for all the soundings in the same area presented in Figure 2, analyzed to a 2.5^{o} grid and imaged using the Off-Line Evaluation system on a VICOM microprocessor

(see Brown et al., 1987, for details of that system). The resulting fields are, therefore, somewhat similar to the AVHRR photos enabling ease of comparison.

Figure 3 gives the TOVS retrieved cloud amount data. White areas depict a higher percentage of cloudiness, darker areas are clearer. Inspection of the figure reveals a large area of little or no cloudiness over the Carribean, southern and eastern U.S. where cloud amounts routinely are 15% or less. Partly cloudy conditions exist in two distinct strips east of the southeastern U.S. with cloud amounts which vary from nearly 0% to over 90%. East of these regions lies a large area of mostly cloudy conditions with cloud amounts reaching 90% or more consistently. Another region of widespread cloudiness is retrieved by the algorithm and shown over the Great Lakes region of the U.S. by cloud amounts generally in the 40-70% range. This figure represents retrievals made with channel pairs 2, 3 and 4 summarized by Table 1.

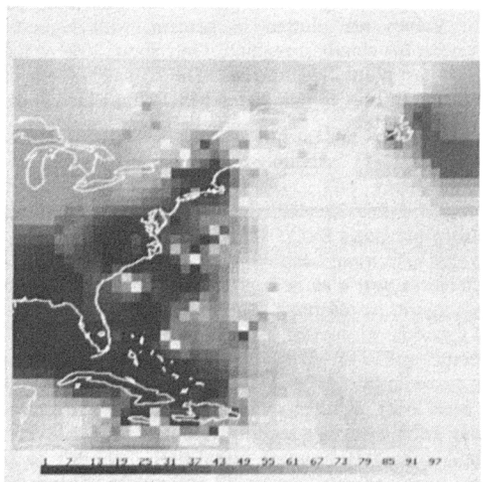

Figure 3. Imaged cloud amount in percent from the TOVS cloud algorithm. Darker areas are clear, whiter areas are cloudy. Scale shows percentage of cloudiness as gray shades.

Figure 4 gives an AVHRR photo for comparison purposes. The actual data shows good agreement, in general, with the cloud algorithm retrievals. Inspection shows the generally clear area over the eastern U.S. and Carribean and two distinct lines of broken to scattered clouds feeding into a wide frontal zone over the ocean. Notice the heavy convective clouds, overshooting tops, and cirrus blow-off in this area. Of special note, is the convective area east of Georgia and South Carolina which is depicted quite well by the algorithm. Further north, the clear area in New England compares favorably with the algorithm data as do the large cloud mass over the ocean and the low cloud area in the vicinity of the Great Lakes.

5. SUMMARY AND CONCLUSIONS

A new operational method of retrieving cloud products from satellite radiance measurements has been presented and preliminary analysis of results is encouraging. This method has the advantage of computing cloud products separately from the temperature retrieval step. The retrieved cloud amount compares favorably with satellite images for a number of different scenarios - over land and ocean, for stratiform cloud, convective cloud and mixed cloud types. More quantitative results, however, are sought for both cloud top temperature and amount on a global scale. These would help discern the accuracy of the algorithm more fully and could lead to further improvements.

6. ACKNOWLEDGEMENTS

The authors wish to acknowledge the following people for their assistance and useful suggestions: Charles Novak and Michael Chalfant of NESDIS and Charles Brown and Kambiz Fakhrai of ST Systems Corp. The authors are also indebted to Christine Mitchell for typing the manuscript.

7. REFERENCES

Brown, C.E., K. Fakhrai, M. Liu, A. Swaroop, and A.L. Reale, 1988: An image processing display system for evaluation of operational meteorological products. Preprint Volume: Fourth Conference on Interactive Information and Processing Systems for Meteorology, Oceanography, and Hydrology, Feb. 1-5, 1988, Anaheim, Calif. Published by Amer. Meteor. Soc., Boston, MA

Chahine, M.T., 1982: Remote sensing of cloud parameters. Journal of Atmospheric Sciences, 39, 159-170.

McMillin, L.M., 1978: An improved technique for obtaining clear column radiances from cloud-contaminated radiances. Monthly Weather Review, 106, 1590-1597.

McMillin, L.M., and C. Dean, 1982: Evaluation of a new operational technique for producing clear radiances. Journal of Applied Meteorology, 21, 1005-1014.

Smith, W., H. Woolf, C. Hayden, D. Wark, and L. McMillin, 1979: The TIROS-N Operational Vertical Sounder. Bulletin of the American Meteorological Society, 60, 1177-1187.

Stowe, L.L., P.P. Pellegrino, P.H. Hwang, P.K. Bhartia, T.F. Eck, C.G. Wellemeyer, S.M. Read, and C.C. Long, 1984: Validation of Nimbus 7 cloud products. Proceedings of the International Radiation Symposium, August 1984, Perugia, Italy.

Susskind, J., D. Reuter, and M.T. Chahine, 1987: Cloud fields retrieved from analysis of HIRS 2/MSU sounding data. Journal of Geophysical Research, 92, No. D4, 4035-4050.

Werbowetzki, A., U.S. Dept. of Commerce, 1981: Atmospheric Sounding Users Guide. NOAA Tech. Re. NESS 83.

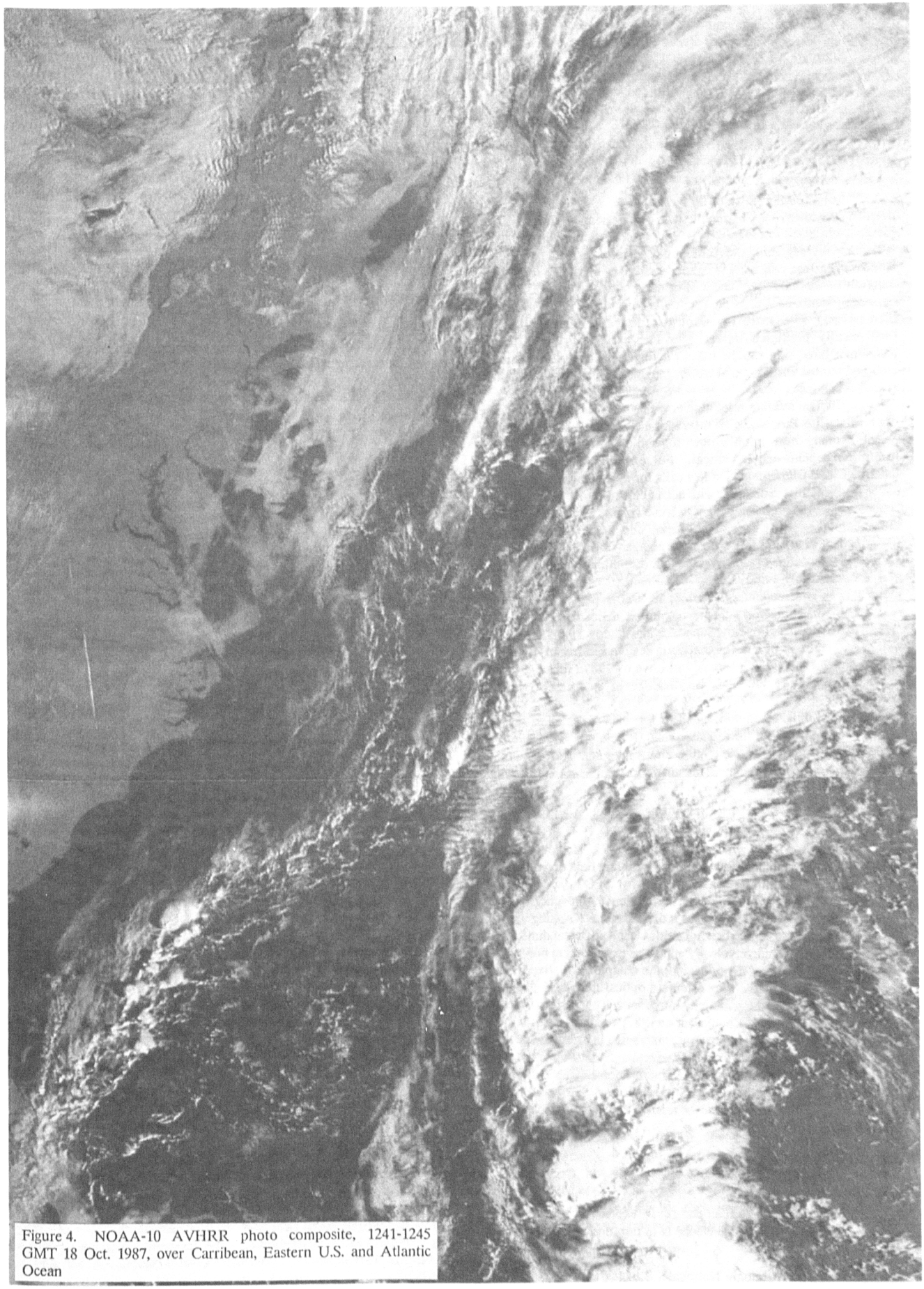

Figure 4. NOAA-10 AVHRR photo composite, 1241-1245 GMT 18 Oct. 1987, over Carribean, Eastern U.S. and Atlantic Ocean

8.8

RESOLUTION DEPENDENCE IN SATELLITE IMAGERY: MULTIFRACTAL ANALYSIS

P. Gabriel, S. Lovejoy, D. Schertzer*

Physics Dept.,
McGill University,
3600 University St.,
Montreal, Que. H3A 2T8

Augmenting a satellite's resolution reveals increasingly detailed structures that are found to occupy a decreasing fraction of the image, while simultaneously brightening to compensate. By systematically degrading the resolution of visible and infra red satellite cloud and surface data as well as radar rain data we define resolution-independent co-dimension functions that describe the spatial distribution of image features as well as the resolution dependence of the intensities themselves. The scale invariant functions so obtained fit into theoretically predicted universality classes. These multifractal techniques have implications for our ability to meaningfully estimate cloud brightness fraction, total cloud amount, as well as other remotely sensed quantities.

Civilian satellite resolution now reaches 10 meters (in the case of the Satellite Probatoire d'Observation Terrestre- SPOT) making possible many new applications for which an understanding of resolution dependence is critical. For example, the International Satellite Cloud Climatology Project calls for measuring monthly cloud cover from satellite radiances, with accuracies of a few percent. Other studies require the radiation budget of some volume of atmosphere from the subcloud scale (Curry et al. 1986) and at the synoptic scale (Ramanathan et al. 1983). To do so, a number of fundamental issues, such as how to define cloud coverage in a resolution-independent way, must be adequately addressed. Studies directed to this end have only recently been undertaken (e.g. Shih et al. 1986). Below, we build on recent work in characterising the resolution dependence of in situ measuring networks (Lovejoy Schertzer and Ladoy 1986a,1986b) as well as on a series of new developments in scaling and fractals (Lovejoy and Schertzer 1986,1987,Schertzer and Lovejoy 1987a for reviews) to systematically study the scale dependence of satellite brightness fractions.

If the satellite resolution scale L is less than the smallest scale η of the inhomogeneities of the radiation field (R being its average over a single image element, R_0 over the entire image and $T'=R/R_0$ is the relative radiance), then we may define the brightness fraction exceeding a given threshold T by:

$$F_T = \frac{\text{Number of resolution elements } T'>T}{\text{Total image elements}} \quad (1)$$

and, as long as $L \leq \eta$, F_T will be independent of L. However, clouds are turbulent fields which interact with the radiation field down to scales of the order of millimeters- hence, even for SPOT, $L \gg \eta$. More precisely, the inhomogeneities of the various atmospheric fields introduce specific types of strong scale dependencies ("scaling") which are associated with scale invariant quantities (such as fractal dimensions, or spectral slopes...) which typically appear as exponents in power laws of scale ratios. Since on the one hand, the complex radiative transfer processes involve only the dimensionless optical thickness (i.e. these processes do not break the scaling by introducing a characteristic length (Gabriel et al 1986,1987, Lovejoy et al 1987)), and on the other, the underlying terrain also involves very small scale inhomogeneities, we may also expect the radiance field to have scaling, fractal structures.

We now seek to express F_T in resolution independent terms. We first introduce the dimensionless ratio $\lambda = L/L_0$ (<1) where L_0 is the image scale. We then characterise the relative radiances by the exponent γ defined by:

$$\gamma = -\frac{\log T}{\log \lambda} \quad (2)$$

or $(R/R_0)=(L/L_0)^{-\gamma}$. We then use (2) to express T, in terms of γ, obtaining F_γ whose scale dependence is in turn described by a simple power law:

$$F_\gamma(\lambda) = \frac{\lambda^{-D(\gamma)}}{\lambda^{-2}} = \lambda^{-c(\gamma)} \quad (3)$$

where we have introduced the completely (scale invariant) codimension function $c(\gamma)=2-D(\gamma)$, where $D(\gamma)$ is the fractal dimension of the (sparse) regions where T exceeds $\lambda^{-\gamma}$. Note that as the resolution is increased ($\lambda \to 0$), $F_\gamma(\lambda) \to 0$ for all $c(\gamma)>0$, while, $T \to \infty$. The multifractal field is thus a superposition of singularities of different orders (γ), distributed over increasingly sparse fractal sets. This is exactly the type of behaviour expected from a multiplicative cascade type process. Study of such processes shows (Schertzer and Lovejoy 1987b,1987c) that $c(\gamma)$ falls into the the following universality classes (e.g. functional forms):

$$c(\gamma) = c(0)\left(1+\frac{\gamma}{\gamma_0}\right)^{\alpha} \quad (4)$$

where $\alpha \geq 2$, with the value $\alpha=2$ corresponding to the case of gaussian cascade generator, and c(0) and γ_0 are parameters characterising respectively the intermittency and smoothness of the process.

To show that eq. (3) holds, define for a given T (or equivalently γ), a series of lower resolution images (size L) by covering the high resolution image, by disjoint "boxes" (squares here), of size L. This is the "functional box counting" described in (Lovejoy,Schertzer and Tsonis 1987) which directly estimates $F_\gamma(\lambda)$ from the number of boxes ($N_T(L)$) size L needed to cover the regions exceeding T ($F_\gamma(\lambda)=N_\gamma(L)/L^{-2}$). $c(\gamma)$ is then obtained as:

$$c(\gamma) = \frac{\log F_\gamma(\lambda)}{\log \lambda} \quad (5)$$

Fig. 1a,b shows the results when the resolution of GOES (geostationary satellite) visible and infra red images are degraded from 8 to 512km on 1024X1024 km image section (The channels cover wavelengths 0.4-0.7μm (reflected solar radiation) and 10.5-12.5μm (black body emitted radiation) respectively. The raw data (at slightly higher resolution) was resampled on a conical projection with an 8X8 grid). The straightness of the lines shows that the scaling is very accurately followed over this range of scales. As T (or γ) increases, the absolute slopes ($D(\gamma)$) monotonically decrease: the most intense regions are the most sparse, hence yield the lowest dimensions (fig 2a,2b).

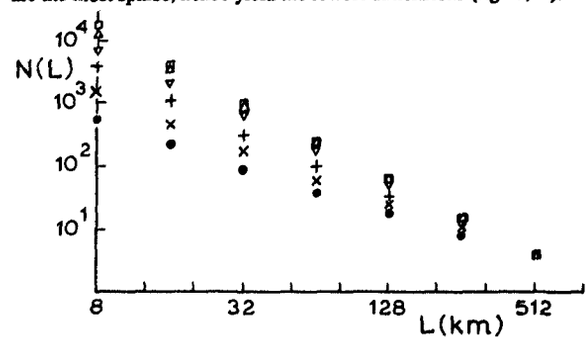

Fig. 1a: A plot of N(L) v.s. L for 11 radiance thresholds with L varying from 8 to 512km at visible wavelengths. The different symbols, top to bottom, indicate thresholds increasing by intervals of 2 satellite counts (these are proportional to the square root of the measured radiance). The straight lines indicate that over this range, scaling is accurately followed. The decreasing (absolute) slopes are D(T). This image was from the Montreal region, summer, and was largely cloud covered.

*EERM/CRMD, Météorologie Nationale, 2 ave. Rapp, Paris 75007, France

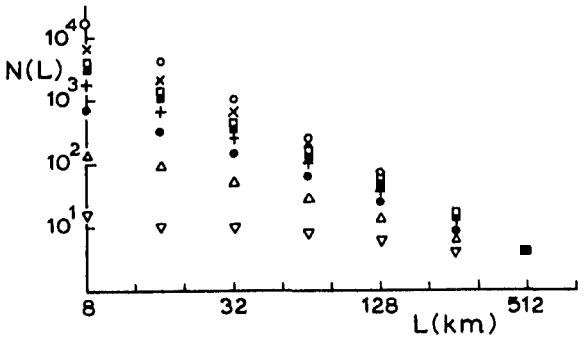

Fig. 1b: The same as 1a, except for the corresponding infra red image. The straight lines are for satellite counts at intervals corresponding to roughly 2K equivalent black body temperature, decreasing from top to bottom. Here the lowest radiances (proportional to the fourth power of the temperature) comes from the sparsest (highest) cloud tops.

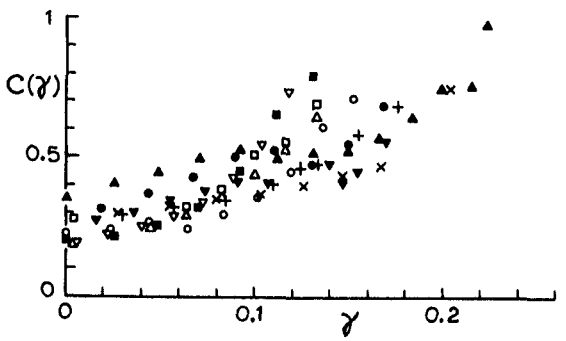

Fig. 2a: The functions c(γ) for the 10 visible cases analysed in the text.

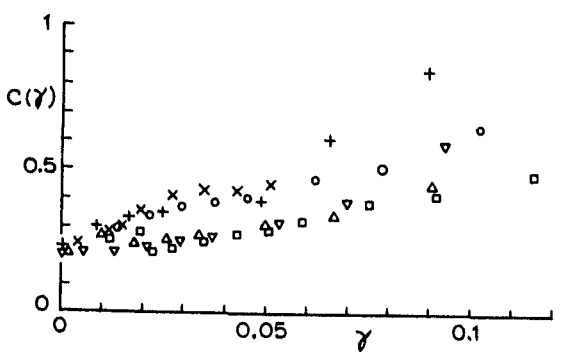

Fig. 2b: Same as 2a, but for the 4 infra red cases.

Since many empirical algorithms designed to exploit remotely sensed data relate radiances above fixed thresholds with specific physical features (such as clouds), it is of some interest to establish whether any such regions can be defined independently of the satellite resolution (i.e. are there values of γ for which $c(\gamma)\approx 0$ and hence $F_\gamma(\lambda)\approx$ constant?). If any of the radiances used by such an algorithm have $c(\gamma)>0$, then, the algorithm will contain hidden resolution dependencies. Accordingly, χ^2 tests were used to test the hypothesis that $F_\gamma(\lambda)=A_\gamma\lambda^{-2}$ where A_γ is the resolution-independent brightness fraction sought. In each of the cases we examined (10 in the visible, 4 in the infra red, spanning nearly cloud free to nearly completely cloud covered situations over Montreal), such a hypothesis could be rejected at very high levels of confidence for all except the very lowest T values. For these very low thresholds (that typically exceed only 1-5% of the data), D(T) was>1.9. For D(T)<1.9, χ^2 with 6 degrees of freedom was typically about 100. This means that the hypothesis that D(T)=2 can be rejected at very high levels of confidence, whereas, for the two parameter fits shown in Fig 1, it was always near unity which is easily compatible with the scaling hypothesis with D(T)<2.. The results were similar at both wavelengths. *For virtually all features of the radiance fields, we could with high confidence, statistically reject the hypothesis of resolution independent brightness fractions.*

We now show that the empirical $c(\gamma)$ functions fit into the universality classes (eq. 4). This is important theoretically because it confirms the predictions of cascade theories (Schertzer and Lovejoy 1987b,1987c,Schertzer and Lovejoy 1985a,1985b,1986), and is important practically, because it permits determination of the fundamental parameters characterising $c(\gamma)$. For the satellite data used here, the empirically accessible range of γ 's is quite small (the maximum is $\approx$0.4). This makes it difficult to accurately estimate α since the latter measures the concavity (In Schertzer and Lovejoy 1987b,1987c it is shown that the concavity of $c(\gamma)$ leads directly to the interesting phenomenon of the divergence of high order statistical moments.) of $c(\gamma)$ which is only pronounced for large γ. The situation is only marginally better for the radar rain reflectivities we examined (using the same data discussed in (Lovejoy,Schertzer and Tsonis 1987), in which a range of γ nearly four times this size was found to be largely compensated by correspondingly larger values of γ_0. To obtain well-defined parameter estimates, we therefore made the plausible assumption that generators were in the gaussian domain of attraction (i.e. α=2), and for each satellite (and radar) image, we empirically estimated the parameter γ_0 via a least squares regression (The standard errors were: visible $\approx$0.037, infra red $\approx$0.063, radar, $\approx$0.062 which are all comparable to the errors in estimating $c(\gamma)$ from functional box-counting which is typically of the order of $\pm$0.05.) using the formula:

$$c_n(\gamma)=c(\gamma)/c(0)=(1+\frac{\gamma}{\gamma_0})^2 \qquad (6)$$

where $c_n(\gamma)$ is the co-dimension "normalised" by c(0) which is the empirically determined co-dimension of the field at image averaged brightness (since $R=R_0 \Rightarrow T=1 \Rightarrow \gamma=0$). We then plot the curves $\langle c_n(\gamma)\rangle$ v.s. $\langle(1+\gamma/\gamma_0)^2\rangle$ fig. 3a,b,c, where the angle brackets indicate ensemble averaging (here over all available cases). As predicted by eq. 6, the curves all closely follow the line x=y (shown for reference). This shows that the main difference between the primarily cloudy, and cloud free cases were in the values of the parameters, which for the visible images were on average 0.21±.07 and 0.41±.16, respectively for γ_0 whereas c(0) was nearly constant (=0.21±.04 and 0.27±.04, respectively).

We have shown clear evidence for the scaling of cloud and surface features over a wide range of scales, radiance intensities, and at several different wavelengths. By constructing scale invariant functions $c(\gamma)$, we have shown that many of the statistical properties of the field along with their variation with scale, can be described by two-parameter universality classes. These findings are important not only for empirical techniques such as those designed to estimate cloud "fraction", but also in modeling (Gabriel et al 1986) the radiative transfer processes in highly variable clouds and over highly variable surfaces.

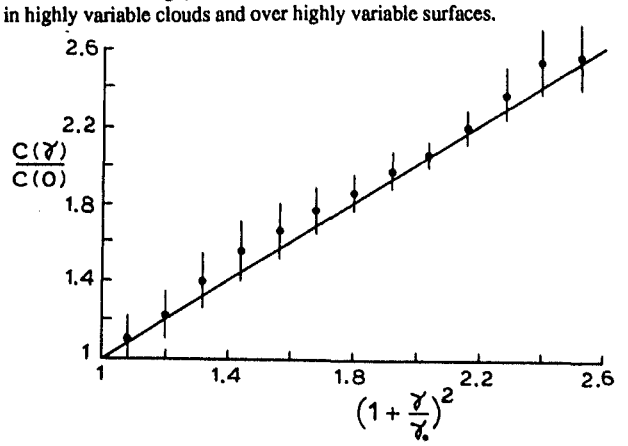

Fig. 3a: The mean normalised co-dimension, $\langle c_n(\gamma)\rangle$ for visible data, (with one standard deviation error bars) plotted against the mean $\langle 1+(\gamma/\gamma_0)\rangle^2$to test whether the empirical $c(\gamma)$ functions belong to the universality class defined by α=2 (c(0)) is measured directly, and γ_0 is ,determined by regression for each image seperately). A perfect fit corrseponding to y=x is shown for refrence.

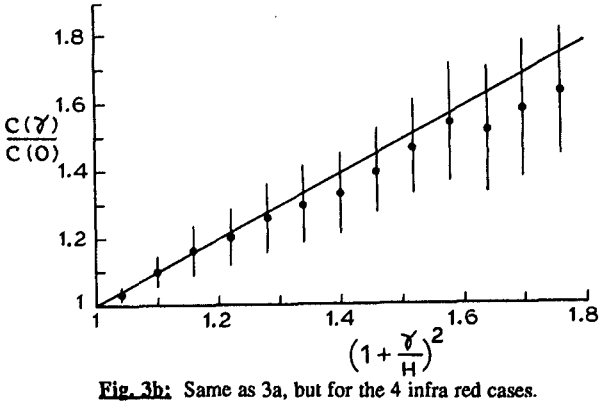

Fig. 3b: Same as 3a, but for the 4 infra red cases.

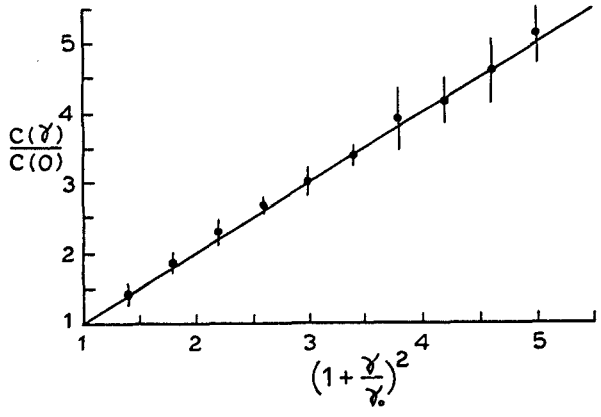

Fig. 3c: Same as 3a, but for 10 radar rain reflectivity fields discussed in detail in (5).

We ackowledge discussions with, G.L. Austin, P. Ladoy, D. Lavallée, E. Levich, J.P. Muller, A. Saucier, A.A. Tsonis, R. Viswanathan, T. Warn.

References

Sci 43,1025-1035.

Curry , J.A.,G.F.Herman, E.E. Ebert,1986: Mean and turbulence structure of the summertime arctic cloudy boundary layer. Quart. J. Roy. Meteor. Soc. (in press)..

Gabriel ,P.,S. Lovejoy, G.L. Austin, D. Schertzer: Radiative transfer in extremely variable fractal clouds, 6th Conference on Atmospheric Radiation, 230-236, AMS, Boston (1986).

Gabriel, P.,S. Lovejoy, G.L. Austin, D. Schertzer:Part II: Discrete Angle Radiative transfer: Applications to fractal clouds J. Geophys. Res. (submitted 22/10/87).

Lovejoy, S., D. Schertzer, P. Ladoy, Nature, 320, 411, (1986a).

Lovejoy, S., D. Schertzer, P. Ladoy, Nature 319, 43-44,(1986b)

Lovejoy, S., D. Schertzer, Bulletin of the AMS, 67, 21-34, (1986).

Lovejoy ,S., D. Schertzer, EOS (in press) 1987.

Lovejoy,S.,D. Schertzer: Scale and Dimension Dependence in the Detection and Calibration of Remotely Sensed Atmospheric Phenomena : Second Conference on Satellite Meteorology/Remote Sensing and Applications., 426-431, AMS, Boston (1986).

Lovejoy,S., D. Schertzer, A.A. Tsonis, Science, 235, 1036-1038, (1987).

Lovejoy, S., P. Gabriel, G. L. Austin, D. Schertzer: Discrete Angle Radiative transfer, Part I: formalism, scaling and universality, J. Geophys. Res. (submitted 28/8/87)

Ramanathan,V.,E.J. Pitcher, R.C. Malone,M.L. Blackmon, 1983: The response of a spectral general circulation model to refinements in radiative processes. J. Atmos. Sci., 40, 605-630.

Schertzer, D., S. Lovejoy, J. Geophys. Res. (in press), (1987b)

Schertzer, S. Lovejoy, Annales Math. du Que. (in press), (1987c).

Schertzer, S. Lovejoy, Scaling, fractals and non-linear variability in geophysics, Reidel (in press) (1987a).

Schertzer D., S. Lovejoy, Turbulent Shear Flow 4, 7, B. Launder ed., Springer (1985a)

Schertzer D., S. Lovejoy, P.C.H. Journal, 6, 623-632, (1985b)

Schertzer D., S. Lovejoy, Fractals in Physics, 457, Eds., Pietronero, Tosatti, North-Holland, (1986)

Shih C.F., G.G Campbell.,T.H. Vonder Haar,: Effects of Data Resolution on Satellite Cloudiness: Second Conference on Satellite Meteorology/Remote Sensing and Applications 398-401, AMS, Boston (1986).

8.9

MODELING THE SCALE DEPENDENCE OF VISIBLE SATELLITE IMAGES BY RADIATIVE TRANSFER IN FRACTAL CLOUDS:

S. Lovejoy, P. Gabriel, G.L. Austin, D. Schertzer*,
Physics dept., McGill University,
3600 University st.,
Montreal Que., H3A 2T8,
CANADA.

1. Introduction

Geophysical and astrophysical systems ranging from clouds to stars involve radiative transfer through extremely inhomogeneous optical media. Structures in both the scattering media and in the associated radiation field frequently occur over wide ranges in scale. Although the radiative transfer equation implies a linear radiative response with respect to the incident radiation, the response relative to the optical properties of the scattering medium (such as optical density) is non-linear. Indeed, from this point of view, we may consider that the incident radiation field is non-linearly smoothed by the scattering process. As a result of this smoothing - and the difficulty in adequately accounting for the variability, their effect is often ignored. Practically all geophysical radiative transfer calculations have been carried out for plane parallel (i.e. horizontally uniform) media. In clouds, (our prime interest here), this assumption has always been ad hoc- lacking both empirical and theoretical bases (at least down to scales of a centimeter or so). With the advent of modern in situ or remote measurements, it is untenable, even for the proto-typical plane parallel arctic stratus clouds (e.g. Tsay and Jayaweera 1983). Real clouds are known to be highly chaotic, turbulent structures with large variation of liquid water down to the smallest observable scales.

The problem of relating the cloud and radiation inhomogeneities has received little attention (see however Stephens 1986, 1987a,b), in part because of the difficulty of theoretically (of even numerically) estimating the radiative transfer properties of extremely inhomogeneous optically thick media. In this paper we outline some recent work (Lovejoy et Al 1987a, Gabriel et Al 1987a) concerning a sub-class of radiative transfer in which the transfer occurs only in discrete directions. A physically realisable example of such a system would be a cloud made up of elements which only scatter along the six directions defined by the normals to a cube all sharing a common orientation. This continuous system is called the Discrete Angle RTE (or DARTE).

Empirical (aircraft) energy spectra of cloud liquid water content (LWC) (such as the power law energy spectra obtained by King et Al (1981)) are scaling (or scale invariant) in form, i.e. the clouds are fractals (Lovejoy (1982), Schertzer and Lovejoy (1985), Lovejoy and Schertzer (1986a,b), Rhys and Waldvogel (1986), Ludwig (1986), Lovejoy et Al (1987)). These results support the idea that clouds have no characteristic length over a wide range, and hence we do not expect to find one in the radiation field: the radiative transfer equation has no characteristic length since radiance depends on the dimensionless optical thickness. Indeed, in a companion paper (Gabriel et Al 1987b), we analysed visible and infra red geostationary satellite data, and showed that far from being uniform, the radiation field could be modelled as a superposition of singularities of various orders, distributed over increasingly sparse fractal sets. This singular multifractal behaviour was shown to give rise to strong resolution dependence in satellite cloud estimates of cloud cover and related cloud quantities.

Our object here is to simplify the radiative transfer problem sufficiently so that it becomes analytically and numerically tractable without losing the essential features of optically thick-cloud radiative transfer with continuous phase functions. In the thick cloud limit, the scale dependence of the scattering medium is of primary importance, hence we simplify further by studying radiative transfer in scaling, uniform or extremely variable (e.g fractal) clouds. For example, we show for clouds of optical thickness τ that as $\tau \to \infty$, the transmission (T) and albedo (R) have the following scaling behaviour: $T \cong \tau^{-\nu_T}$, $1-R \cong \tau^{-\nu_R}$ where $\nu_R < \nu_T$ are universal (phase function independent) scaling exponents. Taking the thick cloud limits of the DARTE yields further insight since it shows that whereas ν_T can be obtained from a diffusion equation (and hence by considereing the photon to "diffuse" through the cloud), ν_R cannot be so obtained: the relevant equations are of higher order and can be approximated by boundary layer methods. We also show how ν_R can be analytically estimated in both uniform and fractal clouds by using renormalisation techniques. Since the notion of diffusion domain only applies to the transmission properties, a more appropriate description of phase function independence is the dynamical systems notion of "universality", justified by the association of the thick cloud limit with a fixed point of a scale changing operation. It is precisely this universal behaviour that assures us that the thick cloud discrete angle behaviour is a good approximation to the continuous angle behaviour. Using Monte Carlo calculations, we verify this quantitatively.

2. Discrete Angle Radiative Transfer:

2.1 Discrete angle discrete space radiative transfer:

Consider the intensity (radiance) $I_{\underline{s}}(\underline{x})$ which is the photon flux per unit area and solid angle at position $\underline{x}$, direction $\underline{s}$. The Discrete Angle, Discrete Space equation is obtained by considering the radiative interaction between d-dimensional cells (refered to below as "cubes" although they could in principle be any regular covering of the space) in a lattice, spacing l. The optical properties of each cube are such that only scattering of light along lattice directions occurs (when the cells are cubes, these are taken to be the the usual coordinate axes in both positive and negative directions). $I_{\underline{s}}(\underline{x})$ is therefore non-zero only for the discrete angles $\underline{s}=\underline{i}$ where $\underline{i}$ represents a unit vector parallel to a coordinate axis $I_{\underline{i}}(\underline{x})$ can therefore be represented as a vector function of position with 2d components. $I_{\underline{i}}(l\underline{m})$ is the intensity in the $\underline{i}$ direction associated with the cell centred at $l\underline{m}$. By convention we can consider this to be the average intensity over an appropriate cell face.

The lattice structure, combined with the discrete angles imply that any individual cube will only be able to interact with the 2d neighbouring cubes at positions $l(\underline{m}-\underline{i})$. The interaction principle, now states that the response $I_{\underline{i}}(l\underline{m})$ must be a linear function of the stimulus, hence there exists as 2dX2d matrix $\sigma_{\underline{i}\,\underline{k}}(l\underline{m})$ such that:

$$I_{\underline{i}}(l\underline{m})=\sum_{\underline{k}}\sigma_{\underline{i}\underline{k}}(l\underline{m})\, I_{\underline{k}}(l(\underline{m}-\underline{k}))+I^{o}_{\underline{i}}(l\underline{m}) \qquad (2.1)$$

where the sum is over the 2d orthogonal directions $\underline{k}$, and $I^{o}_{\underline{i}}(l\underline{m})$ is the source at $l\underline{m}$ (for simplicity, taken as zero below) see fig. 1 for an illustration.

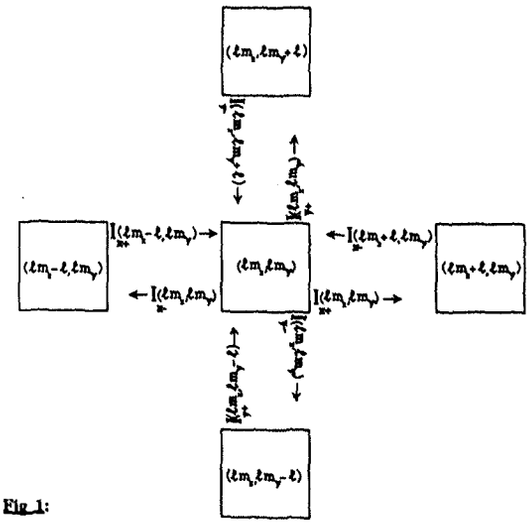

Fig 1:

The radiative interaction between square cells is exemplified. Light only scatters along lattice directions with nearest neighbours scattering elements,here denoted by R,T and S. As an example of the interaction principle: $I_{+y}(l\,m_x,l\,m_y)=RI_{-y}(l\,m_x,l\,m_y+l)+TI_{+y}(l\,m_x,l\,m_y-l)+SI_{+x}(l\,m_x+l,l\,m_y)+SI_{-x}(l\,m_x-l,lm_y)$.

*BERM/CRMD, Météorologie-Nationale, 2 Ave. Rapp, Paris 75007, FRANCE

This discrete angle discrete space equation, while not original, has, to our knowledge, received little attention. A notable exception is Mosher (1979) who referred to it as the "Building Block" model, and studied it purely as a numerical approximation to the usual radiative transfer equation but did not attempt a formal development of the type outlined below.

The simple examples studied here are lattices with orthogonal axes, and with scattering only dependent on the scattering angle. In dimension d= 1, 2, 3 we obtain respectively:

$$\sigma_{ik}=\begin{pmatrix} T & R \\ R & T \end{pmatrix}, \quad \begin{pmatrix} T & R & S & S \\ R & T & S & S \\ S & S & T & R \\ S & S & R & T \end{pmatrix}, \quad \begin{pmatrix} T & R & S & S & S & S \\ R & T & S & S & S & S \\ S & S & T & R & S & S \\ S & S & R & T & S & S \\ S & S & S & S & T & R \\ S & S & S & S & R & T \end{pmatrix} \tag{2.2}$$

where T is the transmission coefficient, R is the reflection coefficient, and S represents scattering through $\pi/2$. We have adopted the convention that the columns left to right and rows top to bottom correspond to the directions $\pm x$, $\pm y$, $\pm z$ respectively. Note that $R+T+2(d-1)S\leq 1$ with the equality holding in conservative scattering.

2.2 The Discrete Angle Radiative Transfer Equation (DARTE):

In the limit $l \to 0$, DADS becomes continuous in space. To obtain the DARTE, however, we need to express σ_{ik} in terms of the discrete scattering matrix P_{ik} which in d=3, using orthogonal directions and the same conventions as for DADS, may be written:

$$P=\begin{pmatrix} t & r & s & s & s & s \\ r & t & s & s & s & s \\ s & s & t & r & s & s \\ s & s & r & t & s & s \\ s & s & s & s & t & r \\ s & s & s & s & r & t \end{pmatrix} \tag{2.3}$$

where the lower case symbols t,r,s have been used to distinguish the scattering elements from the corresponding transfer coefficients (see appendix A for more details). If the optical thickness of the cells is small enough, single scattering dominates, and we obtain:

$$\sigma=1+\tau(l)(P-1)+O(l^2) \tag{2.4}$$

where 1 is the identity and $\tau(l)$ is the optical thickness of the cell:

$$\tau(l)=l^{1-d}\int_{l^d}\rho(\underline{x})\kappa(\underline{x})d^d\underline{x} \tag{2.5}$$

and $\rho(\underline{x})\kappa(\underline{x})$ is the optical density. Dropping the source termin eq. 2.1, and expanding $I_{\underline{k}}(\underline{x}-l\underline{k})$ in a Taylor series, and using the above expression for σ we obtain: we obtain for d=3:

$$\begin{pmatrix} 1-t & -r & -s & -s & -s & -s \\ -r & 1-t & -s & -s & -s & -s \\ -s & -s & 1-t & -r & -s & -s \\ -s & -s & -r & 1-t & -s & -s \\ -s & -s & -s & -s & 1-t & -r \\ -s & -s & -s & -s & -r & 1-t \end{pmatrix}\begin{pmatrix} I_{+x} \\ I_{-x} \\ I_{+y} \\ I_{-y} \\ I_{+z} \\ I_{-z} \end{pmatrix} = -\frac{1}{\rho\kappa}\begin{pmatrix} \partial I_{+x}/\partial x \\ -\partial I_{-x}/\partial x \\ \partial I_{+y}/\partial y \\ -\partial I_{-y}/\partial y \\ \partial I_{+z}/\partial z \\ -\partial I_{-z}/\partial z \end{pmatrix} \tag{2.6}$$

the discrete angle radiative transfer equation (DARTE).

2.3 The DARTE, the diffusion and boundary layer approximations:

In this subsection, we obtain the diffusion equation as a limit of the DARTE, and the albedo as a solution to a boundary value problem. Consider the DARTE (eq. 2.6). Introduce the notation

$$\begin{aligned} I_{x+}&=I_{+x}+I_{-x} \\ I_{x-}&=I_{+x}-I_{-x} \end{aligned} \tag{2.7}$$

and similarly for I_y, I_z, and:

$$\delta_x=\frac{1}{\kappa(\underline{x})\rho(\underline{x})}\frac{\partial}{\partial x} \tag{2.8}$$

and similarly for δ_y, δ_z. Furthermore, define p=1-t-r and q=1-t+r and for simplicity, we assume that the phase functions are constant (only the optical density varies - this does not fundamentally alter any of the results below). Consider the two dimensional case, for which we obtain:

$$\delta_x I_{x+}=-qI_{x-} \tag{2.9a}$$
$$\delta_x I_{x-}=-pI_{x+}+2sI_{y+} \tag{2.9b}$$
$$\delta_y I_{y+}=-qI_{y-} \tag{2.9c}$$
$$\delta_y I_{y-}=2sI_{x+}-pI_{y+} \tag{2.9d}$$

By applying δ_x and δ_y in the above to a, c respectively, and eliminating I_{x-} and I_{y-} we obtain:

$$[\delta_y^2\delta_x^2-pq(\delta_x^2+\delta_y^2)+q^2(2p-\varepsilon)\varepsilon]I_{x+}=0 \tag{2.10a}$$

$$[\delta_x^2\delta_y^2-pq(\delta_x^2+\delta_y^2)+q^2(2p-\varepsilon)\varepsilon]I_{y+}=0 \tag{2.10b}$$

To completely solve the two dimensional DARTE, find I_{x+} and I_{x-} from the above, and then obtain I_{x-} and I_{y-} from equations 2.9 a,c respectively. The fields I_i are obtained by addition and subtraction of the appropriate I_{x+}, I_{x-}, I_{y+} and I_{y-}. In most applications, the primary difficulty with the above is the imposition of boundary conditions which are usually specified by the value of $\underline{I_i}$ at boundaries (for example, unit intensity on only one side of a unit square corresponds to $I_{+x}(0,y)=1$, $I_{-x}(1,y)=0$, $I_{+y}(x,0)=0$, and $I_{-y}(x,1)=0$), whereas to solve the above requires four conditions on the single function I_{x+} (or I_{y+}) such as the values of the function and derivatives of various orders. In practice, it is often easier to solve the DARTE in matrix form (2.6) using the DADS approximation and numerical methods.

We see immediately from the above (by adding eqs 3.16a,b and using $J=I_{x+}+I_{y+}$) that when the highest order terms ($\delta_x^2\delta_y^2$ and $\delta_y^2\delta_x^2$) are negligeable, we obtain a diffusion equation with diffusion coeficient:

$$D(\underline{x})=\frac{1}{\kappa(\underline{x})\rho(\underline{x})}\frac{p}{q[\varepsilon-2p]} \tag{2.11}$$

This condition holds far from sources, hence the diffusion law for thick clouds will be governed by the above diffusion equation (this is also true of the diffusion through fractal clouds, where down to a small inner "cutoff" scale, $\kappa(\underline{x})\rho(\underline{x})$ might be the indicator function of a fractal set, or more generally, a fractal measure). However, near sources (i.e if we seek the cloud albedo), then we run into the classical boundary layer problem, viz., a differential equation whose highest order term is multiplied by a small parameter, and which therefore cannot generally be well approximated everywhere by the solution of a lower order differential equation, since the boundary conditions of the high order equation will generally overdetermine the solution to the lower order one. The scaling of the albedo, must therefore be obtained by studying the boundary layer equation associated with eq. 2.10.

3. Limiting scaling properties of DARTE:

3.1 Introduction:

In the previous section, the scaling of the transmitted radiance was argued from the diffusion limit and the scaling of the boundary conditions. The scaling of 1-R was not propertly justified. In the remainder of this paper, we justify this scaling, making use of a renormalisation type approach which is very similar to invariant embedding. In particular, we obtain approximate doubling relations expressing the transfer matrix $\sigma(2\tau)$ in terms of $\sigma(\tau)$ (i.e. $\sigma(2\tau)=f(\sigma(\tau))$ where f is a non-linear function estimated below). The optical properties of very thick clouds are then obtained by iterating: $\sigma(2^n\tau)=f^{(n)}(\sigma(\tau))$ (where we have used the notation $f^{(n)}$ is the nth iterate of f). The properties of $f^{(n)}$ such as fixed points and scaling exponents can then be studied using functional iteration methods (e.g. Schuster 1984). As the thickness of the cloud is doubled, the albedo approaches 1 and near the fixed point, R=1,T=0, the iteration is approximated by matrix multiplication, yielding a power law (scaling) behaviour governing the approach of R to 1 and T to 0. This approach is actually a type of "real space renormalisation", a method used to study the large scale behaviour of many non-linear physical systems (perhaps the simplest being the percolation problem, e.g. Stauffer 1985). Although

it is only approximate when applied to doubling, we show, by comparing it with quadrupling, octupling and hexatupling etc., that the scaling exponents converge, yielding accurate estimates of ν_R.

3.2 Doubling in two dimensions:

We illustrate this method in detail with d=2 by calculating the radiative transfer properties of the 2X2 square made up of square cells with $S(\tau)$, $T(\tau)$, $R(\tau)$ coefficients (see eq. (2.2)), as shown in fig. 2. We now irradiate the square with unit radiation incident on the top face only (i.e. the boundary conditions are: $I_{-y}(x,2\tau)=1$, $I_{+y}(x,0)=0$ for $0\le x\le 2\tau$, and $I_{-x}(2\tau,y)=0$, $I_{+x}(0,y)=0$ for $0\le y\le 2\tau$). Applying eq. 2.1 to the 2X2 system, interpreting the total +y intensity at the top as $R(2\tau)$, the total -y intensity at the bottom as $T(2\tau)$, and that from the sides as $S(2\tau)$, we obtain:

$$T(2\tau) = \frac{(T(\tau)+\Gamma(\tau))^2}{(1-(R(\tau)+\Gamma(\tau))^2)} \qquad (3.1a)$$

$$R(2\tau) = (R(\tau)+\Gamma(\tau))(1+T(2\tau)) \qquad (3.1b)$$

where:

$$\Gamma(\tau) = \frac{S(\tau)^2}{(1-R(\tau))} \qquad (3.2)$$

When there is absorption, the expression for $S(2\tau)$ is very complicated. However, in the case of interest below, conservative scattering, it is obviously given by $S(2\tau) = \frac{1}{2}(1-T(2\tau)-R(2\tau))$.

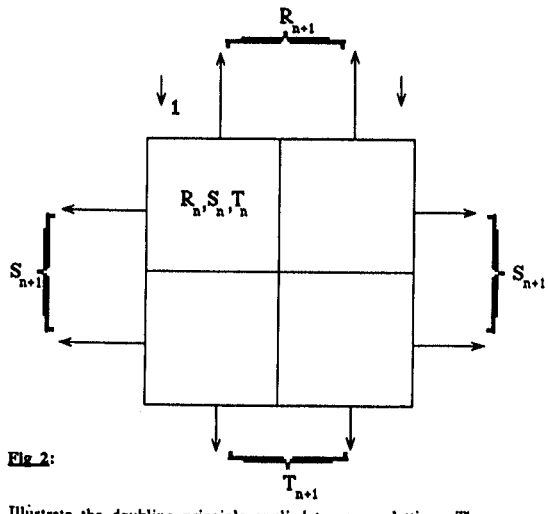

Fig 2:

Illustrate the doubling principle applied to square lattices. The averaged transfer coefficients in the n th iteration can be used as shown to calculate those in the $(n+1)^{th}$ iteration.

The system of non-linear equations (3.1,3.2) can now be regarded as a mapping $(T(2\tau),R(2\tau),S(2\tau)) = f(T(\tau),R(\tau),S(\tau))$ and the functional behaviour of $(T(\tau),R(\tau),S(\tau))$ over the whole range of τ can be analysed by iterating to obtain:

$$(T_n,R_n,S_n) = f^{(n)}(T_0,R_0,S_0) \qquad (3.3)$$

Where we have used the notation $(T(2^n\tau_0),R(2^n\tau_0),S(2^n\tau_0)) = (T_n,R_n,S_n)$.

3.3 Fixed Points and scaling exponents:

In analysing a non-linear mapping such as eq. (3.1), we must first determine its fixed points, i.e. those points which satisfy:

$$(T^*,R^*,S^*)=f(T^*,R^*,S^*) \qquad (3.4)$$

where the asterix indicates a fixed point value. Fixed points are either attractive or repulsive depending on whether the mapping results in points in the infinitesimal neighborhood decreasing or increasing their distance from the fixed point. Mathematically, we require that the largest eigenvalue (Λ) of the Jacobian of f, denoted:

$$\frac{\partial f(T,R,S)}{\partial(T,R,S)}\Big|_{T^*,R^*,S^*} \qquad (3.5)$$

evaluated at the fixed point, is respectively less than or greater than unity (the Jacobians will be explicitely evaluated in the following sections). Continuing our study of the d=2, conservative scattering case, we may drop explicit reference to S (which is given by S=(1-R-T)/2), and consider only the points in (T,R) space. Using f defined by eq. 3.1 and imposing the condition $\Lambda=0$ we obtain the following fixed points:

(1,0)	unstable, infinitely thin cloud
(0,1)	stable, infinitely thick cloud
(1/2,-1/2)	unstable, unphysical
(-1/9,∞)	unstable, unphysical

Since, R,T must be positive, ≤1, physically realisable points (T,R) must lie in the "physical triangle", fig. 3a. Note that although two of the fixed points are unphysical, their existence is important in understanding the physical regime. In particular, as we shall see below, they imply that the actual physical regime is only a subset of the physical triangle.

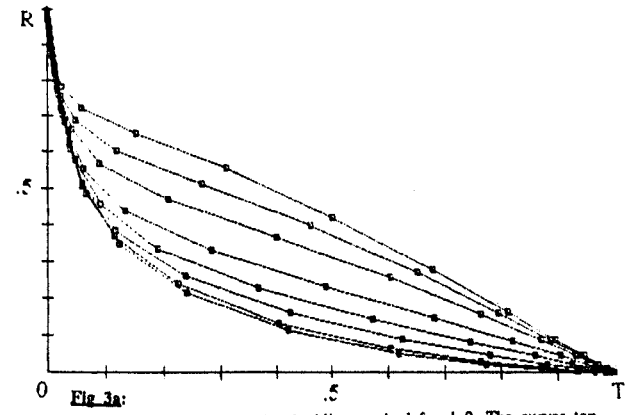

Fig 3a:

Physical triangle estimated by doubling method for d=2. The curves top to bottom are for doubling of t indicated as points $\frac{S}{R}$ = .1, .2, .5, 1, 2, 5, 10, 20 respectively.

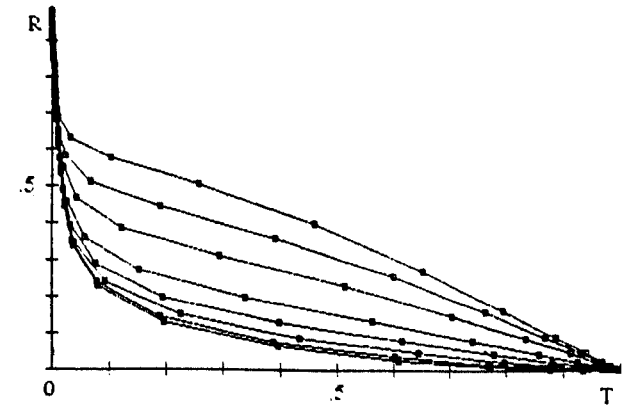

Fig 3b: Same as 5a for d=3.

3.4 Asymptotic non-diffusive limits for thick clouds: scaling exponents and universality:

The analysis of thick cloud behaviour (τ-->∞), is more involved since the Jacobian $\frac{\partial f(T,R)}{\partial(T,R)}\Big|_{0,1}$ depends on the direction in (T,R) space that the fixed point (0,1) is approached. Standard arguments (see Lovejoy et al 1987b for details) yield:

$$\nu_2 = -\frac{\log(\Lambda)}{\log 2} \qquad (3.6)$$

where:

$$\Lambda = \sqrt{3}\left(\frac{627}{32}\right) - \frac{67}{2} + \frac{\sqrt{(2367483-136681\sqrt{3})}}{32} = 0.732... \qquad (3.7)$$

This implies, ν_2=0.450... This may be regarded as an estimate of the true exponent that would be obtained by direct numerical calculation on an enormous grid. To obtain a better estimate we should

compare this result with quadrupling (ν_4) octupling (ν_8) etc. (see fig. 4a), as calculated numerically. As the scale changing factor increases, the value of w increases, since (for conservative scattering) $w = \frac{1-R}{T} = 1+\frac{2S}{T} = \tau^{(\nu_R-\nu_T)}$. On physical grounds, T must approach zero faster than S so that w-->0 hence, $\nu_R<\nu_T$. The dominating exponent obtained as the limit of the above rescaling procedure is the smaller of the two, thus $\nu_\infty=\nu_R$ To obtain ν_T, (which =1 in the homogeneous d = 2, 3 cases) diffusion methods must be used. A similar analysis in d=3, leads to fig.4b and ν_R=1/2 (see Lovejoy et Al 1987b for more details).

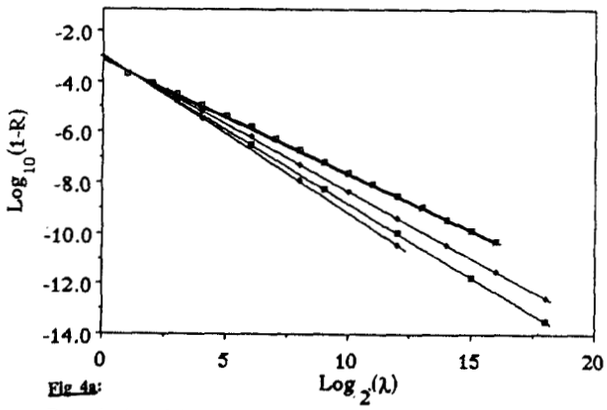

Fig 4a:

Determination of the exponents $\nu_2, \nu_4, \nu_8, \nu_{16}$ for d=2, which determine the rate of convergence to the fixed point R=1 and T=0 for (top to bottom) doubling, quadrupling, octupling and hexatupling respectively. Emphasized line has the theoretical ν_2 slope = 0.447.

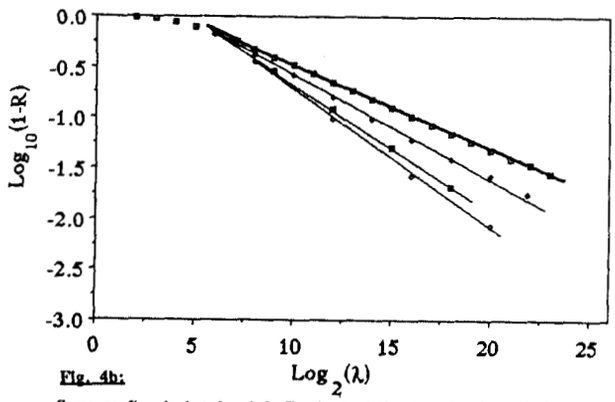

Fig. 4b:

Same as fig. 4a but for d=3. Emphasized line has the theoretical ν_2 slope =0.277.

3.5 Radiative Transfer in a 1.58 Dimensional fractal Cloud:

In this section we apply the doubling method o the simplest fractal cloud imaginable, shown in its early stages of construction in fig. 1. Starting at a small inner scale (below which the cloud has different, e.g. homogeneous behaviour), with optical thickness τ_0, we generate thicker and thicker clouds by placing three squares obtained at a previous iteration in the square pattern shown (this fourth square is empty). At each iteration, the mean optical depth increases by a factor 3/2; from the inner scale up to the resulting outer scale, the cloud is a scaling (mono-dimensional) fractal with dimension D=log3/log2=1.58... Although for the moment, we consider this purely as a simple construct, it is in fact a kind of deterministic "β model" for turbulence (see next section).

As described in part I (section 4.3) for the d=2,3 cases, we can obtain approximate doubling relations for discrete angle fractal clouds. The corresponding doubled transmission and reflection coefficients for this fractal cloud are :

$$T_{n+1}=\frac{T_n}{2}(1+T_n)+\frac{S_n^2}{2}+\frac{\Gamma^2}{2(1-R_n^2\Gamma^2)}\{R_n^2(1-R_n^2)(1+\frac{T_n^2}{S_n^2})+R_n(1-R_n^2)+T_n+R_nS_n^2+R_n^2S_n^2+R_n^2T_n^2+2T_nR_n\}$$

$$R_{n+1}=R_n+\frac{\Gamma^2}{2(1-R_n^2\Gamma^2)}\{T_n(2+R_nT_n)+R_n(1-R_n^2)(1+\frac{T_n^2}{S_n^2})+R_nS_n^2\} \quad (3.9)$$

where:

$$\Gamma=\frac{S_n}{(1-R_n^2)}$$

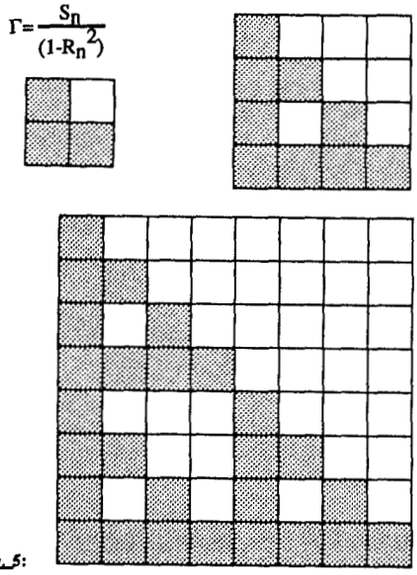

Fig. 5:

Generator for the deterministic fractal cloud discussed in the text with d= $\frac{\mathrm{Log}(3)}{\mathrm{Log}(2)}$ =1.58...showing the first three stages in its construction (top to bottom).

Considering the special case of conservative scattering (R+T+2S=1), we obtain the basic physically significant fixed points (T*,R*)=(0,1), (1,0), corresponding to thick and thin clouds respectively. We also have the following (non-physical but real) fixed points $(\frac{1}{2},\frac{-1}{2})$, (0.3416...,-0.4472...), $(\infty,-\infty)$. As we iterate these equations we systematically build up the fractal cloud (dimension 1.58...) as shown in fig. 5.

Following the above method, we find $\nu_2(1.58)$=0.146... This exponent is an estimate of that which would be obtained by direct numerical calculation on an enormous grid. To obtain better estimates of $\nu_\infty(1.58)$ (recall that this limiting exponent is equal to $\nu_R(1.58)$), this result should be compared to the results of quadrupling, octupling, and hexatupling as calculated in (fig 6b). Using DADS, we obtain, the estimates $\nu_R(1.58)$=0.162.., $\nu_T(1.58)$=0.40... which indicates that the above analytic doubling result is remarkably accurate.

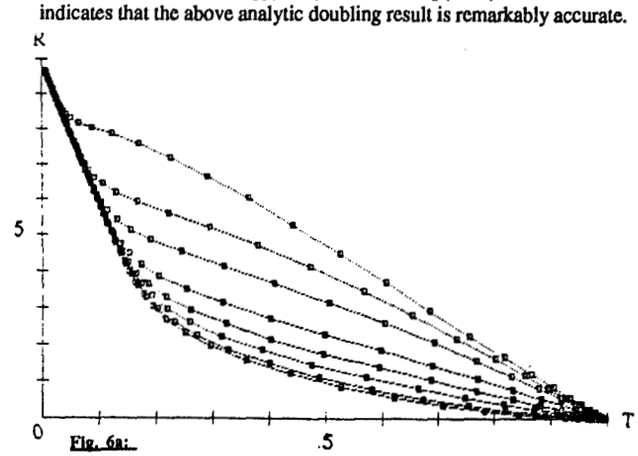

Fig. 6a:

Physical triangle estimated by doubling method for d=1.58... obtained by iterating equation 2.1. The curves top to bottom are for doubling of t indicated as points $\frac{S}{R}$ = .1, .2, .5, 1, 2, 5, 10, 20 respectively.

3.6 Packing Factor :

This analytic result indicates that the albedo of this fractal cloud approaches unity much more slowly than a uniform one, two or three

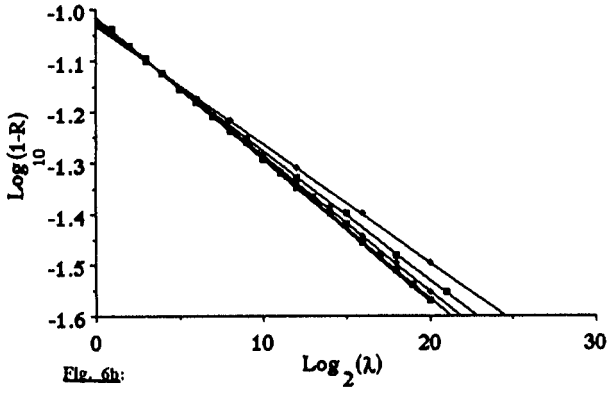

Fig. 6b:

Determination of the exponents ν_2, ν_4, ν_8, ν_{16} for d=1.58..., which determine the rate of convergence to the fixed point R=1 for (bottom to top) doubling, quadrupling, octupling and hexatupling respectively. λ is a scale ratio, λ=1 corresponds to R=0.9,T=0.05. Emphasized line has the theoretical ν_2 slope = 0.147.

dimensional cloud since $\nu_R=1, \frac{3}{4}, \frac{1}{2}$ respectively. In fact, if we define a 'packing factor' ξ as the ratio of optical thickness of a fractal and plane parallel cloud (i.e. one dimensional) with the same albedo, then we obtain:

$$\xi \propto \tau^{\frac{\nu_R(1)-\nu_R(1.58)}{\nu_R(1)}} = \tau^{1-\frac{\nu_R(1.58)}{\nu_R(1)}} \qquad (3.10)$$

Clearly ξ diverges with τ since $\nu_R(1) > \nu_R(1.58)$. The same is true for any cloud (such as a two or three dimensional one) in which ν_R (d)< $\nu_R(1)$.

This result is important since it shows that even when losses through the sides are taken into account, that the inhomogeneities still lead to diverging packing factors (since we have shown $\nu_R(1) > \nu_R(2) > \nu_R(3) > \nu_R(1.58)$). Furthermore, inhomogeneities lead to diverging errors even for the transmitted flux, since $\nu_T(1)=\nu_T(2)=\nu_T(3)> \nu_T(1.58)$.

4. Radiative transfer in random fractal clouds:

4.1 Random Fractal Clouds: Turbulent Cascade Models

A dynamical approach to the interaction of radiation with atmospheric fields has been investigated by Simonin et al (1983), Schertzer and Simonin (1983) and Coantic (1978). By using statistical closure techniques (see also Stephens 1987a,b) this approach directly studied the scaling behaviour of the radiation field and is limited primarily by its inability to properly handle intermittency. Since the latter is important in radiative transfer for the reasons outlined below, we adopt a phenomenological, rather than a dynamical, turbulent approach, relying on extremely variable (intermittent) stochastic fractal models.

In hydrology, stochastic models of rain have been developed for some time (see e.g. Gupta and Waymire 1981 for an early review, and the special issue of JGR, Aug. 1987 for a recent survey). While some of these could be used for cloud modelling, we concentrate here on the sub-class of fractal models. The simplest of these (Lovejoy and Mandelbrot 1985) involves the addition of a large number of "pulses", but has the drawback that it lacks physical motivation, and is characterised by a single fractal dimension. A much more physically based fractal model is the passive scalar turbulent model outlined in Schertzer and Lovejoy 1987a,b. This model has the same symmetries (e.g. scaling) as the dynamical (partial differential) equations governing passive scalar advection in incompressible turbulence, as well as the same cascade phenomenology.

4.2 Fractal Clouds with Cyclic Horizontal Boundary Conditions

As we have already seen, a fractal structure of internal inhomogeneities leads to: a) an albedo varying as a function of spatial resolution (see Gabriel et Al 1987b and below- this is an important issue that appears to have received little attention in the remote sensing literature) and b) we estimate a packing factor ξ>1 whose mean and standard deviation we estimate below. The β model was used to create the cloud model, and the DADS radiation scheme was used to determine the resulting radiation fields.

In fig. 7 the mean and standard deviation of ξ is indicated for clouds with co-dimensions (here C=3-D) varying from 0.2 top 0.8, for clouds with τ=50. For each C calculations were performed on ten samples, and means and standard deviations calculated. We used a 32^3 grid size, a phase function estimated to correspond to a Deirmendjian (1969) C.1 drop size distribution, at 0.45μm wavelength and performed a Monte Carlo calculation to estimate both the end of the linear regime (determined to be at τ=10), and the appropriate R,T,S coefficients. When the cyclical boundary conditions are removed, ξ increases considerably as expected since the albedo is reduced (fig 7). As described in 3.1, except in very artificial mono-dimensional situations, we expect scaling fields to be multifractal; indeed, Gabriel et Al 1987b have shown this to be true of satellite radiation fields at various wavelengths. Gabriel et al 1987a shows that the radiation fields here are also multifractal in spite of the mono-dimensional nature of the cloud field.

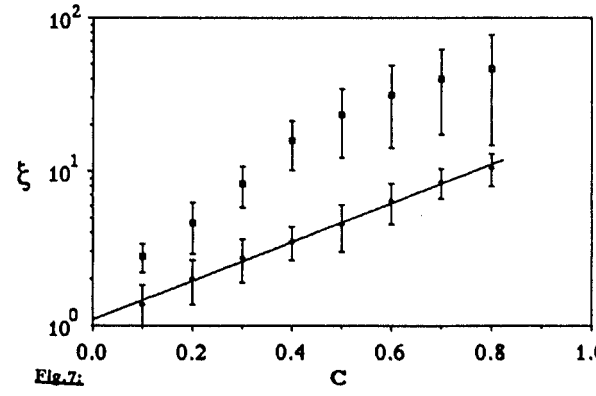

Fig.7:

Packing factors (ξ) estimated for a cubic cloud having cyclic and non-cyclic horizontal boundary conditions (bottom to top) as a function of codimension.

5. Some Meteorological Applications:

We have argued that radiative transfer in clouds depends critically on the assumptions that are made about the variability (or lack of variability) of the optical medium. To date, most radiative transfer calculations have made the totally ad hoc assumption that clouds are plane-parallel. The limitation to this extremely special (and unrealistic) case considerably restricts meteorological and climatological applications of radiative transfer. Areas where our findings are likely to be particularly relevant are discussed briefly below. Other areas include rainfall and cloud estimation algorithms, theoretical radiative transfer calcualtions, stochastic cloud modelling and nuclear winter.

a) The interpretation of high resolution satellite images of clouds: Satellite imagery is widely used to make subjective judgements about meteorological features on a routine basis. The dangers of such naive interpretations of satellite data were underscored in Gabriel et Al 1987 who showed (in contradiction with the plane parallel assumption) that with a high degree of confidence, for virtually every feature of such satellite images at both infra red and visible wavelengths one could statistically reject the hypothesis that the measured fields were independent of the intrinsic sensor resolution.

b) Radiation budget and climate models: The need to relate the spatial and (temporal) variability of clouds to radiation processes of interest arises in many practical problems in remote sensing studies of clouds and precipitation. For example many climatological studies and climate models require estimates of the radiation budget for various regions of the atmosphere and at a variety of scales (e.g Curry et al 1986, Ramanathan et al 1983). The solution to these problems calls for an understanding of how radiance and albedo vary with spatial resolution.

c) The Albedo Paradox: We have seen that because of the very special nature of plane parallel radiative transfer, virtually any non-plane parallel system will be expected to have different thick scaling exponents. In terms of the packing factor ξ this immediately leads to the general (conservative scattering) result:

$$\lim_{\tau \to \infty} \xi(\tau) \longrightarrow \infty$$

This result has implications for the so-called "albedo paradox" (Wiscombe et al, (1984)). Stated simply, the paradox is that optical depths computed from seemingly reasonable liquid water profiles based on actual field measurements reach several hundred for even moderately thick clouds. However, in order to obtain consistency between the value of the planetary albedo ~0.30 , and the globally averaged cloud cover (50%),the latter cannot have a mean albedo greater than 0.5 (Wiscombe et al 1984, Paltridge and Platt 1980), a value which for homogeneous clouds implies optical depths only of order 10. When plane parallel models are used to approximate the radiative properties of real clouds, (and they usually are), then optical depths exceeding 100 imply visible albedoes greater than 0.9, a value rarely observed (Wiscombe et al, 1984). Satellite observations also deduce smaller-than-expected optical depths (e.g. Twomey and Cocks, 1982). As we have seen, the paradox vanishes once we leave the very artificial and special case of plane-parallel clouds.

6. Conclusions:

The major objective of this paper was to study radiative transfer on fractal clouds. To make the problem tractable, we studied the special case involving discrete angle phase functions, in which scattering only occurs along coordinate axes (the DARTE formalism). Furthermore, we only studied the simplest fractal cloud models, involving a single fractal dimension. By comparing the optical thickness of plane parallel and fractal clouds with the same albedoes, we defined a 'packing factor', equal to the ratio of their optical thickness which is a quantitative measure of the non-linear effect of inhomogeneities. We demonstrated that packing factors generally diverge in the limit $\tau \rightarrow \infty$.

Going beyond doubling, large models employing (32^3) grid points were used to analyze the inhomogeneities of the radiation fields. By applying a series of albedo thresholds,and then estimating the fractal dimension of regions exceeding the threshold via a "functional box counting" algorithm, we showed that even when clouds have a single fractal dimension (e.g. clouds generated by the β model) the resulting radiation field is multifractal.

In the meteorological or remote sensing context, this work illustrates that the effects of cloud inhomogeneities can profoundly influence the reflected and transmitted intensities or fluxes. In order to accurately understand the role that clouds in modulating weather and climate, it is necessary to consider non plane-parallel geometries with different scaling characteristics.

We ackowledge discussions with P. Ladoy, D. Lavallée, E. Levich, J.P. Muller, A. Saucier, A.A. Tsonis, R. Viswanathan, T. Warn.

References:

Coantic,M.F.1978: Interaction Between Turbulence and Radiation. AGARDograph 232, 175-236.

Curry J. A., G.F. Herman, E.E. Ebert, 1986: Mean and turbulence structure of the summertime artic cloudy boundary layer. Quart. J. Roy. Meteor. Soc. (in press).

Deirmendjian, D. 1969: Electromagnetic Scattering on Spherical Polydispersions. American Elsevier, NY, 290 pp.

Davies R. 1976: The three dimensional tranfer of solar radiation in clouds. PhD Thesis 219pp U. of Wisc. Mad.

Davies R. 1978: The effect of finite geometry on the dimensional transfer of solar irradiance in clouds. J. Atmos. Sci. 35, 1712-1724.

Gabriel P., Lovejoy, S., G.L. Austin, D. Schertzer, 1987ba Discrete angle radiative transfer part II: applications to fractal clouds. J.Geoph.Res. (submitted 10/87).

Gabriel, P, S. Lovejoy, D. Schertzer, 1987ab Multifractal analysis of satellite resolution dependence. Science (submitted 15/9/87).

Griffith, C. G., W. L. Woodley,P. G. Grube, D. W. Martin, J. Stout, and D. N. Sikdar, 1978: Rain Estimation from Geosynchronous Satellite Imagery, Visible and Infrared Studies. Mon. Wea. Rev.,106, 1153-1171.

King W.D., C.T. Maher, G.A. Hepburn, 1981: Further performace tests on the CSIRO liquid water probe. J. Atmos. Sci., 20, 195-200.

Lovejoy, S., 1982 : The area-perimeter relationship for rain and cloud areas. Science, 216, 185-187.

Lovejoy, S., B. Mandelbrot, 1985: Fractal properties of rain and a fractal model. Tellus, 37A, 209-232.

Lovejoy, S., D. Schertzer, 1985a: Generalized scale invariance in the atmosphere and fractal models of rain. Wat. Resour. Res 21, 1233-1250.

Lovejoy, S., D. Schertzer, 1986b: Scale and dimension dependence in the detection and calibration of remotely sensed atmospheric phenomena. 2nd conf. on sat. meteor. and remote sensing and appl., Williamsburg, May 13-16, p426-431.

Lovejoy, S., D. Schertzer, 1986a: Scale invariance, symmetries fractals and stochastic simulation of atmospheric phenomena. Bull AMS 67, 21-32..

Lovejoy, S., D. Schertzer, A.A. Tsonis, 1987a: Functional box-counting and multiple elliptical dimensions in rain. Science, 235, 1036-1038.

Lovejoy, S., P. Gabriel, G.L. Austin, D. Schertzer, 1987b: Discrete angle radiative transfer part I: formalism, scaling and universality. J.Geoph.Res. (submitted 8/87).

Ludwig, F.L. K.C. Nitz, 1986: Analysis of lidar cross sections to determine the spatial structure of material in smoke plumes. Proc. of Smoke Obscurants symposium vol. 10, Harry Diamond Labs; Adelphis Md. 231-241.

Mosher, F. R. 1979: Visible Flux across Finite Clouds. Ph.D thesis. The University of Wisconsin, Madison, 109 pp.

Paltridge G.W, Platt C.M.R : Radiative Processes in Meteorology and Climatology Developments in Atmospheric Sciences 5, Elsevier Scientific Publishing Company, 1976.

Ramanathan, V., E.J. Pitcher, R. C. Malone, M. L. Blackmon, 1983: The response of a spectral general circulation model to refinements in radiative processes. J. Atmos. Sci., 40, 605-630.

Rhys, F.S., A. Waldvogel, 1986: Fractal shape of hail clouds. Phys. Rev. Lett. 56, 784-787.

Schertzer, D., O. Simonin 1983: A theoretical study of radiative cooling in homogeneous and isotropic turbulence. Turbulent Shear Flow 3, Eds. L.J.S. Bradbury et al , 262-274.

Schertzer, D., S. Lovejoy 1983: On the dimension of atmospheric motions. Preprint Vol., IUT AM Symp on Turbulence and Chaotic Phenomena in Fluids, 141-144.

Schertzer, D., S. Lovejoy, 1985a: The dimension and intermittency of atmospheric dynamics. Turbulent Shear Flow 4, 7-33, B. Launder Ed., Springer, NY.

Schertzer, D., S. Lovejoy, 1985b: Generalised scale invariance in turbulent phenomena P.C.H. Journal, 6, 623-635.

Schertzer, D., S. Lovejoy, 1987a: Singularités anisotropes, et divergence de moments en cascades multiplicatifs. Annales Math. du Que. 11, 139-181.

Schertzer, D., S. Lovejoy, 1987b: Physically based rain and cloud modeling by anisotropic, multiplicative turbulent cascades. J. Geophys. Res. 92, 9693-9714.

Schuster, H.G., 1984: Deterministic Chaos, Physik Verlag, 220pp.

Stauffer D., 1985: Introduction to Percolation Theory, (London: Taylor & Francis).

Simonin,O., Coantic,M.F., Schertzer,D., 1981:Effet du rayonnement infrarouge sur la turbulence de temerature dans l'atmosphere: structure spectrale et taux de dissipation. C.R. Acad Sci. Paris 293, 245-248 .

Stephens G. L., 1986: Radiative Transfer in Spatially Heterogeneous, Two-Dimensional Anisotropically Scattering Media., J.Q.S.R.T , 36 No 1, 51-67.

Stephens G.L. 1987a: Radiative transfer through randomly fluctuating optical media: I General Solution. JGR (submitted 7/87).

Stephens G.L. 1987b: Radiative transfer through randomly fluctuating optical media: II Group theory and closures. JGR (submitted 7/87).

Tsay, S. and K. Jayaweera , 1983: Physical and Radiative properties of Summertime Arctic Stratus Clouds, Final Report, NSI Grant DPP-81-11512, Geophysical Institute, University of Alaska, Fairbanks, Alaska.

Twomey ,S.,and T. Cocks,1982: Spectral reflectance of clouds in the near infrared:comparisons of measurements and calculations. J. Meteor. Soc. Japan, 60,583-592.

Waymire, E, V.K. Gupta, 1981: The mathematical structure of rainfall representations, parts 1-3, Water Res. Res. 17, 1261-1294.

Welch M. R, 1983: Radiation Calculations Based Upon Detailed Microphysics Fifth Confrence on Atmospheric Radiation. p 505 .

Wiscombe, W.J., R.M. Welch, W.D. Hall. 1984: The Effects of Very Large Drops on Cloud Absorption.Part 1: Parcel Models. J. Atmos. Sci. 41, 1336-1355.

EFFECTS OF DATA RESOLUTION ON MARINE STRATIFORM CLOUD DETECTION USING AVHRR AND VISSR SATELLITE DATA

Chi-Fan Shih, Melanie Wetzel and Thomas H. Vonder Haar

Cooperative Institute for Research in the Atmosphere (CIRA)
Colorado State University, Fort Collins, Colorado 80523

1. INTRODUCTION

The extensive stratiform cloudiness commonly found in the California coastal and offshore regions exerts a controlling influence on energy transfer, air motion and local meteorological parameters. A clearer understanding of the evolution and the diurnal fluctuation of this stratiform boundary-layer cloud is crucial to the prediction and numerical modeling of the physical and dynamical processes within cloud-topped boundary layer. At CIRA, we are building a regional marine stratiform cloud climatology for the California coastal ocean area. Since the marine stratiform clouds persist over a large area, only meteorological satellite observation can provide us data that covers the oceanic area continuously. For example, the International Satellite Cloud Climatology Project (ISCCP) has been collecting infrared and visible radiance data from meteorological satellites since July 1983 every three hours (Schiffer and Rossow, 1983). Because this ISCCP data set requires global coverage, its spatial resolution has been reduced to make global processing possible. Therefore, in order for us to use this rich data set to build a satellite climatology of marine stratiform clouds, a very important and necessary requirement is to know the data resolution (including both temporal and spatial resolutions) effects on the derived cloud amounts. In this study, we used both VISSR data from the GOES-6 satellite and AVHRR data from the NOAA-7 satellite to study the spatial resolution effects of ISCCP sampling procedures. The cloud fractions derived from visible and infrared channel data from the AVHRR and VISSR data at full resolution are treated as the "true" fractions. Comparisons of these "true" fractions with cloud fractions from the same data at reduced resolution are presented.

2. DATA ANALYSIS

Figures 1 to 3 are full resolution (1 km at nadir) AVHRR channel 1, 3 and 4 images from the NOAA-7 satellite at 2300Z on 26 June 1986. Twelve trarget areas (boxes A to L) were selected because of their different cloud conditions. The same geographical areas were located on the GOES-6 satellite images of the same time (Figures 4 and 5). Figures 4 and 5 are full resolution visible and infrared channel pictures from the VISSR sensors of the GOES-6 satellite. The sizes of all target areas were 30 pixels by 30 pixels on the AVHRR images. To estimate the satellite cloud fractions, we have analyzed all satellite images subjectively using a threshold method. The threshold value of each target area was chosen while the satellite image was displayed on our Interactive Research Imaging System. The spatial continuity of threshold values was considered when they were determined. Any pixel brighter than the threshold value was counted as a cloudy pixel. The cloud fraction of each box is the percentage of cloudy pixels divided by the total number of pixels in that box. We have applied this simple cloud scheme to the satellite images of Figures 1, 3, 4, 5 and the degraded images of Figure 4 (not shown here). The degradation was done in the same way as in Shih, et al., (1986) using the following formula:

$$\text{Degrade Pixel Count} = \left(\frac{\Sigma_1^N \text{Count}^2}{N}\right)^{1/2}$$

where count is bringhtness count, N is the number of pixels averaged.

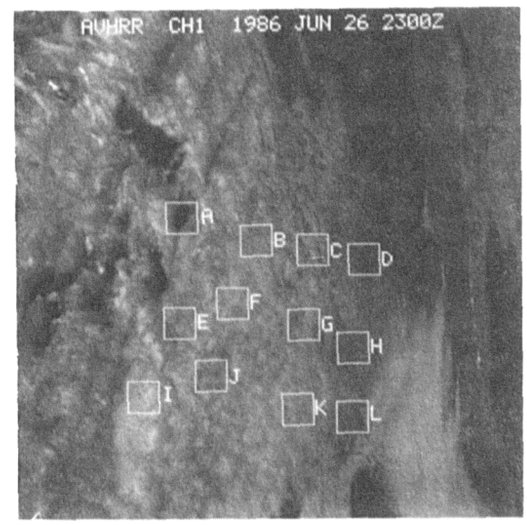

Figure 1. Satellite image of AVHRR Channel 1 data at 2300Z of 26 June 1986. Twelve (boxes A-L) target areas were chosen because of their different cloud conditions.

3. RESULTS

The preliminary results shown here used two different spatial resolutions: full and S8/16. The full resolution used all pixels within the area. The S8/16 resolution utilized only the first pixel within an area of 8 km (longitude) and 16 km (latitude). This latter resolution reduced the number of pixels of a target area to 1/128th of the full resolution for all satellite data used here except the GOES infrared channel which was reduced to 1/4th of its full resolution size. To find out whether the cloud fractions changes when the data resolution changes, we have listed out the current results

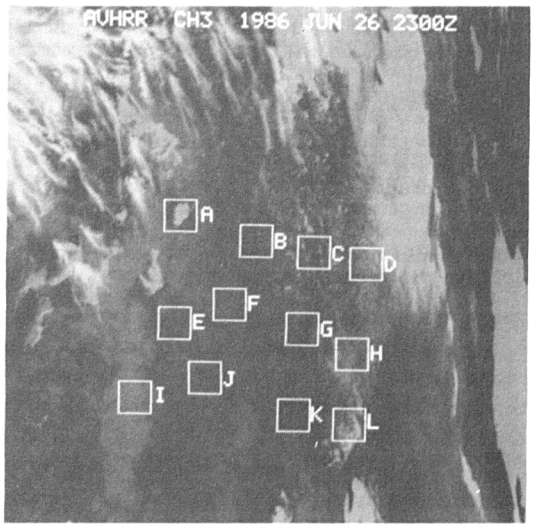

Figure 2. As in Figure 1, but for channel 3 of AVHRR data.

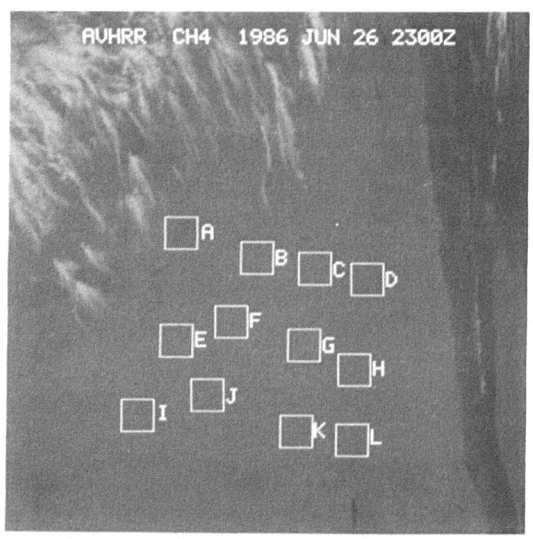

Figure 3. As in Figure 1, but for channel 4 of AVHRR data.

Figure 4. Visible channel image of GOES VISSR data, at the same time as in Figure 1.

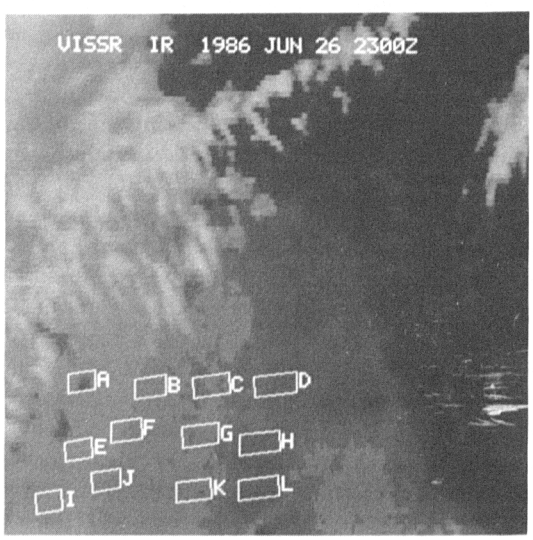

Figure 5. Infrared channel image of GOES VISSR data, at the same time as in Figure 1.

of our cloud alanysis in Table 1. Cloud fractions of five target areas (boxes A, C, D, H and L) are shown in Table 1. Seven other target areas were not shown because their cloud fractions were 100% despite different resolutions used. Thus, sampling or degradation has no effect on cloud fractions when the target areas were completely cloudy. However, whether the characteristic spatial scale from cloud brightness texture analysis would remain unchanged at different resolutions is not yet known. We are working on this subject using digital picture processing technique. The results will be presented at the conference.

To illustrate the effects of reduced resolution on cloud fraction, we have plotted the results of Table 1 in Figures 6 and 7. In Figure 6, the cloud fractions of full resolution samples were plotted against those of the S8/16 resolution without degradation. Ideally, if the sampling has no effects on cloud fraction, the points in Figure 6 would be scattered along the diagonal line of slope one. But the points in Figure 6, except the box A, scatter over a very wide range. This indicates the sampling does change the cloud fractions of target areas C, D, H and L. A visual check of the clouds within these four target areas (Figures 1 to 5) indicates the clouds within these areas were more convective than the other areas. The results of box A were almost unchanged at S8/16 resolution. Similar conclusions are true for Figure 7, which contrasts cloud fractions of full resolution data with those of degraded S8/16 resolution data. All these results point out that in the broken cloud fields often found between clear, near-shore coastal area and completely cloudy, oceanic area, sampling or degradation of satellite data would produce different cloud amount estimates from those generated using full resolution data. Therefore, as we build the marine statiform cloud climatology, different processing strategies have to be adopted to assure accurate cloud amount estimations. This agrees with the results of Hughes and Henderson-Sellers (1983) despite the fact that our data

Table 1. Results of subjective cloud analysis of various channels of satellite data used.

Channel	AVHRR-1		AVHRR-4		GOES-VIS		GOES-IR		GOES-V02	GOES-V04	GOES-V08	GOES-V16
Resolution	Full	S8/16	Full	S8/16	Full	S8/16	Full	S8/16	S8/16	S8/16	S8/16	S8/16
Target Area	Cloud Fractions (%)											
A	68.9	75.0	74.1	75.0	69.6	78.6	79.5	85.7	71.4	85.7	71.4	71.4
C	95.7	75.0	91.7	75.0	93.7	100.0	90.2	95.2	100.0	100.0	100.0	100.0
D	50.4	25.0	36.1	37.5	69.2	72.7	29.7	34.8	72.7	72.7	90.9	100.0
H	89.7	62.5	27.5	62.5	98.2	88.2	86.2	20.0	100.0	100.0	100.0	100.0
L	41.0	50.0	34.7	50.0	82.3	90.0	28.7	26.1	52.6	90.0	100.0	80.0

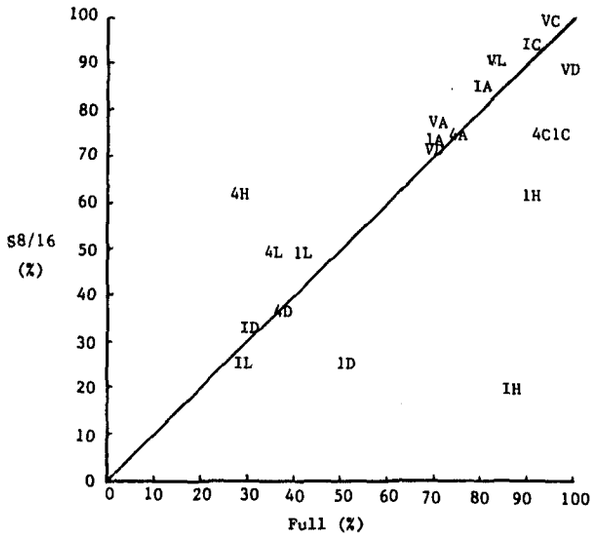

Figure 6. Scatter diagram of cloud fractions of full resolution data versus those of S8/16 undegraded data. Each point is lettered with channel name (1 for AVHRR-1, 4 for AVHRR-4, V for GOES visible, I for GOES infrared) and box name (from A to L).

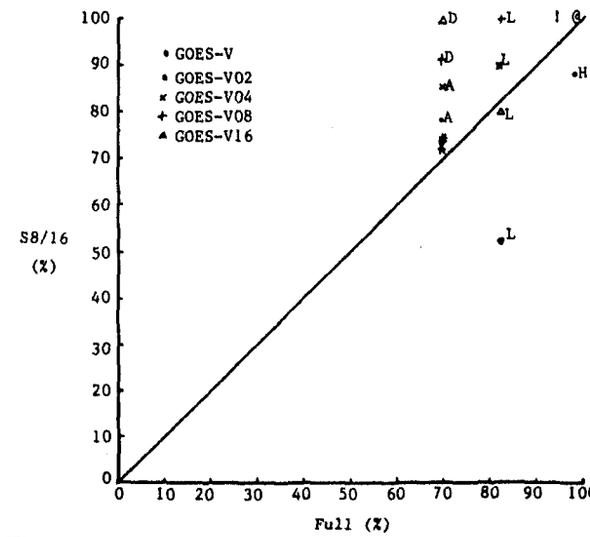

Figure 7. Scatter plot of full resolution GOES visible cloud fractions against degraded S8/16 cloud fractions. The degradation was done at 2 km (V02), 4 km (V04), 8 km (V08) and 16 km (V16). The following symbols represent overlapping points: #: VD, V02D, V04D; *: V02A, V08A, V16A; !: VC, V02C, V04C, V08C, V16C; ◎: V02H, V04H, V08H, V16H.

resolution (1 km) is much higher than theirs (46 km). We are currently testing an objective method to separate the uniform (either clear or cloudy with clear holes) zones from the discrete (convective) zones.

4. SUMMARY

Satellite data from both GOES-VISSR and NOAA-7 AVHRR sensors covering the same marine stratiform cloud were collected for this study. Twelve target areas were chosen for subjective cloud analysis. The results of cloud analysis using two resolutions were presented, and they indicated that cloud fraction varied with data resolution if the target area were located in the discrete zone. For target areas located in the uniform zone, the cloud fractions from reduced resolution data were consistent with those from full resolution data. For completely cloudy area in the uniform zone, whether the characteristic spatial scale of its brightness texture stays unchanged at reduced data resolution is currently under investigation. More results using resolution other than S8/16 will be presented at the conference.

5.0 ACKNOWLEDGEMENTS

We deeply appreciate Mrs. Loretta Wilson for her efforts in preparing this manuscript. We also thank Dr. Phil Durkee at the Naval Postgraduate School for providing us the NOAA-7 AVHRR data. This research was supported by the Office of Naval Research under Contract N00014-86-C-0459.

6.0 REFERENCES

Hughes, N.A. and A. Henderson-Sellers, 1983: The effect of spatial and temporal averaging on sampling strategies for cloud amount data. *Bull. Amer. Meteor. Soc.*, 64, No.3, 250–257.

Schiffer, R.A. and W.B. Rossow, 1983: The international satellite cloud climatology project (ISCCP): The first project of the world climate research programme. *Bull. Amer. Meteor. Soc.*, 64, No.7, 779-784.

Shih, Chi-Fan, G.G. Campbell and T.H. Vonder Haar, 1986: Effects of data resolution on satellite cloudiness estimation. Second Conference on Satellite Meteorology/Remote Sensing and Applications, May 13–16, 1986, Williamsburg, VA. American Meteorological Society.

ANALYSIS OF CLOUD DYNAMICS WITH MULTISPECTRAL TECHNIQUES

Andreas K. Goroch and James R. Clark

Naval Environmental Prediction Research Facility
Monterey, CA 93943-5006

1. INTRODUCTION

The purpose of this article is to describe a technique for simultaneous display of satellite data from the visible and infrared bands. This technique provides a visualization of different atmospheric features, such as fronts, convective areas, cirrus, and stratus occurrence, which are generally inferred from analysis of separate satellite pictures.

2. BACKGROUND

Conventional satellite imagery has been generally provided invisible and infrared bands. The visible band measures reflected properties of the earth surface and cloud structure above it, while the infrared band displays black body and emissivity characteristics of the surface. While the visible information provides information on the density of clouds, the infrared data provides information about the temperature of the cloud top. A combination of the two bands provides a visual indication of the cloud surface while the infrared makes possible the inference of cloud height.

Extensive work has been conducted on the development of three dimensional images of visual and infrared images. These have been very powerful, although requiring extensive hardware support and software development (Von der Haar, et al ., 1987). The procedure described here is an alternate method of displaying multiple frequency satellite data, suitable to less sophisticated image display hardware.

The first section outlines the method of displaying multiple images on a conventional false color image display (NEPRF, 1984). The following sections describe some results and potential advanced applications of these techniques.

3. METHOD

NEPRF uses a GENISCO GCT-3000 graphic display station driven by a Data General Eclipse S-250 minicomputer as its image display system (NEPRF, 1984). The system has 16 refresh memory planes with the capability of displaying either group of eight planes. The screen display is controlled by a video look-up table (VLT) of 256 entries capable of displaying 4096 colors. The gray shade representation is limited to 16 values.

The usual method of display is to load one image into an 8 bit byte. Since only 16 gray shades are displayed, it is possible to display two images simultaneously. This is accomplished by loading two images into one display byte and changing the VLT accordingly.

Prior to loading the two images into a byte, the pixel values may be transformed with a scale and bias to provide a better dynamic range in defining desired features. Our normal procedure is to define the VLT such that the four lower planes drive the green gun, the four upper planes drive the red gun and the blue gun is used to display values above or below some threshold. The choice of color for each image is, of course, arbitrary.

Table 1 shows the scale and bias for visible and infrared GOES VISSR data normally used for display.

Table 1. Typical Image display parameterization.

	Scale	Bias
Visible	0.4	-10
IR	0.63	-50

4. RESULTS

This technique differentiates between cloud structures according to elevation and liquid water content. The technique is useful in the following situations:

Differentiation of Cirrus and Stratus

The height difference between cirrus and stratus is accentuated using color imagery. A frontal region is displayed with cirrus (in red on the SPADS system) ahead of the front, and stratus (in green) in the cold region behind the front.

Identification of Convection Regions

The depth of a convective region is shown in the high reflectivity of visible wavelengths and emissivity of the cloud tops at the infrared wavelengths. The resulting image accentuates the regions in which convective features dominate.

5. CONCLUSIONS

The use of simultaneous display of visible and infrared imagery is a useful technique for the display of three dimensional atmospheric structure. The use of color provides sharp delineation of stratus, cirrus and convective cloud occurrence.

Future Applications

The simultaneous use of images in different spectral regions can be applied to other frequencies in addition to the more or less conventional visible and infrared wavelengths. Initial development has started in using water vapor imager (using the 6.7 micrometer band). It is anticipated that information from the new microwave sensors will be integrated with conventional imagery as well.

6. REFERENCES

Naval Environmental Prediction Research Facility, 1984. Satellite Data Processing and Display System (SPADS) Users Guide, NEPRF Document No. W0523UM02.

Von der Haar, T.H., A.C. Meade, R.J. Craig, and D.L. Reinke, 1987. Four Dimensional Imaging for Meteorological Applications. Accepted for publication in J. Atmos. Ocean Technol.

EVALUATION OF 3.7 μm SPLIT WINDOWS FOR ESTIMATING SURFACE TEMPERATURE

David S. Crosby*
Larry M. McMillin
John C. Alishouse

National Oceanic and Atmospheric Administration
National Environmental Satellite, Data, and Information Service
Satellite Research Laboratory
Washington, D.C. 20233
*Permanent affiliation: The American University, Washington, D.C.

1. INTRODUCTION

Radiometers carried on satellites have been used to provide global estimates of sea surface temperature since 1970. The current operational technique uses a split window in the 11 μm region and a single window in the 3.7 μm region. This technique has been applied to a wide range of conditions (McClain et al. 1985) and is based on an assumption which is valid for transmissivities which are close to one (McMillin and Crosby 1984). When viewing angles are significantly different from nadir, the transmissivities of the 11 μm pair drop to less than 0.7 in moist tropical atmospheres. Because of this difficulty with the 11 μm window, a split window in the 3.7 μm region has been suggested and will be available on future instruments. In this paper we will use simulated data to evaluate the potential gains available from using a short wave split window pair.

2. THEORY

For a general discussion of the multiple window sea surface temperature technique see McMillin and Crosby (1984, 1985). The split window technique requires that τ, the atmospheric transmittance, be close to one. In the 11 μm region transmittances considerably less than 0.7 have been observed in moist tropical atmospheres at viewing angles far from nadir. This occurs because the primary absorber in this window is water vapor. It is also possible to generate a split window in the 3.7 μm region. Compared to the 11 μm windows, the 3.7 μm windows have more absorption due to the fixed gases but less absorption due to water vapor. This gives the 3.7 μm window an advantage in the tropics, namely a higher overall transmittance. A possible disadvantage due to the additional absorption by fixed gases is ameliorated by the fact that the temperature is relatively constant in the tropics and the absorption due to fixed gases tends to take the form of a constant. Hence it is easier to correct. A disadvantage of the short wave windows is that they are sensitive to reflected sunlight.

3. SIGNAL TO NOISE CONSIDERATIONS

One of the parameters required for an evaluation is the instrument noise. Implementation of the short wavelength split window channels requires analysis to insure that adequate signal-to-noise ratios are obtained and that the required components are within the "state-of-the-art". One proposed channel pair is given in Table 1.

The gap between the halfpower points of 2551 cm^{-1} and 2611 cm^{-1} provides room for a dicroic beamsplitter and also avoids a weak atmospheric absorption band of nitrous oxide (N_2O). To estimate signal-to-noise ratios (actually NEΔT's) that might be achieved, results have been extrapolated from those measured for a channel in this spectral region on the Advanced Very High Resolution Radiometer (AVHRR). The AVHRR channel has its center wavelength at 3.7 μm (2703 cm^{-1}) and its halfpower points at 3.56 μm (2809 cm^{-1}) and 3.95 μm (2532 cm^{-1}). For this channel noise equivalent temperature differences (NEΔT's) as small as 0.044 K at 300 K have been measured. This NEΔT was then converted to noise equivalent radiance (NEΔN) and degraded to allow for the smaller spectral bandwidth and reduced transmittance of the optical train. It was assumed that the AVHRR's NEΔN would increase as the ratio of the halfpower bandwidths [(277/151) and (277/112) respectively] and that an extra optical element (a dicroic beamsplitter) would be required. It was assumed that the reflectivity for channel 1 was 0.8 and the transmissivity for channel 2 was also 0.8. NEΔT's were then computed for the new channels at 300 K, the usually specified value, and at 285 K, a more typical value encountered in SST determinations. These results are given in Table 2.

The above NEΔT's were computed for the AVHRR telescope diameter, angular field of view, and a single detector. The AVHRR telescope has a primary mirror of 20 cm diameter, an angular field of view of 1.3 milliradians (1.1 km at nadir), and a single InSb detector. The NEΔT's given in Table 2 could be reduced by increasing the size of the primary mirror, increasing the angular field of view, and the use of multiple detectors. A four element array would provide a factor of 2 increase in signal-to-noise ratio. Increasing the angular field of view will

increase the signal-to-noise ratio, but will also increase the size of the field of view and hence decrease the spatial resolution. Increasing the diameter of the primary mirror will also increase the signal-to-noise ratio, but also increases the volume and weight of the radiometer.

For most of the simulations the random noise in the 11 μm window has been assigned a standard deviation of .125 degrees. Given the results from the AVHRR this value may be too high (McClain et al. 1984). In any case the instrument noise is just a lower bound on the measurement error. The noise may be reduced by averaging.

4. Simulated Data Set

Since no real data are presently available, in order to test, evaluate and compare the 3.7 μm window pairs it was necessary to produce a simulated data set which in turn required a set of atmospheric temperature and humidity profiles. The data set used was the 1200 atmospheres described in Smith et al. 1974. This consists of a geographically and seasonally diverse collection of atmospheres. They are divided into three classes: 400 polar; 400 temperate; 400 tropical. An atmospheric transmittance model (Weinreb and Hill, 1980) was used to generate simulated upwelling radiances which were converted to brightness temperatures. All the channels except the channel centered at 2518.14 cm^{-1} were simulated with the filter shape of the HIRS (High Resolution Infrared Radiation Sounder) channel 19 shifted to the specified center (Schwalb 1978). For the 2518.14 cm^{-1} channel, the filter shape for the HIRS channel 18 was used. The half-widths of these channels are 100 cm^{-1} and 35 cm^{-1} respectively.

To each of the computed brightness temperatures a pseudo-random noise was added. These were normal random variables generated by the SAS package (SAS 1982). The standard deviation of the noise used for most of the simulations were 0.1 and 0.125 in the shortwave and longwave regions respectively. These numbers were compromises arrived at using the analyses of section 3 and the experience with the AVHRR.

5. Results

To evaluate the possible increase in accuracy using windows in the 3.7 μm region, the region was examined for possible split windows. Four pairs of channels were picked: (2518.14-2667.8 cm^{-1}, 2487.14-2529.15 cm^{-1}, 2563.13-2670.52 cm^{-1}, 2813.79-2755.16 cm^{-1}). Except for the channel centered at 2518.44 cm^{-1}, which has a half-width of 35 cm^{-1}, all of these channels have a half-width of 100 cm^{-1}. In each pair, the first is the more absorbing. Pairs were picked to provide different values of absorption at similar wavenumbers. Even though the channels were picked in pairs, each of the four low absorbing channels were paired with the four more absorbing channels, resulting in 16 possible combinations. The first pair consists of the current HIRS channels 18 and 19. Some of the pairs may not be separated far enough in wavenumber to be practical. Simulated brightness temperatures were produced using the technique described in the previous section. The brightness temperatures were used to predict surface temperature. Standard multiple linear regression was used to define the parameters of the relations;

$$T_s = b_0 + b_1*T_1 + b_2*T_2 \quad (1)$$

or

$$T_s = b_0 + b_1*T_1 + b_2*T_2 + b_3*T_3. \quad (2)$$

In equations 1 and 2, T_s is the surface temperature and T_1, T_2, and T_3 are the brightness temperatures in the three windows. RMS errors in the predicted surface temperature were computed for a polar, a midlatitude, a tropical and a global data set. Since T_s, T_1, T_2, and T_3 are approximately equal, it is to be expected that (b_1+b_2) or $(b_1+b_2+b_3)$ should be approximately one. If there is no split window effect then error considerations suggest that $b_1>0$, $b_2>0$ and $b_3>0$. That is, the estimate of T_s is a weighted average of T_1 and T_2 or T_1, T_2 and T_3. (See McMillin and Crosby 1984, 1985). Table 3 gives RMS errors (RMSE) for various possible split windows in the 3.7 μm region. The noise was assumed to have a standard deviation of 0.1 degrees.

Because of the transparency of this window region, all the pairs gave results with an RMSE of less than 0.5. The best results, in a general sense, were produced by the pair 2487.14 and 2529.15, which results in an RMSE of 0.23 for a global sample. The best pair for the tropics is 2813.79 and 2529.15, which gives a RMSE of 0.146. It is worth noting that the best results were obtained when the relationship of b_1 and b_2 is that of a true split window.

The RMSE values for the short wave windows are less than the values of approximately 0.4 K RMSE obtained from an equivalent simulation for the 11 μm window. The noise assumed for the 11 μm window had a standard deviation of 0.125. Reducing the standard deviation of the noise to 0.1 would have slightly reduced the RMSE of the estimated surface temperature. However, instrument noise does differ in the two spectral regions.

Table 4 gives RMSE results for various combinations of 3.7 μm and 11 μm windows. These results show that the 3.7 μm windows give the smallest RMSE's for all regions with the largest difference occurring in the tropics. A probable reason for this is the that there is a much greater absorption due to water vapor in the 11 μm window. This is shown in table 5 which gives the actual regression coefficients for various combinations of the window channels. The windows used where those centered at 907.44, 832.69 and 2670.52 cm^{-1}. The noise factors used were 0.125, 0.125, and 0.10 respectively. It is seen that the coefficients for the 11 μm pair are much larger than those which include the 3.7 μm window. The larger coefficients multiply the measurement errors by larger factors. Table 4 shows that the results obtained by supplementing the 11 μm pair with a single 3.7 μm window are essentially as good as those obtained with the 3.7 μm split window. It also shows that the combinations of one 3.7 μm window with one 11 μm window gives good results.

Even though total atmospheric absorption is larger in the tropics than in the other regions, the 3.7 μm split window accuracies are better in the tropics than in other regions. This is inconsistent with both the simulated and actual results with the AVHRR in the 11 μm region. However, much of the absorption at 3.7 μm is due to the continuum of nitrogen, a fixed gas. Hence,

the variability of the absorption at 3.7 μm depends more on the variability of the temperature profile and less on the changes in water vapor. In this wavelength region, the primary absorption is due to fixed gases and, as a result, the uniformity of the temperature in the tropics becomes a major factor.

6. Conclusions

The results of this study show that the combination of the two split windows provides a complementary set of measurements which serve the intended purpose well. The 11 μm pair provides accurate sea surface temperatures in polar and mid-latitude regions under all lighting conditions. However, the accuracy of this pair is significantly diminished at the high atmospheric absorption frequently experienced in tropical areas. In contrast, while the 3.7 μm pair can experience large errors due to reflection in sunlit areas, it provides the best results in the tropics, thus compensating for the major limitation of the 11 μm pair. The combination of the two pairs can provide accurate estimates of sea surface temperature at all latitudes at night and accurate estimates of the sea surface temperature at high latitudes with partial coverage in the tropics under daylight conditions. Although a single 3.7 μm channel combined with the 11 μm pairs gives almost as good results as the 3.7 μm pair, the shortwave and longwave combination is more subject to errors due to such factors as volcanic aerosols, and is not as effective in correcting for cloud contamination because of the large differences in the relationship between temperatures and radiances in the widely separated spectral regions. It is also subject to larger errors when obtaining surface temperature over areas such a land where the surface temperature varies over a single field of view. None of these effects have been considered in this simulation.

7. References

McClain, E.P., W.G. Pichel, and C.C. Walton, 1985: Comparative performance of AVHRR-based multichannel sea surface temperatures, J. Geophys. Res., 90, 11,587-11,610.

McMillin, L.M. and D.S. Crosby, 1984: Theory and validation of the multiple window sea surface temperature technique. J. Geophys. Res., 89, 3655-3661.

McMillin, L.M. and D.S. Crosby, 1984: Some physical interpretations of statistically derived coefficients for split-window corrections to satellite-derived sea surface temperatures. Quart. J. R. Met. Soc., 111, 867-871.

SAS, 1982: SAS User's Guide: Statistics. SAS Institute, Gary, North Carolina, 584 pp.

Schwalb, A., 1978: The TIROS-N/NOAA A-G satellite series, NOAA Tech. Memo. NESS 95, 75 pp.

Smith, W.L. et al., 1974: NIMBUS-5 sounder data processing system, Part 1 Measurement characteristics and data reduction procedures, NOAA Tech. Memo. NESS 57, 99 pp.

Weinreb, M.P. and M.L. Hill, 1980: Calculations of atmospheric radiances and brightness temperatures in infrared window channels of satellite radiameters, NOAA Tech. Report NESS 80, 40 pp.

Table 1. Proposed 3.7 μm window pair.

Channel	Center frequency (cm^{-1})	Halfpower points (cm^{-1})
1	2688 (3.72 μm)	2611-2762 (3.62-3.83 μm)
2	2494 (4.01 μm)	2439-2551 (3.92-4.10 μm)

Table 2. Estimated NEΔT's for proposed 3.7 μm window pair.

NEΔT Channel	@ 300 K	@ 285 K
1	.12	.20
2	.08	.15

Table 3. RMSE for surface temperature for several combinations of short-wave split windows.

Central frequency	Latitude			
	all	polar	mid lat	tropical
2518.14				
2667.8	*.278	*.227	*.281	.158
2529.15	*.269	*.302	*.273	*.160
2670.52	*.280	*.234	*.285	.157
2755.16	*.281	*.238	*.284	.158
2487.14				
2667.8	*.341	*.240	*.326	.193
2529.15	.233	.239	.217	*.170
2670.52	*.348	*.252	*.335	.191
2755.16	*.346	*.247	*.330	.192
2563.13				
2667.8	*.302	*.232	*.296	.185
2529.15	.270	.302	.270	*.177
2670.52	*.304	*.240	*.301	.182
2755.16	*.304	*.239	*.299	.189
2813.79				
2667.8	.307	.239	.276	.330
2529.15	*.269	*.254	*.272	.146
2670.52	.331	.254	.297	.361
2755.16	.313	.245	.280	.336

Values denoted by an "*" indicate that b_1 and b_2 were both positive and did not form a relationship present in a true split window.

Table 4. RMSE's of surface temperature for several combinations of 3.7 μm and 11 μm windows.

Central Frequencies	Latitude				
	all	polar	mid lat	tropical	noise
2487,2529	.23	.24	.22	.17	.10, .10
2670,907,832	.21	.22	.22	.18	.10, .125, .125
2670,907,832	.20	.20	.20	.17	.10, .10, .10
907,832	.49	.30	.42	.54	.10, .10
907,832	.59	.34	.50	.64	.125, .125
2670,907	.27	.25	.28	.23	.10, .125
2670,832	.22	.23	.22	.18	.10, .125

Table 5. Regression coefficients for various combinations of long and short wave channels.

Central Frequencies	Latitude: all	polar	mid lat	tropical
907.44	1.25	1.02	1.23	1.30
832.69	.40	.53	.50	.26
2670.52	-.63	-.53	-.73	-.55
907.44	3.27	1.68	2.78	3.55
832.69	-2.27	-.66	-1.77	-2.56
2670.52	1.53	1.08	1.55	1.55
907.44	-.51	-.05	-.52	-.52
2670.52	1.39	1.27	1.44	1.39
832.69	-.31	-.25	-.42	-.37

EOF ANALYSIS OF AVHRR AND CZCS IMAGERY

Gary S.E. Lagerloef

Science Applications International Corporation
13400 Northup Way NE, Suite 36B
Bellevue, Wa. 98005

1. INTRODUCTION

Empirical orthogonal function (EOF) analysis, as conventionally applied to oceanographic and meteorological data sets, is used to decompose space-time distributed data into modes ranked by their temporal variance. In the analysis of a set of AVHRR sea surface temperature or CZCS ocean color images, one might be interested in studying the variance associated with frontal, eddy and jet structures which are often clearly evident. However, unless these features are associated with strong temporal variability, they will not be manifested in the most energetic few modes in an EOF decomposition of temporal variance. Because the data are distributed over space and time, EOF modes can be computed ranked by their spatial variance as well as by their temporal variance. Persistent spatial patterns with the strongest horizontal gradients, such as fronts or eddies, will then be evident in the dominant modes. In such an analysis, the space and time axes are reversed relative to the EOF decomposition of temporal variance; the amplitude functions become spatial image patterns, and the eigenvectors become dimensionless time series describing the time histories of the modes.

In this paper, spatial variance EOF decomposition is demonstrated and compared with temporal variance ranked modes. The analyses are applied to the central California shelf and the Santa Barbara Channel region off southern California (Figure 1). In these regions offshore filaments, fronts and eddies are commonly evident in AVHRR and CZCS imagery, and these mesoscale features are the subject of on-going research in the "Coastal Transition Zone".

2. EOF DECOMPOSITION

The key difference between spatially and temporally ranked EOF modes lies in how the data are operated on prior to computing the EOF decomposition. If the time means are first subtracted from each of the timeseries, the resultant mode eigenvalues sum the temporal variance. Conversely, if all data sampled at the same time have the spatial average removed, the modes decompose the spatial variance. Subsequently, the analyses are generic and involve the eigenvalue/eigenvector solution to the smaller of the two possible covariance matrices which can be derived from the adjusted data set (Von Storch and Hannoschock, 1984; Moore, 1974; Hirose and Kutzbach, 1969). This is particularly useful to analyzing data sets considerably more densely sampled in either space or time, relative to the other dimension, such as the satellite image data studied here. An extensive description of the analysis for temporally and spatially ranked modes is given by Lagerloef and Bernstein (1987).

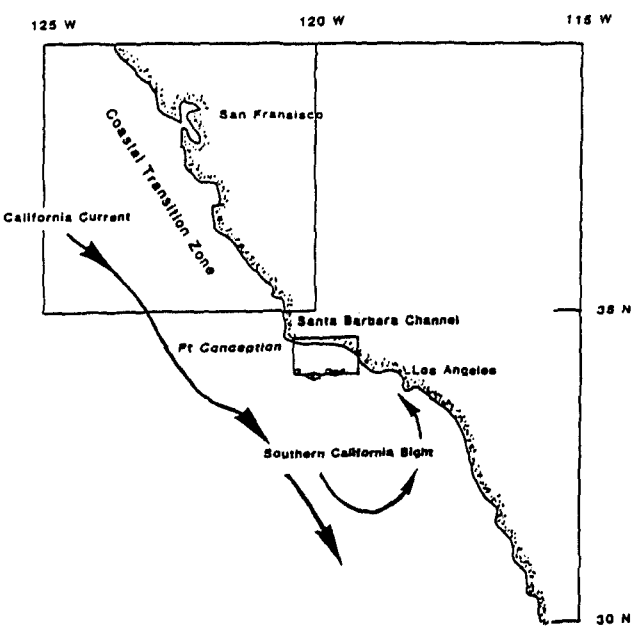

Figure 1: The southern and central California coastal region, showing the location of the Santa Barbara Channel study area, the central California coastal transition zone study area, and a schematic of the California Current and cyclonic circulation of the Southern California Bight.

3. EOF ANALYSES OF AVHRR AND CZCS IMAGES

Two study areas discussed here are the Santa Barbara Channel and the central California coastal transition zone. The Santa Barbara Channel is a semi-enclosed coastal oceanic basin along the south-central California coast (Figure 1), about 100 km long by about 50 km wide, and with a central basin depth of ~500 m. The channel appears to be in a transition region between two coastal water masses. Warmer waters from the Southern California Bight dominate the channel inflow through the eastern boundary and extend into the basin along the northern perimeter. The western channel is influenced by California Current and upwelling waters from the west, with cool eastward inflow along the southern channel perimeter (Lagerloef and Bernstein, 1987; Brink and Muench, 1986). In the channel interior, there is evidence of eddies on the scale of one-half to one-third the channel axis length, particularly in the western portion. These eddies are commonly evident through casual inspection of any large set of AVHRR images of the channel region. This analysis used thirty six cloud-free AVHRR images, sampled an average of every 10 days between January 1984 and January 1985, with a 50x100 km section covering Santa Barbara Channel (see box in Figure 1) extracted from each image, and land areas masked.

The central California shelf study area is dominated by the California Current system, characterized by spring-summer upwelling and, in winter, northward near shore flow commonly referred to as the Davidson Current (Hickey, 1979). During spring and summer cross-shelf filaments of coastal upwelling waters are frequently evident in satellite images, often extending more than 100 km offshore (Bernstein, et al., 1977). At sea measurements have shown these to be associated with energetic cross-shelf current jets (>50 cms) and strong temperature fronts (Flament, et al., 1985). This analysis utilized CZCS data from 1981, in the region 35°N-40°N and 120°W-125°W (Figure 1). Nine composite images were formed from 4-6 week segments in the data to remove contamination from clouds.

3.1 Santa Barbara Channel

Results for the first two modes of both the spatial and temporal variance EOF analyses for Santa Barbara Channel are shown in Figures 2 and 3. It is clear that the spatial and temporal variance approaches yield distinctly different results. The first spatial variance mode (60% of the spatial variance) in Figure 2a shows a distinct NW-SE front in the western half of the channel which separates two water masses dominating the channel circulation. Along channel temperature differences are typically ~1-3°C (CALCOFI, 1982). This pattern closely resembles the mean pattern formed by the time average at each grid point (not shown), suggesting that the dominant temperature pattern represented by this mode is a persistent feature. In contrast, the first temporal variance mode (92% of the temporal variance) has very little spatial structure (Figure 2b).

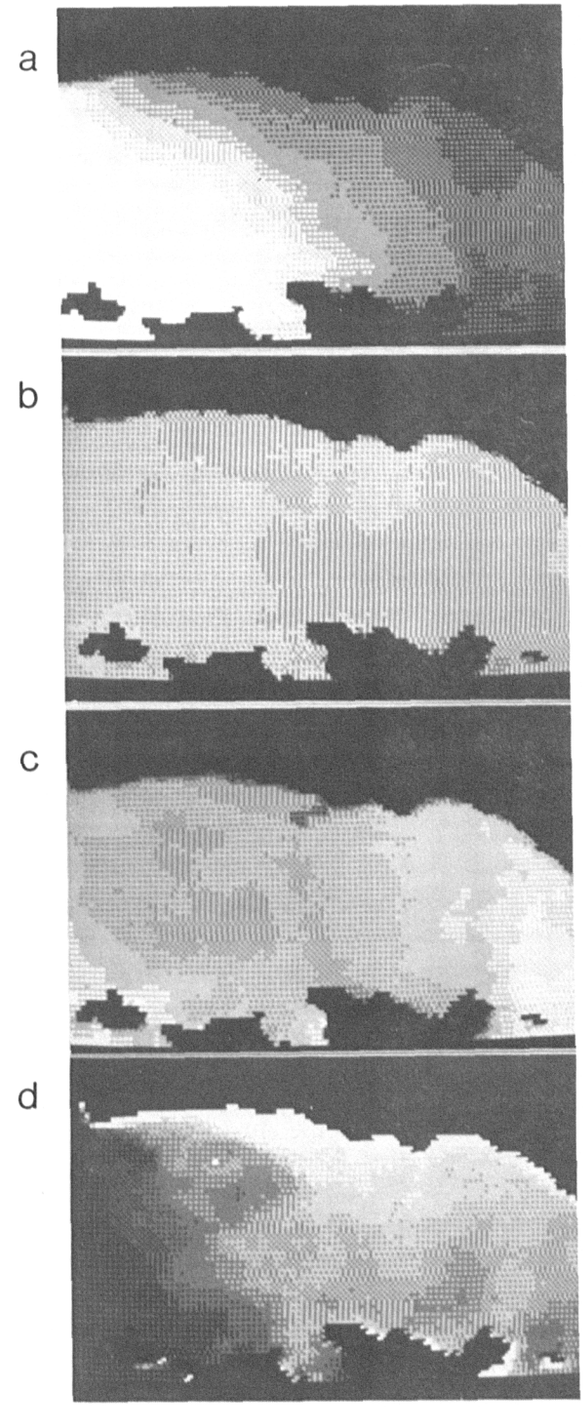

Figure 2: Santa Barbara Channel AVHRR EOF spatial patterns: (a) First spatial variance mode showing the persistent (~2°C) temperature front in the western channel, (b) first temporal variance mode showing little spatial structure, or a basin-wide process, (c) second spatial variance mode resembling an eddy like structure, and (d) second temporal variance mode.

The time variability of these modes is shown in Figures 3a and 3b. The first spatial mode time series leads the first temporal variance mode by ~90°, so that two distinct, uncoupled, seasonal signals are found with these analyses. The first spatial variance mode is seen to increase during the summer months and taper off again during the winter, indicating a summer strengthening of the along-channel temperature gradient and front depicted in Figure 2a. This is consistent with the along-channel temperature difference between moored instruments in the eastern and western channel boundaries and with flow through the eastern channel boundary (Figure 4). The first temporal variance mode (Figure 3b), on the other hand, is consistent with the annual cooling and warming cycle over the region; minimum temperatures in spring, maximum in fall (CALCOFI, 1982). The weak spatial structure of the mode (Figure 2b) indicates that this is a basin-wide signal. A similar first mode result, with a spatially uniform, low frequency temperature variation, was found by Kelly (1986) in a temporal variance EOF analysis of AVHRR images over the northern California shelf.

The image patterns for the second modes of spatial variance and temporal variance are shown in Figures 2c and 2d. The second spatial variance mode (7.7% of the variance) depicts an eddy-like, circular form in the western channel, consistent with the mean cyclonic flow (Lagerloef and Bernstein, 1987). Eddies have been observed in the west central portion of the channel and this mode could represent some of the associated variability. It likely does not represent a permanent warm or cold core eddy mode, but instead may suggest the trapping or entrainment of either warm or cold water mass intrusions in the west-central part of the channel, associated with the eddies and the mean cyclonic flow pattern. For this reason, the eigenvector time series of this mode changes sign frequently over the temporal record of images (Figure 3c). The second temporal variance mode (Figure 2d) has considerably more spatial structure than the first, but accounts for only 2.5% of the temporal variance. The time series of this mode (Figure 3d) shows weak variability with no distinct periodicity, and it is doubtful that this mode has an important physical interpretation.

3.2 California Coastal Transition Region

The analyses of CZCS images of the Central California coastal transition zone are shown in Figures 5 and 6. The first spatial mode (44% spatial variance) again shows a persistent front (Figure 5a), in this case a meandering color front associated with the California Current. This has implications on the persistent structure of the California Current in the region. The mode also strongly resembles the mean color field (not shown). Zones of off shore extending coastal waters adjacent to Pt. Arena and Monterey, indicate that this mode captures much of the structure associated with the prominent cross shelf filaments or jets in those areas. The time series of this mode (Figure 6a) resembles the above Santa Barbara Channel results, with a seasonal signal peaking in summer.

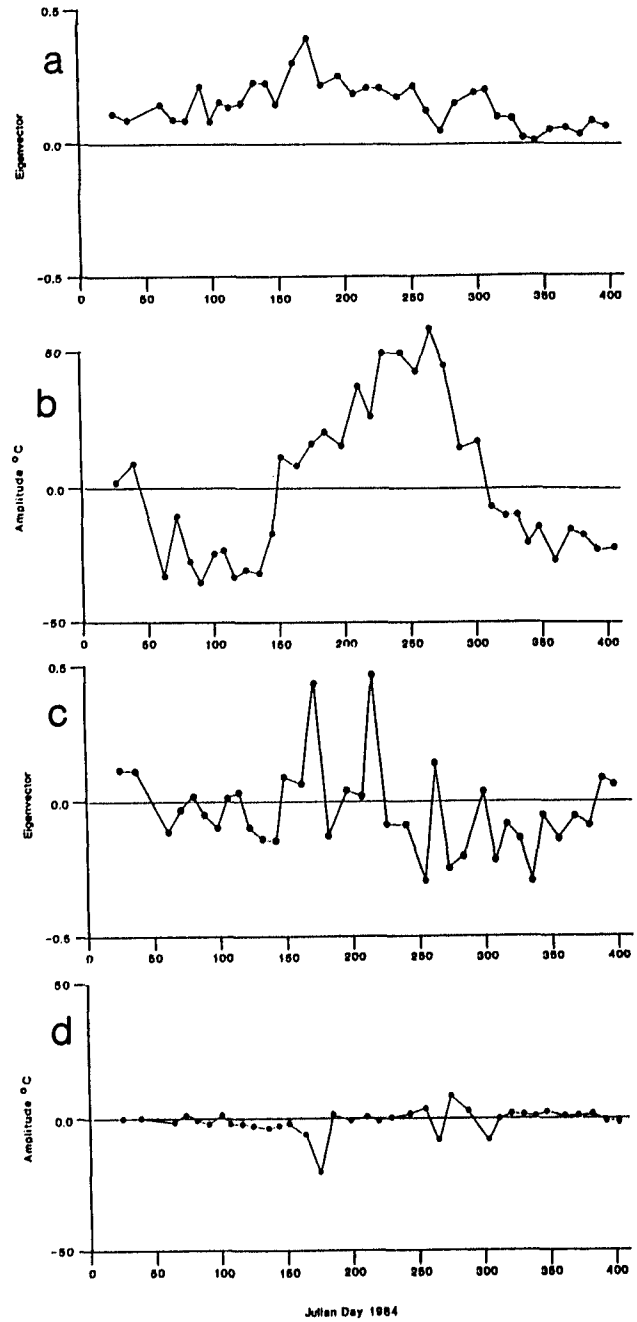

Figure 3: Santa Barbara Channel AVHRR EOF time series: (a) First spatial variance mode showing a seasonal modulation of the frontal gradient which peaked in early summer, (b) first temporal variance mode indicating seasonal basin-wide cooling and warming which peaked in early fall, (c) second spatial variance mode, and (d) second temporal variance mode.

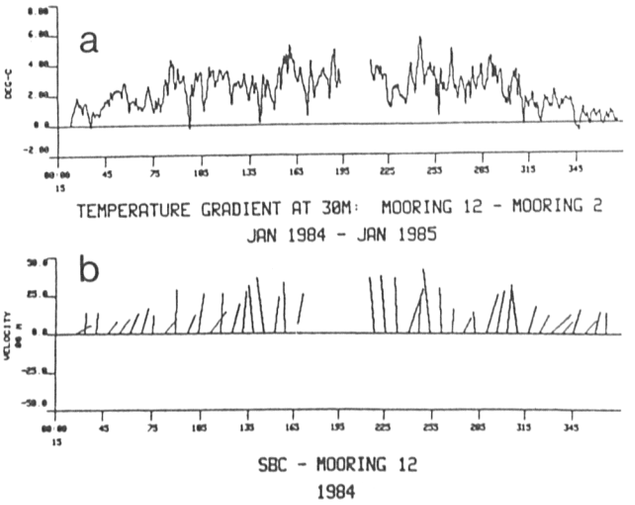

Figure 4: (a) The Santa Barbara Channel along-axis temperature gradient time series, measured from the moored instruments, was stronger in summer than in winter. (b) Flow through the eastern boundary was also somewhat stronger in summer, indicating a response to a strengthening of the steric pressure gradient associated with the stronger temperature gradients. This agrees well with the first spatial variance mode (Figure 3a).

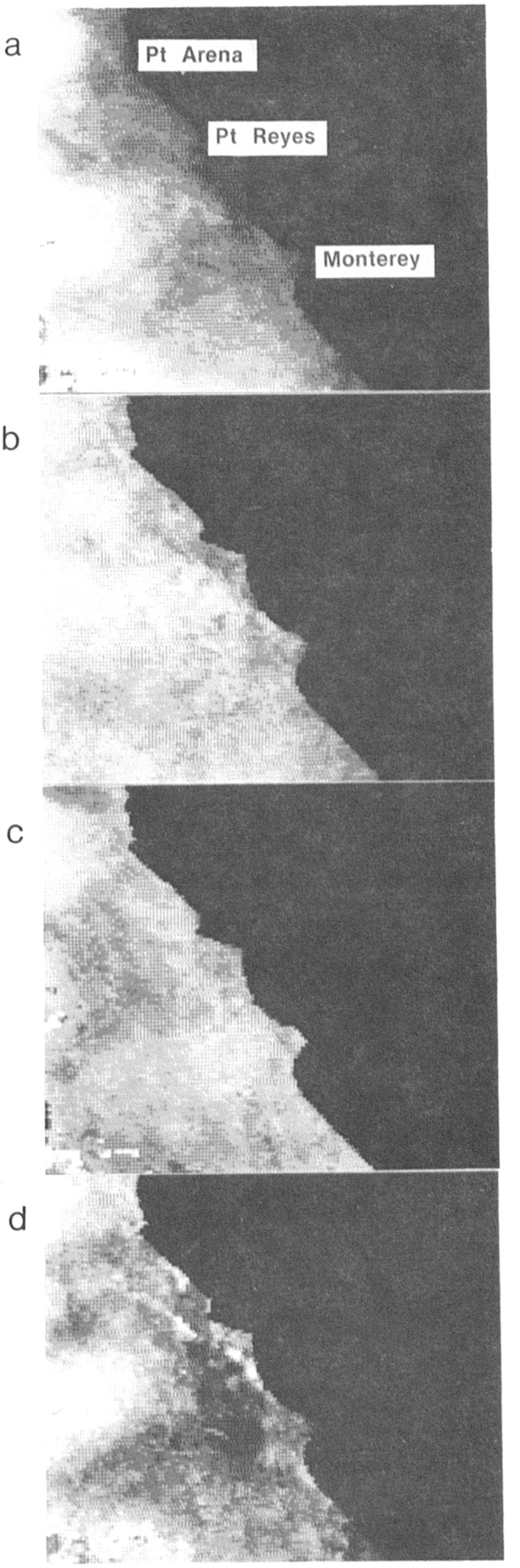

Figure 5: (Facing column) Coastal transition zone CZCS EOF spatial patterns: (a) First spatial variance mode showing a persistent meandering color front in the California Current, (b) first temporal variance mode showing weak spatial structure, but indicative of coastal upwelling, (c) second spatial variance mode, and (d) second temporal variance mode which resembles the first spatial variance mode (a).

The first temporal mode (52% temporal variance) also resembles the Santa Barbara results in having weak spatial structure (Figure 5b). However, the time series of the mode (Figure 6b) lacks the distinct seasonal cycle seen in the Santa Barbara analysis. Instead, there is a sharp rise in spring, followed by a sharp drop, then another broad peak in summer, before declining in the fall. Given that the CZCS measures phytoplankton plant pigment, this scenario is consistent with an interrupted upwelling cycle. Sequential upwelling and relaxation episodes have been observed in the vicinity of Pt. Conception during 1983 (Atkinson, et al., 1986).

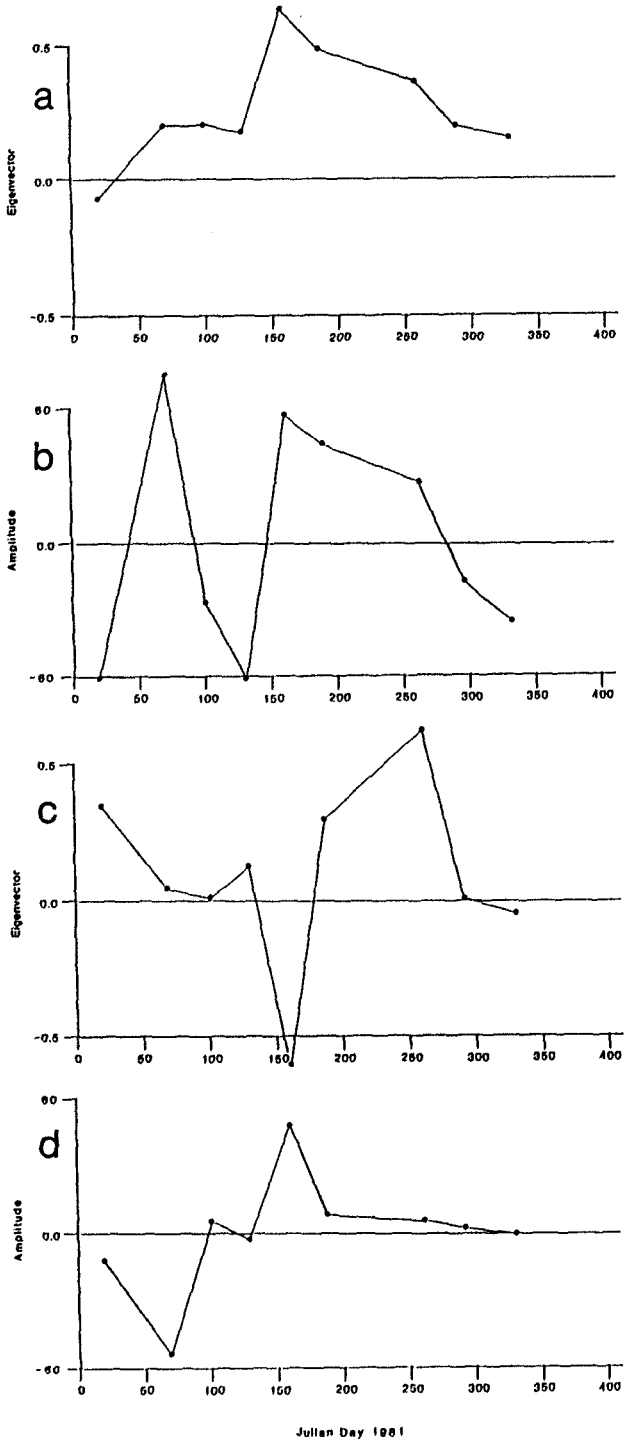

Figure 6: Coastal transition zone CZCS EOF time series: (a) First spatial variance mode showing a seasonal modulation of the frontal gradient which peaked in early summer, (b) first temporal variance mode indicating episodic upwelling as reflected in the CZCS measured phytoplankton pigment, (c) second spatial variance mode, and (d) second temporal variance mode.

The second spatial variance mode (13.6% spatial variance) indicates a patchy region of high pigment waters extending offshore southwest from Pts. Arena and Reyes (Figure 5c), possibly accounting for much of the cross shelf filament structure in this region not accounted for in the first mode. The time series of this mode, however, does not offer a straightforward interpretation (Figure 6c). The spatial pattern (Figure 5d) of the second temporal variance mode (13.2% temporal variance) closely resembles the first spatial variance mode. The time series for this mode (Figure 6d) also reflects a seasonal variation, though not well correlated with the first spatial mode early in the year. Nevertheless, it appears, in this case, that the first spatial mode and second temporal mode captured the same basic patterns in the space-time variability of the CZCS imagery along the central California coastal transition region.

4. SUMMARY

The EOF method used here to extract the dominant spatial variance modes can be very useful for studying quasi-permanent patterns such as fronts, eddies or cross shelf jets often found in satellite image data. Used in conjunction with more traditional temporal variance EOF analyses, considerably more useful information is gained on the modes of spatial and temporal variability, than by use of either technique alone. The analysis and interpretation of satellite remote sensing and other spatially dense oceanographic data will become increasingly more important as future global measurement programs progress. EOFs are a tool which can decompose either the dominant temporal or the dominant spatial modes of a data matrix, giving the investigator considerable versatility depending on what aspects of the data variability are of interest.

Acknowledgements: AVHRR and in situ data presented here were obtained as part of circulation and modelling studies of the Santa Barbara Channel and Central California Shelf sponsored by the Minerals and Management Service, U.S. Department of Interior. CZCS data was furnished by the Jet Propulsion Laboratory West Coast Time Series. The EOF analysis development and application to this data set was supported by the Office of Naval Research under contract number N00014-87-M-0057, and the Science Applications International Corporation Independent Research and Development program.

5. REFERENCES

Atkinson, L.P., K.H. Brink, R.E. Davis, B.H. Jones, T. Paluszkiewicz and D.W. Stuart, 1986: Mesoscale hydrographic Variability in the vicinity of Points Conception and Arguello during April-May 1983: The OPUS 1983 experiment. J. Geophys. Res., 91, 12,899-12,918.

Bernstein, R.L., L. Breaker, and R. Whritner, 1977: California Current eddy formation: ship, air and satellite results. Science, 195, 353-359.

Brink, K.H. and R.D. Muench, 1986: Circulation in the Point Conception-Santa Barbara region. J. Geophys. Res., 91, 877-895.

CALCOFI, 1982: Atlas No. 30. Marine Life Research Program, Scripps Institution of Oceanography, La Jolla, Ca.

Flament, P., L. Armi and L. Washburn, 1985: The evolving structure of an upwelling filament. J. Geophys. Res., 90, 11,765-11,778.

Hickey, B.M., 1979: The California Current System--hypotheses and facts. Prog. Oceanogr., 8, 191-279.

Hirose, M. and J.E. Kutzback, 1969: An alternate method for eigenvector computations. J. Appl. Met, 6, 701.

Kelly, K.A., 1985: The influence of winds and topography on the sea surface temperature patterns over the northern California slope. J. Geophys. Res., 90, 11,783-11,798.

Lagerloef, G.S.E. and R.L. Bernstein, 1987: EOF analysis of AVHRR surface temperature patterns in Santa Barbara Channel. Submitted to J. Geophys. Res.

Moore, D., 1974: Empirical orthogonal functions--a non-statistical view. MODE Hot Line News, 67, 1-6.

Simpson, J.J., C.J. Koblinsky, L.R. Haury and T.D. Dickey, 1984: An offshore eddy in the California Current System. Prog. Ocenogr., 13, 1-111.

Von Storch, H. and G. Hannoschock, 1984: Comments on "Empirical orthogonal function analysis of wind vectors over the tropical Pacific Region". AMS Bull., 65, 162.

9.5

Nimbus-7 SMMR Derived Sea-ice Concentrations Over Antarctica

Ralph R. Ferraro

Eugene R. Major[1]

Research and Data Systems, Corporation
10300 Greenbelt Road
Lanham, MD 20706

Jane D'Aguanno

J. D. Tarpley

NOAA/NESDIS
Washington, DC 20233

1. INTRODUCTION

The monitoring of the polar ice caps has received considerable attention over the last few decades. With many conflicting theories citing that the earth is undergoing a climatic change, an increase or decrease in the extent of the ice at the poles has been targeted as a strong indicator of global temperature change. The implications of such a change in our climate could have catastrophic effects on the world as we know it today. Since continuous ground monitoring of sea-ice is impractical for several reasons, scientists have focused their attention on retrieving sea-ice information from satellite measurements.

Aside from those observations received from aircraft flights, which are primarily used for shipping interests, the only reliable real-time measurements over the high latitudes come from polar orbiting satellites. Visible imagery provide excellent details as to the structure, movement, and extent of the ice during times of polar summer (when the melting occurs) and under cloud-free conditions. However, the primary drawback of visible imagery is their unreliability during periods of prolonged cloudiness. This is compounded by the fact that the region near the ice edge is frequently cloud covered due to the complex interactions between the ice fields, meteorological parameters, and the ocean surface. Both passive and active microwave measurements have demonstrated their ability to retrieve ice concentration, extent, and age. The primary advantage of using microwave measurements to retrieve sea-ice information as opposed to the visible and infrared (IR) is that the microwave measurements can penetrate the cloud cover (especially over the polar regions where cloud liquid water is relatively low), thus providing an all-weather capability. In addition, the microwave measurements are independent of solar illumination. The present disadvantage is the poor spatial resolution of microwave radiometers (25 km versus 1 km). However, future technology will undoubtedly improve the resolution of the microwave measurements.

The motivation for this study is to develop ice-concentration retrieval algorithms for the Advanced Microwave Sounding Unit (AMSU) to be flown aboard the upcoming NOAA-K,L,M satellites scheduled for launch in the 1990's. Near coincident NOAA AVHRR visible and passive microwave measurements from the Nimbus-7 SMMR have been used to develop the algorithms.

2. BACKGROUND

The use of passive microwave measurements to retrieve sea-ice concentration and ice age is not new, although the use on a real-time basis has been limited.

2.1 Basic Microwave Theory

The ratio of the brightness temperature of a medium (TB) to its physical temperature (TS) is called the emissivity (ϵ) of the medium. Simply written, it is

$$\epsilon = TB/TS$$

The emissivity is a highly variable quantity and is primarily a function of the surface type, microwave frequency, view angle, and polarization. For a given surface type, second order variations of emissivity are caused by surface roughness and texture effects, thickness of the emitting medium, etc. Since many of these controlling variables are known when using passive microwave measurements (i.e., frequency, view angle, and

[1]Presently with Science Systems and Applications, Inc.

polarization), much of the brightness temperature variations measured by satellite radiometers are due to changes in surface type and any perturbations within those surfaces.

2.2 The Microwave Response to Sea-Ice

The emissivity of sea-ice is a complex parameter which is a function of ice type. Much research has been done to better understand ice emissivity (Comiso, 1983; Grenfell and Comiso, 1986; Arcone, et al., 1986). The the emissivity of sea-ice is partially controlled by the salinity, which is directly related to the dielectric constant. However, other parameters such as ice wetness, ice age, and snow thickness contribute significantly to the microwave response measured by instruments such as SMMR. Basically, there are three types of sea-ice: new, first-year, and multi-year (Zwally, et al., 1983). A fourth ice type, summer ice, contains melt ponds on top of the standard three ice types. The main factor which separates new and first-year ice from multi-year ice is the presence of air pockets in the multi-year ice. These are the result of brine drainage during the melting and refreeze cycles. These air pockets act as a scattering medium, lowering the emissivity.

2.3 Retrieval of Sea-Ice Parameters

Although the behavior of sea-ice types is well documented, the retrieval of such information via passive microwave measurements is complicated by the large field of view (FOV) of the radiometers. This means that the presence of water and ice (and different ice types) are likely to appear in the FOV of the radiometer.

Much work has been done to create global estimates of sea-ice concentration with measurements from the Nimbus-5 and -6 Electronic Scanning Microwave Radiometer (ESMR). Zwally, et al. (1983) and Parkinson, et al. (1987), have produced a five-year data set of sea-ice concentration over the Antarctic and Arctic, respectively. They use the 19.35 GHz data from the ESMR-5 to produce sea-ice atlases for 1973-1976.

The Nimbus-7 SMMR has been used extensively to produce sea-ice concentration and multi-year fraction. Cavalieri, et al. (1984) and Gloersen, et al. (1984), summarize the algorithms used. The algorithms include the use of dual-polarization measurements at 37 GHz to produce the total sea-ice concentration while dual-frequency measurements at 18 and 37 GHz are used to compute the multi-year fraction. These parameters are investigated in this study.

3. DATA SOURCES

The source of microwave data comes from measurements from the Scanning Multichannel Microwave Radiometer (SMMR) aboard the Nimbus-7 satellite. The SMMR has been observing earth emitted radiation at five frequencies (6.6, 10.7, 18, 21, and 37 GHz) and dual-polarization since launch in November 1978 and at this writing, is still in limited operation. As such, an invaluable data set of nearly nine years is available. More details about SMMR are presented by Gloersen and Barath (1977). In this study, we focus our attention on the dual-polarization measurements at 18 and 37 GHz, which have approximate footprints of 50 and 25 km, respectively.

The Advanced Very High Resolution Radiometer (AVHRR) is operated on the NOAA series of satellites. The NOAA satellites orbit the earth in a nearly circular, sun-synchronous, near-polar orbit. Approximately 14 orbits are made daily at a swath width of 2700 km. Five spectral channels (0.58-0.68, 0.725-1.10, 3.55-3.93, 10.5-11.3, and 11.5-12.5 microns) are available simultaneously over an area. Two types of AVHRR data are available: Global Area Coverage (GAC), which is a reduced data set with a spatial resolution of approximately 4 km, and Local Area Coverage (LAC), which is a full resolution data set with spatial resolution of 1 km. More details on the AVHRR instrument and data format are given by Kidwell (1985). In this study, we have used the 0.725-1.10 micron, or channel 2 data in the LAC format.

4. METHODOLOGY

The Eltanin Bay region (approximately 72.5 S latitude, 82.0 W longitude) in the Bellingshausen Sea in the west Antarctic has been chosen as a test site for the AVHRR and SMMR sea-ice analysis (see Figure 1). This region was selected since it experiences a seasonal ice melting and refreezing.

Two AVHRR/SMMR scenes of approximately 300 km by 300 km have been analyzed in this region. The characteristics of these data sets are summarized in Table 1. The nearest available SMMR observations were matched with nearly cloud-free AVHRR scenes. Exact matchups were not available in November due to unavailable SMMR data. The two time periods selected are representative of late spring and mid-summer ice, and as such, should yield a wide range of ice conditions.

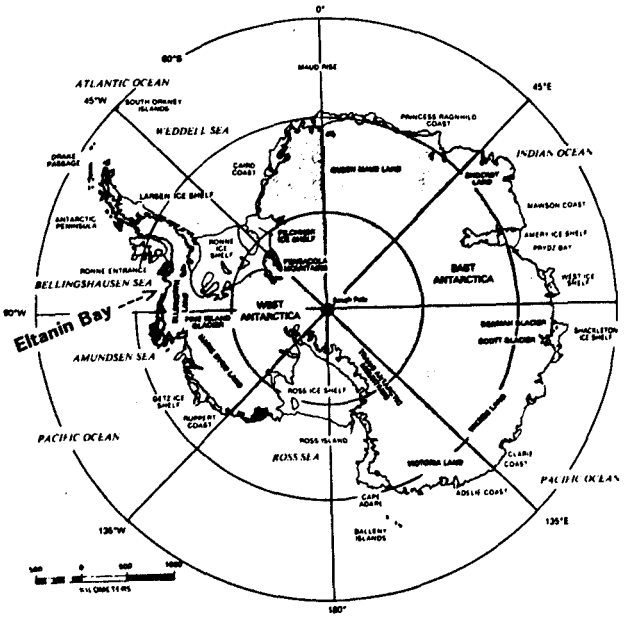

Figure 1. Antarctica, with the Eltanin Bay region of the Bellingshausen Sea indicated (from Zwally, et al., 1983).

Table 1. Times of the data extracted for the Eltanin Bay Region of the Bellingshausen Sea

SMMR	AVHRR
November 21, 1986 18:57 GMT	November 25, 1986 22:08 GMT
February 16, 1983 18:42 GMT	February 16, 1983 22:33 GMT

The AVHRR channel 2 data were used to compute the ice-concentration using a simple thresholding technique. A threshold count is determined through interactive image analysis for open water (0% ice concentration), TW, and 100% ice cover, TI. A similar approach was taken by Comiso and Zwally (1982) comparing Landsat and ESMR-5 data. The algorithm for determining sea-ice concentration, IC, is

$$IC=(C2-TW)/(TI-TW)$$

where C2 is the channel 2 measurement. The counts for open water remained constant throughout the year (TW=40). However, the maximum count for complete ice cover varied for the two scenes (TI=240 in November; TI=190 in February). This difference can be attributed to sun-illumination and possibly a wetter (and hence, "darker") ice from melting during February.

The ice concentration was computed using the above relationship and seasonal values of TI for each AVHRR observation within the test site. Both the AVHRR channel 2 and SMMR 18 and 37 GHz data were gridded to the same projection. This consisted of a 6 by 6 grid with cell size of approximately 50 km. Spatial averaging of all the AVHRR derived ice concentrations within each grid cell was computed. The SMMR 18 and 37 GHz measurements were averaged over the same grid. In addition to the polarized measurements, the vertical and horizontal polarizations were averaged to create a "depolarized" microwave measurement. This was done to simulate the AMSU measurements (Grody, 1988) which will not separate the vertical and horizontal polarizations like the SMMR. The 18 and 37 GHz channels aboard SMMR were used to simulate the 23.8 and 31.4 GHz channels on the AMSU.

5. RESULTS

Data sets consisting of SMMR 18 and 37 GHz depolarized brightness temperatures and AVHRR derived sea-ice concentrations for November 1986 and February 1983 were run through various linear regression models. In addition to matching the ice concentration to each of the SMMR channels, two commonly used parameters in sea-ice retrieval were used (Cavalieri, et al., 1984). Namely, the polarization ratio (PR) and gradient ratio (GR) defined here as

$$PR=(TB(V)-TB(H))/(TB(V)+TB(H))$$

$$GR=(TB^*(18)-TB^*(37))/(TB^*(18)+TB^*(37))$$

where the V and H represent the vertical and horizontal polarizations and the asterisk represents the depolarized measurements at that frequency. The PR was computed for 18 and 37 GHz.

Table 2 summarizes the results of the regression analysis. Several interesting results were found. The most striking was the strong correlations in February and correlations for models using 18 GHz data. The poorer correlations in November can most likely be attributed to the time differences between the AVHRR and SMMR measurements (4 days). Although sea-ice concentration does not change drastically in a few days, the ice does respond rather quickly to changes in meteorological conditions (i.e., wind). Thus, the weaker correlations in November are not surprising. However, the best model (PR18) still yielded a correlation of 0.78 (compared to 0.90 in February). Another contributing factor to the poorer results in November is the narrower range in ice concentration (46-100 percent) compared to February (16-100%).

Table 2. Summary of the regression results

	Correlation Coefficient			
	November 1986		February 1983	
Model	R	R^2	R	R^2
T37 = a ICE + b	0.17	0.03	0.14	0.02
T18 = a ICE + b	0.56	0.31	0.88	0.78
PR37 = a ICE + b	0.10	0.01	0.03	0.001
PR18 = a ICE + b	0.78	0.61	0.90	0.81
GR = a ICE + b	0.52	0.27	0.92	0.84

The weakness of 37 GHz measurements is somewhat surprising. The poor correlations in February may be attributed to the near peak melt conditions, resulting in a mixture of ice-types, including summer ice; those in November again may be caused by the AVHRR/SMMR time differences. Another contributing factor may be the sensitivity of the 37 GHz measurements to ice type. With a rather small sample size, the scatter in the measurements at 37 GHz may be exaggerated. Finally, the use of the 37 GHz data in the GR computation improved the results slightly in February, but not in November.

Figures 2 and 3 show a plot of the 18 GHz depolarized brightness temperatures as a function of ice concentration for November 1986 and February 1983, respectively. The linear regression fit are also indicated. Aside from noting the scatter in the data about the least squares fit, there is a difference in the magnitude of the 18 GHz measurements. The temperatures in February are clearly lower than those in November. This is most likely due to the presence of more water (i.e., lower emissivity) in February from the summer melting. This indicates that seasonal algorithms may be necessary to derive ice concentration.

6. SUMMARY

In this investigation, we have used clear scene AVHRR channel 2 measurements to derive sea-ice concentrations. A test site in the Bellingshausen Sea in West Antarctica, which experiences seasonal melting, was selected as a test site. The nearest available Nimbus-7 SMMR 18 and 37 GHz measurements from November and February were depolarized and spatially matched with the derived sea-ice concentrations. Linear regressions were performed to derive relationships between the microwave brightness temperatures and ice concentrations.

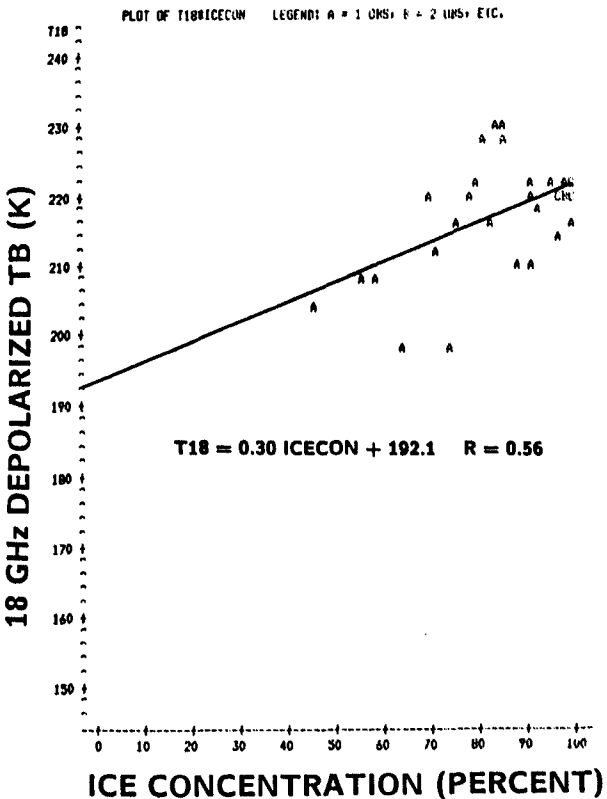

Figure 2. Plot of 18 GHz depolarized brightness temperature (°K) as a function of ice concentration (percent) for November 1986. The linear regression fit is also indicated.

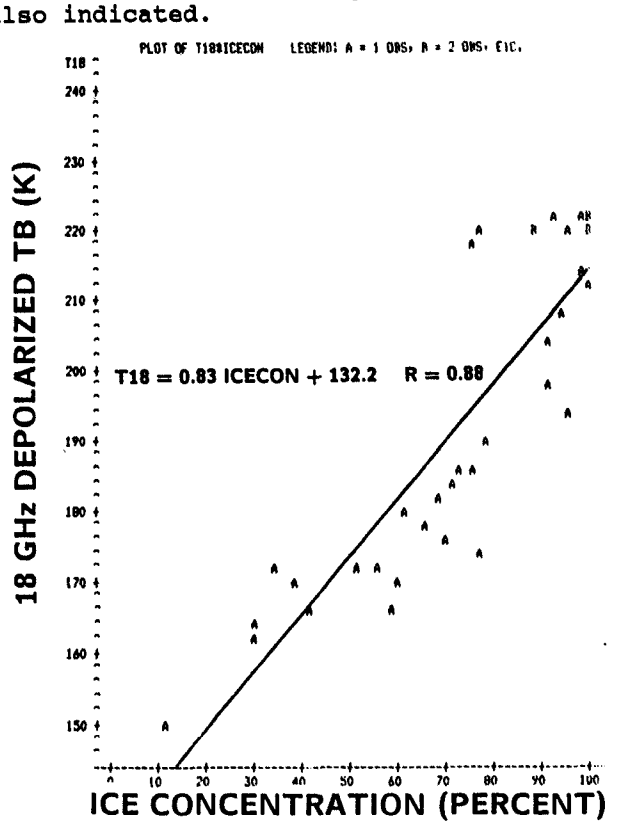

Figure 3. Plot of 18 GHz depolarized brightness temperature (°K) as a function of ice concentration (percent) for February 1983.

Excellent correlations were found between the SMMR 18 GHz measurements and ice concentration. The 37 GHz data alone performed rather poorly, but may add some information when used together with the 18 GHz data. Better results were found in February than in November, which is probably due to the better data matchups in February.

From our investigation, we have shown that the depolarized measurements can yield information on sea-ice concentration. The AMSU 23.8 and 31.4 GHz data are expected to respond in a similar fashion to sea-ice as the SMMR 18 and 37 GHz measurements. We plan to continue our investigations by obtaining AVHRR/SMMR matchups for other summer months. When a large enough data set is acquired, more meaningful algorithms can be developed and applied. In addition, the AVHRR channel 4 measurements will be matched with the SMMR data. The possibility of developing seasonal algorithms will also be pursued. The ultimate goal of this research is to derive prototype operational algorithms for the AMSU.

7. REFERENCES

Arcone, S. A., A. J. Gow, and S. McGrew, 1986: Microwave Dielectric, Structural, and Salinity Properties of Simulated Sea Ice. IEEE Trans. Geosci. Remote Sensing, GE-24, 832-839.

Cavalieri, D. J., P. Gloersen, and W. J. Campbell, 1984: Determination of Sea Ice Parameters with the Nimbus-7 SMMR. J. Geophys. Res., 89, 5355-5369.

Comiso, J. C., 1983: Sea Ice Effective Emissivities from Satellite Passive Microwave and Infrared Observations. J. Geophys. Res., 88, 7686-7704.

Comiso, J. C., and H. J. Zwally, 1982: Antarctic Sea Ice Concentration Inferred from Nimbus-5 ESMR and Landsat Imagery. J. Geophys. Res., 87, 5836-5844.

Gloersen, P., and F. Barath, 1977: A Scanning Multichannel Microwave Radiometer for Nimbus-7 and Seasat-A. IEEE J. Oceanic Eng., OE-02, 172-178.

Gloersen, P, D. J. Cavalieri, A. T. C. Chang, T. T. Wilheit, W. J. Campbell, O. M. Johannessen, K. B. Katsaros, K. F. Kunzi, D. P. Ross, D. Staelin, E. P. L. Windsor, F. T. Barath, P. Gudmandsen, E. Langham, and R. O. Ramseire, 1984: A Summary of the First Nimbus-7 SMMR Observations. J. Geophys. Res., 89, 5335-5344.

Grenfell, T. C., and J. C. Comiso, 1986: Multifrequency Passive Microwave Observations of First-Year Sea Ice Grown in a Tank. IEEE Trans. Geosci. Remote Sensing, GE-24, 826-838.

Grody, N. C., 1988: Determination of Surface and Atmospheric Parameters Using the Advanced Microwave Sounding Unit. Presented at the Third AMS Conference on Satellite Meteorology and Oceanography, Anaheim, CA.

Kidwell, K. B., 1984: NOAA Polar Orbiter Data User's Guide, NOAA/NESDIS, Washington, D.C., 140 pp.

Parkinson, C. L., J. C. Comiso, H. J. Zwally, D. J. Cavalieri, P. Gloersen, and W. J. Campbell, 1987: Arctic Sea Ice, 1973-1976, NASA SP-489, Washington, D.C., 296 pp.

Zwally, H. J., J. C. Comiso, C. L. Parkinson, W. J. Campbell, F. D. Carsey, and P. Gloersen, 1983: Antarctic Sea Ice, 1973-1976, NASA SP-459, Washington, D.C., 206 pp.

MODELLING OF SURFACE WAVES AND SEA STATE-DEPENDENT WIND STRESS FOR THE NORTHEAST PACIFIC OCEAN USING SEASAT SCATTEROMETER DATA

H.C. Graber, K.A. Kelly, R.C. Beardsley

Woods Hole Oceanographic Institution
Woods Hole, MA 02543

S. Hasselmann

Max-Planck Institut für Meteorologie
2000 Hamburg 13, West-Germany

1. INTRODUCTION

There is a substantial growth in evidence that surface waves play a crucial role in air-sea interaction, upper ocean and shelf dynamics. The principal driving force of regional and large-scale ocean circulation models is the surface wind stress. Donelan (1982) and recently Geernaert et al. (1986) have shown that the wind stress cannot be determined from wind speed measurements alone, but must include the presence of waves on the ocean surface. This implies that the wind stress cannot precisely be computed from either scatterometer data or pressure map derived winds alone. Hence, scatterometer wind retrieval algorithms need to account for the joint consideration of radar backscatter and sea state.

In 1978, the SEASAT satellite provided a 96-day record of scatterometer backscatter and altimeter radar measurements over the global ocean. Recently, the full 96-day SEASAT scatterometer data set was assimilated into the Goddard Laboratory for Atmospheres (GLA) analysis/forecasting system to construct de-aliased wind and wind stress fields (Atlas, et al., 1987). The SEASAT altimeter (ALT) derived wave height and wind speed estimates have not yet been fully exploited and extensively compared to ocean wave model predictions.

Here we compare monthly averages of ALT wind stress and significant wave height estimates with fields computed from the global hindcast study of the third generation ocean wave prediction (WAM) model. We also assess the importance of including the sea state in calculations of the surface wind stress.

2. GLOBAL OCEAN WAVE PREDICTIONS

The deep water version of the WAM model developed within the framework of the WAM (Wave Modelling) Program (Hasselmann, et al., 1987) was used to carry out global predictions of the sea state for the entire SEASAT period. The evolution of the two-dimensional ocean wave spectrum $F(f,\theta,\phi,\lambda,t)$ with respect to frequency f and direction θ as a function of latitude ϕ and longitude λ was computed from the integration of the transport equation

$$\frac{\partial \hat{F}}{\partial t} + \frac{\partial}{\partial \phi}(\dot{\phi}\hat{F}) + \frac{\partial}{\partial \lambda}(\dot{\lambda}\hat{F}) + \frac{\partial}{\partial \theta}(\dot{\theta}\hat{F}) = S_{in} + S_{nl} + S_{ds} \quad (1)$$

where $\hat{F} = FR^2 cos\phi$ and R is the radius of the earth. The source terms on the right side of (1) represent atmospheric input, nonlinear energy transfer and dissipation, respectively, and

$$\dot{\phi} = v\,R^{-1}\,cos\theta \quad (2)$$
$$\dot{\lambda} = v\,sin\theta\,(R\,cos\phi)^{-1} \quad (3)$$
$$\dot{\theta} = v\,sin\theta \cdot tan\phi \cdot R^{-1} \quad (4)$$

are the equations for a wave group travelling along a great circle path and the group velocity in deep water is $v = g/4\pi f$.

The global model was implemented on a $3° \times 3°$ latitude-longitude grid. Output of spectral wave parameters was obtained for all grid points at noon and midnight each day, as well as the detailed two-dimensional wave spectrum at pre-selected locations. The input global wind stress fields were derived from the de-aliased GLA data set of Atlas, et al. (1987) and the hindcast study was carried out for the entire SEASAT period, July 7 - October 10, 1978. An example of the predicted significant wave height for the Northeast Pacific and the corresponding custer diagram of wind stress on September 15, 1978 is shown in Figure 1.

The mean significant wave height and wind stress fields for September/October are displayed in Figures 2 and 3, respectively. The region of high sea state ($H_{1/3} > 3\,m$) is confined to the Gulf of Alaska. This corresponds well with the location of the maximum wind stress ($\tau > 2\,dynes/cm^2$). The southern part of the Northeast Pacific

shows less variability in the mean stress and wave height fields. The variance maps (not shown) illustrate the same features.

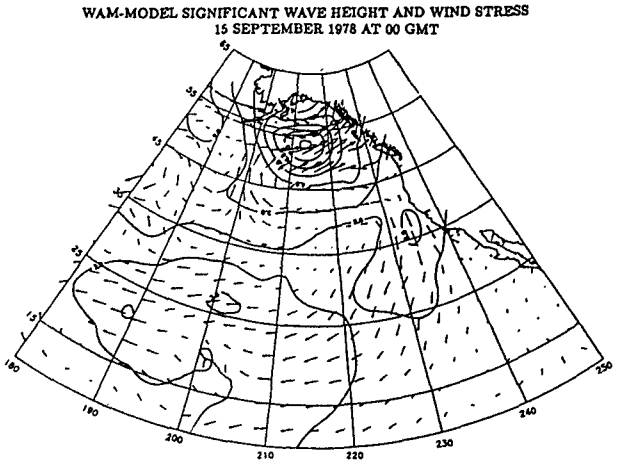

Figure 1. Predicted significant wave height and superimposed surface stress field for 15 September 1978 at 00:00 GMT.

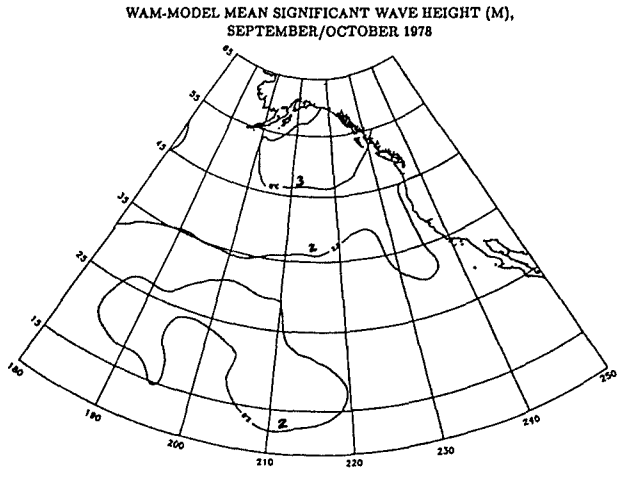

Figure 2. Isolines of computed significant wave height, averaged over the period September/October 1978.

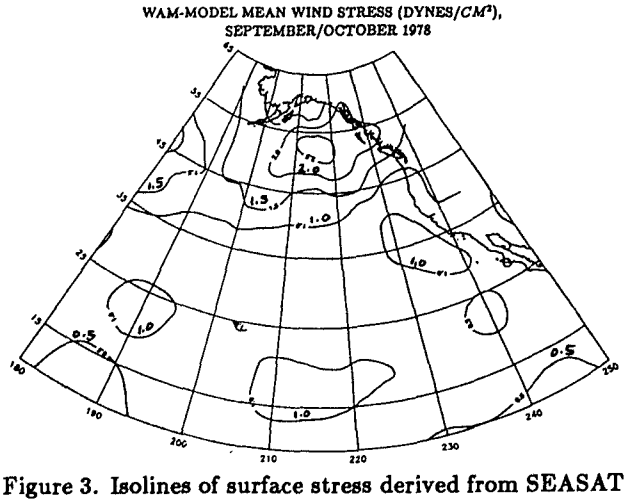

Figure 3. Isolines of surface stress derived from SEASAT scatterometer data, averaged over the period September/October 1978.

3. SEASAT ALTIMETER DATA SET

The usefulness of altimeter observations of the sea surface has been demonstrated in recent studies of synoptic-scale ocean processes. Comparisons of buoy measurements with ALT estimates of significant wave height and wind speeds were presented for SEASAT by Fedor and Brown (1982) and recently for GEOSAT by Dobson et al. (1987). Chelton et al. (1981) provided the first global maps of average wind speed and wave height for the 100 days of SEASAT. Mognard et. al. (1983) constructed monthly mean fields of waves and winds for the southern oceans. It was found that the monthly mean fields were not too different from the 3-month averages obtained by Chelton et al. (1981).

The coarse spatial resolution of altimeter data during September/October (3-day repeat cycle) was not suitable for direct comparison with the evenly gridded model predictions. Therefore, the ALT data was averaged within $3° \times 3°$ bins centered around the WAM model grid points. Altimeter wind speeds were adjusted to 10 m height winds and then converted to surface stress, $\tau = \rho\, C_{10}\, U_{10}^2$, using a wind speed dependent drag coefficient according to Wu (1982)

$$C_{10} = (0.8 + 0.065 U_{10}) \times 10^{-3}\,. \qquad (5)$$

Maps of the monthly mean surface stress and significant wave height fields for September/October are shown in Figures 4 and 5.

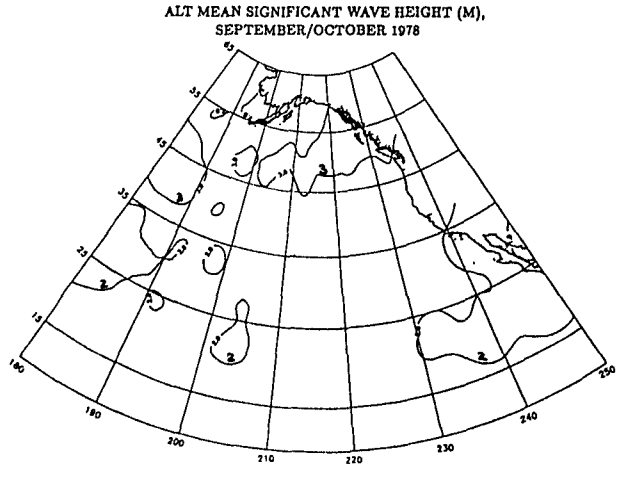

Figure 4. Isolines of ALT significant wave height, averaged over the period September/October 1978.

The largest stresses and waves are confined to a band around the *roaring forties* and extend into the Gulf of Alaska. These results agree well with the monthly maps from the WAM model hindcast study (Fig. 2 and 3) and with the features seen in Chelton et al. (1981). However, two features are noteworthy. First, the band of 3 m wave heights occurs in the Gulf of Alaska for both model and ALT. An aera containing waves greater than 2 m is seen

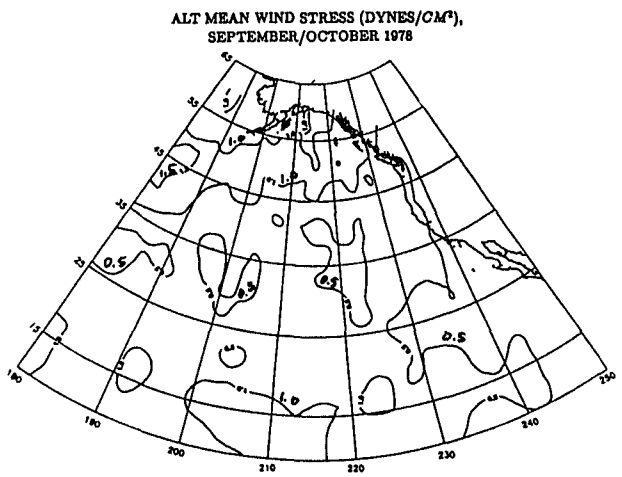

Figure 5. Isolines of ALT surface stress, averaged over the period September/October 1978.

off the California/Mexico border in the ALT averages, but is absent in the WAM model results. Second, the region of maximum wind stress coincides with the area of high waves, but the intensification of stress as exhibited by the model (i.e., scatterometer) winds is absent in the ALT measurements. The coarse across-track spatial resolution of the altimeter could contribute to missing entire storms. However, a closer look of the daily dynamics is needed to determine the cause of this discrepancy.

4. ALT-BUOY AND MODEL-BUOY COMPARISONS

Comparisons of ALT measured oceanic variables with buoy observations are never without uncertainties which are primarily related to temporal and spatial separation, time and area averaging and instrument related errors. Monaldo (1986) investigated the expected differences in wind speed and wave height made by radar altimeters due to the above uncertainties. For the SEASAT hindcast study we calculated the following statistical properties for $H_{1/3}$ and u_* from altimeter and model colocated buoy estimates: the bias, defined as the mean of ALT or model minus observed; the *rms* error or standard deviation; and the scatter index, defined as the ratio of the standard deviation and mean observed value. The sample size of wave and wind stress pairs was 43 and 372 for the ALT-buoy and the model-buoy comparisons, respectively. The results are summarized in Table 1.

ALT-BUOY	Avg. Obs.	Bias	*rms* Error	S. I.
$H_{1/3}$ (m)	1.35	0.38	0.37	27 %
u_* (m/s)	0.22	0.003	0.10	48 %
MODEL-BUOY	Avg. Obs.	Bias	*rms* Error	S. I.
$H_{1/3}$ (m)	1.54	0.60	0.53	34 %
u_* (m/s)	0.22	0.06	0.13	59 %

Table 1. Summary of statistics between ALT-BUOY and MODEL-BUOY estimated significant wave heights and friction velocities.

From these results we can conclude that the mean errors (bias) in the ALT-buoy and model-buoy comparisons of significant wave height are 0.4 and 0.6 m, respectively. Similarly, the *rms* wave height differences are 0.4 and 0.5 m, respectively. For the friction velocities we compute mean and *rms* deviations of 0.003 and 0.10 m/s for ALT-buoy comparisons, and 0.06 and 0.12 m/s for model-buoy pairs. The ALT-buoy values of wave height and wind stress are comparable to the statistics found by Fedor and Brown (1982) and Dobson et al. (1987) in their validation studies of SEASAT and GEOSAT altimeter measurements, respectively. The larger mean error in friction velocity for the model is partially due to spatial separation between model grid point and buoy location, which for some buoys exceeded 100 km. A more appropriate weighted averaging may reduce the mean error and scatter index.

At first glance the above statistics are only slightly better than what can be expected from a finely tuned ocean wave model (Cardone, et al., 1987). However, the spatial resolution for the global hindcast of 3° × 3° is too coarse at present to investigate meso-scale features in both the wind and wave fields. Regional models with spatial resolution of 100 or 50 km will be better suited to study discrepancies in the observed and predicted wave fields and to evaluate the contribution of errors in the wind field which generated the waves.

5. SEA STATE DEPENDENT WIND STRESS

The roughness of the sea surface is strongly coupled to the waves present at the atmosphere-ocean interface. Describing the roughness length characteristic of the sea surface is further complicated by the fact that waves are not fixed in space and time, but continually undergo changes in height, speed, and direction. Donelan (1982) proposed a model for determining the aerodynamic drag over water which accounts for the mobility of the waves as well as including contributions from skin friction (capillary waves) and form drag (gravity waves). However, this model requires knowledge of the two-dimensional ocean wave spectrum, which is not routinely available from conventional measurement techniques and cannot be determined from radar altimeters.

Therefore, we chose a model proposed by Hsu (1974) which incorporates the effect of waves through integral properties of the wave field. Specifically, we need to know the wave height and the mean frequency of the wave energy spectrum to compute the roughness length as a function of sea state. These variables are typically available from conventional as well as remotely sensed measurements of ocean waves.

In order to demonstrate the importance of sea state on the surface wind stress, we computed the stress fields from a wind speed-dependent drag coefficient as given in (5) and directly from the logarithmic profile for winds at height z,

$$U_z = \frac{u_*}{\kappa} \ln \frac{z}{z_o}, \qquad (6)$$

where κ is von Kármán's constant and the roughness length z_o is expressed according to Hsu (1974)

$$z_o = \frac{H_{1/3}}{(2)^{5/2}\pi} (c_o/u_*)^{-2} . \qquad (7)$$

In deep water the mean phase speed can simply be expressed as $c_o = g/2\pi\bar{f}$, where $\bar{f}$ denotes the mean frequency.

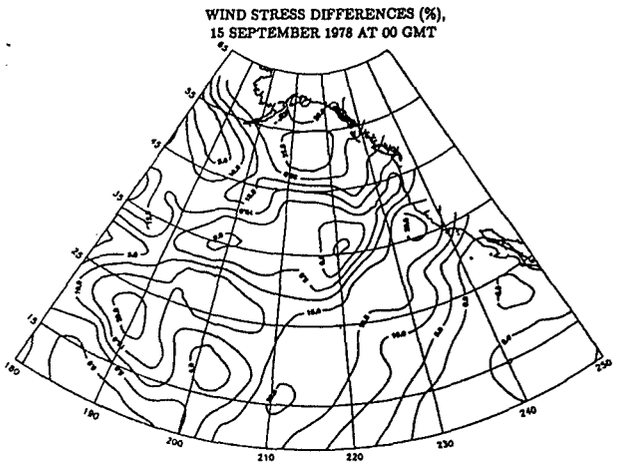

Figure 6. Isolines of differences (%) in surface stress computed from τ(sea state) - τ(wind speed) for 15 September 1978 at 00:00 GMT.

Figure 6 displays the percentage difference in stress when the sea state is taken into consideration over the stress one computes from a wind speed- dependent formula only. Differences in excess of 20 % and more are anticipated in the Gulf of Alaska, where most of the wave action occurs. However, it is surprising to find large areas with subtantial deviations in wind stress in the southwestern part of the Northeast Pacific. These differences are primarily caused by the non-local wave field (swell) which cannot be described by the local wind field.

7. REFERENCES

Atlas, R.A., A.J. Busalacchi, M. Ghil, S. Bloom and E. Kalnay, 1987: Global surface wind and flux fields from model assimilation of SEASAT data. *J. Geophys. Res.*, **92**, 6477-6487.

Cardone, V.J. and J.A. Greenwood, 1987: A sensitivity study of spectral wave growth algorithms. *Proc. Int. Workshop Wave Hindcasting and Forecasting*, 133-144.

Chelton, D.B., K.J. Hussey and M.E. Parke, 1981: Global satellite measurements of water vapor, wind speed and wave height. *Nature*, **294**, 529-532.

Dobson, E., F. Monaldo, J. Goldhirsh and J. Wilkerson, 1987: Validation of GEOSAT altimeter-derived wind speeds and significant wave heights using buoy data. *J. Geophys. Res.*, **92**, 10,719-10731.

Donelan, M.A., 1982: The dependence of the aerodynamic drag coefficient on wave parameters. *Proc. First Int. Conf. Meteorology and Air-Sea Int. of the Coastal Zone*, 381-387.

Fedor, L.A. and G.S. Brown, 1982: Wave height and wind speed measurements from SEASAT radar altimeter. *J. Geophys. Res.*, **87**, 3254-3260.

Geernaert, G.L., K.B. Katsaros and K. Richter, 1986: Variation of the drag coefficient and its dependence on sea state. *J. Geophys. Res.*, **91**, 7667-7679.

Hasselmann, S. and 9 authors, 1987: The WAM model - a third generation ocean wave prediction model. In preparation.

Hsu, S.A., 1974: A dynamic roughness equation and its application to wind stress determination at the air-sea interface. *J. Phys. Oceanogr.*, **4**, 116-120.

Mognard, N.M., W.J. Campbell, R.E. Cheney and J.G. Marsh, 1983: Southern ocean mean monthly waves and surface winds for winter 1978 by SEASAT radar altimeter. *J. Geophys. Res.*, **88**, 1736-1744.

Monaldo, F.M., 1986: Expected differences in the comparison of wind speed and significant wave height made by spaceborne radar altimeters. *Tech. Rep. S1R86U-017*, Appl. Phys. Lab., Johns Hopkins Univ., Laurel, Md.

Wu, J., 1982: Wind-stress coefficients over sea surface from breeze to hurricane. *J. Geophys. Res.*, **87**, 9704-9706.

WIND AND WIND STRESS CURL FIELDS FOR THE NORTHEAST PACIFIC OCEAN USING SATELLITE SCATTEROMETER DATA

K.A. Kelly, H.C. Graber and R.C. Beardsley

Woods Hole Oceanographic Institution
Woods Hole, MA 02543

1. INTRODUCTION

A knowledge of the wind stress and wind stress curl fields is essential to understanding the wind-driven response of ocean circulation. Previous analyses of these fields have been hampered by the poor spatial resolution of conventional wind and pressure measurements. In 1978 the SEASAT-A Satellite Scatterometer (SASS) produced a 96-day record of radar backscatter measurements on an approximately 50 km grid. However, the SASS data were not analyzed extensively because it proved difficult to extract a unique wind vector from the backscatter values. A 14-day segment of that record was processed into unique wind vectors at Jet Propulsion Laboratory (JPL) using the method described by Wurtele et al. (1982); this segment has been analyzed and used in model assimilations by the European Center for Medium-range Weather Forecasting (ECMWF). In 1986 the entire 96-day record was processed into wind vectors on a 100 km grid at Goddard Space Flight Center to use in data assimilation studies (Atlas, et al., 1987). The scatterometer data can provide maps of wind stress and wind stress curl with significantly more spatial detail than conventional measurements or most current numerical models; however an accurate knowledge of the spatial and temporal scales of the wind field is needed to convert the nearly-instantaneous measurements on an uneven grid to maps with regular temporal and spatial sampling. The NASA scatterometer (NSCAT) on NROSS will provide similar longer data sets in the future. We describe here a technique we are developing to generate maps of the wind stress and wind stress curl fields from the 96-day SASS record. This same technique will be used to generate maps from NSCAT data.

2. DEVELOPING A SYNTHETIC DATA SET

To test the procedure for making maps from satellite scatterometer data, we need a synthetic data set with the wavenumber-frequency spectrum we would expect from scatterometer data. The available information from which to obtain this spectrum includes analyses of the wind vectors from conventional sources and analyses of SASS data. Our synthetic set consists of output from the ECMWF model on a 1.875 degree grid for an 11-day period in September 1978 with information added on smaller scales. We first determine the component spectra of the wind velocity vectors in the zonal and meridional directions for the ECMWF data and our best estimate of the spectra for the actual wind field. The difference between the best estimate of the actual velocity spectra and the spectra of the ECMWF output is what we have to add to make a realistic synthetic data set. The ECMWF data are re-gridded with a spacing of 25 km and "noise" with the residual spectrum is added.

The analysis of the ECMWF field is somewhat complicated by the use of a grid evenly spaced in degrees so that data resolution is poorer near the equator. The meridional spectra were computed from the two-dimensional Fourier transform of the field, integrated in the zonal direction. The zonal spectra were computed from one-dimensional Fourier transforms of the data, which were re-gridded to constant wavenumbers in units of rad/km and then averaged. The zonal and meridional spectra of the zonal component (u) are shown in Figure 1 and the same spectra for the meridional component (v) are shown in Figure 2.

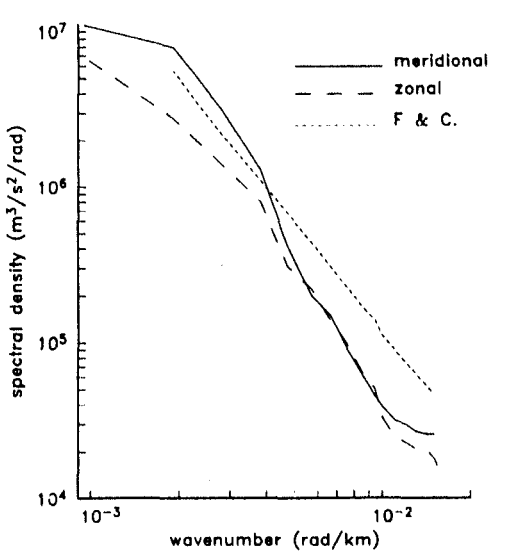

Figure 1. Spectra of the zonal component of the wind for the North Pacific. Solid line is the spectrum in the meridional direction, dashed line is in the zonal direction and dotted line is the power law approximation to the results of Freilich and Chelton (1986). There is less energy in the largest scales for zonal wavenumbers.

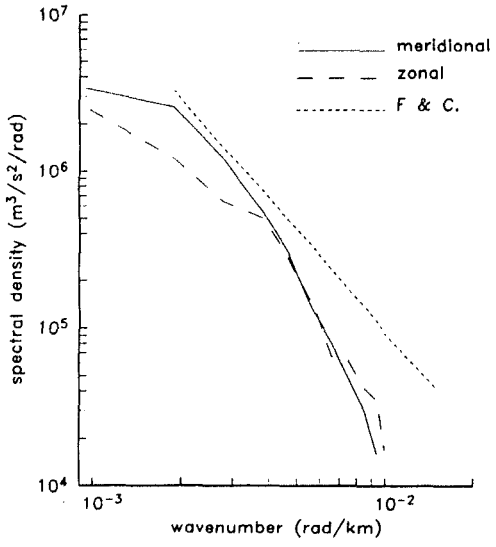

Figure 2. Same as Figure 1, except for the meridional component.

Note that the spectral density falls off somewhat abruptly above $k = 4 \times 10^{-3}$ rad/km, corresponding to a wavelength of about 1600 km, but that there is significant energy down to scales of about 600 km.

3. COVARIANCE FUNCTION FOR MAPPING

For an objective mapping technique it is easiest to use a simple analytic function for the covariance (Bretherton, et al., 1976). We use a simple function of time and two spatial dimensions for each component,

$$C(x,y,t) = V exp(-\sigma t - \alpha x - \beta y)\ cos(\gamma x + \delta y). \quad (1)$$

The exponential functions reflect the decorrelation scales in space and time. The cosine function, which moves the spectral peak away from the wavenumber origin, reflects the maximum finite length scale possible in the atmosphere, which decreases with latitude. The zonal and meridional components of the wind vector are assumed to be uncorrelated as noted by Willebrand (1978). We may be able to obtain a better map by modifying this covariance function to include the effects of the predominately eastward propagation of the wind field for periods of 10 days or less as observed by Willebrand (1978).

In each covariance function and the corresponding spectrum there are five parameters which must be determined. The five parameters can be determined for the ECMWF data by fitting analytic spectra to the computed spectra. The meridional components, β and δ, of the SASS data can be found by fitting an analytic function to the results of Freilich and Chelton (1986); these spectra are well-represented by simple power laws which are also shown on Figures 1 and 2. The zonal spectra could not be obtained from the SASS data because of the narrowness of the swath. We estimate the zonal parameters from the SASS data itself because it has a spatial resolution of 100 km, and we estimate the temporal parameter, γ, from the ECMWF data because it has a temporal resolution of six hours.

4. SAMPLING THE DATA WITH NSCAT

The re-gridded synthetic data are then sampled using the sampling scheme of the NSCAT and the orbit of SEASAT for a three-day repeat cycle (the orbit for NROSS has not yet been finalized). The vector closest to the center of each of the instrument's cells is selected. The sampling pattern for a 24-hour period is shown in Figure 3.

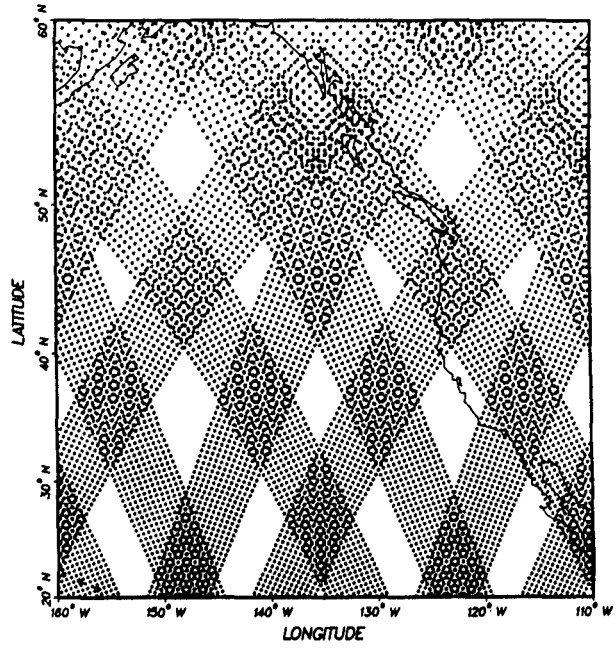

Figure 3. Sampling pattern for NSCAT for a 24-hour period. The gaps of constant width correspond to the "nadir gap" of the instrument. Between consecutive orbits are wedge-shaped gaps which decrease with increasing latitude.

NSCAT has a swath width of about 1575 km with a 375 km "nadir gap", the region directly below the satellite in which no vector wind information will be available. Consecutive (parallel) subtracks are separated by about 2300 km at mid-latitudes, so that the gap between adjacent swaths is about 700 km, about double the size of the "nadir gap". Intersecting subtracks are separated in time by about 12 hours and have the same separations between parallel tracks. SASS had a similar sampling pattern, but with a slightly wider nadir gap and a larger cell size.

5. OBJECTIVE MAPPING WITH CONSTRAINTS

The expected errors in the maps can be minimized by removing a spatially-varying mean from the data, interpolating the residual and then adding the mean back to form the interpolated map (Bretherton, et al., 1976). The 11-day record is so short that the means and variances may be substantially different from the means and variances of the wind field for the entire month of September or for the rest of the SEASAT period. To check this we compared the 11-day means and variances

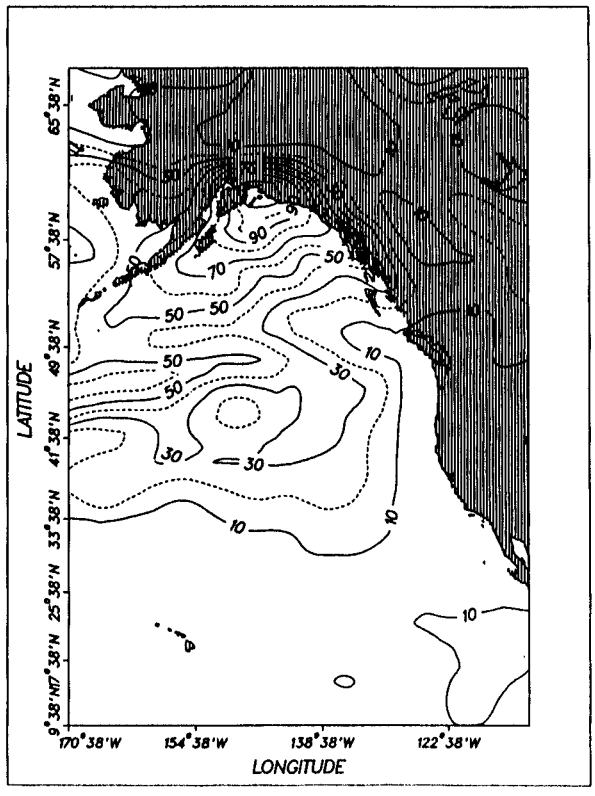

Figure 4. Variance of the zonal component of the wind for 6-17 September 1978 in m^2/s^2. The regions of largest variance are near the coast, particularly in the Gulf of Alaska.

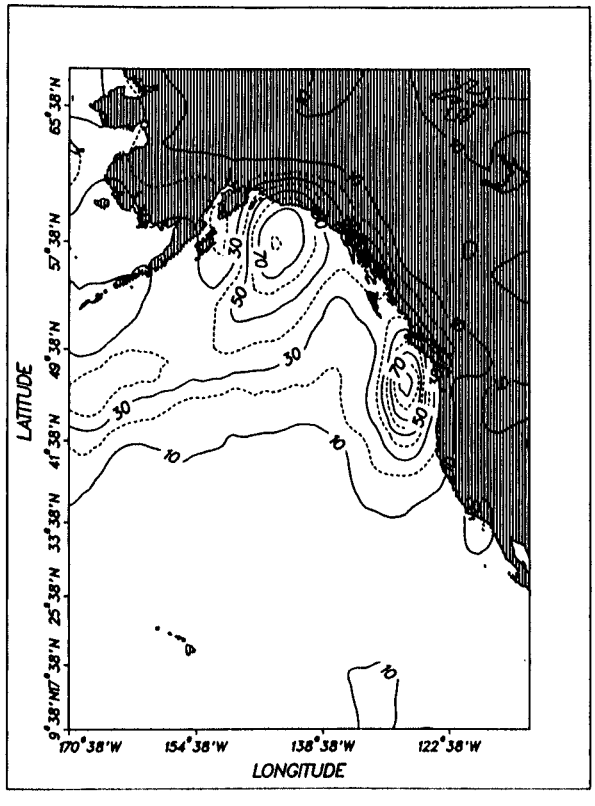

Figure 5. Same as for Figure 4, except the meridional component. There is an additional region of large variance near the Canada-United States border.

with the monthly means and variances on a three-degree grid. The 11-day mean fields (not shown) and the variance fields (Figures 4 and 5) were not substantially different from the monthly fields. The regions of large variance in both the u and v components in the Gulf of Alaska are due to a series of storms which came in from the North Pacific. The regions of large variance in the v component near the Canada-United States border is due to the alongshore motion of the divergence of alongshore winds. In the absence of storms a large region of high pressure in the Northeast Pacific produces equatorward winds all along the coast. As it approaches the coast each storm breaks up this high pressure region and creates poleward winds; after the storm passes the high pressure region is re-established.

The spatial gaps in a 24-hour sample are large compared with the decorrelation scales of the ECMWF data, so that the error estimates associated with objective mapping are quite large. To attempt to decrease the errors, particularly in the gaps, we add physical constraints to the mapping equations. The first and most obvious constraint to apply is a minimum horizontal divergence. Because there is not a straightforward way to compute the new expected error with the constraints, estimates of the errors are computed directly from synthetic examples.

6. CONVERSION TO WIND STRESS

The wind velocity vectors are first interpolated onto an even grid and then these vectors are converted to wind stress using a sea state-dependent drag coefficient. For the SASS wind stress maps, measurements of the sea state are available from a wave model run for the SEASAT period (see Graber, et al., this issue). For NSCAT stress maps we will be examining the possibility of using the sea state as specified by altimeter measurements.

7. REFERENCES

Atlas, R.A. A.J. Busalacchi, M. Ghil, S. Bloom, and E. Kalnay 1987: Global surface wind and flux fields from model assimilation of Seasat data. *J. Geophys. Res.*, *92*, 6477-6487.

Bretherton, F.P., R.E. Davis and C.B. Fandry 1976: A technique for objective analysis and design of oceanographic experiments applied to MODE-73. *Deep-Sea Res.*, *23*, 559-582.

Freilich, M.H. and D.B. Chelton 1986: Wavenumber spectra of Pacific winds measured by the SEASAT scatterometer. *J. Phys. Oceanogr.*, *16*, 741-757.

Willebrand,J. 1978: Temporal and spatial scales of the wind field over the North Pacific and North Atlantic. *J. Phys. Oceanogr.*, *8*, 1080-1094.

Wurtele, M.G., P.M. Woiceshyn, S. Peteherych, M. Borowski and W.S. Appleby, 1983: Wind direction alias removal studies of Seasat scatterometer derived wind fields. *J. Geophys. Res.*, *87*, 3365-3377.

ABSTRACTS

5.1 THE COMBINING OF METEOROLOGICAL RADAR AND SATELLITE DATA FOR THE SHORT-TERM PREDICTION OF RAINFALL AND SEVERE WEATHER. G. L. Austin,* A. Bellon and A. Kilambi, McGill Radar Weather Observatory, Quebec, Canada

The relative advantages of radar and satellite remote sensing techniques for now casting are compared. Statistical and physical techniques are presented for combining the two data sets. Problems associated with short range forecasting wintertime maritime systems and tropical convection are contrasted. The possibilities of making the image processing approach interact with mesoscale models are reviewed.

5.19 SATELLITE-DETERMINED SYMOPTIC AND MESOSCALE VARIATIONS OF LOW CLOUDS AND RADIO PROPAGATION CONDITIONS OVER THE OCEAN. J. S. Rosenthal,* Steven W. Lyons, Alan D. Fox and Roger A. Helvey, Pacific Missile Test Center, Point Mugu, Calif.

Synoptic and mesoscale fluctuations in cloud-top height and radio propagation (duct) conditions over the open ocean are interactively determined on an interactive satellite data processing and display system originally developed by the Naval Environmental Prediction Research Facility using algorithms developed and implemented by Lyons (1985).
Using a built-in capability of this display system to access Fleet Numerical Oceanography Center (FNOC) products, analyses and forecast fields nearly concurrent in time to the processed satellite data are superimposed in order to characterize the mesoscale cloud variability according to types of synoptic regimes. Several characteristic patterns have been observed, associated with strong subsidence from highs, pre-trough convergence, and coastal and latitudinal effects. The technique allows mapping of meteorological conditions vital to Naval operations over vast open-ocean regions void of conventional data, and will be useful in predictive techniques currently under development.

6.6 THE EARTH AS A SYSTEM: STUDYING THE HYDROLOGIC CYCLE WITH THE POLAR-ORBITING, EARTH OBSERVING SYSTEM. James C. Dodge,* NASA Headquarters, Washington, D.C.

In the decade beginning about 1995, NASA is planning a comprehensive, coordinated program of remote sensing based upon collections of state-of-the-art sensors located on polar-orbiting platforms. At least three platforms are currently under consideration, and all involve participation from several international remote sensing partners. The concept is to select sensors which can be used together in a synergistic study of interaction problems within the Earth sciences. While not all of the necessary observations can be made remotely, a crucial part of the concept is to have a massive data system which allows one to retrieve and relate all near-simultaneous data that has been collected by other satellites, aircraft, balloons, surface observations, etc. The total available data will then be scrutinized in numerical physical models to estimate unobservable parameters, supplement missing time and space data, then evaluate the physical processes involved and, eventually, forecast global change in a credible way.

The whole Earth System Science concept involves study of the hydrologic, biogeochemical, and climatic cycles, and involves interrelationships between the atmosphere, the biosphere, the hydrosphere, the cryosphere, and the solid Earth.

This paper will describe the anticipated available sensors and the coordinated remote sensing which can be focused on one aspect of Earth System Science: The Hydrologic Cycle. The most important components of the hydrologic cycle involve variations in soil moisture, evapotranspiration, precipitation, and snow cover area, depth, and water equivalent. It will be shown how remote sensing of the atmosphere and the land/ocean surface layer can help to extend scientific understanding of this critical interdisciplinary problem.

6.8 THE GLOBAL BACKSCATTER EXPERIMENT (GLOBE) MEASUREMENT AND MODELING PROGRAM. David A. Bowdle,* NASA/MSFC, Huntsville, Ala.

The centerpiece of NASA's new GLObal Backscatter Experiment (GLOBE) program is a series of global-scale flights in 1988/1989 over the Pacific Ocean with pulsed CO_2 and Nd:YAG lidars and supporting aerosol optical and microphysical measurements. Also included are backscatter climatologies obtained from a network of ground-based pulsed CO_2 lidars, and global aerosol climatologies obtained from satellite imagery, limb sounding, and surface-based aerosol microphysical measurements. The GLOBE data base is being

used to develop a global-scale model of the typical magnitudes and the spatial / temporal variability of aerosol backscatter. Current model results show a global-scale aerosol background with a volume backscatter coefficient of about 10^{-10} m^{-1} sr^{-1} at CO_2 wavelengths. The model is being used in design and simulation studies for NASA's Laser Atmospheric Wind Sounder (LAWS). The work can be applied to the design of other lidar-based sensors that use atmospheric aerosols as scattering targets for the measurement of primary atmospheric variables.

8.12 DUAL-IMAGE PROCESSING TO ENHANCE LOW CLOUDS AND DELINEATE PRECIPITATION. A. D. Fox,* S. W. Lyons and G. W. Rainey, Pacific Missile Test Center, Point Mugu, Calif.

By processing visual and infrared images together on a satellite image display system, enhancements have been developed which delineate convective, rain-producing clouds, and which on a single image, also separately delineate coastal California low stratus and fog from higher stratocumulus. The technique applies a brightness correction to visual image pixels, then thresholds both visual and infrared images to distinguish between operationally significant categories of rain or low cloud types. The technique is being tested for use in an operational forecasting environment.

9.1 WIDE SWATH RADAR ALTIMETRY: TOPOGRAPHIC MAPPING SYSTEMS OF THE FUTURE. Chester Parsons, NASA/GSFC, Greenbelt, Md. (Invited Paper)

Satellite microwave altimetry is an established remote sensing discipline having a history dating back to the S-193 instrument on SKYLAB. The family of successful radar altimeter missions also includes systems on GEOS-3, SEASAT, and GEOSAT. In the next few years, additional instruments based on this technological heritage will be placed in earth orbit through the TOPEX/POSEIDON and ERS-1 satellite missions. These altimeters all are capable of profiling the ocean's topography along a narrow ground-track at the satellite's nadir. Following TOPEX/POSEIDON, advanced altimeters are being studied that will produce topographic profiles over an extended swath width. In this paper, the characteristics of an aircraft multibeam radar altimeter under development are reviewed. Also, some scientific and

engineering justifications for the new wide swath measurement capability are discussed. The enhanced spatial-temporal resolution resulting from surface topography measurements over an area 100-200 km wide enables the accurate tracking with time of the growth, translation, and decay of mesoscale features such as eddies, major current meanders, and fronts. If the instantaneous field-of-view of the new altimeters includes a surface area in advance of the satellite's ground position, then changes in the surface topography ahead of the nadir spot can be detected and adaptive tracking techniques can be employed to optimize the radar's tracking performance, and knowing the topography over an extended area enables the measurement of the curvature of the surface rather than its slope. The curvature information is shown to be related to the vorticity of the ocean, a parameter of unique importance to physical oceanography. Knowledge of the vorticity is crucial to the inference of momentum and energy sources and sinks within an ocean circulation. And, the curvature measurement diminishes the importance of orbital and platform attitude uncertainties. Hence, a wide swath altimeter is an attractive instrument system for deployment on some of the large space platforms of the future, such as the Earth Observing System.

9.2 TIROS-N MULTICHANNEL SEA SURFACE TEMPERATURE ANALYSES FIELDS FOR THE FGGE PERIOD.

Ziauddin Ahmad,* Jordan L. Sutton and Alan Strong, ST Systems Corp., Lanham, Md.

Satellite data from the TIROS-N AVHRR instrument was reprocessed for the FGGE period using a multichannel (dual window) sea surface temperature (SST) algorithm. Noise filters were developed to reduce noise in the 3.7 μm window channel (channel 3) and separate retrieval algorithms were used for the daytime (solar zenith angle $\leq$ 75 degrees) and the nighttime (solar zenith angle > 75 degrees) measurements. Following the initial data reduction, a monthly mean SST analysis was obtained by grouping the data into 2.5 degree latitude by 2.5 degree longitude grids for each month of 1979. Monthly mean difference fields of satellite SST vs. climatology, multichannel SST vs. GOSSTCOMP SST, and the standard deviation of the multichannel measurements within each grid were examined. In addition, month-to-month changes in satellite and climatological SST as well as daytime vs. nighttime retrievals were also studied.

One of the most notable improvements of the multichannel fields is more accurate and defined coverage in high gradient areas such as the Gulf Stream, Somali current, Falkland current, and Kuro Shio current. In the western Atlantic, multichannel SST comparisons to climatology are much more realistic than the GOSSTCOMP vs. climatology.

J3.12 A SYSTEM FOR GOES RECEPTION AND PROCESSING IN PERU. P. D. Erickson, L. Laba and L. W. Diehl, MacDonald Dettwiler and Associates Ltd., Richmond, B.C., Canada

Peruvian agencies are interested in economic means of expanding their current environmental data collection network. The data are for use in a variety of applications such as oceanography, meteorology, hydrology, geophysical studies, land resources management and the fisheries industry. To meet Peru's requirement for frequent and timely coverage over large geographic areas, a real-time satellite data reception and processing system has recently been installed at the Ancon Observatory of the Geophysical Institute of Peru. The system can receive, process and store complete AAA GOES images and data collection platform information. Using a powerful PC-compatible workstation with an advanced man-machine interface, operators can schedule satellite receptions and control all aspects of product generation. Additional interactive processing for multi-channel monochrome and color image display, image enhancement, zoom, pan, and scroll, latitude/longitude cursor location, basemap overlay, animation sequencing and data collection platform reporting is available.

J3.6

Published in the Preprint Vols., Joint Session of the 4th Intl. Conf. on Interactive and Information Processing Systems for Meteorology, Oceanography and Hydrology and the 3rd Conf. on Satellite Meteorology and Oceanography, Feb.1-5, 1988, Anaheim, Calif., by the American Meteorological Society, Boston, Mass.

A PC-BASED INTERACTIVE GRAPHICS SYSTEM TO PERFORM SATELLITE-DERIVED OCEANOGRAPHIC THERMAL ANALYSIS

Marcia Weaks, Kim Buttleman and W. B. Campbell

National Environmental Satellite, Data and Information Service
Satellite Services Division
Camp Springs, Maryland 20746

1. INTRODUCTION

Oceanographers in the Satellite Services Division (SSD), within the National Environmental Satellite and Data Information Service (NESDIS), have begun a project to improve upon manual methods of ocean feature and isotherm delineation by using a combination of automated and interactive computer techniques. This paper will describe the evolution of the PC-based system which was chosen for the project, and the development of interactive methodology for oceanographic analysis.

2. BACKGROUND

2.1 Current Technology

Presently, oceanographers in the National Ocean Service (NOS) and the National Weather Service (NWS) within the National Oceanic and Atmospheric Administration (NOAA) derive oceanographic information for operational analyses of the Gulf Stream and the Gulf of Mexico using manual methods. These methods have been in place since 1975. An example of one of the analyses is shown in Figure 1. Input to the process are unmapped hard copy channel four (10.5 - 11.5 micrometers) imagery of the Advanced Very High Resolution Radiometer (AVHRR) on the NOAA-N series of polar orbiting spacecraft (Schwalb, 1982). These images provide coverage of an approximately 2000 x 2000 km area at approximately one kilometer spatial resolution at nadir. A grey scale enhancement curve is used to portray cloud, land and water features. Due to periodic changes in the AVHRR calibration, this curve is usually modified seasonally. The output process used in SSD provides a 16 grey shade display.

The analyst identifies ocean features by locating gradients in the gray scale images. Aided by the existence of visual landmarks, plastic grid overlays are used to geolocate the ocean feature locations which are then transferred visually to a Mercator base chart. Location of ocean features are compiled from many images, some from more than four days prior to the analysis. The complete analysis is prepared using a "best guess" position, which is based on analyst experience. Sea surface temperature (SST) information from satellite retrievals, drifting buoys and expendable bathythermographs (XBTs) are plotted as water mass temperatures (Clark, personal communication).

Contour charts of Great Lakes surface temperatures are produced using atmospherically corrected SST information output in alphanumeric computer printouts. These data are gridded, but not mapped, and must be hand contoured. The contour information is visually transferred to a base map. Often the contour charts are produced using only one data set (image).

These manual methods are subject to a number of sources of error. Geolocation inaccuracies may result from satellite navigational errors, geometric distortion of the imagery, and lack of visible geographic reference points due to cloud cover or boundaries of the area analyzed. Cloud cover may also mask large areas of ocean, and other atmospheric effects may substantially effect the interpretation of gradient information. The analysis is subject to the degree of experience of a particular analyst, as well as his familiarity with the recent history of the area. The procedures are also tedious and time consumptive. Clearly, there was a need to standardize and optimize the analysis function.

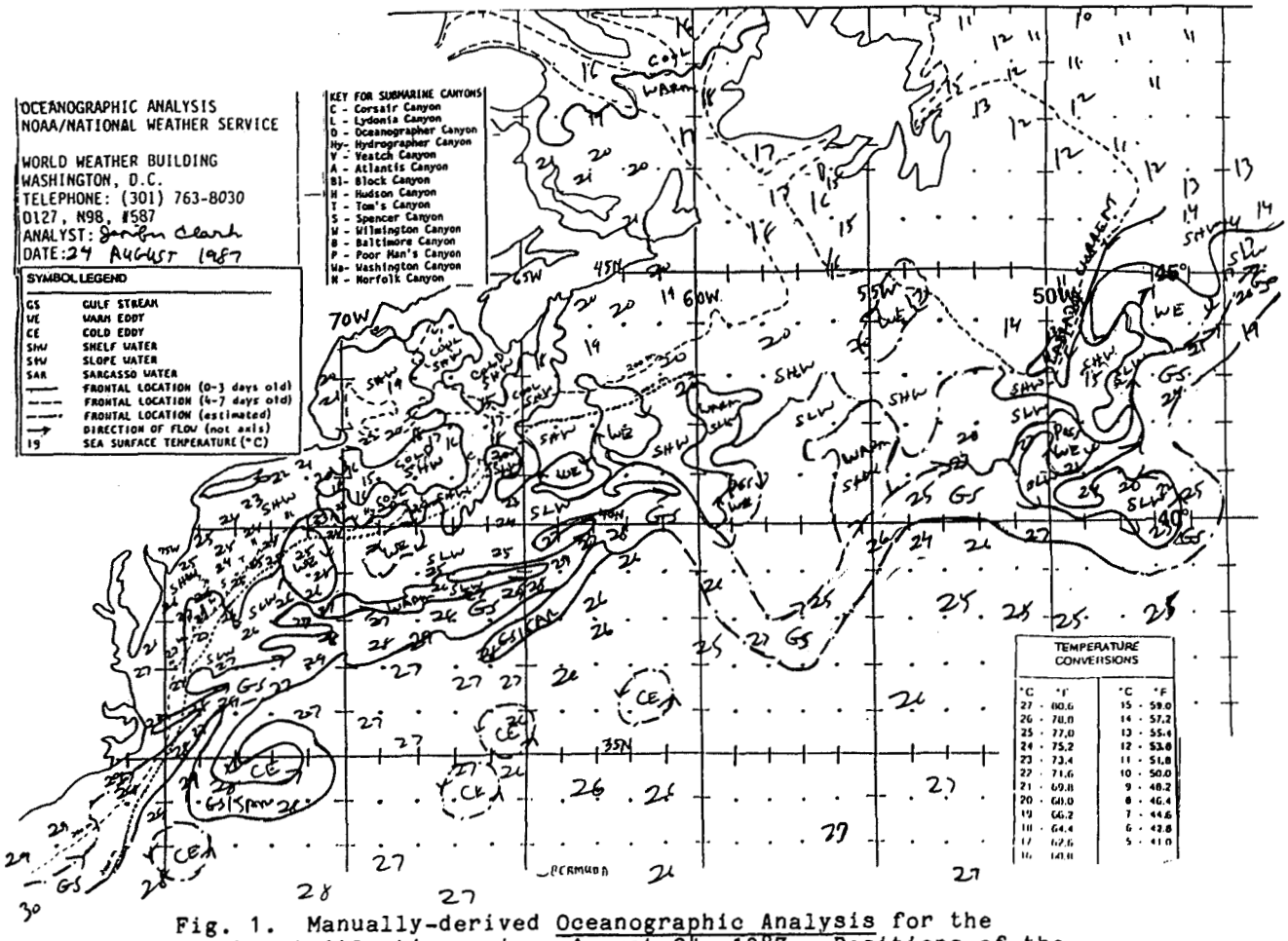

Fig. 1. Manually-derived Oceanographic Analysis for the northwest Atlantic region, August 24, 1987. Positions of the Gulf Stream current, shelf/slope front, and warm and cold eddies are shown. Except for water mass temperatures, positional information is derived primarily from AVHRR HRPT channel four imagery.

2.2 Project Philosophy

Automated computer techniques offer the ability to standardize many of the analysis functions which are subject to error, particularly regarding the preparation of satellite data for use in oceanographic analysis. In addition, interactive computer techniques offer the analyst a powerful set of tools for manipulation of satellite image data in deriving oceanographic information. With this goal in mind, SSD oceanographers surveyed the available hardware and software for application to this project.

Several computer systems already in place within NOAA and others commercially available were considered for the baseline configuration. The IBM Personal Computer (PC) was chosen for development of the interactive portion of the system because it is a relatively inexpensive and widely available system, it is well supported, and many relatively cheap and high quality peripherals and software packages are available for it. The PC can be thought of as a "workstation," where an image is interactively analyzed, collated with other images, and the final analysis prepared.

Since the PC-AT version is presently incapable of many of the satellite image processing functions required in the project, and it has a limited storage capacity, the NOAA "mainframe" computer served as the "preprocessor" and data storage device. Only High Resolution Picture Transmission (HRPT) and Local Area Coverage (LAC) AVHRR digital data was used in the project although incorporation of GOES digital data and sea truth data sets has begun. Figure 2 illustrates the present configuration of the PC/mainframe system, including dissemination capabilities.

Although the project emphasizes development of interactive techniques for oceanographic analysis, another important aspect has been the definition of the hardware and software configuration for an operational oceanographic analysis system. The operational configuration will include many feature of the system described above, and will eventually reside in the NOS/NWS/NESDIS Ocean Products Center, located in Camp Springs, Maryland.

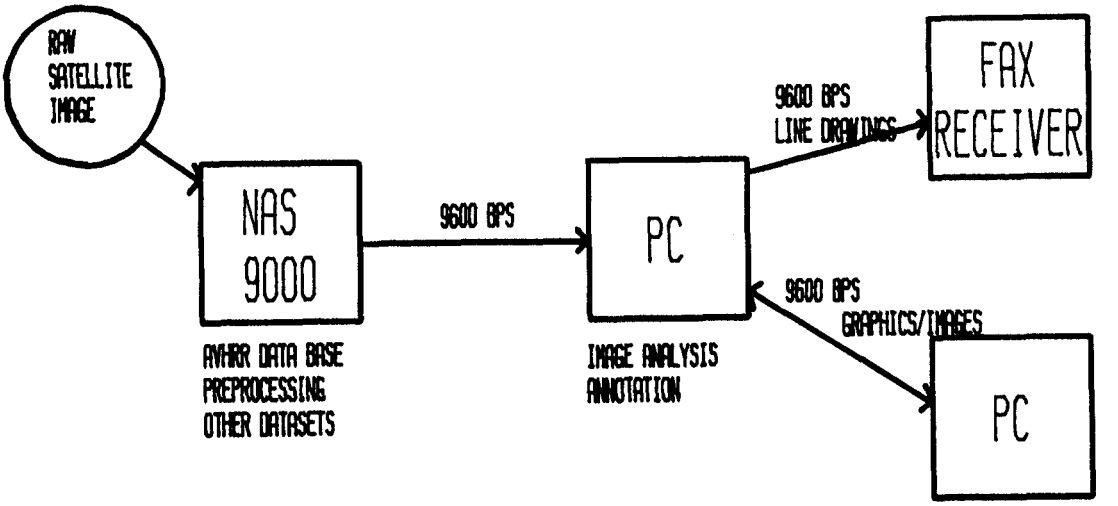

Fig. 2. Communications and product dissemination with the PC image display and analysis system. Processed scenes are received from the NWS/NESDIS computer via up to 56 kbs binary file transfer. Product distribution as shown has been tested for local users only.

3. PC HARDWARE

Hardware components of the PC system include a PC AT with 640 KB of RAM, a 20 MB hard disk, 1.2 MB and 360 KB floppy disk drives, a Number Nine Computer Corporation Revolution 512x32 bit graphics board, a high resolution color monitor, and a color monitor equipped with a color graphics adapter (CGA). The Number Nine graphics board cursor is controlled through a Microsoft mouse or keyboard arrow keys. Hard copy output is provided by an Epson FX100 dot matrix printer or an HP 7475A plotter. Facsimile output is available using a Gammalink board. Communications capabilities are provided by a Hayes 2400 bps modem as well as an IRMA 3278 emulator board.

4. PREPROCESSING COMPONENTS

4.1 Image Preparation

The satellite data used in this project was obtained from the AVHRR data base which resides on the NOAA mainframe computer. This data base is organized as a fixed-sized queue which is continually updated, allowing selection from among approximately forty individual HRPT and LAC data sets. Each data set have a residence time of approximately 24 hours.

A set programs was written to automatically select a HRPT/LAC scene from the data base, based on the desired area of coverage; or, allow for user selectable spatial resolution and center point of the desired ocean area. These routines calculate black body temperatures for the thermal channels, and counts for the visible channels. Sea surface temperatures are calculated using the multichannel atmospheric corrections developed by McClain (1981). Other options are available to map each channel into standard projections such as Mercator and to composite images with previous ones (mapped data only). The mapping routine includes an average or adjacent pixel "fill" procedure.

The processed thermal, visible and SST information is produced in a specific image file format - 512x512 byte x 16 bits. Image information is preserved in eleven bits, while coastlines, latitude and longitude grids and other graphic information is available in the remaining five bits. Also available is housekeeping (header) information for the image files and satellite illumination angle information for each pixel. More infomation on the preprocessing ("SSTMAP") software is available from Tadepalli (1986).

4.2 Image QC

After the preprocessing is completed, the quality of each image file can be checked by using a program which transfers the center portion of the image file of interest as alphanumeric characters to a CRT screen or high speed printer. Statistics are calculated which indicate the average, minimum and maximum image value, and the frequency of occurrence of a particular value. The complete image file, with embedded grids and coastlines, can also be transferred to a printer as alphanumeric characters for subsequent isotherm analysis.

5. TRANSFER TO THE PC

To transfer the image and graphic files to the PC hard disk, two modes are available, one using binary file transfer via commercially available communications (IRMA) software, and the other using ASCII character transfer via an asynchronous modem. At 9600 bps, the binary

file transfer process of a file containing one processed image and the corresponding graphical information takes approximately 20 minutes to transfer; at 56 kbs, the transfer rate is reduced to about 10 minutes. In comparison, the ASCII character transfer, at 1200 bps, takes about two hours. The housekeeping file is appended to each output file prior to transfer.

6. DISPLAY AND ANALYSIS SOFTWARE

6.1 Image Display

A library of FORTRAN callable subroutines for controlling the Number Nine graphics card has been written either in assembly language or C. Programs in this library are used to perform several image display and interactive analysis functions on the PC. To display an image on the high resolution color monitor, the user loads the image data from disk to the Number Nine graphics card through an 11-bit-in, 8-bit-out linear lookup table, which has user-specified temperature bounds. The temperature range thus specified determines the thermal resolution available for image display. For example, 0.1C thermal resolution is displayed by specifying temperature boundaries of 5.0 - 30.6C.

Prior to image analysis, the user may perform histogram equalization on the image. This program effects the displayed image only, leaving the actual temperature data unchanged.

During image analysis, the low resolution color monitor displays two "windows." One shows a menu of options available with the analysis program. These interactive functions include image zoom and roam, pseudocolor temperature slicing or "contouring", graphics and color toggling, and mouse controlled drawing in any of the eight overlay graphics planes. A simple alphanumeric pallet is also available for image annotation. Within the temperature slicing

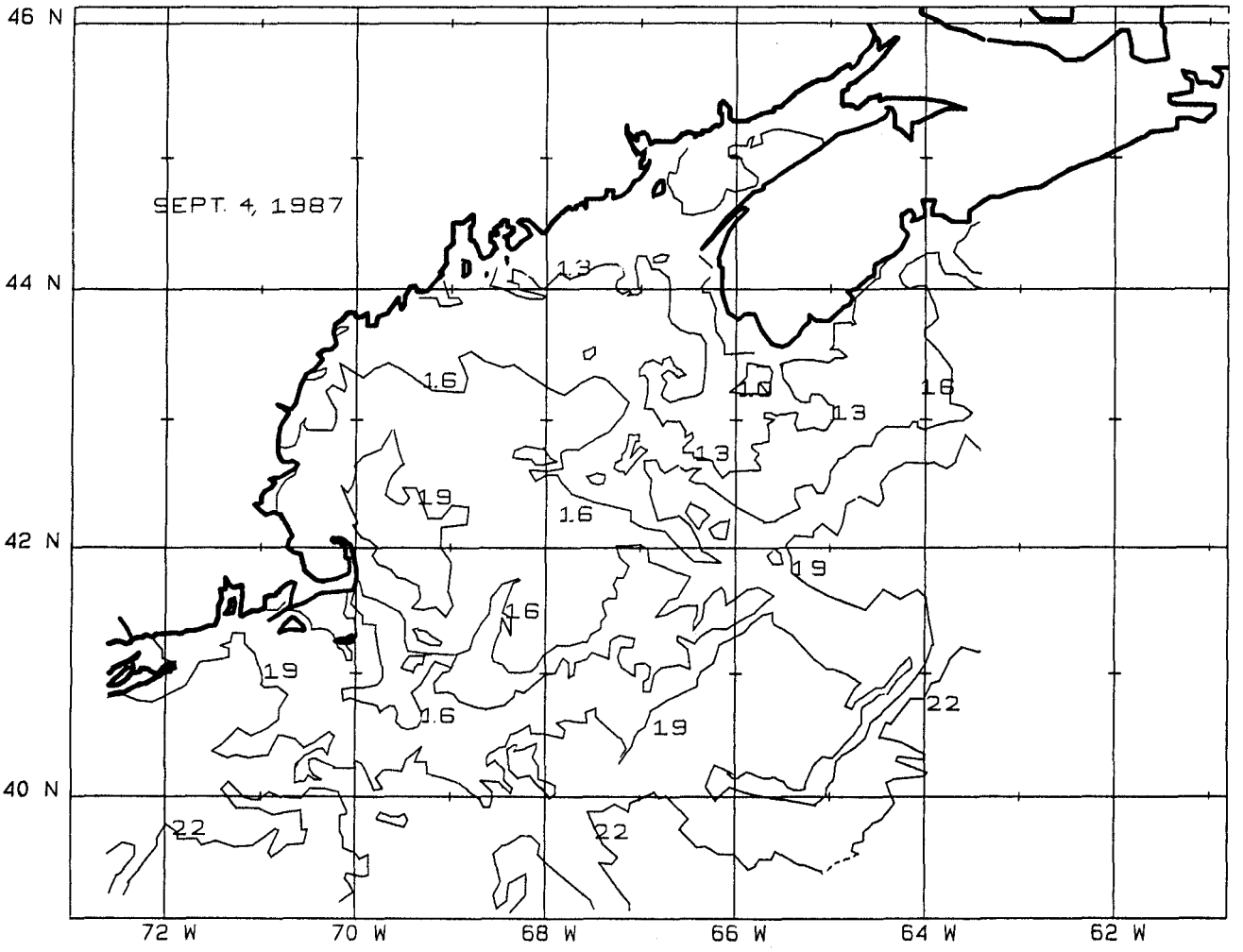

Fig. 3. Plotter output of SST contours in the Gulf of Maine, September 4, 1987. Contours are derived from drawings along individual color temperature "slices" as displayed on a high resolution monitor. Because the analysis was composed of several drawing files from different dates, the contours do not extend to the boundaries of the coastline.

option, the user may select the number of temperature slices, the temperature range of each slice, and the temperature at the warm end of the enhanced slice.

Simultaneously displayed with the analyze window is a "status" window, which describes the overall temperature range and the thermal resolution of the displayed image; the number of contours and their individual and overall range; and information at the cursor location, including temperature, image line and element, and latitude and longitude coordinates.

6.2 Image Analysis

The analyst identifies ocean features or isotherms of interest by highlighting them interactively using a single or series of temperature slices. Because the contour parameters can be adjusted, the analyst has flexibility in identifying features of various temperature ranges within the same image. To assist in the analysis procedure, color contours and graphics planes can be toggled off and on.

Drawings along the color contours are made using the mouse and stored automatically in files as latitude and longitude coordinates. Several drawing files can be placed in different graphics planes and simultaneously or selectively displayed to allow intercomparison (see color plate, next page). Because these files are stored as latitude and longitude coordinate pairs, they are transportable among images of different resolutions, boundaries or times of acquisition. A few examples of this capability include a time series display of drawings or a combination of several higher resolution analyses into one low resolution composite analysis. Oceanographic analyses are then prepared for dissemination by using the annotation capability.

7. PRODUCT DISTRIBUTION

Dissemination of the completed analyses has been tested using several methods. Graphic drawing files can be transferred to other computers via modem or floppy disk, and output as a list of latitude and longitude coordinates. The drawings may be sent to a plotter and drawn onto one of several standard map projections with user specified latitude and longitude boundaries. Thus several drawings may be overlain onto the same chart. An example of the plotted output is shown in Figure 3. Graphic files may be transmitted to facsimile recorders with the aid of the Gammalink board. Also available is a gray scale dot-matrix printer output of the image and/or graphics as displayed on the Number Nine board, Figure 4.

8. DISCUSSION

This PC-based interactive graphics system is still under development. Many of the required hardware and software programs exist, but further testing and integration is required before the system can be considered operational. Some of the outstanding issues include:

A) Modification of the preprocessing programs.

The operational version of this menu-driven program is envisioned to include default values and automated features such as automatic orbit/area and algorithm selection, automatic mapping and possibly, automatic compositing.

B) Integration of preprocessing procedures and PC transfer into an operation.

Currently, a user must initiate the preprocessing procedures separately from the transfer of the processed image to the PC. The current configuration does not support transfer of more than one image at a time, and the overall time for processing and transfer of one SST image may take up to two hours at 9600 bps or about half that at 56 kbs. In an operational environment, the two processes will be integrated and automated.

C) Implementation of cloud/data filtering algorithms.

Analysis of SST images on the PC has shown that cloud and/or data filtering algorithms are necessary, especially when compositing. (Everdale, 1985, contains a complete discussion of AVHRR digital data characteristics regarding use in oceanographic analysis.) These algorithms may be applied automatically or interactively, or by using a combination of both techniques. SSD has begun a development effort to determine appropriate cloud filtering procedures.

D) Determination of appropriate compositing techniques.

To assist in streamlining the analysis operation, compositing procedures may be appropriate. Since compositing tends to smear ephemeral and small scale dynamic features, it may not be appropriate for small scale feature identification over longer time scales. However, identification of small scale dynamic features is important to many user groups. To retain the important features of interest to the user community, several compositing options are under consideration.

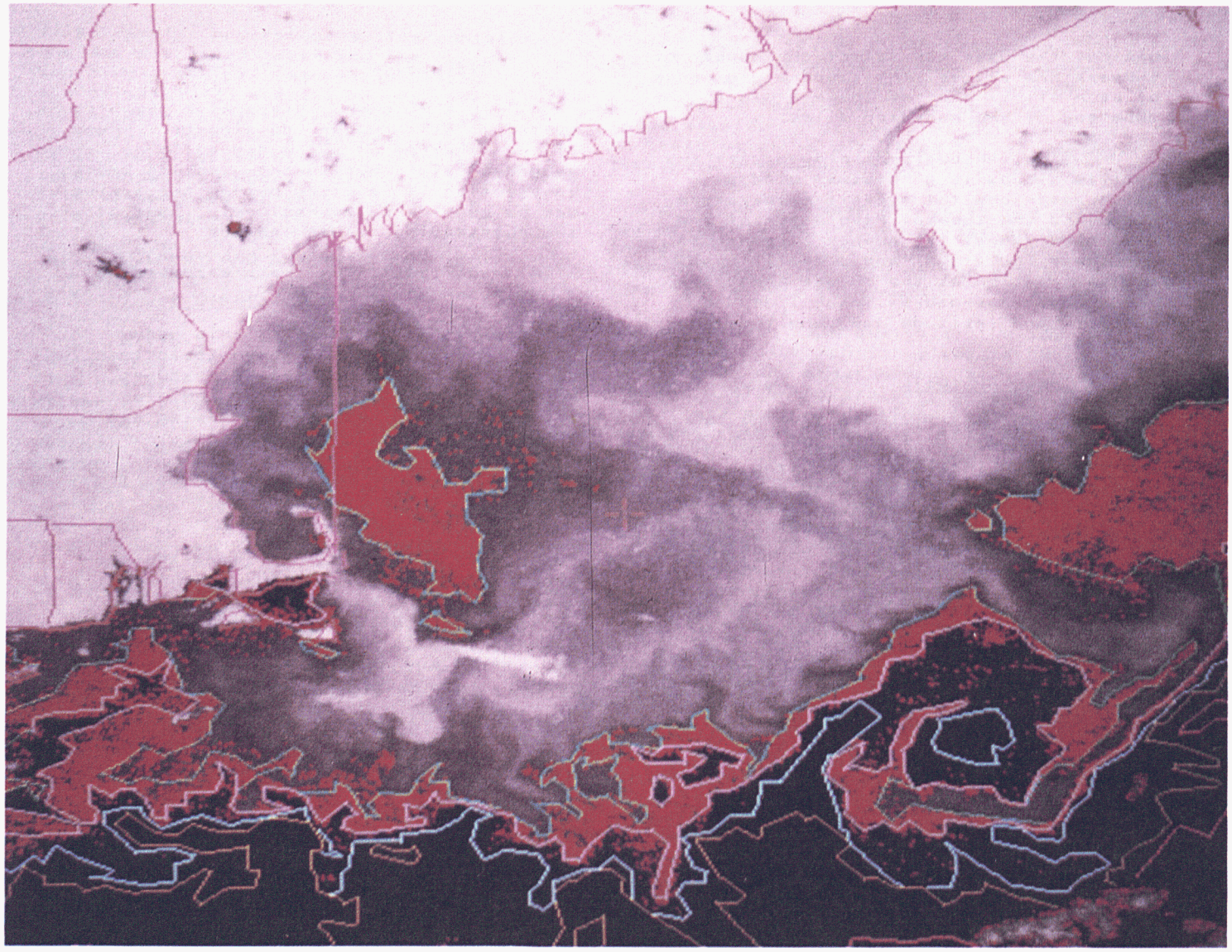

A partial sea surface temperature contour analysis of a September 4, 1987, AVHRR sea surface temperature (SST) image as performed on a IBM PC-AT. The interactive color enhancement program is used to select appropriate temperature "slices", the boundaries of which are traced using the drawing capability. For example, the 22.5-23.2°C temperature range is "painted" in red and outlined in yellow-green. Representing different temperature ranges, three other contours are drawn in white, yellow and pink. The pink vertical line shown east of Cape Cod is an error in the coastline file. Patterns of isotherm locations are apparent when contours are displayed simultaneously.

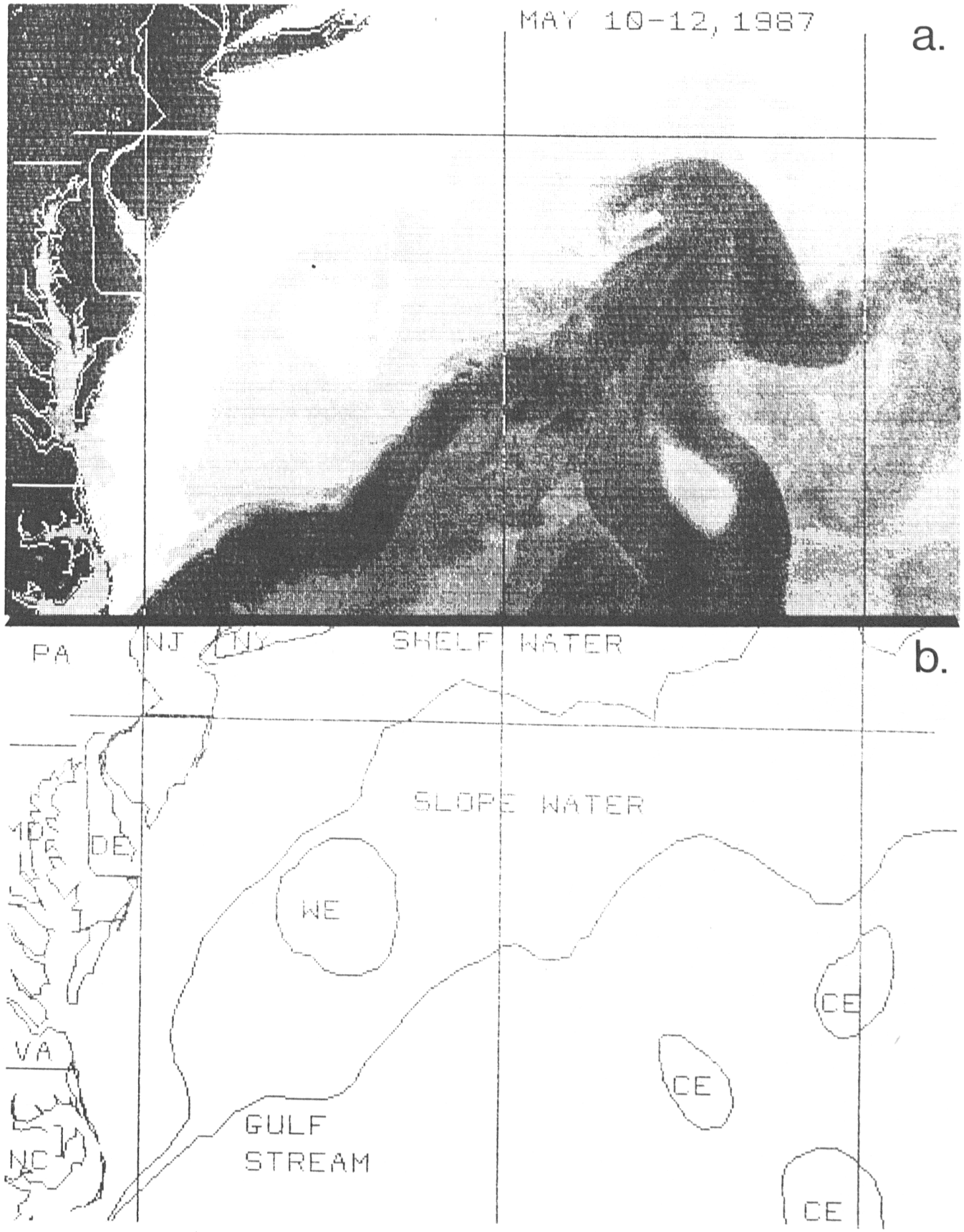

Fig. 4. Dot matrix printer output of the northern Gulf Stream, from a May 10-12, 1987, composite SST image. In (a), a grey scale image of the Gulf Stream, warm and cold eddies and shelf/slope frontal features is shown, while in (b), drawings of these ocean feature locations are shown in graphical form. Both examples are derived directly from the high resolution display of the composite image.

E) Consistent identification of ocean features.

One of the primary goals in implementation of interactive analysis procedures is for consistent identification of the same feature or isotherm from one image to the next. To accomplish this goal, a gradient test for identification of the landward edge (North Wall) of the Gulf Stream is one method under consideration.

F) Integration of image and analysis software into an operational package.

To make the analysis procedures more "user friendly", modifications to the existing programs are required. In addition, several programs need to be added to the system. These include the capability to flicker between two images and to filter or enhance images in various ways. The authors have been working with operational personnel during testing and evaluation of this software, which includes integration into an operational package. To accommodate the additional software capabilities, more hardware may be required. Determination of appropriate software capabilities will help dictate the hardware configuration of the operational system.

G) Determination of appropriate dissemination procedures.

Several output options have been developed for the PC system, many of which are not the traditional forms of dissemination (i.e., mail, telecopier). The OPC is planning for an operational system configuration which minimizes the impact of new technology on users. User input will be solicited prior to operational readiness of the new system.

9. SUMMARY

The purpose of this development project is to improve upon the manual methods of satellite-based oceanographic analysis using a combination of interactive and automated computer techniques. This analysis system is designed to maximize the capabilities of each procedure in order to obtain the best possible oceanographic analysis. A suitable system configuration contains a mainframe computer to perform preprocessing functions, and a PC-class micro-computer to perform image analysis and product generation. Although a basic system has been developed, much testing and evaluation remains before the system can be considered operational.

10. ACKNOWLEDGMENTS

The authors wish to thank the IPB personnel who have contributed to this project, especially Howard Carney (now with NWS) and Dick Garey. Advice and counsel from Ken Barton, NMFS, Fred Everdale and Rick Stumpf, AISC, has been invaluable as well. Finally, many thanks to John Shadid and Zura Hayenga, who helped with the layout.

11. REFERENCES

Everdale, F., 1985: Satellite Oceanography - Volume 1: NOAA-N Advanced Very High Resolution Radiometer Digital Data. NOAA/NESDIS, Assessment and Information Services Ctr., Washington, DC, 63 pp.

McClain, E.P., 1981: Multiple Atmospheric-Window techniques for Satellite-Derived Sea Surface Temperatures. Oceanography from Space, J.F.R. Gower, Ed., Plenum Publishing Corp., New York, 73-85.

Schwalb, A., 1982: The TIROS-N/NOAA A-G Satellite Series. NOAA Tech Memo NESS 95, NOAA/NESDIS, Washington, DC, 20-46.

Tadepalli, K., 1986: Interactive High-Resolution SST and Ocean Feature Analysis. User's Guide and Software Documentation, S M Systems and Research Corp., Landover, Maryland, 165 pp.

VISSR SENSOR INTRODUCED MODIFICATIONS IN THE PRESENCE OF LARGE TEMPERATURE GRADIENTS.

E. V. Cherna, G. L. Austin, A. Bellon and A. Kilambi

McGill Radar Weather Observatory.
Box 241, MacDonald College
Ste. Anne de Bellevue, Quebec,
Canada. H9X 1C0.

1. INTRODUCTION

Since the launch of the meteorological satellite SMS/GOES in 1974, a succession of geostationary satellites have provided a quasi-continuous coverage of the earth disk in both the visible (0.55-0.75μm) and the thermal infrared (IR, 10.5-12.6μm) channels. Cloud top temperature fields, derived from GOES IR images have found applications, alone, or in conjunction with radiances from other spectral regions, in climatology, rainfall estimates and severe storm studies.

Problems peculiar to geostationary satellites arise from the high orbit and the rapid scanning rate. These are manifested by the large field of view (FOV) and by the smoothing of temperature gradients by the finite response time of the IR sensor.

The uncertainties in cloud top temperatures, due to partly filled FOV's have been well documented; local minimum temperatures for example, measured from geostationary altitude, are seriously overestimated (Adler et al., 1983). The unknown cloud filled fractions also account, in part, for the range of temperatures associated with extended features. A number of techniques, summarized by Rossow et al., (1985) have been developed to retrieve cloud type and fractional cloud cover from high orbit measurements. With the exception of spatial coherence method (Coakley and Bretherton, 1982) all these techniques are based on the distribution of radiances in the spectral domain, tacitly assuming that radiances associated with geographic neighbours are essentially independent. Unexplained by FOV considerations alone are the large warm bias found on the upwind anvil edge (Negri and Mack, 1982) and the 30-40K temperature overestimate for small growing storms (Adler et al., 1982). Our thunderstorm studies, from radar, satellite and lightning records, found the spread of IR brightness temperatures associated with thunderstorms excessive, even allowing for the size of the FOV and the viewing angle of the satellite (Wexler, 1983).

Interdependence of neighbouring pixels comes from diffraction, along as well as across scan lines, overlapping FOV's (oversampling) and the finite response time of the IR sensor. Parker et al., (1986) briefly consider response time in conjunction with Landsat data but most texts on remote sensing (Chen, 1985 and Norwood and Lansing, 1983, for example) discuss sensor characteristics under steady state (equilibrium) conditions only.

In view of the rapid data acquisition rate from high orbit the transient response of the IR sensor becomes important in the presence of large temperature gradients. The present study investigates the temperature field retrieved from GOES measurements for evidence of sensor introduced modifications and estimates the response time in the thermal IR channel.

2. THE GOES IR SENSOR

The imaging instrument in early GOES models was a 16 inch aperture scanning telescope, the Visible and Infrared Spin Scan Radiomater (VISSR). The current multichannel Atmospheric Sounder (VAS) has, in the VISSR mode, retained the same imaging characteristics. Sensors for all channels are located in the focal plane of the telescope and view a west to east swath of the earth as the satellite spins at 100 rpm. The IR sensor is a tiny HgCdTe thermistor, radiativey cooled to about 100K. Its area corresponds to an instantaneous FOV of 192 μr by 192 μr (microradians) or 6.9 km by 6.9 km at the satellite subpoint. The IFOV advances at the rate of about 10 $\mu r/(\mu s)^{-1}$, or by 84 μr between successive samplings to give the nominal pixel size of 192 μr by 84 μr. Adjacent scan lines are contiguous with no overlap.

A sensor absorbs radiant energy in a wavelength interval determined by its spectral response function and by external filters. Electron-hole pairs are created by the absorbed photons and depleted by their recombination. As the recombination rate is proportional to the number of electrons in the conduction band (free electrons), equilibrium concentration, in response to a sudden change in irradiation, is reached along a negative exponential, $\exp(-t/\tau)$.

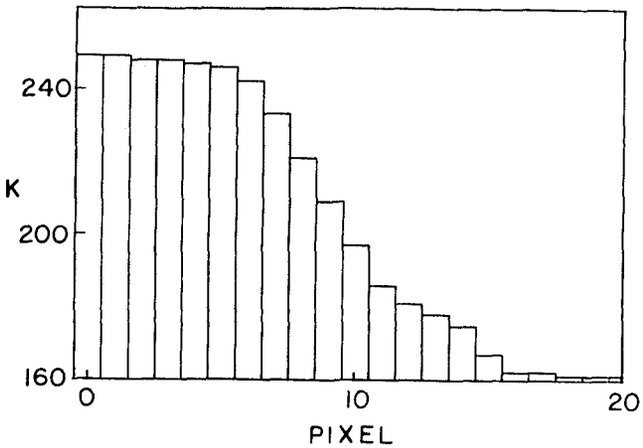

Fig. 1. Pixel by pixel temperatures near the eastern limb.

In the earth-atmosphere system the largest temperature gradients are at the edge of the earth disk. Fig. 1 shows the pixel by pixel variation of the satellite observed temperature T_S along a scan line at 30°N near the eastern limb. In the transition region, between say 250K and 235K, space gradually replaces the atmosphere in the FOV; beyond, T_S decays exponentially with a time constant of about 30 μs. The time constant of the thermistor is, however, likely smaller than the time constant of the system, as estimated from Fig. 1.

3. PARTLY FILLED FOV's

If f_i is the fraction of the FOV filled with cloud at a temperature T_i and emissivity ε_i, radiant energy is absorbed by the sensor at the rate:

$$E_i \propto f_i \varepsilon_i \int_0^\infty E(\lambda, T_i) K(\lambda) d\lambda$$

where $E(\lambda,T)$ is the Planck function and $K(\lambda)$ the spectral response of the sensor. By definition, energy and equivalent black body temperature T_{BB} are related by:

$$E = \sum_i E_i = \int_0^\infty E(\lambda, T_{BB}) K(\lambda) d\lambda$$

In the 200K to 300K range the peak of the Planck function shifts across the absoption band given by $K(\lambda)$ and numerical evaluation of the convolution integral $E(\lambda,T)K(\lambda)d\lambda$ in the interval $10.5\ \mu r < \lambda < 12\ \mu r$ finds that its value is proportional to $T^{5.6}$, that is

$$\sum_i \varepsilon_i f_i T_i^{5.6} = \varepsilon T_{BB}^{5.6}$$

If all T_i's in the FOV are, within say, 20°, the departure from a linear relation is small and

$$\sum_i f_i T_i^{5.6} \sim \sum_i (f_i T_i)^{5.6}$$

and $T_{BB} = \sum_i f_i T_i$, the area (and emissivity) weighted mean temperature in the FOV. In the presence of large temperature gradients T_{BB} is strongly weighted by the warmest temperature in the FOV. This effect is different for positive end negative gradients; in scanning from warm to cold T_{BB} lags, scanning from cold to warm T_{BB} leads the mean temperature in the FOV.

In the wavelength interval given by $K(\lambda)$ the frequency distribution of photon energies is practically independent of temperature hence the $T^{5.6}$ relation applies to the number of incident photons and, with a correction factor for quantum efficiency, to the number of free electrons as well.

Using a conservative estimate of 20 μs for the time constant and the postulated relation between T_{BB} and the number of free electrons we have calculated detector response to an ideal, infinite temperature gradient, a change from 280 K to 220 K, along the scan line with the assumption that the gradient extends over the entire width of the scan line.

Fig. 2a shows the variations of the mean temperature $\overline{T}$ and of T_{BB} with time as the FOV sweeps eastwards. The transition region is 192 μr wide for the infinite gradient, and is wider for more realistic cases. Fig. 2b shows the percent variation of the number of free electrons with time, calculated in time steps of 1 μs; 100% corresponds to the equilibrium concentration at 280 K, and 26% corresponds to the equilibrium concentration at 220 K. Fig. 2c is the variation of the satellite measured temperature as calculated from Fig. 2b. Pixel by pixel temperatures are retrieved stepwise from Fig. 2c, while these depend on the relative position of the gradient and pixel boundaries they agree well with Fig. 1.

We note that the convex part of the temperature graph corresponds to partly filled FOV's and its width depends on the width of the transition region, the point of inflexion of the graph occurs as T_{COLD} just fills the FOV.

Sensor introduced modifications of the temperature field occur near cloud boundaries; the fraction of affected pixels depends on the size of the feature considered and may be disregarded for larger systems (Bellon et al., 1980). For small features, broken clouds or developing thunderstorms for example, the mean temperature in the FOV increases long before the concentration of free electrons has reached its T_{COLD} equilibrium value. In such cases cloud top temperatures may be overestimated by 20-40° even if the cold top is large enough to fill the FOV for a short time.

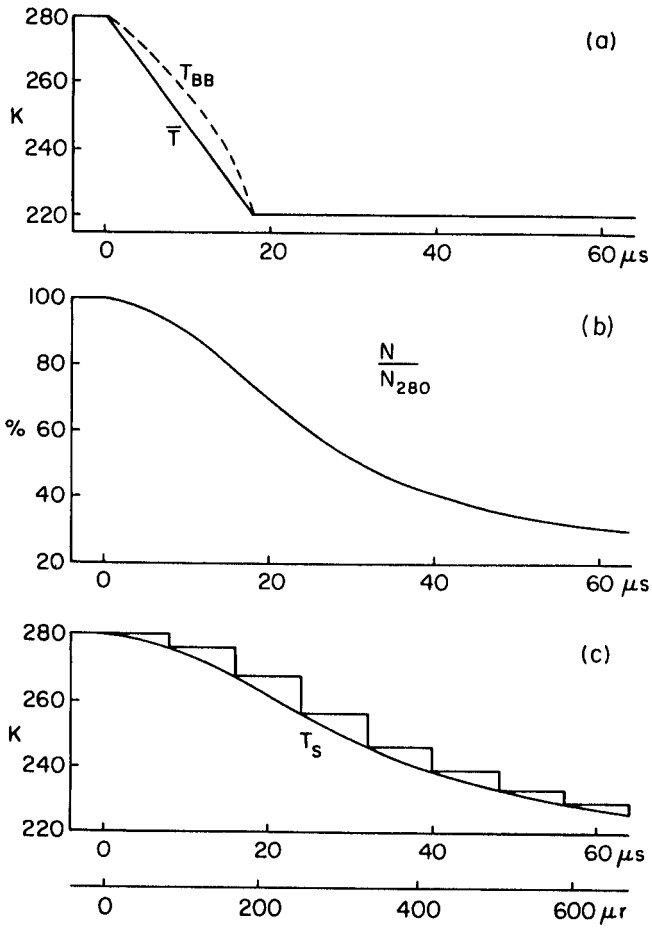

Fig. 2. Sensor response calculated relative to a 60 K gradient:
a) Mean and equivalent black body temparatures.
b) The fraction of free electrons.
c) The corresponding, sensor-indicated, temperature.

Figs. 1 and 2c also indicate that the lowest observed temperature may be offset by 5 to 10 pixels from its geographical location. An analogous, but much smaller offset of 1 to 3 pixels is also found in the visible channel. The different offsets introduce registration problems in the bispectral data and may contribute significantly to the breadth of multispectral histograms.

4. INTERDEPENDENCE OF NEARBY PIXELS

Instrument response is usually evaluated relative to a known, and ideally a square wave input. In the earth-atmosphere system neither the temperature gradients nor their exact location is certain. Sensor response to large gradients must be found indirectly from the observed temperature differences between neighbouring pixels. The statistics are based on the premise that the largest observed differences correspond to the largest actual gradients, located, fortuitously, near pixel boundaries.

We have calculated the temperature differences between neighbouring pixels, both along a scan line and across successive scan lines on 25 GOES IR maps of 512 pixels by 120 scan lines each; a window between 38°N and 48°N latitude, extending from the Great Lakes to the Atlantic Ocean. All data come from two thunderstorm days, May 29, 1986 and June 16, 1986. In each instance the warmest and the coldest temperatures were within two degrees of 298 K and 211 K.

If $P_{j,i}$ is one of the pixels with an equivalent black body temperature T, and if

T_n is the T_{BB} of pixel $P(j+n,i)$ and

T_k is the T_{BB} of pixel $P(j,i+k)$

we set

$\Delta T_n = T - T_n$, associated with T along a scan line and

$\Delta T_k = T - T_k$, associated with T across k scan lines.

If T_{MAX} and T_{MIN} are the warmest and the coldest temperatures on a map, then

$\Delta T_{MAX} = T_{MAX} - T$ and

$\Delta T_{MIN} = T_{MIN} - T$

are the largest possible positive and negative ΔT's associated with T.

In a statistically significant sample of independent pixels we expect that for nearly every temperature T, the largest of all observed ΔT's, $(\Delta T_n)_{MAX}$ along or across scan lines, will equal ΔT_{MAX} and the smallest (the largest negative) of all observed ΔT's $(\Delta T_n)_{MIN}$ will equal to ΔT_{MIN}; at least for a range of temperature differences that represent physically likely gradients. Over this range the plot of $(\Delta T_n)_{MAX}$ vs. ΔT_{MAX} or of $(\Delta T_n)_{MIN}$ vs. ΔT_{MIN} will have unit slope for any "n" or "k". In fact, the departure from unit slope is a reasonable measure of the interdependence of neighbouring pixels.

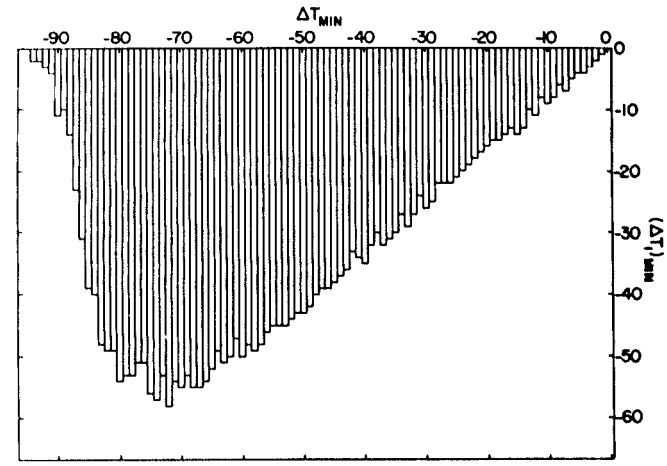

Fig. 3. The largest observed negative temperature difference between adjacent pixels in subsequent scan lines plotted against its possible largest value for every T.

For quantitative comparisons we define the slope of the plot as the slope of the regression line fitted to points $10 < |\Delta T| < 40$. This is an arbitrary, albeit reasonable range; it disregards small differences where interdependence would fail to modify the temperatures and it omits unreasonably large, unlikely ΔT's.

In Fig. 3 the largest negative ΔT_k's are plotted against the corresponding ΔT_{MIN}'s for k = 1. The slope of the plot is 0.84 indicating that the largest observed negative north to south gradients are about 16% smaller than possible. As observations in successive scan lines are separated by one revolution of the satellite and as there is no evidence of oversampling across scan lines, we attribute this modifications of the gradients to diffraction effects; to contributions of radiant energy from outside the pixel. A similar plot, but for k = 2, has a slope of 0.98 indicating that pixels separated by one scan line represent independent data.

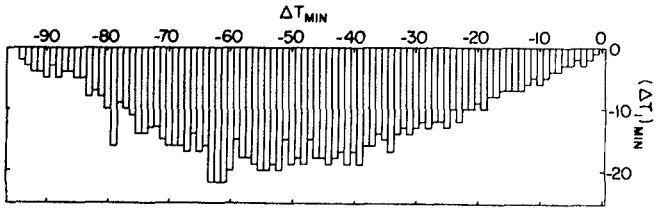

Fig. 4. Same as Fig. 3, but for adjacent pixels along the same scan line.

The above two slopes serve as reference values for analogous slopes along the scan line (n > 1), where the significant temperature modifications take place. Fig. 4 is similar to Fig. 3, but is for the largest negative ΔT's found between adjacent pixels (n = 1) in the same scan line. The difference between the two figures is evident and substantial. The regression line fitted to Fig. 4 has a slope of 0.36, a value interpreted as an indication that the largest west-to-east temperature gradients reach only 36% of their possible value.

For increasing pixel separation (increasing values of n) the slopes of the regression lines increase rapidly. The variation of the slope with n is plotted in Fig. 5 for both positive and negative ΔT's. The initial rapid increase reflects the decreasing importance of the large IFOV; data for every third pixel comes from independent FOV's. For n > 3 Fig. 5 shows that the finite sensor response extends the effective FOV over about seven pixels (22 km) with a weighting that varies inversely with distance.

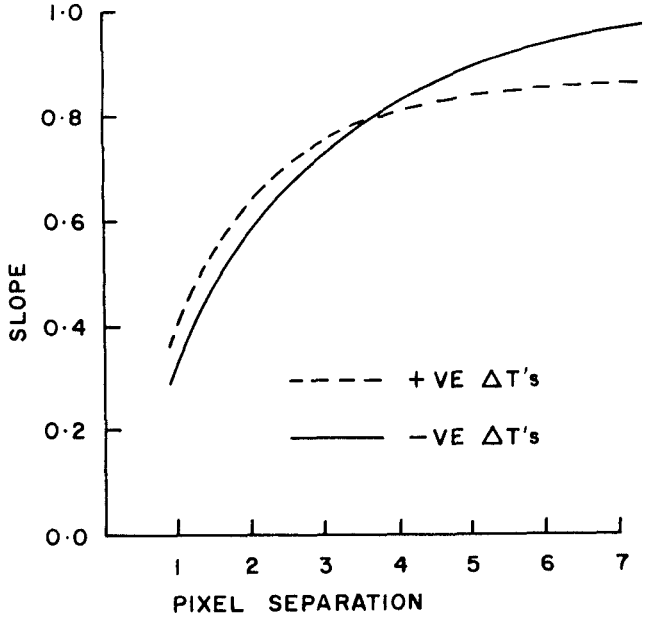

Fig. 5. Variation of the slope with increasing pixel separation.

Positive and negative temperature gradients are similarly rendered by the sensor for small n's; for larger separations however the positive gradients tend to a lower limiting value. In our interpretation this is a physical rather than an instrumental difference. The largest gradients most probably occur at the boundaries of thunderstorm anvils; the negative gradients, on the upwind side, are usually the greater.

5. Conclusions

Examination of GOES East IR data indicates that the response time of the IR sensor is about 20 μs, large compared to the 8 μs sampling interval. In consequence large temperature gradients are stretched over several IR pixels modifying the brightness temperature of these pixels and affecting the registration of diverse spectral bands. Fig. 2 indicates that the equivalent black body temperature may be overestimated by 40° for features of a size comparable to the IFOV. Considering a pixel in the context of neighbouring temperature gradients gives the best estimate of sensor introduced temperature modifications. While small gradients do not necessarily indicate the absence of modifications as FOV effects tend to smooth gradients large gradients point to the sensor operating far from equilibrium conditions. The most severe modifications occur in cases of small local minima or maxima where the gradients along the scan line are large on both sides of the pixel.

REFERENCES

Adler, R.F., M.J. Marcus, D.D. Fenn, G. Szejwach and W.E. Shenk: Thunderstorm Top Structure Observed by Aircraft Overflights with an Infrared Radiometer. J. Clim. App. Meteor., 1983, 22, 579-593.

Bellon, A., S. Lovejoy and G.L. Austin: Combining Satellite and Radar Data for the Short-Range Forecasting of Precipitation. Mon. Weather Rev., 1980, 108, 1554-1566.

Chen, H.S.: Space Remote Sensing Systems. Academic Press, Inc. 1985, 33-50.

Coakley, J.A. and F.P. Bretherton: Cloud Cover from High Resolution Scanner Data. Detecting and Allowing for Partially Filled Fields of View. J. Geophys. Res., 1982, 87, 4917-4932.

Negri, A.J. and R. Mack: Satellite Infrared, Stereo and Radar Observations of Tornadic Thunderstorms on April 10, 1979. Proceeding of the 12th Conference on Severe Local Storms. San Antonio, Texas, 1982. 164-167.

Norwood, V.T. and J.C. Lansing, Jr.: Electro-Optical Imaging Sensors. In "Manual of Remote Sensing". (R.N. Colwell ed.) The Sheridan Press, 1983.

Parker, L., R.M. Welch and D.J. Musil: Analysis of Spatial Inhomogeneities in Cumulus Clouds Using High Spatial Resolution Landsat Data. J. Clim. App. Meteor., 1986, 25, 1301-1314.

Rossow, W.B., F. Mosher, E. Kinsella, A. Arking, M. Desbois, E. Harrison, P. Minnis, E. Ruprecht, G. Seze, C. Simmer and E. Smith: ISCCP Cloud Algorithm Intercomparison. J. Clim. App. Meteor., 1985, 24, 877-903.

Wexler, R.: The Variaton of the Mean Temperature of an Overshooting Top with Angle of View from a Satellite. J. Clim. App. Meteor., 1983, 22, 1468-1471.

OPERATIONAL CALIBRATION OF THE METEOSAT IR CHANNEL USING SEA SURFACE TEMPERATURE OBSERVATIONS

Volker Gaertner

European Space Operations Centre (ESOC)
Darmstadt, West Germany

1. INTRODUCTION

At the European Space Operations Centre (ESOC) in Darmstadt the Meteosat Operational Programme (MOP) is conducted. One important aspect of this programme is the derivation of operational meteorological products from Meteosat image data. The products are:

Sea Surface Temperatures
Cloud Analysis
Cloud Top Height Maps
Cloud Motion Vectors
Upper Tropospheric Humidities

The quantitative exploitation of the Meteosat images is being performed in the Meteorological Information Extraction Centre (MIEC). For this purpose all three spectral channels are used. The channels are:

Visible	channel	(VIS / 0.5 - 0.9 µm)
Water Vapour	channel	(WV / 5.7 - 7.1 µm)
Infrared	channel	(IR /10.5 -12.5 µm)

To derive meteorological products from these image data an operational calibration has to be performed for the water vapour and the infrared channel. Because Meteosat is a spinning satellite, no absolute calibration using a reference black body is feasible. The calibration has to be monitored on a day by day basis as the variation in the internal temperatures of the detectors and the optics within the satellite may vary on this scale and on the longer time scales the contamination of the IR and WV detectors by the ice crystals also contribute to a loss of sensitivity for the received radiance. Therefore at ESOC the Meteosat team has developed methods which allow to monitor and calibrate the WV and the IR channels. The method of the WV calibration is described in a paper of Schmetz/Turpeinen (1988) while the calibration of the IR channel is the scope of this article.

2. OPERATIONAL DERIVATION OF METEOSAT SEA SURFACE TEMPERATURE

To operationally exploit the Meteosat images the whole image is divided into image segments which consist of 32 x 32 image pixels where a pixel is the smallest resolvable image unit (5 x 5 km^2 at the region of the subsatellite point). To identify different physical sources of radiation within an image segment a two dimensional histogram analysis is performed for all segments within the 55 degree great circle arc around the subsatellite point (about 3500 segments). All pixels, which are assigned to the same source of radiation, are grouped together to form a so called 'cluster' for which an average radiance and the standard deviation is specified. For the product derivation the IR radiances are most important and in its basic form the sea surface temperature (SST) product is a direct output of the segment processing analysis.

For any cluster identified as sea it is only necessary to correct the measured radiance for atmospheric absorption before converting the radiance to a temperature using the Planck relationship. These results are produced every three hours for each segment where the sea is visible from geostationary orbit although the results are only made available to the user twice per day. The data distributed to the user are a weighted mean of the results over the last 36 hours and the end result of an automatic and manual quality control scheme applied to the data.

For atmospheric correction an operational fast radiative transfer scheme has been developed at ESOC (Schmetz, 1986) which uses the input data from the European Centre for Medium Range Weather Forecast (ECMWF) to determine for every segment the amount of correction which has to be added to the derived temperatures. In figure 1 for the 6th of October 1987 the atmospheric corrections for the 22 Z SST product are plotted against latitude. It can be seen that the average atmospheric correction varies between 2 and 12 K where the highest values are found for moist tropical regions.

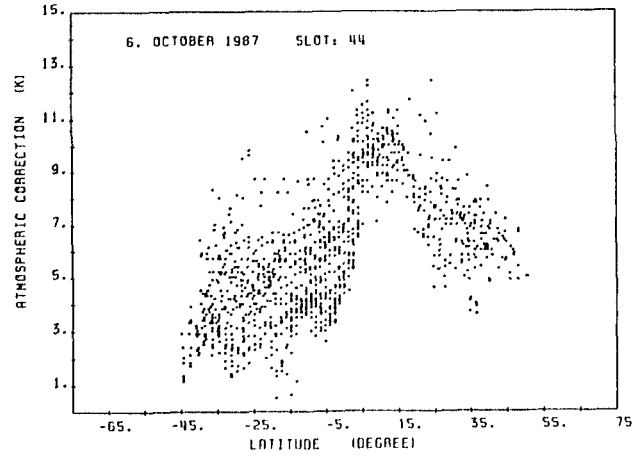

Fig. 1. Atmospheric correction against latitude for SST segments for 6 October 1987 at 22 Z.

The operationally derived SST results for the same date for the Atlantic sector are displayed in figure 2. This plot is a typical example of Meteosat SST results and it shows that for quite a large area of the ocean Meteosat provides SST data.

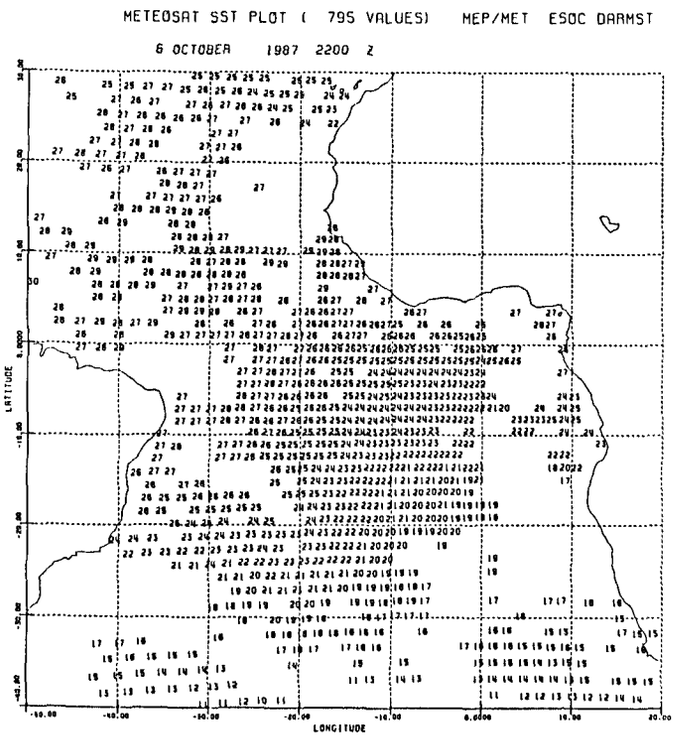

Fig. 2. Meteosat SST results for the Atlantic sector for 6 October 1987 at 22 Z.

3. CALIBRATION OF METEOSAT IR CHANNEL

To calibrate the Meteosat infrared channel the results of the SST derivation for two representative slots close to midday (slot 22) and close to midnight (slot 46) are taken to compare the sea surface temperature readings with conventional SST observations. For these representative slots for all those segments, where sea has been identified and where the total cloud cover is less than a certain threshold, the Meteosat radiances (given in units of digital count rates) are corrected for the effect of attenuatin due to atmospheric absorption. The conventional set of SST observations is operationally received from the National Meteorological Centre (NMC), Washington, via ECMWF. These temperatures are converted to radiances using Planck's law and taking into account the filter function for the Meteosat IR channel:

$$R(T,\lambda) = \int_{\lambda} B(T,\lambda)\ s(\lambda)\ d\lambda$$

where λ - wave length
$R(T,\lambda)$ - Radiance at temperature T
$B(T,\lambda)$ - Black Body radiance according to Planck's law
$s(\lambda)$ - spectral response of the Meteosat IR channel

In figure 3 the relative spectral response function $s(\lambda)$ for the IR channel is shown.

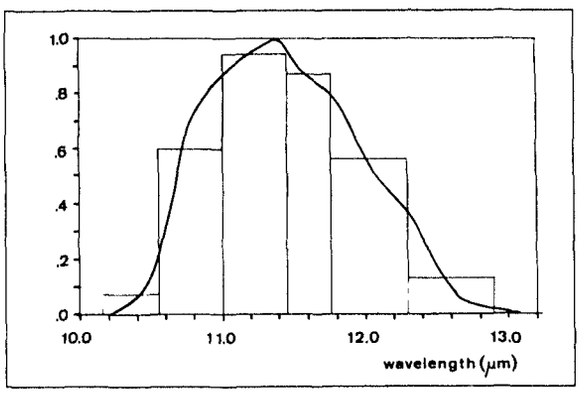

Fig. 3. Relative spectral response function of the Meteosat-2 IR-1 channel and the six spectral bands of the radiation scheme for atmospheric correction calculation.

After having transformed the NMC sea surface observations into radiances they are plotted against the corrected Meteosat SST counts. The calibration slope is determined from that plot to the line which connects the so called 'space count' and the centre of gravity of all displayed points in that scatter plot (see figure 4). The space count is obtained when the radiometer is viewing space (since the beginning of Meteosat-2 lifetime equal to 5).

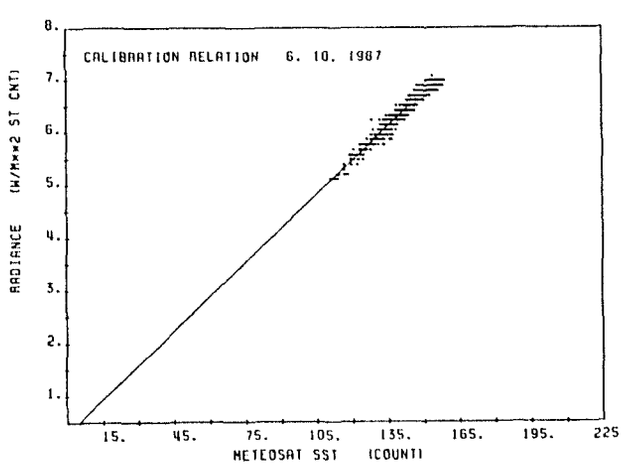

Fig. 4. Calibration relation for Meteosat-2 IR channel for 6 October 1987 (slot 44). The straight line connects the space count and the centre of gravity of the points.

The calibration figure on 6 October 1987 determined from figure 4 was 0.0462 W/(m^2 st cnt). No account is taken for the so called 'skin effect' in radiometric temperature retrieval. This effect results on average in a slightly colder surface temperature derived radiometrically when compared with conventional measurements. An average value of 0.2 degree can be quoted (Grassl (1976), Schluessel (1987)). If this effect had been taken into account, it would have resulted in a calibration coefficient of 0.0461 W/m^2 st cnt) for the above example. Another possible error of the same order of magnitude could result from systematical under- or overestimation of the atmospheric absorption due to the selected parameterization. However, to put the meaning of these deviations in the right perspective, they should be compared with the average RMS error of

about 0.9 degrees which is achieved by the comparison of the Meteosat SST with conventional SST observations, or with the 8-bit digitisation which corresponds to jumps of about 0.5 degrees in the temperature range relevant for sea surfaces.

In figure 5 the history of the derived MIEC IR calibration coefficient for the year 1987 until October 6th is shown. It can be seen that in the beginning of 1987 a dramatic increase in the MIEC calibration coefficient is found which is a result of the contamination of the IR detector. On January 19th the gain setting of the electronics for the IR detector was changed from a value of 9 to a value of 10, which can be clearly seen by the jump on that day. In April 1987, from 21st to 23rd, the detectors were decontaminated which allowed to set the gain afterwards back to a value of 7 from April 23rd (day 113) and later on to a value of 6 (day 132). The decontamination exercise took place immediately after the spring eclipse, and the calibration has since been relatively stable. The calibration coefficient is monitored twice daily, and when the statistical comparison of Meteosat and conventional SST observations shows a bias which exceeds 0.5 degrees an update of the operationally used value is envisaged. The displayed coefficients of figure 5 are just those which would have had to be used to always reduce the bias to zero.

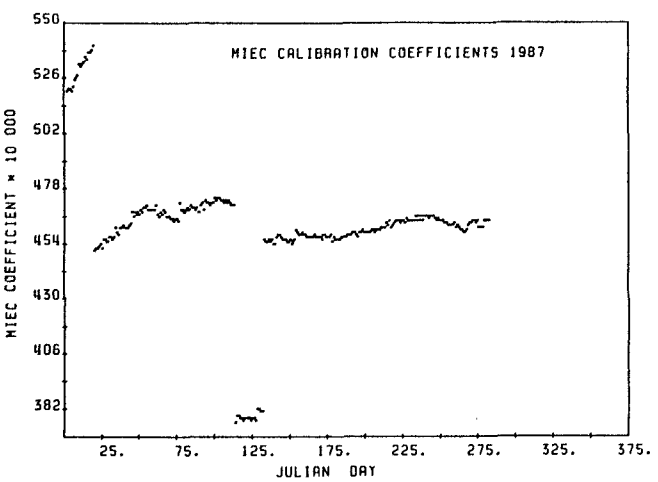

Fig. 5. MIEC IR calibration coefficients which would have reduced the bias between Meteosat and NMC SST observations to zero during 1987.

4. SUMMARY

The operationally applied method of calibrating the Meteosat IR channel provides calibration information on a daily basis. One of the main purposes of retrieving sea surface temperatures from geostationary orbit is just to have the possibility to absolutely calibrate the IR channel of the radiometer. By determining the calibration relation from the two points (space count/centre of gravity) a fairly stable coefficient can be determined which results in reliable SST results from Meteosat.

5. REFERENCES

Grassl H. (1976), The dependence of measured cool skin of the ocean on windstress and total heat flux, Boundary Layer Meteorology, 10, pp 465 - 474.

Schluessel P. (1987), Infraroterkundung von Oberflaechentemperaturen sowie atmosphaerischen Temperatur- und Wasserdampfstrukturen, Berichte aus dem Institut fuer Meereskunde, Nr. 161, Kiel.

Schmetz J., Turpeinen O. (1988), Estimation of the upper tropospheric relative humidity field from Meteosat water vapour image data, (submitted to JCAM)

Schmetz J. (1986), An atmospheric-correction scheme for operational application to Meteosat infrared measurements, ESA Journal, 10, pp 145 - 159.

AUTOMATIC NAVIGATION FOR METEOROLOGICAL SATELLITES

Robert Pyzalski, David A. Santek, J. T. Young

Space Science and Engineering Center
University of Wisconsin
Madison, Wisconsin

1. INTRODUCTION

Navigation of satellite images is accomplished using a set of transformation functions for computing the Earth coordinates (latitude and longitude) from image coordinates (line and element) as well the image coordinates from given Earth coordinates. This set of functions is supplemented by a set of navigation parameters which are common for all points on a given image. Depending on satellite, they include orbital, attitude, camera geometry, and some other parameters.

Precision of the coordinate transformation determines the quality of navigation. It depends mainly on two factors; first, on the correctness of the model of satellite motion which is implemented into the transformation functions, and second, on the correctness and precision of the navigation parameters. The model of the satellite motion is independent of a specific satellite. However, most navigation parameters are satellite dependent and many have to be determined every day. Most users of the meteorological satellite images are provided with the navigation parameters in the data stream.

At the Space Science and Engineering Center (SSEC) a method for manually correcting navigation has been used for years on the Man-computer Interactive Data Access System (McIDAS). The McIDAS manual navigation upgrade procedure is highly interactive relying on the operator for many decisions. It consists of several time-consuming steps and it is based on landmark measurement on images. Landmark selection, measurement, storing, and interpreting the results are all done by an operator. The procedure was applied mainly to geostationary satellite images: SMS, GOES, Meteosat, and GMS.

2. AUTOMATIC NAVIGATION

The intention of the automatic navigation procedure is to implement the decision making mechanism into software. The navigation upgrading will become much faster and available in real-time mode. The automatic navigation scheme developed at SSEC on the McIDAS system consists of two major elements:

- collection of landmark data for every visible image
- upgrading of the navigation parameters.

2.1 Landmark Data Collection

The landmark locations were selected according to the number of cloud-free days over a given area. Collection of landmark data is currently done routinely for three locations. Sample images having the templates of landmarks are matched to a satellite image in areas where the landmarks are expected. The cross-correlation is calculated for each position of template on a 60 line by 60 element sector of an image. If the maximum of the correlation exceeds a threshold value, the landmark is assumed to be found. Its position on an image is stored in the navigation file as a part of navigation for a given day. The matching process is done totally by computer. If the cross-correlation does not reach the threshold value, it means the landmark position cannot be found. Cloudiness is usually the reason.

The landmark collection can be done in real-time mode or for archive data. In the first case the event scheduler calls the matching routine as an image arrives. Currently, on a typical day we collect 20 to 30 landmark measurements for two to three landmark positions.

2.2 Upgrading of Navigation Parameters

Upgrading the navigation parameters from landmarks is done by optimization of the parameters to get minimum residuals for all landmarks measured during the period under consideration. Residuals are the differences between the observed landmark position and the computed position obtained from the navigation functions and current parameters. Two residuals for each landmark are computed for each landmark measurement - line residual and element residual. For the perfect navigation both should be equal to zero for all landmarks during the period under consideration.

The optimization is made by the MINPACK package written at Argonne National Laboratory. MINPACK is a set of routines for unconstrained minimization of nonlinear functions. Line and element residuals for each landmark are input for MINPACK. As an output we get the set of navigation parameters for which the absolute values of all residuals are the smallest.

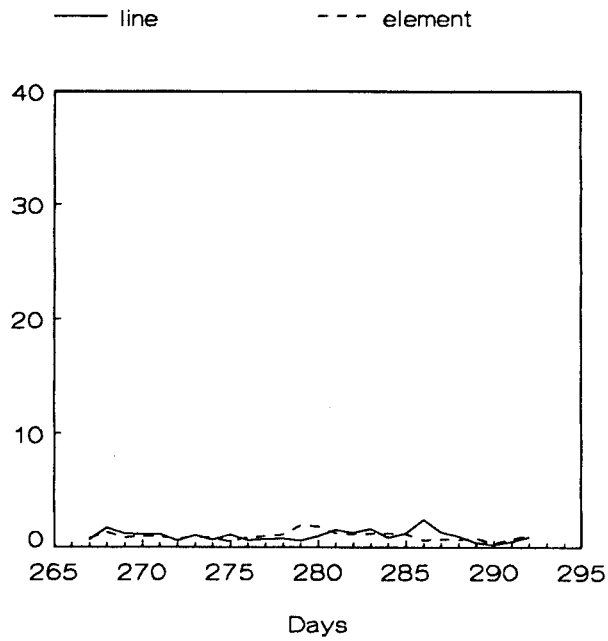

Figure 1

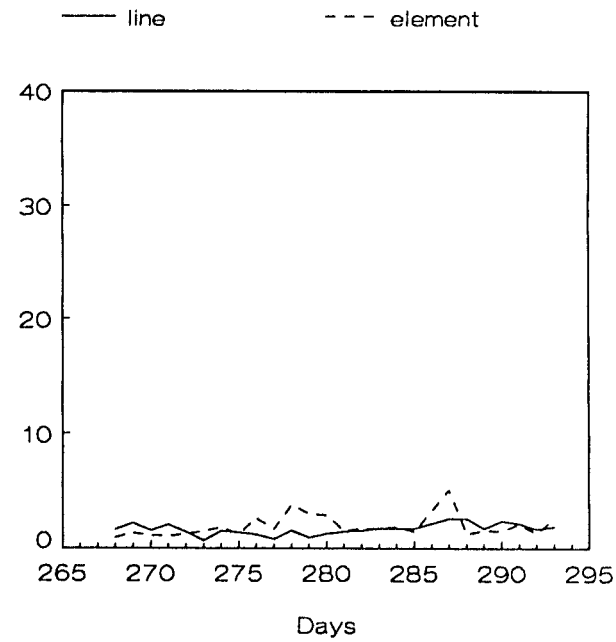

Figure 2

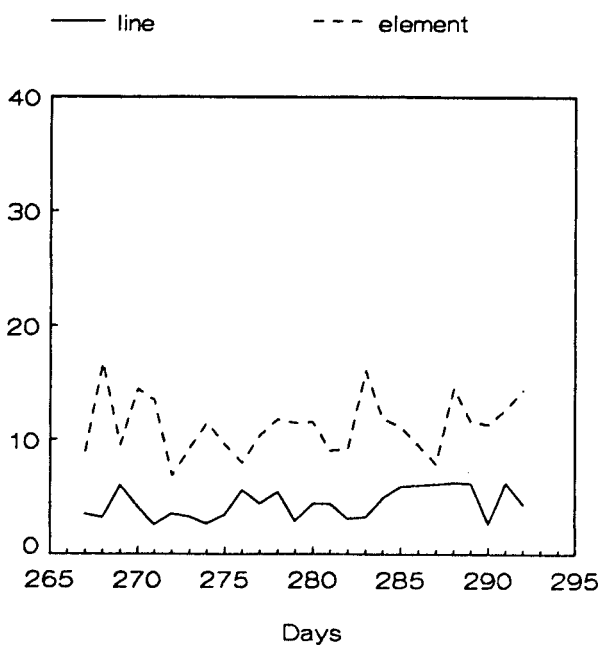

Figure 3

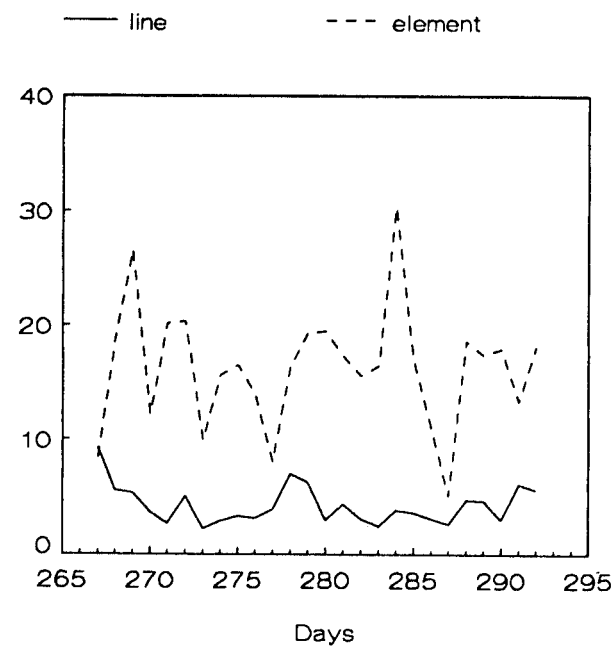

Figure 4

3. RESULTS

The structure of the automatic navigation described above can be applied to upgrade the navigation for images of an arbitrary satellite. The only satellite-dependent element is the transformation function which defines the navigation.

Our tests were performed on images of the GOES 7 satellite. Navigation is based on the algorithms designed by Phillips (Hambrick and Phillips, 1980; Mottershead and Phillips, 1976). The navigation upgrade process can be used in two different ways. For the best navigation for a given day it is sufficient to take landmarks for only that day. It is assumed that at least five measurements are made for each landmark location. The parameters to be upgraded can be chosen by the operator. They may include semimajor axis, eccentricity, right ascension of ascending node, argument of perigee, orbit inclination, eccentric anomaly, attitude declination and right ascension, picture center line, and camera misalignment angles viz. pitch, yaw, and roll.

In order to predict the navigation parameters for a future day, it is necessary to include landmarks for a few previous days (usually three). Using data from the specified previous days, the best orbital parameters are computed. Usually these orbital parameters can be used for about a week into the future. Next, the best attitude is computed for each of the specified previous days from which the orbit has been just computed. Three parameters describe the attitude in our model: declination, right ascension and roll. Although the last parameter is one of the camera misalignment angles, it can be used to describe the third attitude parameter because they are additive in the navigation model. Prediction of the attitude declination and right ascension is obtained by extrapolation using a cubic spline function. Extrapolaton of the roll is made by the parabolic function.

Using test data from the period 24 September 1987 to 22 October 1987 for GOES 7, the upgraded parameters each day have produced an RMS error of 0.927 lines and 0.981 elements for the landmarks of that day. The predicted parameters for the next day produced an RMS error of 1.59 lines and 1.67 elements.

Figures 1 and 2 show the RMS error for line and element as a function of time for the upgraded navigation (1) and predict (2) in comparison with the navigation obtained using the parameters from the GOES data stream (3) and using that set of parameters as a predict for the next day (4).

4. SUMMARY

The automatic navigation system being developed at SSEC shows very promising results. The system provides for the automatic upgrading of navigation parameters for a day to 1.0 pixel accuracy. It also can be used to make a predict of navigation parameters to 1.6 pixels. The tests have been made on GOES images, however, the system can easily modified to work with any satellite.

5. ACKNOWLEDGMENTS

The authors wish to thank Mr. Dennis Phillips for his suggestions.

6. REFERENCES

Hambrick, L. N. and D. R. Phillips, 1980: Earth Locating Image Data of Spin-Stabilized Geosynchronous Satellites, NOAA Technical Memorandum NESS 111, Washington.

MINPACK routines, Argonne National Laboratory, 1980.

Mottershead, T. and D. R. Phillips, 1976: Image Navigation for Geosynchronous Meteorological Satellites, VII Conference on Aerospace and Aeronautical Meteorology and Symposium on Remote Sensing from Satellites, Florida Institute of Technology, Melbourne, FL, 1976.

A SYSTEM FOR MANAGEMENT, DISPLAY AND ANALYSIS OF OCEANOGRAPHIC TIME SERIES AND HYDROGRAPHIC DATA

N.N. Soreide and S.P. Hayes

NOAA/Pacific Marine Environmental Laboratory
7600 Sand Point Way N.E.
Seattle, WA 98115-0070

1. INTRODUCTION

The advent of large-scale, multi-disciplinary ocean climate studies has lead to the requirement for advanced data archival, retrieval, display and analysis systems. EPIC was developed to meet this requirement for the time series and hydrographic data collected as part of NOAA's climate research programs (e.g., EPOCS and TOGA). The system incorporates an easy-to-use, interactive user interface with sophisticated data management techniques, an efficient data file format, a suite of analysis and display programs, and procedures for maintenance and updating the data base. EPIC is written in VAX/VMS DCL and in FORTRAN 77 on a VAX Cluster.

2. DESIGN CRITERIA AND SYSTEM OVERVIEW

The primary objectives in developing the EPIC system were to provide any user with immediate, interactive access to the available data sets (with graphical summarizations of the data sets meeting the selection criteria) and to provide easy and interactive graphics display and data analysis utilities. It should also be flexible in terms of allowing for addition of new data types and easy to maintain and update.

To accomplish these goals, the system includes the following elements: the data sets, a data index (which includes descriptions of the data sets), graphics display and analysis routines, documentation, and maintenance utilities. Figure 1 is a schematic of the system. The data sets and the data index are on-line. Data selection is made interactively by specifying data type, geographic location, depth and time in answer to questions. Plots and listings can be made to summarize the space-time characteristics of the selected data. The data selection process need not be repeated when plotting and analysis is performed, and unwanted data sets are easily eliminated from the selected data. Each data selection can be identified by a name of the users choice (the "EPIC file" in Figure 1).

Once the data selection has been made, any plotting or analysis program can be be started by typing the program name in response to the VAX/VMS prompt. Data display and analysis can be performed interactively, although batch mode operation is available for use when large numbers of data sets have been selected. All plotting and analysis functions are readily accessed without computer sophistication on the part of the user. However, the "layered" nature of the system allows a user to customize many parts of the system.

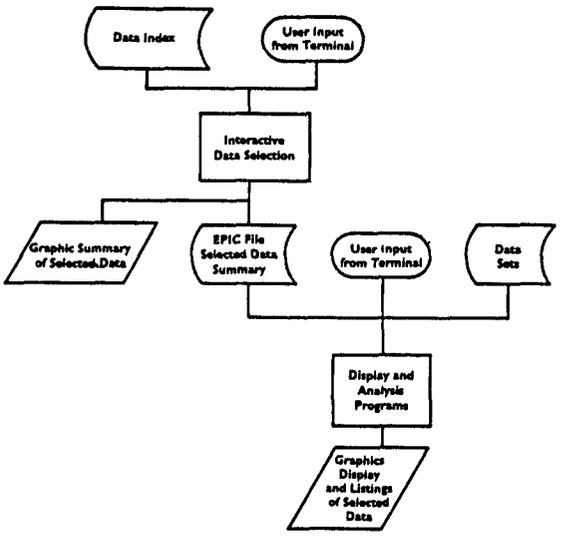

Fig. 1. Flow chart of interactive access to data index and data sets.

Documentation of the EPIC system is extensive and available interactively. All system aspects are included in this documentation. For example, the first-time user can use this on-line "help" for guidance with the data selection process as well as graphics display and analysis programs, and programmers can find detailed descriptions of the data format, utility subroutines, and data management details. The EPIC data sets are documented in two ways: the data file format includes at least one header containing documentation, and the data index which also contains documentation for each data set. Both the data headers and the data index are readily available interactively.

System maintenance and upgrade is accomplished with utilities and is simplified by the fact that each system element functions independently.

3. SYSTEM DESCRIPTION

3.1 The Data Index

The data index, which contains descriptions of the data sets and is used in the data selection process, is based on the RIM relational data base (Ref 1). Each "relation" in this RIM data base contains information about all data sets of a specific data type. In each relation, there is an entry for each data set consisting of descriptive "attributes". For

example, there is a relation for CTD data which contains an entry for each CTD cast. The "attributes" for the CTD relation (Table 1) include parameters such as oceanographic cruise identification, cast identification, date, latitude, longitude, and instrument type and serial number. The data selection process is controlled by a program which uses RIM to search the data index.

The data selection process leaves the user with an "EPIC file", which is an ASCII disk file summarizing the characteristics of the data sets which meet the criteria. Optionally, there are also graphical representations of these characteristics. The EPIC file includes the VAX file specifications and is used by all display and analysis programs to locate the desired data sets. This file is easily edited with the standard VAX editor to eliminate unwanted data sets. It can be given any descriptive name the user chooses. Each EPIC element (data selection, use of a graphics display or analysis program) functions independently. Since the data selection process is independent of using the graphics display or analysis programs, it need not be repeated.

TABLE 1. DESCRIPTIVE INFORMATION IN EPIC DATA BASE TABLES.

NAME	TYPE	DESCRIPTION
CRUISE	TEXT	Cruise ID, e.g., EP3-81-OC
CAST	INTEGER	Cast or Drop Number
ZI	INTEGER	Initial depth (db)
ZF	INTEGER	Final depth (db)
DZ	INTEGER	Incremental depth (db)
LATI	REAL	Laticude North = positive, S = negative (degrees)
LONGI	REAL	Longicude West = positive, East = 360-longitude (degree)
TIMI	REAL	Time in hours since start of century
DATEXT	TEXT	Data type, e.g., CTD
INSTYP	TEXT	Instrument type
DIRECT	TEXT	VAX directory name, e.g., [DATA.EP381.CTD]
FILENAME	TEXT	VAX file name (without directory), e.g., EP381C001.CTD;
DATORIG	TEXT	Data origin
TEMPFLG	TEXT	Flag to indicate if there is good temperature data
SALFLG	TEXT	Flag to indicate if there is good salinity data
UVFLG	TEXT	Flag to indicate if there is good velocity data
FILCREAT	TEXT	File creation date
NVAR	INTEGER	Number of variables in each scan
VAR1	INTEGER	Code for variable 1
VAR2	INTEGER	Code for variable 2
VAR3	INTEGER	Code for variable 3
VAR4	INTEGER	Code for variable 4
VAR5	INTEGER	Code for variable 5
VAR6	INTEGER	Code for variable 6
VAR7	INTEGER	Code for variable 7
VAR8	INTEGER	Code for variable 8
VAR9	INTEGER	Code for variable 9
VAR10	INTEGER	Code for variable 10
VAR11	INTEGER	Code for variable 11
VAR12	INTEGER	Code for variable 12
VAR13	INTEGER	Code for variable 13
VAR14	INTEGER	Code for variable 14
VAR15	INTEGER	Code for variable 15
VAR16	INTEGER	Code for variable 16
VAR17	INTEGER	Code for variable 17
VAR18	INTEGER	Code for variable 18
VAR19	INTEGER	Code for variable 19
VAR20	INTEGER	Code for variable 20
LATITUDE	TEXT	Latitude, e.g., 10 30.1 S
LONGITUD	TEXT	Longitude, e.g., 110 01.3 W
DATE	TEXT	Date, e.g., 0000 14 JUN 81

3.2 The Data Sets

Each data set is an unformatted, variable length record, binary, sequential disk file. These characteristics conserve space on the disk, reduce read/write time, provide flexibility in number of variables which can be included in a data file, and simplify user access to the data. Each data file includes at least one header which contains descriptive information. Analysis programs which manipulate the data and output new data files read these headers for information necessary to process the data and then update the headers to reflect the data treatment. Much of the primary header is fixed format, however, there can be any number of headers following this primary header, allowing ample space for comments. For time series data which is a composite of data from several mooring deployments, there is a secondary header which includes station history information for each series making up the composite. The information in the data file headers for any EPIC file is easily accessed by the user with the EPIC command HEADER. In this way, each data file is self-documenting.

The data files are organized in directories on the disk by data type, experiment identification, and other distinguishing characteristics, utilizing the VAX/VMS hierarchical directory structure. For example, hydrographic data are organized by cruise or experiment, and time series data are organized by data type and geographic location. The data file name incorporates similar identifying information, and is a unique identifier for the data set in the RIM data index.

3.3 Graphics

EPIC graphics includes data plots, contour plots, and plots of the results of data analysis such as spectra, coherences, and EOF decomposition. Although plotting parameters can be specified, defaults are always available, and the plots can be made interactively or obtained in hardcopy. The major EPIC plotting package (PLOT PLUS, Ref 2) is powerful and flexible. It recognizes EPIC data formats, automatically locates the desired data types within the data file, and extracts graph titles and axis labels from the data file headers. Plots are usually generated using the EPIC data plotting interface, without direct user interaction with PLOT PLUS. However, PLOT PLUS can be used interactively in command mode or it can be driven by a PLOT PLUS command file, which is automatically generated by the EPIC plotting interface. By editing this command file, a user can tailor a plot or combine several plots to produce a composite such as the one in Figure 2. Plots of non-EPIC data in almost any VAX file format (e.g., an ASCII file, a binary unformatted file, etc) can be included with EPIC data on a plot using this package, and the plots are of publishable quality.

3.4 Analysis Programs

EPIC includes routines for computing standard oceanographic parameters such as dynamic height, geostrophic velocity, and Brunt-Väisälä frequency. There are also programs for performing analysis such as cross correlation, spectra, and eof decomposition. In addition, there are programs for listing data, and creating ASCII or EBCDIC tapes for transferring data outside our organization. Once an EPIC file has been generated during the data selection process, any of these programs can be initiated interactively from the VAX/VMS prompt. Program input is obtained from the user in answer to questions, and defaults are always available. Program use requires very little computer sophistication on the part of the user. Programs can be run either interactively or in batch mode. Furthermore, since each program runs independently, individual programs can be easily modified and new programs can be added. This feature gives the system great flexibility.

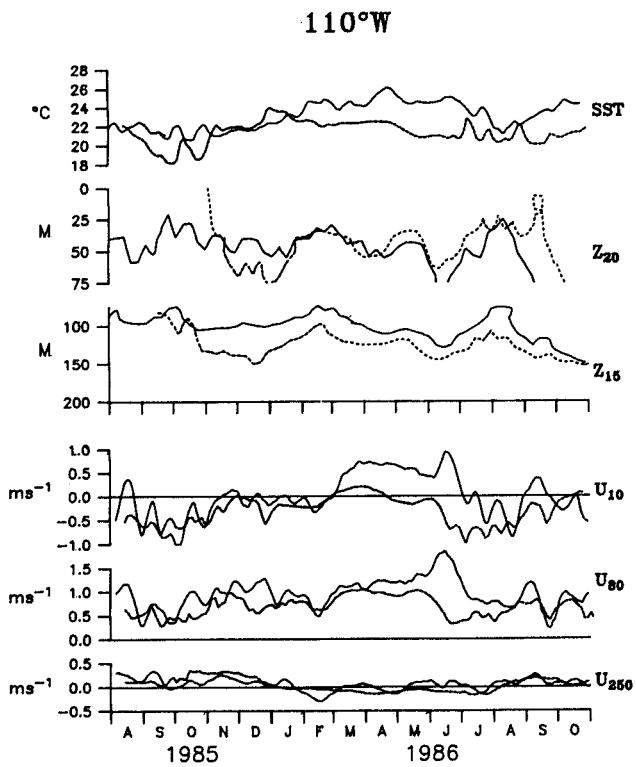

Fig. 2. Composite plot of several EPIC data sets.

3.5 Documentation

Full documentation for all aspects of the system are available interactively with the VAX/VMS help library utility. This on-line help includes an introduction to the system, a description of the data selection process, descriptions of the systems graphic's functions, and a description of each hydrographic and time series display and analysis program. It also includes detailed descriptions of the data file-naming conventions, the data file formats, the utility subroutines used by programmers to write EPIC software, and the updating and maintenance procedures.

3.6 Maintenance

Adding new data sets to the system is a two-step process. First, the new data files are created in the correct directories on the disk, and then the data index is updated to include the new data sets. The new data files are created by utility programs. After their accuracy has been verified, another utility program reads the data files, extracts the needed information from the data file headers, and updates a copy of the data index. The data index is a RIM data base consisting of a set of RIM data base tables. These are updated using RIM's FORTRAN interface. If corrections must be made once the data has been "loaded" into EPIC, these RIM tables can be edited using RIM's interactive editor.

Due to the modular nature of the system, it is possible for several different collections of data, residing on different disks on the VAX, maintained, and updated by different individuals to all be made available during the data selection process.

4. Conclusion

NOAA's participation in major multi-disciplinary climate study programs such as EPOCS and TOGA necessitated the development of a data management, display and analysis system which can accommodate large numbers of hydrographic and time series data sets. EPIC was designed to meet this need. Features include interactive data selection, efficient and flexible data file storage, standard hydrographic and time series analysis and display routines, extensive on-line documentation and ease of maintenance. Over 13,000 data sets are available through EPIC at present, and it is expected to accommodate the data sets collected by PMEL oceanographers during the intense global ocean circulation studies planned as part of the WOCE and global climate change research programs. It is already proving to be a useful tool for oceanographic research.

ACKNOWLEDGMENTS

We wish to thank several people for useful discussions which aided EPIC system development: Linda Green at the University of Washington, Linda Mangum at PMEL, and Bob Millard and Jerry Needal at Woods Hole Oceanographic Institution.

REFERENCES

1. Boeing Computer Services Company, 1983: BCS RIM Relational Management System General Information Manual, The Boeing Company, Seattle, WA.

2. Donald W. Denbo, Harvard University, Department of Earth and Planetary Sciences, Pierce Hall, 29 Oxford St., Cambridge MA 02138, Private Communication.

A SATELLITE DATA PROCESSING AND ANALYSIS SOFTWARE SYSTEM FOR EARTH'S ATMOSPHERE AND SURFACE RESEARCH

B. Dealy, C. Gautier, R. Frouin, J. Bates, D. Lingner, and J.Y. Simonot

California Space Institute, A-021
Scripps Institution of Oceanography
La Jolla, California 92093

1.0 INTRODUCTION

Within the evolution of the Earth sciences two important trends are presently taking place. One, the traditional, discipline-oriented approach to studying earth components is slowly giving way to more comprehensive, interdisciplinary methods that consider the earth and atmosphere as a dynamic and integrated system. Two, space observations, or more precisely, satellite remote sensing is becoming a standard research tool among the Earth science disciplines: oceanography, meteorology, biology, geology, and geophysics.

In view of these trends, the California Space Institute (Cal Space) has been developing a satellite data processing and analysis software system to support its interdisciplinary and integrated research programs. The system, named OASIS (Oceanic and Atmospheric Satellite Imaging System), is geared towards both research and teaching activities dealing with the earth's atmosphere and surface (land and ocean).

1.1 Background

Initially, Cal Space implemented a processing and analysis system based on the original version of the Man computer Interactive Data Access System (McIDAS), developed by the University of Wisconsin for handling imagery from geostationary satellites. Over the last few years capabilities were added to ingest and manipulate polar orbiting satellite data from NIMBUS-7 (CZCS, and SMMR) and the NOAA series (HRPT, AVHRR, and TOVS). More recently, processing packages were acquired from NASA labs (LAS and SEAPAK), which have provided increased capabilities (e.g., LANDSAT data, CZCS and AVHRR) and more sophisticated image manipulation methods.

Taken together, these software packages provided a diverse and complementary set of applications. The overall system, however, still lacked flexibility and integrated structure. In particular, the system lacked uniformity among data set formats and user-interface methods. Thus, it was desired that the system incorporate a minimum amount of facility and unified structure, such as:

o consistant and friendly user interface
o modular design for flexible modifications and additions
o transportable software components
o easy integration of software from other sources

With this in mind, Cal Space decided to integrate the system's software applications under a common executive, namely NASA's Transportable Application Executive (TAE). TAE, developed by NASA, provides an excellent framework for such an integration.

In the remainder of this paper we first we give a more detailed description of TAE and the software system. Second, we briefly describe the system hardware. Third,we present specific techniques used for ingesting, processing, analyzing, and graphically displaying data from many of the sensors presently being flown. Lastly, we describe scientific uses of these capabilities that are, or will shortly be, running under TAE at Cal Space.

2.0 SOFTWARE

2.1 Selection of the TAE Shell.

The Transportable Application Executive was selected as the user interface system because of its applications software, good documentation, ease of expansion, and growing popularity among both scientists and programmers.

Developed by NASA and its contractors, TAE is a well documented and tested set of software that modularizes user interaction requests and provides on-line help facilities as well as screen management. Its menu capability and transparent library search facilities make integration of dissimilar packages easy to accomplish, and it is available for both the VMS and UNIX environments.

The low cost in acquiring TAE and the low level of management required to run the system were major factors in our decision to implement it. Another factor in our decision was the present work at NASA's Goddard Space Flight Center on TAE's networking, window management, and graphics control.

2.2 Selection of a Baseline Design

In order to integrate diverse software packages in an efficient and cost-effective manner, we desired to implement a core of existing generic software. This was done to reduce the amount of software rewriting and conversion. We chose the Land Analysis System (LAS) for several reasons.

The foremost reason for selecting the LAS design was that, having been developed under TAE, it is a well documented and comprehensive set of generic image processing tools. In addition, LAS was specifically designed to handle multi-banded satellite imagery and the ancillary files often associated with such data, such as orbital parameters and geometric positioning data. The LAS Command line syntax supports easy selection of image sub-windows and channel subsets. The programming tools also make possible inclusion of system "niceties" in new functions for even the most hurried scientist or programmer.

As a NASA-developed product, LAS benefits from active support and is currently experiencing a substantial increase in its user base. Moveover, he system is being upgraded to support both the UNIX and VMS operating systems.

2.3 Subsystems Conversion to the LAS/TAE Environment.

Conversion of software components to TAE is a fairly straightforward operation, involving isolation of user interaction and replacement with TAE parameter retreival calls and on line help files. The modular nature of functions under TAE allows for easy software configuration practices. Hierarchical library searchs for functions at runtime are essentially transparent to the user (unless this information is desired). The tree-type menu facility in TAE allows a group of logically interconnected functions to be portrayed in that relationship to the inexperienced system user.

Conversion of the various subsystems to the LAS package design requires a more thorough examination and reworking of the software due to the differences usually encountered in image formats and label fields and ancillary data handling. Since ancillary files and label information records are essentially self-descriptive types of files, the flexibility exists to alter these files and add records or create additional ancillary-associated data sets. This is particularly important given the numerous data sets which are processed at Cal Space, each having a potentially different method of geo-positioning, calibration, and, therefore, different needs for label storage.

2.4 Graphics Interface

There is a subsystem of TAE called the Display Management Subsystem (DMS). This is a layered approach to raster display management. DMS provides inclusion of new raster devices into the TAE environment with a minimum of recoding of graphics applications. The raster display is interfaced by drivers which perform primitive graphics operations. The higher level of DMS routines uses these drivers while shielding the applications routines from device dependent routine calls. Although this approach is correct, the available applications at the time of our implementation were not sufficient to warrant integration into our system. This, in addition to some design considerations which were not optimal for our particular configuration, led us to provide device-specific graphics as an interim solution. DMS implementation is a future goal in furthering the transportability of the Cal Space software system.

The present graphics subsystem permits manipulation of image data and color look up tables as well as merging of vector graphics from the NCAR graphics software. Functions such as interactive geodetic navigation of an image and feature tracking, both of which use a trackball and display, are also available. In order to work efficiently, these types of graphics functions require a tight coupling of data sets, ancillary information, and the display software.

2.5 Costs

Acquisition of TAE and LAS through COSMIC, the distribution agent for NASA-developed software, is fairly inexpensive. TAE and LAS together cost under $5000 for the VMS or UNIX (when completed) version and includes considerable documentation and a user support office located at the Goddard Space Flight Center. This represents a substantial decrease in cost for similar capability.

3.0 HARDWARE SYSTEM

3.1 Computer Resources

Cal Space's computer configuration is composed of a VAX 11-750 with 800 MB of local storage, and two MicroVAX IIs with approximately 600 MB local storage each. These computers are interconnected through DECNET. The systems can also communicate with other computer systems through the University Local Area Network and NASA's Space Physics and Analysis Network (SPAN).

3.2 Display Systems

There are currently two microprocessor-based image display devices: a Raster Technologies Model 180 and a Jupiter Systems Model 7 Plus. The Raster 180 is a 32 bit per pixel device with a considerable library of FORTRAN callable routines for accessing the image memory and various coordinate and value registers. Similarly, the Jupiter 7 has a library of callable FORTRAN routines. The Jupiter, however, is limited to eight bits per pixel, which restricts some applications.

Both devices are driven with Direct Memory Access (DMA) boards which greatly increase data transfer rates. Since we only have one DMA board per machine, data on other machines is transferred to the display through DECNET using in-house developed software. Hardcopies from the image display devices are provided with a DUNN camera, capable of producing both 35mm and 8 x 10 polaroid pictures, and a Seiko Color Thermal Printer.

3.3 Other Peripherals

Other peripherals that reside on the system include: a printer, a laser printer, an HP pen plotter, and approximately two dozen terminals connected through a terminal server. Archival needs are met with a Perceptics 1 GB Write Once Read Many (WORM) optical disk system as well as two 9 track magnetic tape drives.

4.0 PROCESSING

4.1 Radiative Transfer Modeling

An important area of satellite-based research is the radiative transfer in the atmosphere. Whether it is for determining atmospheric corrections, developing algorithms to retrieve surface parameters, or designing new instruments, one must be able to simulate adequately the signal measured at the satellite. In this perspective, we have implemented a hierarchy of radiative transfer routines adapted to various applications. Among those are the line-by-line Fast Atmospheric Signature Code (Clough et al., 1980), the more moderate spectral resolution Lowtran-6 code (Kneizys et al., 1983), wide-band codes currently used in global circulation models (Fouquart and Bonnel, 1978, and Morcrette et al., 1986), and an analytical code (Tanre et al., 1985). This ensemble of codes, allowing for the calculation of radiance and transmittance in the visible, infrared, and microwave regions of the electromagnetic spectrum under most atmospheric conditions, constitutes a powerful research tool that the system provides in a particularly friendly user mode.

4.2 TOVS--TIROS Operational Vertical Sounder

Two complete processing packages are available for producing estimates of atmospheric temperature and moisture profiles from TOVS data. These packages are the Simultaneous Retrieval Export package (referred to as export 3) from the University of Wisconsin, described by Smith et al. (1985), and the Improved Initialization Inversion method (referred to as 3I), described by Chedin et al. (1985). Each package has strengths and weaknesses but both have proven superior to operational retrievals. Export 3 is a simultaneous physical retrieval method that uses all information on temperature and moisture (as well as surface data if available) in the solution of the radiative transfer equation to derive estimates of the temperature and moisture profiles. The package can be

executed on individual fields of view or on a climatological or user-supplied initial guess profile. The 3I method differs from Export 3 in the use of a pattern recognition technique for determining the most appropriate initial guess profile based upon the observed brightness temperatures before solving the radiative transfer equation. Separate retrievals are made for the temperature and moisture retrievals using a physically-based method. Retrievals are made for 100 km square boxes. Profiles can be plotted and compared to in-situ profiles. Horizontal fields of temperature and moisture can also be plotted and contoured.

4.3 AVHRR--Advanced Very High Resolution Radiometer

Software for processing AVHRR data includes routines for ingesting both High Resolution Picture Transmission (HRPT) direct-readout data and Local Area Coverage (LAC) data, orbital prediction for the NOAA polar-orbiting satellites, raw data calibration and earth location, renavigation based on observed landmarks, and various applications routines. All five channels of AVHRR data are usually processed as a subsection of an individual pass and stored as calibrated radiances for visible channels 1 and 2 and as calibrated brightness temperatures for infrared channels 3, 4, and 5. Applications programs include routines to extract any channel in image form for viewing or to produce derived image products. One derived product is a composite sea surface temperature (SST)/cloud image that is produced in a form similar to that described by Bates et al. (1987) for SST/cloud images from the geostationary satellite multichannel data. The user can select which combination of channels (split window, dual window, or triple window from McClain et al., 1985) is to be used and which cloud detection tests may be appropriate. Other derived image products include estimates of trace chemicals (eg., phosphate) and calculations of statistical quantities such as typical shape functions.

4.4 SMMR--Scanning Multichannel Microwave Radiometer

Several algorithms have been developed for processing SMMR cell data, provided by the National Space Science Data Center and the National Geophysical Data Center (NOAA). These data are brightness temperatures in the 6.6, 10.7, 18, 21 and 37 GHz channels with dual polarization. Developed for precipitation retrievals (Gautier and Anderson, 1987), the original algorithm is able to handle any user-requested grid, including a polar grid and the original orbital grid. In the latter case, one should use caution for superimposed orbits. In all other cases, the procedure computes space (user's grid) and time averages of the orbits passing over the requested area. The user must choose the channels according to the physical parameter being retrieved and the lowest spatial resolution of all the sensors used in retrieving this parameter. One can also choose to use night, day, twilight, or all orbits. This choice, however, is not independent of the parameter being retrieved. Finally one has the option to use either oceanic or continental data, or a combination. In the first case the continents are defined on the user's grid by the SMMR data themselves.

The basic retrievable physical parameters are sea surface temperature, wind speed, total water vapor amount, total liquid water content (Wilheit and Chang, 1979), and precipitation amount (Spencer, 1986). Interpretation of time averaged precipitation amounts is difficult due to the lack of knowledge about precipitation time distributions. The number of data on the user's grid is also retrieved by the algorithm as well as the number of precipitating SMMR cells, in the case of precipitation retrieval.

Additional utilities have been implemented, namely rescaling of sea surface temperatures and wind speed and spatial smoothing to reduce noise contamination. Sea surface temperature images may be converted into surface saturation humidity images, and total water vapor images may be converted into surface air humidity images, according to Liu's statistical relationship (Liu, 1986). Finally, latent heat flux (evaporation) images may be obtained through a combination of humidity images and wind speed images. Other utilities include: 1) using total water vapor amount and liquid water content to derive net shortwave radiative flux images, and 2) another version of the SMMR retrieval algorithm that allows one to obtain qualitative information about the size of ice roughness elements on the permanent ice-shelves in the polar regions.

4.5 CZCS--Coastal Zone Color Scanner

The CZCS Calibrated Radiance Tapes (CRT), provided by Goddard Space Flight Center, are being used to estimate concentrations of various chemical and detrital deposits in the oceans. We have adapted a software package, SEAPAK, developed under VAX/VMS and TAE at Goddard. This package has the ability to ingest and remap CZCS CRT tapes. In addition, it enables the user to select various algorithms for retrieving physical and biological parameters from CZCS data.

A good CZCS processing algorithm must extract oceanic information from the overwhelming atmospheric contribution to the signal. The user is given options for multiple or single scattering methods for approximating the Rayleigh component of the CZCS signal. One also has the opportunity to select Angstrom coefficients, for atmospheric aerosol correction, in an automated or interactive mode, using an integrated display function that approximates the effects of changing the Angstrom coefficients on the chlorophyll concentrations. Available CZCS products include: sub-surface radiances for channels 1-3, chlorophyll concentration, and aerosol and water radiances. While this is not a complete implementation of the Goddard SEAPAK system, our conversion effort is ongoing.

4.6 VISSR--Visible and Infrared Spin Scan Radiometer

VISSR data processing on the system follows several steps. First, the system's ingest routines are capable of reading not only VISSR data and navigation from the NESDIS archives, but also SAVE and PUT tape formats from the University of Wisconsin and the International Satellite Cloud Climatology Project (ISCCP). Second, it is important that quality control checks be performed. These include visual inspection to detect missing or bad data lines as well as navigational consistency, which sometimes changes as a result of orbital manuevers. Third, a two point calibration of the visible sensor is performed. The calibrated data is then used as input to our shortwave program, a physical model that uses parameterizations for quantities such as scattering, absorption, and aerosols, and calculates net shortwave downward radiance at the surface. Another by-product is an equivalent cloud measure which is an estimate of fractional cloud and optical cloud thickness.

5.0 SCIENTIFIC APPLICATIONS

5.1 Satellite Sensor Calibration

The system allows one to routinely calibrate satellite sensors while they operate in orbit. This is done by using areas on the earth's surface as calibration targets. Spectral radiances

at satellite altitude are computed from the relevant atmospheric and surface characteristics at the moment of satellite overpass. The calibration data are ingested either from magnetic tape or through a telephone link with the University of Wisconsin, Madison. This link is particularly useful for real-time operations. Such a procedure is currently performed for the AVHRR and VISSR sensors in support of NASA field experiments (Frouin and Gautier, 1987) and will be extended to upcoming satellite programs.

5.2 Primary Productivity

A relatively new project within the remote sensing group of Cal Space is the study of biological primary productivity. Primary productivity is the rate of fixation of carbon dioxide from the atmosphere by plants, mainly phytoplankton in the ocean, to form organic biomass and oxygen. This first step in the carbon cycle is critical to the study of biological, chemical, and geological (sedimentary) processes within the ocean system. A knowledge of the patterns of phytoplankton growth, which attracts zooplankton and larger predators, aids fishermen in predicting where and when fish may appear within a region.

We are developing a method for estimation of marine primary productivity from space using satellite measurements of environmentally forcing parameters. Both empirical and physically-based algorithms are being developed (e.g., Eppley, et al, 1985; Platt, 1986; Collins, et al., 1986; LaFontaine and Peters, 1986) which relate productivity to parameters such as chlorophyll concentration, incident photosynthetically available irradiance and its attentuation with depth, temperature, the depth of the mixed layer, pigment absorption coefficients, and others. Our satellite method incorporates 1) plant biomass, as inferred from CZCS chlorophyll images from the Nimbus-7 satellite; 2) sea-surface temperature, from NOAA/AVHRR scenes; and 3) incident photosynthetically available solar radiation, measured by the VISSR sensor on the GOES satellite series. Other parameters may be added later as predictive algorithms and satellite sensors develop. Each of these parameters is depth dependent so models must be developed which infer depth profiles from surface measurements and typical situations for each particular region.

The image processing tasks for such a program are complex. For example, it is necessary to obtain from GOES not only the irradiance at the time of interest, but also the recent irradiance history of the region, to provide an estimate of the photoadaptive state of the plants there. The images from the three different sensors on satellites having different orbits and resolution then must be geographically corrected and interpolated in time and space to a common grid and combined to form the final product which will be the productivity image.

5.3 Cloud Classification and Feature Tracking

Satellite images, whether visible, infrared, or microwave in origin, contain a wealth of information about the atmosphere and ocean. This information, however, is often incompletely extracted because satellite data are voluminous and require extensive processing. To make fuller and more efficient use of satellite data, we are developing a capability to automatically analyze satellite observations by extracting and tracking recognizable patterns within images.

We have developed, for instance, a technique to automatically classify cloud fields into different cloud situations and cloud types. This method is based on a three-step procedure: First pairs of visible and infrared cloud images are characterized by a number of specific parameters describing the image's spectral and textural features. The spectral parameters chosen are the mean, minimum and maximum of the radiances, and the textural parameters are the moments of the radiance distribution (mean, contrast, entropy, and second angular momentum). In the second step, the images are classified as a function of these parameters, using the Typical Shape Function (TSF) analysis procedure of Jalickee and Ropolevski (1978). This provides sets of TSFs for each image pair, which are each associated with different classes. Once each image pair of an entire data set has been analyzed following this procedure, all the TSFs are regrouped according to a similarity criterion (i.e., correlation) and all the pairs are reclassified over this new TSF basis.

5.4 Radiative Fluxes

Over the last few years we have developed capabilities for computing the net shortwave and downward longwave components of the net surface radiation flux. The shortwave computations are based on combinations of visible data from geostationary satellites (GOES, METEOSAT, and GMS). The algorithm used is that described in Gautier et al. (1980) and later refined by Gautier and Frouin (1985). The downward longwave computations are based on radiative transfer modeling of the longwave radiation in the atmosphere following Morcrette (1984). The necessary input parameters to run this model are obtained from satellite observations. These parameters are: cloud top altitude, cloud optical thickness and emissivity, and atmospheric temperature and moisture profiles. Several approaches have been implemented (see Frouin et al., 1988), the most sophisticated one being updated on a continuous basis.

5.5 Hydrology Cycle

Comprehensive satellite studies are presently underway to better understand the atmospheric hydrological cycle. These studies use satellite-derived estimates of the cycle's principle components. Firstly, estimates of atmospheric total water vapor amounts and liquid water content are derived from SMMR data (Wilheit and Chang, 1979). Vertical moisture profiles are obtained in general from TOVS operational retrievals and more accurately using algorithms of Smith et al. (1985) and Chedin et al. (1985).

Secondly, techniques have been developed to sense oceanic evaporation using SMMR data (Liu, 1986), by relating SMMR total water vapor amount to air surface moisture. In this process SMMR-retrieved SSTs may be replaced soon by TOVS-retrieved SSTs. In the future, SMMR-retrieved wind speed may be replaced by winds estimated from scatterometer equiped satellites.

Thirdly, precipitation estimates can be retrieved from both GOES-VISSR and SMMR data (Gautier and Anderson, 1987). By comparing the time evolution of total water vapor amount and liquid water content with evaporation minus precipitation estimates, one can calculate the horizontal divergence or convergence of atmospheric water content due to atmospheric transport. Information about time statistics of precipitative activity can also be obtained by comparing SMMR- and GOES-retrieved precipitations.

Lastly, one can achieve a better understanding of the cloud and hydrological cycle interaction when comparing GOES-VISSR-retrieved cloud factors (shortwave equivalent cloudiness) and SMMR-retrieved total liquid water content. These studies are also being conducted in the framework of understanding the Indian Monsoon cycle.

5.6 Air-Sea Interactions

The studies of air-sea interactions have been an important area of research at Cal Space. Included in these studies is the net heat flux at the ocean-atmosphere interface. The net heat flux consists of four components: net shortwave flux, net longwave flux, latent heat flux, and sensible heat flux.

The net shortwave radiation flux is derived from GOES-VISSR data and the downward longwave radiation flux estimated from GOES-VISSR and TOVS atmospheric profiles (section 5.4). TOVS/AVHRR SST data are utilized to obtain the upwelling longwave radiation flux, while the latent heat flux due to evaporation can be computed using SMMR data and bulk parameterizations (Liu 1987, Simonot 1987). Finally, through a combination of SMMR or TOVS SSTs and TOVS air temperature profiles, together with SMMR wind speeds, it is possible to estimate the sensible heat flux. This last technique employs a simple boundary layer model developed by Liu et al. (1979).

The oceanic surface net heat flux is calculated from the sum of these four components. In the tropical oceans, however, sensible heat and net longwave fluxes are an order of magnitude less and can be considered constant in a first approximation.

To complement the study of the net surface heat flux, investigations are being conducted of the net water flux at the ocean-atmosphere interface (evaporation minus precipitation). Evaporation can be obtained using SMMR data and precipitation estimates using GOES-VISSR data (section 5.5). Together, estimates of the net heat and water fluxes provide a comprehensive understanding of oceanic surface temperature and salinity changes and, as a result, of surface oceanic density changes. Moreover, they can be used as input forcing parameters for oceanic numerical models (mixed-layer or general circulation models) and for validating atmospheric general circulation numerical models. These studies are taking place in support of the Tropical Ocean and Global Atmosphere program (TOGA), as well as to study the Indian Monsoon onset.

Although the acquisition of all the net surface heat budget components is desirable, it is not a necessary condition for a comprehensive understanding of air-sea interaction processes. The statistical pattern correlation approach has been used by Bates and Gautier (1988) to demonstrate that cloud effects on the net shortwave flux acted as a positive feedback on the SST field during the Frontal Air-Sea INteraction EXperimment (FASINEX). Also, Gautier (1987) has conjectured that feedback mechanisms occurred among net radiative flux diurnal cycles, phytoplankton concentration, and generation of turbulent mixing in the upper ocean during the Tropic Heat experiment.

6.0 REFERENCES

Bates, J.J., W.L. Smith, G.S. Wade, and H.M. Woolf, 1987: An interactive method for processing and display of sea surface temperature fields using VAS multispectral data. Bull. Amer. Meteor. Soc., V. 68 (#6), 602-606.

Chedin, A., N.A. Scott, C. Wahiche, and P. Moulinier, 1985: The improved initialization inversion method: a high resolution physical method for temperature retrievals from the TIROS-N series. J. Clim. Appl. Meteor., 24, 124-143.

Clough, S.A., F.X. Kneizys, R. Davies, R. Gamache, and R. Tipping, 1980: Theoretical line shape for H_2 0 Vapor. Application to continuum. Atmos. Water Vapor, A. Deepak, T.D. Wilkerson, and L.H. Ruhnke, eds., Academic Press, 695 pp.

Collins, D.J., D.A. Kiefer, J.H. SooHoo, C. Stallings, W.-L. Yang, 1986: A model for the use of satellite remote sensing for the measurement of primary production in the ocean. SPIE, Vol. 637, Ocean Optics VIII, 335- 348.

Eppley, R.W., E. Stewart, M.R. Abbott, U. Heyman, 1985: Estimating ocean primary production from satellite chlorophyll. Introduction to regional differences and statistics for the Southern California Bight, J. Plankton Res., 7, 57-70.

Frouin, R., C. Gautier, and J.J. Morcrette, 1988: Downward longwave irradiance at the ocean surface from satellite data: methodology and in-situ validation. J. Climate Appl. Meteor., (to appear).

Frouin, R, and C. Gautier, 1987: Calibration of NOAA-7 AVHRR, GOES-5, and GOES-6 VISSR/VAS solar channels. Rem. Sens. Environ., 22, 73-101.

Gautier, C., G. Diak, and S. Masse, 1980: A simple physical model to estimate incident solar radiation at the surface from GOES satellie data. J. Appl. Meteor., 19, 1005-1012.

Gautier, C. and R. Frouin, 1985: Satellite-derived ocean surface radiation fluxes. In Adv. Rem. Sens. Ret. Meth., A. Deepak Publishing, Hampton, VA, 311-329.

Gautier, C. and M. Anderson, 1987: Satellite-derived Indian Ocean precipitation activity during summer MONEX (May-June July 1979). 17th Conf. on Hurr. and Trop. Met. of the A.M.S., April 7-10, 1987.

Gautier, C. 1987: Radiative processes affecting mixed-layer heat content and their monitoring from satellite. (submitted) Proc. from 'AHA HULIKO'A workshop, Univ. of Hawaii.

Jalickee, J.B. and C.F. Ropolewski, 1978: An objective analysis of the boundary-layer thermodynamic structure during GATE part I: method. Mon. Wea. Rev., 107, 68-76.

Kneizys, F.X., E.P. Shettle, W.O. Gallery, J.H. Chetwynd, L.W. Abreu, J.E.A. Selby, S.A. Clough, and R.W. Fenn, 1983: Atmospheric transmittance/radiance: computer code LOWTRAN 6. Air Force Geophy. Lab. Pub., pp 200.

La Fontaine, Y. and R.H. Peters, 1986: Empirical relationship for marine primary production: the effect of environmental variables, Oceanolog. Acta, 9, 65-72.

Liu, T.W., K.B. Katsaros, and J.A. Businger, 1979: Bulk parameterization of air-sea exchanges of heat and water vapor including the molecular constraints at the interface. J. Atmos. Sci., 36(9), 1722-1735.

Liu, T.W. 1986: Statistical relation between mean precipitable water and surface level humdity over global oceans. Mon. Wea. Rev., 114, 1591-1602.

Liu, T.W. 1987: 1982-1983 El Nino atlas Nimbus 7 microwave radiometer data. NASA Jet Propulsion Laboratory Publication 87-5, 68pp.

McClain, E.P., W.G. Pichel, and C.C. Walton, 1985: Comparative performance of AVHRR-based multichannel sea surface temperatures. J. Geophys. Res., V. 90 (C6), 11,587-11,601.

Morcrette, J.J. 1984: Sur la parametrisation du rayonnement dans les modeles de la circulation generale atmospherique. These de Doctorat d'Etat, No. 630, Univ. of Lille, France.

Morcrette, J.J., L. Smith, and Y. Fouquart, 1986: Pressure and temperature dependence of the absorbtion in longwave radiation parameterizations. Beitr. Phys. Atmos., 59, 455-469.

Platt, T.,1986: Primary production of the ocean water column as a function of surface light intensity: algorithms for remote sensing. Deep-Sea Res, 33, 149-163.

Simonot, J.Y. 1988: Satellite estimates of surface evaporation in the Indian Ocean during the 1979 Monsoon. (to appear) Workshop Proc. Climate Rem. Sens., Cal. Space Inst., La Jolla, CA.

Smith, W.L., H.M. Woolf, C.M. Hayden, and A.J. Schriener, 1985: The simultaneous retrieval export package. The Technical Proceedings of the Second International TOVS Study Conference, W.P. Menzel, editor, pp. 224-253.

Spencer, R.W., 1986: A satellite passive 37-GHz scattering-based method for measuring oceanic rainrates. J. Climate and Appl. Meteor., 25, 754-766.

Tanre, D., C. Derro, P. Duhaut, M. Herman, J.J. Morcrette, J. Perbos, and P.Y. Deschamps, 1985: Effets atmospheriques en teledetection--Logiciel de simulation du signal satellitaire dans le spectre solaire. Proc. 3rd Int. Coll. on Spec. Sig. of Obj. in Rem. Sen., Les Arcs, Fr. 16-20 Dec.

Wilheit. T.T., and A.T.C. Chang 1979: An algorithm for retrieval of ocean surface and atmospheric parameters from the observations of the Scanning Multichannel Microwave Radiometer (SMMR). NASA, Goddard Space Flight Center, Tech. Memo. 80277.

7.0 ACKNOWLEDGEMENTS

This work has been supported in part through grant #NAGW-1141 from NASA. We wish to acknowledge B. Bloomfield's help in preparing the manuscript.

SATELLITE TRAINING DEVELOPMENT ACTIVITIES: A STATUS REPORT

H. Michael Mogil

National Environmental Satellite, Data and Information Service, NOAA
Camp Springs, Maryland 20746

1. INTRODUCTION

Prior to 1985, the National Weather Service (NWS), the Air Weather Service (AWS), the National Environmental Satellite, Data and Information Service (NESDIS), and the Naval Oceanography Command (NAVOCEANCOMFAC) generally undertook applied weather/oceanography satellite training independently. In addition, NESDIS' international satellite training activities were largely addressed apart from those done domestically.

The situation was recognized by agency representatives at the Fall 1985 National Weather Association (NWA) Annual Meeting. At that time, two special training focus sessions opened opportunities to explore multi-agency training development, particularly in the area of satellite imagery interpretation. Budgetary and personnel cutbacks, the imminent arrival of satellite imagery-in-motion display systems at both NWS and AWS sites, and a more realistic determination of training needs sparked the first Interagency Training Coordination Working Group (ITCWG) meeting at Scott Air Force Base (AFB), IL on February 24-25, 1986. Attendees included members of the operational meteorological community's working level trainers. Thus, instead of policy making, the attendees focused on actually making the training happen.

Subsequent meetings of the ITCWG were held in Kansas City, MO in 1986 and in Camp Springs, MD and Houston, TX in 1987. Each meeting further enhanced establishment and maintenance of a more fully coordinated training development program. Additionally, the AWS estimated training development savings of more than $20K and over an 18 month manpower savings due to initial training coordination activities alone (Guard, 1986). Similar savings and/or creation of additional training materials resulted within NESDIS and NWS due to non-duplication of effort.

2. THE TRAINING UNIVERSE

Training, no matter good, doesn't just happen. It requires a multi-faceted approach (figure 1) and the involvement of large numbers of people, including agency management, operational forecasters, local weather office management, and training developers. Fortunately, such a team exists in the satellite training area.

NESDIS has assumed the leadership and coordination role in satellite training development activities. This has involved extensive discussions with the users of training materials, as well as the creation of a large, albeit ad hoc, force of training developers. Whereas in past years, NESDIS created its own training materials, there is now a coordinated program involving NWS, AWS, and Navy forecasters, contract support, and applied NESDIS research scientists.

The program relies heavily on ensuring that training development activities meet training needs and that duplicity of efforts is minimized. Further, NESDIS ensures that satellite training materials receive a critical, multi-agency evaluation prior to being released for use.

Training workshops, audio-cassette tape-slide programs, videotape and videodisk production, training laboratory exercises, and creation of a satellite technical reference handbook and correspondence course round out the overall satellite training program.

Once developed, distribution of training materials remains a problem. The materials are sent to remote sites where they are added to existing training aids. There may not be a person designated as a training coordinator. Hence, materials may not reach the people intended, they may not be used correctly, or they may be misplaced. Efforts are being made to overcome this. Within the NWS, serious consideration is being given to creating a training position at forecast offices as part of the proposed NWS reorganization. This person would create and administer training in a broad range of programs, not just satellite imagery interpretation.

There are other shortfalls in interagency training coordination activities, especially as personnel involved in the program change. Budgetary constraints have impacted training efforts, as well. International activities have been especially hard hit due to compounding of constraints by a larger number of organizations and nations.

3. NEEDS ASSESSMENT

3.1 Coordination

Besides formal ITCWG meetings, ITCWG members routinely discuss training needs and activities. In 1986, early in the ITCWG's history, the Navy and Air Force learned about the development of Forecasting Handbook No. 6 - Satellite Imagery Interpretation for Forecasters. This compendium of selected operational articles, technical memoranda, and other publications provided an unparalleled technical reference resource for field forecasters. Many of the articles included in the Handbook would not have been available at remote weather sites. The handbook was organized by topics (e.g., tropical weather, convection, aviation) and was printed in loose-leaf format for later updating. The Air Force and Navy both joined in the initial and subsequent reprintings of the Handbook.

In addition, NESDIS' Training and Information Services Branch (TISB) coordinates closely with two NOAA International Relations Offices (NWS and NESDIS). Recently NWS' International Relations Office determined, through discussions with southeast

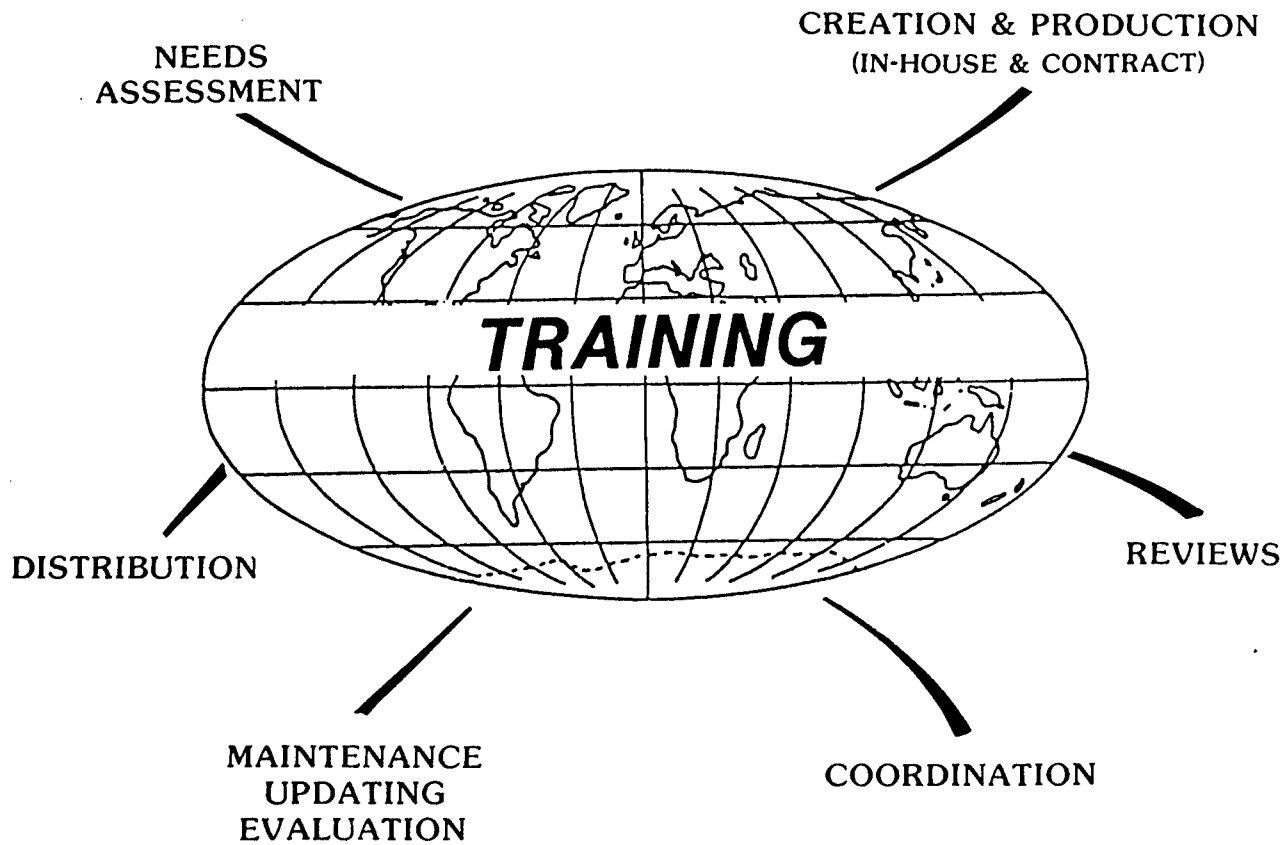

Figure 1. Conceptual model of the "training universe". All six areas must be successfully addressed to have an effective training program.

Asian Nations, that there was a need for a specialized Satellite Interpretation Handbook on tropical meteorology (not just tropical cyclones). NESDIS and NWS have already begun exploring options for preparing such a Handbook.

NESDIS is also in touch with various international organizations. The World Meteorological Organization (WMO) is very interested in training, but lacks sufficient fiscal resources to implement a major worldwide training program throughout **all** meteorological, hydrological, and oceanographic disciplines. However, they do provide insight into international training needs, sponsor or co-sponsor numerous workshops and courses, and help distribute some training materials. Other groups, such as the International Civil Aviation Organization (ICAO), have training offices throughout the world and encourage training and/or distribute or market training materials.

NESDIS also undertakes a major training workshop program. In addition to effecting training, these workshops provide unparalleled opportunities for NESDIS instructors to interact with practicing meteorologists and oceanographers. Thus, training development, as well as applied projects, can be more tailored to meet operational needs.

Some of the topics for which satellite interpretation training materials were needed in late 1987 included:

- moisture channel imagery
- imagery-in-motion
- techniques for assessing numerical model initial analysis accuracy
- oceanic cyclogenesis
- mesoscale analysis
- sea surface temperature analysis techniques

Although training materials, once developed, could be used throughout the world, there is always the need to tailor materials, especially case study laboratory exercises, to specific geographical areas.

3.2 Professional Society Involvement

The NWA has been an active supporter of meteorological training activities. In 1986, they republished a satellite imagery interpretation handbook (NWS Forecasting Handbook No. 6 - Satellite Imagery Interpretation For Forecasters), and made it available, at low cost, throughout the meteorological community (figure 2). At least three universities have used the reprinted handbook as a textbook (selected readings) as part of various courses in instruments and/or synoptic meteorology. The NWA has also included two training focus sessions at each of their last three annual meetings, and in 1987 hosted the annual ITCWG meeting. Due to this commitment to training, the ITCWG agreed to tie all of its future meetings to the NWA Annual Conference and invite the Executive Director of NWA to participate.

The American Meteorological Society (AMS) is also taking a more active role in training. As part of the 1987 Annual AMS Weathercasters Conference, a special full-day forecasting workshop was held. More than 100 weathercasters attended. And dozens of weathercasters, and others, have benefitted from a videotape/workbook program derived from the workshop. The AMS plans another such weathercasters workshop in 1988 focusing on satellite and radar applications.

3.3 Training Workshops

NESDIS carries out an extensive training workshop program in support of both domestic and international users of

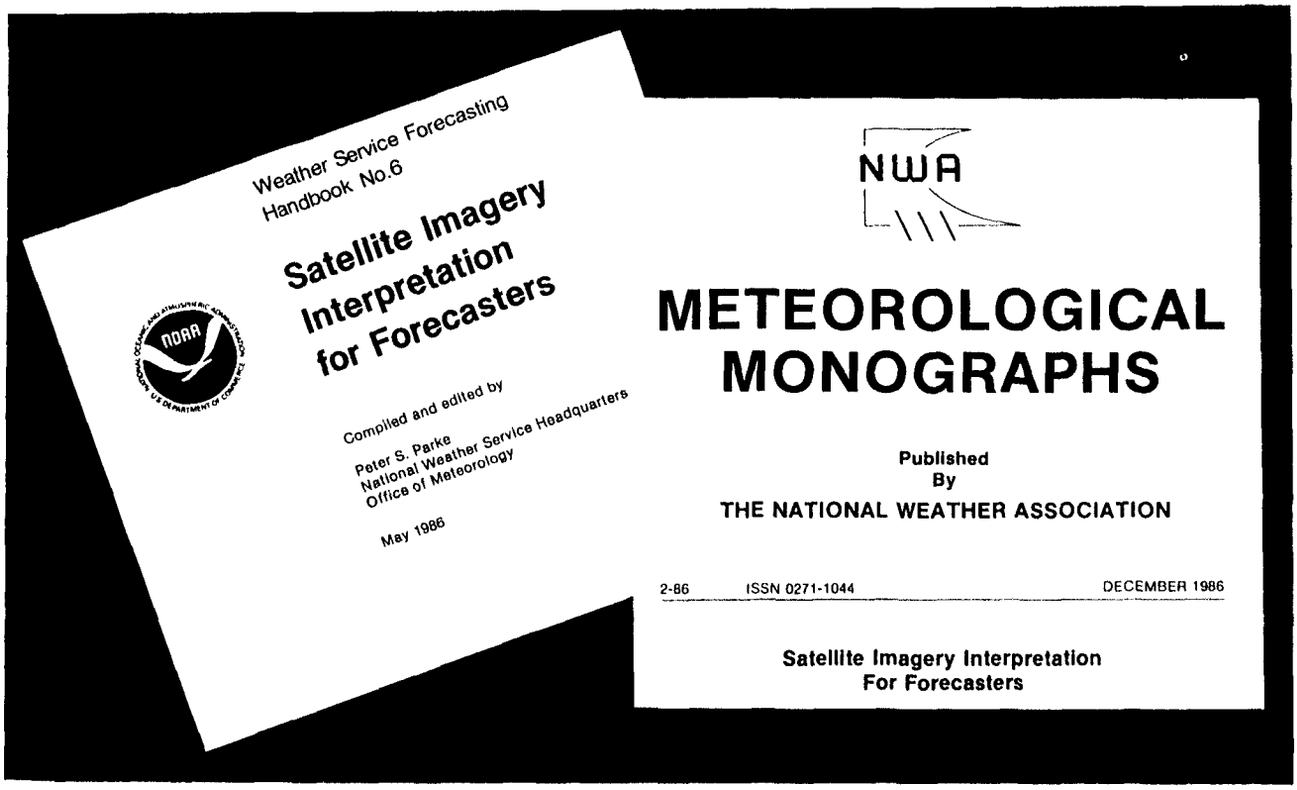

Figure 2. Covers of NWS and NWA versions of Forecasting Handbook No. 6. The NWA version is available by contacting the NWA Executive Offices, 4400 Stamp Road, Room 404, Temple Hills, MD 20748 (301- 899-3784).

satellite imagery. Internationally, NESDIS has provided instructors and/or training support to workshops on tropical cyclones, precipitation, and agricultural assessments. Numerous scientists from other Nations have visited NESDIS laboratories to learn firsthand about satellite research and operational applications. However, due to personnel cutbacks, the one-on-one visitation program is being downplayed as a viable training option.

Domestically, NESDIS instructors teach workshops at NWS Forecast Offices, NWS National Centers, Air Force and Navy Bases, and at other selected sites. They also participate in teaching the flash flood course at the NWS Training Center.

During the three-year period 1985-1987, NESDIS instructors conducted nearly 90 training workshops in the U.S. and abroad, training almost 2400 people (figure 3). These workshops have addressed severe weather, mesoscale and synoptic scale meteorology, aviation and oceanography applications, and heavy rainfall. Figure 4 shows some of the workshops conducted during the period October 1986 - September 1987 (FY87).

In addition, instructors at the Chanute AFB Weather School conduct workshops at many overseas sites in various weather topics, including satellite imagery interpretation. NESDIS has begun providing videotapes, slides, and transparencies to Chanute in support of these efforts. Recently, Air Weather Service Headquarters provided individual instructor copies of Forecasting Handbook No. 6 to Chanute Weather School. Workshops taught by Chanute Weather School instructors were **not** included in the workshop totals listed above.

4. CREATION AND PRODUCTION

The creation process involves coordinating with governmental developers, monitoring non-government contractor development, and pooling scarce governmental finances for training contracts. NESDIS' Training and Information Services Branch (TISB) has taken the lead in this area during the past two years.

Internal NESDIS coordination is primarily with the Physical Sciences and Regional and Mesoscale Meteorology Branches (both within the Office of Research and Applications). Additionally there is close cooperation between TISB and the Satellite Services Division, part of the operational arm of NESDIS. Scientists and forecasters in these offices develop satellite interpretation applications, conduct training workshops and develop training materials or courseware.

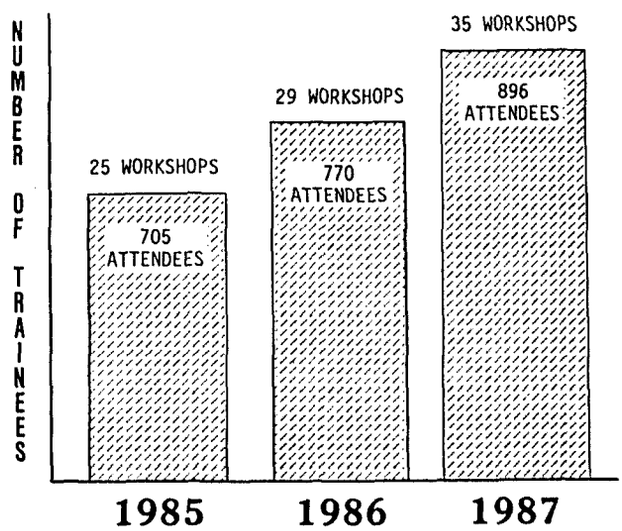

Figure 3. Training workshop summary for fiscal years (FYs) 1985-1987. The increasing number of workshops and people trained occurred during a period of decreasing staff resources within NESDIS.

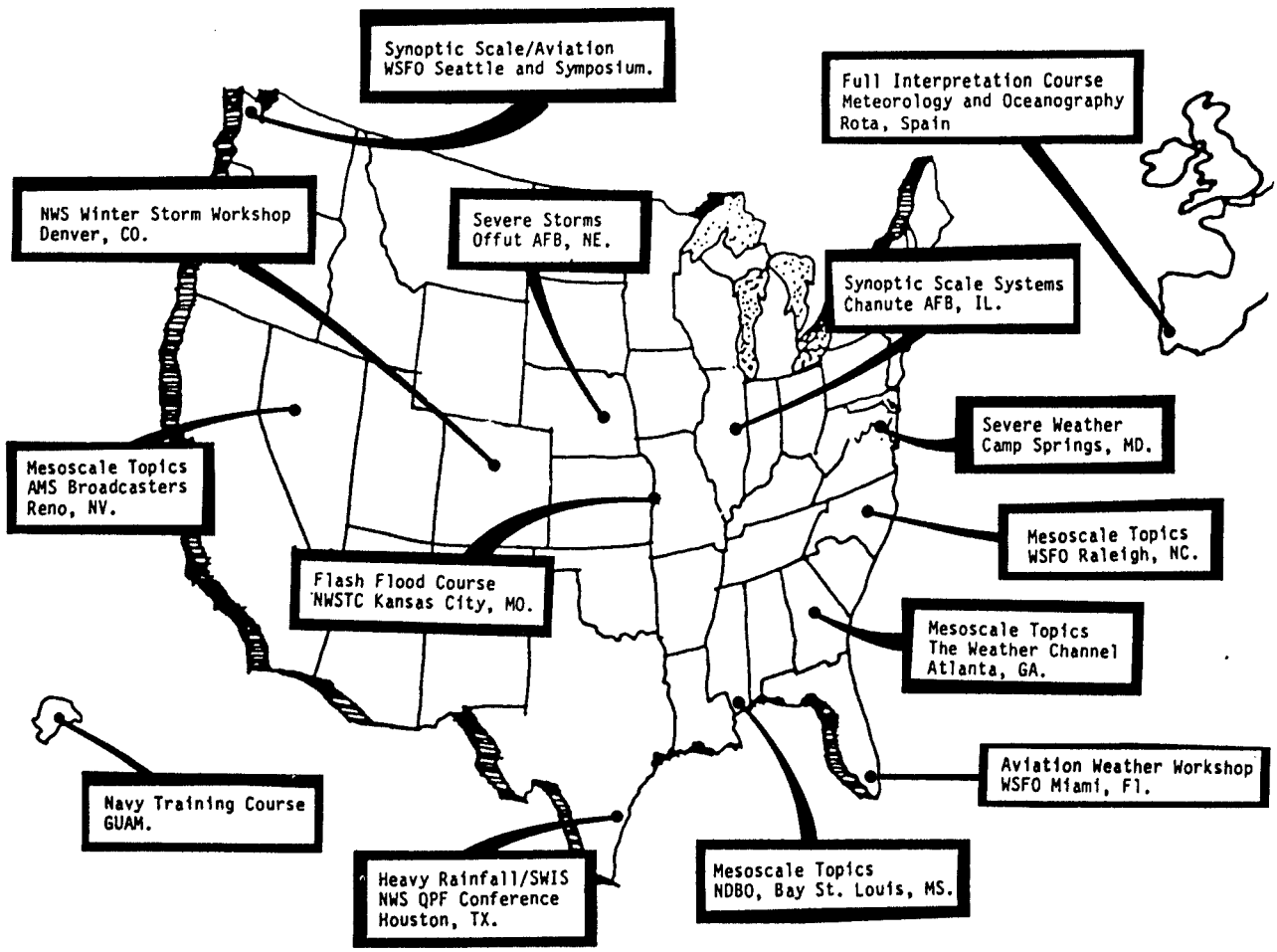

Figure 4. Representative sampling of training workshops conducted by NESDIS instructors during FY87. Workshops range from a half-day to 8 days in length.

TISB routinely coordinates with NWS National and Regional Headquarters, as well as with the National Meteorological Center (Hurricane, Severe Storms, and Operations Divisions), and the NWS Training Center. There is also frequent coordination with AWS Headquarters, The Air Force's Training Center at Chanute AFB, IL, and with various Air Force sites (e.g., Kennedy Space Center). Navy coordination is done primarily through the Naval Oceanography Command Facility at Bay St. Louis, MS.

There is also coordination, albeit limited, between TISB and the FAA Academy in Oklahoma City and with the Canadian Atmospheric Environment Service. These groups are being brought into the training effort more fully due to their growing involvement in the ITCWG.

While government employees and contractors create the training materials, it is primarily government personnel who are preparing the final products at this time. NWS and NESDIS worked together to organize, reconstruct, and publish NWS Forecasting Handbook No. 6 and its associated correspondence course. NESDIS rewrote and reorganized several contractor-developed training packages and laboratory exercises and is preparing final photography and layout/design. NESDIS has begun working with the AWS to transform audio-cassette tape-slide and videotape programs to videodisk. NWS and AWS are both exploring videodisk systems for use in remote site, self-study training.

The training development effort is being directed to ensure that materials will be suited for videodisk use in future years (figure 5). Step one currently involves creation of a script-slide program because it is the easiest to produce and modify, and because instructors can more easily use materials in slide format. Once completed, the program will be transformed into videotape, with addition of imagery in motion, where appropriate. From this step, interactive videodisk production follows, "relatively" easily.

Wherever possible, training, regardless of which step is being used, will be interactive and/or will involve hands-on laboratory experiences, and Handbook No. 6 as a reference source and correspondence course. This is based on extensive workshop evaluations and discussions with forecasters.

5. REVIEW PROCESS

It's one thing to produce a training package; it's quite another to complete it. During the development phase, several reviews of a training package are often undertaken. In addition to verifying technical content and training effectiveness, reviews center on ensuring proper annotating, satellite image clarity and photographic contrast, and other audiovisual aspects.

Once the product is completed, a more formal review, involving as many as a dozen different groups, is in order. For example, a recently completed training program on basic polar orbiter image interpretation was sent to NWS and AWS Headquarters, the Navy, the NWS Alaska Region Headquarters, Chanute AFB, the FAA Academy, Johnson Space Center's Space Flight Meteorology Group, and at least three NESDIS Branches not involved in the program's original development. The goal is to ensure the most complete, most accurate training package as possible. This will speed transformation to videotape/videodisk formats.

SCRIPT-SLIDE ➡ VIDEOTAPE ➡ VIDEODISK

- INSTRUCTOR USE
- REVIEW
- FINALIZE

- WIDESPREAD DISTRIBUTION
- SELF STUDY USE

- WIDESPREAD DISTRIBUTION
- SELF STUDY USE
- INTERACTIVE

LABORATORIES - USE SEPARATELY OR WITH A/V ABOVE
AND/OR FORECASTING HANDBOOK #6

CORRESPONDENCE COURSE

Figure 5. Developmental self-study training development approach within NESDIS. Script-slide programs provide the easiest and lowest cost method of development, but are the least effective training technique.

6. COORDINATION

Coordination never really ceases. There are always opportunities to reassess training needs, formats, and courseware content. ITCWG members discuss these and other topics routinely. Again, workshops provide opportunities for courseware to be "field-tested". Based on this feedback, materials may be changed prior to final production or they may be updated once in use.

7. FOLLOW UP ACTIVITIES

Operational forecasters (meteorologists and oceanographers) eventually define the success of the training materials. They may alert their agency and/or ITCWG member about a newly developed technique or procedure, or a modification to an existing one. Perhaps, they'll experience a significant weather event which provides valuable training information. In the case of NWS Forecasting Handbook No. 6, routine updating is planned, with removal of certain papers and addition of others. This will require changes to the satellite interpretation correspondence course. Regardless, the ITCWG members fully support updating to ensure the latest, most accurate information is available. It is recognized that updating is far superior than recreation.

8. PRODUCTION AND DISTRIBUTION

Once developed, training materials must be produced and distributed by the various agencies. To date, each agency has paid for its own materials. However, through coordinated purchasing, agencies have saved large amounts of money over what individual printing costs would have been.

Distribution of training materials must also be considered. In some cases, it may be desirable to house copies of materials at a central site(s) and loan them to interested users, as needed. NESDIS' Training and Information Services Branch (5200 Auth Road, Room 601, Camp Springs, MD 20746 - 301-763-8204) does this for intra-governmental loan of films and videotapes. NESDIS' Satellite Data Services Division (5200 Auth Road, Room 101, Camp Springs, MD 20746 - 301-763-8111) provides film rental service for non-governmental users. The Air Force and Navy also have central distribution sites for videotape loan within their respective agencies. However, the preferred approach is to have copies of training materials resident at each forecast site for use by operational staff whenever they can find the time to use them.

Each agency currently maintains its own distribution lists and basically prints and/or reproduces its own training materials. However, due to coordination efforts, it is becoming rarer for one agency to produce and/or distribute a training program without others knowing about and being involved in it.

Distribution of technical reports and technical memoranda are needed to ensure proper interagency development of training materials. The ITCWG recently agreed to undertake a review of the present distribution lists for its technical and scientific publications. Each agency has agreed to update these lists.

9. OTHER TRAINING ASPECTS

There are still a great number of unsolved training issues before the ITCWG. These include:

--determining methods for purging old and outdated training materials

--ensuring compatibility of training systems (e.g., videotape, videodisk, computer)

--providing the needed staffing and fiscal resources to keep developing and improving training materials.

--administering training programs at remote sites to ensure accomplishment of training.

--assessing the training requirements associated with new technology well-before implementation, and ensuring that training is available prior to operational use.of the systems.

--determining ways to publish and provide government-developed training materials to non-government users at a time when "give-aways" are no longer permitted.

How these and similar issues are addressed will define the state of training in years to come.

Finally, let me restate that training doesn't just happen. It requires involvement, commitment and resources. Although the emphasis in this paper was on the governmental sector's involvement, Mark Shulman, past National Weather Association president, put it this way in his outgoing presidential address (1987). "..it is through education and training at the university and elsewhere that we (the meteorological, hydrological, and oceanographic community) will be able to meet the challenge of service to the public. The rigor of a thorough...education...must be maintained...with an indepth comprehension of the physical principles underlying the profession...the forecaster must be retrained to understand the capabilities and limitations of new observing systems and...be able to use the (new and growing) wealth of data..."

Through the ITCWO and its own agency's representatives, NESDIS, NWS, the Air Weather Service, the Navy, and the FAA have begun to realize this training goal. Further involvement and cooperation of others, such as the universities, professional society's, and other agencies, will certainly keep training in the spotlight and ensure that it serves the operational needs of forecasters throughout the world.

10. REFERENCES

Guard, C., 1986: Some results from interagency cooperation on the development of meteorological training materials. Paper presentated at, Eleventh Conference on Weather Analysis and Forecasting (Kansas City, MO).

Shulman, M., 1987: Remarks given at Outgoing Presidential Address at National Weather Association Annual Meeting (Houston, TX).

INTEGRATED SATELLITE APT AND WEATHER RADIO BROADCAST PROCESSOR

Kenneth W. Ruggles

Systems West Incorporated
27880 Dorris Drive, Carmel, California, 93923 (408-625-6911)

1. BACKGROUND DISCUSSION

In the past 25 years, numerical weather prediction, remote sensing and collection of data by satellites and high-speed, global communications networks have revolutionized the weather services industry. Unfortunately, only the largest and wealthiest countries and/or commercial enterprises have had the resources to take full advantage of these technological advances. Smaller or less-developed nations and the more remote end users of weather information have not benefited commensurately for several reasons:

- The equipments to receive and process the data are too large and too complex.
- The costs of the systems are too high.
- The technology is beyond the capabilities of operating and maintenance personnel.

A number of the larger nations now operate regional or global forecast centers which routinely receive/process conventional observations as well as the latest satellite data and prepare state-of-art analyses and prognoses using advanced mathematical/-physical models. The World Meteorological Organization (WMO) distributes global collections of observations and finished products (numerical fields, messages or graphics) to major hubs through the Global Telecommunications System (GTS) and local or regional collectives and products to smaller, more remote users through radio broadcasts in either voice, teletype or facsimile mode. A number of countries transmit satellite data for local applications, such as Automatic Picture Transmission (APT) and other image broadcasts from their spacecraft.

A substantial amount of data are available to the smaller forecast office or other user of weather data. What is needed to use these data at remote stations is an integrated system which is affordable and semi-portable. The system should be capable of receiving, processing and displaying satellite data (such as APT data), radio-teletype broadcast data and radiofacsimile broadcast data simultaneously. It must be easy to operate and maintain, should possess enough central processor capacity for the user to run special-purpose software modules and should be capable of serving as a vehicle for further technological advances at the local level.

2. THE TECHNICAL OPPORTUNITY

The explosive growth in the speed and capacity of Personal Computers (PCs) coupled with the availability of powerful but tiny microchips provide a unique opportunity to assemble a truly low-cost Integrated Satellite APT and Weather Radio Broadcast Processor. The wide acceptance and use of PCs means that smaller users can now obtain computing systems capable of supporting multiple functions such as data receipt, image processing/display and algorithm solution at reasonable costs. Systems West's approach to an integrated system is to use a standard microcomputer of the IBM PC/AT class as a Central Processor, augment it with proprietary communications and display boards and combine it with a small but sensitive satellite receiver to realize an affordable, desk-top system which can simultaneously receive, process and display satellite images, radio-teletype messages and radiofacsimile graphics.

3. DESIGN REQUIREMENTS FROM THE USER VIEWPOINT

Remote users of weather data include fishing vessels, merchant ships, smaller detached weather service centers/offices, remote airport forecast offices, local government entities such as transportation and harbor master offices, field military units, etc. All of these require that the system be at least semi-portable, but the marine and military users also require a more rugged version which can withstand the shocks of ship motion and/or frequent moves to new locations. The special requirements of the marine and military user dictate that tape capsules and "Hi-G" disks rather than standard disks be considered as the main data storage device(s) in the Central Processor.

Since very few of the projected users now have VHF radio receivers capable of handling APT signals from NOAA or foreign satellites equipped for this type of broadcast, the system design must include a computer-tunable VHF radio, an omni-directional (monopole) VHF antenna and a low-noise VHF amplifier. At the same time, since many potential users already have H/F receivers to copy radioteletype and /or radiofacsimile

broadcasts, the system design should also contain provisions to connect to existing H/F radios (or to include high-quality H/F receivers if not already available).

Some of the projected users already have graphics printers and/or facsimile recorders; the system design should permit them to make use of existing output devices. Some users also originate local landline or radio-teletype/radio-facsimile broadcasts; the system should be able to function as a driver for these outgoing broadcasts.

Many of the prospective users have rigid operating schedules and must be able to receive and process satellite, radioteletype and radiofacsimile data simultaneously. The system design needs to accommodate this special requirement for timely receipt and processing.

Conventional weather data terminals have focused on display in straight black/-white or in shades of grey (typically for satellite images only). To obtain maximum definition of the detail available in APT broadcasts, it is desirable to have a display system which is also capable of handling an extended palette of colors. The system design should provide for display in multiple shades of grey AND in high-resolution color.

Finally, many users have expressed an interest in a system with enough capacity to permit the running of local/regional analysis and forecast models and/or special-purpose applications algorithms. The system design should recognize this requirement even to the extent of including optional higher-level (faster) chips or math co-processors to accelerate special problem solving.

Table 1 contains a summary of the design requirements which have been considered in Systems West's approach to an integrated system.

4. SYSTEM CHARACTERISTICS

Figure 1 presents an artist's concept of the Systems West Integrated Satellite APT and Weather Radio Broadcast Processor. This unit has been designed in response to the user requirements listed in Section 3. The Model 1000 meets the requirements for marine and military users who want a more rugged system, while the Model 2000 is a desk-top version suitable for use by weather services centers/offices and land-based commercial users. The primary differences in the two models are the data storage components and overall portability.

4.1 The Central Processor

The Central Processor selected for this system is a fully-compatible PC/AT micro-computer which is capable of running any existing software available for this class of computer. The general specifications for the Central Processor are given in Table 2; notice that the only difference in the Central Processors for the Model 1000 and Model 2000 are the use of a tape drive versus hard disk for data storage. The system is augmented with an 80287 math coprocessor and additional RAM memory to improve its overall performance.

4.2 The Data Manager System

Figure 2 is a schematic layout of the Data Manager Board (Card) showing how it connects to the Satellite APT (VHF) receiver, the HF/SSB (Single Side Band) receiver(s) for radio-teletype and/or radio-facsimile intercept and to output devices or broadcast channels. Some of the key features of this proprietary board are shown at the right side of the Figure. The board has self-contained computers to process all incoming data on the fly, and store the data in local memory. When a local memory buffer is full, data are transferred to the main computer using direct memory-to-memory transfer independent of the processor. It is this unique assembly of four miniature processors (CPUs), a DMA Controller and a Large Memory Buffer (Cache) on the Data Manager Board which permits the simultaneous handling of all these data streams.

Table 1. User Requirements Which Were Considered in Systems West's Design of an Integrated Satellite APT and Weather Radio Broadcast Processor.

- Affordable and Semi-Portable.
- Easy to Operate and Maintain.
- Rugged Version for Marine and Military Users.
- Desk-Top Version for All Other Users.
- Simultaneous Receipt and Processing of Satellite APT, Radio-Teletype and Radio-Facsimile Broadcasts.
- IBM PC/AT-Compatible Central Processor.
- Integrated VHF Satellite Receiver including Antenna and Low-Noise Amplifier.
- Optional Use of Existing H/F Radio Receivers, Facsimile Recorders, Graphics Printers.
- Capability to Drive Local Landline or Radio-Teletype/Radio-Facsimile Broadcast Networks.
- Display in Multiple Grey Shades and High-Resolution Color.
- Sufficient Central Processor Capacity and Flexibility to Run Local Analysis/Forecast Models, User Algorithms and Existing General-Purpose PC Software.
- Options to Add Higher-Speed Chips and/or Math Co-Processors.

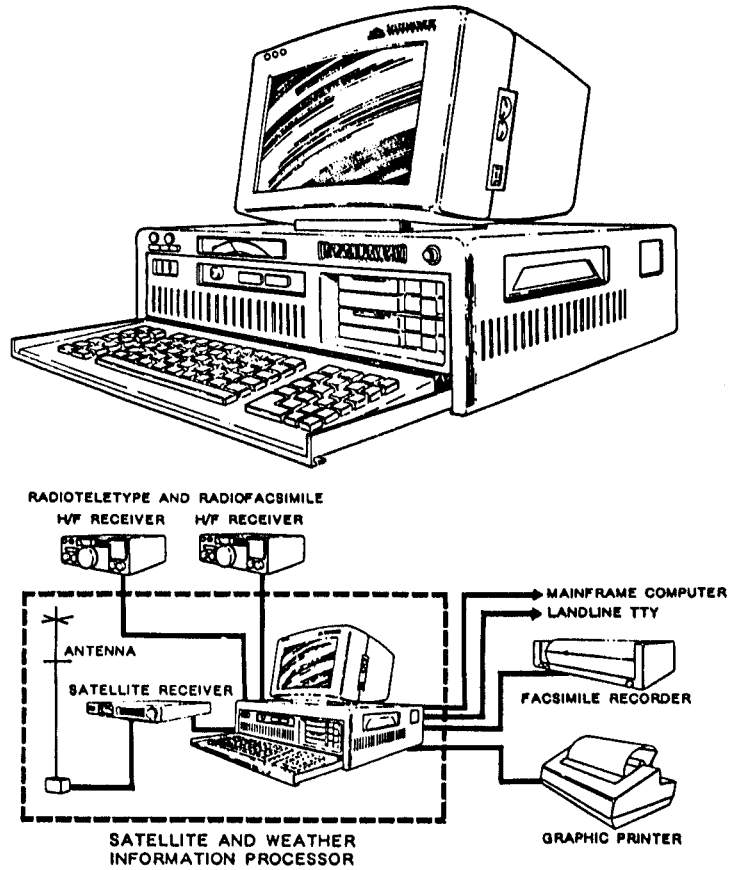

Figure 1. Systems West Integrated Satellite APT and Weather Radio Broadcast Processor (Artist's Concept)

Table 2. Characteristics of the Central Processor in the Systems West Integrated Satellite APT and Weather Radio Broadcast Processor

- Fully PC/AT Compatible
- 80287 Math Coprocessor
- 30MB Addressable Tape (Model 1000)
- 30MB Ruggedized Disk (Model 2000)
- 1.2MB Floppy Disk Drive
- 2MB Main Memory
- Special Data Manager Board (see Section 4.2)
- Special Video Display Board (see Section 4.3)
- Serial Port
- Parallel Port
- Keyboard
- Mouse or Joystick
- Analog Multisync Monitor
- Conventional and Special Systems West Software

4.3 The Video Display System

The video display system provides very high quality imagery using standard video monitors. Table 3 presents a summary of the capabilities which are achievable through the Video Display Board which Systems West has added to the Central Processor. This very advanced display board and its accompanying software give the user a variety of options concerning the number of grey shades, number of colors and/or resolution of the image he/she wishes to use for the particular product to be displayed. The system supports a full 64 shades of grey, while the color slicing which can be done on cloud or Sea Surface Temperatures is virtually unlimited.

4.4 Software

4.4.1 System Software. The computer operates two operating systems simultaneously. Foreground processing for user applications is performed by standard DOS 3.X, while the real-time background processing is performed by the Systems West real-time executive. This approach permits the user to use the computer for standard applications processing in the DOS environment, while data collection and transmission is proceeding unattended by the operator. This allows the user to run special applications models using the data bases or to run any other standard personal computer software.

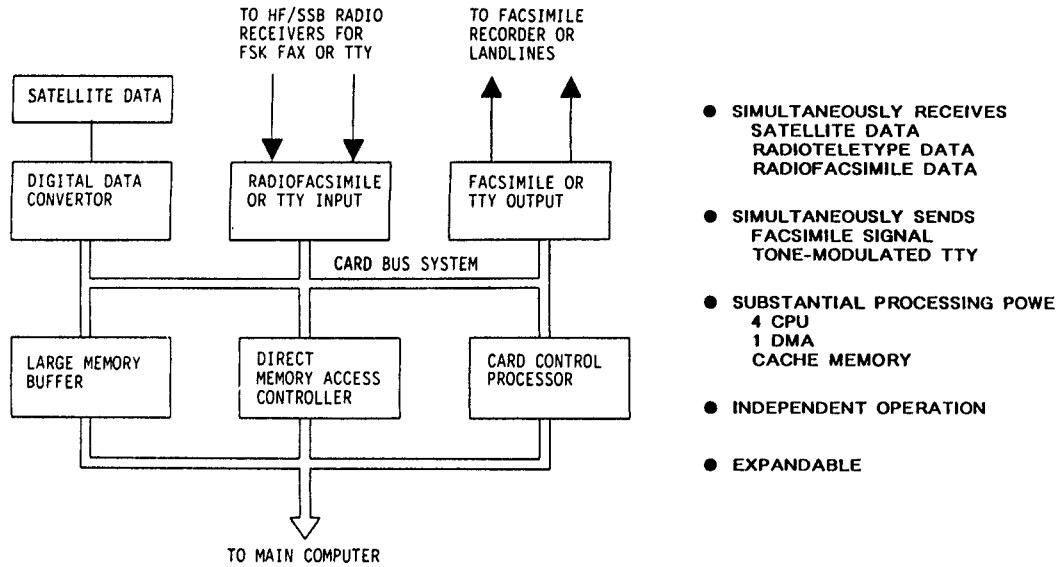

Figure 2. Schematic Layout of the Systems West Data Manager Board

Table 3. Video Display Board Capabilities

- 960 x 350 x 16 Color
- 640 x 480 x 16 Color

  [For Graphics, Facsimile & Text]

- 480 x 350 x 256 Color (22,000 Color Palette)
  x 64 Grey Shades

  [For Pictures]

- Mode Switching in Image
  - Pop-Up Windows

- Software Controlled
  - Mouse Windows, Graphics

Figure 3 shows the overview of the Systems West software from a user perspective. Those modules in the "systems area" on the figure are wholly under the control of the Systems West real-time executive, while those modules in the applications area are standard DOS programs. In consideration of the user interface issues, the interfaces between programs running in the real-time environment and the DOS environment are through standard DOS functions. The entire real-time executive is defined as a standard DOS device, allowing applications programmers to access the real-time executive through standard interfaces. This gives applications programmers full access to system control functions and data bases through high-level languages.

4.4.2 Satellite Data Processing. Satellite imagery are collected, calibrated, and placed into imagery files for display. The digitizing approaches and data storage algorithms are designed to extract the maximum amount of usable data from the signal and organize it into a rational data base.

The data base is organized into coherent visual and temperature pixels, allowing full overlay of the visual and temperature data. The data are located and a 5° lat-lon grid is placed on the image. The lat-lon grid can be any color the user chooses. The IR data are corrected using a secant curve correction for limb darkening.

The user has a wide variety of visual processing capabilities including pan, zoom, density slicing, false coloring, and temperature recalibration. The user can locate his own position on the screen, and can overlay other graphics and images if he wishes. A pop-up window can be retrieved at any time to show statistics about the cursor location, or to execute commands. Again, the system provides wide flexibility for user programmability for his own applications.

5.0 PLANNED AT-SEA EVALUATION

In the past several years, the American Tropical Tuna Fleet, operating mostly out of San Diego, has been fishing in a newly-opened Albacore Tuna fishery in the western South Pacific Ocean. These vessels typically follow the eastward migration of the Albacore toward the coast of South America and have found that this species of tuna has the same preference for environmental conditions as do their cousins in the Northern Hemisphere. That is, the Albacore prefer waters where the Sea Surface Temperature (SST) is between

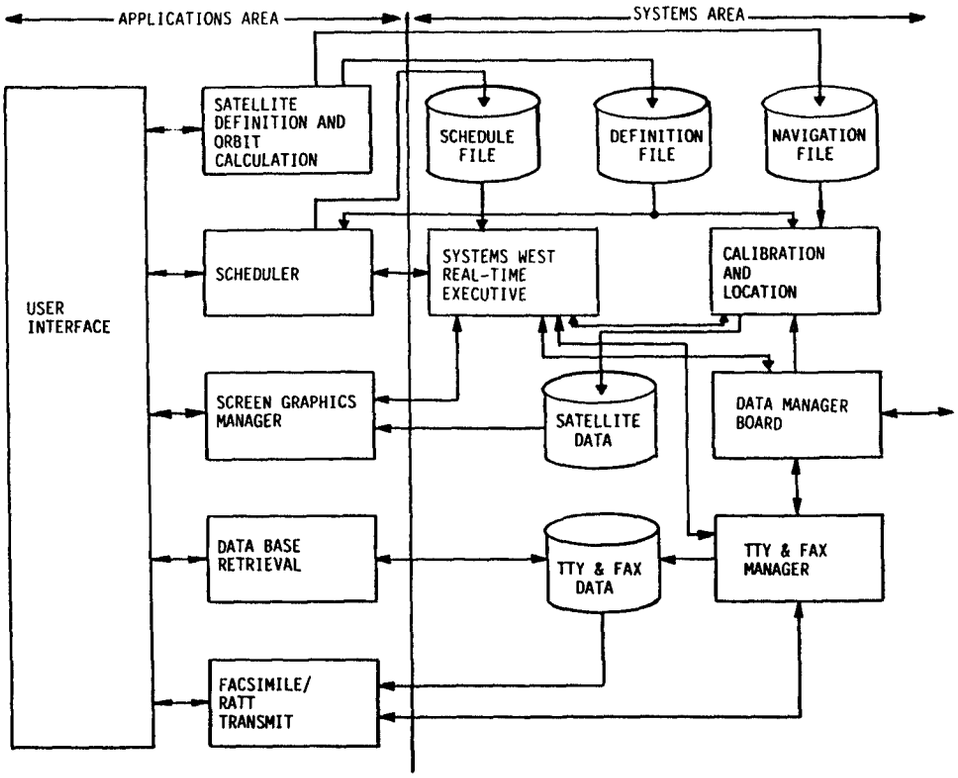

Figure 3. Overview of the Systems West Software

58F and 64F and tend to congregate within this SST band at locations where there is a local convergence.[1] These convergences are typically correlated with ocean color boundaries and/or local current boundaries as indicated by stronger horizontal gradients in the SST.[2]

Since the satellite data which will be copied by the Integrated Satellite APT and Weather Radio Broadcast Processor system receives both cloud images and SST values for cloud-free areas, Systems West has proposed an at-sea evaluation of the system to demonstrate its utility in locating optimum fishing areas for this new South Pacific fisheries. It has been proposed that the demonstration be jointly sponsored and funded by the National Marine Fisheries Service (NMFS), the Western Fishboat Owners Association and Systems West. Mr. Art Haworth, the owner and Captain of the American tuna clipper BARBARA H., has volunteered to make space available on his vessel for the equipment and an operator/-evaluator. Dr. William Hubert of Systems West, a recognized authority on fisheries applications, will conduct the experiment if approved. The vessel will operate as far south as 40 degrees South latitude.

IBM is a registered trademark and PC/AT is a trademark of International Business Machines, Inc.

The area to be fished by the BARBARA H. is quite remote and not characterized by good observational coverage or particularly good weather forecast services; therefore, the proposed demonstration project also provides a good opportunity to assess the value of the system for general weather forecasting for day-by-day safety of operations. The cloud images (and radio-teletype/radio-facsimile information if that processing software is ready in time) will be used by Dr. Hubert to monitor the synoptic situation and to prepare tailored operational forecasts for the vessel's Captain.

The at-sea evaluation will be used by Systems West to determine ways in which the system can be improved to:

- Locate optimum fishing areas for specific species of fish (Albacore tuna in this case).
- Maximize safety of operations in remote fishing areas.

6.0 REFERENCES

1. Jet Propulsion Laboratory, Users Guide: An Experimental Satellite-Oriented Observation Program for Commercial Fisheries. JPL 400 - 122 8/81. (1981)

2. W. E. Hubert, Seminar on Marine Meteorology/Oceanography for Fishermen and Other Mariners. Cal Tech-JPL-Univ. of Alaska Marine Advisory Program. (1982)

J3.4 A REAL-TIME INTERACTIVE SYSTEM TO PROCESS TIROS ASVHRR, TOVS, AND ARGOS DATA FOR USE IN METEOROLOGY, OCEANOGRAPHY, AND OTHER APPLICATIONS. Charles H. Vermillion and F. Stetina, NASA/GSFC, Greenbelt, Md.; J. Hill, Louisiana State Univ., Baton Rouge, La.; G. Shaffer, Science Systems and Applications, Inc., Beltsville, Md.

NASA Goddard Space Flight Center has developed a HRPT real-time ground station based on a program tracking antenna, MicroVAX II, and I2S IVAS image processor. The system receives in real time and processes the entire HRPT data stream including AVHRR imagery, the TOVS vertical sounder, and the ARGOS data collection platform data. Data processing software and image processing software has been developed for applications in meteorology, oceanography and hydrology. The data processing system produces information to help in the analysis of severe storm detection, cloud top temperatures, vegetation indexing, atmospheric stability, sea surface temperatures, water turbidity, and river flood stages. All imagery and data products are fully registered to allow overlay of a latitude/longitude grid and geographic information. Data products such as TOVS and ARGOS are overlayed on AVHRR images along with annotation and data field contouring. The TOVS analysis includes displays of temperature and dew point vertical profiles on a skew-t/log-p thermodynamic diagram. Other data products (LANDSAT, IEMIS, etc.) may be brought into the system to be combined with the HRPT data products for further analysis such as storm surge prediction. The software package developed for the ground station is interactive, user friendly, and menu driven.

J3.8 A SOFTWARE SYSTEM FOR PROCESSING TOVS ON A PERSONAL COMPUTER. W. L. Smith, R. G. Redecker, H. M. Woolf, H. B. Howell, W. P. Menzel and Qu Wanni, Cooperative Inst. for Meteorological Satellite Studies (CIMSS), Univ. of Wisconsin, Madison, Wis.

A software system has been developed for ingesting, calibrating, and earth locating TOVS (TIROS Operational Vertical Sounder) radiance data and then producing soundings and image/graphic products for real-time weather analysis/forecast applications. The system runs on IBM, or compatible, AT personal computers. In addition to a manuscript describing the software and associated hardware requirements for running it, a real-time demonstration of the system will be given at the conference.

J3.9 AN OVERVIEW OF INTERAGENCY TRAINER COORDINATED WORKING GROUP ACTIVITIES. Michael F. Squires, Dept. of the Air Force (DNTN), Scott AFB, Ill.

The Interagency Training Coordination Working Group (ITCWG) is a cooperative effort among several governmental agencies to crossfeed meteorological training materials and information. The ITCWG includes members from the Air Force, FAA, Navy, NESDIS, and NWS. To date there have been four coordination conferences.

Under the ITCWG, agencies can indicate their training priorities. Where mutual interest exists, joint production becomes possible. The most significant effort has involved the reprinting of NWS Forecasting Handbook #6 - " Satellite Imagery Interpretation for Forecasters". Rather than have each agency develop a similar publication, the same publication was shared among many agencies.

The purpose of this paper is to describe the evolution, accomplishments, and plans of the ITCWG. Specific attention will be focused on sharing of information to minimize duplication of training development efforts. The presentation by Mike Mogil will describe, in detail, training materials which have been developed and/or are under development.

X-BAND SCATTEROMETER MEASUREMENTS AT LOW WINDS IN A WAVETANK

Mary R. Keller and William J. Plant

Space Sensing Branch
Space Systems Technology Department
Naval Center for Space Technology
Naval Research Laboratory
Washington, DC 20375-5000

1. INTRODUCTION

For intermediate incidence angles, Bragg scattering of microwave signals from the ocean surface is the accepted explanation for radar returns from wind-generated waves. Recently, two models using Bragg scattering to relate wind waves and scatterometer measurements, both based on field results, have been published (Plant, 1986, and Donelan and Pierson, 1987). The models predict similar X-band backscatter values at high winds, for low winds, however, the model of Donelan and Pierson predicts a sharp drop-off to -50 dB while the model of Plant predicts a gentle roll-off to about -30 dB. While concentrating on the low wind speed range, we report experimental results, from a wavetank, for radar backscatter at X-band and compare them with the two models. Future work will expand comparisons to other models, such as those of Wentz (1984) and of Durden and Vesecky (1985).

2. EXPERIMENTAL CONDITIONS

The wavetank used to obtain these data is 30.5 m long, 2.4 m wide, and filled to a depth of 0.5 m. Winds are generated with a fixed speed, variable vane blower 29 m away from the measurement site. The upwind fetch was 16.5 m. Long waves are generated by a paddle 19.5 m upwind of the radar. The paddle is driven by a HP3325A synthesizer/function generator and a HP6824A DC power supply amplifier. Waves are damped at a beach at the far end of the tank, 10 m downwind of the measurement site. The antenna for the CW, 10 GHz radar is mounted 2.9 m above the water level and can be rotated for incidence angles from 2° to 87°. Wind speeds are measured by a pitot tube mounted 0.5 m away from the side of the tank and 23 cm above the water level. Hot film crossed wire anemometers mounted next to the pitot tube are used, when functional, to calculate wind stress and friction velocity.

The outputs, in voltages, from the radar, pitot tube, and hot film anemometers were sampled every eighth of a second for 2.1 minutes with a DEC MINC-11CA computer. Means and standard deviations were calculated for the radar cross-section and wind speed. Means only were calculated for the wind stress and friction velocity. Air and water temperatures were measured periodically using mercury thermometers suspended in the air channel and the water. Long wave amplitudes were set with the function generator and checked with a meter stick. The averaged values were stored on hard disk and transferred to a MICROVAX II for further analysis.

While operating at 48° incidence angle, the water in the tank was heated and cooled to measure temperature effects predicted by the Donelan and Pierson model. The tank was drained and refilled with heated (38°C) water and measurements were collected as the water cooled. Later, by adding dry ice to the tank, the temperature dropped to 14°C and measurements were collected as the water warmed. The lowest wind speeds the blower can generate, with the vanes completely closed, is 4 m/s (all wind speeds reported are for 19.5 meter neutral winds, which yield equivalent stresses under neutral conditions to those measured in the tank), well above the fall-off predicted by the Donelan and Pierson model. For winds below 4 m/s, the blower output was partially blocked at the point the air enters the fetch channel with plastic stretched over a screen. The plastic panel was removed for high winds and reinserted to generate the low winds at all incidence angles.

3. RESULTS

Vertical polarization backscatter measurements were made at 48°, 68°, and 28° incidence angles. Wind speed ranged from 1 m/s to 22 m/s. The temperature of the water and air, other than when the water temperature was deliberately varied, drifted with ambient conditions. Long wave effects were measured only for the 28° incidence angle. With a constant frequency of 1 Hz, long wave amplitudes of 4.5 cm, 2.5 cm, 0.5 cm, and 0.25 cm were generated to observe the effect of varying amplitude on low wind speed backscatter measurements. The experimental results are plotted versus wind

speed in Figures 1-5 against calculated values from the Donelan and Pierson and Plant models. The data show about a 3 dB scatter in cross-section and about 0.2 m/s in wind speed. The water temperature was varied from 14°C to 36°C and the winds from 4 m/s to 22 m/s while at 48° incidence angle. As shown in Figure 1, within the data scatter, no dependence on temperature was found. No further temperature dependence was examined, although the air and water temperatures were carefully monitored.

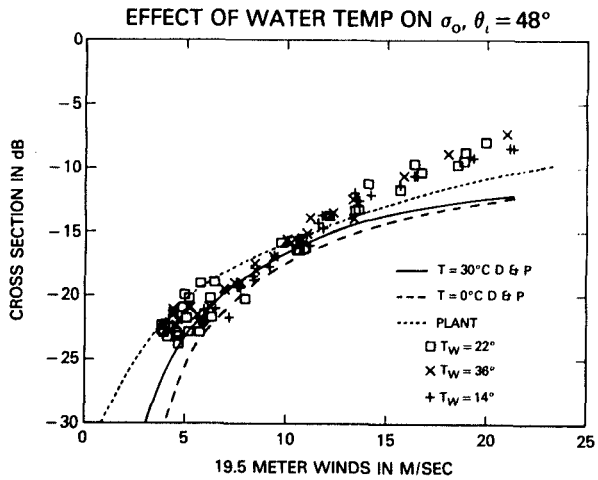

Figure 1. Cross section as a function of 19.5 meter winds at 48° incidence angle showing the effects of water temperature on the backscatter. Model calculations are for 50° incidence angle.

4. COMPARISON WITH MODEL CALCULATIONS

In the absence of long waves, the Donelan and Pierson model predictions compared well to the experimental data. At 48° incidence angle (Figure 2), both models predicted lower values than the measurements for wind speeds above 11 m/s. At the 68° incidence angle (Figure 3), the distributions of the wavetank cross sections with wind speed have the same slope as the 48° data above 4 m/s, but are about 9 dB lower. Neither model agrees with the data in this wind speed range for 68° incidence angle. At the 28° incidence angle (Figure 4), the data follow the predictions of the Donelan and Pierson model up to 16 m/s, where the cross sections increase faster at low winds than Plant's predictions. Above 16 m/s, the data follow the Plant model, which crosses over the Donelan and Pierson model and predicts higher values.

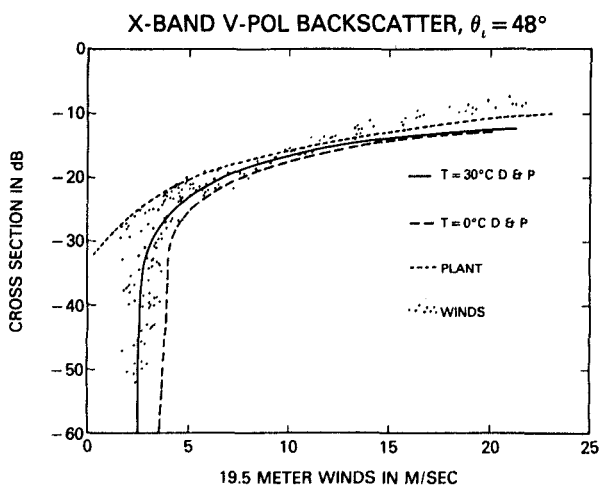

Figure 2. Cross section as a function of 19.5 meter winds at 48° incidence angle across the entire wind range. Model calculations are for 50° incidence angle.

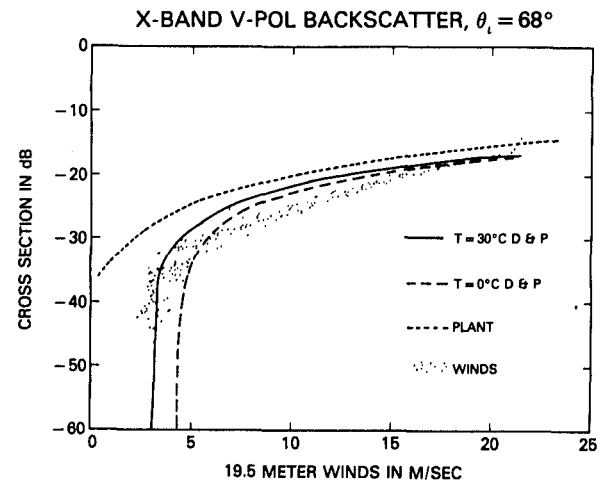

Figure 3. Cross section as a function of 19.5 meter winds at 68° incidence angle across the entire wind range. Model calculations are for 70° incidence angle.

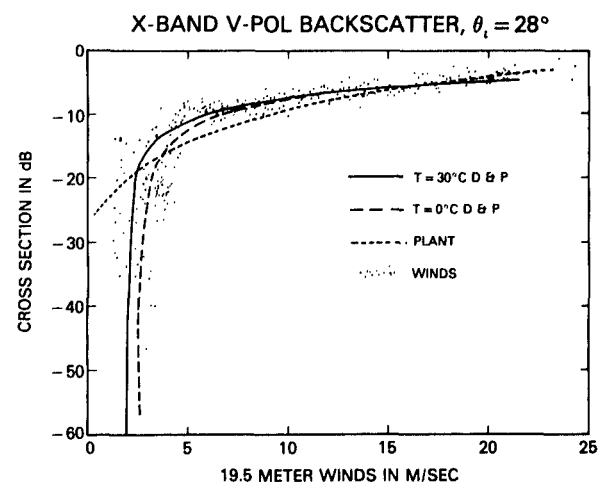

Figure 4. Cross section as a function of 19.5 meter winds at 28° incidence angle across the entire wind range. Model calculations are for 30° incidence angle.

The addition of long waves to wind-generated waves effectively eliminated the sharp drop-off in mean cross-section at low winds (Figure 5). A long wave amplitude of 4.5 cm allowed only 3 dB variation in backscatter as the wind was varied from 1.5 m/s to 5.5 m/s. Over this same range, the backscatter with no long waves present had shown a 40 dB variation.

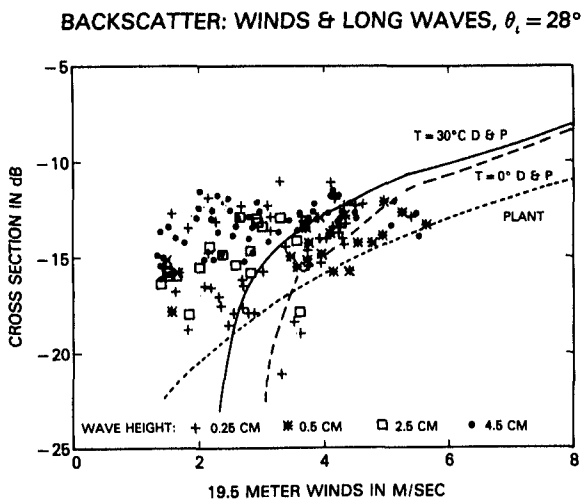

Figure 5. Cross section as a function of 19.5 meter winds and long wave height at 28° incidence angle. Model calculations are for 30° incidence angle.

As the long wave amplitude decreased, the variation in backscatter increased, from 3 dB at 4.5 cm amplitude to 5 dB at 2.5 cm amplitude, 6 dB at 0.5 cm amplitude, and 10 dB at 0.25 cm amplitude. In the presence of long waves, the cross sections never fall much below the higher calculations of the Plant model, which has a wind-speed dependence at low winds similar to that of the measurements generated in the presence of the 0.5 cm amplitude long wave.

5. CONCLUSION

The results of this study, when compared with the calculations of the Donelan and Pierson and Plant models, show strengths and weaknesses for both. Although the Donelan and Pierson model predicted the observed sharp drop-off in cross section at low winds, no temperature dependence was observed. The Plant model, although not predicting this sharp roll-off, yielded good results at high winds and at low winds when small-amplitude, low frequency long waves were present. Wind-generated waves in the tank have characteristically steeper slopes than those encountered in the field, which may explain some of the discrepancies between the Plant model and the wavetank data. Based on these results, further refinements are called for in both models. Our future work will look into other models, polarization and frequency effects, backscatter at other azimuth angles, and scattering effects which may be specifically related to the wavetank.

6. REFERENCES

Donelan, M. A., and W. J. Pierson, 1987: Radar scattering and equilibrium ranges in wind-generated waves with application to scatterometry, J. Geophys. Res., 92(C5), 4971-5029.

Durden, S. L., and J. F. Vesecky, 1985: A physical radar cross-section model for a wind driven sea with swell, IEEE J. Ocean Eng., OE-10, 451-454.

Keller, W. C., W. J. Plant, and D. E. Weissman, 1985: The dependence of X band microwave sea return on atmospheric stability and sea state, J. Geophys. Res., 90, 1019-1029.

Plant, W. J., 1986: A two-scale model of short wind-generated waves and scatterometry, J. Geophys. Res., 91(C9), 10,735-10,749.

Plant, W. J., and J. W. Wright, 1977: Growth and equilibrium of short gravity waves in a wind-wave tank, J. Fluid Mech., 82, 767-793.

Wentz, F. J., S. Peteherych, and L. A. Thomas, 1984: A model function for ocean radar cross sections at 14.6 GHz, J. Geophys. Res., 89, 3689-3704.

Wright, J. W., 1966: Backscattering from capillary waves with application to sea clutter, IEEE Trans. Antennas Propag., AP-14, 749-774.

Wright, J. W., 1968: A new model for sea clutter, IEEE Trans. Antennas Propag., AP-16, 217-223.

Wright, J. W., and W. C. Keller, 1971: Doppler spectra in microwave scattering from wind waves, Phys. Fluids, 14, 466-474.

USING SATELLITE SCATTEROMETER DETERMINED WINDFIELDS TO OBTAIN SYNOPTIC-SCALE SURFACE PRESSURE FIELDS

R. A. Brown
University of Washington
Seattle, Washington

The successful derivation of surface pressure maps from a satellite microwave scatterometer plus a single surface pressure data point was demonstrated by Brown and Levy (1986). The implications of the agreement between these pressure fields and those produced with the National Weather Service analysis are significant.

Thus, the well-known caveats to the relation between microwave scale water waves and surface winds or stress (e.g. Brown, 1986) are not enough to dismiss the correlation. The scatterometer winds, including direction, must be accurate to about ± 2 m/s and 20° in order to have produced the agreement with the NWS maps, which were determined for regions using relatively dense (at least one measurement per 200-400 km) surface pressure measurements accurate to ± 2 mb. This is the agreement accuracy found in the SEASAT scatterometer (SASS) verification procedure, for windfields with good horizontal uniformity (Brown, 1983).

In addition, the Planetary Boundary Layer (PBL) model which was used to relate the surface winds to gradient winds and thereby pressure gradient fields, must not have introduced significant error. Our initial comparisons covered two regions in the north Pacific, one in the Atlantic. The Pacific areas were well covered by ships and buoys, while the Atlantic case (the QE II storm) featured a carefully reworked surface pressure analysis. In sensitivity studies with this model, we found that the effects of PBL stratification, when included in both the surface layer and the Ekman layer (via organized large-eddies), produced changes commensurate with the differences between satellite derived and NWS analyzed fields. Since the inclusion of these effects generally led to smaller differences between the fields, it was assumed that the optimal model must include them.

Finally, it is evident that the NWS smoothed pressure fields eliminated any pressure variations on scales less than about 400 km. Since the scatterometer can produce 100 wind measurements in a square this size, there is possibly more information on pressure field variability in the satellite derived fields. The comparison fields in figure 1 show increased variability in the satellite-PBL

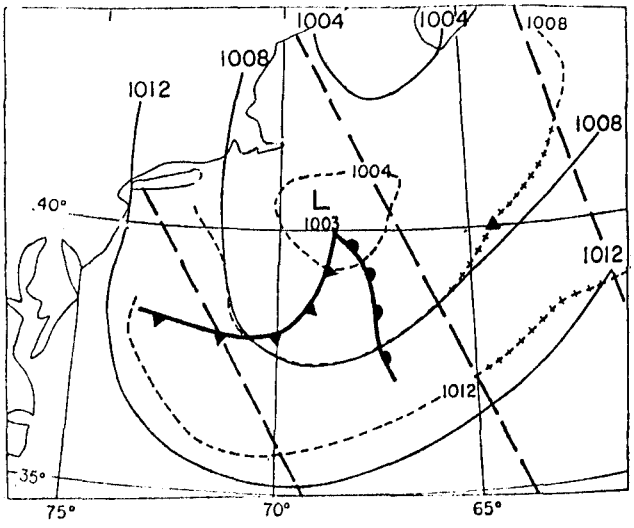

Figure 1. Conventional (solid) and Model (dashed, from SASS) derived pressure fields for Atlantic storm, 1200 GMT, 9 Sep 1978. Bold lines mark scatterometer data swath, triangle is pressure data.

model fields. A priori, it is difficult to determine whether these variations are geophysical or artifacts produced by our processing, which includes smoothing. This question cannot be resolved by comparison with surface observations, since they are not sufficiently accurate or dense. However, we have checked our predicted pressure fields against all available surface pressure information, and there are no inconsistencies. More information can be gained from statistics obtained from numerous comparison fields, and we have begun this process.

There are 100 days of global coverage from SEASAT. We have found that a combination of SASS and SMMR works well to locate significant mesoscale weather patterns (generally, cyclones). The scatterometer pattern in its multiple vector form (chicken tracks) serves well to locate storms and fronts, as discussed by Brown (1983). The SMMR water content information also has a characteristic frontal signature, as discussed by McMurdie, Levy and Katsaros (1987), although this is not as evident in southern hemisphere storms as in the northern hemisphere. Once the storm center and any fronts are located, the SASS wind-

field can be uniquely determined, using characteristic patterns for cyclonic storms. The SASS data is then sufficient to produce surface pressure fields for a neutrally stratified PBL, given a single surface pressure measurement. In the absence of the surface pressure measurement, an arbitrary value can be assigned with no information lost on the dynamics of the system.

When a system is found that is well covered by SASS and/or SMMR, corrections for PBL stratification, and possibly thermal wind are merited. The model predicts that major changes in the speed ratio of surface to geostrophic winds and in the turning angle occur very near the neutral stratification point. Therefore, the large variations, as shown in figure 2, can be incorporated by simply denoting

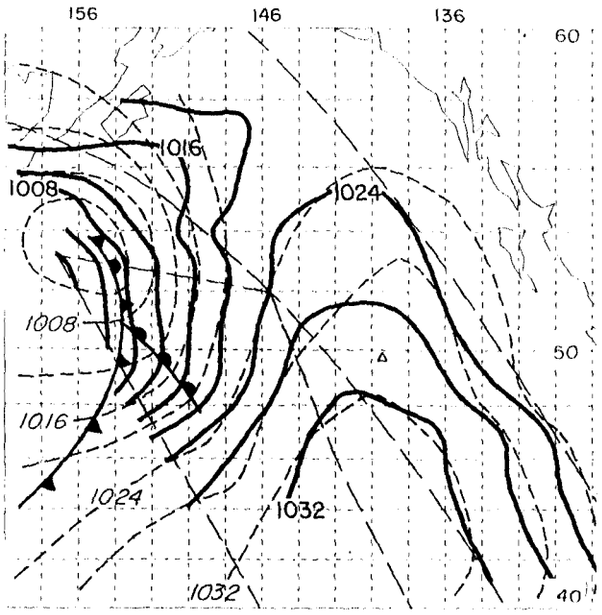

Figure 2. Model (solid) and NWS (dashed) derived pressure fields for the north Pacific, 17 Sep 1978.

unstably and stably stratified regimes. These regimes can be taken from characteristics of such cyclonic storms as discussed by Bond and Fleagle (1985) and Nuss and Brown (1987). When satellite derived SST are available, they provide part of the information needed to evaluate stratification. However, the air temperature is generally not available from satellite data. Currently, for the purpose of obtaining the best possible pressure fields, we resort to ancillary temperature data when available to quantify the stratification. In a similar fashion, we can evaluate the effect of baroclinicity, which generally serves to enhance the effects of stratification (Levy, 1987).

We have identified ten cases of Southern Hemisphere storm systems identified in quick-look surveys of SASS and SMMR swath data. The analysis of these systems form the basis for determining pressure field details, an evaluation of microwave remote sensing capability in examining mesoscale storm systems, and an assessment of characteristics of these storms.

References:

Bond, N.A. and R.G. Fleagle, 1985: Structure of a cold front over the ocean. Quart. J. R. Soc., 111, 739-756.

Brown, R.A., and G. Levy, 1986; Ocean Surface Pressure Fields from Satellite Sensed Winds, Monthly Weather Review 114, pp 2197-2206,.

Brown, R.A., 1983; On a Scatterometer as an Anemometer. J. Geophys. Res., 88, C3, 1663-1673.

Brown, R.A., 1986: On Satellite Scatterometer Capabilities in Air-Sea Interaction. J. of Geophysical Res., 91, 2221-2232.

Levy, G., 1987; A Study of the Dynamics of Maritime Fronts Using Remotely Sensed Wind and Stress Measurements, PhD Thesis, University of Washington.

McMurdie, L. A., G. Levy, and K. B. Katsaros, 1987; On the relationship between scatterometer derived convergences and atmospheric moisture. Monthly Weather Review, 115, 7, 1281-1294.

Nuss, W. and R.A. Brown, 1987; Evaluation of Surface Winds and Flux Analysis in Mid-Latitude Marine Cyclones, J. Dynamics of Atmospheres/Oceans, 10, 291-315.

Determining Equivalent Depths of the Atmospheric Boundary Layer Over the Oceans

Tsann-wang Yu
National Meteorological Center
NWS/NOAA, Washington, D. C., 20233

1. INTRODUCTION

In a previous study, the writer proposed a technique to deduce wind directions from the SEASAT altimeter and scatterometer wind speed measurements (Yu, 1987a). This technique is based on simple vertically integrated Ekman boundary layer dynamics and uses the sea level pressure analyses together with satellite measured wind speeds. Implied in this technique is a parameter, hereafter referred to as "the atmospheric boundary layer equivalent depth", $\hat{h}$. The equivalent depth is defined as $\hat{h} \equiv \int_0^h A\,dz / A_0$, where h is the height of the atmospheric boundary layer above which the effect of the surface stress becomes negligible, and A_0 refers to surface value of quantity A. Thus the equivalent depth is a characteristic length scale which, together with the surface value of any quantity enables one to estimate the integral value of that quantity within the atmospheric boundary layer.

This study presents a method for determining the equivalent depths of the atmospheric boundary layer over the oceans. However, it should be pointed out that the method may be equally applicable over land. Section 2 discusses the computational procedure which may apply to all sources of wind speed data including reports from ships and buoys over the oceans and surface reports over land. But for this study, we shall deal exclusively with the space borne wind speed measurements. Section 3 presents results calculated by using three days of the altimeter wind speed data taken from SEASAT. It will be shown that the equivalent depths thus computed are generally of the same order of magnitude as the height of the atmospheric boundary layer in mid-latitude regions. Further, the $\hat{h}$ values are quite realistic and remain bounded in the tropics. In view of the fact that GEOSAT now operationally provides altimeter wind speed measurements over the global oceans, the method discussed here permits one to routinely compute the equivalent depths of the atmospheric boundary layer. These equivalent depths should be particularly useful for initialization of atmospheric mixed layer models over the oceans (e.g., Suarez et al, 1983, and Yu, 1986).

2. THE ANALYSIS PROCEDURE

The method is based on Ekman boundary layer dynamics which assume a balance between the pressure gradient, Coriolis, and frictional forces in the atmospheric boundary layer. The reader is referred to Yu (1987b) for a more detailed description of the analysis technique. Here we shall briefly summarize the analysis procedure. If we integrate the Ekman boundary layer dynamics from surface to the top the boundary layer where the momentum fluxes are assumed to be zero, and assume that the surface momentum fluxes can be represented by a quadratic law in terms of surface drag coefficient, C_D, and surface wind speeds, one can derive the equations of motion valid over the ocean surface, i.e.,

$$-f v_0 = -\frac{1}{\rho}\left(\frac{\partial P}{\partial x}\right)_0 - \hat{C}_D |S_0| u_0$$

$$f u_0 = -\frac{1}{\rho}\left(\frac{\partial P}{\partial y}\right)_0 - \hat{C}_D |S_0| v_0 \qquad (1)$$

where P is atmospheric pressure, f is Coriolis parameter, ρ is density of the air, u and v are wind components in the east-west and north-south directions respectively, and S_0 is the surface wind speed, i.e., $S_0 = (u_0^2 + v_0^2)^{1/2}$. Note that $\hat{C}_D$ is an effective surface drag coefficient. It is defined as, $\hat{C}_D \equiv C_D / \hat{h}$. It follows from (1),

$$\hat{C}_D = \left[\left(\frac{1}{\rho} |\nabla P|_0 \right)^2 - f^2 S_0^2 \right]^{1/2} / S_0^2 \qquad (2)$$

From equation (2), one can uniquely

determine the effective surface drag coefficient from given pressure gradient and wind speed measurements and does not require any a priori specification of the surface drag coefficient. From (2), one can write,

$$\hat{h} = C_D S_0^2 / \left[\left(\frac{1}{\rho}|\nabla p|_0\right)^2 - f^2 S_0^2 \right]^{1/2} \qquad (3)$$

Equation (3) establishes a relationship between the equivalent depth of the boundary layer and wind speed, surface pressure gradient, and a chosen value of the surface drag coefficient. Therefore, if we know the pressure gradient from any conventional meteorological analysis, the wind speed from conventional or space borne measurements, we can compute the equivalent depth from (3) once a value of surface drag coefficient is specified. Moreover, it is seen from (3) that the equivalent depth of the boundary layer is well defined at the equator where f = 0. An important point to note in connection with equation (3) is that if the wind speed is provided from a measurement, the other variable that is required to determine $\hat{h}$ is the surface pressure field. The latter is an integral of the mass through the depth of an atmospheric column, and is not influenced by the details of boundary layer physics. Hence the surface pressure is probably the most reliable analysis field available on a global basis as compared to other meteorological variables from routine numerical weather prediction models.

From equation (3), we see that in order to compute the equivalent depth ,one needs to specify the surface drag coefficient. Garrat (1977) has recently made a thorough review of previously reported values of surface drag coefficients in relation to the ocean surface winds. He compiled observations of wind stress and wind profiles reported in the literature, and found them to be consistent with the Charnock's (1955) relation between aerodynamic roughness (z_0) and friction velocity (u_*); that is, $z_0 = \alpha u_*^2 / g$, with α = 0.0144, and g = 9.8 m / sec^2. He further argues that for practical purposes, Charnock's relation may be closely approximated (in the range of wind speed between 4 m/sec and 21 m/sec) by a neutral drag coefficient (referred to 10 meters above the ocean surface) varying with the 10 m wind speed in a linear form,

$$C_D = (0.75 + 0.67\ S_0) \times 10^{-3} \qquad (4)$$

In this study, we shall adapt this formulation for surface drag coefficient over the oceans. Based on equations (3) and (4), we see that if the surface drag coefficient is a linear function of surface wind speed, the equivalent depth is proportional to the cubic power of wind speed at low latitudes. In higher latitudes, it depends on the square of the wind speed and the ageostrophic contribution of the wind fields.

According to Blackadar and Tennekes (1968), the height of the boundary layer may be estimated by a relationship between surface friction velocity and Coriolis parameter. Since the surface friction velocity u_* is related to the surface wind speed and drag coefficient by the relationship, i.e., $u_* = \sqrt{C_D}\, S_0$ (e.g., Hasse and Dunkel, 1974) , we shall also calculate heights of the atmospheric boundary layer using the altimeter wind speeds according to the formulation, i.e.,

$$h = \varepsilon u_* / |f| \quad ; \quad \varepsilon = 0.25 \qquad (5)$$

The formulation for the atmospheric boundary layer according to equation (5) is reasonable in mid-latitudes, but is not valid in the tropics, where the height becomes unbounded as one approaches the equator. In order to apply equation (5), we shall make use of the beta plane approximation for the tropical region, that is $|f| > f_0 = \beta y$ = 2.5 x 10^{-5} sec^{-1}, where β = 2.2 x 10^{-11} m^{-1} sec^{-1} , and y = 1200 km are used in this study. This is equivalent to limiting values of the Coriolis parameter to be no less than the value at 10 degrees north latitude.

3. RESULTS FROM SEASAT WIND SPEED DATA

For this study, wind speeds were taken from the altimeter wind speed measurements from SEASAT, and the corresponding surface pressure gradients from the National Meteorological Center (NMC) analyses. These three days altimeter data from SEASAT are identical to those used in a previous study of vector retrievals from the altimeter wind speeds reported in Yu (1987a). Further, the altimeter wind speed measurements were taken at all points along the satellite tracks that fall within one and half hours before and after the surface pressure analysis time. On the average, the altimeter measures ocean surface winds every second or so, which can in principle result in nearly a maximum of ten thousand data points for a three hour window. Since the computational procedure laid out in equations (6), (7) and (11) depends on the use of NMC's sea level pressure fields which are analyzed on a 2.5 by 2.5 degrees longitude-latitude grid, we also applied an averaging procedure in this study as discussed in Yu (1987a) to obtain the satellite altimeter wind speeds on the

same grid. The averaging procedure is such that the weighting of each data point is inversely proportional to the distance between the data and the grid point to which the average will be assigned. Typically about 40 data points are used to generate an average grid point value. The total number of altimeter data after the averaging is about 300 for the SEASAT period (N=276 for September 17, N =279 for September 18, and N = 317 for September 19, 1978) during the three hour window.

Following the previous discussions, we see that equivalent depths and effective surface drag coefficients are functions of three variables, that is, surface pressure gradient, wind speed, and latitude. Since the surface wind speed is somewhat correlated with the surface pressure gradient, we shall group the results into two independent categories, namely, latitude ϕ , and surface wind speed, S . Further, we shall classify the wind speed into two ranges: light wind speed range for S < 5 m/sec , and medium wind speed range for 15 m/sec > S > 5 m/sec. During the two three day periods, there were only few observations with wind speeds greater than 15 m/sec and these were ignored. Similarly, we shall classify the latitudinal dependency into three regions: polar region for $|\phi| > 60^\circ$, mid-latitude region for $60^\circ > |\phi| > 20^\circ$, and the tropics for $|\phi| < 20^\circ$. From Table 1, one can see that during the three days period, the wind speeds do not show a large variability within the two speed ranges. The mean SEASAT altimeter wind speed for the light wind speed range is about 2 m/sec in the polar region, and about 3-4 m/sec in the mid-latitudes and tropics; and for the medium wind speed range, the means are about 8-9 m/sec from the polar region to the tropics. On the other hand, for each wind speed range, the analyzed NMC's sea surface pressure gradients show a large variability, being much larger in the polar region than are at the tropics. Further, the standard errors (the bracketed values in Table 1) for the NMC's pressure gradients are about 10% of the means, which is much larger than those for the altimeter wind speeds. This relatively large uncertainly about the means in the NMC's pressure gradient term clearly indicates a large variability within the three latitude categories used for this study, and will undoubtedly contribute to larger variances in the other derived quantities.

Before discussing the calculated results of equivalent depths, and heights of the atmospheric boundary layer, it is instructive to examine the calculated values of the surface drag coefficient and the effective surface drag coefficient and their dependency on wind speeds and latitudes shown in Table 1. The mean value of the surface drag coefficient is nearly constant (C_D = 0.0013) in the wind speed range of 15 m/sec > S > 5 m/sec. For wind speeds less than 5 m/sec, the values of the surface drag coefficient decrease to about 0.0008-0.0010. These mean values with very small standard errors, as expected, compare favorably with the values of surface drag coefficient reported in the literature (e.g., Garrat, 1977).

From equation (2), the values of the effective surface drag coefficient are directly proportional to the departure of surface wind speeds from geostrophy, and inversely proportional to the square of surface wind speeds. Hence the calculated values of the effective surface drag coefficient are larger in the light wind category than they are in the medium wind speed range. Moreover, values of the effective surface drag coefficients are calculated to vary between 2.02×10^{-6} meter^{-1} in the tropics to 8.87×10^{-6} meters^{-1} in the polar region (see Table 1) . The large values in the polar region may be explained by much larger values of the NMC's surface pressure gradient term as discussed earlier. It may be pointed out that the NMC's surface pressure analysis is produced by updating the forecast model's first guess by surface ship observations of winds and pressures over the oceans through a multivariate optimum interpolation analysis scheme (Dey and Morone, 1984). If the observed altimeter wind speeds represent the true state over the ocean surface, the large values of the effective surface drag coefficient which is indicative of large departure from the geostrophy in the polar region, would seem to suggest that the first guess of surface pressure from the NMC's forecast model is far from being in geostrophic equilibrium with the observed altimeter surface winds. To a lesser degree the same consideration may also be applied in the tropics. On the other hand, one can similarly postulate that in mid-latitudes where there are more surface observations to update the model first guess of surface pressure, and therefore, the observed altimeter wind speeds are in a closer balance with the analyzed NMC's surface pressure fields.

The equivalent depths calculated for the mid-latitude region are found to be comparable but slightly less than heights of the atmospheric boundary layer. That is, the values of equivalent depths are about 700-800 meters in the range of surface wind speeds between 5 m/s and 15 m/s for the SEASAT period (Table 1). These values

should be compared with heights of the boundary layer, which are about 800 - 900 meters. When the surface wind speed is less than 5 m/sec, the equivalent depths decrease to about 300 - 500 meters, which are quite comparable to the values of about 300 -400 meters for boundary layer . Note that in each category, the standard errors for both the equivalent depths and the atmospheric boundary layer heights are calculated to amount to about 15-20 % of the mean values.

The equivalent depths calculated for the polar region are smaller than those in mid-latitudes and tropics. Similarly, the heights of the atmospheric boundary layer calculated according to equation (5) exhibit their minimum values in the polar region. In the light wind category, (i.e., S < 5 m/sec) the calculated equivalent depths are quite comparable to those calculated by the conventional scale height formulation, and the values are found to vary between 100 and 200 meters. In the medium wind speed range (i.e., 15 m/sec > S > 5 m/sec), the equivalent depths are found to vary between 200 and 600 meters whereas the heights of the atmospheric boundary layer are about 600 meters for all cases. This large variation in the values of equivalent depths calculated for the polar region is clearly caused by the large values of the effective surface drag coefficients as explained previously.

The main advantage of using the equivalent depth as a scale height is that at the equator it is well defined, and the values in the tropics in general are about 650 - 900 meters in the wind speed between 5 m/sec and 15 me/sec (Table 1). These values are quite realistic over the tropical oceans where the height of the boundary layer should be expected to correspond to approximately the top of lifting condensation level, or the cloud base corresponding to the top of the tropical atmospheric mixed layer. This is consistent with the results reported in Betts (1976) which based on the BOMEX tropical data show that the top of the mixed layer occurred at a height between 500 and 1500 meters. On the other hand, the use of equation (13) for the boundary layer depths leads to unacceptable values, which can be as large as about 2500 meters even with the tropical beta- plane approximation.

4. SUMMARY

This study discusses a method by which the equivalent depths of the atmospheric boundary layer may be computed from sea level pressure analyses and ocean surface wind speed measurements. An explicit representation for the equivalent depth has been given in terms of the sea level pressure gradient, wind speed and the surface drag coefficient. The equivalent depths were calculated from a three-days periods of altimeter wind speed data taken from SEASAT. For comparison, a conventional scale height formula is used to calculate the heights of the atmospheric boundary layer. This study shows that: over the mid-latitudes and in the range of wind speeds between 5 m/sec and 15 m/sec, the equivalent depths, calculated to vary between 700 and 800 meters, are found to be quite comparable to the heights of the atmospheric boundary layer which are calculated to vary between 800 and 900 meters. When the surface wind speeds decrease to less than 5 m/sec, both the equivalent depths and the atmospheric boundary layer decrease to about 300-500 meters in the mid-latitudes. In the polar region, both scale heights are found to be smaller and quite comparable in values, ranging between 200 and 600 meters. In the tropics, however, use of the conventional scale height for the atmospheric boundary layer gives unreasonably large values whereas the equivalent depths are calculated to be about 600-1000 meters. These values compare favorably with the observed heights of the atmospheric mixed layer over the tropical oceans. It is therefore argued that the equivalent depths may be more appropriately used as scale heights over the tropical atmospheric boundary layer, and can be used for initialization of tropical mixed layer models.

Acknowledgements:

The writer would like to express his sincere thanks to D.B. Rao for suggesting the concept of the equivalent depths, and for the time spent in many stimulating discussions and reviews of the paper.

REFERENCES

Betts, A. K., (1976): The thermodynamic transformation of the tropical subcloud layer by precipitation downdrafts, J. of Atmos. Sciences, vol (34), pp. 1008-1020.

Blackadar, A. K.,and H. Tennekes,(1968): Asymptotic similarity in neutral barotropic planetary boundary layer, J. of Atmos. Sciences, vol.(25), pp 1015-1020.

Charnock, H., (1955): Wind stress on a water surface, Quarterly Journal of the Royal Meteorological Society, vol.(81), p 639

Dey, C.H., and L.L. Morone(1985): Evolution of the National Meteorological Center global data assimilation system: January 1982-December 1983, Monthly Weather Review, vol 113 (3), pp. 304-318

Hasse, L., and M. Dunkel (1974): Direct determination of geostrophic drag coefficients at sea. Boundary Layer Meteorology, vol (7), 3, pp. 323-329

Garrat, J.R.,(1977): Review of drag coefficient over oceans and continents, Monthly Weather Review, vol.(105), pp 915-928

Suarez, M., A. Arakawa, and D. A. Randell (1983): The parameterization of the planetary boundary layer in the UCLA general circulation model: Formations and results, Monthly Weather Review, vol (111), pp. 2224-2243

Yu, T. W., (1986): A global atmospheric mixed layer model designed for operational marine weather prediction, a poster session paper presented at WMO/IUGG International Symposium on short and medium range numerical weather prediction, Tokyo, Japan, August 4-8, 1986. (WMO PSMP Report Series 19, page 291.)

Yu, T. W., (1987a): A technique for deducing wind direction from satellite microwave measurements of wind speed, Monthly Weather Review, (to appear in the September issue).

Yu, T.W., (1987b): Determining Equivalent depths of the atmospheric boundary layer over the oceans, submitted to Boundary Layer Meteorology.

Table 1: Means and standard errors of the means (values inside the brackets) calculated for equivalent depth $\hat{h}$ (meters), atmospheric boundary layer depth h (meters), surface drag coefficient C_D (10^{-3}), effective surface drag coefficient $\hat{C}_D$ (10^{-5} meters^{-1}), NMC's sea level pressure gradient $\frac{1}{\rho}|\nabla p|$ (10^{-4} meter/sec^2),and altimeter wind speed S (m/sec) for three days of altimeter data from SEASAT satellite.

Dates		9/17/78 00z		9/18/78 00z		9/19/78 00z	
Wind speeds (m/s)		$S < 5$	$15 > S > 5$	$S < 5$	$15 > S > 5$	$S < 5$	$15 > S > 5$
Polar Region $\lvert\phi\rvert > 60^\circ$	N	35	40	51	53	63	35
	$\hat{h}$	190 (44)	579 (88)	156 (30)	341 (56)	110 (13)	197 (36)
	h	113 (12)	599 (30)	134 (11)	588 (22)	106 (8)	632 (22)
	C_D	.885 (.014)	1.332 (.022)	.971 (.012)	1.307 (.017)	.877 (.009)	1.355 (.018)
	$\hat{C}_D$	.809 (.043)	.571 (.058)	.846 (.027)	.734 (.041)	.887 (.013)	.839 (.028)
	S	2.01 (.21)	8.69 (.32)	2.36 (.17)	8.48 (.25)	1.89 (.13)	9.03 (.27)
	$\frac{1}{\rho}\lvert\nabla p\rvert$	9.329 (.849)	14.506 (1.094)	11.432 (.706)	16.679 (.795)	14.680 (.845)	17.665 (.483)
Mid-latitude Region $60^\circ > \lvert\phi\rvert > 20^\circ$	N	26	105	31	98	28	119
	$\hat{h}$	359 (78)	831 (52)	483 (81)	712 (58)	312 (70)	720 (51)
	h	370 (32)	912 (29)	311 (23)	885 (35)	393 (24)	854 (31)
	C_D	.968 (.012)	1.331 (.013)	.974 (.013)	1.323 (.012)	.994 (.009)	1.304 (.010)
	$\hat{C}_D$	.656 (.069)	.371 (.034)	.565 (.071)	.476 (.038)	.698 (.062)	.437 (.033)
	S	3.25 (.18)	8.67 (.19)	3.35 (.19)	8.55 (.17)	3.64 (.14)	8.26 (.15)
	$\frac{1}{\rho}\lvert\nabla p\rvert$	4.266 (.558)	8.524 (.611)	4.039 (.647)	8.910 (.570)	4.627 (.647)	8.747 (.489)
Tropics $\lvert\phi\rvert < 20^\circ$	N	35	33	15	31	21	50
	$\hat{h}$	172 (27)	630 (78)	384 (97)	888 (69)	272 (71)	851 (65)
	h	996 (59)	2214 (116)	915 (90)	2593 (118)	850 (77)	2451 (84)
	C_D	.976 (.012)	1.259 (.012)	.971 (.021)	1.307 (.016)	.959 (.016)	1.288 (.011)
	$\hat{C}_D$	.751 (.039)	.360 (.046)	.555 (.089)	.202 (.027)	.693 (.068)	.237 (.025)
	S	3.37 (.18)	7.60 (.18)	3.30 (.32)	8.32 (.23)	3.12 (.23)	8.03 (.17)
	$\frac{1}{\rho}\lvert\nabla p\rvert$	1.719 (.167)	2.860 (.282)	1.118 (.162)	2.465 (.306)	1.767 (.277)	2.279 (.192)

J9.4

Marine Boundary Layer Depth and Humidity Estimation From Satellite Measured Optical Depth and Total Water Content

PHILIP A. DURKEE, RICHARD KREN AND STEVEN SMOLINSKI

Department of Meteorology
Naval Postgraduate School
Monterey, CA 93943-5000

1. Introduction

Knowledge of the characteristics of the marine atmospheric boundary layer (MABL) is critical to large scale investigations of the interactions between the oceans and atmosphere. Conventional means of *in situ* observation are necessarily limited in horizontal extent. Therefore the development of satellite-based MABL characterization methods would be valuable for regional and global scale investigations. Direct methods related to atmospheric sounding techniques are limited by broad weighting functions resulting in poor resolution of the sharp temperature and moisture gradients at the top of the MABL. This paper describes an indirect method of MABL characterization by balancing estimates of aerosol optical depth (τ_A) and total water vapor (W) with the relationship between relative humidity (RH) and radiative extinction (β_{EXT})to estimate MABL depth and RH. We present here a brief description of the technique and a study of the effects of measurement errors. A more detailed description of the the technique and the initial performance has been presented by Kren (1987).

2. Physical Basis of the Technique

The method described here relies on previously developed techniques for estimating aerosol optical depth and total column water vapor. Aerosol optical depth techniques have been developed by several investigators (Griggs, 1982; Durkee et al., 1986). This study uses red-visible radiance measurements of the NOAA AVHRR (channel 1) and the direct relation to τ_A (Durkee et al., 1986). Also, several techniques have been developed to detect atmospheric water vapor variations from satellite measurements (Prabhakara et al., 1979; Dalu, 1986). The method used here follows Dalu (1986) which relates total column water vapor to the difference between split window brightness temperatures from the NOAA AVHRR sensor (channels 4 and 5). Since both estimates are derived from the same sensor the boundary layer estimates described below can be derived from a single data source.

Two assumptions about the vertical profile of extinction and water vapor are needed to relate τ_A and W to MABL depth and humidity. First, the only significant contribution to τ_A results from extinction by aerosols in the MABL. The validity of this assumption rests on the moisture profile above the MABL and sources of mid-tropospheric aerosols (mostly continental). Second, the only significant contribution to W results from water vapor in the MABL. As above, the upper level moisture profile is important for this assumption.

Values of τ_A and W are given by vertical integration of β_{EXT} and ρ_w:

$$\tau_A = \int_0^\infty \beta_{EXT}\, dz \approx H\beta_{EXT}(MABL) \qquad (1)$$

$$W = \int_0^\infty \rho_w\, dz \approx H\rho_w(MABL) \qquad (2)$$

Where H is the depth of the MABL. From these relations, τ_A and W are related to the boundary layer values of β_{EXT} and ρ_w through the MABL depth. Further, β_{EXT} can be related to relative humidity as can ρ_w following assumptions about the temperature profile. Therefore, the measured τ_A and W values provide information about MABL depth and RH.

The relation between β_{EXT} and RH is taken from Durkee et al. (1986) for this study and it is noted that the extent to which this or any other relation is representative must still be determined. The form of the relation however is understood (Fitzgerald et al., 1982) and we proceed on the assumption that representative relationships between β_{EXT} and RH exist.

Following these assumptions, MABL depth is related to measurements of τ_A and W by:

$$H = \frac{AB-[AB-ARH(0)]\exp(-\tau AC)-ARH(0)}{AC} \qquad (3)$$

and

$$H = -\frac{RH(0)\pm\sqrt{RH(0)^2+200CW/\rho_{ws}(T_l)}}{C} \qquad (4)$$

where A and B are coefficients from $\beta_{EXT}(RH)$, C is the coefficient describing the vertical variation of RH from its surface value, RH(0), and is consistent with well mixed potential temperature and specific humidity, and ρ_{ws} is saturation vapor density here evaluated at the average layer temperature, T_l. The temperature of the layer is derived from an estimate of the sea surface temperature (SST) and varies vertically according to the well mixed assumption.

Finally, these two relations can be used to solve for the two unknowns H and RH(0). Eq. (3) is quadratic in RH(0) so two solutions exist. One solution matches a very dry boundary layer but of sufficient thickness to match τ_A and W. This solution is discarded and the solution corresponding to a moist boundary layer is accepted as the estimation of RH(0).

Since the vertical profile of RH depends on the MABL thickness and the thickness is not initially known, an iterative approach is needed and proceeds as follows. The estimation is first run assuming constant RH within the MABL. The resulting MABL depth is used to specify the vertical variation of RH and the estimation is rerun. The iteration on MABL depth continues until convergence occurs.

3. Sensitivity of the Estimation to Measurement Error

The estimation scheme was initially tested on a model atmosphere that matched the assumptions discussed above. The inputs necessary (τ_A, W, and SST) are assumed to be known for what we call the "model values". The estimation was run at 1000 m MABL depth, 70 and 80 % RH(0), and 20 and 25°C SST. The maximum RH within the MABL was set at

97% to avoid saturation. Avoidance of saturation is appropriate since τ_A cannot be determined the for cloudy conditions. A test of changing to 96% for a max RH was also run.

Table 1 lists the results of the estimation. The model value of RH(0) and MABL depth for each case is within about 2% of the correct value. Kren (1987) showed results for depths of 500 and 1500 m as well as 1000 m and found that errors increase slightly as depth increases.

A statistical analysis was performed to assess the cumulative effects of errors in the measurement of the three parameters, SST, τ_A and W. The input values were varied within a normal distribution around the correct value with standard deviations of 20% for τ_A, 0.2 g/m^2 for W and 1K for SST. Histograms were generated based on 30 random combinations of inputs and are presented in Figs 1 and 2.

A t-test was run on all cases and the results are presented in the Table 1. The minimum and maximum values represent the range of possibilities for the mean at the 90% confidence level. All of the model values fall within the 90% confidence range. For RH, the spread is approximately 3% to 10% of the value. Considering the present ability to accurately measure RH, these are very reasonable results. For MABL depth, the spread is approximately 10% to 18% of the value.

The difference between the 96% and 97% cap is evident in both the relative humidity and boundary layer results. Since a cap at 96% would mean significantly less extinction in the upper portion of the layer, a decrease in both relative humidity and boundary layer depth is found when compared to the 97% cap case.

4. Conclusions

A technique has been developed to estimate MABL depth and RH from satellite-based estimates of aerosol optical depth, total column water vapor and sea surface temperature. For an atmosphere that matches the assumptions applied to the technique, estimations are within a few percent of the correct values. Naturally as the atmosphere deviates from the applied assumptions, the accuracy of the estimations will decrease.

The sensitivity of the estimation to errors in the input variables was presented. Given random occurance of expected errors, the estimations are within 10-20% of the correct value. These results represent significant success and should directly apply to cases when the atmosphere fits the assumptions of the method. As application of the technique develops, methods to identify cases that match the assumptions must also be developed. In addition, the relationship between β_{EXT} and RH and its effects on the estimation technique must be more fully examined.

5. Acknowledgements

This study has been supported by the ONR Marine Meteorology Element under Contract No. N0001487AF00001.

6. References

Dalu, G., 1986: Satellite remote sensing of atmospheric water vapor. *Intl. J. Remote Sensing*, 7, 1089-1097.

Durkee, P. A., D. R. Jensen, E. E. Hindman and T. H. Vonder Haar, 1986: The relationship between marine aerosol particles and satellite-detected radiance. *J. Geophys. Res.*, 91, 4063-4072.

Fitzgerald, J. W., W. A. Hoppel and M. A. Vietti, 1982: The size and scattering coefficient of urban aerosol particles at Washington, DC as a function of relative humidity. *J. Atmos. Sci.*, 39, 1838-1852.

Griggs, M., 1983: Satellite measurements of tropospheric aerosols. *Adv. Space Res.*, 2, 109-118.

Prabhakara, C., G. Dalu, R. C. Lo and N. R. Nath, 1979: Remote sensing of seasonal distributions of precipitable water vapour over the oceans and the inference of boundary layer structure. *M. Wea. Rev.*, 107, 1388-1401.

Kren, R., 1987: Marine boundary layer depth and relative humidity from multispectral satellite-detected radiance. Masters Thesis, Naval Postgraduate School, Monterey, California, 73 pp.

SST	Sfc. Relative Humidity	
20	70	
25	70	
20	80	96% cap
20	80	97% cap
25	85	

The 96% cap represents the highest possible relative humidity value within the layer. The comparison between 96% and 97% capping was made to asses the model's treatment of the effect of extinction on relative humidity. In all other cases, the cap was 97%. The histograms are presented on the following pages.

While the histograms present a graphical view of the effect of measurement errors, they do not identify the specific mean values and ranges expected from the model. A t-test was run on all cases and the results are presented in the table below

	SST	RH	Min.	Mean	Max.	Model Value
RELATIVE HUMIDITY (%)	20	70	65.4	68.6	71.8	69.2
	25	70	66.7	69.5	72.3	70.7
	20	80	79.0	80.2	81.4	80.3
	20	80	78.4	79.5	80.6	78.8 (cap 96%)
	25	80	77.7	78.9	80.1	78.8
BOUNDARY LAYER HEIGHT (m)	20	70	908.9	995.3	1081.7	991.1
	25	70	951.2	999.9	1048.5	994.0
	20	80	961.2	1024.0	1086.8	1014.7
	20	80	932.8	982.6	1032.3	1011.8 (cap 96%)
	25	80	980.6	1032.3	1084.0	1018.7

Table 1. Relative humidity and MABL depth model values and t-test results from error sensitivity analysis.

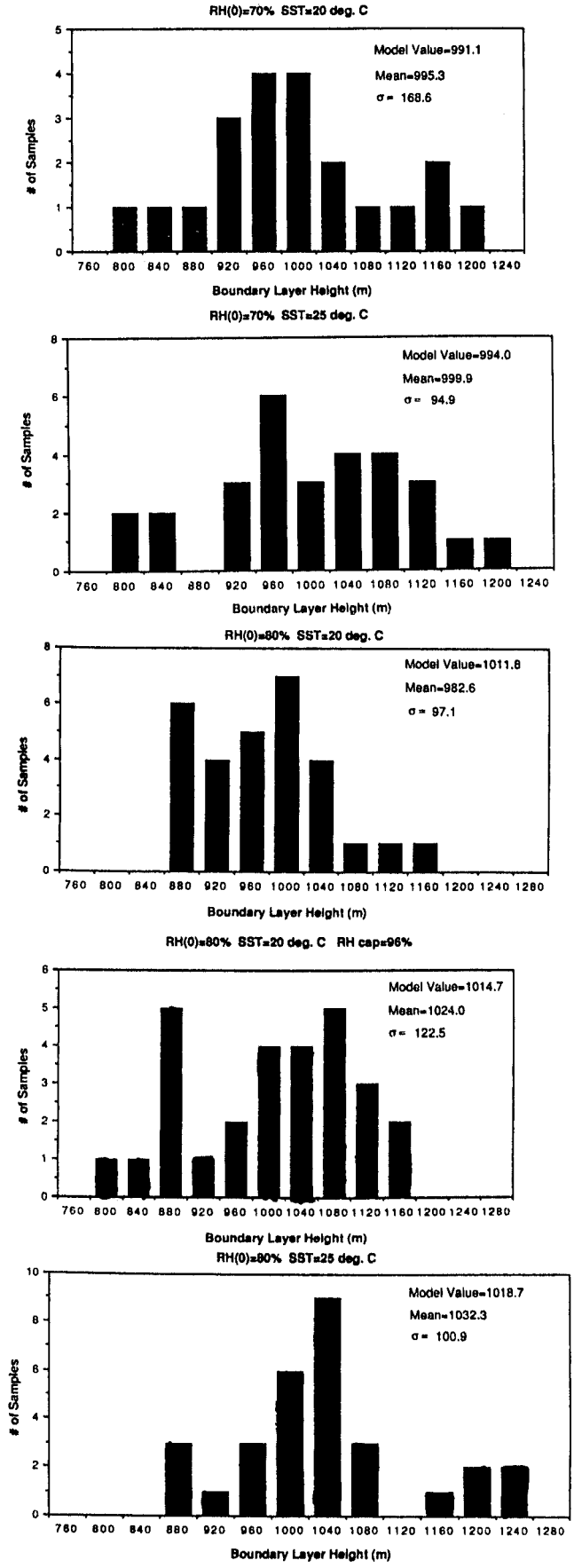

Fig. 1. Histogram of MABL depth estimates from cases listed in Table 1.

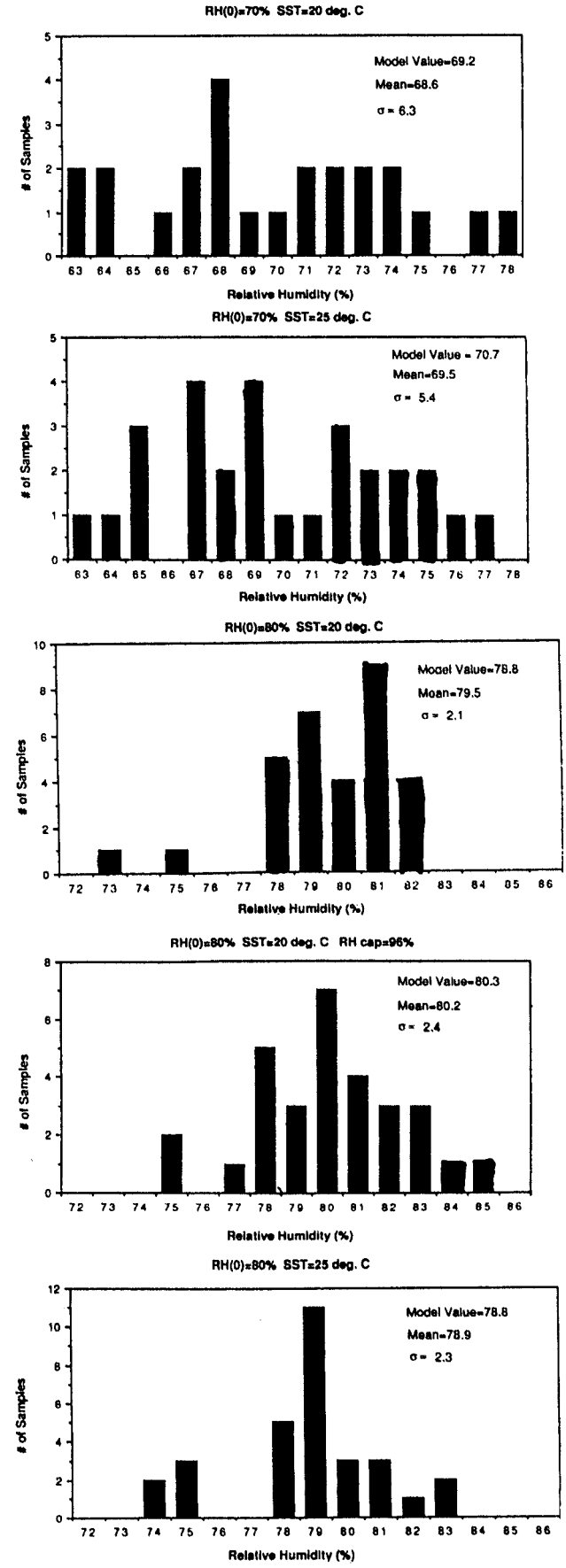

Fig. 2. Histogram of MABL relative humidity estimates from cases listed in Table 1.

J9.5

MESOSCALE SATELLITE DERIVED TEMPERATURE AND HUMIDITY PROFILES FOR THE FASINEX CAMPAIGN. COMPARISONS WITH CONVENTIONAL PRODUCTS.

C.Lévy, F.M.Bréon, A.Chédin, N.A.Scott

Lab. de Météorologie Dynamique, FRANCE

1. INTRODUCTION

During February and March 1986,the FASINEX (Frontal Air-Sea INteraction EXperiment) experiment was in its intensive phase. It was designed to study the response of the upper ocean to atmospheric forcing, the response of the atmosphere in the vicinity to the oceanic front, and the associated two ways interaction between ocean and atmosphere. During the same period of February 1986, The GALE experiment (Genesis of Atlantic Lows Experiment) went on over the same area, on a somewhat larger scale. This experiment intended to study the atmospheric cyclogenesis over the american East coast. February, 24th was seen as the biggest cyclogenesis day. TOVS data have been analyzed using the "3I" method (Improved Initialisation Inversion) for days February 22 and 24th. Preliminary results for satellite retrieved atmospheric parameters are presented here and compared to conventional analyses and radiosondes data.

2. THE 3I RETRIEVAL METHOD

The "3I" procedure (Improved Initialisation Inversion) is a physico-statistical type method for retrievals of atmospheric parameters from satellite data. It is a physical type method since it requires a theoretical simulation of atmospheric transmittances which directly enter the inversion process itself. It is a statistical type method since it relies upon an a priori knowledge of the observations (the brightness temperatures in each channel of the vertical sounder) as well as of the parameters (the atmospheric structure). This a priori knowledge is contained in a large dataset, the TIGR (Tovs Initial Guess Retrieval) data set, precomputed once and for all. Provided the observed brightness temperatures correspond to clear areas, or have been properly "cleared" (decontaminated from clouds) using the so called ψ-method (Chedin and Scott 1984), the 3I procedure follows two principal steps: search of the "best" initial guess solution using the TIGR dataset, and retrieval of the "exact" solution by a maximum probability estimation procedure using the jacobian associated with the initial guess, in the TIGR data set.

At present, the spatial resolution of the 3I algorithm is a compromise between the spatial resolutions of the two major sounders of TOVS: HIRS2 and MSU. Retrievals are made for fields of view -or boxes- of 3 HIRS-2 spots along the sub-orbital track by 4 to 2 HIRS-2 spots along the scan line according to the viewing angle. Such boxes approximately represent a surface of 100x100 km^2.

The physical parameters retrieved by the "3I" method over the area covered by the satellite passes are: air mass types (see P.Moine et al.) temperatures profiles, geopotential thicknesses, thermal winds, cloud heights, cloud amounts (equivalent of black clouds), total water vapor content, and three layers relative humidities.

3. RESULTS

On Feb. 22, geopotential thicknesses from 1000 to 500 HPa deduced from satellite data (Fig. 1) show a strong north-south gradient associated with zonal oscillations over of the FASINEX area. East of this area, a cyclonic structure can be seen and confirmed by the associated thermal wind structure. The wind speeds are quite intense (from 25m/s west of FASINEX area, to 50m/s at the centre of the cyclonic structure.

On Feb. 24, results of the cloud detection algorithm are presented on Fig 2a. The scene appears very cloudy, especially on the FASINEX area. On the west, a clear area is detected over Florida. Those results are in reasonable agreement with the AVHRR image (Fig 2b).

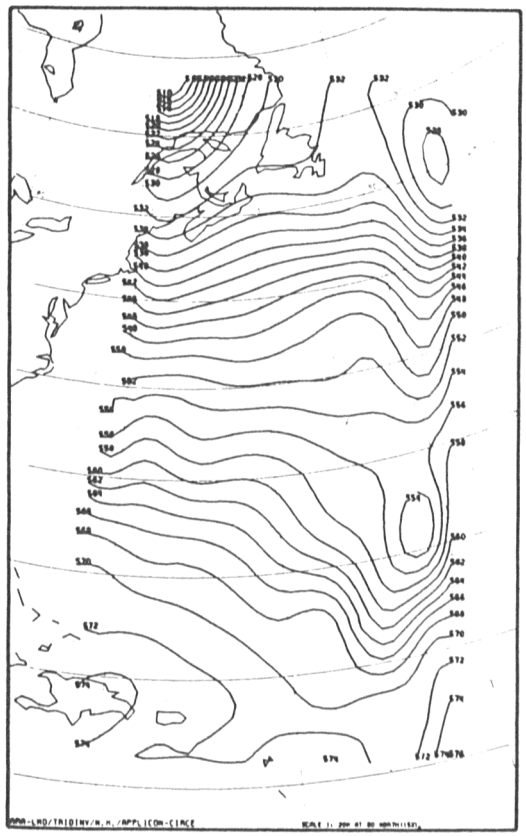

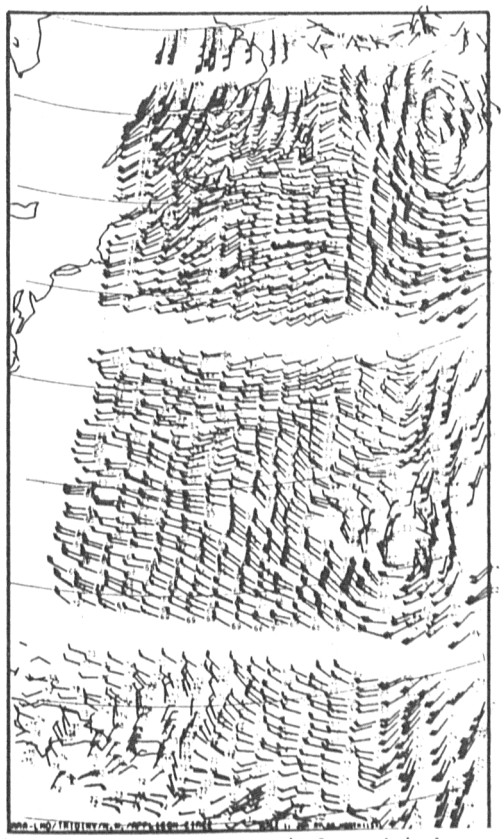

Fig 1: Geopotential thicknesses 1000-500HPa (top, contours in decameters), and associated thermal winds (bottom) retrieved from NOAA9 orbit number 6162 (Feb. 22, 1986, 6.46a.m).

Fig 2a: Cloud detection in "3I boxes" for NOAA9 orbit 6198 (Feb. 24, 1986, 7.32p.m). Full dots are cloud free boxes as seen by the "3I" method.

Fig 2b: AVHRR picture. Orbit nb.6198 (NOAA9). February 24, 1986 7.32p.m. Circle is centered on FASINEX area.

4. COMPARISON OF SATELLITE DATA WITH CONVENTIONAL ANALYSES AND RADIOSONDES DATA

Fig 3 shows comparisons between "3I" temperature and dew-point temperature profiles; and radiosondes data. Although the space and time coincidence of satellite retrieval and in situ measurements are not complete, the comparison shows very little differences in temperatures (less than 2K nearly everywhere). Dew-point temperature profile, when retrieved, is in good agreement with radiosonde data.

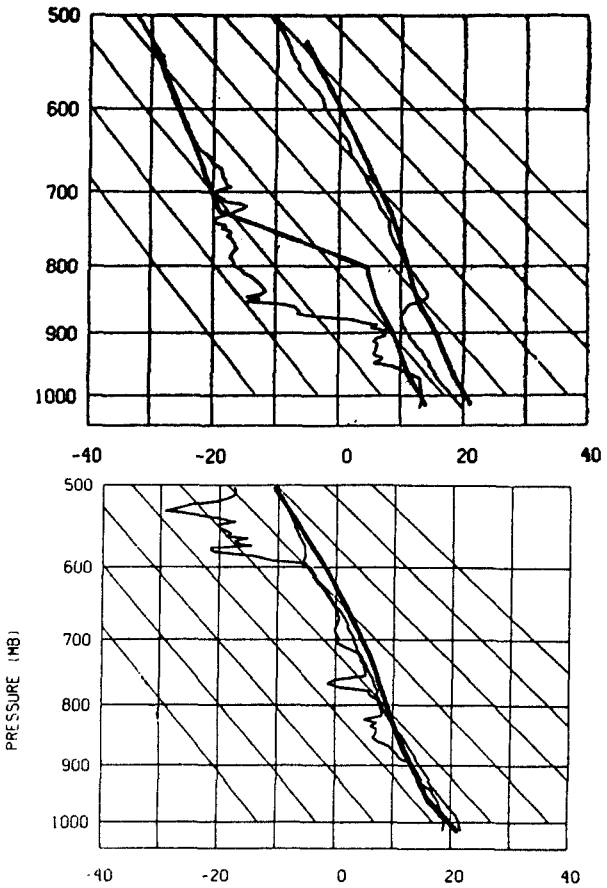

Fig 3: Comparison between radiosondes data and nearest (in space and time) "3I-retrieved" temperature and dew-point temperature profiles. The thick lines are for "3I" retrievals. Top: FASINEX FL31 (22/2/86, 28.18N, 69.20W, 7.19p.m) compared to orbit 6169 at 6.10p.m. Bottom: FASINEX FL37 (24/2/86, 27.53N, 69.47W, 6.32p.m) compared to orbit 6198 at 7.32p.m (dew-point temperature not retrieved).

Fig 4 shows the geopotential thicknesses produced by the analysis from ECMWF(Reading), which may be directly compared with Fig 1. Although the general pattern are in agreement, the satellite derived field shows stronger gradients and steeper ridges and troughs.

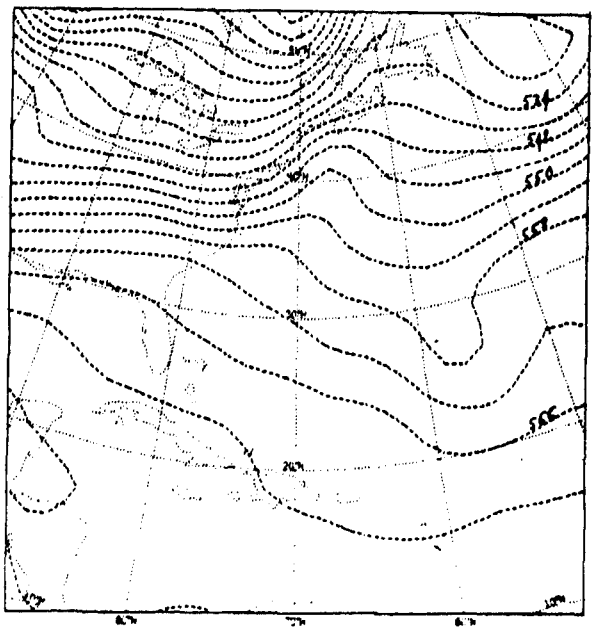

Fig 4: Geopotential thickness for the layer 1000-500HPa. Analysis from European Center for Medium Range Weather Forecast on Feb. 22, 1986 at 6a.m.

5. PRELIMINARY CONCLUSIONS

The agreement between 3I results and conventional data shows the robustness of this method in its present form against the known perturbing factors in remote sounding of the atmosphere, in particular the presence of clouds. More specific work concerning the effect of the oceanic front is going on and will be presented jointly with results involving additional satellite observations.

6. ACKNOWLEDGEMENTS

We wish to thank Drs C. Gautier and J.Bates, and all the members of the California Space Institute, especially Brian Dealy and Bob Wylie, for fruitfull discussion and assistance. We are indebted to Drs G.Rochard and J.Quéré from CMS Lannion (France) for preparing the satellite data.

7. REFERENCES:

-CHEDIN A. and N.A.SCOTT 1984:Improved Initialisation Inversion Procedure. Proc. of the 1st Int. TOVS Study Conference. Igls, Austria. August 1983. A report from the CIMSS, Ed P.Menzel, p14-79. See also J. Clim. Appl. Meteor. 24, 124-143 (1985)

-CHEDIN A. and N.A.SCOTT 1985: Initialisation of the radiative transfer equation inversion problem from a pattern recognition type approach. Applications to the satellites of the TIROS-N series. In: "Advances in Remote Sensing Retrieval Methods", Academic Press, A.Deepak Ed. pp495-515.

-P. MOINE, A.CHEDIN, and N.A.SCOTT, 1987: Automatic classification of air mass type from satellite vertical sounding data. Application to NOAA-7 observations. Ocean-Air Interaction 1, pp95-108.

J9.6

Hurricane - Ocean Interaction near the Subtropical Front

Peter G. Black
NOAA - AOML - Hurricane Research Division
Miami, Florida

ABSTRACT

Scales of variability in ocean current and temperature observations were studied in the vicinity of the Sargasso Sea subtropical front during and following the passage of Hurricanes Josephine (1984) and Gloria (1985). Data were obtained from 30 Airborne Expendable Current Probes (AXCP's) deployed from a NOAA WP-3D research aircraft and 8 air-deployed drifting buoys (four deployed from the NOAA WP-3D). These mixed layer and surface observations indicated a complex mixed layer flow pattern in the two storms consisting of a storm-induced divergent, cyclonic vortex superimposed on a pre-existing couplet of cyclonic and anticyclonic eddies associated with the front. The strength and orientation of these background eddies was different for the two cases. Mean eddy diameters were on the order of 150-200 km and mean eddy currents of order 20 cm s^{-1}. The storm induced vortex, which travelled with the storm, was about 200 km in diameter and had a mean swirl velocity of 60 cm s^{-1}. Maximum mixed layer velocities in excess of 150 cm s^{-1} were observed just beyond the radius of maximum winds in the right-rear quadrant of the storm. Downward propagating, near-inertial oscillations were also observed from thermistor chain data and buoy trajectories. They decayed to negligable amplitudes within seven days of storm passage. Interpretation of these data were aided by enhanced, water vapor corrected infrared satellite images from NOAA polar orbiting satellites.

INFLUENCE OF SEA SURFACE TEMPERATURE ON INTRA- AND INTER-ANNUAL VARIATIONS OF ITCZ

Jaime M. Daniels
ST Systems Corporation (STX)
4400 Forbes Boulevard, Lanham, MD. 20706

Anandu D. Vernekar
University of Maryland
College Park, MD 20742

1. INTRODUCTION

Most of the earlier studies on ITCZ were based on brightness values derived from ESSA series of satellites. The ITCZ position over the oceans were determined by following the locus of the brightest zone in the monthly mean brightness data which was mapped on a 5°x5° lat-long grid (see Gruber, 1972). Over the land it was difficult to distinguish between cloud brightness and the brightness of the underlying surfaces whose albedos were large. These studies were not able to determine the intensity of the ITCZ. Since June 1974 outgoing longwave radiation (OLR) data derived from measurements made by the NOAA polar orbiting satellites became available. The OLR is sensitive to cloud top temperatures. In the troposphere the deeper the clouds the colder the cloud tops, and hence, OLR is a good indicator of the depth of convective clouds. These data are measured twice daily and mapped on 2.5°x2.5° lat-long grid. By utilizing these data it is possible to estimate the position and intensity of the ITCZ.

The purpose of the present study is to utilize OLR data to determine the intra-annual and inter-annual variability of the ITCZ position and intensity and their relationship with the SST.

2. DATA AND ANALYSIS

The OLR data were obtained from the National Environmental Satellite, Data and Information Service (NESDIS). These data have been derived from twice daily measurements made by radiometers aboard the NOAA polar orbiting satellite series since June 1974 with a gap from March 1978 to December 1978 due to satellite failure. Gruber and Krueger (1984) provide the algorithm for converting window measurements to total flux.

For this study, monthly mean OLR data on 2.5°x2.5° lat-long grid are used. The monthly mean OLR for the period June 1974 to April 1984, with exception of missing data period, March 1978 - December 1978, were computed from the daily mean values.

The sea surface temperature (SST) data were obtained from the Climate Analysis Center. The monthly mean sea surface temperature fields were available for the period January 1970 - June 1984 (See Reynolds and Gemmil, 1984). For this study a SST climatology based on the period June 1974 - April 1984 is computed. All SST anomalies presented in this paper are deviations from this climatology.

The monthly mean position and intensity of ITCZ was determined by following the locus of minimum OLR in the tropics. The minimum value at any meridian was computed by taking a smooth derivative (see Lanczos, 1961) with respect to latitude of each meridional OLR profile from 45°N to 45°S. The minimum of the OLR profile was determined by noting where this derivative changes sign. The latitude of minimum OLR gives the position of ITCZ for the month and the magnitude of the minimum value gives the intensity of ITCZ for the month. The mean position and intensity based on approximately a 10 year period were computed by averaging over the appropriate number of years.

3. INTRA-ANNUAL VARIATIONS OF ITCZ

The means and standard deviations of the ITCZ position and intensity for January and July are shown in Figs. 1 and 2 respectively. The position of the ITCZ shown in the lower panel of the figures varies more with longitude in January than in July. The difference in position from January to July is largest over continents, exceeding 20° latitude, whereas in the mid-Pacific and mid-Atlantic Oceans it is about 5° latitude. The ITCZ position over land and ocean follow the seasonal march of the sun. The standard deviation of the position in January is large compared to July exceeding 3° latitude in several regions. The large variability in mid Pacific Ocean is due to effects of two El Niño's, 1976-77 and 1982-83 in the data period. In July the standard deviation exceeds 3° latitude only over Monsoon region and in the eastern Pacific Ocean. The zonally averaged position is 5°S of the equator in January and 10°N in July. The intensity of the ITCZ shown in the middle panel ranges from 250 W/m^2 (low intensity) to 190 W/m^2 (high intensity). The intensity is higher over land than over ocean. A linear relationship between OLR and precipitation derived by Arkin (1984) yields ~7.5 mm/day or ~2°C/day heating in the atmospheric column for 250 W/m^2 OLR and ~19 mm/day or ~4.5°C/day heating in the atmospheric column for 190 W/m^2 OLR. As in the case of the position the standard deviation of the intensity is higher in January than in July. As the position of the ITCZ follows the seasonal march the sun from January to July the intense centers in the ITCZ, especially over the

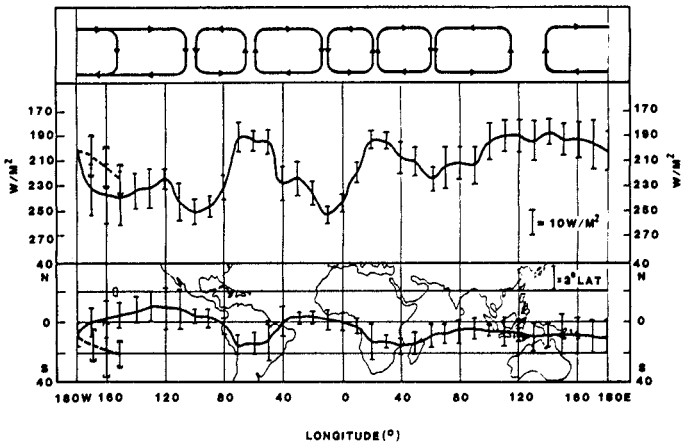

Fig. 1. Lower panel: January position of ITCZ (solid line) and SPCZ (dashed line). The vertical bars indicate the magnitude of one standard deviation (SD) of position (unit is shown in top right hand corner). The SD for SPCZ is indicated with vertical bar with 'T'. Middle panel: January intensity of ITCZ (solid line) and SPCZ (dashed line). The vertical bars give the magnitude of one SD of intensity (unit is shown in top right hand corner). The SD for SPCZ is indicated with 'T'. Top panel: Schematic east-west circulation implied by the intensity of ITCZ.

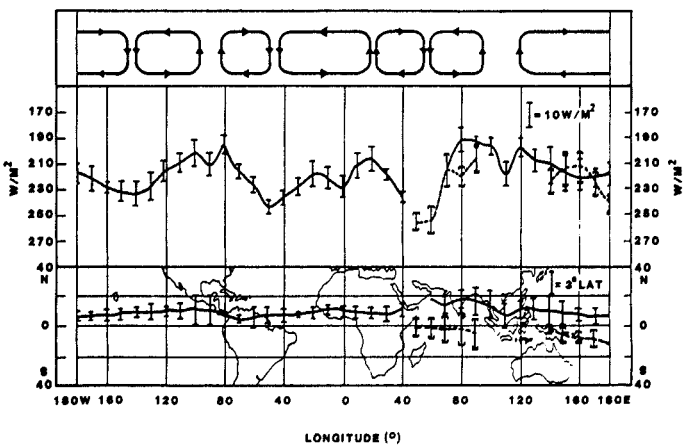

Fig. 2. Same as Fig. 1 but for July.

continents, moves toward the west by about 20° longitude. The top panels of the figures show sketches of the zonal circulation cells or the so-called Walker Circulations implied by the intensity of the ITCZ. Although the Walker Circulation was described by Bjerknes (1969) in relation to the zonal circulation cell over the Pacific Ocean, it may be applied to the east-west circulation around the equatorial belt. A strong seasonal variation is apparent in the intensity and position of the ascending and descending branches of the Walker Circulation cells. During January the Walker Circulation appears to be best developed with ascent over Brazil, Central Africa, and Indonesia-western Pacific and subsidence over the eastern Pacific, eastern south Atlantic, and the central Indian Ocean. During July there is ascent over Central America, Central Africa, India, and the western Pacific Ocean and subsidence over the eastern Pacific, north Atlantic, and western Indian Ocean. These extended views of the Walker Circulations which have been derived from OLR data are consistent with those derived from wind observations (see Newell et al 1972; Kidson (1975)).

To assess the influence of mean sea surface temperature variations during the year on the intensity and position of the ITCZ we present Figs. 3a and b which represent the sector averages of 150°E-170°E, and 100°W-120°W in the Pacific Ocean respectively. The annual variation of the ITCZ position in the western Pacific Ocean (Fig. 3a) is to some extent in phase with the variation of maximum temperature but it does not coincide with the maximum temperature. In July the latitude of maximum temperature is 3°S whereas the latitude of ITCZ is 6°N. During the year the maximum temperature is almost constant, varying only 0.5°C, whereas the intensity of the ITCZ is high in January and low in July. In the eastern Pacific Ocean both the position and the intensity show a good relation with latitude and magnitude of the maximum temperature there.

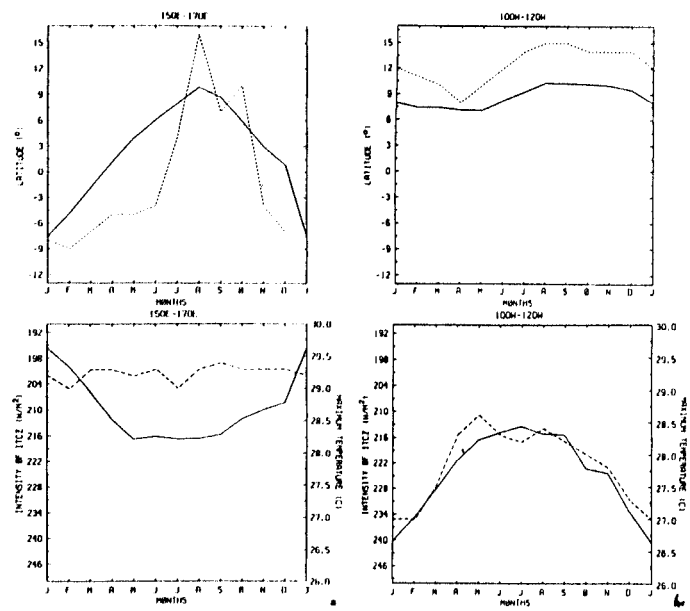

Fig. 3. (a) Upper panel: latitude of ITCZ position (solid line) and latitude of maximum temperature (dashed line). Lower panel: intensity of ITCZ (solid line) and magnitude of maximum temperature (dashed line) average of sector 150°E-170°E. (b) Same as 3a but for sector, 100°W-120°W.

In the mid-Atlantic Ocean (figure not shown) the position of the ITCZ and the latitude of maximum SST are pretty much in phase even though they do not coincide. The intensity of the ITCZ, however, shows no relation with the magnitude of maximum SST.

If the ITCZ position and intensity were mainly controlled by the sea surface temperature then the position should coincide with the axis of maximum temperature and the magnitude of maximum temperature should have a perfect

correlation with the intensity of ITCZ. With the exception of intensity variations in the eastern Pacific, there is no evidence to support the hypothesis that the position of the ITCZ coincides with the latitude of maximum SST or that the intensity increases with the SST.

4. INTER-ANNUAL VARIATIONS OF ITCZ

While the results on the annual variations of ITCZ intensity and position presented in the previous section do not fully support the claim that the ITCZ is maintained by the SST, there is abundance of observational evidence to suggest that the warm (cold) anomalies in SST increase (decrease) convection over shorter time scales (see Bjerkness, 1966). Recently, Gadgil et al (1984) show that convection increases with the SST, but the deep persistent convection, as in ITCZ, occurs only when SST is equal to or exceeds 28°C. Hence, it is the magnitude of the SST rather than the magnitude of the anomaly that maintains the deep convection.

To study the year-to-year variability of SST we define a "key region" which represents the temporal variability of the entire eastern equatorial Pacific Ocean. The key region is centered at 2°S, 130°W extending latitudinally from 6°N to 10°S and longitudinally from 120°W to 140°W. Figure 4a shows the time series of SST anomaly for the key region. The inter-annual variability is mainly dominated by the two El Niño periods (1976-77) and (1982-83), and non-El Niño periods. Time series of ITCZ intensity anomaly for the central Pacific (165°E-165°W), the Atlantic (50°W-10°E) and the maritime continent of Indonesia (100°E-120°E) are shown in Figs. 4b, 4c and 4d respectively. Over the central Pacific the ITCZ time series exhibits two distinct modes of variation - one related to a 2-3 month oscillation in tropical cloudiness and one related to a clear inter-annual variation represented by shifts from a less intense ITCZ to a more intense ITCZ during periods when eastern Pacific sea surface temperatures become anomalously warm. This is especially apparent during the 1982/1983 warming event where OLR anomalies approached -50 W/m^2 over the central Pacific. Similar shifts in ITCZ intensity are seen to occur over the maritime continent (Fig. 4d), but with opposite sign to that over the central Pacific. The inverse relationship between the two time series in the monthly oscillation is an indication of a strong Walker-type circulation connecting the two regions. The intensity of Atlantic ITCZ (Fig. 4b) is also inversely related to the ITCZ intensity over the central Pacific. Similar results were obtained by Lau and Chan (1983) and Ramage (1973). Hence the Fig. 4 suggests that the inter-annual variability of SST in the eastern Pacific Ocean influences the intensity of ITCZ in the Pacific Ocean, Atlantic Ocean and over the maritime continent of Indonesia.

The second warming period in our data record, 1982/83, was by far associated with the strongest global-scale climatic fluctuations on record. Fig. 5 shows the time evolution of Pacific sea surface temperature anomalies and the ITCZ intensity for the period January 1982 - April 1984. The ITCZ intensity shows increased convective activity just east of the dateline at nearly the same time sea surface temperatures began rising. Enhanced convective activity associated with the ITCZ was seen to be propagating eastward, developing slowly at first till October 1982, even though sea surface temperatures were continuing to rise rapidly and were approaching 2°C above normal. During this time the ITCZ across the central and eastern Pacific was at its normal position. Suddenly, in October 1982 an explosive growth of the ITCZ

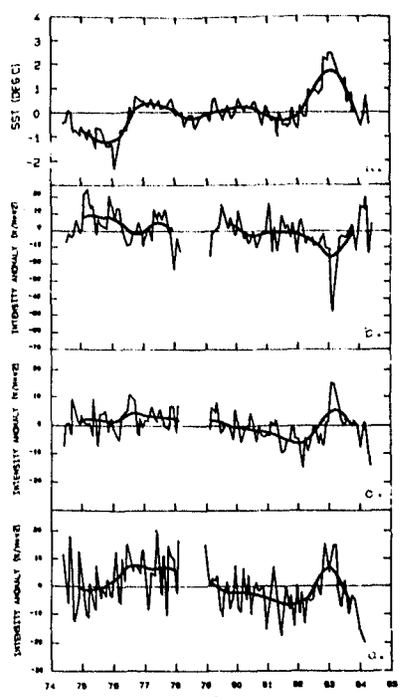

Fig. 4. (a) Time series of monthly mean SST anomaly for the key region (see text). (b) Time of Pacific ITCZ intensity anomaly averaged between 165°E-165°W. (c) Time series of Indonesian region ITCZ intensity anomaly averaged between 100°E-120°E. The smooth lines were obtained by applying a 15-point Gaussian-type filter.

became evident and quickly spread west and east till it engulfed nearly the entire Pacific from 160°E-80°W during February/March 1983. OLR anomalies approached -70 W/m^2 along the ITCZ. In the western Pacific, west of 160°E the ITCZ is weakened west of 160°E. During this time the ITCZ across the central and eastern Pacific moved quickly equatorward and attained a highly anomalous southward position between 170°W and 135°W reaching 7.5°S in March 1983. It is interesting to note that maximum ITCZ intensity did not occur where sea surface temperature anomalies were largest, but west of the sea surface temperature anomaly maximum. This suggests the intensity depends on the magnitude of the SST. Also the ITCZ did not reach maximum intensity until nearly two months after the maximum in SSTA.

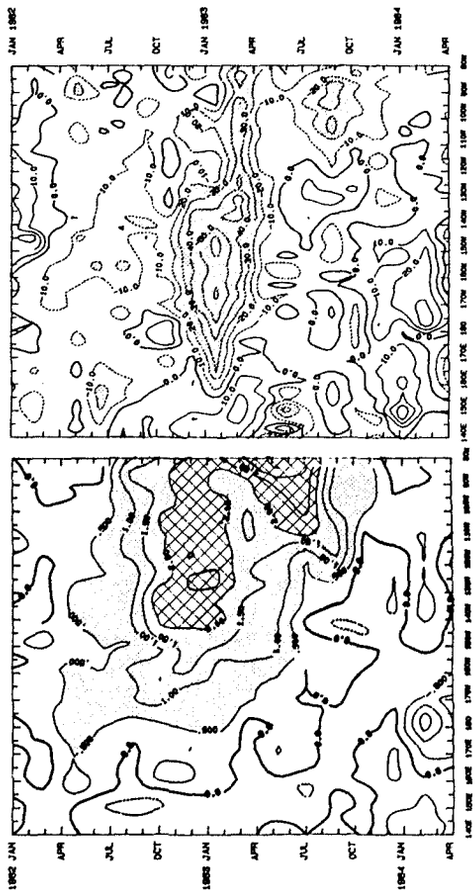

Fig. 5. Left panel: time-longitude cross-section of Pacific Ocean SST anomalies averaged between 6°N-10°S. Contour interval 0.5°C values greater than 0.5 are hatched. Right panel: time-longitude cross-section for ITCZ intensity anomaly for the period January 1982 - April 1984. Contour interval: 10 W/m^2.

5. SUMMARY

The OLR data derived from measurements made by the polar orbiting satellites are utilized to estimate inter- and intra-annual variations of monthly mean position and intensity of ITCZ. These variations are compared with corresponding variations of SST to assess the influence of SST in maintaining the position and intensity of ITCZ.

The range of ITCZ position is a maximum over land and a minimum over mid-ocean. The position follows the annual march of the sun. The intensity of ITCZ is a maximum over land or in the vicinity of land masses and a minimum over mid-ocean. The annual variation of ITCZ position is in phase with maximum temperature but it does not coincide with the latitude of maximum temperature. The annual variations of intensity does not show any relationship with the magnitude of SST except in the eastern Pacific Ocean.

The inter-annual variability of ITCZ intensity in all oceans is dominated by the SST anomalies associated with El Niño. During El Niño the ITCZ intensity increases in the Pacific Ocean but decreases in the Atlantic Ocean as well as in Indian Ocean. The ITCZ variations due to local SST variation in the Atlantic Ocean do not appear to be significant. In the Pacific Ocean the convection is intense to the west of the maximum SST anomaly where the SST is higher. The maximum ITCZ intensity lags the SST anomaly maximum by 2 months.

6. REFERENCES

Arkin, P. A., 1984: An examination of Southern Oscillation in the upper tropical and subtropical wind field. Ph.D. Thesis, University of Maryland.

Bjerknes, J., 1966: A possible response of the atmospheric Hadley circulation to equatorial anomalies of ocean temperature. Tellus, 18, 820-828.

Bjerknes, J., 1969: Atmospheric teleconnections from the equatorial Pacific. Mon. Wea. Rev., 97, 163-172.

Gadgil, S., P.V. Joseph, and N.V. Joshi, 1984: Ocean-atmosphere coupling over monsoon regions, Nature, 312, 141-143.

Gruber, A., 1972: Fluctuations in the position of the ITCZ in the Atlantic and Pacific Ocean. J. Atmos. Sci., 29, 193-197.

_____ and A.F. Krueger, 1984: The status of the NOAA outgoing longwave radiation data set. Bull. Amer. Meteor. Soc., 65, 958-962.

Kidson, J.W., 1975: Tropical eigenvector analysis and the southern oscillation. Mon. Wea. Rev., 103, 187-196.

Lanczos, C., 1964: Applied Analysis, Prentice Hall Inc., N.Y., 539 pp.

Lau, K. and P.H. Chan, 1983: Short-term climate variability and atmospheric teleconnections from satellite-observed outgoing longwave radiation. Part I: Simultaneous relationships. J. Atmos. Sci., 40, 2735-2750.

Newell, R.E., J.E. Kidson, D.G. Vincent and G.J. Boer, 1972: The general circulation of the tropical atmosphere and interactions with extratropical latitudes. Volume 2. The MIT Press, pp. 371.

Ramage, C.S., 1973: Preliminary discussion of the meteorology of the 1972-73 El Niño. Bull. Amer. Meteor. Soc., 56, 234-242.

Reynolds, R.W. and W.H. Gemmil, 1984: An objective global monthly mean sea surface temperature analysis. Tropical Ocean-Atmosphere Newsletter, 22, 4-5.

[Reprinted from BULLETIN OF THE AMERICAN METEOROLOGICAL SOCIETY, Vol. 68, No. 8, August 1987]
Printed in U. S. A.

PUBLICATIONS OF THE AMS

Nonmember Prices Effective August 1, 1987*

BOOKS

Compendium of Meteorology, 1951—Out of Print
Dynamic Meteorology and Weather Forecasting, 1957—Out of Print
Glossary of Meteorology, 1959; fourth printing, 1986—$25
Vilhelm Bjerknes Memorial Volume, 1962—$12
A Century of Weather Progress, 1970—$10
Workshop on Micrometeorology, 1973—$35
Atmospheric Science and Public Policy, 1976—$6
Workshop on the Future of National Atmospheric Research, 1977—$6
Curricula in the Atmospheric, Oceanic and Related Sciences, 1986—$15
Workshop on the Planetary Boundary Layer, 1980—$25
Lectures on Air Pollution and Environmental Impact Analyses, 1975; second printing, 1982—$30
Probing the Atmospheric Boundary Layer, 1986—$40
Mesoscale Meteorology and Forecasting, 1987—$45 (postage and handling $5.25)

Distributed by AMS:

Weather Modification in the Public Interest, 1974—$10.50
A Field Guide to the Atmosphere, 1981–(HC $15.95; SC $10.95)
The American Weather Book, 1982—(HC $14.95; SC $8.95)
Proceedings of the First Sino-American Workshop on Mountain Meteorology, 1984—$42.50
Proceedings of the International Symposium on the Qinghai Xizang (Tibet) Plateau and Mountain Meteorology, 1986—$47.50
The above two proceedings available as a set for $75
Handbook of Applied Meteorology, 1986—$90.00 (postage and handling $4)
Some Meteorological Aspects of the D-Day Invasion of Europe, 6 June 1944, 1986—$20
Monsoons, 1987—$74.95

METEOROLOGICAL MONOGRAPHS (ISSN 0065-9401)

No. 1 Wartime Developments in Applied Climatology, 1947—$12
No. 2 The Observations and Photochemistry of Atmospheric Ozone, 1950—$12
No. 3 On the Rainfall of Hawaii, 1951—$12
No. 4 On Atmospheric Pollution, 1951—$12
No. 5 Forecasting in Middle Latitudes, 1952—Out of Print
No. 6 Thirty-Day Forecasting, 1953—$12
No. 7 The Jet Stream, 1954—$12
No. 8 Recent Studies in Bioclimatology, 1954—$12
No. 9 Industrial Operations under Extremes of Weather, 1957—$12
No. 10 Interaction of Sea and Atmosphere, 1957—$12
No. 11 Cloud and Weather Modification, 1957—$12
Nos. 12–20 Meteorological Research Reviews, 1957. Review of Climatology; Meteorological Instruments; Radiometeorology; Weather Observations, Analysis and Forecasting; Applied Meteorology; Physics of the Upper Atmosphere; Physics of Clouds; Physics of Precipitation; Atmospheric Electricity. (In 1 vol.)—$24
No. 21 Studies of Thermal Convection, 1959—$12
No. 22 Topics in Engineering Meteorology, 1960—$12
No. 23 Atmospheric Radiation Tables, 1960—$12
No. 24 Fluctuations in the Atmospheric Inertia, 1961—$12
No. 25 Statistical Prediction by Discriminant Analysis, 1962—$12
No. 26 The Dynamical Prediction of Wind Tides on Lake Erie, 1963—$12
No. 27 Severe Local Storms, 1963—$20 Paperbound.
No. 28 Agricultural Meteorology, 1965—$20 Paperbound; $22 Clothbound.
No. 29 Scattered Radiation in the Ozone Absorption Bands at Selected Levels of a Terrestrial. Rayleigh Atmosphere, 1966—$20 Paperbound; $22 Clothbound.
No. 30 The Causes of Climatic Change, 1968—$20
No. 31 Meteorological Investigations of the Upper Atmosphere, 1968—$18
No. 32 On the Distribution and Continuity of Water Substance in Atmospheric Circulations, 1969—$18
No. 33 Meteorological Observations and Instrumentation, 1970—$25
No. 34 Long-Period Global Variations of Incoming Solar Radiation, 1971—$20
No. 35 Meteorology of the Southern Hemisphere, 1972—$25
No. 36 Alberta Hailstorms, 1973—$18
No. 37 The Dynamic Meteorology of the Stratosphere and Mesosphere, 1975—$35
No. 38 Hail: A Review of Hail Science and Hail Suppression, 1977—$35
No. 39 Solar Radiation and Clouds, 1980—$35
No. 40 METROMEX: A Review and Summary, 1981—$35
No. 41 Tropical Cyclones—Their Evolution, Structure, and Effects, 1982—$40
No. 42 Statistical Inference and Prediction in Climatology: A Bayesian Approach, 1985—$45
No. 43 Precipitation Enhancement—A Scientific Challenge—$45

HISTORICAL MONOGRAPHS

The History of American Weather (All 4 vols.—$40)
Early American Hurricanes (1492–1870), 1963—$12
Early American Winters (2 vols.—$22)
(1604–1820), 1966—$12
(1821–1870), 1967—$12
Early American Tornadoes (1586–1870), 1970—$12
The History of Meteorology (to 1800), 1977; second printing, 1983—$20
The Thermal Theory of Cyclones: A History of Meteorological Thought in the Nineteenth Century, 1979—$35

TRANSLATIONS

No. 76 Problems of Dynamic Meteorology and Climatic Theory—Out of Print
No. 82 Question of Physics of the Atmosphere—$5
Studies of Clouds, Precipitation, and Thunderstorm Electricity—$10

CONFERENCE PREPRINTS/PROCEEDINGS

$20 each (unless other price is given)

Second National Conf. on Weather Modification, 1970
Seventh Conf. on Severe Local Storms, 1971
International Conf. on Weather Modifications, 1971
Second Symp. on Meteorological Observations and Instrumentation, 1972—Out of Print
Third Conf. on Weather Modification, 1972
Conf. on Atmospheric Radiation, 1972—Out of Print
15th Conf. on Radar Meteorology, 1972—Out of Print
Third Conf. on Probability and Statistics in Atmospheric Science, 1973
International Tropical Meteorology Meeting, 1974 (2 vols.)—$25
Second International Conf. on the Environmental Impact of Aerospace Operations in the High Atmosphere, 1974
Sixth Conf. on Aerospace and Aeronautical Meteorology, 1974
Fourth Conf. on Weather Modification, 1974
Third Symp. on Meteorological Observations and Instrumentation, 1975
Fourth Conf. on Probability and Statistics in Atmospheric Sciences, 1975—Out of Print

*Add $3 per item for postage and handling. Prices subject to future changes without notice.

PUBLICATIONS OF THE AMS

Nonmember Prices Effective August 1, 1987*

(continued)

Conf. on Hydrometeorology, 1976
International Conf. on Cloud Physics, 1976—$35
Third Conf. on Numerical Weather Prediction, 1977
Sixth Conf. on Planned and Inadvertent Weather Modification, 1977
10th Conf. on Severe Local Storms, 1977
Second Conf. on Hydrometeorology, 1977
Fifth Conf. on Probability and Statistics in Atmospheric Sciences, 1977
Joint Conf. on Applications of Air Pollution Meteorology, 1977
11th Technical Conf. on Hurricanes and Tropical Meteorology, 1977—$25
Fifth Joint Conf. on Fire and Forest Meteorology, 1978
18th Conf. on Radar Meteorology, 1978—Out of Print
Conf. on Flash Floods: Hydrometeorological Aspects, 1978
Conf. on Climate and Energy: Climatological Aspects and Industrial Operations, 1978
Conf. on Sierra Nevada Meteorology, 1978
Third Conf. on Atmospheric Radiation, 1978 (Abstracts)
Conf. on Cloud Physics and Atmospheric Electricity, 1978—$25
Conf. on Weather Forecasting and Analysis and Aviation Meteorology, 1978—Out of Print
Conf. on Atmospheric Environment of Aerospace Systems and Applied Meteorology, 1978
Conf. and Workshop on Wind Energy Characteristics and Wind Energy Siting, 1979—$25
Third Conf. on Hydrometeorology, 1979
11th Conf. on Severe Local Storms, 1979—Out of Print
Seventh Conf. on Inadvertent and Planned Weather Modification, 1979 (Extended Abstracts)
Sixth Conf. on Probability and Statistics in Atmospheric Sciences, 1979
Second Conf. on Coastal Meteorology, 1980—Out of Print
Second Conf. on Flash Floods, 1980
Second Joint Conf. on Applications of Air Pollution Meteorology and Second Conf. on Industrial Meteorology, 1980—$32
Eighth Conf. on Weather Forecasting and Analysis, 1980
13th Technical Conf. on Hurricanes and Tropical Meteorology, 1980
Fifth Symp. on Turbulence, Diffusion, and Air Pollution, 1981 (Extended Abstracts)
15th Conf. on Agriculture and Forest Meteorology and Fifth Conf. on Biometeorology, 1981 (Extended Abstracts)
Fourth Conf. on Atmospheric Radiation, 1981
Eighth Conf. on Inadvertent and Planned Weather Modification. 1981 (Extended Abstracts)
Fourth Conf. on Hydrometeorology, 1981
Fifth Conf. on Numerical Weather Prediction, 1981
Seventh Conf. on Probability and Statistics in Atmospheric Sciences, 1981
Second Conf. on Mountain Meteorology, 1981
20th Conf. on Radar Meteorology, 1981—$25
12th Conf. on Severe Local Storms, 1981—$25
Third Joint Conf. on Applications of Air Pollution Meteorology (Extended Abstracts), 1982
First International Conf. on Meteorology and Air Sea Interaction of the Coastal Zone, 1982—$25
Second Symp. on the Composition of the Nonurban Troposphere (Extended Abstracts), 1982
Ninth Conf. on Weather Forecasting and Analysis, 1982
Conf. on Cloud Physics (Extended Abstracts), 1982
Proceedings of the International Conf. on the Aviation Weather System, 1981 (published 1982)—$25
Proceedings of the International Conf. on Climate and Offshore Energy Resources, 1980 (published 1982)—$25
Sixth Symp. on Turbulence and Diffusion (Extended Abstracts), 1983
Fifth Symp. on Meteorology Observations and Instrumentation, 1983—$25
16th Conf. on Agriculture and Forest Meteorology and Sixth Conf. on Biometeorology (Extended Abstracts), 1983
Seventh Conf. on Fire and Forest Meteorology, 1983
Sixth Conf. on Numerical Weather Prediction, 1983
Ninth Conf. on Aerospace and Aeronautical Meteorology, 1983
First International Conf. on Southern Hemisphere Meteorology (Extended Abstracts), 1983
21st Conf. on Radar Meteorology, 1983—$32
13th Conf. on Severe Local Storms (Extended Abstracts), 1983—$25
Fifth Conf. on Hydrometeorology, 1983
Fifth Conf. on Atmospheric Radiation (Extended Abstracts), 1983
Eighth Conf. on Probability and Statistics in Atmospheric Sciences, 1983
15th Technical Conf. on Hurricanes and Tropical Meteorology, 1984—$30
Third Conf. on Meteorology of the Coastal Zone, 1984
Ninth Conf. on Weather Modification, 1984
Seventh International Conf. on Atmospheric Electricity, 1984—$30
10th Conf. on Weather Forecasting and Analysis, 1984—$30
Conf. on Satellite Meteorology/Remote Sensing and Applications, 1984—$30
22nd Conf. on Radar Meteorology, 1984—$32
Fourth Joint Conf. on Applications of Air Pollution Meteorology, 1984—$30
Third Conf. on Mountain Meteorology, 1984
Third Conf. on Climate Variations: Symp. on Contemporary Climate: 1850–2100, 1985
International Conf. on Interactive Information and Processing Systems for Meteorology, Oceanography and Hydrology, 1985—$30
17th Conf. on Agriculture and Forest Meteorology and Seventh Conf. on Biometeorology & Aerobiology, 1985—$30
16th Conf. on Hurricanes & Tropical Meteorology, 1985
7th Conf. on Numerical Weather Prediction, 1985—$30
Second International Conf. on the Aviation Weather System, 1985
Conf. on Aerospace and Range Meteorology, 1985—Out of Print
Ninth Conf. on Probability and Statistics in Atmospheric Sciences, 1985—$30
14th Conf. on Severe Local Storms, 1985—$30
Sixth Conf. on Hydrometeorology, 1985—$30
Seventh Symp. on Turbulence and Diffusion, 1985—$30
National Conf. on the Scientific Results of the First GARP Global Experiment, 1986—$30
2nd International Conf. on Interactive Information and Processing Systems for Meteorology, Oceanography, 1986—$30—Out of Print
Second Conf. on Satellite Meteorology/Remote Sensing and Applications, 1986—$30
Sixth Conf. on Atmospheric Radiation, 1986—$30
10th Conf. on Weather Modification, 1986—$30
11th Conf. on Weather Forecasting and Analysis, 1986—$30
Conf. on Climate and Water Management—A Critical Era and Conf. on Human Consequences of 1985's Climate, 1986—$30
23rd Conf. on Radar Meteorology and Conf. on Cloud Physics and Papers from Joint Sessions, 3 Vols., 1986—$90
Fifth Joint Conf. on Applications of Air Pollution Meteorology with APCA, 1986—$30

*Add $3 per item for postage and handling. Prices subject to future changes without notice.

PUBLICATIONS OF THE AMS

Nonmember Prices Effective August 1, 1987*

(continued)

Second International Conf. on Southern Hemisphere Meteorology, 1986—$30
3rd International Conf. on Interactive Information and Processing for Meteorology, Oceanography, Hydrology, 1987—$30
Sixth Symp. on Meteorological Observations and Instrumentation, 1987—$30
Fifth Conference on Applied Climatology, 1987—$30
17th Conf. on Hurricanes and Tropical Meteorology, 1987—$30
Ninth Conf. on Fire and Forest Meteorology, 1987—$30
Third Conf. on Mesoscale Processes, 1987—$30
Fourth Conf. on Mountain Meteorology, 1987—$30
18th Conf. on Agricultural & Forest Meteorology and Eighth Conf. on Biometeorology & Aerobiology, 1987—$30
Seventh Conf. on Hydrometeorology & 11th Weather Modification, 1987—$30
10th Conf. on Probability & Statistics, 1987—$30

BIBLIOGRAPHIES ON OCEANOGRAPHY

Physical Oceanography of the Indian Ocean, 1965—Out of Print
Collected Bibliographies on Physical Oceanography (1953–1964), 1966—Out of Print
Marine Corrosion, 1967—$5
Marine Seismics, 1967—$5
Oceanography of the Tropical Atlantic, 1967—Out of Print
Marine Atlases, 1968—$10

ABSTRACTS

Meteorological & Geoastrophysical Abstracts (Monthly)

Volumes 1–10 (1950–1959)—$50/volume; $10/issue
complete set, volumes 1–10, $200
Volumes 11–20 (1960–1969)—$100/volume; $15/issue
complete set, volumes 11–20, $400
Volumes 21–30 (1970–1979)—$200/volume; $20/issue
complete set, volumes 21–30, $800
Volumes 31–33 (1980–1982)—$400/volume; $40/issue
Volumes 34–38 (1983–1987)—$450/volume; $50/issue

INDEXES

Meteorological & Geoastrophysical Abstracts (Annual Indexes)
Volumes 11–14—$50/volume
Volumes 16–22—$50/volume
Volumes 27–37—$150/volume
Meteorological & Geoastrophysical Abstracts (Cumulative Indexes)
Volumes 1–10 (1950–1959), Author Index (A–K) } $200
Volumes 1–10 (1950–1959), Author Index (L–Z) } per
Volumes 1–10 (1950–1959), Geographic } set
Volumes 21–26 (1970–1975), Author Index—$200
Volumes 21–26 (1970–1975), Subject Index—$200
Journal of Physical Oceanography
Volumes 1–10 (1971–1980)—$10

GUIDES

Authors' Guide, 1983—$5

*Add $3 per item for postage and handling. Prices subject to future changes without notice.

Handbook of

APPLIED METEOROLOGY

Edited by
David D. Houghton

The 46 chapters in the *Handbook of Applied Meteorology* are organized into five main sections: Part 1 deals with fundamental meteorological information; Part 2 addresses the topic of measurements; Part 3 focuses on specific major applications of meteorology; Part 4 provides a general discussion on some major impacts of meteorology on society; and Part 5 summarizes a wide range of resources available for meteorological data and knowledge. Two appendixes give additional information on terminology, units, and climatic data. This handbook presents, for the first time, an authoritative, comprehensive reference on meteorological knowledge and technology. Designed for professionals and technicians both within and outside the meteorological profession, this broad-ranging book offers general guidelines for those who need information on the effects of weather.

The *Handbook of Applied Meteorology* was awarded honorable mention in the category for best physical science book of 1985 in the Tenth Annual Professional and Scholarly Book Awards sponsored by the Association of American Publishers.

To order please send $94.50 plus $4.00 postage and handling to:

AMERICAN METEOROLOGICAL SOCIETY
45 BEACON ST.
BOSTON, MA 02108

[Reprinted from BULLETIN OF THE AMERICAN METEOROLOGICAL SOCIETY, Vol. 68, No. 5, May 1987]
Printed in U. S. A.

SELECTED LIST OF WMO PUBLICATIONS

Distributed by
The American Meteorological Society
45 Beacon Street
Boston, MA 02108

All prices listed below are quoted in U.S. Dollars. (Availability and prices are subject to change without notice.) Orders and inquiries from residents of U.S.A. and Canada should be directed to: American Meteorological Society, Attn: WMO Publication Center, 45 Beacon Street, Boston, MA 02108, U.S.A. Residents of all other countries should direct orders and inquiries to: World Meteorological Organization, Publications Sales Unit, P.O. Box No. 5, CH-1211 Geneva 20, Switzerland.

Remittance must accompany all orders; only after receipt of payment will the order be processed. Add $3.00 per book for postage and handling. Payment from Canadian clients must be made by a draft on a U.S. Bank or by International Money Order. Checks or money orders should be made payable to the AMS in U.S. dollars.

Recent WMO Publications

WMO *Cloud Sheet*, 1986.

The dimensions of the new edition of the WMO *Cloud Sheet* are 39 × 83 cm. This popular sheet is printed on glossy paper and can be mounted on a hard backing. There are 38 color photographs from the *International Cloud Atlas*. These were selected to assist not only the marine observer, but also as a general reference for all professional or amateur meteorological observers.

QUANTITY	PRICE PER CLOUD SHEET
1-10	$ 5.00*
11-30	$ 4.00*
31-50	$ 3.00*
51-100	$ 2.75*
101-500	$ 2.50**
501-1000	$ 2.25**
1000+	$ 2.00**

* Ten (10) sheets fit into a mailing tube. For orders less than 10 add $4.00/order for shipping and handling. For orders of 10-100 add $4.00/ten sheets for shipping and handling.
** Contact AMS for shipping and handling costs for orders over 100 sheets.

WMO 622 *Compendium of Lecture Notes on Meteorological Instruments for Training Class III and Class IV Meteorological Personnel*, 1986 (Vol. I $39.00; Vol. II $37.00)

Vol. I Part 1 *Meteorological Instruments*
Part 2 *Meteorological Instrument Maintenance Workshops, Calibration Laboratories and Routines*
Vol. II Part 3 *Basic Electronics for the Meteorologist*

WMO 629 *The Analysis of Data Collected From International Experiments on Lucerne*, T.N. 182; 1986 ($21.00)

"Lucerne, known also as alfalfa, widely adopted for its high productivity and nutrient value, is an important forage crop for livestock and poultry. However, the agrometeorology of this crop, with a perennial cycle of development and multiple cuttings during a single vegetation season, is little known. Study was therefore initiated, resulting in the present report by the Working Group on International Experiments for the Acquisition of Lucerne/Weather Data."

"The international experiments are described in Chapter 2. Chapter 3 deals with micro-climatological aspects of this crop; and the growth and development of lucerne, including its productivity for individual cuttings, are presented in Chapter 5. Analysis of the results for the experiments on the growth, development and yield is contained in Chapter 8. Lucerne-weather models are presented in Chapter 9, and Chapter 10 contains recommendations on the cultivation and adoption of this forage crop. An extensive bibliography is given at the end of the report." (WMO)

WMO 633 *Land Use and Agrosystem Management Under Severe Climatic Conditions*, T.N. 184; 1986 ($25.00)

"Each type of crop or livestock has its own particular climatic requirements and tolerances for growth, development and yield. The requirements and tolerances vary according to the species and the various stages in their life cycle. The sensitivity to environmental deterioration also varies greatly among different types of agriculture and climatic regime. The climatic severity for agricultural purposes is therefore complex to understand and can only be defined in a very general way."

"The validity of criteria for specifying climatic severity for agriculture depends on the extent to which (within each region defined by them) the biomes, the ecosystems and agrosystems, and the most suitable management practices are uniform, well defined, characteristic and distinct from those of other regions."

WMO 633 (continued)

"For the purpose of this Technical Note on the general principles of land use in regions with severe climates, the regions have been defined according to the macro-environment they represent: arid regions, semi-arid regions, extreme monsoon regions, humid tropical regions and cold regions." (WMO)

WMO 649 *El Niño* Phenomenon and Fluctuations of Climate, Lectures Presented at the 36th Session of the WMO Executive Council, 1986 ($12.00)

Chapter 1: *The characteristics of the 1982/83 El Niño off the Pacific coast of South America*, by S. Zuta.
Chapter 2: *The ecological and economic impacts of the El Niño phenomenon in the south-east Pacific*, by R. Jordan Sotelo.
Chapter 3: *El Niño - Southern Oscillation and investigations of short-range climate variations according to the "Sections" programme*, by A. S. Sarkisyan.

WMO 658 *Methods of Measurement and Estimation of Discharges at Hydraulic Structures*, O.H.R. 26; 1986 ($10.00)

"This report is a review of methods for the measurement and estimation of discharges at hydraulic structures and pressure conduits with the aim of utilizing such facilities, where they already exist, as an alternative to the construction of discharge measurement stations. It focuses largely on methods of flow estimation at structures commonly installed in reservoirs, dams and canals as well as standard methods for the measurement of open-channel and pipe flow. Mention is also made of the use of pumping stations and navigation locks. In the majority of cases the discussion is brief and the reader is referred to the literature for further information. In many cases, flow estimation formulae are given." (WMO)

WMO Bulletin - Quarterly Subscription*			*WMO 5 - Composition of the WMO* - Quarterly Subscription*		
Number of Years	Surface Mail	Airmail	Number of Years	Surface Mail	Airmail
1	$ 48.00	$ 66.00	1	$ 60.00	$ 77.00
2	78.00	107.00	2	110.00	145.00
3	109.00	150.00	3	150.00	200.00
			Single issue	17.00	20.00

*Subscriptions to WMO Bulletin and WMO 5 are accepted on calendar year basis

WMO No.	$ Unit Price
Atlases	
Climatic Atlas of Europe. Volume I: Maps of Mean Temperature and Precipitation	$172.00
Climatic Atlas of South America. Volume I: Maps of Mean Temperature and Precipitation	197.00
Climatic Atlas of North and Central America. Volume I: Maps of Mean Temperature and Precipitation	172.00
Climatic Atlas of Asia. Volume I: Maps of Mean Temperature and Precipitation	202.00
International Cloud Atlas, Abridged Edition, 1956	47.00
International Cloud Album for Observers in Aircraft, 1956	15.00
International Cloud Atlas - Manual on the Observation of Clouds and other Meteors, 1987	
Volume I - Text (out of print)	
Volume II - Color Plates	78.00
Basic Documents	
15 - *Basic Documents No. 1* - (Excluding Technical Regulations), 2nd Edition, 1984	$34.00
60 - *Basic Documents No. 3 - Agreements and Working Arrangements With Other International Organizations*, 1983	21.00
Technical Regulations	
49 - *Technical Regulations* - Basic Documents No. 2 (loose leaf; please specify if cover is needed)	
Vol. I *General*, 2nd Edition, 1984	$28.00
Vol. II *Meteorological Services for International Air Navigation*, 1976	**
Vol. III *Hydrology*, 1979	15.00
555 - *Technical Regulations - Hydrology and International Hydrological Codes*, 1980	24.00
558 - *Manual on Marine Meteorological Services*, 1981	26.00
Weather Reporting: Stations, Data Processing and Transmission	
9 - *Weather Reporting*	
Vol. A *Observing Stations:* Basic Volume:	$145.00
Subscription to Supplement Service (Semi-Annual): surface mail	134.00
airmail	174.00

* In preparation
** Currently out of stock and unavailable from AMS or WMO

Weather Reporting: Stations, Data Processing and Transmission (continued)		
Vol. B *Data Processing:* Basic Volume:		78.00
Subscription to Supplement Service (Semi-Annual):	surface mail	30.00
	airmail	46.00
Vol. C *Transmissions:* Basic Volume:		152.00
Subscription to Supplement Service (Bi-Monthly):	surface mail	132.00
	airmail	184.00
Vol. D *Information for Shipping:* Basic Volume:		183.00
Subscription to Supplement Service (Bi-Monthly):	surface mail	96.00
	airmail	158.00
Operational Manuals		
306 - *Manual on Codes*		
Vol. I *International Meteorological Codes*, 1984 Edition	(w/out cover)	$87.00
	(w/cover)	100.00
Vol. II *Regional Codes and National Coding Practices*, 1982 Edition	(w/out cover)	47.00
	(w/cover)	60.00
386 - *Manual on the Global Telecommunication System*, 1986	(w/out cover)	$140.00
Vol. I *Global Aspects*		
Vol. II *Regional Aspects*		
Cover only		21.00
485 - *Manual on the Global Data-Processing System* (Vol. I and II one binder)		48.00
Vol. I *Global Aspects*, 1977		
Vol. II *Regional Aspects*, 1980		
491 - *International Operations Handbook for Measurement of Background Atmospheric Pollution*, 1978		35.00
544 - *Manual on the Global Observing System* (Vol. I and II one binder), 1981		27.00
Guides		
8 - *Guide to Meteorological Instruments and Observing Practices*, 5th Edition, 1983		$47.00
100 - *Guide to Climatological Practices*, 2nd Edition, 1983		39.00
114 - *Guide to Qualifications and Training of Meteorological Personnel Employed in the Provision of Meteorological Services for International Air Navigation*, 1974		13.00
134 - *Guide to Agricultural Meteorological Practices*, 2nd Edition, 1981		29.00
168 - *Guide to Hydrological Practices* -		
Vol. I *Data Acquisition and Processing*, 1981		38.00
Vol. II *Analysis, Forecasting and other Applications*, 1983		46.00
305 - *Guide on the Global Data-Processing System*, 1982		27.00
471 - *Guide to Marine Meteorological Services*, 2nd Edition, 1982		34.00
488 - *Guide on the Global Observing System*, 1977		47.00
623 - *Guide to the IGOSS Data-Processing and Services System*, 1983		7.00
634 - *Guidelines for Computerized Data Processing in Operational Hydrology and Land and Water Management*, 1985		34.00
636 - *Guide on the Automation of Data-Processing Centers*, 1985		25.00
Training Manuals		
240 - *Compendium of Training Facilities for Meteorology and Operational Hydrology*, 6th Edition, 1982		$64.00
258 - *Guidelines for Education and Training of Personnel in Meteorology and Operational Hydrology*, 3rd Edition, 1984		39.00
266 - *Compendium of Lecture Notes for Training Class IV Meteorological Personnel*		
Vol. I *Earth Science*, 1970		23.00
Vol. II *Meteorology*, 2nd Edition, 1984		47.00
364 - *Compendium of Meteorology for use by Class I and II Meteorological Personnel*		
Vol. I Part 1 *Dynamic Meteorology*, 1973		**
Part 2 *Physical Meteorology*, 1973		**
Part 3 *Synoptic Meteorology*, 1978		39.00
Vol. II Part 1 *General Hydrology*, 1977		13.00
Part 2 *Aeronautical Meteorology*, 1978		19.00
Part 3 *Marine Meteorology*, 1979		16.00
Part 4 *Tropical Meteorology*, 1979		40.00
Part 5 *Hydrometeorology*, 1985		19.00
Part 6 *Air Chemistry and Air Pollution Meteorology*, 1985		26.00
432 - *Proceedings of the WMO/IAMAP Symposium on Education and Training in Meteorology and Meteorological Aspects of Environmental Problems* (Caracas, February 1975); 1975		58.00
489 - *Compendium of Training Facilities in Environmental Problems Related to Meteorology and Operational Hydrology*, 1977		28.00
493 - *Proceedings of the Meeting on Education and Training in Meteorological Aspects of Atmospheric Pollution and Related Environmental Problems*, Research Triangle Park, U.S.A., January-February 1977; 1977		49.00

* In preparation
** Currently out of stock and unavailable from AMS or WMO

Training Manuals (continued)

593 - *Lecture Notes for Training Class IV Agricultural Meteorological Personnel*, 1982 — 19.00

622 - *Compendium of Lecture Notes on Meteorological Instruments for Training Class III and Class IV Meteorological Personnel*, 1986
- Vol. I Part 1 *Meteorological Instruments* — 39.00
- Part 2 *Meteorological Instrument Maintenance Workshops, Calibration Laboratories and Routines*
- Vol. II Part 3 *Basic Electronics for the Meteorologist* — 37.00

669 - *Workbook on Numerical Weather Prediction for the Tropics for the Training of Class I and Class II Meteorological Personnel, 1986* — 39.00

Operational Hydrology Reports

332 - *Manual for Estimation of Probable Maximum Precipitation*, O.H.R. 1; 1986 — 33.00
341 - *Benefit and Cost Analysis of Hydrological Forecasts. A State-of-the-Art Report*, O.H.R. 3; 1973 — 15.00
419 - *Meteorological and Hydrological Data Required in Planning and Development of Water Resources*, O.H.R. 5; 1975 — **
425 - *Hydrological Forecasting Practices*, O.H.R. 6; 1975 — 26.00
433 - *Hydrological Network Design and Information Transfer. Proceedings of the International Seminar, Newcastle upon Tyne, U.K., August 1974*, O.H.R. 8; 1976 — 36.00
461 - *Casebook of Examples of Organization and Operation of Hydrological Services*, O.H.R. 9; 1977 — 27.00
476 - *Hydrological Application of Atmospheric Vapour Flux Analyses*, O.H.R. 11; 1977 — 13.00
513 - *Applications of Remote Sensing to Hydrology*, O.H.R. 12; 1979 — 14.00
519 - *Manual on Stream Gauging* (2 Vol. set in one binder), O.H.R. 13; 1980 — 61.00
559 - *Hydrological Data Transmission*, O.H.R. 14; 1981 — 8.00
560 - *Selection of Distribution Types for Extremes of Precipitation*, O.H.R. 15; 1981 — 9.00
561 - *Measurement of River Sediments*, O.H.R. 16; 1981 — 10.00
576 - *Case Studies of National Hydrological Data Banks (Planning, Development and Organization)*, O.H.R. 17; 1981 — 15.00
577 - *Flash Flood Forecasting*, O.H.R. 18; 1981 — 9.00
580 - *Concepts and Techniques in Hydrological Network Design*, O.H.R. 19; 1982 — 9.00
587 - *Long-Range Water-Supply Forecasting*, O.H.R. 20; 1982 — 9.00
589 - *Methods of Correction for Systematic Error in Point Precipitation Measurement for Operational Use*, O.H.R. 21; 1982 — 14.00
635 - *Casebook on Operational Assessment of Areal Evaporation*, O.H.R. 22; 1985 — 23.00
646 - *Intercomparison of Models of Snowmelt Runoff*, O.H.R. 23; 1986 — 51.00
650 - *Level and Discharge Measurement Under Difficult Conditions*, O.H.R. 24; 1986 — 10.00
655 - *Tropical Hydrology*, O.H.R. 25; 1986 — *
658 - *Methods of Measurement and Estimation of Discharges at Hydraulic Structures*, O.H.R. 26; 1986 — 10.00

Reports on Marine Science Affairs

499 - *Meteorological Aspects of the Contributions Presented at the Joint Oceanographic Assembly (Edinburgh, September, 1976)*, M.S.A. 12; 1978 — $13.00
548 - *Satellite Data Requirements for Marine Meteorological Services*, M.S.A. 14; 1980 — 20.00
595 - *The Preparation and Use of Weather Maps by Mariners (update of T.N. 72)*, M.S.A. 15; 1982 — 15.00

Special Environment Reports

372 - *A Brief Survey of Meteorology as Related to the Biosphere*, S.E.R. 4; 1973 — $15.00
403 - *Drought (Lectures from 25th WMO Executive Committee)*, S.E.R 5; 1975 — 22.00
440 - *Determination of the Atmospheric Contribution of Petroleum Hydrocarbons to the Ocean*, S.E.R. 6; 1976 — 19.00
448 - *Weather, Climate and Human Settlements*, S.E.R. 7; 1976 — 15.00
455 - *The Quantitative Evaluation of the Risk of Disaster from Tropical Cyclones*, S.E.R. 8; 1976 — 55.00
459 - *An Evaluation of Climate and Water Resources for Development of Agriculture in the Sudano-Sahelian Zone of West Africa*, S.E.R. 9; 1976 — 48.00
460 - *Report and Proceedings of the WMO Air Pollution Measure Techniques Conference (APOMET), Gothenburg, October 1976*, S.E.R. 10; 1977 — $42.00
496 - *Systems of Evaluating and Predicting the Effects of Weather and Climate on Wildland Fires*, S.E.R. 11; 1978 — 13.00
504 - *Implementation Plan for the Determination of the Atmospheric Contribution of Petroleum Hydrocarbons to the Oceans*, S.E.R. 12; 1979 — 13.00
517 - *Meteorology and the Human Environment - Lectures Presented at the 29th Session of the WMO Executive Committee*, S.E.R. 13; 1979 — 9.00
563 - *Proceedings of the Symposium on the Development of Multi-Media Monitoring of Environmental Pollution (Riga 1978)*, S.E.R. 15; 1980 — 57.00
647 - *Lectures Presented at the WMO Technical Conference on Observation and Measurements of Atmospheric Contaminants (TECOMAC)*, S.E.R. 16; 1985 — 67.00

* In preparation
** Currently out of stock and unavailable from AMS or WMO

Technical Notes

391 - *Meteorology and the Colorado Potato Beetle*, T.N. 137; 1975 — $18.00
392 - *Drought and Agriculture*, T.N. 138; 1975 — 35.00
394 - *Upper-Air Sounding Studies*, T.N. 140; 1975 — 30.00
400 - *Utilization of Aircraft Meteorological Reports (Rev. of T.N. 80)*, T.N. 141; 1975 — 13.00
423 - *Rice and Weather*, T.N. 144; 1975 — 18.00
424 - *Economic Benefits of Climatological Services*, T.N. 145; 1975 — 18.00
426 - *Cost and Structure of Meteorological Services with Special Reference to the Problem of Developing Countries*, T.N. 146; 1975 — 21.00
431 - *Review of the Present Knowledge of Plant Injury by Air Pollution*, T.N. 147; 1976 — 15.00
436 - *Controlled Climate and Plant Research*, T.N. 148; 1976 — 15.00
438 - *Urban Climatology and its Relevance to Urban Design*, T.N. 149; 1976 — **
441 - *Application of Building Climatology to Problems of Housing and Building for Human Settlements*, T.N. 150; 1976 — 20.00
467 - *Radiation Regime of Inclined Surfaces*, T.N. 152; 1977 — 22.00
478 - *The Scientific Planning and Organization of Precipitation Enhancement Experiments, With Particular Attention to Agricultural Needs*, T.N. 154; 1977 — 14.00
482 - *Forecasting Techniques of Clear Air Turbulence Including that Associated with Mountain Waves*, T.N. 155; 1977 — 13.00
487 - *Techniques of Frost Prediction and Methods of Frost and Cold Protection*, T.N. 157; 1978 — 40.00
495 - *Handbook of Meteorological Forecasting for Soaring Flight*, T.N. 158; 1978 — 23.00
497 - *Weather and Parasitic Animal Disease*, T.N. 159; 1978 — 36.00
498 - *Soya Bean and Weather*, T.N. 160; 1978 — 24.00
507 - *The Application of Atmospheric Electricity Concepts and Methods to other Parts of Meteorology*, T.N. 162; 1978 — 25.00
530 - *The Planetary Boundary Layer*, T.N. 165; 1980 — 26.00
532 - *Meteorological Factors Affecting the Epidemiology of the Cotton Leaf Worm and Pink Bollworm*, T.N. 167; 1980 — 13.00
536 - *The Role of Agrometeorology in Agricultural Development and Investment Projects*, T.N. 168; 1980 — 14.00
550 - *Meteorological and Hydrological Aspects of Siting and Operation of Nuclear Power Plants*, T.N. 170
- *Vol. I Meteorological Aspects*, 1985 — 18.00
- *Vol. II Hydrological Aspects*, 1981 — 30.00

554 - *Fog and Reduced Visibility Due to Fog at Aerodromes*, T.N. 171; 1985 — *
557 - *Meteorological Aspects of the Utilization of Solar Radiation as an Energy Source + Annex: World Maps of Relative Global Radiation*, T.N. 172; 1981 — 58.00
566 - *The Effect of Meteorological Factors on Crop Yields and Methods of Forecasting the Yield*, T.N. 174; 1982 — 10.00
575 - *Meteorological Aspects of the Utilization of Wind as an Energy Source*, T.N. 175; 1981 — 41.00
583 - *Tropospheric Chemistry and Air Pollution*, T.N. 176; 1982 — 17.00
581 - *Review of Atmospheric Diffusion Models for Regulatory Applications*, T.N. 177; 1982 — 10.00
591 - *Meteorological Aspects of Certain Processes Affecting Soil Degradation - Especially Erosion*, T.N. 178; 1983 — 57.00
620 - *Weather-Based Mathematical Models for Estimating Development and Ripening of Crops*, T.N. 180; 1983 — 16.00
625 - *Use of Radar in Meteorology*, T.N. 181; 1985 — 30.00
629 - *Analysis of Data from International Experiments on Lucerne*, T.N. 182; 1985 — 21.00
630 - *Severe Convective Weather in Relation to Inflight Phase*, T.N. 183; 1985 — *
633 - *Land Use and Agro-System Management Under Severe Climatic Conditions*, T.N. 184; 1985 — 25.00
641 - *Meteorological Observations using NAVAID Methods*, T.N. 185; 1985 — 14.00

World Weather Watch Planning Reports

494 - *The Role of Satellites in WMO Programmes in the 1980's*, W.W.W. 36; 1977 — $45.00
528 - *World Weather Watch - WMO Tropical Cyclone Project - Sub Project No. 6 - Operational Techniques for Forecasting Tropical Cyclone Intensity and Movement*, 1979 — 45.00
535 - *World Weather Watch - The Plan and Implementation Programme 1980-1983*, 1979 — 29.00
553 - *Conversion of Grid-Point Data into Meteorological Maps with a Mini-Computer System*, W.W.W. 37; 1980 — 8.00
617 - *World Weather Watch - The Plan and Implementation Programme (1984-1987)* — 18.00

World Weather Watch Status Reports

601 - *World Weather Watch - 11th Status Report on Implementation*, 1982 — $30.00
639 - *World Weather Watch - 12th Status Report on Implementation*, 1984 — 30.00

General Reference Publications

2 - *Meteorological Services of the World*, 1985 — 64.00
47 - *International List of Selected, Supplementary and Auxilliary Ships*, 1985 — 55.00
174 - *Catalogue of Meteorological Data for Research*
- Part I *Published Synoptic and Climatological Data*, 1965 — 38.00
- Part II *Meteorological Stations with Observational Series Extending Over 80 Years or More*, 1970 — 25.00
- Part III *Meteorological Data Recorded on Media Usable by Automatic Data-Processing Machines*, 1972 — 57.00
- Part IV *Sources of Additional Data Needed for Research on Climatic Change*, 1979 — 20.00

* In preparation
** Currently out of stock and unavailable from AMS or WMO

General Reference Publications (continued)

259 - *WMO Sea-Ice Nomenclature*, 1970 (Vol I and III one binder)	34.00
Vol. I *Terminology and Codes*	
Vol. II *Illustrated Glossary* (out of print)	
Vol. III *International System of Sea Ice Symbols*	
634 - *Guidelines for Comprehensive Data-Processing in Operational Hydrology and Land Water Management*, 1985	34.00

Publications of General Interest

385 - *International Glossary of Hydrology*, 1974	$50.00
420 - *Proceedings of a WMO Technical Conference on Automated Meteorological Systems (TECAMS), Washington, D.C., February 1975*; 1975	67.00
463 - *Weather and Water*, 1977	6.00
477 - *Solar Energy. Proceedings of the WMO/UNESCO Symposium, Geneva, August–September 1976*; 1977	65.00
481 - *Proceedings of the Symposium on the Agrometeorology of the Maize (Corn) Crop, July 1976*; 1977	67.00
510 - *Papers Presented at the WMO Symposium on Boundary Layer Physics Applied to Specific Problems of Air Pollution (Norrkoping, June 1978)*; 1978	43.00
523 - *The Atmosphere Boundary Layer*, 1979	24.00
537 - *Proceedings of the World Climate Conference - A Conference of Experts on Climate and Mankind, Geneva, February 1979*; 1979	55.00
542 - *Climatic Changes and Their Effects on the Biosphere*, 1980	34.00
543 - *Man and Climatic Variability*, 1980	5.00
573 - *Typhoon Operational Experiment - A General Description (TOPEX Report No. 3)*, 1981	10.00
574 - *Sea-Ice Information Services in the World*, 1981	20.00
578 - *Proceedings of the Technical Conference on Climate - Asia and West Pacific (Guangzhou, China, 15–20 December 1980)*; 1981	36.00
582 - *Integrated Global Ocean Services Systems - General Plan and Implementation Programme 1982–1985*, 1982	9.00
585 - *Satellites in Meteorology, Oceanography and Hydrology*, 1982	8.00
596 - *Proceedings of the Technical Conference on Climate - Africa (Arusha, 25–30 January 1982)*; 1982	49.00
608 - *Twentieth Anniversary of the World Weather Watch - Opportunities and Outlook for Improved World Weather Watch*, 1983	14.00
613 - *Monsoons*, 1986	43.00
616 - *First WMO Long-Term Plan Part I: Overall Policy and Strategy (1984–1993)*; 1983	15.00
624 - *Meteorology Aids Food Production*, 1985	7.00
627 - *The Next Decade Meteorology and Operational Hydrology in the Service of Mankind - A Policy for Advancement*, 1985	8.00
632 - *Proceedings of the Climate Conference for Latin America and the Carribean 1983*, 1984	55.00
637 - *Meteorology and Public Safety*, 1985	7.00
643 - *Meteorology and Society*, 1985	**
652 - *Proceedings of the Technical Conference on Urban Climatology and Its Applications With Special Regard to Tropical Areas (Mexico D.F., 26–30 November 1984)*; 1986	53.00
653 - *Climate Variations, Drought and Desertification*, 1985	7.00
661 - *Report of the International Conference on the Assessment of the Role of Carbon Dioxide and of Other Greenhouse Gases in Climate Variations and Associated Impacts*, 1986	14.00
667 - *Meteorology - A Model of International Cooperation*, 1986	7.00

Commission, Congress, Executive, and Annual Reports

508 - *Resolutions of Congress and Executive Committee*, 1985	$45.00
547 - *8th World Meteorological Congress - Proceedings*, 1980	35.00
568 - *Scientific Lectures Presented at the 8th World Meteorological Congress, Geneva 1979*; 1981	15.00
590 - *Commission for Instruments and Methods of Observation - Abridged Final Report of the 8th Session (1981)*; 1982	24.00
598 - *Commission for Atmospheric Sciences - Abridged Final Report of the 8th Session*, 1982	29.00
599 - *WMO Executive Commission 34th Session - Abridged Report with Resolutions*, 1982	31.00
602 - *Commission for Aeronautical Meteorology - Abridged Final Report of the 7th Session*, 1982	29.00
603 - *Long-Range Transport of Sulphur in the Atmosphere and Acid Rain - Lectures Presented at the 33rd Session of the WMO Executive Committee*, 1983	$12.00
606 - *Consolidated Report on the Voluntary Co-operation Programme Including Projects Approved for Circulation in 1982–1983*; 1983	21.00
609 - *Annual Report of the World Meteorological Organization, 1982–83*; 1983	31.00
611 - *Commission for Basic Systems - Abridged Final Report of the 8th Session*, 1983	31.00
614 - *Scientific Lectures Presented at the 9th World Meteorological Congress, Geneva 1983*; 1985	14.00
615 - *Ninth World Meteorological Congress - Abridged Report with Resolutions*, 1983	39.00
619 - *WMO Executive Council 35th Session - Abridged Final Report with Resolutions*, 1983	29.00
628 - *Annual Report of the World Meteorological Organization (1983)*; 1984	31.00

* In preparation

** Currently out of stock and unavailable from AMS or WMO

Commission, Congress, Executive, and Annual Reports (continued)

638 - *Commission for Hydrology (CHY) - Abridged Final Report of the 7th Session*, 1985	30.00
640 - *Commission for Marine Meteorology (CMM) - Abridged Final Report of the 9th Session*, 1985	29.00
644 - *Annual Report of the World Meteorological Organization (1984)*; 1985	32.00
645 - *Ninth World Meteorological Congress - Proceedings*, 1985	35.00
648 - *WMO Executive Committee 36th Session - Abridged Final Report with Resolutions*, 1984	31.00
649 - *Scientific Lectures Presented at the 36th Session of the WMO Executive Committee*, 1984	12.00
651 - *Commission for Instrument and Methods of Observation - Abridged Final Report of the 9th Session (1982)*, 1986	30.00
656 - *Annual Report of the World Meteorological Organization (1985)*; 1986	33.00

Reports of Sessions of Regional Associations

524 - *Regional Association IV (North and Central America) - Hurricane Operational Plan*, 1985	$27.00
594 - *Regional Association III (South America) - Abridged Final Report of the 8th Session*, 1982	25.00
604 - *Regional Association V (South-West Pacific) - Abridged Final Report of the 8th Session (1982)*; 1983	30.00
605 - *Regional Association VI (Europe) - Abridged Final Report of the 8th Session (1982)*; 1983	31.00
607 - *Regional Association I (Africa) - Abridged Final Report of the 8th Session (1982)*; 1983	31.00
642 - *Regional Association II (Asia) - Abridged Final Report of the 8th Session (1982)*; 1983	33.00
657 - *Regional Association IV (North and Central America) - Abridged Final Report of the 9th Session (1985)*; 1986	28.00
666 - *Regional Association III (South America) - Abridged Final Report of 9th Session*, 1986	25.00

GARP Publication Series

International Conference on the Results of the Global Weather Experiment and Their Implications for The World Weather Watch, No. 26; 1986	
Volume I (limited supply available)	32.00
Volume II	31.00
Scientific Results of the Alpine Experiment (ALPEX), No. 27; 1986 (2 Volume Set)	64.00

GARP Special Reports

Report of the Seminar on Progress in Diagnostic Studies of the Global Atmospheric Circulation as a Result of the Global Weather Experiment (August 1984), No. 42; 1985	$35.00
Report of the Seminar on Progress in Numerical Modelling and the Understanding of Predictability as a Result of the Global Weather Experiment (October 1984), No. 43; 1985	37.00
Report of the Seminar on Progress in Tropical Meteorology as a Result of the Global Weather Experiment (October 1984), No. 44; 1985	51.00

* In preparation

** Currently out of stock and unavailable from AMS or WMO

MESOSCALE METEOROLOGY AND FORECASTING

Edited by PETER S. RAY

This volume provides a comprehensive survey of the important topics in mesoscale meteorology. It is designed to supplement a practicing meteorologist's experience with new material and ideas on mesoscale processes, and to acquaint the student meteorologist with the broad range of topics embraced by the classification "mesoscale" meteorology.

Illustrations, complete bibliographic references, and a comprehensive index are included. The text comprises contributions from 44 distinguished scientists in mesoscale meteorology. The 31 chapters are organized within these general headings:

INTRODUCTION

Kerry A. Emanuel
Glen Rasch
Daniel Smith
T.T. Fujita
Joseph T. Schaefer
Fred L. Zuckerberg

OBSERVING TECHNIQUES

Donald Burgess
Joseph H. Golden
Ronald D. McPherson
Peter S. Ray
Robert Serafin
Joseph Facundo
Vincent Lally
James F.W. Purdom
Roderick A. Scofield
Dennis W. Thomson

INTERNALLY GENERATED CIRCULATIONS

Robert W. Burpee
William H. Hooke
Douglas Lilly
Howard B. Bluestein
Charles F. Chappell
Daniel Keyser

MESOSCALE CONVECTIVE SYSTEMS

Diana L. Bartels
Kenneth W. Howard
Robert Maddox
Richard Rotunno
Carl Hane
Joseph B. Klemp
Dennis M. Rodgers
Morris L. Weisman

EXTERNALLY FORCED CIRCULATIONS

Joe F. Boatman
Roger A. Pielke
Roger F. Reinking
Moti Segal
Dale R. Durran
Raymond T. Pierrehumbert
Joseph T. Schaefer

MESOSCALE MODELING

Richard A. Anthes
John B. Hovermale
William R. Cotton
Donald J. Perkey

SHORT-RANGE FORECASTING TECHNIQUES

Charles A. Doswell
Bruce B. Ross
John McGinley
Thomas W. Schlatter

As a textbook of mesoscale meteorology, the volume will provide to the operational and practicing meteorologist, as well as student meteorologists, the principal new observations and theories in this interdisciplinary topic.

List price $45*
AMS Member/NOAA Employee $30*
Course Participant/Student $20*
*(Plus $3.75 shipping & handling)

Send order and remittance to:
AMERICAN METEOROLOGICAL SOCIETY
45 Beacon Street
Boston, MA 02108

WORLD METEOROLOGICAL ORGANIZATION

INTERNATIONAL CLOUD ATLAS

Volume II

The World Meteorological Organization, a specialized agency of the United Nations, is pleased to announce the forthcoming publication of new editions of the INTERNATIONAL CLOUD ATLAS (Vol. **II**) (English and French editions), the MARINE CLOUD ALBUM (English edition), and the CLOUD SHEET.

INTERNATIONAL CLOUD ATLAS - Volume II

English and French editions

196 pages of photographs, 161 of which are in colour, 29.7 × 21 cm, art paper, superb hardback cover.

Each photograph is accompanied by a concise yet detailed legend.

A must for college and school libraries, aviation and shipping (airline pilots, flying clubs, ships' masters, yachting enthusiasts), as well as agriculture, this Atlas, which is a complete reference book on clouds and meteors for professionals, will also fascinate all amateurs who wish to deepen their knowledge of clouds.

MARINE CLOUD ALBUM

38 colour pictures of cloud formations found at sea, 29.7 × 21 cm.

Of particular value to ships' officers and other professional marine cloud observers, the Album also provides an essential and stimulating source of information for all who have an interest in, and love of, the marine environment.

CLOUD SHEET

Poster 39 × 83 cm illustrating 38 different cloud formations.

Attractive educational document particularly suited for the class-room and places accessible to cloud observers, professional or amateur.

The above publications will be available in May 1987. **ORDER NOW!**

I wish to order the following WMO publications:

WMO-No.	*Title*	*No. of copies*	*List price (US$)*
407	*International cloud atlas, Volume II*	_____	*78.— (English edition)*
407	*Atlas international des nuages, Volume II*	_____	*78.— (French edition)*
–	*Marine cloud album*	_____	*20.— (in English)*
____	_____	_____	_____

+ $3.00 per book for handling: _____ _____

☐ check payable to the AMS;
☐ money order payable to the AMS;
☐ draft on a US bank, payable to the AMS (Canadian c
☐ international money order payable to the AMS (Cana

Total: ____

(*Residents of other countries than the USA and Canac orders to:* The Secretary-General, World Meteorologic P.O. Box No. 5, CH-1211 GENEVA 20, Switzerland.)

NAME AND ADDRESS (IN BLOCK LETTERS):

Name: _____

Address: _____

City: _____ Postal code: ____

Country: _____

Send order and remittance to:
AMERICAN METEOROLOGICAL SOCIETY
45 Beacon Street
Boston, MA 02108